The international journal of science / 16 January 2020

nature



BORDER CONTROL

Four rules for synthesizing nanocrystals with defined grain boundaries

Human screenome
Capture complexities of media use in a public project

Out on a limb
Leg protein helps mosquitoes to evade bed-net insecticides

Final stand
Last known occurrence of *Homo erectus* identified in Java

Vol. 577 | No. 7789
nature.com

The international journal of science / 16 January 2020

nature

Protect India's universities

The government and state authorities must step in and stop violent attacks on campuses.

For several weeks the world has watched as India's citizens — including academics and students — have taken to the streets. Tens of thousands have been gathering to read out the preamble to the Indian constitution, as a mark of protest against a discriminatory new citizenship law.

The law provides a path to citizenship for recent refugees from Afghanistan, Bangladesh and Pakistan. It is a means to providing permanent sanctuary for religious minorities fleeing hardship or persecution in these countries — an intention that is to be commended. What is troubling is that decisions on who can — and cannot — apply for citizenship will be made on the basis of religious belief. Muslims are to be excluded, which is a violation of the foundational principle that people of all faiths and none must be equal in law.

Tragically, some of the peaceful protests are being met with violence, and university campuses are not immune. The latest high-profile incident took place at Jawaharlal Nehru University (JNU) in New Delhi, where students have also been protesting over an increase in accommodation fees. On the evening of 5 January, people wearing masks and carrying iron rods, stones and wooden clubs entered the campus and launched an attack. The city's police failed to provide protection, according to the international advocacy organization Human Rights Watch.

Videos of bloodied and bruised students and staff have been widely shared. Surya Prakash, a student of Sanskrit texts who is visually impaired, was beaten in his room. And Sucharita Sen, a researcher at JNU's Centre for the Study of Regional Development, confirmed to *Nature* that she was hit on the head "with a stone the size of half a brick".

In mid-December, police entered two of India's older universities — Jamia Millia Islamia in New Delhi and Aligarh Muslim University in the neighbouring state of Uttar Pradesh. Students were beaten, property was damaged and tear gas used. Both institutions had to close temporarily, disrupting teaching and research. Jamia Millia's vice-chancellor, Najma Akhtar, said that it is not acceptable for police to harm innocent students.

The severity of the police action has rightly prompted a chorus of international concern. Among those speaking up are the Nobel prizewinners Abhijit Banerjee, an economist and JNU alumnus now at the Massachusetts Institute of Technology in Cambridge, and Venki Ramakrishnan, a biologist and the president of the Royal Society in London, who received his undergraduate education in India, and who is also critical of the new law.

Many of the government's supporters are upset that university students, academics and scientists are also opposing the new law. But they must know that freedom of expression is core to a university's mission; that the ability of citizens to protest peacefully against government policies is a right, not a privilege; and that the state should provide protection for such dissent. Without it, no opposition would be able to present its case to the public — as members of the current government and its supporters did in the years they were out of power.

> "Freedom of expression is core to a university's mission."



Academics in India and around the world are right to be alarmed and to speak up, because force has been used on university campuses, causing fear. India's authorities must take the necessary steps to protect their nation's universities and their people's freedom of speech.

They must heed the words of the prime minister's principal scientific adviser, Krishnaswamy VijayRaghavan, who said unequivocally: "Campuses are places for learning, discussion, collegial debate amongst diverse opinions, and research. There is no place at all for violence."

Solve hunger with systems thinking

Feeding the world involves tackling all aspects of the food system.

"What would the world be if there were no hunger?" It's a question that the late ecologist Donella Meadows would ask her students at Dartmouth College in Hanover, New Hampshire, back in the 1970s. They found it hard to answer, she later wrote, because imagining something that isn't part of real life — and learning how to make it real — is a rare skill. It is taught to artists, writers and engineers, but much less often to scientists. Meadows set out to change that, and helped to create a global movement. The result — an approach known as systems thinking — is now seen as essential in meeting big global challenges such as the Sustainable Development Goals.

Systems thinking is crucial to achieving targets such as zero hunger and better nutrition because it requires considering the way in which food is produced, processed, delivered and consumed, and looking at how those things intersect with human health, the environment, economics and society. Doing this is genuinely difficult, but it's not impossible if the barriers are known. Some of these obstacles — along with potential solutions — are explored this week in a series of articles in the first issue of *Nature Food*, one of three journals in the Nature Research portfolio (along with *Nature Cancer* and *Nature Reviews Earth & Environment*) to launch this month.

According to systems thinking, changing the food

© 2020 Springer Nature Limited. All rights reserved.

nature

system — or any other network — requires three things to happen. First, researchers need to identify all the players in that system; second, they must work out how they relate to each other; and third, they need to understand and quantify the impact of those relationships on each other and on those outside the system.

Take nutrition. In its latest report on global food security, the United Nations Food and Agriculture Organization says that the number of undernourished people in the world has been rising since 2015, despite great advances in nutrition science. For example, tracking of 150 biochemicals in food by the US Department of Agriculture and various databases has been important in revealing the relationships between calories, sugar, fat, vitamins and the occurrence of common diseases. But using machine learning and artificial intelligence, network scientist Albert László Barabási at Northeastern University in Boston, Massachusetts, and his colleagues propose that human diets consist of at least 26,000 biochemicals — and that the vast majority are not known (*Nature Food* **1**, 33–37; 2020). This shows that we have some way to travel before achieving the first objective of systems thinking — which, in this example, is to identify more components of the nutrition system.

A systems approach to creating change is also built on the assumption that everyone in the system has equal power and status — or agency, to use the academic term. But as health-equity researcher Sharon Friel at the Australian National University in Canberra and her colleagues show, the food system is not an equal one, and the power of world trade can override environmental and nutritional needs (S. Friel *et al. Nature Food* **1**, 51–58; 2020). Countries need to pass relevant laws and regulations to meet global goals for nutrition and climate change. But this becomes difficult because the global trade rules set by the World Trade Organization (WTO) are legally binding on countries, whereas policies on climate change or nutrition are often not.

The need for a global counterweight to the WTO has led to calls for a World Environmental Organization (see, for example, go.nature.com/2th18yc). Another way to redress such power imbalances is for more universities to do what Meadows did and teach students how to think using a systems approach.

A team of researchers has done just that, through the Interdisciplinary Food Systems Teaching and Learning programme (J. Ingram *et al. Nature Food* **1**, 9–10; 2020). Students from disciplines including agriculture, ecology and economics learn together by drawing on their collective expertise in tackling real-world problems, such as how to reduce food waste. Since its launch in 2015, the programme has trained more than 1,500 students from 45 university departments.

More researchers, policymakers and representatives from the food industry must learn to look beyond their direct lines of responsibility and embrace a systems approach, as the editors of *Nature Food* advocate in their launch editorial (*Nature Food* **1**, 1; 2020). Meadows knew that visions alone don't produce results, but concluded that "we'll never produce results that we can't envision".

> **"The food system is not an equal one."**

The life of archaea

Cultivation of Asgard archaea brings us closer to understanding how complex life evolved.

Hilaire Belloc's 'The Microbe' opens with the words:

> The microbe is so very small,
> You cannot make him out at all.

The poem lists the wonders of microorganisms, and they continue to reveal their secrets to researchers more than a century after his book *The Bad Child's Book of Beasts* (1896) excited and delighted children.

In 2015, researchers published the metagenome of a member of the Asgard group of archaea called Lokiarchaeota (A. Spang *et al. Nature* **521**, 173–179; 2015). These are descended from an ancient lineage of archaea, simple cells lacking a nucleus and distinct from bacteria. This discovery was exciting because the genes were found to have similarities with those of eukaryotes — the group of organisms whose cells have nuclei and other structures, and which include plants, fungi, humans and other animals. That suggested a stronger connection between archaea and eukaryotes than had previously been thought.

Now, after a heroic effort that took 12 years, researchers led by Hiroyuki Imachi, a microbiologist at the Japan Agency for Marine-Earth Science and Technology, Yokosuka, have successfully grown a new Asgard lineage (H. Imachi *et al. Nature* https://doi.org/10.1038/s41586-019-1916-6; 2020). This achievement puts to rest concerns that the genes sequenced in 2015 were the result of contamination, or the initial sample being a mix of cells.

Imachi and his colleagues grew cells from sediment that had been collected below the sea bed. But why did the cells take so long to grow? The problem in culturing cells from sediment is that most microbes aren't as obliging as familiar lab workhorses such as *Escherichia coli*. The researchers took up the challenge and with much patience, trial and error, they found that the cells grew best on a diet of peptides, amino acids and even baby-milk powder.

The resulting cells are tiny spheres 300–750 nanometres in diameter, but they often extrude longer, branched filaments that reach out to meet neighbouring bacteria. The researchers think that such a partnership, both biochemical and physical, could tell us more about the processes that led to the eukaryote cell being formed — a question more researchers must surely try to tackle.

Despite the promise of what is to come, a degree of caution is needed. Eukaryotes evolved more than two billion years ago, possibly coincident with an episode of global climatic change called the Great Oxidation Event. Nonetheless, the achievement brings us closer to meeting living relatives of our ancestors. We await the next chapter with anticipation.

© 2020 Springer Nature Limited. All rights reserved.

World view



By Hetan Shah

Global problems need social science

Without human insights, data and the hard sciences will not meet the challenges of the next decade, says Hetan Shah.

At the beginning of the year, Dominic Cummings, a senior adviser to the UK government, posted an unusual advert on his blog, calling for data scientists, mathematicians and physicists to join him at the heart of government. As outgoing director of the Royal Statistical Society in London and soon-to-be chief executive of the British Academy, I support the sentiment behind the call: data do have huge power to inform government policy.

But I worry about the fact that the call prioritized science and technology over the humanities and social sciences. Governments must make sure they also tap into that expertise, or they will fail to tackle the challenges of this decade.

For example, we cannot improve global health if we take only a narrow medical view. Epidemics are social as well as biological phenomena. Anthropologists such as Melissa Leach at the University of Sussex in Brighton, UK, played an important part in curbing the West African Ebola epidemic with proposals to substitute risky burial rituals with safer ones, rather than trying to eliminate such rituals altogether.

Treatments for mental health have made insufficient progress. Advances will depend, in part, on a better understanding of how social context influences whether treatment succeeds. Similar arguments apply to the problem of antimicrobial resistance and antibiotic overuse.

Environmental issues are not just technical challenges that can be solved with a new invention. To tackle climate change we will need insight from psychology and sociology. Scientific and technological innovations are necessary, but enabling them to make an impact requires an understanding of how people adapt and change their behaviour. That will probably require new narratives — the purview of rhetoric, literature, philosophy and even theology.

Poverty and inequality call even more obviously for expertise beyond science and maths. The UK Economic and Social Research Council has recognized that poor productivity in the country is a big problem, and is investing up to £32.4 million (US$42 million) in a new Productivity Institute in an effort understand the causes and potential remedies.

Policy that touches on national and geographical identity also needs scholarly input. What is the rise of 'Englishness'? How do we live together in a community of diverse races and religions? How is migration understood and experienced? These intangibles have real-world consequences, as demonstrated by the Brexit vote and ongoing discussions about whether the United Kingdom has a future as a united kingdom. It will take the work of historians, social psychologists and political scientists to help shed light on these questions. I could go on: fighting against misinformation; devising ethical frameworks for artificial intelligence. These are issues that cannot be tackled with better science alone.

> "These are issues that cannot be tackled with better science alone."

Consider how life-enhancing — and even life-saving — technologies have failed to be taken up. 'Vaccine hesitancy' is more a social phenomenon than a technical one, and the main cause of measles resurgence. Solutions depend not on medical breakthroughs, but on insight from anthropologists such as Heidi Larson at the London School of Hygiene & Tropical Medicine, who have done much to understand people's decisions about whether to vaccinate themselves and their children.

In diverse cases, social factors — cultural norms, educational understanding, kin and social networks, power dynamics, or simply the layout of a building — must be accounted for before policy can succeed. Blind faith in data science without an understanding of what data are missing, or how algorithms can exacerbate existing biases, can lead to policy failure.

A good example of the incorporation of appropriate expertise is the UK government's Behavioural Insights Team, which has run more than 750 projects around the world, in particular randomized control trials of policy interventions. Work on the treatment of tuberculosis in Moldova brought the rate of adherence to daily medical regimes up from 44% to 84%.

Downing Street is right to look for data scientists, but must not overlook the benefits brought by the humanities and social science. This expertise is embedded in existing staff and structures and should not be overlooked. There are many successes, from the creation of the 'nudge units' to the use of social-science expert panels. Detailed policy histories — compiled by agencies such as the British Academy and the UK Institute for Government — can provide surprising and valuable insights.

More could be done to connect the policy community with external social science and humanities expertise. Chile's innovation-focused Government Laboratory, the Bridging the Gap programme in Washington DC, and the Centre for Science and Policy in Cambridge, UK, have all used a variety of mechanisms — among them workshops, funding schemes and policy fellowships — to bring expert voices into the policymaking process.

In a democracy, expert advice must be balanced with considerations such as public opinion, financial costs and political demands. Still, without the humanities and social sciences, hard science and technology can do little to resolve complex societal challenges. Wise governments will find ways to incorporate that insight.

Hetan Shah is the incoming chief executive of the British Academy in London.
e-mail: h.shah@thebritishacademy.ac.uk
Twitter @HetanShah

CLIVE SHERLOCK

© 2020 Springer Nature Limited. All rights reserved.

News in brief

PREDATORY-JOURNAL PAPERS HAVE LITTLE SCIENTIFIC IMPACT

Papers published in 'predatory' journals attract little attention from scientists, and get cited much less than those in reputable publications, an analysis shows.

Predatory journals charge authors high article-processing fees, but don't provide expected publishing services, such as peer review. Researchers have long voiced fears that these practices could be harming research by flooding the literature with poor-quality studies.

But the authors of the 21 December analysis say their findings suggest papers in predatory journals have a "very limited readership among academics" (B.-C. Björk *et al.* Preprint at https://arxiv.org/abs/1912.10228; 2019).

The researchers picked 250 predatory journals from more than 10,000 titles on a list of such publications curated by Cabells, a publishing analytics company in Beaumont, Texas. They then selected one paper published in 2014 from each of the 250 journals. Using the Google Scholar search engine, they manually checked how many times each paper had been cited since its publication.

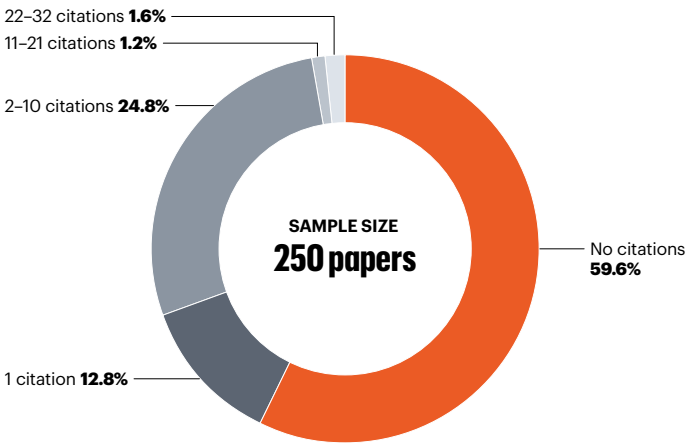
Around 60% of the papers hadn't attracted any citations at all, and 38% were cited up to 10 times. Less than 3% of the papers attracted more than 10 citations, and none got more than 32 citations (see 'Limited readership').

The lack of citations could indicate that the harm predatory-journal articles cause might have been exaggerated, says Bo-Christer Björk, an information-systems scientist at the Hanken School of Economics in Helsinki who co-authored the study. "If people don't cite, they probably don't read those articles," he says.

The results aren't surprising — not many academics thought predatory-journal papers were highly cited, says Matt Hodgkinson, head of research integrity at the open-access publisher Hindawi in London. But he argues that predatory journals still pose a threat to science and to scholarly publishing in several ways. They trick researchers and institutions out of payments, refuse to reject flawed papers and tarnish the reputation of legitimate open-access journals, he says.

LIMITED READERSHIP

Papers published in predatory journals five years ago have attracted few or no citations.





ANIMAL-CLONING SCIENTIST GETS PRISON SENTENCE

Leading animal-cloning researcher Li Ning has been sentenced to 12 years in prison in China for allegedly embezzling research funding.

Li's team famously engineered cows to produce milk containing a human milk protein (B. Yang *et al. PLoS ONE* **6**, e17593; 2011).

On 3 January, a court in Jilin Province found that Li, formerly a researcher at the China Agricultural University in Beijing and a member of the Chinese Academy of Engineering (CAE), had stolen 34.1 million yuan (US$4.9 million) in research grants, and invested the money in his own companies, according to Xinhua, China's state news agency. His former assistant, Zhang Lei, received a sentence of more than 5 years for allegedly helping.

Zhang admitted to the charges, according to Xinhua. But Li denied stealing the money, and said that he had invested unused grant funding with the intention of using it for future research, according to the Chinese newspaper *Economic Observer*.

Li's lawyer did not respond to a request for comment. Some Chinese media reported that Li is likely to appeal.

In 2018, 15 members of the CAE and the Chinese Academy of Sciences urged the president of China's supreme court to finalize Li's case and praised his research achievements.

EARTH-SIZED EXOPLANET SPIED IN 'HABITABLE ZONE'

Astronomers have discovered a world only a little bit bigger than Earth, whirling around a bright star about 31 parsecs from our planet. The world, known as TOI 700 d, orbits in its star's 'habitable zone' — the region in which liquid water could exist. Astronomers know of only a handful of such worlds.

"We don't have that many Earth-sized planets in the habitable zone," says Elisa Quintana, an astronomer at NASA's Goddard Space Flight Center in Greenbelt, Maryland. "Having one around a nearby bright star is exciting," she adds, because it is easier to study planets around nearby stars than around distant ones.

Emily Gilbert, an astronomer at the University of Chicago in Illinois, and her colleagues discovered the planet (depicted below) using NASA's Transiting Exoplanet Survey Satellite (TESS). It is the first Earth-sized planet discovered by TESS that lies in its star's habitable zone. Gilbert reported the discovery on 6 January at a meeting of the American Astronomical Society in Honolulu, Hawaii.

TESS, which launched in 2018, sweeps the night sky, looking for stars that periodically dim as an orbiting planet passes in front of them. It has found more than 1,500 planet candidates using this method.



L TO R: SOURCE: B.-C. BJÖRK *ET AL.* PREPRINT AT HTTPS://ARXIV.ORG/ABS/1912.10228 (2019); ALAMY: NASA/GODDARD SPACE FLIGHT CENTER; ANDY WONG/AP/SHUTTERSTOCK

© 2020 Springer Nature Limited. All rights reserved.

Nature Briefing

Sign up to get essential science news, opinion and analysis delivered to your inbox daily. Visit go.nature.com/newsletter



Chinese respiratory illness claims first life

Researchers have identified a new virus as the cause of a respiratory illness that has affected dozens of people in China, one of whom has died. One case of the virus has also been detected outside China, in Thailand.

The pneumonia-like illness surfaced last December, mostly in people who worked at or regularly visited a live-animal and seafood market in the city of Wuhan, China.

On 9 January, Chinese state media reported that scientists had sequenced the genome of the culprit: a previously unknown member of the coronavirus family, which also includes the virus that causes the highly contagious severe acute respiratory syndrome (SARS) that killed hundreds of people in China in 2002–03. China has now publicly shared the virus's genetic sequence.

Forty-one people have been confirmed as being infected with the virus. The World Health Organization (WHO) says that the infected person in Thailand had travelled there from Wuhan. Authorities in Hong Kong and South Korea have been screening travellers (see picture) who have recently been to Wuhan.

There is no clear evidence of human-to-human transmission, the WHO says. Scientists suspect that an animal is passing the virus to people.

MIT RELEASES REPORT ON EPSTEIN DONATIONS

Sex offender and alleged sex trafficker Jeffrey Epstein donated US$850,000 to the Massachusetts Institute of Technology (MIT) in Cambridge between 2002 and 2017, and visited the prominent US university at least nine times.

Those are the findings of an investigation conducted by law firm Goodwin Procter on the university's behalf. MIT released the report on 10 January.

MIT president Rafael Reif did not know that the university was accepting money from Epstein while it was taking place, the report found, but three senior administrators drew up an "informal framework" in 2013 to accept money from Epstein. "No Senior Team member violated any law, breached any MIT policy, or acted in pursuit of personal gain in connection with Epstein's donations," the report says.

In 2008, Epstein pleaded guilty in Florida to two felony charges of soliciting a minor for prostitution and served more than a year in prison. He died by suicide in August while awaiting trial on federal charges of trafficking under-age girls.

The bulk of Epstein's donations to MIT occurred after his guilty plea. The report found that former director of the MIT Media Lab Joi Ito and mechanical-engineering professor Seth Lloyd were key to maintaining the relationship with Epstein.

Lloyd received $225,000 in research funds and $60,000 as a personal gift. He "purposefully failed to inform MIT" that Epstein was funding his work, the report said. MIT has placed Lloyd on paid administrative leave. "Just heard myself and so can't comment right now," Lloyd said. Ito did not respond to a request for comment.

© 2020 Springer Nature Limited. All rights reserved.

News in focus



DAVE CHAN/GETTY

Residents of Ottawa held a vigil for people killed when a Ukraine International Airlines jet crashed in Iran.

CANADIAN UNIVERSITIES MOURN RESEARCHERS WHO DIED IN IRAN PLANE CRASH

Victims include two computer scientists returning from their wedding in Iran and a student about to begin his PhD.

By Nidhi Subbaraman

Canadian universities are mourning more than two dozen faculty members and students who died when Ukraine International Airlines flight PS752 crashed in Iran on 8 January.

One hundred and seventy-six people were killed when the Boeing 737-800 crashed shortly after take-off from Tehran. At least 57 victims were Canadian, and, according to the country's prime minister, Justin Trudeau, 138 people on the flight were en route to Canada.

"What happened yesterday was a tragedy, a tragedy that shocked not only Canada but the world," Trudeau said at a news conference on 9 January, calling for a "thorough investigation" into the causes of the crash. Initial reports from the United States and Canada pointed to an Iranian surface-to-air missile.

On 11 January, Iran's military announced that it had unintentionally shot down the plane. "The Islamic Republic of Iran deeply regrets this disastrous mistake," Iran's President Hassan Rouhani said on Twitter.

Across Canada, universities lowered flags to half mast and planned gatherings to honour the dead. "I want to express my heartfelt grief. Words simply cannot express the loss I know we all are feeling," David Turpin, president and vice-chancellor at the University of Alberta in Edmonton, wrote on 8 January. About 50 people attended a vigil at the Alberta Legislature Building on 8 January, lighting candles and placing photos on the steps, the Canadian Broadcasting Corporation reported.

University of Alberta engineers Pedram Mousavi and Mojgan Daneshmand and their two young daughters were among those who died. "They were big deals," says James Hogan, a materials engineer at Alberta.

© 2020 Springer Nature Limited. All rights reserved.

Hogan lost a graduate student, Amir Saeedinia, who was travelling from Iran to begin his PhD in Hogan's lab. "He worked very hard to create this opportunity for himself. This was just a start for him in Canada – he was coming to join the group today."

On 9 January, the university identified seven other community members who were listed as passengers. They include Arash Pourzarabi and Pouneh Gorji, graduate students in computer science who were returning to Canada after their wedding in Iran. Turpin said that university flags would be lowered to half mast to remember the victims, and a memorial service would be held.

'We are all heartbroken'

Peyman Servati, an electrical engineer at the University of British Columbia in Vancouver, said on Twitter that he was "so so devastated" by the deaths of Mousavi, Daneshmand and their daughters – his "smart and kind friends".

The University of Toronto announced that flags at its three campuses would fly at half mast in memory of at least six students who were expected to have been on the plane. "We are all heartbroken," university president Meric Gertler said in a statement.

At least five University of Windsor community members were also listed as passengers, the Ontario university said in a statement. They included Hamidreza Setareh Kokab, who had begun studying for a PhD in mechanical engineering last January in Jill Urbanic's lab. "He would have been successful in both academia and industry. We lost a bright light," says Urbanic. Kokab's wife Samira Bashiri, a biology research assistant, also died on the flight.

At Western University in London, Ontario, about 250 people gathered on 8 January to remember 4 students who were killed in the crash. And the University of Waterloo confirmed that two of its students had died.

Flags at the University of Guelph were lowered to mourn for two university graduate students: Ghanimat Azhdari of the Department of Geography, Environment and Geomatics, and Milad Ghasemi Ariani of the Department of Marketing and Consumer Studies.

"Milad had just started his PhD with us in the fall, so much hope, gone," said Statia Elliot, a marketing academic at the University of Guelph, on Twitter. "My heart goes out to family and friends."

Faisal Moola, an ecologist at the University of Guelph, said that it had been an "awful 48 hours for our students and faculty". "Ghanimat was such a proud member of the Qashqai Indigenous tribe in Iran and spoke with such love for her people and her ancestral territories," he wrote on Facebook. "She was a powerful and passionate young leader in defence of Indigenous Peoples across the planet and her life's work continues."



SIGRID GOMBERT/CULTURA/SPL

Chinese scientists are encouraged to study abroad and then return home.

CHINESE ACADEMICS WHO WORK ABROAD ARE SLOWER TO WIN HONOUR

Local networks help to speed researchers to highly prestigious Changjiang scholarship.

By Hepeng Jia

Does working in a foreign country enhance the career of a Chinese scientist? For years, China has been encouraging researchers to study abroad and then bring their expertise home. But a study finds that returnees take longer than peers who remained in China to win one of the country's highest scientific honours.

Of the roughly 1,500 Chinese nationals awarded a Changjiang scholarship in the sciences between 1999 and 2015, those who received a PhD from a foreign university had held their doctorate for 25% longer – about an extra 2.3 years – when they won the scholarship than those who earnt their PhD in China. That's the finding of a study led by Tang Li, a public-policy researcher at Fudan University in Shanghai, China.

The prestigious Changjiang scholarship is awarded by the Chinese Ministry of Education. It comes with a yearly stipend of 200,000 yuan (US$29,000) and is seen as more important than a salary or even individual professorships in terms of conferring respect among peers and indicating scientific achievement.

International mobility has been shown to boost scientists' skills and networks and, once academics return to their homelands, to increase the country's international expertise and exposure to global research practices. Institutions need to better recognize the benefits of international training and reward it, Tang says. But the results of the study, published last year, suggest that the advantages of overseas training might not be well recognized (F. Li and L. Tang *Sci. Public Policy* **46**, 518–529; 2019). The researchers also report that local connections help academics obtain the honour faster, and that this could explain why returnees are at a disadvantage.

The results of the study suggest that the advantages of overseas training might not be well recognized.

Over the past decade, numerous national recruitment programmes have attracted Chinese-born academics back to the country from foreign institutions, often with promises of higher salaries and research funding. The best known, the Thousand Talents Plan, has come under scrutiny in the United States in the past year for potentially being a threat to US research and intellectual property. Academics returning to China from leading international

© 2020 Springer Nature Limited. All rights reserved.

universities are promised relocation packages of up to one million yuan, as well as top salaries and millions in research grants. To learn more about the impact of working abroad, Tang and her colleague Li Feng at Hohai University in Nanjing, China, decided to review the career trajectories of 1,447 Changjiang scholars. About one-third held PhDs from overseas universities, and about half had short-term overseas experience.

The average time between graduating with a PhD and becoming a Changjiang scholar is 10.3 years, Tang and Feng report. But it took researchers with any type of overseas experience longer to receive the honour than it took those with no international experience. Even Chinese scholars who left the country temporarily to be visiting scholars at international institutions waited 12% longer (about a year extra) for the title than did peers who remained in China.

The researchers controlled for factors that could influence the timing of the award, such as gender, research field, where academics trained overseas and the status of the academic's university when they received the award.

In the second part of the study, the researchers examined the Changjiang scholars' networks. They found that academics with strong local connections — measured as having obtained a bachelor's degree and PhD at the same institution in which they work — were faster to obtain the title. Scholars working at their alma mater received the honour, on average, about 2 to 8 months faster than did those working at a different university.

Tang suggests that because award recipients are nominated by their university, researchers who have spent their academic career in China might be more likely to be nominated — and more familiar to the reviewers — than are academics who have been out of China for years.

Dong Jielin, a guest researcher in science policy at Tsinghua University in Beijing, says that the results support the belief among some that China has an unhealthy academic environment that rewards personal connections over skills and experience. Efforts to reform this culture are needed, she says.

But Cao Cong, a science-policy researcher at the University of Nottingham Ningbo China, has another theory. He suggests that in the past, researchers with overseas training might have been slower to obtain the award because they were not as academically competitive as the best locally trained scientists. Before programmes such as Thousand Talents, many overseas-trained PhD graduates preferred to apply for foreign faculty positions, and so academics who returned to China might have done so because they couldn't secure an overseas position, he says.

Cao suggests that a future study should examine overseas-trained scientists who have returned more recently, to see whether the study's conclusion still holds.

SPACEX TESTS BLACK SATELLITE TO REDUCE REFLECTIVITY

'DarkSat' prototype could help to address 'megaconstellation' threat to astronomy.

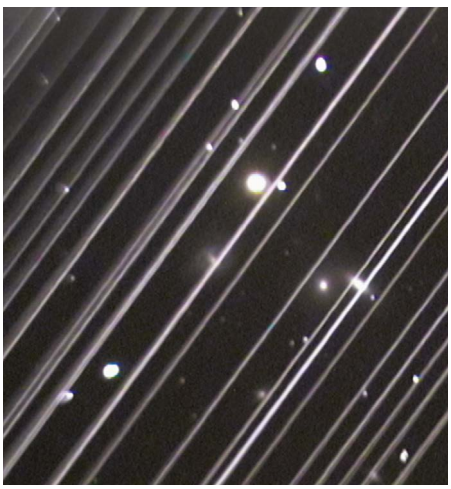
By Alexandra Witze in Honolulu, Hawaii

The SpaceX company launched 60 of its Starlink broadband Internet satellites into orbit on 6 January — including one, called DarkSat, that is partially painted black. The probe is testing one strategy to reduce the brightness of satellite 'megaconstellations', which scientists fear could interfere with astronomical observations.

Various companies plan to launch thousands of Internet satellites in the coming years; SpaceX, of Hawthorne, California, aims to launch 24 batches of Starlinks this year. By the mid-2020s, thousands to tens of thousands of new satellites could be soaring overhead. Bright streaks caused by light reflecting off them could degrade astronomical images.

"I was complaining to my wife that I can't sleep very well these days because of this," says Tony Tyson, a physicist at the University of California, Davis, and chief scientist of the Vera C. Rubin Observatory, a major US telescope under construction in Chile.

Astronomers discussed the potential impact of the satellites on various telescopes, and what could be done about the problem, on 8 January at a meeting of the American Astronomical Society in Honolulu, Hawaii. "2020 is the window to figure out what makes a difference in reducing the impact," says Jeffrey Hall, director of Lowell Observatory in Flagstaff, Arizona, and chair of the society's committee on light pollution.



VICTORIA GIRGIS/LOWELL OBSERVATORY

The diagonal lines in this image show light reflected from SpaceX's Starlink satellites.

"SpaceX is absolutely committed to finding a way forward so our Starlink project doesn't impede the value of the research you all are undertaking," Patricia Cooper, SpaceX's vice-president for satellite government affairs, told a session at the astronomy meeting.

Three batches of Starlinks have been launched, totalling about 180 satellites so far. They are most obvious in the night sky immediately after launch, before they boost their orbits to higher altitudes where they are farther away and look dimmer. It's not yet clear how significant a problem Starlinks will be for astronomy, although scientists have complained about trails in their images.

Many astronomers panicked in June, soon after SpaceX launched the first batch of 60 Starlinks and telescopes began photographing their trails. Their brightness came as a surprise, says Patrick Seitzer, an astronomer at the University of Michigan in Ann Arbor. "The new megaconstellations coming online have the potential to be brighter than 99% of everything else in Earth orbit, and that's where the concern comes from," he says.

Several factors contribute to the puzzling brightness, astronomers reported at the meeting. SpaceX says the position of the solar panels might have something to do with it: at lower elevations, before the orbit boost, the satellites' panels are positioned like an open book to reduce drag. That temporary orientation could make them reflect more sunlight. The speed at which a satellite moves across a telescope's field of view is also important — the more slowly it moves, the more brightness accumulates per pixel of imagery.

There are no regulations that control how bright or dim a satellite needs to be, notes Ralph Gaume, director of the astronomical-sciences division of the US National Science Foundation in Alexandria, Virginia.

Calculations suggest that the Starlink trails will interfere with astronomy most significantly during the hours surrounding twilight and dawn. That's a particular problem for observations that need to be made during twilight, such as searches for some near-Earth asteroids. And on short summer nights, the satellite trails could be visible all night long.

© 2020 Springer Nature Limited. All rights reserved.

Q&A



TESS FLYNN/LA TROBE UNIVERSITY

Ecologist Michael Clarke describes Australian wildfires' devastating aftermath

Australia is in the grip of its worst wildfire season on record. The human death toll stands at 28, and thousands of homes have been destroyed across more than 10 million hectares of land — an area larger than Portugal. An estimated 1 billion wild mammals, birds and reptiles have perished. Michael Clarke, an ecologist at La Trobe University in Bundoora, Melbourne, has been studying the effect of fires on native ecosystems — and how they recover — ever since a fire tore through his field site 15 years ago. Clarke spoke to *Nature* about how animals fare in the wake of wildfires, and why this season's fires could prove particularly devastating.

What happens in the aftermath of a wildfire?
It is deathly silent when you go into a forest after a fire. Apart from the undertakers — the carrion eaters like currawongs, ravens and shrike-thrushes — picking off the dead bodies, there's nothing much left in the forest. It's a chilling experience.

Any animal that manages to make it through the fire uninjured faces three major challenges. One is finding shelter from climatic extremes, the second is the risk of starvation. And third, they've got to avoid predators. They're exposed; there's nowhere to hide in a barren landscape.

Even if an animal makes it to an unburnt patch, the density of organisms trying to eke out a living will be way beyond the area's carrying capacity. After fires in 2007, one unburnt patch I visited in the Mallee [a region in the far north of Victoria] was literally crawling with birds, all chasing one another, trying to work out who owned the last bit of turf. It was insufficient to sustain them all.

Which animals are likely to be most affected?
Animals like koalas that live above ground in small, isolated populations and have a limited capacity to flee are in all sorts of trouble. During past fires, we've seen some really surprising creative behaviours, like lyrebirds and wallabies going down wombat burrows to escape fire. But a large majority of animals are simply incinerated. Even really big, fast-flying birds like falcons and crimson rosellas can succumb to fire.

How are this season's fires different from those in previous years?
The scale is unprecedented: such synchronous loss of vast areas of habitat. The ferocity of the fires, which can create their own weather, means the wildlife is at a loss to respond.



WOLTER PEETERS/*THE SYDNEY MORNING HERALD*/GETTY

Animals that survive the fires, like this wombat pictured in New South Wales, will struggle to find food and shelter.

The fires are also burning differently to how they have in the past. Previously, you could rely on wet gullies acting as natural barriers to the spread of a fire. This year, with the dryness, the fires are just going straight through gullies and rainforest pockets that would otherwise be places where animals could take refuge afterwards.

How long will it take for ecosystems to recover?
Recovery will probably be slower than for previous fires. Re-vegetation depends on rainfall, and that's become so unpredictable. Tree hollows and nectar-producing trees, key resources for animals, take years or decades to recover.

One concern is the future of several migratory bird species that fly between Tasmania, Victoria and southern Queensland. They make pit stops on the coastal heathlands along the east coast, precisely where a lot of these fires have been happening. It'll be years before those habitats are back in production as stop-over points for migratory birds.

Other animals are being pushed closer to extinction. There are real concerns for the brush-tailed rock wallaby, and the Kangaroo Island dunnart — a small marsupial — which has lost nearly all of its habitat.

What does the future hold for these ecosystems?
The challenge will be to work out how to protect the pockets of forest habitat that are left. We may need to be proactive and carry out controlled burns near areas that become wildlife refuges during fires to keep future fires out. That doesn't sit well with me, but it may be the new normal that we're facing.

These fires are unprecedented but not unexpected. Thirty years ago, scientists predicted that there would be more severe fires due to climate change. We are seeing three big changes: increased frequency of fire, increased severity, and increased extent of these blazes. That triple whammy reduces fauna's capacity to recover.

Interview by Dyani Lewis
This interview has been edited for length and clarity.

© 2020 Springer Nature Limited. All rights reserved.



MUJAHID SAFODIEN/AFP/GETTY

An existing 64-dish array in South Africa is set to become part of the Square Kilometre Array.

WORLD'S LARGEST RADIO TELESCOPE NEEDS TO HIT US$1-BILLION TARGET

Countries won't say how much they have pledged to the Square Kilometre Array in Australia and South Africa.

By Sarah Wild

An independent panel of reviewers has approved the design of what will be the world's largest telescope — the Square Kilometre Array (SKA). But the final design and construction timetable depend on whether the SKA collaboration can raise its first €940 million (US$1 billion).

The amount that countries have already committed to the SKA is confidential, but it is understood to be less than is needed for construction to begin on schedule in 2021. When asked, SKA director-general Philip Diamond would not say how much money the project expects to have in the bank when building starts, but SKA officials say that pledges must be confirmed by the middle of 2020.

The design was agreed by the review panel last month. "We are aggressively seeking the full funding commitment," Diamond says. But he adds that if sufficient funds are not pledged in time, the collaboration will turn to a scaled-back design costing €691 million. This design has reduced computing power, and its dishes and antennas are squeezed closer together.

If the full plan is achieved, the SKA will be able to create images 50 times more detailed than those produced by current instruments, such as the Hubble Space Telescope, and will shed light on some of the most enigmatic problems in astronomy and science, such as the nature of dark matter and how galaxies form.

The gigantic telescope will be able to detect signals from the 'epoch of reionization', when the first stars and galaxies began to give off light, says Francisco Colomer, director of the Joint Institute for Very Long Baseline Interferometry European Research Infrastructure Consortium in Dwingeloo, the Netherlands, which coordinates a network of radio telescopes in 13 countries.

Budgetary barriers

The SKA will be built in stages, but once complete, it will include around 2,000 radio dishes in 9 African countries and up to one million antennas in Australia. The array will have a total signal-collecting area of roughly 1 square kilometre, hence its name. Designs for the first phase — known as SKA1 — account for roughly 10% of the finished project, and will include 194 dishes in South Africa, along with about 130,000 antennas in Australia.

The project is being coordinated by ten member governments: those of Australia, Canada, China, India, Italy, Spain, South Africa, Sweden, the Netherlands and the United Kingdom, as well as a group of French research organizations and Germany's Max Planck Society.

But it's not clear how much of the $1-billion construction cost has already been raised. The United Kingdom — which houses the project's headquarters at the Jodrell Bank Observatory near Manchester — has contributed £119 million ($154 million) to the SKA project so far, and other countries have also provided funds.

Around 100 organizations from 20 countries have worked on prototype dish and antenna designs, as well as the information-technology infrastructure needed to collect data. SKA spokesperson William Garnier says the amounts that these countries have contributed are confidential for now, but he confirms that the construction funds will need to be banked before the collaboration can award building contracts.

Costs of cutbacks

Astronomers have voiced concerns that — if the project cannot raise its first $1 billion — the scaled-back plan would reduce the telescope's sensitivity. But Diamond told *Nature* that this design can be upgraded if more money comes through — or if more countries become part of the consortium.

Extra countries have joined the project since it officially kicked off in 2013. But of the founding partners, the German government left the project in 2014 and New Zealand pulled out in July last year, the latter because officials were not convinced that its researchers would gain enough benefits from the project to justify the membership cost, estimated at NZ$40 million (US$26 million) over 10 years.

The telescope's budget and its start date have changed before, and it is possible that the 2021 target might be revised again. This is because SKA member countries have not yet finished creating the intergovernmental SKA Observatory, which will be the legal entity responsible for managing the project and collecting and spending funds.

The SKA Observatory must be established before governments can formally begin depositing project funds. For this to happen, at least five member countries — including Australia, South Africa and the United Kingdom, which all host parts of the project — must each pass a law pledging that the country will become part of the body. Australia, China, Italy, the Netherlands, Portugal, South Africa and the United Kingdom have all agreed to enact relevant legislation, but so far only the Netherlands has done so.

A source who has knowledge of the project, but who asked not to be named, is confident that the SKA will be built despite delays and fluctuating costs, and that it will be an impressive instrument irrespective of the chosen design. "SKA is too big to fail: there's too much involvement at a senior level, too much money," they say.

© 2020 Springer Nature Limited. All rights reserved.

US DATA SUGGEST HUMAN BODIES ARE COOLING DOWN

Normal body temperatures are a fraction of a degree colder than they were in the nineteenth century.

By Ewen Callaway

The human body is getting colder. Since the nineteenth century, normal body temperatures have dropped by a fraction of a degree, finds a study[1] that looked at more than 150 years of data.

People's bodies are now, on average, cooler than the textbook figure of 37 °C, having fallen by a few hundredths of a degree per decade, estimates a team led by Julie Parsonnet, an infectious-disease epidemiologist at Stanford University in California (M. Protsiv *et al. eLife* **9**, e49555; 2020).

German physician Carl Reinhold August Wunderlich determined the 37 °C figure in 1851. But later research found that the average body temperature is slightly cooler. A 2017 study of some 35,000 people found a temperature of 36.6 °C (Z. Obermeyer *et al. Br. Med. J.* **359**, j5468; 2017). Scientists suspected that measurement error explained the discrepancy.

But Parsonnet says her team's data and modelling suggest bodies really are cooling. The researchers looked at three data sets – 83,900 temperatures taken between 1862 and 1930 from American Civil War veterans, and hundreds of thousands of measurements collected in the 1970s and between 2007 and 2017.

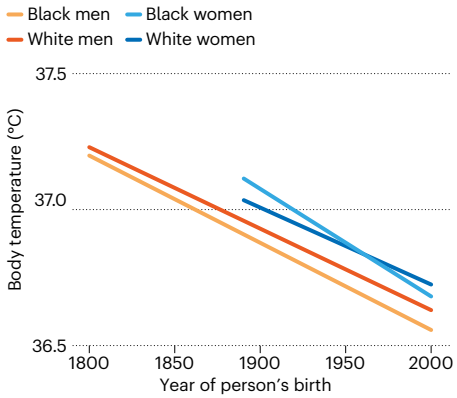
The team found that women born in the first decade of the nineteenth century had temperatures 0.32 °C higher than those of women born in the late 1990s; for men, the difference was 0.59 °C. Overall, temperatures dropped by 0.03 °C per decade (see 'Chilling effect').

Parsonnet thinks that lower rates of long-term infections such as tuberculosis, which can elevate body temperature, explains the trend. In the nineteenth century, chronic infections were common, she says.

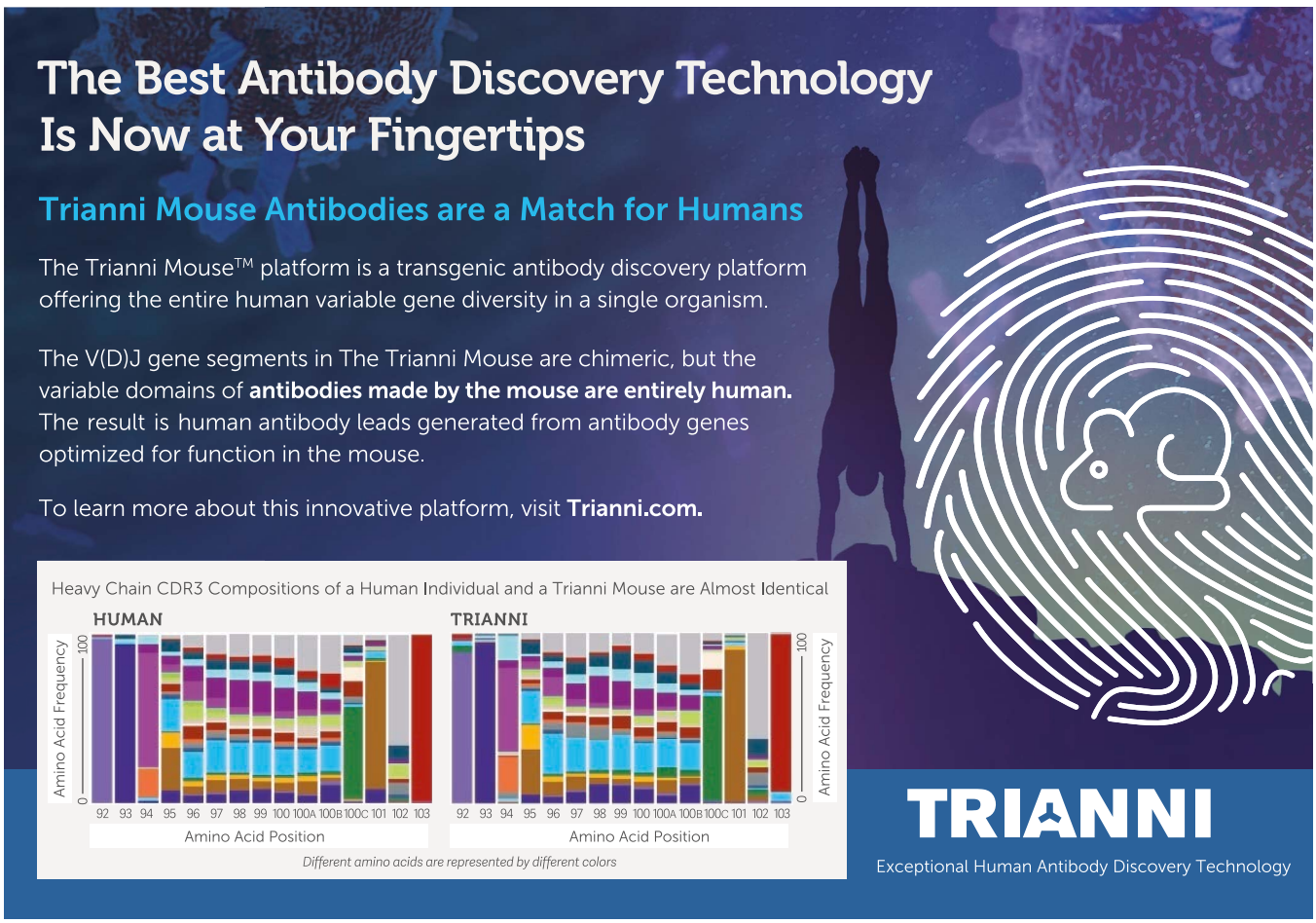
That suggestion is "intriguing and plausible", says Jill Waalen, an epidemiologist at the Scripps Research Translational Institute in La Jolla, California. But none of the measurements the researchers used came from the period beginning in the 1940s, when antibiotics were widely introduced. Waalen says that a marked drop in body temperatures at this time would support Parsonnet's infection theory.

CHILLING EFFECT

Average normal body temperatures have dropped by about 0.03 °C per decade since the nineteenth century, according to a study of hundreds of thousands of temperature measurements taken from people in the United States.



SOURCE: *ELIFE*



© 2020 Springer Nature Limited. All rights reserved.



FINDING THE CRISPR OFF-SWITCH

Researchers have identified a bevy of anti-CRISPR tools that could aid in medicine and biosecurity. **By Elie Dolgin**

It started out as "sort of a stupid thing to do", recalls Joe Bondy-Denomy, a microbiologist at the University of California, San Francisco. As a graduate student in the early 2010s, he tried to infect bacteria with viruses that, on paper, shouldn't have stood a chance. He knew that these viruses, or phages, were susceptible to CRISPR–Cas, the bacterial defence system that scientists have harnessed as a powerful tool for gene editing. And in most cases, he was right: the CRISPR machinery chopped the incoming phages into bits. But in a few instances, against the odds, the intruders survived.

Bondy-Denomy thought he had messed up. "Then a light bulb went off," he says. Maybe something inside the bacterial genome was disarming its defences. And maybe that self-sabotaging bit of DNA was coming from previous viral invaders.

A quick comparison of DNA sequences proved Bondy-Denomy's intuition correct. Phage genes nestled inside the bacterial genome were completely shutting down the CRISPR–Cas system, making the bacteria vulnerable[1].

"Joe got the result that changed everything," says Alan Davidson, a phage biologist at the University of Toronto in Canada, who was Bondy-Denomy's PhD adviser at the time. "He found something amazing that we never expected."

Bondy-Denomy — together with Davidson, microbiologist Karen Maxwell and fellow graduate student April Pawluk — had stumbled onto tools now known as anti-CRISPRs. These proteins serve as the rocks to CRISPR's molecular scissors. And soon, they were popping up everywhere: more than 50 anti-CRISPR proteins have now been characterized, each with its own means of blocking the cut-and-paste action of CRISPR systems.

ILLUSTRATION BY SÉBASTIEN THIBAULT

© 2020 Springer Nature Limited. All rights reserved.

The expansive roster opens up many questions about the archaic arms race between bacteria and the phages that prey on them. But it also provides scientists with a toolkit for keeping gene editing in check.

Some are using these proteins as switches to more finely control the activity of CRISPR systems in gene-editing applications for biotechnology or medicine. Others are testing whether they, or other CRISPR-stopping molecules, could serve as biosecurity countermeasures of last resort, capable of reining in some genome-edited bioweapon or out-of-control gene drive.

"For any reason you can think of to turn off CRISPR systems, anti-CRISPRs come into play," says Kevin Forsberg, a microbial genomicist at the Fred Hutchinson Cancer Research Center in Seattle, Washington.

Yet, despite a growing number of proposed applications and proof-of-concept experiments in the laboratory, researchers have yet to pin down the therapeutic potential of these anti-CRISPR systems. Jennifer Doudna, a biochemist at the University of California, Berkeley, and one of the pioneers of CRISPR gene editing, voices a question that she says is on everyone's lips: "How do you actually use these in a way that will provide meaningful control?"

"That's certainly where that whole anti-CRISPR field needs to go," she says. "It just hasn't gone there yet."

All hell breaks loose

Despite the growing focus on anti-CRISPRs — with about one paper a week published on the topic in 2019 — the initial discovery by Davidson and his students flew under the radar.

To most scientists, it seemed like an esoteric example of evolutionary warfare — especially given that the anti-CRISPR proteins discovered were all specific to one particular form of bacterial defence, known as the type I CRISPR system. The darling of genome editing has been the type II system and its archetypal DNA-cutting protein, Cas9.

"For the wider biological audience to really take notice," says Pawluk, now an editor at *Cell*, "it had to be Cas9".

In December 2016, Pawluk, still working in Davidson's lab, and Bondy-Denomy, leading his own independent research group, each identified inhibitors to the Cas9 enzyme[2,3]. This time, researchers around the world seized on the findings. "Like everything else in the CRISPR world, the thin edge of the wedge comes in, and the next thing you know all hell breaks loose," says Erik Sontheimer, a molecular biologist at the University of Massachusetts Medical School in Worcester and a co-author on Pawluk's paper[2].

In less than three months, structural biologists at the Harbin Institute of Technology in China had deciphered the molecular mechanism by which one of Bondy-Denomy's anti-CRISPR proteins, called AcrIIA4, shut off Cas9 activity[4] (see 'CRISPR correctives'). A few months later, Doudna, working with Bondy-Denomy and biochemist Jacob Corn, now at the Swiss Federal Institute of Technology in Zürich, offered the first demonstration that anti-CRISPRs had practical value: they showed that delivering AcrIIA4 into human cells, either alongside or right after introducing Cas9, could halt gene-editing activity in its tracks[5].

That's useful, because if Cas9 remains active for too long, it raises the risk of unintended edits. Doudna and her collaborators reported that an anti-CRISPR protein could limit the 'off-target' effects that researchers and investors have fretted over since early in CRISPR's development.

> "JOE GOT THE RESULT THAT CHANGED EVERYTHING. HE FOUND SOMETHING AMAZING THAT WE NEVER EXPECTED."

Curbing off-target activity would be a big contribution to the field of CRISPR therapeutics, says David Rabuka, chief executive and cofounder with Bondy-Denomy of Acrigen Biosciences, based in Berkeley. The company's pitch: "We're going to make gene editing more efficient and safer," Rabuka says.

Anti-CRISPRs could also help to confine editing activity to particular cells and tissues in the body. In 2019, research teams in Germany, Japan and the United States independently attempted to use the proteins in tandem with small regulatory molecules called microRNAs to bring about tissue-specific editing[6–8]. The US team, led by Sontheimer, even showed that the approach could work in mice — theirs is the only published study so far to demonstrate that anti-CRISPR proteins can work in a living animal, and not just cells[8].

Sontheimer and his colleagues wanted to allow editing in the liver while suppressing it in all other tissues of the mouse. So they designed an anti-CRISPR protein that would be active everywhere except in the presence of microRNA-122, which is found only in the liver. In the mice, the anti-CRISPR successfully blocked Cas9 editing throughout the body, except in that one organ.

Although the paper focused on liver-directed editing, the platform is "plug and play", says Sontheimer: any organs that produce a unique microRNA at high expression levels could be targeted in this way, provided that the anti-CRISPR proteins don't trigger unwanted immune effects.

Not immune to challenges

Because of previous exposure to microbes harbouring CRISPR–Cas systems, many people have immune systems that are already primed to attack and disable the Cas9 protein. That could pose a challenge. In mice, just one dose of a CRISPR-based medicine can elicit a strong enough immune response to render subsequent treatments ineffective.

According to Sontheimer, anti-CRISPR proteins could be prone to the same rejection issue, potentially imperilling the technology and triggering dangerous, inflammatory reactions in patients.

Other types of CRISPR inhibitor shouldn't have the same limitation. Last May, a team led by Amit Choudhary, a chemical biologist at the Broad Institute of MIT and Harvard in Cambridge, Massachusetts, described a new way of identifying small-molecule drugs capable of disrupting Cas9 activity[9]. The compounds his team identified are not as potent as natural anti-CRISPR proteins, but they are more likely to sneak past the immune system, to cross cell barriers and to allow for reversible control of Cas9 activity.

Elsewhere, researchers have designed short strings of nucleic acids that grab onto two parts of the Cas9 complex and completely shut down gene editing in human cells[10]. "We're pretty sure that what we have works better than all the best anti-CRISPR proteins out there already," says Keith Gagnon, an RNA biochemist at Southern Illinois University in Carbondale who led the research. And other groups, including virologist Brooke Harmon's at Sandia National Laboratories in Livermore, California, have synthesized tiny protein fragments that show potential as anti-CRISPR agents. "It's nice to have a lot of different options," Harmon says.

That diversity could be important in medical applications: for example, in limiting the editing activity of gene-targeted medicines, or fashioning phage therapies capable of wiping out difficult-to-treat bacteria without being stymied by the pathogen's own CRISPR defences. It might also help in other proposed applications of CRISPR-blocking technologies.

Take gene-drive systems, in which scientists deploy CRISPR gene editing to spread a DNA modification swiftly through an entire population. Some public-health officials hope that the technique might allow for the complete eradication of disease-carrying mosquitoes or ticks, for example.

But concerns over unforeseen ecological impacts abound. Many public officials and researchers also worry about gene drives being weaponized to wipe out agricultural systems or to spread a deadly disease.

Anti-CRISPRs could provide a molecular

© 2020 Springer Nature Limited. All rights reserved.

safety net against these potential bio-attacks, says Sandia biochemist Joe Schoeniger. "You need to have an off-button," he says.

For now, such applications are mostly hypothetical. The only published report of researchers using anti-CRISPR proteins to inhibit a gene drive comes from a proof-of-principle experiment in yeast[11]. However, the idea is gaining traction, including among researchers hoping to halt the spread of malaria by forcing harmful genes to spread through an entire population of mosquitoes.

Andrea Crisanti, a molecular parasitologist at Imperial College London, says that he has used anti-CRISPR genes to halt a mosquito-eradicating gene-drive system. The gene drive, which disrupts female fertility, can wipe out mosquitoes in the lab in about ten generations[12]. But in unpublished work, his team has added anti-drive mosquitoes to the mix, and "they can completely, 100% block the drive", Crisanti says. "We can stop the population from crashing."

Insurance policy

As Crisanti looks ahead to field-testing his sterilization strategy, he imagines having cages of anti-drive mosquitoes at the ready, just in case things go awry. "It's kind of like buying an insurance," he says.

But the need for CRISPR containment goes beyond gene drives. "If there's an adverse event in a clinical trial or a nefarious use of a genome editor, we're not going to know what that looks like until it happens," says Renee Wegrzyn, a biosecurity scientist at the US government's Defense Advanced Research Projects Agency (DARPA) in Arlington, Virginia.

That's why DARPA, in 2017, launched the Safe Genes programme, a four-year, US$65-million initiative aimed at combating the dangers of CRISPR technologies. This has involved discovering new inhibitors against all types of CRISPR–Cas system and finding anti-CRISPRs that function in unique and useful ways. Bondy-Denomy, Choudhary, Crisanti, Doudna and the Sandia team, among others, are all recipients of this funding.

Beyond its biotechnology applications, the anti-CRISPR strategy is opening up fresh possibilities for basic research, too. "It's become one of our favourite tools," says Shawn Liu, a neuro-epigeneticist at Columbia University Medical Center in New York City. Liu studies how a modified CRISPR–Cas9 system can change the expression levels of a gene through epigenetic modifications — that is, without altering the underlying sequence. Anti-CRISPR proteins helped him to show how long the effects lasted[13].

They also came in handy when researchers were looking for mutant strains of bacteria that could fend off phage attacks more effectively than standard ones. A team led by Sylvain Moineau, a phage biologist at Laval University in Quebec City, Canada, focused on *Streptococcus thermophilus*, a microbe used to make cheese and yoghurt[14]: "We used a phage containing an anti-CRISPR protein as a tool to find other defence mechanisms," he explains.

Other scientists are incorporating anti-CRISPRs into tools such as biosensors that can track how much of a therapeutic gene editor is active inside cells, and optogenetic control strategies that allow researchers to switch on Cas9 genome targeting at the flick of a laser beam.

"A lot of it is still in the stage of 'toy' systems," says Chase Beisel, a bioengineer at the Helmholtz Institute for RNA-based Infection Research in Würzburg, Germany. "But the concept is there, at least."

Open questions

As bioengineers continue to tinker with anti-CRISPRs, and as companies such as Acrigen move to introduce the inhibitors into therapeutic platforms, some biologists have also begun to grapple with more philosophical questions about the evolution of CRISPR–Cas systems in the first place. If bacteria with intact CRISPR protections commonly harbour phage-derived sequences for inhibitors that neutralize this immunity, then "CRISPR is clearly not doing its defence role in many of those cases", says Edze Westra, who studies the ecology of CRISPR systems at the University of Exeter, UK. And yet, natural selection seems to maintain the system in working order. So, he asks, "what is its role apart from fuelling biotech start-up companies?"

Some studies point to bacteria using CRISPR–Cas systems in forming biofilms, repairing DNA and conducting other regulatory processes involved in enhancing virulence. And it's possible that once anti-CRISPRs have defanged Cas enzymes of their DNA-cutting abilities, bacteria will have repurposed the gene editors for other uses, says Maxwell, the University of Toronto microbiologist.

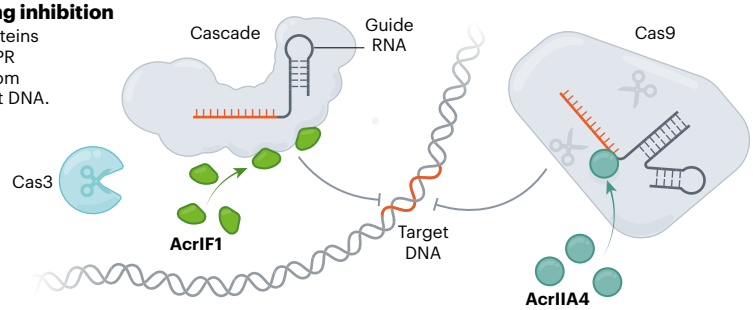
Those bedevilling mysteries won't halt the steady march of CRISPR gene editing into human therapeutics, pest control and more. And for many, that's why anti-CRISPRs are so important.

"There needs to be this shift to really controlling these editors so we make sure that you get the change you want and nothing else," says Doudna. And just as the CRISPR–Cas systems that ushered in a biotechnology revolution started with a few curious observations in a laboratory, she notes, so too did the discovery of the inhibitors that could be a much-needed corrective.

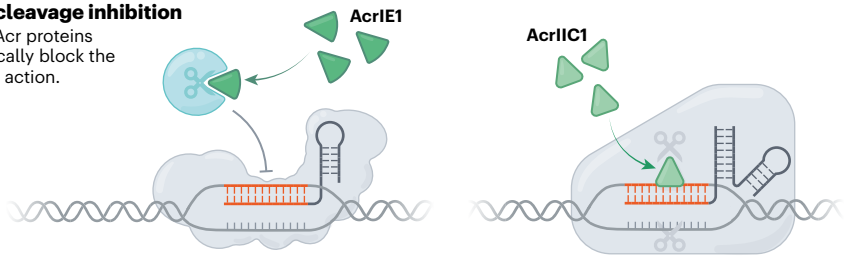
CRISPR CORRECTIVES

There are two particularly well-studied types of CRISPR DNA editing. Type I uses a Cascade complex and guide RNA to bind a DNA target, which is then cut with the Cas3 enzyme. Type II uses a single enzyme, such as Cas9, to bind and cut the target sequence. Researchers have discovered more than 50 anti-CRISPR (Acr) proteins that turn off DNA-editing activity in a variety of ways. Here are two commonly observed mechanisms.

DNA-binding inhibition
Some Acr proteins prevent CRISPR complexes from binding target DNA.



DNA-cleavage inhibition
Some Acr proteins specifically block the cutting action.

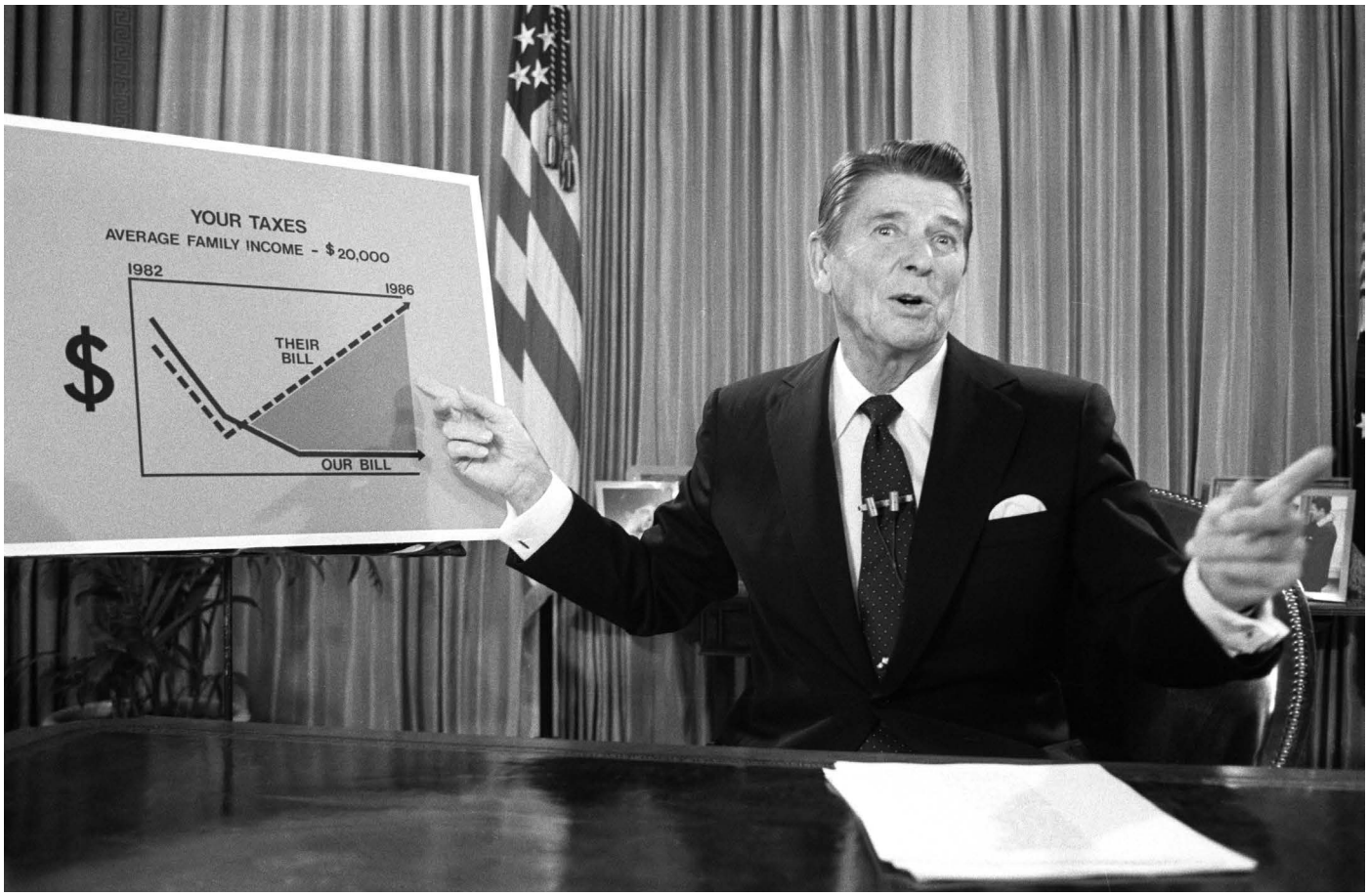


Elie Dolgin is a science journalist in Somerville, Massachusetts.

1. Bondy-Denomy, J., Pawluk, A., Maxwell, K. L. & Davidson, A. R. *Nature* **493**, 429–432 (2013).
2. Pawluk, A. *et al. Cell* **167**, 1829–1838.e9 (2016).
3. Rauch, B. J. *et al. Cell* **168**, 150–158.e10 (2017).
4. Dong, D. *et al. Nature* **546**, 436–439 (2017).
5. Shin, J. *et al. Sci. Adv.* **3**, e1701620 (2017).
6. Hoffmann, M. D. *et al. Nucleic Acids Res.* **47**, e75 (2019).
7. Hirosawa, M., Fujita, Y. & Saito, H. *ACS Synth. Biol.* **8**, 1575–1582 (2019).
8. Lee, J. *et al. RNA* **25**, 1421–1431 (2019).
9. Maji, B. *et al. Cell* **177**, 1067–1079.e19 (2019).
10. Barkau, C. L., O'Reilly, D., Rohilla, K. J., Damha, M. J. & Gagnon, K. T. *Nucleic Acid Ther.* **29**, 136–147 (2019).
11. Basgall, E. M. *et al. Microbiology* **164**, 464–474 (2019).
12. Kyrou, K., Hammond, A., Galizi, R. *et al. Nature Biotechnol.* **36**, 1062–1066 (2018).
13. Liu, X. S. *et al. Cell* **172**, 979–992.e6 (2018).
14. Labrie, S. J. *et al. Sci. Rep.* **9**, 13816 (2019).

© 2020 Springer Nature Limited. All rights reserved.

Books & arts



BETTMANN

US president Ronald Reagan based his tax cuts of the 1980s on questionable ideas.

The dangers of fringe economics

Governments need to heed the evidence. Three books warn of the perils of untested ideas. **By Ehsan Masood**

In November 2017, the economist Vera Shlakman died at the age of 108. Her 1935 *Economic History of a Factory Town* is a landmark in the field. Chronicling how textile manufacturing transformed Chicopee, Massachusetts, Shlakman zeroed in on working women's lives, vaulting beyond analyses of data on wages and shift lengths to include the value of dowries and information in letters and diaries. Ousted from teaching economics during the McCarthy era of the 1950s, she never published another book.

I thought of Shlakman, and how far we have strayed from such integrated analyses of economic realities, while combing through Simon Bowmaker's 2019 *When the President Calls*. Over the past half-century, Bowmaker shows, economic advisers to US presidents from Richard Nixon to Donald Trump have enabled central bankers and treasury officials to implement untethered ideas. Often described in terms borrowed from mathematics or physics (such as the 'velocity of money'), these concepts neither command an expert consensus nor are they necessarily reproducible.

Two other new books, both by economics Nobel laureates, also capture the spirit of Shlakman's diverse thinking: Paul Krugman's *Arguing with Zombies*, and *Good Economics for Hard Times* by Abhijit Banerjee and Esther Duflo.

Banerjee and Duflo's book appeared a month before they were awarded the 2019 Nobel, which they shared with Michael Kremer. It encapsulates nearly two decades of research bringing field trials of policies in low-income countries into the mainstream — from improving educational outcomes, to uptake of vaccination. Krugman's tome, meanwhile, mulls over the mistakes of the past two decades. The 'zombies' of his title are economic theories and policies that should have been killed by evidence, but keep coming back — such as the idea that inequality is necessary for growth. In a world still reeling from the impact of the 2008 financial crisis, Krugman (who was awarded his Nobel that year) has harsh words for practitioners clinging to the old ways.

© 2020 Springer Nature Limited. All rights reserved.



JIM DAVIS/*THE BOSTON GLOBE* VIA GETTY

Abhijit Banerjee and Esther Duflo advocate field trials of economic policies, notably in low-income nations.

A prominent example is the 'Laffer curve', named after Arthur Laffer, who later became Ronald Reagan's economic adviser. Bowmaker clearly relished the chance to quiz Laffer, who is reported to have sketched the idea out on a napkin over a 1974 lunch with two White House officials: Donald Rumsfeld and Dick Cheney. If governments raise taxes for people with modest incomes and cut taxes for the wealthy, Laffer argued, they can raise revenue and boost growth. The former, because lower-income earners far outnumber the rich, thus amplifying their total tax contribution; the latter, because wealthy business owners are likely to use cash saved from tax cuts to invest in new products, more jobs or equipment, thus boosting growth.

Untested tax cuts

There is no consensus on whether the Laffer curve is accurate — even some leading conservative economists, such as Gregory Mankiw, are critical. Yet it became the basis for tax cuts, beginning with Reagan's decision to slash the top rate of income tax from 70% down to 28% over the early to mid-1980s. Bowmaker found Laffer still buoyant. "That's my baby and I just loved it," Laffer said. "It was the best tax bill in US history." Trump awarded him the Presidential Medal of Freedom in 2019.

As these three books reveal, however, the ideas that Laffer and others came to represent are now under severe pressure, even from the centre-right parties in high-income nations that initially backed them. Decades of falling or flat public spending, unrestricted free trade, relatively light regulations on financial institutions and low taxes on businesses and top earners have not translated into across-the-board prosperity. That is seen especially in the United States and Britain, now among the most unequal countries in their peer group. In 2016, six out of northern Europe's ten poorest regions, as measured by gross domestic product per person, were in the United Kingdom.

When the President Calls: Conversations with Economic Policymakers
Simon W. Bowmaker
MIT Press (2019)

Arguing with Zombies: Economics, Politics, and the Fight for a better Future
Paul Krugman
W. W. Norton (2020)

Good Economics for Hard Times
Abhijit V. Banerjee and Esther Duflo
PublicAffairs (2019)

Economic nationalism has emerged from these trends, under slogans ranging from "America First" to the UK "Take Back Control". The real results are the Trump administration's public disavowal and renegotiation of the North American Free Trade Agreement — and Brexit.

At the same time, the collapse of what were once seen as mainstream economic ideas by politicians right and left has opened up space for more conventionally green-left approaches to policymaking. That explains in part why the Italian American economist Mariana Mazzucato is being heard across political divides. In books such as *The Value of Everything* (2018), Mazzucato makes a strong case for the state as enabler in an economic policy that privileges well-being and sustainability. That is also the space into which Banerjee and Duflo enter in *Good Economics for Hard Times*. Like Krugman, they are critical of policies based on weak or non-existent evidence. But their approach is less argument than stepping back to let the research do the talking.

Consensus and controversy

The studies they cite probe hot topics such as climate change, immigration and the viability of continued economic growth. Banerjee and Duflo synthesize the literature on what is agreed and what is controversial in an accessible, often entertaining way. There are gaps, however. Mentioning the work of Kate Raworth and Tim Jackson on the environmental impacts of constant growth, and of Partha Dasgupta on the value of biodiversity, would have enriched and unified their thinking on the impact of consumption-fuelled growth on climate change, and on biodiversity and

© 2020 Springer Nature Limited. All rights reserved.

ecosystem services.

Grand narratives, which smack of the old economic thinking, are not the goal of Banerjee and Duflo. The authors do, however, need to articulate their approach in narrative terms, or they will struggle to be heard. As Bowmaker demonstrates, US presidents want to hear happy endings, rather than sit through a menu of options communicated seminar-style. Harry Truman is reported to have said that he preferred one-handed economists, because he didn't like hearing "on the other hand". Barack Obama was an exception, making decisions after hearing arguments pro and con.

"There is strength in numbers and robustness in diversity."

Sadly, neither *Arguing with Zombies* nor *Good Economics for Hard Times* tackles in depth what I feel is the defining challenge for newer generations of economic policy advisers. That is, how to mitigate the risks of expert-shopping by policymakers. If researchers with fringe ideas continue to validate untested theories, yet more zombies will invade the corridors of power.

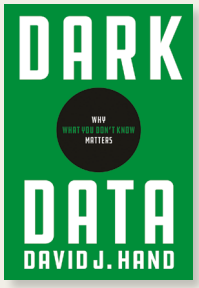
This happens to scientific advisers, too – although perhaps less often. In the 1990s, governments with significant oil and gas interests joined the powerful fossil-fuel industry lobby in seeking experts who could cast doubt on human influence on climate change. The consensus view of the Intergovernmental Panel on Climate Change – backed as it was by a huge number of heavyweight researchers – was essential in preventing such dubious ideas from penetrating the mainstream (although it has not stopped Trump's withdrawal from the 2015 Paris climate agreement).

Economists need to organize similarly across different schools of thought – and to include development economics as well as ecological and environmental economics and feminist economics. There is strength in numbers and robustness in diversity. That can go some way towards curbing the unworkable concepts that continue to emerge.

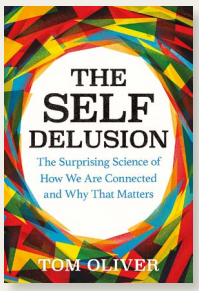
As these three thoughtful, timely books demonstrate in their own ways, a space has opened up for new ideas in economics at a time of widespread inequality, social and cultural schisms, and environmental crisis. That is an opportunity to avoid another 50 years of theories that inform the highest levels of policy as if evidence didn't matter.

Ehsan Masood is Editorials editor and bureau chief for the Middle East and Africa at *Nature* in London. His latest book is *The Great Invention: The Story of GDP and the Making and Unmaking of the Modern World*.

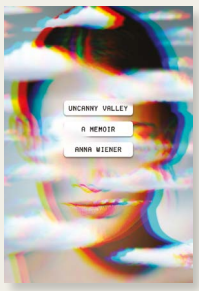
Books in brief



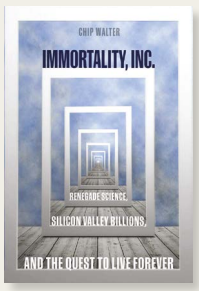
Dark Data
David J. Hand Princeton Univ. Press (2020)
We are deluged with billions of bytes of data, yet much crucial information goes unseen and unreported. So reveals statistician David Hand in this penetrating study of missing ('dark') data and its impacts on decisions — skewing stats, enabling fraud, embedding inequity and triggering preventable catastrophes. Advocating "data science judo", Hand offers expert training, from recognizing when facts are being cherry-picked to designing randomized trials. A book illuminating shadowed corners in science, medicine and policy.



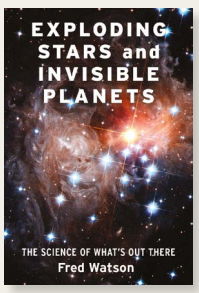
The Self Delusion
Tom Oliver Weidenfeld & Nicolson (2020)
Humans are less discrete entities than mash-ups of microbiota and shifting beliefs, declares ecologist Tom Oliver in this rich, intriguing book. We are, he shows, so interfused with the environment that all life might be seen as a web of genes, and all minds a web of memes. Oliver reframes the self as a fleeting union of molecules, a target for manipulation by parasites, a cooperative co-creator who is also destroying the biosphere. But by recognizing our connectedness, he argues, we enable needed societal and environmental change.



Uncanny Valley
Anna Wiener Farrar, Straus and Giroux (2020)
Start-ups have long been seen as a geek-driven, idealistic antidote to corporate culture. Anna Wiener's unsettling memoir may muddy that image. In 2013, a 20-something Wiener was drawn to the digital economy of California's Silicon Valley. Soon enough she recognized it as a reckless, male-dominated world of barely regulated surveillance. She witnessed the boom in online abuse and political trolling from the inside, and the growing inequity in San Francisco fuelled by venture capitalists. An acute eye on a dystopia in the making.



Immortality, Inc.
Chip Walter National Geographic (2020)
Extreme longevity might seem a seductive concept to some. To a handful of prominent researchers, it's an experimental goal. Venturing into that rarefied world, journalist Chip Walter interviewed stars such as biotechnologist J. Craig Venter and X Prize founder Peter Diamandis. Their eventful stories are woven through Walter's tour of biotech research centres Calico and Celularity, and fields from cryopreservation to regeneration. Results remain broadly inconclusive, but this witty look at 'curing' death is worth the ride.



Exploding Stars and Invisible Planets
Fred Watson Columbia Univ. Press (2020)
Astronomer Fred Watson is a science communicator par excellence. Here, with infectious enthusiasm, he plunges the reader into the science on sky-watching and space observation. Kicking off with a nuanced discussion of twilight — covering everything from crepuscular rays to the 'green flash' — he moves on to meteor showers, the potential contamination of the Solar System's ice moons by earthly microbes, the mystery of a hypothesized Planet Nine and the real origins of the Moon. **Barbara Kiser**

© 2020 Springer Nature Limited. All rights reserved.

Comment

Time for the Human Screenome Project

Byron Reeves, Thomas Robinson & Nilam Ram



To understand how people use digital media, researchers need to move beyond screen time and capture everything we do and see on our screens.

There has never been more anxiety about the effects of our love of screens — which now bombard us with social-media updates, news (real and fake), advertising and blue-spectrum light that could disrupt our sleep. Concerns are growing about impacts on mental and physical health, education, relationships, even on politics and democracy. Just last year, the World Health Organization issued new guidelines about limiting children's screen time; the US Congress investigated the influence of social media on political bias and voting; and California introduced a law (Assembly Bill 272) that allows schools to restrict pupils' use of smartphones.

All the concerns expressed and actions taken, including by scientists, legislators, medical and public-health professionals and advocacy groups, are based on the assumption that digital media — in particular, social media — have powerful and invariably negative effects on human behaviour. Yet so far, it has been a challenge for researchers to demonstrate empirically what seems obvious experientially. Conversely, it has also been hard for them to demonstrate that such concerns are misplaced.

A major limitation of the thousands of studies, carried out over the past decade or so, of the effects of digital media is that they do not analyse the types of data that could reveal exactly what people are seeing and doing on their screens — especially in relation to the problems that doctors, legislators and parents worry most about. Most use self-reports of 'screen time'. These are people's own estimates of the time they spend engaging with screens or with platforms that are categorized as 'smartphone', 'television', 'social media', 'political news' or 'entertainment media'. Yet today's media experiences defy such simplistic characterization: the range of content has become too broad, patterns of consumption too fragmented[1], information diets too idiosyncratic[2], experiences too interactive and devices too mobile.

Policies and advice must be informed by accurate assessments of media use. These should involve moment-by-moment capture of what people are doing and when, and machine analysis of the content on their screens and the order in which it appears.

Technology now allows researchers to record digital life in exquisite detail. And thanks to shifting norms around data sharing, and the accumulation of experience and tools in fields such as genomics, it is becoming easier to collect data while meeting expectations and legal requirements around data security and personal privacy.

We call for a Human Screenome Project — a collective effort to produce and analyse recordings of everything people see and do on their screens.

Screen time

According to a 2019 systematic review and meta-analysis[3], over the past 12 years, 226 studies have examined how media use is related to psychological well-being. These studies consider mental-health problems such as anxiety, depression and thoughts of suicide, as well as degrees of loneliness, life satisfaction and social integration.

The meta-analysis found almost no systematic relationship between people's levels of exposure to digital media and their well-being. But almost all of these 226 studies used responses to interviews or questionnaires about how long people had spent on social media, say, the previous day.

The expectation is that if someone reports being on Facebook a lot, then somewhere among all those hours of screen time are the ingredients that influence well-being, for better or worse. But 'time spent on Facebook' could involve finding out what your friends are doing, attending a business meeting, shopping, fundraising, reading a news article, bullying, even stalking someone. These are vastly different activities that are likely to have very different effects on a person's health and behaviour.

Another problem is that people are unlikely to recollect exactly when they did what[4,5]. Recent studies that compared survey responses with computer logs of behaviour indicate that people both under- and over-report media exposure — often by as much as several hours per day[6–8]. In today's complex media environment, survey questions about the past month or even the past day might be almost useless. How many times did you look at your phone yesterday?

The US National Institutes of Health (NIH) is

© 2020 Springer Nature Limited. All rights reserved.



A participant in a traditional Chinese opera competition plays on her phone.

THOMAS PETER/REUTERS

currently spending US$300 million on a vast neuroimaging and child-development study, eventually involving more than 10,000 children aged 9 and 10. Part of this investigates whether media use influences brain and cognitive development. To indicate screen use, participants simply pick from a list of five standard time ranges, giving separate answers for each media category and for weekdays and weekends. (The first report about media use from this study, published last year, showed a small or no relationship between media exposure and brain characteristics or cognitive performance in computer-based tasks[9].)

Digital life

Instead, researchers need to observe in exquisite detail all the media that people engage with, the platforms they use and the content they see and create. How do they switch between platforms and between content within those? How do the moments of engagement with various types of media interact and evolve? In other words, academics need a multidimensional map of digital life.

To illustrate, people tend to use their laptops and smartphones in bursts of, on average, 10–20 seconds[10]. Metrics that quantify the transitions people make between media segments within a session, and between media and the rest of life, would provide more temporally refined representations of actual use patterns. A session begins when the screen lights up and ends when it goes dark, and might last less than a second if it entails checking the time. Or it could start with a person responding to their friend's post on Facebook, and end an hour later when they click on a link to read an article about politics.

"In today's complex media environment, survey questions about the past month or even the past day might be almost useless."

Measures of media use must also take account of the scattering of content. Today's devices allow digital content that used to be experienced as a whole (such as a film, news story or personal conversation) to be atomized, and the pieces viewed across several sessions, hours or days. We need measures that separate media use into content categories (political news, relationships, health information, work productivity and so on) — or, even better, weave dissimilar content into sequences that might not make sense to others but are meaningful for the user.

To try to capture more of the complexity, some researchers have begun to use logging software. This was developed predominantly to provide marketers with information on what websites people are viewing, where people are located, or the time they spend using various applications. Although these data can provide more-detailed and -accurate pictures than self-reports of total screen time, they don't reveal exactly what people are seeing and doing at any given moment.

A better way

To record the moment-by-moment changes on a person's screen[2,11], we have built a platform called Screenomics. The software records, encrypts and transmits screenshots automatically and unobtrusively every 5 seconds, whenever a device is turned on (see go.nature.com/2fsy2j2). When it is deployed on several devices at once, the screenshots from each one are synced in time.

This approach differs from other attempts to track human–computer interactions — for instance, through the use of smartwatches and fitness trackers, or diaries. It is more accurate, it follows use across platforms, and it samples more frequently. In fact, we are working on software that makes recordings every second.

We have now collected more than 30 million screenshots — what we call 'screenomes' — from more than 600 people. Even just two of these reveal what can be learnt from a fine-grained look at media use (see 'Under the microscope' and All in the details').

This higher-resolution insight into media use could help answer long-held questions and lead to new ones. It might turn out, for

© 2020 Springer Nature Limited. All rights reserved.

UNDER THE MICROSCOPE

Recordings of smartphone use by two 14-year-olds living in the same northern California community reveal what can be learnt from a fine-grained analysis of media use (see 'All in the details').

Dose. A typical question that researchers might ask is whether study participants are 'heavy' or 'light' phone users. Both adolescents might have characterized their phone use as 'substantial' had they been asked the usual survey questions. Both might have reported that they used their smartphones 'every day' for '2 or more hours' each day, and that looking at their phones was the first thing they did each morning and the last thing they did every night.

But detailed recordings of their actual phone use over 3 weeks in 2018 highlight dramatic differences[2]. For participant A, median use over the 3 weeks was 3.67 hours per day. For participant B, it was 4.68 hours, an hour (27.5%) more.

Pattern. The distribution of time spent using phones during the day differed even more. On average, participant A's time was spread over 186 sessions each day (with a session defined as the interval between the screen lighting up and going dark again). For A, sessions lasted 1.19 minutes on average. By contrast, participant B's time was spread over 26 daily sessions that lasted, on average, 2.54 minutes. So one of the adolescents turned their phone on and off seven times more than the other, using it in bursts that were about one-third the length of the other's sessions.

These patterns could signal important psychological differences. Participant A's days were more fragmented, maybe indicating issues with attentional control, or perhaps reflecting an ability to process information faster.

Interactivity. Both adolescents spent time creating content as well as consuming it. They wrote text messages, recorded photos and videos, entered search terms and so on. On a questionnaire, both might have reported that they posted original material 'sometimes' or maybe 'often'. But the screenshot data reflect patterns of interactivity that would be almost impossible for them to recall accurately.

Participant A spent 2.6% of their screen time in production mode, creating content evenly throughout the day and usually within social-media apps. By contrast, participant B spent 7% of their total screen time producing content (and produced 2.5 times more). But they did so mainly in the evening while watching videos.

Content. During the 3 weeks, participant A engaged with 26 distinct applications. More than half of these (53.2%) were social-media apps (mostly Snapchat and Instagram). Participant B engaged with 30 distinct applications, mostly YouTube (50.9% of the total).

Zooming deeper into specific screen content reveals even more. For participant B, on average, 37% of the screenshots for a single day included food — pictures of food from various websites, photos of B's own food, videos of other people eating or cooking, and food shown in a game involving the running of a virtual restaurant.

In a survey, both adolescents might have reported that they used 'a lot' of apps, and might have given the names of some of them. But the content of their media diets would be impossible to capture. **B.R. *et al.***

instance, that levels of well-being are related to how fragmented people's use of media is, or the content that they engage with. Differences in brain structure might be related to how quickly people move through cycles of production and consumption of content. Differences in performance in cognitive tasks might be related to how much of a person's multitasking involves switching between content (say, from politics to health) and applications (social media to games), and how long they spend on each task before switching.

The Human Screenome Project

So, how can we do better? What's needed is a collective effort to record and analyse everything people see and do on their screens, the order in which that seeing and doing occurs, and the associated metadata that are available from the software and sensors built into digital devices (for instance, on time of day, location, even keystroke velocity).

In any one screenome, screenshots are the fundamental unit of media use. But the particular pieces or features of the screenome that will be most valuable will depend on the question posed — as is true for other 'omes'. If the concern is possible addiction to mobile devices, then arousal responses (detected by a change in heart rate, say) associated with the first screen experienced during a session might be important to measure. If the concern is the extent to which social relationships dictate how political news is evaluated, then the screenshots that exist between 'social' and 'political' fragments in the screenome sequence might be the crucial data to analyse. (News items flagged by a close friend might be perceived as more trustworthy than the same news obtained independently, for example.)

How can researchers get access to such high-resolution data? And how can they extract meaning from data sets comprising millions of screenshots?

One option is for investigators to collaborate with the companies that own the data, and that have already developed sophisticated ways to monitor people's digital lives, at least in certain domains, such as Google, Facebook, Amazon, Apple and Microsoft. The Social Science One programme, established in 2018 at Harvard University in Cambridge, Massachusetts, involves academics partnering with companies for exactly this purpose[12]. Researchers can request to use certain anonymized Facebook data to study social media and democracy, for example.

Largely because of fears about data leaks or study findings that might adversely affect business, such collaborations can require compromises in how research questions are defined and which data are made available, and involve lengthy and legally cumbersome administration. And ultimately, there is nothing to compel companies to share data relevant to academic research.

To explore more freely, academics need to collect the data themselves. The same is true if they are to tackle questions that need answers within days — say, to better understand the effects of a terrorist attack, political scandal or financial catastrophe.

Thankfully, Screenomics and similar platforms are making this possible.

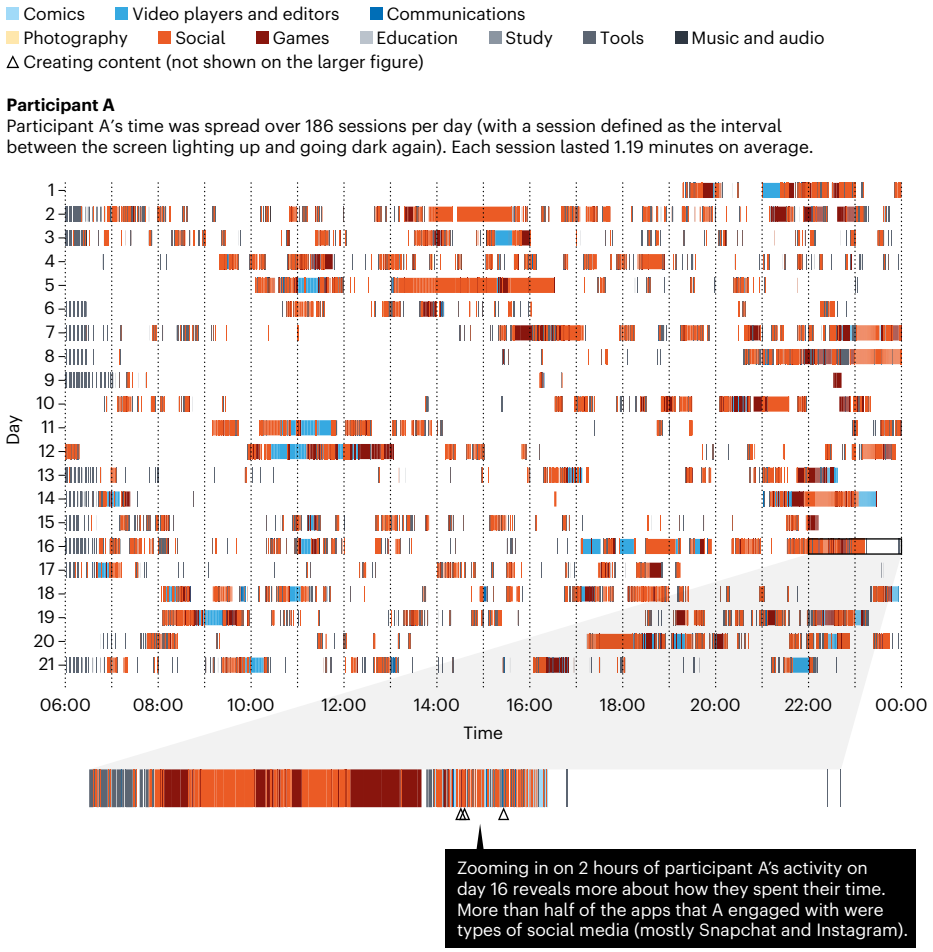
In our experience, people are willing to share their data with academics. The harder problem is that collecting screenomics data rightly raises concerns about privacy and surveillance. Through measures such as encryption, secure storage and de-identification, it is possible to collect screenomes with due attention to personal privacy. (All our project proposals are vetted by university institutional review boards, charged with protecting human participants.) Certainly, social scientists can learn a lot from best practice in the protection and sharing of electronic medical records[13] and genomic data.

Screenomics data should be sifted using a gamut of approaches — from deep-dive qualitative analyses to algorithms that mine and classify patterns and structures. Given how quickly people's screens change, studies should focus on the variation in an individual's use of media over time as much as on differences between individuals and groups. Ultimately, researchers will be able to investigate moment-by-moment influences on physiological and psychological states, the sociological dynamics of interpersonal and group relations over days and weeks, and even cultural and historical changes that accrue over months and years.

© 2020 Springer Nature Limited. All rights reserved.

ALL IN THE DETAILS

Recordings of screenshots every five seconds reveal substantial differences in how two adolescents use their smartphones over 21 days (see 'Under the microscope').



Some might argue that screenomics data are so fine-grained that they invite researchers to focus on the minutiae rather than the big picture. We would counter that today's digital technology is all about diffused shards of experience. Also, through the approach we propose, it is possible to zoom in and out, to investigate how the smallest pieces of the screenome relate to the whole. Others might argue that even with this better microscope, we will not find anything significant. But if relationships between the use of media and people's thoughts, feelings and behaviours continue to be weak or non-existent, at least we could have greater confidence as to whether current concerns are overblown.

The approach we propose is complex, but no more so than the assessment of genetic predictors of mental and physical states and behaviours. Many years and billions of US dollars have been invested in other 'omics' projects. In genomics, as in neuroscience, planetary science and particle physics, governments and private funders have stepped up to help researchers gather the right data, and to ensure that those data are accessible to investigators globally. Now that so much of our lives play out on our screens, that strategy could prove just as valuable for the study of media.

The authors

Byron Reeves is a professor of communication at Stanford University, California, USA. **Thomas Robinson** is a professor of child health, paediatrics and medicine, and director of the Stanford Solutions Science Lab at Stanford University, California, USA. **Nilam Ram** is a professor of human development and psychology, and director of the Quantitative Developmental Systems Group at Pennsylvania State University, University Park, Pennsylvania, USA.
e-mails: reeves@stanford.edu; tom.robinson@stanford.edu; nur5@psu.edu

1. Yeykelis, L., Cummings, J. J. & Reeves, B. *J. Commun.* **64**, 167–192 (2014).
2. Ram, N. *et al. J. Adolesc. Res.* **35**, 16–50 (2020).
3. Hancock, J., Liu, X., French, M., Luo, M. & Mieczkowski, H. *Social media use and psychological well-being: a meta-analysis.* Paper presented at 69th Annu. Conf. Int. Commun. Assoc., Washington DC (2019).
4. Prior, M. *Polit. Commun.* **30**, 620–634 (2013).
5. Niederdeppe, J. *Commun. Meth. Measures* **10**, 170–172 (2016).
6. Araujo, T., Wonneberger, A., Neijens, P. & de Vreese, C. *Commun. Meth. Measures* **11**, 173–190 (2017).
7. Naab, T. K., Karnowski, V. & Schlütz, D. *Commun. Meth. Measures* **13**, 126–147 (2019).
8. Junco, R. *Comp. Human Behav.* **29**, 626–631 (2013).
9. Paulus, M. P. *et al. Neuroimage* **185**, 140–153 (2019).
10. Yeykelis, L., Cummings, J. J. & Reeves, B. *Media Psychol.* **21**, 377–402 (2018).
11. Reeves, B. *et al. Human–Comp. Interact.* **34**, 1–52 (2019).
12. King, G., & Persily, N. *PS: Polit. Sci. Polit.* https://doi.org/10.1017/S1049096519001021 (2019).
13. Parasidis, E., Pike, E. & McGraw, D. *N. Engl. J. Med.* **380**, 1493–1495 (2019).

© 2020 Springer Nature Limited. All rights reserved.

Correspondence

Rooibos settlement: a crucial omission

We celebrate the compensation agreement between the rooibos-tea industry and South Africa's Indigenous peoples (see *Nature* **575**, 258; 2019). As researchers in the field, what concerns us are those left out of the story: small-scale farmers who have worked rooibos land for generations.

It is their oral histories that informed how rooibos seeds were originally unearthed by following the paths of ants (a finding that led to the birth of the industry at scale), and how rooibos was used alongside breast milk to nurture their children. Yet these farmers do not fit neatly into the compensation-agreement narrative because most do not self-identify as Indigenous San or Khoi. Traditional knowledge does not necessarily have a clear-cut ethnic provenance.

Although some small-scale rooibos farmers are descended from San and Khoi, many trace back to slaves and labourers brought in from other parts of Africa and from southeast Asia. The group was largely left out of the compensation negotiations and was eventually included only through a gesture by the National Khoisan Council. Whether the group will benefit in practice remains to be seen.

If not, these communities will be further marginalized: by their exclusion from an Indigenous heritage, by their dearth of land and resources, and because they lack the power of a government-recognized council.

Sarah Ives City College of San Francisco, California, USA.
sarah.f.ives@gmail.com

Rachel Wynberg University of Cape Town, South Africa.

Graham Dutfield University of Leeds, UK.

Sahel crisis: cut global emissions

The recommendations by Alisha Graves and her colleagues for averting catastrophe in Africa's Sahel overlook the need to address the drivers of its climate and ecological crises (*Nature* **575**, 282–286; 2019).

Although the authors' recommendations could help to prevent catastrophe in the short to medium term, immediate action is also needed against the fundamental causes if we are to mitigate crises of rapidly escalating scale and severity in the longer term.

This might seem obvious, but it must be emphasized repeatedly if we are to ramp up our currently woefully inadequate action against the global climate and ecological emergency. Otherwise, there is an implicit acceptance of the status quo and the current trajectory. And the catastrophe in the Sahel, and others like it around the world, will not be averted, but at best delayed.

Keir Philip Imperial College London, UK.
k.philip@imperial.ac.uk

Kurdistan: stop the cycle of strife

I agree with some of the scientists who wrote to *Nature* from nations experiencing civil unrest: instability can wreck educational and research infrastructure (*Nature* **576**, 382–384; 2019). Several civil wars over the past half-century have certainly done so in Kurdistan — the geographical region divided between Iran, Iraq, Turkey and Syria. The continuing conflict against the Islamist terrorist group ISIS and Turkey is making matters worse. And civil war now looms in Rojava, the autonomous Kurdish region in northern Syria.

The Kurds have been considered second-class citizens in their homelands for centuries. Other than in Iraqi Kurdistan, they have no right to speak in their own language or to wear traditional attire in state institutions. Research students must undergo security screening and are excluded from some subjects, including electronics and aerospace engineering.

It pains me to think what another generation might have to live through in the region. I was a child in the 1980s, when Iraq's President Saddam Hussein's use of chemical weapons killed more than 3,000 Kurdish civilians in one day. He bombarded my city, Saqqez in Iran, forcing my family and thousands of others to flee. After the war, the damaged infrastructure of Iraq's and Iran's Kurdish regions — often there was electricity for just a few hours each day — prevented most research laboratories from functioning.

Ebrahim Karimi University of Ottawa, Canada.
ekarimi@uottawa.ca

Futures: lost to the past

I am deeply disappointed to see the loss of the Futures section from the print version of *Nature*. I read only the hard copy of the magazine, and I looked forward every week to the science fiction on its last page. To be able to think deeply about contemporary problems and then abruptly shift to a more creative turn of mind was, to my knowledge, unique among scientific publications.

The Futures section offered me an opportunity to make connections. For example, the mind- and time-bending short story 'You will remember this' by Justen Russell brought to life an illustration of two universes governed by different laws (*Nature* **574**, 144; 2019). For me, this imaginative story found a route to reality as I read Philip Ball's Comment article 'Science must move with the times', which speculated on the future scientific advances of humanity (*Nature* **575**, 29–31; 2019).

My more playful side will miss such indulgences when I am reading *Nature* to further my personal and professional development.

Joseph Moore, Wilmington, Delaware, USA.
jdmoorephd@gmail.com

HOW TO SUBMIT

Correspondence may be submitted to correspondence@nature.com after consulting the author guidelines and section policies at go.nature.com/cmchno.

© 2020 Springer Nature Limited. All rights reserved.

News & views

Malaria

Mosquitoes get a leg up on insecticides

Flaminia Catteruccia

A chemosensory protein enriched in the legs of malaria-carrying mosquitoes gives them resistance to insecticides used to treat bed nets. This discovery points to the challenges of tackling malaria. See p.376

The wide distribution of insecticide-treated mosquito nets across malaria-endemic regions has drastically reduced the incidence of the disease over the past 20 years, and so has saved millions of lives[1]. However, malaria-carrying mosquitoes have now developed strong resistance to the pyrethroid chemicals used in these long-lasting insecticidal nets (LLINs)[2]. An understanding of the mechanisms underlying resistance should reveal ways to make mosquitoes susceptible to insecticides once more. On page 376, Ingham *et al.*[3] demonstrate an unexpected way in which mosquitoes in Africa neutralize pyrethroids: they use a class of small proteins normally involved in chemical communication.

Malaria parasites are transmitted to humans by female mosquitoes of the genus *Anopheles*, with *Anopheles gambiae* being a major carrier of the disease. The first identified mechanism of pyrethroid resistance in wild *Anopheles* populations was a phenomenon called knockdown resistance, which involves mutations in a voltage-gated sodium channel protein that reduce neuronal sensitivity to the insecticide[4]. Other mechanisms have also been identified, including enhanced metabolic activity of detoxifying enzymes such as cytochrome P450s (CYPs), which bind to and promote the breakdown of insecticides[5] (Fig. 1).

The emergence of strong pyrethroid resistance in West African populations of *A. gambiae*[6] prompted Ingham *et al.* to search for more mediators of resistance. The authors analysed the gene-expression profiles of insecticide-resistant *A. gambiae* populations from Burkina Faso and Côte d'Ivoire. To the authors' surprise, they discovered higher-than-normal expression of genes that encode a family of chemosensory proteins, called sensory appendage proteins (SAPs).

SAPs, like all chemosensory proteins, are found only in insects. They are small, soluble proteins that typically transmit chemical signals by transporting small hydrophobic molecules between cells. Ingham and colleagues found that reducing the levels of one of these proteins, SAP2, in pyrethroid-resistant *A. gambiae* significantly restored the mosquitoes' susceptibility to pyrethroids. Conversely, overexpressing SAP2 in an otherwise susceptible *A. gambiae* colony boosted the mosquitoes' resistance levels.

How does a chemosensory protein interfere with insecticide activity? Ingham *et al.* show that SAP2 binds to pyrethroids with high specificity, and that its expression is enhanced in the legs of mosquitoes. These data suggest that SAPs sequester pyrethroids that penetrate the mosquito's hard exterior when it lands on a bed net, perhaps preventing the insecticide from exerting its toxic effect on the nervous system by promoting its breakdown.

Finally, Ingham *et al.* analysed the genomes of West African *Anopheles* populations collected over time, making use of an existing database as well as sequences that they had gathered. They found that a 'selective sweep' had occurred near the genomic region that encodes SAP2 – a phenomenon in which one particular version of a genomic region becomes more prevalent in a population as a result of natural selection. The authors showed that the sweep had occurred over the time in which pyrethroid resistance sharply increased, maybe owing to the beneficial effects of one version of this genomic region on survival. Taken together, Ingham and colleagues' data unveil chemosensory proteins

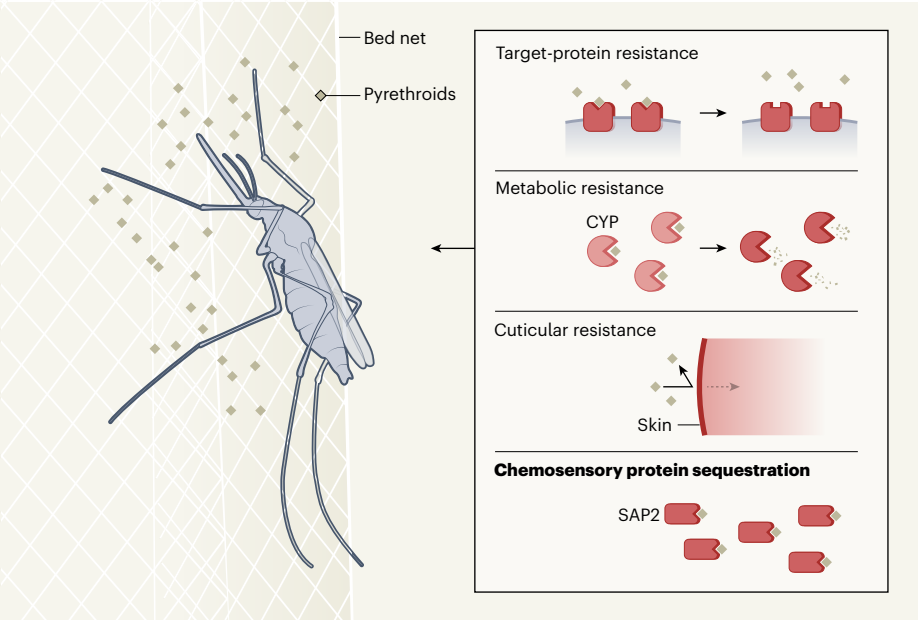


Figure 1 | Multiple lines of resistance. Malaria-carrying mosquitoes in West Africa have developed several mechanisms of resistance to insecticides called pyrethroids, which are used to treat bed nets[2]. Mutations in a voltage-gated sodium channel protein to which pyrethroids bind reduce the chemicals' ability to recognize their target. Enhanced activity of metabolic enzymes such as the cytochrome P450s (CYPs) can break down the pyrethroids before they kill the insect. Thickening of the mosquito's outer cuticular layer can slow insecticide penetration into the skin, thereby reducing the chemicals' concentration. Ingham *et al.*[3] now show that, in the insect's legs, the chemosensory protein SAP2 binds to pyrethroids, sequestering them and so preventing them from functioning.

© 2020 Springer Nature Limited. All rights reserved.

as a key component of insecticide resistance in *Anopheles* mosquitoes.

Chemosensory proteins represent a previously unknown class of resistance-causing factor, and so Ingham and co-workers' finding points to a fresh opportunity to restore full susceptibility to pyrethroids in West African *Anopheles* populations. Resistance caused by CYP enzymes has been mitigated by adding compounds that interfere with CYPs to bed nets[7]; similarly, compounds that inhibit binding between SAP2 and insecticides could be generated and incorporated into next-generation LLINs. Moreover, the genomic region associated with SAP2 resistance can now be used as a molecular marker for tracking the spread of this resistance mechanism. In the future, it will be crucial to determine whether and how chemosensory proteins interact both functionally and spatially with other mechanisms of resistance, to inform the optimal design of resistance-management strategies.

Although Ingham and co-workers' study provides hope of reversing mosquitoes' resistance to insecticides, it also highlights how skilled these insects are at escaping unwanted attention. Clearly, our understanding of insecticide resistance is far from complete, and we should expect other studies in different locations to identify yet more such mechanisms, acting at local or continental levels. *Anopheles* species have been populating Africa for more than 100 million years — considerably longer than humans and our ancestors[8]. Such an enduring connection with their natural habitat is a testament to the challenge that we face when targeting these insects.

The next generation of LLINs and indoor residual sprays (another method of delivering insecticides) is currently being deployed in Africa[9]. Simultaneously, new insecticide-based methods such as insect-attractive targeted sugar baits are being tested[10]. But, like previous interventions, these tools will probably undergo cycles of impactful but relatively short-lived success, followed by decreased effectiveness owing to the emergence of resistance. Beyond insecticides, other mosquito-control strategies will probably encounter similar resistance issues. These include methods that rely on mosquito killing, such as mosquitocidal drugs[11], and genetic systems designed to suppress *Anopheles* populations (reviewed in ref. 12).

It is possible that the combined use of multiple strategies will break mosquito endurance and lead to population collapse. However, work from my group recently showed that strong selective pressures imposed on *Anopheles* females could actually favour malaria transmission, for instance by triggering acceleration of parasite growth rates[13]. To avoid this issue, mosquito-targeting interventions could be integrated with approaches that block parasite development in the insects without causing them harm, thus reducing selective pressures. Furthermore, mathematical models suggest that our chances of achieving sustainable malaria control could be improved by incorporating antimalarials into LLINs or indoor residual sprays, to kill parasites and prevent their transmission even when mosquitoes become resistant to insecticides[14]. Similar results could be obtained by delivering antiparasitic agents through biological or genetic means[12].

Whatever the eventual solution, the road to malaria elimination remains long. Mosquitoes are sending clear signals that they will fight for their survival.

Flaminia Catteruccia is in the Department of Immunology and Infectious Diseases, Harvard T.H. Chan School of Public Health, Boston, Massachusetts 02115, USA.
e-mail: fcatter@hsph.harvard.edu

1. Bhatt, S. *et al. Nature* **526**, 207–211 (2015).
2. Ranson, H. & Lissenden, N. *Trends Parasitol.* **32**, 187–196 (2016).
3. Ingham, V. A. *et al. Nature* **577**, 376–380 (2020).
4. Martinez-Torres, D. *et al. Insect Mol. Biol.* **7**, 179–184 (1998).
5. Stevenson, B. J. *et al. Insect Biochem. Mol. Biol.* **41**, 492–502 (2011).
6. Churcher, T. S., Lissenden, N., Griffin, J. T., Worrall, E. & Ranson, H. *eLife* **5**, e16090 (2016).
7. Protopopoff, N. *et al. Lancet* **391**, 1577–1588 (2018).
8. Neafsey, D. E. *et al. Science* **347**, 1258522 (2015).
9. N'Guessan, R., Odjo, A., Ngufor, C., Malone, D. & Rowland, M. *PLoS ONE* **11**, e0165925 (2016).
10. Qualls, W. A. *et al. Malar. J.* **14**, 301 (2015).
11. Kobylinski, K. C. *et al. Acta Trop.* **116**, 119–126 (2010).
12. Shaw, W. R. & Catteruccia, F. *Nature Microbiol.* **4**, 20–34 (2019).
13. Werling, K. *et al. Cell* **177**, 315–325 (2019).
14. Paton, D. G. *et al. Nature* **567**, 239–243 (2019).

This article was published online on 25 December 2019.

Nanotechnology

Evolution of circuits for machine learning

Cyrus F. Hirjibehedin

The fundamental machine-learning task of classification can be difficult to achieve directly in ordinary computing hardware. Unconventional silicon-based electrical circuits can be evolved to accomplish this task. **See p.341**

Artificial intelligence (AI) has allowed computers to solve problems that were previously thought to be beyond their capabilities, from defeating the best human opponents in complex games[1] to automating the identification of diseases[2]. There is therefore great interest in developing specialized circuits that can complete AI calculations faster and with lower energy consumption than can current devices. On page 341, Chen *et al.*[3] demonstrate an unconventional electrical circuit in silicon that can be evolved *in situ* to carry out basic machine-learning operations.

Although computers excel at performing calculations that have well-defined answers, they have not been good at making guesses. For example, if you are thinking about selling your car, a computer is ideally suited for calculating the average price that similar cars have sold for, to help you determine your selling price. But by analysing the enormous digital data sets that are currently available, AI techniques such as machine learning can now teach computers to make sensible predictions. One of the most basic operations that machine-learning algorithms can carry out when provided with a large set of inputs (such as the age of a car and how many kilometres it has been driven) is classification into one of a set of categories, such as whether the car is in poor, fair or good condition and therefore whether you can expect to get the price you want for it.

Using the structure of the human brain as inspiration, scientists and engineers have made substantial progress in developing specialized hardware to greatly reduce the amount of time and energy needed to perform tasks such as classification[4]. There are also many unconventional device concepts for machine learning that are still in the early stages of development but that could offer radical new capabilities. For example, researchers are exploring whether superconductor-based electrical circuits that work at only a few degrees above absolute zero, and that operate at gigahertz frequencies with high energy efficiency, could enable machine-learning applications that are currently infeasible using conventional approaches[5].

Chen and co-workers' circuit is also inspired by the brain, and represents a major departure from typical electrical circuits. Normally, electrical current flows through circuits like water flowing in a river. If the river becomes so shallow that it is reduced to a set of small

© 2020 Springer Nature Limited. All rights reserved.

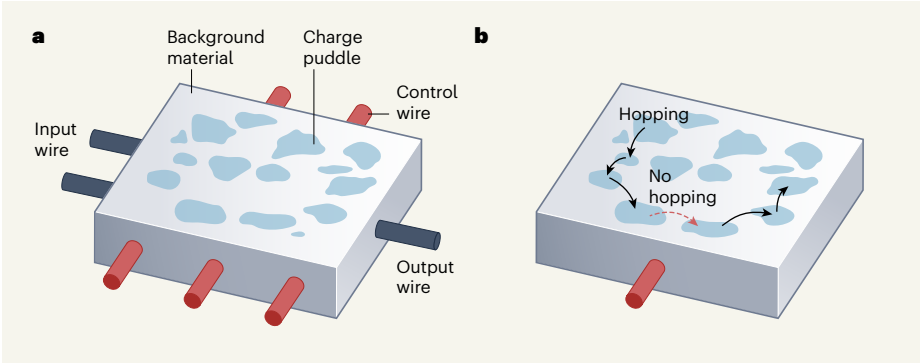


Figure 1 | An unconventional circuit for machine learning. a, Chen *et al.*[3] demonstrate an electrical circuit in which charge hops between 'puddles' of charge in a background material. The operation of the circuit is tuned by applying voltages to control wires. Inputs to the circuit are provided by voltages on input wires, and the circuit's output is determined by whether or not charge flows through an output wire. **b**, The control wires modify the regions of the circuit in which charge hopping can occur, thereby modifying which hopping paths can exist. An example of the effect produced by changing the voltage for a single control wire is shown here. The authors use their circuit to carry out basic machine-learning operations.

puddles, the water can no longer flow because the puddles are isolated from each other by barriers formed by the riverbed.

Although the barriers between water puddles are too wide for a water molecule to hop from one puddle to the next, this is not the case for electrical charge in 'puddles' of charge separated by nanoscale distances. Tools such as scanning tunnelling microscopes use the high sensitivity of a hopping process called quantum-mechanical tunnelling to routinely image features as small as individual atoms on surfaces[6]. This tunnelling is also at the heart of quantum-computing technologies that have made impressive advances in the past decade[7].

Previous work by some of the current authors[8] produced isolated charge puddles from a collection of gold nanoparticles that were randomly deposited on a silicon surface, with insulating molecules between them. These puddles were used to implement circuits that carried out conventional calculations, rather than machine learning, and are at the heart of Chen and colleagues' circuit design (Fig. 1a). Information is input into such a circuit through electrical voltages that are applied using ordinary wires. The electric fields from these wires can alter whether or not hopping between neighbouring puddles can occur, and therefore can modify the hopping path for electrical charge through the circuit (Fig. 1b). The output of the circuit is determined by whether or not electrical current flows through another designated wire.

Because the distribution of charge puddles is random, it would seem impossible to predict how such a circuit would behave. However, the high sensitivity of tunnelling makes it possible to strongly modify the behaviour of the circuit using different control wires. This behaviour also cannot be easily predicted, but the previous work showed that configurations could be reliably found that carried out logic operations for two inputs, such as indicating whether at least one or both of the inputs were on (called an OR gate and an AND gate, respectively, in binary logic).

Although these earlier circuits did not perform machine-learning operations, the researchers did use a machine-learning algorithm to determine the control parameters needed to make the circuits carry out different operations. This algorithm is inspired by biological evolution, starting from a set of random control parameters and using only the most promising outcomes to 'breed' new parameter sets for successive generations. The previous study was groundbreaking because it showed that a single circuit could be reprogrammed *in situ* to execute any two-input logic operation by simply changing the voltages applied to five control wires.

In the present work, Chen *et al.* greatly expanded this basic idea by overcoming some of its key limitations and using the circuits to perform AI operations. First, the authors found a way to produce charge puddles directly in silicon by randomly implanting atoms that donate small amounts of charge to the silicon itself. This method makes the devices more broadly manufacturable than they previously were and potentially compatible with the current generation of electronics, which are also mainly based on silicon. Second, in this new material system, the maximum temperatures at which hopping dominates the electrical flow in these circuits, and therefore at which the desired operation is viable, is increased from barely above absolute zero to room temperature.

To demonstrate the increased potential of these devices, Chen *et al.* evolved circuits that could classify all 16 possible sets of 4 binary inputs (0000, 0001, …, 1111, where 0 represents no input on a given wire and 1 represents an input on a given wire). This classification was possible even when the number of control voltages was reduced from five to three.

The authors then incorporated this *in silico* 4-input classifier into the more complex AI task of classifying a standard set of black and white images of handwritten digits, which were encoded as a 28 × 28 array of pixels, each with a value of either 0 (white) or 1 (black) (see Fig. 4 of the paper[3]). To do this, Chen *et al.* subdivided the original array into sets of 2 × 2 neighbouring pixels and fed the value of each of these 4 pixels into the 4-input classifier's input wires. The authors then set the control wires to perform classification for each of the 16 possible sets of 4 inputs, and passed all 16 outputs for each set of 2 × 2 pixels to a machine-learning algorithm run on conventional hardware that identified the digit in the full image.

Chen and colleagues' hardware platform for classification is inherently scalable, and individual classifier devices can be run in parallel without any conflicts. In the current incarnation of the platform, the set-up used to perform the measurements limits the speed at which the classifiers can be operated and, in turn, the energy efficiency. The authors suggest alternative ways in which the measurements could be implemented to greatly improve the speed and energy efficiency of the circuits; demonstrating such improvement will be crucial if these designs are to move from the research laboratory to real-world applications.

Because the random distribution of charge puddles in both the previous and current designs is difficult to model, the circuits' high sensitivity to the control voltages is essential for evolving a set of control parameters after fabrication. Although the absence of the need to precisely position the puddles makes the circuits easier to fabricate, their performance might be further enhanced by having predefined, atomically precise arrangements of the individual impurity atoms that donate charge to the silicon[9]. Such enhancements could include reproducibility of control parameters for different devices, improved reliability of operation at higher temperatures and reduced energy consumption.

Cyrus F. Hirjibehedin is in the Quantum Information and Integrated Nanosystems group, Lincoln Laboratory, Massachusetts Institute of Technology, Lexington, Massachusetts 02421, USA.
e-mail: cyrus.hirjibehedin@ll.mit.edu

1. Silver, D. *et al. Nature* **529**, 484–489 (2016).
2. Liu, X. *et al. Lancet Dig. Health* **1**, e271–e297 (2019).
3. Chen, T. *et al. Nature* **577**, 341–345 (2020).
4. Merolla, P. A. *et al. Science* **345**, 668–673 (2014).
5. Day, A., Wynn, A. & Golden, E. *APS March Meet. 2020* abstr. L48.00008 (2020); go.nature.com/2ti4zt1
6. Binnig, G., Rohrer, H., Gerber, Ch. & Weibel, E. *Phys. Rev. Lett.* **50**, 120–123 (1983).
7. Arute, F. *et al. Nature* **574**, 505–510 (2019).
8. Bose, S. K. *et al. Nature Nanotechnol.* **10**, 1048–1052 (2015).
9. Schofield, S. R. *et al. Phys. Rev. Lett.* **91**, 136104 (2003).

© 2020 Springer Nature Limited. All rights reserved.

Alzheimer's disease

T cells make a home in the degenerating brain

Michael T. Heneka

A subpopulation of adaptive immune cells patrols the brain and cerebrospinal fluid in people who have Alzheimer's disease. This discovery should broaden our understanding of how the immune system can influence neurodegeneration. **See p.399**

For decades, research into Alzheimer's disease has centred on neurons. Only in the past few years have scientists identified a role for immune cells in the progression of this neurodegenerative disorder[1]. Most research has focused on the nonspecific, innate branch of the immune system. But Gate *et al.*[2] report on page 399 that an immune-cell subpopulation belonging to the adaptive immune system – which remembers and responds to specific foreign invaders – might also have a role in Alzheimer's disease.

The authors isolated and analysed immune cells from the blood of healthy people and people who had Alzheimer's disease or a precursor of the disease known as mild cognitive impairment (MCI). They discovered an immune-cell subpopulation called $CD8^+$ T effector memory $CD45RA^+$ (T_{EMRA}) cells that was associated with MCI and Alzheimer's disease. T_{EMRA} cells have previously been linked to immunological memory, and they release inflammatory and cytotoxic (cell-death-promoting) molecules[3].

Analysis of a separate cohort of people who had Alzheimer's disease revealed that an increased presence of T_{EMRA} cells in the blood was associated with compromised cognitive performance. This finding could indicate that T_{EMRA} cells contribute to neuronal dysfunction by secreting inflammatory and cytotoxic molecules in the brain (Fig. 1). Alternatively, a damaging mechanism that causes cognitive dysfunction might also elicit an inflammatory T_{EMRA}-cell response in the blood.

Gate *et al.* corroborated their findings *in vitro*, showing that stimulation with an inflammatory molecule caused immune cells from people who had MCI or Alzheimer's disease to release more interferon-γ (a key pro-inflammatory protein) than did immune cells from people who did not have these conditions. This is consistent with another study[4], which demonstrated that T cells derived from people who have Alzheimer's disease become more active than do those from healthy people when exposed to β-amyloid, a protein associated with this disorder.

The authors then asked whether the presence of T_{EMRA} cells could be used to predict disease status. Indeed, a machine-learning algorithm could use measurements of T_{EMRA} cells (together with information about other immune-cell populations) to distinguish between healthy people and those with MCI or Alzheimer's disease with about 80% accuracy. Many immune processes alter during ageing and so are of limited use for predictive clinical testing, but age did not influence the level of T_{EMRA} cells. This type of technique, once refined, might therefore be used alongside biomarkers of neuronal damage and degeneration for blood-based diagnostic tests, improving our ability to detect Alzheimer's disease at an early stage.

> **"This is perhaps the first evidence that clonally expanded T cells invade the cerebrospinal fluid in age-related neurodegenerative diseases."**

Next, Gate and colleagues analysed the brains of people who had died with Alzheimer's disease. This revealed $CD8^+$ T cells (which might be T_{EMRA} cells) in the perivascular space around the brain's blood vessels, and at sites of β-amyloid deposition, as previously reported for T cells in Alzheimer's disease[5,6]. $CD8^+$ T cells are known to physically contact and sever neuronal processes, causing structures called neuritic spheroids to form nearby – another hallmark of Alzheimer's disease[7]. Thus, it is conceivable that T_{EMRA} cells contribute to neuronal damage not only by secreting immune molecules, but also by directly damaging neuronal processes[7].

MCI and Alzheimer's disease are associated with changes in the number and proportion of T cells in the cerebrospinal fluid (CSF) that surrounds the brain and spinal cord[8,9]. The investigators therefore asked whether T_{EMRA} cells were found in the CSF and whether there was evidence of 'clonal expansion' of this cellular subpopulation. Naive T cells each have different T cell receptor (TCR) proteins, but when the receptor is stimulated by a particle called an antigen, the cell proliferates to form clones of itself. The presence of more than one cell with the same TCR therefore indicates clonal expansion – a sign that T cells have been activated previously. The authors sequenced TCRs from an independent cohort of people and identified several T-cell clones, including

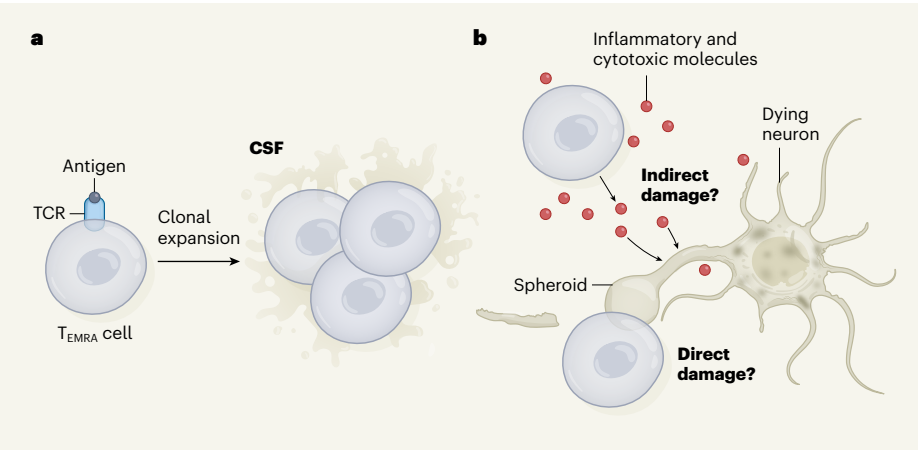


Figure 1 | T_{EMRA} cells and age-related neurodegeneration. Gate *et al.*[2] report that the presence of immune cells called $CD8^+$ T effector memory $CD45RA^+$ (T_{EMRA}) cells in the brain is associated with Alzheimer's disease. **a**, Evidence from a few people suggests that the cells are activated by binding between the T-cell receptor (TCR) and an antigen molecule (which can be from a host cell or a foreign invader). The cells then proliferate to produce an expanded pool of T_{EMRA}-cell clones. The cells patrol the cerebrospinal fluid (CSF). **b**, T_{EMRA} cells might promote neuronal damage indirectly, by releasing inflammatory and cytotoxic (death-promoting) molecules, or directly, by physically interacting with and severing neuronal processes, causing the formation of structures called spheroids that are associated with Alzheimer's disease. Alternatively, they might have no role in disease progression (not shown).

© 2020 Springer Nature Limited. All rights reserved.

T_{EMRA} cells, in people with Alzheimer's disease. This is perhaps the first evidence that clonally expanded T cells invade the CSF in age-related neurodegenerative diseases.

Gate *et al.* then validated their result using gene-expression analysis. This revealed that the T_{EMRA}-cell population was the predominantly expanded T-cell clone in each person who had Alzheimer's disease. The population expressed various cytotoxic genes, and was enriched in the hippocampus — a brain region crucial for human memory. In line with this observation, hippocampal T-cell infiltration promotes cognitive decline in a mouse model of Alzheimer's disease[10]. The authors also found evidence for T_{EMRA}-cell clones and gene-expression changes in the CSF of people who had another neurodegenerative disorder, Parkinson's disease, highlighting the possibility that different age-related neurodegenerative diseases share similar molecular underpinnings.

Which antigens drive clonal expansion of T_{EMRA} cells? By comparing TCR sequences from people who had MCI and Alzheimer's disease, the investigators found evidence that clonally expanded T_{EMRA} cells had been bound by two antigens produced by a virus of the herpes family, Epstein–Barr virus (EBV). However, it is important to note that a role for EBV infection in neurodegeneration has not yet been reported, and Gate *et al.* make no suggestion that EBV is involved in the development of Alzheimer's disease.

Gate and colleagues' data involve only a few patients and should be interpreted with great care, particularly given that EBV infects about 95% of people during early life[11]. Previous work[12] has shown a complex relationship between herpes viruses and Alzheimer's disease in mice. One the one hand, β-amyloid fibres can entrap herpes viruses, extending survival in mouse models of Alzheimer's disease. But on the other hand, virus infection strongly increases β-amyloid deposition in these animals.

In addition, a study[11] of 85 people who had Alzheimer's disease found evidence of EBV DNA in the brains of only 6% of cases. All of these people carried the gene *APOE4*, which is associated with a high risk of Alzheimer's disease and could explain why they developed the disorder. The same study did find that antibody responses against EBV increased during cognitive deterioration and progression of Alzheimer's disease[11]. However, these responses are quite common in older people. Moreover, a recent meta-analysis found no correlation between herpes-virus infection and dementia[13]. Longitudinal studies involving many more people will be needed before solid conclusions can be drawn.

It will be interesting to reconcile Gate and colleagues' data with the finding[14] that T cells can restrain cognitive deficits in mouse models of Alzheimer's disease. Analysis of less-prominent T-cell clones in people with and without disease might reveal other, potentially harmful — or even protective — subclones. In addition, the current study will no doubt renew efforts to define the cross-talk between innate and adaptive immunity in general, as well as in neurodegeneration. Perhaps, in the future, these interactions could be harnessed for diagnostic purposes or to develop therapeutic interventions.

Michael T. Heneka is in the Department of Neurodegenerative Diseases and Geriatric Psychiatry, University of Bonn Medical Center, and at the German Center for Neurodegenerative Disease, Bonn 53127, Germany.
e-mail: michael.heneka@ukbonn.de

1. Labzin, L. I., Heneka, M. T. & Latz, E. *Annu. Rev. Med.* **69**, 437–449 (2018).
2. Gate, D. *et al. Nature* **577**, 399–404 (2020).
3. Sallusto, F., Geginat, J. & Lanzavecchia, A. *Annu. Rev. Immunol.* **22**, 745–763 (2004).
4. Monsonego, A. *et al. J. Clin. Invest.* **112**, 415–422 (2003).
5. Togo, T. *et al. J. Neuroimmunol.* **124**, 83–92 (2002).
6. Town, T., Tan, J., Flavell, R. A. & Mullan, M. *Neuromol. Med.* **7**, 255–264 (2005).
7. Medana, I., Martinic, M. A., Wekerle, H. & Neumann, H. *Am. J. Pathol.* **159**, 809–815 (2001).
8. Monson, N. L. *et al. J. Cereb. Blood Flow Metab.* **34**, 30–33 (2014).
9. Lueg, G. *et al. Neurobiol. Aging* **36**, 81–89 (2015).
10. Laurent, C. *et al. Brain* **140**, 184–200 (2017).
11. Carbone, I. *et al. Neurobiol. Aging* **35**, 122–129 (2014).
12. Eimer, W. A. *et al. Neuron* **99**, 56–63.e3 (2018).
13. Warren-Gash, C. *et al. Sci. Rep.* **9**, 4743 (2019).
14. Dansokho, C. *et al. Brain* **139**, 1237–1251 (2016).

This article was published online on 8 January 2020.

Cardiovascular biology

Platelets have a hold over immune cells

Filip K. Swirski

Plaques are lipid-rich structures in the blood-vessel wall that can cause heart attacks or strokes if they rupture. It now seems that blood-cell fragments called platelets alter the function of immune cells in ways that accelerate plaque formation.

Heart attacks or strokes might seem to be sudden events, but they are the consequences of a condition called atherosclerosis, which can be decades in the making. Atherosclerosis involves the accumulation of lipids and immune cells into structures called plaques in the blood-vessel wall. If these plaques become unstable they can rupture, blocking blood flow and so depriving tissues such as the heart and brain of oxygen, respectively triggering a heart attack or a stroke. Identifying precisely how plaques grow at cellular and molecular scales is therefore crucial for understanding and so treating atherosclerosis. Writing in *Science Translational Medicine*, Barrett *et al.*[1] enrich our thinking about how atherosclerosis evolves, providing evidence that platelets in the blood promote the formation of bigger, more dangerous plaques by shaping the function of immune cells.

Monocytes are a class of short-lived immune cell crucial to host defence. They survey their environment, patrolling the vasculature and frequently migrating in and out of the blood to scout for injuries or infections. This movement is aided by endothelial cells, which demarcate the border between blood and tissue, and which produce a panoply of monocyte-attracting chemical messengers, enabling monocyte surveillance of and migration across the blood-vessel wall. Platelets — blood-cell fragments best known for making blood clots — likewise help monocytes to infiltrate the vessel wall by adhering to the cells to form monocyte–platelet aggregates. Precisely how such aggregates promote migration is not clear, but it is known that platelets can deliver a variety of mediators to which monocytes can respond[2].

Because of their role in monitoring the vasculature, monocytes are key to the development of atherosclerosis. Voracious eaters, they ingest lipids that accrue in plaques, before morphing into larger, less agile macrophages. As this transformation occurs, the cells can wreak inflammatory havoc, contributing to a feed-forward loop that generates bigger, rupture-prone plaques[3]. But because monocytes are crucial for host defence, eliminating them entirely is not therapeutically viable. Identifying and blocking factors involved in monocyte recruitment to plaques might, however, be an alternative strategy.

Barrett and colleagues investigated interactions between platelets, monocytes and their descendent macrophages in mice that have abnormally high levels of cholesterol — a risk factor for atherosclerosis. They observed that platelets adhere to monocytes in blood more readily when mice have high cholesterol levels, bolstering the idea that monocyte–platelet

© 2020 Springer Nature Limited. All rights reserved.

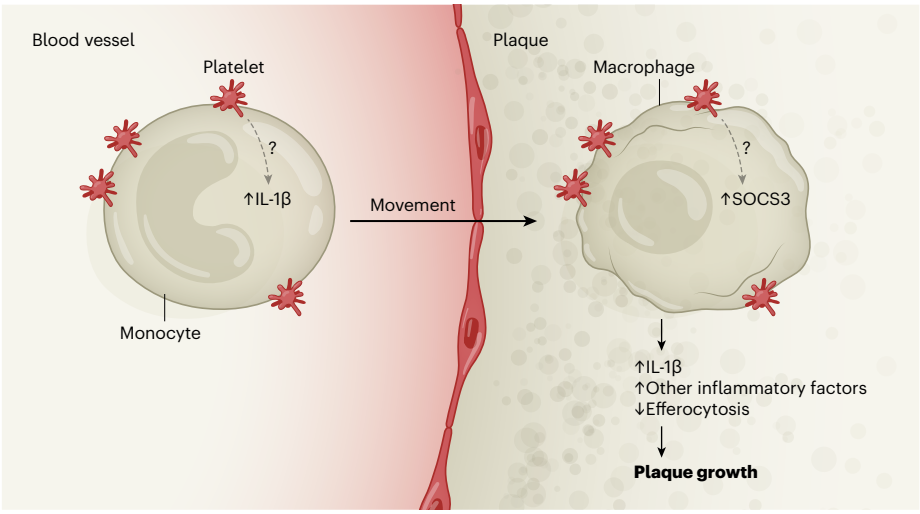


Figure 1 | How platelets might promote plaques. Atherosclerosis is a condition in which immune cells and lipids aggregate in structures called plaques in the blood-vessel wall. Barrett *et al.*[1] provide evidence for a model in which blood-cell fragments called platelets promote plaque build-up in mice that have high cholesterol levels. In this model, platelets adhere to immune cells called monocytes, and promote (through an unknown mechanism) both production of inflammatory signalling molecules such as interleukin-1β (IL-1β) and movement to plaques. In plaques, monocytes ingest lipids and transform into macrophage cells. Platelets promote expression of SOCS3, a protein that induces macrophages to adopt inflammatory characteristics. The cells then secrete high levels of IL-1β and other inflammatory factors, and have a low capacity to ingest dying cells through efferocytosis. Together, these factors promote plaque growth.

aggregates augment monocyte recruitment to growing plaques. In parallel, the authors performed single-cell RNA sequencing of immune cells retrieved from plaques, and found an increase in platelet-specific factor Pf4 on macrophages, suggesting that platelet adherence persisted beyond monocyte recruitment. Platelets, it seemed, were also aggregating with macrophages.

This liaison spells trouble. The group used specific antibodies to deplete platelets in a genetically engineered strain of mouse susceptible to atherosclerosis, and compared the macrophages of these animals with those of counterparts that had not received platelet-depleting antibodies. Single-cell RNA sequencing revealed that exposure to platelets triggers increased production and release of plaque-enhancing inflammatory molecules by macrophages. Interleukin-1β is one such mediator — and, indeed, therapeutic blockade of this protein in humans attenuates cardiovascular disease[4].

Next, Barrett *et al.* provided further evidence that the presence of platelets accelerates plaque growth. In addition to inducing inflammatory-molecule production, platelets impaired macrophages' capacity to ingest dying cells through efferocytosis, increasing the number of undigested dying cells in plaques — a phenomenon that increases the likelihood of plaque rupture. Thus, platelets promote atherosclerosis by fostering monocyte recruitment to plaques and by reprogramming macrophage function (Fig. 1).

The authors next investigated the factors that govern the switch in macrophage function. Two transcription factors, suppressor of cytokine signalling 1 (SOCS1) and SOCS3, are known to influence macrophage behaviour[5]. Specifically, a low ratio of SOCS1 to SOCS3 triggers gene-expression patterns that lead to inflammatory characteristics, whereas a high ratio prompts tissue-repairing traits. The team found that macrophages taken from plaques in platelet-depleted mice had a higher SOCS1:SOCS3 ratio than did macrophages from untreated animals, indicating that platelets somehow alter this pathway in macrophages to trigger inflammatory characteristics.

Finally, Barrett *et al.* asked whether their findings might be applicable to humans. They found that, in a group of women, the platelet count — and expression of genes that encode SOCS3 and interleukin-1β — was higher in those who had had a heart attack than in those who had not had one. Moreover, the authors report an inverse relationship between the SOCS1:SOCS3 ratio and markers of platelet activation in people with peripheral-artery disease. Thus, this mechanism is potentially relevant to human disease.

Barrett and colleagues' results are intriguing. Platelet blood-clotting ability serves an essential function in wound healing, but it can be detrimental in the wrong context. Blood-thinning, anti-clot drugs, such as clopidogrel or aspirin, have well-documented therapeutic effects in preventing blood clots. The current study suggests that blocking platelets might have collateral antiatherosclerotic benefits, which aligns with previous work[6].

Of course, many questions remain. For instance, it is unclear precisely how platelets foster monocyte recruitment and how they reprogram macrophages. There are clues to be found in other work, given that platelets are a source of various immune mediators[2,7]. Barrett *et al.* suggest that platelets stimulate macrophages by releasing the protein S100A9, which triggers the inflammatory TLR signalling pathway in macrophages, but this possibility requires further exploration. Another question is whether distinct types of platelet have evolved for specialized cell communication. In support of this idea, research[8] suggests that large platelet-producing cells called megakaryocytes, which reside in different locations, have differing functions. Finally, it will be important to know whether all macrophages are equally affected by platelet instruction, or whether the partnership is specific to certain stages of development, anatomical locations or times.

The authors caution against drawing sweeping conclusions, and, indeed, there are caveats to the study that should be considered. For instance, it would be useful to reduce platelet levels by approaches other than the anti-CD42b antibody used here. This antibody is expected to deplete platelets only transiently, and it might have collateral, unforeseen effects. In addition, it would be valuable to visualize the aggregates *in vivo*, perhaps using electron microscopy, to obtain a clear picture of what a macrophage–platelet aggregate really looks like. Finally, future work will need to determine whether this phenomenon occurs broadly in other situations involving monocyte recruitment and consequent macrophage activity, for instance in infected or injured tissue.

Nevertheless, the study builds on a long line of work implicating platelets, monocytes and macrophages as key contributors to atherosclerosis. The conceptual power of exploring how immune and blood-clotting pathways intersect, the insights into monocyte and macrophage function, and the corroborating human data, are all worthy of further exploration.

Filip K. Swirski is in the Center for Systems Biology, Massachusetts General Hospital, Boston, Massachusetts 02114, USA, and in the Department of Radiology, Harvard Medical School, Boston.
e-mail: fswirski@mgh.harvard.edu

1. Barrett, T. J. *et al. Sci. Transl. Med.* **11**, eaax0481 (2019).
2. Morrell, C. N., Aggrey, A. A., Chapman, L. M. & Modjeski, K. L. *Blood* **123**, 2759–2767 (2014).
3. Swirski, F. K. & Nahrendorf, M. *Science* **339**, 161–166 (2013).
4. Ridker, P. M. *et al. N. Engl. J. Med.* **377**, 1119–1131 (2017).
5. Wilson, H. M. *Front. Immunol.* **5**, 357 (2014).
6. Heim, C. *et al. Heart Vessels* **31**, 783–794 (2016).
7. Hilt, Z. T. *et al. JCI Insight* **4**, e122943 (2019).
8. Lefrançais, E. *et al. Nature* **544**, 105–109 (2017).

This article was published online on 9 December 2019.

© 2020 Springer Nature Limited. All rights reserved.

Materials science

Transparent crystals with ultrahigh piezoelectricity

Jurij Koruza

It has been difficult to make transparent materials that have extremely high piezoelectricity — a useful property related to the coupling of electric fields and mechanical strain. This hurdle has now been overcome. See p.350

Piezoelectric materials show high electromechanical coupling, which means that they can generate large strains if an electric field is applied to them, and can transform external mechanical stimuli into electric charge or voltage[1]. They are widely used in electronic applications, including sensors, small motors and actuators — devices that convert electrical energy into movement. In addition, their high energy efficiency and ease of miniaturization are driving the development of new technologies, such as energy harvesters for the growing network of Internet-connected devices known as the Internet of Things, actuators for touch screens and microrobots. On page 350, Qiu *et al.*[2] report the preparation of high-performance piezoelectrics that have the long-desired property of near-perfect transparency to light. This breakthrough could lead to devices that combine excellent piezoelectricity with tunable optical properties.

Most high-performance piezoelectrics are ferroelectrics — materials that have a spontaneous electric polarization that can be reversed by the application of an external electric field. At the atomic level, ferroelectrics have a local polarization that is caused by the displacements of certain ions from their symmetric positions. Regions that have a uniform direction of polarization are referred to as ferroelectric domains and are separated by boundaries called domain walls. The material's crystal structure determines the possible directions of polarization and, in turn, the types of domain wall. For example, a rhombohedral crystal structure enables 8 possible domain variants and 71°, 109° and 180° domain walls (where the angle refers to the difference in polarization direction between the domains separated by the wall).

For these ferroelectrics to be used as piezoelectrics, they must first undergo a process known as poling, in which an external electric field is applied to the material to reorient unfavourably oriented domains and induce macroscopic polarization. Poled ferroelectrics show a large electromechanical response to an external electric field or to mechanical force, and this response is typically characterized by a quantity dubbed the piezoelectric coefficient. The magnitude of this coefficient depends to a large extent on the domain configuration; the other major contribution comes from the crystal lattice. Some of the largest coefficients known today were reported[3,4] for ferroelectric crystals based on lead magnesium niobate–lead titanate (PMN-PT). These crystals have piezoelectric coefficients above 1,500 picocoulombs per newton (pC N^{-1}), which is about ten times higher than those of most other ferroelectrics.

The poling process is conventionally carried out using direct-current (d.c.) electric fields. In rhombohedral PMN-PT crystals that are [001] oriented (a particular crystallographic orientation), d.c. poling results in the removal of 180° domain walls and the formation of a laminar (layered) domain structure consisting of 71° and 109° walls (Fig. 1a). When light propagates through such a structure, the difference between the refractive indices at each side of an encountered 71° wall induces scattering, resulting in the poled crystal having an overall opaque appearance. The 109° walls in this configuration, however, do not give rise to scattering.

Qiu and colleagues exploited this difference in light scattering between 71° and 109° domain walls. The authors simulated the evolution of domains in [001]-oriented rhombohedral PMN-PT crystals that were subjected to either d.c. or alternating-current (a.c.) electric fields. These simulations showed that the application of an a.c. poling field (a method reported only in the past few years[5,6]), instead of a d.c. one, greatly reduces the number of 71° domain walls (Fig. 1b). Qiu *et al.* attributed this effect to a process referred to as domain swinging, whereby the 71° walls alternate between two crystallographic planes and tend to merge, thereby decreasing their number. The 109° walls, by contrast, remain almost unaffected by the a.c.-poling process.

The authors then compared their simulation results with d.c.- and a.c.-poled [001]-oriented rhombohedral PMN-PT crystals that had been

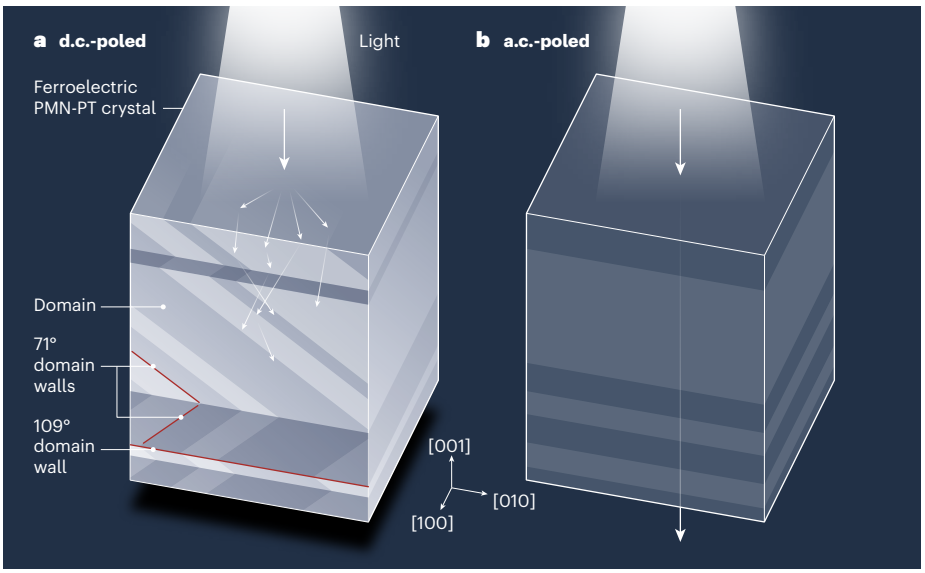


Figure 1 | Near-perfect light transmittance in a high-performance piezoelectric. a, Materials known as ferroelectrics contain regions of uniform electric polarization called domains (the different shades represent different orientations of polarization). These domains are separated by boundaries dubbed domain walls. When [001]-oriented rhombohedral ferroelectric crystals of lead magnesium niobate–lead titanate (PMN-PT) undergo a process called poling using direct-current (d.c.) electric fields, they contain both 71° and 109° domain walls (where the angle indicates the difference in polarization orientation between the domains separated by the wall). The 71° walls cause incident light to be scattered, such that the crystals are opaque. **b**, Qiu *et al.*[2] demonstrate that, when the poling is carried out using alternating-current (a.c.) electric fields, the number of 71° domain walls is greatly reduced. The crystals show near-perfect light transmittance and ultrahigh piezoelectricity — a property associated with the coupling of electric fields and mechanical strain.

© 2020 Springer Nature Limited. All rights reserved.

grown by a modified version of a widely used approach called the Bridgman method. They studied the domain structure of the crystals using three techniques (high-resolution X-ray diffraction, polarized-light microscopy and birefringence imaging spectroscopy), and confirmed the removal of 71° domain walls throughout the a.c.-poled samples. These samples exhibited near-perfect light transmittance, large birefringence (an effect in which a material's refractive indices are different along different axes) and ultrahigh piezoelectric coefficients, exceeding 2,100 pC N^{-1}. For comparison, ferroelectrics that have a similar level of transparency to these crystals, such as lithium niobate or polyvinylidine fluoride, typically have piezoelectric coefficients[1] of less than 40 pC N^{-1}.

The report by Qiu *et al.* adds the optical component to high-performance piezoelectric crystals and therefore opens the door to the design of electro-optical-mechanical devices. Transparent actuators or motors could be used for touch screens in consumer electronics or for the development of invisible microrobots. Moreover, the crystals' high electromechanical performance and transparency could be harnessed in an imaging technology known as photoacoustic imaging or in piezoelectric light guides.

"Transparent actuators or motors could be used for touch screens or for the development of invisible microrobots."

Although the authors demonstrated the applicability of their approach to several PMN-based crystals, it remains to be seen whether similar principles can be applied to other ferroelectric systems. Of particular interest are systems that remain polarized at high temperatures (above 100–150 °C), unlike PMN-based materials. Nevertheless, Qiu and colleagues' discovery has arrived just in time to meet the growing demand for multitasking smart materials and hybrid devices.

Jurij Koruza is at the Institute of Materials Science, Technische Universität Darmstadt, 64287 Darmstadt, Germany.
e-mail: koruza@ceramics.tu-darmstadt.de

1. Heywang, W., Lubitz, K. & Wersing, W. (eds) *Piezoelectricity: Evolution and Future of a Technology* (Springer, 2008).
2. Qiu, C. *et al. Nature* **577**, 350–354 (2020).
3. Park, S.-E. & Shrout, T. R. *J. Appl. Phys.* **82**, 1804–1811 (1997).
4. Zhang, S. *et al. Prog. Mater. Sci.* **68**, 1–66 (2015).
5. Yamamoto, N., Yamashita, Y., Hosono, Y., Itsumi, K. & Higuchi, K. US Patent 2014/0062261 A1 (2014).
6. Yamashita, Y., Yamamoto, N., Hosono, Y. & Itsumi K. US Patent 2015/0372219 A1 (2015).



© 2020 Springer Nature Limited. All rights reserved.

The arms race between bacteria and their phage foes

https://doi.org/10.1038/s41586-019-1894-8

Received: 24 July 2019

Accepted: 13 November 2019

Published online: 15 January 2020

Hannah G. Hampton[1,3], Bridget N. J. Watson[1,2,3] & Peter C. Fineran[1]*

Bacteria are under immense evolutionary pressure from their viral invaders—bacteriophages. Bacteria have evolved numerous immune mechanisms, both innate and adaptive, to cope with this pressure. The discovery and exploitation of CRISPR–Cas systems have stimulated a resurgence in the identification and characterization of anti-phage mechanisms. Bacteriophages use an extensive battery of counter-defence strategies to co-exist in the presence of these diverse phage defence mechanisms. Understanding the dynamics of the interactions between these microorganisms has implications for phage-based therapies, microbial ecology and evolution, and the development of new biotechnological tools. Here we review the spectrum of anti-phage systems and highlight their evasion by bacteriophages.

Bacteriophages (phages) are viruses that infect bacteria and it has been estimated that there are 10^{31} phages present in the biosphere[1]. Their abundance accounts for 20–40% of bacterial mortality daily[2], and has a considerable impact on biogeochemical cycles[3]. The pressure of phage infection on bacteria has resulted in the evolution of multiple bacterial immune systems, each of which hampers different stages of the phage life cycle[4,5] (Fig. 1). Unsurprisingly, phages have evolved a myriad of ways to overcome these defences[5,6], which in combination with phage diversity, has contributed to the diversity of bacterial immune mechanisms.

Research interests in bacterial–phage interactions, and in particular bacterial defences, are manifold. First, although the importance of these interactions for global ecology is accepted, large sequencing efforts, such as the *Tara* Oceans project, are furthering our understanding by showing that phages drive rapid evolution through the daily transfer of approximately 10^{29} genes between bacteria[7]. Second, phage-based therapies are becoming feasible antibacterial treatments as alternatives to antibiotics, owing to the rise of antibiotic resistance[8]. For successful therapy, it is critical to understand how bacterial pathogens might become resistant to phages and, therefore, recalcitrant to treatment. Finally, phage-resistant strains are required in different industries[9] and fundamental research into phage-defence mechanisms has underpinned the development of these, and other, applications, such as gene editing and diagnostics[10]. The importance of bacterial immune systems to these areas has led to a resurgence in the discovery and characterization of phage-resistance mechanisms. Here we focus on the diverse systems that bacteria use to resist phages and how their phage invaders can evade these immune mechanisms.

Preventing adsorption

Phages exploit at least three different lifestyles to reproduce. Virulent phages replicate exclusively through the lytic cycle, exploiting bacteria to make new phages before their release by cell lysis[11] (Fig. 1). Alternatively, in addition to the lytic cycle, temperate phages can enter the lysogenic cycle and form prophages that are integrated into the bacterial chromosome or maintained extrachromosomally[1] (Fig. 1). By contrast, filamentous phages cause chronic infections and are continuously secreted from the bacterium without lysis[12]. For infection to occur, phages must adsorb to the cell surface by binding to phage receptors, and inject their genome (Fig. 2a). To prevent adsorption, bacteria can alter or disguise receptors through surface modification (Fig. 2a). For example, receptor mutations in *ompU* in *Vibrio cholerae* confer resistance to the vibriophage ICP2[13]. Bacteria can also use receptors as phage decoys. In this case, outer membrane vesicles (OMVs) that contain receptors bud off from *Escherichia coli* and *Vibrio*, and can bind to phages, reducing productive infections[14,15] (Fig. 2a). Nonetheless, OMVs have complex effects on phage dynamics because they can also extend the host range of phages. Indeed, phage receptors were transferred by OMVs to *Bacillus subtilis* cells that previously lacked the receptor, rendering *B. subtilis* and other phage-resistant species susceptible to phages[16] (Fig. 2b). Although this provides only transient susceptibility, the receptors may subsequently facilitate the transfer of receptor genes through generalized transduction, which could lead to a permanent heritable change in phage susceptibility. Inhibiting DNA entry into the bacterial cell is another defence strategy. For example, the Imm and Sp proteins of phage T4 prevent the DNA of other T-even phages from being translocated across the membrane[4]. However, systems that prevent DNA entry are typically encoded on prophages and inhibit infection by subsequent phages[4].

The fitness costs of receptor mutations have led to other strategies that impede attachment[5]. Phase variation enables the reversible expression of phage receptors, resulting in phage-resistant bacterial subpopulations[5,17]. Furthermore, receptors can be masked, preventing recognition while retaining function. For example, capsules or exopolysaccharides provide phage resistance in *Staphylococcus*, *Pseudomonas* and other species[18,19] (Fig. 2a). Subtle modifications can also disguise receptors from phages, such as in *Pseudomonas aeruginosa*, in which pilus and O-antigen modifications and type IV pili glycosylation occludes phages[20,21].

Receptor modification can select for phages that recognize the mutated, or alternative, receptors. In coevolution studies, it was shown

[1]Department of Microbiology and Immunology, University of Otago, Dunedin, New Zealand. [2]Environment and Sustainability Institute, Biosciences, University of Exeter, Cornwall Campus, Penryn, UK. [3]These authors contributed equally: Hannah G. Hampton, Bridget N. J. Watson. *e-mail: peter.fineran@otago.ac.nz

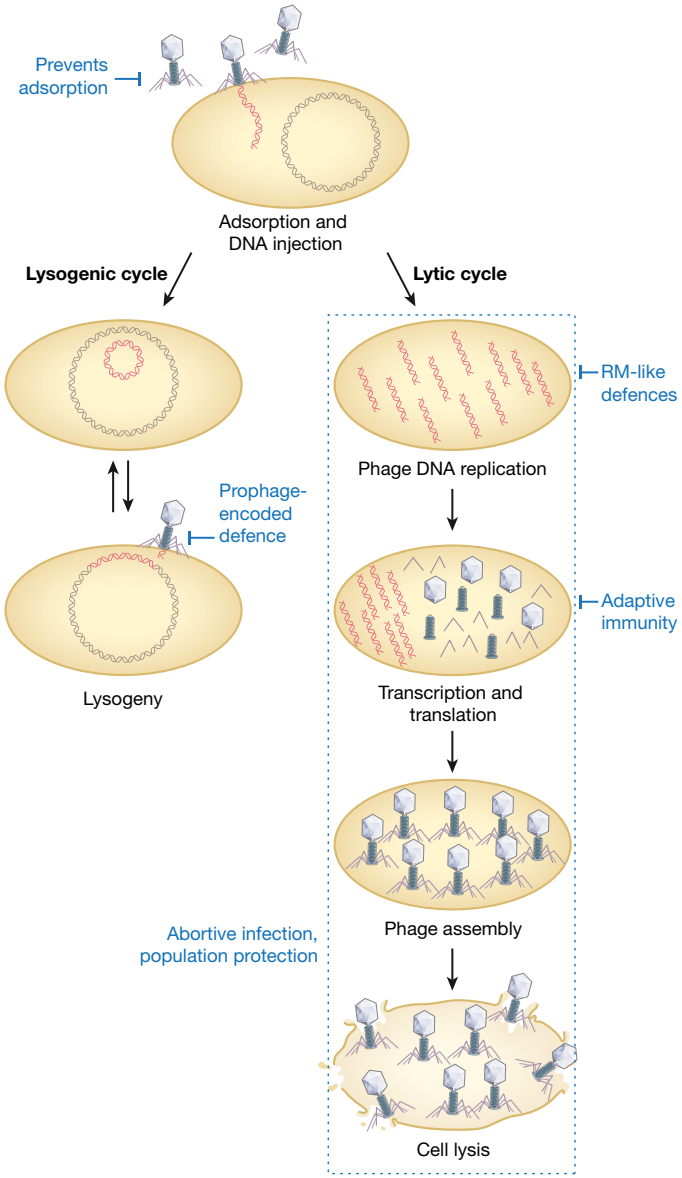


Fig. 1 | Anti-phage mechanisms act at different stages of the phage life cycle. Virulent phages replicate exclusively through the lytic cycle, whereas temperate phages may replicate through either the lytic or the lysogenic cycle. Bacteria have numerous anti-phage systems that function at different stages of the phage life cycle to prevent productive phage replication. Abortive infection mechanisms provide population protection and function at different stages of the phage life cycle, indicated by the blue dashed line.

that the receptor-binding proteins (RBPs) of phages—which bind to the bacterial receptors—are often mutated (Fig. 2b). For example, phage λ overcame a LamB receptor mutant of *E. coli* through tail fibre mutations, some of which caused stochastic protein folding into different forms that enabled the recognition of a new receptor (OmpF) or mutated LamB[22,23]. Access to a new receptor occurred through baseplate and tail fibre mutations in *B. subtilis* phage SPO1, which also resulted in an extended range of *Bacillus* hosts[24]. Instead of mutating, some phages—such as the *E. coli* phage phi92—have more than one RBP, enabling the recognition of multiple receptors[25]. RBP variability can be further expanded by diversity-generating retroelements that result in hypervariable RBPs. For example, the diversity-generating retroelement of the *Bordetella* phage BPP-1 creates variable tail fibres, changing the receptor tropism of the phage[4]. Finally, when receptors are masked by exopolysaccharide capsules, some phages produce depolymerases that enable them to gain access[26] (Fig. 2b). Recent research on receptor interactions is driven by the goal to understand and manipulate phage–receptor interactions to extend the host range for biotechnological and medical applications[27].

Restriction–modification and related defences

The biotechnological use of restriction–modification (RM) systems has led to these systems being the most well-characterized phage-resistance mechanism—they are highly diverse and ubiquitous, and are present in around 90% of bacterial genomes[28]. These systems distinguish self from non-self DNA to recognize and destroy phage DNA after its injection. Discrimination is due to DNA modifications at specific sequences and is characteristic of a number of anti-phage systems. Two components that are typically present in RM systems are a methyltransferase and a restriction endonuclease (Fig. 3a, b). Both recognize restriction-site sequences; the methyltransferase methylates DNA and the restriction endonuclease cleaves the unmethylated sequence. A comprehensive review of RM systems has been published previously[29]. A range of other phage-resistance systems have similarities to RM systems, but their functions appear to be more complex owing to the presence of additional genes.

One RM-like phage-defence mechanism is the phage growth limitation (Pgl) system in *Streptomyces coelicolor*, which modifies and cleaves phage DNA[30,31]. Pgl has three phases and requires four genes, *pglW*, *pglX*, *pglY* and *pglZ* (Fig. 3a, c). Phages become methylated after infecting Pgl$^+$ bacteria and, following release, these phages can infect other cells. During subsequent infections, the modified phage DNA is cleaved. Hence, although the initial infected cell does not survive phage infection, it is able to mark the phage to 'warn' neighbouring cells[31]. Genes similar to *pglZ* from the Pgl system were identified in six-gene clusters, including *brxABCL* and *pglX*[32] (Fig. 3a). These were termed bacteriophage exclusion (BREX) genes and have been characterized in Gram-positive (*B. subtilis*[32]) and Gram-negative (*E. coli*[33]) bacteria. Akin to RM, BREX acts after DNA injection to prevent phage replication and lysogen formation, but differs as DNA cleavage was undetectable[32]. BREX further differs from Pgl in that it restricts phages upon first exposure[32,33]; however, the precise mechanism by which BREX prevents infection remains unresolved.

Another RM-like system was recently identified—termed defence island associated with restriction–modification (DISARM)[34] (Fig. 3a). Class 1 and 2 DISARM share three core genes, with each class having two distinct additional genes. Class 2 DISARM includes a five-cytosine DNA methyltransferase and a system from *Bacillus paralicheniformis* prevented phage DNA accumulation by distinct families of double-stranded (ds)DNA phages. Notably, phages modified at a specific sequence, and therefore presumably masked from the RM-like system, were inhibited. Furthermore, DISARM offered protection against phages that lacked the sequence recognized by the RM-like system. These results indicate that the mechanism differs from classic RM systems. To add further mystery to the DISARM mechanism, the candidate nuclease was dispensable for resistance[34].

Phages have amassed strategies to counteract RM, and potentially RM-like, systems[6,35,36]. Phage DNA can become methylated by the host methyltransferase on entry, disguising the DNA from the host restriction endonuclease. The resulting phages become phenotypically RM-insensitive; however, this epigenetic avoidance is transient and is lost following infection of methyltransferase-deficient bacteria. In addition, RM sites are mutated, underrepresented or absent in phage genomes to prevent restriction[35,37,38] (Fig. 3d). Phages also exploit modified or unusual bases, such as hydroxymethylation, glycosylation, glucosylation and acetamidation to make these sites unrecognizable to the restriction endonuclease[36]. Specifically, coliphage 9g utilizes a deoxyarchaeosine modification to avoid restriction[39]. Some phage proteins (for example, Ral from λ and P22 phages) activate host methyltransferases

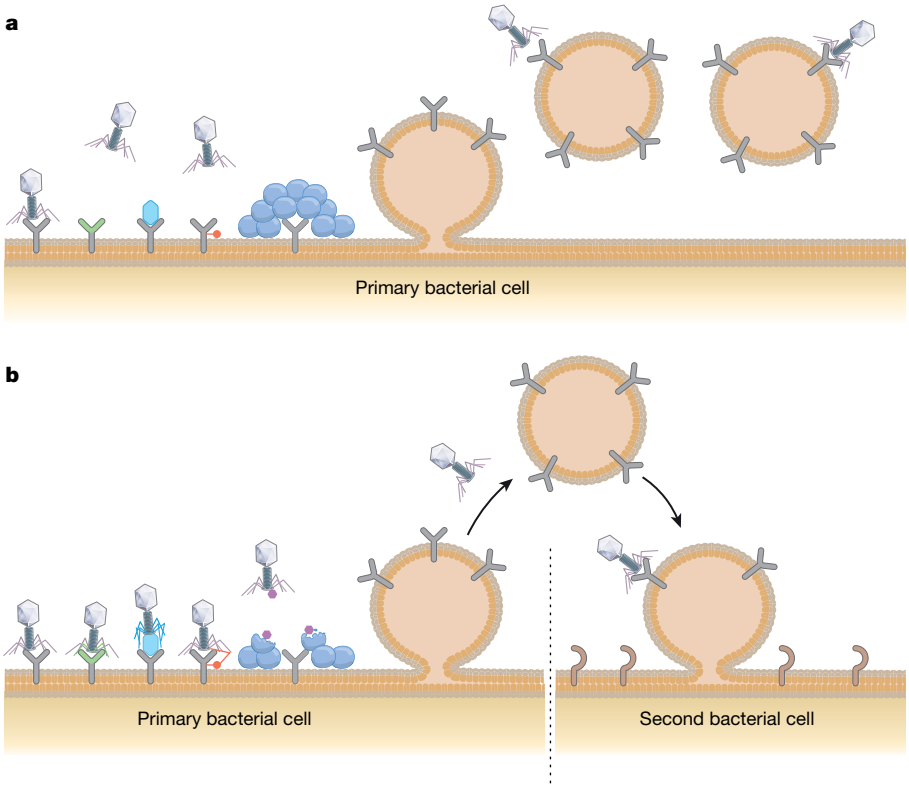


Fig. 2 | Preventing phage adsorption. a, Bacteria have developed a number of methods to prevent phage adsorption. These include altering (green), disguising (blue), modifying (red) or masking (blue circles) receptors and the use of decoy OMVs. **b**, Phages can co-evolve to recognize the modified receptor, through mutations, and produce extracellular-matrix-degrading enzymes. OMVs can also extend the host range of phages, by transferring receptors used by the phage to cells that previously lacked those specific phage receptors.

and promote DNA modification to protect against restriction endonucleases[40,41]. Phages can also encode methyltransferases, which protect their DNA from restriction[42,43] (Fig. 3d), such as the methyltransferase of the *Bacillus* phage SPR, which can modify three sites to protect against multiple nucleases[42,44]. Phages can also prevent degradation of their genomes using the defence against restriction (Dar) system. The Dar system of coliphage P1 limits DNA degradation by type I restriction endonucleases[45,46]. Dar proteins are injected along with the phage DNA and function in *cis*. Another successful anti-RM strategy is the direct inactivation of restriction endonucleases. The overcome classical restriction (Ocr) protein of coliphage T7 is expressed immediately after DNA injection, mimics DNA, and tightly binds and sequesters the EcoKI restriction endonuclease[47,48]. Routes of phage escape from the recently discovered, RM-like systems have yet to be thoroughly investigated. However, phages are likely to use similar anti-restriction mechanisms for DISARM and BREX. No phages that have escaped Pgl systems have been isolated[31,49], suggesting that bacterial protection by this system may be more robust than other RM-like systems.

CRISPR–Cas adaptive immunity

The ability to cleave phage DNA in a sequence-specific manner is shared by both RM and clustered regularly interspaced short palindromic repeats (CRISPR)–CRISPR-associated protein (Cas) systems. However, CRISPR–Cas provides 'adaptive' immunity through the generation of memories of past phage encounters that guide sequence-specific immunity[50]. CRISPR–Cas immunity is present in about half of sequenced bacteria and is mediated by three stages[51–53]: adaptation, expression and interference (Fig. 4a). The mechanistic diversity of CRISPR–Cas systems is considerable—currently there are two classes, six types and more than 30 subtypes[54,55].

Class 1 systems include types I, III and IV, which have multi-subunit Cas complexes. Various type I CRISPR–Cas subtypes have been shown to provide phage resistance[56–62], whereas type IV systems—which are most-closely related to type I—are poorly characterized and their role in phage resistance is unknown[63,64]. Type III systems differ from other class 1 systems, because they target both RNA and DNA[65,66]. Resistance to lytic infection has been demonstrated by the type III systems of *Staphylococcus epidermidis*[66–68], *Lactococcus lactis*[69] and *Streptococcus thermophilus*[70]; however, the RNA-dependent targeting provides tolerance to prophages[71]. An interesting feature of type III systems is that Cas10 synthesizes intracellular signals (cyclic oligoadenylates) that bind an accessory RNase and unleash its promiscuous activity[67,72,73]. The RNase may have an abortive infection effect (see 'Protecting the bacterial population' section), adding a further layer of defence by inducing dormancy through unspecific cleavage of both host and phage transcripts[74,75].

Class 2 CRISPR–Cas includes type II, V and VI systems, which are characterized by single-subunit effectors. The first direct evidence that CRISPR–Cas provides immunity against phages was provided by the type II-A system of *S. thermophilus*[50] and was later shown in *Streptococcus pyogenes*[76]. Type II systems use Cas9 to generate dsDNA breaks, whereas type V systems use Cas12[77]. Although there are few studies that have investigated phage resistance by type V systems, it has been shown that the *Francisella novicida* system protects against phage infection in *E. coli*[78]. The dsDNA breaks induced by class 2 systems have been exploited in biotechnology, but may be less effective for clearing phages. In support of this idea, class 2 systems are less common than type I, which have a potentially more destructive DNA-shredding mechanism[55]. Finally, class 2 systems can recognize and cleave phage RNA. Indeed, Cas13 from the type VI system of *Leptotrichia shahii* cleaved phage MS2 RNA in *E. coli*[79]. Upon target recognition, Cas13 not only

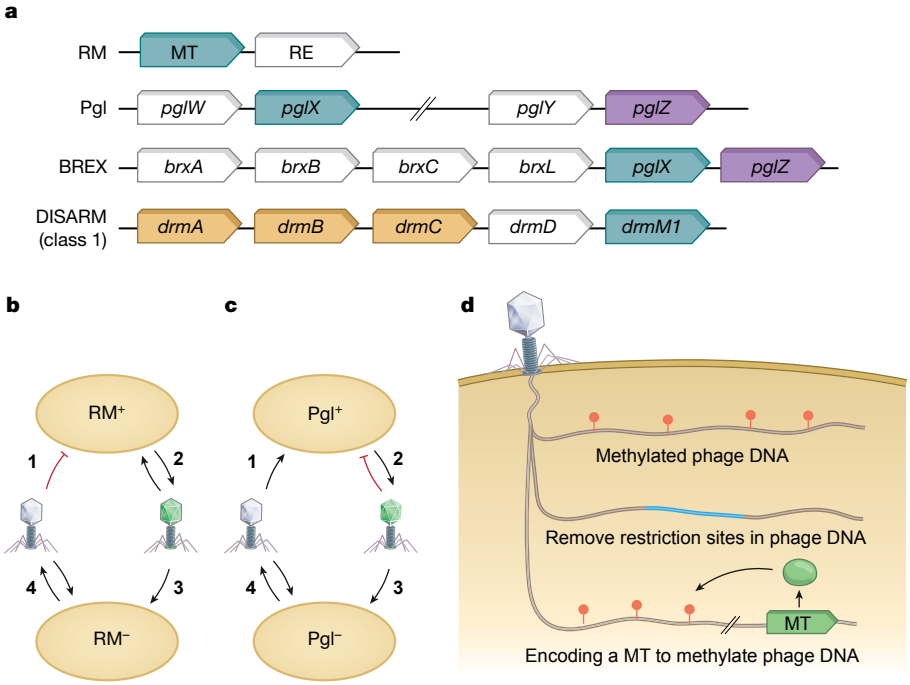


Fig. 3 | RM-like systems. a, Many proteins and protein domains are shared between the RM, Pgl, BREX and DISARM systems. The blue genes indicate enzymes that are responsible for DNA modification (methyltransferases (MT)), the purple gene (*pglZ*) encodes a conserved protein (an alkaline phosphatase) and orange genes in the DISARM system indicate core genes. RE, restriction endonuclease. *pglW* encodes a serine/threonine kinase; *pglX* encodes an adenine-specific methyltransferase; *pglY* encodes an ATP-binding protein; *brxA* encodes an RNA-binding anti-terminase; *brxB* encodes a protein with an unknown function; *brxC* encodes an ATP-binding protein; *brxL* encodes a protease; *drmA* encodes a putative helicase; *drmB* encodes a helicase-associated protein; *drmC* encodes phospholipase D/nuclease; *drmD* encodes an SFN2 helicase; and *drmM1* encodes an N^6-adenine DNA methyltransferase. **b**, (1) RM restricts any phage DNA that is not modified by methylation; (2) however, modified phages (green phage; see **d**) can replicate on RM^+ strains. (3) Modified or (4) unmodified phages can replicate on an RM^- strain but will lose any modifications. **c**, Pgl systems only restrict phages that have been previously exposed to the system. (1) A naive phage can replicate on Pgl^+, (2) but upon secondary infection of a Pgl^+ strain, the phage (shown in green) is restricted. (3) Modified (yellow) or (4) unmodified (grey) phages can replicate on Pgl^- strains. **d**, Mechanisms of phages for avoiding RM and RM-like systems include methylation of DNA, removing recognition sequences from their genome and encoding a methyltransferase to methylate the phage DNA.

cuts complementary transcripts, but also becomes a promiscuous RNase[79,80]. This promiscuous RNase activity can cleave phage mRNAs and host RNAs, inducing dormancy and providing Cas13-mediated resistance against dsDNA phages[80].

The sequence specificity of CRISPR–Cas selects for phages with mutations in targeted regions (Fig. 4b). Indeed, mutations in protospacer-adjacent motifs and spacer targets (i.e. protospacers) enable phages to overcome type I systems[57,59–61,81] and type II systems[82–85]. Insertions, deletions and recombination events can also mediate phage escape[50,59,81,84,85]. However, type I systems have a positive feedback mechanism to restore or enhance immunity by acquiring multiple new spacers that target escape phages—a process called priming[51]. There is now bioinformatic and experimental evidence that priming occurs in type II systems[86,87]. Nevertheless, phages can evade primed strains with multiple spacers by deleting the target region[81].

As type V and VI systems can also degrade non-specific single-stranded (ss)DNA (type V) or RNA (type VI), they might provide an additional layer of resistance, which may explain why escape phages are yet to be identified for these systems[75]. In agreement with this notion, dormancy induced by type VI systems suppressed the emergence of escape mutants and protected the bacterial population against phages[80]. Similar to RM system evasion, phages can modify DNA to reduce Cas complex binding and cleavage—as seen for T4 evasion of type I-E and II-A systems[59,78].

Escape mutations can lead to phage fitness defects, and if essential genes are targeted, escape might be impossible. As an alternative, some phages have anti-CRISPR (Acr) proteins that inactivate CRISPR–Cas systems[88,89] (Fig. 4b). Acrs have been identified for type I, II, III, V and VI systems and most interact with the Cas proteins to block activity[89–91]. Recently, an Acr has been shown to acetylate a type V system to prevent DNA binding[92], and another inactivates Cas12 by triggering cleavage of CRISPR RNA bound to Cas12[93]. Notably, some phages must cooperate to exploit their Acrs. Acrs produced by the first phage that infects can immunosuppress the host, but may fail to fully protect the phage from CRISPR–Cas, while enabling a productive infection by successive phages[94,95]. It is possible that Acrs have provided a selection for CRISPR–Cas diversity, but the ecological importance of their mechanistic diversity is unclear (see Box 1).

Phage defences such as CRISPR–Cas are sometimes encoded by phages[96,97]. For example, CRISPR arrays occur in prophages of *Clostridium difficile*, which target other *C. difficile* phages, and CRISPR–Cas systems are also present in 'huge' phages[98–100]. In many phages, these systems are incomplete—lacking genes for adaptation or interference[97,101]. Phages that contain these incomplete systems have been proposed to co-opt the required proteins from the host, or repress transcription without cleavage, akin to RNA interference[101]. These phage-encoded CRISPR–Cas components may also eliminate competing phages and manipulate the hosts[102]. Indeed, a complete system expressed by a *Vibrio* phage can protect against a host defence island[96]. Phages can also transduce CRISPR–Cas systems between bacteria, which can provide immunity against other phages[62,75]. These examples highlight how some phages have manipulated CRISPR–Cas systems as a way to avoid defence systems in the host and endow them with an advantage over competing phages.

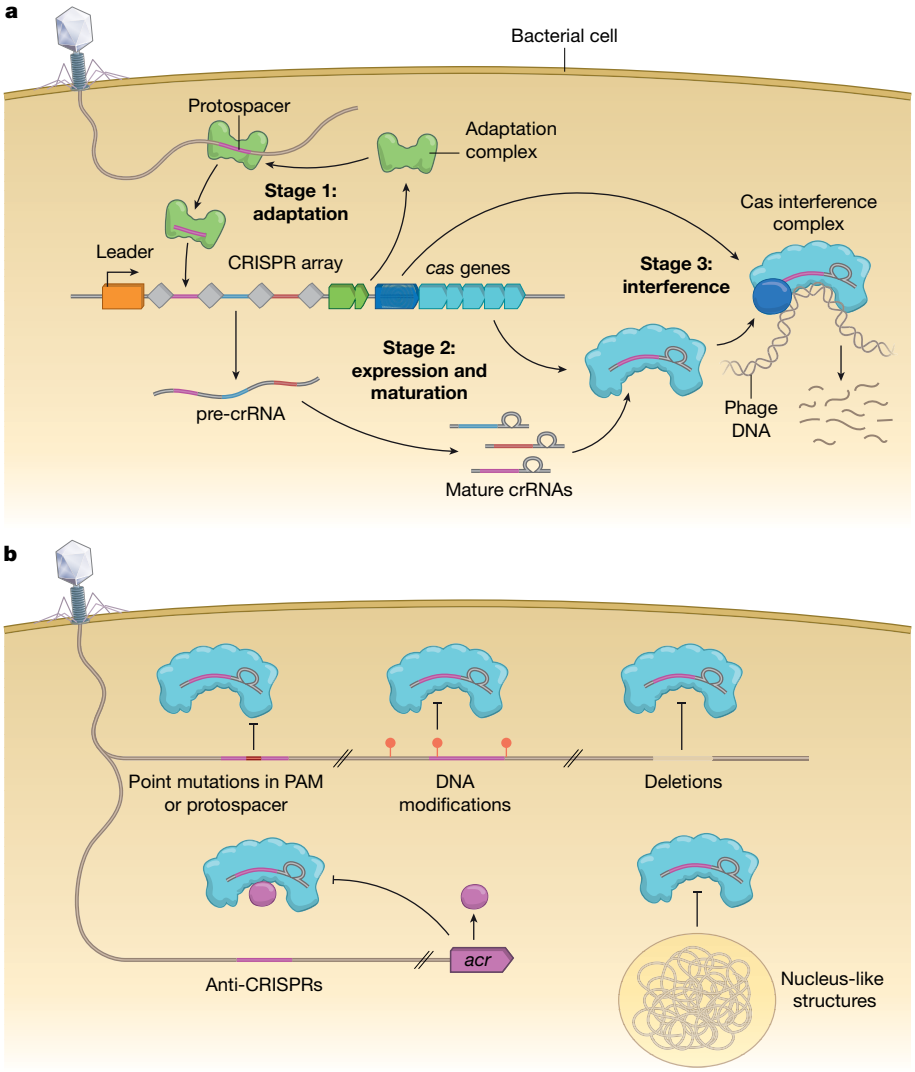


Fig. 4 | CRISPR–Cas adaptive immunity and how phages overcome the CRISPR–Cas adaptive immune system. a, Schematic of the three stages of CRISPR–Cas immunity, including adaptation (stage 1), expression and maturation (stage 2), and interference (stage 3). crRNA, CRISPR RNA. **b**, Phages have the ability to overcome CRISPR–Cas defences through point mutations in the protospacer-adjacent motif (PAM) or protospacer, deletions or modifications of the DNA so that the DNA cannot be bound by Cas complexes. Phages can also encode protein anti-CRISPRs that can interfere with CRISPR immunity, and jumbo phages produce a nucleus-like structure that excludes Cas complexes, thus preventing DNA targeting.

Protecting the bacterial population

In contrast to RM and adsorption inhibition, which confer individual benefits, abortive infection (Abi) anti-phage systems protect the bacterial population[5]. Abi is characterized by successful phage entry; however, development is interrupted, resulting in the release of few, if any, phages and the host cell dies, which prevents a phage epidemic and protects the bacterial population[103]. 'Altruistic' Abi systems are widespread in Gram-positive and Gram-negative bacteria[103]; however, as Abi systems are defined by phenotype, rather than genotype, their discovery has been sporadic[103]. Nevertheless, the presence of many Abi systems on plasmids has been used successfully to identify these systems, particularly in lactococci[103]. The mechanistic details of phage abortion are unknown for many systems, although disruption of essential processes, such as replication, transcription, translation and DNA packaging is common[4,104].

An Abi mechanism in *S. epidermidis* was recently shown to involve a serine/threonine kinase (Stk)[105]. Activated Stk phosphorylates proteins involved in translation, transcription, cell cycle control, the stress response, central metabolism, and DNA topology and repair[105]. Death of infected bacteria occurs through this phosphorylation pathway, decreasing phage release and protecting the population[105]. The presence of serine/threonine kinases in eukaryotic viral defences suggests there are shared immune strategies between these kingdoms. Kinases also play wider roles in viral defence in bacteria, with examples in the BREX and Pgl systems[30–32].

The phenotypic definition of Abi systems is also reflected in their mechanistic diversity. For example, *E. coli* lambda lysogens encode RexAB, which is activated by a poorly-characterized T4 phage protein-DNA complex[104,106]. When triggered, RexA activates RexB, which forms a membrane channel that leads to ATP leakage, lost membrane potential and phage exclusion[106]. RexAB-like systems are widespread, with their recent identification in actinobacteriophages. For example, *rexAB*-like genes in *Mycobacterium smegmatis* and *Gordonia terrae* prophages abort multiple phages[98,107]. In each host, phage escape mutants were identified and all contained mutations in the proteins that triggered RexAB activity[98].

A subset of Abi systems function through a toxin–antitoxin mechanism. Toxin–antitoxin systems are composed of a toxin and an antitoxin

Box 1

Ecology, evolution and phage defence systems

Interactions between bacteria and phages can have important consequences for microbial communities and it is essential to study these in more natural contexts[157–159]. Cocultures of bacteria and phages, which enable the assessment of changes in phage resistance and susceptibility, can provide insights into coevolutionary dynamics. For example, in early experiments with *E. coli* and T-even phages, bacteria became resistant through surface modification[160,161], whereas experiments with *Pseudomonas fluorescens* SBW25 and phage Φ2 showed coevolution of these microorganisms over time[162–164]. When monitored in soil, the coevolution of *P. fluorescens* and Φ2 still occurred, but in a different manner[165]. The differences that were observed were due to the reduced nutrients, which increased the growth-rate costs of phage resistance. This example highlights the importance of considering the ecological context and communities when studying phage resistance.

Evolutionary studies also provide insights into conditions in which bacteria might favour different resistance mechanisms. For example, *P. aeruginosa* used CRISPR–Cas when grown under nutrient-limiting conditions, whereas excess nutrients typically led to surface mutations[61]. Both resistance outcomes were costly to bacteria, yet each mechanism was favoured under different ecological conditions[61].

Although laboratory experiments that mimic natural ecological and evolutionary scenarios benefit from being easy to manipulate, they cannot replicate environmental complexities. Metagenomics provides one way to complement the laboratory approach and has enabled the high-resolution examination of bacterial and phage communities from complex environments[159]. This technique has been useful for following the evolution of CRISPR–Cas resistance and subsequent phage escape in diverse environments, including acid mine drainage, the human gut, hyper saline lakes and a fish farm[166–169]. Phages and bacteria can be monitored over time, providing valuable insights into the role of CRISPR–Cas immunity in shaping microbial communities. Furthermore, metagenomics has been key for identifying new anti-phage systems[127] and CRISPR–Cas variants[170,171].

Finally, mathematical modelling of bacteria–phage interactions provides insights into coevolutionary dynamics, helps to explain experimental observations and predict the influence of other ecological variables that can be difficult to manipulate experimentally[161,172,173]. To gain a more complete understanding of phage–bacteria interactions and phage resistance, we must use a multidisciplinary approach by combining these complementary research areas with molecular studies.

that are usually co-transcribed. The toxins targets essential cellular processes, leading to bacterial dormancy or death. There are six types of toxin–antitoxin systems, based on the identity of the gene products (RNA or protein) and whether, and how, the toxin and antitoxin interact[99]. ToxIN, a type III system from *Pectobacterium atrosepticum* was the first example of an Abi system that was shown to function as a toxin–antitoxin mechanism[100] and this has now been observed for other Abi systems[108,109]. Different toxin–antitoxin types can elicit phage resistance, but have not been strictly classified as Abi systems, as the outcome for the infected bacterium was not defined. Examples in *E. coli* include *hok/sok* (type I) and *rnlA/rnlB* (type II), which exclude phage T4[110,111], and *mazEF* (type II), which excludes phage P1[112]. Many of these toxins are RNases, a characteristic shared by several Abi systems. For example, *E. coli* PrrC is an RNase that cleaves lysine transfer RNA ($tRNA^{Lys}$) during infection, and only T4 phages that are able to repair this cleavage can replicate[4]. Thus, mutant T4 phages that lack a polynucleotide kinase or RNA ligase are aborted due to $tRNA^{Lys}$ cleavage[113].

To bypass toxin–antitoxin systems, phages can encode antitoxins. For example, T4 produces Dmd, an antitoxin that inhibits *E. coli* RnlA and LsoA toxins[114]. Dmd differs from the RnlB or LsoB antitoxins, suggesting it evolved independently, which is highlighted by its different toxin neutralization mechanism[114]. Phages can generate diversity for escape by acquiring host genetic material through recombination. Indeed, recombination between lytic phages and resident lactococcal prophages led to Abi escape through gene loss or gain[115]. Recombination can also promote antitoxin acquisition by phages. For example, to escape ToxIN, phages containing a short *toxI*-like sequence recombined with *toxIN* and directly gained *toxI*[116]. Notably, in other escape phages, *toxI*-like sequence duplications produced pseudo-ToxI RNAs that inhibited ToxN[116]. Rather than encoding its own antitoxin, coliphage T7 evades a toxin–antitoxin system by producing a protein that has been proposed to prevent antitoxin degradation by the Lon protease. This ensures that the toxin remains inactive by increasing the stability of the host antitoxin[117]. Finally, the T4 protein Alt (an ADP-ribosyltransferase) is injected with phage DNA, which chemically modifies the MazF toxin[118]. ADP-ribosylated MazF has reduced cleavage activity, enabling the survival of the phage[118].

Many new Abi systems await discovery and, indeed, new systems in different strains are still being uncovered. For example, Abiα was recently identified in *Enterococcus faecalis* and leads to asynchronous lysis[119]. To understand Abi responses, the phage genes involved can be revealed by isolating escape mutants. For example, ToxIN can be overcome by specific mutations in ϕM1 and T4-like phage proteins[120,121]. However, the often toxic and poorly characterized nature of the phage Abi-triggering proteins is a frequent challenge for mechanistic studies.

Prophage-encoded defence systems

Prophages can have immune systems that prevent subsequent phage infection of lysogens (for example, *rexAB*). These non-essential transcribed regions or genes within prophage genomes have been called 'morons' and can encode factors that benefit the host, such as defence systems[122]. For example, morons (or 'immunity cassettes') within *M. smegmatis* prophages provide phage defence by encoding RM and toxin–antitoxin components, and other defence systems[123]. These systems can be remarkably specific; for example, prophage Charlie encodes a defence system that offered protection against only one phage of many tested. A different *M. smegmatis* prophage encoded a (p)ppGpp synthetase similar to RelA/SpoT that is proposed to be inactivated by a prophage 'regulator' protein. Lytic phage replication leads to rapid dissociation of the synthetase from the regulator, (p)ppGpp accumulation, growth cessation and stalled phage development[123]. Another phage, Fruitloop, encodes an immunity protein that interacts with Wag31, a cell-wall synthesis protein in *M. smegmatis*. Fruitloop inhibits superinfection by other phages that are thought to require Wag31 for DNA injection[124]. Prophage-mediated phage defences are widespread. Indeed, a systematic study revealed that *Pseudomonas* lysogens have diverse prophage-encoded defences[21]. Furthermore, filamentous phages of the *Inoviridae* family that cause chronic infections were recently shown to have multiple toxin–antitoxin systems and superinfection systems[125]. As these systems are encoded by the phage, phage escape represents phage–phage coevolution. Accordingly, many genes of unknown function in prophages, especially within morons, may protect from superinfection and this knowledge may accelerate the identification of candidate resistance systems.

A new world of diverse resistance systems

Defence systems are often clustered in defence islands in bacterial genomes and unknown genes within these regions have been proposed to encode anti-phage systems[54,126]. This was supported by the discovery of BREX, DISARM and the Stk2 kinase[31,32,34,105], and was the premise for a search that uncovered 26 broadly distributed candidate defence systems[127]. Nine systems have been validated as anti-phage systems, some of which protect against specific phages, whereas others provided broader defence. Although the mechanisms are undetermined, multiple protein domains have been identified that are typical for phage-defence systems (for example, helicases and nucleases), in addition to proteins that have been proposed to be repurposed for phage defence. For example, components of the Zorya system, which is proposed to be an Abi system, show homology to the MotAB proteins that form the stator of the flagella complex, and are hypothesized to form a membrane channel that results in depolarization and cell death upon phage infection[127].

Prokaryotic Argonaute (Ago) proteins are also found in defence islands nearby other newly discovered and validated systems (for example, Thoeris), suggesting that they may also elicit phage defence[127,128]. Moreover, the eukaryote Ago proteins are key proteins in RNA-interference systems, and prokaryotic Ago proteins function as nucleic-acid-guided nucleases[129]. Generally, prokaryotic Ago proteins generate and associate with short-interfering DNA or RNA guides. The single-stranded guides facilitate the identification of the complementary sequence by prokaryotic Ago, which cleaves the target strand or produces double-stranded breaks[130–133]. Following the discovery of prokaryotic Ago proteins, further parallels are being drawn with the eukaryotic immune systems—for example, with the eukaryotic cGAS–STING pathway that senses viral DNA and activates an innate immune response. Recently, prokaryotic cGAS homologues, which cluster near defence islands, have been identified[134]. These cGAS-encoding genes reside in operons that include a phospholipase and two other genes that contain eukaryotic-like domains that are required for defence against some phages, but are dispensable for the defence against others. This pathway was named CBASS (cyclic-oligonucleotide-based anti-phage signalling system) and is triggered by an unidentified signal that causes cGAS to produce cyclic GMP–AMP (cGAMP). cGAMP activates the phospholipase, which aborts a range of dsDNA phages by eliciting membrane damage and cell death[134]. A second example is the eukaryotic-like HORMA proteins that are present in various bacteria, including *E. coli*[135]. These proteins sense unknown phage product(s) and, once activated, the HORMA domain activates a cGAS/DncV-like nucleotidyltransferase that produces the second messenger cyclic tri-AMP. Cyclic tri-AMP causes dsDNA cleavage by activating an endonuclease, which in *E. coli* confers λ immunity[135]. It is currently unknown whether this results in abortive infection or targeted destruction of the phage[135,136]. The discovery of eukaryotic-like defences in prokaryotes suggest that systematic searches for homologues in bacteria may uncover many new anti-phage systems.

Recently, a new type of phage defence was discovered that relies on small molecules rather than proteins[137]. This chemical defence is widespread in *Streptomyces*, a genus known for the prolific production of bioactive secondary metabolites. The metabolites block genome propagation by intercalating dsDNA. Because many secondary metabolites can diffuse and thus function outside of the cell, this has been proposed as an innate defence that protects bacteria before phage infection[137]. However, various aspects of the chemical defence strategy remain unclear, such as how the phage DNA is recognized as non-self.

With such a diversity of defence systems, the arms race has escalated. Indeed, jumbo phages produce nucleus-like structures inside the infected bacterium, in which phage DNA replication and transcription occur[138,139]. In *P. aeruginosa*, this nucleus-like structure protects ϕKZ from type I-C, II-A and V-A CRISPR–Cas and a type I RM system[139]. Moreover, in *Serratia*, a distinct nucleus-forming jumbo phage evades the native DNA-targeting type I-F and I-E CRISPR–Cas systems[140]. However, phage mRNA translated in the cytoplasm is susceptible to RNA-targeting by Cas13[139] or type III-A defence[140] in *P. aeruginosa* and *Serratia*, respectively. Therefore, this physical occlusion of the phage genome appears to be a widespread method to overcome anti-phage systems and this is supported by a paucity of type I spacers that target jumbo phages in nature, whereas type III-A spacers are over-represented[140].

Finally, extracellular chemicals not only engage in direct resistance against phages (for example, chemical defence[137]), but also facilitate communication to pre-empt bacteria to increase their immunity. Indeed, quorum sensing—cell-density-dependent signalling—upregulates bacterially encoded CRISPR–Cas and downregulates surface receptors when populations would otherwise be at increased risk of a phage epidemic[141–143]. Perhaps unsurprisingly, phages also use communication to ensure productive infection[144,145]. These peptide communication systems (which are also known as arbitrium) are diverse and widespread, and inform phages about host availability. Arbitrium has been proposed to limit phage-induced host decimation by determining whether phages enter the lytic or lysogenic life cycle[144–148]. Phages also encode LuxR-type proteins, which respond to Gram-negative quorum-sensing signals[149,150] and quorum-sensing genes are also present in Gram-positive phages[151]. Although the function of phage quorum-sensing genes remains to be elucidated, they might allow phages to sense host density[149]. These examples of communication between phages and bacteria raise the question whether bacteria and phages engage in 'espionage', where either party listens in to, or interferes with, the communications of the other to manipulate the outcome for their own benefit. However, the roles and implications of phage–phage and phage–bacteria communications remain to be understood.

Perspectives

There is a clear diversity of phage-resistance mechanisms and ways that phages evade these systems. This knowledge is informing microbiology, the potential of phage-inspired therapeutics and new biotechnological tools. Despite considerable advances, we are far from understanding bacterial defences and phage counter-adaptation across scales—from molecules, single cells, communities, ecosystems and through to the global scale (Box 1). Furthermore, the recent discovery of completely new systems demonstrates that our view of the defence arsenal is incomplete, and that their identification requires more systematic approaches. Increased sequencing data will expand the success of bioinformatics strategies, but these need to be complemented by high-throughput experimental techniques. For example, phage-based positive selection of new anti-phage systems from metagenomic libraries could be exploited in a similar manner to those reported for anti-CRISPR discovery[152]. To advance the field, both sides of this arms race, the bacteria and the phages, must be considered.

In terms of bacterial defences, critical gaps exist in our understanding of molecular mechanisms—for both old and new systems—and new techniques should be applied to uncover their mode of action. Determining the molecular mechanisms of diverse defences will undoubtedly lead to both fundamental biological knowledge and new technologies—as exemplified by the exploitation of CRISPR–Cas and RM systems. Furthermore, most defence systems have been studied without considering other co-existing immune mechanisms. Indeed, bacteria often have multiple CRISPR–Cas systems, in addition to other innate defences. How these function together—whether redundantly or synergistically—is not well understood, but they may help bacteria to resist diverse phages and overcome escape phages[153]. In fact, RM and CRISPR–Cas act together to increase phage resistance, and crosstalk between CRISPR–Cas systems can provide protection against escape phages[154,155]. In addition, each defence system is likely to have different

costs and benefits that depend on the niche inhabited and these factors may be key drivers in the evolutionary selection of defences.

Our understanding of phages is improving, in part due to the increased availability of sequencing data, but given their global abundance, we only have a tiny snapshot of this ever-changing community. Poor functional gene annotations highlight the gaps in fundamental phage biology and hinder our ability to understand their interactions with bacterial immune systems. We can focus on genes that probably influence bacterial immunity. For example, prophage-encoded defences and anti-defences are commonly found in particular genomic locations and their discovery has been facilitated by comparative genomics of phage families. Moreover, early expressed genes often have important roles in anti-defence or bacterial takeover[156]; however, studying these genes has been hampered by the paucity of genetic tools for phages. Reassuringly, phages are becoming genetically tractable due to CRISPR–Cas methods. To realize the ecological importance, and the therapeutic and biotechnological implications of bacterial immune systems, mechanistic studies must be complemented with evolutionary and ecological experiments to illuminate how molecular events scale to global microbial processes.

1. Fortier, L.-C. & Sekulovic, O. Importance of prophages to evolution and virulence of bacterial pathogens. *Virulence* **4**, 354–365 (2013).
2. Suttle, C. A. Marine viruses—major players in the global ecosystem. *Nat. Rev. Microbiol*. **5**, 801–812 (2007).
3. Hurwitz, B. L., Hallam, S. J. & Sullivan, M. B. Metabolic reprogramming by viruses in the sunlit and dark ocean. *Genome Biol*. **14**, R123 (2013).
4. Dy, R. L., Richter, C., Salmond, G. P. C. & Fineran, P. C. Remarkable mechanisms in microbes to resist phage infections. *Annu. Rev. Virol*. **1**, 307–331 (2014).
5. van Houte, S., Buckling, A. & Westra, E. R. Evolutionary ecology of prokaryotic immune mechanisms. *Microbiol. Mol. Biol. Rev*. **80**, 745–763 (2016).
6. Samson, J. E., Magadán, A. H., Sabri, M. & Moineau, S. Revenge of the phages: defeating bacterial defences. *Nat. Rev. Microbiol*. **11**, 675–687 (2013).
7. Gregory, A. C. et al. Marine DNA viral macro- and microdiversity from pole to pole. *Cell* **177**, 1109–1123 (2019).
8. Dedrick, R. M. et al. Engineered bacteriophages for treatment of a patient with a disseminated drug-resistant *Mycobacterium abscessus*. *Nat. Med*. **25**, 730–733 (2019).
The first published study in which a genetically engineered phage cocktail is used to treat a bacterial infection in a human patient.
9. O'Sullivan, L., Bolton, D., McAuliffe, O. & Coffey, A. Bacteriophages in food applications: from foe to friend. *Annu. Rev. Food Sci. Technol*. **10**, 151–172 (2019).
10. Foss, D. V., Hochstrasser, M. L. & Wilson, R. C. Clinical applications of CRISPR-based genome editing and diagnostics. *Transfusion* **59**, 1389–1399 (2019).
11. Ackermann, H. W. Tailed bacteriophages: the order *Caudovirales*. *Adv. Virus Res*. **51**, 135–201 (1998).
12. Clokie, M. R. J., Millard, A. D., Letarov, A. V. & Heaphy, S. Phages in nature. *Bacteriophage* **1**, 31–45 (2011).
13. Seed, K. D. et al. Evolutionary consequences of intra-patient phage predation on microbial populations. *eLife* **3**, e03497 (2014).
14. Manning, A. J. & Kuehn, M. J. Contribution of bacterial outer membrane vesicles to innate bacterial defense. *BMC Microbiol*. **11**, 258 (2011).
15. Reyes-Robles, T. et al. *Vibrio cholerae* outer membrane vesicles inhibit bacteriophage infection. *J. Bacteriol*. **200**, e00792-17 (2018).
16. Tzipilevich, E., Habusha, M. & Ben-Yehuda, S. Acquisition of phage sensitivity by bacteria through exchange of phage receptors. *Cell* **168**, 186–199 (2017).
This study showed that co-culturing of cells allowed for the transfer of phage receptors from sensitive bacteria to resistant bacteria.
17. Moxon, R., Bayliss, C. & Hood, D. Bacterial contingency loci: the role of simple sequence DNA repeats in bacterial adaptation. *Annu. Rev. Genet*. **40**, 307–333 (2006).
18. Ohshima, Y., Schumacher-Perdreau, F., Peters, G. & Pulverer, G. The role of capsule as a barrier to bacteriophage adsorption in an encapsulated *Staphylococcus simulans* strain. *Med. Microbiol. Immunol*. **177**, 229–233 (1988).
19. Scanlan, P. D. & Buckling, A. Co-evolution with lytic phage selects for the mucoid phenotype of *Pseudomonas fluorescens* SBW25. *ISME J*. **6**, 1148–1158 (2012).
20. Harvey, H. et al. *Pseudomonas aeruginosa* defends against phages through type IV pilus glycosylation. *Nat. Microbiol*. **3**, 47–52 (2018).
21. Bondy-Denomy, J. et al. Prophages mediate defense against phage infection through diverse mechanisms. *ISME J*. **10**, 2854–2866 (2016).
22. Meyer, J. R. et al. Repeatability and contingency in the evolution of a key innovation in phage lambda. *Science* **335**, 428–432 (2012).
23. Petrie, K. L. et al. Destabilizing mutations encode nongenetic variation that drives evolutionary innovation. *Science* **359**, 1542–1545 (2018).
24. Habusha, M., Tzipilevich, E., Fiyaksel, O. & Ben-Yehuda, S. A mutant bacteriophage evolved to infect resistant bacteria gained a broader host range. *Mol. Microbiol*. **111**, 1463–1475 (2019).
25. Schwarzer, D. et al. A multivalent adsorption apparatus explains the broad host range of phage phi92: a comprehensive genomic and structural analysis. *J. Virol*. **86**, 10384–10398 (2012).
26. Fernandes, S. & São-José, C. Enzymes and mechanisms employed by tailed bacteriophages to breach the bacterial cell barriers. *Viruses* **10**, 396 (2018).
27. Nobrega, F. L. et al. Targeting mechanisms of tailed bacteriophages. *Nat. Rev. Microbiol*. **16**, 760–773 (2018).
28. Oliveira, P. H., Touchon, M. & Rocha, E. P. C. The interplay of restriction–modification systems with mobile genetic elements and their prokaryotic hosts. *Nucleic Acids Res*. **42**, 10618–10631 (2014).
29. Loenen, W. A. M., Dryden, D. T. F., Raleigh, E. A., Wilson, G. G. & Murray, N. E. Highlights of the DNA cutters: a short history of the restriction enzymes. *Nucleic Acids Res*. **42**, 3–19 (2014).
30. Sumby, P. & Smith, M. C. M. Genetics of the phage growth limitation (Pgl) system of *Streptomyces coelicolor* A3(2). *Mol. Microbiol*. **44**, 489–500 (2002).
31. Hoskisson, P. A., Sumby, P. & Smith, M. C. M. The phage growth limitation system in *Streptomyces coelicolor* A(3)2 is a toxin/antitoxin system, comprising enzymes with DNA methyltransferase, protein kinase and ATPase activity. *Virology* **477**, 100–109 (2015).
32. Goldfarb, T. et al. BREX is a novel phage resistance system widespread in microbial genomes. *EMBO J*. **34**, 169–183 (2015).
This study describes an RM-like system that prevents infection through a mechanism other than DNA cleavage or degradation.
33. Gordeeva, J. et al. BREX system of *Escherichia coli* distinguishes self from non-self by methylation of a specific DNA site. *Nucleic Acids Res*. **47**, 253–265 (2019).
34. Ofir, G. et al. DISARM is a widespread bacterial defence system with broad anti-phage activities. *Nat. Microbiol*. **3**, 90–98 (2018).
Discovery of a type of widespread RM-like phage-resistance system.
35. Krüger, D. H. & Bickle, T. A. Bacteriophage survival: multiple mechanisms for avoiding the deoxyribonucleic acid restriction systems of their hosts. *Microbiol. Rev*. **47**, 345–360 (1983).
36. Vasu, K. & Nagaraja, V. Diverse functions of restriction–modification systems in addition to cellular defense. *Microbiol. Mol. Biol. Rev*. **77**, 53–72 (2013).
37. Korona, R., Korona, B. & Levin, B. R. Sensitivity of naturally occurring coliphages to type I and type II restriction and modification. *J. Gen. Microbiol*. **139**, 1283–1290 (1993).
38. Pleška, M. & Guet, C. C. Effects of mutations in phage restriction sites during escape from restriction–modification. *Biol. Lett*. **13**, 20170646 (2017).
39. Kulikov, E. E. et al. Genomic sequencing and biological characteristics of a novel *Escherichia coli* bacteriophage 9g, a putative representative of a new Siphoviridae genus. *Viruses* **6**, 5077–5092 (2014).
40. Loenen, W. A. M. & Murray, N. E. Modification enhancement by the restriction alleviation protein (Ral) of bacteriophage λ. *J. Mol. Biol*. **190**, 11–22 (1986).
41. Semerjian, A. V., Malloy, D. C. & Poteete, A. R. Genetic structure of the bacteriophage P22 PL operon. *J. Mol. Biol*. **207**, 1–13 (1989).
42. Murphy, J., Mahony, J., Ainsworth, S., Nauta, A. & van Sinderen, D. Bacteriophage orphan DNA methyltransferases: insights from their bacterial origin, function, and occurrence. *Appl. Environ. Microbiol*. **79**, 7547–7555 (2013).
43. Schlagman, S. L. & Hattman, S. Molecular cloning of a functional *dam*$^+$ gene coding for phage T4 DNA adenine methylase. *Gene* **22**, 139–156 (1983).
44. Günthert, U. & Reiners, L. *Bacillus subtilis* phage SPR codes for a DNA methyltransferase with triple sequence specificity. *Nucleic Acids Res*. **15**, 3689–3702 (1987).
45. Iida, S., Streiff, M. B., Bickle, T. A. & Arber, W. Two DNA antirestriction systems of bacteriophage P1, *darA*, and *darB*: characterization of *darA*$^-$ phages. *Virology* **157**, 156–166 (1987).
46. Piya, D., Vara, L., Russell, W. K., Young, R. & Gill, J. J. The multicomponent antirestriction system of phage P1 is linked to capsid morphogenesis. *Mol. Microbiol*. **105**, 399–412 (2017).
47. Atanasiu, C., Su, T. J., Sturrock, S. S. & Dryden, D. T. F. Interaction of the ocr gene 0.3 protein of bacteriophage T7 with EcoKI restriction/modification enzyme. *Nucleic Acids Res*. **30**, 3936–3944 (2002).
48. Walkinshaw, M. D. et al. Structure of Ocr from bacteriophage T7, a protein that mimics B-form DNA. *Mol. Cell* **9**, 187–194 (2002).
49. Laity, C., Chater, K. F., Lewis, C. G. & Buttner, M. J. Genetic analysis of the φC31-specific phage growth limitation (Pgl) system of *Streptomyces coelicolor* A3(2). *Mol. Microbiol*. **7**, 329–336 (1993).
50. Barrangou, R. et al. CRISPR provides acquired resistance against viruses in prokaryotes. *Science* **315**, 1709–1712 (2007).
51. Jackson, S. A. et al. CRISPR–Cas: adapting to change. *Science* **356**, eaal5056 (2017).
52. Hille, F. et al. The biology of CRISPR–Cas: backward and forward. *Cell* **172**, 1239–1259 (2018).
53. Koonin, E. V. & Makarova, K. S. Origins and evolution of CRISPR–Cas systems. *Phil. Trans. R. Soc. B* **374**, 20180087 (2019).
54. Koonin, E. V., Makarova, K. S. & Zhang, F. Diversity, classification and evolution of CRISPR–Cas systems. *Curr. Opin. Microbiol*. **37**, 67–78 (2017).
55. Makarova, K. S., Wolf, Y. I. & Koonin, E. V. Classification and nomenclature of CRISPR–Cas systems: where from here? *CRISPR J*. **1**, 325–336 (2018).
56. Brouns, S. J. J. et al. Small CRISPR RNAs guide antiviral defense in prokaryotes. *Science* **321**, 960–964 (2008).
57. Semenova, E. et al. Interference by clustered regularly interspaced short palindromic repeat (CRISPR) RNA is governed by a seed sequence. *Proc. Natl Acad. Sci. USA* **108**, 10098–10103 (2011).
58. Datsenko, K. A. et al. Molecular memory of prior infections activates the CRISPR/Cas adaptive bacterial immunity system. *Nat. Commun*. **3**, 945 (2012).
59. Strotskaya, A. et al. The action of *Escherichia coli* CRISPR–Cas system on lytic bacteriophages with different lifestyles and development strategies. *Nucleic Acids Res*. **45**, 1946–1957 (2017).
60. Cady, K. C., Bondy-Denomy, J., Heussler, G. E., Davidson, A. R. & O'Toole, G. A. The CRISPR/Cas adaptive immune system of *Pseudomonas aeruginosa* mediates resistance to naturally occurring and engineered phages. *J. Bacteriol*. **194**, 5728–5738 (2012).
61. Westra, E. R. et al. Parasite exposure drives selective evolution of constitutive versus inducible defense. *Curr. Biol*. **25**, 1043–1049 (2015).

62. Watson, B. N. J., Staals, R. H. J. & Fineran, P. C. CRISPR–Cas-mediated phage resistance enhances horizontal gene transfer by transduction. *mBio* **9**, e02406-17 (2018).
63. Taylor, H. N. et al. Structural basis of type IV CRISPR RNA biogenesis by a Cas6 endoribonuclease. *RNA Biol*. **16**, 1438–1447 (2019).
64. Özcan, A. et al. Type IV CRISPR RNA processing and effector complex formation in *Aromatoleum aromaticum*. *Nat. Microbiol*. **4**, 89–96 (2019).
65. Deng, L., Garrett, R. A., Shah, S. A., Peng, X. & She, Q. A novel interference mechanism by a type IIIB CRISPR–Cmr module in *Sulfolobus*. *Mol. Microbiol*. **87**, 1088–1099 (2013).
66. Samai, P. et al. Co-transcriptional DNA and RNA cleavage during type III CRISPR–Cas immunity. *Cell* **161**, 1164–1174 (2015).
67. Jiang, W., Samai, P. & Marraffini, L. A. Degradation of phage transcripts by CRISPR-associated RNases enables type III CRISPR–Cas immunity. *Cell* **164**, 710–721 (2016).
68. Pyenson, N. C., Gayvert, K., Varble, A., Elemento, O. & Marraffini, L. A. Broad targeting specificity during bacterial type III CRISPR–Cas immunity constrains viral escape. *Cell Host Microbe* **22**, 343–353 (2017).
69. Millen, A. M., Horvath, P., Boyaval, P. & Romero, D. A. Mobile CRISPR/Cas-mediated bacteriophage resistance in *Lactococcus lactis*. *PLoS ONE* **7**, e51663 (2012).
70. Tamulaitis, G. et al. Programmable RNA shredding by the type III-A CRISPR–Cas system of *Streptococcus thermophilus*. *Mol. Cell* **56**, 506–517 (2014).
71. Goldberg, G. W., Jiang, W., Bikard, D. & Marraffini, L. A. Conditional tolerance of temperate phages via transcription-dependent CRISPR–Cas targeting. *Nature* **514**, 633–637 (2014).
72. Kazlauskiene, M., Kostiuk, G., Venclovas, Č., Tamulaitis, G. & Siksnys, V. A cyclic oligonucleotide signaling pathway in type III CRISPR–Cas systems. *Science* **357**, 605–609 (2017).
73. Niewoehner, O. et al. Type III CRISPR–Cas systems produce cyclic oligoadenylate second messengers. *Nature* **548**, 543–548 (2017).
74. Rostøl, J. T. & Marraffini, L. A. Non-specific degradation of transcripts promotes plasmid clearance during type III-A CRISPR–Cas immunity. *Nat. Microbiol*. **4**, 656–662 (2019).
75. Varble, A. & Marraffini, L. A. Three new Cs for CRISPR: collateral, communicate, cooperate. *Trends Genet*. **35**, 446–456 (2019).
76. McGinn, J. & Marraffini, L. A. CRISPR–Cas systems optimize their immune response by specifying the site of spacer integration. *Mol. Cell* **64**, 616–623 (2016).
77. Zetsche, B. et al. Cpf1 is a single RNA-guided endonuclease of a class 2 CRISPR–Cas system. *Cell* **163**, 759–771 (2015).
78. Vlot, M. et al. Bacteriophage DNA glucosylation impairs target DNA binding by type I and II but not by type V CRISPR–Cas effector complexes. *Nucleic Acids Res*. **46**, 873–885 (2018).
79. Abudayyeh, O. O. et al. C2c2 is a single-component programmable RNA-guided RNA-targeting CRISPR effector. *Science* **353**, aaf5573 (2016).
80. Meeske, A. J., Nakandakari-Higa, S. & Marraffini, L. A. Cas13-induced cellular dormancy prevents the rise of CRISPR-resistant bacteriophage. *Nature* **570**, 241–245 (2019).
This study demonstrates that a CRISPR–Cas variant can provide broad phage protection by inducing bacterial dormancy.
81. Watson, B. N. J. et al. Different genetic and morphological outcomes for phages targeted by single or multiple CRISPR–Cas spacers. *Phil. Trans. R. Soc. B* **374**, 20180090 (2019).
82. Deveau, H. et al. Phage response to CRISPR-encoded resistance in *Streptococcus thermophilus*. *J. Bacteriol*. **190**, 1390–1400 (2008).
83. Sun, C. L. et al. Phage mutations in response to CRISPR diversification in a bacterial population. *Environ. Microbiol*. **15**, 463–470 (2013).
84. Martel, B. & Moineau, S. CRISPR–Cas: an efficient tool for genome engineering of virulent bacteriophages. *Nucleic Acids Res*. **42**, 9504–9513 (2014).
85. Paez-Espino, D. et al. CRISPR immunity drives rapid phage genome evolution in *Streptococcus thermophilus*. *mBio* **6**, e00262-15 (2015).
86. Nicholson, T. J. et al. Bioinformatic evidence of widespread priming in type I and II CRISPR–Cas systems. *RNA Biol*. **16**, 566–576 (2019).
87. Nussenzweig, P. M., McGinn, J. & Marraffini, L. A. Cas9 cleavage of viral genomes primes the acquisition of new immunological memories. *Cell Host Microbe* **26**, 515–526 (2019).
88. Bondy-Denomy, J., Pawluk, A., Maxwell, K. L. & Davidson, A. R. Bacteriophage genes that inactivate the CRISPR/Cas bacterial immune system. *Nature* **493**, 429–432 (2013).
The discovery and characterization of anti-CRISPRs.
89. Hwang, S. & Maxwell, K. L. Meet the anti-CRISPRs: widespread protein inhibitors of CRISPR–Cas systems. *CRISPR J*. **2**, 23–30 (2019).
90. Trasanidou, D. et al. Keeping CRISPR in check: diverse mechanisms of phage-encoded anti-CRISPRS. *FEMS Microbiol. Lett*. **366**, fnz098 (2019).
91. Bhoobalan-Chitty, Y., Baek Johansen, T., Di Cianni, N. & Peng, X. Inhibition of type III CRISPR–Cas immunity by an archaeal virus-encoded anti-CRISPR protein. *Cell* **179**, 448–458 (2019).
92. Dong, L. et al. An anti-CRISPR protein disables type V Cas12a by acetylation. *Nat. Struct. Mol. Biol*. **26**, 308–314 (2019).
93. Knott, G. J. et al. Broad-spectrum enzymatic inhibition of CRISPR–Cas12a. *Nat. Struct. Mol. Biol*. **26**, 315–321 (2019).
94. Landsberger, M. et al. Anti-CRISPR phages cooperate to overcome CRISPR–Cas immunity. *Cell* **174**, 908–916 (2018).
This study demonstrates that phages cooperate through their anti-CRISPRs to immunosuppress the host CRISPR–Cas system.
95. Borges, A. L. et al. Bacteriophage cooperation suppresses CRISPR–Cas3 and Cas9 immunity. *Cell* **174**, 917–925 (2018).
This work describes how phages cooperate through their anti-CRISPRs to inhibit bacterial adaptive immunity.
96. Seed, K. D., Lazinski, D. W., Calderwood, S. B. & Camilli, A. A bacteriophage encodes its own CRISPR/Cas adaptive response to evade host innate immunity. *Nature* **494**, 489–491 (2013).
97. Hargreaves, K. R., Flores, C. O., Lawley, T. D. & Clokie, M. R. J. Abundant and diverse clustered regularly interspaced short palindromic repeat spacers in *Clostridium difficile* strains and prophages target multiple phage types within this pathogen. *mBio* **5**, e01045-13 (2014).
98. Montgomery, M. T., Guerrero Bustamante, C. A., Dedrick, R. M., Jacobs-Sera, D. & Hatfull, G. F. Yet more evidence of collusion: a new viral defense system encoded by *Gordonia* phage CarolAnn. *mBio* **10**, e02417-18 (2019).
99. Page, R. & Peti, W. Toxin–antitoxin systems in bacterial growth arrest and persistence. *Nat. Chem. Biol*. **12**, 208–214 (2016).
100. Fineran, P. C. et al. The phage abortive infection system, ToxIN, functions as a protein–RNA toxin–antitoxin pair. *Proc. Natl Acad. Sci. USA* **106**, 894–899 (2009).
101. Al-Shayeb, B. et al. Clades of huge phage from across Earth's ecosystems. Preprint at *bioRxiv* https://doi.org/10.1101/572362 (2019).
102. Faure, G. et al. CRISPR–Cas in mobile genetic elements: counter-defence and beyond. *Nat. Rev. Microbiol*. **17**, 513–525 (2019).
103. Chopin, M.-C., Chopin, A. & Bidnenko, E. Phage abortive infection in lactococci: variations on a theme. *Curr. Opin. Microbiol*. **8**, 473–479 (2005).
104. Labrie, S. J., Samson, J. E. & Moineau, S. Bacteriophage resistance mechanisms. *Nat. Rev. Microbiol*. **8**, 317–327 (2010).
105. Depardieu, F. et al. A eukaryotic-like serine/threonine kinase protects Staphylococci against phages. *Cell Host Microbe* **20**, 471–481 (2016).
This study describes the discovery of an Abi system with similarities to eukaryotic defences.
106. Parma, D. H. et al. The Rex system of bacteriophage lambda: tolerance and altruistic cell death. *Genes Dev*. **6**, 497–510 (1992).
107. Gentile, G. M. et al. More evidence of collusion: a new prophage-mediated viral defense system encoded by mycobacteriophage Sbash. *mBio* **10**, e00196-19 (2019).
108. Samson, J. E., Spinelli, S., Cambillau, C. & Moineau, S. Structure and activity of AbiQ, a lactococcal endoribonuclease belonging to the type III toxin–antitoxin system. *Mol. Microbiol*. **87**, 756–768 (2013).
109. Dy, R. L., Przybilski, R., Semeijn, K., Salmond, G. P. C. & Fineran, P. C. A widespread bacteriophage abortive infection system functions through a type IV toxin–antitoxin mechanism. *Nucleic Acids Res*. **42**, 4590–4605 (2014).
110. Pecota, D. C. & Wood, T. K. Exclusion of T4 phage by the *hok/sok* killer locus from plasmid R1. *J. Bacteriol*. **178**, 2044–2050 (1996).
111. Koga, M., Otsuka, Y., Lemire, S. & Yonesaki, T. *Escherichia coli rnlA* and *rnlB* compose a novel toxin–antitoxin system. *Genetics* **187**, 123–130 (2011).
112. Hazan, R. & Engelberg-Kulka, H. *Escherichia coli mazEF*-mediated cell death as a defense mechanism that inhibits the spread of phage P1. *Mol. Genet. Genomics* **272**, 227–234 (2004).
113. Snyder, L. Phage-exclusion enzymes: a bonanza of biochemical and cell biology reagents? *Mol. Microbiol*. **15**, 415–420 (1995).
114. Otsuka, Y. & Yonesaki, T. Dmd of bacteriophage T4 functions as an antitoxin against *Escherichia coli* LsoA and RnlA toxins. *Mol. Microbiol*. **83**, 669–681 (2012).
115. Labrie, S. J. & Moineau, S. Abortive infection mechanisms and prophage sequences significantly influence the genetic makeup of emerging lytic lactococcal phages. *J. Bacteriol*. **189**, 1482–1487 (2007).
116. Blower, T. R., Evans, T. J., Przybilski, R., Fineran, P. C. & Salmond, G. P. C. Viral evasion of a bacterial suicide system by RNA-based molecular mimicry enables infectious altruism. *PLoS Genet*. **8**, e1003023 (2012).
117. Sberro, H. et al. Discovery of functional toxin/antitoxin systems in bacteria by shotgun cloning. *Mol. Cell* **50**, 136–148 (2013).
118. Alawneh, A. M., Qi, D., Yonesaki, T. & Otsuka, Y. An ADP-ribosyltransferase Alt of bacteriophage T4 negatively regulates the *Escherichia coli*|MazF toxin of a toxin–antitoxin module. *Mol. Microbiol*. **99**, 188–198 (2016).
119. Lossouarn, J. et al. *Enterococcus faecalis* Countermeasures defeat a virulent *Picovirinae* bacteriophage. *Viruses* **11**, 48 (2019).
120. Blower, T. R. et al. Evolution of *Pectobacterium* bacteriophage ΦM1 to escape two bifunctional type III toxin–antitoxin and abortive infection systems through mutations in a single viral gene. *Appl. Environ. Microbiol*. **83**, e03229-16 (2017).
121. Chen, B., Akusobi, C., Fang, X. & Salmond, G. P. C. Environmental T4-family bacteriophages evolve to escape abortive infection via multiple routes in a bacterial host employing 'altruistic suicide' through type III toxin–antitoxin systems. *Front. Microbiol*. **8**, 127 (2018).
122. Cumby, N., Davidson, A. R. & Maxwell, K. L. The moron comes of age. *Bacteriophage* **2**, e23146 (2012).
123. Dedrick, R. M. et al. Prophage-mediated defence against viral attack and viral counter-defence. *Nat. Microbiol*. **2**, 16251 (2017).
Demonstration that mycobacterial prophages encode diverse anti-phage defence systems and the ways that phages can evade these defences.
124. Ko, C.-C. & Hatfull, G. F. Mycobacteriophage Fruitloop gp52 inactivates Wag31 (DivIVA) to prevent heterotypic superinfection. *Mol. Microbiol*. **108**, 443–460 (2018).
125. Roux, S. et al. Cryptic inoviruses revealed as pervasive in bacteria and archaea across Earth's biomes. *Nat. Microbiol*. **4**, 1895–1906 (2019).
126. Makarova, K. S., Wolf, Y. I., Snir, S. & Koonin, E. V. Defense islands in bacterial and archaeal genomes and prediction of novel defense systems. *J. Bacteriol*. **193**, 6039–6056 (2011).
127. Doron, S. et al. Systematic discovery of antiphage defense systems in the microbial pangenome. *Science* **359**, eaar4120–13 (2018).
This study describes the identification of numerous new anti-phage systems in defence islands.
128. Willkomm, S., Makarova, K. S. & Grohmann, D. DNA silencing by prokaryotic Argonaute proteins adds a new layer of defense against invading nucleic acids. *FEMS Microbiol. Rev*. **42**, 376–387 (2018).
129. Hegge, J. W., Swarts, D. C. & van der Oost, J. Prokaryotic Argonaute proteins: novel genome-editing tools? *Nat. Rev. Microbiol*. **16**, 5–11 (2018).
130. Swarts, D. C. et al. DNA-guided DNA interference by a prokaryotic Argonaute. *Nature* **507**, 258–261 (2014).
131. Swarts, D. C. et al. Autonomous generation and loading of DNA guides by bacterial Argonaute. *Mol. Cell* **65**, 985–998 (2017).

132. Olovnikov, I., Chan, K., Sachidanandam, R., Newman, D. K. & Aravin, A. A. Bacterial Argonaute samples the transcriptome to identify foreign DNA. *Mol. Cell* **51**, 594–605 (2013).
133. Zander, A. et al. Guide-independent DNA cleavage by archaeal Argonaute from *Methanocaldococcus jannaschii*. *Nat. Microbiol.* **2**, 17034 (2017).
134. Cohen, D. et al. Cyclic GMP–AMP signalling protects bacteria against viral infection. *Nature* **574**, 691–695 (2019).
This study showed that a eukaryotic anti-viral signalling pathway is also present in prokaryotes, and that this pathway offers protection from a range of phages.
135. Ye, Q. et al. HORMA domain proteins and a Pch2-like ATPase regulate bacterial cGAS-like enzymes to mediate bacteriophage immunity. Preprint at *bioRxiv* https://doi.org/10.1101/694695 (2019).
136. Lau, R. K. et al. Structure and mechanism of a cyclic trinucleotide-activated bacterial endonuclease mediating bacteriophage immunity. Preprint at *bioRxiv* https://doi.org/10.1101/694703 (2019).
137. Kronheim, S. et al. A chemical defence against phage infection. *Nature* **564**, 283–286 (2018).
The first example of chemical defences against phages.
138. Chaikeeratisak, V. et al. Assembly of a nucleus-like structure during viral replication in bacteria. *Science* **355**, 194–197 (2017).
This study describes how jumbophages can produce nucleus-like protein shells inside a bacterium for phage replication.
139. Mendoza, S. D. et al. A bacteriophage nucleus-like compartment shields DNA from CRISPR nucleases. *Nature* https://doi.org/10.1038/s41586-019-1786-y (2019).
140. Malone, L. M. et al. A jumbo phage that forms a nucleus-like structure evades CRISPR–Cas DNA targeting but is vulnerable to type III RNA-based immunity. *Nat. Microbiol.* https://doi.org/10.1038/s41564-019-0612-5 (2019).
141. Høyland-Kroghsbo, N. M., Maerkedahl, R. B. & Svenningsen, S. L. A quorum-sensing-induced bacteriophage defense mechanism. *mBio* **4**, e00362-12 (2013).
142. Høyland-Kroghsbo, N. M. et al. Quorum sensing controls the *Pseudomonas aeruginosa* CRISPR–Cas adaptive immune system. *Proc. Natl Acad. Sci. USA* **114**, 131–135 (2017).
143. Patterson, A. G. et al. Quorum sensing controls adaptive immunity through the regulation of multiple CRISPR–Cas systems. *Mol. Cell* **64**, 1102–1108 (2016).
Demonstration that bacteria use quorum-sensing communication to coordinate multiple CRISPR–Cas systems at a population level
144. Erez, Z. et al. Communication between viruses guides lysis–lysogeny decisions. *Nature* **541**, 488–493 (2017).
This study reveals that phages use communication to guide the replication strategy used by progeny phages.
145. Stokar-Avihail, A., Tal, N., Erez, Z., Lopatina, A. & Sorek, R. Widespread utilization of peptide communication in phages infecting soil and pathogenic bacteria. *Cell Host Microbe* **25**, 746–755 (2019).
146. Dou, C. et al. Structural and functional insights into the regulation of the lysis–lysogeny decision in viral communities. *Nat. Microbiol.* **3**, 1285–1294 (2018).
147. Gallego del Sol, F., Penadés, J. R. & Marina, A. Deciphering the molecular mechanism underpinning phage arbitrium communication systems. *Mol. Cell* **74**, 59–72 (2019).
148. Guan, Z. et al. Structural insights into DNA recognition by AimR of the arbitrium communication system in the SPbeta phage. *Cell Discov.* **5**, 29 (2019).
149. Silpe, J. E. & Bassler, B. L. Phage-encoded LuxR-type receptors responsive to host-produced bacterial quorum-sensing autoinducers. *mBio* **10**, e00638-19 (2019).
150. Silpe, J. E. & Bassler, B. L. A Host-Produced Quorum-Sensing Autoinducer Controls a Phage Lysis-Lysogeny Decision. *Cell* **176**, 268–280 (2019).
151. Hargreaves, K. R., Kropinski, A. M. & Clokie, M. R. J. What does the talking?: quorum sensing signalling genes discovered in a bacteriophage genome. *PLoS ONE* **9**, e85131 (2014).
152. Uribe, R. V. et al. Discovery and characterization of Cas9 inhibitors disseminated across seven bacterial phyla. *Cell Host Microbe* **25**, 233–241 (2019).
153. Koonin, E. V., Makarova, K. S. & Wolf, Y. I. Evolutionary genomics of defense systems in archaea and bacteria. *Annu. Rev. Microbiol.* **71**, 233–261 (2017).
154. Dupuis, M.-È. V., Villion, M., Magadán, A. H. & Moineau, S. CRISPR–Cas and restriction–modification systems are compatible and increase phage resistance. *Nat. Commun.* **4**, 2087 (2013).
155. Silas, S. et al. Type III CRISPR–Cas systems can provide redundancy to counteract viral escape from type I systems. *eLife* **6**, e27601 (2017).
156. Van den Bossche, A. et al. Systematic identification of hypothetical bacteriophage proteins targeting key protein complexes of *Pseudomonas aeruginosa*. *J. Proteome Res.* **13**, 4446–4456 (2014).
157. Buckling, A. & Brockhurst, M. in *Evolutionary Systems Biology* Vol. 751 (ed. Soyer O.) 347–370 (Springer, 2012).
158. Koskella, B. & Brockhurst, M. A. Bacteria–phage coevolution as a driver of ecological and evolutionary processes in microbial communities. *FEMS Microbiol. Rev.* **38**, 916–931 (2014).
159. Scanlan, P. D. Bacteria–bacteriophage coevolution in the human gut: implications for microbial diversity and functionality. *Trends Microbiol.* **25**, 614–623 (2017).
160. Horne, M. T. Coevolution of *Escherichia coli* and bacteriophages in chemostat culture. *Science* **168**, 992–993 (1970).
161. Lenski, R. E. & Levin, B. R. Constraints on the coevolution of bacteria and virulent phage: a model, some experiments, and predictions for natural communities. *Am. Nat.* **125**, 585–602 (1985).
162. Buckling, A. & Rainey, P. B. Antagonistic coevolution between a bacterium and a bacteriophage. *Proc. R. Soc. Lond. B* **269**, 931–936 (2002).
163. Buckling, A. & Rainey, P. B. The role of parasites in sympatric and allopatric host diversification. *Nature* **420**, 496–499 (2002).
164. Brockhurst, M. A., Morgan, A. D., Fenton, A. & Buckling, A. Experimental coevolution with bacteria and phage: the *Pseudomonas fluorescens*—Φ2 model system. *Infect. Genet. Evol.* **7**, 547–552 (2007).
165. Gómez, P. & Buckling, A. Bacteria–phage antagonistic coevolution in soil. *Science* **332**, 106–109 (2011).
166. Andersson, A. F. & Banfield, J. F. Virus population dynamics and acquired virus resistance in natural microbial communities. *Science* **320**, 1047–1050 (2008).
167. Stern, A., Mick, E., Tirosh, I., Sagy, O. & Sorek, R. CRISPR targeting reveals a reservoir of common phages associated with the human gut microbiome. *Genome Res.* **22**, 1985–1994 (2012).
168. Emerson, J. B. et al. Virus–host and CRISPR dynamics in Archaea-dominated hypersaline Lake Tyrrell, Victoria, Australia. *Archaea* **2013**, 370871 (2013).
169. Laanto, E., Hoikkala, V., Ravantti, J. & Sundberg, L. R. Long-term genomic coevolution of host–parasite interaction in the natural environment. *Nat. Commun.* **8**, 111 (2017).
170. Shmakov, S. et al. Discovery and Functional characterization of diverse class 2 CRISPR–Cas systems. *Mol. Cell* **60**, 385–397 (2015).
171. Burstein, D. et al. New CRISPR–Cas systems from uncultivated microbes. *Nature* **542**, 237–241 (2017).
172. Weissman, J. L. et al. Immune loss as a driver of coexistence during host–phage coevolution. *ISME J.* **12**, 585–597 (2018).
173. Jackson, S. A., Birkholz, N., Malone, L. M. & Fineran, P. C. Imprecise spacer acquisition generates CRISPR–Cas immune diversity through primed adaptation. *Cell Host Microbe* **25**, 250–260 (2019).

Acknowledgements Research in the Fineran laboratory on phage defence systems is supported by the Marsden Fund, Royal Society of New Zealand, the Bio-Protection Centre of Research Excellence and the University of Otago. We thank N. Birkholz for providing input on the figures and members of the Fineran laboratory for discussions and comments on the manuscript.

Author contributions H.G.H., B.N.J.W. and P.C.F. contributed equally to all aspects of the manuscript.

Competing interests The authors declare no competing interests.

Additional information

Correspondence and requests for materials should be addressed to P.C.F.

Reprints and permissions information is available at http://www.nature.com/reprints.
Publisher's note Springer Nature remains neutral with regard to jurisdictional claims in published maps and institutional affiliations.

© Springer Nature Limited 2020

Article

A population of dust-enshrouded objects orbiting the Galactic black hole

https://doi.org/10.1038/s41586-019-1883-y

Received: 5 June 2019

Accepted: 2 October 2019

Published online: 15 January 2020

Anna Ciurlo[1]*, Randall D. Campbell[2], Mark R. Morris[1], Tuan Do[1], Andrea M. Ghez[1], Aurélien Hees[3], Breann N. Sitarski[4], Kelly Kosmo O'Neil[1], Devin S. Chu[1], Gregory D. Martinez[1], Smadar Naoz[1] & Alexander P. Stephan[1]

The central 0.1 parsecs of the Milky Way host a supermassive black hole identified with the position of the radio and infrared source Sagittarius A* (refs. [1,2]), a cluster of young, massive stars (the S stars[3]) and various gaseous features[4,5]. Recently, two unusual objects have been found to be closely orbiting Sagittarius A*: the so-called G sources, G1 and G2. These objects are unresolved (having a size of the order of 100 astronomical units, except at periapse, where the tidal interaction with the black hole stretches them along the orbit) and they show both thermal dust emission and line emission from ionized gas[6–10]. G1 and G2 have generated attention because they appear to be tidally interacting with the supermassive Galactic black hole, possibly enhancing its accretion activity. No broad consensus has yet been reached concerning their nature: the G objects show the characteristics of gas and dust clouds but display the dynamical properties of stellar-mass objects. Here we report observations of four additional G objects, all lying within 0.04 parsecs of the black hole and forming a class that is probably unique to this environment. The widely varying orbits derived for the six G objects demonstrate that they were commonly but separately formed.

We used near-infrared (NIR) spectro-imaging data obtained over the past 13 years[11] at the W. M. Keck Observatory with the OSIRIS integral field spectrometer[12], coupled with laser guide star adaptive optics wave front corrections[13]. OSIRIS data-cubes have two spatial dimensions—about 3 arcsec × 2 arcsec surrounding Sgr A* with a plate-scale of 35 mas—and one wavelength dimension that covers the Kn3 band, 2.121–2.229 μm, with a spectral resolution of $R \approx 3{,}800$. We selected 24 data-cubes based on image quality and signal-to-noise ratio; see Methods section 'Observations'. These cubes were processed through the OSIRIS pipeline[14]. We also removed the stellar continua to isolate emission features associated with interstellar gas (Methods section 'Continuum subtraction'). The reduced data-cubes were analysed with a three-dimensional visualization tool, OsrsVol[15], that simultaneously displays all dimensions of the data-cube. This helps disentangle the many features of this crowded region, which are often superimposed in the spatial dimension but are separable in the wavelength dimension (Fig. 1).

Analysing the data with OsrsVol as well as conventional two-dimensional (2D) and one-dimensional (1D) tools, we identify four new compact objects in Brackett-γ line emission (Brγ; 2.1661 μm rest wavelength) that consistently appear in the data across the observed timeline. In addition to Brγ, all four objects show two [Fe III] emission lines (at 2.1457 μm and 2.2184 μm; ref. [16]).

The four objects show many properties in common with G1 and G2 (compact Brγ emission and coherent orbital motion) and we therefore name them G3, G4, G5 and G6. G3 was previously identified (D2[7,17]). For this work we independently identified G3 in Brγ emission, and G4, G5 and G6 are newly reported. Recently, G6 has been independently examined[18], and interpreted as a bow shock source rather than a G object. We estimate that we are able to detect G objects having Brγ flux densities of at least 0.02 mJy, if they lie in a non-confused location.

Several other infrared-excess sources have been identified with L′ and K′ observations (central wavelengths of 2.2 μm and 3.8 μm, respectively[7,17], see Extended Data Fig. 1). We do not include these other sources in this work (except for G3/D2), either because they lie outside the OSIRIS field of view, or because they have not been detected in Brγ, or because they have not been consistently detected throughout the 13 years of data. We use Keck/NIRC2 L′ imaging data to investigate whether G3, G4, G5 and G6 have detectable L′ counterparts, as G1 and G2 do (Methods section 'L′ detection analysis'). No L′ counterpart was detected for G4, G5 and G6, with upper limits to the flux density of 0.4 mJy, 0.6 mJy and 0.5 mJy, respectively. G3 is detected in L′ with a dereddened flux density of 2.5 mJy, consistent with a previous report[17].

None of the G objects was detected in the K continuum. Our detection limit in the K continuum is 0.01 mJy in the OSIRIS spectra (Kn3 filter) and in the K′ broadband (2.12 μm central wavelength) a limit of 0.07 mJy was reported for G2[19] (but see ref. [20]).

The Brγ emission is a key defining feature of the G objects because it probably results from external ionization and does not depend on the mass of a putative central object, and hence its presence is independent of the nature of the G objects (low-mass cloud or extended stellar-mass object). The compactness of such emission is what distinguishes the G objects from other presumably short-lived gas blobs that have become detached from larger-scale interstellar structures. The dust heating can be attributed to some combination of the external radiation field and an internal stellar core, if present. Therefore, the

[1]Department of Physics and Astronomy, University of California, Los Angeles, CA, USA. [2]W. M. Keck Observatory, Waimea, HI, USA. [3]SYRTE, Observatoire de Paris, Université PSL, CNRS, Sorbonne Université, LNE, Paris, France. [4]Giant Magellan Telescope Organization, Pasadena, CA, USA. *e-mail: ciurlo@astro.ucla.edu

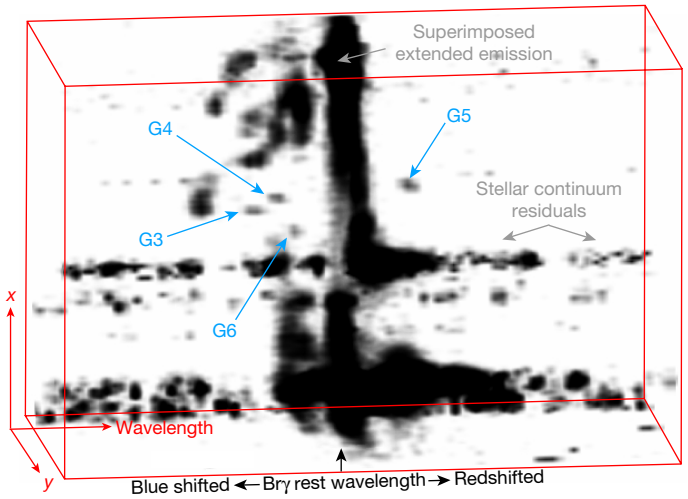


Fig. 1 | 2006 OSIRIS data-cube visualized with OsrsVol. The spatial dimensions ($x-y$) cover the OSIRIS field of view. The wavelength dimension is centred around Brγ (±1,500 km s^{-1}). G3, G4 and G6 are blueshifted, whereas G5 is redshifted. G1 and G2 are not visible here because they have larger velocities. The extended emission in the middle is near the rest wavelength and it arises from foreground or background gas ('superimposed extended emission'). The emission extending the full length of the wavelength axis at a few positions ('stellar continuum residuals') is associated with continuum subtraction residuals. For this analysis, we only use sources that appear throughout the observed timeline.

lack of detection of the G objects in the L′ band does not necessarily have implications for the existence of a stellar object embedded within the ionized external envelope.

The proper motions of the G objects were determined from the Brγ centroid in the OSIRIS data (Methods sections 'Aligning OSIRIS epochs' and 'Astrometric measurements and uncertainty'). We furthermore determined the radial velocity of each object by extracting its spectrum over a 1.5-pixel-radius aperture on each data-cube and performing a Gaussian fit to the Brγ profile (Methods section 'Radial velocity measurements and uncertainty').

All G objects show large proper motions and have substantial radial velocity shifts; the radial velocity of G3 changed by about 300 km s^{-1} over 13 years (see Fig. 2b and Methods section 'Radial velocity measurements and uncertainty').

Using these measurements (Extended Data Table 2), we determined the orbits of the new G objects with a Keplerian model, using a fitting algorithm[11] (Methods section 'Orbit fitting') with six orbital parameters, two parameters accounting for systematic errors in both astrometric positions and radial velocities, and one parameter accounting for correlation within the astrometric measurements. The black hole parameters (mass and Galactic Centre distance) are considered fixed[11]. The best-fit orbits are illustrated in Fig. 3 and the orbital parameters are reported in Extended Data Table 3. These fits indicate that: (1) G3, G4 and G6 have orbits with modest eccentricities ($e \approx 0.15$, 0.3 and 0.3, respectively), whereas G5 has a very eccentric orbit ($e \approx 0.9$); (2) the orbital periods range between 170 years (for G3) and 1,600 years (for G5); (3) all orbits lie on different planes, none of which contains G1 and G2 orbits or the clockwise stellar disk[21–23]; and (4) the orbits all have periods much longer than the 13 years of observations, which implies a small orbital phase coverage (~9% and ~2% in true anomaly for G3 and G5, respectively). We have run coverage tests to assess the bias attributable to the low phase coverage (Methods section 'Dependence on priors') and the results show that the obtained orbital parameters are not significantly biased (consistent with an unbiased result to within 1σ).

We used a Gaussian fit to the Brγ and the brightest [Fe III] line (2.2184 μm) profiles to extract fluxes. There is no noticeable flux variation for any of the four newly reported G objects in the 13 years of observations (Methods sections 'Flux calibration', 'Flux measurements' and 'Flux and FWHM summary table'). Nor can we detect any variation in the line width, given the variations in the data quality, instrumental upgrades and the emission line blending with other features.

Our analysis shows that the new objects show many of the same characteristics as G1 and G2, enough to justify defining them as members of a common new class. We define the G objects to have the following characteristics: (1) presence of a distinct source of Brγ emission; (2) spatially compact emission; (3) relatively weak K-band continuum emission (such that $K'-L' \geq 4.5$); and (4) large proper motion and radial velocity shifts over time. By 'compact' we mean that they are unresolved (<0.03″) or slightly resolved (~0.05″).

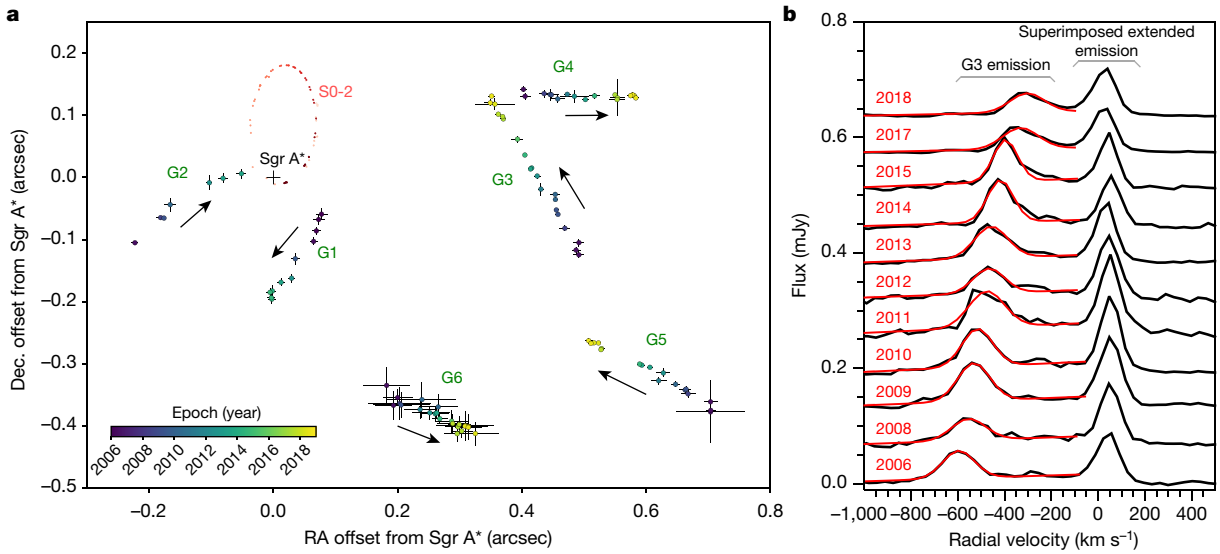


Fig. 2 | Proper motion and spectrum of the G objects. a, Observed proper motions (with error bars showing standard deviations) of G objects and S0-2 on the plane of the sky. RA, right ascension; dec., declination. **b**, G3 spectrum (black) and Gaussian fit to the G3 Brγ emission (red) in each year. There is no detected variation in the line width, but the G3 emission line blends with neighbouring features as it changes radial velocity. The large changes in the radial velocity of G3 contrast with the static extended foreground (or background) emission at the rest velocity ('superimposed extended emission'). G objects have Brγ emission, large proper motion and radial velocity shift, and are not detected in the K continuum.

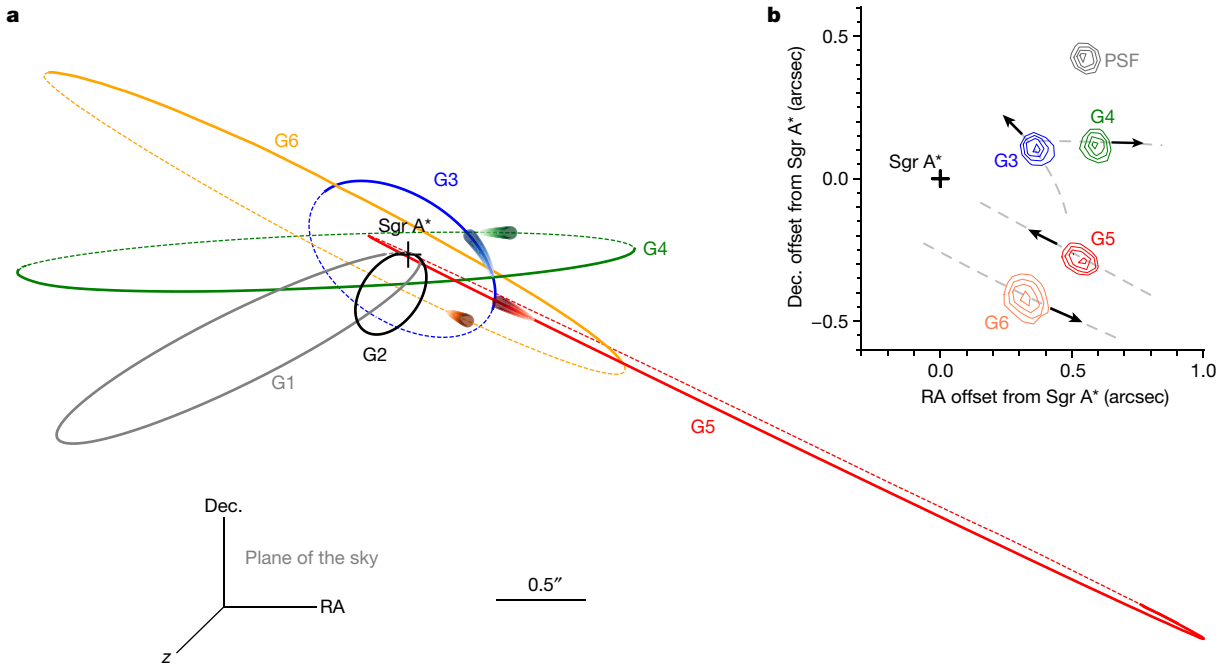


Fig. 3 | Orbits of the G objects. a, Orbit models in three dimensions: the portion of the orbit behind the plane of the sky containing Sgr A* is represented as a dashed line, and the part between the observer and Sgr A* is represented as a solid line. The thick short line indicates the time span of the observations (2006–18) and it gets darker and thicker in the direction of the object's motion. All orbits have different inclinations, eccentricities and periods. **b**, Contour plots of intensity (in the Kn3 band) of the new G objects in 2018, their orbits (dashed grey lines) and the point-spread function (PSF). All G objects are unresolved or only marginally resolved.

These characteristics distinguish G objects clearly from normal stars. In general, the G objects seem to have very red $K-L$ colours ($K'-L'>5.2$, 6 and 4.5 for G1, G2 and G3, respectively[17]), indicating that they are probably enshrouded by dust.

There are also some differences and peculiarities: G3, G4, G5 and G6 are all brighter in Brγ than G1 and G2 by about a factor of 2. G1, G2 and G3 have a clear L-band counterpart, unlike G4, G5 and G6. G3, G4, G5 and G6 show [Fe III] emission, whereas G1 and G2 do not. G3 and G4 are unresolved, while G5 and G6 are slightly extended (Fig. 3 inset). G1 was extended after periapse[9], as G2 was before and after periapse (but reverted to being compact[10]). Despite these differences, the shared properties of the G sources warrant their aggregation into a new class with an appreciable population.

G2 was originally interpreted as an ionized gas cloud[6] and later it was argued that G1 and G2 were knots within a common orbiting filament[24]. However, this interpretation cannot apply to the new sources as they have completely different orbits. G1 and G2 have remained intact after passing through periapse and, whereas G2 clearly underwent tidal interaction during its periapse passage[10], its dust component has remained unresolved. This has led several authors[8,9,25–27] to suggest that there might be a stellar core shielded by an extended envelope of gas and dust. The star needs to have a relatively low mass (less than a few solar masses[21]) in order to be compatible with the weakness of the stellar continuum.

Several models (Methods section 'G-object formation scenarios') have been proposed to account for G2 in terms of an optically thick distribution of dust surrounding a star: a young, low-mass star (T Tauri star) that has retained a protoplanetary disk[26] or that generates a mass-loss envelope[27], or the merger of a binary system[8,9,25,28].

The binary merger hypothesis (in which the influence of the black hole enhances the probability of a merger through eccentricity oscillations[29]) can also account for the presence of a population of G objects by interpreting them as relatively long-lived, distended post-merger objects. Assuming the binary merger hypothesis, we have used the number of observed G objects to estimate the required binary fraction[30] in the central 0.1 pc, obtaining a lower limit of about 5% for low-mass stars (Methods section 'Binary fraction estimate'). This is compatible with the expected binary fraction[31], based on dynamical simulations[30] and taking into account the physical characteristics of the Galactic Centre. In the most likely scenario[30] for the merger hypothesis, the original binaries would have been formed in the last major star formation event at the Galactic Centre (4–6 Myr ago[23]).

Therefore, the binary merger hypothesis offers a compelling explanation for the origin of the population of G objects for several reasons: (1) it fits well with the three-body dynamics that are necessarily at play in a dense stellar environment; (2) it is compatible with the observed wide range of G-object eccentricities[28]; and (3) it fits well with the known star formation history and observed stellar population.

The random distribution of the orbital planes and the broad range of eccentricities of the G objects very closely resemble the characteristics of the orbits of the S stars, which more or less occupy the same volume. In all of the star-centred hypotheses for the G objects, the stellar object must have a relatively small mass (less than a few solar masses). At present, in the central parsec, we can directly detect stars with masses down to ~1.5 solar masses[22]. Therefore, the G objects could be offering a unique window on the low-mass, currently undetectable, part of the S-star cluster.

Online content

Any methods, additional references, Nature Research reporting summaries, source data, extended data, supplementary information, acknowledgements, peer review information; details of author contributions and competing interests; and statements of data and code availability are available at https://doi.org/10.1038/s41586-019-1883-y.

1. Schödel, R. et al. A star in a 15.2-year orbit around the supermassive black hole at the centre of the Milky Way. *Nature* **419**, 694–696 (2002).
2. Ghez, A. M. et al. Stellar orbits around the Galactic center black hole. *Astrophys. J.* **620**, 744–757 (2005).

3. Eckart, A. & Genzel, R. Stellar proper motions in the central 0.1 pc of the Galaxy. *Mon. Not. R. Astron. Soc.* **284**, 576–598 (1997).
4. Morris, M. & Serabyn, E. The Galactic center environment. *Annu. Rev. Astron. Astrophys.* **34**, 645–701 (1996).
5. Genzel, R., Eisenhauer, F. & Gillessen, S. The Galactic center massive black hole and nuclear star cluster. *Rev. Mod. Phys.* **82**, 3121–3195 (2010).
6. Gillessen, S. et al. A gas cloud on its way towards the supermassive black hole at the Galactic Centre. *Nature* **481**, 51–54 (2012).
7. Eckart, A. et al. Near-infrared proper motions and spectroscopy of infrared excess sources at the Galactic center. *Astron. Astrophys.* **551**, A18 (2013).
8. Witzel, G. et al. Detection of Galactic center source G2 at 3.8 μm during periapse passage. *Astrophys. J.* **796**, L8 (2014).
9. Witzel, G. et al. The post-periapsis evolution of Galactic center source G1: the second case of a resolved tidal interaction with a supermassive black hole. *Astrophys. J.* **847**, 80 (2017).
10. Gillessen, S. et al. Detection of a drag force in G2's orbit: measuring the density of the accretion flow onto Sgr A* at 1000 Schwarzschild radii. *Astrophys. J.* **871**, 126 (2019).
11. Do, T. et al. Relativistic redshift of the star S0-2 orbiting the Galactic center supermassive black hole. *Science* **365**, 6454 (2019).
12. Larkin, J. et al. OSIRIS: a diffraction limited integral field spectrograph for Keck. *Proc. SPIE* **6269**, 62691A (2006).
13. Wizinowich, P. L. et al. The W. M. Keck Observatory laser guide star adaptive optics system: overview. *Publ. Astron. Soc. Pacif.* **118**, 297–309 (2006).
14. Lockhart, K. E. et al. Characterizing and improving the data reduction pipeline for the Keck OSIRIS integral field spectrograph. *Astron. J.* **157**, 75 (2019).
15. Campbell, R., Kjær, K. & Amico, P. 3D visualisation of integral field spectrometer data. *ESO Messenger* **148**, 28–31 (2012).
16. Bautista, M. A. & Pradhan, A. K. Ionization structure and spectra of iron in gaseous nebulae. *Astrophys. J.* **492**, 650–676 (1998).
17. Sitarski, B. N. *Characterizing Infrared Excess Sources in the Galactic Center with Adaptive Optics*. PhD thesis, Univ. California, Los Angeles (2016).
18. Peißker, F. et al. New bow-shock source with bipolar morphology in the vicinity of Sgr A*. *Astron. Astrophys.* **624**, A97 (2019).
19. Phifer, K. et al. Keck observations of the Galactic center source G2: gas cloud or star? *Astrophys. J.* **773**, L13 (2013).
20. Shahzamanian, B. et al. Polarized near-infrared light of the dusty S-cluster object (DSO/G2) at the Galactic center. *Astron. Astrophys.* **593**, A131 (2016).
21. Paumard, T. et al. The two young star disks in the central parsec of the Galaxy: properties, dynamics, and formation. *J. Phys. Conf. Ser.* **54**, 199–207 (2006).
22. Do, T. et al. Stellar populations in the central 0.5 pc of the Galaxy. I. A new method for constructing luminosity functions and surface-density profiles. *Astrophys. J.* **764**, 154 (2013).
23. Lu, J. R. et al. Stellar populations in the central 0.5 pc of the Galaxy. II. The initial mass function. *Astrophys. J.* **764**, 155 (2013).
24. Pfuhl, O. et al. The Galactic center cloud G2 and its gas streamer. *Astrophys. J.* **798**, 111 (2015).
25. Prodan, S., Antonini, F. & Perets, H. B. Secular evolution of binaries near massive black holes: formation of compact binaries, merger/collision products and G2-like objects. *Astrophys. J.* **799**, 118 (2015).
26. Murray-Clay, R. A. & Loeb, A. Disruption of a proto-planetary disc by the black hole at the Milky Way centre. *Nat. Commun.* **3**, 1049 (2012).
27. Scoville, N. & Burkert, A. The Galactic center cloud G2: young low-mass star with a stellar wind. *Astrophys. J.* **768**, 108 (2013).
28. Stephan, A. P. et al. Merging binaries in the Galactic center: the eccentric Kozai-Lidov mechanism with stellar evolution. *Mon. Not. R. Astron. Soc.* **460**, 3494–3504 (2016).
29. Naoz, S. The eccentric Kozai-Lidov effect and its applications. *Annu. Rev. Astron. Astrophys.* **54**, 441–489 (2016).
30. Stephan, A. P. et al. The fate of binaries in the Galactic center: the mundane and the exotic. *Astrophys. J.* **878**, 58 (2019).
31. Raghavan, D. et al. A survey of stellar families: multiplicity of solar-type stars. *Astrophys. J. Suppl. Ser.* **190**, 1–42 (2010).

Publisher's note Springer Nature remains neutral with regard to jurisdictional claims in published maps and institutional affiliations.

© The Author(s), under exclusive licence to Springer Nature Limited 2020

Methods

Observations

The observations were carried out with OSIRIS LGSAO covering 13 years, as tabulated in Extended Data Table 1. For each epoch of observations, the OSIRIS configuration with a plate-scale of 0.035″ per lenslet was used with the Kn3 (2.121–2.229 μm) bandpass. A dither sequence with 900 s per integration using a square box pattern centred on Sgr A* with 1.0 arcsec spacing was employed to increase the field of view and to help average-out systematic instrumental features. The data were reduced using the OSIRIS data reduction package, DRP[14]. The DRP produces a wavelength-calibrated data-cube with two spatial dimensions and one spectral dimension, with the dither sequence median combined into a mosaic.

Continuum subtraction

In order to extract the emission line of the interstellar medium we need to remove the continuum emission coming from the numerous stars in the field. To do so, we selected several spectral ranges devoid of spectral features. These spectral ranges are the same for all epochs and they are chosen to optimize the continuum estimation across the field and across the spectral band. Afterwards, we model the continuum pixel-by-pixel using a spline function. The continuum subtraction is somewhat more complex at the edges of the filter's band but this does not affect our measurements: the continuum around the emission line closest to the edge of the band that we are considering, [Fe III] 2.2184 μm, is still well modelled. We then produce new data-cubes in which the modelled continuum has been subtracted from each spectrum and use those for the rest of the analysis.

L′ detection analysis

The Galactic Center Group has gathered L′ (at 3.8 μm) imaging data in the L′ bandpass (at 3.8 μm) with the NIRC2 imager at the W. M. Keck Observatory over several of the same epochs observed by OSIRIS and used in this study. These data were analysed to determine whether there are L′ sources coincident with the OSIRIS-detected Brγ sources via the PSF-fitting tool StarFinder[32]. We chose the deepest L′ epoch (2012.551[17]) to search for coincident L′ sources.

No L′ counterpart was detected for G4, G5 and G6 and we perform star-planting simulations to determine an upper flux limit. We used the Brγ positions of the sources and transformed them into the 2012.551 L′ coordinate system using a series of linear transformations that take into account stretching, linear offsets, and rotation. For each source, neighbouring L′ sources were subtracted out using the flux values identified with StarFinder. K′-identified sources that were not associated with the L′ sources based on proper motions were also subtracted from the analysis image assuming that they had the same magnitude and colour profiles as our flux calibration sources (S0-2, S0-12, S1-20 and S1-1[9,17]). The images were then background-subtracted and Lucy–Richardson deconvolved using the background map and model PSF generated from StarFinder. We deconvolved for 8,196 iterations and re-convolved each image with a 3-pixel full-width at half-maximum (FWHM) two-dimensional Gaussian PSF. Point sources of varying magnitude were planted in the image at the positions of G4, G5 and G6 at varying magnitude until they could no longer be detected with a modified version of StarFinder[9,19,33]. These magnitudes were then corrected for Galactic Centre extinction[34] and converted to flux densities. The L′ flux density values for G4, G5 and G6 represent upper limits, but the G5 value may still be contaminated by structured background in that region. The flux density values for G3 are consistent with previous reports[17]. All flux densities are reported in Extended Data Table 4. In all the above analyses, the single PSF model generated by StarFinder is adequate to use in this case as the off-axis positions of the candidate G sources do not experience a strong effect of the field-dependent PSF. A by-eye search for G4, G5 and G6 was performed using the L′ data coincident with the other OSIRIS epochs, but no sources were cleanly identified as being associated with the three candidate G sources. All deconvolved images in the L′-coincident epochs are shown in Extended Data Fig. 2.

Aligning OSIRIS epochs

For our measurements and analysis, we used 24 epochs of OSIRIS observations. Each epoch consists of a mosaic constructed from frames that have been observed while dithering around the position of the star S0-2. The mosaic is obtained through a median-combine procedure applied through the OSIRIS DRP[14,35]. In order to extract the astrometry of the G objects, we shifted all mosaics into a common reference frame. To do so we measured the position of two reference stars: S0-12 and S0-14. The choice of these two specific stars was made because they are reasonably well-isolated in this crowded field, they are reasonably bright (for S0-12 $K \approx 14.3$, and for S0-14 $K \approx 13.7$; ref. [22]), and they are close to the observed G objects, thereby minimizing possible systematics in the alignment procedure due to distortion. We have accurate knowledge of the orbital motions—and thus astrometric positions—of these two stars with respect to Sgr A* from previous publications[11]. Taking into account the reference stars' motions we can put all observations in a common reference frame with Sgr A* at the centre. However, this assumes there is no significant differential distortion from epoch to epoch and that Sgr A* does not move. Given the small field of view covered by OSIRIS at this platescale, any differential distortion should be insignificant. The main source of uncertainty in this procedure comes from the centroid of the G objects. On the other hand, the position of the reference stars is very well measured because of the very high signal-to-noise. We also consider an additional systematic uncertainty on the astrometric position in the orbital fit (Methods section 'Orbit fitting').

Astrometric measurements and uncertainty

Analysis of the proper motion of the G objects was performed using two sets of cubes: those that had been processed to remove the continuum (Methods section 'Continuum subtraction') and those with the stellar continuum included. The G sources do not have a continuum detection in the Kn3 bandpass and thus we used the continuum-subtracted cubes to measure their positions. The positions of the G objects were measured in a median-collapsed 2D image produced by combining five spectral channels centred on the peak wavelength of the Brγ emission from each G source for each epoch. The peak-fit IDL routine was used to measure the X–Y position in each cube. The X–Y positions were transformed into RA–dec. coordinates relative to Sgr A* using the positions for S0-12 and S0-14 to establish the frame of reference.

S0-12 and S0-14 are stellar sources with well-established position offsets from Sgr A*, they are relatively isolated spatially, and their motion on the plane of the sky is relatively small over this time frame. The stellar positions were measured using the IDL peak-fit routine of a median-combined 2D image produced from collapsing the spectral dimension of the cube over the range of 2.133–2.158 μm (corresponding to channels 50–150). This wavelength range was chosen because it is a clean part of the spectrum that avoids emission, stellar absorption and atmospheric absorption features. The stellar point sources were mapped to a coordinate system in which Sgr A* is at rest[36,37]. The errors of the position measurements were estimated using a Monte Carlo method with many trials of centroid measures over variable aperture size and position. The measurements are reported in Extended Data Table 2.

Radial velocity measurements and uncertainty

The spectra for each G object were extracted from the continuum-subtracted data-cubes. To extract a 1D spectrum for the purpose of measuring radial velocity, the intensity of each Brγ emission feature was measured at each spectral channel of the data-cube, summing over a 1.5-pixel-radius aperture centred on the peak position of the emission feature.

The emission-line profile was analysed using a Gaussian fitting routine on the emission feature. The fits were performed on a wavelength range that isolates the feature under study as much as possible from other nearby emission features, such as the ambient gas and other G objects. The Gaussian parameter fit yields the central wavelength of the Brγ emission line, from which the radial velocity can be calculated relative to the local standard of rest.

Extended Data Fig. 3 displays the extracted spectrum and Gaussian fit for each object as it progresses over time. Changes in radial velocity over the 13-year period are evident for each G object. The velocity measurement errors were computed using the statistical errors of the Gaussian fit. In addition to the detection of Brγ emission, G3, G4, G5 and G6 display [Fe III] emission at the same Doppler shift, as shown in Extended Data Fig. 4, which displays the full Kn3 bandpass spectra from 2006-combined data sets for G3, G4, G5 and G6 (as well as G1 and G2 for comparison). G3, G4, G5 and G6 have [Fe III] detections at 2.2184 μm and 2.1457 μm (ref. [16]), whereas G1 and G2 show only Brγ emission. None of the G objects shows H_2 emission (2.1220 μm), although H_2 is evident in the ambient background material near zero velocity. The measurements are reported in Extended Data Table 2.

Orbit fitting

The astrometric and radial velocity measurements (Extended Data Table 2) are combined in a global orbit fit. The software used for orbit fitting has been previously used for the detection of the relativistic redshift on S0-2[11]. The orbital modelling assumes Keplerian motion parameterized by the six following orbital elements[2]: the period (P), the time of closest approach (T_0), the eccentricity (e), the inclination (i), the argument of periastron (ω) and the longitude of the ascending node (Ω). The G objects do not have enough orbital coverage and information to constrain the parameters related to the central mass (the mass of the black hole, the distance to our Galactic Centre R_0, the position and velocity of the central mass). Therefore, we fixed the values of the black hole mass and R_0 to the ones obtained from S0-2's measurements[11], that is, to $M = 3.964 \times 10^6 M_\odot$ (where $M_\odot$ is the solar mass) and $R_0 = 7.971$ kpc.

Our orbital fits are performed using Bayesian inference with a MultiNest sampler[38,39]. The radial velocity measurements are assumed to be independent and normally distributed. To take into account possible systematics at the level of the orbital fit, we use a likelihood that includes a systematic uncertainty (σ_{RV}) for the radial velocities. In summary, the radial velocity (RV) measurements are assumed to be distributed following:

$$\mathrm{RV}_i \sim \mathrm{N}\left[\mathrm{RV}(t_i),\ \sigma_{\mathrm{RV}_i}^2 + \sigma_{\mathrm{RV}}^2\right]$$

where $\mathrm{RV}_i(t)$ are the predicted radial velocity values, σ_{RV_i} are the measurement uncertainties and where $x \sim \mathrm{N}[\mu, \sigma^2]$ denotes that x is normally distributed around μ with a variance of σ^2. On the other hand, the astrometric measurements are assumed to be correlated, that is, the likelihood is assumed to be a multivariate normal distribution characterized by a covariance matrix. In addition, to take into account possible systematics at the level of the orbital fit, we also include an additional parameter: a systematic uncertainty for the astrometry, σ_{astro}. The astrometric measurements are therefore assumed to be distributed as:

$$\mathbf{x} \sim \mathrm{N}[x(\mathbf{t}_{\mathrm{astro}}),\ \Sigma_x] \text{ and } \mathbf{y} \sim \mathrm{N}[y(\mathbf{t}_{\mathrm{astro}}),\ \Sigma_y]$$

where $x(\mathbf{t}_{\mathrm{astro}})$ and $y(\mathbf{t}_{\mathrm{astro}})$ are the predicted astrometric values, Σ_x and Σ_y are the covariance matrices, and $\mathbf{x} \sim \mathrm{N}[\boldsymbol{\mu}, \Sigma]$ denotes that the vector $\mathbf{x}$ is normally distributed around the vector $\boldsymbol{\mu}$ with a covariance matrix of Σ. We model the covariance matrices[11] by:

$$[\Sigma_x]_{ij} = [\rho]_{ij} \sqrt{\sigma_{x_i}^2 + \sigma_{\mathrm{astro}}^2} \sqrt{\sigma_{x_j}^2 + \sigma_{\mathrm{astro}}^2}$$
$$[\Sigma_y]_{ij} = [\rho]_{ij} \sqrt{\sigma_{y_i}^2 + \sigma_{\mathrm{astro}}^2} \sqrt{\sigma_{y_j}^2 + \sigma_{\mathrm{astro}}^2}$$

where σ_{astro} is the systematic uncertainty and ρ is the correlation matrix that characterizes the correlation of the measurement errors. This correlation matrix is given by[11]:

$$[\rho]_{ij} = (1 - c)\delta_{ij} + c\mathrm{e}^{|-d_{ij}|/\Lambda}$$

where δ_{ij} is the Kronecker delta and d_{ij} is the 2D projected distance between point i and point j:

$$d_{ij} = \sqrt{(x_i - x_j)^2 + (y_i - y_j)^2}$$

Here Λ is a correlation length scale that typically takes the value of half the diffraction limit of the detector[11], and is fixed here at a value of 35 mas; c is a mixing parameter that is fitted simultaneously with all parameters and that characterizes the strength of the correlation. Corner plots of the best fit are shown in Extended Data Fig. 5 and the best fit parameters are reported in Extended Data Table 3.

In addition, we use uniform priors on all fitted parameters. We show in the next Methods section that this does not bias our estimates.

Dependence on priors

To estimate the orbits of the G objects, we use uniform priors on all eight fitted parameters (six orbital parameters and two systematic uncertainty parameters). Although uniform priors are commonly assumed in orbit fitting, this choice has been shown to cause potential biases in estimated parameters when orbital periods are much longer than the time baseline of observations[40,41]. To assess the impact of our fitting procedure in this context, we ran simulations to assess possible biases in the estimated parameters and to test the accuracy of confidence intervals obtained in our analysis[41]. We generated 100 mock data sets with simulated measurements at epochs corresponding to our observations. The simulated measurements were randomly drawn from a normal distribution about an assumed 'true' value, with a dispersion equal to the true measurement error at that epoch. We fit each of these 100 mock data sets with the same orbit fitting procedure as described above. The bias on each fitted parameter is computed from the difference between the estimated parameter value and the input parameter value, normalized by the 1σ confidence interval on the corresponding parameter. For all eight fitted parameters, the distribution of bias values is centred around zero for G3, G4, G5 and G6 within the 68% confidence interval, indicating non-biased parameter estimates.

In addition, we evaluate statistical efficiency to demonstrate that the confidence intervals used in this analysis are well-defined and have close to exact coverage. According to the classical definition of a confidence interval, 1σ confidence intervals inferred from each orbit fit should cover the 'true' value (from the simulated data) 68% of the time. In other words, given 100 randomly drawn simulated data sets, a 68% confidence interval requires that about 68 out of 100 fits produce a confidence interval that covers the true value[42]. However, effective coverage (defined as the experimentally determined percentage of data sets in which the inferred confidence interval covers the true value) is rarely exact. Statistical efficiency, defined as the ratio of effective coverage to stated or expected coverage (for example, 68% for a 1σ confidence interval), is thus a powerful performance diagnostic that can be used to investigate the accuracy of calculated confidence intervals[41]. By definition, a statistical efficiency of one indicates exact coverage. The statistical efficiencies for all parameters for G3, G4 and G6 are

consistent with one. For G5, the period is slightly under-covered with a statistical efficiency of 0.81 ± 0.09, indicating that the inferred confidence interval on G5's period is slightly underestimated. The statistical efficiencies for all other parameters for G5 are consistent with one. This analysis indicates that, in general, confidence intervals calculated in this work provide robust estimates of the statistical uncertainty.

Flux calibration

For this project we perform the absolute flux calibration of OSIRIS data. To do so, we need to apply aperture photometry to isolate sources of known magnitude. Even though many of the stellar sources are well-known, the Galactic Centre is a very crowded environment: no source is truly isolated and the combined background of underlying sources is challenging to determine. To measure the flux of stars on the field we would need to use a very small aperture radius. However, the PSF cannot be easily modelled, since the observations are taken through adaptive optics. Moreover, the OSIRIS field of view is very small, making an accurate empirical knowledge of the PSF impossible.

Instead we use observations of standard A stars, obtained the same night as the Galactic Centre observations. We used: HD 155379, HD 195500 and HD 146606 with 2MASS K magnitudes of 6.52, 7.19 and 7.04 respectively. These stars are chosen to be at around the same airmass as the science targets and their observations are taken as close in time as possible to the science observations (within a few hours). These are well-known, bright and isolated sources for which we can use aperture photometry over a very large radius that encompasses almost all of the source. In this way we can gather close to 100% of the flux and avoid problems related to the PSF shape.

The A-star frames are obtained by dithering around the star's position and are treated with the standard calibration procedure to remove atmospheric effects. Here, for each epoch, we use all available frames independently to measure the counts-to-Jy conversion factor and use their dispersion to estimate the corresponding uncertainty. Both the science mosaic and the A-star frames are calibrated in the standard way of the group. For each epoch, for each frame, we perform a 2D Gaussian fit to get the centroid of the source and an estimate of the Gaussian σ. We extract the A-star flux (F_{ap}) within a ~12-pixel aperture radius, which is ~6 times the σ of the 2D Gaussian fit (that is, that encompass ~100% of the stars' flux). We subtract the sky background through an annulus 1 pixel larger than the aperture size and of 1-pixel thickness (F_{an}). We use the known magnitude of the star (from the 2MASS catalogue) to compute its expected flux in the Kn3 band (F_{th}) using Vega as zero-point. The conversion factor is computed as follows:

$$\mathrm{CF} = \frac{F_{th}}{F_{ap} - F_{an}} \frac{1}{\mathrm{d}f}$$

where df is the width of the spectral channel in hertz. The same process is repeated for all frames within one given epoch and the median is adopted as the value for that epoch and the dispersion as the uncertainty. We checked other potential sources of error, such as imprecise pointing on the centre of the star, but we always obtained uncertainties several orders of magnitude smaller than the one coming from the dispersion.

The disadvantage of not using sources within the science field for calibration is that there could be variations of the fraction of photons reaching the detector surface between the science target and calibrator observations—for example, because of variations in the extinction due to passing clouds at the telescope site. However, the variation in extinction due to clouds is usually less than 0.5 mag and should have an impact smaller than the final calibration error. Indeed, the final calibration factor does not vary much from night to night or even year to year. The most dramatic variations are related to instrumental hardware upgrades. Therefore, we have chosen to divide the OSIRIS instrument timeline into three parts[14]: (1) 2006–12 before the grating upgrade; (2) 2012–16 before the spectrograph upgrade; and (3) from 2017 on.

For each of these periods, we consider the median of the conversion factors as the final value and the dispersion of the measurements as its uncertainty. This way we obtain three calibration factors with an error of about 10%.

We also compare the conversion factor obtained with the A stars to the one obtained using multiple stars on the field. In the case of the field stars the values are very sensitive to the applied correction to the aperture flux, and the conversion factor therefore varies more dramatically (even within close epochs) than in the case of the A stars (Extended Data Fig. 6). Therefore, we can affirm that the flux calibration obtained through standard stars is more robust.

Flux measurements

In order to maximize the signal-to-noise ratio, we measured the flux on data-cubes combined year by year (hence 1 cube per year). Multiple datasets were combined for each year using all available epochs to enhance the signal-to-noise ratio in the emission lines, resulting in 11 data-cubes corresponding to 11 years of data taken between 2006 and 2018 (except for 2007 and 2016, where the image quality was too poor and no Kn3 data cube was obtained, respectively).

The Brγ line fluxes of the G objects are obtained for each combined data-cube by extracting its spectrum and performing a Gaussian fit to the emission line. Flux measurements were derived from each line profile using an equivalent width method. The equivalent width was computed from the Gaussian fit parameters of the emission features from Brγ and [Fe III]. A conversion from measured flux to W m^{-2} was established using the flux calibration performed for each epoch from observations of A standards (Methods section 'Flux calibration'). Note that the absolute flux calibration can have relatively high errors in AO systems where the image quality and encircled energy in the data collection can change substantially on short timescales and from night to night. The measured fluxes are dereddened[34]. The measurements are reported in the following Methods section and in Extended Data Table 4.

Flux and FWHM summary table

The measured flux densities for all objects are reported in Extended Data Table 4, along with measurements of the spatial and spectral width. We do not detect any continuum in the Kn3 band in any of the G sources (we find a detection limit of 0.01 mJy). However, G2 detection in K-broadband imaging data has been claimed[20], finding a dereddened flux of about 0.25 mJy in K_s (2.18 μm central wavelength), which compares to a detection limit of 0.07 mJy in the K′ band[19] (2.12 μm central wavelength).

G-object formation scenarios

Although many hypotheses have been proposed to explain the origin of G1 and G2, the principal debate has centred on whether they are compact, dusty gas clouds or gaseous features anchored on stellar cores. G1 and G2 were first interpreted as purely gas and dust clouds[6]. However, G1 and G2 have remained intact after passing through periapse, which has led some[8,25–27] to argue that they must have a stellar core shielded by an extended opaque envelope of gas and dust.

Given the absence of photospheric emission, the original G2 hypothesis[6] interpreted it as an ionized gas cloud of 3 Earth masses. Since its discovery, the gas has been tidally interacting with the black hole. It was argued[10,24] that G1 and G2 are knots of gas and dust that have formed within a common orbiting filament. Indeed, their orbits are similar, but substantially different[9]. A drag force has been invoked to explain this difference[10]. However, the common filament interpretation cannot apply to the new sources we present here because of their very different location and orbit.

Given the strong tidal forces near the black hole, and the high flux of ultraviolet radiation in this region, compact gas clouds would supposedly be transient phenomena, unless they could be stably confined by a high external pressure[43]. Otherwise, they would need to be continuously produced in order to account for the sizable population we observe. The region is rich in gaseous interstellar medium structures, including the Epsilon source[44] (a nearby feature immediately west of the field), the Minispiral[45] and the Circumnuclear Disk[46]. It is possible that small pieces of these larger structures get detached and stay in the region for a few decades before getting destroyed, but it is not clear that such gas blobs would be as compact as the observed G sources.

The alternative hypothesis is that the G objects host a star. Whereas G2 is tidally interacting during its closest approach to Sgr A*[10], the dust component of G2 has remained unresolved. The emitting gas is unbound at closest approach[10], but that is not inconsistent with the existence of a stellar mass keeping the dust emission compact[8].

Several models have been proposed to account for G2 in terms of an optically thick distribution of dust surrounding a star: a young, low-mass star (T Tauri star) that has retained a protoplanetary disk[26] (scenario 1) or that generates a mass-loss envelope[27] (scenario 2); or alternatively, the merger of a binary system[9,25,28] (scenario 3).

In the first scenario, G2 could be a young star that has retained a protoplanetary disk and that was scattered inwards from the massive cluster of young stars distributed on larger scales[37]. Stars having protoplanetary disks are common in young clusters, but it is unclear whether such disks would survive the abrupt scattering event needed to transfer the protostars onto such tight orbits around the black hole. Furthermore, protoplanetary disks do not last very long except under the most benign conditions (up to 5–7 Myr; ref. [47]), therefore a population of such objects in the particularly hostile Galactic Centre environment is not obviously compatible with the timescale of the last star formation event (4–6 Myr ago[23]). Therefore, the protostellar disk hypothesis might be ruled out as an explanation for the common origin of these objects unless star formation is continuous at the Galactic Centre, as some have argued[48,49]. This matter is still under debate, but any demonstration that a substantial number of protoplanetary disks have survived in the central 0.05 pc of the Galactic Centre would have important implications for our understanding of star formation in this region.

In the second scenario, G2 was proposed to be the product of the mass-losing envelope of a young, low mass, T Tauri star. One open question is whether the observed Brγ emission is caused by collisions or ionization by Galactic Centre stars. In the case of emission by collisions the emission is unrelated to the G objects being located in the vicinity of the black hole, which raises the question of why these objects have not been seen elsewhere.

In the third scenario, G1 and G2 are proposed to be binary merger products. The influence of the black hole will enhance the probability that binary systems merge through eccentricity oscillations due to the eccentric Kozai–Lidov (EKL) mechanism[29]. The merging process would inflate the outer layers of the merging binaries, which would produce an extended envelope of dust and gas around the merger product, hiding the central mass for an extended period of time. A few binary mergers are known in the Galaxy[50–52]. However, such mergers took place recently and were discovered because of the strong variability that probably characterizes the early stages of a merger. According to the merger hypothesis, the G objects are more likely to be in a much quieter long-term phase in which the merger has stabilized and is evolving slowly on a Kelvin–Helmholtz timescale. For this reason, it is not meaningful to compare the G objects to presently known mergers, especially because we still have scant quantitative knowledge of how a merger evolves.

The binary merger hypothesis could offer a mechanism to rejuvenate stars in the Galactic Centre, as in the case of blue stragglers[53,54] (but see ref. [55]): some of the observed young stars orbiting closely around the central black hole (the S stars) could be the product of the merger of older stars. However, it is unclear whether this process can produce sufficiently massive stars to account for the S stars (typically (10–30)$M_{\odot}$; ref. [21]). The new star resulting from a merger can appear to be from a few Myr to several Gyr younger, depending on the merging circumstances[30].

Even if the G objects cannot account for the origin of the S stars, they are possibly connected to them. Here we have shown that the orbits of G3, G4, G5 and G6 have very different inclinations. This random distribution of the orbital planes very closely resembles the distribution of the orbits of S stars. If a stellar object is hidden inside a G object it must have a relatively small mass (less than a few solar masses), given the weakness of the continuum emission from these objects. In the central parsec, given the K′ detection limit[19], we can detect stars with masses down to ~1.5$M_{\odot}$ (ref. [56]). However, we could detect low-mass binary systems that merge, producing a shell of dust and gas: gas would be ionized by the environmental radiation, whereas dust would be heated by both environmental radiation and the luminous energy emerging from the interior of the G object. The G objects could therefore offer a unique window on the low-mass, currently undetectable, part of the S-star cluster.

As a consistency check, we investigated whether the number of observed G objects is consistent with the expected number of binary mergers (see the following Methods section).

The EKL-induced binary merger hypothesis offers a compelling explanation for the origin of G objects that fits well with the three-body dynamics that are necessarily at play in a dense stellar environment, with the third body being a supermassive black hole. Moreover, a wide range of eccentricities is expected for such binary merger products[28], in agreement with what we observe.

Binary fraction estimate

To estimate the binary fraction from the current number of G objects, we assume that all observed G objects are binary merger products (indeed we expect a large fraction of binaries in the Galactic Centre based on the orbital configuration of the stellar disk[57]). We assume that all six of the G objects discussed here are relatively recent binary mergers, and that their progenitor binary systems were formed in the latest known star formation event 4–6 Myr ago. This assumption is supported by the fact that older binaries can only survive in the Galactic Centre if they are very tight, and therefore have a very low probability of merging[30]. They would consequently not contribute substantially to the observed population of G objects. We use binary merger rates[30] and the initial mass function[23]. Given the absence of continuum emission, we assume the G objects come from only the low-mass part of the population. Therefore, the binary fraction of low-mass stars is given by:

$$R = \frac{1}{2}\frac{N_{\mathrm{B}}}{N_{\mathrm{m}}} \quad (1)$$

where N_{B} is the number of binaries and N_{m} the number of low-mass stars. We should expect about 10% of all binary systems to have merged within a few million years from a given star formation event in the Galactic Centre[30]. Also, 20%–25% of the initial binary population will have evaporated within the first few million years. So, given the observed number of G objects in the OSIRIS field of view ($N_{\mathrm{G}} = 6$), the number of binaries present today is given by:

$$N_{\mathrm{B}} = \frac{N_{\mathrm{G}}}{0.1}(1 - 0.25 - 0.1) \quad (2)$$

The initial mass function inferred by Lu et al.[23] is:

$$\frac{\mathrm{d}N}{\mathrm{d}m} = \xi m^{-\alpha} \text{ with } \alpha = 1.7$$

where ξ is a normalization factor. Using this we can compute the number of low-mass stars ($1M_{\odot} < M < 10M_{\odot}$), N_{m}:

$$\int_{1M_\odot}^{10M_\odot} N_{\rm m} = \xi \int_{1M_\odot}^{10M_\odot} m^{-\alpha} \quad (3)$$

Given the number of stars we detect in the OSIRIS field of view ($N_{\rm M} \approx 64$ stars with $M > 10M_\odot$ is the average for 2018 data), we can determine the normalization factor and estimate the number of low-mass stars from equation (3):

$$\int_{10M_\odot}^{30M_\odot} N_{\rm M} = \xi \frac{M^{1-\alpha}}{1-\alpha} \Rightarrow \xi \approx 0.15 \Rightarrow N_m \approx 478$$

From equations (1) and (2), it follows that the current binary fraction is $R \approx 5\%$.

Locally in the Galaxy, the binary fraction of solar-type stars[31] is ~50%. Only about 20% of such binaries—which would be stable in the field—can be stable in the Galactic Centre[28], which leads to 10% solar-type star binaries in the Galactic Centre. 35% of these binaries have already evaporated after formation[30], resulting in a surviving binary fraction of 6%–7%, compatible with what we deduce from the observed abundance of G objects.

Data availability

All data generated or analysed during this study are included in this published article.

Code availability

The orbit fit code is publicly available at https://zenodo.org/record/3305315#.XXmLPC3MzUY.

32. Diolaiti, E. et al. Analysis of isoplanatic high resolution stellar fields by the StarFinder code. *Astron. Astrophys. Suppl. Ser.* **147**, 335–346 (2000).
33. Boehle, A. et al. An improved distance and mass estimate for Sgr A* from a multistar orbit analysis. *Astrophys. J.* **830**, 17 (2016).
34. Schödel, R., Najarro, F., Muzic, K. & Eckart, A. Peering through the veil: near-infrared photometry and extinction for the Galactic nuclear star cluster. *Astron. Astrophys.* **511**, A18 (2010).
35. Lyke, J. et al. *OSIRIS Toolbox: OH-Suppressing InfraRed Imaging Spectrograph pipeline*. (Code Record ascl:1710.021, Astrophysics Source Code Library, 2017).
36. Yelda, S. et al. Improving Galactic center astrometry by reducing the effects of geometric distortion. *Astrophys. J.* **725**, 331–352 (2010).
37. Yelda, S. et al. Properties of the remnant clockwise disk of young stars in the Galactic center. *Astrophys. J.* **783**, 131 (2014).
38. Feroz, F. & Hobson, M. P. Multimodal nested sampling: an efficient and robust alternative to Markov Chain Monte Carlo methods for astronomical data analyses. *Mon. Not. R. Astron. Soc.* **384**, 449–463 (2008).
39. Feroz, F., Hobson, M. P. & Bridges, M. MULTINEST: an efficient and robust Bayesian inference tool for cosmology and particle physics. *Mon. Not. R. Astron. Soc.* **398**, 1601–1614 (2009).
40. Lucy, L. B. Mass estimates for visual binaries with incomplete orbits. *Astron. Astrophys.* **563**, A126 (2014).
41. Kosmo O'Neil, K. et al. Improving orbit estimates for incomplete orbits with a new approach to priors — with applications from black holes to planets. *Astron. J.* **158**, 1 (2019).
42. Neyman, J. Outline of a theory of statistical estimation based on the classical theory of probability. *Phil. Trans. R. Soc. Lond. A* **236**, 333–380 (1937).
43. Schartmann, M. et al. 3D adaptive mesh refinement simulations of the gas cloud G2 born within the disks of young stars in the Galactic center. *Astrophys. J.* **811**, 155 (2015).
44. Yusef-Zadeh, F., Morris, M. & Ekers, R. D. New structures near the compact radio source at the Galactic centre. *Nature* **348**, 45–47 (1990).
45. Lo, K. Y. & Claussen, M. J. High-resolution observations of ionized gas in central 3 parsecs of the Galaxy — possible evidence for infall. *Nature* **306**, 647–651 (1983).
46. Becklin, E. E., Gatley, I. & Werner, M. W. Far-infrared observations of Sagittarius A – the luminosity and dust density in the central parsec of the Galaxy. *Astrophys. J.* **258**, 135–142 (1982).
47. Russell, S. S. et al. in *Meteorites and the Early Solar System II* (eds Lauretta, D. S. & McSween, H. Y. Jr) 233–251 (Univ. Arizona Press, 2006).
48. Jalali, B. et al. Star formation in the vicinity of nuclear black holes: young stellar objects close to Sgr A*. *Mon. Not. R. Astron. Soc.* **444**, 1205–1220 (2014).
49. Yusef-Zadeh, F. et al. Sgr A* and its environment: low-mass star formation, the origin of X-ray gas and collimated outflow. *Astrophys. J.* **819**, 60 (2016).
50. Tylenda, R., Soker, N. & Szczerba, R. On the progenitor of V838 Monocerotis. *Astron. Astrophys.* **441**, 1099–1109 (2005).
51. Tylenda, R. & Kamiński, T. Evolution of the stellar-merger red nova V1309 Scorpii: spectral energy distribution analysis. *Astron. Astrophys.* **592**, A134 (2016).
52. MacLeod, M. et al. Lessons from the onset of a common envelope episode: the remarkable M31 2015 luminous red nova outburst. *Astrophys. J.* **835**, 282 (2017).
53. Genzel, R. et al. The stellar cusp around the supermassive black hole in the Galactic center. *Astrophys. J.* **594**, 812–832 (2003).
54. Naoz, S. & Fabrycky, D. C. Mergers and obliquities in stellar triples. *Astrophys. J.* **793**, 137 (2014).
55. Antonini, F., Faber, J., Gualandris, A. & Merritt, D. Tidal breakup of binary stars at the Galactic center and its consequences. *Astrophys. J.* **713**, 90–104 (2010).
56. Do, T. et al. *Envisioning the next decade of Galactic Center science: a laboratory for the study of the physics and astrophysics of supermassive black holes*. Preprint at https://arXiv.org/abs/1903.05293 (2019).
57. Naoz, S. et al. Confusing binaries: the role of stellar binaries in biasing disk properties in the Galactic center. *Astrophys. J.* **853**, L24 (2018).

Acknowledgements We thank G. Witzel, R. Schödel and E. Becklin for providing insight and expertise. Support for this work was provided by NSF AAG grant AST-1412615, Jim and Lori Keir, the W. M. Keck Observatory Keck Visiting Scholar programme, the Gordon and Betty Moore Foundation, the Heising-Simons Foundation, and Howard and Astrid Preston. A.M.G. acknowledges support from her Lauren B. Leichtman and Arthur E. Levine Endowed Astronomy Chair. The W. M. Keck Observatory is operated as a scientific partnership among the California Institute of Technology, the University of California, and the National Aeronautics and Space Administration. The Observatory was made possible by the generous financial support of the W. M. Keck Foundation. The authors wish to recognize and acknowledge the very significant cultural role and reverence that the summit of Maunakea has always had within the indigenous Hawaiian community. We are most fortunate to have the opportunity to conduct observations from this mountain.

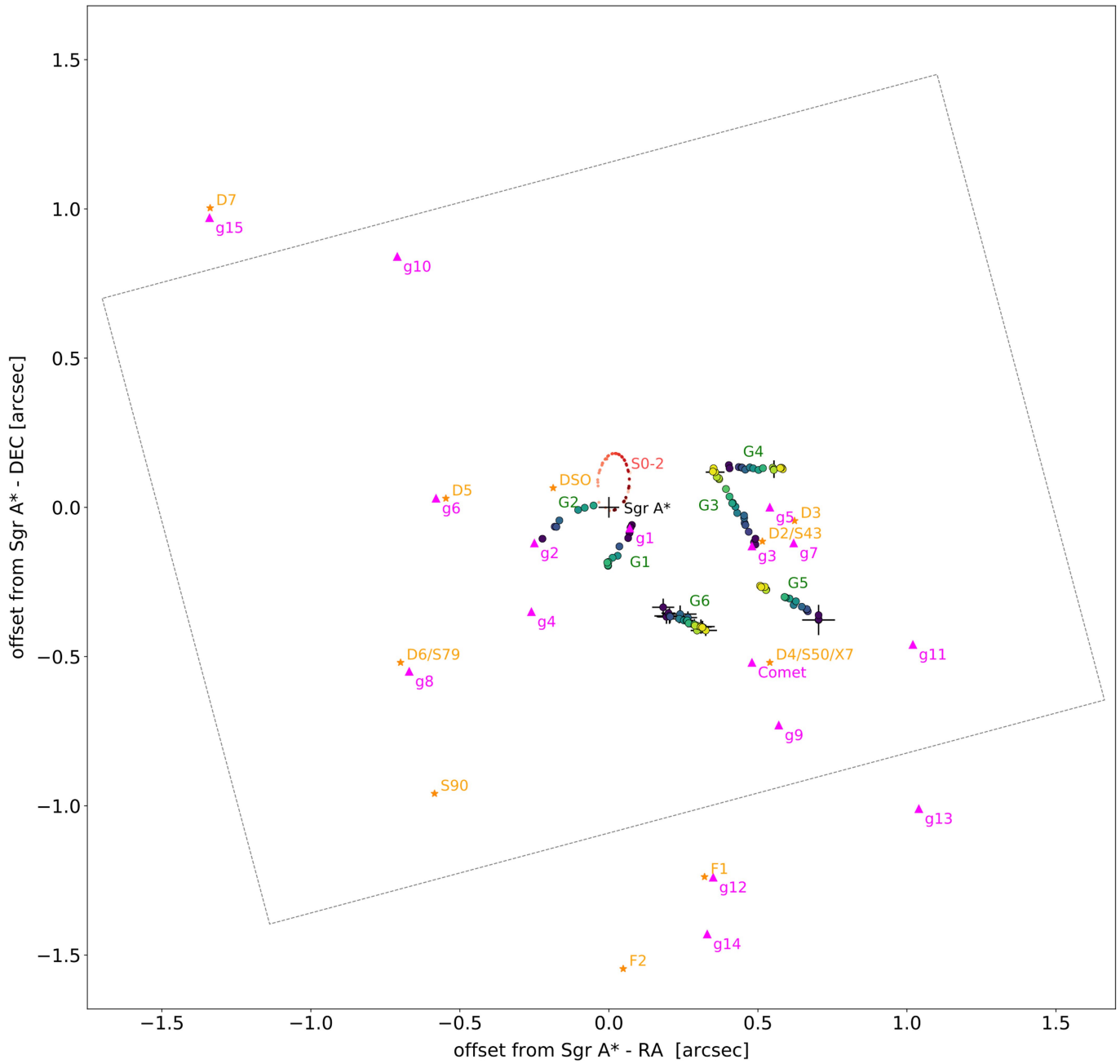
Author contributions A.C., R.D.C. and M.R.M. designed the project, and carried out the analysis and the interpretation of the results. A.M.G. supervised the observing, data acquisition and data reduction. T.D. and D.S.C. obtained and reduced the data. A.H., K.K.O'N. and B.N.S. contributed to the analysis and to the manuscript. A.C. wrote the manuscript with support from M.R.M. and R.N.C., and with contributions from all other authors. All authors provided critical feedback and helped gather data.

Competing interests The authors declare no competing interests.

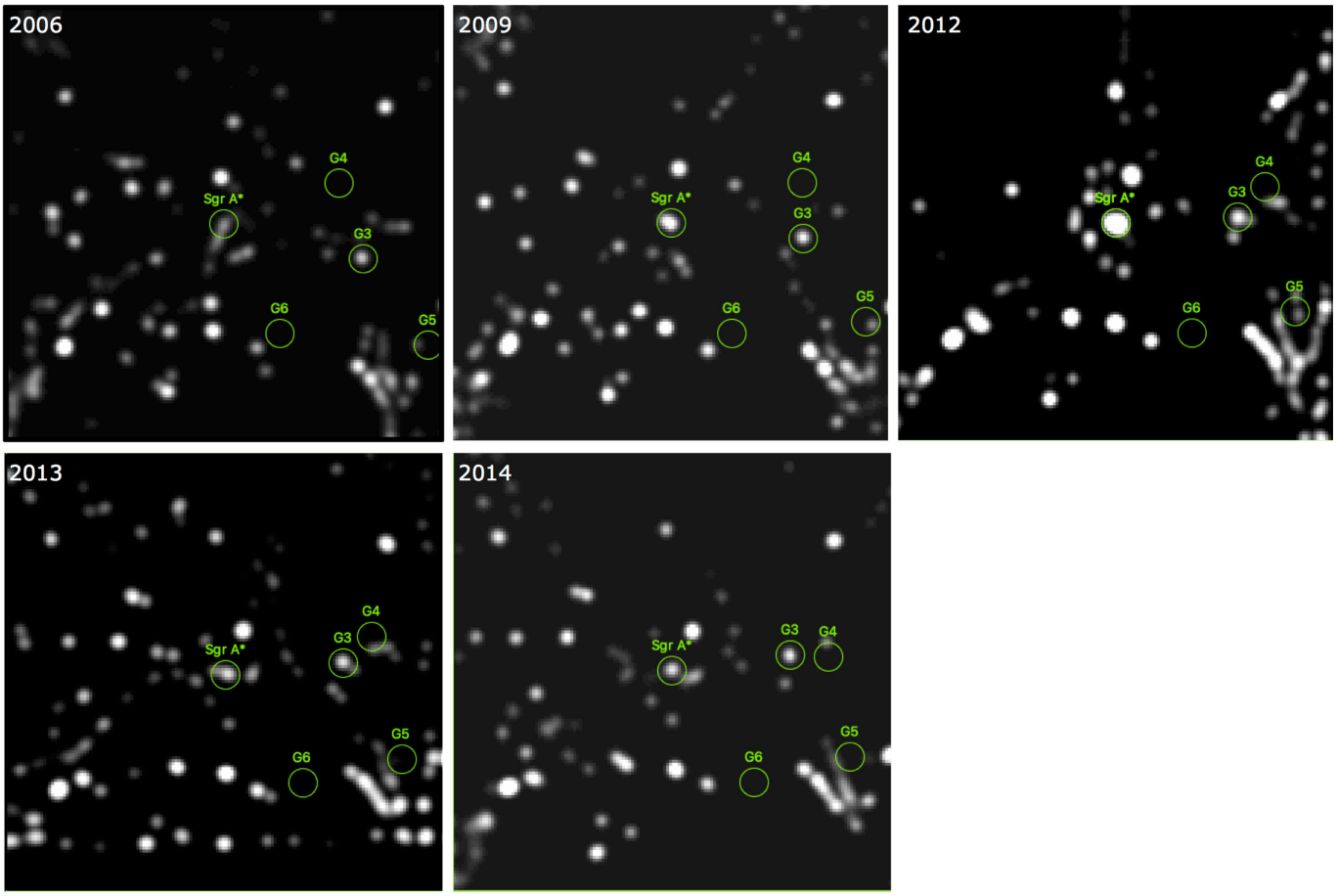
Additional information

Correspondence and requests for materials should be addressed to A.C.

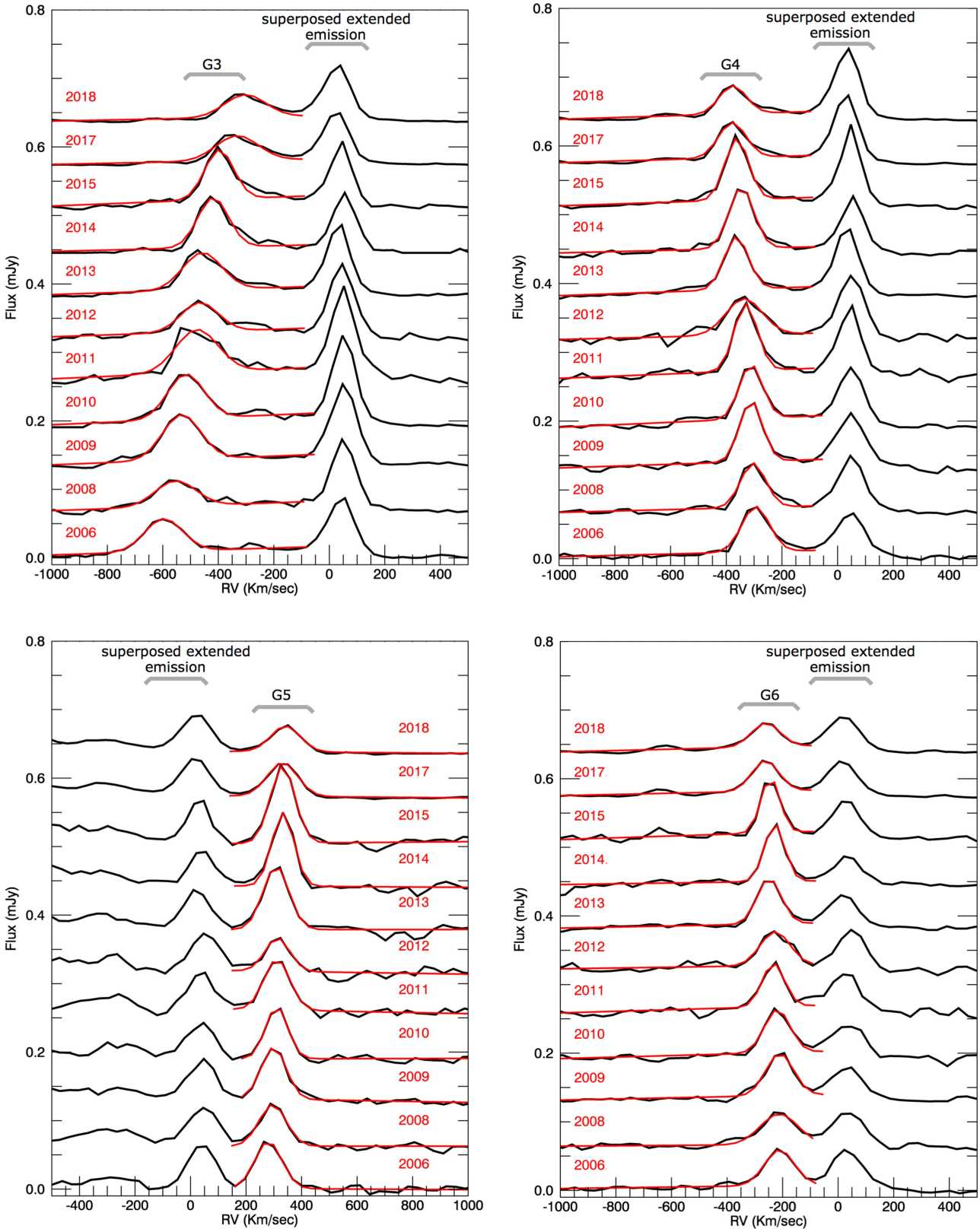
Reprints and permissions information is available at http://www.nature.com/reprints.



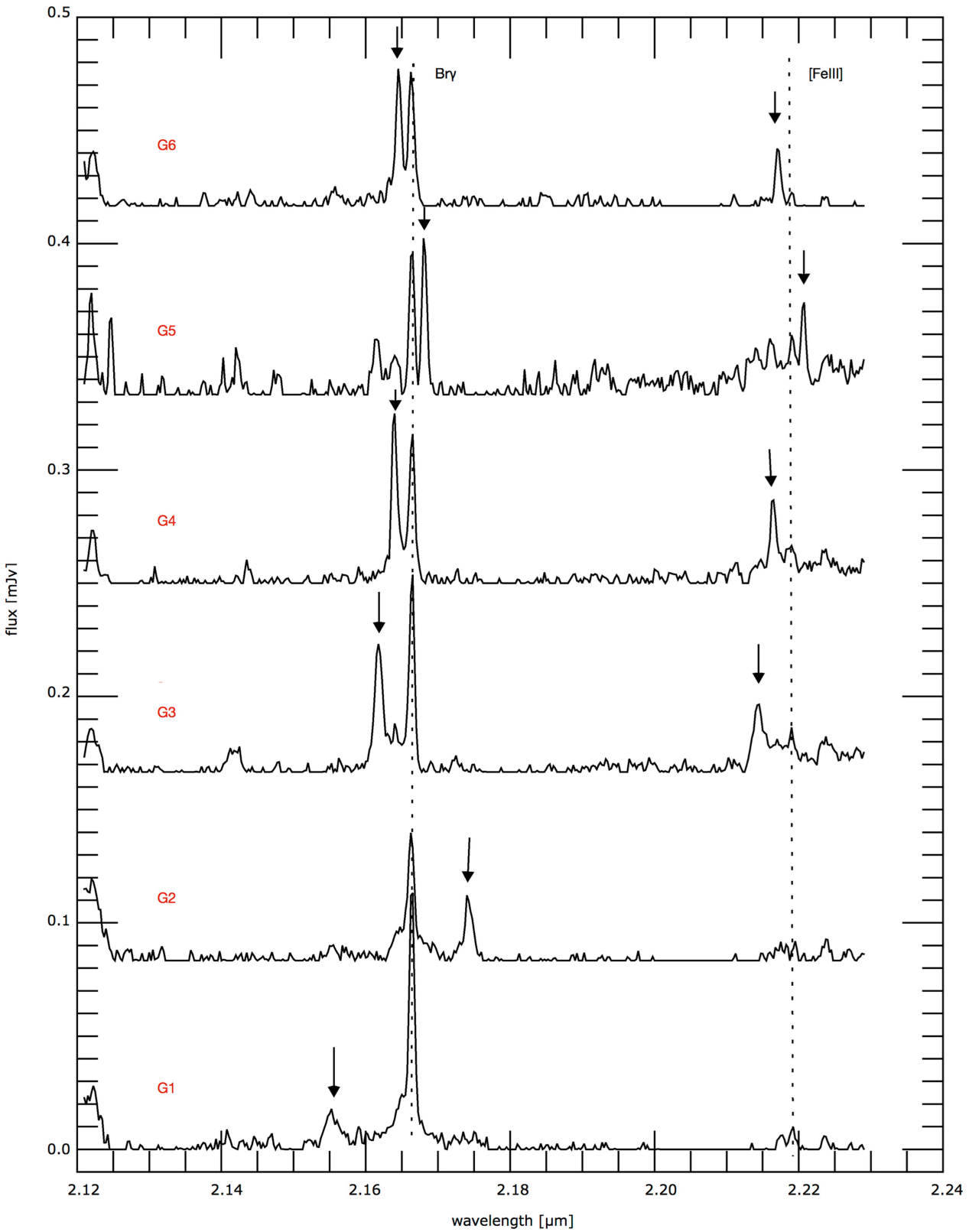
Extended Data Fig. 1 | Infrared-excess sources and G objects. Shown are the proper motions of the G sources (from 2006, in blue, to 2018, in yellow) along with the positions of infrared-excess sources[7] in orange (data obtained with NACO at the VLT in 2005) and[17] in magenta (data obtained with NIRC2 at Keck in 2005). The red trace shows the proper motion of S0-2 (from NIRC2) as reference. The average OSIRIS field is displayed as a dotted rectangle.



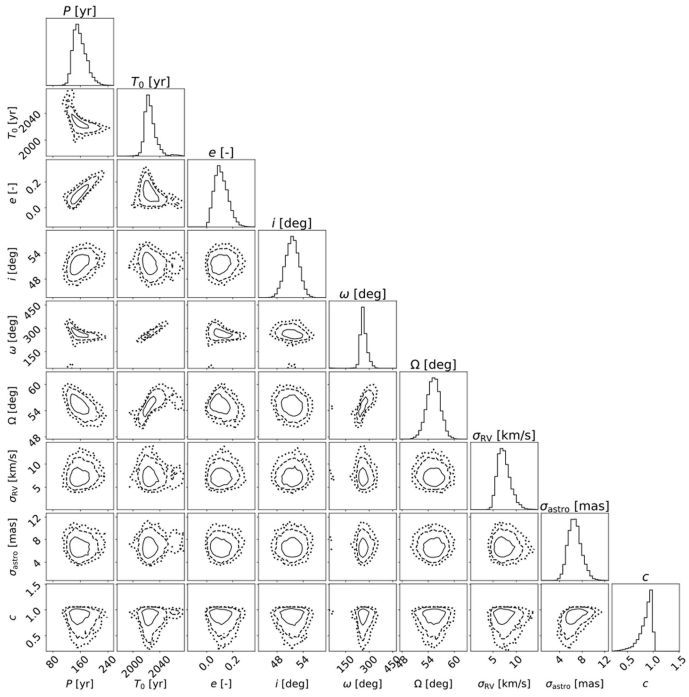
Extended Data Fig. 2 | New G objects in the L band. We show the deconvolved L′ images from NIRC2 for several epochs (each year is reported in the top-left corner). The green circles indicate the position of the G objects in the Kn3 OSIRIS band and of Sgr A*.



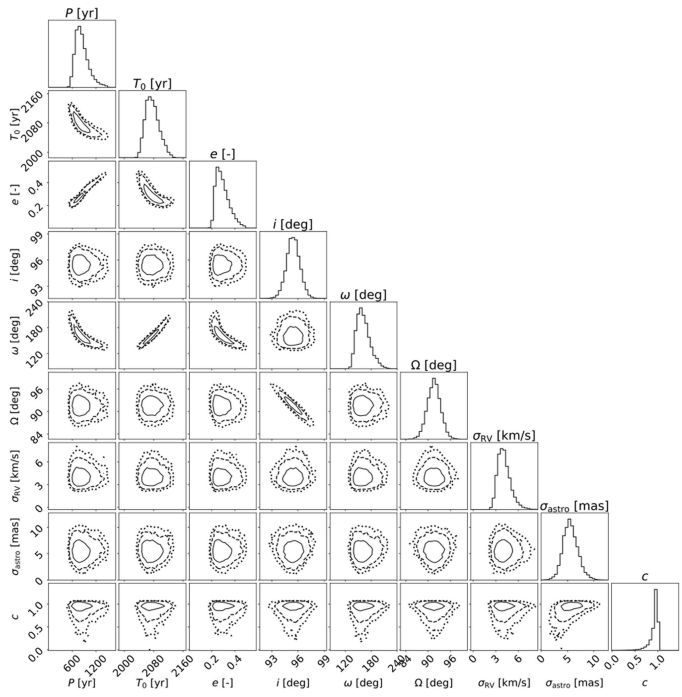
Extended Data Fig. 3 | Spectra of the new G objects showing the Brγ emission line over time. Top row, G3 (left) and G4 (right); bottom row, G5 (left) and G6 (right). The spectra are extracted epoch by epoch (black). The Gaussian fit of the Brγ emission line (red) is superimposed. There is no significantly detected variation (all values are compatible within 1σ) in the linewidth for any of the objects. The data quality varies and the emission of the objects blends with neighbouring features as it changes radial velocity (RV) and position: this gives sometimes the impression of a broadening of the line which is not real. The emission line at the rest velocity is part of the extended emission present across the field and does not change with time.



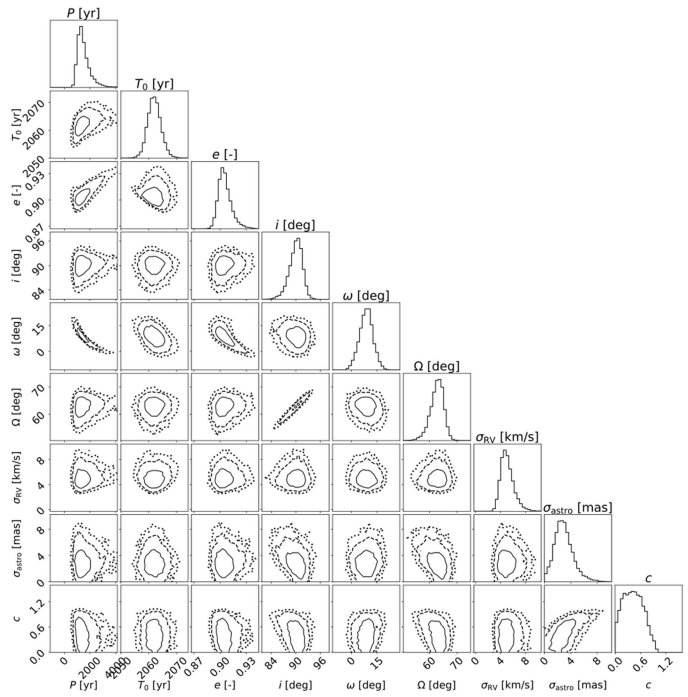
Extended Data Fig. 4 | Spectra of the G objects showing Brγ and [Fe III] emission lines. The Kn3 spectra of G objects G6–G1 are extracted over an aperture of 1.5-pixel radius from the 2006 combined dataset. The dotted lines show the rest-frame velocity of the Brγ and [Fe III] emission lines. G3, G4, G5 and G6 show both Brγ and [Fe III] emission moving at the same velocity (Doppler-shifted emission indicated by the arrows), whereas G1 and G2 show only Brγ emission.



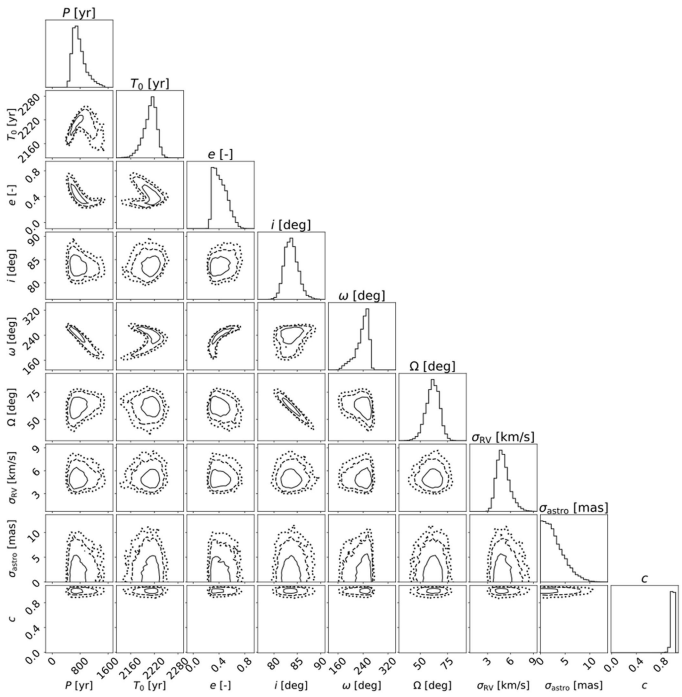
G3



G4

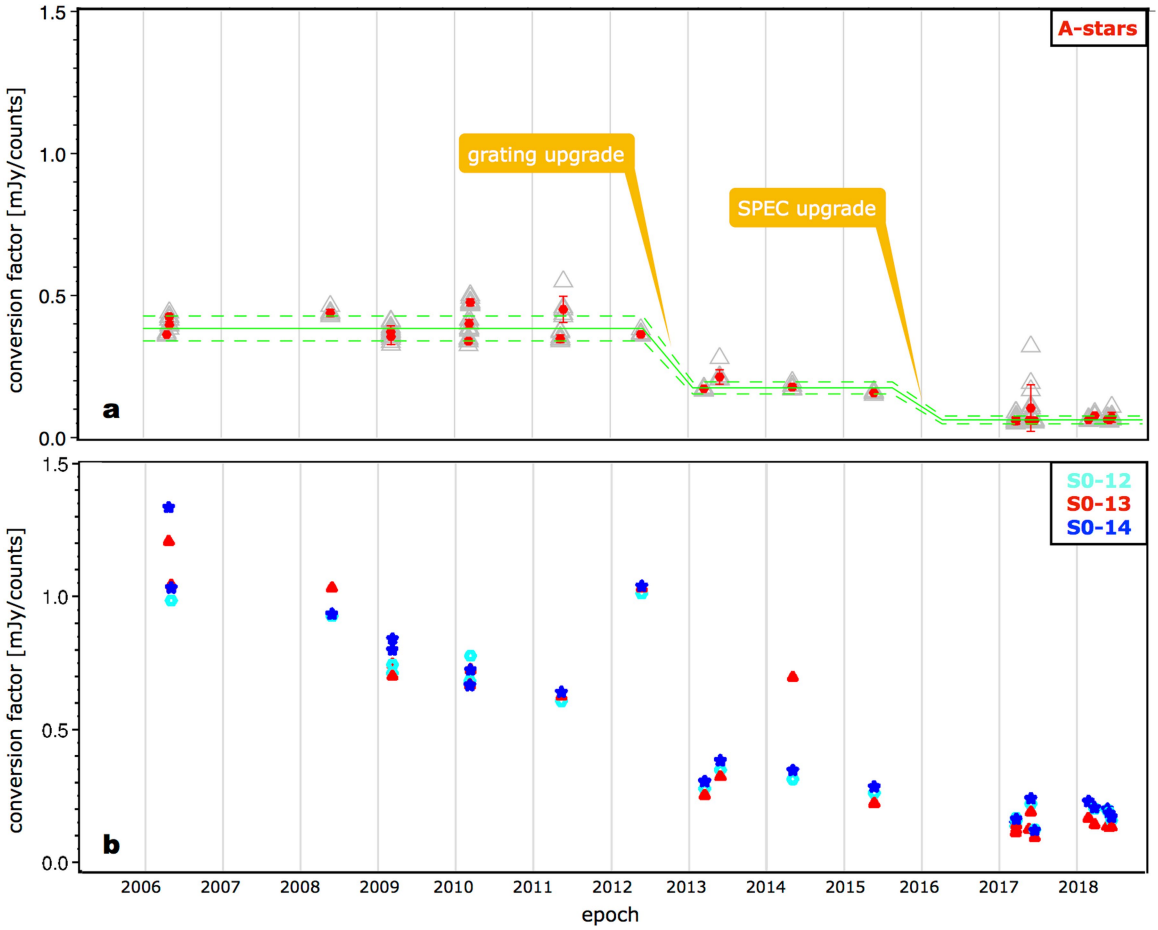


G5



G6

Extended Data Fig. 5 | Corner plots for orbit fitting of G3, G4, G5 and G6. See Methods section 'Orbit fitting' for details of the parameters displayed.



Extended Data Fig. 6 | Unit conversion factors as a function of time. a, Factor obtained using calibration A stars (single frames in grey triangles, median for each epoch in red dots, dispersion used as error bar). **b**, Factor obtained using stars in the science field. The dispersion when using stars in the science field is much larger. We use the A stars, for which most of the variation corresponds to hardware changes in the instrument. We use the median value for each instrument period (green solid line) and use the dispersion as an estimate of the uncertainty (green dashed lines). See Methods section 'Flux calibration' for details.

Extended Data Table 1 | OSIRIS observations used for the orbital fit

Date	Used for orbit fit	# of frames	FWHM [mas]	LSR corr [km/s]
2006-06-18	G3 G4 G5 G6	9	65	10
2006-06-30	G3 G4 G5 G6	9	59	4
2006-07-01	G3 - G5 G6	9	64	4
2008-07-25	G3 G4 G5 G6	11	60	-7
2009-05-05	G3 G4 G5 -	12	60	30
2009-05-06	G3 G4 G5 G6	12	69	30
2010-05-05	G3 G4 G5 G6	6	67	30
2010-05-08	G3 - - G6	11	69	29
2011-07-10	G3 G4 G5 G6	6	71	0
2012-07-22	G3 G4 G5 G6	9	81	-6
2013-05-14	G3 G4 G5 G6	11	91	27
2013-07-27	G3 - G5 G6	11	66	-8
2014-07-03	G3 G4 G5 G6	9	66	3
2015-07-21	G3 - - G6	7	56	-5
2017-05-17	G3 G4 G5 G6	11	73	25
2017-05-18	- G4 - G6	9	94	25
2017-05-19	- G4 - G6	6	86	24
2017-07-19	G3 - - G6	12	77	-4
2017-08-14	G3 - G5 G6	8	75	-14
2018-04-24	G3 - G5 G6	7	73	34
2018-05-23	- G4 G5 G6	14	91	23
2018-07-22	- G4 - G6	11	77	-6
2018-07-31	G3 G4 G5 G6	11	73	-9
2018-08-11	G3 G4 G5 G6	9	79	-13

The date is reported in YYYY-MM-DD format. All frames had integration times of 900 s. The FWHM value reported is for the star S0-2. To obtain radial velocities in the local standard of rest (LSR) reference frame, each observed radial velocity is corrected for the Earth's rotation, its motion around the Sun, and the Sun's peculiar motion with respect to the LSR.

Extended Data Table 2 | Measured values of positions and radial velocities

G3

epoch	RA	err	DEC	err	RV	err
53904.4	0.487	0.007	-0.117	0.005	-594	2
53916.3	0.492	0.009	-0.125	0.006	-600	2
53917.3	0.492	0.009	-0.105	0.006	-592	2
54672.3	0.469	0.009	-0.082	0.005	-555	3
54956.5	0.455	0.004	-0.052	0.001	-536	2
54957.5	0.458	0.004	-0.059	0.003	-531	2
55321.5	0.454	0.003	-0.035	0.003	-518	1
55324.5	0.454	0.008	-0.027	0.002	-512	2
55752.3	0.431	0.004	-0.019	0.010	-478	3
56130.3	0.425	0.005	0.002	0.004	-464	3
56426.5	0.416	0.002	0.015	0.001	-450	2
56500.3	0.414	0.004	0.014	0.002	-438	2
56841.3	0.405	0.002	0.036	0.001	-419	1
57224.3	0.393	0.009	0.062	0.005	-398	1
57890.4	0.370	0.005	0.094	0.002	-324	3
57953.3	0.369	0.003	0.098	0.002	-312	2
57979.2	0.362	0.005	0.102	0.003	-318	2
58232.5	0.356	0.032	0.118	0.010	-298	3
58330.3	0.351	0.005	0.131	0.003	-288	2
58341.3	0.349	0.009	0.120	0.005	-300	2

G4

epoch	RA	err	DEC	err	RV	err
53904.4	0.402	0.005	0.142	0.004	-293	1
53916.3	0.405	0.009	0.131	0.006	-291	2
54672.3	0.436	0.008	0.135	0.006	-304	1
54956.5	0.445	0.009	0.133	0.009	-310	1
54957.5	0.447	0.012	0.133	0.004	-313	1
55321.5	0.458	0.012	0.126	0.006	-314	1
55752.3	0.473	0.005	0.134	0.004	-330	1
56130.3	0.484	0.023	0.131	0.010	-334	2
56426.5	0.502	0.005	0.125	0.002	-345	1
56841.3	0.517	0.009	0.131	0.005	-346	1
57890.4	0.550	0.004	0.133	0.003	-360	1
57891.5	0.554	0.012	0.128	0.029	-360	1
57892.5	0.553	0.012	0.125	0.008	-360	1
58261.4	0.581	0.004	0.132	0.003	-361	1
58321.3	0.583	0.005	0.128	0.002	-368	2
58330.3	0.578	0.005	0.133	0.004	-363	2
58341.3	0.575	0.006	0.132	0.003	-365	1

G5

epoch	RA]	err	DEC	err	RV	err
53904.4	0.70	0.06	-0.38	0.05	267	2
53916.3	0.70	0.01	-0.37	0.01	281	2
53917.3	0.70	0.01	-0.36	0.01	276	1
54672.3	0.67	0.01	-0.35	0.01	296	2
54956.5	0.66	0.01	-0.34	0.00	297	1
54957.5	0.66	0.01	-0.34	0.00	304	1
55321.5	0.65	0.01	-0.33	0.00	311	1
55752.3	0.62	0.01	-0.33	0.01	311	1
56130.3	0.63	0.01	-0.31	0.01	314	2
56426.5	0.61	0.00	-0.31	0.00	327	0
56500.3	0.59	0.00	-0.30	0.00	329	1
56841.3	0.59	0.00	-0.30	0.00	331	0
57890.4	0.53	0.00	-0.28	0.00	352	0
57979.2	0.53	0.00	-0.28	0.00	354	1
58232.5	0.52	0.01	-0.27	0.00	360	1
58261.4	0.52	0.00	-0.27	0.00	358	1
58330.3	0.51	0.01	-0.26	0.00	363	2
58341.3	0.51	0.00	-0.27	0.00	358	2

G6

epoch	RA	err	DEC	err	RV	err
53904.4	0.19	0.03	-0.37	0.02	-210	2
53916.3	0.18	0.04	-0.33	0.03	-207	2
53917.3	0.20	0.02	-0.35	0.01	-209	1
54672.3	0.20	0.05	-0.36	0.03	-210	2
54957.5	0.21	0.05	-0.37	0.02	-210	1
55321.5	0.24	0.05	-0.36	0.03	-212	2
55324.5	0.27	0.03	-0.37	0.02	-225	1
55752.3	0.24	0.03	-0.37	0.01	-232	2
56130.3	0.25	0.03	-0.38	0.01	-227	2
56426.5	0.26	0.02	-0.38	0.01	-230	1
56500.3	0.26	0.02	-0.38	0.01	-230	1
56841.3	0.27	0.01	-0.39	0.01	-229	1
57224.3	0.29	0.03	-0.39	0.02	-244	1
57890.4	0.30	0.02	-0.40	0.01	-238	1
57891.5	0.30	0.02	-0.41	0.01	-237	1
57892.5	0.30	0.02	-0.41	0.01	-240	2
57953.3	0.30	0.02	-0.40	0.01	-245	1
57979.2	0.29	0.03	-0.40	0.01	-240	1
58232.5	0.31	0.05	-0.40	0.02	-253	2
58261.4	0.32	0.04	-0.41	0.02	-244	1
58321.3	0.31	0.03	-0.40	0.02	-237	1
58330.3	0.31	0.02	-0.40	0.01	-241	1
58341.3	0.31	0.02	-0.40	0.01	-244	1

Data are shown for G3, G4, G5 and G6. The epochs are reported as modified Julian date (MJD). The positions (RA and dec.) are offsets from Sgr A* in arcseconds. The position uncertainties are the standard deviation obtained through a Monte Carlo method. The radial velocities (RV) are in km s^{-1} and have been corrected for the local standard of reference (LSR). The reported radial velocity uncertainties (err.) are purely statistical (1σ of the line fit). There is an additional systematic uncertainty that we fold into the orbit fit.

Extended Data Table 3 | Best fit orbital parameters

	P [yr]	T0 [yr]	e	i [deg]	ω	Ω	σ_{astro}	σ_{RV}	c
G3	156^{+22}_{-16}	2024^{+9}_{-6}	$0.11^{+0.06}_{-0.05}$	$52^{+1.5}_{-1.6}$	261^{+23}_{-16}	$55^{+1.5}_{-1.6}$	$6.7^{+1.3}_{-1.1}$	$7.2^{+1.6}_{-1.1}$	$0.89^{+0.08}_{-0.15}$
G4	815^{+190}_{-126}	2075^{+21}_{-16}	$0.28^{+0.07}_{-0.05}$	$95.4^{+0.8}_{-0.7}$	160^{+18}_{-13}	$92^{+1.7}_{-1.8}$	$5.5^{+1.5}_{-1.3}$	$4^{+0.9}_{-0.7}$	$0.96^{+0.03}_{-0.1}$
G5	1392^{+555}_{-315}	2062^{+2}_{-2}	$0.9^{+0.01}_{-0.01}$	$90.1^{+1.4}_{-1.7}$	$8.8^{+3.7}_{-4.1}$	$62.9^{+2.1}_{-2.6}$	$2.8^{+1.5}_{-1.2}$	$4.9^{+1.1}_{-0.8}$	$0.42^{+0.27}_{-0.25}$
G6	732^{+224}_{-136}	2211^{+13}_{-19}	$0.41^{+0.13}_{-0.09}$	$83.6^{+1.5}_{-1.3}$	$242^{+13.8}_{-26.7}$	$61.7^{+5.8}_{-6.4}$	$2.4^{+2.6}_{-1.7}$	$5^{+0.9}_{-0.7}$	$0.99^{+0.01}_{-0.02}$

We show the median and central 68% confidence interval of the best-fit orbital parameters for G3, G4, G5 and G6. See Methods section 'Orbit fitting' for nomenclature.

Extended Data Table 4 | Emission from the G objects

	NIRC2	OSIRIS					
		flux density		FWHM		S/N	
	L' [mJy]	**Brγ** [mJy]	**[FeIII]** [mJy]	**spectral** [km/s]	**spatial** ["]	**Brγ**	**[FeIII]**
G3	2.5±0.5	1.16±0.15	0.59±0.11	156±5	0.10±0.02	24	14
G4	<0.38±0.08	1.10±0.14	0.49±0.09	117±2	0.10±0.02	34	16
G5	<0.57±0.11	0.99±0.13	0.44±0.08	110±2	0.12±0.02	17	16
G6	<0.54±0.10	0.82±0.12	0.37±0.07	127±5	0.13±0.02	28	19
G1	0.6±0.05	0.48±0.15	<0.027±0.005	293±20	0.10±0.04	8	-
G2	2.12±0.15	0.65±0.19	<0.027±0.003	174±14	0.08±0.04	13	-

We report properties of this emission: flux densities, spectral and spatial widths (as FWHM), and signal-to-noise ratios (*S*/*N*). The L' flux densities come from NIRC2 2012 measurements (G1 is brighter in earlier epochs[17]). The total flux density for Brγ and [Fe III] (2.2184 μm) come from OSIRIS (average of all observing). For comparison, we report G1 and G2 measurements from 2006 where all G objects are detectable in OSIRIS data. All fluxes are dereddened[34]. The spectral and spatial FWHM (an average of the *x*- and *y*-FWHM) are measured for Brγ. These values are not corrected for instrumental line width and PSF size (respectively ~100 km s^{-1} and ~75 mas). The *S*/*N* of the other [Fe III] line has a value of ~6 for all objects.

Article

Classification with a disordered dopant-atom network in silicon

https://doi.org/10.1038/s41586-019-1901-0

Received: 4 December 2018

Accepted: 13 November 2019

Published online: 15 January 2020

Tao Chen[1], Jeroen van Gelder[1], Bram van de Ven[1], Sergey V. Amitonov[1], Bram de Wilde[1], Hans-Christian Ruiz Euler[1], Hajo Broersma[2], Peter A. Bobbert[1,3], Floris A. Zwanenburg[1] & Wilfred G. van der Wiel[1]*

Classification is an important task at which both biological and artificial neural networks excel[1,2]. In machine learning, nonlinear projection into a high-dimensional feature space can make data linearly separable[3,4], simplifying the classification of complex features. Such nonlinear projections are computationally expensive in conventional computers. A promising approach is to exploit physical materials systems that perform this nonlinear projection intrinsically, because of their high computational density[5], inherent parallelism and energy efficiency[6,7]. However, existing approaches either rely on the systems' time dynamics, which requires sequential data processing and therefore hinders parallel computation[5,6,8], or employ large materials systems that are difficult to scale up[7]. Here we use a parallel, nanoscale approach inspired by filters in the brain[1] and artificial neural networks[2] to perform nonlinear classification and feature extraction. We exploit the nonlinearity of hopping conduction[9–11] through an electrically tunable network of boron dopant atoms in silicon, reconfiguring the network through artificial evolution to realize different computational functions. We first solve the canonical two-input binary classification problem, realizing all Boolean logic gates[12] up to room temperature, demonstrating nonlinear classification with the nanomaterial system. We then evolve our dopant network to realize feature filters[2] that can perform four-input binary classification on the Modified National Institute of Standards and Technology handwritten digit database. Implementation of our material-based filters substantially improves the classification accuracy over that of a linear classifier directly applied to the original data[13]. Our results establish a paradigm of silicon-based electronics for small-footprint and energy-efficient computation[14].

Doping is a crucial process in semiconductor electronics, where impurity atoms are introduced to modulate the charge carrier concentration. Conventional semiconductor devices operate in the band regime of charge transport, where the delocalization of the charge carriers gives rise to high mobility and a linear response to an applied electric field. At sufficiently low doping concentration and temperature[9,15], however, delocalization is lost, and carriers move sequentially from dopant atom to dopant atom. This is referred to as the hopping regime[10,11,16], which exhibits higher resistivity and nonlinearity. Nonlinearity is often undesired, but it is a valuable asset for unconventional computing, that is, for systems that do not follow the Turing model of computation[6–8,17–19]. Rather than excluding nonlinearity, we can exploit it[12] and manipulate our physical system with artificial evolution to solve computational problems[17]. This evolution in materio has been used, for example, for frequency distinguishing by liquid crystals[18] and robot control with carbon nanotubes[19]. We recently showed that a disordered network of gold nanoparticles acting as single-electron transistors can be evolved into any Boolean logic gate at sub-kelvin temperatures[12]. By exploiting the physics of materials for computation at the nanoscale through evolution, we may realize systems with unprecedented computational density and efficiency that are too complex to design[20].

Here, we fundamentally advance our previous work[12] by expanding the functionality, exploiting the well established platform of silicon technology and demonstrating operation up to room temperature. According to Cover's theorem[4], complex, linearly inseparable classification problems, when nonlinearly and sparsely mapped to a higher-dimensional space, can transform into linearly separable problems. The essence of this nonlinear mapping is illustrated in Fig. 1a for the XOR classification problem. To save resources, this projection is often done implicitly by using kernel functions in machine learning, that is, without explicit computation of high-dimensional coordinates[3]. In artificial neural networks (ANNs), the nonlinear projection is learned by adjusting internal weights, traditionally through back-propagation, leading to powerful feature extractors[2]. However, emulating ANNs with

[1]NanoElectronics Group, MESA+ Institute for Nanotechnology and BRAINS Center for Brain-Inspired Nano Systems, University of Twente, Enschede, The Netherlands. [2]Programmable Nanosystems and Formal Methods and Tools, MESA+ Institute for Nanotechnology, DSI Digital Society Institute and BRAINS Center for Brain-Inspired Nano Systems, University of Twente, Enschede, The Netherlands. [3]Molecular Materials and Nanosystems and Center for Computational Energy Research, Department of Applied Physics, Eindhoven University of Technology, Eindhoven, The Netherlands. *e-mail: W.G.vanderWiel@utwente.nl

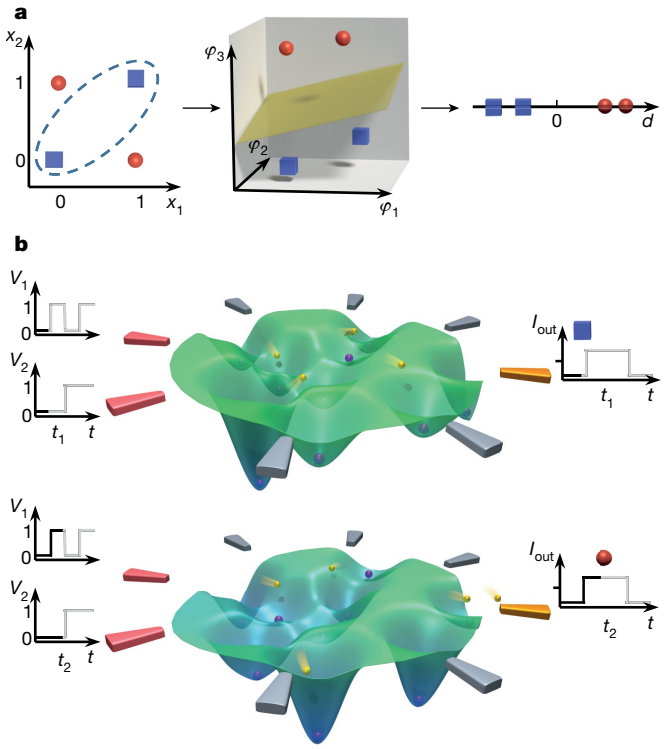


Fig. 1 | Simplifying classification by nonlinear projection. a, In the XOR classification problem two classes of data (red circles for (1,0), (0,1) and blue squares for (0,0), (1,1)) cannot be linearly separated in two dimensions (x_1, x_2; left). When nonlinearly transformed to three dimensions (φ_1, φ_2, φ_3; middle), the data can be linearly separated according to their distances d (right) to a decision boundary (yellow plane in the middle panel). **b**, Schematic representation of the potential landscape of the dopant network. In the hopping regime, the potentials of N dopants (purple spheres) span a high-dimensional feature space. Yellow spheres represent charge carriers. The voltage–time (V–t) diagrams on the left schematically show the voltage combinations applied to the input electrodes (red), affecting the potential landscape and projecting information nonlinearly to the feature space. Note the difference between the potential landscapes in the top and bottom panels for different input voltages. The characteristics of the output current (yellow electrode) are tunable by the control voltages (grey electrodes).

conventional complementary metal–oxide–semiconductor (CMOS) technology is known to be power-inefficient[21], and CMOS scaling is not keeping pace with ANNs[14]. To avoid the area and power costs of emulating neurons and synapses, reconfigurable[2] material systems with intrinsic complexity and diversity of nonlinear operations[6,22,23] are strongly sought after.

Our system consists of a disordered network of boron dopants in silicon (Si:B) and is illustrated in Fig. 2a, b. The boron atoms were implanted in n-type silicon with a concentration of 2×10^{19} cm^{-3} at the surface (Methods, Extended Data Fig. 1). A 300-nm-diameter active region was defined by eight electrodes. The central silicon region was etched (about 80 nm deep) so that the boron concentration at the receded surface was reduced to about 5×10^{17} cm^{-3}, as confirmed by secondary-ion mass spectroscopy. The current–voltage (I–V) characteristics (Fig. 2c, Extended Data Fig. 2) become increasingly nonlinear with decreasing T, and can be modelled as electric-field-activated hopping conduction at low temperatures (Supplementary Notes 1, 2). The network's potential landscape (Fig. 1b) depends in a highly nonlinear way on the input and control voltages, and spans a high-dimensional space. The output current is determined by this complex potential landscape. The nonlinear projection is realized when a combination of two or more input voltages is converted to an output current.

To identify the charge transport regimes, we focus on the low-bias conductance[11] $G = \mathrm{d}I_\mathrm{D}/\mathrm{d}V_\mathrm{SD}|_{V_\mathrm{SD}=-10\,\mathrm{mV}}$, where I_D is the drain current and V_SD is the source–drain voltage:

$$G(T) = G_\mathrm{b} e^{(-\varepsilon_\mathrm{b}/k_\mathrm{B}T)} + G_\mathrm{h} e^{-(T_\mathrm{h}/T)^p} \quad (1)$$

where the first term describes band (b) conduction and the second term describes hopping (h) conduction. G_b and G_h are pre-factors with a much weaker temperature (T) dependence than the exponential terms, ε_b is the dopant ionization energy, T_h is a characteristic temperature of hopping conduction and k_B is the Boltzmann constant. The exponent p depends on the specific hopping model[11]. The resistance $R = 1/G$ as a function of inverse temperature $1/T$ is shown in Fig. 2d. At $T > 250$ K, hole-band conduction dominates. The extracted ε_b is about 130 meV, three times larger than the value of boron in bulk silicon, about 45 meV. We attribute this increased ionization energy to dopant deactivation[24,25]: for hydrogen-like dopants near the silicon surface, the decreased dielectric screening leads to stronger electron confinement, and therefore a larger ionization energy.

We adopt the method proposed by Zabrodskii et al.[15] to distinguish the hopping regime and extract p (Methods). For 70–160 K, we find $p = 0.342 \pm 0.023$, in agreement with $p = 1/3$ predicted for two-dimensional Mott variable-range hopping (Mott-VRH)[11,26] (Fig. 2e). The two-dimensional nature implies that the dopants participating in transport are located close to the silicon surface, because the hopping resistance increases exponentially with inter-dopant distance[11], which is lowest near the surface. This is consistent with the dopant deactivation observed in the band-conduction regime. Above about 160 K, band conduction starts to contribute, becoming dominant above about 250 K.

To demonstrate classification in the hopping regime (Supplementary Notes 3–7), we followed the evolutionary approach of ref. [12] (Methods) and configured the system into Boolean logic (Fig. 3a–c, Extended Data Figs. 3–5) at 77 K. The working-temperature window for a set of control voltages (about 30 K) is approximately 15 times wider than in our previous nanoparticle system[12] (about 2 K). The retention period of the gates is over two months in liquid nitrogen, and the device characteristics remain virtually unchanged after thermal cycling, indicating the robustness of the dopant network. Boolean logic represents a prototypical two-input binary classification problem[3], and the XOR classification problem is a poignant example of a single-layer perceptron's inability to solve problems with linearly inseparable vectors[27]. Hence, solving the linearly inseparable X(N)OR problem demonstrates the system's separation ability[3,22,23] (Fig. 1a).

As realizing all Boolean logic gates with a standard ANN requires at least one hidden layer of two neurons[3] (corresponding to nine linear and three nonlinear operations), our dopant network can be considered to emulate at least such a neural network in hardware (Fig. 3d). Importantly, the dopant network has only a 300-nm-diameter footprint and an average power consumption of about 1 μW (Methods). Using established monolithically integrated readout circuits (Methods, Extended Data Fig. 6), the bandwidth of the readout circuitry can be increased from 40 Hz in our current setup to over 100 MHz. With optimization (Methods and Supplementary Note 8), the energy efficiency of the dopant network at 77 K is projected to exceed 100 tera-operations per second per watt (TOP s^{-1} W^{-1}, where OP is one typical linear operation of a neural network[28]), one order of magnitude higher than a state-of-the-art customized CMOS neural network accelerator[29] (Supplementary Notes 8, 9, Extended Data Fig. 7b).

To investigate the correlation between the functionality of our devices and the transport mechanism, we performed random searches with 10,000 sets of control voltages as a function of temperature. We define the total abundance A, representing the overall probability of finding Boolean logic, with two fitness F thresholds for each logic gate[12] (Methods). For both fitness thresholds $F > 1, 2$, the total abundance drops to below 5% when band conduction sets in at around

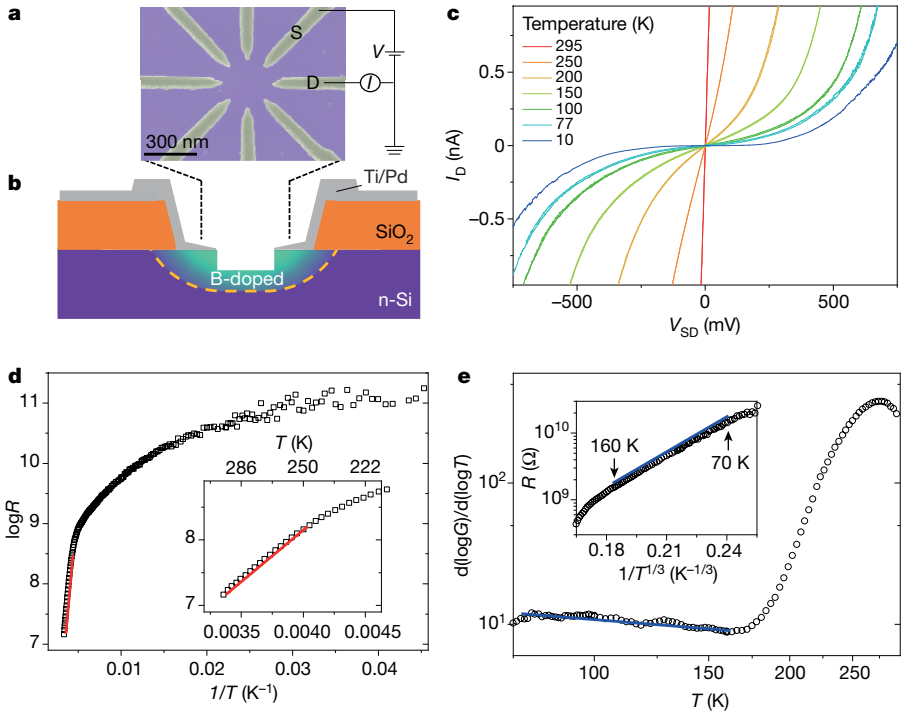


Fig. 2 | Device structure and charge transport mechanism. a, Scanning electron microscope image, indicating the source (S) and drain (D) contacts for *I*–*V* measurements. **b**, Schematic cross-section, illustrating the doping profile and the p–n junction (yellow dashed line). **c**, *I*–*V* characteristics at different temperatures (*T*) showing nonlinear behaviour below about 250 K. **d**, Resistance *R* versus inverse temperature at $V_{SD} = -10$ mV. Band transport is observed for 250–295 K (indicated by the red line in the main figure and the inset, which shows the high-*T* region). **e**, Logarithmic derivative of the low-bias conduction *G* with respect to *T*. The linear segment for 70–160 K indicates hopping conduction (blue line). Inset, semi-logarithmic plot of *R* versus $1/T^{1/3}$, indicating two-dimensional variable-range hopping for 70–160 K (blue line) with $T_h = 7.7 \times 10^4$ K, falling well within the range reported for Mott's VRH model[16].

160 K (Fig. 3e). Hence, functionality is highly correlated to the hopping regime.

Led by this correlation, we tried to increase the operating temperature by suppressing band conduction. With increasing temperature, dopants near the p–n junction (Fig. 2b) are expected to be ionized first, as they are less subject to deactivation than dopants far away from the junction. By depleting the junction using a backgate, we indeed observe nonlinearity, and can evolve all six major logic gates at room temperature (Fig. 3f, Extended Data Fig. 8). The confirmed correlation between functionality and the charge transport mechanism can serve as a guiding tool towards robust functionality at room temperature.

To demonstrate the ability of our device to perform more complicated classification tasks, we performed four-input binary classification in the form of filtering 16 2 × 2 black (1) and white (0) pixel features, as shown in the inset of Fig. 4a. The four pixel values are encoded as four input voltages to our dopant network, together with three control voltages and one output current. We use the three control voltages to evolve a single network into 16 different filters at 77 K. Each filter should

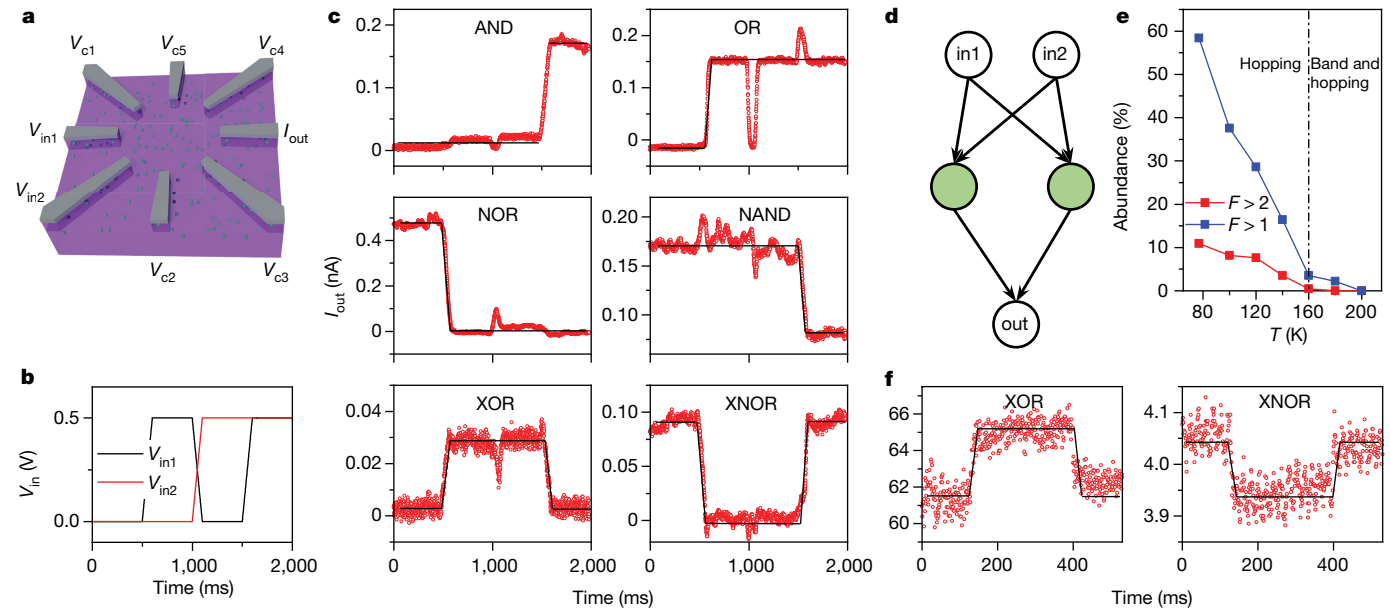


Fig. 3 | Evolution of Boolean logic. a, Schematic electrode configuration, indicating input voltages (V_{in1}, V_{in2}), control voltages (V_{c1}–V_{c5}) and output current (I_{out}). **b**, Input waveforms. The logic 0 and 1 are represented here by two different voltages, 0 V and 0.5 V, respectively (see also Supplementary Note 6). **c**, Major Boolean logic gates at 77 K (experimental current values in red, desired output normalized to the experimental data in black). We reproduced all Boolean logic gates in seven devices. **d**, ANN with two hidden neurons (green filled circles) emulated by the dopant network device. The ANN requires six (linear) weight multiplications, three (linear) summations and three (nonlinear) activations. **e**, Total abundance of logic gates (defined in Methods) as a function of temperature. The dashed line marks the onset of band conduction. The blue and red curves correspond to fitness thresholds of $F > 1$ (noise level) and $F > 2$, respectively. **f**, XOR and XNOR gates evolved at room temperature with a backgate voltage of about 12 V.

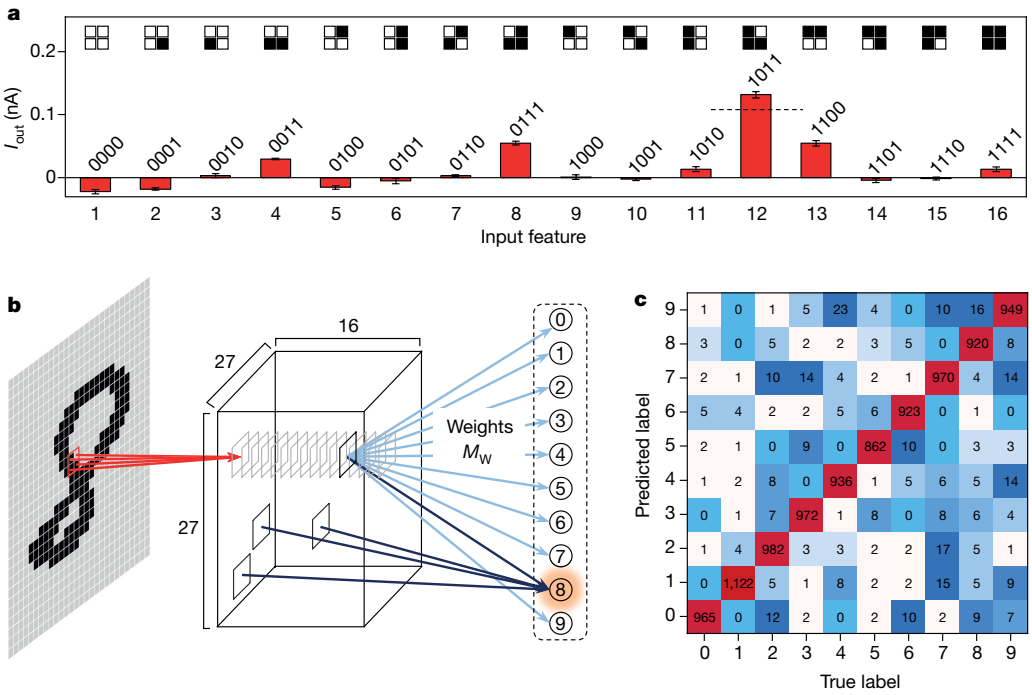


Fig. 4 | Feature filtering and handwritten digit classification. a, Current response of one of the 16 filters. The 2 × 2 pixel black/white patterns (inset) are represented by '0000', '0001', ..., '1111', with black (1) and white (0) mapped to input voltages 0.5 V and −0.5 V, respectively. The output current of this filter is maximal when the '1011' pattern is presented. Error bars represent the standard deviation of ten tests. **b**, Feature mapping for digit recognition. Specific filters are activated (bold dark squares) depending on the features presented to them. For clarity, most of the 27 × 27 × 16 filters are not shown. The output of the filters is obtained from the experimental data shown in **a** and Extended Data Fig. 9. The ten output nodes, representing digits 0 to 9, are connected to the filters through a weight matrix M_W of a linear classifier. **c**, Confusion matrix of classification with the 10,000 MNIST test dataset, showing that 96.0% of the digits are correctly classified.

make one of the 16 features distinguishable from all the others, which is realized by evolving the dopant network such that it yields the maximal or minimal output current for that specific feature (Fig. 4a, Extended Data Fig. 9). If we feed a feature to a group of 16 filters, each of which distinguishes one feature, then the 4-dimensional data are mapped to a 16-dimensional vector, and each feature vector is separated from the others in one of the dimensions (Supplementary Note 9).

Our approach allows the separation of data by evolving filters that are capable of processing data in parallel and with high throughput. Compared with optical networks, which also allow parallel processing, our dopant networks feature tunability and have much smaller dimensions: about 100 nm instead of centimetres[7].

Taking advantage of the separation ability of our nanomaterial system, we used the evolved filters as the core ingredient to classify the Modified National Institute of Standards and Technology (MNIST) digits[13]. The whole classification procedure consists of a feature mapping layer of the evolved filters inspired by the convolutional neural network[2], followed by a linear classifier in a traditional computer, which can in principle also be realized in materio[30] (Fig. 4b). The 28 × 28 greyscale pixels of each MNIST digit are converted to black and white using a threshold and divided into 2 × 2 pixel receptive fields (overlapping in one row/column with neighbours). The receptive fields feed their signal to the cluster of 16 filters, each filtering out one of the features. The (28 × 28)-dimensional MNIST data are hence mapped onto (27 × 27 × 16)-dimensional feature vectors. The linear classifier then converts these high-dimensional feature vectors to a 10-dimensional output by a weight matrix M_W (Fig. 4b), obtained by pseudo-inverse learning[31] with the 60,000 MNIST training data (Methods). The largest of the ten outputs finally determines the recognized digit.

Application to 10,000 test digits shows 96.0% accuracy (Fig. 4c, Supplementary Note 9, Extended Data Fig. 10), which is better than the accuracy obtained with state-of-the-art physical reservoir computing[8] and optical networks[7]. We note that differences in the output current scales of the different filters are irrelevant, because the weight matrix will automatically compensate for those (Supplementary Note 9). We also simulated feature filters with ideal characteristics, which are only activated when presented with its corresponding feature (output 1 for target feature and 0 otherwise). The classification of the MNIST dataset with these ideal filters results in an accuracy of 96.2%. Therefore, as long as the data mapped to the feature space are sufficiently separated, a linear classifier can learn the decision boundaries. The underlying reason is that every complete set of independent vectors, be it orthogonal (ideal) or not, can represent other vectors by linear combination. This shows the power of our dopant network in making data linearly separable, owing to its intrinsic nonlinear transformation. The ability to separate data, when combined with an adaptable linear readout in a scaled-up system, can achieve universal computational power[8,22,23]. For instance, in ANNs, perceptrons can be cascaded to solve more complex problems[3]. This analogy strongly suggests that a system of interconnected dopant networks can address a much wider range of tasks, particularly because the computational power of a single dopant network is larger than that of a single perceptron (it can solve XNOR whereas a single perceptron cannot).

At the system level, we anticipate a number of necessary developments. First, the total evolution time of the filters, which scales linearly with their number, can be reduced (by a factor 10^6; Methods and Supplementary Notes 7, 8). Besides competitive evolutionary approaches[32], we will also explore gradient-based methods[33]. Second, it will be highly advantageous to store the evolved control voltages locally, employing,

for example, memristors[30] (Supplementary Note 8). Third, memristive technology is also suitable for in materio implementation of the linear classification step in our scheme with energy efficiency comparable to our material-based nonlinear feature filters. Fourthly, processing analogue instead of binary signals would be more natural for our devices. To filter more complex, non-binary features, such as edge detection by the brain[1], more electrodes per device are needed and/or multiple devices need to be interconnected, so that more input signals can be processed in parallel. This will also allow for more control voltages per filter (at present, three) to improve the signal-to-noise ratio. Lastly, for practical applications, room-temperature operation with long retention, low-voltage supplies and without a backgate is desired, which we deem possible by engineering the deactivation effect in a silicon-on-insulator-based system.

Our silicon-based system provides a powerful platform for carrying out machine learning tasks in hardware. By material learning, we harness the intrinsic nonlinearity and tunability of a nanomaterial system to efficiently realize functional tasks without the need to design circuitry for the underlying elementary operations. The small footprint and silicon-compatible fabrication process facilitates scaling up for massively parallel, high-throughput information processing platforms for complex computational tasks. Whereas the randomness and discreteness of dopants pose challenges on conventional silicon electronics, we have presented a computational paradigm that takes full advantage of these properties. When integrated with other technologies, complex classification problems can be solved fully in materio, potentially achieving ultrahigh computational density and energy efficiency[14].

Online content

Any methods, additional references, Nature Research reporting summaries, source data, extended data, supplementary information, acknowledgements, peer review information; details of author contributions and competing interests; and statements of data and code availability are available at https://doi.org/10.1038/s41586-019-1901-0.

1. Hubel, D. H. & Wiesel, T. N. Receptive fields of single neurones in the cat's striate cortex. *J. Physiol.* **148**, 574–591 (1959).
2. LeCun, Y., Bengio, Y. & Hinton, G. Deep learning. *Nature* **521**, 436–444 (2015).
3. Haykin, S. *Neural Networks and Learning Machines* (Pearson Prentice Hall, 2008).
4. Cover, T. M. Geometrical and statistical properties of systems of linear inequalities with applications in pattern recognition. *IEEE Trans. Electron. Comput.* **EC-14**, 326–334 (1965).
5. Torrejon, J. et al. Neuromorphic computing with nanoscale spintronic oscillators. *Nature* **547**, 428–431 (2017).
6. Tanaka, G. et al. Recent advances in physical reservoir computing: a review. *Neural Netw.* **115**, 100–123 (2019).
7. Lin, X. et al. All-optical machine learning using diffractive deep neural networks. *Science* **361**, 1004–1008 (2018).
8. Du, C. et al. Reservoir computing using dynamic memristors for temporal information processing. *Nat. Commun.* **8**, 2204 (2017).
9. Hung, C. S. & Gliessman, J. R. Resistivity and Hall effect of germanium at low temperatures. *Phys. Rev.* **96**, 1226–1236 (1954).
10. Mott, N. F. Conduction in glasses containing transition metal ions. *J. Non Cryst. Solids* **1**, 1–17 (1968).
11. Gantmakher, V. F. *Electrons and Disorder in Solids* (Clarendon Press, 2005).
12. Bose, S. K. et al. Evolution of a designless nanoparticle network into reconfigurable Boolean logic. *Nat. Nanotechnol.* **10**, 1048–1052 (2015).
13. Lecun, Y., Bottou, L., Bengio, Y. & Haffner, P. Gradient-based learning applied to document recognition. *Proc. IEEE* **86**, 2278–2324 (1998).
14. Xu, X. et al. Scaling for edge inference of deep neural networks. *Nat. Electron.* **1**, 216–222 (2018).
15. Zabrodskii, A. G. & Zinov'eva, K. N. Low-temperature conductivity and metal-insulator transition in compensate n-Ge. *Sov. Phys. JETP* **59**, 425–433 (1984).
16. Jenderka, M. et al. Mott variable-range hopping and weak antilocalization effect in heteroepitaxial Na_2IrO_3 thin films. *Phys. Rev. B* **88**, 045111 (2013).
17. Miller, J. F. & Downing, K. Evolution in materio: looking beyond the silicon box. In *Proc. 2002 NASA/DoD Conference on Evolvable Hardware* 167–176 (IEEE, 2002).
18. Harding, S. & Miller, J. F. Evolution in materio: a tone discriminator in liquid crystal. In *Proc. 2004 Congress on Evolutionary Computation* 1800–1807 (IEEE, 2004).
19. Mohid, M. & Miller, J. F. Evolving robot controllers using carbon nanotubes. In *Proc. 13th European Conference on Artificial Life* 106–113 (MIT Press, 2015).
20. Wolfram, S. Approaches to complexity engineering. *Physica D* **22**, 385–399 (1986).
21. Backus, J. Can programming be liberated from the von Neumann style? A functional style and its algebra of programs. *Commun. ACM* **21**, 613–641 (1978).
22. Maass, W., Natschläger, T. & Markram, H. Real-time computing without stable states: a new framework for neural computation based on perturbations. *Neural Comput.* **14**, 2531–2560 (2002).
23. Dale, M., Stepney, S., Miller, J. F. & Trefzer, M. Reservoir computing in materio: an evaluation of configuration through evolution. In *2016 IEEE Symposium Series on Computational Intelligence, SSCI* 1–8 (IEEE, 2016).
24. Björk, M. T., Schmid, H., Knoch, J., Riel, H. & Riess, W. Donor deactivation in silicon nanostructures. *Nat. Nanotechnol.* **4**, 103–107 (2009).
25. Pierre, M. et al. Single-donor ionization energies in a nanoscale CMOS channel. *Nat. Nanotechnol.* **5**, 133–137 (2010).
26. Hartstein, A. & Fowler, A. B. High temperature 'variable range hopping' conductivity in silicon inversion layers. *J. Phys. C* **8**, L249–L253 (1975).
27. Minsky, M. & Papert, S. *Perceptrons: An Introduction to Computational Geometry* (MIT Press, 1969).
28. Chen, T. et al. DianNao: a small-footprint high-throughput accelerator for ubiquitous machine-learning. *ACM SIGPLAN Not.* **49**, 269–284 (2014).
29. Lee, J. et al. UNPU: an energy-efficient deep neural network accelerator with fully variable weight bit precision. *IEEE J. Solid-State Circuits* **54**, 173–185 (2019).
30. Li, C. et al. Analogue signal and image processing with large memristor crossbars. *Nat. Electron.* **1**, 52–59 (2018).
31. Tapson, J. & van Schaik, A. Learning the pseudoinverse solution to network weights. *Neural Netw.* **45**, 94–100 (2013).
32. Such, F. P. et al. Deep neuroevolution: genetic algorithms are a competitive alternative for training deep neural networks for reinforcement learning. Preprint at http://arxiv.org/abs/1712.06567 (2017).
33. Kingma, D. P. & Ba, L. J. Adam: a method for stochastic optimization. Preprint at https://arxiv.org/abs/1412.6980 (2015).

Publisher's note Springer Nature remains neutral with regard to jurisdictional claims in published maps and institutional affiliations.

© The Author(s), under exclusive licence to Springer Nature Limited 2020

Methods

Samples

300 nm of thermal oxide was grown on an n-type silicon substrate (Extended Data Fig. 1a), in which $26 \times 60\ \mu m^2$ implantation windows were defined by photolithography and wet etching. Another 35 nm of oxide was thermally grown in the implantation window to serve as a stopping layer (Extended Data Fig. 1b). After boron implantation (9 keV equivalent, $3.5 \times 10^{14}\ cm^{-2}$), and activation via rapid thermal annealing (1,050 °C, 7 s; Extended Data Fig. 1c), the 35-nm stopping layer was removed by wet etching. The boron concentration near the silicon surface exceeds $2 \times 10^{19}\ cm^{-3}$ to ensure Ohmic contact with the electrodes, and decreases monotonically with depth (Extended Data Fig. 1h). After lift-off of the wire-bonding pads (1.5 nm Ti/40 nm Pd) defined by photolithography (Extended Data Fig. 1d), eight 1.5 nm Ti/40 nm Pd nanoelectrodes were patterned on top of the silicon by electron-beam lithography (Extended Data Fig. 1e). The devices were annealed at 160 °C for 10 min to promote the metal/silicon contact quality. The silicon surface was further etched by reactive ion etching to reduce the boron concentration in the active gap area (Extended Data Fig. 1f, g; see also Supplementary Note 6). The surface was finally treated with mild oxygen plasma, followed by 1% HF etching to remove possible contaminants.

Charge transport

Following Zabrodskii et al.[15], we introduce the logarithmic derivative $w = \mathrm{d}(\log G)/\mathrm{d}(\log T)$. From equation. (1), we see that if the hopping term $G_h e^{-(T_h/T)^p}$ dominates, $\log w \approx \log p + p(\log T_h - \log T)$, and p can be derived from the slope of the $\log w - \log T$ curve (Fig. 2e), thus allowing us to identify the exact hopping conduction model. For $T < 70$ K, the measurement noise level prevents unambiguous identification of the charge transport mechanism (Fig. 2d), but probably VRH continues[34]. The charge transport behaviour described in the main text has been observed in the two devices we characterized.

Measurements

We conducted the charge transport measurements and evolution of logic gates at different temperatures in a customized flow cryostat. The cryostat is equipped with 12 coaxial cables to reduce capacitive cross-talk. We use a battery-powered electronics rack (IVVI rack and matrix rack; http://qtwork.tudelft.nl) composed of digital-to-analogue converters (DACs) and *I*/*V* converters for low-noise measurements (Extended Data Fig. 6). The output range of the DACs is from −2 V to 2V. The *I*/*V* converter has four amplification settings, 1 GΩ, 100 MΩ, 10 MΩ and 1 MΩ, each corresponding to a different measurement range. For measurements at cryogenic temperatures, 1 GΩ amplification is chosen as default, by which currents from −3.4 nA to 3.4 nA can be measured. The output of the *I*/*V* converter is sampled by a multimeter (Keithley 2000) or digitizer (ADwin-Gold II). For room-temperature evolution, the *I*/*V* converter amplification is set to 10 MΩ, resulting in a current measurement range from −340 nA to 340 nA. The measurements are automated with either LabVIEW or Python scripts. For fixed-temperature measurements, the devices were inserted into a liquid-helium (4.2 K) or liquid-nitrogen (77 K) dewar with a customized dipstick.

Readout speed

In our system, the relaxation time of hopping conduction is less than 10 ns at 77 K and even smaller at higher temperatures (Supplementary Note 8), so it is not the dominant timescale in our present devices. Like in all measurements on resistive devices[35], the readout speed of our dopant networks is constrained by a large capacitive load (Extended Data Fig. 6b). The long, twisted pairs (about 3 m) as well as the filters of the matrix rack amount to a large load capacitance C_L (about 4 nF) that limits the signal speed. With the existing setup, we have a bandwidth (cutoff frequency of the resistor–capacitor (RC) circuit in Extended Data Fig. 6b)

$$\mathrm{BW} = \frac{1}{2\pi C_L (R_{out} || R_{IV})} \approx 40\ \mathrm{Hz}$$

where $R_{IV} = 1$ MΩ is the input resistance of the *I*/*V* converter at 1 GΩ amplification, and the dopant network output resistance R_{out} is typically hundreds of MΩ (Extended Data Fig. 7d).

By monolithically integrating a transistor-based readout circuitry close to the dopant network[35] (Extended Data Fig. 6c), we can reduce the capacitive load for fast readout, and also enable interconnection with other devices. With existing CMOS technology, the load capacitance can be easily reduced to below 1 fF, and the RC-related bandwidth can reach 160 MHz, or even more, by reducing R_{IV}.

Given a signal intensity (the difference between high and low output current levels; see 'Fitness functions' below), the signal-to-noise ratio (SNR) is predominantly set by the Johnson–Nyquist noise from R_{IV}, because its noise power is proportional to the bandwidth. Therefore, for a required SNR (computation precision), the bandwidth and the subsequent energy efficiency, are determined by the signal intensity (Supplementary Note 8). The signal intensity of our devices ranges from the order of 0.1 nA to the order of 1 nA (Supplementary Note 6), thus allowing over 100 MHz bandwidth (Extended Data Fig. 7a).

Fitness functions

For Boolean logic gate evolution, the input sequences, representing the four input entries of truth tables (Fig. 3b), were fed to the input electrodes (Fig. 3a) after the control voltages were set. We monitored the output current waveform $\overline{Y}$ and fitted it with $\overline{Y} = m\overline{X} + C$, where $\overline{X}$ is the expected output waveform of a logic gate (logic high and low taking numerical values of 1 and 0, respectively). m is the proportionality factor and its value thus equals the separation of the high and low levels (signal intensity). C represents the offset. For each set of control voltages, a fitness is evaluated by $F = m/\left(\sqrt{r_{ss}} + kC\right)$, with r_{ss} being the fitting residual[12] and k an empirical constant. A larger k puts more emphasis on minimizing the offset C in the evolution process. For the evolution of logic gates, we found that there is minimal offset for $k = 0.2$ (Fig. 3c). In the random search of logic gates at different temperatures, k has been set to 0.01 to give the waveform shape more weight than the offset. Then, a fitness value of $F = 1$ implies that the signal intensity (related to m) almost equals the noise intensity (related to $\sqrt{r_{ss}}$), and a fitness value of $F = 2$ corresponds to more robust logic gates. Based on the fitness, we define the abundance of each gate. For the 10,000 output waveforms from a random search, we assessed the fitness of each output waveform for six major logic gates. In this way, each logic gate is associated with 10,000 fitness values. The abundance of a gate A_i (where i is AND, OR, NAND, NOR, XOR, XNOR) is defined as the number of fitness values larger than a threshold, divided by 10,000. The total abundance is then defined as $A = 1/\sum_i (1/A_i)$. The fitness function for the feature filter evolution was defined as $F = |I_{out,i}|/[\mathrm{avg}(|I_{out,j\neq i}|) + \mathrm{std}(I_{out,j\neq i})]$, where $I_{out,i}$ is the output current corresponding to feature f_i, and avg and std stand for the average and standard deviation, respectively, of all the other feature outputs $I_{out,j\neq i}$. Here, i runs from 1 to 16.

Genetic algorithm

The genetic algorithm mimics natural evolution. An initial generation of 20 genomes, with the length of each genome equal to the number of control electrodes, is first randomly generated and mapped to control voltages. The fitnesses of the 20 genomes are evaluated and ranked. Then the off-spring generation of 20 genomes is produced in the following way: (1) inheriting the five elite genomes (with highest fitnesses) from the previous generation; (2) cross-breeding of the elite genomes to produce five off-spring genomes; (3) mutation of the five elite genomes

by a probability of 0.1, then cross-breeding with the five elite genomes to generate five other genomes; (4) cross-breeding of the five elite genomes with five random genomes to generate five other genomes. The genetic algorithm keeps iterating until it reaches a satisfactory fitness value (Extended Data Fig. 4a; see also Supplementary Note 7). A more detailed description of the evolution procedure is given in our previous work[12].

Power consumption

To estimate the power consumption and energy efficiency of our device, we measured the static power consumption of the six major Boolean logic gates for four different input voltage combinations, so in total 24 configurations. To measure the current of the ith (i running from 1 to 8) electrode, the voltage V_i (current I_i) is set (measured) by a source meter (Keithley 2401), while the voltages on the other electrodes are set by either the DACs (control voltages and input voltages) or an I/V converter (output electrode). For each of the 24 configurations, the total power P is calculated as $P = \sum_{i=1}^{8} V_i I_i$. The average power of the 24 configurations is found to be about 1 μW. Under operational conditions, the voltage changes on the electrodes are accompanied by charging and discharging of wire capacitances. As mentioned above ('Readout speed' section), the capacitances can be reduced to below 1 fF, making the dynamical power consumption negligible compared with the static power consumption. The static power consumption could be substantially reduced by using electrostatic electrodes (see also Supplementary Note 8).

Weight matrix training and test

In the digit classification task, each 28 × 28 pixel digit is divided into 27 × 27 receptive fields of 2 × 2 pixels, overlapping by one row/column of pixels. The pixels of each receptive field are mapped to the 4 inputs of 16 filters (with their experimentally determined response), each of which filters 1 of the 16 distinctive 2 × 2 pixel features shown in the inset of Fig. 4a. For the dth digit in the N_d = 60,000 MNIST training database, we stack the $N_f = 27 \times 27 \times 16 = 11{,}664$ outputs of the filters in a feature vector $\mathbf{O}_d = (O_{d,1}, \cdots, O_{d,N_f})$. Combining the vectors $\mathbf{O}_d$ of 60,000 training digits together, we obtain an $N_d \times N_f$ output matrix $\mathbf{O} = (\mathbf{O}_1, \cdots, \mathbf{O}_{N_d})^{\mathrm{T}}$.

The true label of each digit is represented by a ten-dimensional label vector $\mathbf{L}_d$, whose elements are all zeros except for the $(l+1)$th entry being 1, where $l \in \{0, \ldots, 9\}$ is the true label of the dth MNIST digit. Ideally, the weight matrix M_W converts the feature vector of a digit to its corresponding label vector $\mathbf{O}_d M_W = \mathbf{L}_d$. So, in matrix form, $\mathbf{O}M_W = \mathbf{L}$, where $\mathbf{L} = (\mathbf{L}_1, \cdots, \mathbf{L}_{N_d})^{\mathrm{T}}$. The weight matrix M_W has a dimension of $N_f \times 10$, and is simply obtained by $M_W = O^+\mathbf{L}$, where O^+ is the pseudoinverse of matrix O. Once the weight matrix is trained, we test it with the N_t = 10,000 MNIST test data. The feature vector of each test digit $\mathbf{O}_t$, $(t = 1, \ldots, N_t)$, is multiplied by the weight matrix to acquire the predicted label vector $\mathbf{P}_t$, $\mathbf{O}_t M_W = \mathbf{P}_t$.

The index of the maximal element of $\mathbf{P}_t$ minus one gives the predicted label. The accuracy is calculated as the ratio of the total counts of the correctly classified digits, that is, the sum of diagonal entries in Fig. 4c, to the total number of test digits N_t.

Data availability

Data are available from the corresponding author upon reasonable request.

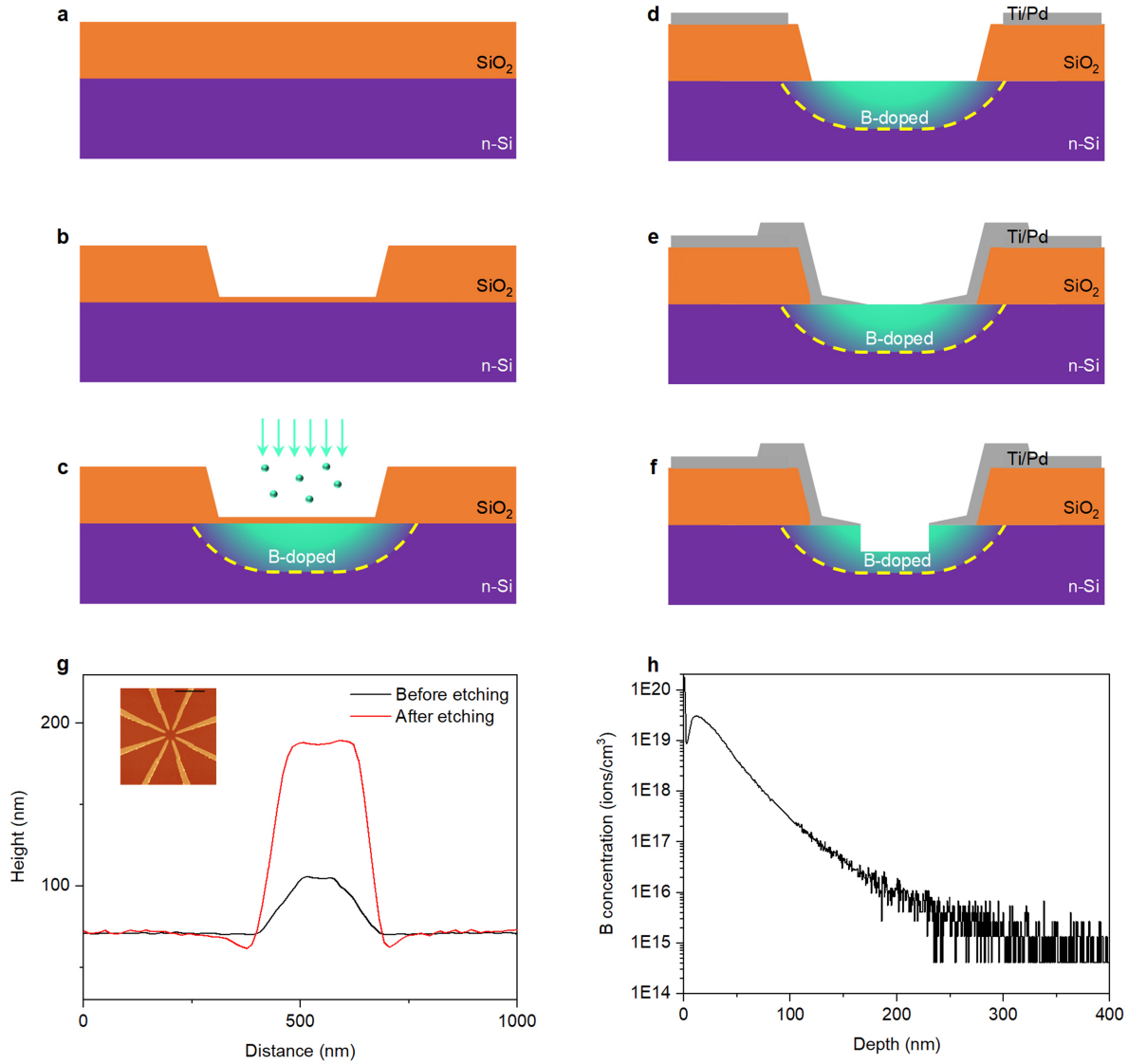
34. Aharony, A., Zhang, Y. & Sarachik, M. P. Universal crossover in variable range hopping with Coulomb interactions. *Phys. Rev. Lett.* **68**, 3900–3903 (1992).
35. Pettersson, J. et al. Extending the high-frequency limit of a single-electron transistor by on-chip impedance transformation. *Phys. Rev. B* **53**, R13272–R13274 (1996).
36. The Green500 *TOP500.org* https://www.top500.org/green500/ (2019).
37. Hu, M. et al. Memristor-based analog computation and neural network classification with a dot product engine. *Adv. Mater.* **30**, 1705914 (2018).

Acknowledgements We thank T. Bolhuis, M. H. Siekman and J. G. M. Sanderink for technical support. We thank C. P. Lawrence, B. J. Geurts, M. Nass, A. J. Annema, M. Dale and J. Dewhirst for discussions. We thank W. M. Elferink, R. Hori, J. Wildeboer and T. Dukker for help with measurements. We acknowledge financial support from the MESA+ Institute for Nanotechnology, and the Netherlands Organisation for Scientific Research (NWO): NWA Startimpuls grant number 680-91-114 and Natuurkunde Projectruimte grant number 400-17-607.

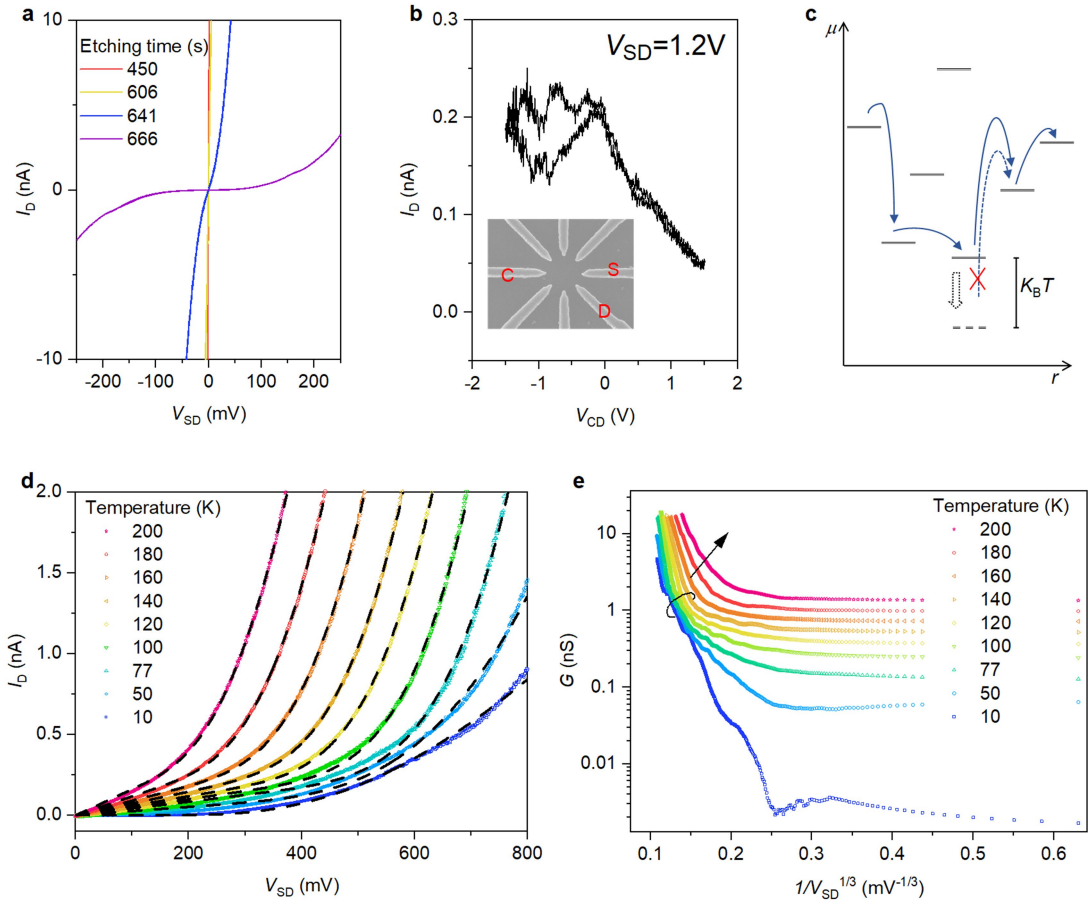
Author contributions T.C. and W.G.v.d.W. designed the experiments. J.v.G., T.C., B.v.d.V. and S.V.A. fabricated the samples. T.C., J.v.G. and B.v.d.V. performed the measurements and simulations. T.C. analysed the data with input from all authors. H.B., H.C.R.E. and P.A.B. provided theoretical inputs. B.d.W. and H.C.R.E. contributed to measurement script. T.C. and W.G.v.d.W. wrote the manuscript and all the authors contributed to revisions. W.G.v.d.W. and F.A.Z. conceived the project. W.G.v.d.W. supervised the project. F.A.Z. co-supervised the sample fabrication.

Competing interests The authors declare no competing interests.

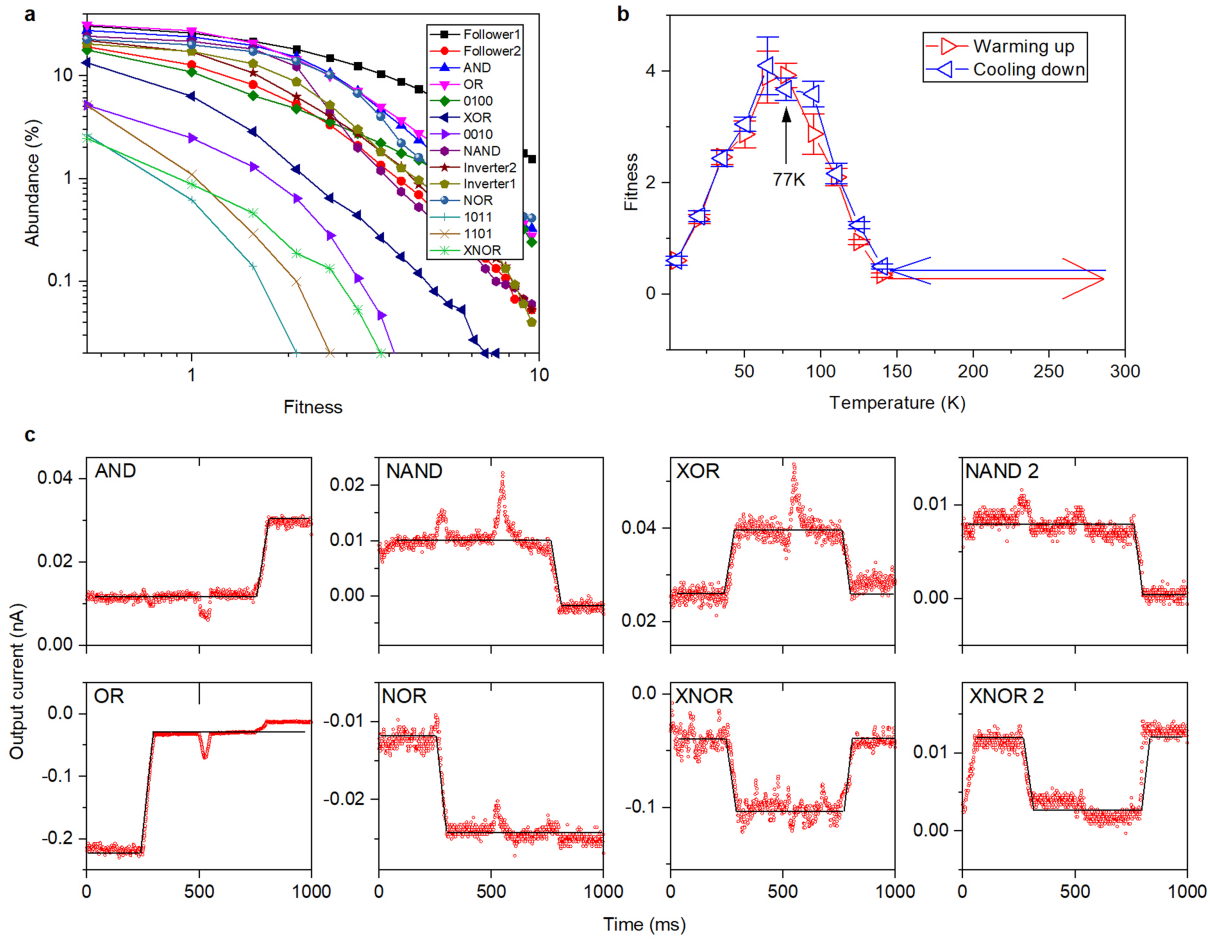
Additional information
Supplementary information is available for this paper at https://doi.org/10.1038/s41586-019-1901-0.
Correspondence and requests for materials should be addressed to W.G.v.W.
Peer review information *Nature* thanks Cyrus Hirjibehedin and the other, anonymous, reviewer(s) for their contribution to the peer review of this work.
Reprints and permissions information is available at http://www.nature.com/reprints.



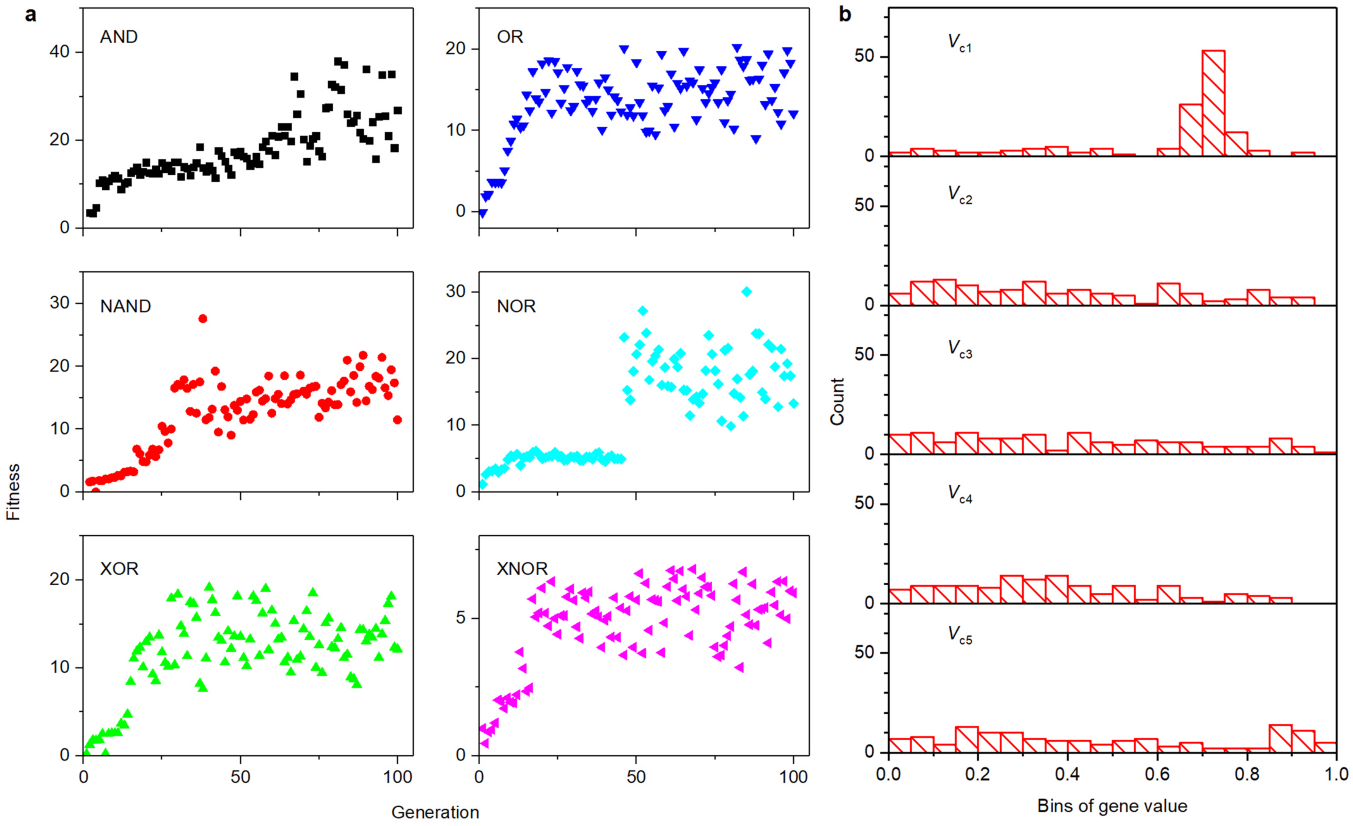
Extended Data Fig. 1 | Fabrication steps and dopant concentration. **a**, Thermal oxidation. **b**, Implantation window definition and growth of 35 nm oxide. **c**, Ion implantation. **d**, Photolithography and contact pads lift-off. **e**, Electron-beam lithography and nanoelectrodes lift-off. **f**, Reactive ion etching (RIE) of silicon. **g**, Height profile of the metal electrodes with respect to silicon before (black) and after (red) RIE etching. The etch depth of silicon is estimated by measuring the height change of the metal electrodes with respect to the silicon surface (indicated by the black line on the atomic force microscopy image in the inset, not to scale). Assuming that the metal is not etched by RIE, the etch depth of silicon is around 83 nm. **h**, Secondary ion mass spectroscopy of the boron dopant depth profile after implantation. On the basis of the etch depth, the boron concentration near the recessed silicon surface is of the order of 5×10^{17} cm^{-3}.



Extended Data Fig. 2 | Nonlinear and tunable hopping conduction. a, *I*–*V* characteristics at 4.2 K with different total etching time by RIE. As the total etching time increases, the nonlinearity becomes increasingly prominent, signalling the dominance of hopping conduction. **b**, Drain current versus control voltage for constant source–drain voltage V_{SD} = 1.2 V at 4.2 K. The source (S), drain (D) and control (C) electrodes are shown in the inset. The hysteresis for negative gate voltage is probably due to charging of the other five floating electrodes. **c**, Schematic plot of electrochemical potential μ versus position *r*, illustrating the tunability. The solid lines represent impurity states and the arrows represent hopping of carriers among states. See Supplementary Note 3 for detailed discussion. **d**, Fitting the temperature-dependent *I*–*V* curves with the model described by equation (2) in Supplementary Note 2. Black dashed lines represent the fitted curves. **e**, Conductance versus the reciprocal of the cube root of the source–drain voltage at different temperatures. The black circle groups data at temperatures below 140 K. See also Supplementary Note 2 for more discussion.



Extended Data Fig. 3 | Evolved logic gates at 77 K. a, Abundance plot of 14 non-trivial truth tables at 77 K. From a search with 10,000 sets of randomly generated control voltages, we found all 16 possible truth tables that can be realized for a two-input–one-output configuration. **b**, Thermal stability of a NAND gate evolved at 77 K. Above 140 K, the output current clipped to compliance, and therefore the fitness was not extracted. The error bars represent the standard deviation of ten tests (see also Supplementary Note 4). **c**, Boolean logic gates evolved at 77 K in a device other than the one in Fig. 3c. Red circles are experimental output currents, and black lines represent the normalized desired output currents. The left six panels show the six major logic gates evolved with input voltage levels 0 V and 0.5 V. The right two panels show a NAND and a XNOR gate evolved with input voltage levels of −0.25 V and 0.25 V, showing the adaptability of the dopant network to different voltage levels (see also Supplementary Note 6).



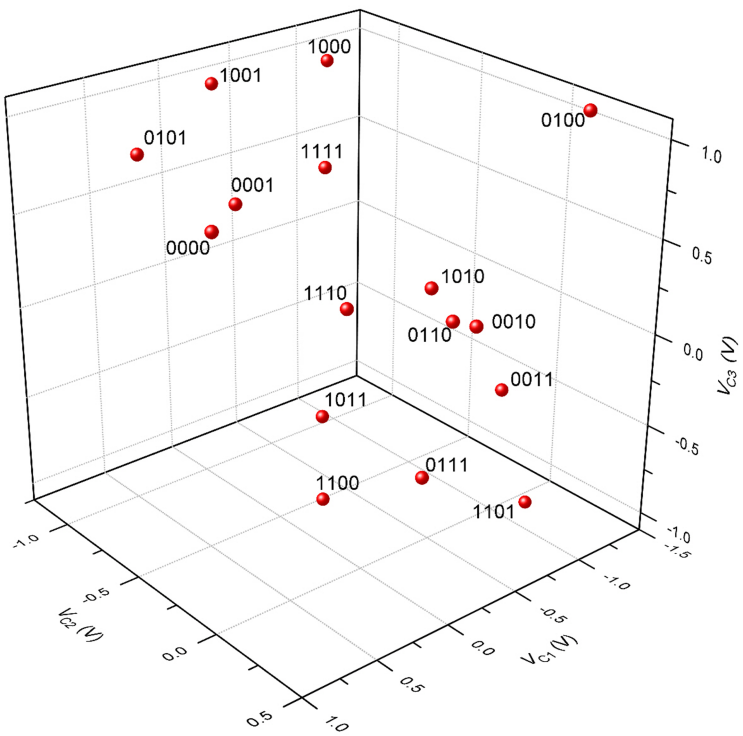
c

	V_{C1} (V)	V_{C2} (V)	V_{C3} (V)	V_{C4} (V)	V_{C5} (V)
AND	0.261	0.299	-0.619	-0.579	-0.221
OR	-0.266	-0.68	0.515	-0.175	-0.199
NAND	-0.298	0.177	0.515	0.244	-0.32
NOR	0.346	-0.25	0.328	1.18	-0.124
XOR	0.442	0.314	0.487	0.144	-0.209
XNOR	-0.279	0.018	0.038	-0.73	-0.256

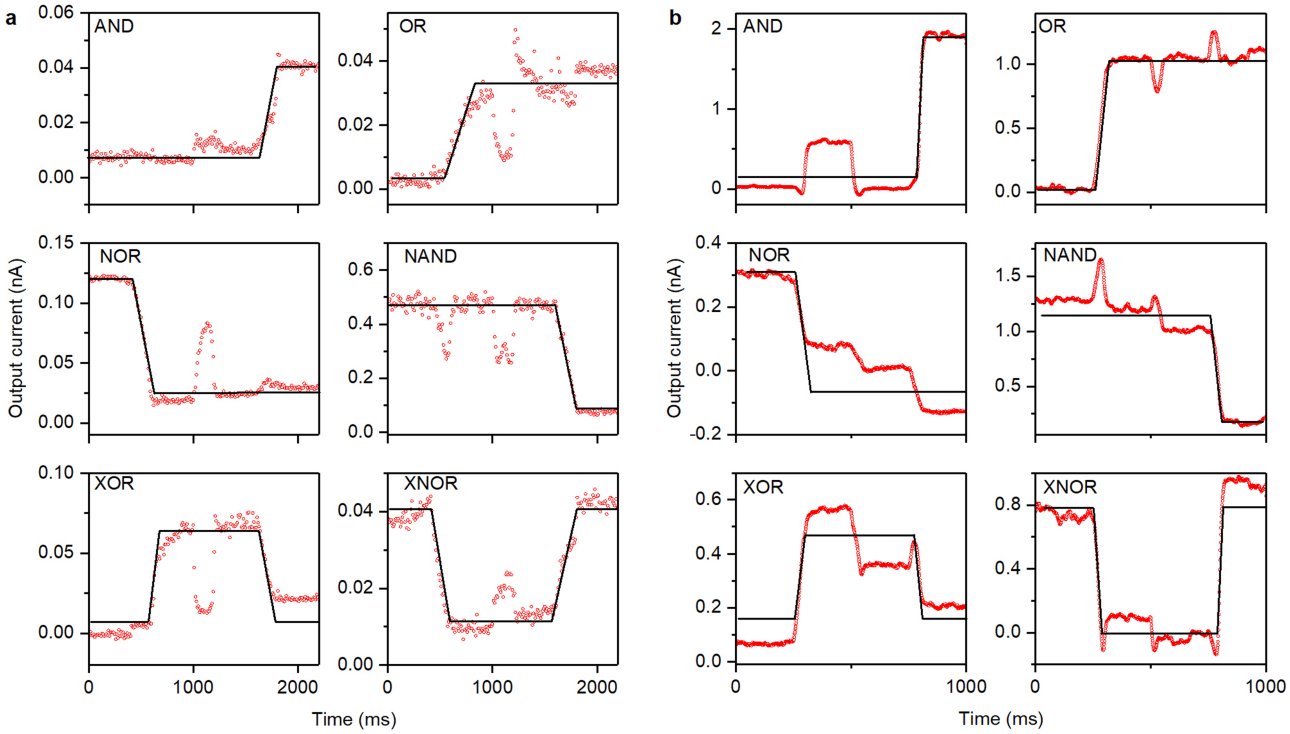
d

	V_{C1} (V)	V_{C2} (V)	V_{C3} (V)
0000	0.60509	-0.34386	0.69212
0001	0.20454	-0.57179	0.64293
0010	-0.41105	0.29822	0.2447
0011	-0.82728	0.15518	-0.27901
0100	-1.29545	0.22605	1.08706
0101	0.54342	-0.86175	0.85753
0110	-0.32769	0.23459	0.26238
0111	-0.12659	0.24267	-0.49213
1000	-0.77783	-0.86176	1.07511
1001	-0.1088	-1.00302	1.03481
1010	-0.39624	0.06503	0.3365
1011	-0.07965	-0.30009	-0.43787
1100	0.02196	-0.21027	-0.82176
1101	-0.97294	0.21243	-0.92759
1110	0.01541	-0.07923	0.27283
1111	-0.38757	-0.54464	0.70877

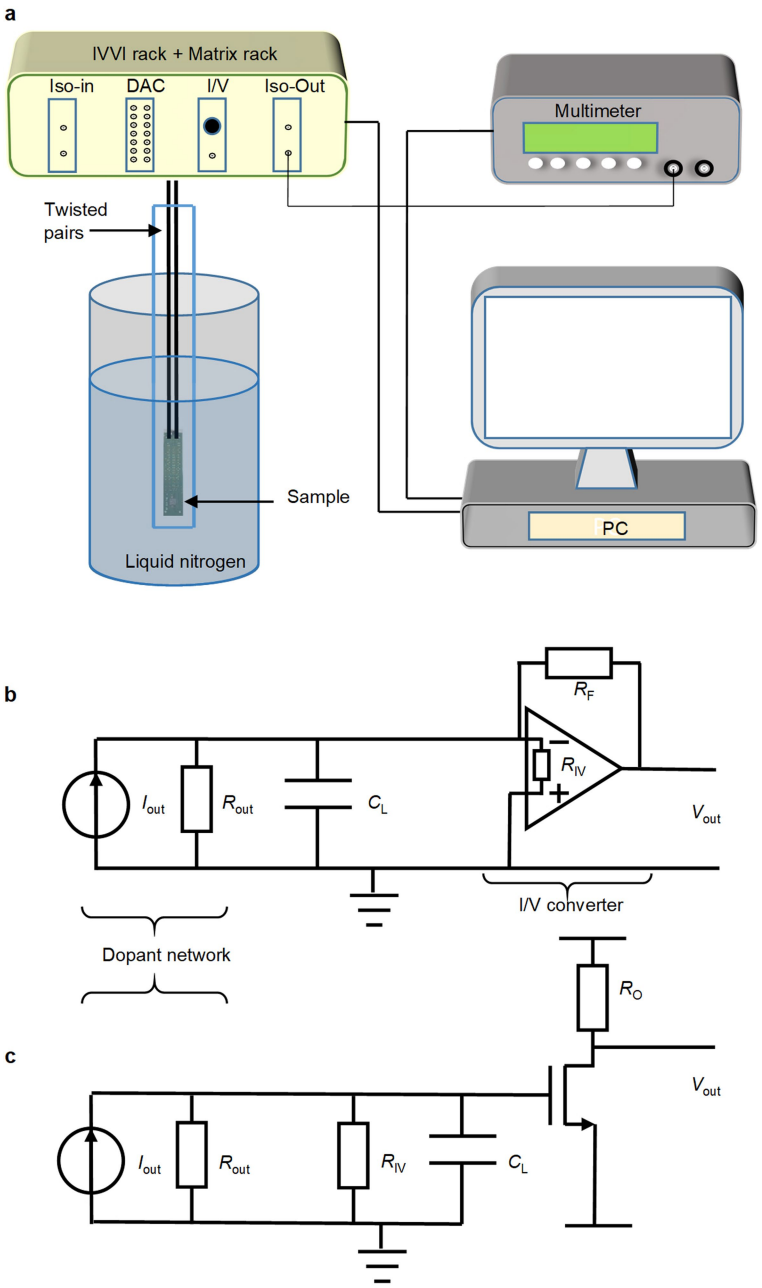
e



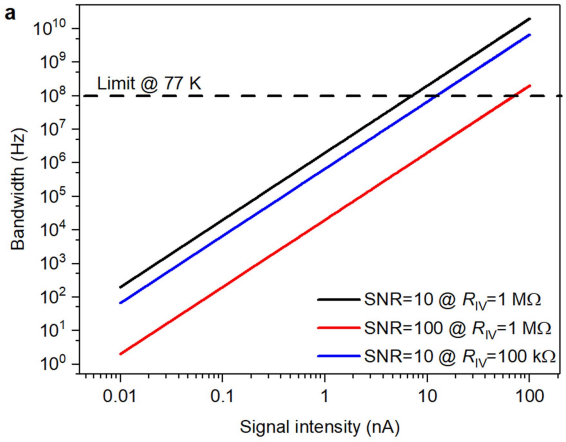
Extended Data Fig. 4 | Convergence of genetic algorithm in the configuration space. a, Genetic algorithm convergence for the six major Boolean logic gates at 77 K. The best fitness of the 20 genomes is plotted against generation. **b**, Histograms of the control voltages that configure the dopant network to the XNOR gates with fitness *F* larger than 1.5. The first control voltage is prominently concentrated in a small range, but the others do not show a favourite range. The ranges of the five control voltages are (−600, 600), (−1,200, 1,200), (−1,200, 1,200), (−1,200, 1,200) and (−600, 600). **c**, Control voltages for the six major logic gates. **d**, Control voltages for the 16 filters, which are visualized in **e**. The filters '0110' and '0010' have the smallest separation. See Supplementary Notes 3 and 7 for more discussion.

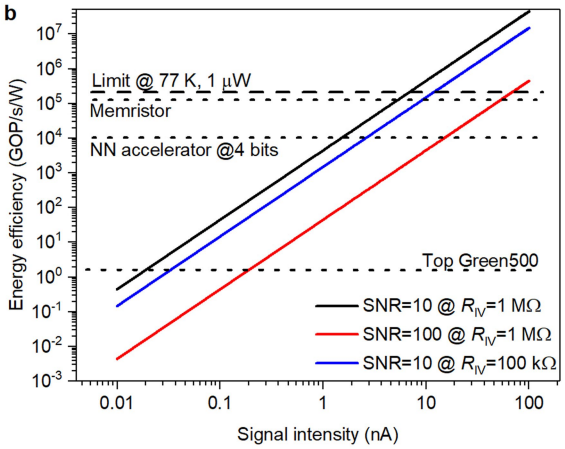


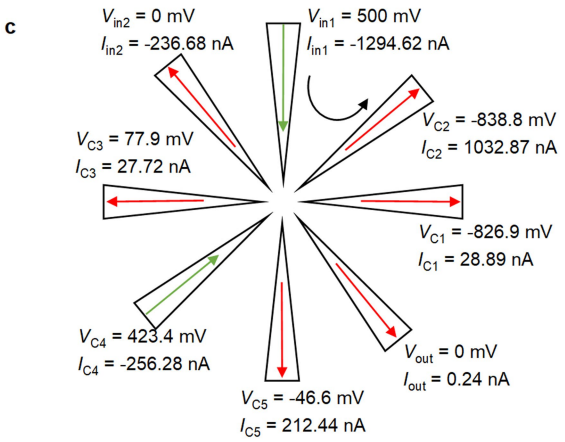
Extended Data Fig. 5 | Evolution of logic gates at two ends of hopping conduction. a, Evolved logic gates at 4.2 K, at which the charge transport mechanism is still VRH (Methods). **b**, Evolved logic gates at 140 K. Red circles are experimental output currents and black lines represent the normalized desired output currents. See Supplementary Note 5 for a detailed discussion.



Extended Data Fig. 6 | Measurement setup. a, Schematics of the existing measurement setup. **b**, Equivalent circuit of the current measurement setup. I_{out} and R_{out} represent the output current and output resistance of the device. C_L is the parasitic capacitance of about 4 nF. R_{IV} and R_F are the input resistance and feedback resistance of the *I*/*V* converter, respectively. **c**, Schematic of an integrated high-speed current reading circuit. Here, R_{IV} is a resistor to convert current to voltage, C_L is the parasitic capacitance that can be reduced to below 1fF. R_O is a resistor that sets the amplification.







d

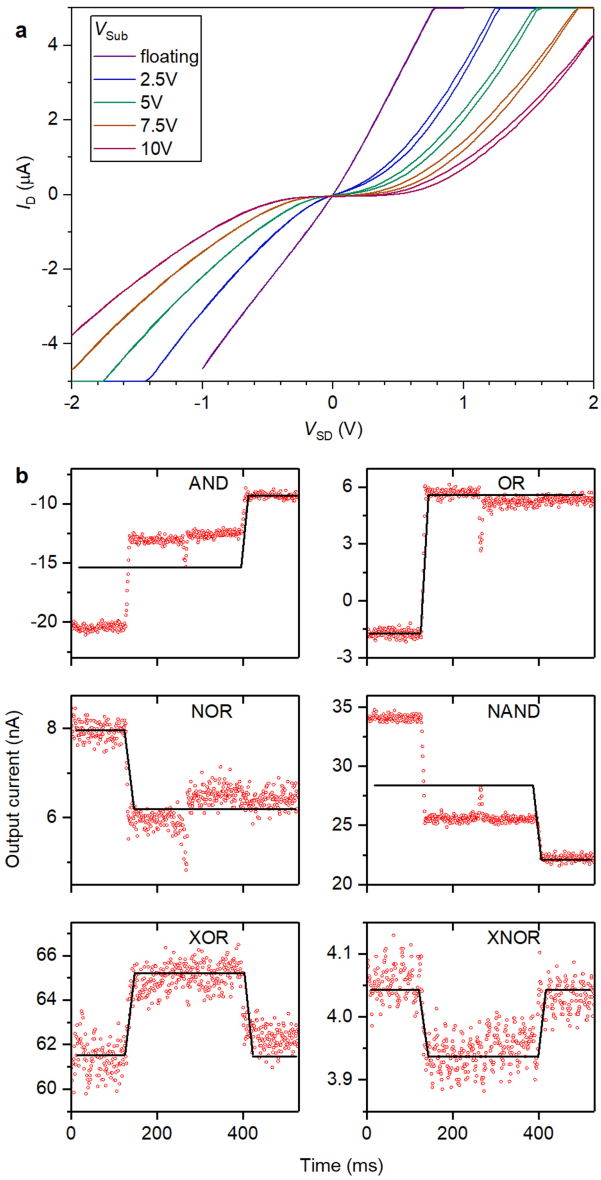
NAND00	V (mV)	I (nA)	I_{std} (nA)	R_{diff} (MΩ)
Input 1	0.00	-81.81	0.84	1.22
Input 2	0.00	14.74	0.08	8.49
Control 1	-826.90	10.79	0.12	21.75
Control 2	-838.80	119.42	1.16	1.99
Control 3	77.90	24.33	0.22	7.99
Control 4	423.40	-339.16	1.50	0.43
Control 5	-46.60	251.61	1.47	0.96
Output	0.00	0.28	0.01	48.19
Power		0.26 μW		

NAND01	V (mV)	I (nA)	I_{std} (nA)	R_{diff} (MΩ)
Input 1	0.00	77.73	0.88	0.98
Input 2	500.00	-276.23	2.11	0.42
Control 1	-826.90	9.76	0.13	28.85
Control 2	-838.80	147.69	1.21	1.91
Control 3	77.90	48.95	0.22	2.74
Control 4	423.40	-203.48	1.12	0.57
Control 5	-46.60	182.3	1.06	1.38
Output	0.00	0.16	0.02	138.59
Power		0.36 μW		

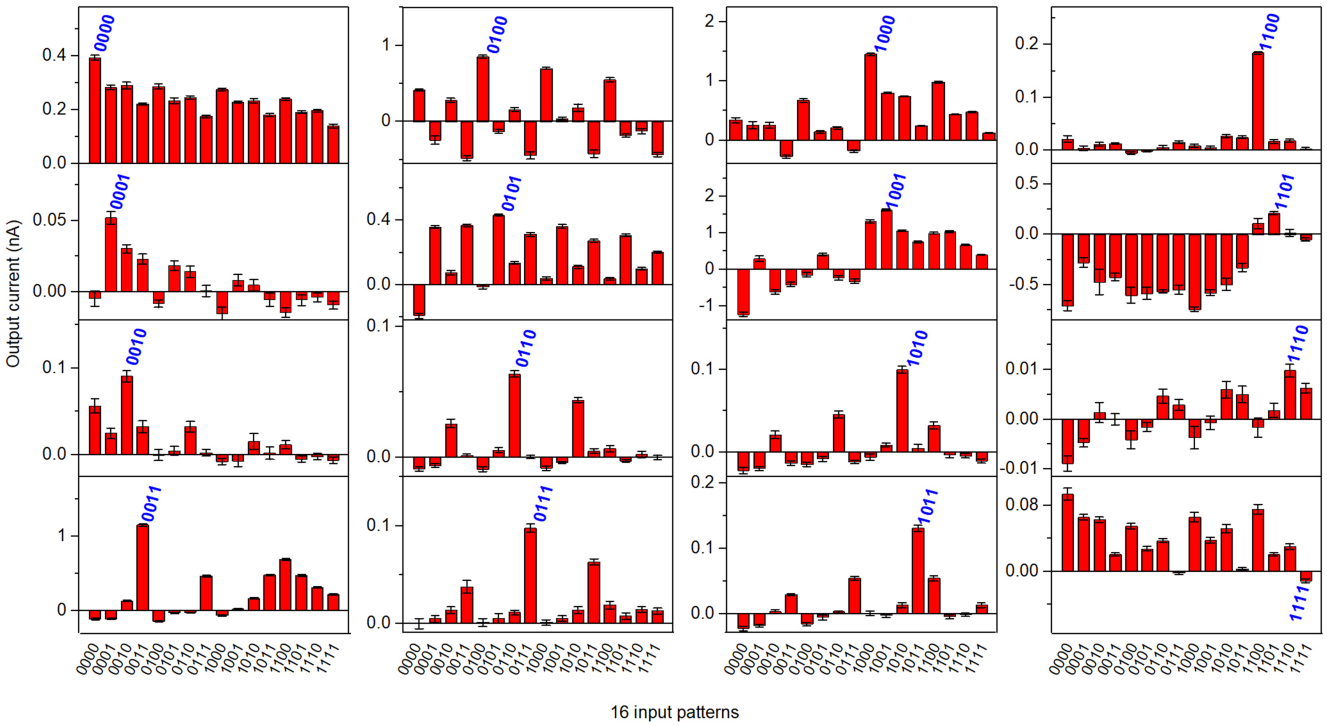
NAND10	V (mV)	I (nA)	I_{std} (nA)	R_{diff} (MΩ)
Input 1	500.00	-1294.62	4.09	0.23
Input 2	0.00	236.68	2.06	0.75
Control 1	-826.90	28.89	0.25	12.94
Control 2	-838.80	1032.87	5.09	0.63
Control 3	77.90	27.72	0.21	6.37
Control 4	423.40	-256.28	1.96	0.52
Control 5	-46.60	212.44	1.39	1.11
Output	0.00	0.24	0.02	105.88
Power		1.65 μW		

NAND11	V (mV)	I (nA)	I_{std} (nA)	R_{diff} (MΩ)
Input 1	500.00	-795.46	4.23	0.30
Input 2	500.00	-101.46	0.92	0.82
Control 1	-826.90	20.07	0.35	17.53
Control 2	-838.80	836.29	4.42	0.71
Control 3	77.90	48.01	0.35	2.70
Control 4	423.40	-173.57	1.19	0.64
Control 5	-46.60	161.28	1.10	1.20
Output	0.00	0.02	0.01	231.38
Power		1.24 μW		

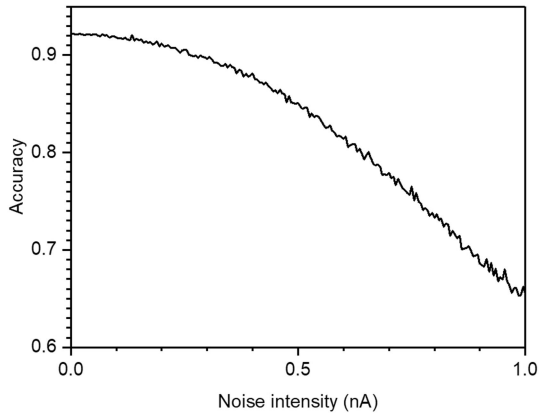
Extended Data Fig. 7 | Bandwidth and energy efficiency scaling. a, The scaling of allowed bandwidth with signal intensity in a log–log plot. The back, blue and red solid lines represent three different indicated cases. Larger required SNR (red) and smaller R_{IV} (blue) lower the bandwidth. The horizontal black dashed line represents the limit set by the hopping relaxation time at 77 K, which increases with temperature. **b**, The scaling of equivalent energy efficiency with signal intensity in a log–log plot. Larger SNR (red) and smaller R_{IV} (blue) lowers the energy efficiency. The horizontal black dashed line represents the limit at 77 K and fixed power consumption. If the dopant network power consumption is lowered, then the limit and all three scaling trends shift upwards. The three black dotted lines mark three representative computational technologies, the most energy efficient high-performance computer[36], the neural network (NN) accelerator[29] and memristors[37] (Supplementary Note 8). **c**, Current flow pattern of a NAND gate (NAND10 in **d**) with inputs 500 and 0 mV. There is a large parasitic current flowing from input 1 to control electrode 2 (black curved arrow). This parasitic current limits the energy efficiency. This can be solved by using electrostatically coupled electrodes (Supplementary Note 8). **d**, Measured power consumption of a NAND gate for the four input combinations. The standard deviations in the current are calculated from ten measurements. The differential resistances R_{diff} are measured around the voltages in the second column.



Extended Data Fig. 8 | Backgate-induced nonlinearity and evolved logic gates at room temperature. a, A positive voltage V_{Sub} with respect to the drain voltage is applied to the n-type substrate (Fig. 2b) to make the depletion region wider at the p–n junction, and to suppress the band conduction. **b**, Evolved gates at room temperature. Red circles are experimental outputs, and black lines represent the normalized desired outputs. The output current levels, and also the separation between these levels, are more than one order of magnitude larger than those of the logic gates evolved at 77 K, owing to the increased hopping conductance (Supplementary Note 3). The increased noise intensity is mainly due to the settings of the current measurement circuit (Methods).



Extended Data Fig. 9 | Experimental response of the 16 filters. Each of them is evolved to filter the feature given in blue. The output currents corresponding to features other than the desired one are not zero, but the output current of the targeted feature is clearly separated from the other currents. Error bars represent the standard deviation obtained from ten tests.



Extended Data Fig. 10 | Enhancing robustness of the linear classifier against noise. Besides optimizing the SNR, the linear classifier's tolerance to noise can also be increased by taking noise into account during the training phase. The accuracy remains over 92% at 0.05 nA noise amplitude (see Supplementary Note 8 for a detailed discussion).

Direct thermal neutron detection by the 2D semiconductor $^{6}LiInP_2Se_6$

https://doi.org/10.1038/s41586-019-1886-8

Received: 28 April 2019

Accepted: 8 October 2019

Published online: 15 January 2020

Daniel G. Chica[1,5], Yihui He[1,5], Kyle M. McCall[1,2], Duck Young Chung[3], Rahmi O. Pak[3], Giancarlo Trimarchi[1], Zhifu Liu[2], Patrick M. De Lurgio[4], Bruce W. Wessels[2] & Mercouri G. Kanatzidis[1,3]*

Highly efficient neutron detectors are critical in many sectors, including national security[1,2], medicine[3], crystallography[4] and astronomy[5]. The main neutron detection technologies currently used involve ^{3}He-gas-filled proportional counters[6] and light scintillators[7] for thermalized neutrons. Semiconductors could provide the next generation of neutron detectors because their advantages could make them competitive with or superior to existing detectors. In particular, solids with a high concentration of high-neutron-capture nuclides (such as ^{6}Li, ^{10}B) could be used to develop smaller detectors with high intrinsic efficiencies. However, no promising materials have been reported so far for the construction of direct-conversion semiconductor detectors. Here we report on the semiconductor $LiInP_2Se_6$ and demonstrate its potential as a candidate material for the direct detection of thermal neutrons at room temperature. This compound has a good thermal-neutron-capture cross-section, a suitable bandgap (2.06 electronvolts) and a favourable electronic band structure for efficient electron charge transport. We used α particles from an ^{241}Am source as a proxy for the neutron-capture reaction and determined that the compact two-dimensional (2D) $LiInP_2Se_6$ detectors resolved the full-energy peak with an energy resolution of 13.9 per cent. Direct neutron detection from a moderated Pu–Be source was achieved using ^{6}Li-enriched (95 per cent) $LiInP_2Se_6$ detectors with full-peak resolution. We anticipate that these results will spark interest in this field and enable the replacement of ^{3}He counters by semiconductor-based neutron detectors.

Direct neutron detection presents a tremendous challenge because neutrons interact weakly with most matter[8]. Neutron detectors exploit the properties of certain nuclides that decay into highly energetic charged fragments upon capture of a neutron, providing easily detectable signals through ionization products[9]. In practice, only ^{3}He, ^{10}B and ^{6}Li combine high neutron-capture cross-sections with detectable decay products, and these isotopes have been incorporated into various detector architectures. The detector of choice for several decades has been the ^{3}He-gas-filled proportional counter. However, in the past two decades, the stockpile of ^{3}He has been greatly depleted with no viable means for increasing production to meet demand[6]. Therefore, many alternative technologies have attracted interest, including $^{10}BF_3$-filled tubes, ^{10}B-lined tubes, ^{6}LiF-based scintillators, lithium-loaded plastic scintillators[7],^{6}LiF-filled micro-structured semiconductor detectors[10] and neutron-sensitive semiconductors. These technologies have advantages and disadvantages[11], but so far no widespread replacement for ^{3}He tubes has been found.

^{6}Li- and ^{10}B-containing semiconductors are emerging technologies that promise highly efficient detectors because the concentration of neutron-absorbing isotopes is much greater in solids. There are two classes of semiconductor neutron detectors: indirect- and direct-conversion detectors[12]. The thermal-neutron detection efficiency for indirect-conversion semiconductors reaches a maximum of about 40%[13]. Direct-conversion semiconductors use a single material for both neutron capture and charge collection, enabling a simpler detector geometry, with intrinsic thermal-neutron detection efficiencies approaching 100%. The semiconductors, however, must be extremely pure and with low carrier trapping because neutron fluxes can be very low, creating very small numbers of excited charges. Materials used for direct conversion include $LiInSe_2$[14–16] and hexagonal-BN (h-BN)[17], both of which suffer from severe drawbacks that limit their performance. Despite these challenges, we demonstrate here the development and outstanding neutron detection capabilities of the layered semiconductor $LiInP_2Se_6$.

The selenophosphate compound $LiInP_2Se_6$ is a 2D layered semiconductor that offers the requisite properties needed to achieve direct thermal neutron detection. Bulk $LiInP_2Se_6$ was synthesized phase pure (see Extended Data Fig. 1a–c) via a slightly off-stoichiometric solid-state reaction at 750 °C (see Methods). $LiInP_2Se_6$ crystallizes in the trigonal space group $P\bar{3}1c$ with lattice parameters $a = b = 6.3975(9)$ Å, $c = 13.351(3)$ Å (estimated standard deviations in parentheses), $\alpha = \beta = 90°$ and $\gamma = 120°$ (details of the refinement and structure can be

[1]Department of Chemistry, Northwestern University, Evanston, IL, USA. [2]Department of Materials Science and Engineering, Northwestern University, Evanston, IL, USA. [3]Materials Science Division, Argonne National Laboratory, Argonne, IL, USA. [4]Strategic Security Sciences Division, Argonne National Laboratory, Argonne, IL, USA. [5]These authors contributed equally: Daniel G. Chica, Yihui He. *e-mail: m-kanatzidis@northwestern.edu

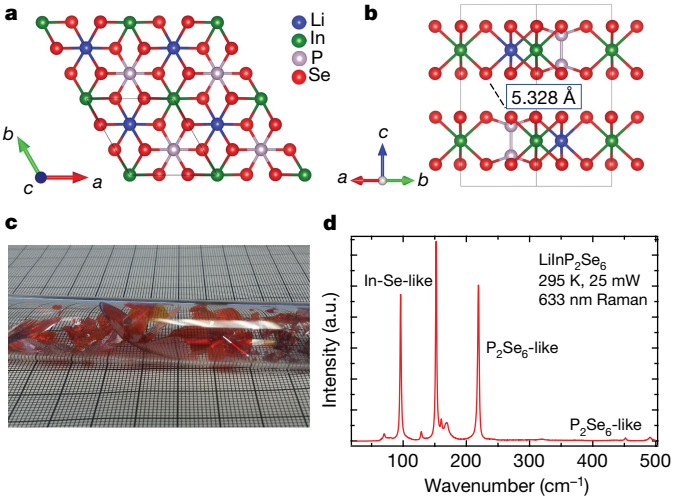


Fig. 1 | Structural properties of $LiInP_2Se_6$. a, **b**, Crystal structure of $LiInP_2Se_6$: a 2 × 2 unit cell looking down the *c* axis (**a**) and a single unit cell looking down the *a*–*b* plane, showing layered structure. **c**, Source side of the reaction vessel containing plate-like crystals of CVT-grown $LiInP_2Se_6$. **d**, Raman spectrum of $LiInP_2Se_6$ acquired at room temperature, showing characteristic vibrational modes associated with In–Se bonds and P_2Se_6 units. a.u., arbitrary units.

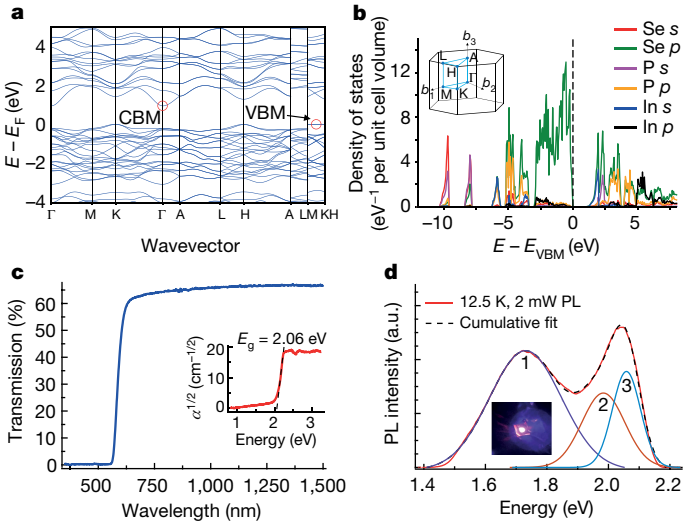


Fig. 2 | Band structure and optical properties of $LiInP_2Se_6$ single crystals. **a**, **b**, Electronic band structure (**a**) and density of states (number of states per unit cell volume per electronvolt) (**b**) for $LiInP_2Se_6$ calculated using the PBE+vdW functional on a fully relaxed structure. The inset in **b** shows the Brillouin zone. CBM, conduction band minimum; VBM, valence band maximum; *E*, energy; E_F, Fermi energy. **c**, UV-Vis-NIR transmission spectrum of $LiInP_2Se_6$. The inset shows the corresponding Tauc plot. *α*, absorbance; E_g, bandgap energy. **d**, PL spectrum of $LiInP_2Se_6$ obtained at 12.5 K and 2 mW, with three Gaussian fit peaks. The inset shows an image of the PL emission.

found in Extended Data Tables 1, 2). $LiInP_2Se_6$ comprises polyhedral layers separated by van der Waals gaps. Scanning electron microscopy images show a clear layered nature for this compound (Extended Data Fig. 2c–d). Each individual layer has the structure of CdI_2, where Li, In and P_2 dimers each occupy one-third of the octahedral Cd sites in an ordered manner and Se occupies the I site, as illustrated in Fig. 1a. The stacking of these layers follows an ABAB sequence such that the $InSe_6$ polyhedra align whereas the $LiSe_6$ and P_2Se_6 polyhedra alternate along the *c* axis (Fig. 1b). This structure is typical among metal selenophosphates with the general formula $M^+M^{3+}P_2Se_6$ (M, metal; refs. [18,19]) and derives from a larger layered family based on divalent metal cations $M^{2+}{}_2P_2Se_6$ (ref. [20]). Raman spectroscopy at an excitation of 633 nm shows several well-resolved peaks consistent with the vibrational modes of the $InSe_6$ octahedra and the $[P_2Se_6]^{4-}$ unit seen in Fig. 1d (see Extended Data Fig. 3 for details).

The melting behaviour of $LiInP_2Se_6$ was determined through differential thermal analysis (DTA), giving melting and crystallization points of 717 °C and 695 °C, respectively (Extended Data Fig. 2a). The compound melts congruently, as a single thermal event is observed upon heating or cooling, and the powder diffraction pattern after DTA shows only $LiInP_2Se_6$ present (Extended Data Fig. 1g) .

We then developed a more effective approach to grow detector-grade, large-size $LiInP_2Se_6$ single crystals using the chemical vapour transport (CVT) method. The temperature of the hot zone (660 °C) was below the melting point because otherwise the atmosphere would saturate with volatile components and inhibit the transport of the other constituents. The cold zone was set to 560 °C, creating a driving force for the transport of material from the hot to the cold zone. The initial transport reactions of $LiInP_2Se_6$ were carried out without a transporting agent and produced tiny $LiInP_2Se_6$ crystals with a low yield (about 1 mg out of ~0.7 g of starting material) even after a few days of transport owing to decomposition into amorphous P_xSe_y (Extended Data Fig. 1d).

This issue was resolved by the use of iodine as a transporting agent, as the formation of InI_3 and LiI enables the transport of each metal component to balance the vapour transport[21]. Iodine-assisted CVT enabled the growth of large single $LiInP_2Se_6$ crystals with an area of about 1 cm^2 and thickness of ~0.05–1 mm for the week-long reactions in Fig. 1c. To reduce the number of nucleation sites and improve the yield of large crystals, we reversed the zones for 24 h to ensure that all $LiInP_2Se_6$ was at the source side. The crystals produced by the transport reactions without this first step are smaller and often intergrown with each other owing to multiple nucleations (Extended Data Fig. 1e). The reversal of the hot and cold sides at the end of the reaction limits the deposition of the gas phase species onto the as-grown crystal surfaces, which is necessary for high-quality, clean surfaces that permit good electrical contact with the electrodes. The X-ray powder diffraction pattern of ground CVT-grown $LiInP_2Se_6$ crystals matches the simulated pattern and exhibits identical thermal behaviour to the bulk material (Extended Data Figs. 1f, h, 2b), confirming the purity of the transported $LiInP_2Se_6$ single crystals.

Density functional theory calculations of the electronic band structure were carried out using the PBE+vdW functional, revealing $LiInP_2Se_6$ to be an indirect-gap semiconductor with a bandgap transition from near the K point at the valence band maximum to the Γ point at the conduction band minimum for a bandgap of 0.94 eV (Fig. 2a). The conduction band is composed of hybridized In *s* and Se *p* states associated with the empty In 5*s* lone pair, whereas the valence band is made up of Se *p* states, as seen in Fig. 2b. The conduction band has a high curvature, corresponding to a low effective electron mass (m_e^*) of $0.16m_e$ and $0.30m_e$ for the in- and out-of-plane directions, respectively (m_e, electron mass). The valence band maximum lies along the out-of-plane direction in reciprocal space (K to H), and the band in this direction is very flat, so the hole effective mass in the out-of-plane direction will be immense. Accordingly, we expect that the electron mobility should be vastly superior in $LiInP_2Se_6$, especially given that the planar nature of the material forces devices to operate in the out-of-plane direction.

Ultraviolet–visible–near infrared (UV-Vis-NIR) transmission and reflection measurements on a $LiInP_2Se_6$ single crystal were used to measure the bandgap, which was determined to be 2.06 eV (Fig. 2c). Photoluminescence (PL) measurements on $LiInP_2Se_6$ at low temperature (12.5 K) under an excitation of 405 nm showed red–orange emission from the as-grown surface of the single crystal, with two broad emission bands observed with peak maxima near 1.73 eV and 2.05 eV (Fig. 2d). Excitation intensity and temperature-dependent PL measurements support the assignment of the 1.73 eV peak to donor–acceptor pair recombination

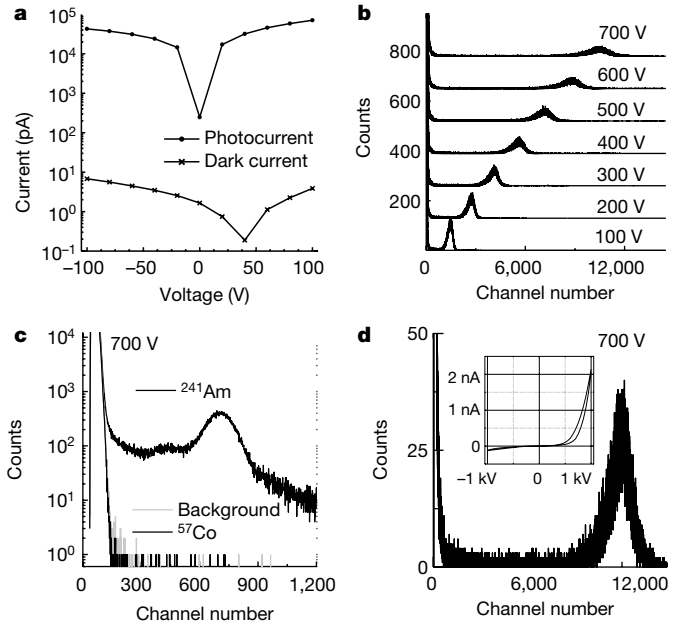


Fig. 3 | Electrical characteristics and pulse-height spectra of $LiInP_2Se_6$ devices irradiated by α-particle and γ-ray sources. a, Dark current and photocurrent (absolute values) as a function of voltage (from −100 V to 100 V) for CVT-grown $LiInP_2Se_6$ (~0.3 mm thickness) with gold electrodes illuminated by ambient light (~0.2 mW cm^{-2}). **b**, Pulse-height spectra of α particles from ^{241}Am for a $LiInP_2Se_6$ device (~120 μm thickness) for electron collection at various voltages, collected for 60 s each. **c**, Pulse-height spectrum of a $LiInP_2Se_6$ detector (~0.5 mm thickness) under a bias of 700 V illuminated by γ-rays from ^{241}Am and ^{57}Co, and without a source. The counts for ^{57}Co γ-rays and for the natural background are negligible, as shown. The spectra were collected for 200 s each. **d**, Pulse-height spectrum at 700 V with the same conditions as in **b**. Inset, Dark current measured with the voltage varying from 0 to 1 kV, to −1 kV, and to 0 V under the same conditions as in **a**. The contact area on the crystals in **a**–**d** was 3 × 3 mm^2. The shaping time in **b**–**d** was 1 μs.

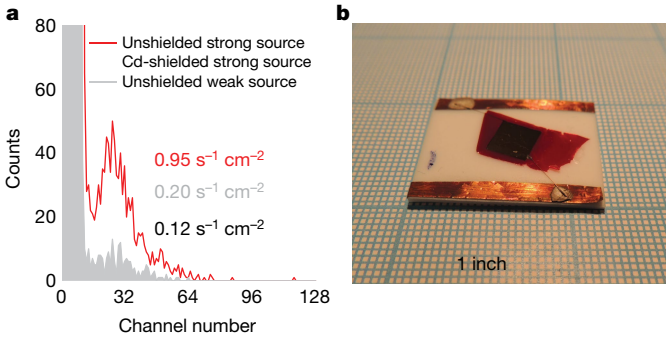


Fig. 4 | Thermal-neutron spectra resolved by $^6LiInP_2Se_6$ devices. a, Binned pulse-height spectrum of a $^6LiInP_2Se_6$ device (shown in **b**) exposed to a moderated Pu–Be source without shielding (red) and with Cd shielding (0.125 inch thick; black) and to a source ~5 times weaker (grey) for 300 V bias, 3 μs shaping time and 30-min measurements. The counts from channel 16 and above correspond to neutron-capture events. The count rate for the unshielded measurement was 0.95 s^{-1} cm^{-2}. **b**, The 7 × 7 mm^2 $^6LiInP_2Se_6$ device (90 μm thickness) used for the measurements shown in **a**.

and of the 2.05 eV peak to a free-to-bound transition; a detailed discussion may be found in Methods section 'Notes on Extended Data Fig. 3'. Despite these defect-related peaks, a strong PL signal from an indirect-gap material is an indication of good optical quality.

$LiInP_2Se_6$ detector devices were fabricated from large CVT-grown single crystals using evaporated planar gold contacts. Pristine $LiInP_2Se_6$ devices exhibit very low dark current, of the order of picoamperes (Fig. 3a), corresponding to a high electrical resistivity of around 10^{13} Ω cm. The dark-current plot shows a non-zero current at 0 V, though the dark current exhibits linearity in this range (Extended Data Fig. 4a). When larger voltages are applied a diode-like current–voltage curve is observed, whereas the low dark current is maintained at 2 nA at 1,000 V (Fig. 3d), which is more than sufficient for effective α- and neutron-detection measurements. This behaviour might originate from blocked/injected current from the electrodes under a large electric field of up to tens of kilovolts per centimetre. When exposed to ambient light (~0.2 mW cm^{-2}), photogenerated charge carriers in the $LiInP_2Se_6$ detector increase the current by three to four orders of magnitude (Fig. 3a). This is an exceptional photoresponse that indicates favourable charge transport properties in $LiInP_2Se_6$, as the photogenerated carriers efficiently traverse the detector thickness.

As a direct-conversion semiconductor based on lithium, neutrons (n) are captured in $LiInP_2Se_6$ through the following nuclear reaction: $n + {}^6Li = {}^4He + {}^3H$ (energy Q = 4.78 MeV). Thus, the interaction of α particles produced by the decay of ^{241}Am (Q = 5.486 MeV) mimics the energy deposition of a neutron-capture event at the detector surface.

The pulse-height spectrum of a $LiInP_2Se_6$ device with a thickness of 120 μm irradiated by 5.486 MeV ^{241}Am α particles for electron collection can be seen in Fig. 3b. Here the channel number reflects the charge collection efficiency (CCE), which is the ratio of collected and generated charge from a single event (for example, neutron capture), and under constant bias can be considered proportional to the energy of the incident particle. The peak from the interaction of α particles shifts to higher channel numbers with increasing voltage (Extended Data Fig. 5), as higher CCE can be achieved with higher applied electric field. The energy resolution for the full-energy peak at 700 V is 13.9% for the $LiInP_2Se_6$ detector, confirming that $LiInP_2Se_6$ can accurately resolve the charged particles generated by neutron interaction. To our knowledge, this is the highest energy resolution reported for ^{241}Am α particles for any direct-conversion thermal-neutron semiconductor detector, surpassing the 23.3% resolution[15] of $LiInSe_2$ or the non-resolution of the full-energy peak in h-BN due to poor CCE.

These results are reproducible for different growth sizes, and the α-particle response of other $LiInP_2Se_6$ devices with crystals grown under identical conditions can be seen in Extended Data Fig. 6a–h. For hole collection in a typical sample, a shoulder, instead of a full-energy peak, is usually observed, implying relatively poor CCE of holes. Nevertheless, several devices were able to resolve the ^{241}Am peak for both holes and electrons. This is because the high electric field that this material can withstand (at least 60 kV cm^{-1}) allows the generated carriers to be swept out to the contacts before trapping or recombination can occur, resulting in a spectroscopic response even for the relatively low-mobility holes. For a constant applied voltage across various samples, the CCE is higher for thinner samples because of the larger external electric field. These results conclusively demonstrate that $LiInP_2Se_6$ devices can achieve a high-resolution spectroscopic response to ^{241}Am α particles.

Isotopically enriched lithium (95% ^6Li) was used to grow $LiInP_2Se_6$ crystals (hereafter labelled $^6LiInP_2Se_6$) with maximal ^6Li to maximize the thermal-neutron-capture cross-section. The α-particle response of the $^6LiInP_2Se_6$ devices is similar to that of their unenriched analogues, with full resolution of the ^{241}Am peak for electron collection (Extended Data Fig. 7a–e). Hole collection of $^6LiInP_2Se_6$ devices also demonstrates some level of α-particle response.

The thermal-neutron response of the 95% ^6Li-enriched detectors was tested at room temperature using a moderated and very weak Pu–Be source, which generated roughly 75 neutrons per second per square centimetre. The absorption probability for thermalized neutrons versus the thickness of $^6LiInP_2Se_6$ is shown in Extended Data Fig. 8. The device had an active area of 7 × 7 mm^2 and a thickness of ~90 μm, and was subjected to a bias of 300 V. The binned pulse-height spectrum of a $^6LiInP_2Se_6$ device under neutron irradiation shows a defined peak

that is clearly resolved from the background, demonstrating successful direct detection of neutrons (Fig. 4a). The pulse-height spectrum shows a broad full-energy peak corresponding to the neutron-capture reaction close to the dark-current noise background edge. When cadmium shielding (0.125-inch-thick; 1 inch = 2.54 cm) was placed in front of the device to block most of the thermalized neutrons, the count rate was reduced by 87%. This reduction stems from the high absorption of neutrons below the cadmium cutoff energy (0.5 eV; ref. [22]). The energy resolution of this neutron-capture peak was 69.7%. This response is very promising at this early stage.

An ideal neutron detector should be insensitive to γ-rays to ensure that false neutron counts are not generated from incident γ radiation. The ability of the $LiInP_2Se_6$ device to discriminate against γ-rays was evaluated on a thicker detector (~0.5 mm) exposed to a 0.2-mCi ^{57}Co γ-radiation source (a photon flux multiple orders of magnitude higher than the neutron source discussed earlier). Despite the higher flux, the pulse-height spectra of the ambient background and under direct γ irradiation shown in Fig. 3c are essentially identical, demonstrating the negligible γ sensitivity of this material.

In conclusion, $LiInP_2Se_6$ is the first, to our knowledge, direct thermal-neutron semiconductor detector with intrinsic ^6Li to demonstrate a resolved full-energy neutron peak above the background. Further improvements in the neutron detection efficiency could be achieved by the growth of larger single crystals, such as through the Bridgman growth method. Furthermore, spectroscopic ^{241}Am α-particle detection is achieved with 13.9% energy resolution. The excellent semiconducting properties and radiation response achieved here demonstrate that $LiInP_2Se_6$ has the potential to transform neutron detection technology, which relies almost exclusively on scintillation paradigms, and usher in the semiconductor modality for direct-conversion thermal-neutron detection.

Online content

Any methods, additional references, Nature Research reporting summaries, source data, extended data, supplementary information, acknowledgements, peer review information; details of author contributions and competing interests; and statements of data and code availability are available at https://doi.org/10.1038/s41586-019-1886-8.

1. *Detection of Radioactive Materials at Borders* (International Atomic Energy Agency, 2002).
2. Runkle, R. C., Bernstein, A. & Vanier, P. E. Securing special nuclear material: recent advances in neutron detection and their role in nonproliferation. *J. Appl. Phys.* **108**, 111101 (2010).
3. Barth, R. F., Coderre, J. A., Vicente, M. G. H. & Blue, T. E. Boron neutron capture therapy of cancer: current status and future prospects. *Clin. Cancer Res.* **11**, 3987–4002 (2005).
4. Wollan, E. O. & Shull, C. G. The diffraction of neutrons by crystalline powders. *Phys. Rev.* **73**, 830–841 (1948).
5. Ruffolo, D. et al. Monitoring short-term cosmic-ray spectral variations using neutron monitor time-delay measurements. *Astrophys. J.* **817**, 38–50 (2016).
6. Kouzes, R. T. The ^3He Supply Problem. Report No. PNNL-18388 (Pacific Northwest National Laboratory, 2009).
7. Breukers, R. D., Bartle, C. M. & Edgar, A. Transparent lithium loaded plastic scintillators for thermal neutron detection. *Nucl. Instrum. Methods Phys. Res. A* **701**, 58–61 (2013).
8. Dunning, J. R., Pegram, G. B., Fink, G. A. & Mitchell, D. P. Interaction of neutrons with matter. *Phys. Rev.* **48**, 265–280 (1935).
9. Knoll, G. F. in *Radiation Detection and Measurement* 505–535 (John Wiley & Sons, 2000).
10. Ochs, T. R. et al. Present status of the microstructured semiconductor neutron detector-based direct helium-3 replacement. *IEEE Trans. Nucl. Sci.* **64**, 1846–1850 (2017).
11. Simpson, A. P., Jones, S., Clapham, M. J. & Mcelhaney, S. A. A review of neutron detection technology alternatives to helium-3 for safeguards applications. In *INMM 52nd Annual Meeting* **Vol. 8** (2011).
12. Caruso, A. N. The physics of solid-state neutron detector materials and geometries. *J. Phys. Condens. Matter* **22**, 443201 (2010).
13. Shultis, J. K. & Mcgregor, D. S. Design and performance considerations for perforated semiconductor thermal-neutron detectors. *Nucl. Instrum. Methods Phys. Res. A* **606**, 608–636 (2009).
14. Tupitsyn, E. et al. Lithium containing chalcogenide single crystals for neutron detection. *J. Cryst. Growth* **393**, 23–27 (2014).
15. Guo, L. et al. Stoichiometric effects on the photoelectric properties of $LiInSe_2$ crystals for neutron detection. *Cryst. Growth Des.* **18**, 2864–2870 (2018).
16. Hamm, D. S. et al. Semiconducting lithium indium diselenide: charge-carrier properties and the impacts of high flux thermal neutron irradiation. *Appl. Phys. Lett.* **112**, 242104 (2018).
17. Maity, A., Grenadier, S. J., Li, J., Lin, J. Y. & Jiang, H. X. High-efficiency and high-sensitivity thermal neutron detectors based on hexagonal BN epilayers. In *Proc. SPIE Hard X-Ray, Gamma-Ray, and Neutron Detector Physics XIX*, **10392** (2017).
18. Pfeiff, R. & Kniep, R. Quaternary selenodiphosphates(IV): $M^IM^{III}[P_2Se_6]$, (M^I = Cu, Ag; M^{III} = Cr, Al, Ga. *J. Alloys Compd.* **186**, 111–133 (1992).
19. Seidlmayer, S. *Strukturchemische Untersuchungen an Hexachalkogenohypodiphosphaten und Verwandten Verbindungen*. PhD Thesis, University of Regensburg (2009).
20. Wang, F. et al. New frontiers on van der Waals layered metal phosphorous trichalcogenides. *Adv. Funct. Mater.* **28**, 1–24 (2018).
21. Binnewies, M., Glaum, R., Schmidt, M. & Schmidt, P. in *Chemical Vapor Transport Reactions* 360–369 (De Gruyter, 2012).
22. Knoll, G. F. *Radiation Detection and Measurement* 757–775 (John Wiley & Sons, 2000).

Publisher's note Springer Nature remains neutral with regard to jurisdictional claims in published maps and institutional affiliations.

© The Author(s), under exclusive licence to Springer Nature Limited 2020

Methods

Chemical reagents

Lithium (99.9% Sigma Aldrich), indium (99.99% American Elements), phosphorus (99.999% Alfa Aesar), selenium (99.99% American Elements) and iodine (99.999% Sigma Aldrich) were used as received. For the material used in the detectors, high-purity indium (99.9999% Alfa Aesar) and selenium (99.999% Alfa Aesar) were used. Isotopically enriched lithium (95% ^{6}Li) was used to synthesize materials for the neutron detection measurements.

Synthesis of Li_2Se

Li_2Se was synthesized using a modified literature procedure[23,24]. In an argon-filled glovebox, lithium metal was removed from mineral oil and the oxidized edges were cut off. The lithium metal, selenium and a stir bar were added into a 500-mL three-neck flask. The reaction vessel was attached to a custom apparatus that allowed an ammonia stream to condense liquid ammonia into the vessel under flowing argon. In a typical reaction, ~300 mL of ammonia was condensed using a cold finger containing an acetone–dry-ice mixture. The reaction continued under reflux and stirring until the ammonia colour changed from deep blue to clear. After the completion of the reaction, the liquid ammonia was boiled off and the vessel material was placed under vacuum overnight. The material was stored in a N_2 glovebox. In a typical reaction, 15 g of material was synthesized with a Li:Se ratio of 2:1.002. The slight excess of selenium was to ensure that the reaction goes to completion.

Synthesis of $Li_{1.03}In$

In an argon-filled glovebox, In (2.535 g) and Li (0.147 g) chunks were loaded into a glassy carbon crucible with a lid. This crucible was then placed in a fused quartz silica tube and the tube was flame-sealed under a pressure of ~2×10^{-3} mbar. The tube was placed in a vertical furnace and subjected to the following heating profile: heat to 700 °C over 10 h, soak for 2 h, and then cool to ambient temperature. The ingot was extracted and stored in a nitrogen box.

Synthesis of P_2Se_5

For P_2Se_5, red phosphorus pieces (1.356 g) and selenium shot (8.644 g) were loaded into a 13-mm fused-silica tube in a stoichiometric ratio. The tube was flame-sealed under vacuum (~2×10^{-3} mbar). The reagents were physically mixed by shaking the tube. The tubes were placed in a tilted tube furnace so that the tops of the tubes were at the centre of the furnace. The following temperature profile was used: heat to 500 °C over 12 h, hold the temperature for 72 h and then furnace-cool to ambient temperature. The tubes were opened in a nitrogen-filled glovebox for storage.

Synthesis of bulk $LiInP_2Se_6$

Owing to the air-sensitive nature of Li_2Se, the reagents were manipulated in a nitrogen-filled glovebox. For the bulk synthesis of $LiInP_2Se_6$, Li_2Se (0.437 g), In (1.030 g), P_2Se_5 (4.181 g) and Se (0.351 g) were loaded into a carbon-coated, 13-mm fused-silica tube at a molar ratio of Li:In:P:Se = 1.05:1:2.04:6.12. Alternatively, $Li_{1.03}In$ (2.500 g), P_2Se_5 (9.643 g) and Se (1.667 g) could be used as the starting reagents, and were used for the synthesis of detector-grade crystals. Synthesis of chalcogenides containing Li typically require crucibles that can withstand chemical attack from Li, such as glassy carbon or pyrolytic BN[14]. In the present synthesis, the tubes were carbon-coated to prevent glass attack. The tubes were flame-sealed under vacuum (~2×10^{-3} mbar). The tubes and thermocouple were placed in the same manner as in the reaction of P_2Se_5. The following optimized heating profile was used: heat to 750 °C over 10 h, hold the temperature for 24 h, cool to 350 °C over 12 h and then furnace-cool to ambient temperature. The tubes were opened in air, revealing an ingot comprised of deep red plates. The synthesis of bulk $^6LiInP_2Se_6$ was performed using $^6Li_{1.03}In$, P_2Se_5 and Se as the starting reagents.

CVT

Preformed material from the bulk synthesis was used as the source for the CVT growth of $LiInP_2Se_6$. In a typical synthesis, approximately 0.5–5 g of source material was used, accompanied by 16–30 mg of I_2—the amount of I_2 used depends on the inner diameter of the fused-silica tube (11–16 mm). The tube was sealed to a length of 17 cm while the bottom was submerged in liquid nitrogen to prevent loss of iodine. The tube was then placed in a two-zone furnace and subjected to the following heating profile: source zone: heat to 560 °C over 6 h, hold the temperature for 12 h, heat to 660 °C over 6 h, hold for 168 h and then cool to ambient temperature over 6 h; sink zone: heat to 660 °C over 6 h, hold for 12 h, heat to 560 °C over 6 h, hold for 170 h and then cool to ambient temperature over 10 h. After the transport process, deep-red plates were found on the sink side, and the source material was consumed. The vacuum of the tube was carefully breached by slowly cutting into the tube at the source side with a diamond saw to make a pinhole opening. This step was necessary to prevent damage to the thinner crystals from the influx of air.

X-ray diffraction

A Rigaku Miniflex600 X-ray diffraction system equipped with a Dtex silicon 1-D detector was used to obtain powder X-ray diffraction patterns. Cu Kα radiation (wavelength λ = 1.5406 Å) was produced using a voltage of 40 kV and a current of 15 mA and filtered with a graphite monochromator and a Kβ foil filter. A zero-background silicon holder was used. Crystals suitable for single-crystal diffraction were obtained using CVT reactions. Single-crystal X-ray diffraction was performed using a STOE IPDS II diffractometer operating at 50 kV and 40 mA with Mo Kα radiation (λ = 0.71073 Å) with a graphite monochromatizer. Data reduction, integration and absorption correction were performed using the X-area software package. The program XPREP was used to determine the space group and prepare the data for the structure solution. Structure solutions using intrinsic phasing and refinements were obtained using SHELXT[25] and SHELXL[26], respectively. OLEX2 was used as a GUI[27]. VESTA was used to produce crystal structure figures[28].

Optical property characterization

UV-Vis-NIR transmission and reflection were measured on a PerkinElmer LAMBDA 1050 UV/Vis spectrophotometer in the range 1,500–250 nm on a single crystal of $LiInP_2Se_6$ at room temperature. These were used to obtain the absorption and thereby determine the bandgap using a linear fit of the Tauc plot. Raman spectroscopy was conducted on a single crystal of $LiInP_2Se_6$ at room temperature using a confocal Horiba LabRAM HR Evolution spectrometer with an excitation wavelength of 633 nm and a laser power of 25 mW.

Room-temperature PL was measured in the range 475–1,000 nm with the same spectrometer using an above-bandgap excitation wavelength of 473 nm. The laser power (25 mW) was varied in the range 0.25–12.5 mW using neutral density filters. Laser powers above 1.25 mW led to visible damage to the sample, and below this threshold no PL was observed. Above this point, a broad band appears from 1.4 eV to 2 eV, probably due to an impurity phase formed upon decomposition of the sample.

The temperature and excitation intensity dependence of the PL were measured on a $LiInP_2Se_6$ single crystal in a closed-cycle He cryostat (SHI Cryogenics DE-202). The single crystal was mounted on the stage using Apiezon N grease. The excitation source was a continuous-wave diode laser (OBIS 405 nm LX; beam diameter 0.8 mm) with the power digitally adjusted in the range of 0.5–21 mW. A 405-nm bandpass filter (full-width at half-maximum 10 nm; Thorlabs) screened the laser light focused onto the sample, and the emitted light was filtered by a 450-nm long-pass filter (Thorlabs) before reaching the monochromator entrance slit (width 200 μm). A chopper was used at 710 Hz to increase the signal-to-noise ratio. PL spectra were resolved by a 500M SPEX

grating monochromator with a Hamamatsu R928 photomultiplier tube biased at 500 V, which was read into a SR810 lock-in amplifier (Stanford Research Systems). PL spectra were collected over the range of 530–900 nm at a rate of 1 nm s^{-1}.

DTA

For the determination of the thermal properties of $LiInP_2Se_6$, a Netzch Simultaneous Thermal Analysis (STA 449F3) instrument was employed. Approximately 25 mg of the sample was sealed in a fused-silica ampoule. An alumina ampoule of similar mass was used as a reference. The heating and cooling rates were 10 K min^{-1}.

Band structure

The band structure calculations were performed using VASP (Vienna ab initio simulation package) within the framework of density functional theory. The symmetry-unconstrained lattice parameters and atom coordinates were relaxed to the local total energy minimum, starting from the structure that we measured experimentally. The structure optimization was performed by applying the Perdew–Burke–Ernzerhof exchange and correlation functional with the van der Waals extension (PBE+vdW) using the optB88-vdW functional[29]. The electronic-band dispersions were calculated for the fully relaxed structures using the special k points and the high-symmetry path in the Brillouin zone defined by Setyawan and Curtarolo[30]. The analysis of the data generated by the ab initio calculations was carried out with Python scripts with extensive use of the Atomic Simulation Environment (ASE)[31] and the Python Materials Genomics (pymatgen) materials analysis libraries[32]. The effective masses were calculated using the set of python scripts available at the emc repository[33].

Scanning electron microscopy

A Hitachi 3400 scanning electron microscope was used to image the microstructure. The accelerating voltage and probe current were set to 20 keV and 70 mA, respectively. Energy-dispersive X-ray spectroscopy (EDS) was performed using a PGT energy-dispersive X-ray analyser. Aztec software from Oxford Instruments was used to analyse the EDS data.

Device fabrication

Planar-type devices were fabricated using single crystals grown by CVT without cutting or polishing, owing to the high surface quality of the as-grown crystals. Translucent and flat crystals that were visibly defect-free were selected. Gold electrodes with a typical area of 3 × 3 mm^2 (unless otherwise stated) and thickness of ~70 nm were deposited on both sides of the crystal by thermal evaporation at a rate of ~1 Å s^{-1} using an SQC-310 Inficon deposition controller. Cu wires were attached to the gold electrodes using graphite paste, allowing the crystals to be connected to the external circuit used for property measurements.

Electrical properties and α-particle response

The electrical resistivity was measured using a Keithley 6517B electrometer. For dark-current measurements, the device was enclosed in a light-tight metal box. The photoconductivity was measured using ambient light (0.2 mW cm^{-2}, 400–800 nm) as the source of excitation. Current–voltage characteristic curves from 100 V to −100 V were used to calculate the electrical resistivity. To enable collection of the α-particle spectrum, planar-type detectors with evaporated gold contacts were used for pulse-height spectroscopy. The α-particle source employed was ^{241}Am, with a typical α-particle kinetic energy of 5.486 MeV. The detectors were enclosed in a light-tight metal box with the source ~3 mm away from the top electrode. The device was connected to an eV-550 preamplifier and a voltage source that applied a voltage of ±20–1,000 V to the bottom electrode. An ORTEC amplifier (model 572A) was used to amplify and shape the signal from the preamplifier. The gain and shaping time were set to 100–200 and 0.5–2 μs, respectively. A dual 16K-input multichannel analyser (model ASPEC-927) and MAESTRO-32 software were used to process the amplified signal and display the response spectrum, respectively. The Hecht equation for a single carrier type is a common way to estimate the mobility–lifetime product $\mu\tau$ (ref. [34]) as $\mathrm{CCE} = \frac{(\mu\tau)_e V}{d^2}\left[1 - \exp\left(\frac{-d^2}{(\mu\tau)_e V}\right)\right]$, where d is the thickness of the semiconducting region through which the charge carrier travels and V is the applied voltage. The charge collection efficiency (CCE) refers to the fraction of charge that is collected versus the generated charge.

Neutron detection

The same setup used to measure the pulse-height spectrum of α particles was used to determine the neutron response. The source of neutrons used was a polyethylene-moderated PuBe source. A ^3He proportional tube was used to determine the neutron flux of the source so that the absolute efficiency of the devices could be calculated. The $^6LiInP_2Se_6$ device was placed at the same distance away from the source as the ^3He detector. Collection times were 30 min. The number of channels was reduced from 16,384 to 128 by summing the counts from 128 channels into a single channel.

Notes on Extended Data Fig. 1

Note for bulk synthesis and chemical stability. The optimized synthesis of $LiInP_2Se_6$ involves a relatively small excess of Li/P/Se to synthesize phase-pure material. When a stoichiometric ratio of reagents was used, secondary phases were present (see Extended Data Fig. 1c). The need for additional P and Se may stem from the imbalanced vapour pressure of different vapour components, which probably induces a P/Se-rich atmosphere, leaving the melt deficient in P/Se. For a few reactions, even when the carbon coat peeled off the silica wall, there were no signs of glass attack, suggesting that the as-formed $LiInP_2Se_6$ material does not react with silica. Bulk $LiInP_2Se_6$ shows good stability under ambient atmospheric conditions. However, when the ingot is finely ground, the resulting powder turns from bright orange to dark brown after several minutes of air exposure. Both the ingot and powder were very sensitive to liquid water and appeared to exfoliate after several seconds in water, potentially from water intercalating into the layers.

Gas phase equilibrium in the CVT reaction. Because this vapour transport experiment involves a quinary system when considering the iodine, the gas–solid phase equilibrium is quite complex. For a given material to transport, every element present in the material must have some species that favours the gas phase. Typically, metal selenides can be transported using iodine through the formation of the gas phase species, $M^{n+}I_n$, and Se_2 dimers[21]. Phosphorus is relatively volatile and transports well through the formation of either P_4 tetramers or PI_3 (ref. [35]). By contrast, the transport of alkali metals is more difficult[36] as alkali metal compounds typically have low vapour pressures at moderate temperatures and thus transport poorly. Li is probably transported as LiI, given its relatively low melting point of 469 °C and boiling point of 1,171 °C. For crystals grown without employing the reversal of zones at the end of the growth, EDS mapping (Extended Data Fig. 2e) of the surface demonstrated a growth front rich in iodine, demonstrating the involvement of iodine in the transport of $LiInP_2Se_6$.

Notes on Extended Data Fig. 3

Room-temperature PL measurements on a $LiInP_2Se_6$ single crystal showed no response to excitation at 473 nm except upon decomposition at high laser powers, when a broad band centred at 1.7 eV appears (Extended Data Fig. 3). This lack of PL response may be due to the indirect gap of the compound, which reduces the probability of radiative recombination due to the momentum difference between the band edge states, requiring phonons to mediate the transition. Thus, low-temperature PL was used to determine the optical quality of these

crystals and investigate whether any defects were present. As observed in Fig. 2d, $LiInP_2Se_6$ exhibits two broad PL peaks at low temperature (12.5 K), which can be modelled by three Gaussian peaks. A two-peak fit was attempted, but it was found to require the use of an exponentially modified Gaussian peak as described in ref. [37] to adequately model the asymmetry of the higher energy band. However, the use of such a peak is not justified here because the source of emission is not the result of a distribution of phonon-related peaks. Hence, these emission bands are best fitted using three Gaussian peaks, where peaks 2 and 3 correspond to the same broad band so they are expected to show similar behaviour. To further characterize the PL emission at 12.5 K, the PL dependence on the excitation intensity was tested by increasing the laser power from 0.5 mW to 21 mW, resulting in corresponding enhancements in the emission intensity and a slight blueshift in the peak maxima for all three peaks (Extended Data Fig. 3a).

The PL intensity I has a power-law dependence on the laser power L in the form $I \propto L^k$ with the behaviour governed by the exponent k (ref. [38]). Excitonic emission shows superlinear behaviour with increasing excitation intensity, corresponding to a coefficient of $1 < k < 2$, whereas free-to-bound and donor–acceptor pair (DAP) recombination processes have a power-law coefficient k below 1. This coefficient can be derived from the slope of a plot of log$I$ versus log$L$ for each peak, as shown in Extended Data Fig. 3b. Each of the three peaks observed in $LiInP_2Se_6$ has a power-law coefficient below 1 (Extended Data Fig. 3b), so these emissions are a result of either free-to-bound transitions or DAP recombination. We note the essentially identical behaviour of peaks 2 and 3; these peaks correspond to the same band and thus have the same power-law coefficient of 0.91 ± 0.04. The temperature dependence of PL at 2 mW demonstrates that the higher-energy emission quenches first, with peaks 2 and 3 merging at 70 K and vanishing by 90 K, and peak 1 persisting until about 150 K (Extended Data Fig. 3c). The energies of peaks 2 and 3 blueshift slightly as the temperature rises, whereas peak 1 redshifts dramatically between 12.5 K and 150 K (Extended Data Fig. 3d). This redshift causes the low-energy tail of peak 1 to fall past the response limit of the photomultiplier tube (1.46 eV), producing an artificial asymmetry; thus, above 55 K the fit ignores data below 1.48 eV to accurately reproduce the Gaussian peak shape.

PL quenching occurs when a nonradiative recombination process competes for the photogenerated carriers involved in the emission. The temperature dependence of this quenching behaviour can be modelled using an Arrhenius plot, following the frequently used expression[39]:

$$I(T) = I_0\left[1 + a\,\exp\left(-\frac{E_a}{kT}\right)\right]^{-1} \quad (1)$$

where I_0 is the PL intensity at 0 K, a is a constant, k is the Boltzmann constant and E_a is the activation energy corresponding to the competing nonradiative recombination. This model corresponds to the simple case of a single nonradiative transition, and adequately describes the Arrhenius plots of the integrated PL intensity versus the inverse temperature, as indicated by the solid lines in Extended Data Fig. 3e. The activation energies of the nonradiative quenching processes are determined to be 40.0 ± 6.6 meV, 15.2 ± 6.2 meV and 16.8 ± 3.4 meV for peaks 1, 2 and 3, respectively. Again, the behaviours of peaks 2 and 3 are quite similar, indicating that they should have the same emission mechanism.

The power-law coefficients of all three peaks are consistent with either DAP recombination or free-to-bound transitions, whereas the energy of each peak blueshifts with increasing excitation intensity, as expected for DAP recombination[40]. However, the temperature-dependent behaviour of peak 1 is markedly different from that of peaks 2 and 3, with different energy shifts as the temperature increases and distinct quenching processes for the two bands. To assign these accurately, we compare the relatively 'deep' energy of peak 1 (coming from energy levels in the middle of the bandgap) to the 'shallower' peaks 2 and 3 that emit from energy levels closer to the band edge. DAP recombination occurs between a donor and an acceptor band, both of which must lie deep enough within the bandgap to avoid being ionized, whereas a free-to-bound transition is between a single defect band and the opposite band edge, so it is only as deep as the defect band. At 1.73 eV, peak 1 lies well below the band edge (2.06 eV at room temperature) while peaks 2 and 3 are much closer to the bandgap at 1.98 eV and 2.06 eV, respectively. Together with the difference in temperature-dependent behaviour, this supports the assignment of peak 1 to DAP recombination and of peaks 2 and 3 to a free-to-bound transition. The PL measurements are summarized in Extended Data Fig. 3f, along with these tentative peak assignments. These results reveal the presence of at least two defect levels, which should be identified and removed. Nevertheless, the presence of a strong PL signal from an indirect-gap material is an indication of good optical quality and the removal of these defects promises further improvements in the detector performance of $LiInP_2Se_6$.

Data availability

The data that support the findings of this study are available from the corresponding author upon request.

23. Feher, F. *Handbuch der Präparativen Anorganischen Chemie* (F. Enke, 1954).
24. Aitken, J. A., Cowen, J. A. & Kanatzidis, M. G. Metamagnetic transition in $EuSe_2$: a new, metastable binary rare-earth polychalcogenide. *Chem. Mater.* **10**, 3928–3935 (1998).
25. Sheldrick, G. M. SHELXT – integrated space-group and crystal- structure determination. *Acta Crystallogr. A* **71**, 3–8 (2014).
26. Sheldrick, G. M. Crystal structure refinement with SHELXL. *Acta Crystallogr. C* **71**, 3–8 (2015).
27. Dolomanov, O. V., Bourhis, L. J., Gildea, R., Howard, J. A. K. & Puschmann, H. OLEX2: a complete structure solution, refinement and analysis program. *J. Appl. Crystallogr.* **42**, 339–341 (2009).
28. Momma, K. & Izumi, F. VESTA 3 for three-dimensional visualization of crystal, volumetric and morphology data. *J. Appl. Crystallogr.* **44**, 1272–1276 (2011).
29. Klimeš, J., Bowler, D. R. & Michaelides, A. Chemical accuracy for the van der Waals density functional. *J. Phys. Condens. Matter* **22**, 022201 (2010).
30. Setyawan, W. & Curtarolo, S. High-throughput electronic band structure calculations: challenges and tools. *Comput. Mater. Sci.* **49**, 299–312 (2010).
31. Larsen, A. et al. The atomic simulation environment - a Python library for working with atoms. *J. Phys. Condens. Matter* **29**, 273002 (2017).
32. Ong, S. P. et al. Python Materials Genomics (pymatgen): a robust, open-source python library for materials analysis. *Comput. Mater. Sci.* **68**, 314–319 (2013).
33. Fonari, A. & Sutton, C. Effective mass calculator https://github.com/afonari/emc (2012).
34. Owens, A. & Peacock, A. Compound semiconductor radiation detectors. *Nucl. Instrum. Methods Phys. Res. A* **531**, 18–37 (2004).
35. Binnewies, M., Glaum, R., Schmidt, M. & Schmidt, P. in *Chemical Vapor Transport Reactions* 452–457 (De Gruyter, 2012).
36. Binnewies, M., Glaum, R., Schmidt, M. & Schmidt, P. in *Chemical Vapor Transport Reactions* 165–166 (De Gruyter, 2012).
37. McCall, K. M., Stoumpos, C. C., Kostina, S. S., Kanatzidis, M. G. & Wessels, B. W. Strong electron–phonon coupling and self-trapped excitons in the defect halide perovskites $A_3M_2I_9$(A = Cs, Rb; M = Bi, Sb). *Chem. Mater.* **29**, 4129–4145 (2017).
38. Schmidt, T., Lischka, K. & Zulehner, W. Excitation-power dependence of the near-band-edge photoluminescence of semiconductors. *Phys. Rev. B* **45**, 8989–8994 (1992).
39. Pankove, J. I. *Optical processes in semiconductors* (Dover, 1971).
40. Pelant, I. & Valenta, J. *Luminescence Spectroscopy of Semiconductors* (Oxford Univ. Press, 2012).
41. Veale, M. C. et al. X-ray spectroscopy and charge transport properties of CdZnTe grown by the vertical Bridgman method. *Nucl. Instrum. Methods Phys. Res. A* **576**, 90–94 (2007).
42. Watanabe, S. et al. Stacked CdTe gamma-ray detector and its application to a range finder. *Nucl. Instrum. Methods Phys. Res. A* **505**, 118–121 (2003).

Acknowledgements The exploratory synthesis and materials characterization work was supported by the National Science Foundation through grant DMR-1708254. The device fabrication and neutron response measurements were supported by Laboratory Directed Research and Development (LDRD) funding from Argonne National Laboratory, provided by the Director, Office of Science of the US Department of Energy under contract number DE-AC02-06CH11357. PL measurements were supported by the Murphy Fellowship from Northwestern University. This work made use of the SPID and EPIC facilities of Northwestern University's NUANCE Center, which has received support from the Soft and Hybrid Nanotechnology Experimental (SHyNE) Resource (NSF ECCS-1542205); the MRSEC programme (NSF DMR-1720139) at the Materials Research Center; the International Institute for Nanotechnology (IIN); the Keck Foundation; and the State of Illinois, through IIN. This work used the Northwestern University's Keck Biophysics Facility, which is funded by a Cancer Center Support Grant (NCI CA060553). This work made use of IMSERC at Northwestern University, which has received support from the Soft and Hybrid Nanotechnology Experimental (SHyNE) Resource (NSF ECCS-1542205), the State of Illinois and IIN.

Author contributions The idea for this project was conceived by M.G.K., D.Y.C., D.G.C. and Y.H. The manuscript was written by D.G.C., Y.H. and M.G.K. with input from all authors. D.G.C. developed the synthetic and crystal growth methods. The crystal structure and physical properties, excluding the optical properties, were measured by D.G.C. The band structure and effective-mass calculations were conducted by G.T. Optical transmission measurements were performed by K.M.M. and Z.L. K.M.M. measured the variable-temperature and power-dependent PL and the Raman spectra. Y.H. and D.G.C. fabricated the devices and performed pulse-height spectrometry of the ^{241}Am and ^{57}Co sources. Neutron measurements were performed by R.O.P., Y.H., D.G.C., D.Y.C. and P.M.D.L. M.G.K. and B.W.W. supervised the project.

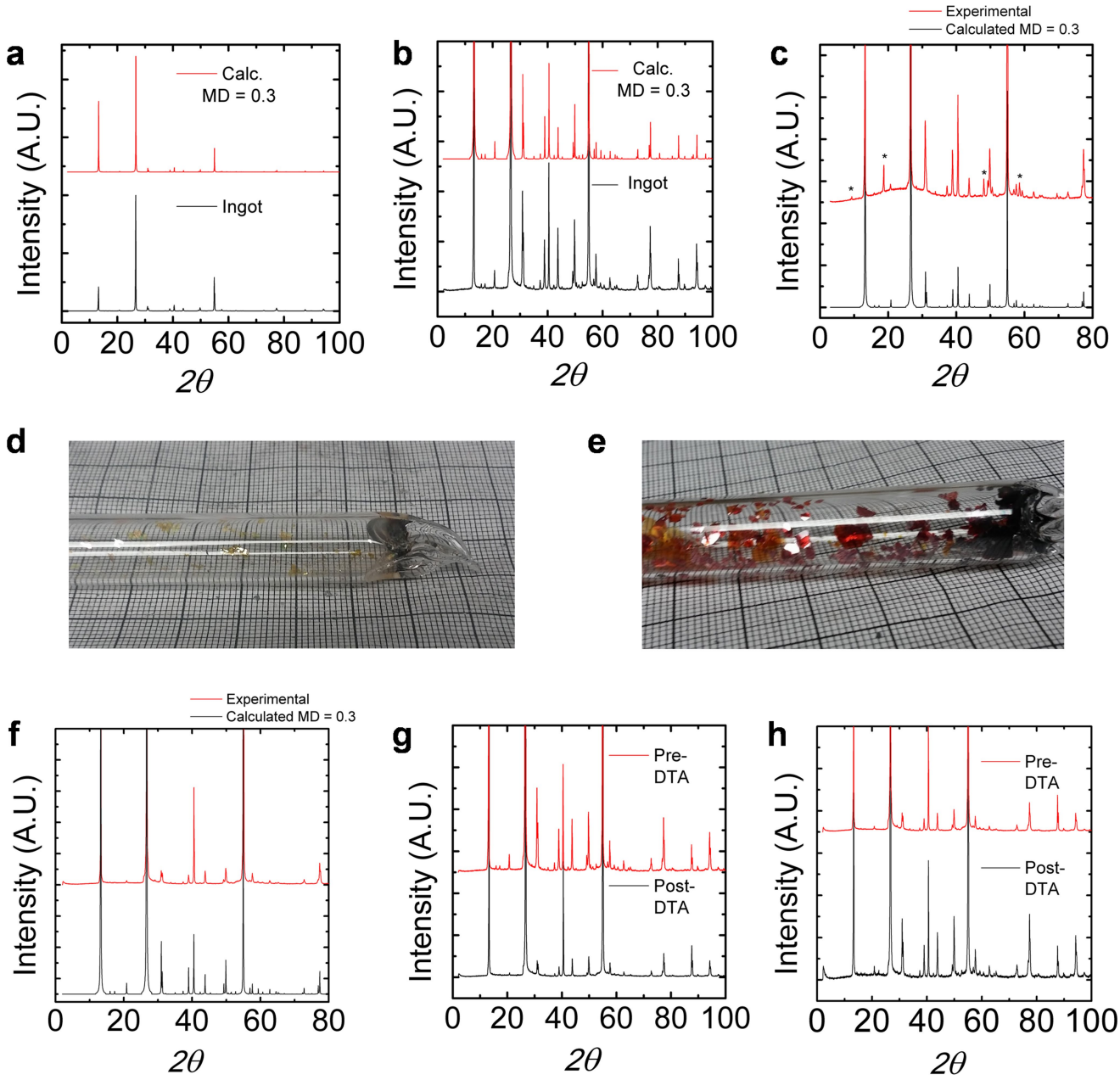
Competing interests The authors declare the U.S. patent application 62/701,144.

Additional information

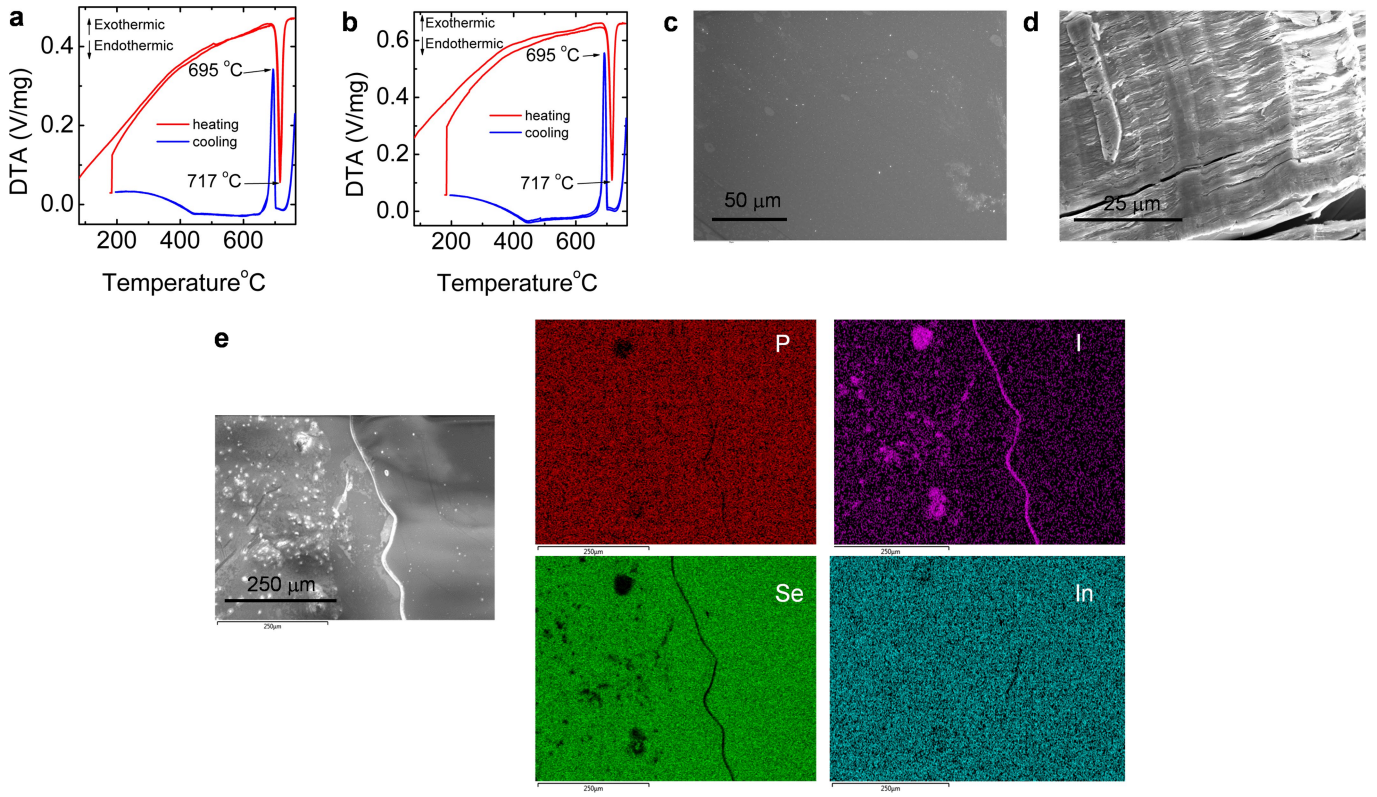
Correspondence and requests for materials should be addressed to M.G.K.

Peer review information *Nature* thanks Paul Sellin and Mariya Zhuravleva for their contribution to the peer review of this work.

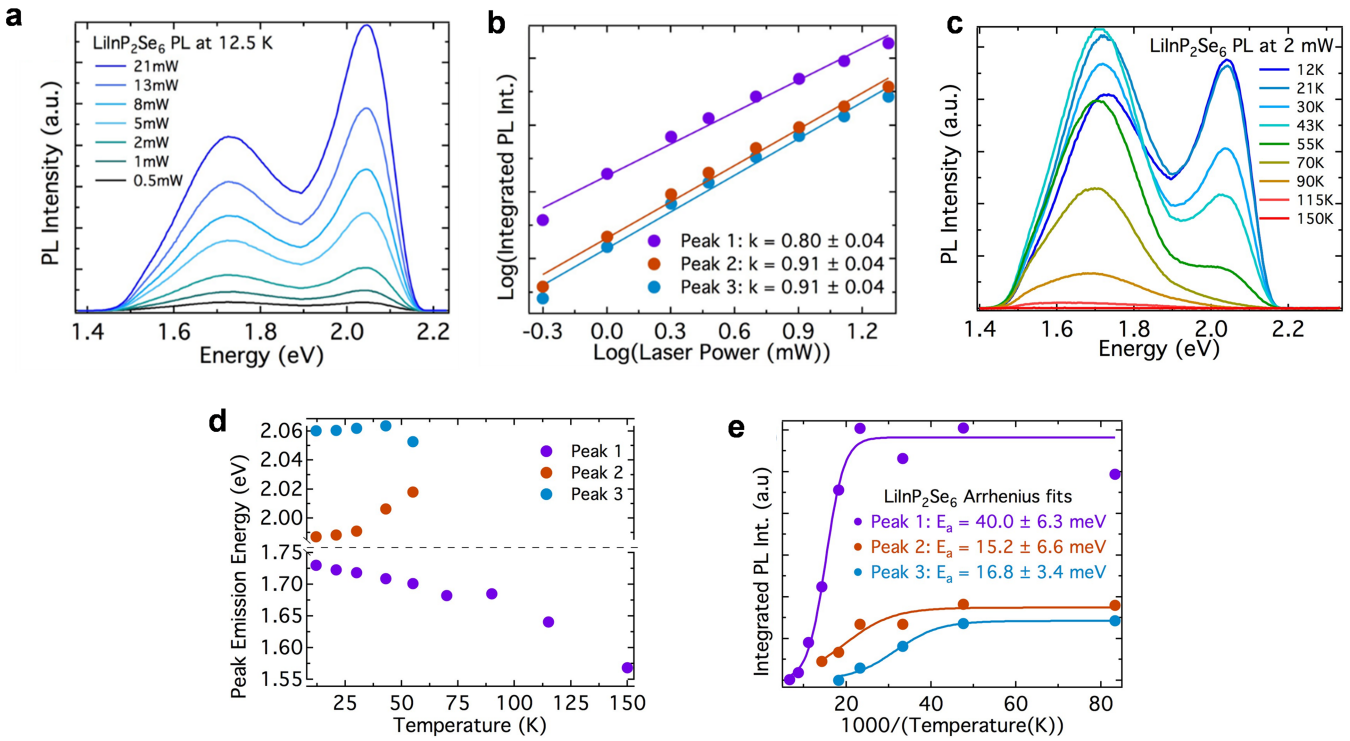
Reprints and permissions information is available at http://www.nature.com/reprints.



Extended Data Fig. 1 | X-ray powder diffraction patterns of $LiInP_2Se_6$ prepared under different conditions. a, **b**, Experimental versus simulated powder diffraction pattern of $LiInP_2Se_6$ scaled to the largest peak (**a**) and scaled by a factor of 20 (**b**). The simulated pattern has a March–Dollase parameter of 0.3. The X-ray powder diffraction pattern of $LiInP_2Se_6$ in **a** shows a considerable preference to orientation along ⟨0 0 1⟩, that is, the peaks with the largest intensity correspond to the (0 0 2), (0 0 4) and (0 0 8) planes. This preferred orientation stems from the layered nature of this compound, which causes the layers to lie parallel to the sample holder. The simulated pattern with a March–Dollase parameter of 0.3 was the reference pattern used to compare with the experimental pattern, and accurately accounts for the sample's preferred orientation. When the patterns are zoomed-in closer to the baseline, the reflections with contributions from the *h* and *k* directions can be seen and match well with the simulated pattern (**b**). **c**, Experimental versus simulated powder diffraction pattern of $LiInP_2Se_6$ obtained using a stoichiometric amount of reagents. The unknown secondary phases are marked by asterisks. **d**, Sink side of the reaction tube used for CVT with no iodine charged into the tube. **e**, Sink side of the reaction tube used for CVT with iodine as the transporting agent. This reaction did not employ an initial reverse transport step. **f**, Experimental versus simulated powder diffraction pattern of $LiInP_2Se_6$ grown using CVT. The simulated pattern has a March–Dollase coefficient of 0.3. **g**, Experimental powder diffraction pattern of bulk $LiInP_2Se_6$ before (red) and after (black) DTA up to 760 °C. **h**, Experimental diffraction pattern of $LiInP_2Se_6$ grown by CVT before (red) and after (black) DTA up to 760 °C.



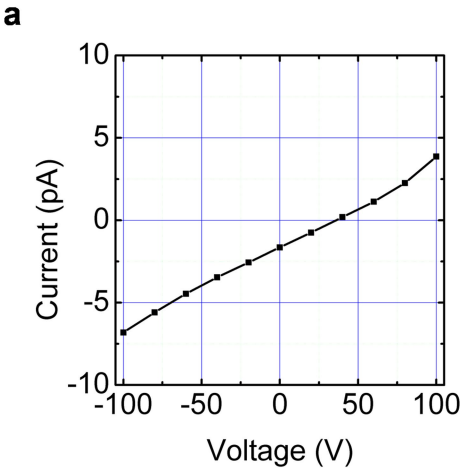
Extended Data Fig. 2 | Thermal analysis, morphology and compositional analysis for $LiInP_2Se_6$. **a**, **b**, DTA measurement of bulk-synthesized (**a**) and CVT-grown (**b**) $LiInP_2Se_6$ up to 760 °C. The vertical axis is a measure of the voltage difference of the thermocouples on the sample and the alumina standard as the temperature is varied; thus, the spikes correspond to a transfer of heat from the sample to the environment and vice versa. The melting point of $LiInP_2Se_6$ is considerably lower than that of $LiInSe_2$ (~915 °C)[14], which yields several practical benefits, including the reduction of thermally induced defects and improved stoichiometry from reduced evaporative losses of the volatile Li, P and Se. **c**, **d**, Scanning electron microscopy images of bulk $LiInP_2Se_6$ in the basal plane (**c**) and a cross-section of the layers (**d**). The lamellar crystal morphology of the bulk ingot can be clearly seen in the images. A large flake with a smooth surface was selected to examine the surface of the basal plane. **c** shows a typical image of the smooth basal plane. The composition obtained from EDS from both orientations yielded the semiquantitative formula $In_{1.1}P_{2.0}Se_{6.0}$, which is consistent with the expected ratio of 1:2:6 determined from the crystal structure. The lithium content could not be determined from EDS because of the insensitivity of EDS to lithium. **e**, EDS mapping of the surface of $LiInP_2Se_6$ grown using CVT without reverse transport. The growth front of the layer appears rich in iodine.

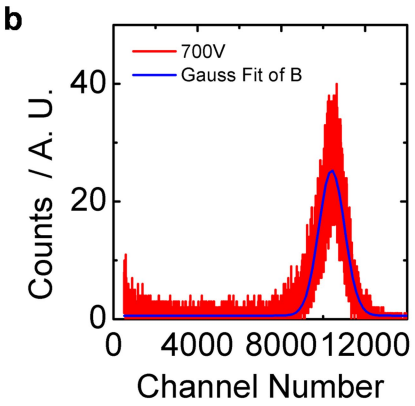


f

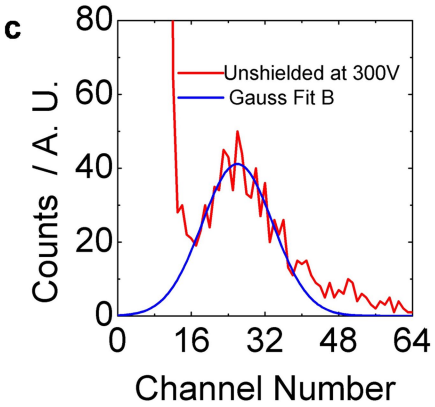
Peak #	E_{PL} @ 2 mW, 12.5 K	E_{PL} shift w/T	E_{PL} IV trend	FWHM (meV)	Power Law	E_a (meV)	Assignment
Peak 1	1.73 eV	Redshift	Blueshift	275	0.80(4)	40.0(6.3)	DAP
Peak 2	1.98 eV	Slight Blueshift	Blueshift	160	0.91(4)	15.2(6.6)	Free-to-bound
Peak 3	2.06 eV	Blueshift	Slight Blueshift	103	0.91(4)	16.8(3.4)	Free-to-bound

Extended Data Fig. 3 | PL characterization of $LiInP_2Se_6$. **a**, Dependence of the PL spectra of $LiInP_2Se_6$ at 12.5 K on laser power. **b**, Power-law fits of the integrated PL intensity versus power for each peak. **c**, Temperature dependence of the PL spectra of $LiInP_2Se_6$ at 2 mW. **d**, PL peak energy versus temperature. **e**, Arrhenius plots of integrated PL intensity versus inverse temperature. The solid lines are the least-squares best fit for each peak according to Eq. (1). **f**, Tabulated PL peak properties for $LiInP_2Se_6$ at 12.5 K. See Methods for further discussion.



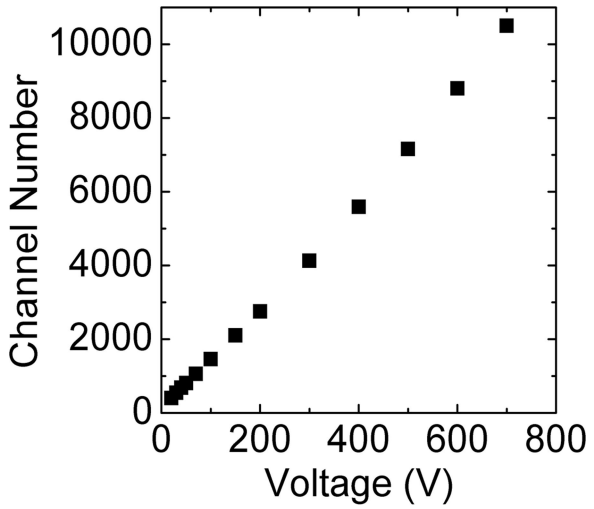


Equation	y=y0 + (A/(w*sqrt(PI/2)))*exp(-2*((x-xc)/w)^2)		
Adj. R-Sq	0.91032		
		Value	Standard
B	y0	0.58252	0.0168
B	xc	10404.96	2.01122
B	w	1229.551	4.19256
B	A	38077.32	121.0528
B	sigma	614.7759	
B	FWHM	1447.686	
B	Height	24.70925	

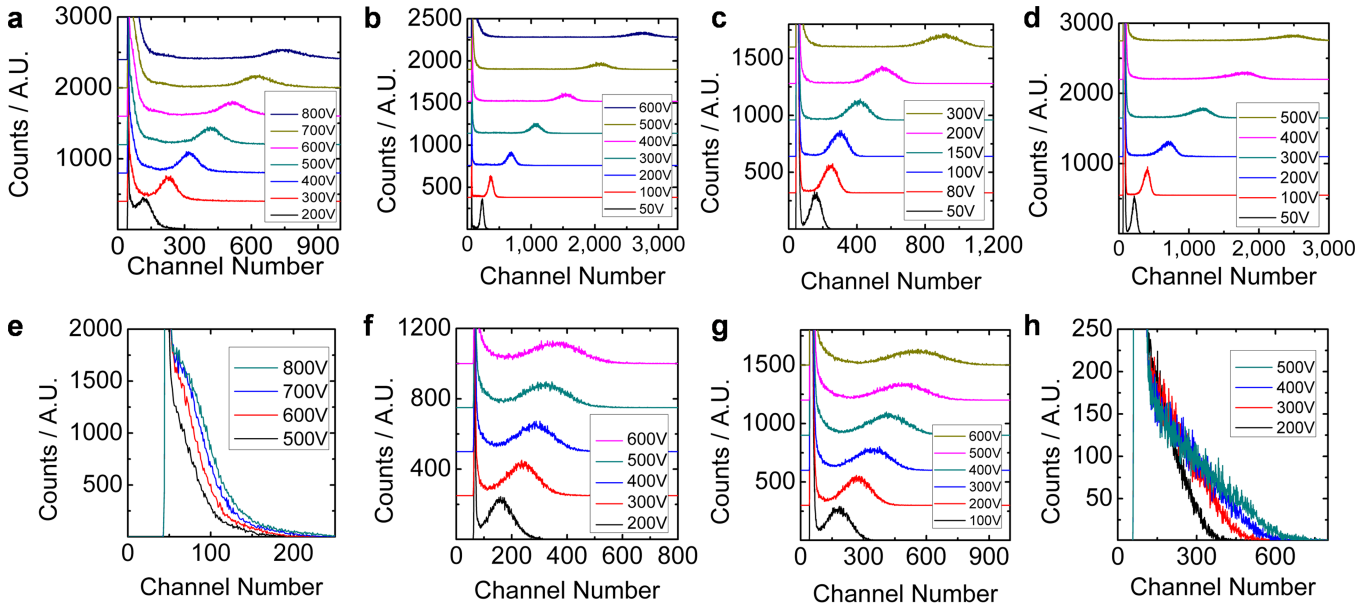


Equation	y=y0 + (A/(w*sqrt(PI/2)))*exp(-2*((x-xc)/w)^2)		
Adj. R-Sq	0.72822		
		Value	Standard
B	y0	0	0
B	xc	26.00778	0.46723
B	w	15.39988	1.24503
B	A	794.052	49.392
B	sigma	7.69994	
B	FWHM	18.13197	
B	Height	41.148	

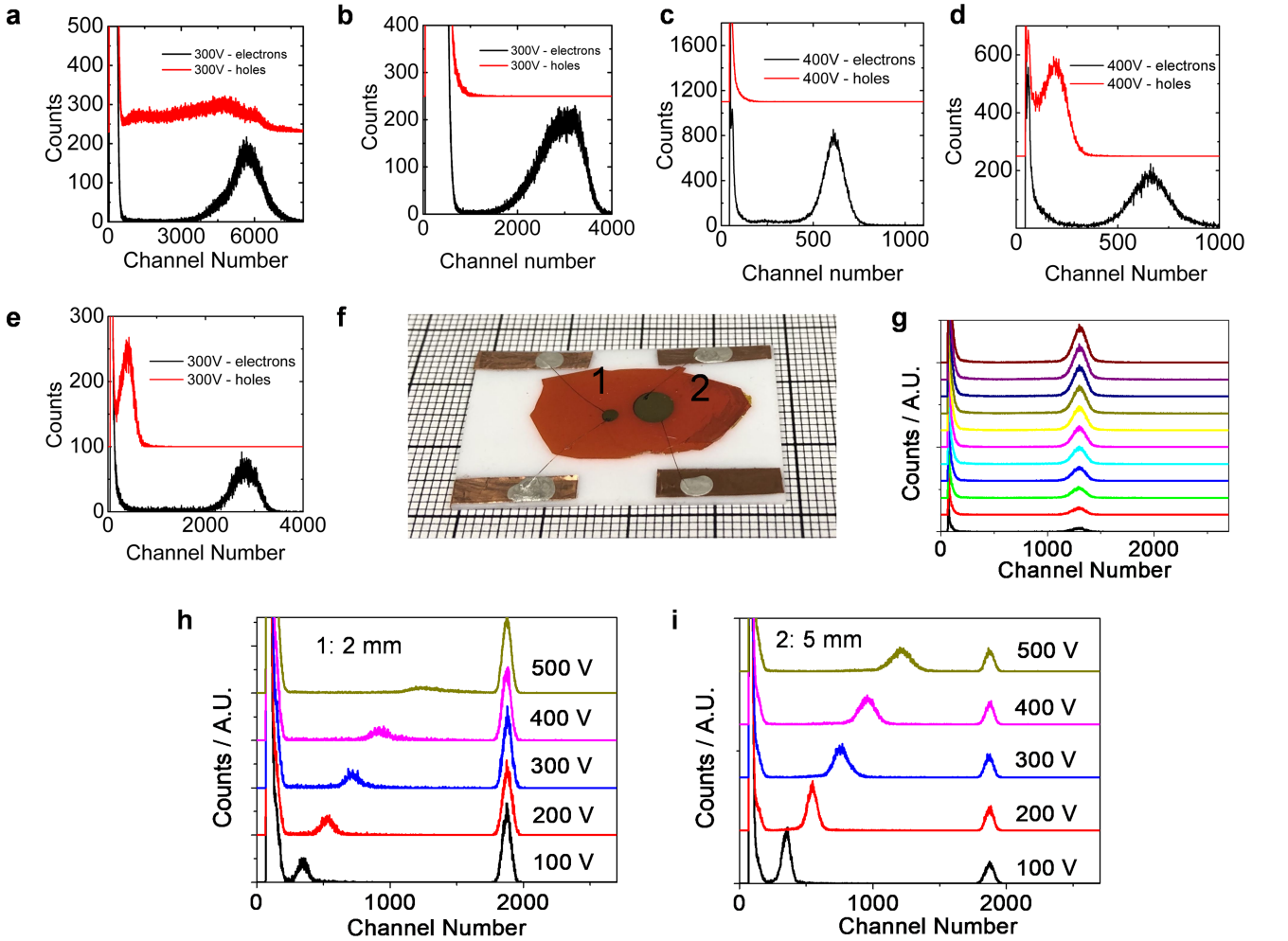
Extended Data Fig. 4 | Electrical properties and spectroscopic response of $LiInP_2Se_6$ device. a, Current–voltage plot (from −100 V to 100 V) of a pristine $LiInP_2Se_6$ device showing linear behaviour. **b**, Pulse-height spectra of α particles from an ^{241}Am source at 700 V with a Gaussian fit (blue curve). **c**, Binned pulse-height spectrum of a 7 × 7 mm^2 $^6LiInP_2Se_6$ device (90 µm thickness) exposed to a moderated Pu–Be source while unshielded under 300 V bias for 30 min, and the corresponding Gaussian fit (blue curve). The tables in **b**, **c** show the Gaussian equation used to fit the full-energy peak and values of the peak parameters. y_0, vertical offset; x_c, centre; w, width; A, area; FWHM, full-width at half-maximum.



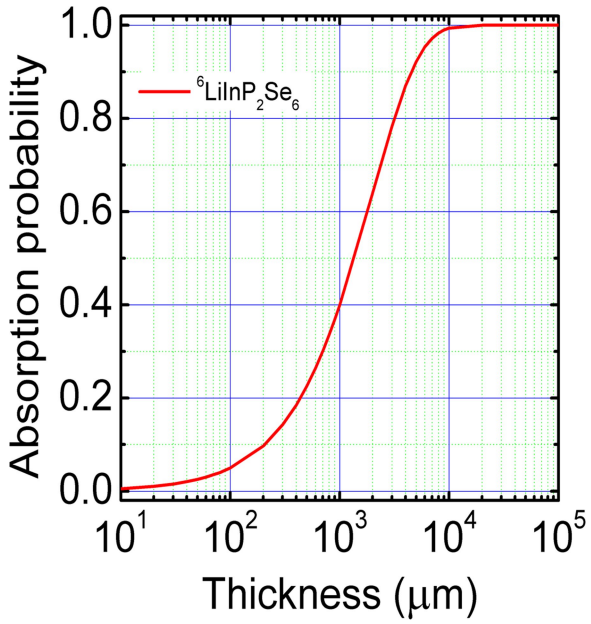
Extended Data Fig. 5 | Channel number versus voltage for $LiInP_2Se_6$ devices collecting electrons. The figure of merit for charge transport in semiconductor radiation detectors is the mobility–lifetime product, $\mu\tau$. For reliable neutron detection, $\mu\tau$ must be sufficient so that counts from neutron capture are at a sufficiently high channel number to be distinct from the background to allow accurate discrimination. Here the channel number is plotted versus voltage for a typical device, and surprisingly the curve exhibits two slopes in different voltage ranges. The Hecht equation cannot model these data because the model assumes linear behaviour at low voltages, which then saturate towards a maximum channel number as the CCE reaches unity. The observed behaviour has the opposite concavity to the model, with a slight rise in slope as voltage increases. This change in slope can be explained by the reduction of the effective voltage from an internal polarization antiparallel to the applied field. Similarly atypical behaviour has been observed in the α-particle response of cadmium zinc telluride at $T = 200$ K, where this effect was attributed to polarization from deep-level traps[41].



Extended Data Fig. 6 | Pulse-height spectra of four other samples. a–**h**, Pulse-height spectra are shown for electron (**a**–**d**) and hole (**e**–**h**) collection. The growth conditions of these samples were the same as those used for the samples that gave the spectra shown in the main-text figures. For hole collection, the spectra had lower channel numbers than the electron-collection spectra, indicating lower CCE for hole transport.



Extended Data Fig. 7 | Pulse-height spectrum for ^{6}Li-enriched $LiInP_2Se_6$ devices. a–**e**, Data are shown for ^{6}Li-enriched $LiInP_2Se_6$ devices with areas of $7 \times 7\,mm^2$ (**a**, **b**), $5 \times 5\,mm^2$ (**c**) and $3 \times 3\,mm^2$ (**d**, **e**). Devices with larger electrode areas had lower energy resolutions for electron collection, possibly owing to property variation among different samples. **f**, As-made $LiInP_2Se_6$ detectors with a diameter of 2 mm ('1') and 5 mm ('2') on the same single crystal. **g**, Time-dependent α-particle spectra collection by $LiInP_2Se_6$ detector 2 in **f**. We note that the peak channel number and count rate per second were constant over time. **h**, Collection of α-particle spectra by detector 1 in **f** with a pulse generator. **i**, Collection of α-particle spectra by detector 2 in **f** with a pulse generator. We note that the positions of the pulser peak in **h** and **i** are the same and the corresponding energy resolution is (3.5 ± 0.1)%, indicating the same electronics noise during collection.



Extended Data Fig. 8 | Absorption probability versus ^{6}LiInP$_2$Se$_6$ thickness for thermalized neutrons. In addition to charge transport properties, the neutron-capture cross-section of LiInP$_2$Se$_6$ must be considered, as this directly correlates with the intrinsic maximum of the detector efficiency. A linear attenuation coefficient can be used to quantify the percentage of incident neutrons absorbed in a given material through the equation: fraction of neutrons captured (%) = $(1 - e^{-l\alpha}) \times 10\%$, where l is the thickness of the active region and α is the linear attenuation coefficient, which is calculated using the capture cross-section of thermalized neutrons for each element and its molar density. The calculated mass attenuation coefficient for thermalized neutrons is 5.1 cm^{-1} and 1.4 cm^{-1} for LiInP$_2$Se$_6$ fully enriched in ^{6}Li and natural-abundance Li, respectively. A detector with a thickness of about 9 mm would be able to absorb 99% of the incident neutrons. Here we achieved the successful growth of crystals with thickness of ~1 mm, which would absorb ~40% of incident neutrons. Increases in efficiency would be achievable through scaled-up growth of thicker crystals or stacking of several thinner detectors[42]. When ^{115}In (the most common isotope in natural indium) absorbs a neutron, the nuclide produces a γ-ray instead of a highly energetic charged particle. Thus, about 20% of the neutrons absorbed do not contribute to the signal, which sets the maximum theoretical detector efficiency of ^{6}LiInP$_2$Se$_6$ to approximately 80%.

Extended Data Table 1 | Crystal data and structure refinement for $LiInP_2Se_6$ at 293 K

Empirical formula	$LiInP_2Se_6$	θ range for data collection	3.052 to 29.197°
Formula weight	657.46	Index ranges	-8<=h<=8, -8<=k<=8, -17<=l<=18
Temperature	293 K	Reflections collected	4045
Wavelength	0.71073 Å	Independent reflections	437 [R_{int} = 0.0438]
Crystal system	Trigonal	Completeness to θ = 25.242°	98.6%
Space group	*P-31c*	Refinement method	Full-matrix least-squares on F^2
Unit cell dimensions	a = 6.3971(4) Å, α = 90° b = 6.3971(4) Å, β = 90° c = 13.3505(12) Å, γ = 120°	Data / restraints / parameters	437 / 0 / 17
Volume	473.15(7) $Å^3$	Goodness-of-fit	1.335
Z	2	Final R indices [I > 2σ(I)]	R_{obs} = 0.0277, wR_{obs} = 0.0592
Density (calculated)	4.615 g/cm^3	R indices [all data]	R_{all} = 0.0361, wR_{all} = 0.0616
Absorption coefficient	25.832 mm^{-1}	Extinction coefficient	.
F(000)	572	Largest diff. peak and hole	0.680 and -0.835 $e·Å^{-3}$
Crystal size	0.4 x 0.2 x 0.05 mm^3		

$R = \Sigma||F_o|-|F_c|| / \Sigma|F_o|$, $wR = \{\Sigma[w(|F_o|^2 - |F_c|^2)^2] / \Sigma[w(|F_o|^4)]\}^{1/2}$ and $w=1/[\sigma^2(Fo^2)+(0.0302P)^2+0.0582P]$ where $P=(Fo^2+2Fc^2)/3$

Extended Data Table 2 | Atomic coordinates (×10^4), equivalent isotropic and anisotropic displacement parameters (×10^3 Å^2), selected bond lengths (Å) and angles (°) for $LiInP_2Se_6$ at 293(2) K, with estimated standard deviations in parentheses

Label	x	y	z	Occupancy	U_{eq}^*	U_{11}	U_{22}	U_{33}	U_{12}	U_{13}	U_{23}
In(01)	10000	10000	7500	1	16(1)	12(1)	12(1)	25(1)	6(1)	0	0
Se(01)	6613(1)	6677(1)	6204(1)	1	15(1)	10(1)	15(1)	21(1)	7(1)	1(1)	-2(1)
P(01)	3333	6667	6672(2)	1	11(1)	8(1)	8(1)	17(1)	4(1)	0	0
Li(01)	6667	3333	7500	1	37(5)	13(4)	13(4)	85(18)	7(2)	0	0

*U_{eq} is defined as one third of the trace of the orthogonalized U_{ij} tensor.
The anisotropic displacement factor exponent takes the form: $-2\pi^2[h^2a^{*2}U_{11} + \ldots + 2hka^*b^*U_{12}]$.

	Label	Distances (Å)	Angles (°)
Bond length label	In(01)-Se(01)	2.7576(4)	-
	P(01)-Se(01)	2.1859(6)	-
	P(01)-P(01)	2.212(3)	-
	Li(01)-Se(01)	2.7650(4)	-
Bond angle label	Se(01)-In(01)-Se(01)#3	-	178.527(13)
	Se(01)-In(01)-Se(01)#4	-	94.232(16)
	Se(01)-In(01)-Se(01)'	-	84.780(13)
	Se(01)-In(01)-Se(01)'	-	96.227(16)
	Se(01)-In(01)-Se(01)'	-	94.233(16)
	In(01)-Se(01)-Li(01)	-	83.944(12)
	P(01)-Se(01)-In(01)	-	101.88(4)
	P(01)-Se(01)-Li(01)	-	101.65(4)
	Se(01)'-P(01)-Se(01)	-	112.17(4)
	Se(01)'-P(01)-P(01)'	-	106.61(5)
	Se(01)-Li(01)-Se(01)'	-	178.760(12)
	Se(01)-Li(01)-Se(01)'	-	94.205(16)
	Se(01)-Li(01)-Se(01)'	-	95.887(15)
	Se(01)'-Li(01)-Se(01)	-	84.962(13)

Article

Transparent ferroelectric crystals with ultrahigh piezoelectricity

https://doi.org/10.1038/s41586-019-1891-y

Received: 30 May 2019

Accepted: 18 November 2019

Published online: 15 January 2020

Chaorui Qiu[1,9], Bo Wang[2,9], Nan Zhang[1,9], Shujun Zhang[2,3], Jinfeng Liu[1], David Walker[4], Yu Wang[5], Hao Tian[5], Thomas R. Shrout[2], Zhuo Xu[1]*, Long-Qing Chen[2,6,7,8]* & Fei Li[1]*

Transparent piezoelectrics are highly desirable for numerous hybrid ultrasound–optical devices ranging from photoacoustic imaging transducers to transparent actuators for haptic applications[1–7]. However, it is challenging to achieve high piezoelectricity and perfect transparency simultaneously because most high-performance piezoelectrics are ferroelectrics that contain high-density light-scattering domain walls. Here, through a combination of phase-field simulations and experiments, we demonstrate a relatively simple method of using an alternating-current electric field to engineer the domain structures of originally opaque rhombohedral $Pb(Mg_{1/3}Nb_{2/3})O_3$-$PbTiO_3$ (PMN-PT) crystals to simultaneously generate near-perfect transparency, an ultrahigh piezoelectric coefficient d_{33} (greater than 2,100 picocoulombs per newton), an excellent electromechanical coupling factor k_{33} (about 94 per cent) and a large electro-optical coefficient γ_{33} (approximately 220 picometres per volt), which is far beyond the performance of the commonly used transparent ferroelectric crystal $LiNbO_3$. We find that increasing the domain size leads to a higher d_{33} value for the [001]-oriented rhombohedral PMN-PT crystals, challenging the conventional wisdom that decreasing the domain size always results in higher piezoelectricity[8–10]. This work presents a paradigm for achieving high transparency and piezoelectricity by ferroelectric domain engineering, and we expect the transparent ferroelectric crystals reported here to provide a route to a wide range of hybrid device applications, such as medical imaging, self-energy-harvesting touch screens and invisible robotic devices.

Achieving simultaneous high piezoelectricity and perfect transparency in a piezoelectric material has long been a challenge. For example, traditional high-performance piezoelectric transducers are typically made from perovskite ferroelectric ceramics and crystals with chemical compositions that are close to their morphotropic phase boundaries (MPBs), such as $Pb(Zr,Ti)O_3$ (PZT) ceramics and domain-engineered PMN-PT crystals. These materials possess very high d_{33} and k_{33} values[11–14], but they are usually opaque in the visible-light spectrum. On the other hand, the commonly used transparent piezoelectric $LiNbO_3$ crystals and polyvinylidine fluoride (PVDF) polymers[6,7] have good transparency but much lower d_{33} and k_{33} values ($LiNbO_3$: $d_{33} < 40$ pC N^{-1}, $k_{33} \approx 47\%$; PVDF: $d_{33} \approx 20$ pC N^{-1}, $k_{33} \approx 16\%$) that severely limit the acoustic source level, bandwidth and sensitivity of the transducers.

In addition to the extrinsic effects, such as porosity and grain boundaries, which are ubiquitous in ceramics, the poor transparency in PZT ceramics and domain-engineered PMN-PT crystals is closely associated with light scattering and reflection from their ferroelectric domain walls. There are two possible approaches to reducing the light-scattering domain walls. The first is to pole a ferroelectric crystal along the polar direction to achieve a single-domain state. However, the d_{33} value of such single-domain PMN-PT crystals is generally very low[13,14]—much lower than that of [001]-poled multidomain rhombohedral PMN-PT crystals (>1,500 pC N^{-1}). In principle, one could first pole a rhombohedral PMN-PT crystal along the [111] direction to achieve a single-domain state with good transparency, then rotate the crystal to the [001] direction to guarantee high longitudinal piezoelectricity. However, this approach is not feasible in practice (see Methods for a detailed explanation). The second approach is to dramatically reduce the domain sizes by breaking the domains into polar nanoregions with spatial sizes (a few to tens of nanometres) much smaller than the wavelength of visible light, thus greatly improving their light transparency—as observed in La-doped PZT[15,16]. However, improving the transparency using polar nanoregions is achieved at the expense of a markedly reduced remanent polarization and thus very low d_{33} values; therefore, despite more than 50 years of effort, optical functionalities in high-performance piezoelectrics have not been realized.

[1]Electronic Materials Research Laboratory (Key Lab of Education Ministry), State Key Laboratory for Mechanical Behavior of Materials and School of Electronic and Information Engineering, Xi'an Jiaotong University, Xi'an, China. [2]Department of Materials Science and Engineering, The Pennsylvania State University, University Park, PA, USA. [3]ISEM, Australian Institute for Innovative Materials, University of Wollongong, Wollongong, New South Wales, Australia. [4]Department of Physics, University of Warwick, Coventry, UK. [5]School of Physics, Harbin Institute of Technology, Harbin, China. [6]Materials Research Institute, The Pennsylvania State University, University Park, PA, USA. [7]Department of Engineering Science and Mechanics, The Pennsylvania State University, University Park, PA, USA. [8]Department of Mathematics, The Pennsylvania State University, University Park, PA, USA. [9]These authors contributed equally: Chaorui Qiu, Bo Wang, Nan Zhang.
*e-mail: xuzhuo@xjtu.edu.cn; lqc3@psu.edu; ful5@xjtu.edu.cn

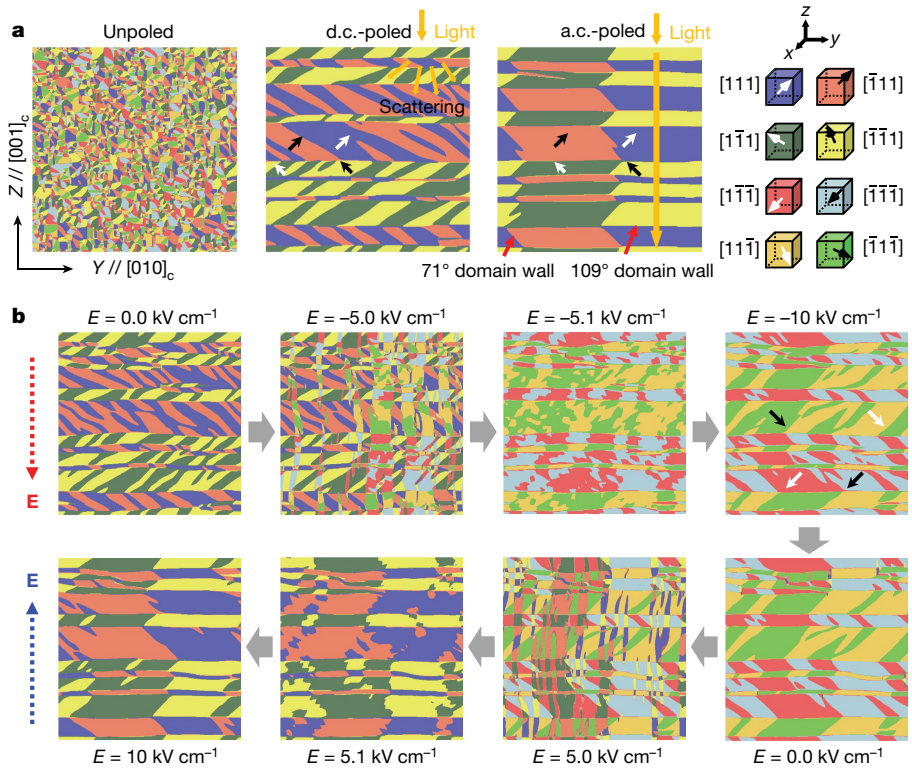


Fig. 1 | Phase-field simulations of the domain structures and evolution of [001]-oriented rhombohedral PMN-28PT single crystals via d.c. and a.c. poling. a, Domain structures for unpoled, d.c.- and a.c.-poled samples. The subscript c denotes pseudo-cubic coordinates. The black and white vectors on the right show the polarization directions, and the colour denotes the positive (white) and negative (black) polarization components along the [100] direction. The other colours represent different ferroelectric domains (the corresponding polar directions are illustrated on the right). Examples of 71° and 109° domain walls are indicated by the red arrows. A beam of light is schematically illustrated in the d.c.- and a.c.-poled cases, indicating that the light may not be scattered as it travels through the a.c.-poled sample. **b**, Snapshots of the domain pattern evolution during the reversal of polarization under a.c. poling. The initial state (that is, electric field $E = 0.0$ kV cm^{-1}) is the d.c.-poled sample. The blue and red arrows represent the applied electric fields along the [001] and [00$\bar{1}$] directions, respectively. The dimensions of all of the domain structure plots are 512 nm × 512 nm. The domain evolution under an a.c. electric field is shown in Supplementary Videos 1, 2. For comparison, the domain evolution under a d.c. electric field is shown in Supplementary Video 3.

In this work, we show that a.c. electric fields can be used to effectively eliminate light-scattering 71° domain walls for [001]-oriented rhombohedral PMN-PT crystals to achieve both near-perfect transparency and ultrahigh piezoelectricity. We first perform phase-field simulations to study the domain evolution of a [001]-oriented 0.72Pb($Mg_{1/3}Nb_{2/3}$)O_3-0.28$PbTiO_3$ (PMN-28PT) rhombohedral crystal using conventional d.c. and a.c. electric fields. We generate the initial pristine unpoled state starting from a random distribution of small polarizations that represent a high-temperature paraelectric state. The obtained multi-domain state contains all eight possible ⟨111⟩ rhombohedral domain variants with an average size of ~20 nm. Three types of domain wall are present in the unpoled rhombohedral crystal: 71°, 109° and 180° domain walls.

Under a d.c. electric field along the [001] direction, the four domain variants with polarizations along [11$\bar{1}$], [$\bar{1}$1$\bar{1}$], [$\bar{1}\bar{1}\bar{1}$] or [1$\bar{1}$1] are switched to the [111], [1$\bar{1}$1], [$\bar{1}\bar{1}$1] or [$\bar{1}$11] directions. Thus, only 71° and 109° domain walls survive, whereas the 180° domain walls are eliminated, as shown Fig. 1a. The horizontal layers are separated by a set of 109° domain walls parallel to the (001) plane, whereas within each lamina there are 71° domain walls approximately parallel to {011} planes. It should be noted that 71° domain walls can scatter light because the refractive indices n_o and n_e (where o and e represent ordinary and extraordinary light, respectively) change as light travels across a 71° domain wall, as shown in Extended Data Fig. 1. By contrast, 109° domain walls do not induce light scattering as the refractive indices are the same for the domains on both sides of the wall.

Our phase-field simulations demonstrate that the application of an a.c. electric field effectively reduces the number of 71° domain walls, with only two 71° domain walls left in each lamina after a.c. poling, leading to a much larger domain size within each lamina. To understand the reason for the elimination of 71° domain walls by a.c. poling, we analyse the domain evolution during the polarization reversal process, as shown in Fig. 1b and Supplementary Videos 1, 2. One can see that the reversal of the electric field causes 'swinging' of 71° domain walls: that is, 71° domain walls alternate between the (011) and (01$\bar{1}$) planes. During this process, the contiguous 71° domains tend to merge with each other, resulting in a considerable increase in 71° domain size after a.c. poling. In addition (Extended Data Fig. 2), the total free energy of the system is reduced during this poling process as the energies arising from the discontinuities of polarization/strain associated with domain walls decrease when the domain wall density decreases. In other words, alternating the polarity of the electric field lowers the free energy of a ferroelectric crystal, leading to a domain structure with reduced domain wall density. As discussed above, owing to the substantially decreased 71° domain wall density, the light transmission of the a.c.-poled sample is expected to be superior to that of a corresponding d.c.-poled sample.

Following the phase-field simulations, we characterized the domain structures of a.c.-poled and d.c.-poled PMN-28PT crystals. Using birefringence imaging microscopy (BIM)[17], we characterized the orientation (φ) of the principal axis of the optical indicatrix projected on the (001) planes, as shown in Fig. 2a. For a rhombohedral single domain,

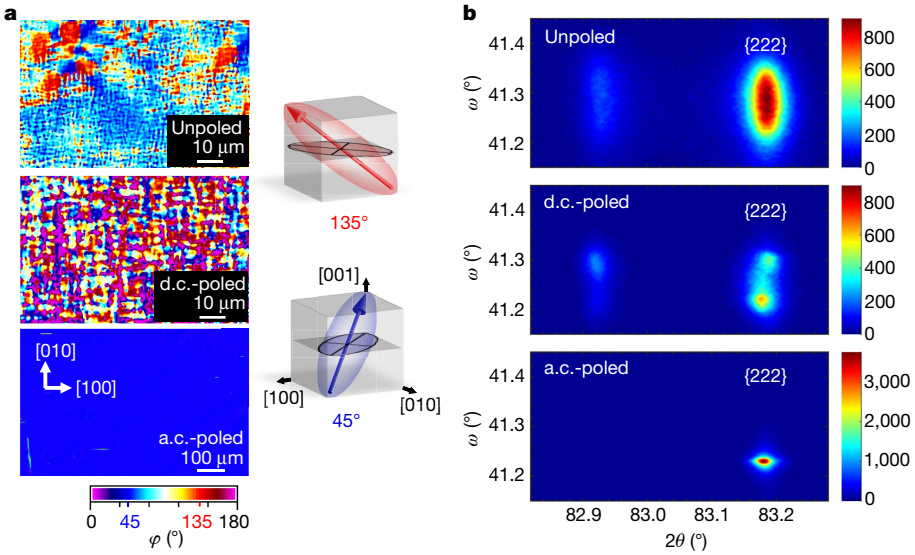


Fig. 2 | Analysis of the domain structures for the [001]-oriented PMN-28PT crystals. a, BIM image; the colours indicate the orientation angles (φ) of the projection of the principal optical axis on the (001) plane. Red and blue represent the projection of the principal axis of the optical indicatrix along the diagonal faces on the (001) plane, that is, φ of 45° and 135°, respectively. As an example, the projections of the principal axis of the optical indicatrix of the $[\bar{1}\bar{1}1]$ and $[1\bar{1}1]$ domains are illustrated in the schematics on the right of the figure. **b**, Reciprocal space maps of the {222} reflections from the samples under different poling conditions, measured with high-resolution single-crystal X-ray diffraction. The colour bars indicate the intensity of the diffraction. The thickness of the samples is 175 μm.

the projection of the optical axis is along the diagonal face. Therefore, the φ value of a rhombohedral domain would be 45° or 135°, which are represented by blue and red colours, respectively (colour bar in Fig. 2a). A multidomain crystal may show two or more colours simultaneously in the projection map owing to the overlap of ferroelectric domains and domain walls along the light propagation path.

The orientation map for the unpoled sample shows an irregular colour distribution on a very fine scale. This is because the domain size of the as-grown PMN-PT is much smaller than the experimental resolution (the wavelength of the light is 590 nm); therefore, the exact domain pattern may not be clearly revealed. Compared with classical ferroelectrics (for example, $BaTiO_3$), the relatively small domain size in relaxor ferroelectrics (of the order of several tens of nanometres before poling[18–20]) is attributed to the presence of random fields/bonds that inhibit the growth of ferroelectric domains[21–24].

After d.c. poling, the domains represented by regions with the same colour increase in size, and the boundaries between the domains are approximately along the [100] and [010] directions, which are associated with the projections of 71° domain walls ((101), (10$\bar{1}$), (011) or (01$\bar{1}$) planes) on the (001) plane. In this image, the colours of most regions are neither red nor blue. Of particular importance is the substantially enlarged domain size in the a.c.-poled sample, where the in-plane size of the rhombohedral domain is on the millimetre scale. It should be noted that the domain size obtained from the phase-field simulation is much smaller than that from experiments. This is because the spatial scale in the phase-field simulation (512 nm) is much smaller than that of the materials in the experiments (at the millimetre scale). By coarsening the scale in the phase-field simulation, the domain size of the a.c.-poled crystal is found to increase (Extended Data Fig. 3). It is difficult to perform a phase-field simulation on the millimetre scale and simultaneously resolve the polarization profiles across domain walls of ~1 nm in thickness. In this work, we used phase-field simulations to qualitatively analyse the domain evolution of PMN-28PT crystals during a.c. poling. We also characterized the cross-section domain structure of a.c.-poled and d.c.-poled samples to investigate the domain size in the out-of-plane direction. As shown in Extended Data Fig. 4, we found that the width between two neighbouring 109° domain walls is similar for both samples (~1 μm), indicating that most 109° domain walls survived after a.c. poling, which is consistent with the phase-field simulations.

X-ray diffraction patterns confirm the main observations from the BIM images. Figure 2b shows the {222} reflections for the [001]-oriented PMN-28PT crystals. If the rhombohedral domain variants are evenly distributed in the sample, there should be two diffraction peaks in the 2θ–ω map (2θ is the angle between the transmitted and reflected X-ray beams; ω represents the angle between the incident beam and the sample surface): one peak is associated with the (222) plane at a lower 2θ, and the other peak is associated with the remaining three {222} planes at a higher 2θ. Thus, the integrated intensity of the high-2θ reflection is supposed to be three times that of the low-2θ reflection. This is approximately what is observed in the unpoled sample. The diffused distribution of the diffraction along the ω axis is associated with the lattice distortions due to the existence of domain walls. The diffraction peaks converge into distinctive sharper reflections after d.c. poling, indicating that the domains become larger and that the volume fraction of domain walls decreases. Eventually, in the a.c.-poled sample, only the high-2θ diffraction peak is observed, and the diffusiveness of the diffraction peak along the ω axis is much smaller than that of the d.c.-poled and unpoled samples (Extended Data Fig. 5). These features reveal that the X-ray beam is approximately incident on a single domain of the a.c.-poled sample. The size of the beam here is about 1 mm^2, which indicates that the in-plane domain size of the a.c.-poled sample is equal to or larger than 1 mm^2.

Owing to the unique domain structure, a.c.-poled PMN-28PT crystals exhibit numerous attractive properties in addition to their ultrahigh piezoelectricity, including an electro-optical coefficient γ_{33} of 220 pm V^{-1}, near-perfect light transmittance and enhanced birefringence (Extended Data Table 1). Figure 3a shows photographs of the a.c.- and d.c.-poled samples: the a.c.-poled samples are clearly transparent. The light transmittance of the a.c.-poled sample is found to be very close to its theoretical limit and is much higher than that of the d.c.-poled sample, especially for the visible-light spectrum (Fig. 3b). The light with wavelengths below 400 nm is completely absorbed because of the optical absorption edge (~3.10 eV), which is similar to most oxygen

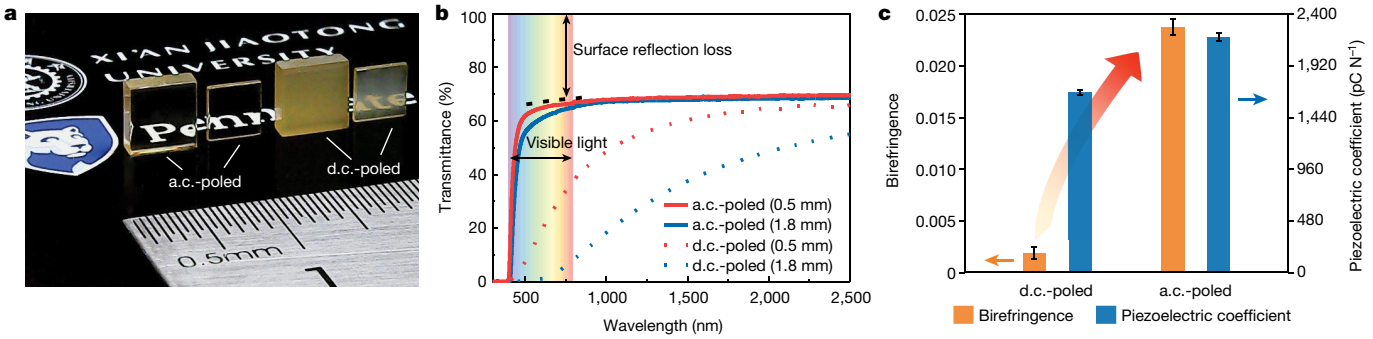


Fig. 3 | Comparison of the properties of a.c.-poled and conventional d.c.-poled [001]-oriented PMN-28PT crystals. a, Photograph of a.c- and d.c.-poled PMN-28PT crystals. The thicknesses of the crystals are 0.5 mm and 1.8 mm, respectively. **b**, Light transmittance of the a.c.- and d.c.-poled PMN-28PT crystals. **c**, d_{33} and birefringence of the a.c.- and d.c.-poled PMN-28PT crystals. Ten a.c.-poled and ten d.c.-poled samples are used for the characterization of d_{33}, whereas the birefringence is determined from seven points of the a.c.- and d.c.-poled samples. The red graded arrow indicates the increase in d_{33} and birefringence for PMN-PT crystals after a.c. poling. The error bars in **c** present the standard deviation of the corresponding data.

octahedral perovskites[25,26]. The light absorption coefficient of the a.c.-poled sample is found to be almost zero at wavelengths longer than 400 nm, whereas the absorption coefficient of the d.c.-poled sample remains large and decreases monotonically with increasing wavelength (Extended Data Fig. 6).

The birefringence of the a.c.-poled crystals is approximately one order of magnitude higher than that of their d.c.-poled counterparts (Fig. 3c). This difference is associated with the different domain structures. The principle axis of the optical indicatrices of the domains on both sides of a 71° domain wall are perpendicular to each other on the (001) plane, resulting in cancellation of the birefringence as light travels through a 71° domain wall (see Methods section 'PLM'). For a.c.-poled crystals, however, the birefringence is approximately equal to that of the intrinsic value of a single-domain rhombohedral PMN-28PT crystal because of the substantially decreased number of 71° domain walls.

The a.c.-poled crystals also exhibit a 30% enhancement in d_{33} over the d.c.-poled crystals. This phenomenon was observed in many a.c.-poled relaxor–PT crystals[27–30]. To understand the mechanism for the enhanced piezoelectricity, we conducted phase-field simulations to calculate the piezoelectricity of PMN-28PT with different 71° domain sizes, as shown in Fig. 4a. The variation of polar vectors around a 71° domain wall is depicted in Fig. 4b. For an ideal rhombohedral domain, the polar vectors are along the ⟨111⟩ directions, and the angle between the polar vector and the [011] direction is 35.3°. However, the presence of 71° domain walls causes the polar vectors to rotate towards the [011] direction to minimize the polarization gradient and elastic energies associated with the polarization/strain discontinuities around the

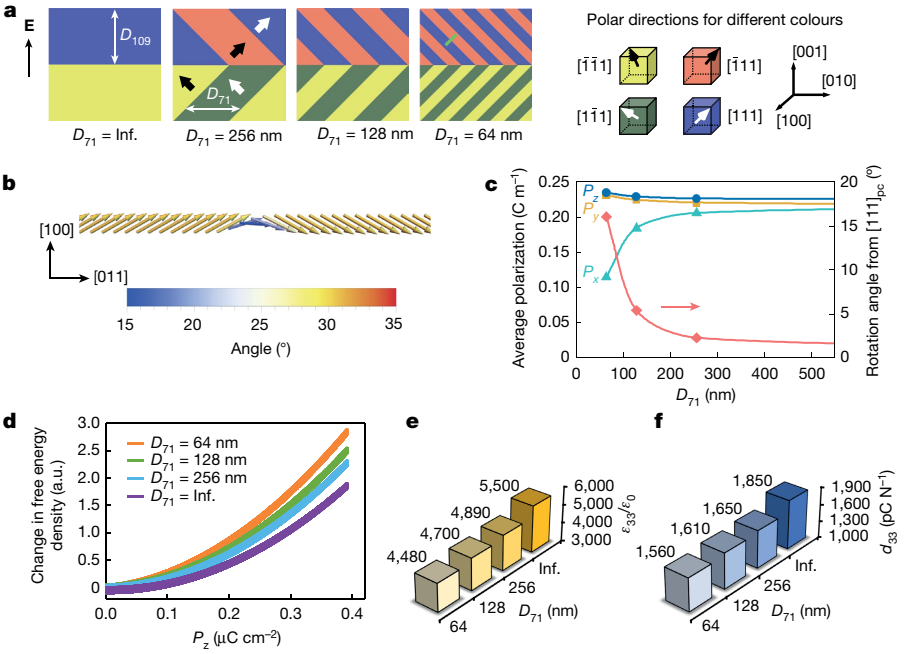


Fig. 4 | Phase-field simulations of the effect of domain size on the polarization, free-energy density and properties of the PMN-28PT crystal. a, Two-dimensional schematic of a [001]-poled PMN-28PT with various 71° domain widths (D_{71}). 'Inf.', no 71° domain walls are present in the system. The polar directions for different colours are depicted on the right. **b**, Schematic of polar vectors around a 71° domain wall (marked by the green line in **a**). The colours of the arrows represent the angles between each polar vector and the [011] direction. D_{71} in this schematic is 64 nm. **c**, The average magnitude of the spontaneous polarization components P_x ([100]), P_y ([010]) and P_z ([001]) of a ferroelectric domain as a function of D_{71}. The red line describes the angle between the overall polarization and the [111] direction as a function of D_{71}. **d**, The average free-energy density of the system with respect to P_z. The free-energy density at the stable state (that is, $\Delta P = 0$) is selected as the reference. **e**, Dielectric permittivity ($\varepsilon_{33}/\varepsilon_0$) as a function of D_{71}. **f**, d_{33} as a function of D_{71}.

domain walls. With decreasing domain size, the impact of the domain walls on the polarization becomes more prominent, resulting in a larger deviation of the polarization from the ⟨111⟩ directions, as shown in Fig. 4c. The free-energy profile of the system is also affected by the variation in polarization. As shown in Fig. 4d, the average free-energy profile of the system as a function of ΔP_z (the change in polarization P along the z direction; that is, the [001] direction) is flattened with the increase in the width of the 71° domains; that is, the curvature of the free-energy profile ($\partial^2 G/\partial P_z^2|_{\Delta P_z=0}$) decreases with increasing 71° domain width. Thus, the calculated ε_{33} and d_{33} increase with enlarging 71° domain widths, as shown in Fig. 4e, f.

It should be noted that the observed enhancement in piezoelectricity with increasing domain size is not universal to all ferroelectric crystals. It is expected that the piezoelectricity of ferroelectrics is also related to the symmetry of the ferroelectric phase and domain configurations[31,32]. For example, in tetragonal $BaTiO_3$ (refs. [8–10]) and high-temperature-poled PZN-PT crystals[33], where domain configurations are very different from PMN-28PT, the domain-size dependence of piezoelectricity shows an opposite trend to that observed here.

For the purpose of practical applications, we also studied the temperature stability of the properties of a.c.-poled PMN-28PT crystals (Extended Data Fig. 7), which indicates that the temperature-dependent electromechanical behaviours of a.c.- and d.c.-poled samples are very similar. Of particular interest is the fact that at temperatures below the rhombohedral–tetragonal phase transition temperature (~95 °C), the domain structure remains essentially the same, and no depolarization behaviour is observed, indicating that a.c.-poled crystals can be used up to their respective phase transition temperatures.

In summary, we report a simple approach that uses a.c. electric fields to simultaneously achieve near-perfect transparency, enhanced piezoelectricity and birefringence in rhombohedral PMN-PT crystals. Such transparent crystals are expected to find a wide range of applications in coupled electro-optical–mechanical devices. Both experimental and simulated results demonstrate that the enhanced piezoelectricity of [001]-oriented rhombohedral PMN-PT crystals achieved through a.c.-poling is due to the increased domain size, in contrast to the long-standing belief that decreasing domain size always leads to higher piezoelectricity.

Online content

Any methods, additional references, Nature Research reporting summaries, source data, extended data, supplementary information, acknowledgements, peer review information; details of author contributions and competing interests; and statements of data and code availability are available at https://doi.org/10.1038/s41586-019-1891-y.

1. Wang, L. V. Multiscale photoacoustic microscopy and computed tomography. *Nat. Photon.* **3**, 503–509 (2009).
2. Chen, X. et al. Transparent lead lanthanum zirconate titanate (PLZT) ceramic fibers for high-frequency ultrasonic transducer applications. *Ceram. Int.* **42**, 18554–18559 (2016).
3. Tshering, C. & Tshering, D. Renewable mobile charger using piezoelectric transducer. *Res. J. Recent Sci.* **7**, 20–23 (2018).
4. Sette, D. et al. Transparent piezoelectric transducers for large area ultrasonic actuators. In *2017 IEEE 30th International Conference on Micro Electro Mechanical Systems (MEMS)*. 793–796 (IEEE, 2017).
5. Modarres, A., Ramstein, C., Cruz-Hernandez, J. M., Danny, A. & Grant, A. G. Transparent composite piezoelectric combined touch sensor and haptic actuator. US Patent 2011/0261021 A1 (2011).
6. Thalhammer, G., McDougall, C., MacDonald, M. P. & Ritsch-Marte, M. Acoustic force mapping in a hybrid acoustic-optical micromanipulation device supporting high resolution optical imaging. *Lab Chip* **16**, 1523–1532 (2016).
7. Niederhauser, J. J., Jaeger, M., Hejazi, M., Keppner, H. & Frenz, M. Transparent ITO coasted PVDF transducer for optoacoustic depth profiling. *Opt. Commun.* **253**, 401–406 (2005).
8. Wada, S., Yako, K., Kakemoto, H., Tsurumi, T. & Kiguchi, T. Enhanced piezoelectric properties of barium titanate single crystals with different engineered-domain sizes. *J. Appl. Phys.* **98**, 014109 (2005).
9. Hlinka, J., Ondrejkovic, P. & Marton, P. The piezoelectric response of nanotwinned $BaTiO_3$. *Nanotechnology* **20**, 105709 (2009).
10. Ahluwalia, R., Lookman, T., Saxena, A. & Cao, W. Domain-size dependence of piezoelectric properties of ferroelectrics. *Phys. Rev. B* **72**, 014112 (2005).
11. Jaffe, B., Cook, W. R. & Jaffe, H. *Piezoelectric Ceramics* (Academic, 1971).
12. Damjanovic, D. Comments on origins of enhanced piezoelectric properties in ferroelectrics. *IEEE Trans. Ultrason. Ferroelectr. Freq. Control* **56**, 1574–1585 (2009).
13. Sun, E. W. & Cao, W. W. Relaxor-based ferroelectric single crystals: growth, domain engineering, characterization and applications. *Prog. Mater. Sci.* **65**, 124–210 (2014).
14. Zhang, S. J. et al. Advantages and challenges of relaxor-PT ferroelectric crystals for electroacoustic transducers—a review. *Prog. Mater. Sci.* **68**, 1–66 (2015).
15. Haertling, G. H. Ferroelectric ceramics: history and technology. *J. Am. Ceram. Soc.* **82**, 797–818 (1999).
16. Ruan, W. et al. Large electro-optic effect in La-doped $0.75Pb(Mg_{1/3}Nb_{2/3})O_3$-$0.25PbTiO_3$ transparent ceramic by two-stage sintering. *J. Am. Ceram. Soc.* **93**, 2128–2131 (2010).
17. Glazer, A. M., Lewis, J. G. & Kaminsky, W. An automatic optical imaging system for birefringent media. *Proc. R. Soc. Lond. A* **452**, 2751–2765 (1996).
18. Shvartsman, V. & Kholkin, A. Domain structure of $0.8Pb(Mg_{1/3}Nb_{2/3})O_3$-$0.2PbTiO_3$ studied by piezoresponse force microscopy. *Phys. Rev. B* **69**, 014102 (2004).
19. Bai, F., Li, J. & Viehland, D. Domain hierarchy in annealed (001)-oriented Pb $(Mg_{1/3}Nb_{2/3})O_3$-*x*% $PbTiO_3$ single crystals. *Appl. Phys. Lett.* **85**, 2313–2315 (2004).
20. Sato, Y., Hirayama, T. & Ikuhara, Y. Real-time direct observations of polarization reversal in a piezoelectric crystal: $Pb(Mg_{1/3}Nb_{2/3})O_3$-$PbTiO_3$ studied via in situ electrical biasing transmission electron microscopy. *Phys. Rev. Lett.* **107**, 187601 (2011).
21. Kleemann, W. Relaxor ferroelectrics: cluster glass ground state via random fields and random bonds. *Phys. Stat. Sol. B* **251**, 1993–2002 (2014).
22. Bokov, A. A. & Ye, Z. G. Recent progress in relaxor ferroelectrics with perovskite structure. *J. Mater. Sci.* **41**, 31–52 (2006).
23. Krogstad, M. J. et al. The relation of local order to material properties in relaxor ferroelectrics. *Nat. Mater.* **17**, 718–724 (2018).
24. Takenaka, H., Grinberg, I., Liu, S. & Rappe, A. M. Slush-like polar structures in single-crystal relaxors. *Nature* **546**, 391–395 (2017).
25. Wan, X. M., Luo, H. S., Wang, J., Chan, H. L. W. & Choy, C. L. Investigation on optical transmission spectra of $(1–x)Pb(Mg_{1/3}Nb_{2/3})O_3$-$xPbTiO_3$ single crystals. *Solid State Commun.* **129**, 401–405 (2004).
26. Wemple, S. Polarization fluctuations and the optical-absorption edge in $BaTiO_3$. *Phys. Rev. B* **2**, 2679–2689 (1970).
27. Ogawa, T., Matsushita, M. & Tachi, Y. Domain controlled piezoelectric single crystal and fabrication method therefor. US Patent 2003/0178914 A1 (2003).
28. Yamashita, Y., Yamamoto, N., Hosono, Y. & Itsumi, K. Piezoelectric transducer, ultrasonic probe, and piezoelectric transducer manufacturing method. US Patent 2015/0372219 A1 (2015).
29. Chang, W. Y. et al. Dielectric and piezoelectric properties of $0.7Pb(Mg_{1/3}Nb_{2/3})O_3$-$0.3PbTiO_3$ single crystal poled using alternating current. *Mater. Res. Lett.* **6**, 537–544 (2018).
30. Xu, J. et al. Piezoelectric performance enhancement of $Pb(Mg_{1/3}Nb_{2/3})O_3$-$0.25PbTiO_3$ crystals by alternating current polarization for ultrasonic transducer. *Appl. Phys. Lett.* **112**, 182901 (2018).
31. Budimir, M., Damjanovic, D. & Setter, N. Piezoelectric response and free-energy instability in the perovskite crystals $BaTiO_3$, $PbTiO_3$, and $Pb(Zr,Ti)O_3$. *Phys. Rev. B* **73**, 174106 (2006).
32. Sluka, T., Tagantsev, A. K., Damjanovic, D., Gureev, M. & Setter, N. Enhanced electromechanical response of ferroelectrics due to charged domain walls. *Nat. Commun.* **3**, 748 (2012).
33. Xiang, Y., Zhang, R. & Cao, W. Optimization of piezoelectric properties for $[001]_c$ poled 0.94 Pb $(Zn_{1/3}Nb_{2/3})O_3$–0.06 $PbTiO_3$ single crystals. *Appl. Phys. Lett.* **96**, 092902 (2010).

Publisher's note Springer Nature remains neutral with regard to jurisdictional claims in published maps and institutional affiliations.

© The Author(s), under exclusive licence to Springer Nature Limited 2020

Methods

Sample preparation

To achieve high transparency in the rhombohedral PMN-PT crystals, we choose crystal compositions that avoid the presence of multiple phases, such as a mixture of rhombohedral, monoclinic and orthorhombic phases within an MPB region. In particular, we selected the 28% PT composition to circumvent the MPB region (around 33% PT). The PMN-28PT single crystals were grown by a modified Bridgman method at Xi'an Jiaotong University. The crystals were oriented by an X-ray diffraction (XRD) method with the x, y and z axes along the [100], [010] and [001] directions, respectively, and then cut to the required dimensions for different experiments. The thickness of the samples for the domain observations and birefringence measurements was 0.175 mm. For the other experiments, the thickness of the samples was in the range of 0.5 mm to 4 mm. Vacuum-sputtered gold was applied to both (001) faces of the samples to act as electrodes.

The a.c.- and d.c.-poling experiments were performed with a ferroelectric test system (TF Analyzer 2000E, aixACCT) with a high-voltage amplifier (TREK 610E). The samples were immersed in silicone oil during the poling process. For a.c. poling, a bipolar triangle wave was applied to the samples with a frequency of 0.1–100 Hz, a cycle number of 5–20, an amplitude of 5 kV cm^{-1} and a poling temperature of 20–60 °C (ref. [34]). We discovered that essentially all of the 71° domain walls could be effectively eliminated by using a.c. electric fields with a broad range of frequencies from 0.1 to 100 Hz (see Extended Data Fig. 8). The cycle number was selected to be larger than 10, as the enhancement of dielectric permittivity was found to saturate after 10 cycles, as shown in Extended Data Fig. 9. To minimize the fluctuations in dielectric and piezoelectric properties among different samples, the frequency of the a.c. electric field was selected to be below 10 Hz, as shown Extended Data Fig. 9. To minimize the influence of internal stresses generated during polishing and sputtering of PMN-28PT crystals, a thermal annealing process was applied to the PMN-28PT crystals before a.c. poling[34]. Specifically, the samples were first annealed at 300 °C for 5 h and then slowly cooled to room temperature. The samples then remained at room temperature for 5–7 days until the dielectric loss was reduced from approximately 4–5% after the annealing to around 2%. For the d.c. poling, a conventional poling process used for PMN-PT crystals was adopted, with a d.c. electric field amplitude of 5 kV cm^{-1} and a dwelling time of 5 min.

For the optical and XRD experiments, the gold electrodes were removed by a solution of potassium iodide and iodine (the mass ratio of KI:I_2:H_2O was 4:1:40) without affecting the polarization. The (001) surfaces were then carefully polished to optical quality using diamond polishing paste and decreasing the average grit size down to 0.05 μm. For the electro-optic measurements, a thin layer of gold film (~15 nm) was deposited on the polished surfaces to act as electrodes. Silver leads were attached using conductive epoxy to apply a voltage.

Here, we would like to note that there are two technical issues associated with the idea of using crystals poled along the [111] direction and then cut along the [001] direction to achieve both a high d_{33} and light transparency rather than the a.c. poling employed in this work.

(1) The limitations of crystal size and difficulty in achieving a single domain state by poling [111] oriented rhombohedral crystals. For example, if one needs a [001]-oriented crystal plate with a size of 20 mm × 20 mm × 1 mm (the practical size of piezoelectric materials for medical transducers is in the range of 20–60 mm), one first needs a [111]-oriented crystal with the size of ~30 × 30 × 30 mm^3. It is almost impossible to pole a crystal with a thickness of 30 mm along its spontaneous polarization direction as the internal stresses that develop during poling induce severe cracking[35]. In addition, one cannot guarantee a homogeneous composition for the [001]-oriented crystal plates made using this process because of the composition segregation along the growth direction of Bridgman-grown PMN-PT crystal boules.

(2) The instability of a single-domain state and the issue of depolarization. Preparing the [111]-poled samples with a rotated d_{33} involves high-temperature processes, such as attaching a crystal to a sample holder for cutting, heat generation during cutting and sputtering transparent electrodes (the temperature required for sputtering ITO electrodes is approximately 300–600 °C). One may argue that we can adopt careful, low-temperature processes and utilize low-temperature transparent electrodes (such as silver nanowires) to prepare the samples. However, based on our experience, this is a difficult task, as we need to use special binders and sample holders and drastically slow down the cutting speed of the cutting machine; the adhesion of electrodes would also be substantially affected by using silver nanowires in place of ITO. Even if all of these precautions and approaches are followed, the samples are still likely to be depolarized to some extent because of the instability of a single-domain state. In addition, the [001]-oriented samples made by this process cannot be re-poled if they are de-poled accidentally. This is due to the fact that we cannot recover the original [111]-oriented samples.

Dielectric and piezoelectric measurements

The d_{33} values were determined by a combination of a quasi-static d_{33} meter (ZJ-6A) and an electric-field-induced strain measurement. The electric-field-induced strain was measured by a ferroelectric test system (TF Analyzer 2000E, aixACCT) with a laser interferometer (SIOS SP-S 120E). The dielectric permittivity was measured using an LCR meter (E4980A, KEYSIGHT technologies). To study the temperature stability of the properties, the d_{33} and k_{33} values of PMN-PT crystals are determined by the resonance method according to IEEE standard.

Optical transmittance measurements

Transmission spectra were measured with an ultraviolet–visible–infrared spectrophotometer (JASCO V-570) at wavelengths ranging from 300 to 2,500 nm. The incident light was set to transmit through the crystal along the poling direction, which was perpendicular to the (001) surface.

According to the Fresnel equations, the reflection loss at two faces of the crystal plate was calculated from 450 to 850 nm through:

$$R = \frac{(n-1)^2}{n^2+1} \tag{1}$$

where n is the wavelength-dependent index of refraction, calculated from the Sellmeier equation for a PMN-28PT single crystal given in refs. [36,37].

The effective loss coefficient α_{eff}, a combination of the scattering coefficient κ and the absorption coefficient α ($\alpha_{\text{eff}} = \kappa + \alpha$), was calculated using the transmission data from samples of different thicknesses:

$$\alpha_{\text{eff}} = -\frac{\ln(T_2/T_1)}{t_2 - t_1} \tag{2}$$

where T_1 and T_2 are the transmittances of the two samples with thicknesses t_1 and t_2, respectively.

Optical domain characterizations

PLM. The domain patterns and their extinction behaviours were observed using a PLM with a 0°/90° crossed polarizer/analyser pair (OLYMPUS BX51). The optical retardation was measured using a thick Berek compensator (OLYMPUS U-CTB, ~0–10λ) and an interference filter (IF546; wavelength, λ = 546.1 nm). The birefringence was calculated as the ratio of the retardation to the sample thickness. In the following, we would like to explain the cancellation effect of birefringence as light travels across a 71° domain wall. For a single-domain rhombohedral ferroelectric, the parameters Δn_1 and Δn_2 are the birefractive indices of two different domains on both sides of a 71° domain wall.

Because the principal axes of the optical indicatrices of the domains on both sides of a 71° domain wall (for example, the domains with polar vectors along [111] and [1$\bar{1}$1] directions) are perpendicular to each other on the (001) plane, the relation between Δn_1 and Δn_2 is $\Delta n_1 = -\Delta n_2$. Thus as the light travels across a 71° domain wall, the measured birefringence can be expressed by the following equation:

$$\Delta n^* = \frac{\Delta L}{d} = \frac{\Delta n_1 d_1 + \Delta n_2 d_2}{d_1 + d_2} = \Delta n_1 \frac{d_1 - d_2}{d} \quad (3)$$

where d_1 and d_2 are the lengths of optical path within the [111] and [1$\bar{1}$1] domains, respectively, ΔL is the optical retardation caused by birefringence, and d is a sum of d_1 and d_2. It is obvious that the measured birefringence will be quite small if the values of d_1 and d_2 are similar.

BIM. The domain orientation measurements were performed using BIM equipment (Metripol, Oxford Cryosystems). Monochromatic light with a wavelength of 590 nm was used as the light source. A quarter-wave plate and a polaroid (P_2) were placed at a 45° position to produce circularly polarized light. The circularly polarized light was converted to elliptical polarization after passing through an optically anisotropic specimen. The light then transmits through a linear analyser (P_2) rotating about the microscope axis at a frequency of ω. Finally, the intensity measured by the charge-coupled device (CCD) camera as a function of ω is given by

$$I = \frac{1}{2} I_0 \{1 + \sin[2(\omega t - \varphi)] \sin\delta\} \quad (4)$$

where t is the time, φ is the angle between the horizontal direction and the principal axis of the optical indicatrix, δ is the phase shift introduced to the light rays passing through the anisotropic sample with a certain thickness, and I_0 is the intensity of the unpolarized light. After rotating the analyser ten times, it is possible to obtain the intensity of each pixel on the recorded image, refine the I_0, $|\sin\delta|$ and φ values, and construct the false-colour images.

High-resolution XRD experiments

High-resolution, single-crystal XRD experiments were carried out to analyse the {222} Bragg reflections for (001)-oriented PMN-PT crystals. A high-resolution diffractometer (PANalytical X'Pert Pro MRD), equipped with Cu $K\alpha_1$ radiation, a hybrid mirror monochromator, an open Eulerian cradle and a solid-state PIXcel detector, was used for a precise two-dimensional 2θ–ω scan of the {222} Bragg peaks. The reciprocal space maps were collected with step sizes of 0.004° in ω and 0.004° in 2θ. The intensity of the patterns was accumulated along the ω or 2θ directions and then fitted to the pseudo-Voigt function:

$$f(x) = a_1 \left\{ a_4 \frac{1}{1 + \left(\frac{x - a_2}{a_3}\right)^2} + (1 - a_4) \exp\left[-\left(\frac{x - a_2}{a_3}\right)^2 \right] \right\} \quad (5)$$

where a_1 is the intensity of the peak, a_2 is the position of the peak, a_4 is the mixing parameter of the Gaussian and Lorentzian profiles, and a_3 is proportional to the full-width at half-maximum (FWHM), which can be calculated using the equation,

$$\mathrm{FWHM} = 2\sqrt{\ln 2}\, a_3 \quad (6)$$

Electro-optic measurements

The electro-optic coefficients of the samples were measured using a modified Mach–Zehnder interferometer. The light source was a 632.8-nm He–Ne laser. For the longitudinal mode, the light beam and the applied electric field were both parallel to the poling direction. In this mode, the longitudinal effective linear electro-optic coefficient γ_c^{L*} was measured, where the subscript c indicates that the coefficient is a composite of several electro-optic coefficients in the standard coordinate system (for example, r_{13} and r_{33}).

For the transverse mode, the light beam travels along the [110] direction, and the electric field was applied along the [001] poling direction of the sample. The linear electro-optic coefficients γ_{13}^* and γ_{33}^* were measured when the polarization directions of the laser beam were perpendicular and parallel to the poling direction, respectively. The transverse effective linear electro-optic coefficient (γ_c^{T*}) was calculated by the equation:

$$\gamma_c^{T*} = \gamma_{33}^* - n_0^3 \gamma_{13}^* / n_e^3 \quad (7)$$

The refractive indices were calculated from the data of single-domain crystals[36,37]. The asterisk indicates that the measured electro-optic coefficient is a combination of the inverse piezoelectric effect and the intrinsic electro-optic effect.

Phase-field simulations

The domain evolution and piezoelectric responses were obtained by performing phase-field simulations. A domain structure is described by the spatial distribution of the ferroelectric polarization **P**. The temporal evolution of the polarization and thus the domain structure is described by the time-dependent Ginzburgh–Landau equation:

$$\frac{\partial \mathbf{P}}{\partial t} = -L \frac{F(\mathbf{P})}{\delta \mathbf{P}} \quad (8)$$

where t is the time, F is the total free energy and L is the kinetic coefficient. The total free energy contains contributions from the bulk, elastic, electric and gradient energies. Details of how the phase-field method can be used to simulate the switching behaviours of ferroelectric single crystals can be found in refs. [38,39]. The Landau coefficients were adapted from ref. [40] using the experimental ferroelectric, piezoelectric and dielectric properties of PMN-28PT crystals at room temperature. On the basis of this thermodynamic potential, the calculated equilibrium phase is rhombohedral at room temperature with a spontaneous polarization of ~0.38 C m^{-2}, a relative dielectric constant of ~5,500 along [001] and a longitudinal piezoelectric coefficient of ~1,850 pC N^{-1} along [001], which are in reasonable agreement with our experiments. The electrostrictive coefficients measured by Li et al.[41] for PMN-28PT were adopted. The gradient energy coefficients were assumed to be isotropic, and the domain wall width was assumed to be ~2 nm. It should be noted here that the Landau potential used in this work represents the average free energy of a single-domain PMN-28PT crystal, which incorporates the impacts of the nanoscale heterogeneous polar regions (several nanometres) in the free energy and electromechanical properties[42].

To simulate the a.c. and d.c. poling processes, we first obtained an unpoled domain structure from a random noise distribution of the polarization within a quasi-two-dimensional grid with $512\Delta x \times 512\Delta x \times 1\Delta x$ grid points ($\Delta x = 1$ nm). A low-frequency triangle wave was then applied to mimic the a.c. poling, whereas a single-step square wave was used to represent the d.c. poling. The magnitude of the poling electric field was 10 kV cm^{-1}. We performed phase-field simulations at different mechanical boundary conditions: the stress-free condition, which assumes the averaged stress of the simulated system is zero; and the clamped condition, which assumes the averaged strain is zero. Figure 1 shows the simulated results for the clamped condition, and the simulation results under stress-free conditions are presented in Extended Data Fig. 3b. The practical condition in the experiments is probably between these two extreme mechanical conditions. The conclusion that the sizes of the 71° domains in a.c.-poled samples are always much larger than the d.c.-poled ones holds for both mechanical boundary conditions, while the 109° domain layer thickness is similar

in both a.c.- and d.c.-poled samples. It is interesting to note that the a.c. poling can lead to a completely layered 109° domain structure without 71° domain walls under the stress-free condition.

The ε_{33} and d_{33} values were obtained by evaluating the variations of polarization and longitudinal strain under a small electric field of 0.5 kV cm^{-1} along the [001] direction. We also calculate the free energy by applying small test electric fields (E_z is from 0 to 1 kV cm^{-1}, which is sufficiently small to avoid domain wall motion or phase transitions) and plot the average free-energy density as a function of the change of P_z along the poling direction.

The computer simulations were performed using the commercial software package μ-PRO (http://mupro.co/contact/) on the ICS-ACI Computing Systems at Pennsylvania State University and at the Extreme Science and Engineering Discovery Environment cluster, which used the Bridges system at the Pittsburgh Supercomputing Center[43,44].

Data availability

The data that support the findings of this study are available on request from the corresponding authors.

34. Li, F. et al. Transparent ferroelectric crystals with ultrahigh piezoelectricity. Provisional US Patent 16/541,309 (2019).
35. Li, F., Wang, L., Jin, L., Xu, Z. & Zhang, S. J. Achieving single domain relaxor-PT crystals by high temperature poling. *CrystEngComm* **16**, 2892–2897 (2014).
36. Wan, X. M., Chan, H. L. W., Choy, C. L., Zhao, X. & Luo, H. Optical properties of (1–x) $Pb(Mg_{1/3}N_{b2/3})O_3$-x$PbTiO_3$ single crystals studied by spectroscopic ellipsometry. *J. Appl. Phys*. **96**, 1387–1391 (2004).
37. Wan, X. M. et al. Refractive indices and linear electro-optic properties of (1–*x*) $Pb(Mg_{1/3}N_{b2/3})O_3$-*x*$PbTiO_3$ single crystals. *Appl. Phys. Lett*. **85**, 5233–5235 (2004).
38. Wang, J., Shi, S. Q., Chen, L.-Q., Li, Y. & Zhang, T. Y. Phase-field simulations of ferroelectric/ferroelastic polarization switching. *Acta Mater*. **52**, 749–764 (2004).
39. Wang, J., Wang, B. & Chen, L.-Q., Understanding, predicting, and designing ferroelectric domain structures and switching guided by the phase-field method. *Annu. Rev. Mater. Res*. **49**, 127–152 (2019).
40. Khakpash, N., Khassaf, H., Rossetti, G. A. Jr & Alpay, S. P. Misfit strain phase diagrams of epitaxial PMN-PT films. *Appl. Phys. Lett*. **106**, 082905 (2015).
41. Li, F., Jin, L., Xu, Z., Wang, D. & Zhang, S. J. Electrostrictive effect in $Pb(Mg_{1/3}Nb_{2/3})O_3$-*x* $PbTiO_3$ crystals. *Appl. Phys. Lett*. **102**, 152910 (2013).
42. Li, F. et al. The origin of ultrahigh piezoelectricity in relaxor-ferroelectric solid solution crystals. *Nat. Commun*. **7**, 13807 (2016).
43. Towns, J. et al. XSEDE: accelerating scientific discovery. *Comput. Sci. Eng*. **16**, 62–74 (2014).
44. Nystrom, N. A., Levine, M. J., Roskies, R. Z. & Scott, J. R. Bridges: a uniquely flexible HPC resource for new communities and data analytics. In *Proc. 2015 Annual Conference on Extreme Science and Engineering Discovery Environment* (ACM, 2015); https://doi.org/10.1145/2792745.2792775.

Acknowledgements F.L. and Z.X. acknowledge the support of the National Natural Science Foundation of China (grant numbers 51922083, 51831010 and 51761145024), the development programme of Shaanxi province (grant number 2019ZDLGY04-09) and the 111 Project (B14040). B.W. and L.Q.C. acknowledge the support of the US National Science Foundation under the grant number DMR-1744213 and Materials Research Science and Engineering Center (MRSEC) grant number DMR-1420620. N.Z. thanks the NSFC for support under grant number 1604123. The computer simulations were performed on the ICS-ACI Computing Systems at Pennsylvania State University through the Penn State Institute for Cyber Science and at the Extreme Science and Engineering Discovery Environment cluster supported by National Science Foundation grant number ACI-1548562; the Bridges system was used, which is supported by NSF award number ACI-1445606 at the Pittsburgh Supercomputing Centre under the allocation DMR170006. S.Z. thanks the ONRG (grant number N62909-18-12168) and ARC (grant number FT140100698) for support. T.R.S. was supported by the US ONR.

Author contributions The work was conceived and designed by S.Z., L.Q.C. and F.L. C.Q. performed the piezoelectric and optical experiments. F.L. and Z.X. supervised the piezoelectric and dielectric measurements. N.Z. and F.L. supervised the optical experiments. B.W. performed the phase-field simulations and discussed with F.L. L.Q.C. supervised the simulation work. J.L. assisted with the piezoelectric measurements. N.Z. and D.W. performed XRD experiments. Y.W. and H.T. assisted with the optical measurements. F.L. drafted the manuscript, S.Z., N.Z., L.Q.C. and T.R.S. revised the manuscript and all authors discussed the results.

Competing interests The authors declare no competing interests.

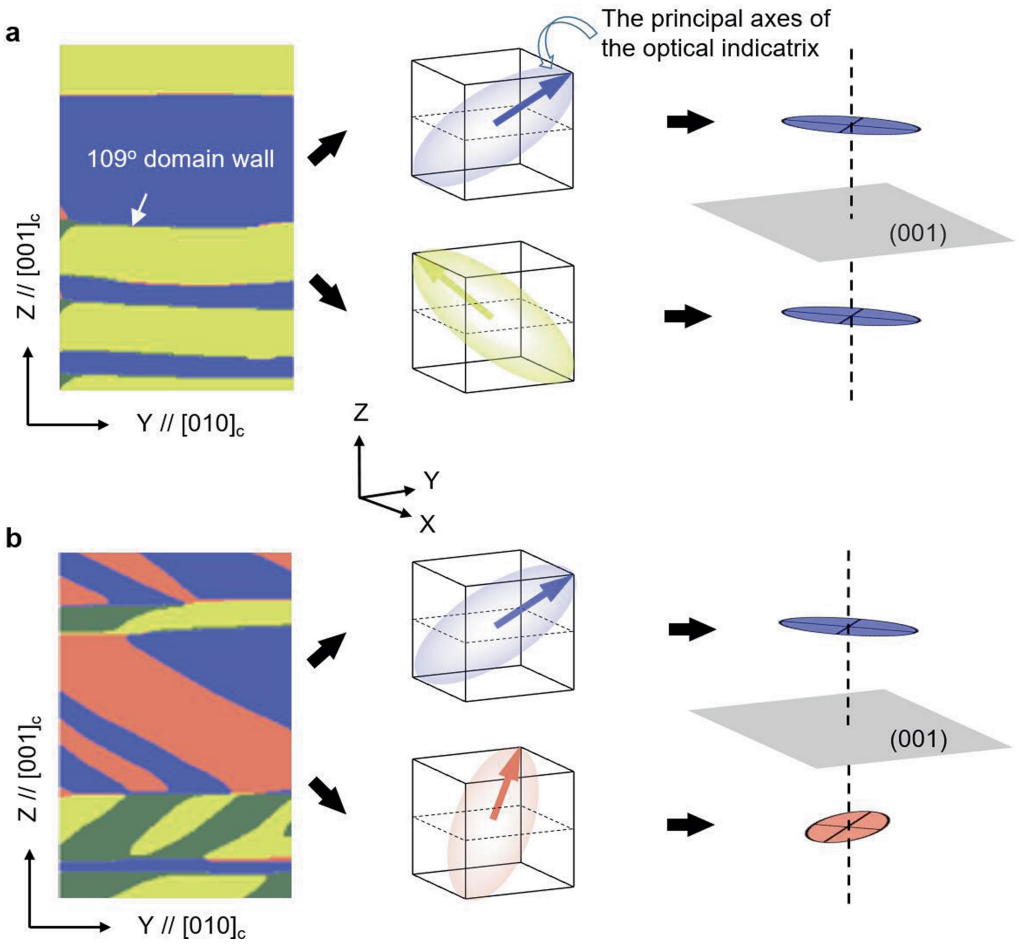
Additional information

Supplementary information is available for this paper at https://doi.org/10.1038/s41586-019-1891-y.

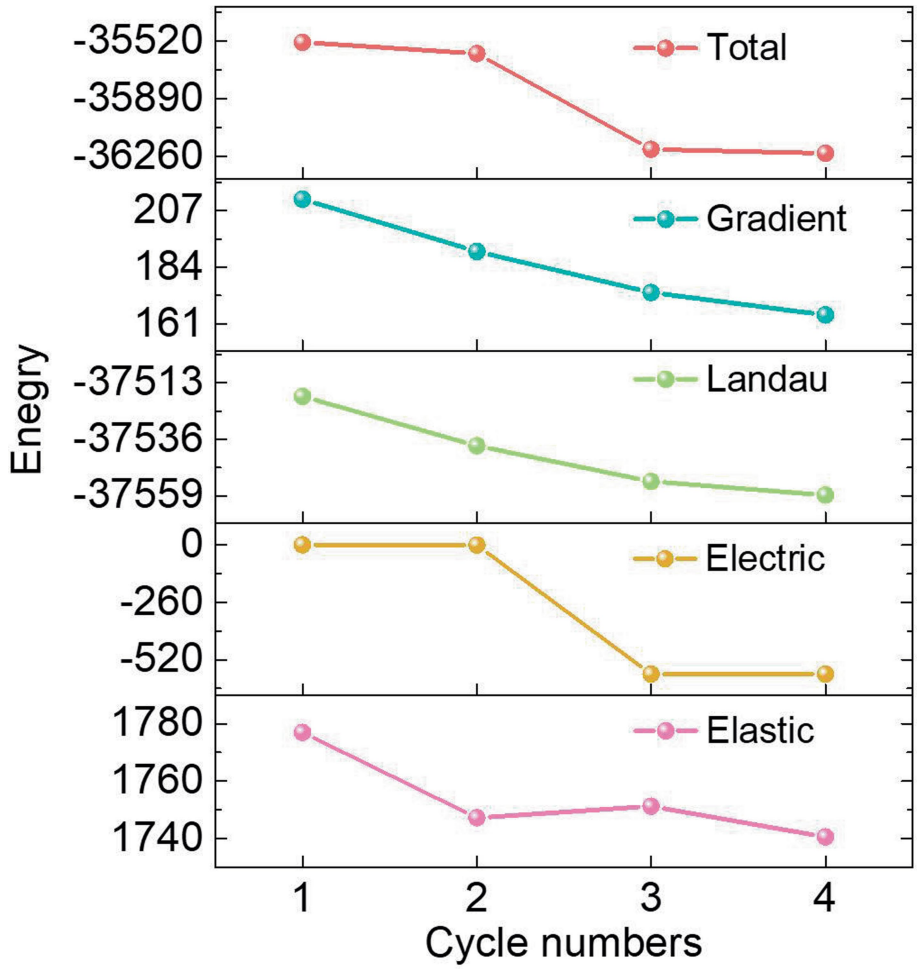
Correspondence and requests for materials should be addressed to Z.X., L.-Q.C. or F.L.

Peer review information *Nature* thanks Wook Jo and the other, anonymous, reviewer(s) for their contribution to the peer review of this work.

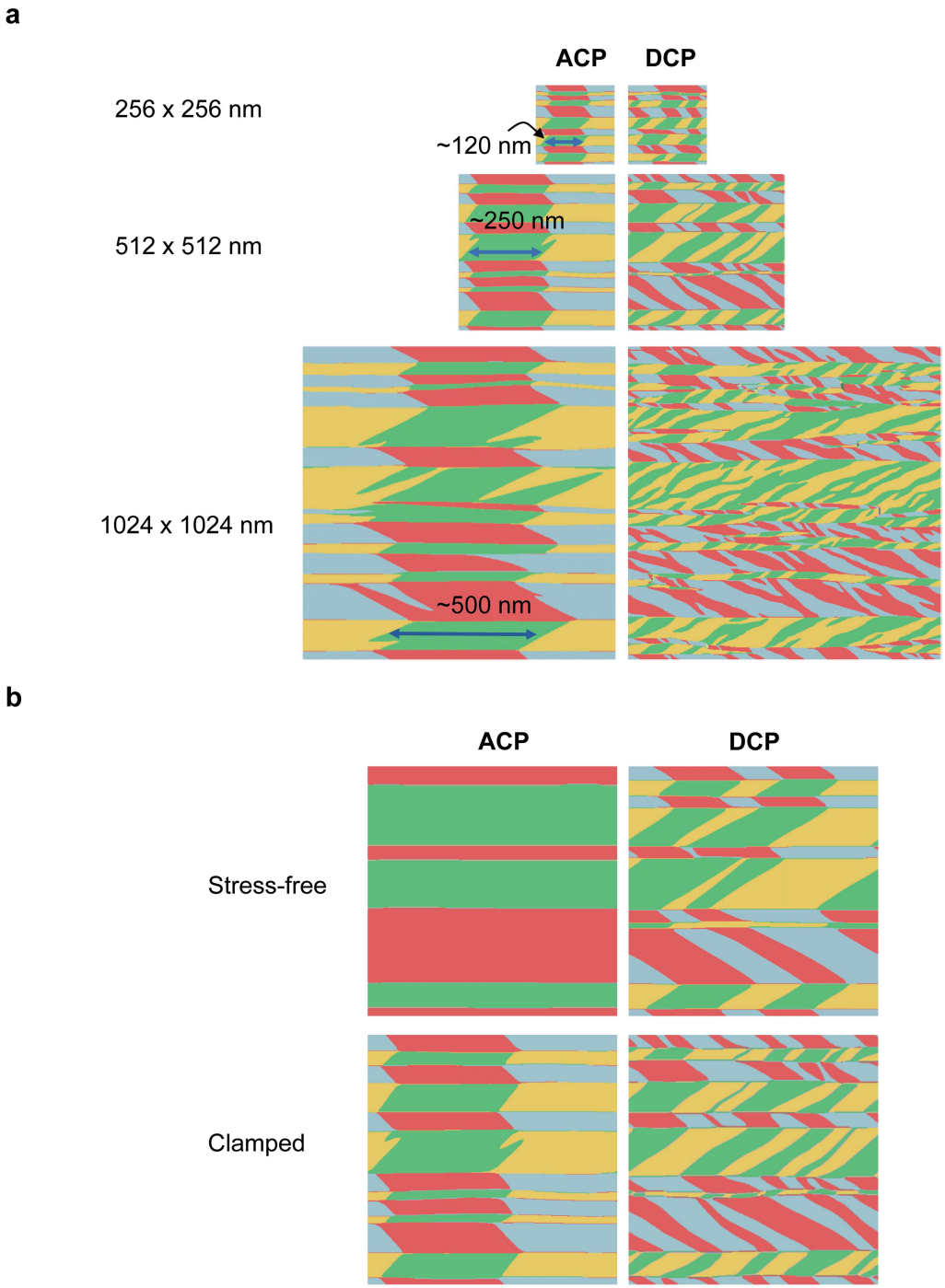
Reprints and permissions information is available at http://www.nature.com/reprints.



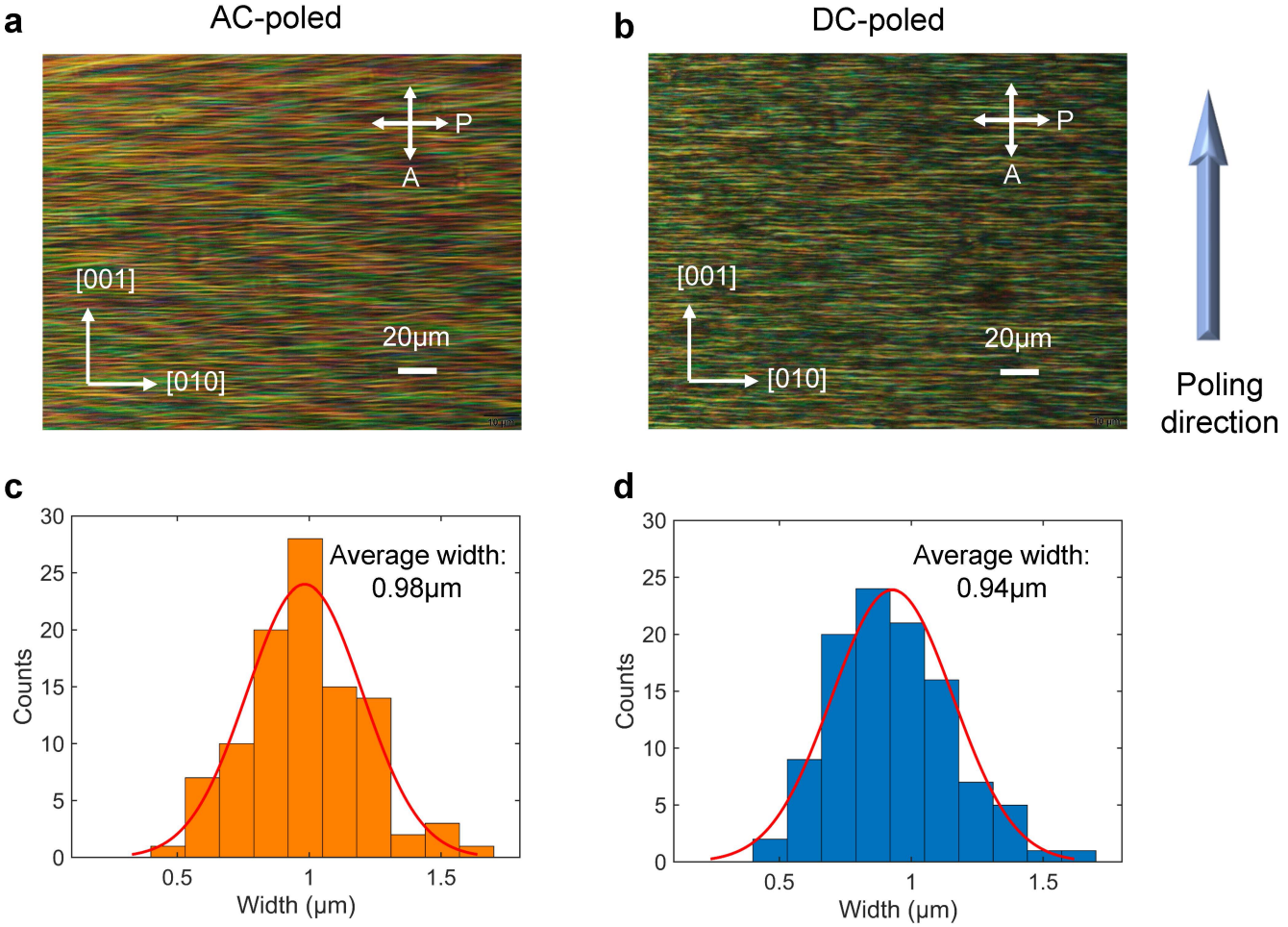
Extended Data Fig. 1 | Schematic diagrams of the projections of optical indicatrices on both sides of a domain wall. a, 109° domain wall; **b**, 71° domain wall. The prerequisite for the light scattering and reflection at an interface is the difference in refractive indices between the optical media on each side of the interface. As shown here, the principal axes of the optical indicatrix projected on the (001) plane are the same for domains on each side of a 109° domain wall. Thus, n_o and n_e do not change as the light crosses a 109° domain wall, resulting in the absence of light scattering and/or reflection. In contrast, the principal axis of the optical indicatrix projected on the (001) plane rotates by 90° as the light travels across a 71° domain wall, resulting in the alternating of refractive indices n_o and n_e. This is the reason that 71° domain walls scatter and/or reflect the light.



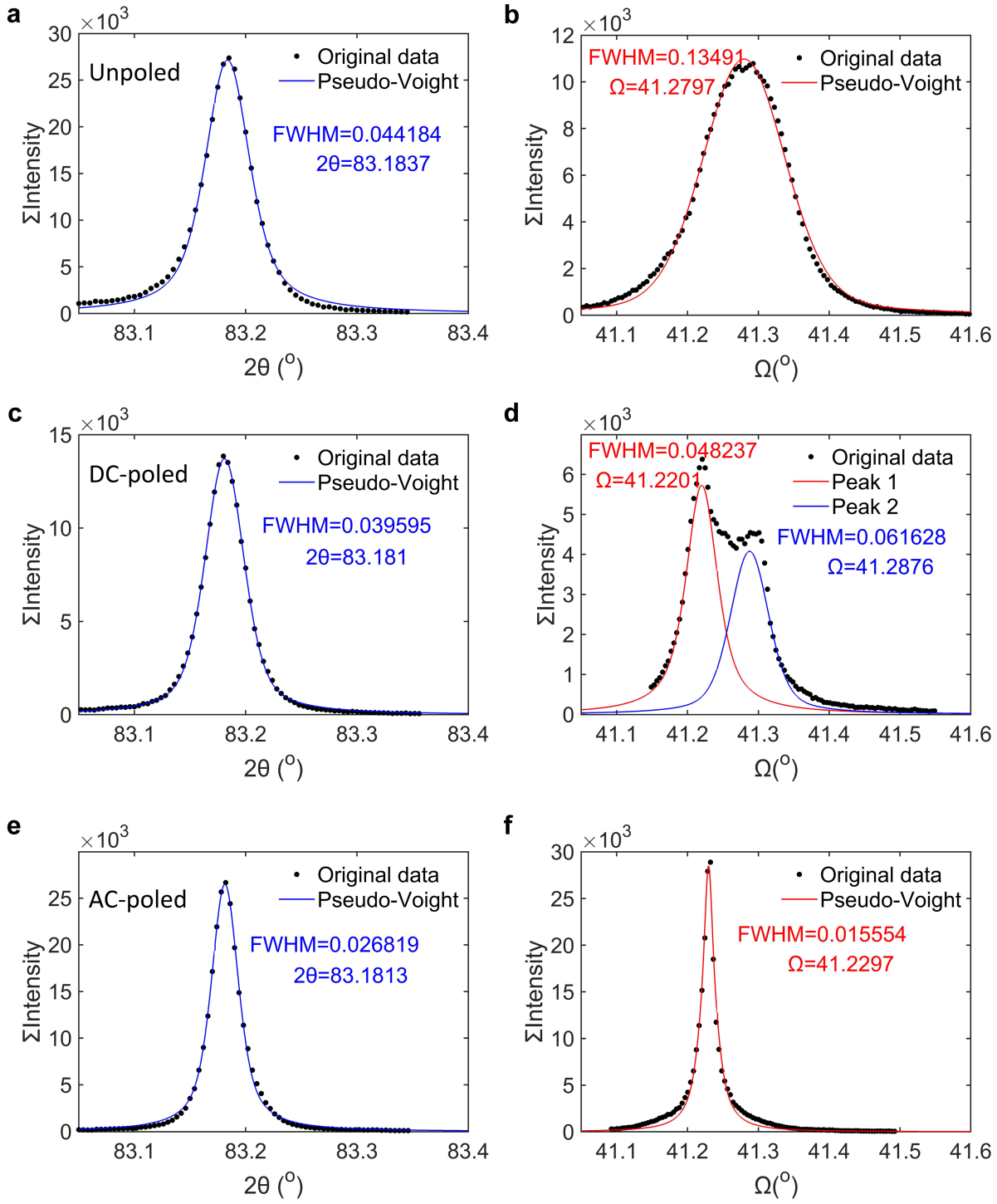
Extended Data Fig. 2 | The variation in various energies of PMN-28PT during the first four cycles of a.c. poling. The data are obtained by phase-field simulations. Here we plot the normalized energies, which are dimensionless.



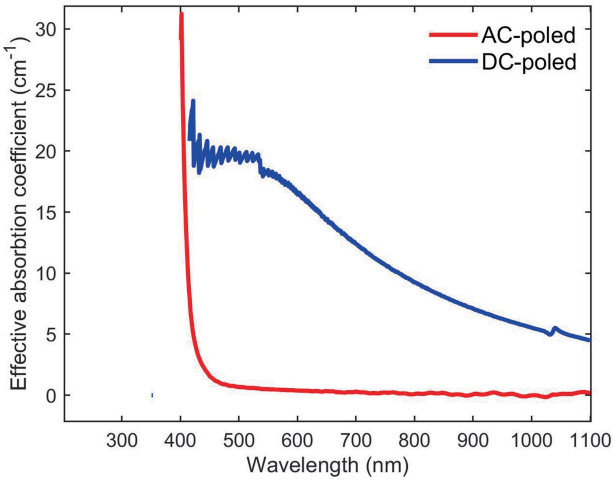
Extended Data Fig. 3 | Effects of system size and mechanical boundary conditions on the a.c.- and d.c.-poled domain structures from phase-field simulations. **a**, Effects of system size (at the clamped boundary condition). **b**, Effects of the mechanical boundary condition (the scale of the simulation is 512 × 512 nm).



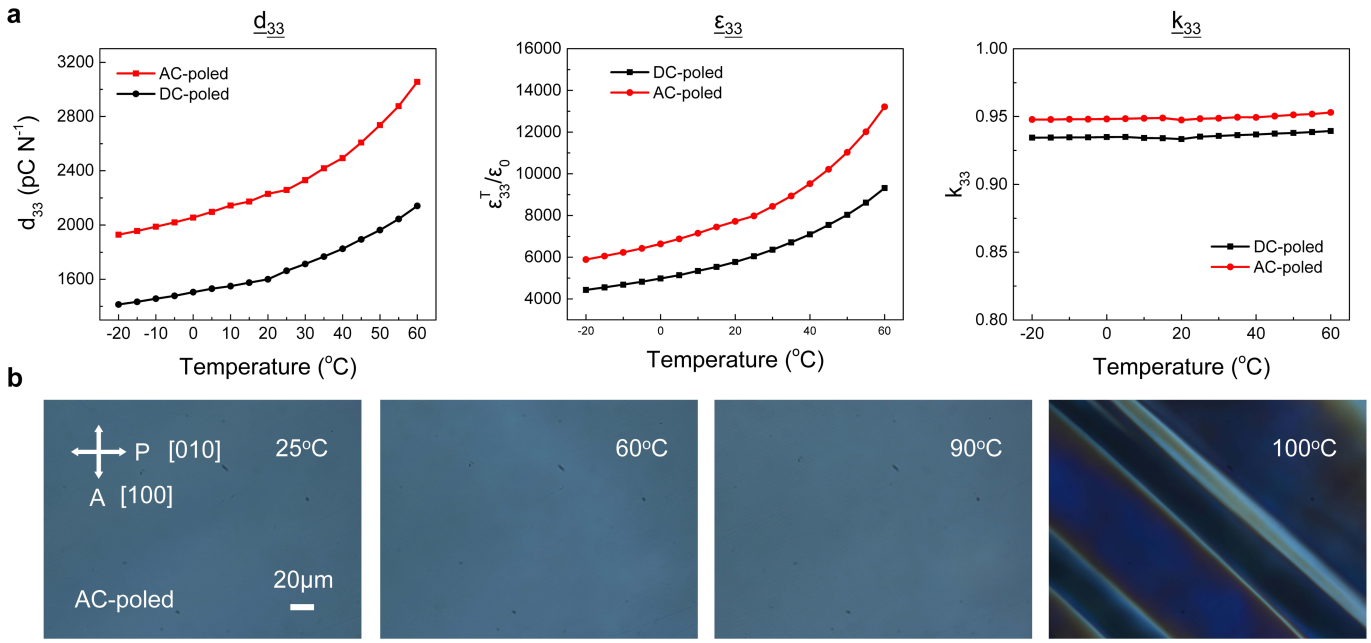
Extended Data Fig. 4 | Characterization of the domain size along the poling direction for [001]-oriented rhombohedral PMN–PT crystals. a, PLM images on the (100) face for [001]-poled PMN-28PT crystals under a.c. poling. **b**, PLM images on the (100) face for [001]-poled PMN-28PT crystals under d.c. poling. **c**, Distribution of the thickness of laminar domains for the a.c.-poled sample measured from **a**. **d**, Distribution of the thickness of laminar domains for the d.c.-poled sample measured from **b**. The thickness of the samples is around 100 μm. As shown in this figure, no clear difference is observed for the thickness of laminar domains between a.c.- and d.c.-poled samples.



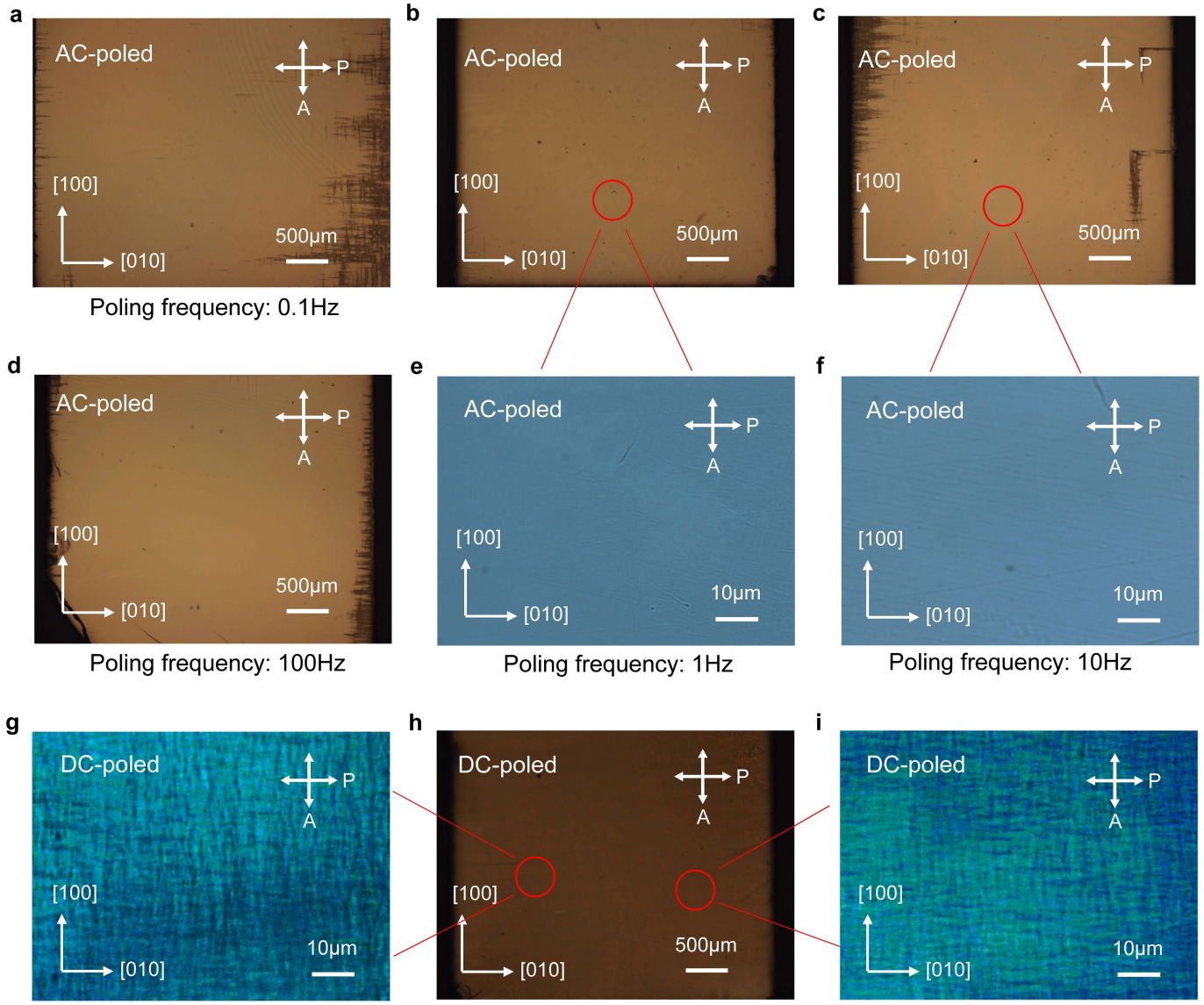
Extended Data Fig. 5 | Pseudo-Voight fittings of the {222} diffraction peaks at high-2θ. a,**b**, The unpoled sample. **c**,**d**, The d.c.-poled sample. **e**,**f**, The a.c.-poled sample. **a**,**c**,**e**, The intensity of the patterns accumulated along Ω. **b**,**d**,**f**, The intensity of the patterns accumulated along 2θ.



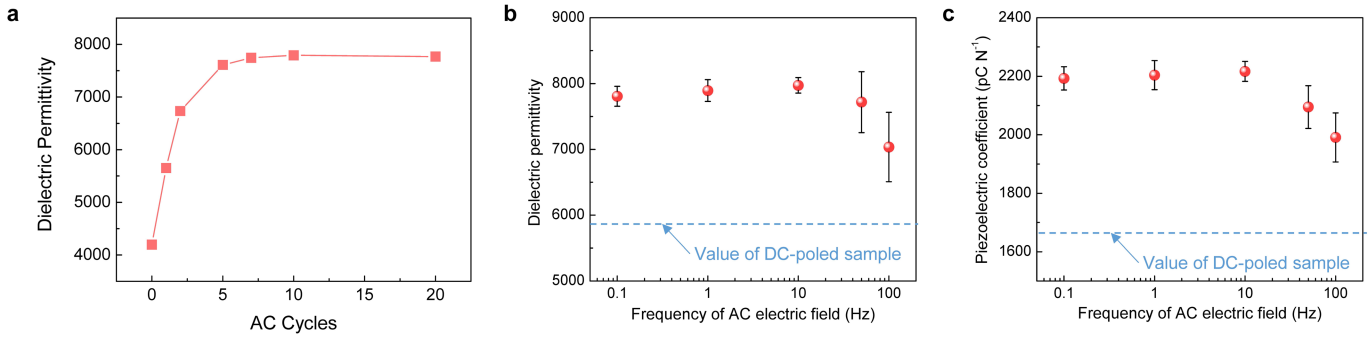
Extended Data Fig. 6 | Effective light absorption coefficients of a.c.- and d.c.-poled PMN-28PT crystals.



Extended Data Fig. 7 | The temperature stability of a.c.- and d.c.-poled PMN-28PT crystals. a, d_{33}, $\varepsilon_{33}^{T}/\varepsilon_0$ and k_{33} as a function of temperature. The dwelling time for each testing temperature is 10 min. **b**, Domain structure of a.c.-poled PMN-28PT crystals as a function of temperature. The temperature is increased from 25 to 100 °C at a rate of 1 °C min^{-1}. The dwelling time for each testing temperature is 30 min.



Extended Data Fig. 8 | PLM images of [001]-oriented PMN-28PT crystals with different poling conditions. a–**d**, Images obtained from the crystals poled by an a.c. electric field at frequencies of 0.1 Hz (**a**), 1 Hz (**b**), 10 Hz (**c**) and 100 Hz (**d**), respectively. **e**, **f**, Enlargements of the regions in **b** and **c**, respectively. **g**–**i**, Images obtained from the crystals poled by a d.c. electric field. **g**, **i**, Magnifications of the two regions circled in **h**. The thickness of the samples is 0.5 mm. There are numerous cross-like domain walls in d.c.-poled samples, whereas these types of domain wall are removed by an a.c. electric field.



Extended Data Fig. 9 | Dielectric permittivity and piezoelectric coefficient of the a.c.-poled PMN-28PT crystal as a function of the cycle number and frequency. a, Dielectric permittivity as a function of the cycle number. **b**, Dielectric permittivity as a function of the frequency. **c**, Piezoelectric coefficient as a function of the frequency. Five samples are used for each frequency. The error bars indicate the s.d. of the corresponding data.

Extended Data Table 1 | Electromechanical and electro-optical properties of [001]-oriented PMN-28PT crystals via a.c.- and d.c.-poling

Properties of PMN-28PT	*DC*-poled	*AC*-poled
Free dielectric permittivity ($\varepsilon_{33}^{T}/\varepsilon_0$)	5800±120	7800±230
Clamped dielectric permittivity	780±50	840±60
Dielectric loss at 1 kHz (%)	0.48±0.02	0.30±0.04
Piezoelectric coefficient (pC N^{-1})	1670±30	2190±40
Electromechanical coupling factor k_{33}	0.93±0.01	0.94±0.01
Phase transition temperature T_{RT} (°C)	93±1	93±1
Curie temperature T_C (°C)	132±2	132±2
Birefringence (10^{-3})	1.89±0.55	23.7±0.7
Effective electro-optical coefficient γ_{33}^{*} (pm V^{-1}) @633nm light beam//[110]	-	227±23
Effective electro-optical coefficient γ_{13}^{*} (pm V^{-1}) @633nm light beam//[110]	-	115±11
Effective electro-optical coefficient γ_c^{L*} (pm V^{-1}) @633nm light beam//[001]	-	153±20

To measure γ_c^{L*}, both the applied electric field and the light beam are along the [001] direction. To measure coefficients γ_{33}^{*} and γ_{13}^{*}, the applied electric field is along the [001] direction, and the light beam is along the [110] direction. Note: it is difficult to obtain accurate electro-optical coefficients for d.c.-poled samples owing to the strong light scattering by the high density of ferroelectric domain walls. The errors indicate the s.d. of the corresponding data (more than five samples/data points are used for each measurement).

Archimedean lattices emerge in template-directed eutectic solidification

https://doi.org/10.1038/s41586-019-1893-9

Received: 1 April 2019

Accepted: 11 October 2019

Published online: 15 January 2020

Ashish A. Kulkarni[1,2,3], Erik Hanson[4], Runyu Zhang[1,2,3], Katsuyo Thornton[4] & Paul V. Braun[1,2,3,5]*

Template-directed assembly has been shown to yield a broad diversity of highly ordered mesostructures[1,2], which in a few cases exhibit symmetries not present in the native material[3–5]. However, this technique has not yet been applied to eutectic materials, which underpin many modern technologies ranging from high-performance turbine blades to solder alloys. Here we use directional solidification of a simple AgCl-KCl lamellar eutectic material within a pillar template to show that interactions of the material with the template lead to the emergence of a set of microstructures that are distinct from the eutectic's native lamellar structure and the template's hexagonal lattice structure. By modifying the solidification rate of this material–template system, trefoil, quatrefoil, cinquefoil and hexafoil mesostructures with submicrometre-size features are realized. Phase-field simulations suggest that these mesostructures appear owing to constraints imposed on diffusion by the hexagonally arrayed pillar template. We note that the trefoil and hexafoil patterns resemble Archimedean honeycomb and square–hexagonal–dodecagonal lattices[6], respectively. We also find that by using monolayer colloidal crystals as templates, a variety of eutectic mesostructures including trefoil and hexafoil are observed, the former resembling the Archimedean kagome lattice. Potential emerging applications for the structures provided by templated eutectics include non-reciprocal metasurfaces[7], magnetic spin-ice systems[8,9], and micro- and nano-lattices with enhanced mechanical properties[10,11].

Eutectic materials have been considered for use as optical metamaterials[12,13] and plasmonic structures[14], and for mechanical[15] and energy-harvesting[16] applications. During solidification, the constituent species in the molten eutectic diffuse perpendicular to the solidification direction near the solidification front. The kinetics of this mass transport in the liquid just ahead of the solidification front drives arrangement of the solid phases in patterns with generally consistent length scales that are roughly inversely proportional to the square root of the solidification velocity[17]. Decades of research on solidification of binary and ternary eutectic systems indicate that only a limited set of regular mesostructures emerge, even over a broad range of processing conditions[17–21]. By engineering the heat removal, for example, the microstructure could be modified from straight to curved lamellae[21,22], or from lamellar to rod-like[23]; however, the resulting microstructures are still quite similar to those found in the native eutectic. As we describe here, this limitation can be overcome by introducing a template phase into which the eutectic melt is solidified. Although the introduction of a template has been demonstrated to drive the self-assembly of organic molecules[24] into highly ordered patterns[1,2,25,26] and new symmetries[3–5,27–29], such an approach has not been applied to any eutectic system. As we previously reviewed[30], only now is the promise of the effects of a template on a solidifying eutectic for forming new and complex eutectic mesostructures beginning to be exploited[31,32].

Here, starting with the well-studied AgCl-KCl eutectic[31–33] (see Methods for details), we examine how a template affects what would otherwise be a regular lamellar microstructure (see the scanning electron microscopy (SEM) image in Fig. 1a). The templates used in this work consist of a hexagonal lattice of Ni pillars that are 4–6 μm tall and 500–620 nm in diameter (see Fig. 1b and Methods for details), with edge gaps, g (defined in the inset of Fig. 1b), of 160–290 nm. Pillar diameters and g were selected to be comparable to the accessible range of the average lamellar spacing, λ (defined in the inset of Fig. 1a), in the AgCl-KCl lamellar eutectic. Outside the template, a lamellar structure emerges with a λ that depends on the solidification rate (see Extended Data Fig. 1a), as expected. However, inside the pillar template, there is a remarkable transition, and a broad array of solidification-rate-dependent complex mesostructures appear. When λ is commensurate with the edge gaps in the template, the pillars modify the phase separation of the eutectic such that spoke-like patterns in AgCl and KCl are realized instead of the regular lamellar structure. We designate the resultant structures as trefoil (see Fig. 1c), quatrefoil (see Fig. 1e), cinquefoil (see Fig. 1f) and hexafoil (see Fig. 1g), based on the number of KCl spokes per unit cell of the template (see schematic in Extended Data Fig. 2). Remarkably, the trefoil pattern resembles the Archimedean honeycomb lattice (see schematic in Fig. 1d) of roughly hexagonally shaped AgCl and KCl domains. In contrast, the hexafoil pattern resembles the Archimedean

[1]Department of Materials Science and Engineering, University of Illinois at Urbana-Champaign, Champaign, IL, USA. [2]Materials Research Laboratory, University of Illinois at Urbana-Champaign, Champaign, IL, USA. [3]Beckman Institute for Advanced Science and Technology, University of Illinois at Urbana-Champaign, Champaign, IL, USA. [4]Department of Materials Science and Engineering, University of Michigan, Ann Arbor, MI, USA. [5]Department of Chemistry, University of Illinois at Urbana-Champaign, Champaign, IL, USA. *e-mail: pbraun@illinois.edu

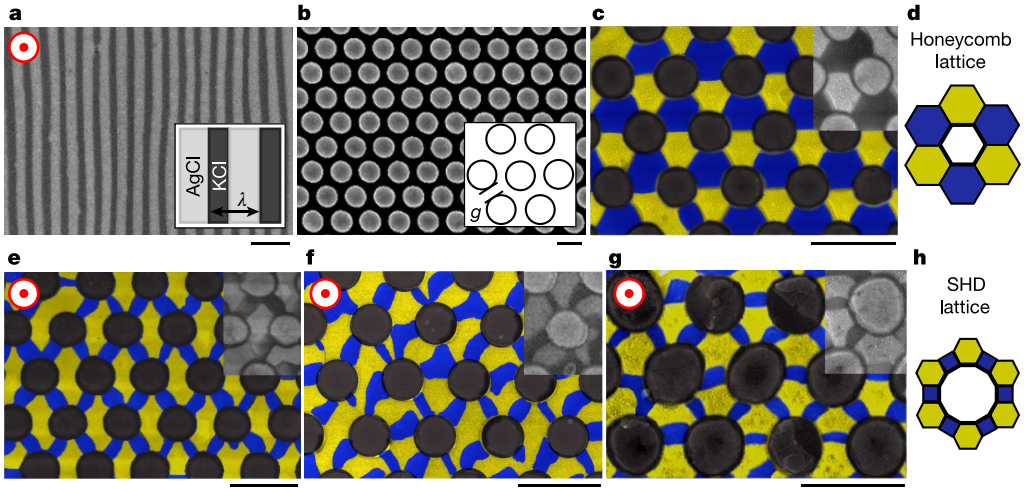


Fig. 1 | Selected microstructures formed by template-directed eutectic solidification. a, SEM image of AgCl (bright)-KCl (dark) eutectic solidified at a cooling rate of 22 °C min^{-1}. Average λ as defined in the inset is 420 nm. The solidification direction is out of the image (z axis), as indicated by the red dotted circle. **b**, Plan-view SEM image of a pillar template sample showing the hexagonal arrangement of pillars; here g = 220 nm, as defined in the inset. **c**–**h**, SEM images of microstructures, with lattice schematics shown for selected cases. **c**, Trefoil, **e**, quatrefoil, **f**, cinquefoil and **g**, hexafoil patterns with 3, 4, 5 and 6 KCl spokes per unit cell of the template (see schematic in Extended Data Fig. 2), respectively, were obtained by varying the solidification conditions. **d**, Schematic of the Archimedean honeycomb lattice (for **c**); **h**, schematic of the Archimedean SHD lattice (for **g**). Parts of the SEM images (in **c** and **e**–**g**) are false-coloured, with AgCl as yellow, KCl as blue and Ni pillars as black. Uncoloured SEM images are displayed in Extended Data Figs. 3g, 4b, c, d. All scale bars, 1 µm.

square (KCl)–hexagonal (pillars)–dodecagonal (AgCl) lattice (the SHD lattice, see schematic in Fig. 1h).

Pillar templates were infilled by molten AgCl-KCl eutectic that was directionally solidified at various rates (see Extended Data Fig. 1b and Methods for details), leading to different values of g/λ (λ determined outside the template region; see Extended Data Fig. 1c). When $g/\lambda \leq 0.25$, a disordered pattern (termed no-foil) persists (see Extended Data Fig. 3a–d). Upon increasing the solidification rate such that $0.4 < g/\lambda < 0.75$, trefoil patterns were formed (see Extended Data Fig. 3f–i). In the transition region when $g/\lambda \approx 0.3$, a mixed, predominantly trefoil, structure is present (see Extended Data Fig. 3e). For $g/\lambda \approx 0.95$, quatrefoil patterns dominate (see Extended Data Fig. 4a, b). When $g/\lambda \approx 1$, the cinquefoil pattern appears (see Extended Data Fig. 4c), and for $g/\lambda \geq 1.05$, the hexafoil pattern is obtained (see Extended Data Fig. 4d–f). In Extended Data Fig. 5 we include quantitative image analysis (see Methods for details) of the local and long-range order in these patterns. The cross-sectional view of these spoke-like patterns shows a tilted alignment of the eutectic phase boundaries (Extended Data Fig. 6a). Thermal simulations based on our experimental setup suggest that the solidification front within the bulk of the template would be slanted (Extended Data Fig. 6b) owing to the nonplanar geometry of the sample (see Methods for details). In experiments, there may be other factors that affect the orientation of the solidification front, including inhomogeneities in thermal properties. These factors are ignored in the phase-field simulations, which assume a linear thermal gradient parallel to the pillar axis, leading to a generally planar solidification front perpendicular to the pillar axis; additionally, differences in the thermal conductivities of the eutectic phases and pillars are not considered (see Methods for details). Despite these simplifications, the phase-field simulations (Fig. 2) produce structures that match the experimentally observed structure of the eutectic (Fig. 1).

In phase-field simulations (see Methods for details), when $g/\lambda = 0.163$, λ is substantially larger than the edge gap (g = 220 nm) of the template and the template does not impose order on the eutectic pattern, resulting in a no-foil structure (see Fig. 2c, j). For increased solidification rates, the simulations predict the trefoil pattern for $0.325 \leq g/\lambda \leq 0.651$ (see Fig. 2d–f, k–m), the cinquefoil pattern for $g/\lambda = 0.814$ (see Fig. 2g, n), and the hexafoil pattern for $g/\lambda \geq 0.976$ (see Fig. 2h, i, o, p). We note that phase-field simulations suggest that it is necessary to have the solidification direction parallel to the template pillar axis (that is, along the z axis; see Fig. 2a, b), rather than perpendicular to it, for these highly ordered patterns to emerge. These results reveal that at the solidification front within the template, the pillars disrupt the natural edgewise diffusion of the lamellar eutectic by compelling the diffusion fields to obey constraints set by the template geometry. To maintain the requirement of consistent diffusion path lengths[17] within this modified diffusion field, the eutectic solidifies in spoke-like patterns while preserving the overall hexagonal symmetry imposed by the template.

The patterns observed for various g/λ in experiments and phase-field simulations are mapped in Fig. 3. This map suggests that certain ranges of lamellar spacings and template edge gaps will result in a single type of spoke-like pattern, a useful finding for setting the parameters to achieve a specific mesostructure. While some experimentally observed patterns were not observed in the simulations, this is probably due to enforcement of periodic boundary conditions and the use of a domain size of one template unit cell, which constrains the system and prevents the emergence of asymmetric patterns or patterns with larger periodicities. Simulations were also performed for g = 440 nm (see Extended Data Fig. 7), showing the possibility of obtaining additional patterns by changing the pillar diameter as well as g/λ. The effects of the shape of the pillars (circular and oval) were also investigated via phase-field modelling (see Extended Data Fig. 8). The eutectic maintains the overall pattern expected for a hexagonal arrangement of pillars, but the morphologies of individual phases are strongly dependent on the exact shape of those pillars, showing the versatility of this process.

Building on these findings, template-directed eutectic solidification was also explored within a monolayer silica colloidal crystal in which spherical silica colloidal particles are assembled into a two-dimensional hexagonally close-packed structure (see Fig. 4a, b, and Extended Data Fig. 9a). The sphere diameter, d, was 560 nm (comparable to the pillars). At a solidification rate where $\lambda \approx d$, the eutectic pattern organized into a trefoil pattern (see Fig. 4c), while a hexafoil pattern (see Fig. 4d) was observed when $\lambda < d$. As expected, when the solidification rate was slow such that $\lambda \gg d$, the colloidal crystal template imposes no order on the eutectic pattern, resulting in a disordered structure (see Extended Data Fig. 9b). The trefoil pattern in this template resembles the Archimedean

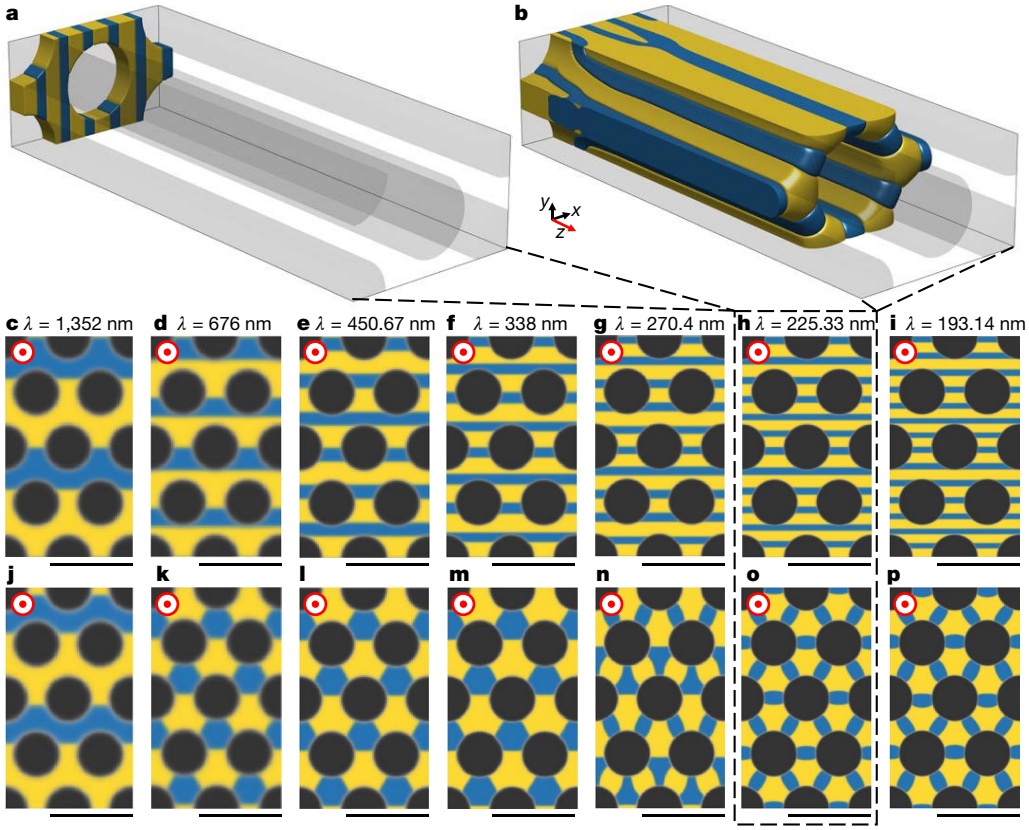


Fig. 2 | Patterns observed in phase-field simulations. a, **b**, Three-dimensional views of the phase-field simulation domain showing the evolution of the initial lamellar seed (**a**; cross-section shown in **h**) into the hexafoil structure (**b**; cross-section shown in **o**). The solidification direction in **a** and **b** is along the *z* axis. **c**–**i**, Images of the initial conditions of simulations performed using the given lamellar spacing. **j**–**p**, Images showing the corresponding steady-state patterns: **j**, no-foil; **k**–**m**, trefoil; **n**, cinquefoil; **o**, **p**, hexafoil. The solidification direction in **c**–**p** is out of the image (*z* axis), as indicated by the red dotted circles. The images in **c**–**p** show the *x*–*y* plane cross-section of the simulation domain repeated once in each direction. The template pillars are displayed as semitransparent grey in **a** and **b**, and as black in **c**–**p**, while AgCl is shown as yellow, and KCl as blue. All scale bars, 1 µm.

kagome lattice (see schematic overlaid on Fig. 4c), approximating AgCl and KCl as triangles and silica colloids as hexagons. These results suggest that such patterns can be obtained not only from pillar templates, but also from other two-dimensionally arranged obstacles. Owing to the planar geometry of the sample, the solidification front appears to remain parallel to the substrate throughout the template (see Extended Data Fig. 9c, d).

The realization of complex mesostructures from solidification of a simple system consisting of a lamellar eutectic in a hexagonally arranged template indicates that the complex thermal and diffusion landscapes imposed by a template on a solidifying eutectic can lead to intricate and rather unexpected patterns. Given the classes of patterns observed, we suggest it would be interesting to consider whether templates could modify the structure of metal-dielectric eutectics (for example, Ge-Al and Cu-Cu_3P) to form non-reciprocal metasurfaces[7], Co-based eutectics to form magnetic spin-ice systems[8,9], and mechanically robust eutectics such as NiAl-Mo or Al_2O_3-ZrO_2 to form mechanical microlattices[10,11]. It is important to keep in mind that the template can provide additional functionality (for example, being formed from a

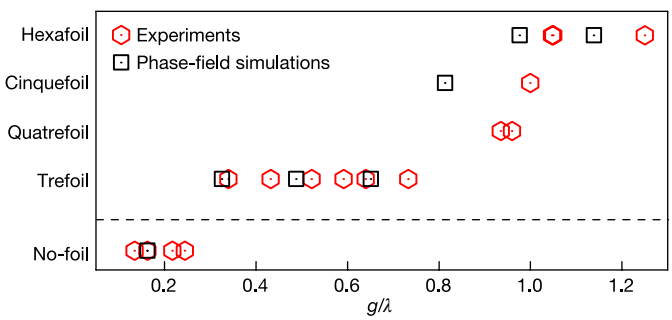


Fig. 3 | Mesostructure phase map. Map of experimentally observed (red) and phase-field simulated (black) mesostructures (shown on the vertical axis) as a function of g/λ. The plotted data are displayed in Fig. 2 and in Extended Data Figs. 3 and 4.

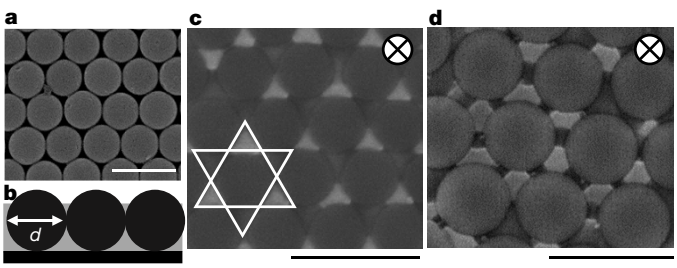


Fig. 4 | Pattern formation by a monolayer colloidal crystal template. a, SEM image of the monolayer silica colloidal crystal (sphere diameter $d = 560$ nm) template. **b**, Schematic of eutectic-infilled monolayer colloidal crystal template (see Methods for details). **c**, SEM image of the trefoil pattern (a schematic of the Archimedean kagome lattice is overlaid on the image at bottom left) obtained when $\lambda \approx d$ ($\lambda = 500$ nm). **d**, SEM image of the hexafoil pattern obtained when $\lambda < d$ ($\lambda = 160$ nm). The solidification direction in **c** and **d** is into the image (*z* axis), as indicated by the black crossed circle. All scale bars, 1 µm.

diamagnetic material), and also that in some systems it is possible for one of the eutectic phases to be selectively etched and replaced with a different material[13].

Online content

Any methods, additional references, Nature Research reporting summaries, source data, extended data, supplementary information, acknowledgements, peer review information; details of author contributions and competing interests; and statements of data and code availability are available at https://doi.org/10.1038/s41586-019-1893-9.

1. Braun, P. V., Osenar, P. & Stupp, S. I. Semiconducting superlattices templated by molecular assemblies. *Nature* **380**, 325–328 (1996).
2. Tavakkoli, K. G. A. et al. Templating three-dimensional self-assembled structures in bilayer block copolymer films. *Science* **336**, 1294–1298 (2012).
3. Wu, Y. et al. Composite mesostructures by nano-confinement. *Nat. Mater*. **3**, 816–822 (2004).
4. Tavakkoli, K. G. A. et al. Rectangular symmetry morphologies in a topographically templated block copolymer. *Adv. Mater*. **24**, 4249–4254 (2012).
5. Urgel, J. I. et al. Quasicrystallinity expressed in two-dimensional coordination networks. *Nat. Chem*. **8**, 657–662 (2016).
6. Grünbaum, B. & Shephard, G. C. Tilings by regular polygons. *Math. Mag*. **50**, 227–247 (1977).
7. Yu, N. & Capasso, F. Flat optics with designer metasurfaces. *Nat. Mater*. **13**, 139–150 (2014).
8. Wang, R. F. et al. Artificial 'spin ice' in a geometrically frustrated lattice of nanoscale ferromagnetic islands. *Nature* **439**, 303–306 (2006); addendum 446, 102 (2007).
9. Ladak, S., Read, D. E., Perkins, G. K., Cohen, L. F. & Branford, W. R. Direct observation of magnetic monopole defects in an artificial spin-ice system. *Nat. Phys*. **6**, 359–363 (2010).
10. Schaedler, T. A. et al. Ultralight metallic microlattices. *Science* **334**, 962–965 (2011).
11. Meza, L. R., Das, S. & Greer, J. R. Strong, lightweight, and recoverable three-dimensional ceramic nanolattices. *Science* **345**, 1322–1326 (2014).
12. Pawlak, D. A. et al. How far are we from making metamaterials by self-organization? The microstructure of highly anisotropic particles with an SRR-like geometry. *Adv. Funct. Mater*. **20**, 1116–1124 (2010).
13. Acosta, M. F., Rodrigo, S. G., Martín-Moreno, L., Pecharromán, C. & Merino, R. I. Micropillar templates for dielectric filled metal arrays and flexible metamaterials. *Adv. Opt. Mater*. **5**, 1600670 (2017).
14. Sadecka, K. et al. When eutectics meet plasmonics: nanoplasmonic, volumetric, self-organized, silver-based eutectic. *Adv. Opt. Mater*. **3**, 381–389 (2015).
15. Bei, H., Pharr, G. & George, E. A review of directionally solidified intermetallic composites for high-temperature structural applications. *J. Mater. Sci*. **39**, 3975–3984 (2004).
16. Wysmulek, K. et al. A $SrTiO_3$-TiO_2 eutectic composite as a stable photoanode material for photoelectrochemical hydrogen production. *Appl. Catal. B* **206**, 538–546 (2017).
17. Jackson, K. & Hunt, J. Lamellar and rod eutectic growth. *Trans. Metall. Soc. AIME* **236**, 1129–1142 (1966).
18. Himemiya, T. & Umeda, T. Three-phase planar eutectic growth models for a ternary eutectic system. *Mater. Trans. JIM* **40**, 665–674 (1999).
19. Choudhury, A., Plapp, M. & Nestler, B. Theoretical and numerical study of lamellar eutectic three-phase growth in ternary alloys. *Phys. Rev. E* **83**, 051608 (2011).
20. Dennstedt, A. & Ratke, L. Microstructures of directionally solidified Al–Ag–Cu ternary eutectics. *Trans. Indian Inst. Met*. **65**, 777–782 (2012).
21. Akamatsu, S. & Plapp, M. Eutectic and peritectic solidification patterns. *Curr. Opin. Solid State Mater. Sci*. **20**, 46–54 (2016).
22. Boley, J. W. et al. High-operating-temperature direct ink writing of mesoscale eutectic architectures. *Adv. Mater*. **29**, 1604778 (2017).
23. Choi, J. et al. Processing-dependent microstructure of AgCl–$CsAgCl_2$ eutectic photonic crystals. *Adv. Opt. Mater*. **6**, 1701316 (2018).
24. Darling, S. B. Directing the self-assembly of block copolymers. *Prog. Polym. Sci*. **32**, 1152–1204 (2007).
25. Ouk Kim, S. et al. Epitaxial self-assembly of block copolymers on lithographically defined nanopatterned substrates. *Nature* **424**, 411–414 (2003).
26. Shin, D. O. et al. Multicomponent nanopatterns by directed block copolymer self-assembly. *ACS Nano* **7**, 8899–8907 (2013).
27. Choi, Y. J. et al. Hierarchical directed self-assembly of diblock copolymers for modified pattern symmetry. *Adv. Funct. Mater*. **26**, 6462–6470 (2016).
28. Jung, H. et al. Hierarchical multi-level block copolymer patterns by multiple self-assembly. *Nanoscale* **11**, 8433–8441 (2019).
29. Ding, Y. et al. Emergent symmetries in block copolymer epitaxy. *Nat. Commun*. **10**, 2974 (2019).
30. Kulkarni, A. A. et al. Template-directed solidification of eutectic optical materials. *Adv. Opt. Mater*. **6**, 1800071 (2018).
31. Kim, J. et al. Template-directed directionally solidified 3D mesostructured AgCl-KCl eutectic photonic crystals. *Adv. Mater*. **27**, 4551–4559 (2015).
32. Kulkarni, A. A., Kohanek, J., Hanson, E., Thornton, K. & Braun, P. V. Control of lamellar eutectic orientation via template-directed solidification. *Acta Mater*. **166**, 715–722 (2019).
33. Yan, Z. et al. Three-dimensional mesostructures as high-temperature growth templates, electronic cellular scaffolds, and self-propelled microrobots. *Proc. Natl Acad. Sci. USA* **114**, E9455–E9464 (2017).

Publisher's note Springer Nature remains neutral with regard to jurisdictional claims in published maps and institutional affiliations.

© The Author(s), under exclusive licence to Springer Nature Limited 2020

Methods

AgCl-KCl eutectic synthesis

As-received AgCl (99.999%, Sigma Aldrich) and KCl (99.99%, Sigma Aldrich) were mixed as per the binary eutectic composition[34] of 81.77 wt% AgCl and 18.23 wt% KCl, and melted in a glass vial (covered with aluminium foil to exclude light) on a hotplate at 470 °C for 1 h, and subsequently cooled to room temperature.

Fabrication of pillar templates

Under dark-room conditions, SU-8 (MicroChem, SU-8 2000 series) photoresist was mixed with 0.5 wt% photo-initiator, cyclopentadienyl(fluorene)iron(II) hexafluorophosphate (Aldrich). Indium tin oxide coated glass substrates (with a sheet resistance of 70–100 Ω; Delta Technologies Ltd) were cleaned with acetone and isopropanol, followed by O_2 reactive ion etching (RIE) at 100 W for 5 min (with an O_2 flow of 19.6 $cm^3 min^{-1}$ at STP at 10 mtorr chamber pressure; Plasma-Therm 790 MF RIE Plasma System). Immediately after RIE, the SU-8 solution was spin-coated (2,000 r.p.m. for 30 s) on the substrates. These SU8 layers were soft baked on hotplates first at 65 °C for 10 min and then at 90 °C for 20 min, followed by slow cooling. A laser interference lithography setup[35] (laser output of 5.0 W, frequency-doubled Nd:YVO_4 laser, 532 nm) was used to create a hexagonal pattern in the SU8 film, by focusing three identical beams (arranged at 120° to each other) onto the sample plane for 0.8 s. The parameters of this pattern (with a lattice constant of 760–810 nm, and diameter of 500–620 nm) were adjusted by controlling the exposure time and the incident angles of each beam. All the beams were linearly polarized in their incident planes. After exposure, the samples were oven-baked at 85 °C for 20 min in dry air followed by slow cooling. The post-baked samples were then developed in propylene glycol monomethyl ether acetate for 4 h, followed by rinsing in an isopropanol bath for 10 min. The samples were gently blow dried with N_2 and then baked at 90 °C for 15 min. To create the pillar template, Ni electrodeposition was carried out within the SU8 scaffold. The electrodeposition was performed potentiostatically at −1.8 V in a commercial sulfamate nickel plating solution (Transene, SN-10). A drop of isopropanol was put on the scaffold before dipping it in the electroplating solution to improve the infiltration of the solution into the hydrophobic scaffold. By controlling the electrodeposition time, we were able to control the pillar height. The SU8 scaffold was then etched using O_2 plasma RIE (Nordson March RIE Plasma System) with 500 mtorr pressure and 200 W power for 15 min, thus exposing the Ni pillars. Subsequently, the exposed pillars were surface-protected with a conformal coating of ~25 nm of alumina using atomic layer deposition (300 cycles of the standard recipe; Savannah S100 Cambridge Nanotech). The usable spot size of the pillar template was about 2 mm in diameter.

Eutectic solidified in pillar templates

Directional solidification experiments were performed using two techniques, a Linkam THMS 600 hot-stage (with a TMS 94 controller) that sets a cooling rate, and a tube-furnace setup[23] where a syringe pump draws the samples out of the heated furnace at fixed speeds. The rate of solidification (controlled by either a set cooling rate or the draw rate) was varied to obtain a certain λ of the eutectic (see Extended Data Fig. 1a). With the hot-stage setup, the stage was first heated to 470 °C and then the sample was placed on it. For the tube-furnace setup, the temperature was first set to 550 °C, and then the samples were placed at the location where the temperature reached 470 °C. A small piece of the prepared eutectic (around 150 mg) was placed on top of the pillar templates (see schematic in Extended Data Fig. 1b), and heated to 470 °C for 8–10 min to enable complete infiltration of the molten eutectic. Partial infilling was obtained with the dwell time less than 5 min. Subsequently, the infilled samples were directionally solidified at various rates, such that the nominal direction of solidification was along the axis of the pillars, until the sample cooled to room temperature.

Microstructure characterization

Directionally solidified solid eutectic samples were peeled off from the substrate and their bottom surface was characterized (see schematic in Extended Data Fig. 1b) by scanning electron microscopy (SEM) using a Hitachi S4800-SEM. SEM images from all the samples are shown in Extended Data Figs. 3 and 4. Note that we did not coat the samples during the SEM visualization: to visualize the cross-section, the samples were mechanically cleaved. After SEM imaging, the samples were stored in an argon glove-box to minimize the corrosive reaction between the chloride salts and the exposed Ni pillars.

Image analysis

The average lamellar spacing values (from samples without pillar templates) were determined by performing the fast Fourier transform function of ImageJ on the SEM images. For templated eutectic samples, λ was determined outside the template region (see Extended Data Fig. 1c), whereas g and the emergent patterns were determined from SEM images taken around the centre of the pillar template samples. Patterns were analysed using a custom MATLAB code based on ref. [36]. The SEM images were first false-coloured to match the colour scheme of the simulated patterns, and the false-coloured SEM images were used in further analysis. These images were divided into unit cells and these unit cells were stacked together, followed by averaging the intensity at each pixel (shown in Extended Data Fig. 5). Moreover, the deviation between the simulated pattern and the SEM image was calculated for each unit cell and mapped over the entire SEM image. The unit cells having the lowest deviation are denoted in blue and those with the greatest deviation in red. Cells where the template pillars appeared damaged were not included in the analysis.

Eutectic solidified in colloid template

Silica microspheres (Fibre Optic Center Inc.) were dispersed in ethanol (1% by weight). Using a vertical deposition method[37], the 560 nm diameter silica colloids were deposited as a monolayer (2D colloidal crystal) and as multilayers (3D colloidal crystal) on (piranha cleaned) silicon substrates in an incubator (Isotemp 125D, Fisher) set at 50 °C. Multilayer regions were scratched off before the directional solidification experiments. The eutectic was side-infilled (as demonstrated in ref. [31]) into the template, using a hotplate set at 470 °C, and subsequently directionally solidified using the hot-stage setup. The patterns were imaged with top-view SEM.

Thermal profile simulations

The temperature profile in the eutectic during solidification was calculated using COMSOL in order to evaluate the assumptions regarding the orientation of the solidification front. For the pillar template case, the heat equation was solved in a two-dimensional axisymmetric domain consisting of (from bottom to top) an aluminium plate (1 cm thick, 8 cm in diameter, thermal conductivity (κ) = 238 $W m^{-1} K^{-1}$), a glass substrate (0.7 mm thick, 20 mm in diameter, κ = 1.38 $W m^{-1} K^{-1}$), a pillar-eutectic composite layer (6 μm thick, 2 mm in diameter, κ = 23.4 $W m^{-1} K^{-1}$), and a eutectic overlayer (a truncated hemisphere with a base diameter of 5 mm and a height of 2 mm). Unless otherwise noted, the thermal conductivity values were assumed from COMSOL's default material library. The thermal conductivity of the pillar-eutectic composite (κ = 23.4 $W m^{-1} K^{-1}$, as previously stated) was determined by weighting the thermal conductivity of each material by its volume fraction—namely, the Ni pillar (κ = 90.7 $W m^{-1} K^{-1}$, taken from a pure Ni value) and the eutectic (κ = 3.25 $W m^{-1} K^{-1}$, based on the solid value[22])—along with an assumption of a volume fraction of 23% and 77%, respectively, which is for the case when the pillar diameter and the edge gap are equal. The thermal properties of the ~25 nm alumina layer on the surface of the Ni pillars were not considered. Since the overlayer would solidify before the composite layer, the overlayer is assumed to have the average

thermal conductivity of AgCl-KCl eutectic solid ($\kappa = 3.25\ W\ m^{-1}\ K^{-1}$)[22]. A cooling rate of 10 °C min^{-1} was enforced on the bottom surface of the aluminium plate (that is, the cooling stage). Newton's law of cooling was applied to all other surfaces, with an air temperature of 300 K and a thermal transfer coefficient of 10 W m^{-2} K^{-1} (ref. [38]). The evolution of the shape of the solidification front (approximated by the eutectic temperature isocontour at 591.73 K) was calculated using element sizes, ensuring a minimum of five elements across each feature. A simulation was also performed with a eutectic thermal conductivity corresponding to the liquid eutectic ($\kappa = 0.45\ W\ m^{-1}\ K^{-1}$)[22]. The result was qualitatively similar to that of $\kappa = 3.25\ W\ m^{-1}\ K^{-1}$ case, but the tilt of the solidification front was more pronounced in the outer region of the disk and there was almost no tilt in the inner region. While we find that changing thermal conductivity has minimal impact on the shape of the solidification front, we note that there are other simplifications made in our model. First, the electrodeposited Ni pillars probably have a lower thermal conductivity than pure Ni, and second, the alumina layer will serve as a thermal barrier between the pillars and the eutectic (the thermal conductivity of amorphous alumina grown by atomic layer deposition is[39] ~2 W m^{-1} K^{-1}, similar to the thermal conductivity of the eutectic). This alumina layer may reduce thermal coupling between the pillars and the solidifying eutectic. For simulations of monolayer silica colloidal crystal templates, the substrate was instead assumed to be a silicon layer (0.6 mm thick, $\kappa = 130\ W\ m^{-1}\ K^{-1}$). The bulk layer was assumed to be a composite of silica colloidal crystal and eutectic (560 nm thick, $\kappa = 2.8\ W\ m^{-1}\ K^{-1}$) with no overlayer.

Phase-field simulations

Solidification of the AgCl-KCl eutectic along the axis of the pillars was simulated using a template-directed eutectic solidification model based on the phase-field model developed by Folch and Plapp[40] and as applied in other templated-eutectic cases[31,32]. Model parameters, including material properties, were taken from refs. [22,32]. Simulations of template-directed solidification were conducted over computational domains representing a unit cell of the hexagonal lattice of pillars, with dimensions of 780.6 nm and 1,352 nm and an edge gap of 220 nm. Periodic boundary conditions were assumed at the unit-cell boundaries, and no-flux boundary conditions were imposed at the template-eutectic interfaces through the use of the smoothed boundary method[41]. The initial lamellar spacings were chosen such that their integer multiples (1 to 7) would fit in the 1,352 nm domain width (see Fig. 2c–i), and the solidification velocities were set such that they would result in these lamellar spacings in the absence of a template. These initial lamellae act as a solid seed in the simulations. The grid size of the computational domain is set to provide sufficient resolution over the diffuse interface, which must in turn be sufficiently smaller than the lamellar spacing, to ensure numerical accuracy without unnecessary expenditure of computational resources. Thus, the simulations with smaller lamellar spacing have higher resolutions, resulting in the sharper appearance of interfaces than those with larger spacing in Fig. 2. A linear thermal gradient of 10^5 K m^{-1} was applied in the solidification direction. This thermal gradient is probably larger than that found in the physical system, but it allowed the simulation to reach a steady-state structure more quickly without affecting the final morphology. The linear thermal gradient forced the solidification front to be perpendicular to the axis of the pillars (that is, parallel to the x–y plane; see Fig. 2a, b). The solidification of the eutectic was simulated along the axis of the pillars (that is, along the z axis; see Fig. 2a, b) until a stable, steady-state structure was attained. While this model does not explicitly specify the contact angle, it closely approximates the model that specifies a 90° contact angle on a flat surface of the template material, corresponding to a system with both solid phases having the same interfacial energy. This assumption of equal interfacial energy can be justified by examining the experimental images, which show most of the interfaces intersecting the pillar surface at approximately 90°. Phase-field simulations were only performed for the solidification direction parallel to the axis of the pillars because a tilted solidification front requires a much larger computational domain. Phase-field simulations were not performed for the monolayer colloidal-crystal case because the level of resolution necessary to resolve the evolution in the small gaps between spheres made the simulation costly.

Data availability

Data that support the findings of this study are available within the paper, and from the corresponding author on reasonable request.

Code availability

The phase-field simulations were performed using a custom code written in Fortran 90. The code is available from K.T. (kthorn@umich.edu) on reasonable request.

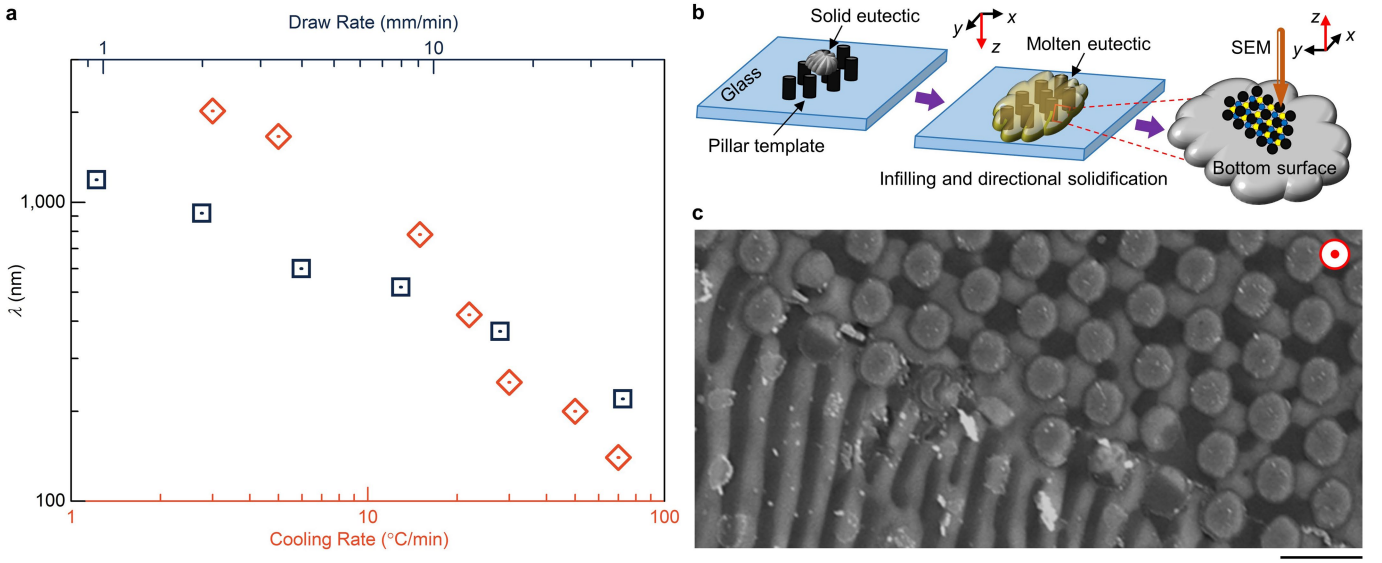
34. Fischer, E. Thermodynamic optimization of the AgCl-KCl and $BaCl_2$-LiCl systems. *J. Phase Equilibria* **24**, 228–235 (2003).
35. Chen, Y., Geddes, J. III, Lee, J., Braun, P. & Wiltzius, P. Holographically fabricated photonic crystals with large reflectance. *Appl. Phys. Lett*. **91**, 241103 (2007).
36. Kim, J., Ou, Z., Jones, M. R., Song, X. & Chen, Q. Imaging the polymerization of multivalent nanoparticles in solution. *Nat. Commun*. **8**, 761 (2017).
37. Ma, J. et al. Coherent phonon-grain boundary scattering in silicon inverse opals. *Nano Lett*. **13**, 618–624 (2013).
38. Whitelaw, J. H. Convective heat transfer. In *Thermopedia* (ed. Hewitt, G. F.) https://doi.org/10.1615/AtoZ.c.convective_heat_transfer (Begell House Inc., 2011).
39. Cappella, A. et al. High temperature thermal conductivity of amorphous Al_2O_3 thin films grown by low temperature ALD. *Adv. Eng. Mater*. **15**, 1046–1050 (2013).
40. Folch, R. & Plapp, M. Quantitative phase-field modeling of two-phase growth. *Phys. Rev. E* **72**, 011602 (2005).
41. Yu, H.-C., Chen, H.-Y. & Thornton, K. Extended smoothed boundary method for solving partial differential equations with general boundary conditions on complex boundaries. *Model. Simul. Mater. Sci. Eng*. **20**, 075008 (2012).

Acknowledgements This work was supported through the Air Force Office of Scientific Research Multidisciplinary University Research Initiative FA9550-12-1-0471. This work was carried out in part in the Materials Research Laboratory Central Facilities, and in the Beckman Institute for Advanced Science and Technology, University of Illinois. E.H. and K.T. acknowledge use of the computational resources in the Department of Defense High-Performance Computing Modernization Program. We thank J. Kohanek for suggestions and discussions on solidification in pillar templates, Z. Ou and Q. Chen for help with image analysis, G. Huang for help with thermal profile simulations, and K. Tyler and V. Mohan for critical feedback on the manuscript.

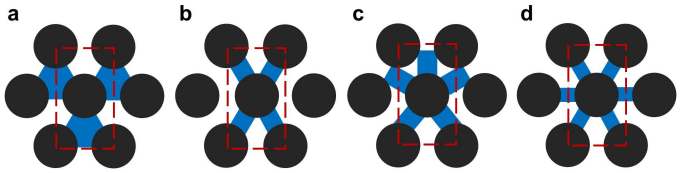
Author contributions A.A.K. and E.H., under the supervision of P.V.B. and K.T., respectively, designed the study. A.A.K. and R.Z. fabricated the templates. A.A.K. performed solidification experiments and sample characterization. E.H. performed the simulations. A.A.K., E.H. and R.Z. analysed the data. All authors prepared the manuscript.

Competing interests The authors declare no competing interests.

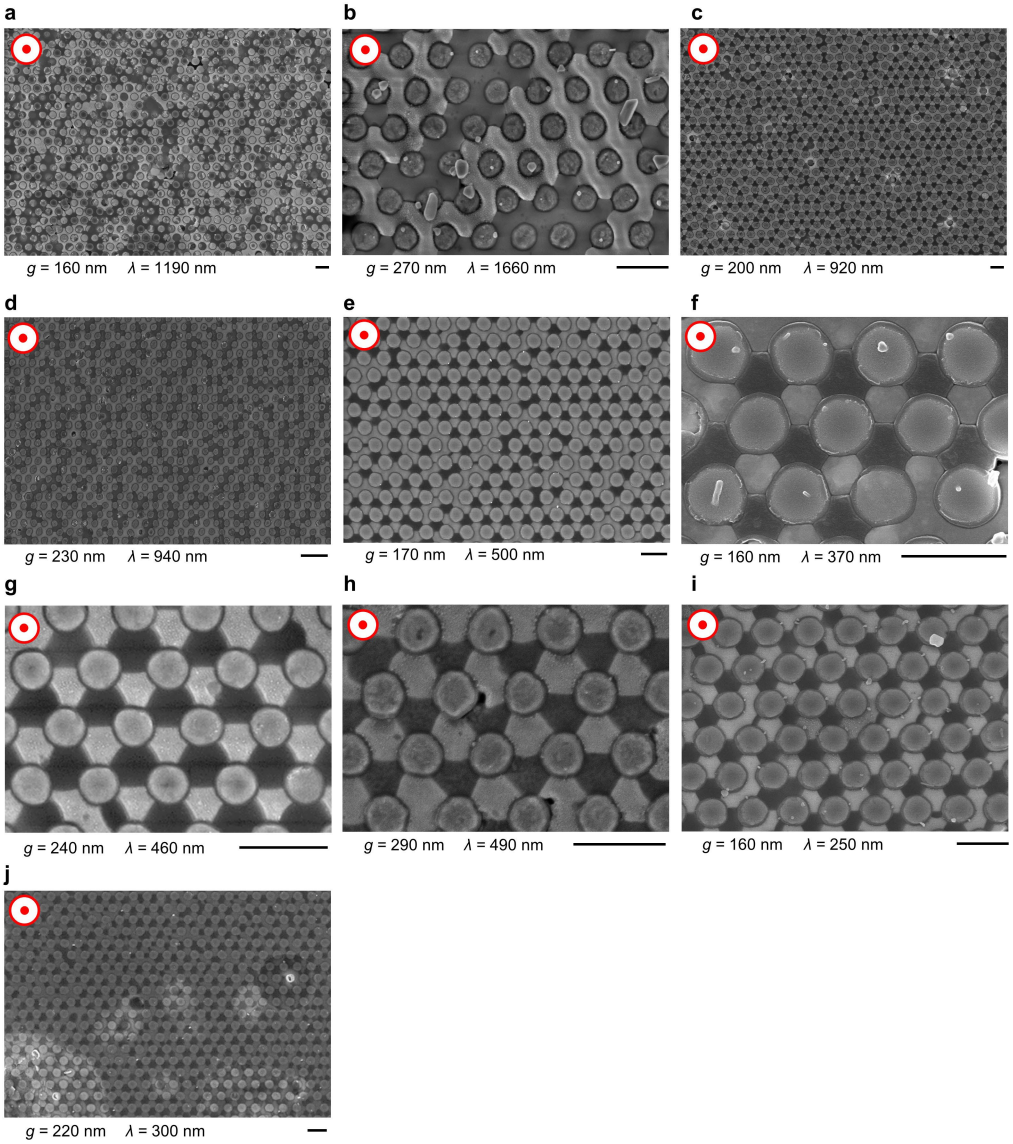
Additional information
Correspondence and requests for materials should be addressed to P.V.B.
Peer review information *Nature* thanks Elizabeth Dickey, Alain Karma and the other, anonymous, reviewer(s) for their contribution to the peer review of this work.
Reprints and permissions information is available at http://www.nature.com/reprints.



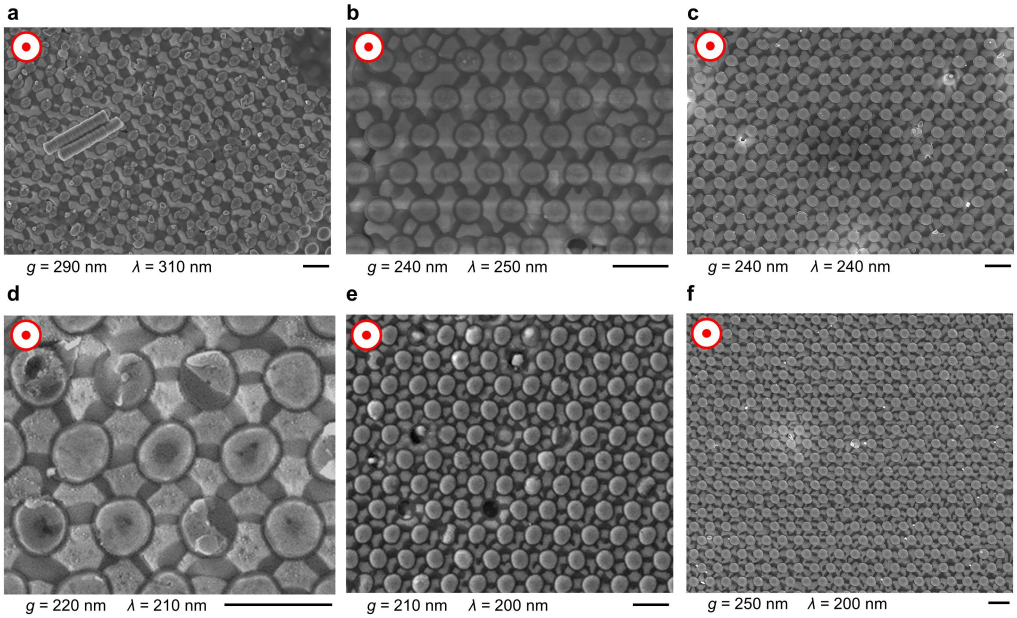
Extended Data Fig. 1 | Directional solidification of AgCl-KCl lamellar eutectic and experiment schematic for pillar-template-directed eutectic solidification. a, Plot of the average lamellar spacing (λ) of AgCl-KCl eutectic directionally solidified using the hot-stage setup at set cooling rates (plotted in orange) and the tube-furnace setup at set draw rates (plotted in blue). **b**, Experiment schematic for infilling the pillar template with eutectic, subsequent directional solidification of the eutectic in the pillar template, and characterization of the resultant microstructures. **c**, SEM image showing the eutectic solidified within and outside the pillar template. The solidification direction is out of the image (z axis), as indicated by the red dotted circle. See Methods for details. Scale bar, 1 µm.



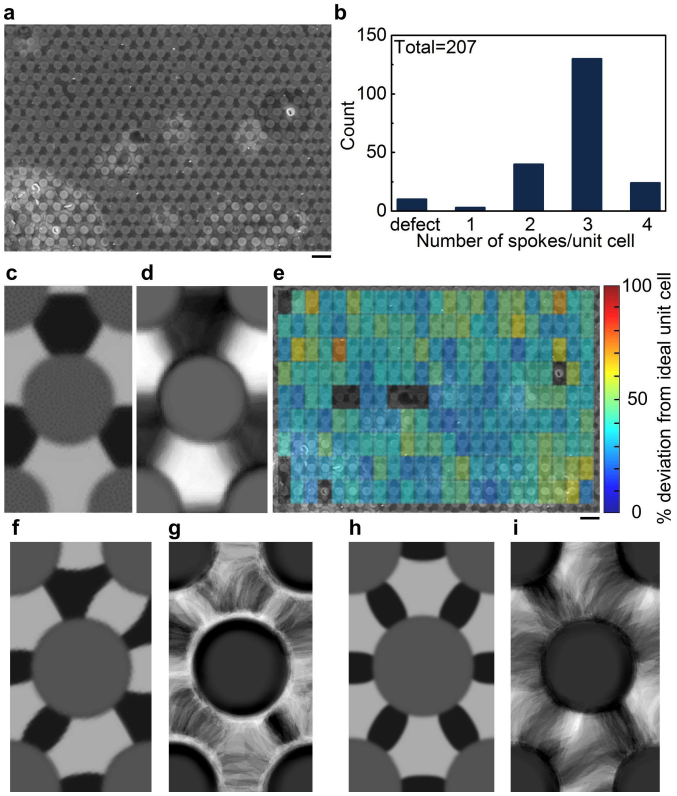
Extended Data Fig. 2 | Nomenclature of the patterns. a–**d**, Schematic showing the number of KCl spokes per unit cell of the pillar template for **a**, trefoil (three), **b**, quatrefoil (four), **c**, cinquefoil (five) and **d**, hexafoil (six) patterns. The KCl spokes are coloured blue, pillars black, and the unit cell is marked by red dashed lines.



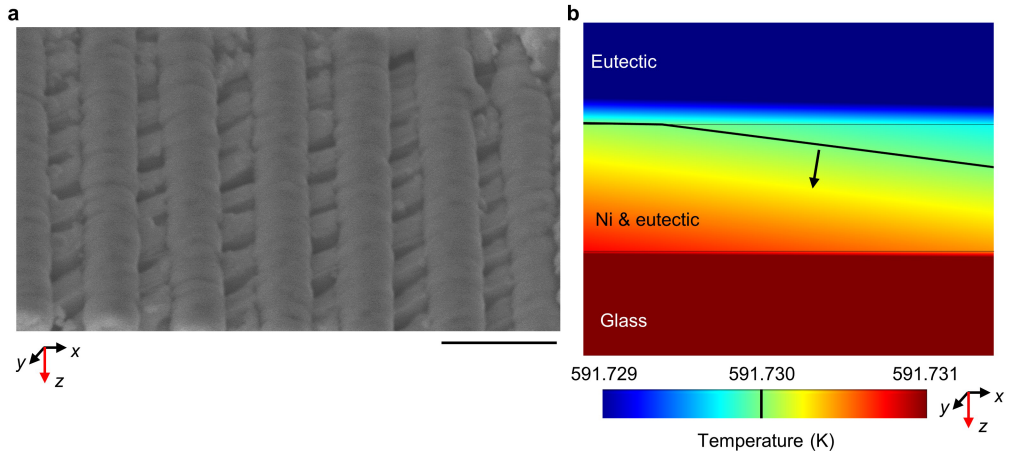
Extended Data Fig. 3 | No-foil and trefoil patterns. Uncoloured SEM images of the samples, showing the variety of no-foil (**a**–**d**) and trefoil (**e**–**j**) patterns mapped in Fig. 3. Values of edge gap, g, and average lamellar spacing, λ, are given under each image. The solidification direction is out of the image (z axis), as indicated by the red dotted circle. All scale bars, 1 µm.



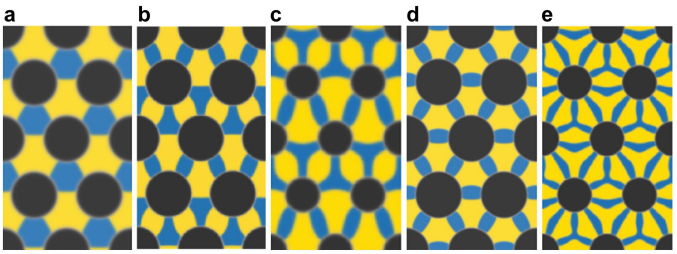
Extended Data Fig. 4 | Quatrefoil, cinquefoil and hexafoil patterns. Uncoloured SEM images of the samples showing the variety of quatrefoil (**a**, **b**), cinquefoil (**c**) and hexafoil (**d**–**f**) patterns mapped in Fig. 3. Values of edge gap, g, and average lamellar spacing, λ, are given under each image. The solidification direction is out of the image (z axis), as indicated by the red dotted circle. All scale bars, 1 µm.



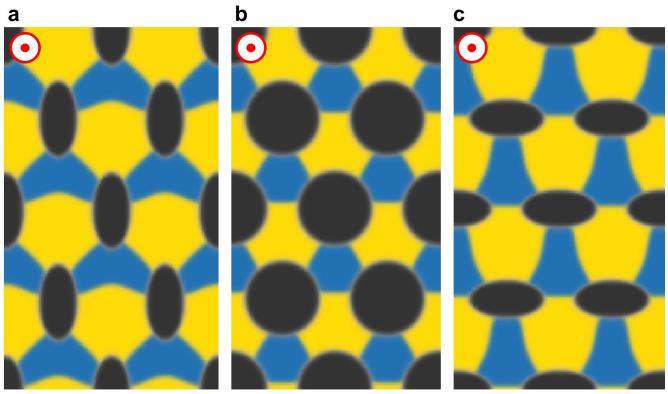
Extended Data Fig. 5 | Image analysis of local and long-range order in the patterns. a, SEM image of a trefoil pattern. **b**, Histogram representing a simple counting of the number of spokes in each unit cell. The dominant feature in the 12 μm × 17 μm SEM image in **a** is the three-spoke pattern. We also include in the histogram the number of unit cells that have missing pillars or other defects. **c**, A unit cell of the phase-field-simulated trefoil pattern. **d**, Mean unit cell obtained by averaging the intensity at each pixel from a false-coloured version of the SEM image in **a**. The experimental average matches the ideal simulated unit cell well. **e**, Map of deviation between the simulated trefoil pattern and each unit cell of the experimental image. The unit cells having the lowest deviation are denoted in blue and those with the greatest deviation in red. Cells where the template pillars appeared damaged were not included in the analysis. **f**, Unit cell of the simulated cinquefoil pattern. **g**, Averaged unit cell obtained from the SEM image shown in Extended Data Fig. 4c. **h**, Unit cell of the simulated hexafoil pattern. **i**, Averaged unit cell obtained from the SEM image shown in Extended Data Fig. 4e. All scale bars, 1 μm.



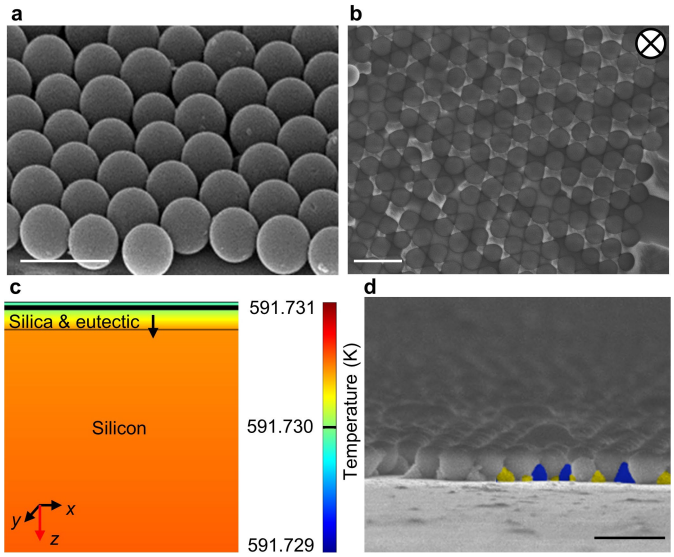
Extended Data Fig. 6 | Eutectic phase boundary alignment and thermal profile in the bulk of the pillar template. a, SEM image of a cross-section, showing a tilted alignment of eutectic phase boundaries within the pillars. **b**, Calculated thermal profile in the bulk of the template during directional solidification of eutectic-infiltrated Ni pillar template at a set cooling rate of 10 °C min^{-1}. The isothermal solidification front at the eutectic temperature (591.73 K) is denoted by a thick black line; the eutectic temperature is also indicated by a black line in the key. The black arrow denotes the direction of solidification. Scale bar, 1 µm.



Extended Data Fig. 7 | Effect of pillar diameter on the emergence of patterns. **a**–**e**, Phase-field-simulated steady-state patterns for a fixed lattice constant of 780.6 nm, varying edge gaps, g, and lamellar spacing, λ. These results suggest the possibility of obtaining new patterns by varying the parameter associated with pillar diameter as well as g/λ. The solidification direction is out of the image (z axis). The images show the x–y plane cross-section of the simulation domain repeated once in each direction. The template pillars are displayed as black, AgCl as yellow, and KCl as blue.



Extended Data Fig. 8 | Phase-field simulations for different shapes of pillars. **a**–**c**, A variety of patterns in templated-eutectic obtained by changing the shapes and orientations of the pillars: **a**, oval; **b**, circle; **c**, same as **a** but rotated by 90°. Characteristic features depend on the pillar shape and orientation. The solidification direction is out of the image (*z* axis), as indicated by the red dotted circle. The images show the *x*–*y* plane cross-section of the simulation domain repeated once in each direction. The template pillars are displayed as black, AgCl as yellow, and KCl as blue.



Extended Data Fig. 9 | Solidification of AgCl-KCl eutectic in a monolayer silica colloidal crystal. a, An oblique-view SEM image of the monolayer silica colloidal crystal used as a template. **b**, Plan-view SEM image of a disordered structure observed in AgCl-KCl eutectic solidified (with $\lambda = 1.7$ µm) within a monolayer silica colloidal crystal of diameter 560 nm. The solidification direction in **b** is into the image (z axis), as indicated by the black crossed circle. **c**, Calculated thermal profile in the bulk of the template during directional solidification of the eutectic-infilled silica colloidal crystal template at a set cooling rate of 10 °C min^{-1}. The isothermal solidification front at the eutectic temperature (591.73 K) is denoted by a thick black line; the eutectic temperature is also indicated by a black line in the key. The black arrow denotes the direction of solidification. **d**, Cross-sectional-view SEM image, with false colouring denoting AgCl as yellow, and KCl as blue. All scale bars, 1 µm.

Design and synthesis of multigrain nanocrystals via geometric misfit strain

https://doi.org/10.1038/s41586-019-1899-3

Received: 15 June 2018

Accepted: 30 October 2019

Published online: 15 January 2020

Myoung Hwan Oh[1,2,3,4,5,13], Min Gee Cho[1,2,5,13], Dong Young Chung[1,2], Inchul Park[1,6], Youngwook Paul Kwon[7], Colin Ophus[8], Dokyoon Kim[1,2,9], Min Gyu Kim[10], Beomgyun Jeong[11], X. Wendy Gu[12], Jinwoung Jo[1,2], Ji Mun Yoo[1,2], Jaeyoung Hong[1,2], Sara McMains[7], Kisuk Kang[1,6], Yung-Eun Sung[1,2], A. Paul Alivisatos[3,4,5,14]* & Taeghwan Hyeon[1,2,14]*

The impact of topological defects associated with grain boundaries (GB defects) on the electrical, optical, magnetic, mechanical and chemical properties of nanocrystalline materials[1,2] is well known. However, elucidating this influence experimentally is difficult because grains typically exhibit a large range of sizes, shapes and random relative orientations[3–5]. Here we demonstrate that precise control of the heteroepitaxy of colloidal polyhedral nanocrystals enables ordered grain growth and can thereby produce material samples with uniform GB defects. We illustrate our approach with a multigrain nanocrystal comprising a Co_3O_4 nanocube core that carries a Mn_3O_4 shell on each facet. The individual shells are symmetry-related interconnected grains[6], and the large geometric misfit between adjacent tetragonal Mn_3O_4 grains results in tilt boundaries at the sharp edges of the Co_3O_4 nanocube core that join via disclinations. We identify four design principles that govern the production of these highly ordered multigrain nanostructures. First, the shape of the substrate nanocrystal must guide the crystallographic orientation of the overgrowth phase[7]. Second, the size of the substrate must be smaller than the characteristic distance between the dislocations. Third, the incompatible symmetry between the overgrowth phase and the substrate increases the geometric misfit strain between the grains. Fourth, for GB formation under near-equilibrium conditions, the surface energy of the shell needs to be balanced by the increasing elastic energy through ligand passivation[8–10]. With these principles, we can produce a range of multigrain nanocrystals containing distinct GB defects.

The geometric misfit strain in core/shell nanocrystals was investigated using nanocrystals of a polyhedral Co_3O_4 core and a heteroepitaxial Mn_3O_4 shell as a model system. We prepared ~11-nm-side Co_3O_4 nanocubes with {100} facets as substrates for the growth of Mn_3O_4 (Supplementary Fig. 1a). The formation of Mn_3O_4 grains on the nanocube was carried out by the reaction of $MnCl_2$ or $Mn(HCOO)_2$ in an organic/aqueous (xylene/water) reverse micelle solution in the presence of oleylamine, oleic acid and HCl[11,12] (Supplementary Methods). X-ray diffraction (XRD) data confirm that the deposited phase is tetragonal Mn_3O_4 ($a = b = 5.765$ Å, $c = 9.442$ Å; JCPDS #80-0382) (Supplementary Fig. 1b), which has a spinel structure elongated along the c axis owing to the Jahn–Teller effect of Mn^{3+}, with an electron configuration of $t_{2g}^3 e_g^1$, whereas the Co_3O_4 core has a cubic spinel structure ($a = b = c = 8.084$ Å; JCPDS #42-1467). As shown in Fig. 1a, the lattice of Mn_3O_4 {220} coincides with Co_3O_4 {400} at a misfit of less than 1%, explaining the consistent values in the in-plane interatomic distance (d_{in}) for both phases (Supplementary Figs. 1–3, Supplementary Table 1, Supplementary Discussion).

In Fig. 1a, the high-resolution high-angle annular dark-field scanning transmission electron microscope (HAADF-STEM) images and the Fourier-filtered images reveal that for each facet of the cubic core, a Mn_3O_4 grain grows in ⟨001⟩ directions perpendicular to Co_3O_4 {100}, and Mn_3O_4 {110} are parallel to Co_3O_4 {010}. The growth direction of the shell is guided by the lattice matching along six {100} surface planes of the Co_3O_4 core, which leads to the segmentation of the shell into multigrains. An irregularly shaped core induces an inconsistent lattice

[1]Center for Nanoparticle Research, Institute for Basic Science (IBS), Seoul, South Korea. [2]School of Chemical and Biological Engineering and Institute of Chemical Processes, Seoul National University, Seoul, South Korea. [3]Department of Chemistry and Department of Materials Science and Engineering, University of California Berkeley, Berkeley, CA, USA. [4]Materials Sciences Division, Lawrence Berkeley National Laboratory, Berkeley, CA, USA. [5]Kavli Energy NanoScience Institute, University of California Berkeley and Lawrence Berkeley National Laboratory, Berkeley, CA, USA. [6]Department of Materials Science and Engineering, Research Institute of Advanced Materials (RIAM), Seoul National University, Seoul, South Korea. [7]Department of Mechanical Engineering, University of California Berkeley, Berkeley, CA, USA. [8]National Center for Electron Microscopy, Molecular Foundry, Lawrence Berkeley National Laboratory, Berkeley, CA, USA. [9]Department of Bionano Engineering and Bionanotechnology, Hanyang University, Ansan, South Korea. [10]Beamline Research Division, Pohang Accelerator Laboratory, Pohang University of Science and Technology, Pohang, South Korea. [11]Advanced Nano Surface Research Group, Korea Basic Science Institute, Daejeon, South Korea. [12]Department of Mechanical Engineering, Stanford University, Stanford, CA, USA. [13]These authors contributed equally: Myoung Hwan Oh, Min Gee Cho. [14]These authors jointly supervised this work: A. Paul Alivisatos, Taeghwan Hyeon. *e-mail: paul.alivisatos@berkeley.edu; thyeon@snu.ac.kr

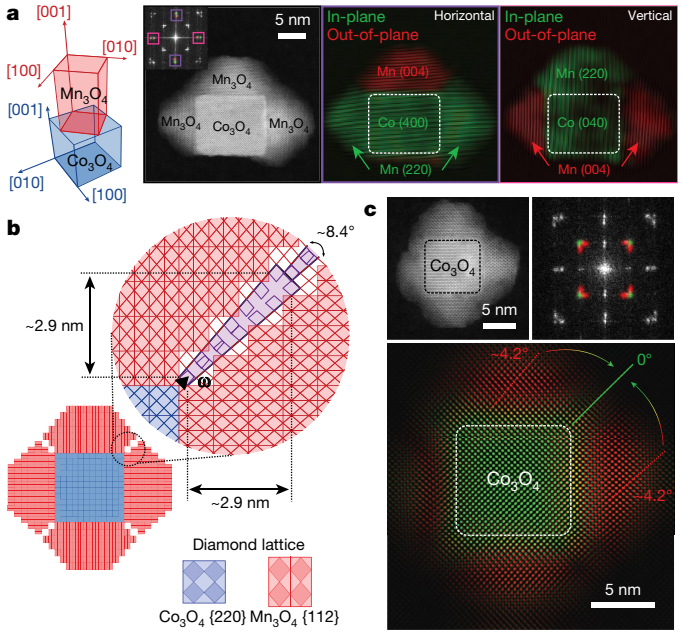


Fig. 1 | Epitaxially guided growth and gap closing of Mn_3O_4 grains on a Co_3O_4 nanocube. a, Left, relative orientation between Mn_3O_4 and Co_3O_4 unit cells. HAADF-STEM image (centre) and corresponding Fourier-filtered images (right) of the Co_3O_4/Mn_3O_4 nanocrystal taken along the Co_3O_4 ⟨100⟩ and Mn_3O_4 ⟨110⟩ zone axes, showing the relative orientation between the Co_3O_4 core and Mn_3O_4 grains. Horizontal and vertical lattices are shown in the purple and pink box, respectively. The in-plane (outer) spots in the FFT pattern are mapped in green (2.04 Å) and the out-of-plane (inner) spots are mapped in red (2.36 Å). **b**, Gaps between adjacent Mn_3O_4 grains resulting in disclinations at the Mn_3O_4 GBs. The misorientation angle between neighbouring Mn_3O_4 {112} planes is about 8.4°. The disclination line is shown as a black triangle with Frank vector **ω**. **c**, The GBs observed in the HAADF-STEM image and the corresponding lattice spacing map. The green and red spots in the FFT image were used to visualize the lattice spacing distribution in the nanocrystal. In the map, the interface between the Co_3O_4 nanocrystal and the Mn_3O_4 GBs is shown in the same green colour as Co_3O_4, giving a lattice spacing at the interface of 2.85 Å. (The lattice spacings of the Mn_3O_4 {112} planes, which are not affected by the Co_3O_4 core, range from 2.96 Å to 3.09 Å (red)).

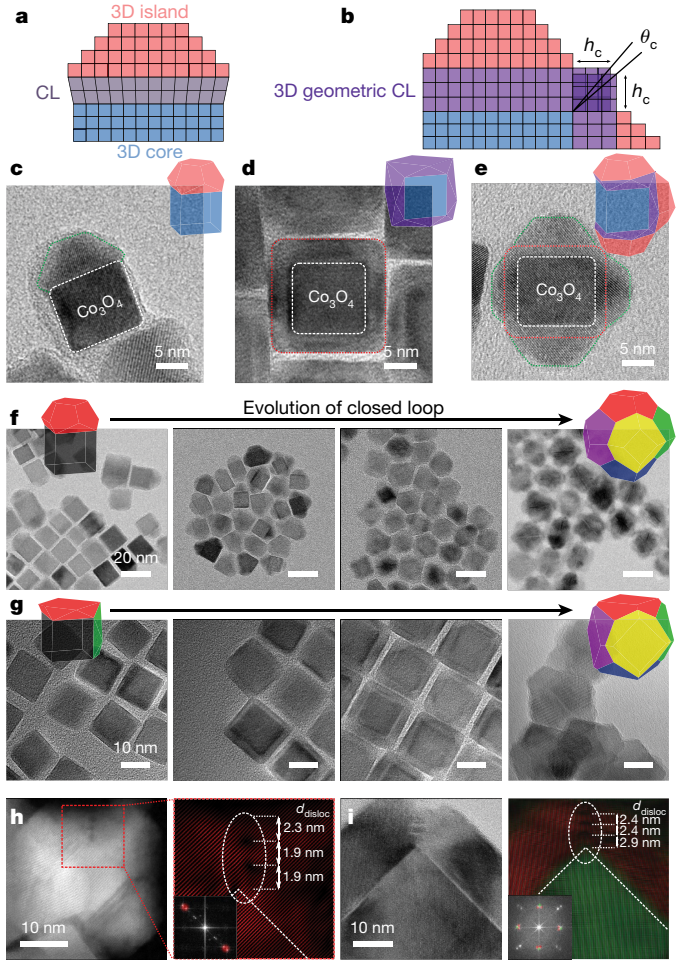


Fig. 2 | Extension of SK growth to 3D polyhedral substrates. a, **b**, Schematic illustration of traditional SK growth without geometric misfit strain (**a**) and extended SK growth with a 3D geometric CL induced by geometric misfit strain along the sharp edges of the core (**b**). **c**, TEM image of a Co_3O_4/Mn_3O_4 nanocrystal without GBs. **d**, **e**, TEM images showing the effects of counteranions in manganese (II) precursors on the morphology of Mn_3O_4 grains without islands (**d**) and with islands (**e**). Red and green lines in the high-resolution TEM images indicate the CL and the islands of Mn_3O_4, respectively. **f**, **g**, Monitoring of the development of grains and GBs while repeating the synthetic procedure using chloride (**f**) and formate (**g**) ligands with an 11-nm core. **h**, **i**, STEM, TEM, FFT and Fourier-filtered images of Co_3O_4/Mn_3O_4 nanocrystals synthesized using 11-nm (**h**) and 30-nm (**i**) Co_3O_4 nanocubes as cores and with GBs longer than one critical thickness. The Fourier-filtered images show the induced dislocation and its spacing at the Mn_3O_4 GB.

coincidence, which prevents the formation of an ordered grain structure[13] (Supplementary Fig. 4a–c).

The tetragonal symmetry of Mn_3O_4 produces a gap with an angle of about 8.4° between the {112} planes of adjacent Mn_3O_4 grains along the edges of the Co_3O_4 core[14] (Fig. 1b). Twinned disclinations of Mn_3O_4 {112} with respect to Co_3O_4 {110} are thus formed around the boundary to close the gap. Accordingly, the fast Fourier transform (FFT) of a TEM image with the zone axis along Co_3O_4 [100] shows the extension of the square lattice of Co_3O_4 into Mn_3O_4 (Fig. 1c). A similar FFT analysis with the zone axis along Co_3O_4 [110] further supports the distortion of the Mn_3O_4 lattice structure near the Co_3O_4 nanocube edges (Supplementary Fig. 4d). Each Mn_3O_4 grain has a truncated square pyramidal shape enclosed by {100} and {011} facets (Supplementary Fig. 1c, d). The overall morphology of each Co_3O_4/Mn_3O_4 multigrain nanocrystal can be described as a truncated octahedron consisting of a cubic Co_3O_4 core and Mn_3O_4 grains orthogonally grown from the basal planes of the core.

The overall growth process can be considered to be a generalization or extension of the Stranski–Krastanov (SK) mode growth of a thin film on a two-dimensional (2D) substrate to a finite-sized three-dimensional (3D) case. In SK growth, the thin film grows up to a critical layer thickness (h_c), which is determined by the interplay between the strain and the surface energy, followed by 3D island growth[15,16]. From the perspective of extending the SK growth to 3D nanocrystal substrates, as illustrated in Fig. 2a, b, the mechanism by which the grains grow to form the core/shell nanocrystals can be described as follows. The shell initially grows via a layer-by-layer mode on the facets of the polyhedral nanocrystal core, forming a coherent layer (CL) and accumulating epitaxial strain (Fig. 2a). When the growth thickness exceeds h_c, the growth mode changes to island growth for strain relaxation. In particular, unless there is a GB that exerts geometric-misfit-induced stress (Fig. 1c), the Co_3O_4/Mn_3O_4 core/shell nanocrystals with minimal lattice mismatch exhibit almost no CL characteristics because the strain energy is very small (Fig. 2c, Supplementary Fig. 2a).

The CLs grown on the facets of the core are differently oriented and meet each other at a certain angle (θ_c) around the sharp edges of the core, forming tilt boundaries (Fig. 2b). Consequently, a geometric strain arises due to the mismatch between the CL lattices, which is rendered by anisotropic strain relaxation of the shell material[17–19]. The mismatch is particularly pronounced in nanocrystals with an isotropic lattice core

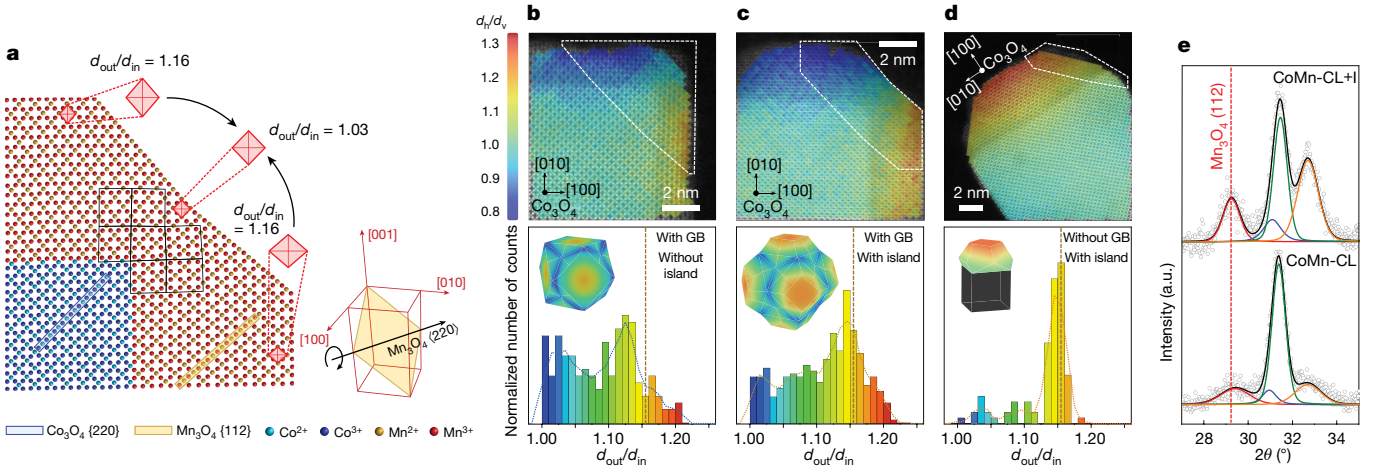


Fig. 3 | GB defects in Co_3O_4/Mn_3O_4 nanocrystals. a, 2D illustration of the atomic arrangement of the nanocrystal with both a GB and an island. Black rectangles represent the distorted Mn_3O_4 unit cells viewed along the [110] direction. The Mn_3O_4 {112} planes rotate around ⟨220⟩. **b**–**d**, Computer-vision-based image-processing results for diamond lattices consisting of Co_3O_4 {220} or Mn_3O_4 {112} planes (top) and histograms (bottom) showing the aspect ratio distribution of the diamond lattices in the outlined regions of the nanocrystals with a GB and without an island (**b**), with both a GB and an island (**c**), and without a GB and with an island (**d**). Colour maps show the distribution of strained diamond lattice cells. In the maps, the horizontal length (d_h; Co_3O_4 [100] direction) of the lattice cells is divided by the vertical length (d_v; Co_3O_4 [010] direction) to distinguish the orientations of the grains. In the histogram, ratios greater than 1 are used to obtain the d_{out}/d_{in} values; that is, the larger of d_h/d_v and d_v/d_h. The insets show 3D models illustrating the strain field of the Mn_3O_4 grains. Vertical dotted lines represent the aspect ratio (1.16) of unstrained Mn_3O_4. **e**, XRD patterns and calculated peak profiles of Co_3O_4/Mn_3O_4 nanocrystals with GBs. Individual peak profiles are Mn_3O_4 (112) (red), (020) (blue), (013) (orange) and Co_3O_4 (220) (green). The full-width at half-maximum of the Mn_3O_4 (112) peak increases considerably from 0.90° for CoMn-CL+I to 1.56° for CoMn-CL.

(for example, cubic lattice) and an anisotropic lattice shell (for example, tetragonal lattice). The h_c value of the CL observed for 2D epitaxy is modified in 3D epitaxy to the value at which the geometric misfit strain, in addition to the epitaxial strain, can be accommodated by the shell material. For example, the Mn_3O_4 lattice at the GBs can accommodate the elastic distortion required to create a continuous disclination with a length of three Mn_3O_4 unit cells (~2.9 nm; h_c)[20]. Therefore, each Mn_3O_4 shell can be divided into two regions: the '3D geometric CL' with GBs and the islands grown farther from the CL (Fig. 2b).

When the GB formation is driven energetically, precise management of the kinetic effects during the shell growth is the key to obtaining the desired coverage and morphology of the shell grains[21]. In our synthetic method using oleylammonium salts, the acid/base ratio of the solution and the concentration of counteranions can be varied (Supplementary Fig. 5). The deposition rate—a kinetic parameter—and the surface energy of the growing nanocrystals—a thermodynamic parameter—are affected by both the acid/base ratio and the counteranion concentration. The former is more sensitive to the acid/base ratio that controls the supersaturation level, and the latter is responsive to the counteranions bound to the surface. Using this synthetic system, we can limit the shell growth in a near-equilibrium thin-film growth regime.

By changing the counteranions that passivate the surface of the shell, the morphology of the grains could be controlled to produce CLs with (CoMn-CL+I) or without islands (CoMn-CL) (Fig. 2d, e, Supplementary Fig. 5c–e). To compare the stabilizing effects of different types of counteranions, $MnCl_2$ and $Mn(HCOO)_2$ were tested. With $HCOO^-$ ions, lateral growth (that is, wetting of the core surface) of the grains is promoted without the formation of the islands because the low surface energy can compensate for the energy expended on the epitaxial strain and even the large geometric strain to form the GBs (Fig. 2d). On the other hand, when $MnCl_2$ is used, Mn_3O_4 islands with high surface energy tend to grow on the CLs to relax the strain, and the creation of CLs/GBs is inhibited (Fig. 2e). For almost the same elemental composition, the Mn_3O_4 shell of CoMn-CL has larger coverage, meaning not only more grains and GBs, but also a lower height/edge-length ratio than those of CoMn-CL+I. This behaviour of the shell material, which switches the growth mode between lateral and vertical, depending on the ligand stabilization capability, minimizes the total free energy while incorporating the geometric misfit strain[9]. To further drive near-equilibrium growth, we designed experiments that repeat the shell growth under the same supersaturated conditions (Fig. 2f, g, Supplementary Discussion). As a result, the shell coverage increases and subsequently the GB number also rises, producing nanocrystals with a near-equilibrium structure in which the grains form a closed loop.

Furthermore, we could tailor the structures of the GB defects (for example, disclinations and dislocations) either by using different types of counteranions that can promote non-equilibrium shell growth or by changing the core size (Fig. 2h, i, Supplementary Figs. 5f, 6, Supplementary Discussion). Because of the stress relief through the formation of dislocations at the core/shell interface or in the GBs, the GBs are extended along with the periodic/zigzag dislocations.

The structure of the GB defects is illustrated using the area marked by the green square in the HAADF-STEM image of a nanocrystal with both GBs and islands in Supplementary Fig. 7a (Fig. 3a). Here, d_{in} and d_{out} are defined as the interatomic spacings among the M^{2+} cations (M = Co, Mn) that are parallel (in-plane) and perpendicular (out-of-plane) to the interface, respectively, on the 2D projection of the lattice. The d_{out}/d_{in} ratio of 1.03 and the square-like shape of the unit cell at the GB in Fig. 3a result from the rotation of Mn_3O_4 {112} planes around the Mn_3O_4 ⟨220⟩ axes. The FFTs of the STEM images of all the CoMn-CL and CoMn-CL+I samples with GBs taken along the Co_3O_4 [100] zone axis consistently show the Bragg peaks of Mn_3O_4 (112) dispersed towards Co_3O_4 (220) reflections (Supplementary Fig. 7).

Strain field mapping was conducted by image-processing the atomic-resolution HAADF-STEM image (Fig. 3b–d, Supplementary Fig. 8, Supplementary Methods). The extent of local distortion is presented in terms of the aspect ratio of a diamond lattice consisting of Co_3O_4 {220} or Mn_3O_4 {112} planes. The colour map images clearly show that the strain field has narrow bands of reduced d_{out}/d_{in} lattices at the GBs around the nanocube edges. The statistical distributions of the aspect ratios are extracted from the regions defined by the white dashed outlines, which correspond to the lateral views of two adjacent grains sharing a GB. The most frequent d_{out}/d_{in} values for the nanocrystals with islands are near 1.16, which is close to the $c/(\sqrt{2}a)$ value of the

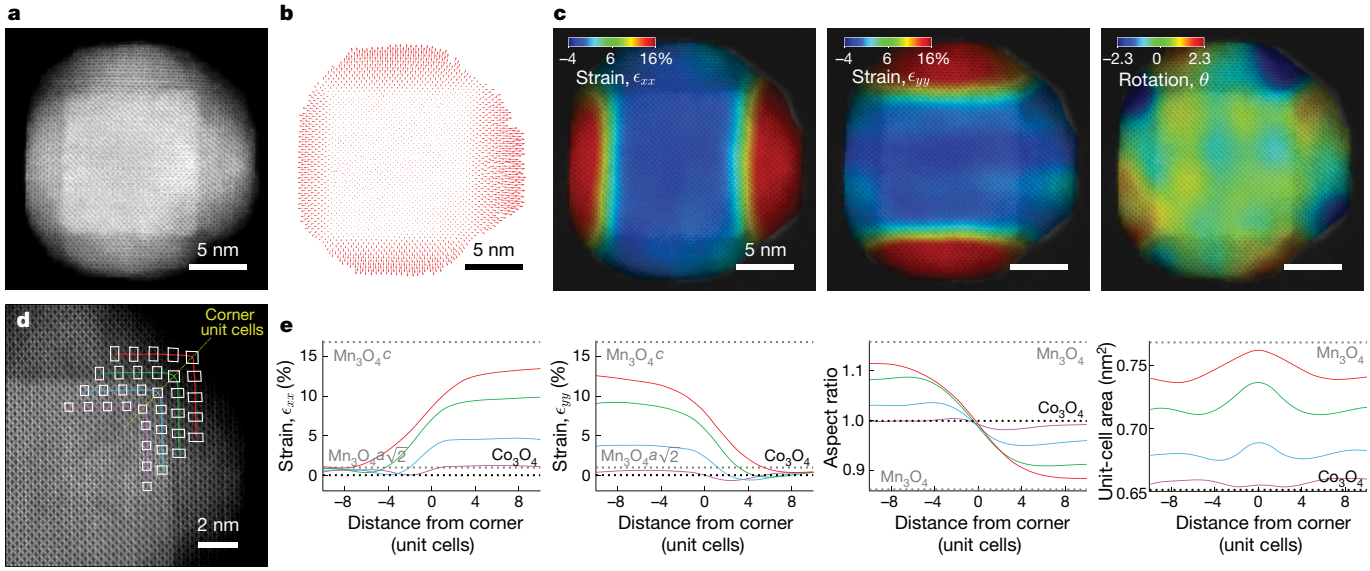


Fig. 4 | Strain tensor measurements of Co_3O_4/Mn_3O_4 nanocrystal. a, HAADF-STEM image of the nanocrystal. **b**, Map of displacement based on the atomic position of Co_3O_4. **c**, Infinitesimal strains and rotation in the *x* and *y* directions and rotation of the unit cell. **d**, Line traces (coloured lines) and unit cells (white rectangles) showing the change in aspect ratio and volume of the unit cells. **e**, Infinitesimal strains in the *x* and *y* directions, aspect ratio and unit cell area over the line traces shown in **d**.

regular Mn_3O_4 lattice (also see Supplementary Fig. 9). On the other hand, lower values are observed for the nanocrystals without islands, which can be attributed to the distribution of tensile and compressive strains induced along Mn_3O_4 [220] and [004], respectively, owing to the gap closing.

The local strain distribution is reflected in the electron diffraction patterns and powder XRD data through a reasonably uniform grain configuration in the nanocrystals (Fig. 3e, Supplementary Figs. 9, 10). The GB areas and gap angles are almost identical for all the GBs, implying that the residual stresses associated with the gap closing between two grains near each GB are almost the same. At a given residual stress, an island appears to have less normal strain per plane than a CL according to the strain field mapping. The Mn_3O_4 (112) XRD peak for the CoMn-CL nanocrystals is broader than that for the CoMn-CL+I nanocrystals at a similar Mn content, which indicates a higher proportion of nonuniform deformation due to the smaller volume or the absence of islands. Such uniformity in the GB structure provides a valuable opportunity to investigate the properties of strained GB structures, which are otherwise hard to achieve. For instance, one can obtain the correlation between the microscopic defect structures and the ensemble properties.

When the gap closes, we observe not only normal strain and the accompanying Poisson effect, but also shear strain and rotation of unit cells at the GBs due to the high elastic anisotropy of orthotropic Mn_3O_4[22]. The more accurate strain tensor measurement[23], which is of the order of 0.5 nm, shows that the normal strain and the rotation are the principal deformation components (Fig. 4, Supplementary Fig. 11; see Supplementary Methods for the algorithm). In both the nanocrystals with and without islands, the aspect ratios of the unit cells at the GBs are close to unity. Furthermore, the sizes of the unit cells increase with increasing distance from the Co_3O_4/Mn_3O_4 interface, with very similar values are for unit cells at the same distance. Interestingly, the Mn_3O_4 shell accommodates a large 3D strain (~8% for each axis) per GB without producing any dislocations. The value is quite large compared to that of decahedral Au nanoparticles—another material well known to exhibit GBs within nanocrystals[14]. Moreover, GBs in the form of disclinations could also be created in the core/shell nanocrystals of other material combinations, such as Fe_3O_4/Mn_3O_4, Mn_3O_4/Co_3O_4, Fe_3O_4/Co_3O_4 and Pd/Au, via geometric misfit strain (Supplementary Figs. 12–15, Supplementary Discussion).

Thin films in 2D SK growth mode often exhibit periodic ripple patterns along with island formation, which is mainly attributed to the epitaxial strain[9,24]. Pre-patterned substrates with ordered pit arrays and stripes are used for directing the island growth and ordering[25]. In our demonstration of the 3D analogy of the SK growth, each of the well-defined polyhedral nanocrystals (that is, the core) acts as a pre-patterned substrate. Consequently, a thin film (that is, the shell) grows with a strain field patterned along the sharp edges owing to the geometric misfit strain in addition to the epitaxial strain. This 3D network of strains also organizes the grains into a 3D superlattice[26]. Given that the self-organization of lattice domains in 2D epitaxial thin films has been a key element for various physical phenomena, this utilization of geometric misfit strains in 3D shell growth could facilitate the engineering of the properties of nanocrystalline materials for improved applications, such as in mechanics, catalysis and dielectrics[27–30].

Online content

Any methods, additional references, Nature Research reporting summaries, source data, extended data, supplementary information, acknowledgements, peer review information; details of author contributions and competing interests; and statements of data and code availability are available at https://doi.org/10.1038/s41586-019-1899-3.

1. Siegel, R. W. & Thomas, G. J. Grain boundaries in nanophase materials. *Ultramicroscopy* **40**, 376–384 (1992).
2. Ovid'ko, I. A. Deformation of nanostructures. *Science* **295**, 2386 (2002).
3. Read, W. T. & Shockley, W. Dislocation models of crystal grain boundaries. *Phys. Rev.* **78**, 275–289 (1950).
4. Liu, H. H. et al. Three-dimensional orientation mapping in the transmission electron microscope. *Science* **332**, 833–834 (2011).
5. Feng, B. et al. Atomic structures and oxygen dynamics of CeO_2 grain boundaries. *Sci. Rep.* **6**, 20288 (2016).
6. Lu, K. Stabilizing nanostructures in metals using grain and twin boundary architectures. *Nat. Rev. Mater.* **1**, 16019 (2016).
7. Klapper, H. & Rudolph, P. in *Handbook of Crystal Growth* 2nd edn 1093–1141 (Elsevier, 2015).
8. Kwon, S. G. et al. Heterogeneous nucleation and shape transformation of multicomponent metallic nanostructures. *Nat. Mater.* **14**, 215–223 (2015).
9. Dixit, G. K. & Ranganathan, M. Consequences of elastic anisotropy in patterned substrate heteroepitaxy. *Nanotechnology* **29**, 365305 (2018).
10. Yang, B., Liu, F. & Lagally, M. G. Local strain-mediated chemical potential control of quantum dot self-organization in heteroepitaxy. *Phys. Rev. Lett.* **92**, 025502 (2004).

11. Oh, M. H. et al. Galvanic replacement reactions in metal oxide nanocrystals. *Science* **340**, 964–968 (2013).
12. Pan, A. et al. Insight into the ligand-mediated synthesis of colloidal $CsPbBr_3$ perovskite nanocrystals: the role of organic acid, base, and cesium precursors. *ACS Nano* **10**, 7943–7954 (2016).
13. Tsivion, D., Schvartzman, M., Popovitz-Biro, R., von Huth, P. & Joselevich, E. Guided growth of millimeter-long horizontal nanowires with controlled orientations. *Science* **333**, 1003–1007 (2011).
14. Johnson, C. L. et al. Effects of elastic anisotropy on strain distributions in decahedral gold nanoparticles. *Nat. Mater.* **7**, 120–124 (2008).
15. Shklyaev, O. E., Beck, M. J., Asta, M., Miksis, M. J. & Voorhees, P. W. Role of strain-dependent surface energies in Ge/Si(100) island formation. *Phys. Rev. Lett.* **94**, 176102 (2005).
16. Chen, G. et al. Formation of Ge nanoripples on vicinal Si (1110): from Stranski–Krastanow seeds to a perfectly faceted wetting layer. *Phys. Rev. Lett.* **108**, 055503 (2012).
17. Sneed, B. T., Young, A. P. & Tsung, C.-K. Building up strain in colloidal metal nanoparticle catalysts. *Nanoscale* **7**, 12248–12265 (2015).
18. Foster, C. M., Pompe, W., Daykin, A. C. & Speck, J. S. Relative coherency strain and phase transformation history in epitaxial ferroelectric thin films. *J. Appl. Phys.* **79**, 1405–1415 (1996).
19. Sun, Y. et al. Ambient-stable tetragonal phase in silver nanostructures. *Nat. Commun.* **3**, 971–976 (2012).
20. Romanov, A. E. & Kolesnikova, A. L. Application of disclination concept to solid structures. *Prog. Mater. Sci.* **54**, 740–769 (2009).
21. Gránásy, L., Podmaniczky, F., Tóth, G. I., Tegze, G. & Pusztai, T. Heterogeneous nucleation of/on nanoparticles: a density functional study using the phase-field crystal model. *Chem. Soc. Rev.* **43**, 2159–2173 (2014).
22. Gaillac, R., Pullumbi, P. & Coudert, F. X. ELATE: An open-source online application for analysis and visualization of elastic tensors. *J. Phys. Condens. Matter* **28**, 275201–275205 (2016).
23. Ophus, C., Ciston, J. & Nelson, C. T. Correcting nonlinear drift distortion of scanning probe and scanning transmission electron microscopies from image pairs with orthogonal scan directions. *Ultramicroscopy* **162**, 1–9 (2016).
24. Hu, H., Gao, H. J. & Liu, F. Theory of directed nucleation of strained islands on patterned substrates. *Phys. Rev. Lett.* **101**, 216102 (2008).
25. Zhong, Z. & Bauer, G. Site-controlled and size-homogeneous Ge islands on prepatterned Si (001) substrates. *Appl. Phys. Lett.* **84**, 1922–1924 (2004).
26. Damodaran, A. R. et al. New modalities of strain-control of ferroelectric thin films. *J. Phys. Condens. Matter* **28**, 263001 (2016).
27. Li, X., Wei, Y., Lu, L., Lu, K. & Gao, H. Dislocation nucleation governed softening and maximum strength in nano-twinned metals. *Nature* **464**, 877–880 (2010).
28. Mariano, R. G., Mckelvey, K., White, H. S. & Kanan, M. W. Selective increase in CO_2 electroreduction activity at grain-boundary surface terminations. *Science* **358**, 1187–1192 (2017).
29. Fan, F. et al. Continuous-wave lasing in colloidal quantum dot solids enabled by facet-selective epitaxy. *Nature* **544**, 75–79 (2017).
30. Gao, P. et al. Atomic-scale mechanisms of ferroelastic domain-wall-mediated ferroelectric switching. *Nat. Commun.* **4**, 2791 (2013).

Publisher's note Springer Nature remains neutral with regard to jurisdictional claims in published maps and institutional affiliations.

© The Author(s), under exclusive licence to Springer Nature Limited 2020

Data availability

The data that produced and support the findings of this study are available from the corresponding author upon request.

Code availability

Strain and rotation mapping using real-space peak fitting, geometric phase analysis and other Fourier filtering measurements were performed using custom MATLAB scripts. The raw image data and analysis codes are available upon reasonable request.

Acknowledgements Synthesis and image analysis of the nanocrystal samples were supported by the Research Center Program of IBS in Korea (IBS-R006-D1 to T.H.; IBS-R006-G1 to Y.-E.S. and K.K. The theoretical part of this work was also supported by the US Department of Energy, Office of Science, Office of Basic Energy Sciences, Materials Sciences and Engineering Division, under contract number DE-AC02-05-CH11231 within the Physical Chemistry of Inorganic Nanostructures Program (KC3103 to A.P.A.). The computational work was supported by the Supercomputing Center/Korea Institute of Science and Technology Information with supercomputing resources including technical support (KSC-2014-C3-037 to K.K.). Work at the Molecular Foundry was supported by the Office of Science, Office of Basic Energy Sciences, of the US Department of Energy under contract number DE-AC02-05CH11231. Experiments at PLS-II were supported in part by MSIP and POSTECH.

Author contributions M.H.O., M.G.C., A.P.A. and T.H. conceived the research. M.H.O. and M.G.C. designed and performed the experiments and analysed the results. I.P. and K.K. performed the density functional theory calculations and analysis. Y.P.K. and S.M. conducted the computer-vision-based image processing of HAADF-STEM images. C.O. conducted the strain tensor measurements for the HAADF-STEM micrographs. M.G.K. and B.J. contributed to the analysis of X-ray absorption spectroscopy and X-ray photoelectron spectroscopy data, respectively. D.Y.C., J.M.Y., D.K., X.W.G. and Y.-E.S. discussed and commented on the results. J.J. and J.H. prepared the samples for the TEM analysis. M.H.O., M.G.C., D.K., A.P.A. and T.H. wrote the manuscript. A.P.A. and T.H. supervised the project. All the authors commented on the manuscript.

Competing interests The authors declare no competing interests.

Additional information
Supplementary information is available for this paper at https://doi.org/10.1038/s41586-019-1899-3.
Correspondence and requests for materials should be addressed to A.P.A. or T.H.
Peer review information *Nature* thanks Laura Bocher, Yong Ding and the other, anonymous, reviewer(s) for their contribution to the peer review of this work.
Reprints and permissions information is available at http://www.nature.com/reprints.

Article

Importance and vulnerability of the world's water towers

https://doi.org/10.1038/s41586-019-1822-y

Received: 27 May 2019

Accepted: 11 November 2019

Published online: 9 December 2019

W. W. Immerzeel[1,2,26]*, A. F. Lutz[1,2,26]*, M. Andrade[3,4], A. Bahl[5], H. Biemans[6], T. Bolch[7], S. Hyde[5], S. Brumby[5], B. J. Davies[8], A. C. Elmore[5], A. Emmer[9], M. Feng[10], A. Fernández[11], U. Haritashya[12], J. S. Kargel[13], M. Koppes[14], P. D. A. Kraaijenbrink[1], A. V. Kulkarni[15], P. A. Mayewski[16], S. Nepal[17], P. Pacheco[18], T. H. Painter[19], F. Pellicciotti[20], H. Rajaram[21], S. Rupper[22], A. Sinisalo[17], A. B. Shrestha[17], D. Viviroli[23], Y. Wada[24], C. Xiao[25], T. Yao[10] & J. E. M. Baillie[5]

Mountains are the water towers of the world, supplying a substantial part of both natural and anthropogenic water demands[1,2]. They are highly sensitive and prone to climate change[3,4], yet their importance and vulnerability have not been quantified at the global scale. Here we present a global water tower index (WTI), which ranks all water towers in terms of their water-supplying role and the downstream dependence of ecosystems and society. For each water tower, we assess its vulnerability related to water stress, governance, hydropolitical tension and future climatic and socio-economic changes. We conclude that the most important (highest WTI) water towers are also among the most vulnerable, and that climatic and socio-economic changes will affect them profoundly. This could negatively impact 1.9 billion people living in (0.3 billion) or directly downstream of (1.6 billion) mountainous areas. Immediate action is required to safeguard the future of the world's most important and vulnerable water towers.

The term 'water tower' is used to describe the water storage and supply that mountain ranges provide to sustain environmental and human water demands downstream[1,2]. Compared to its downstream area, a water tower (seasonally) generates higher runoff from rain as a result of orographic precipitation and delays the release of water by storing it in snow and glaciers (because of lower temperatures at high altitude) and lake reserves. Because of their buffering capacity, for instance by supplying glacier melt water during the hot and dry season, water towers provide a relatively constant water supply to downstream areas. We define a water tower unit (WTU; see Methods, Extended Data Fig. 1) as the intersection between major river basins[5] and a topographic mountain classification based on elevation and surface roughness[6]. Since water supply and demand are linked at the river basin scale, the basin is the basis for the WTU. One WTU can therefore contain multiple topographically different mountain ranges and we assume that it provides water to the areas in the downstream river basin that are hydrologically connected to the WTU (Extended Data Fig. 1, Extended Data Table 1 and 2). Subsequently, we consider only cryospheric WTUs by imposing thresholds on satellite-derived snow-cover data[7] and a glacier inventory[8], because the buffering role of glaciers and snow and the delayed supply of melt water is a defining feature of water towers. Consequently, there are regions (for example, in Africa), which do contain mountain ranges, but because of their small snow and ice reserves they do not meet the WTU criteria. In total, we define 78 WTUs globally (see Methods), which are home to more than 250 million people. However, more than 1.6 billion people live in areas receiving water from WTUs, which is about 22% of the global population[9] (Fig. 1).

Water towers have an essential role in the Earth system and are particularly important in the global water cycle[1,2]. In addition to their water supply role, they provide a range of other services[10,11]. About 50% of the global biodiversity hotspots on the planet are located in mountain regions[12], they contain a third of the entire terrestrial species diversity[13], and are extraordinarily rich in plant diversity[14]. Moreover, mountain ecosystems provide key resources for human livelihoods, host important cultural and religious sites, and attract millions of tourists globally[6]. Economically, 4% and 18% of the global gross domestic product (GDP) is generated in WTUs and WTU-dependent basins respectively[15]. Furthermore, mountains are highly sensitive to climate change[3,4] and are warming faster than low-lying areas owing to elevation-dependent warming[16]. Climate change therefore threatens the entire mountain

[1]Faculty of Geosciences, Department of Physical Geography, Utrecht University, Utrecht, The Netherlands. [2]FutureWater, Wageningen, The Netherlands. [3]Universidad Mayor de San Andrés, Institute for Physics Research, La Paz, Bolivia. [4]University of Maryland, Department of Atmospheric and Oceanic Science, College Park, MD, USA. [5]National Geographic Society, Washington, DC, USA. [6]Wageningen University and Research, Water and Food Group, Wageningen, The Netherlands. [7]School of Geography and Sustainable Development, University of St Andrews, St Andrews, UK. [8]Centre for Quaternary Research, Department of Geography, Royal Holloway University of London, Egham, UK. [9]Czech Academy of Sciences, Global Change Research Institute, Brno, Czech Republic. [10]Institute of Tibetan Plateau Research, Chinese Academy of Sciences, Beijing, China. [11]Department of Geography, Universidad de Concepción, Concepción, Chile. [12]Department of Geology, University of Dayton, Dayton, OH, USA. [13]Planetary Science Institute, Tucson, AZ, USA. [14]Department of Geography, University of British Columbia, Vancouver, British Columbia, Canada. [15]Indian Institute of Science, Divecha Center for Climate Change, Bangalore, India. [16]University of Maine, Climate Change Institute, Orono, ME, USA. [17]International Centre for Integrated Mountain Development, Kathmandu, Nepal. [18]Agua Sustentable, Irpavi, La Paz, Bolivia. [19]Joint Institute for Regional Earth System Science and Engineering, University of California, Los Angeles, CA, USA. [20]Swiss Federal Research Institute WSL, Birmensdorf, Switzerland. [21]Johns Hopkins University, Department of Environmental Health and Engineering, Baltimore, MD, USA. [22]University of Utah, Department of Geography, Salt Lake City, UT, USA. [23]University of Zurich, Department of Geography, Zurich, Switzerland. [24]International Institute for Applied Systems Analysis, Laxenburg, Austria. [25]State Key Laboratory of Earth Surface Processes and Resource Ecology, Beijing Normal University, Beijing, China. [26]These authors contributed equally: W. W. Immerzeel, A. F. Lutz. *e-mail: w.w.immerzeel@uu.nl; a.f.lutz@uu.nl

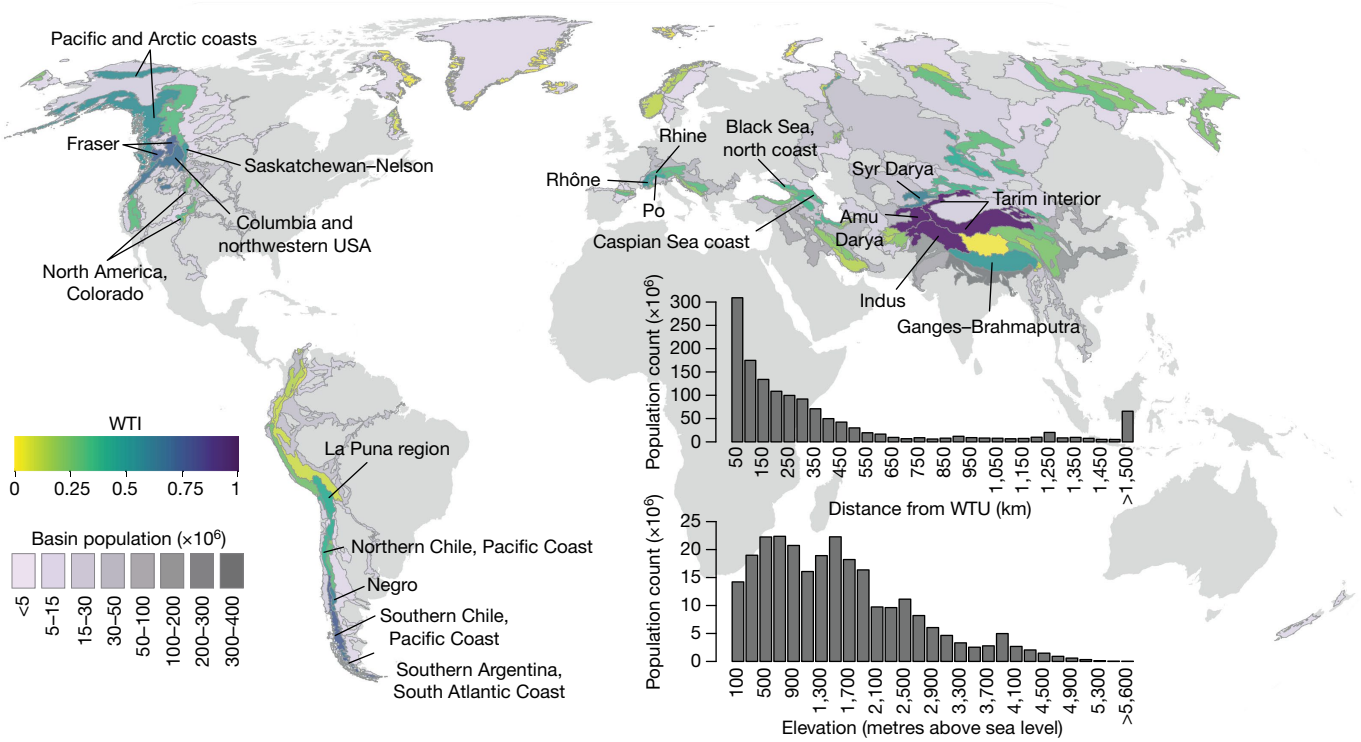


Fig. 1 | The WTI, the population in WTUs and their downstream basins. The WTI, derived from the SI and the DI, is shown for all 78 WTUs, in combination with the shaded total population in all WTU-dependent river basins. Labels indicate the five water towers with the highest WTI value per continent. The insets show the number of people living in WTUs as a function of elevation and of the downstream population's proximity to the WTUs[9].

ecosystem. Worldwide, the vast majority of glaciers are losing mass[17], snow melt dynamics are being perturbed[18–21], and precipitation and evapotranspiration patterns are shifting, all leading to future changes in the timing and magnitude of mountain water availability[22]. Besides, the combination of cryosphere degradation and increases in climate extremes implies changing sediment loads affecting the quality of water supplied by mountains[23].

Not only are the world's water towers crucial to human and ecosystem survival, the steep terrain in combination with extreme climatic conditions, and in some regions seismic or volcanic activity, frequently triggers landslides, rock fall, debris flows, avalanches, glacier hazards and floods[24,25]. Since 2000, over 200,000 people have died in WTUs as a result of natural disasters[26]. Climate change, in combination with population growth, urbanization and economic and infrastructural developments, is likely to exacerbate the impact of natural hazards and further increase the vulnerability of these water towers[23,27–30].

Quantifying importance of water towers

Consequently, there is a strong need for a consistent framework within which to assess and rank the importance and vulnerability of individual WTUs in order to guide global research, as well as conservation and policy-making efforts. Here we develop such a framework according to quantifiable indicators for both the water supply and demand sides of each WTU. Conceptually, a WTU is deemed to be important when its water resources (liquid or frozen) are plentiful relative to its downstream water availability and when its basin water demand is high and cannot be met by downstream water availability alone. Ideally, such an assessment would require a global-scale, high-resolution, fully coupled atmospheric–cryospheric–hydrological model that can resolve the interactions between extreme topography and the atmosphere, fully account for snow and ice dynamics, and incorporate anthropogenic interventions in the hydrological cycle. It would also require models that include socio-economic impacts on sectoral water demands and a spatially explicit attribution of water sources (for example, meltwater, groundwater, surface runoff) to water use. Although excellent progress has been made in specific regions and for specific sectors[31], at the global scale this is not yet feasible. We therefore derive indices covering relevant drivers for both the water supply and demand of a WTU's water budget (see Methods), which we combine to derive a water tower index (WTI).

The supply index (SI) is based on the average of four indicators that are quantified for each WTU: precipitation, snow cover, glaciers and surface water (Fig. 2a, Extended Data Table 3, Supplementary Table 1 and Methods). If the precipitation in the WTU (Extended Data Fig. 3a) is high relative to the overall basin precipitation and if the inter-annual and intra-annual variation is low (that is, the supply is constant), a WTU scores highly on the precipitation indicator. If a WTU has persistent snow cover (Extended Data Fig. 3b) throughout the year and the snowpack shows lower inter-annual variation, this will result in a high snow indicator. Similarly, if the total glacier ice volume (Extended Data Fig. 4a) and glacier water yield in a WTU are high relative to the basin precipitation then a WTU has a high glacier indicator value. Finally, we assess the amount of water stored in lakes and reservoirs in a WTU (Extended Data Fig. 4b) compared to basin precipitation to derive a surface water indicator.

There is considerable variability in the power of WTUs to supply water. In Asia, the Tibetan Plateau has the highest ranking because of the large amounts of water stored in lakes, but a large part of the Tibetan Plateau is endorheic and its water resources are disconnected from the downstream demand. The Indus WTU has an important water-supplying role with a balanced mix of precipitation, glaciers, snow and surface water. In Europe, the Arctic Ocean islands, Iceland and Scandinavia have extensive stocks of water stored in their WTUs. Iceland stands out with some of the thickest glaciers in the world and a glacier ice storage (about

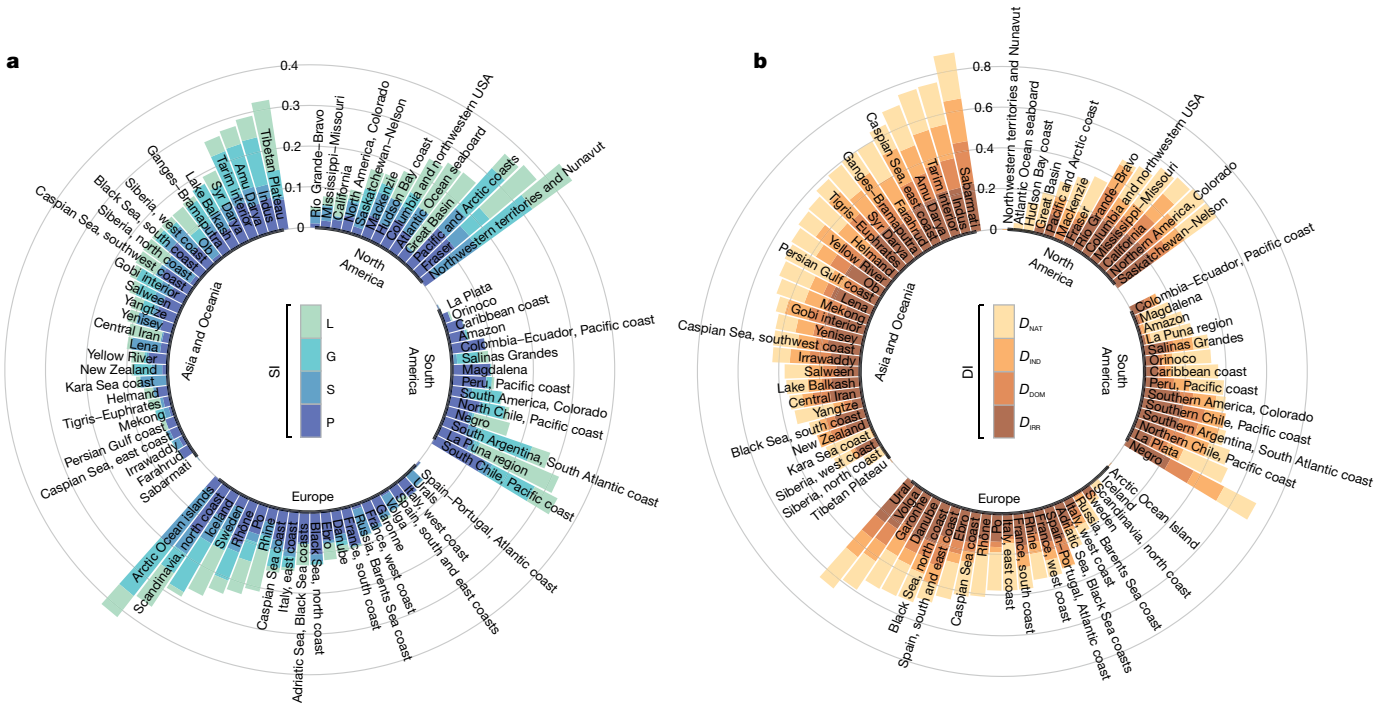


Fig. 2 | The SI and DI. a, **b**, The SI (**a**) and the DI (**b**) of each WTU grouped by continent and ordered by SI or DI value, respectively. The stacked bars show the four indicator values for surface water (*L*), glacier (*G*), snow (*S*) and precipitation (*P*). In **b**, the stacked bars show the four indicator values for natural (D_{NAT}), industrial (D_{IND}), domestic (D_{DOM}) and irrigation demands (D_{IRR}). Calculation details of the indicators and indices are provided in Extended Data Tables 3, 4.

1,027 km^3) that is 15 times as large as its total annual WTU precipitation (about 67 km^3). In South America, the mountain ranges (Extended Data Tables 1, 2) supplying the Southern Chilean Pacific coast regions and La Puna Region are the most prominent water towers, because of large glacier ice reserves and high orographic precipitation rates and because of the large amount of water stored in lakes (in the La Puna region). The Northwest Territories and Nunavut, Fraser and the Pacific and Arctic coast are the key WTUs in North America. In the Northwest Territories and Nunavut the relevance of the WTU is primarily driven by the abundance of glaciers, snow and surface water. However, the precipitation indicator value is low, meaning that mountain precipitation is low relative to the overall basin precipitation.

To derive a demand index (DI) for each WTU, we quantify the monthly water requirements to be supplied by the water towers to sustain the WTU basin's net sectoral water demand for irrigation, industrial (energy and manufacturing) and domestic purposes, and monthly natural water demand, relative to the total annual demand (Fig. 2b, Extended Data Table 4, Supplementary Table 1). Monthly sectoral water requirements are estimated by subtracting the monthly water availability downstream (ERA5 precipitation minus natural evapotranspiration[32]) from the monthly net demands[33]. The DI is the average of the four indicators (see Methods). Figure 2b demonstrates considerable variability, globally and within continents, in the demands that WTUs need to sustain. Irrigation water demands are the highest of the four demand types, and this is relatively consistent across the continents. The Asian river basins, specifically the heavily irrigated and densely populated basins such as the Indus, Amu Darya, Tigris, Ganges-Brahmaputra and Tarim, score more highly on the DI than other basins across the world and they score highly on each sectoral demand indicator. In those basins, the water required to close the gap between demand and downstream supply may also originate from (unsustainable) groundwater use[34,35]. However, in those cases, when there is a large water gap being (partly) closed by unsustainable groundwater pumping, the WTU water supply is critical both to meet the demand and to recharge the aquifers.

In Europe, the Volga and Ural in Russia show the highest DI values, including high values for the natural demand indicator, whereas the Negro basin has the highest DI in South America. In North America a range of basins scores equally highly, but for different reasons. For example, the Mississippi–Missouri basin scores highly particularly because of a high natural demand indicator value, whereas the California basin scores highly on all four demand indicators.

Ultimately, the presence of mountain water resources, either as additional rain or stored in snow, ice or lakes, in conjunction with a high demand downstream, determines whether a WTU has an indispensable role (Extended Data Fig. 2). The WTI is the product of the SI and the DI, for which the values are subsequently normalized over the range of WTI values found for all 78 WTUs (Fig. 1, Supplementary Table 1). Globally, the upper Indus basin is the most critical water tower unit (WTI = 1.00 ± 0.03) with abundant water resources in the Karakoram, Hindu-Kush, Ladakh and Himalayan mountain ranges in combination with a densely populated and intensively irrigated downstream basin[22,36]. In North America, the Fraser and Columbia river basins are the most critical WTUs (WTI = 0.62 ± 0.07 and 0.58 ± 0.06, respectively). The Fraser basin is rich in surface water resources, and has a high natural water demand downstream, whereas the Columbia basin is rich in snow and glacier resources in combination with a high irrigation demand. In South America, the Cordillera Principal, the Cordillera Patagónica Sur and the Patagonian Andes are key WTUs in the supply of water to the South Atlantic and Pacific coastal regions and the Negro basin. In Europe, the Alps are the most relevant water-supplying mountain range, meeting the demands of the Rhône (WTI = 0.45 ± 0.07), Po (WTI = 0.39 ± 0.07) and Rhine (WTI = 0.32 ± 0.11) basins. We note that several WTUs that score highly on either the SI or the DI do not rank highly in the final WTI. For example, the Tibetan Plateau and Arctic Ocean islands WTUs score highly on the SI, but have the lowest scores on the DI, owing to low water demands (Fig. 2b). By contrast, the Sabarmati in Asia with a small portion of its water coming from the Himalayas has the highest DI, but a low SI.

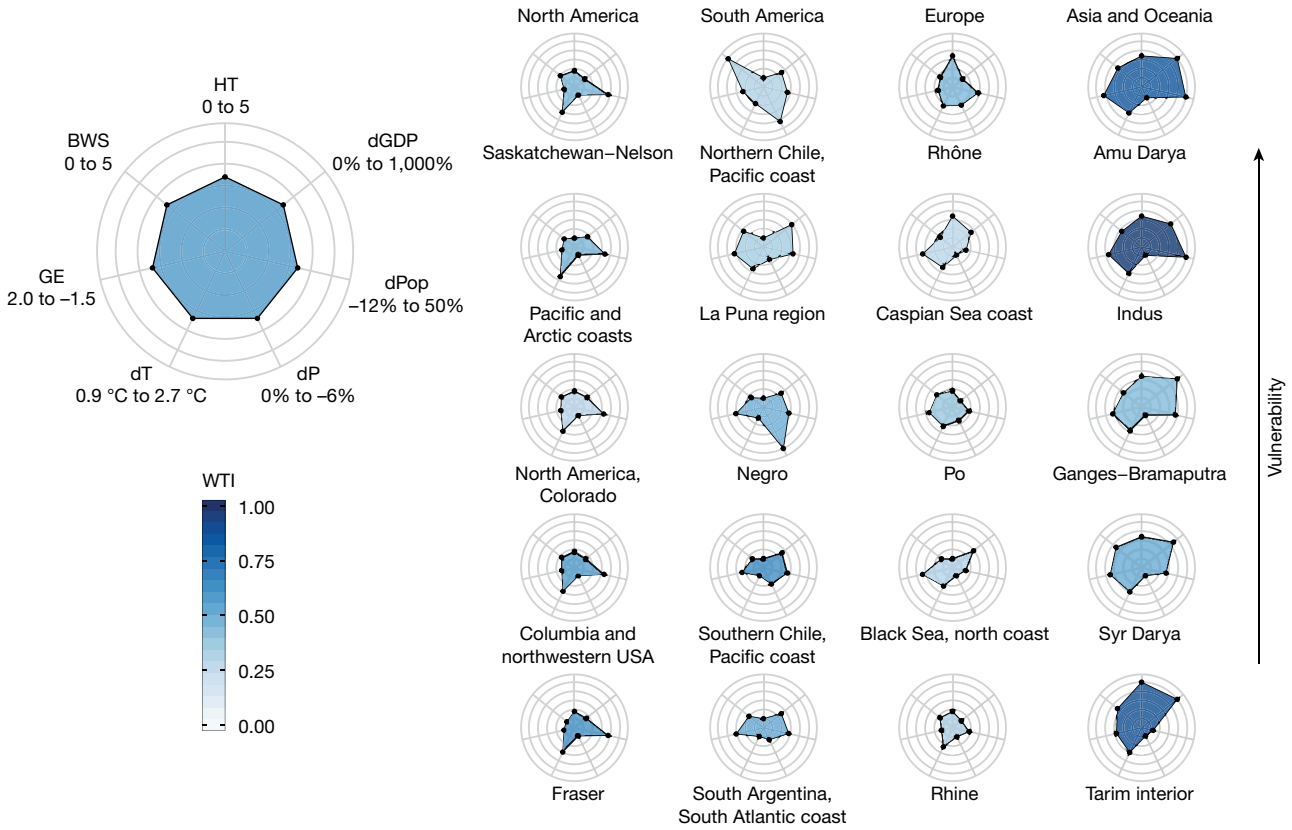


Fig. 3 | The vulnerability and projected change of the top five WTUs of each continent. The total vulnerability (indicated by larger polygons), and projected change indicators of the five most important WTUs on each continent. BWS is the baseline water stress indicator of the basin[38]; GE is an indicator for government effectiveness in the basin[39]; HT is hydro-political tension[37]; dGDP[41] and dPop[9] are the projected changes in gross domestic product and population between 2000 and 2050, according to Shared Socioeconomic Pathway 2 (SSP2)[67]; dP[40] and dT[40] are the projected precipitation and temperature changes between 2000 and 2050 according to the CMIP5 multi-model ensemble mean for Representative Concentration Pathway (RCP) 4.5[40]. WTUs are ranked by vulnerability (highest vulnerability on top); colour filling indicates the WTU's WTI value. See Methods for calculation details.

Vulnerability of the water towers

We assess the vulnerability of each WTU and show this for the five most important (that is, with highest WTI values) WTUs in Asia and Oceania, Europe, North America and South America (Fig. 3, Supplementary Table 2). For this analysis, we include the hydro-political tension[37], baseline water stress[38], government effectiveness[39], projected climate change[40], projected change in GDP[41], and projected population change[9] (see Methods). The highest-ranking WTUs of South America and Asia in particular are more vulnerable than those in North America and Europe. Strikingly, the Indus, which is globally the most important water tower (Fig. 4), is also very vulnerable. The Indus is a transboundary basin with considerable hydro-political tension between its riparian countries Pakistan, India, China and Afghanistan. The population of approximately 235 million people in the basin in 2016 is projected to increase by 50% by 2050, and the basin's GDP is projected to encounter a nearly eightfold increase[41]. The average annual temperature in the Indus WTU is projected to increase by 1.9 °C between 2000 and 2050, compared to 1.8 °C in the downstream section[40]. The average annual precipitation in the Indus WTU is projected to increase by 0.2%, compared to 1.4% downstream[40]. It is evident that, owing to the expected strong growth in population and economic development, the demand for fresh water will rise exponentially[42]. Combined with increased climate change pressure on the Indus headwaters, an already high baseline water stress and limited government effectiveness, it is uncertain whether the basin can fulfil its water tower role within its environmental boundaries. It is unlikely that the Indus WTU can sustain this pressure.

The Indus does not stand alone, however. Nearly all important WTUs in Asia are also highly vulnerable (Fig. 3). Most WTUs are transboundary, densely populated, heavily irrigated basins and their vulnerability is primarily driven by high population and economic growth rates and, in most cases, ineffective governance. Moreover, the Syr Darya, Amu Darya and Indus, in particular, are characterized by considerable hydro-political tension[37]. In most cases, downstream riparian states are dependent on mountain water resources provided by bordering upstream states to supply the competing irrigation, hydropower and domestic demands. In South America, the vulnerability is less than for the Asian WTUs, and the drivers are variable. On northern Chile's Pacific coast, the baseline water stress and a projected decrease in precipitation (−4.8%) cause the vulnerability, whereas population and economic growth render the La Puna region's WTU vulnerable. In North America, the vulnerabilities are related to population growth and temperature increase.

Global assets with increasing importance

Planetary boundaries (for example, the CO_2 concentration, global freshwater use and biosphere integrity) are defined as thresholds within which humanity can safely function without abrupt large-scale changes to the environment[43]. Climate change and biosphere integrity have been identified as the core planetary boundaries with the potential to change the state of the Earth system should they be consistently transgressed for a prolonged period of time[44]. The global food system, in particular, has been identified as a major pressure on the planetary

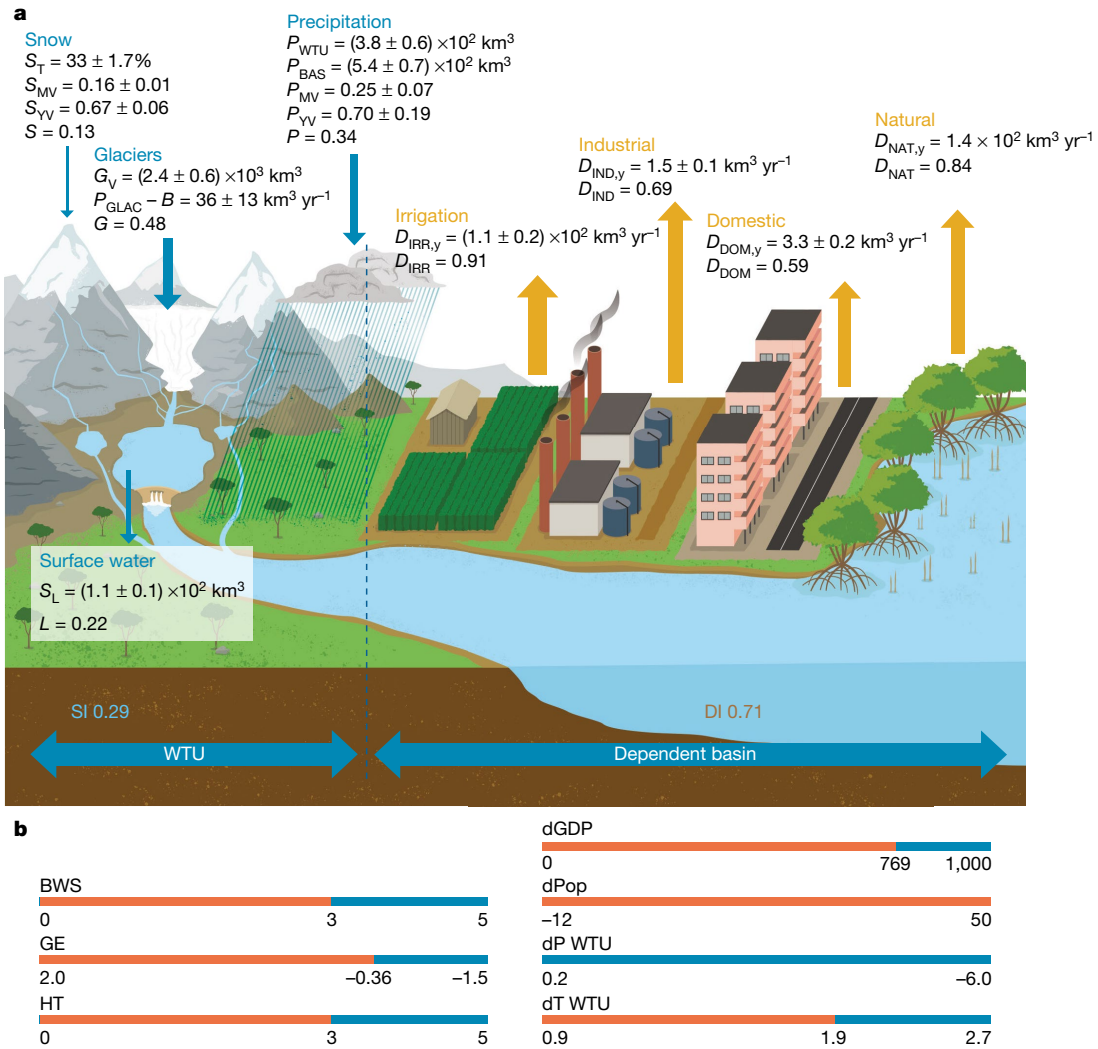


Fig. 4 | WTI and vulnerabilities of the Indus basin. a, The supply and demand indicators. **b**, The vulnerabilities. See Methods for details on the supply and demand indicators and the meaning of the vulnerability ranges. S_T, snow cover; S_{MV}, intra-annual snow cover variability; S_{YV}, inter-annual snow cover variability; S, snow indicator; S_L, lake and reservoir volume; L, surface water indicator; G_V, glacier ice volume; $P_{GLAC} - B$, glacier water yield; G, glacier indicator; P_{WTU}, WTU precipitation; P_{BAS}, basin precipitation; P_{MV}, WTU intra-annual precipitation variability; P_{YV}, WTU inter-annual precipitation variability; P, precipitation indicator; $D_{IND,y}$, net industrial demand; D_{IND}, industrial demand indicator; $D_{NAT,y}$, natural demand; D_{NAT}, natural demand indicator; $D_{DOM,y}$, net domestic demand; D_{DOM}, domestic demand indicator; $D_{IRR,y}$, net irrigation demand; D_{IRR}, irrigation demand indicator.

boundaries[45]. Without targeted technological changes and mitigation measures, it is expected that the adverse environmental effects of the food system could increase by more than 50% by 2050 relative to 2010, thus crossing the planetary boundaries[45]. In relation to the planetary boundaries, water towers are of particular importance. They are highly vulnerable to climate change, a key water supply that sustains the major global food systems in the world and rich in biodiversity.

A clear implication is that vulnerability can be decreased with conservation, or increased with inefficient water use. This may seem logical and obvious, but it also means that the priorities for the most urgent action can be shifted as the nations of WTUs practice conservation or grow in an unsustainable way. Although irreversible changes in the buffering capacity of water towers are underway, conservation of the water towers in the broadest sense starts with the global task to mitigate further global climate warming leading to cryosphere degradation and its adverse effects on the water towers' buffering role. In a more local or regional context, water conservation is the one part of the equation that is under the control of an individual nation's part of a water tower system, calling for transboundary cooperation. Specific conservation can, for example, imply preserving the buffering capacity of mountain ranges in newly established protected areas, increasing the buffering capacity with reservoirs, and conservation of water by increasing water-use efficiency. Efficient use of scarce water resources can translate into improved wellbeing of people and increased economic and food security.

The vulnerability of these water towers in the future is controlled by the trajectory of change that a WTU and its associated downstream basin will follow. At the global scale we made a first-order assessment for a middle-of-the-road scenario both in terms of climate change and of socio-economic pathway (see Methods). However, it is important to acknowledge that the future pathways are extremely precarious and the outcomes diverging and uncertain. A recent assessment for the Hindu-Kush Himalayan region concluded that there is no single likely future: the region may run downhill, may do business as usual or it may advance to prosperity[46]. Each of those future pathways will result in systematically different demands for water and may cross the planetary boundaries in varying degrees and this will probably hold for most WTUs, but those in Asia and South America in particular.

Mountains are also an essential resource in the context of the United Nations' Sustainable Development Goals (SDGs) that have been

targeted towards the year 2030[47]. Mountains play a key part in achieving the SDGs for water (SDG 6), food (SDG 2) and energy (SDG 7). Given the projected change in climate and socioeconomic development in mountain-dependent basins, it is evident that if the SDGs are to be achieved the water resources of the water towers need to be harnessed within safe environmental limits.

We therefore make three essential recommendations. First, mountain regions must be recognized as a global asset of the Earth system. Second, it must be acknowledged that vulnerability of the world's water towers is driven both by socio-economic factors and climate change. Third, we must develop international, mountain-specific conservation and climate-change adaptation policies (such as national parks, pollutants control, emission reductions, erosion control and dam regulations) that safeguard the mountain ecosystems and mountain people and simultaneously ensure water, food and energy security of the millions of people downstream.

Online content

Any methods, additional references, Nature Research reporting summaries, source data, extended data, supplementary information, acknowledgements, peer review information; details of author contributions and competing interests; and statements of data and code availability are available at https://doi.org/10.1038/s41586-019-1822-y.

1. Viviroli, D., Dürr, H. H., Messerli, B., Meybeck, M. & Weingartner, R. Mountains of the world, water towers for humanity: typology, mapping, and global significance. *Wat. Resour. Res.* **43**, 1–13 (2007).
2. Immerzeel, W. W., Van Beek, L. P. & Bierkens, M. F. P. Climate change will affect the Asian water towers. *Science* **328**, 1382–1385 (2010).
3. Viviroli, D. et al. Climate change and mountain water resources: overview and recommendations for research, management and policy. *Hydrol. Earth Syst. Sci.* **15**, 471–504 (2011).
4. IPCC *Special Report on the Ocean and Cryosphere in a Changing Climate* https://www.ipcc.ch/report/srocc/ (IPCC, 2019).
5. Lehner, B., Verdin, K. & Jarvis, A. New global hydrography derived from spaceborne elevation data. *Eos* **89**, 93–104 (2008).
6. Körner, C. et al. A global inventory of mountains for bio-geographical applications. *Alp. Bot.* **127**, 1–15 (2017).
7. Hall, D. K. & Riggs, G. A. *MODIS/Terra Snow Cover Monthly L3 Global 0.05Deg CMG Dataset Version 6* https://nsidc.org/data/MOD10CM (2015).
8. Pfeffer, W. et al. The Randolph Glacier Inventory: a globally complete inventory of glaciers. *J. Glaciol.* **60**, 537–552 (2014).
9. Klein Goldewijk, K., Beusen, A., Van Drecht, G. & De Vos, M. The HYDE 3.1 spatially explicit database of human-induced global land-use change over the past 12,000 years. *Glob. Ecol. Biogeogr.* **20**, 73–86 (2011).
10. Xiao, C.-D., Wang, S. J. & Qin, D. H. A preliminary study of cryosphere service function and value evaluation. *Adv. Clim. Chang. Res.* **6**, 181–187 (2015).
11. Wang, X., Liu, S. W. & Zhang, J. L. A new look at roles of the cryosphere in sustainable development. *Adv. Clim. Chang. Res.* **10**, 124–131 (2019).
12. Chape, S., Spalding, M. D. & Jenkins, M. D. *The World's Protected Areas* (UNEP-World Conservation Monitoring Centre, 2008).
13. Körner, C. & Paulsen, J. A world-wide study of high altitude treeline temperatures. *J. Biogeogr.* **31**, 713–732 (2004).
14. Körner, C., Paulsen, J. & Spehn, E. M. A definition of mountains and their bioclimatic belts for global comparisons of biodiversity data. *Alp. Bot.* **121**, 73–78 (2011).
15. Nordhaus, W. D. Geography and macroeconomics: new data and new findings. *Proc. Natl Acad. Sci.* **103**, 3510–3517 (2006).
16. Pepin, N. et al. Elevation-dependent warming in mountain regions of the world. *Nat. Clim. Chang.* **5**, 424–430 (2015).
17. Zemp, M. et al. Global glacier mass changes and their contributions to sea-level rise from 1961 to 2016. *Nature* **568**, 382–386 (2019).
18. Hammond, J. C., Saavedra, F. A. & Kampf, S. K. Global snow zone maps and trends in snow persistence 2001–2016. *Int. J. Climatol.* **38**, 4369–4383 (2018).
19. Bormann, K. J., Brown, R. D., Derksen, C. & Painter, T. H. Estimating snow-cover trends from space. *Nat. Clim. Chang.* **8**, 924–928 (2018).
20. Sarangi, C. et al. Impact of light-absorbing particles on snow albedo darkening and associated radiative forcing over High Mountain Asia: high resolution WRF-Chem modeling and new satellite observations. *Atmos. Chem. Phys. Discuss.* https://doi.org/10.5194/acp-2018-979 (2018).
21. Painter, T. H. et al. Impact of disturbed desert soils on duration of mountain snow cover. *Geophys. Res. Lett.* **34**, L12502 (2007).
22. Lutz, A. F., Immerzeel, W. W., Shrestha, A. B. & Bierkens, M. F. P. Consistent increase in High Asia's runoff due to increasing glacier melt and precipitation. *Nat. Clim. Chang.* **4**, 587–592 (2014).
23. Huss, M. et al. Toward mountains without permanent snow and ice. *Earth. Future* **5**, 418–435 (2017).
24. Kargel, J. S. S. et al. Geomorphic and geologic controls of geohazards induced by Nepal's 2015 Gorkha earthquake. *Science* **351**, aac8353 (2016).
25. Kirschbaum, D. et al. The state of remote sensing capabilities of cascading hazards over high mountain Asia. *Front. Earth Sci.* https://doi.org/10.3389/feart.2019.00197 (2019).
26. Guha-Sapir, D., Below, R. & Hoyois, P. *EM-DAT: International Disaster Database* www.emdat.be (2019).
27. Mal, S. *Climate Change, Extreme Events and Disaster Risk Reduction* (Springer, 2018).
28. Mann, M. E. et al. Influence of anthropogenic climate change on planetary wave resonance and extreme weather events. *Sci. Rep.* **7**, 45242 (2017).
29. Fischer, E. M. & Knutti, R. Anthropogenic contribution to global occurrence of heavy-precipitation and high-temperature extremes. *Nat. Clim. Chang.* **5**, 560–564 (2015).
30. Haeberli, W., Schaub, Y. & Huggel, C. Increasing risks related to landslides from degrading permafrost into new lakes in de-glaciating mountain ranges. *Geomorphology* **293**, 405–417 (2017).
31. Biemans, H. et al. Importance of snow and glacier meltwater for agriculture on the Indo-Gangetic Plain. *Nat. Sustain.* **2**, 594–601 (2019).
32. Hersbach, H. et al. *Operational global reanalysis: progress, future directions and synergies with NWP*. ECMWF ERA Report Series No. 27, https://www.ecmwf.int/node/18765 (ECMWF, 2018).
33. Wada, Y., De Graaf, I. E. M. & van Beek, L. P. H. High-resolution modeling of human and climate impacts on global water resources. *J. Adv. Model. Earth Syst.* **8**, 735–763 (2016).
34. Wada, Y. et al. Global depletion of groundwater resources. *Geophys. Res. Lett.* **37**, https://doi.org/10.1029/2010GL044571 (2010).
35. Wada, Y., Van Beek, L. P. H. & Bierkens, M. F. P. Nonsustainable groundwater sustaining irrigation: a global assessment. *Wat. Resour. Res.* **48**, https://doi.org/10.1029/2011WR010562 (2012).
36. Immerzeel, W. W. & Bierkens, M. F. P. Asia's water balance. *Nat. Geosci.* **5**, 841–842 (2012).
37. De Stefano, L., Petersen-Perlman, J. D., Sproles, E. A., Eynard, J. & Wolf, A. T. Assessment of transboundary river basins for potential hydro-political tensions. *Glob. Environ. Change* **45**, 35–46 (2017).
38. Hofste, R. W. et al. *Aqueduct 3.0: Updated Decision-Relevant Global Water Risk Indicators*. Technical Note https://www.wri.org/publication/aqueduct-30 (World Resources Institute, 2019).
39. Kaufmann, D., Kraay, A. & Mastruzzi, M. *The Worldwide Governance Indicators. Methodology and Analytical Issues*. World Bank Policy Research Working Paper No. 5430 https://elibrary.worldbank.org/doi/abs/10.1596/1813-9450-5430 (The World Bank Development Research Group, 2010).
40. Taylor, K. E., Stouffer, R. J. & Meehl, G. A. An overview of CMIP5 and the experiment design. *Bull. Am. Meteorol. Soc.* **93**, 485–498 (2012).
41. Murakami, D. & Yamagata, Y. Estimation of Gridded Population and GDP Scenarios with Spatially Explicit Statistical Downscaling. *Sustainability* **11**, 2106 (2019).
42. Wijngaard, R. R. et al. Climate change vs. socio-economic development: understanding the South-Asian water gap. *Hydrol. Earth Syst. Sci.* **22**, 6297–6321 (2018).
43. Rockström, J. et al. Planetary boundaries: exploring the safe operating space for humanity. *Ecol. Soc.* **14**, 32 (2009).
44. Jaramillo, F. & Destouni, G. Comment on "Planetary boundaries: Guiding human development on a changing planet". *Science* **348**, 1217 (2015).
45. Springmann, M. et al. Options for keeping the food system within environmental limits. *Nature* **562**, 519–525 (2018).
46. Roy, J. et al. Exploring futures of the Hindu Kush Himalaya: scenarios and pathways. In *The Hindu Kush Himalaya Assessment: Mountains, Climate Change, Sustainability and People* (eds Wester, P., Mishra, A., Mukherji, A. & Shrestha, A. B.) 99–125 (Springer International Publishing, 2019).
47. United Nations. *Transforming Our World: The 2030 Agenda For Sustainable Development*. A/RES/70/1 Resolution adopted by the United Nations General Assembly. https://sustainabledevelopment.un.org/index.php?page=view&type=111&nr=8496&menu=35 (UN, 2015).

Publisher's note Springer Nature remains neutral with regard to jurisdictional claims in published maps and institutional affiliations.

© The Author(s), under exclusive licence to Springer Nature Limited 2019

Methods

Delineation of WTUs

In this study, we define a WTU as the intersection of major river basins[5] and a topographic mountain classification based on elevation and surface roughness developed in the framework of the Global Mountain Biodiversity Assessment (GMBA)[6]. Although other similar mountain classification datasets exist[1] that are also based on a combination of elevation and surface roughness, we use the GMBA classification (version 1.2) because topographical names of mountain ranges have been assigned to each of the mountain regions classified. The original GMBA inventory contains 1,048 mountain regions worldwide. We make a subset of this dataset by imposing minimum thresholds for glacier area, glacier ice volume and snow persistence. We retain those mountain regions which have an ice volume larger than 0.1 km^3 (ref. [48]) or an average annual areal snow persistence larger than 10%[7]. After imposing these thresholds, 174 mountain regions remain. We intersect those regions with the major river basins and dissolve the result based on major river basin ID; that is, all selected GMBA regions within a basin are grouped as a single WTU (Extended Data Fig. 1, Extended Data Table 1, Extended Data Table 2). The final WTU delineation contains 78 units (Extended Data Fig. 1). For each WTU we also define the downstream area that directly depends on the WTU using the river sub-basin delineation[5], and we specify which mountain ranges are part of the WTU (Extended Data Fig. 1, Extended Data Table 1, Extended Data Table 2). This dependent downstream area is smaller than the total downstream basin because not every downstream sub-basin is hydrologically connected to the WTU. To this end we start at the WTU and iteratively select each connected downstream sub-basin until the basin outlet, or lowest sub-basin in case of an endorheic system, is reached (Extended Data Fig. 1).

Quantifying the WTI

We combine an SI and a DI into a WTI with which to rank WTUs. All grid calculations are performed at 0.05° resolution.

The SI (see Extended Data Table 3 for all equations) is based on indicators for precipitation, snow cover, glaciers and surface water storage. For the precipitation indicator, the 2019 released ERA5 reanalysis dataset is used[32]. As sub-indicators, we first compute the total annual average (2001–2017) WTU precipitation (Extended Data Fig. 3a) relative to the overall basin precipitation (P_T). We then include the inter-annual variation in WTU precipitation (P_{YV}) and the intra-annual monthly WTU variation (P_{MV}) based on the 2001–2017 time series. We combine these three sub-indicators into a precipitation indicator (P), giving the variation (P_{YV} and P_{MV}) the same weight as P_T. The underlying assumption of including the variation is that if the variation is low, the WTU will provide a constant flow of water to the downstream basin, and therefore it is a more important WTU. For the snow cover indicator, we use the MODIS MOD10CM1 product[7]. We derive an average annual snow cover (S_T) in each WTU for the 2001–2017 period (Extended Data Fig. 3b). Here too, we derive both an inter-annual (S_{YV}) and intra-annual (S_{MV}) variation in snow cover, and using the same rationale as for the precipitation indicator, we combine the average snow persistence with the variation to derive a final snow indicator (S). For the glacier indicator, we compute the glacier ice volume in a WTU[48] (Extended Data Fig. 4a) relative to the average annual WTU precipitation (G_S). We also compute the annual glacier water flux relative to the WTU precipitation on non-glacierized terrain (G_Y). We estimate the glacier water yield as the sum of the on-glacier precipitation and the mass balance per WTU. The WTU mass balance is based on the area-weighted average annual mass balance from all geodetic and direct mass balance measurements made available by the World Glacier Monitoring Service[49]. However, if there are fewer than ten glaciers with data available within a WTU then we use the regional average[17]. We average G_S and G_Y to derive a final glacier indicator (G). For the surface water indicator (L), we compute the total volume of water that is stored in lakes and reservoirs in a WTU[50] (Extended Data Fig. 4b) relative to the average annual WTU precipitation. The SI is the average of P, S, G and L.

The DI is based on net human water demands for domestic, industrial and irrigation purposes[33], and natural demand (see Extended Data Table 4 for all equations, Extended Data Fig. 5, Extended Data Fig. 6). Since data for the natural demand, defined as the minimum river flow required to sustain the ecosystem, are not readily available, we estimate it with the environmental flow requirement computed with the 90th-percentile exceedance value of the natural flow[33,51,52]. First, the average monthly sectoral demands are computed based on a 2001–2014 time series ($D_{DOM,m}$, $D_{IRR,m}$, $D_{IND,m}$, $D_{NAT,m}$). Part of each sectoral demand can potentially be met by downstream water availability that does not have its origin in the mountains. For each grid cell with a positive demand we therefore compute the average monthly water availability ($WA_{DOM,m}$, $WA_{IRR,m}$, $WA_{IND,m}$, $WA_{NAT,m}$; see Extended Data Table 4) as the precipitation minus the actual natural evapotranspiration[32]. We subtract this amount from the average monthly sectoral water demands as an estimate for the monthly demand that needs to be met by other sources, including the WTUs. We assume that the entire water deficit has to be provided by the WTU, although other water sources, such as groundwater[51], can also be important. We acknowledge that the global scale of our assessment also prevents us from fully taking into account the distribution and allocation of water within different portions of our spatial units of calculation. Finally, we aggregate these monthly net demands to be sustained by the WTU over all months and we divide it by the total annual sectoral demand to get four demand indicators (D_{DOM}, D_{IND}, D_{IRR}, D_{NAT}). The DI is the average of the indicators D_{DOM}, D_{IND}, D_{IRR} and D_{NAT}.

The final WTI is the product of SI and DI, for which the values are subsequently normalized over the range of WTI values found for all 78 WTUs. By using a multiplicative approach, we ensure that a WTU only ranks highly when it has considerable water resources (either as precipitation, glacier ice, snow and surface water or a combination) in the mountains, and the demand for those resources downstream is likewise high (Extended Data Fig. 2).

Uncertainty

It is acknowledged that the SI, DI and WTI are based on partly arbitrary choices of indicators and sub-indicators. In our assessment we have assigned an equal weight to each of the indicators constituting SI and DI. To account for uncertainty in the weight of each indicator in the WTI calculation we have performed a sensitivity analysis in which we randomly vary the weights of each of the eight indicators that constitute the SI and DI and assess the impact on the WTI ranking of the WTUs. We assume that the weight of each indicator is uniformly distributed and can be a maximum of three times as high or low as another indicator, and we assess through a 10,000-member Monte Carlo analysis how sensitive the rank of the WTU is as a result of this uncertainty (Extended Data Fig. 7). The analysis shows that the top and bottom of the ranking are robust and only limited shifts in the ranking occur (<5 positions). However, the middle part of the ranking is more sensitive to the weights of the indicators and there is a considerable number of WTUs where, in more than 25% of the total runs, the rank changes more than 5 positions.

In addition, we also include a 1,000-member Monte Carlo analysis to assess the propagation of uncertainty in the datasets used in the WTI calculation. For each input dataset we estimate a standard deviation and assuming a normally distributed error we sample from the distribution to assess how the input data uncertainty affects the WTI value (Supplementary Table 1) and WTU ranking (Extended Data Fig. 7). For precipitation we compute the standard deviation per WTU and per downstream basin based on nine different precipitation datasets (CRU bias-corrected with ERA-Interim, CRU TS2.1 downscaled with ERA-40, CRU TS3.21 downscaled with ERA-40, CRU TS3.21 downscaled with ERA-Interim, WFDEI, NCEP-NCAR Reanalysis, WATCH, WATCH corrected with GPCC, and ERA5)[32,53–59]. For evapotranspiration we take a similar approach using four different datasets (ERA-Interim, GLEAM,

MERRA-2, PCR-GLOBWB forced with ERA-Interim, and ERA5)[32,54,60–62]. Values for snow persistence, ice volumes, glacier mass balance, and the domestic, industrial and irrigation water demands are derived from the literature[17,48,63–65]. For the uncertainty in lake and reservoir volume we assume a standard deviation of 10% and we keep the environmental flow requirement constant. The ranking is also sensitive to input data uncertainty; however, the ranking is robust, in particular in the top 20 places of the ranking where only limited shifts in positions occur. Here, too, most shifts are observed in the middle part of the ranking.

Assessing vulnerabilities

For the WTUs, we assess the vulnerability of their role as water tower based on three static indicators for water stress, government effectiveness and the potential for hydro-political tension in case of transboundary basins (Supplementary Table 2). In addition, we include four change indicators: the projected change in temperature, precipitation, population and gross domestic product between 2000 and 2050. In all cases we use the ensemble mean RCP4.5 climate change scenario[66] in combination with the SSP2 shared socio-economic pathway[67] as a middle-of-the-road scenario, both in terms of economic development and associated climate change (Supplementary Table 2). We scale the different vulnerability indicators between 0 (minimum vulnerability) and 1 (maximum vulnerability) considering the thresholds defined below.

For water stress, we use the baseline water stress (BWS) indicator[38]. BWS measures the ratio of total water withdrawals to the available renewable surface and groundwater supplies; higher values indicate more competition among users. The index value is derived from an ordinary least-squares regression fitted through raw monthly water-stress values for 1960–2014, taking the fitted BWS value for 2014[38]. We compute the area-averaged BWS for all WTUs, including their downstream dependent areas and scale between 0 and 5, which is the range of the BWS scale in ref. [38]. High BWS is associated with high vulnerability and low BWS is associated with low vulnerability. Since no global dataset for water management capacity is available at the global scale we validated the indicators gross domestic product (GDP)[68], human development index (HDI)[68] and government effectiveness (GE)[39] as proxies for water management capacity, which is available for selected mountainous basins only[3]. GE shows the best correlation with water management capacity in the selection of basins, and we calculate the area-averaged value for each WTU including its downstream dependent area. We scale between −1.5 and 2.0, which are the minimum and maximum values found for the WTUs. A low value for GE implies high vulnerability whereas a high value for GE indicates low vulnerability. Lastly, all transboundary basins are assessed on the risk for potential hydro-political tensions based on a global mapping of basins that are ill-equipped to deal with transboundary disputes triggered by the construction of new dams and diversions[37]. We compute the WTU basin aggregated score provided by the cited study and the range of the original scale in the cited study (0 to 5) is used to scale between minimum and maximum.

For each WTU we compute a projected multi-model ensemble mean change in precipitation (measured as a percentage) and temperature (measured in kelvin) between 2000 and 2050 for RCP4.5 for 35 different CMIP5 climate models[40]. For projected changes in temperature the scores for the individual WTUs are linearly scaled between 0 and 1 for the full range of projected temperature increases of all WTUs. For precipitation projections, only decreases in precipitation are assumed to contribute to vulnerability (that is, projections of increases in precipitation and unchanged precipitation are classified as minimum vulnerability). The scores for the individual WTUs are scaled linearly between 0 and 1, where 0 indicates unchanged or increasing precipitation and 1 indicates the largest precipitation decrease projected for all 78 WTUs. The projected population change between 2016 and 2050 for SSP2 is derived from the HYDE database[9] and the relative increase for each of the WTU basins is computed. All WTUs are scaled between a growth of 0% and a maximum of 50%, that is, if the projected population growth is more than 50%, a WTU has maximum vulnerability. The relative increase in GDP between 2000 and 2050 is computed per WTU basin, with the assumption that a strong projected increase in GDP is indicative of a strong growth in water demand. Data for the SSP2 shared socio-economic pathway are used[41]. All WTU basins are scaled between the minimum and the maximum, which is capped by a growth rate of 1000%.

We assess indicators of various nature for vulnerability and future changes. To assess a complete vulnerability based on this set of indicators is challenging and requires knowledge of the weights of the individual indicators in assessing the total vulnerability for each WTU. The caveat is made that we consider a middle-of-the-road scenario both in terms of projected climate change and socio-economic development as a first-order assessment. The future development pathway in most WTUs, in particular in Asia and South America, is uncertain and highly diverging and depends on the global economy, regional growth rates and geopolitical tensions, which are difficult to project or quantify. In addition, a satisfactory representation of mountainous climate in General Circulation Models is difficult, leading to large uncertainty in particular for future precipitation projections.

In our study we assess impacts-driven vulnerability, where vulnerability is defined in direct proportion to the magnitude of hydrological change. However, we note that recent work on the human dimensions of climate change have demonstrated that vulnerability emerges from the interaction of both environmental and social dynamics in specific contexts[69,70].

Data availability

The data generated to support the findings of this study are available in an online data repository at zenodo.org at https://doi.org/10.5281/zenodo.3521933. Third party data used in this study are available as follows. Hydrological basin boundaries[5] used in this study are available online at http://www.fao.org/nr/water/aquamaps/. Mountain definition data[6] used in this study are available online at https://ilias.unibe.ch/goto_ilias3_unibe_file_1047348.html. Precipitation and evaporation data used in this study[32] are available online at https://cds.climate.copernicus.eu. Snow cover data used in this study[7] are available online at https://nsidc.org/data/MOD10CM. Glacier volume data[48] used in this study are available online at https://doi.org/10.3929/ethz-b-000315707. Glacier mass balance data[17,49] are available online at https://wgms.ch/. Lake and reservoir storage data[50] used in this study are available online at https://www.hydrosheds.org/pages/hydrolakes. Water demand data used in this study are available upon request from Y.W. (wada@iiasa.ac.at). BWS data[38] used in this study are available online at https://www.wri.org/aqueduct. GE data[39] used in this study are available online at https://info.worldbank.org/governance/wgi/#home. Data on hydro-political tensions for transboundary river basins[37] used in this study are available online at https://transboundarywaters.science.oregonstate.edu/content/transboundary-freshwater-spatial-database. Data for future projections of population count[9] used in this study are available online at ftp://ftp.pbl.nl/hyde/SSPs/SSP2/zip/. Data for future projections of GDP[41] used in this study are available online at http://www.cger.nies.go.jp/gcp/population-and-gdp.html. Data for future projections of temperature and precipitation[40] used in this study are available online at https://climexp.knmi.nl. An online interactive visualization of the water tower index and vulnerability is available at https://www.nationalgeographic.com/environment/perpetual-planet/.

Code availability

The code developed for the WTI calculations performed for this study are publicly available in a Github repository at https://github.com/mountainhydrology/pub_ngs-watertowers.

48. Farinotti, D. et al. A consensus estimate for the ice thickness distribution of all glaciers on Earth. *Nat. Geosci*. **12**, 168–173 (2019).
49. World Glacier Monitoring Service *Fluctuations of Glaciers (FoG) Database* https://doi.org/10.5904/wgms-fog-2018-06 (2018).
50. Messager, M. L., Lehner, B., Grill, G., Nedeva, I. & Schmitt, O. Estimating the volume and age of water stored in global lakes using a geo-statistical approach. *Nat. Commun*. **7**, 13603 (2016).
51. Gleeson, T., Wada, Y., Bierkens, M. F. P. & Van Beek, L. P. H. Water balance of global aquifers revealed by groundwater footprint. *Nature* **488**, 197–200 (2012).
52. Smakhtin, V., Revenga, C. & Döll, P. A pilot global assessment of environmental water requirements and scarcity. *Water Int*. **29**, 307–317 (2004).
53. Harris, I., Jones, P. D., Osborn, T. J. & Lister, D. H. Updated high-resolution grids of monthly climatic observations—the CRU TS3.10 dataset. *Int. J. Climatol*. https://doi.org/10.1002/joc.3711 (2013).
54. Dee, D. P. et al. The ERA-Interim reanalysis: configuration and performance of the data assimilation system. *Q. J. R. Meteorol. Soc*. **137**, 553–597 (2011).
55. Weedon, G. P. et al. The WFDEI meteorological forcing data set: WATCH Forcing Data methodology applied to ERA-Interim reanalysis data. *Wat. Resour. Res*. **50**, 7505–7514 (2014).
56. Weedon, G. P. et al. Creation of the WATCH Forcing Data and its use to assess global and regional reference crop evaporation over land during the twentieth century. *J. Hydrometeorol*. **12**, 823–848 (2011).
57. Schneider, U. et al. GPCC's new land surface precipitation climatology based on quality-controlled in situ data and its role in quantifying the global water cycle. *Theor. Appl. Climatol*. **115**, 15–40 (2014).
58. Uppala, S. M. et al. The ERA-40 re-analysis. *Q. J. R. Meteorol. Soc*. **131**, 2961–3012 (2005).
59. Kalnay, E. et al. The NCEP/NCAR 40-Year Reanalysis Project. *Bull. Am. Meteorol. Soc*. **77**, 437–471 (1996).
60. Martens, B. et al. GLEAM v3: Satellite-based land evaporation and root-zone soil moisture. *Geosci. Model Dev*. **10**, 1903–1925 (2017).
61. Rienecker, M. M. et al. MERRA: NASA's modern-era retrospective analysis for research and applications. *J. Clim*. **24**, 3624–3648 (2011).
62. Sutanudjaja, E. H. et al. PCR-GLOBWB 2: a 5 arcmin global hydrological and water resources model. *Geosci. Model Dev*. **11**, 2429–2453 (2018).
63. Riggs, G. A., Hall, D. K. & Román, M. O. Overview of NASA's MODIS and VIIRS Snow-Cover Earth System Data Records. *Earth Syst. Sci. Data* **9**, 765–777 https://doi.org/10.5194/essd-9-765-2017 (2017).
64. Wada, Y. et al. Modeling global water use for the 21st century: the Water Futures and Solutions (WFaS) initiative and its approaches. *Geosci. Model Dev*. **9**, 175–222 (2016).
65. Wada, Y. et al. Multimodel projections and uncertainties of irrigation water demand under climate change. *Geophys. Res. Lett*. **40**, 4626–4632 (2013).
66. van Vuuren, D. P. et al. The representative concentration pathways: an overview. *Clim. Change* **109**, 5–31 (2011).
67. O'Neill, B. C. et al. The roads ahead: narratives for shared socioeconomic pathways describing world futures in the 21st century. *Glob. Environ. Change* **42**, 169–180 (2017).
68. Kummu, M., Taka, M. & Guillaume, J. H. A. Gridded global datasets for gross domestic product and human development index over 1990-2015. *Sci. Data* **5**, 180004 (2018).
69. McDowell, G. et al. Adaptation action and research in glaciated mountain systems: Are they enough to meet the challenge of climate change? *Glob. Environ. Change* **54**, 19–30 (2019).
70. Conway, D. et al. The need for bottom-up assessments of climate risks and adaptation in climate-sensitive regions. *Nat. Clim. Chang*. **9**, 503–511 (2019).

Acknowledgements This project was funded as part of the National Geographic Society and Rolex Partnership to Support a Perpetual Planet. We are grateful to the Strategic Priority Research Program of the Chinese Academy of Sciences for their support, to D. Farinotti for providing the data on glacier volume, and to N. Wanders for providing precipitation datasets used in the uncertainty analysis.

Author contributions W.W.I. and A.F.L. contributed equally to the study; they designed the study, performed the analysis, prepared figures and tables and drafted the manuscript. P.D.A.K. contributed to the data analysis and prepared Fig. 3. Y.W. provided the dataset used to calculate demand indicators. S.B., S.H., A.B. and A.C.E contributed to the design of the index and analysis methods. All authors contributed to developing the theory and conception of the study by providing regional (M.A., A.F. and P.P. for the Andes; T.B., U.H., P.D.A.K., A.V.K., P.A.M., S.N., F.P., A.B.S., A.S., C.X. and T.Y. for High Mountain Asia; T.B., A.E., F.P. and D.V. for the Alps; and S.R., T.H.P., J.S.K. and M.K. for North America) or subject-specific expertise (B.J.D., J.S.K., A.B.S., P.P., A.S. and S.R. for glacial volume; U.H., M.K. and F.P. for meltwater discharge; H.B., A.F. and Y.W. on irrigation demand; T.B., A.E., J.S.K. and A.V.K. for glacial lakes; M.F. and T.H.P. for global snow cover, P.D.A.K. for volume ice loss; A.F., P.A.M., A.S. and T.Y. for climatology; S.N. and S.R. for hydrology; M.K., A.B.S. and D.V. for water demand, conflicts and vulnerability; H.R. for preferential flow; S.R. for glacier accumulation mass loss and its effects on downstream populations; D.V. for water management capacity; C.X. for global cryospheric functions and processes; and Y.W. for environmental flow requirements). All authors discussed and provided feedback on the manuscript. The study was initiated by J.E.M.B. and facilitated by A.C.E.

Competing interests The authors declare no competing interests.

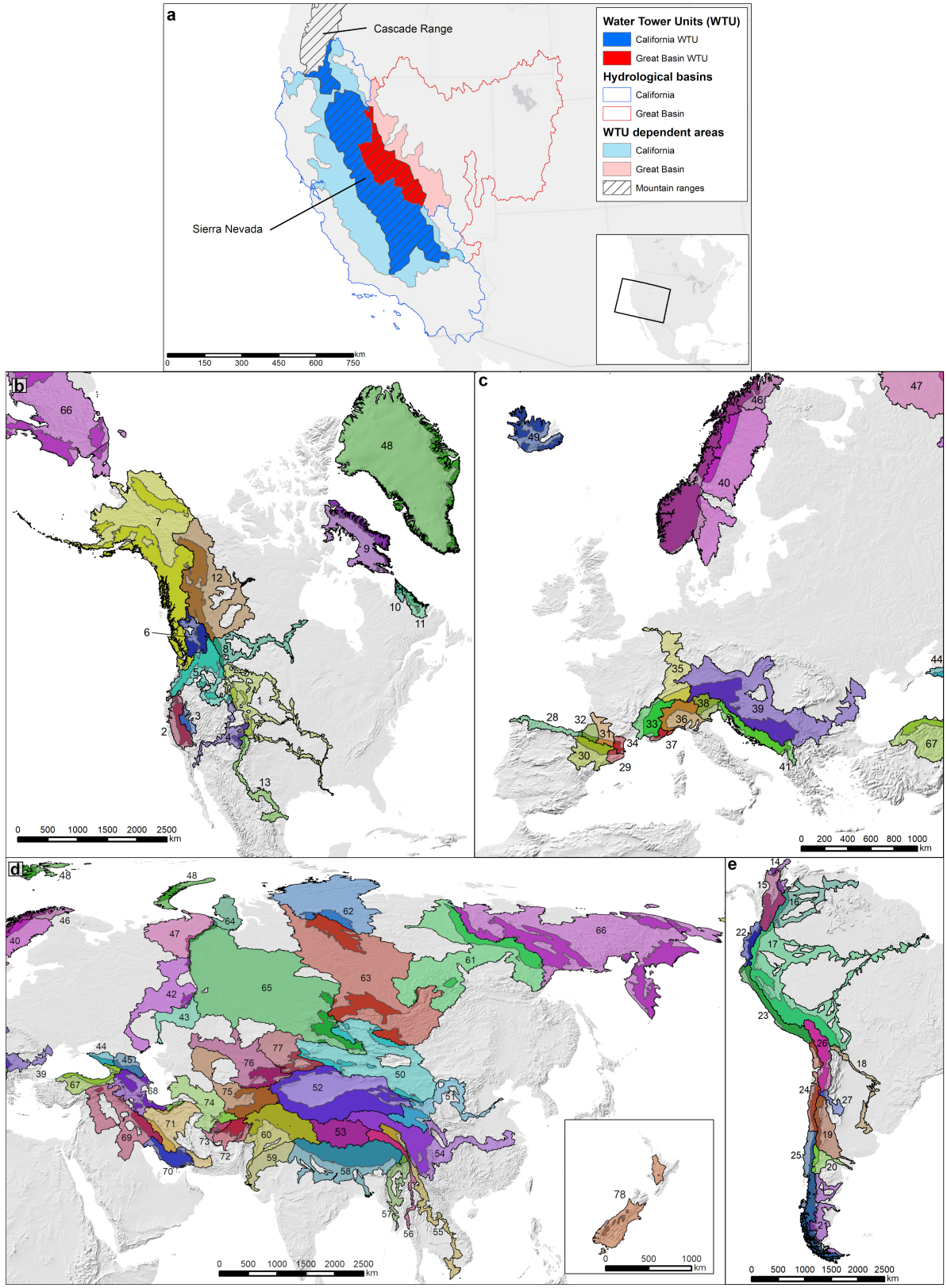
Additional information

Supplementary information is available for this paper at https://doi.org/10.1038/s41586-019-1822-y.

Correspondence and requests for materials should be addressed to W.W.I. or A.F.L.

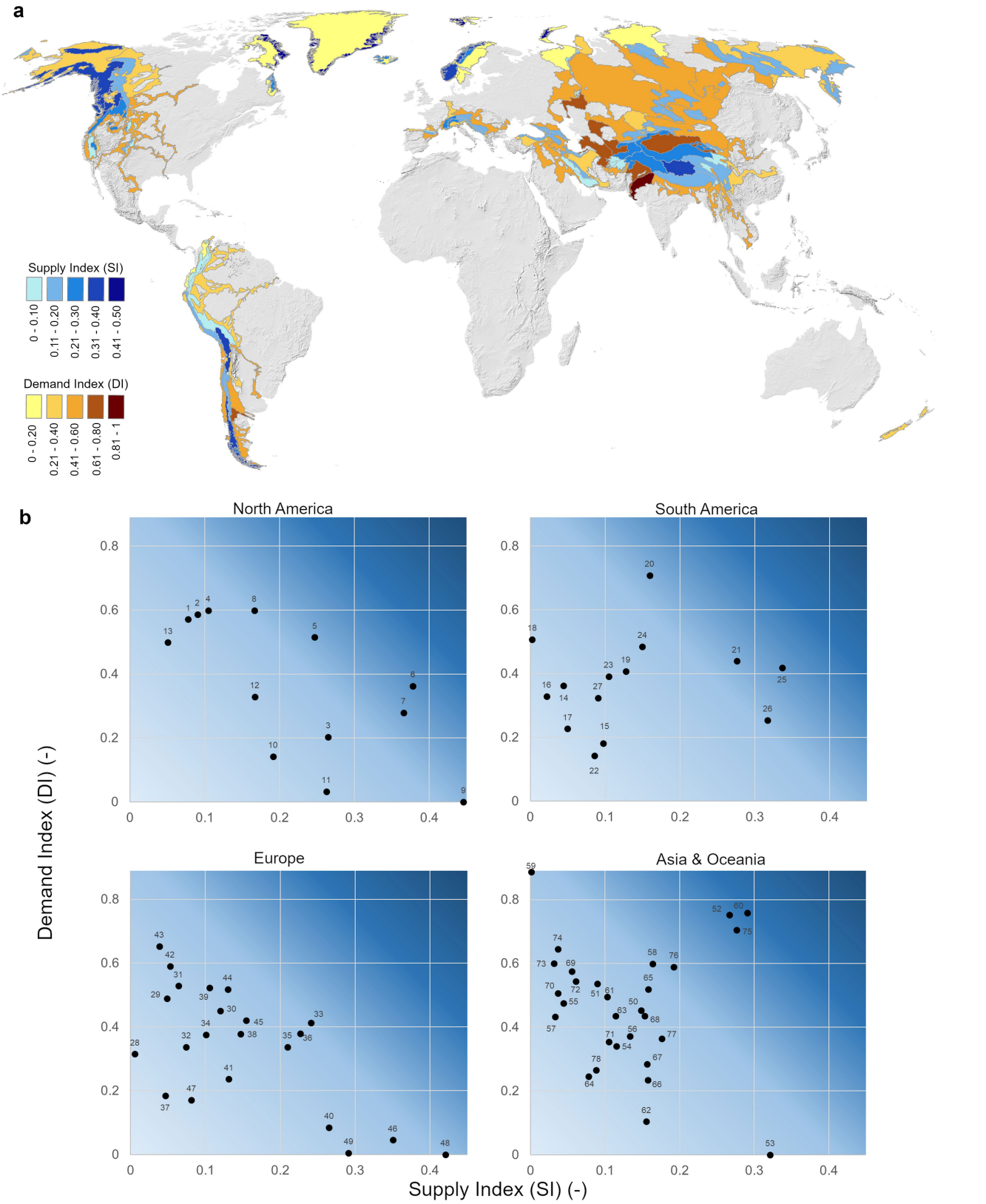
Peer review information *Nature* thanks Günther Grill and the other, anonymous, reviewer(s) for their contribution to the peer review of this work.

Reprints and permissions information is available at http://www.nature.com/reprints.

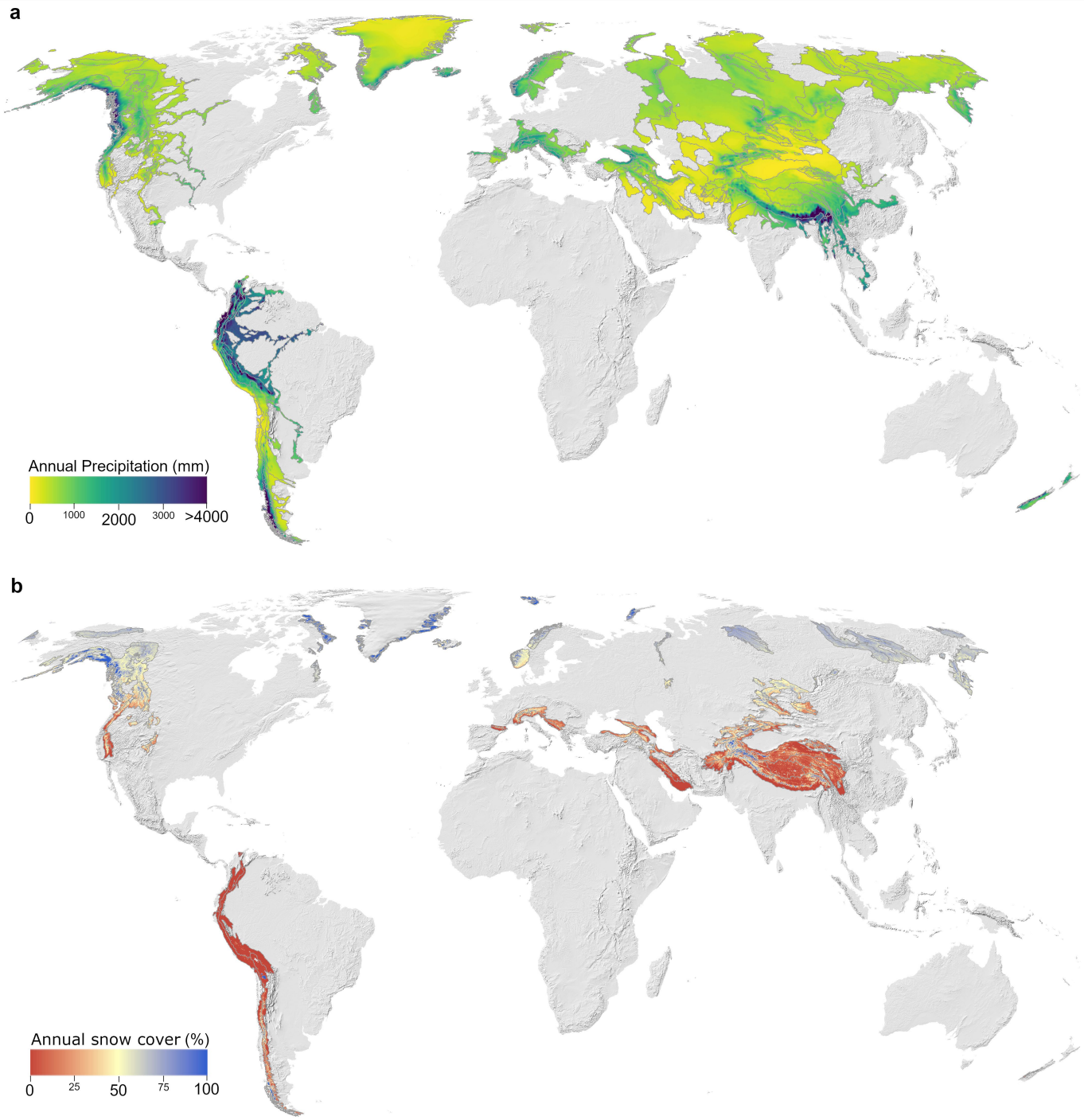


Extended Data Fig. 1 | See next page for caption.

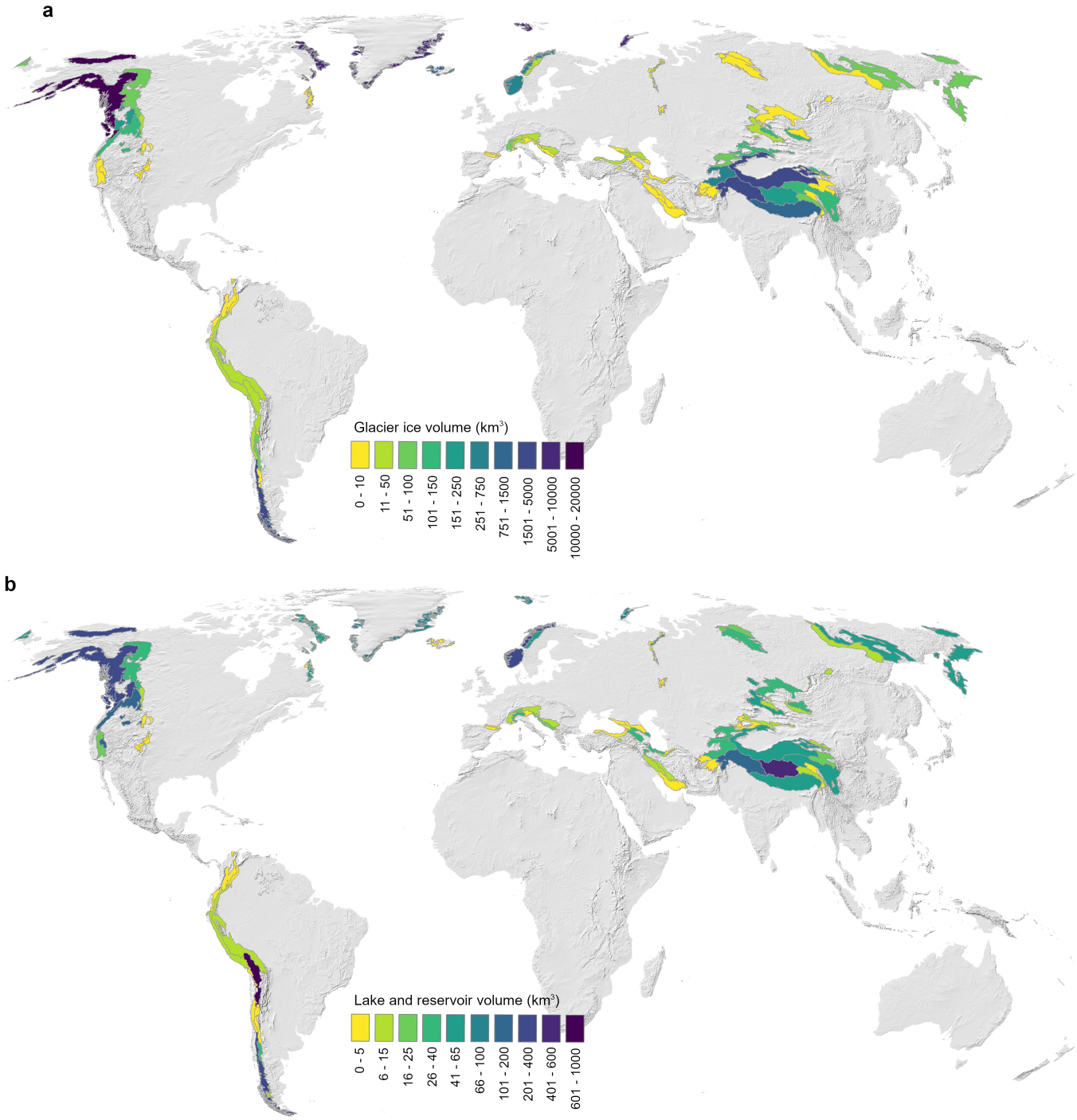
Extended Data Fig. 1 | Concept and global spread of WTUs. a, The WTUs are defined as the intersection of Earth's major hydrological basins[5] and mountain ranges[6] meeting predefined thresholds for ice volume or snow persistence (see Methods section). One WTU can consist of (parts of) multiple mountain ranges and one mountain range can be part of multiple WTUs. The example shows two hydrological basins in North America: the Great Basin (red outline) and California (blue outline). The striped areas indicate two mountain ranges: the Sierra Nevada and the Cascade Range. The intersection of the hydrological basins and the mountain ranges defines the WTUs (dark colours). For example, the Great Basin WTU is defined as the portion of the Sierra Nevada that is part of the Great Basin hydrological basin (dark red), and the California WTU is defined as the portion of the Sierra Nevada that is part of the California hydrological basin as well as a portion of the Cascade Range that is part of the California hydrological basin (dark blue). The WTU's dependent area (light colours) is defined as the sub-basins within the hydrological basin that are overlapping the WTU or downstream of sub-basins overlapping the WTU. **b**–**e**, The WTUs (dark colours) and associated WTU basins (light colours) for all 78 WTUs and WTU basins, grouped by continents: North America (**b**), Europe (**c**), Asia and Oceania (**d**), South America (**e**). Number labels indicate the WTU IDs (see Extended Data Tables 1, 2 for corresponding names).



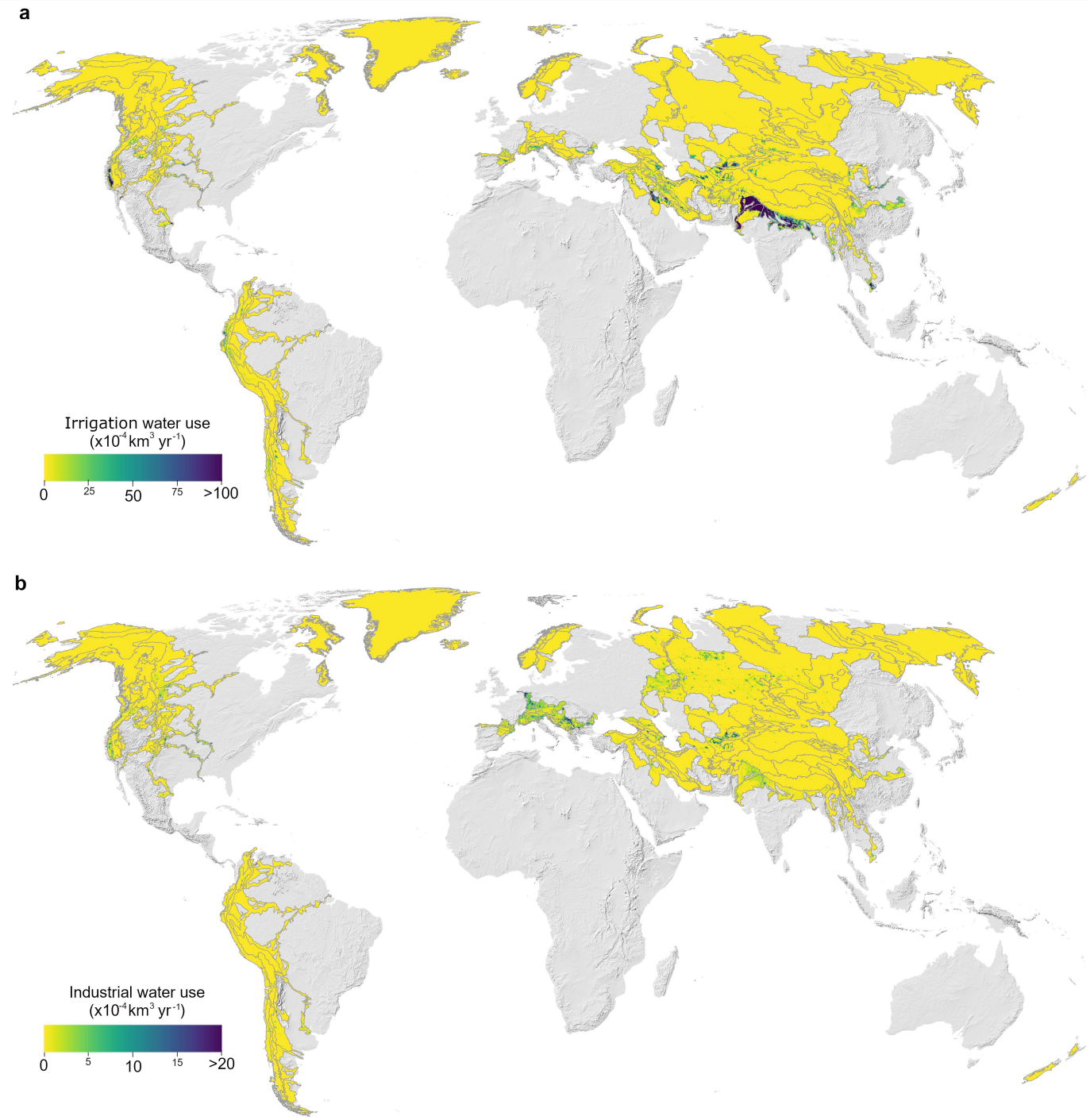
Extended Data Fig. 2 | SI and DI. a, The WTU SI (blue colourscale) and downstream DI (brown colourscale) for all 78 WTUs and WTU basins. **b**, Supply index (SI) and demand index (DI) for each WTU grouped per continent. Background colour gradient indicates water tower importance (that is, darker shades represent higher SI and DI values). Points are labelled with WTU IDs (see Extended Data Tables 1, 2, Extended Data Fig. 1).



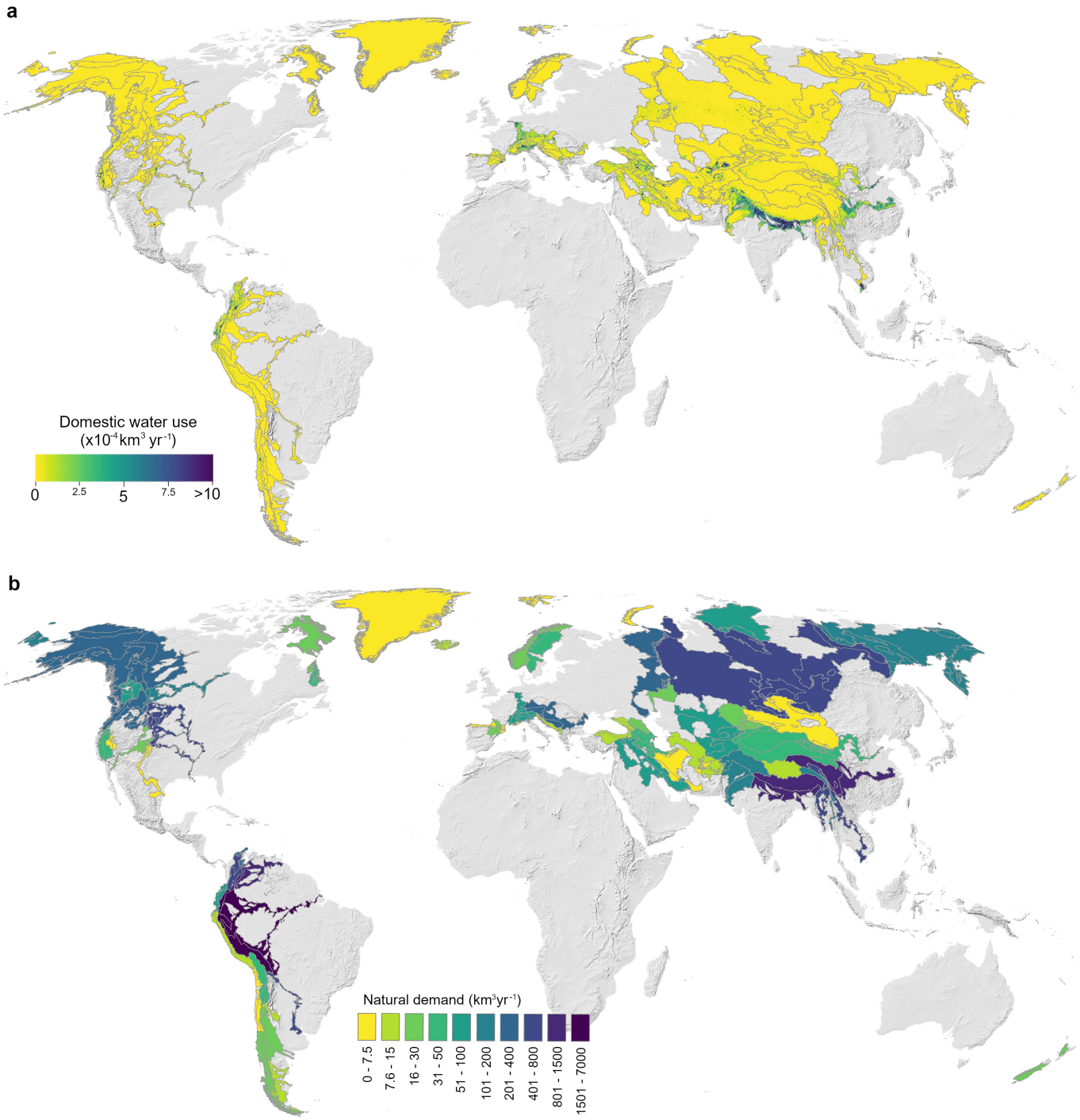
Extended Data Fig. 3 | Annual precipitation and snow cover. a, Average annual precipitation between 2001 and 2017, resampled bilinearly to 0.05° resolution based on ERA5[32]. **b**, Average snow persistence between 2001 and 2017, resampled to 0.05° resolution based on MODIS MOD10CM1[7].



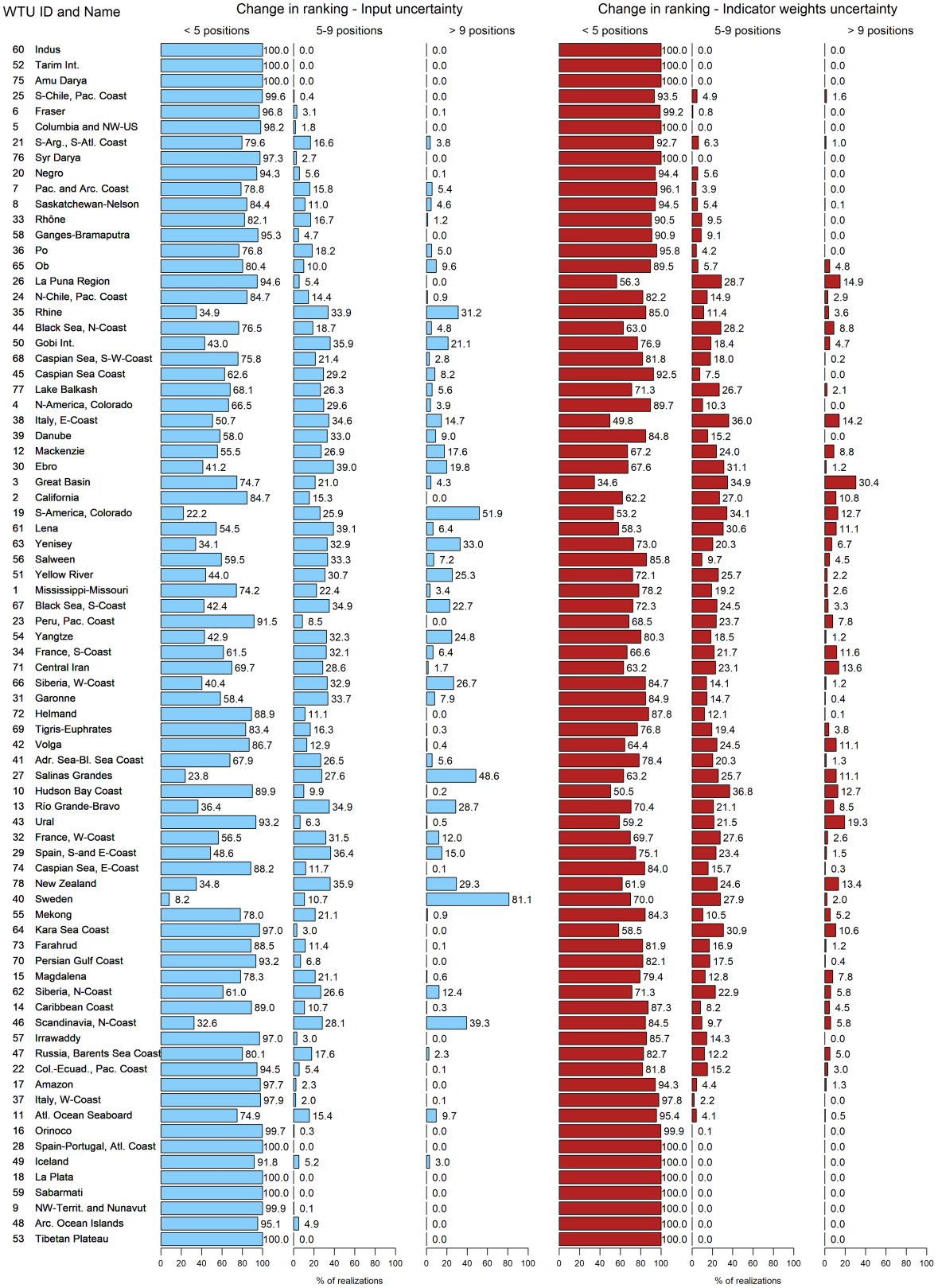
Extended Data Fig. 4 | Glacier ice volume and lake and reservoir volume. a, Total aggregated glacier ice volume per WTU[48]. **b**, Total aggregated lake and reservoir water volume per WTU[50].



Extended Data Fig. 5 | Water use for irrigation and industry. a, Average annual irrigation water use per 0.05 × 0.05° grid cell 2001–2014[33]. **b**, Average annual industrial water use per 0.05 × 0.05° grid cell 2001–2014[33].



Extended Data Fig. 6 | Domestic water use and natural water demand. a, Average annual domestic water use per 0.05 × 0.05° grid cell 2001–2014[33]. **b**, Total aggregated average annual natural water demand 2001–2014 per WTU basin based on the Environmental Flow Requirement[33,51,52].



Extended Data Fig. 7 | Sensitivity of WTU ranking to uncertainty in input data and indicator weights. Position change in ranking of WTUs by WTI resulting from uncertainty in input data (blue), expressed as a percentage of 1,000 realizations of the WTI index calculation. Position change in ranking of WTUs by WTI resulting from uncertainty in the weights of individual indicators (red), expressed as a percentage of 10,000 realizations of the WTI index calculation.

Extended Data Table 1 | List of WTUs and the GMBA mountain ranges that are (partly) covered by each WTU, for North America and South America

WTU ID	WTU Name	GMBA mountain ranges (partly) covered by WTU
1	Mississippi-Missouri	Bighorn Mountains, Absaroka Range, Crazy Mountains, Lewis Range, Swan Range, Flathead Range, Wind River Range, Front Range, Medicine Bow Mountains, Gore Range, Sawatch Range
2	California	Sierra Nevada, Cascade Range
3	Great Basin	Sierra Nevada
4	N-America, Colorado	San Juan Mountains, Wind River Range, Front Range, Medicine Bow Mountains, Gore Range, Sawatch Range
5	Columbia and NW-US	Absaroka Range, Lewis Range, Swan Range, Mission Range, Flathead Range, Purcell Mountains, Cabinet Mountains, Sawtooth Mountains, Teton Range, Wind River Range, Wallowa Mountains, Cariboo Mountains, Monashee Mountains, Selkirk Mountains, Coast Mountains, Rocky Mountains Calgary, Scrip Range, Cascade Range
6	Fraser	Coast Mountains, Skeena Mountains, Omineca Mountains, Cariboo Mountains, Monashee Mountains, Hazelton Mountains, Rocky Mountains Calgary, Scrip Range, Cascade Range
7	Pac. and Arc. Coast	Chugach Mountains, Kenai Mountains, Alaska Range, Coast Mountains, Aleutian Range, Kodiak and Afognak Island, Alexander Archipelago, Vancouver Island, Brooks Range, Saint Elias Mountains, Wrangell Mountains, Kilbuck Mountains, Talkeetna Mountains, Mackenzie Mountains, Wernecke Mountains, Selwyn Mountains, Pelly Mountains, Skeena Mountains, Stikine Ranges, Cassiar Mountains, Omineca Mountains, Hazelton Mountains, Cascade Range, Olympic Mountains
8	Saskatchewan-Nelson	Lewis Range, Rocky Mountains Calgary
9	NW-Territ. and Nunavut	Baffin Island
10	Hudson Bay Coast	Torngat Mountains
11	Atl. Ocean Seaboard	Torngat Mountains
12	Mackenzie	Mackenzie Mountains, Wernecke Mountains, Selwyn Mountains, Pelly Mountains, Stikine Ranges, Cassiar Mountains, Omineca Mountains, Rocky Mountains Calgary
13	Río Grande-Bravo	San Juan Mountains, Sawatch Range
14	Caribbean Coast	Sierra Nevada de Santa Marta, Cordillera Oriental Colombia Venezuela
15	Magdalena	Sierra Nevada de Santa Marta, Cordillera Central Colombia, Cordillera Oriental Colombia Venezuela
16	Orinoco	Cordillera Oriental Colombia Venezuela
17	Amazon	Cordillera Central Colombia, Cordillera Oriental Colombia Venezuela, Cordillera Central Ecuador, Cordillera Oriental Peru Bolivia, Cordillera Occidental Peru Bolivia Chile, Altiplano
18	La Plata	Cordillera Oriental Peru Bolivia
19	S-America, Colorado	Cordillera principal, Cordillera de Oliva, Cordillera de Ollita, Cerro de Ansilta, Central Volcanic Zone, Cordillera Frontal
20	Negro	Cordillera principal, Northern Patagonian Andes
21	S-Arg., S-Atl. Coast	Cordillera Patagonica Sur, Northern Patagonian Andes, Andes fueginos
22	Col.-Ecuad., Pac. Coast	Cordillera Central Colombia, Cordillera Central Ecuador
23	Peru, Pac. Coast	Cordillera Central Ecuador, Cordillera Occidental Peru Bolivia Chile
24	N-Chile, Pac. Coast	Cordillera principal, Cordillera Occidental Peru Bolivia Chile, Sierra de la Punilla, Sierra de Tatul, Cordillera de Oliva, Cordillera de Ollita, Cerro de Ansilta, Central Volcanic Zone, Cordillera Frontal
25	S-Chile, Pac. Coast	Northern Patagonian Andes, Cordillera Patagonica Sur, Andes fueginos, Cordillera principal, Cordillera Frontal
26	La Puna Region	Cordillera Oriental Peru Bolivia, Cordillera Occidental Peru Bolivia Chile, Altiplano, Central Volcanic Zone, Cordillera Frontal
27	Salinas Grandes	Central Volcanic Zone, Cordillera Frontal

Extended Data Table 2 | List of WTUs and the GMBA mountain ranges that are (partly) covered by each WTU, for Europe, Asia and Oceania

WTU	WTU Name	GMBA mountain ranges (partly) covered by WTU
28	Spain-Portugal, Atl. Coast	Pyrenees
29	Spain, S-and E-Coast	Pyrenees
30	Ebro	Pyrenees
31	Garonne	Pyrenees
32	France, W-Coast	Pyrenees
33	Rhône	European Alps
34	France, S-Coast	European Alps, Pyrenees
35	Rhine	European Alps
36	Po	European Alps, Pyrenees
37	Italy, W-Coast	European Alps
38	Italy, E-Coast	European Alps
39	Danube	European Alps, Dinaric Alps
40	Sweden	Scandinavian Mountains, Jotunheimen
41	Adr. Sea-Bl. Sea Coast	Dinaric Alps, European Alps
42	Volga	Ural Mountains
43	Ural	Ural Mountains
44	Black Sea, N-Coast	Greater Caucasus
45	Caspian Sea Coast	Greater Caucasus
46	Scandinavia, N-Coast	Scandinavian Mountains, Jotunheimen
47	Russia, Barents Sea Coast	Ural Mountains
48	Arc. Ocean Islands	Svalbard, Greenland Kalaallit Nunaat, Novaya Zemlya
49	Iceland	Iceland
50	Gobi Int.	Haanhöhiy Uul, Borohoro-Shan, Khrebet Dzhungarskiy Alatau, Khrebet Saur, Bogda Shan, Karlik Shan, Tulai Nanshan,
51	Yellow River	Lenglong Ling, Datong Shan, Banyan Har Shan, Qionglai Shan, Anyemaqen Shan
52	Tarim Int.	Alayskiy Khrebet, Ferganskiy Khrebet, Terskey Ala Too, Kokshaal Too, Borohoro-Shan, Narat Shan, Horo Shan, Eren
53	Tibetan Plateau	Nganglong Kangri, Gangdise Shan, Nyainqentanglha Shan, Tanggula Shan, Tibetan Plateau
54	Yangtze	Tanggula Shan, Banyan Har Shan, Ningjing Shan, Chola Shan, Shaluli Shan, Daxue Shan, Qionglai Shan, Tibetan
55	Mekong	Tanggula Shan, Ningjing Shan, Patkai Hills, Mishmi Hills, Tibetan Plateau, Yun Range
56	Salween	Nyainqentanglha Shan, Tanggula Shan, Patkai Hills, Mishmi Hills, Tibetan Plateau
57	Irrawaddy	Patkai Hills
58	Ganges-Bramaputra	Gangdise Shan, Nyainqentanglha Shan, Tanggula Shan, Himalaya, Patkai Hills, Mishmi Hills
59	Sabarmati	Himalaya
60	Indus	Himalaya, Ladakh Range, Pamir Mountains, Karakorum, Hindu Kush, Nganglong Kangri, Gangdise Shan, Malakand
61	Lena	Baykal'skiy Khrebet, Khrebet Kodar, Verkhoyanskiy Khrebet, Khrebet Suntar Khayata
62	Siberia, N-Coast	Gory Putorana
63	Yenisey	Haanhöhiy Uul, Shopshal'skiy Khrebet, Kuznetskiy Alatau, Zapadnyy Sayan, Vostochnyy Sayan, Baykal'skiy Khrebet,
64	Kara Sea Coast	Ural Mountains
65	Ob	Khrebet Saur, Seminskiy Khrebet, Aygulakskiy Khrebet, Kuroyskiy Khrebet, Shopshal'skiy Khrebet, Kuznetskiy Alatau,
66	Siberia, W-Coast	Chukotskiy (Anadyrskiy) Khrebet, Koryakskiy Khrebet, Sredinnyy Khrebet, Verkhoyanskiy Khrebet, Momskiy Khrebet,
67	Black Sea, S-Coast	Kuzey Anadolu Daglari / Pontus Mountains, Lesser Caucasus, Greater Caucasus
68	Caspian Sea, S-W-Coast	Agri Dagi, Süphan Dagi, Küh-e haye Sabalan, Alborz Mountains, Zagros Mountains, Lesser Caucasus, Greater
69	Tigris-Euphrates	Mercan Daglari, Hakkari Daglari, Süphan Dagi, Zagros Mountains
70	Persian Gulf Coast	Zagros Mountains
71	Central Iran	Alborz Mountains, Zagros Mountains
72	Helmand	Hindu Kush
73	Farahrud	Hindu Kush
74	Caspian Sea, E-Coast	Hindu Kush, Alborz Mountains
75	Amu Darya	Zeravshan, Pamir-Alay, Turkestainskiy Khrebet, Gory Baysun Tau, Pamir, Karakorum, Hindu Kush, Malakand Range
76	Syr Darya	Turkestanskiy Khrebet, Pamir-Alai, Ferganskiy Khrebet, Chatkal'skiy Khrebet, Talas Alatau, Kyrgyz Ala Too, Terskey Ala
77	Lake Balkash	Kyrgyz Ala Too, Kungey Ala Too, Ile Alatau, Borohoro-Shan, Dzhungarskiy Alatau, Narat Shan, Tien Shan
78	New Zealand	Ruapehu, Rolleston Range, Two Thumb Range, Liebig Range, Ben Ohau Range, Young Range, Olivine Range,

Extended Data Table 3 | Overview of WTU supply indicators used

Indicator	Symbol	Input	Equation	Reference
Precipitation contribution WTU/basin	P_T	Average annual WTU precipitation sum (2001-2017): P_{WTU} (km^3)	$P_T = P_{WTU} / P_{BAS}$	32
		Average annual basin precipitation sum (2001-2017): P_{BAS} (km^3)		32
Inter-annual variability in precipitation	P_{YV}	Annual WTU precipitation for individual years (2001-2017): P_y (km^3)	$P_{YV} = 1 - ((max(P_y)-min(P_y)) / max(P_y)$	32
Intra-annual variability in precipitation	P_{MV}	Average monthly WTU precipitation sum (2001-2017): P_m (km^3)	$P_{MV} = 1 - ((max(P_m)-min(P_m)) / max(P_m)$	32
Precipitation	P	-	$P = 0.5*(P_{YV}+P_{MV})*P_T$	32
WTU snow cover	S_T	Average annual WTU snow cover: S (-)		7
Inter-annual variability in snow cover	S_{YV}	Annual average WTU snow cover (2001-2017): S_y (-)	$S_{YV} = 1 - ((max(S_y)-min(S_y)) / max(S_y)$	7
Intra-annual variability in snow cover	S_{MV}	Average monthly snow cover (2001-2017): S_m (-)	$S_{MV} = 1 - ((max(S_m)-min(S_m)) / max(S_m)$	7
Snow	S	-	$S = 0.5*(S_{YV}+S_{MV})*S_T$	7
Glacier ice storage	G_S	Total glacier ice volume in WTU: G_V (km^3)	$G_S = G_V / (G_V+P_{WTU})$	48
		Average annual WTU precipitation sum (2001-2017): P_{WTU} (km^3)		32
Glacier water yield	G_Y	Average annual WTU precipitation sum (2001-2017): P_{WTU} (km^3)	$G_Y = (P_{GLAC} – B) / (P_{GLAC} – B + P_{WTU})$	32
		Average annual precipitation sum glaciated area (2001-2017): P_{GLAC} (km^3)		32
		WTU average annual glacier mass balance: B (km^3)		17
Glaciers	G	-	$G = (G_S+G_Y) / 2$	
Lake and reservoir storage	L	Total volume stored in lakes and reservoirs in WTUs: S_L (km^3)	$L = S_L / (S_L+P_{WTU})$	50
		Average annual WTU precipitation sum (2001-2017): P_{WTU} (km^3)		32
Final supply index	**SI**		**(P + S + G + L) / 4**	

Extended Data Table 4 | Overview of WTU demand indicators used

Indicator	Symbol	Input	Equation	Reference
Domestic demand	D_{DOM}	Average annual downstream domestic water use (2001-2014): $D_{DOM,y}$ (km^3) Average monthly downstream domestic water use (2001-2014): $D_{DOM,m}$ (km^3) Average monthly P-ET (2001-2017) for downstream cells with domestic demand above threshold: $WA_{DOM,m}$ (km^3) Threshold is $1*10^{-6}$ km^3 per 0.05° grid cell	$\Sigma (D_{DOM,m} - WA_{DOM,m}) / D_{DOM,y}$	64
Industrial demand	D_{IND}	Average annual downstream industrial water use (2001-2014): $D_{IND,y}$ (km^3) Average monthly downstream industrial water use (2001-2014): $D_{IND,m}$ (km^3) Average monthly P-ET (2001-2017) for downstream cells with industrial demand above threshold: $WA_{IND,m}$ (km^3) Threshold is $1*10^{-6}$ km^3 per 0.05° grid cell	$\Sigma (D_{IND,m} – WA_{IND,m}) / D_{IND,y}$	64
Irrigation demand	D_{IRR}	Average annual downstream irrigation water use (2001-2014): $D_{IRR,y}$ (km^3) Average monthly downstream irrigation water use (2001-2014): $D_{IRR,m}$ (km^3) Average monthly P-ET (2001-2017) for downstream cells with irrigation demand above threshold: $WA_{IRR,m}$ (km^3) Threshold is $1*10^{-6}$ km^3 per 0.05° grid cell	$\Sigma (D_{IRR,m} – WA_{IRR,m}) / D_{IRR,y}$	64
Natural demand	D_{NAT}	Average annual Environmental Flow Requirement at river basin outlet (2001-2014): $D_{NAT,y}$ (km^3) Average monthly Environmental Flow Requirement at river basin outlet (2001-2014): $D_{NAT,m}$ (km^3) Average monthly P-ET for downstream basin (2001-2017): $WA_{NAT,m}$ (km^3)	$\Sigma (D_{NAT,m} – WA_{NAT,m}) / D_{NAT,y}$	51,52,64
Final demand index	**DI**		**$(D_{IRR} + D_{IND} + D_{DOM} + D_{NAT}) / 4$**	

Article

Ocean acidification does not impair the behaviour of coral reef fishes

https://doi.org/10.1038/s41586-019-1903-y

Received: 25 April 2019

Accepted: 21 November 2019

Published online: 8 January 2020

Timothy D. Clark[1]*, Graham D. Raby[2], Dominique G. Roche[3,4,5], Sandra A. Binning[4,5], Ben Speers-Roesch[6], Fredrik Jutfelt[7] & Josefin Sundin[7,8,9]*

The partial pressure of CO_2 in the oceans has increased rapidly over the past century, driving ocean acidification and raising concern for the stability of marine ecosystems[1–3]. Coral reef fishes are predicted to be especially susceptible to end-of-century ocean acidification on the basis of several high-profile papers[4,5] that have reported profound behavioural and sensory impairments—for example, complete attraction to the chemical cues of predators under conditions of ocean acidification. Here, we comprehensively and transparently show that—in contrast to previous studies—end-of-century ocean acidification levels have negligible effects on important behaviours of coral reef fishes, such as the avoidance of chemical cues from predators, fish activity levels and behavioural lateralization (left–right turning preference). Using data simulations, we additionally show that the large effect sizes and small within-group variances that have been reported in several previous studies are highly improbable. Together, our findings indicate that the reported effects of ocean acidification on the behaviour of coral reef fishes are not reproducible, suggesting that behavioural perturbations will not be a major consequence for coral reef fishes in high CO_2 oceans.

The partial pressure of CO_2 in the oceans has increased from average pre-industrial levels of around 280 μatm to present-day levels of approximately 410 μatm, driving a process known as ocean acidification. End-of-century levels of CO_2 in the oceans are expected to reach 900–1,000 μatm, exceeding what most marine species have experienced in the past 30 million years[1,2], and raising concerns over biodiversity loss and the stability of marine ecosystems[3].

Fishes have well-developed acid–base regulatory systems to maintain tissue pH, even when faced with partial pressure levels of CO_2 (p_{CO_2}) that exceed the end-of-century forecasts by 15 times (that is, 15,000 μatm)[6]. Therefore, physiologists have historically considered fishes to be robust to near-future CO_2 levels[7,8]. Notably, a number of highly publicized studies have reported detrimental effects of elevated CO_2 levels on the sensory systems and behaviours of fishes[4,9], with coral reef fishes appearing to be the most sensitive despite experiencing large daily and seasonal CO_2 fluctuations in nature (for example, 100–1,300 μatm)[7,10]. Indeed, CO_2 levels of around 1,000 μatm appear to alter or impair all of the sensory systems and associated behaviours of coral reef fishes studied to date[7,11]. Reported effects across a range of life stages include alterations in olfaction, hearing, vision, learning, behavioural lateralization, activity levels, boldness, anxiety and susceptibility to predation[11]. This literature has contributed to dire predictions for fish populations and marine ecosystems that are at risk of ocean acidification[12,13].

Although the reported effects of ocean acidification on the sensory systems and behaviours of fishes are considerable, there are substantial disparities among studies and species, even when methodological approaches are similar[14,15]. This discrepancy is surprising given that many of the most prominent studies that describe detrimental effects of ocean acidification on fish behaviour report exceptionally low variability and large effect sizes[4,5,9,16,17], which should maximize the probability of successful replication[18]. Moreover, the proposed mechanism that underlies the sensory impairments (interference with the function of the neurotransmitter $GABA_A$ (γ-aminobutyric acid) in the brain[17]) is reported to transcend animal phyla[11] and therefore should apply to all species of fish.

In response to the 'reproducibility crisis' that affects many scientific disciplines[19], the scientific community is demanding that studies are rigorously conducted and independently replicated before drawing broad conclusions and implementing management measures, particularly when describing widespread phenomena of global importance[20]. Establishing a robust and independently replicated database of the effects of ocean acidification on fishes is essential to gain a reliable understanding of the consequences of climate change on marine ecosystems[21].

To this end, we commenced a three-year research program in 2014 to quantify the effects of end-of-century ocean acidification on the sensory and behavioural ecology of coral reef fishes. Our objectives were to replicate and build on some of the most prominent studies in

[1]School of Life and Environmental Sciences, Deakin University, Geelong, Victoria, Australia. [2]Great Lakes Institute for Environmental Research, University of Windsor, Windsor, Ontario, Canada. [3]Department of Biology, Carleton University, Ottawa, Ontario, Canada. [4]Institut de Biologie, Éco-Éthologie, Université de Neuchâtel, Neuchâtel, Switzerland. [5]Département de Sciences Biologiques, Université de Montréal, Montréal, Québec, Canada. [6]Department of Biological Sciences, University of New Brunswick, Saint John, New Brunswick, Canada. [7]Department of Biology, Norwegian University of Science and Technology, Trondheim, Norway. [8]Department of Neuroscience, Uppsala University, Uppsala, Sweden. [9]Department of Aquatic Resources, Swedish University of Agricultural Sciences, Drottningholm, Sweden. *e-mail: t.clark@deakin.edu.au; josefin@teamsundin.se

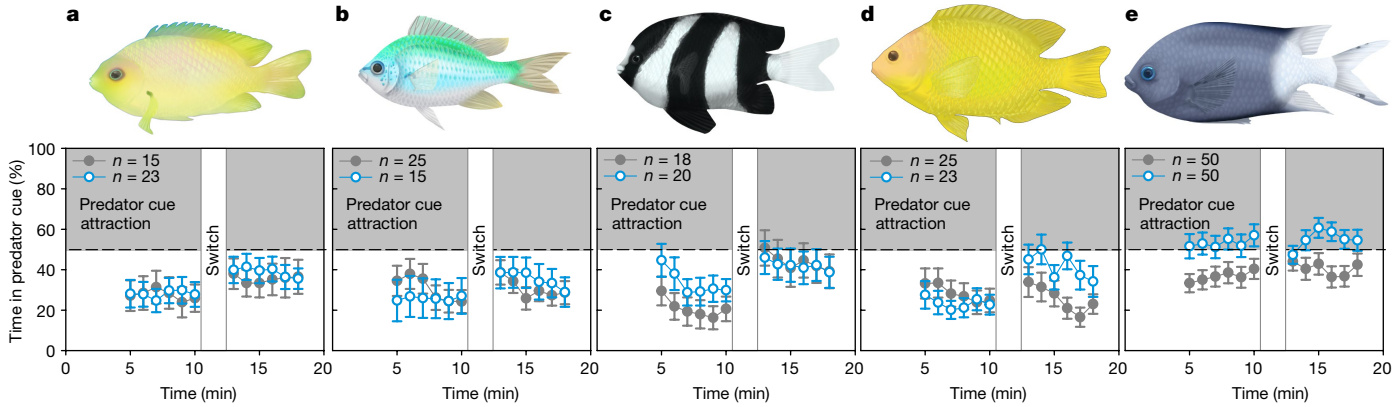


Fig. 1 | Widespread avoidance of predator chemical cues in coral reef damselfishes exposed to present-day and end-of-century levels of CO_2. **a**, *P. amboinensis*. **b**, *C. atripectoralis*. **c**, *D. aruanus*. **d**, *P. moluccensis*. **e**, *A. polyacanthus*. **a**–**e**, Percentage of time (mean ± s.e.m.) that fishes spent in water containing chemical cues of a predator (*C. cyanostigma* (**a**–**d**) or *C. urodeta* (**e**)) during two-current choice flume tests at the Lizard Island Research Station in 2014 (**a**–**d**, sub-adults and adults) and at the Australian Institute of Marine Science in 2015 (**e**, juveniles). Control fish (maintained in water containing around 410 µatm CO_2) in closed grey circles, CO_2-exposed fish (maintained in water containing around 1,000 µatm CO_2) in open blue circles (*n* of biologically independent animals are shown in the figure panels). Data were excluded between 10 min and 13 min for the predator cue switch. See Extended Data Table 2 for statistics. Fish illustrations by E. Walsh and S. Rowan.

this field to understand the diversity in behavioural responses within and across species. Notably, we aimed to enhance transparency and reduce methodological biases[22] by ensuring that our methods were fully documented and reproducible, and that raw data and videos of behavioural trials were publicly available and open to external review[23,24].

Responses to chemical cues from predators

In fishes, the reversal of chemical cue preferences is one of the most alarming effects of elevated CO_2 reported to date. Initial studies on this phenomenon used choice flumes and reported that larval clownfish (*Amphiprion percula*) and damselfish (*Pomacentrus wardi*) exposed to elevated CO_2 (850–1,050 µatm for 3–11 days) chose to spend a remarkable 90–100% of their time in water containing the chemical cues of predators (*Cephalopholis cyanostigma* or *Pseudochromis fuscus*) instead of avoiding these cues like conspecifics that were maintained at present-day CO_2 levels (0–10% of time in predator cues)[4,5]. These reports concluded that prey species will be attracted to their predators in a high CO_2 world. Many reports of cue preference reversal in coral reef fishes have since been published, including for fishes obtained from natural CO_2 seeps[16] and those experiencing transgenerational acclimation to elevated CO_2 under laboratory conditions[25].

Our experiments used established protocols in choice flume methodology (see Methods), including video footage of experiments (with pre-trial notes indicating the treatment history of each fish; see https://youtu.be/iH0w7Wqztjo) and the use of automated tracking software. We quantified the effects of elevated CO_2 on predator cue avoidance across 3 consecutive years in 560 individuals from 6 species of pomacentrid coral reef fishes (*Acanthochromis polyacanthus*, *Chromis atripectoralis*, *Dascyllus aruanus*, *Dischistodus perspicillatus*, *Pomacentrus amboinensis* and *Pomacentrus moluccensis*). Experiments covered a range of temperatures (Extended Data Table 1), CO_2 acclimation protocols were kept consistent with previous studies (4 or more days at around 1,000 µatm)[4,5,17] and four of our study species (*A. polyacanthus*, *D. aruanus*, *P. amboinensis* and *P. moluccensis*) have previously been reported to exhibit severe behavioural impairments following exposure to high CO_2 levels[16,25,26].

All four species of adult and sub-adult wild fishes tested in 2014 (*C. atripectoralis*, *D. aruanus*, *P. amboinensis* and *P. moluccensis*) significantly avoided the predator cue (*C. cyanostigma*) in both control and high CO_2 groups (Fig. 1a–d and Extended Data Table 2; pooled across all species, $n = 164$, all $P > 0.21$). The following year (2015), we detected a CO_2 treatment effect for *A. polyacanthus* juveniles reared in captivity (Extended Data Table 2; $n = 100$, $P < 0.001$): control fish spent 39 ± 2% (model estimate ± s.e.) of their time in the predator cue (*Cephalopholis urodeta*) whereas fish acclimated to high CO_2 levels spent 54 ± 3% of their time in the predator cue (Fig. 1e). This CO_2 treatment effect was not replicated in wild *A. polyacanthus* of any life stage in 2016 (Fig. 2a, b and Extended Data Table 2; $n = 94$, $P = 0.86$), nor were there any treatment effects for any of the life stages of *D. aruanus* ($n = 83$, $P = 0.09$) or *D. perspicillatus* ($n = 119$, $P = 0.30$) tested in that same year (Fig. 2c–e and Extended Data Table 2).

Overall, we detected a modest CO_2 treatment effect (no avoidance of predator cue) in one of six species in one of the two years in which that species was examined. These findings demonstrate that none of the coral reef fishes that we examined exhibited attraction to predator cues when acclimated to high CO_2 levels, in contrast to previous reports on the same and other species[4,5,16,27].

To investigate the marked disparity between our findings and previous reports for coral reef fishes, we took subsets of our choice flume data ($n = 247$ control, $n = 239$ high CO_2; 4 min per trial) to replicate the 4-min analysis approaches used previously (that is, around 9-min trials, using 2 min of data before and after the cue switch)[4,5,16,17,25,27]. We then used bootstrapping simulations to compare our data with previous datasets (Supplementary Information). On the basis of 10,000 bootstrap samples per scenario, we demonstrate using our large dataset that the results reported previously for coral reef fishes are highly improbable (probability of 0 out of 10,000): our frequency histograms of bootstrapping outputs show no evidence of CO_2 effects on chemical cue avoidance (Fig. 3a–c), and the within-group variance reported in previous studies is typically lower than what is statistically realistic (Fig. 3d–f).

Activity levels

Coral reef fishes exposed to end-of-century CO_2 levels have been stated to exhibit up to 90-fold higher levels of activity[27], prompting suggestions that these changes could underlie the higher mortality rates reported for fish that have been briefly exposed to high CO_2 and then placed onto patch reefs in the wild under present-day CO_2 conditions[5]. Notably, most activity measurements (for example, distances moved) from coral reef fishes have not used video footage but have been made

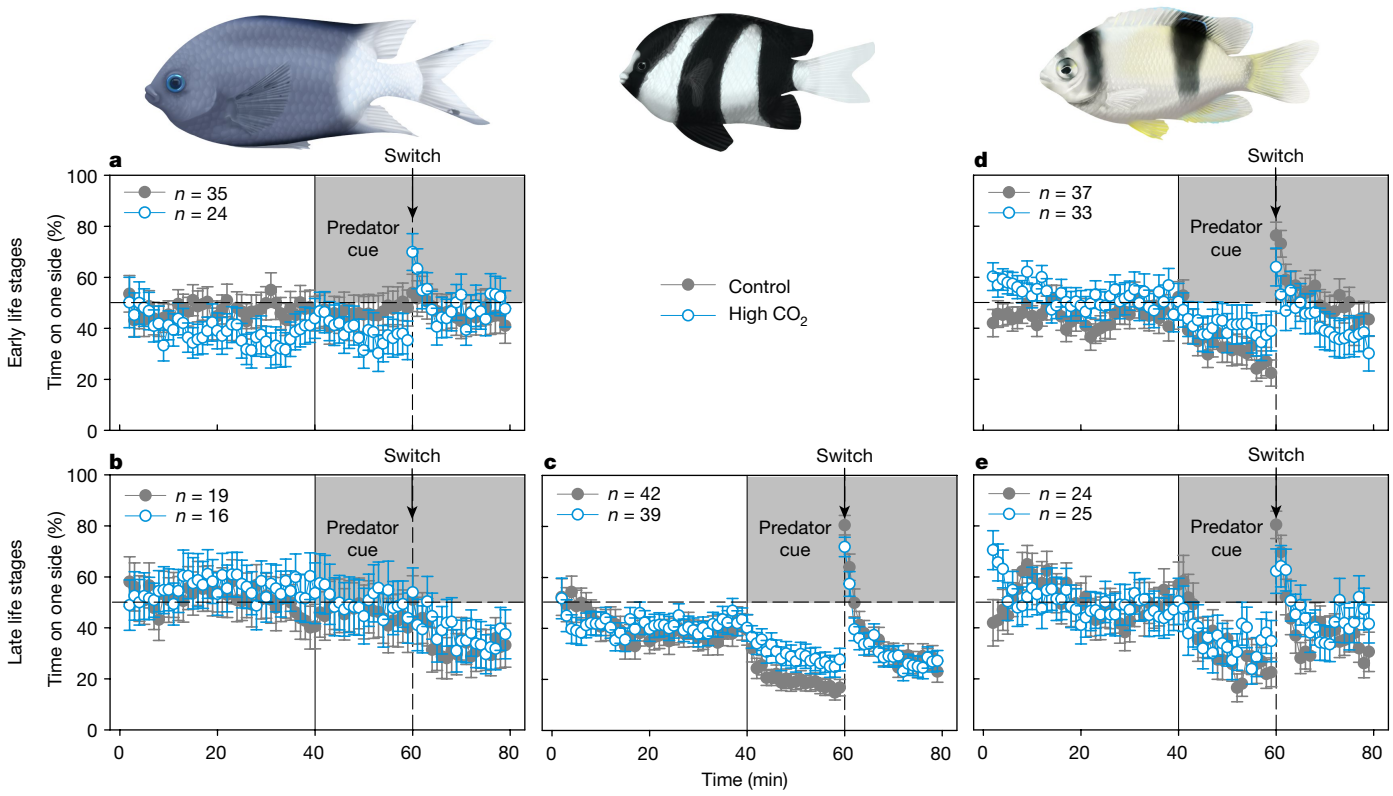


Fig. 2 | Damselfishes avoid predator chemical cues to the same degree when exposed to present-day or end-of-century CO_2 levels irrespective of life stage. a, **b**, *A. polyacanthus*. **c**, *D. aruanus*. **d**, **e**, *D. perspicillatus*. **a**–**e**, Percentage of time (mean ± s.e.m.) that fishes from early life stages and later life stages (including mid and late life stages) spent on one side of a two-current choice flume during experiments at the Lizard Island Research Station in 2016. Control fish (maintained at approximately 520 µatm) in closed grey circles, CO_2-exposed fish (maintained at around 1,090 µatm) in open blue circles. Fish were given 40 min to habituate to the flume (during which time their activity was quantified; see Fig. 4). Predator chemical cues (*C. cyanostigma*) were introduced to one side of the flume for 20 min and then switched to the other side for another 20 min. *n* of biologically independent animals are shown in the figure panels. See Extended Data Table 2 for statistics. Fish illustrations by E. Walsh.

using direct manual observations, either by SCUBA divers or by an observer counting the number of gridlines crossed by fish in aquaria[5,26].

We filmed 582 individuals from 6 species across 3 years and quantified swimming activity in behavioural arenas using automated tracking software. Activity levels were assessed in adults and sub-adults of 5 species in 2014, with 3 species showing no detectable effects of CO_2 treatment (*C. atripectoralis*, *P. amboinensis* and *P. moluccensis*; Fig. 4c–e and Extended Data Table 3; pooled across all species, $n = 126$, $P > 0.08$). We found some evidence that activity was affected by high CO_2 in *D. aruanus*, for which an interaction between CO_2 treatment and standard length suggested that activity was elevated by approximately 59–92% in smaller individuals (<37 mm standard length) in high CO_2 levels (Fig. 4b, Extended Data Fig. 1a and Extended Data Table 3; $n = 46$, $P = 0.03$). In *A. polyacanthus*, activity levels were increased by around 50% ($P = 0.009$) in fish acclimated to elevated CO_2 levels after controlling for a strong main effect of standard length (Fig. 4a, Extended Data Fig. 1b and Extended Data Table 3; $n = 16$, $P < 0.001$).

When we extended our experiments in 2015 using captive-reared juvenile *A. polyacanthus* with greater sample sizes and longer-duration trials (Supplementary Information), the effect of CO_2 on activity disappeared (Extended Data Table 3; $n = 66$, $P = 0.1$). There was, however, a weak interaction ($P = 0.04$); activity decreased in the high CO_2 fish (but not controls) with increasing body size (Fig. 4a, Extended Data Fig. 1c and Extended Data Table 3). In 2016, we conducted additional tests of activity in wild fish across various life stages and found no effects of CO_2 nor any interactions with body size in any of the three species ($n = 122$ *D. perspicillatus*, $n = 112$ *A. polyacanthus*, $n = 94$ *D. aruanus*; all CO_2 main effects $P > 0.24$; Fig. 4 and Extended Data Table 3).

Overall, we found that fish exposed to high CO_2 did not exhibit consistently elevated activity levels compared with conspecifics under control conditions (Fig. 4). Rather, we found that activity levels were highly variable among individuals, increasing the risk of type-I errors in experiments using small sample sizes[18], and possibly in large-sample experiments that rely on human observation rather than automated video analysis[22–24].

Behavioural lateralization

A tendency to favour the left or right side during behavioural activities (that is, behavioural lateralization) is thought to be an expression of functional asymmetries of the brain; this is important for tasks such as schooling and predator avoidance[28]. Elevated CO_2 has been reported to reduce or abolish behavioural lateralization in fishes[17,25], presumably as a result of brain dysfunction[17]. Population-level lateralization is present when a group of individuals collectively exhibits a side bias (the mean number of turns to one side significantly exceeds 50%), whereas individual-level lateralization is present when more individuals within a tested group exhibit a side bias than expected by chance (based on a binomial distribution with $\alpha = 0.5$). Both types of lateralization are independent of each other, but are not mutually exclusive (see Methods and Supplementary Information for details).

Using a standard detour test in a double T-maze, we quantified the effects of elevated CO_2 levels on behavioural lateralization using 175 fishes across four species in 2014 (*C. atripectoralis*, *D. aruanus*, *P. amboinensis* and *P. moluccensis*). None of the species exhibited population-level lateralization under control conditions (Extended

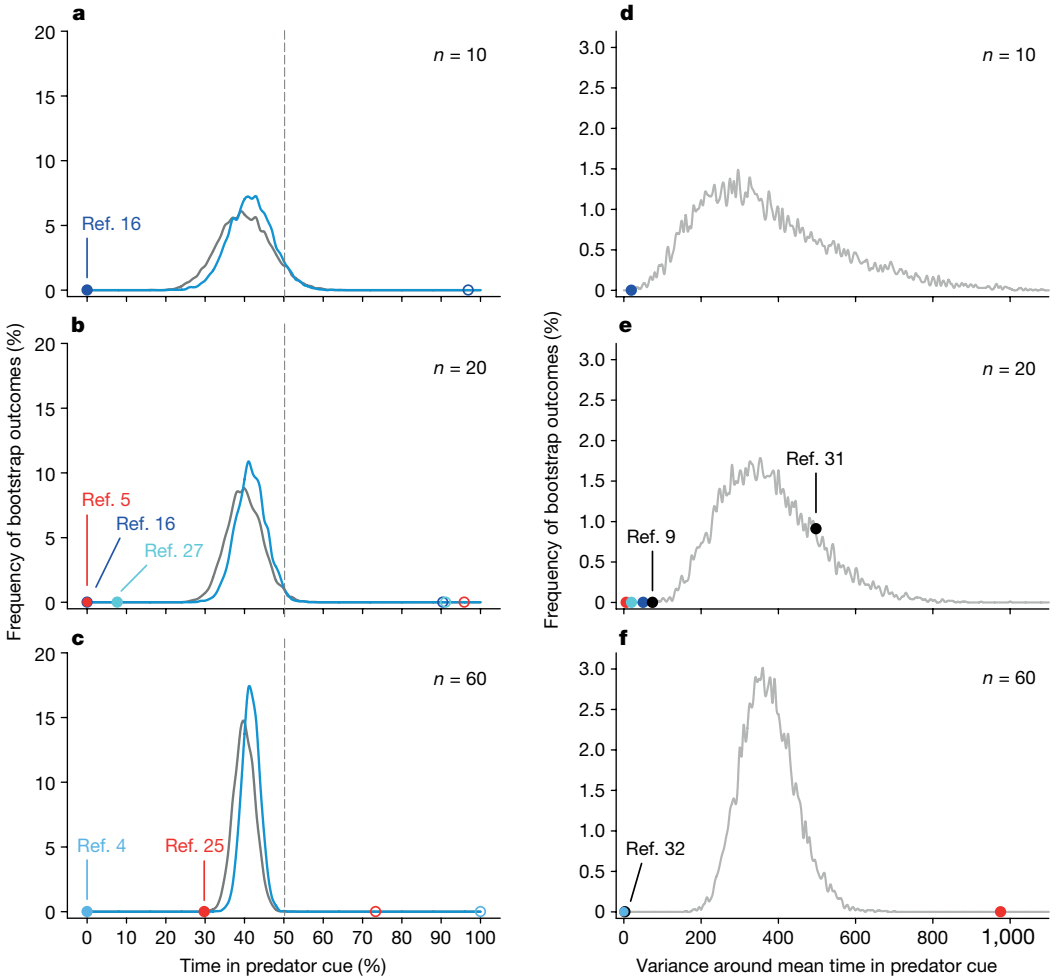


Fig. 3 | Bootstrapping data simulations of predator chemical cue avoidance and within-group variance. Bootstrapping data simulations reveal that fish avoid predator chemical cues regardless of whether they are acclimated to present-day or end-of-century CO_2 levels (**a**–**c**), and the within-group variance in many previous studies is lower than statistically reasonable (**d**–**f**). **a**–**c**, Frequency outputs from bootstrapping simulations of the mean percentage of time spent in water containing predator cues when $n = 10$ (**a**), $n = 20$ (**b**) or $n = 60$ (**c**) fish were sampled from each of the control (grey) and high CO_2 (blue) treatment groups (total n in sampled dataset: 247 control, 239 high CO_2; sample sizes represent biologically independent animals). The frequency distributions fall to the left of 50% (dashed vertical line) in both treatment groups, indicating similar avoidance of predator chemical cues under control and high CO_2 conditions. This is markedly different from previous reports of major effects of high CO_2 levels on predator and alarm cue avoidance in coral reef fishes (examples presented in coloured circles, selected to match the group sample sizes presented in figure panels: closed circles, control; open circles, high CO_2). **d**–**f**, Frequency histograms (light grey) of the associated variance around the means from bootstrapping simulations presented in **a**–**c** (control and high CO_2 fish pooled for simplicity). Also presented are results of previous studies of coral reef fish (variance around the group mean, where similar groups were combined for simplicity) that have used choice flumes to examine chemical cue preferences. **a**, **d**, Dark-blue circle, data from ref. [16]. **b**, **e**, Dark-blue circle, data from ref. [16] (this circle overlaps with the red circle in **b**); red circle, data from ref. [5]; light-blue circle, data from ref. [27]. **c**, **f**, Blue circle, data from ref. [4]; red circle, data from ref. [25]. **e**, **f**, Black circles indicate references that did not examine the effects of high CO_2 and/or predator or alarm cue avoidance and thus do not appear in **a**–**c**. **e**, Left black circle, data from ref. [9]; right black circle, data from ref. [31]. **f**, Black circle, data from ref. [32]. For additional details, see Supplementary Information.

Data Fig. 2a–d and Extended Data Table 4), and only *C. atripectoralis* showed slight population-level lateralization under high CO_2 ($P = 0.047$; Extended Data Table 4). Three species (*C. atripectoralis*, *D. aruanus* and *P. moluccensis*) exhibited no individual-level lateralization under control conditions, which remained unchanged under high CO_2 conditions (Extended Data Fig. 2a–c and Extended Data Table 4). A treatment effect was detected for individual-level lateralization in *P. amboinensis*, with the high CO_2 group displaying reduced individual-level lateralization compared with controls (Extended Data Fig. 2d and Extended Data Table 4). However, this effect was no longer present when a subset of the same individuals was retested 7–8 days later ($n = 15$ control, $n = 15$ high CO_2; Extended Data Fig. 2e and Extended Data Table 4). Although our sample sizes were comparable to many similar studies (for example, ref. [17]), our inconsistent findings for *P. amboinensis* are likely to be a consequence of low statistical power in a behavioural test that exhibits high inter-individual variability[18] (Extended Data Fig. 2).

We increased statistical power in 2015 when behavioural lateralization was tested in wild and captive-reared *A. polyacanthus* ($n = 120$ control, $n = 104$ high CO_2), a species for which impairments in lateralization caused by high CO_2 levels have been reported[25]. In contrast to previously reported results, we found no effect of CO_2 levels on behavioural lateralization: *A. polyacanthus* exhibited individual-level lateralization and no population-level lateralization, both under control and high CO_2 conditions (Extended Data Fig. 2f and Extended Data Table 5). On the basis of the previous studies that have reported that elevated CO_2 levels impair visual acuity[26,29], we slightly offset the barrier at one end of the lateralization arena, creating a shorter path around the barrier to the left. We predicted that fish under high CO_2 levels would not visually

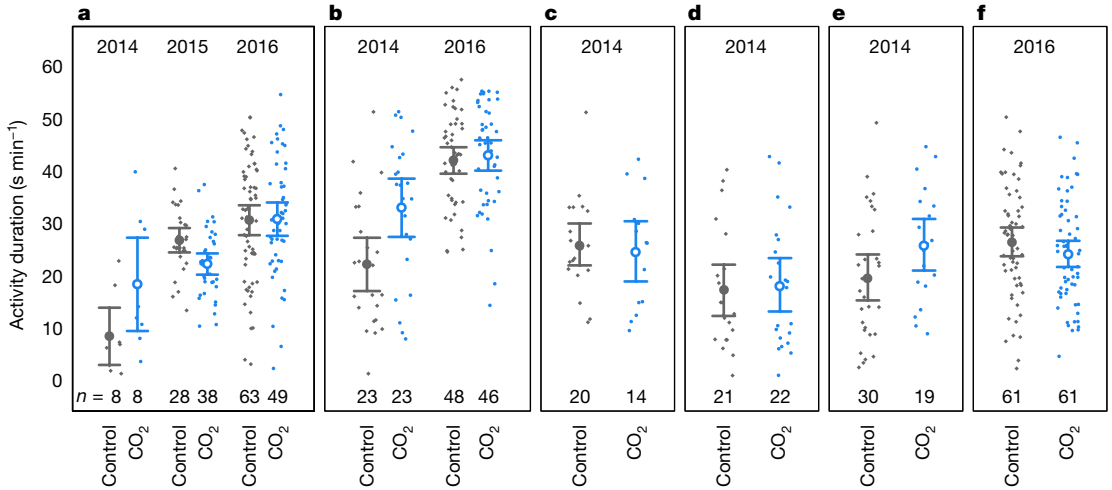


Fig. 4 | Widespread similarities in the activity levels of six species of coral reef damselfish regardless of whether acclimated to present-day or end-of-century levels of CO_2. a–**f**, Activity levels (s min^{-1}) after acclimation to control (around 450 µatm; closed grey circles) or end-of-century (about 1,000 µatm; open blue circles) levels of CO_2. Mean values for individual animals are shown (small symbols). The large symbols and error bars represent the mean ± 95% confidence intervals for each group. Data for *A. polyacanthus* (**a**) and *D. aruanus* (**b**) were collected across multiple years (indicated at the top of each panel), whereas data for *C. atripectoralis* (**c**), *P. amboinensis* (**d**) and *P. moluccensis* (**e**) were collected in 2014 and data for *D. perspicillatus* (**f**) were collected in 2016. *n* numbers along the bottom of the figure panels represent biologically independent animals. Note that there were some statistically significant (two-tailed tests), context-dependent effects of CO_2 treatment for *A. polyacanthus* and *D. aruanus*, including interactions with body size (see Extended Data Fig. 1; statistics are included in Extended Data Table 3).

detect the shortcut as strongly as control fish. By contrast, we found that fish from both treatment groups exhibited a preference for the shorter path (Extended Data Fig. 2g and Extended Data Table 5).

Conclusions and implications

Here we present a multi-species, multi-year and multi-life-stage examination of the sensory and behavioural impairments that have been reported for coral reef fishes under end-of-century levels of CO_2, thus answering an international call for comprehensive replication studies on issues of global importance[21]. Notably, we took great care to enhance transparency by systematically documenting our experiments and providing raw data and analysis code. In contrast to previous studies on the same and closely related species, we found no consistent detrimental effects of end-of-century CO_2 levels on the avoidance of predator chemical cues, activity levels or behavioural lateralization. Although CO_2 emissions are an environmental threat[3,30], the catastrophic projections for fish sustainability based on CO_2-induced behavioural impairments[12,13] must be reassessed in light of our findings.

We went to great lengths to match the species, life stages, location and season of previous studies, yet the discrepancies in findings were considerable. This was most apparent for the responses of fish to predator chemical cues, for which previous studies have reported extreme effect sizes (in which control fish spent <10% of their time in predator cues compared with >90% of time for fish under high CO_2; Fig. 3a–c) with exceedingly low variability around the group means (Fig. 3d–f). The research community in the field of ocean acidification and coral reef fish behaviour has remained small, and the study systems are often remote and expensive to access, both of which have precluded independent assessments of previous findings. Small sample sizes[18] and other methodological or analytical weaknesses[22] in previous studies could potentially explain the discrepancies between our results and the majority of articles that have reported minor impacts (small effect sizes) of CO_2 on fish behaviour. However, we cannot reconcile our findings with those that show extremely large effect sizes and small within-group variance in experiments with large sample sizes (Fig. 3). Inter-individual variation enables the persistence of populations and species and is a fundamental biological phenomenon on which selection acts; results showing negligible variation (particularly for behaviours that are inherently variable) should be viewed with caution (see Supplementary Information).

On the basis of our findings on more than 900 wild and captive-reared individuals of 6 species across 3 years, we conclude that acclimation to end-of-century levels of CO_2 does not meaningfully alter important behaviours of coral reef fishes. Reasonably large sample sizes and consistent results across species, locations, life stages and years suggest that the probability of false-negative results (type-II errors) in our study is low. Given the importance of these issues to the management of coral reefs and other aquatic ecosystems[12,13], we encourage further replication of previous studies using the transparent and objective approaches described here (for example, video footage with pre-trial notes, complete data and code archiving)[22,23]. Only then will the research community be equipped to reach a consensus on whether end-of-century ocean acidification could have direct effects on the behaviour of fishes. Nonetheless, it should be firmly emphasized that there is strong evidence that increasing atmospheric CO_2 is causing ocean warming, which can profoundly affect marine fishes[30].

Online content

Any methods, additional references, Nature Research reporting summaries, source data, extended data, supplementary information, acknowledgements, peer review information; details of author contributions and competing interests; and statements of data and code availability are available at https://doi.org/10.1038/s41586-019-1903-y.

1. Hönisch, B. et al. The geological record of ocean acidification. *Science* **335**, 1058–1063 (2012).
2. Lüthi, D. et al. High-resolution carbon dioxide concentration record 650,000–800,000 years before present. *Nature* **453**, 379–382 (2008).
3. Riebesell, U. & Gattuso, J.-P. Lessons learned from ocean acidification research. *Nat. Clim. Change* **5**, 12–14 (2015).
4. Dixson, D. L., Munday, P. L. & Jones, G. P. Ocean acidification disrupts the innate ability of fish to detect predator olfactory cues. *Ecol. Lett.* **13**, 68–75 (2010).
5. Munday, P. L. et al. Replenishment of fish populations is threatened by ocean acidification. *Proc. Natl Acad. Sci. USA* **107**, 12930–12934 (2010).
6. Ishimatsu, A., Hayashi, M., Lee, K.-S., Kikkawa, T. & Kita, J. Physiological effects on fishes in a high-CO_2 world. *J. Geophys. Res. Oceans* **110**, C09S09 (2005).

7. Heuer, R. M. & Grosell, M. Physiological impacts of elevated carbon dioxide and ocean acidification on fish. *Am. J. Physiol. Regul. Integr. Comp. Physiol.* **307**, R1061–R1084 (2014).
8. Melzner, F. et al. Physiological basis for high CO_2 tolerance in marine ectothermic animals: pre-adaptation through lifestyle and ontogeny? *Biogeosciences* **6**, 2313–2331 (2009).
9. Munday, P. L. et al. Ocean acidification impairs olfactory discrimination and homing ability of a marine fish. *Proc. Natl Acad. Sci. USA* **106**, 1848–1852 (2009).
10. Shaw, E. C., McNeil, B. I. & Tilbrook, B. Impacts of ocean acidification in naturally variable coral reef flat ecosystems. *J. Geophys. Res. Oceans* **117**, C03038 (2012).
11. Clements, J. C. & Hunt, H. L. Marine animal behaviour in a high CO_2 ocean. *Mar. Ecol. Prog. Ser.* **536**, 259–279 (2015).
12. McNeil, B. I. & Sasse, T. P. Future ocean hypercapnia driven by anthropogenic amplification of the natural CO_2 cycle. *Nature* **529**, 383–386 (2016).
13. Leis, J. M. Paradigm lost: ocean acidification will overturn the concept of larval-fish biophysical dispersal. *Front. Mar. Sci.* **5**, 47 (2018).
14. Bignami, S., Sponaugle, S. & Cowen, R. K. Response to ocean acidification in larvae of a large tropical marine fish, *Rachycentron canadum*. *Glob. Change Biol.* **19**, 996–1006 (2013).
15. Sundin, J., Amcoff, M., Mateos-González, F., Raby, G. D. & Clark, T. D. Long-term acclimation to near-future ocean acidification has negligible effects on energetic attributes in a juvenile coral reef fish. *Oecologia* **190**, 689–702 (2019).
16. Munday, P. L., Cheal, A. J., Dixson, D. L., Rummer, J. L. & Fabricius, K. E. Behavioural impairment in reef fishes caused by ocean acidification at CO_2 seeps. *Nat. Clim. Change* **4**, 487–492 (2014).
17. Nilsson, G. E. et al. Near-future carbon dioxide levels alter fish behaviour by interfering with neurotransmitter function. *Nat. Clim. Change* **2**, 201–204 (2012).
18. Button, K. S. et al. Power failure: why small sample size undermines the reliability of neuroscience. *Nat. Rev. Neurosci.* **14**, 365–376 (2013).
19. Baker, M. 1,500 scientists lift the lid on reproducibility. *Nature* **533**, 452–454 (2016).
20. Eisenstein, M. Public health: an injection of trust. *Nature* **507**, S17–S19 (2014).
21. Browman, H. I. Applying organized scepticism to ocean acidification research. *ICES J. Mar. Sci.* **73**, 529–536 (2016).
22. Parker, T. H. et al. Transparency in ecology and evolution: real problems, real solutions. *Trends Ecol. Evol.* **31**, 711–719 (2016).
23. Clark, T. D. Science, lies and video-taped experiments. *Nature* **542**, 139 (2017).
24. Clark, T. D. et al. Scientific misconduct: the elephant in the lab. A response to Parker et al. *Trends Ecol. Evol.* **31**, 899–900 (2016).
25. Welch, M. J., Watson, S.-A., Welsh, J. Q., McCormick, M. I. & Munday, P. L. Effects of elevated CO_2 on fish behaviour undiminished by transgenerational acclimation. *Nat. Clim. Change* **4**, 1086–1089 (2014).
26. Ferrari, M. C. O. et al. Effects of ocean acidification on visual risk assessment in coral reef fishes. *Funct. Ecol.* **26**, 553–558 (2012).
27. Munday, P. L. et al. Elevated CO_2 affects the behavior of an ecologically and economically important coral reef fish. *Mar. Biol.* **160**, 2137–2144 (2013).
28. Vallortigara, G. & Rogers, L. J. Survival with an asymmetrical brain: advantages and disadvantages of cerebral lateralization. *Behav. Brain Sci.* **28**, 575–589 (2005).
29. Chung, W.-S., Marshall, N. J., Watson, S.-A., Munday, P. L. & Nilsson, G. E. Ocean acidification slows retinal function in a damselfish through interference with $GABA_A$ receptors. *J. Exp. Biol.* **217**, 323–326 (2014).
30. Pecl, G. T. et al. Biodiversity redistribution under climate change: impacts on ecosystems and human well-being. *Science* **355**, eaai9214 (2017).
31. Gould, A. L., Harii, S. & Dunlap, P. V. Cues from the reef: olfactory preferences of a symbiotically luminous cardinalfish. *Coral Reefs* **34**, 673–677 (2015).
32. Dixson, D. L., Abrego, D. & Hay, M. E. Chemically mediated behavior of recruiting corals and fishes: a tipping point that may limit reef recovery. *Science* **345**, 892–897 (2014).

Publisher's note Springer Nature remains neutral with regard to jurisdictional claims in published maps and institutional affiliations.

© The Author(s), under exclusive licence to Springer Nature Limited 2020

Methods

Experiments were conducted across 3 years (2014–2016), at 2 locations in Australia (the Lizard Island Research Station (LIRS) and the Australian Institute of Marine Science (AIMS) in Townsville), and on a total of more than 900 individuals from 6 species across an ontogenetic range. The experimental designs and CO_2 dosing systems (described below) followed best practices for ocean acidification research[33–35]. For all experiments, fish were given at least 4 days to acclimate to the CO_2 treatment before trials commenced. Although an acclimation period of 4 days is short, this duration was chosen because it has been reported to be sufficient to maximize behavioural and/or sensory impairments in fishes[5,27]. Fish were placed in the two treatment groups at random. Other aspects of water chemistry (that is, the water supply used and the temperature it was kept at), lighting and feeding were kept constant among replicate tanks across the two acclimation treatments. Juvenile fish were mostly used in the experiments but when adult fish were used, we did not determine their sex in order to minimize handling. The sample sizes used in each experiment were based on previous studies and fish availability. Complete blinding regarding CO_2 treatment was not possible as the CO_2 dosing system was visible (both visually and auditory) to any observer physically present during the experiments. However, all activity and predator cue avoidance experiments were recorded on video and analysed using automated tracking software. Lateralization experiments could not be tracked using automated tracking software but were scored in real-time. A detailed description of the methods is included in the Supplementary Information. All experiments were conducted in compliance with relevant ethical regulations under approval from the James Cook University Animal Ethics Committee in association with the AIMS (permit A1924).

Animals and holding conditions

LIRS August 2014. Sub-adult and adult wild fishes (humbug dascyllus (*D. aruanus*), $n = 46$; Ambon damsel (*P. amboinensis*), $n = 43$; lemon damsel (*P. moluccensis*), $n = 49$; black-axil chromis (*C. atripectoralis*), $n = 43$; and spiny chromis (*A. polyacanthus*), $n = 16$) were collected from around Lizard Island at the northern end of the Great Barrier Reef, Australia (14° 40′ S, 145° 28′ E), by SCUBA divers using hand and/or barrier nets and spray bottles of clove oil anaesthetic (mixed 1:4 with ethanol). To produce predator chemical cues, predatory blue-spotted rock cods (*C. cyanostigma*; $n = 24$) were collected using hook and line. All fishes were transported in aerated seawater to LIRS, where they were placed in tanks with flow-through seawater (35 PSU) at ambient temperature (Extended Data Table 1). The damselfishes were divided in approximately even numbers between eight identical tanks (25 l each; 3 l min^{-1} flow-through). *C. cyanostigma* were divided in even numbers between two identical tanks (200 l each; 12 l min^{-1} flow-through) and fed pieces of sardine (*Sardinops sagax*) every 2–3 days.

After 1–2 days in captivity, the CO_2 of half of the tanks (including one of the *C. cyanostigma* tanks) was gradually increased to 945 ± 117 µatm (mean ± s.d.) (pH_{total} of around 7.72, calculated using previously published constants[36,37]; Extended Data Table 1) over 24 h using a CO_2 dosing system (pH stat Computers, Aqua Medic) connected to solenoid valves that regulate the administration of 100% CO_2 gas (as previously described[38]). Although 24 h may seem a short duration over which to increase CO_2 to end-of-century levels, fish have a well-developed physiological capacity to endure much larger and/or quicker changes in p_{CO_2} levels[6,39]. In addition, some previous studies have reported that fish were simply transferred to end-of-century p_{CO_2} treatments rather than using a gradual change[27,40,41] and others did not report how fish were transferred to high p_{CO_2} levels[4,5,17]. The other half of the tanks remained at ambient CO_2 levels of 406 ± 21 µatm (pH_{total} of approximately 8.04; Extended Data Table 1). Levels of CO_2 in each tank were checked twice daily using a handheld CO_2 meter (GMT 222, Vaisala) connected to an aspiration pump (Vaisala) and a submerged gas-permeable PFTE probe (Qubit Systems) as described previously[42]. The CO_2 meter was factory-calibrated by Vaisala before experiments. Water samples (60-ml samples of water with 30 µl of mercury chloride to poison any microorganisms) were taken at 10 different points throughout the experiment for subsequent measurements of total alkalinity (Extended Data Table 1). Fish were fed to satiation 1–2 times per day with a commercial pellet food, but food was withheld for around 12 h before experiments. Tanks were cleaned every 3–4 days. Individual fish were reused for each of the three response variables that we measured (activity, behavioural lateralization and predator chemical cue avoidance) in a randomized order. At the end of the experiments, fish were released at their site of capture.

AIMS May and June 2015. Juvenile spiny chromis (*A. polyacanthus*) (age, 3–14 days after hatching, 0.019 ± 0.015 g (mean ± s.d.) initial wet weight, 9.1 ± 2.3 mm initial standard length) were obtained from the Reef HQ aquarium in Townsville, Australia (total $n = 1{,}494$). In addition, groups of wild *A. polyacanthus* juveniles (10–15 days after hatching) from four distinct schools (four breeding pairs) were corralled into clear containers by SCUBA divers at depths of 8–10 m at Davies Reef (18.8238° S, 147.6429° E) in April 2015 ($n = 481$ collected). Fish were transported in aerated seawater to AIMS, where they were placed in 25-l tanks with seawater recirculating (around 3.5 l min^{-1}) to one of four independent 200-l sumps, which themselves were continuously flushed with fresh seawater (4–7 l min^{-1}). Subsets of fish from Reef HQ were used for assessments of predator cue avoidance, activity levels and behavioural lateralization, whereas wild fish were only used in behavioural lateralization experiments. Four wild predatory fish (flagtail grouper (*C. urodeta*)) were freighted to AIMS and split evenly between two tanks after being caught from the northern Great Barrier Reef by Cairns Marine. The effluent water from the grouper tanks went straight to the drains to ensure that the *A. polyacanthus* did not habituate to predator chemical cues. *C. urodeta* were fed freshly killed juvenile *A. polyacanthus* every 1–2 days as previously described[43].

After at least 24 h to recover from transport, the CO_2 of half of the *A. polyacanthus* tanks ($n = 10$) and one of the C. *urodeta* tanks was gradually increased to 1,021 ± 156 µatm (mean ± s.d.) (pH_{total} of around 7.70; Extended Data Table 1) over 24 h using a CO_2 dosing system (pH stat Computers, Aqua Medic) connected to solenoid valves that regulate the administration of 100% CO_2 gas into two of the partial-recirculation sump systems. The remaining tanks ($n = 10$ for *A. polyacanthus* and $n = 1$ for *C. urodeta*) were kept at ambient CO_2 levels (428 ± 13 µatm, pH_{total} of around 8.03; Extended Data Table 1). Three large air stones in each sump ensured that the water remained well mixed and maintained dissolved oxygen at >90% air saturation. The CO_2 levels of the holding tanks were checked every 1–4 days using a LI-820 CO_2 Gas Analyzer (LI-COR). Fish were exposed to natural water temperatures for the region (quantified using thermal data-loggers sampling every 30 min; iButton, Maxim Integrated). Temperature decreased seasonally from 26.1 ± 0.2 °C during the first week of acclimation (May 2015) to 24.8 ± 0.5 °C during the final week of experiments (June 2015; Extended Data Table 1). Salinity was regulated through the AIMS SeaSim aquarium system (35.8 ± 0.15 PSU). Water samples for alkalinity were taken as described above for LIRS 2014 (five samples per treatment, Extended Data Table 1). Fish were fed ad libitum 1–2 times per day using commercial aquaculture pellets crushed to a powder and/or *Artemia* spp. nauplii, but food was withheld for 12–18 h before experiments. Tanks were cleaned weekly. Individual fish were used once; that is, for one of the three response variables that we measured (activity, behavioural lateralization or predator chemical cue avoidance). All fish used at AIMS in 2015 were euthanized with an overdose of tricaine methanesulfonate (MS-222, around 500 mg l^{-1}) at the end of the experiments, or at intermittent times during the experiments when they were euthanized to take precise length and weight measurements for another study[15].

LIRS January 2016. Wild fishes were collected from around Lizard Island, as described above for LIRS 2014. Adult predatory *C. cyanostigma*

(n = 15) were caught using hook and line, and three damselfish species were caught using clove oil spray and hand or barrier nets (sub-adult and adult *D. aruanus* (n = 96); juvenile, sub-adult and adult *A. polyacanthus* (n = 112); sub-adult and adult white damsel (*D. perspicillatus*; n = 50)). Note that *A. polyacanthus* does not have a pelagic larval phase (see Supplementary Information). In addition, larval *D. perspicillatus* (n = 72) were caught near the end of their pelagic phase using established light-trapping techniques[44]. Fishes were placed in tanks with flow-through seawater at ambient temperature (Extended Data Table 1). The damselfishes were divided in approximately even numbers between 22 identical tanks that each received constant flow-through (one species per tank, 7–8 tanks per species; 10–25 l each and 1–3 l min^{-1} flow-through, depending on fish size). *C. cyanostigma* were divided in even numbers between four identical flow-through tanks (60 l each; 3 l min^{-1} flow-through) and fed sardine pieces and freshly killed adult damselfish every 2–3 days. All tanks were provided with pieces of PVC piping to act as shelter for the fish.

After 1–2 days in captivity, the CO_2 of half of the tanks (n = 11 damselfish tanks, n = 2 *C. cyanostigma* tanks) was gradually increased to 1,089 ± 326 µatm (mean ± s.d.) over 24 h using a CO_2 dosing system as described above for LIRS 2014, while the other half of the tanks remained at ambient CO_2 levels of 521 ± 93 µatm (Extended Data Table 1). Levels of CO_2 in each tank were checked twice daily using the handheld Vaisala as described above for LIRS 2014. Damselfishes were fed to satiation 1–2 times per day with a commercial fish flake–saltwater slurry (TetraMin Tropical Flakes, Tetra), but food was withheld for around 12 h before experiments. Tanks were cleaned every 3–4 days. Individual fish were used once; the two measured response variables were obtained from a single, continuous behavioural trial (activity followed by predator chemical cue avoidance). At the end of the experiments, fish were released at the approximate site of capture.

Response to predator chemical cues

LIRS 2014. Four species were examined for their responses to predator chemical cues (*P. amboinensis* (standard length range, 23–53 mm), *C. atripectoralis* (standard length, 15–43 mm), *D. aruanus* (standard length, 16–63 mm) and *P. moluccensis* (standard length, 19–34 mm); sample sizes are provided in Fig. 1 and Extended Data Table 2), using a two-current choice flume. The setup for the two-current choice flume followed established protocols[45] (for details, see Supplementary Information). The fish in the high CO_2 group had been acclimated to the CO_2 treatment for 5–16 days before commencement of experiments, while control fish had been held for 4–16 days. The choice flume was a custom-built, larger version ($L \times W \times H$ = 580 × 260 × 280 mm^3; water depth, 80 mm) of a two-current choice flume used in previous studies[46]. Detailed information on the design and function of two-current choice flumes has been described previously[45] (for details, see Supplementary Information). *C. cyanostigma* was used to create predator chemical cues (see Supplementary Information for details). All trials in the choice flume were recorded using a computer with a webcam (Logitech HD Pro C920) positioned 45 cm above the choice arena. At the beginning of a trial, a paper note detailing the treatment history of the individual fish was placed in view of the camera before the fish was placed into the centre of the choice arena within a bottomless mesh cylinder (70-mm diameter) for 1.5–2 min. This step was included to ensure that the fish had the opportunity to receive sensory input from both sides of the choice flume—one side flowing with unmanipulated water and the other side flowing with water containing the predator cue. After the settling period, the mesh cylinder was carefully lifted and the fish was allowed to select its position within the flume. After a further 8 min, the configuration of flow through each side of the flume was switched using a series of valves such that water containing the predator cue now flowed through the opposite side of the flume. The valves were positioned near the secondary header tanks and could be adjusted without visually or physically disturbing the fish. The fish was given a further 8 min to select its position in the flume with the new flow configuration before being removed and returned to its holding tank. The video files were analysed using tracking software (ViewPoint, Zebralab) to automatically quantify time spent in the flow of water (side of the flume) containing the predator cue.

AIMS 2015. The general flume setup used at AIMS followed the design described above, with some exceptions. Two choice flumes were used side-by-side under the view of a single camera (Microsoft LifeCam HD 5000, mounted around 45 cm above the tank) recording at 10 frames per second with a resolution of 1,280 × 720 pixels. To match the smaller size of the fish (compared with the fish of the LIRS 2014 dataset), we used choice flumes with an arena that was 90 mm long × 45 mm wide with a water depth of 22 mm (4.9 mm s^{-1} water speed, around 135 ml min^{-1} per current). We initially tested flumes built to the exact specifications of those used in previous papers[4,5,9,25]. However, we were unable to produce laminar flow using this setup; both incoming streams of water mixed in the test section of the flume, meaning that the fish would not be able to make a choice between the different currents (https://youtu.be/jrtyc-rLGWc?t=705, see Supplementary Information for details).

The fish (*A. polyacanthus* (standard length, 9–11 mm) from Reef HQ aquarium) were acclimated to their respective CO_2 conditions for 6–13 days before being used in choice flume trials. The predator chemical cue avoidance trials (n = 50 control, n = 50 high CO_2) followed the same protocol as at LIRS 2014 (see above; total duration of 18 min), including the presentation of an explanatory note in front of the camera before each trial. *C. urodeta* was used to create predator chemical cues (see Supplementary Information for details).

LIRS 2016. Three species across an ontogenetic range were examined for their responses to predator chemical cues at LIRS in January 2016 (*A. polyacanthus*, *D. aruanus* and *D. perspicillatus* from early life stages (7.5–14.5 mm standard length) and later life stages (15.0–51.0 mm standard length; sample sizes listed in Fig. 2 and Extended Data Table 2). Five two-current choice flumes were used in parallel (one 610 mm × 200 mm, two 290 mm × 93 mm, and two 235 mm × 45 mm, for details see Supplementary Information). All trials in the choice flumes were recorded using a computer with webcams (Logitech HD Pro C920, FireWire camera, Dragonfly 2, Point Gray; Microsoft LifeCam HD 5000 webcam) positioned 45–130 cm above the choice arenas (depending on camera type and flume size). Trials were executed in a similar manner as at LIRS in 2014. At the commencement of a trial, a paper note detailing the treatment history of each fish was placed in view of the relevant camera before the fish was placed into the centre of the choice arena (no mesh cylinder was used) of the flume. Unlike during the predator chemical cue trials described for LIRS 2014 and AIMS 2015, the fish were given 40 min to settle in the flumes with unmanipulated water running down both sides (that is, no predator cue) before the cue was added to one side for 20 min, before switching the predator cue to the other side for the final 20 min. *C. cyanostigma* was used to create predator chemical cues (see Supplementary Information for details). The video files were analysed using tracking software (ViewPoint, Zebralab) for subsequent analyses of activity levels (defined as seconds per minute spent swimming more than 0.5 standard lengths per second) and time spent in the side of the flume containing the predator cue. An example of a full day of flume trials can be found at https://youtu.be/iH0w7Wqztjo.

Activity levels

LIRS 2014. Eight tanks (2 × 4 arrangement) were used to monitor activity in five species (Extended Data Table 3). Each tank was 220 mm × 140 mm × 140 mm ($L \times W \times H$; water depth, 105 mm) and contained 3.2 l of flow-through water (70 ml min^{-1}, using the same header tank system as described above for LIRS 2014). Each tank was equipped with a halved piece of 50-mm diameter PVC pipe standing on its end (height 50 mm), which provided a vertical structure for the fish to use as

shelter. A video camera (Panasonic HC-V130) was positioned 1 m above the tanks to monitor fish activity at all times. At the commencement of each trial, a paper note detailing the treatment history of the fish was placed in view of the camera before introducing individual fish into each tank. The fish were then video-monitored for activity levels for 27 min. Sample sizes for 2014 swimming activity trials are included in Fig. 4 and Extended Data Table 3.

AIMS 2015. The two choice flumes described above for use at AIMS in 2015 were also used for separate assessments of the activity levels of captive-reared *A. polyacanthus* for the two acclimation treatments ($n = 28$ fish from control; $n = 38$ fish from high CO_2; fish standard length, 11.7 ± 1.6 mm (mean ± s.d.); Extended Data Table 3) in unmanipulated acclimation water (that is, no predator cue). For these trials, fish were transferred from their home tank (without air exposure) into a flume and recorded for 2 h (Microsoft LifeCam HD 5000, mounted around 45 cm above the flume).

LIRS 2016. Activity trials were conducted in the choice flumes described above for LIRS 2016; activity levels were monitored for the first 40 min of the experimental trials before releasing any chemical stimulus into either side of the flume. Five flumes were used in parallel and the flume dimensions and water velocities are described above. Additional large adult *A. polyacanthus* ($n = 9$ control, 9 high CO_2) and *D. aruanus* ($n = 6$ control, 7 high CO_2) were tested in white opaque tanks (43×32.5 cm^2, water depth, 10 cm). Sample sizes are provided in Fig. 4 and Extended Data Table 3.

Behavioural lateralization

LIRS 2014. A double-ended opaque plastic T-maze ($39 \times 29 \times 20$ cm^3, $L \times W \times H$) was constructed to perform detour tests to examine behavioural lateralization in juveniles and adults of four species (*P. amboinensis*, control $n = 21$, high CO_2 $n = 22$; *C. atripectoralis*, control $n = 26$, high CO_2 $n = 17$; *D. aruanus*, control $n = 19$, high CO_2 $n = 21$; *P. moluccensis*, control $n = 29$, high CO_2 $n = 20$). The double T-maze was a modified version of those used in experiments that have been described previously[47,48]. Individual fish were netted from their tanks and transferred immediately to the double-ended T-maze. Fish were given 1 min to settle in the central channel of the T-maze before the trial commenced. Lateralization experiments consisted of an experimenter first manoeuvring the fish to the starting point of the channel and then coaxing it down the channel with perforated plastic paddles for 10 consecutive runs. Fish had to make a decision to turn left or right each time they reached the perpendicular barrier at the end of the channel. All lateralization tests were recorded on video (using an Olympus Tough TG1 or a Panasonic Lumix DMC-FT4 camera).

AIMS 2015. A double-ended T-maze ($31 \times 11 \times 13$ cm^3, $L \times W \times H$) similar to the maze described above was constructed to perform detour tests in juvenile *A. polyacanthus*. Wild-caught fish (10–33 mm standard length; control $n = 54$; high CO_2 $n = 42$) as well as captive-reared fish from Reef HQ aquarium (8–33 mm standard length; control $n = 66$; high CO_2 $n = 62$) were used. The lateralization trials at AIMS followed the method described above for LIRS with the exception that 20 rather than 10 consecutive turns were recorded and the fish were given 2 min rather than 1 min of settling time upon entrance to the arena. In addition, the barrier at one end of the central channel was offset by 5 mm to create a situation in which the path around the barrier was shorter if the fish turned left rather than right (rationale and further details are provided in the Supplementary Information).

Statistics

General analyses. Time spent in predator cue and activity levels were quantified for each min of the behavioural trial for each fish using tracking software, which meant many repeat observations for each individual. However, three limitations prevented us from analysing the data over time. First, the effect of time was nonlinear. Second, the data were temporally auto-correlated. Third, the data were bimodal around the minimum and maximum values (see Extended Data Fig. 3 for an example) and did not conform to any distribution readily available for use in generalized additive mixed models (with the mgcv package in R). For simplicity, we took a mean across the entire trial for each fish (for choice flume and activity data; see below), which resulted in data being normally distributed and without auto-correlated repeated measurements, allowing us to use general linear models (see Supplementary Information for additional details).

Response to predator chemical cues. General linear models were used to test for the effects of CO_2 treatment (present-day versus end-of-century levels) and fish size (standard length in mm) on the percentage of time that fish spent on the side of the flume that contained the predator cue. Among the six species, there were different sample sizes, size ranges and years (or locations, for details see Supplementary Information) in which the fish were tested. Therefore, we built separate models for each species–year combination ($n = 9$ models). We used backwards model selection, beginning by including an interaction between the two fixed effects (treatment, standard length): *F*-tests were used to assess the significance of removal of model terms on the Akaike information criterion (AIC) (using the 'drop1' function in R). For model selection, α was set to 0.05. We acknowledge that these (two-tailed) tests were repeated on multiple species and multiple response variables, inflating the potential for type-I errors; however see a previous study[49]. Therefore, in our interpretations, although we refer to effects with $P < 0.05$ as 'significant', we emphasize the strength and size of effects, recognizing that *P* values have limitations[18] and represent a continuum of statistical significance. Model assumptions were assessed with *q*–*q* plots of residuals and by plotting residuals against fitted values and against each of our predictor variables[50].

Bootstrapping. Most previous studies have used more rapid assessments of cue preferences than in the present study, in which 4 min of measurements have been taken during 9–11 min trials (typically a 2-min post-handling settling period, 2 min measurement, 3 min for side switch and post-switch settling, 2 min measurement)[4,5,9,16,25,27,32]. For direct comparisons with these studies in our bootstrapping simulations (see Supplementary Information), we averaged 2 min of data after a 2-min post-handling settling period and 2 min of data 3 min after the cue side switch (2014 and 2015), or we averaged 2 min of data 2 min after the predator cue was first introduced to the choice flume and 2 min of data 3 min after the cue side switch (2016). The bootstrapping results are presented in Fig. 3, with comparisons to seven papers[4, 5, 9, 16, 25, 27, 32]. Note that another study[31]—which is also included in Fig. 3—is included for comparative purposes. The extremely high variance in one paper[25] (Fig. 3f) was caused by an exceedingly high proportion of control individuals reported to have spent 0% of their time in the conspecific chemical alarm cue (grey solid bars in Extended Data Fig. 4a) and an equally high proportion of high CO_2 individuals reported to have spent 100% of their time in the cue (blue solid bars in Extended Data Fig. 4b). Additionally, control and high CO_2 data were pooled to calculate the associated variance around the group means for each of the sample size scenarios (Fig. 3d–f), similar to a previously published method[51]. For additional details on the bootstrapping, see Supplementary Information.

Activity levels. Time spent active (s) was calculated on a minute-by-minute basis (to give s min^{-1}). However, data were analysed as one value (mean of the trial for each fish) per individual, using the same general linear modelling procedures outlined above for 'Response to predator chemical cues'. See Supplementary Information for further details.

Behavioural lateralization. Data collected from each location and year were analysed separately owing to the differences in time of year, species used and exposure duration. Testing for lateralization is not straightforward because it involves multiple binomial experiments with structure; a description of issues with the statistical approaches used by previous studies to assess lateralization can be found elsewhere[52]. A test for detecting lateralization at the population level requires examining the mean lateralization score across all individuals in the sample as population-level lateralization is present when a group of individuals collectively exhibits a side bias. By contrast, a test for detecting individual-level lateralization requires examining the sample variance as individual-level lateralization is present when more individuals exhibit a side bias than expected by chance (irrespective of whether it is to the left or to the right). Explanations and examples of these two concepts have been published previously[48,53,54]. We tested population-level lateralization with a generalized linear mixed model (with glmer function in R) that sets the intercept equal to the grand mean of the data[52]. We tested individual-level lateralization with a χ^2 test comparing the observed variance (numerator) to the expected variance (denominator) assuming a normal approximation to the binomial distribution[52]. This is analogous to testing for overdispersion (that is, are there more observations in the tail ends of the distribution than expected by chance). See Supplementary Information for further details.

Reporting summary

Further information on research design is available in the Nature Research Reporting Summary linked to this paper.

Data availability

The data necessary to reproduce figures and results in this study are publicly archived in Figshare following best-practice guidelines[55], and were made available to editors and reviewers at the time of submission: https://doi.org/10.6084/m9.figshare.7871522. We place no restrictions on data availability.

Code availability

Scripts for statistical analyses are available from Figshare (https://doi.org/10.6084/m9.figshare.7871522). We place no restrictions on code availability.

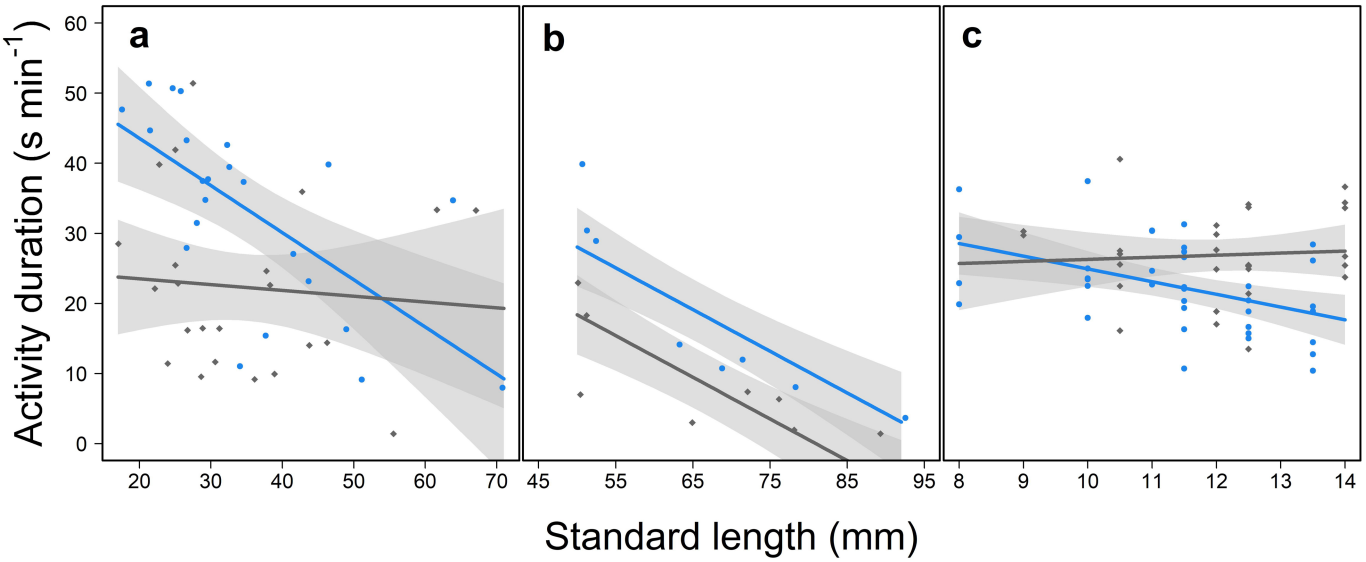
33. Riebesell, U., Fabry, V. J., Hansson, L. & Gattuso, J.-P. *Guide to Best Practices for Ocean Acidification Research and Data Reporting* (Publications Office of the European Union Luxembourg, 2010).
34. Moran, D. The importance of accurate CO_2 dosing and measurement in ocean acidification studies. *J. Exp. Biol.* **217**, 1827–1828 (2014).
35. Cornwall, C. E. & Hurd, C. L. Experimental design in ocean acidification research: problems and solutions. *ICES J. Mar. Sci.* **73**, 572–581 (2016).
36. Dickson, A. G. Standard potential of the reaction: $AgCl(s) + 1_2H_2(g) = Ag(s) + HCl(aq)$, and the standard acidity constant of the ion HSO_4^- in synthetic sea water from 273.15 to 318.15 K. *J. Chem. Thermodyn.* **22**, 113–127 (1990).
37. Lueker, T. J., Dickson, A. G. & Keeling, C. D. Ocean pCO_2 calculated from dissolved inorganic carbon, alkalinity, and equations for K_1 and K_2: validation based on laboratory measurements of CO_2 in gas and seawater at equilibrium. *Mar. Chem.* **70**, 105–119 (2000).
38. Jutfelt, F., Bresolin de Souza, K., Vuylsteke, A. & Sturve, J. Behavioural disturbances in a temperate fish exposed to sustained high-CO_2 levels. *PLoS One* **8**, e65825 (2013).
39. Ishimatsu, A., Hayashi, M. & Kikkawa, T. Fishes in high-CO_2, acidified oceans. *Mar. Ecol. Prog. Ser.* **373**, 295–302 (2008).
40. Ou, M. et al. Responses of pink salmon to CO_2-induced aquatic acidification. *Nat. Clim. Change* **5**, 950–955 (2015).
41. Munday, P. L. et al. Selective mortality associated with variation in CO_2 tolerance in a marine fish. *Ocean Acidif.* **1**, 1–5 (2012).
42. Green, L. & Jutfelt, F. Elevated carbon dioxide alters the plasma composition and behaviour of a shark. *Biol. Lett.* **10**, 20140538 (2014).
43. Sundin, J. et al. Long-term exposure to elevated carbon dioxide does not alter activity levels of a coral reef fish in response to predator chemical cues. *Behav. Ecol. Sociobiol.* **71**, 108 (2017).
44. Doherty, P. J. Light-traps: selective but useful devices for quantifying the distributions and abundances of larval fishes. *Bull. Mar. Sci.* **41**, 423–431 (1987).
45. Jutfelt, F., Sundin, J., Raby, G. D., Krang, A.-S. & Clark, T. D. Two-current choice flumes for testing avoidance and preference in aquatic animals. *Methods Ecol. Evol.* **8**, 379–390 (2017).
46. Atema, J., Kingsford, M. J. & Gerlach, G. Larval reef fish could use odour for detection, retention and orientation to reefs. *Mar. Ecol. Prog. Ser.* **241**, 151–160 (2002).
47. Bisazza, A., Facchin, L., Pignatti, R. & Vallortigara, G. Lateralization of detour behaviour in poeciliid fish: the effect of species, gender and sexual motivation. *Behav. Brain Res.* **91**, 157–164 (1998).
48. Bisazza, A., Pignatti, R. & Vallortigara, G. Detour tests reveal task- and stimulus-specific behavioral lateralization in mosquitofish (*Gambusia holbrooki*). *Behav. Brain Res.* **89**, 237–242 (1997).
49. Nakagawa, S. A farewell to Bonferroni: the problems of low statistical power and publication bias. *Behav. Ecol.* **15**, 1044–1045 (2004).
50. Zuur, A. F., Ieno, E. N., Walker, N. J., Saveliev, A. A. & Smith, G. M. *Mixed Effects Models and Extensions in Ecology with R* (Springer, 2009).
51. Simonsohn, U. Just post it: the lesson from two cases of fabricated data detected by statistics alone. Psychol. *Sci.* **24**, 1875–1888 (2013).
52. Roche, D. et al. Replication alert: behavioural lateralisation in a detour test is not repeatable in fishes. Preprint at *EcoEvoRxiv* https://doi.org/10.32942/osf.io/6kcwa (2019).
53. Domenici, P., Allan, B., McCormick, M. I. & Munday, P. L. Elevated carbon dioxide affects behavioural lateralization in a coral reef fish. *Biol. Lett.* **8**, 78–81 (2012).
54. Roche, D. G., Binning, S. A., Strong, L. E., Davies, J. N. & Jennions, M. D. Increased behavioural lateralization in parasitized coral reef fish. *Behav. Ecol. Sociobiol.* **67**, 1339–1344 (2013).
55. Roche, D. G., Kruuk, L. E. B., Lanfear, R. & Binning, S. A. Public data archiving in ecology and evolution: how well are we doing? *PLoS Biol.* **13**, e1002295 (2015).
56. Clark, T. D., Roche, D. G., Binning, S. A., Speers-Roesch, B. & Sundin, J. Maximum thermal limits of coral reef damselfishes are size dependent and resilient to near-future ocean acidification. *J. Exp. Biol.* **220**, 3519–3526 (2017).

Acknowledgements T.D.C. was funded by a Future Fellowship Grant (FT180100154) from the Australian Research Council. J.S. was funded by a Mobility Grant from the Swedish Research Council Formas (2013-947). G.D.R. was funded by a Postdoctoral Fellowship from the Natural Sciences and Engineering Research Council of Canada (NSERC). S.A.B. and B.S.-R. were funded by Discovery Grants from NSERC. B.S.-R. was also funded by a Harrison McCain Young Scholars Award. F.J. was funded by Formas (2009-596), the Swedish Research Council VR (621-2012-4679) and the Research Council of Norway (262942). Additional funding was obtained from the Society for Experimental Biology and Company of Biologists Travel Grants (J.S., JEBTF-150422), Magnus Bergvalls Stiftelse (J.S., 2014-00620), Australian Endeavor Research Fellowship (G.D.R.), IRIS stipendiet (J.S., 2015-0264), Stiftelsen Lars Hiertas Minne (J.S., FO2014-0659), the Wenner-Gren Foundation (J.S.), Wallenbergstiftelsen (J.S.), Inez Johanssons stiftelse (J.S.) and Sederholms utrikes stiftelse (J.S.). We thank N. Sopinka and A. Yu for assistance with behavioural lateralization trials in 2015, S. Noonan for analysing water samples for total alkalinity, R. Streit for assistance with some experiments in 2014, A. Severati and C. Schlott for wild fish collections in 2015, K. Stark for assistance with the R script for bootstrapping simulations, and V. Messmer, A. Hoey and A. Tobin for assisting with the collection of fishes for the 2014 experiments. Thanks to the SeaSim staff at AIMS for logistical support.

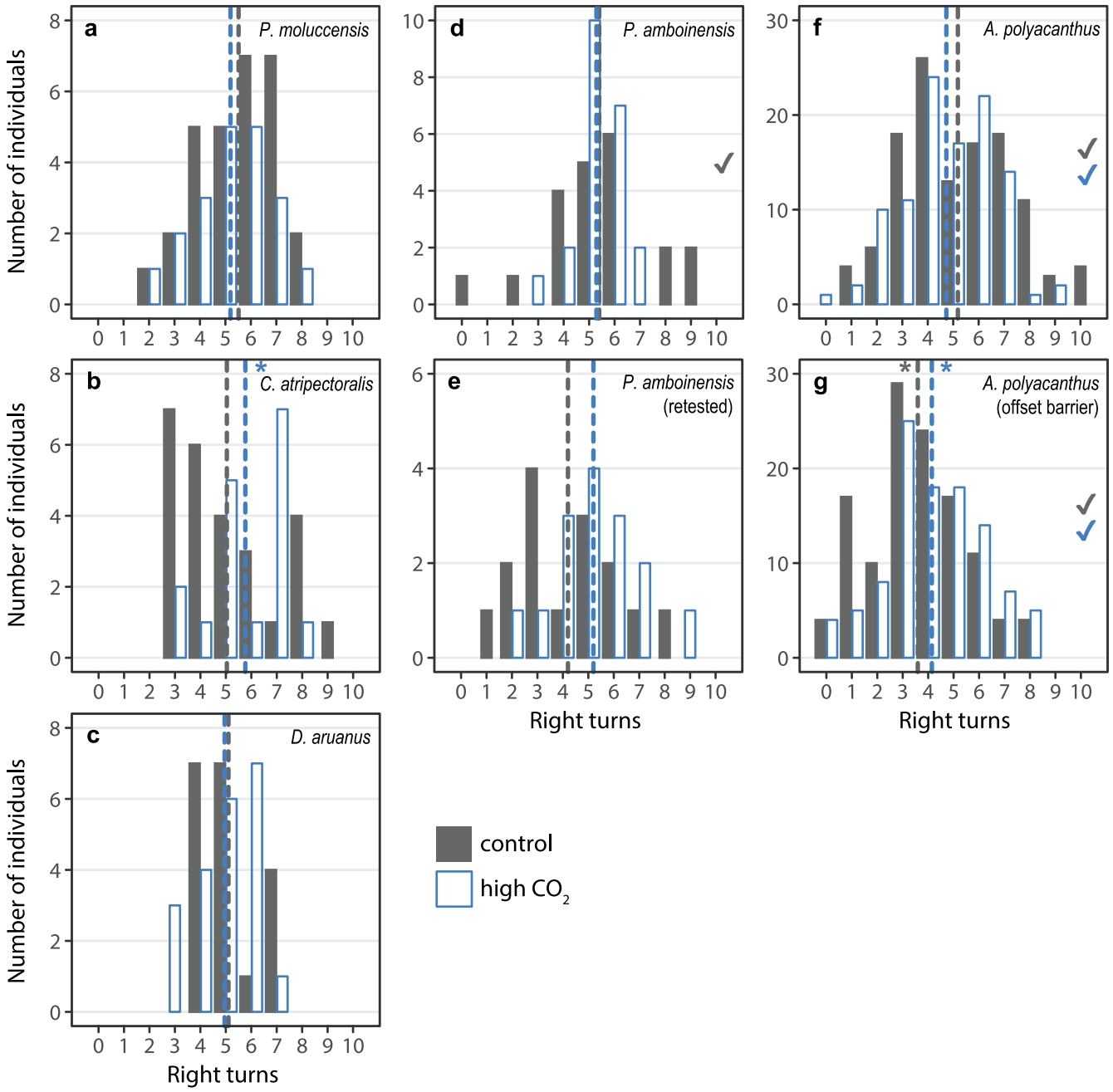
Author contributions All authors contributed to the design and execution of behavioural experiments; T.D.C. drafted the manuscript and Supplementary Information with assistance from all authors; T.D.C. and J.S. managed and prepared the raw data with assistance from co-authors; G.D.R., D.G.R. and T.D.C. conducted the statistical analyses and created the figures. J.S. managed the revisions with assistance from all co-authors.

Competing interests The authors declare no competing interests.

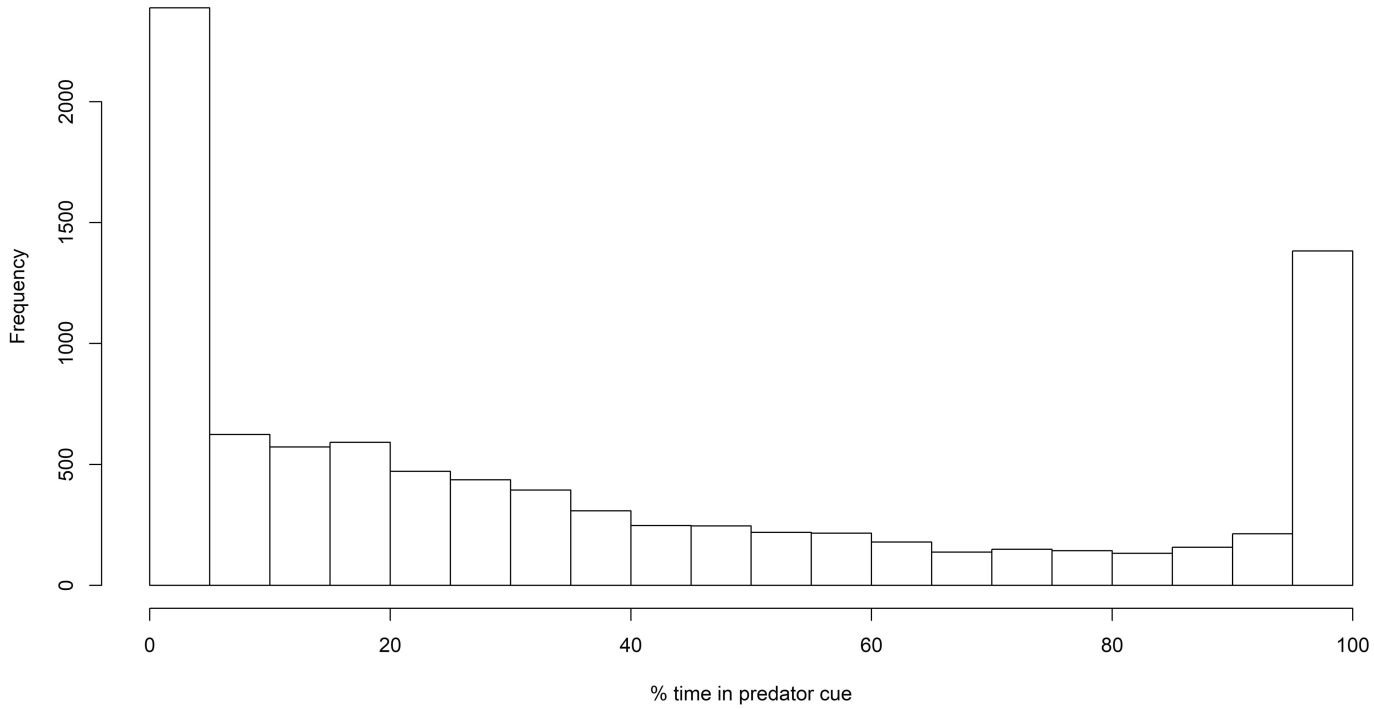
Additional information
Supplementary information is available for this paper at https://doi.org/10.1038/s41586-019-1903-y.
Correspondence and requests for materials should be addressed to T.D.C. or J.S.
Peer review information *Nature* thanks David Bierbach and the other, anonymous, reviewer(s) for their contribution to the peer review of this work.
Reprints and permissions information is available at http://www.nature.com/reprints.



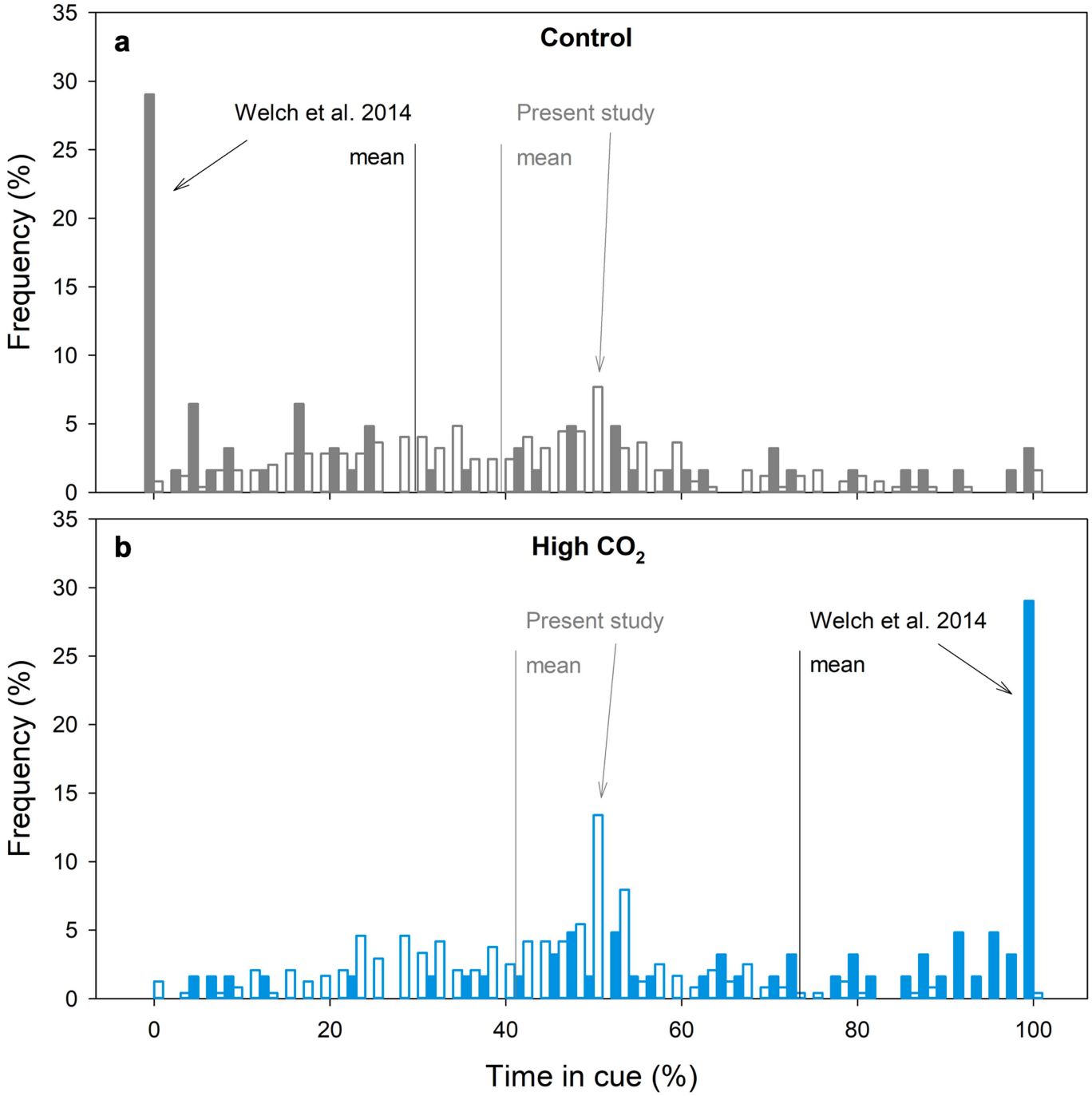
Extended Data Fig. 1 | Interactions between CO_2 treatment and size for fish activity. a–**c**, Raw data points and fitted model estimates for activity in *D. aruanus* in 2014 (**a**), *A. polyacanthus* in 2014 (**b**) and *A. polyacanthus* in 2015 (**c**) as a function of acclimation treatment (grey diamonds, control; blue circles, high CO_2) and size (*x* axis), with shaded areas indicating 95% confidence intervals of model estimates. Model parameter estimates are included in Extended Data Table 3. **a**, $n = 23$ per treatment. **b**, $n = 8$ per treatment. **c**, Control, $n = 28$; CO_2, $n = 38$. Sample sizes represent biologically independent animals.



Extended Data Fig. 2 | Widespread resilience of behavioural lateralization in coral reef damselfishes when faced with end-of-century levels of CO_2. **a**–**g**, Number of right turns (out of 10) under control (closed grey bars) and high CO_2 (open blue bars) conditions for fishes facing either a centred barrier at one end of the T-maze (**a**–**f**) or an offset barrier at the other end of the T-maze (**g**). Sample sizes represent biologically independent animals). **a**, *P. moluccensis*. Control, $n = 29$; CO_2, $n = 20$. **b**, *C. atripectoralis*. Control, $n = 26$; CO_2, $n = 17$. **c**, *D. aruanus*. Control, $n = 19$; CO_2, $n = 21$. **d**, *P. amboinensis*. Control, $n = 21$; CO_2, $n = 22$. **e**, *P. amboinensis* retested. Control, $n = 15$; CO_2, $n = 15$. **f**, *A. polyacanthus*. Control, $n = 120$; CO_2, $n = 104$. **g**, *A. polyacanthus* (same sample sizes as in **f**). **a**–**e**, Data were obtained at the LIRS in 2014. **f**, **g**, Data were obtained at the AIMS in 2015. Dashed lines represent the mean number of right turns for each treatment group. A tick mark on the panel (coloured according to treatment) indicates significant individual-level lateralization, whereas an asterisk at the top of the panel indicates significant population-level lateralization. See Extended Data Tables 4, 5 for statistics.



Extended Data Fig. 3 | Histogram of the percentage of time in predator cue data for fish used in choice flume trials at LIRS in 2016. Each data point included in this summary represents analysis of one minute of behavioural data for a fish; the plot contains many repeated measurements for each fish.



Extended Data Fig. 4 | Histogram of representative data for percentage of time spent in water containing predator cue or conspecific alarm cue. Histograms of representative data (4-min means) from a previous study[25] (solid bars) showing the disproportionate number of fish that were reported to spend 0% of time in conspecific chemical alarm cue when acclimated to control water (**a**) or 100% of time in the cue when acclimated to water with elevated CO_2 levels (**b**). The representative treatment groups[25] are juvenile *A. polyacanthus* in control water from parents acclimated to high CO_2 water (**a**, $n = 62$) and juvenile *A. polyacanthus* in high CO_2 water from parents acclimated to high CO_2 water (**b**, $n = 62$). Also presented are data (4-min means) from the present study (6 species, open bars; $n = 247$ control, $n = 239$ high CO_2) showing peak frequencies around 50% of time in predator cue for both control (**a**) and high-CO_2-exposed (**b**) fish. Sample sizes represent biologically independent animals. Mean values for each of the datasets are indicated with vertical lines, and arrows are directed at modal values in each of the datasets.

Extended Data Table 1 | Water chemistry data for the two sites for the three years of the study

Location/year	Treatment	pCO_2 (µatm)	pCO_2 *n*	Temperature (°C)	Temperature *n*	Alkalinity (µmol kg^{-1})	Alkalinity *n*	pH_{total} (calc.)
LIRS 2014	Control	406 (21)	19	23.1 (0.9)	2,048	2,292 (2.9)	10	8.04
	High CO_2	945 (117)	66	23.1 (0.9)	2,048	2,298 (4.7)	10	7.72
AIMS 2015	Control	428 (13)	1,907	25.8 (1.0)	5,747	2,356 (5.8)	5	8.03
	High CO_2	1,021 (156)	11,537	25.8 (1.0)	3,831	2,355 (5.5)	5	7.70
LIRS 2016	Control	521 (93)	8	29.4 (0.8)	147	-	-	-
	High CO_2	1,089 (326)	234	29.6 (0.8)	388	-	-	-

Data were obtained from the LIRS and AIMS between 2014 and 2016. p_{CO_2} was measured every 1–4 days, temperature was logged using iButton data-loggers (1 sample per 30 min), and alkalinity was measured from 10 samples at LIRS in 2014 and from five samples at AIMS in 2015. Data are presented as mean ± s.d. Sample sizes are included in the table. Some of the data for AIMS (2015)[15,43] and LIRS (2016)[56] have previously been published previously.

Extended Data Table 2 | Model predictions of time spent in predator chemical cue

Parameter name	Parameter estimate (± SE)	*t*	*P*
Humbug, *D. aruanus* (2014)			
n = 38, model R^2 = 0.03			
Model intercept	32.36 ± 3.59	9.02	<.001
Acclimation (CO_2)	5.67 ± 4.94	1.14	0.26
Humbug, *D. aruanus* (2016)			
n = 83, model R^2 = 0.13			
Model intercept	11.95 ± 4.07	2.93	0.004
Acclimation (CO_2)	4.23 ± 2.47	1.71	0.09
SL (mm)	0.44 ± 0.13	3.47	**<.001**
Spiny chromis, *A. polyacanthus* (2015)			
n = 100, model R^2 = 0.19			
Model intercept	38.57 ± 2.29	16.87	<.001
Acclimation (CO_2)	15.69 ± 3.23	4.85	**<.001**
Spiny chromis, *A. polyacanthus* (2016)			
n = 94, model R^2 = -0.01			
Model intercept	43.58 ± 1.93	22.56	<.001
Acclimation (CO_2)	-0.54 ± 2.96	-0.18	0.86
Ambon damsel, *P. amboinensis* (2014)			
n = 38, model R^2 = -0.02			
Model intercept	31.47 ± 3.51	8.98	<.001
Acclimation (CO_2)	1.95 ± 4.51	0.43	0.67
White damsel, *D. perspicillatus* (2016)			
n = 119, model R^2 = 0.04			
Model intercept	39.83 ± 1.73	22.98	<.001
Acclimation (CO_2)	2.26 ± 2.16	1.05	0.30
Size class (large)	-5.19 ± 2.19	-2.37	**0.02**
Lemon damsel, *P. moluccensis* (2014)			
n = 48, model R^2 = 0.01			
Model intercept	27.05 ± 3.04	8.90	<.001
Acclimation (CO_2)	5.50 ± 4.39	1.25	0.22
Black-axil chromis, *C. atripectoralis* (2014)			
n = 40, model R^2 = -0.03			
Model intercept	30.58 ± 4.99	6.13	<.001
Acclimation (CO_2)	-0.03 ± 6.31	-0.005	0.996

Parameters (± standard error) and their statistical significance for general linear models that predict the mean percentage of time spent on the side of the choice flume containing the predator chemical cue for an individual fish for six species of coral reef fishes tested in this study. We used backwards model selection using *F*-tests to compare the AIC of models with and without each predictor variable using the 'drop1' function in R. Only the parameter estimates for the final (best) models are given, although we always kept the main effect of acclimation treatment (that is, the effect of acclimation to elevated CO_2) in place because it was the key variable of interest. Note that for the *D. perspicillatus* model, the baseline factor level for size class was 'early-stage juveniles' (<15 mm standard length). Sample sizes represent biologically independent animals. Statistical significance is indicated in bold (α = 0.05).

Extended Data Table 3 | Model predictions of mean activity levels

Parameter name	Parameter estimate (± SE)	*t*	*P*
D. aruanus (2014), *n* = 46, model R^2 = 0.31			
Model intercept	25.19 ± 7.05	3.57	<.001
Acclimation (CO_2)	31.83 ± 9.91	3.21	**0.003**
SL (mm)	-0.08 ± 0.19	-0.44	0.66
CO_2 × SL (mm)	-0.59 ± 0.26	-2.23	**0.03**
D. aruanus (2016), *n* = 94, model R^2 = 0.00			
Model intercept	41.14 ± 1.37	30.78	<.001
Acclimation (CO_2)	0.96 ± 1.96	0.49	0.63
A. polyacanthus (2014), *n* = 16, model R^2 = 0.71			
Model intercept	48.11 ± 7.81	6.16	<.001
Acclimation (CO_2)	9.66 ± 3.12	3.10	**0.009**
SL (mm)	-0.59 ± 0.11	-5.28	**<.001**
A. polyacanthus (2015), *n* = 66, model R^2 = 0.19			
Model intercept	23.33 ± 9.60	2.43	0.01
Acclimation (CO_2)	19.76 ± 11.81	1.67	0.10
SL (mm)	0.30 ± 0.79	0.38	0.71
CO_2 × SL (mm)	-2.11 ± 0.99	-2.13	**0.04**
A. polyacanthus (2016), *n* = 112, model R^2 = 0.34			
Model intercept	38.24 ± 1.53	24.98	<.001
Acclimation (CO_2)	0.34 ± 1.77	0.19	0.85
SL (mm)	-0.32 ± 0.04	-7.64	**<.001**
P. amboinensis (2014), *n* = 43, model R^2 = -0.02			
Model intercept	17.34 ± 2.58	6.71	<.001
Acclimation (CO_2)	1.05 ± 3.61	0.29	0.77
D. perspicillatus (2016), *n* = 122, model R^2 = 0.21			
Model intercept	35.47 ± 1.96	18.10	<.001
Acclimation (CO_2)	-1.93 ± 1.69	-1.15	0.25
SL (mm)	-0.64 ± 0.11	-5.71	**<.001**
P. moluccensis (2014), *n* = 49, model R^2 = 0.05			
Model intercept	19.80 ± 2.15	9.21	<.001
Acclimation (CO_2)	6.44 ± 3.45	1.81	0.08
C. atripectoralis (2014), *n* = 34, model R^2 = -0.03			
Model intercept	26.10 ± 2.22	11.77	<.001
Acclimation (CO_2)	-1.32 ± 3.46	-0.38	0.71

Parameters and their statistical significance for general linear models that predict the individual mean activity levels (swimming (s min^{-1})) for six species of coral reef fishes tested in this study. We used backwards model selection using *F*-tests to compare the AIC of models with and without each predictor variable using the 'drop1' function in R. Only the parameter estimates for the final (best) models are given, although we always kept the main effect of acclimation treatment in place because it was the key variable of interest. Sample sizes represent biologically independent animals. Statistical significance is indicated in bold (α = 0.05).

Extended Data Table 4 | Individual- and population-level lateralization of coral reef fishes

Treatment	Species	*n*	ind χ^2	ind *P*	$\bar{X}$	pop *z*	pop *P*
Control	*P. amboinensis*	21	36.38	**0.014**	5.38	0.83	0.404
	C. atripectoralis	26	37.18	0.055	5.04	0.11	0.912
	D. aruanus	19	9.52	0.947	5.11	0.29	0.772
	P. moluccensis	29	26.89	0.524	5.52	1.76	0.079
	P. amboinensis (retest)	15	22.56	0.068	4.20	-1.59	0.112
High CO_2	*P. amboinensis*	22	7.51	0.997	5.31	0.943	0.346
	C. atripectoralis	17	14.82	0.538	5.76	1.99	**0.047**
	D. aruanus	21	10.78	0.952	4.95	-0.138	0.890
	P. moluccensis	20	18.08	0.517	5.20	0.566	0.572
	P. amboinensis (retest)	15	16.96	0.258	5.20	0.463	0.644

Individual- and population-level lateralization was tested for four species of coral reef fishes (*P. amboinensis*, *C. atripectoralis*, *D. aruanus* and *P. moluccensis*) in a detour test (LIRS 2014) under control (around 400 µatm CO_2) and high CO_2 (about 1,000 µatm) conditions. The sample size (*n*) and mean number of right turns ($\bar{X}$) out of a total of 10 turns is indicated for each species and treatment group (sample sizes represent biologically independent animals). χ^2 statistics (ind χ^2) and *P* values (ind *P*) are presented for tests of individual-level lateralization. *z* values (pop *z*) and *P* values (pop *P*) are presented for tests of population-level lateralization. $P < 0.05$ indicates lateralization. 'retest' indicates a subset of individuals that underwent a second trial in an effort to validate the findings from their first trial. Statistical significance is indicated in bold ($\alpha = 0.05$).

Extended Data Table 5 | Individual- and population-level lateralization of wild and captive-reared *A. polyacanthus*

Treatment	Species	*n*	ind χ^2	ind *P*	$\bar{X}$	pop *z*	pop *P*
Control	*A. polyacanthus* (cantered end)	120	219.18	**6.28E-08**	5.18	0.974	0.33
	A. polyacanthus (offset end)	120	170.79	**0.001**	3.59	-7.76	**8.24E-15**
High CO_2	*A. polyacanthus (cantered end)*	104	130.58	**0.034**	4.73	-1.56	0.119
	A. polyacanthus (offset end)	104	152.33	**0.001**	4.14	-4.51	**6.56E-06**

The individual- and population-level lateralization of wild (n = 96) and captive-reared (n = 128) *A. polyacanthus* (mean ± s.d. standard length, 20 ± 7 mm) was tested in a detour test (AIMS 2015) under control (around 400 µatm CO_2; n = 54 wild, n = 66 captive-reared) and high CO_2 (about 1,000 µatm; n = 42 wild, n = 62 captive-reared) conditions. 'offset end' indicates the end of the lateralization arena where the barrier was offset by 5 mm to create a situation in which the path around the barrier was shorter if the fish turned left rather than right. The sample size (n) and mean number of right turns ($\bar{X}$) out of a total of 10 turns (per arena end) is indicated for each treatment group (sample sizes represent biologically independent animals). χ^2 statistics (ind χ^2) and *P* values (ind *P*) are presented for tests of individual-level lateralization. *z* values (pop *z*) and *P* values (pop *P*) are presented for tests of population-level lateralization. $P < 0.05$ indicates lateralization. Statistical significance is indicated in bold (α = 0.05).

nature research

Corresponding author(s): Timothy Clark and Josefin Sundin

Last updated by author(s): Oct 6, 2019

Reporting Summary

Nature Research wishes to improve the reproducibility of the work that we publish. This form provides structure for consistency and transparency in reporting. For further information on Nature Research policies, see Authors & Referees and the Editorial Policy Checklist.

Statistics

For all statistical analyses, confirm that the following items are present in the figure legend, table legend, main text, or Methods section.

n/a	Confirmed	
☐	☒	The exact sample size (*n*) for each experimental group/condition, given as a discrete number and unit of measurement
☐	☒	A statement on whether measurements were taken from distinct samples or whether the same sample was measured repeatedly
☐	☒	The statistical test(s) used AND whether they are one- or two-sided *Only common tests should be described solely by name; describe more complex techniques in the Methods section.*
☐	☒	A description of all covariates tested
☐	☒	A description of any assumptions or corrections, such as tests of normality and adjustment for multiple comparisons
☐	☒	A full description of the statistical parameters including central tendency (e.g. means) or other basic estimates (e.g. regression coefficient) AND variation (e.g. standard deviation) or associated estimates of uncertainty (e.g. confidence intervals)
☐	☒	For null hypothesis testing, the test statistic (e.g. *F*, *t*, *r*) with confidence intervals, effect sizes, degrees of freedom and *P* value noted *Give P values as exact values whenever suitable.*
☒	☐	For Bayesian analysis, information on the choice of priors and Markov chain Monte Carlo settings
☒	☐	For hierarchical and complex designs, identification of the appropriate level for tests and full reporting of outcomes
☒	☐	Estimates of effect sizes (e.g. Cohen's *d*, Pearson's *r*), indicating how they were calculated

Our web collection on statistics for biologists contains articles on many of the points above.

Software and code

Policy information about availability of computer code

Data collection	To extract fish behavioural data from videos we recorded of fish in behavioural arenas, we used the commercial software ViewPoint (version 3, 20, 5, 83) (details given in the Supplementary Information).
Data analysis	For data analyses, we used a combination of Microsoft Excel (for organizing and summarizing outputs from the ViewPoint video tracking software) and R (versions 3.5.0 and 3.5.2, for doing statistical analyses and making most of the figures). Within R, we specifically used glmer which is a function of the analysis package lme4 (version 1.1-20). For data exploration we used mgcv (version 1.8-26). Further details are given in the statistical analyses section of the Methods and Supplementary Information.

For manuscripts utilizing custom algorithms or software that are central to the research but not yet described in published literature, software must be made available to editors/reviewers. We strongly encourage code deposition in a community repository (e.g. GitHub). See the Nature Research guidelines for submitting code & software for further information.

Data

Policy information about availability of data

All manuscripts must include a data availability statement. This statement should provide the following information, where applicable:

- Accession codes, unique identifiers, or web links for publicly available datasets
- A list of figures that have associated raw data
- A description of any restrictions on data availability

The data necessary to reproduce figures and results in this study are publicly archived in the repository figshare and were made available to editors and reviewers at the time of submission: https://figshare.com/s/99f6b8973bfd0bb234e8. We place no restrictions on data availability.

Field-specific reporting

Please select the one below that is the best fit for your research. If you are not sure, read the appropriate sections before making your selection.

☐ Life sciences ☐ Behavioural & social sciences ☒ Ecological, evolutionary & environmental sciences

For a reference copy of the document with all sections, see nature.com/documents/nr-reporting-summary-flat.pdf

Ecological, evolutionary & environmental sciences study design

All studies must disclose on these points even when the disclosure is negative.

Study description	We tested the effect of elevated CO2 on predator cue avoidance, swimming activity and behavioural lateralisation. Experiments were conducted across three years (August-September 2014, April-July 2015, January 2016), at two locations, and on a total of >900 individuals from six species. Predator cue avoidance and activity trials were conducted at the Lizard Island Research Station (LIRS) in 2014 and 2016, and at the Australian Institute of Marine Science (AIMS) in Townsville in 2015. Behavioural lateralisation trials were conducted at LIRS in 2014 and at AIMS in 2015. We used General Linear Models to test for the effect of elevated CO2 on predator cue avoidance. We built separate models for each species × year combination due to the many differences between years. Fish size was included as a fixed effect. Swimming activity was analysed using the same general linear modelling procedures as for predator cue avoidance. Population-level lateralisation was analysed with a generalized linear random-effects model, and individual-level lateralisation was analysed with a chi-square test comparing the observed variance (numerator) to the expected variance (denominator) assuming a normal approximation to the binomial distribution. All statistical procedures are described in detail in the Methods section and in the Supplementary Information.
Research sample	We used six species of coral reef fish (humbug dascyllus Dascyllus aruanus, ambon damsel Pomacentrus amboinensis, lemon damsel Pomacentrus moluccensis, black-axil chromis Chromis atripectoralis, spiny chromis Acanthochromis polyacanthus, white damsel Dischistodus perspicillatus) and two species of predators (bluespotted rock cod Cephalopholis cyanostigma and flagtail grouper Cephalopholis urodeta). Species were selected based on previously used coral reef fishes (for direct replication) and two species not previously used in ocean acidification research (for conceptual replication). Fish were collected from the wild at Lizard Island, obtained from a public aquarium (Reef HQ Aquarium, Townsville) and obtained from the northern Great Barrier Reef (by Cairns Marine Pty Ltd). Fish were juveniles, sub-adults and adults. No fish were sexed. Fish were exposed to CO2, no additional manipulations were applied.
Sampling strategy	Sample sizes were based on previous studies and fish availability. Previous studies have typically used 10 fish or less per treatment group, which formed the lowest sample size used in this study. When possible, we used a higher sample size (e.g., n = 50) to increase statistical power but without depleting any wild fish populations.
Data collection	For predator cue avoidance and activity, trials were video recorded and analysed using tracking software. Data from lateralisation trials was collected manually in real-time (video recorded at LIRS in 2014, data collected by JS, for AIMS 2015, data was collected by GDR, NS and AY).
Timing and spatial scale	Timing: For LIRS 2014, data was collected in August and September (Aug 30-Sept 10, data was collected every day). For AIMS 2015, predator cue avoidance trials were conducted on May 21, 22, 27, and 27; activity trials were conducted on May 24, 26, 29, 30, 31, and June 1 and 2-9; behavioural lateralization trials were done on April 15-17, April 23, 27, 28, and May 17, 19, 23, and 24. Temporal gaps in data collection at AIMS was related to logistical factors, including days off, and availability of experimental equipment and personnel. For LIRS 2016, data was collected in January (16-31, data collection every day except for Jan 24 which was a day off). Rationale for data collection was to perform the maximum number of experiments per day after the fish had been exposed to CO2 for an adequate amount of time. Spatial scale: For LIRS 2014 and 2016, the experiments were performed at the Lizard Island Research Station, Great Barrier Reef, Australia. The fish were collected from around Lizard Island at the northern end of the Great Barrier Reef, Australia (14°40' S; 145° 28' E). For AIMS 2015, the experiments were performed at the Australian Institute of Marine Science, Townsville, Australia. Fish were obtained from the Reef HQ Aquarium in Townsville. Additionally, groups of wild fish were collected at Davies Reef (18.8238° S, 147.6429° E) Great Barrier Reef, Australia (in April 2015) and transported to AIMS.
Data exclusions	Data where excluded in instances where the automated tracking software we used failed, causing erroneous tracks of animal movement.
Reproducibility	Activity and predator cue avoidance was replicated across three years. Lateralisation was replicated across two years.
Randomization	Fish were placed in the two treatment groups (control and elevated CO2) at random. Other aspects of water chemistry (i.e., the water supply used and the temperature it was kept at), lighting, and feeding were kept constant among replicate tanks across the two acclimation treatments.
Blinding	Complete blinding was not possible since the CO2 dosing system was visible (both visually and auditory) to any observer physically present for the experiments, making it obvious which replicate tanks contained the elevated CO2 treatment. However, all activity and predator cue avoidance experiments were video recorded and analysed using automated tracking software rather than being manually scored by a human observer.

Did the study involve field work? ☐ Yes ☒ No

Reporting for specific materials, systems and methods

We require information from authors about some types of materials, experimental systems and methods used in many studies. Here, indicate whether each material, system or method listed is relevant to your study. If you are not sure if a list item applies to your research, read the appropriate section before selecting a response.

Materials & experimental systems

n/a	Involved in the study
☒	☐ Antibodies
☒	☐ Eukaryotic cell lines
☒	☐ Palaeontology
☐	☒ Animals and other organisms
☒	☐ Human research participants
☒	☐ Clinical data

Methods

n/a	Involved in the study
☒	☐ ChIP-seq
☒	☐ Flow cytometry
☒	☐ MRI-based neuroimaging

Animals and other organisms

Policy information about studies involving animals; ARRIVE guidelines recommended for reporting animal research

Laboratory animals	The study did not involve laboratory animals
Wild animals	Lizard Island Research Station 2014 Sub-adult and adult wild fishes were collected in August 2014 from around Lizard Island at the northern end of the Great Barrier Reef, Australia (14°40′ S; 145° 28′ E), on SCUBA using hand- and/or barrier-nets and spray bottles of clove oil anaesthetic (mixed 1:4 with ethanol). Five species of damselfishes were collected: humbug dascyllus (Dascyllus aruanus), ambon damsel (Pomacentrus amboinensis), lemon damsel (Pomacentrus moluccensis), black-axil chromis (Chromis atripectoralis), and spiny chromis (Acanthochromis polyacanthus). Predatory bluespotted rock cod (Cephalopholis cyanostigma) were collected using hook and line. Fish were not sexed. All fish were transported in aerated seawater to LIRS. At the end of the experiments, fish were released at the site of capture. Australian Institute of Marine Science 2015 A. polyacanthus juveniles (~10-15 days post-hatching) were corralled into clear containers by SCUBA divers from four distinct schools (four breeding pairs) at depths of 8-10 m at Davies Reef (18.8238° S, 147.6429° E), Lizard Island, in April 2015. Fish were transported in aerated seawater to AIMS. Fish were not sexed. All fish were euthanized with an overdose of tricaine methanesulfonate (MS-222, ca. 500 mg L-1) at the end of the experiments, or at intermittent times through experiments when they were sacrificed to take precise length and weight measurements for another study (Sundin et al., 2019). Lizard Island Research Station 2016 Wild fishes were collected in January 2016 from around Lizard Island, as detailed above for LIRS 2014. Adult predatory bluespotted rock cod (C. cyanostigma) were caught using hook-and-line, and three damselfish species were caught using clove oil spray and hand- or barrier-nets (subadult and adult humbug dascyllus [D. aruanus]; juvenile, subadult and adult spiny chromis [A. polyacanthus]; subadult and adult white damsel [Dischistodus perspicillatus]). Additionally, larval white damsels were caught near the end of their pelagic phase using established light trapping techniques. Fish were not sexed. At the end of the experiments, fish were released at the site of capture.
Field-collected samples	Lizard Island Research Station 2014 Damselfishes were placed in tanks with flow-through seawater (35 PSU) at ambient temperature (23±1oC, actual range), divided in approximately even numbers between eight identical tanks (25 L each; 3 L min-1 flow-through). Fish were fed to satiation 1-2 times per day with a commercial pellet food. C. cyanostigma were divided in even numbers between two identical tanks (200 L each; 12 L min-1 flow-through) and fed pieces of sardine (Sardinops sagax) every 2-3 d. Tanks were cleaned every 3-4 days. Australian Institute of Marine Science 2015 Juvenile spiny chromis (A. polyacanthus) were obtained from the Reef HQ Aquarium in Townsville, Australia in May. The fish were housed in 25 L tanks with seawater recirculating (~3.5 L min-1), connected to one of four independent 200 L sumps, which themselves were continuously flushed with fresh seawater at 4-7 L min-1. Fish were fed ad libitum 1-2 times per day using commercial aquaculture pellets crushed to a powder and/or Artemia nauplii. Four wild predatory fish (flagtail grouper; Cephalopholis urodeta) were freighted to AIMS and split evenly between two tanks after being caught from the northern Great Barrier Reef by Cairns Marine Pty Ltd. C. urodeta were fed freshly killed juvenile A. polyacanthus every 1-2 days. Fish were exposed to natural water temperatures for the region (quantified using thermal data-loggers sampling every 30 min; iButton, Maxim Integrated, San Jose, CA, USA). Temperature declined seasonally from 26.1±0.2°C during the first week of acclimation (May 2015) to 24.8±0.5°C during the final week of experiments (June 2015; Table S1). Salinity was regulated through the AIMS SeaSim aquarium facility and remained at 35.8±0.15 PSU. Tanks were cleaned weekly. Lizard Island Research Station 2016 Fishes were placed in tanks with flow-through seawater at ambient temperature (29.5±1oC, actual range). The damselfishes were divided in approximately even numbers between 22 identical tanks (one species per tank, 7-8 tanks per species; 10-25 L each and 1-3 L min-1 flow-through, depending on fish size). Fish were fed to satiation 1-2 times per day with a commercial fish flake-saltwater slurry (TetraMin Tropical Flakes, Tetra, Blacksburg, VA). C. cyanostigma were divided in even numbers between

four identical tanks (60 L each; 3 L min-1 flow-through) and fed sardine pieces and freshly killed adult damselfish every 2-3 d. All tanks were provided with pieces of PVC piping to act as shelter for the fish. Tanks were cleaned every 3-4 days.

Ethics oversight

All experiments were conducted in compliance with all relevant ethical regulations under approval from the James Cook University Animal Ethics Committee in association with the Australian Institute of Marine Science (permit A1924).

Note that full information on the approval of the study protocol must also be provided in the manuscript.

A sensory appendage protein protects malaria vectors from pyrethroids

https://doi.org/10.1038/s41586-019-1864-1

Received: 2 May 2019

Accepted: 24 November 2019

Published online: 25 December 2019

Victoria A. Ingham[1]*, Amalia Anthousi[1], Vassilis Douris[2,3], Nicholas J. Harding[4], Gareth Lycett[1], Marion Morris[1], John Vontas[2,5] & Hilary Ranson[1]*

Pyrethroid-impregnated bed nets have driven considerable reductions in malaria-associated morbidity and mortality in Africa since the beginning of the century[1]. The intense selection pressure exerted by bed nets has precipitated widespread and escalating resistance to pyrethroids in African *Anopheles* populations, threatening to reverse the gains that been made by malaria control[2]. Here we show that expression of a sensory appendage protein (SAP2), which is enriched in the legs, confers pyrethroid resistance to *Anopheles gambiae*. Expression of *SAP2* is increased in insecticide-resistant populations and is further induced after the mosquito comes into contact with pyrethroids. *SAP2* silencing fully restores mortality of the mosquitoes, whereas *SAP2* overexpression results in increased resistance, probably owing to high-affinity binding of SAP2 to pyrethroid insecticides. Mining of genome sequence data reveals a selective sweep near the *SAP2* locus in the mosquito populations of three West African countries (Cameroon, Guinea and Burkina Faso) with the observed increase in haplotype-associated single-nucleotide polymorphisms mirroring the increasing resistance of mosquitoes to pyrethroids reported in Burkina Faso. Our study identifies a previously undescribed mechanism of insecticide resistance that is likely to be highly relevant to malaria control efforts.

Anopheline mosquitoes are the only genus that is capable of transmitting human malaria. Targeting the mosquito has proven to be the most effective means of reducing the incidence of malaria, and the massive scale-up of insecticide-based interventions, most notably long-lasting insecticidal nets (LLINs), has driven the considerable reductions in malaria cases in Africa in the twenty-first century[1]. However, worryingly, after many years of progress, gains in malaria control are now stalling, with an estimated 219 million cases and 435,000 malaria-associated deaths across Africa in 2017 prompting a re-examination of the effectiveness of the primary prevention tools[2]. LLINs have proven so effective in preventing malaria because they not only provide personal protection to LLIN users by reducing biting by *Anopheles* mosquitoes that feed at night, but also have a community effect, whereby contact with the insecticide decreases the likelihood that mosquitoes will survive long enough for the development and transmission of the *Plasmodium* parasite[3]. The scale-up of LLINs has exerted intense selection pressure on *Anopheles* vectors to develop resistance to pyrethroids, the insecticide class used to treat all LLINs and, as a result, the community effect of LLINs is being eroded[4]. To prevent catastrophic failure of insecticide-based vector control tools, the resistance mechanisms must be identified and targeted. Successful management of insecticide resistance has been demonstrated by trials using pyrethroid nets that contain the synergist piperonyl butoxide (PBO)[5], a potent inhibitor of metabolic resistance caused by cytochrome P450s, one of the most widespread, and hitherto most potent, resistance mechanisms[6,7]. By blocking this resistance mechanism, PBO–pyrethroid nets restore insecticide susceptibility, leading to a reduction in malaria cases in areas in which metabolic resistance prevails[5].

Although PBO–pyrethroid nets are now replacing standard pyrethroid-only nets in many regions across Africa[8], not all pyrethroid-resistant populations can be effectively targeted by this synergist[8,9] as additional mechanisms are contributing to the resistance phenotype. Recently, using a meta-analysis approach of transcriptomic data from pyrethroid-resistant *A. gambiae* populations from across Africa, multiple new resistance mechanisms—including upregulation of putative insecticide-binding proteins—have been identified[10]. By screening these transcriptomic data from Burkina Faso and Côte d'Ivoire—areas with particularly high pyrethroid resistance and low PBO synergism[9,11]—we found that one family of binding proteins, the sensory appendage proteins, were particularly highly overexpressed in these populations (Extended Data Table 1).

Sensory appendage proteins are members of the chemosensory protein (CSP) family—small soluble proteins that are found only in arthropods[12] and that mediate the transport of hydrophobic compounds through the sensillum lymph[13]. Eight CSP genes are present in the genome of *A. gambiae*, seven of which are clustered on chromosome 3R (Extended Data Fig. 1). Four members of this family have previously been expressed in vitro and have been shown to bind aromatic compounds[14]. Members of the CSP family have been shown to be induced

[1]Vector Biology, Liverpool School of Tropical Medicine, Liverpool, UK. [2]Foundation for Research and Technology - Hellas (FORTH), Institute of Molecular Biology and Biotechnology, Heraklion, Greece. [3]Department of Biological Applications and Technology, University of Ioannina, Ioannina, Greece. [4]The Big Data Institute, University of Oxford, Oxford, UK. [5]Pesticide Science Laboratory, Department of Crop Science, Agricultural University of Athens, Athens, Greece. *e-mail: victoria.ingham@lstmed.ac.uk; hilary.ranson@lstmed.ac.uk

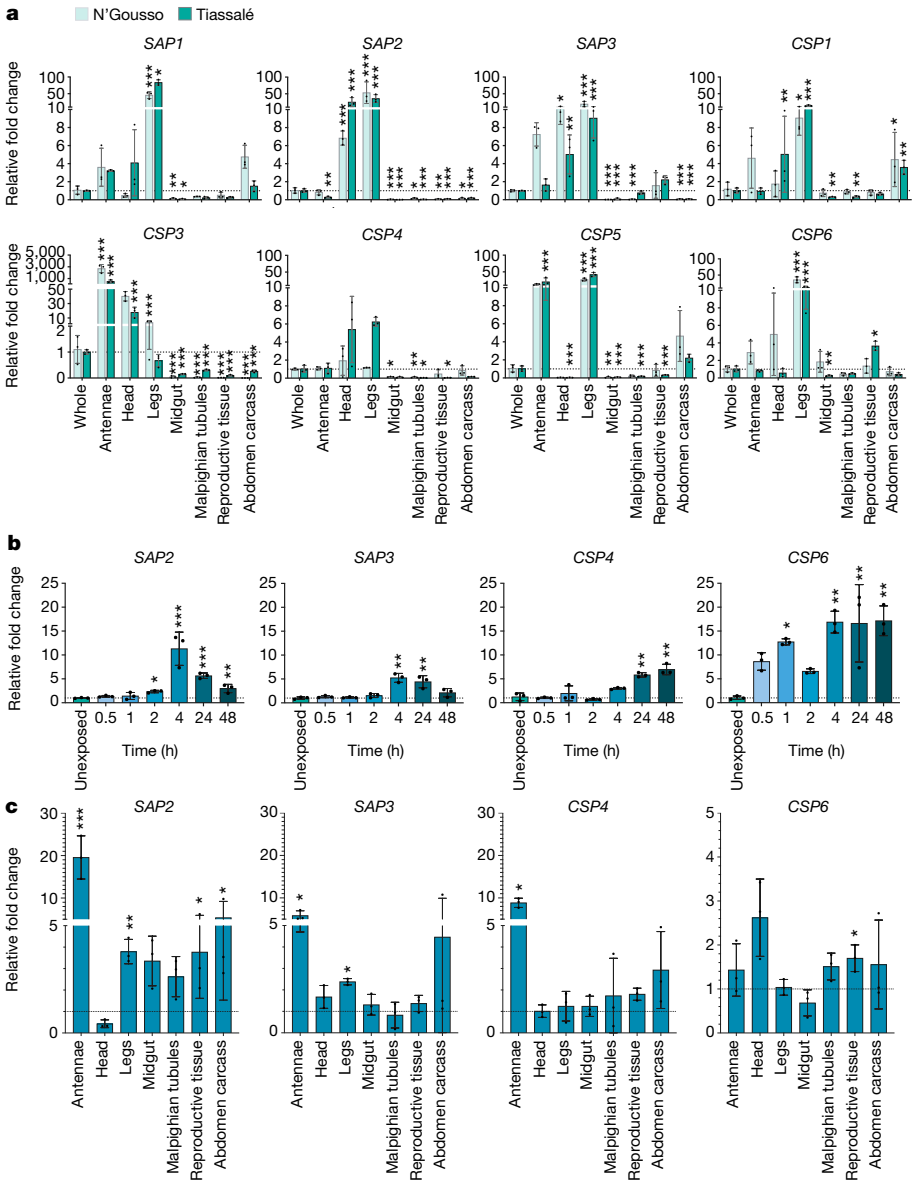


Fig. 1 | CSP expression profiles. a, Constitutive expression of CSPs in resistant and susceptible strains. mRNA localization in antennae, head, legs, midgut, Malpighian tubules, reproductive tissue and the remaining abdominal tissues (abdominal carcass) in N'Gousso and Tiassalé mosquitoes for each member of the CSP family compared to the whole body. **b**, Induction of CSPs in Tiassalé mosquitoes following pyrethroid exposure. Four CSPs show significant induction of mRNA expression at different time points after exposure to the pyrethroid insecticide deltamethrin in Tiassalé mosquitoes (results for the non-induced CSPs are shown in Extended Data Fig. 3a). **c**, Tissue-specific profile of the induction of CSPs in Tiassalé mosquitoes. Tissue-specific induction for the 4 significantly induced CSPs in the Tiassalé strain, shown 4-h after exposure to deltamethrin, each data point shows the exposed compared to unexposed tissues from the same generation (see Extended Data Fig. 3b for the remaining CSPs). The quantitative PCR data show mean ± s.d. of three biological replicates. $^{*}P \leq 0.05$; $^{**}P \leq 0.01$; $^{***}P \leq 0.001$. Statistical significance was calculated by an ANOVA followed by Dunnett's post hoc test; in cases in which normalization was not possible, data were analysed using a Kruskall–Wallis test followed by a Dunn's post hoc test in **a** and **b**. In **c**, significance was calculated using a two-tailed Student's *t*-test; *P* values are included in Supplementary Table 2; $n = 3$ for each replicate.

by insecticide exposure, for example by avermectin in the silkworm *Bombyx mori*[15], pyrethroids in the diamondback moth *Putella xylostella*[16] and noenicitinoids in the whitefly *Bemiscia tabaci*[17].

CSP expression and localization

To determine whether elevated CSP expression was associated with pyrethroid resistance in *A. gambiae*, we characterized the expression of all eight members of the family in females of a multi-insecticide-resistant laboratory colony that originated from Côte d'Ivoire (Tiassalé mosquitoes). We found that two CSPs, *SAP2* (VectorBase ID: AGAP008052) and *CSP6* (AGAP001303), had significantly higher constitutive expression compared to two separate susceptible control mosquito lines (Extended Data Fig. 2). We next determined the localization of CSP expression in multiple tissues, including body areas that are the primary points of mosquito contact with LLINs: the legs, head and antennae; the major detoxification tissues: the Malpighian tubules and the midgut; the reproductive tissues; and the remaining abdominal carcass (Fig. 1a). Six of the eight CSPs, including both *SAP2* and *CSP6*, were enriched in the legs of both resistant and susceptible *Anopheles* mosquito populations, two of the CSPs were enriched in the head (*SAP2* and *SAP3* (AGAP008054)); two in the antennae

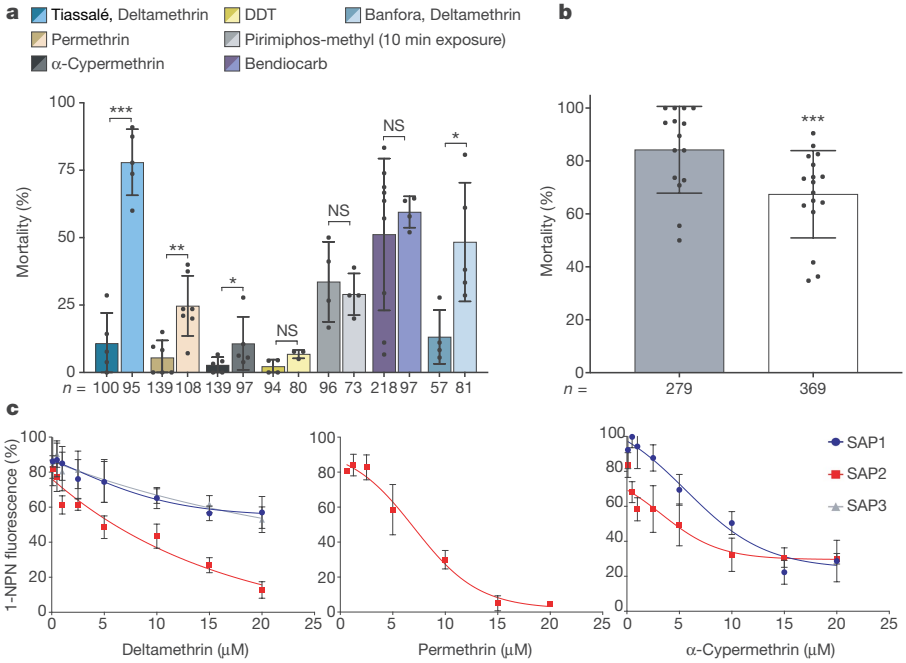


Fig. 2 | SAP2 mediates resistance to pyrethroid insecticides. a, Effect of *SAP2* knockdown on mortality in multi-insecticide-resistant *Anopheles* populations in response to a panel of insecticides (right bar) compared with GFP-injected controls (left bar). Tiassalé, deltamethrin (blue; GFP, $n = 5$; SAP2, $n = 5$); permethrin (brown; GFP, $n = 6$; SAP2, $n = 7$); α-cypermethrin (dark grey; GFP, $n = 5$; SAP2, $n = 5$); DDT (yellow; GFP, $n = 4$; SAP2, $n = 3$), primiphos-methyl (light grey; GFP, $n = 4$; SAP2, $n = 4$), bendiocarb (purple0; GFP, $n = 9$; SAP2, $n = 4$) and Banfora, deltamethrin (grey blue; GFP, $n = 4$; SAP2, $n = 5$). Indicated n numbers are the total number of females used across all replicates. **b**, Transgenic overexpression of *SAP2* in susceptible G3 mosquitoes reduces mortality after permethrin exposure. Bars represent control (grey; $n = 15$) and *SAP2* overexpression (white; $n = 17$). Indicated n numbers are the total number of females used across all replicates. **c**, Competitive binding assays of the three SAP proteins to three pyrethroid insecticides. Only instances with binding shown; no binding was found for SAP3 and SAP1 with permethrin; SAP3 with α-cypermethrin; any SAP with bendiocarb or pirimiphos-methyl. 1-NPN, *N*-phenyl-1-naphthylamine. The data are mean ± s.d. $^{*}P \leq 0.05$; $^{**}P \leq 0.01$; $^{***}P \leq 0.001$; NS, not significant ($P > 0.05$). Statistical significance in **a** and **b** was calculated using an ANOVA test followed by a Tukey post hoc test; *P* values are included in Supplementary Table 2.

(*CSP3* (AGAP008055) and *CSP5* (AGAP008058)) and one in the abdomen carcass (*CSP1* (AGAP008059)).

We performed a time course to determine whether any of the eight CSPs were induced by exposure to pyrethroids in the resistant strain (Fig. 1b and Extended Data Fig. 3a) and found that four of the eight CSPs were significantly induced by deltamethrin, the pyrethroid that is most widely used in LLINs, including the constitutively overexpressed *SAP2* and *CSP6*, in addition to *SAP3* and *CSP4* (AGAP008062) (Fig. 1b). Examining the tissue specificity of the induction 4 h after exposure showed that *SAP2*, *SAP1* (AGAP008051) and *CSP3* were induced in multiple tissues, including the legs, whereas *CSP4*, *CSP6* and *CSP1* showed induction in a single tissue (Fig. 1c and Extended Data Fig. 3b).

CSPs confer resistance

Having established that CSPs are highly overexpressed in the appendages of pyrethroid-resistant mosquitoes, and expression of a subset of this family is further induced by insecticide exposure, we next silenced these CSPs using RNA interference (RNAi) (Extended Data Fig. 4) in females from the highly pyrethroid-resistant Tiassalé colony before exposing the mosquitoes to a panel of insecticide classes (pyrethroids, carbamates and organophosphates) that are widely used in public health initiatives. Notably, silencing of *SAP2* almost completely restored susceptibility to the pyrethroid deltamethrin, and also significantly increased the susceptibility to the other two pyrethroids (permethrin and α-cypermethrin) that were used in these analyses (Fig. 2a). No change in mortality was observed after exposure to the other insecticide classes, indicating that this mechanism is specific to pyrethroid insecticides. We further explored this notable phenotype in a second multi-insecticide-resistant population from Burkina Faso (Banfora) and again found that mortality of the mosquitoes was significantly restored after exposure to deltamethrin (Fig. 2a). Knockdown of the other three CSPs (*SAP3*, *CSP4* and *CSP6*) had no effect on mortality to any insecticide class, except in the case of *CSP6* knockdown, which also significantly increased susceptibility to deltamethrin in Tiassalé mosquitoes—although not to the same extent as *SAP2* knockdown (Extended Data Fig. 5). Conversely, overexpression of *SAP2* in an insecticide-susceptible population (Extended Data Fig. 6) significantly increased pyrethroid resistance, directly linking the function of this protein to insecticide resistance (Fig. 2b). To check for adverse changes to the life-history traits of mosquitoes owing to the disruption of *SAP2* expression, we recorded the survival, blood-feeding ability and egg production in *SAP2* RNAi-injected females and found no significant changes compared to a GFP-injected control, indicating that the mortality that is observed is due to a direct effect of SAP2 on the insecticide and not reduced overall fitness (Extended Data Fig. 7).

To determine a putative mode of action through which a chemosensory protein could confer resistance, we next investigated whether these proteins act as pyrethroid-binding proteins. We heterologously expressed SAP2 and two closely related CSPs (SAP1 and SAP3) in *Escherichia coli* and carried out competitive binding assays with the fluorescent marker *N*-phenyl-1-naphthylamine and a panel of insecticides (Fig. 2c). SAP2 bound to all three pyrethroid insecticides tested: deltamethrin (half-maximum inhibitory concentration (IC_{50}) = 3.99 μM); permethrin (IC_{50} = 4.77 μM); and α-cypermethrin (IC_{50} = 3.74 μM), but did not bind to pirimiphos-methyl (an organophosphate) or bendiocarb (a carbamate). The IC_{50} values were similar to those found for the most important cytochrome p450s that are responsible for metabolic clearance

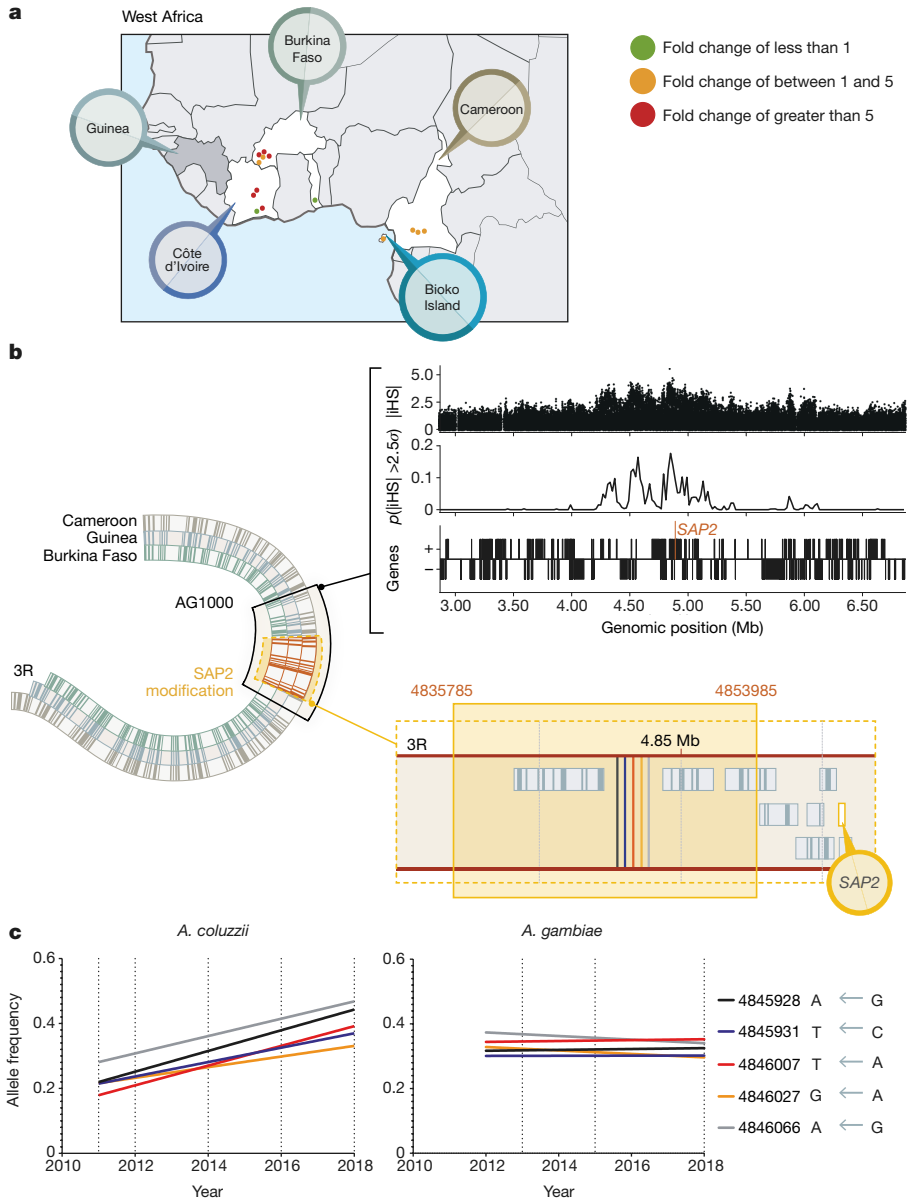


Fig. 3 | *SAP2* is upregulated and under selection in multiple countries across West Africa. a, Points represent significantly differential expression of *SAP2* in pyrethroid-resistant mosquitoes in two sister species (*A. coluzzii* and *A. gambiae*) compared with susceptible populations (supplementary table 1 from a previously published study[10]). Significant (limma; Benjamini–Hochberg-corrected *P* value[10], $P \leq 0.05$) fold changes are shown in green, orange and red. Countries in which SAP2 is significantly upregulated and/or involved in the selective sweep are highlighted with a pin. No transcriptomic data are available for Guinea. The map was created specifically for this manuscript by M. Bernardi. **b**, Left, schematic of the range of the selective sweep found in Guinea, Burkina Faso and Cameroon with a selective sweep found across these regions in the *Anopheles gambiae* 1000 Genomes Project highlighted in grey[19]. Right, the observed iHS signal from Guinea is shown as follows (from top to bottom): raw iHS statistics per SNP, normalized by chromosome in allele frequency bins; summarized iHS in windows of 20 kb by proportion (*p*) of SNPs exceeding 2.5 standard deviations[20]; and genes in this region with *SAP2* annotated. The range of the 55 SNPs with this haplotype across the three countries is highlighted in yellow. Bottom right, a magnified area shows the approximate location of the five haplotype-associated SNPs in proximity to *SAP2* (Extended Data Fig. 1a). **c**, Fitted trend in frequency of the derived haplotype-associated SNPs in field populations from Burkina Faso. *A. coluzzii* populations collected from Tengrela from 2011 to 2018 (left) and *A. gambiae* s.s. samples collected in 2013 and 2015 from Bakaridjan, Burkina Faso and 2018 from Tiefora, Burkina Faso (right). Dates when samples were sequenced are indicated by a dotted line. SNP data are shown in the legend, including the locus and the alternate allele (left) and PEST allele (right).

of pyrethroid insecticides[6,7] (deltamethrin: CYP6M2, IC_{50} = 4.24 μM and CYP6P3, IC_{50} = 3.17 μM; permethrin: CYP6M2, IC_{50} = 8.07 μM and CYP6P3, IC_{50} = 6.77 μM)[18]. The binding of the pyrethroids to SAP2 had significantly higher specificity (analysis of variance (ANOVA), $P < 0.0001$) than the other SAP proteins; however, both SAP1 and SAP3 bound weakly to deltamethrin (IC_{50} > 10 μM) and SAP1 bound moderately to α-cypermethrin (IC_{50} = 9.02 μM).

Having established the importance of SAP2 expression for the resistance of mosquitoes to pyrethroids in a laboratory setting, and having detected the overexpression of this transcript in available transcriptomic data from multiple resistant West African field populations (Fig. 3a and Extended Data Table 1), we next looked for evidence of selection at this locus, using data from the *Anopheles gambiae* 1000 Genomes Project[19] and further de novo sequencing. We computed

the selection statistics—integrated Haplotype Score (his)[20] and XP-EHH (Cross Population Extended Haplotype Homozygosity)[21]—using 1,142 wild-caught *A. gambiae*[19] for the region in which the CSP cluster is found on chromosome 3R (Fig. 3b). Evidence for a selective sweep at this locus was observed in *A. gambiae* from Guinea and Burkina Faso. The swept haplotype is present at a low frequency but there is evidence of haplotype sharing between Guinea, Burkina Faso and Cameroon. We next identified single-nucleotide polymorphisms (SNPs) that are diagnostic of the derived haplotype in this selective sweep (Fig. 3b) and sequenced this region in individual mosquitoes that were collected in the Banfora region of Burkina Faso from 2011 to 2018. This haplotype was stable in frequency in *A. gambiae* sensu stricto (s.s.), indicating that this sweep occurred before the collections of mosquitoes by the *Anopheles gambiae* 1000 Genomes Project[19] in 2012 and pre-dating our collection dates (Fig. 3c and Supplementary Table 1). Conversely, *Anopheles coluzzii* samples collected from 2011 to 2018 showed a large increase in frequency of the SNPs associated with the sweep (Fig. 3c and Supplementary Table 1), and this corresponded with a sharp increase in the prevalence of pyrethroid resistance that occurred during this time period (Extended Data Fig. 8).

Discussion

Our results show that SAP2, a chemosensory protein with no previous known function in insecticide resistance, has a key role in conferring pyrethroid resistance in the *A. gambiae* species complex through the binding of insecticides at the first point of mosquito contact with bed nets. When *SAP2* was overexpressed in an otherwise-susceptible background, the transgenic line was more resistant to pyrethroids, but the phenotype was less marked than the phenotypes found in the *SAP2* knockdown lines, perhaps indicating that SAP2 acts in conjunction with other resistance mechanism(s) to provide an additive effect. Given its strong binding to pyrethroid insecticides, it is possible that SAP2 acts by sequestering the insecticide directly, thus either preventing the function of the insecticide on the nervous system or facilitating its detoxification. Notably, longitudinal sequencing of field samples and available transcriptomic data from wild collections show that this mechanism is being selected for in multiple countries in West Africa, highlighting its relevance in field settings. Nationwide distribution of LLINs has not affected malaria transmission in Burkina Faso, where cases continue to rise annually[22]. Our finding of a potent mechanism that has rapidly swept across anopheline populations in this region will help to address the contribution of insecticide resistance to the persistence of malaria, and the identification of the corresponding SNPs will facilitate tracking its spread. Finally, the identification of this previously undescribed insecticide sequestration mechanism offers the concrete possibility to restore the effectiveness of pyrethroid insecticides in natural mosquito populations through the identification of new targets for inhibitors that can be incorporated into bed nets, in an analogous manner to the incorporation of PBO into nets—this may prove to be critical for the elimination of malaria across Africa.

Online content

Any methods, additional references, Nature Research reporting summaries, source data, extended data, supplementary information, acknowledgements, peer review information; details of author contributions and competing interests; and statements of data and code availability are available at https://doi.org/10.1038/s41586-019-1864-1.

1. Bhatt, S. et al. The effect of malaria control on *Plasmodium falciparum* in Africa between 2000 and 2015. *Nature* **526**, 207–211 (2015).
2. WHO. *World Malaria Report* (WHO, 2018).
3. Hawley, W. A. et al. Community-wide effects of permethrin-treated bed nets on child mortality and malaria morbidity in western Kenya. *Am. J. Trop. Med. Hyg.* **68**, 121–127 (2003).
4. Churcher, T. S., Lissenden, N., Griffin, J. T., Worrall, E. & Ranson, H. The impact of pyrethroid resistance on the efficacy and effectiveness of bednets for malaria control in Africa. *eLife* **5**, e16090 (2016).
5. Protopopoff, N. et al. Effectiveness of a long-lasting piperonyl butoxide-treated insecticidal net and indoor residual spray interventions, separately and together, against malaria transmitted by pyrethroid-resistant mosquitoes: a cluster, randomised controlled, two-by-two factorial design trial. *Lancet* **391**, 1577–1588 (2018).
6. Stevenson, B. J. et al. Cytochrome P450 6M2 from the malaria vector *Anopheles gambiae* metabolizes pyrethroids: sequential metabolism of deltamethrin revealed. *Insect Biochem. Mol. Biol.* **41**, 492–502 (2011).
7. Müller, P. et al. Field-caught permethrin-resistant *Anopheles gambiae* overexpress CYP6P3, a P450 that metabolises pyrethroids. *PLoS Genet.* **4**, e1000286 (2008).
8. Gleave, K., Lissenden, N., Richardson, M. & Ranson, H. Piperonyl butoxide (PBO) combined with pyrethroids in long-lasting insecticidal nets (LLINs) to prevent malaria in Africa. *Cochrane Database Syst. Rev.* **8**, CD012776 (2017).
9. Toe, K. H. et al. Do bednets including piperonyl butoxide offer additional protection against populations of *Anopheles gambiae* s.l. that are highly resistant to pyrethroids? An experimental hut evaluation in Burkina Fasov. *Med. Vet. Entomol.* **32**, 407–416 (2018).
10. Ingham, V. A., Wagstaff, S. & Ranson, H. Transcriptomic meta-signatures identified in *Anopheles gambiae* populations reveal previously undetected insecticide resistance mechanisms. *Nat. Commun.* **9**, 5282 (2018).
11. Edi, C. V. et al. CYP6 P450 enzymes and ACE-1 duplication produce extreme and multiple insecticide resistance in the malaria mosquito *Anopheles gambiae*. *PLoS Genet.* **10**, e1004236 (2014).
12. Vieira, F. G. & Rozas, J. Comparative genomics of the odorant-binding and chemosensory protein gene families across the Arthropoda: origin and evolutionary history of the chemosensory system. *Genome Biol. Evol.* **3**, 476–490 (2011).
13. Leal, W. S. Odorant reception in insects: roles of receptors, binding proteins, and degrading enzymes. *Annu. Rev. Entomol.* **58**, 373–391 (2013).
14. Iovinella, I., Bozza, F., Caputo, B., Della Torre, A. & Pelosi, P. Ligand-binding study of *Anopheles gambiae* chemosensory proteins. *Chem. Senses* **38**, 409–419 (2013).
15. Xuan, N. et al. Increased expression of CSP and CYP genes in adult silkworm females exposed to avermectins. *Insect Sci.* **22**, 203–219 (2015).
16. Bautista, M. A. M. et al. Evidence for trade-offs in detoxification and chemosensation gene signatures in *Plutella xylostella*. *Pest Manag. Sci.* **71**, 423–432 (2015).
17. Liu, G. X. et al. Biotype expression and insecticide response of *Bemisia tabaci* chemosensory protein-1. *Arch. Insect Biochem. Physiol.* **85**, 137–151 (2014).
18. Yunta, C. et al. Pyriproxyfen is metabolized by P450s associated with pyrethroid resistance in *An. gambiae*. *Insect Biochem. Mol. Biol.* **78**, 50–57 (2016).
19. The *Anopheles gambiae* 1000 Genomes Consortium. Genetic diversity of the African malaria vector *Anopheles gambiae*. *Nature* **552**, 96–100 (2017).
20. Voight, B. F., Kudaravalli, S., Wen, X. & Pritchard, J. K. A map of recent positive selection in the human genome. *PLoS Biol.* **4**, e72 (2006).
21. Sabeti, P. C. et al. Genome-wide detection and characterization of positive selection in human populations. *Nature* **449**, 913–918 (2007).
22. Pombi, M. et al. Unexpectedly high *Plasmodium* sporozoite rate associated with low human blood index in *Anopheles coluzzii* from a LLIN-protected village in Burkina Faso. *Sci. Rep.* **8**, 12806 (2018).

Publisher's note Springer Nature remains neutral with regard to jurisdictional claims in published maps and institutional affiliations.

© The Author(s), under exclusive licence to Springer Nature Limited 2019

Methods

Data reporting

No statistical methods were used to predetermine sample size. The experiments were not randomized and the investigators were not blinded to allocation during experiments and outcome assessment.

Mosquito strains

The populations, each belonging to the *A. gambiae* species complex, used in these experiments were reared and maintained at the Liverpool School of Tropical Medicine, under standard insectary conditions at 27 °C, 70–80% humidity, under a 12:12-h photoperiod. Both the Tiassalé (*A. gambiae* sensu lato (s.l.)) strain from Côte d'Ivoire[11] and the Banfora strain (*A. coluzzii*) from Burkina Faso[23] are from insecticide-resistant populations and have been maintained under insecticide pressure since colonization in 2009 and 2014, respectively. The laboratory-maintained insecticide-susceptible populations N'Gousso (*A. coluzzii*)[24], Kisumu (*A. gambiae* s.s.) and G3 (*A. gambiae* s.l.) originate from Cameroon, Kenya and The Gambia, respectively. *A. gambiae* s.l. here refers to a mixture of *A. gambiae* and *A. coluzzii*.

RNAi

PCR was performed on cDNA from Tiassalé mosquitoes using Phusion High-Fidelity DNA Polymerase (Thermo Scientific) following the manufacturer's instructions and primer sets with a T7 docking sequence at the 5′ end of both the sense and antisense primers. Primers were designed using NCBI Primer BLAST to produce an asymmetric product with a length of 300–600 bp, a GC content of 20–50% and no more than three consecutive equivalent nucleotides (Supplementary Table 3). PCR was performed with the following cycles: 3 min at 98 °C; 35 cycles of 7 s at 98 °C; 7 s at calculated T_m; and 10 s at 72 °C; followed by a final hold at 72 °C for 7 min. PCR products were purified using a Qiagen QIAquick PCR Purification kit following the manufacturer's instructions. dsRNA was synthesized using a Megascript T7 Transcription kit (Ambion), with a 16-h 37 °C incubation, following the manufacturer's instructions. The dsRNA was cleaned using a MegaClear Transcription Clear Up kit (Ambion), with nuclease-free DEPC-treated water, heated twice at 65 °C for 10 min, to elute the sample. The resultant dsRNA product was analysed using a Nanodrop spectrometer (Nanodrop Technologies) and subsequently concentrated to 3 μg μl^{-1} using a vacuum centrifuge at 37 °C. Presumed mated, 3–5-day-old, non-blood-fed females were immobilized on a CO_2 block and 69 nl dsRNA was injected directly into the thorax, between the cuticle plates of the abdomen, underneath the wing. As a control, non-endogenous GFP dsRNA was injected at the same amount and concentration.

UAS:SAP2 plasmid construction

Owing to the difficulty of the transformation of a UAS:SAP2 construct into *E. coli* with a complete open-reading frame (ORF), a fusion gene was created that was interrupted by a synthetic intron directly after the start codon. Two fragments were amplified separately and fused together through 40-bp overlapping nucleotides (20 final nucleotides of the synthetic intron and 20 nucleotides downstream of the SAP2 start codon). The 5′ fragment containing a start codon, intron and SAP2 overlap was amplified from pSL-attB-Gyp-UAS14i-Cyp6P3-eYFP (A. Adolfi and G.L., unpublished data). In parallel, *SAP2* was amplified from gDNA of Tiassalé mosquitoes using the following primers: forward, 5′-TTCTGAATTCCATCATGAAACTGTTCGTCGCC-3′ and reverse 5′-TTCTCTCGAGTTATTCCAGCTTGATG-3′. The 3′ fragment for fusion was amplified from the *SAP2* PCR product with the overlapping sequences indicated above. The primers used were: forward, 5′-TTCTGAATTCCATCATGGTAAGTATCAAGGTTACA-3′, reverse 5′-GCGATGGCGACGAACAGTTTCTGTGGAGAGAAAGGCAAAG-3′ and forward 5′-CTTTGCCTTTCTCTCCACAGAAACTGTTCGTCGCCATCGC-3′, reverse 5′-TTCTCTCGAGTTATTCCAGCTTGATG, respectively. The two fragments were fused together by PCR using the outer amplification primers, subcloned into pJET1.2 (Thermo Scientific) and inserted into pSL-attB-Gyp-UAS14-eYFP-gyp-attB (G.L., unpublished data), which carries an inverse attB site for RCME (recombinase-mediated cassette exchange) flanking, the 3×P3-YFP transformation marker and multiple cloning site through the EcoRI/XhoI restrictions sites, to generate the plasmid pUAS:SAP2. Sequence analysis indicated a point mutation within the synthetic intron but outside of the splice and acceptor donor sites.

Transgenic lines

The CFP-marked A10 Ubi-GAL4 line[25] was used as the RCME docking line to establish the UAS:SAP2 line. The A10 promoter, polyubiquitin c (PUBc), has previously been characterized, and shows high levels of expression throughout adult male and female mosquitoes[25]. mCherry under the PUBc promoter in the A10 line has fluorescence in the thorax, non-sclerotized abdomen and appendages (wing veins, antennae, palps, proboscis/labium and legs)[25] (Extended Data Fig. 6b). Microinjections were performed on approximately 200 embryos with 350 ng μl^{-1} of UAS:SAP2 responder plasmid and 150 ng μl^{-1} of phiC31 integrase helper plasmid pKC40 (gift from L. Ringrose). Subsequently, 38 F_0 L1 larvae that transiently expressed the YFP marker were obtained, reared separately and crossed into G3 mosquitoes of the opposite sex. Three YFP-positive F_1 male adults were identified from screening, which were backcrossed with wild-type G3 mosquitoes, and characterized for orientation of the exchange cassette through a diagnostic PCR. All males showed identical orientation in the expected genomic site. From these F_1 crosses, a single isofemale line was selected, which showed the expected 50% YFP inheritance in F_2. This line was further characterized after crossing with the parental A10 Ubi-Gal4 driver line for correct splicing of the inserted intron (Extended Data Fig. 6c) and for insecticide bioassays.

Bioassays

At 72-h after injection, 3–5-day-old adult females were exposed to a panel of insecticides using standard insecticide impregnated papers in WHO tubes[26]. In each case, 15–30 adult females were exposed to insecticide for 1 h and then left in a control tube for 24 h in insectary conditions before mortality was scored (minimum biological replicates, $n = 3$; maximum, $n = 17$). For each experiment, mosquitoes were simultaneously exposed to untreated control papers. GFP-injected mosquitoes were used as controls for the RNAi bioassays and the GAL4-driver line acted as a control for the bioassays on the transgenic strains. For the induction experiments, no 24-h recovery period was allowed, and mosquitoes were taken at the time point directly after 1-h exposure; this experiment was only possible on the resistant population, owing to mortality in the susceptible control. Bartlett and Shapiro tests were used to confirm homogeneity of variance and normality of data, respectively. For non-normal data, transformations were performed to achieve normality. Analysis of mortality data was done using an ANOVA followed by a Tukey post hoc test. Graphs were produced using GraphPad Prism 8.0.2. Mortalities and significance levels for figure panels are shown in Supplementary Table 2.

RNA extraction

RNA was extracted and purified in each experimental set using an Arcturus PicoPure RNA Isolation Kit (Thermo Fisher Scientific) following the manufacturer's instructions. Whole-body resistant and susceptible experiments, and RNAi-knockdown efficiency checks, used 5–7, 3–5-day-old adult female mosquitoes. For insecticide induction, 3–5-day-old female mosquitoes were snap-frozen pre-exposure and at 30 min, 1 h, 2 h, 4 h, 24 h and 48 h after deltamethrin exposure and RNA was extracted as above. For tissue experiments, 50–100 3–5-day-old females had heads, legs, antennae, midgut, Malpighian tubules, reproductive tissues (and hindgut), along with the remaining abdominal carcass in which fat body cells predominate[27], removed

with microdissection scissors and tweezers on iced PBS, alongside 5–7 age-matched whole females from the same cage. The quality of the RNA was assessed using a Nanodrop spectrophotometer (Nanodrop Technologies).

Quantitative PCR

RNA (1–4 μg) from each biological replicate was reverse-transcribed using oligodT (Invitrogen) and Superscript III (Invitrogen) according to the manufacturer's instructions. Quantitative PCR (qPCR) was performed using SYBR Green Supermix III (Applied Biosystems) using an MX3005 and the associated MxPro software v.4.10 (Agilent). Primer BLAST (NCBI) was used to design primer pairs. Where possible, primers were designed to span an exon junction (Supplementary Table 3). Each 20-μl reaction contained 10 μl SYBR Green Supermix, 0.3 μM of each primer and 1 μl of 2 ng μl^{-1} cDNA. Standard curves for each primer set were used to calculate efficiency, using five 1:5 dilutions of cDNA to ensure that all primer sets met the MIQE guidelines (90–120%). qPCR was performed with the following conditions: 3 min at 95 °C, with 40 cycles of 10 s at 95 °C, followed by 10 s at 60 °C. Relative expression was normalized to two housekeeping genes: *EF* (AGAP005128) and *S7* (AGAP010592). Analysis was performed on ΔC_t values[28]; Bartlett and Shapiro tests were used to confirm homogeneity of variance and normality of data, respectively. For non-normal data, transformations were performed where possible to achieve normality. Normal data were analysed using an ANOVA followed by a Dunnett's post hoc test, non-normal data were analysed using a Kruskall–Wallis test followed by a Dunn's post hoc test. Graphs were produced using GraphPad Prism 8.0.2. All qPCR analysis had three biological replicates and three technical replicates within each biological replicate, with the exception of the transgenics experiments, which had two biological replicates. Relative fold changes and significance levels for each figure panel are shown in Supplementary Table 2; primers are shown in Supplementary Table 3 and *SAP2* sequences to demonstrate conservation of the binding site are shown in Extended Data Fig. 9. The PCR for sequencing was performed in two reactions, and sequenced using the primers, region1-F 5′-CACAACGATTCGTGGTCACC-3′, region1-R 5′-CACTTCACAACTTGC AATGAA-3′, sequenced using region1-R. The second region was similarly amplified and sequenced using region2-F 5′-TTCATTGCAAGTTGTGAAG TG-3′, region2-R 5′-GCACCAGCTGATCGTTGA-3′, and sequenced using region2-F. PCR used Phusion High-Fidelity DNA Polymerase (Thermo Fisher Scientific) with a cycle at 98 °C for 30 s followed by 40 cycles of 98 °C for 7 s, 64 °C for 10 s, 72 °C for 2 min and a final hold at 72 °C for 10 min. Gel extraction used the Qiagen Gel Extraction Kit (Qiagen) following the manufacturer's instructions and PCR products were Sanger-sequenced at Eurofins Genomics.

SAP constructs

SAP1, SAP2 and SAP3 proteins were expressed in bacteria (SAP1 and SAP3 were expressed as N-terminal His-tagged proteins, and SAP2—which is secreted in the periplasmic space—was expressed as a C-terminal His-tagged protein). The bacterial expression constructs used for SAP1 and SAP3 expression were generated by directly subcloning the *SAP1* and *SAP3* ORFs (as EcoRI–NdeI fragments) from the relevant constructs used in a previous study[14] (provided by A. della Torre) into the pET16bTeV vector to generate plasmids pET16TeV.SAP1 and pET16TeV.SAP3, which expressed the N-terminal His-tagged versions of SAP1 and SAP3, respectively. For SAP2 expression, a stepwise cloning strategy into the pET22b vector was used, as follows: *A. gambiae* cDNA (made from RNA from mosquito heads of the N'Gousso strain) was used as a template for PCR amplification of a 384-bp *SAP2* ORF with Kapa Taq polymerase (Roche) using primers *SAP2* forward (5′-ATGAAACTGTTCGTCGCCATC-3′) and *SAP2* reverse (5′-TTATTCCAGCTTGATGCCCTC-3′) using the following conditions: 95 °C for 5 min and 30 cycles of 95 °C for 30 s, 60 °C for 30 s and 72 °C for 30 s, followed by a final extension step at 72 °C for 5 min. The amplified *SAP2* ORF was subcloned into the pGEM-T-Easy vector (Promega) and sequence-verified. Plasmid DNA from a positive pGEM.SAP2 clone was used as a template for the amplification of the mature *SAP2* ORF (that is, without the native signal peptide sequence to enable cloning in frame with the pET22-encoded bacterial signal peptide), using primers NcoSAP2-F 5′-TAACCATGGCCCAGGAGCAGT ACACCACC-3′ (to generate an NcoI site in frame with the pelB ORF in pET-22b) and XhoSAP2Δ-R 5′-GTCTCGAGTTCCAGCTTGATGCCCTC CTT-3′ (to remove the termination codon, thus enabling C-terminal His tagging, and also to introduce an XhoI site). The amplified product was digested with NcoI and XhoI and subcloned into the relevant cloning sites of pET-22b. The recombinant plasmid pET22.SAP2His was sequence-verified and used for periplasmic protein expression.

Protein expression and purification

Expression of *SAP1* and *SAP3* was carried out in BL21-Codon Plus (DE3) *E. coli* cells (Agilent) containing pET16TeV.SAP1 and pET16TeVSAP3, respectively. A single colony was selected and cultured overnight at 37 °C in 80 ml of terrific broth containing 100 μg ml^{-1} ampicillin and 34 μg ml^{-1} chloraphenicol. The 80-ml overnight bacterial culture was used to inoculate a 4-l culture of terrific broth containing 100 μg ml^{-1} ampicillin and 34 μg ml^{-1} chloramphenicol. Cells were cultured at 37 °C until an optical density at 595 nm (OD_{595}) of 0.8. Recombinant protein expression was induced by addition of 0.4 mM isopropyl-β-D-thiogalactoside (IPTG) and the bacteria were cultured for an additional 4 h at 30 °C. Bacteria were collected by centrifugation (5,000 rpm for 30 min) and the pellet was resuspended in 1 M NaCl, 50 mM Tris-HCl pH 8.0, 0.2 mM EDTA, 0.2 mM PMSF buffer and sonicated for 30 min at 4 °C. Following sonication, samples were centrifuged by high-speed centrifugation at 20,000*g* for 30 min at 4 °C, and the supernatant was collected and processed in a purification step.

The supernatant containing soluble SAP1 or SAP3 was purified by Ni^{2+}-affinity chromatography as follows: a 5.5-ml Ni-NTA agarose column was equilibrated with a buffer containing 1 M NaCl, 50 mM Tris-HCl pH 8.0 and 5 mM imidazole. The supernatant was loaded onto the column and washed with equilibration buffer for 10 column volumes. Another wash of 10 column volumes was performed with 25 mM NaCl, 50 mM Tris-HCl pH 8.0, 10% glycerol and 10 mM imidazole. Bound protein was eluted with 5 column volumes of 50 mM Tris pH 8.0, 25 mM NaCl, 10% glycerol and 300 mM imidazole. Fractions with an absorbance at 595 nm (Bradford assay) greater than 3 mg ml^{-1} were pooled, concentrated and buffer-exchanged into 50 mM Tris-HCl pH 8.0, 25 mM NaCl and 10% glycerol with dialysis membrane (6–8 kDa) overnight at 4 °C.

For expression of *SAP2*, *E. coli* BL21-Codon Plus (DE3) cells transformed with pET22.SAP2His were cultured overnight at 37 °C in 20 ml terrific broth containing 100 μg ml^{-1} ampicillin and 34 μg ml^{-1} chloramphenicol. The 20-ml overnight *E. coli* culture was used to inoculate a 2-l culture of terrific broth containing 100 μg ml^{-1} ampicillin and 34 μg ml^{-1} chloramphenicol. Cells were cultured at 37 °C until an OD_{595} of 0.8. Protein expression was induced by addition of 0.1 mM IPTG and the bacteria were cultured for an additional 16–18 h at 25 °C. Cells were collected by centrifugation (5,000 rpm for 30 min) and the periplasmic *E. coli* fraction was extracted by osmotic shock as previously described[29]. In brief, collected cells were suspended in a hypertonic solution of 30 mM Tris, 20% w/v sucrose, 1 mM EDTA, pH 8.0 (25 ml per 1-l culture) and incubated for 30 min at 4 °C. Then, cells were centrifuged at 20,000*g* at 4 °C for 20 min and the supernatant was collected. Cells were resuspended in a hypotonic solution of 5 mM $MgSO_4$ (25 ml per 1-l culture), incubated for 30 min at 4 °C, followed by an additional centrifugation at 20,000*g* at 4 °C for 20 min, and the supernatant was collected. The supernatant from the hypotonic solution was used for the purification step.

The periplasmic solution containing secreted *SAP2* was purified by Ni^{2+}-affinity chromatography as follows. A 6.5-ml Ni-NTA agarose column was equilibrated with 20 mM Tris, 300 mM NaCl, 40 mM imidazole, pH 8.0. The clarified osmotic shock fluid (supernatant from the hypotonic solution) was loaded onto the column and washed with

equilibration buffer for 15 column volumes. Bound protein was eluted with 5 column volumes of 20 mM Tris, 300 mM NaCl, 500 mM imidazole, pH 8.0. Fractions with an absorbance at 59 nm (Bradford assay) greater than 0.5 were pooled, concentrated and buffer-exchanged into 50mM Tris-HCl pH 8.0, 25mM NaCl, 10% glycerol with dialysis membrane (6-8kDa MWCO) overnight at 4 °C.

1-NPN binding competition assays

The affinity of various insecticides for SAP1, SAP2 and SAP3 was measured indirectly by competitive binding assays, which determined the displacement of the ligands from the SAPs by the fluorescent probe 1-NPN. Purified recombinant SAP proteins were mixed with different concentrations of insecticides (in methanol) and 1-NPN (in methanol) in a final volume of 200 µl of 20 mM Tris-HCl, pH 8.0, 100 mM NaCl (containing 1.5% methanol). The final concentration of recombinant SAP protein and 1-NPN in the assays was 10 µM and 5 µM, respectively. Insecticide concentration ranged from 0.0625 to 20 µM. The probe was excited at 337 nm and emission spectra were recorded between 380 nm and 460 nm (peak emission in the presence of recombinant SAP is at 386–388 nm). Emission spectra were recorded on an Infinite M-200 fluorimeter (Tecan Trading) using black 96-well plates (Greiner Bio-One). Graphs were produced using GraphPad Prism 8.0.2. A non-linear fit using logged concentrations were used to fit best-fit lines and calculate the IC_{50} values. The calculated log(IC_{50}) values and associated standard errors were used to fit an ANOVA to compare the binding specificity of the three proteins.

Microarray data

Microarray data were retrieved from the IR-TEx application[10] (https://www.lstmed.ac.uk/projects/ir-tex).

Field collections

Field collections of *A. gambiae* s.l. were performed by colleagues at the Liverpool School of Tropical Medicine in collaboration with the Centre National de Recherche sur le Paludsime (CNRFP) in Banfora district, Burkina Faso. The mosquitoes used in this study originated from Tengrela, (10° 38′ 7.53″ N; 4° 48′ 48.35″ W) in 2011, 2012, 2014, 2016 and 2018, Bakaridjan (10° 24′ 26.34″ N; 4° 33′ 44.78″ W) in 2013 and 2015 and from Tiefora (10° 37′ 54.02″ N; 4° 33′ 22.85″ W) in 2018. All gDNA extractions were subject to SINE PCR[30] to determine the species of each mosquito before sequencing.

Scan for natural selection

We computed iHS[20] and XP-EHH[21] statistics on phased sequences for regions 1.5 Mb upstream and downstream of the chemosensory locus for all available *A. gambiae* West African mosquito populations found in phase 2 of the *Anopheles gambiae* 1000 Genomes Project using scikit-allel v.1.1.10 (https://doi.org/10.5281/zenodo.822784). A peak was apparent in iHS in the Guinean *A. gambiae* population (highest value at 3R: 4,845,138) and a smaller peak was present in Burkina Faso, and a XPEHH peak was present in Cameroon.

Clustering analysis and SNP panel

We carried out haplotype clustering analysis around the chemosensory locus and identified 13 haplotypes that differed by fewer than 20 SNPs across a window 25 kb upstream and downstream of the limits of *SAP2*. This is a firm proxy for identity by descent[19] in an organism with $\pi \approx 0.01$, indicative of selection acting at this region. These 13 shared haplotypes were observed in Guinea, Burkina Faso and Cameroon.

These 13 haplotypes were used to define 55 SNPs with high F_{ST} between this cluster and the wild-type *A. gambiae* populations. A SNP panel screen was designed to encompass a range of these SNPs showing the highest difference between wild-type and cluster SNPs, primers for the two panels were as follows: forward, CAAGCATTGCGCCATCGT; reverse, GAGAAGATGATACTGAGCGG. PCR was performed on gDNA from individual *A. gambiae* from Bakaridjan in 2013 (42 individuals) and 2015 (50 individuals) and Tiefora in 2018 (40 individuals). SNP genotypes from genomic sequence data from individual *A. coluzzii* samples from Tengrela from 2011 (21 individuals), 2012, 2014 and 2016 (72 individuals for each year) were provided by the Broad Institute; the PCR panel was carried out on samples from the same site in 2018 (20 samples). The panel was analysed using Phusion High-Fidelity DNA Polymerase (Thermo Fisher) following the manufacturer's instructions and the following cycles were used: 98 °C for 30 s, 35 cycles of 98 °C for 7 s, 65 °C for 10 s, 72 °C for 15 s and a final hold at 72 °C for 15 min. The resultant product was purified using a QiaQuick Gel Extraction Kit (Qiagen) following the manufacturer's instructions and sent for Sanger sequencing at Eurofins Genomics using the reverse primer. SNPs were identified using Benchling (Biology Software; https://benchling.com), the resultant change in minor allele frequency was calculated and a trend line was fitted to each SNP using GraphPad Prism 8.0.2.

Phylogeny

cDNA sequences for each of the CSPs were retrieved from VectorBase[31] and aligned using Clustal Omega (https://www.ebi.ac.uk/Tools/msa/clustalo/). These data were loaded into Mega 7.0[32] and a maximum likelihood tree with 1,000 bootstraps was performed.

Reporting summary

Further information on research design is available in the Nature Research Reporting Summary linked to this paper.

Data availability

All data analysed during this current study are described in the Article, Extended Data Fig. 1–9, Extended Data Table 1 and the Supplementary Information, or are available from the corresponding authors upon reasonable request. Source Data for Figs. 1, 2 are provided with the paper.

23. Namountougou, M. et al. Multiple insecticide resistance in *Anopheles gambiae* s.l. populations from Burkina Faso, West Africa. *PLoS ONE* **7**, e48412 (2012).
24. Harris, C. et al. Polymorphisms in *Anopheles gambiae* immune genes associated with natural resistance to *Plasmodium falciparum*. *PLoS Pathog.* **6**, e1001112 (2010).
25. Adolfi, A., Pondeville, E., Lynd, A., Bourgouin, C. & Lycett, G. J. Multi-tissue GAL4-mediated gene expression in all *Anopheles gambiae* life stages using an endogenous polyubiquitin promoter. *Insect Biochem. Mol. Biol.* **96**, 1–9 (2018).
26. WHO. *Test Procedures for Insecticide Resistance Monitoring in Malaria Vector Mosquitoes* (WHO, 2016).
27. Severo, M. S. et al. Unbiased classification of mosquito blood cells by single-cell genomics and high-content imaging. *Proc. Natl Acad. Sci. USA* **115**, E7568–E7577 (2018).
28. Schmittgen, T. D. & Livak, K. J. Analyzing real-time PCR data by the comparative C_t method. *Nat. Protocols* **3**, 1101–1108 (2008).
29. Sockolosky, J. T. & Szoka, F. C. Periplasmic production via the pET expression system of soluble, bioactive human growth hormone. *Protein Expr. Purif.* **87**, 129–135 (2013).
30. Santolamazza, F. et al. Insertion polymorphisms of SINE200 retrotransposons within speciation islands of *Anopheles gambiae* molecular forms. *Malar. J.* **7**, 163 (2008).
31. Giraldo-Calderón, G. I. et al. VectorBase: an updated bioinformatics resource for invertebrate vectors and other organisms related with human diseases. *Nucleic Acids Res.* **43**, D707–D713 (2015).
32. Kumar, S., Stecher, G. & Tamura, K. MEGA7: molecular evolutionary genetics analysis version 7.0 for bigger datasets. *Mol. Biol. Evol.* **33**, 1870–1874 (2016).
33. Carpenter, B. et al. Stan: a probabilistic programming language. *J. Stat. Softw.* **76**, 1–32 (2017).

Acknowledgements We thank N. Grisales (Bakaridjan in 2013 and 2015), A. Sanou, M. Guelbeogo (Tiefora 2018, Tengrela 2011, 2012, 2014, 2016) and N. Lissenden (Tengrela 2018) for providing field collections; D. Neafsey and J. Tennessen for sharing Tengrela whole-genome sequence data; I. Iovinella for the provision of SAP1 and SAP3 plasmids; M. Bernardi for help with the generation of the map in Fig. 3a and the preparation of figures; F. Brown, S. Elg, P. Pignatelli and D. Au for providing technical support; H. Toé, B. Lambert and T. Churcher for supplying both the field data and figure in Extended Data Fig. 8; and D. Tsakireli and E. Morou for their help with the expression and characterization of SAP proteins. This study was funded by an MRC Skills Development Fellowship (MR/R024839/1) to V.A.I. and a Royal Society Challenge Grant (CH160059) to H.R. Mosquito collections in Burkina Faso were supported by EC FP7 Project grant no: 265660 'AvecNet' and Wellcome Trust Collaborative Award (200222/Z/15/Z).

Author contributions V.A.I. and H.R. conceived the experimental design. V.A.I. performed all transcriptomic expression experiments, RNAi and phenotyping experiments, data analysis,

and PCR and associated sequencing experiments. A.A. and G.L. produced the transgenic lines and associated phenotypic characterisation. V.D. and J.V. performed the binding assays and associated protein expression experiments. N.J.H. analysed the data from the *Anopheles gambiae* 1000 Genomes Project and produced the haplotype SNP panel. M.M. provided all insectary support. V.A.I. and H.R. drafted the manuscript.

Competing interests The authors declare no competing interests.

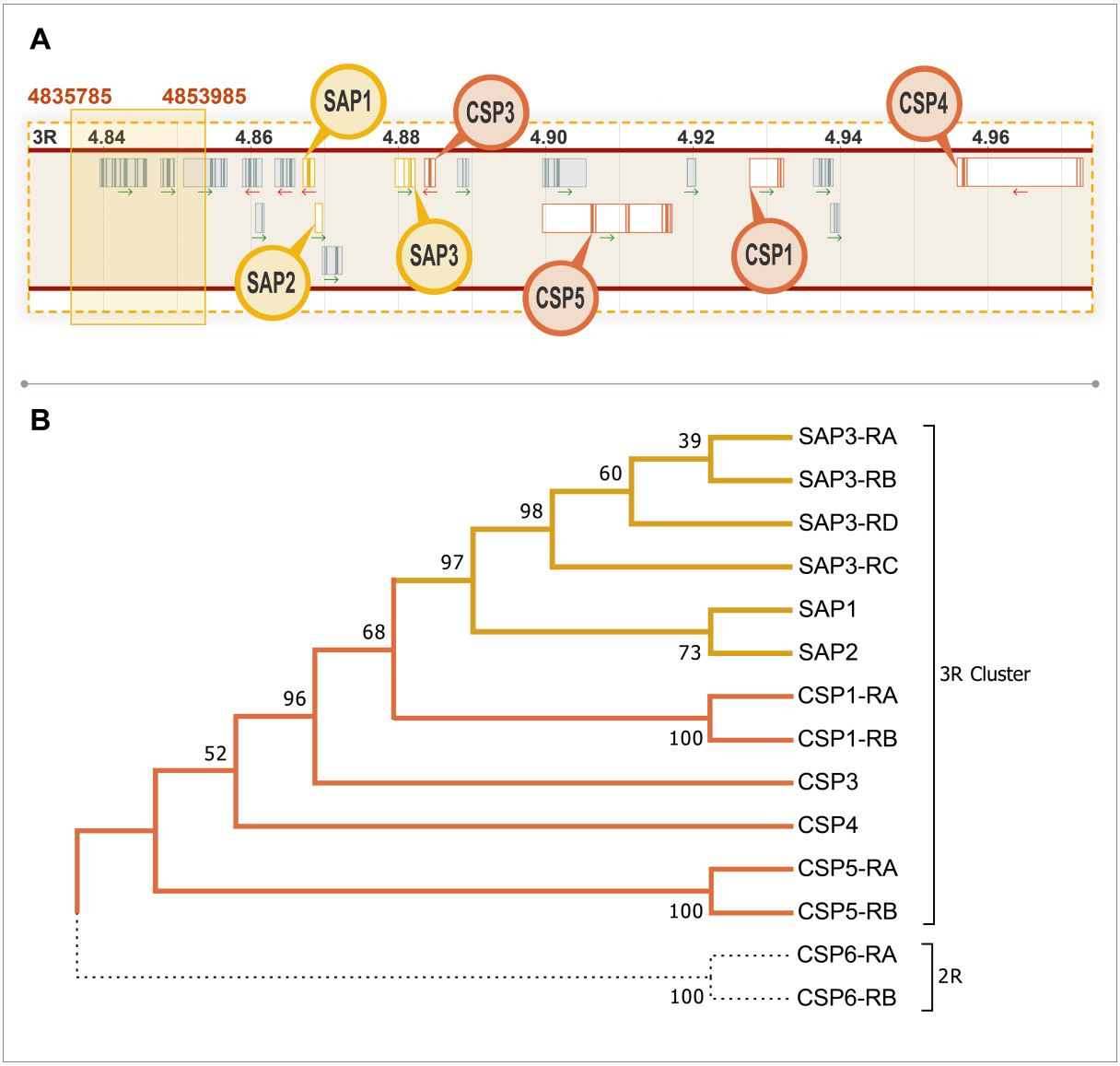
Additional information

Supplementary information is available for this paper at https://doi.org/10.1038/s41586-019-1864-1.

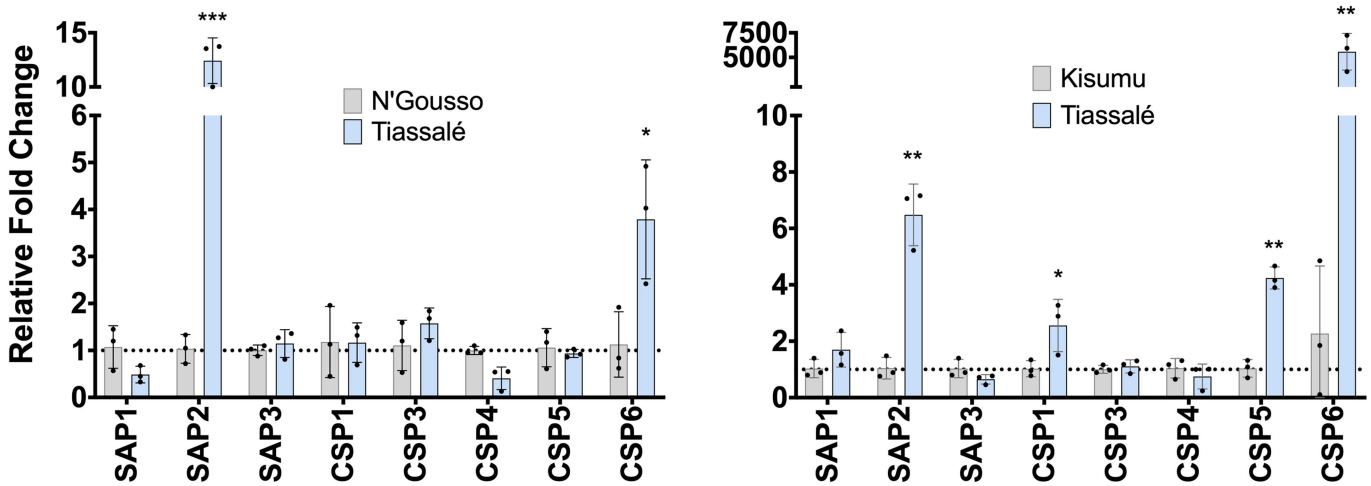
Correspondence and requests for materials should be addressed to V.A.I. or H.R.

Peer review information *Nature* thanks Mara Lawniczak, James G Logan and the other, anonymous, reviewer(s) for their contribution to the peer review of this work.

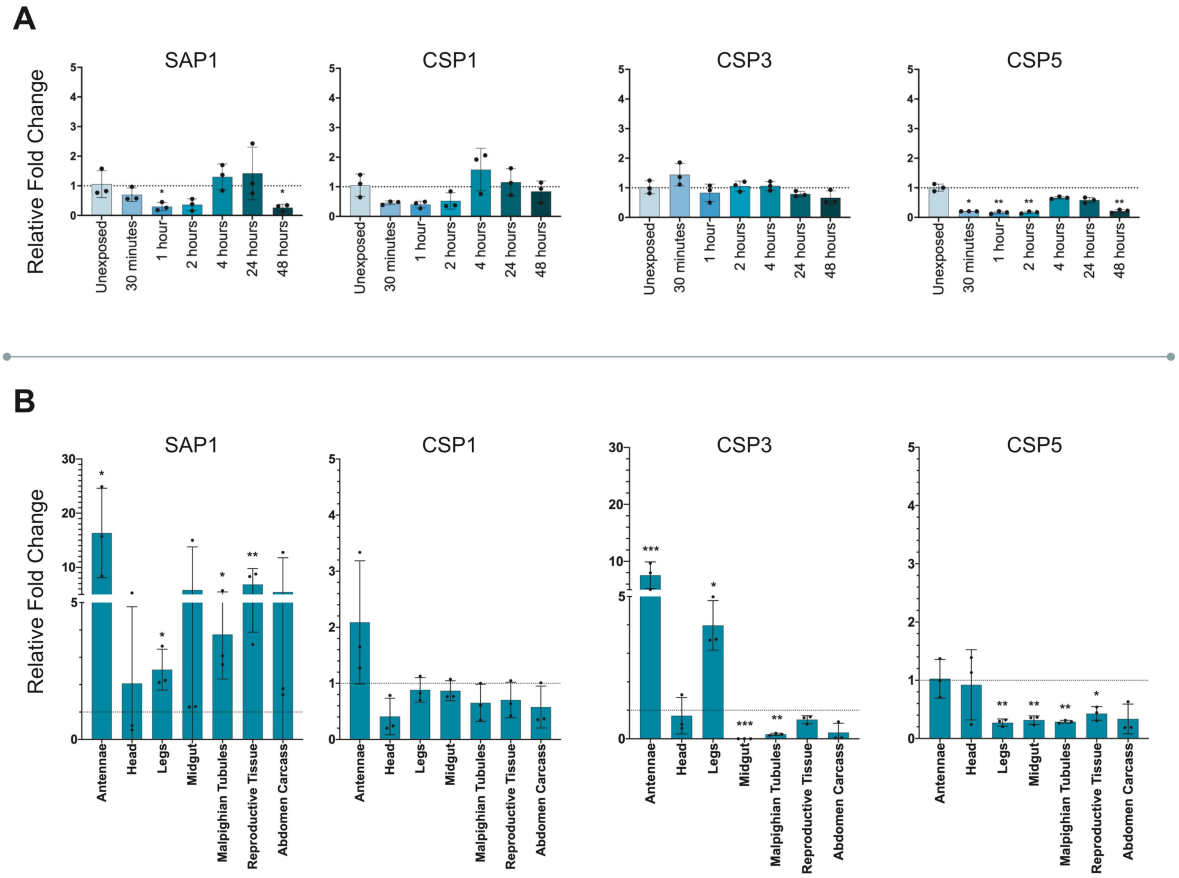
Reprints and permissions information is available at http://www.nature.com/reprints.



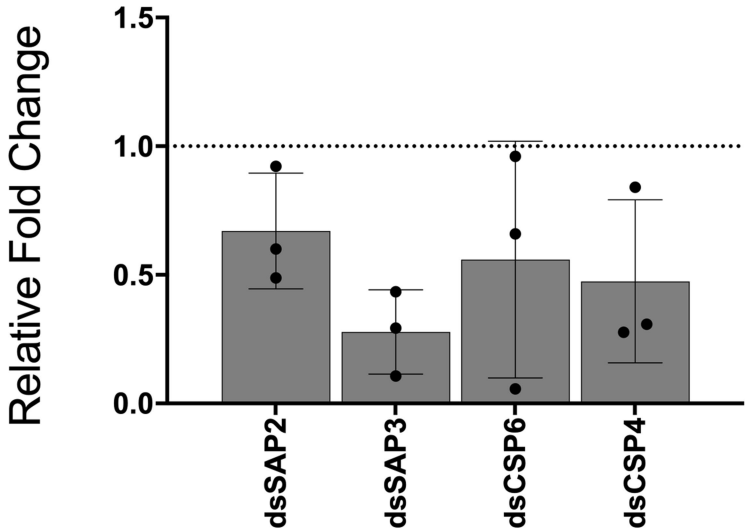
Extended Data Fig. 1 | Chemosensory protein cluster. a, Schematic of the region surrounding the shared haplotype block found in the *Anopheles gambiae* 1000 Genomes Project data with all chemosensory proteins in the cluster highlighted in yellow. Genes displayed in order of appearance, from left to right, are as follows: AGAP008046, AGAP013713, AGAP008047, AGAP008048, AGAP008049, AGAP008050, AGAP008051 (*SAP1*), AGAP008052 (*SAP2*), AGAP008053, AGAP008054 (*SAP3*), AGAP008055 (*CSP3*), AGAP008056, AGAP029127 (*CSP5*, previously AGAP008058), AGAP008059 (*CSP1*), AGAP008060, AGAP008061 and AGAP008062 (*CSP4*). **b**, cDNA bootstrap consensus tree inferred from 1,000 replicates using the maximum likelihood method; the percentage of replicate trees with the associated clustering are shown next to the branches. Yellow indicates the sensory appendage proteins, orange the remaining chemosensory proteins in the 3R cluster and black dotted lines show *CSP6*, which is located on 2R. Alternative isoforms are represented with '-R*X*', with '*X*' proceeding alphabetically dependent on number of splice variants.



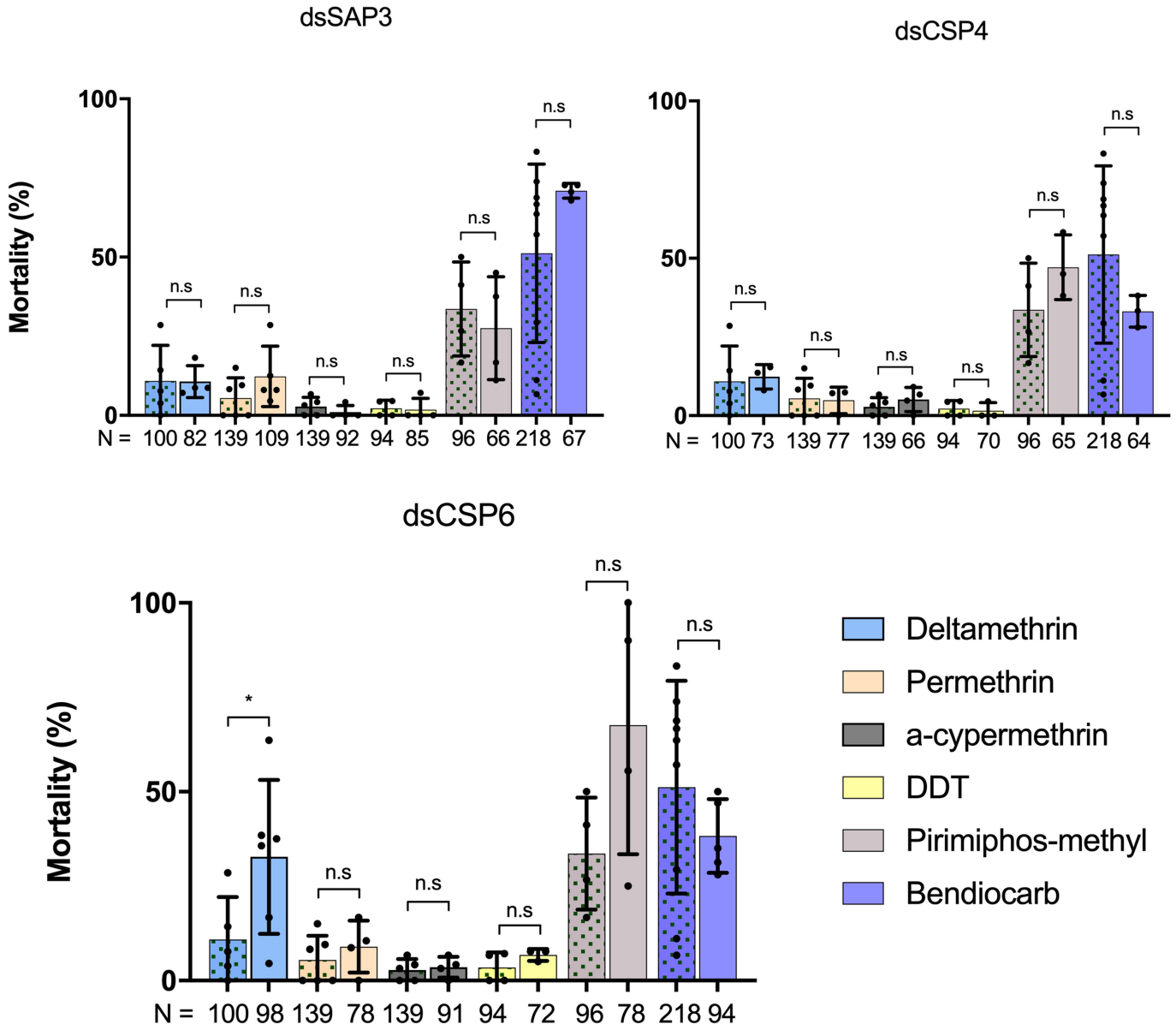
Extended Data Fig. 2 | Overexpression of the CSP family in a multi-insecticide-resistant *Anopheles* population. Left, mean relative fold change of each CSP in Tiassalé mosquitoes (blue) compared with the susceptible control N'Gousso mosquitoes (grey) as determined by qPCR. Right, mean relative fold change of each CSP in Tiassalé mosquitoes (blue) compared with the susceptible Kisumu population (grey). Points show three biological replicates. Data are mean ± s.d. $^{*}P \leq 0.05$; $^{**}P \leq 0.01$; $^{***}P \leq 0.001$. Statistical significance was calculated by an ANOVA followed by Dunnett's post hoc test; *P* values are included in Supplementary Table 2.



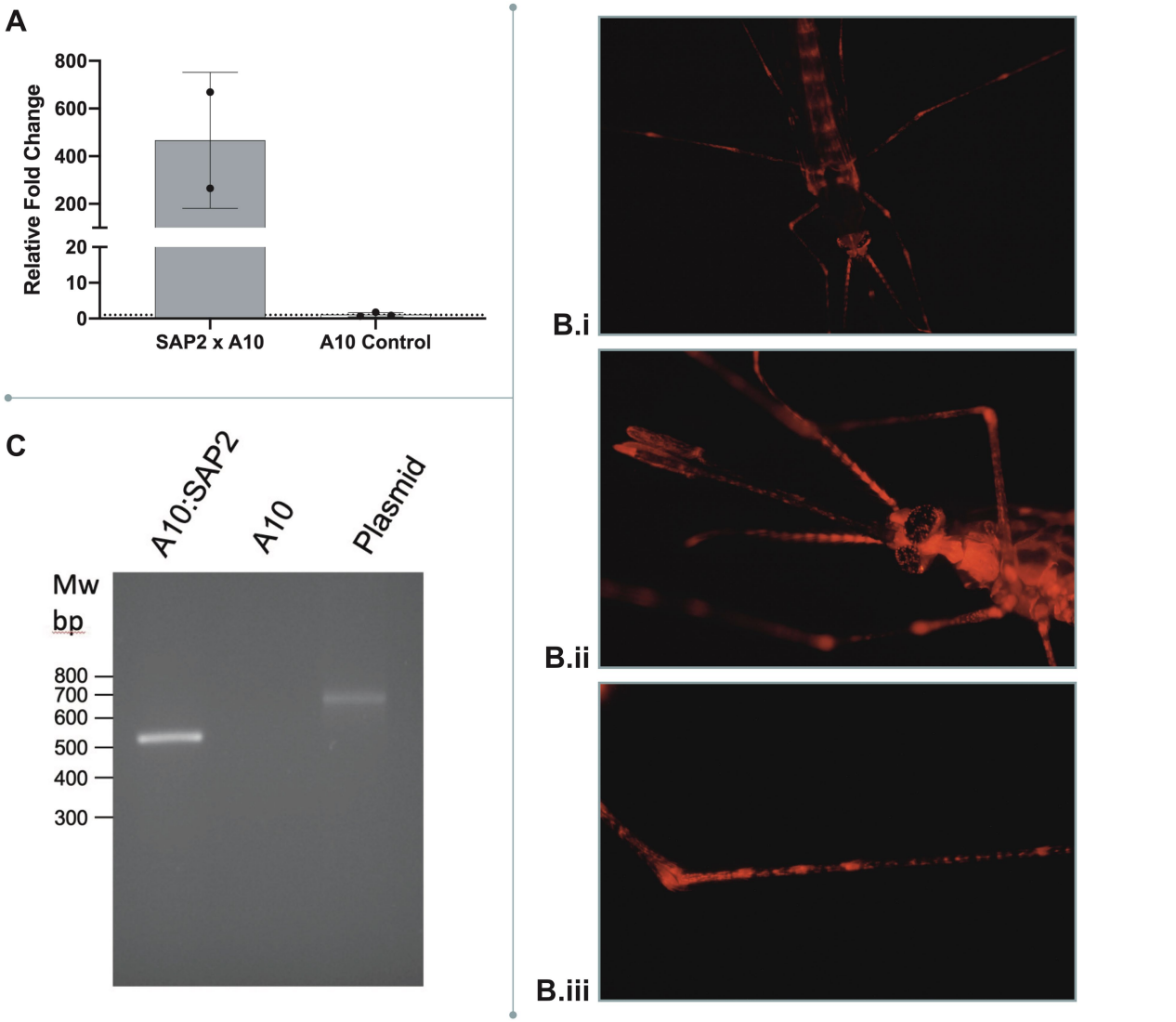
Extended Data Fig. 3 | Expression levels of non-induced chemosensory proteins after exposure to deltamethrin in Tiassalé mosquitoes. **a**, Expression levels of the remaining four CSPs at various time points after exposure to deltamethrin in the multi-insecticide-resistant Tiassalé population. **b**, Tissue-specific induction of these four CSPs 4-h after exposure to deltamethrin. Data are mean ± s.d. of three biological replicates. *$P \leq 0.05$; **$P \leq 0.01$; ***$P \leq 0.001$. Statistical significance was calculated by an ANOVA followed by Dunnett's post hoc test. If the data were non-normal, data were analysed using a Kruskall–Wallis test followed by a Dunn's post hoc test; *P* values are included in Supplementary Table 2.



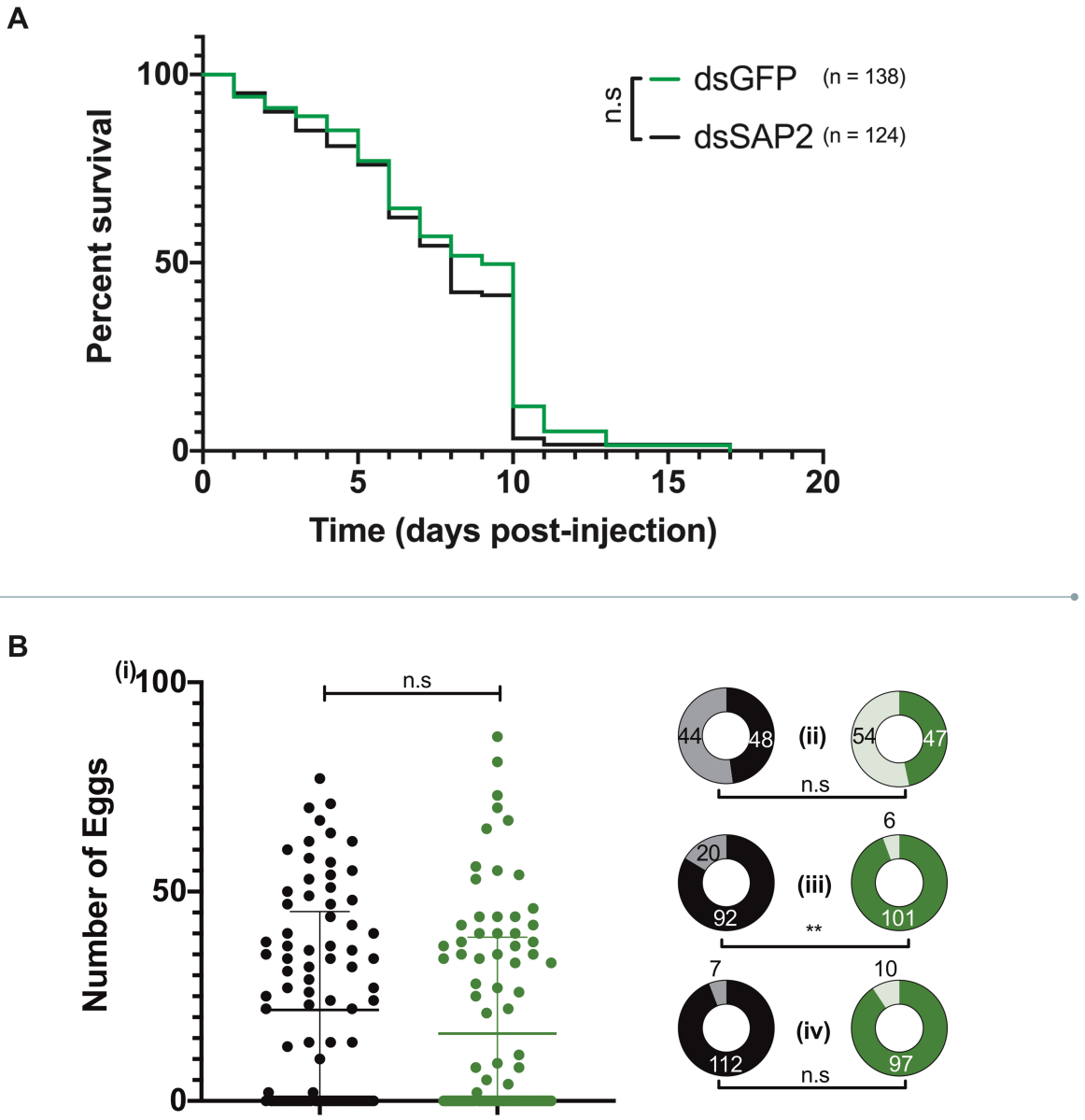
Extended Data Fig. 4 | Efficacy of RNAi. mRNA knockdown of whole female mosquitoes 72 h after injection compared with GFP-injected controls. Data are mean ± s.d. of three biological replicates.



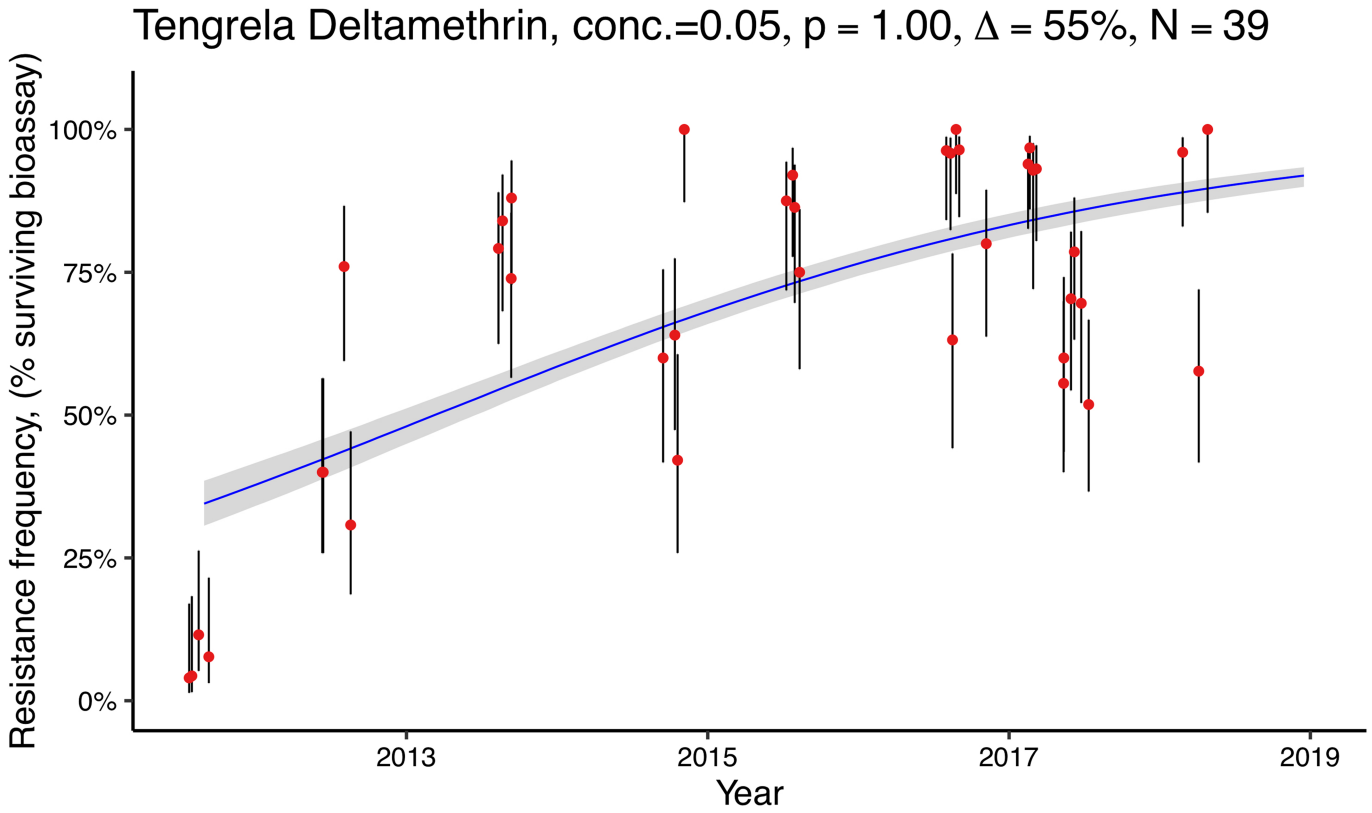
Extended Data Fig. 5 | Phenotype of other induced CSPs to a panel of insecticides. a, Effect of attenuation of dsSAP3 on mortality after insecticide exposure in Tiassalé mosquitoes (right bars; deltamethrin, $n = 4$; permethrin, $n = 5$; α-cypermethrin, $n = 3$; DDT, $n = 3$; pirimiphos-methyl, $n = 3$; bendiocarb, $n = 4$) compared with dsGFP-injected controls (left bars, green patterned; deltamethrin, $n = 5$; permethrin, $n = 5$; α-cypermethrin, $n = 5$; DDT, $n = 4$; pirimiphos-methyl, $n = 4$; bendiocarb, $n = 8$). **b**, Effect of attenuation of dsCSP4 on mortality after insecticide exposure in Tiassalé mosquitoes (right bars; deltamethrin, $n = 3$; permethrin, $n = 3$; α-cypermethrin, $n = 3$; DDT, $n = 3$; pirimiphos-methyl, $n = 3$; bendiocarb, $n = 3$) compared with dsGFP-injected controls (left bars, green patterned; deltamethrin, $n = 5$; permethrin, $n = 5$; α-cypermethrin, $n = 5$; DDT, $n = 4$; pirimiphos-methyl, $n = 4$; bendiocarb, $n = 8$). **c**, Effect of attenuation of dsCSP6 on mortality after insecticide exposure in Tiassalé mosquitoes (right bars; deltamethrin, $n = 6$; permethrin, $n = 4$; α-cypermethrin, $n = 4$; DDT, $n = 3$; pirimiphos-methyl, $n = 4$; bendiocarb, $n = 5$) compared with dsGFP-injected controls (left bars, green patterned; deltamethrin, $n = 5$; permethrin, $n = 5$; α-cypermethrin, $n = 5$; DDT, $n = 4$; pirimiphos-methyl, $n = 4$; bendiocarb, $n = 8$). Analysis of mortality data was done using an ANOVA followed by a Tukey post hoc test; n.s indicates a non-significant change in mortality; $^*P \leq 0.05$. dsCSP6 $\mu_{mortality} = 11.7–31.6\%$, $P = 0.0474$. N indicates the number of individual mosquitoes used for phenotyping; points show the number of bioassay replicates per group. Data are mean ± s.d.



Extended Data Fig. 6 | Characterization of SAP2 in the transgenic line. **a**, Mean mRNA expression after *SAP2* overexpression in the SAP2 × A10 transgenic line ($n = 2$) compared with *SAP2* expression in the A10 × G3 control ($n = 3$). Data are mean ± s.d. and points show each biological replicate. **b**, mCherry under the PUBc A10 promoter demonstrating (i) ubiquitous expression; (ii) expression in the head; and (iii) expression in the legs as previously shown[25]; these results were tested across more than 100 independent mosquito screens. **c**, Intron splicing confirmed by PCR in A10 × SAP2 and negative control A10 mosquitoes compared with plasmid DNA of pUAS:SAP2. The size of the PCR product with and without the synthetic intron is 647 bp and 534 bp, respectively. MW, 100-bp DNA ladder. $n = 2$ A10 × SAP2 samples and $n = 2$ A10 control samples (each sample consists of a pool of 5 4-day-old, unfed females) were tested and experiments were repeated in 2 PCRs.



Extended Data Fig. 7 | Effect of *SAP2* RNAi injection on the fitness of Tiassalé mosquitoes. a, Longevity of SAP2 RNAi (dsSAP2)-expressing mosquitoes (black) compared with dsGFP-expressing control mosquitoes (green). N indicates the number of individual mosquitoes used in each group; n.s represents $P = 0.113$ as calculated by a two-sided Mantel–Cox test. **b**, Life-history traits of dsSAP2-injected (black) and dsGFP-injected (green) females. (i) Number of eggs in each group 72-h after a blood meal (the median and interquartile range are shown). (ii) Proportion of females with eggs (dark shading indicates females with eggs, light shading without; $P = 0.4382$). (iii) Mortality after a blood meal (dark shading are females that are alive after a blood meal, light those that are dead; $P = 0.0052$). (iv) Blood feeding proportions (dark shading are blood-fed females, light non-blood-fed; $P = 0.3257$). Numbers show total numbers of individual females in each group. Significance in (i) was calculated by a two-tailed Mann–Whitney *U*-test (n.s represents $P = 0.0657$); significance in (ii), (iii) and (iv) was calculated using a χ^2 test. $^{**}P \leq 0.01$.



Extended Data Fig. 8 | Mortality of *A. coluzzii* field populations. Temporal plot of mortality from 2011 to 2018 of *A. coluzzii* mosquitoes to 0.05% WHO tube deltamethrin exposure. Δ is the posterior median change in mortality from 2011 to 2018. N indicates the number of experiments included (minimum sample size for any given data point is 14). p indicates the posterior probability that resistance (the proportion of posterior samples for which the April 2018 mean exceeds the corresponding value in January 2011) has increased over the time period. The blue line indicates the posterior median of a logistic model fit to binomial test results; the two parameters of the logistic function were assigned using uninformative (Cauchy(0, 1)) priors. The model was fitted using Stan[33] with 4 chains and 800 iterations per chain (400 of which were discarded as burn-in in each case); all parameters had Rhat < 1.1, indicating convergence. The shading indicates the 90% predictive interval on the mean. Data and figure were provided by H. Toé, B. Lambert and T. Churcher.



Extended Data Fig. 9 | Sequencing of SAP2 primer binding sites. Four N'Gousso and four Tiassale mosquitoes were sequenced across the primer binding sites. **a**, Complete conservation of the sequence was seen in the forward binding site. **b**, One N'Gousso mosquito was heterozygous at one base in the centre of the reverse primer binding site.

Extended Data Table 1 | Expression of the CSP family in western Africa

Dataset		Banfora	Tiefora13	Tiefora14	Tengrela	VK72011	VK72012	VK6
AGAP008051-RA	SAP1	0.827	3.320	5.414	2.229	2.006	0.370	0.402
AGAP008052-RA	**SAP2**	**2.218**	**2.947**	**7.912**	**6.102**	**6.322**	**0.953**	**0.949**
AGAP008054-RA	SAP3	1.040	0.882	0.736	1.052	1.729	0.858	1.329
AGAP008055-RA	CSP3	0.960	2.516	1.994	3.086	3.866	0.914	1.419
AGAP008058-RA	CSP5	1.060	1.252	1.824	1.074	1.231	0.649	0.997
AGAP008059-RA	CSP1	0.506	3.628	4.146	1.738	1.247	0.466	0.877
AGAP008062-RA	CSP4	0.921	0.992	1.024	0.948	1.048	0.985	1.162
AGAP001303-RA	CSP6	0.869	1.772	2.118	0.961	0.704	0.463	0.782
AGAP001303-RB	CSP6	0.864	1.821	2.164	0.969	0.711	0.444	1.195

Country		**Burkina Faso**	**Burkina Faso**	**Burkina Faso**	**Burkina Faso**	**Burkina Faso**	**Burkina Faso**	**Burkina Faso**
Species		**An. coluzzii**	**An. gambiae**	**An. gambiae**	**An. coluzzii**	**An. coluzzii**	**An. coluzzii**	**An. coluzzii**
Exposure Status		Unexposed	Unexposed	Unexposed	Unexposed	Deltamethrin	Deltamethrin	Unexposed
Susceptible Comparator		N'Gousso	Kisumu	Kisumu	Mali	Mali	N'Gousso	N'Gousso

Dataset		Bouake	M'Be	Tiassale	TiassaleMali	TiassaleOkyero	Tiassale2011	Nkolondom
AGAP008051-RA	SAP1	1.889	1.726	4.257	1.106	0.620	0.385	1.374
AGAP008052-RA	**SAP2**	**10.486**	**8.882**	**51.346**	**1.360**	**0.419**	**0.768**	**1.415**
AGAP008054-RA	SAP3	2.585	1.683	5.516	0.822	0.623	0.681	1.844
AGAP008055-RA	CSP3	1.157	1.549	1.247	1.091	0.672	0.569	2.259
AGAP008058-RA	CSP5	0.946	1.134	1.008	1.038	0.833	0.688	1.330
AGAP008059-RA	CSP1	1.609	1.932	2.505	1.067	0.844	0.638	1.331
AGAP008062-RA	CSP4	0.992	0.980	0.995	1.076	0.990	1.128	1.100
AGAP001303-RA	CSP6	0.610	0.635	0.856	0.848	1.130	0.456	2.384
AGAP001303-RB	CSP6	0.584	0.604	0.819	0.850	1.065	0.458	2.463

Country		**Cote D`Ivoire**	**Cote D`Ivoire**	**Cote D`Ivoire**	**Cote D`Ivoire**	**Cote D`Ivoire**	**Cote D`Ivoire**	**Cameroon**
Species		**An. coluzzii**	**An. coluzzii**	**An. coluzzii**	**An. coluzzii**	**An. coluzzii**	**An. coluzzii**	**An. gambiae**
Exposure Status		Deltamethrin	Deltamethrin	Deltamethrin	Unexposed	Unexposed	Unexposed	DDT
Susceptible Comparator		N'gousso	N'gousso	N'gousso	Mali	Okyero	N'Gousso	Kisumu

Dataset		Garre	Messa	Youande	Bioko	KovieOkyero	KovieMalanville
AGAP008051-RA	SAP1	0.659	0.702	0.978	0.782	1.171	0.519
AGAP008052-RA	**SAP2**	**3.024**	**1.673**	**2.009**	**4.094**	**0.871**	**0.473**
AGAP008054-RA	SAP3	1.480	1.842	1.412	0.962	0.605	1.065
AGAP008055-RA	CSP3	1.023	0.795	0.952	0.754	0.723	0.844
AGAP008058-RA	CSP5	0.774	0.681	1.298	0.734	0.842	0.956
AGAP008059-RA	CSP1	0.481	0.492	1.297	0.472	1.535	1.293
AGAP008062-RA	CSP4	0.958	0.870	0.993	0.848	0.821	0.826
AGAP001303-RA	CSP6	0.452	0.423	1.387	0.458	1.135	0.896
AGAP001303-RB	CSP6	0.450	0.393	1.431	0.435	1.232	0.908

Country	**Cameroon**	**Cameroon**	**Cameroon**	**Equatorial Guinea**	**Togo**	**Togo**
Species	**An. coluzzii**	**An. coluzzii**	**An. gambiae**	**An. coluzzii**	**An. coluzzii**	**An. coluzzii**
Exposure Status	DDT	DDT	Bendiocarb	Deltamethrin	Unexposed	Unexposed
Susceptible Comparator	N'Gousso	N'Gousso	N'Gousso	N'gousso	Okyero	Malanville

Microarray fold-change data from microarray datasets were retrieved from IR-TEx[10] across western Africa for *A. coluzzii* and *A. gambiae* populations for each member of the CSP family. Fold changes showing significant overexpression in the respective datasets are highlighted in green, yellow indicates underexpression and white backgrounds show no significant change. SAP2 is shown in bold. The country of origin, species and exposure status of the resistant population are given below each table, as well as the susceptible population used as for comparison.

Corresponding author(s): Hilary Ranson
Victoria A Ingham

Last updated by author(s): Oct 14, 2019

Reporting Summary

Nature Research wishes to improve the reproducibility of the work that we publish. This form provides structure for consistency and transparency in reporting. For further information on Nature Research policies, see Authors & Referees and the Editorial Policy Checklist.

Statistics

For all statistical analyses, confirm that the following items are present in the figure legend, table legend, main text, or Methods section.

n/a	Confirmed	
☐	☒	The exact sample size (*n*) for each experimental group/condition, given as a discrete number and unit of measurement
☐	☒	A statement on whether measurements were taken from distinct samples or whether the same sample was measured repeatedly
☐	☒	The statistical test(s) used AND whether they are one- or two-sided *Only common tests should be described solely by name; describe more complex techniques in the Methods section.*
☒	☐	A description of all covariates tested
☐	☒	A description of any assumptions or corrections, such as tests of normality and adjustment for multiple comparisons
☐	☒	A full description of the statistical parameters including central tendency (e.g. means) or other basic estimates (e.g. regression coefficient) AND variation (e.g. standard deviation) or associated estimates of uncertainty (e.g. confidence intervals)
☐	☒	For null hypothesis testing, the test statistic (e.g. *F*, *t*, *r*) with confidence intervals, effect sizes, degrees of freedom and *P* value noted *Give P values as exact values whenever suitable.*
☒	☐	For Bayesian analysis, information on the choice of priors and Markov chain Monte Carlo settings
☒	☐	For hierarchical and complex designs, identification of the appropriate level for tests and full reporting of outcomes
☒	☐	Estimates of effect sizes (e.g. Cohen's *d*, Pearson's *r*), indicating how they were calculated

Our web collection on statistics for biologists contains articles on many of the points above.

Software and code

Policy information about availability of computer code

Data collection	GraphPad Prism 8 Benchling MxPro software version 4.10 IR-TEx (https://www.lstmed.ac.uk/projects/ir-tex)
Data analysis	GraphPad Prism 8 Benchling scikit-allel v1.1.10 (DOI: 10.5281/zenodo.822784) Mega 7 Clustal Omega

For manuscripts utilizing custom algorithms or software that are central to the research but not yet described in published literature, software must be made available to editors/reviewers. We strongly encourage code deposition in a community repository (e.g. GitHub). See the Nature Research guidelines for submitting code & software for further information.

Data

Policy information about availability of data

All manuscripts must include a data availability statement. This statement should provide the following information, where applicable:

- Accession codes, unique identifiers, or web links for publicly available datasets
- A list of figures that have associated raw data
- A description of any restrictions on data availability

All data analysed during this current study are available on public repositories and detailed in the present paper, or in the Extended Data files, or are available from the authors upon request.

Field-specific reporting

Please select the one below that is the best fit for your research. If you are not sure, read the appropriate sections before making your selection.

☒ Life sciences ☐ Behavioural & social sciences ☐ Ecological, evolutionary & environmental sciences

For a reference copy of the document with all sections, see nature.com/documents/nr-reporting-summary-flat.pdf

Life sciences study design

All studies must disclose on these points even when the disclosure is negative.

Sample size	In all cases experiments were carried out in at least biological triplicate and in the case of qPCR and the binding assays technical triplicate, as previously published in the MIQE guidelines. In each case a minimum number of mosquitoes were included in biological replicate in qPCR analysis (5-10) to ensure enough RNA was produced. For each bioassay over 20 individuals per WHO tube for diagnostic assay, with n greater than or equal to 3 following standard procedure specified by WHO's Testing Procedures document stating around 120-150 mosquitoes minimum should be used in these assays (combined exposed+control). In the case of field sample sequencing, we were constrained by the number of individuals available of the correct species in historical samples.
Data exclusions	No data was excluded from the analysis
Replication	As described above all experiments were performed with at least three biological replicates and were required, at least three technical replicated. All experiments were successful; however only 2 samples were available for qPCR of the SAP2 over-expressing line.
Randomization	This is not relevant as mosquitoes are reared in large cases, often with over 200 females so selection of females is inherently random.
Blinding	Blinding is not possible in this study design as it is necessary to know which tubes contain insecticides and the relevant meta-data for the sequencing experiments.

Reporting for specific materials, systems and methods

We require information from authors about some types of materials, experimental systems and methods used in many studies. Here, indicate whether each material, system or method listed is relevant to your study. If you are not sure if a list item applies to your research, read the appropriate section before selecting a response.

Materials & experimental systems

n/a	Involved in the study
☒	☐ Antibodies
☒	☐ Eukaryotic cell lines
☒	☐ Palaeontology
☐	☒ Animals and other organisms
☒	☐ Human research participants
☒	☐ Clinical data

Methods

n/a	Involved in the study
☒	☐ ChIP-seq
☒	☐ Flow cytometry
☒	☐ MRI-based neuroimaging

Animals and other organisms

Policy information about studies involving animals; ARRIVE guidelines recommended for reporting animal research

Laboratory animals	Anopheles gambiae sl female mosquitoes, 3-5 days old
Wild animals	No wild animals were involved in this study.
Field-collected samples	No mosquitoes were directly collected from field in this study.
Ethics oversight	No ethical approval is needed for use of mosquitoes

Note that full information on the approval of the study protocol must also be provided in the manuscript.

Article

Last appearance of *Homo erectus* at Ngandong, Java, 117,000–108,000 years ago

https://doi.org/10.1038/s41586-019-1863-2

Received: 29 May 2019

Accepted: 4 November 2019

Published online: 18 December 2019

Yan Rizal[1,21], Kira E. Westaway[2,21]*, Yahdi Zaim[1], Gerrit D. van den Bergh[3], E. Arthur Bettis III[4], Michael J. Morwood[3,22], O. Frank Huffman[5], Rainer Grün[6], Renaud Joannes-Boyau[7], Richard M. Bailey[8], Sidarto[9], Michael C. Westaway[6,10], Iwan Kurniawan[9], Mark W. Moore[11], Michael Storey[12], Fachroel Aziz[9], Suminto[9,22], Jian-xin Zhao[13], Aswan[1], Maija E. Sipola[14], Roy Larick[15], John-Paul Zonneveld[16], Robert Scott[17], Shelby Putt[18,19] & Russell L. Ciochon[20]*

Homo erectus is the founding early hominin species of Island Southeast Asia, and reached Java (Indonesia) more than 1.5 million years ago[1,2]. Twelve *H. erectus* calvaria (skull caps) and two tibiae (lower leg bones) were discovered from a bone bed located about 20 m above the Solo River at Ngandong (Central Java) between 1931 and 1933[3,4], and are of the youngest, most-advanced form of *H. erectus*[5–8]. Despite the importance of the Ngandong fossils, the relationship between the fossils, terrace fill and ages have been heavily debated[9–14]. Here, to resolve the age of the Ngandong evidence, we use Bayesian modelling of 52 radiometric age estimates to establish—to our knowledge—the first robust chronology at regional, valley and local scales. We used uranium-series dating of speleothems to constrain regional landscape evolution; luminescence, ^{40}argon/^{39}argon (^{40}Ar/^{39}Ar) and uranium-series dating to constrain the sequence of terrace evolution; and applied uranium-series and uranium series–electron-spin resonance (US–ESR) dating to non-human fossils to directly date our re-excavation of Ngandong[5,15]. We show that at least by 500 thousand years ago (ka) the Solo River was diverted into the Kendeng Hills, and that it formed the Solo terrace sequence between 316 and 31 ka and the Ngandong terrace between about 140 and 92 ka. Non-human fossils recovered during the re-excavation of Ngandong date to between 109 and 106 ka (uranium-series minimum)[16] and 134 and 118 ka (US–ESR), with modelled ages of 117 to 108 thousand years (kyr) for the *H. erectus* bone bed, which accumulated during flood conditions[3,17]. These results negate the extreme ages that have been proposed for the site and solidify Ngandong as the last known occurrence of this long-lived species.

Our current understanding of *H. erectus* in Asia largely derives from evidence from the Solo River region of central Java in the Indonesian archipelago[7]. However, this region presents great challenges to constructing solid chronologies for hominin occupation, evolution and dispersal[9]. These problems relate to finding appropriate materials for dating, confusion over the location of previous excavations and find spots, a lack of direct association between the fossils and material being dated, taphonomic differences within the faunal assemblages, reworking of surrounding fluvial deposits and fossils and the leaching of uranium from the fossils being dated. Nowhere are these complications and misperceptions more apparent than at the site of Ngandong[12,18–20].

In 1996, late-Pleistocene age estimates from uranium-series (U-series) and ESR dating were reported for mammalian bone within the 20-m terrace fill at Ngandong and other nearby localities[9]. These unexpectedly young results (corresponding to ages of 53 to 27 kyr) triggered debate regarding the taphonomy of the Ngandong fossil assemblage and the sedimentological context of the dated material[12]. More dating followed: direct gamma-spectrometric ^{230}Th/^{234}U dating of *H. erectus*

[1]Department of Geology, Institute of Technology Bandung, Bandung, Indonesia. [2]Department of Earth and Environmental Sciences, Macquarie University, Sydney, New South Wales, Australia. [3]Centre for Archaeological Science, School of Earth, Atmospheric and Life Sciences, University of Wollongong, Wollongong, New South Wales, Australia. [4]Department of Earth and Environmental Sciences, University of Iowa, Iowa City, IA, USA. [5]Department of Anthropology, University of Texas at Austin, Austin, TX, USA. [6]Australian Research Centre for Human Evolution (ARCHE), Environmental Futures Research Institute, Griffith University, Nathan, Queensland, Australia. [7]Southern Cross GeoScience, Southern Cross University, Lismore, New South Wales, Australia. [8]School of Geography and the Environment, University of Oxford, Oxford, UK. [9]Geology Museum, Geological Agency, Bandung, Indonesia. [10]School of Social Science, University of Queensland, Brisbane, Queensland, Australia. [11]Archaeology and Palaeoanthropology, University of New England, Armidale, New South Wales, Australia. [12]Quadlab, Natural History Museum of Denmark, University of Copenhagen, Copenhagen, Denmark. [13]School of Earth and Environmental Sciences, University of Queensland, Brisbane, Queensland, Australia. [14]Chemistry and Geology Department, Minnesota State University, Mankato, MN, USA. [15]Bluestone Heights, Shore Cultural Center, Cleveland, OH, USA. [16]Department of Earth and Atmospheric Sciences, University of Alberta, Edmonton, Alberta, Canada. [17]Department of Anthropology and Center for Human Evolutionary Studies, Rutgers University, New Brunswick, NJ, USA. [18]The Stone Age Institute, Indiana University, Bloomington, IN, USA. [19]Department of Sociology and Anthropology, Illinois State University, Normal, IL, USA. [20]Department of Anthropology and Museum of Natural History, University of Iowa, Iowa City, IA, USA. [21]These authors contributed equally: Yan Rizal, Kira E. Westaway. [22]Deceased: Michael J. Morwood, Suminto. *e-mail: kira.westaway@mq.edu.au; russell-ciochon@uiowa.edu

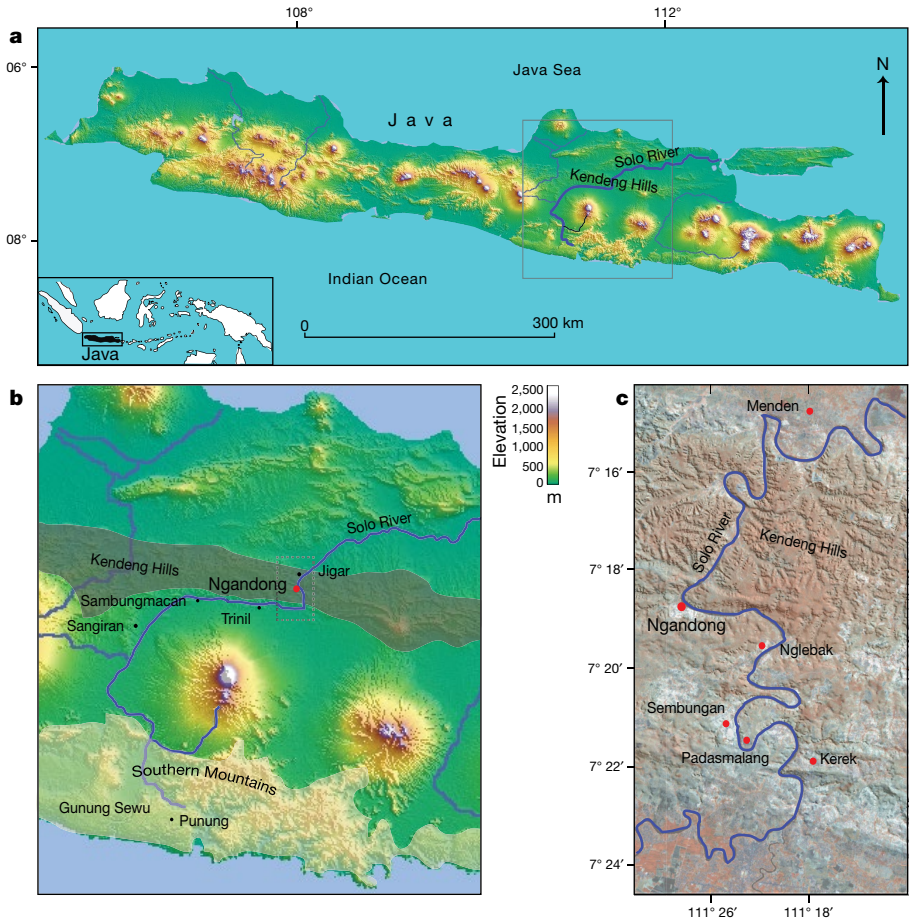


Fig. 1 | Location of Java with *H. erectus* sites and key study sites on the terraces. a, Java and study sites, and the location of Java in the Indonesian archipelago (inset). **b**, The location of the key study areas; the Southern Mountains, Kendeng Hills (Kendeng anticlinorium), Solo River terraces and the *H. erectus* sites of Sangiran, Trinil, Sambungmacan and Ngandong, as well as the other Javanese sites (Jigar and Punung). The scale bar for the elevation changes relates to both **a** and **b**. Topographical map redrawn from the US Geological Survey's Earth Resources Observation and Science Center (USGS EROS). **c**, A section of the Solo River system, from Kerek village in the south to Menden village in the north, showing our key study sites (including Ngandong, Sembungan, Padasmalang, Nglebak, Kerek and Menden). USGS Landsat image with digital elevation model[31,32].

cranial bone from Ngandong and Sambungmacan, giving ages of 40 and 60–70 kyr, respectively[13]; U-series and ESR dating of mammalian bone from Jigar I (downstream of Ngandong), which gave an age of 143 +20 or −17 kyr[14]; and $^{40}Ar/^{39}Ar$ dating of pumice hornblende from Ngandong II and Jigar, giving an age of 546 ± 12 kyr[14] (Fig. 1; uncertainties are defined in figure legends).

To address these chronological inconsistencies, we applied a regional approach to establishing a chronology for the re-excavations that we conducted at Ngandong (Fig. 2). First, to establish a landscape context, we used U-series dating of speleothems to constrain the tectonic uplift of the Southern Mountains that caused the Solo River to divert northward to flow through the Kendeng Hills and form the Solo River strath terrace sequence (Fig. 3, Extended Data Fig. 1). Second, to establish a terrace context, we applied red thermoluminescence, post-infrared infrared-stimulated luminescence (pIR-IRSL) and $^{40}Ar/^{39}Ar$ dating techniques to terrace sediments at localities covering the entire incision sequence: Kerek (upper), Padasmalang (middle), Ngandong (lower), Sembungan terrace (lower, contemporaneous with Ngandong), Ngleback (lowermost) and Menden terrace (outside of the Kendeng Hills and the Solo terrace sequence). We used the terrace chronology to identify the incision phases and constrain the age of the Ngandong terrace by its relative position in the terrace sequence (Extended Data Fig. 2). Third, we established a fossil context by re-excavating the Ngandong bone bed (Extended Data Fig. 6, Supplementary Information section 2) to better understand the sedimentology of the terrace fill, the taphonomy of the Ngandong fossil assemblage and to provide context-supported datable material. We applied laser-ablation U-series analyses[16] to 8 bovid teeth and 15 mammalian long bones (Supplementary Information section 7) and coupled US–ESR analyses to 3 additional fossil bovid teeth (Supplementary Information section 6).

According to the U-series-derived speleothem chronology (Supplementary Table 13), the Gunung Sewu section of the Southern Mountains had been uplifted and the Solo River had been diverted by >500 ka, which places a maximum age on the formation of the terrace sequence. Consistent with this, the red thermoluminescence, pIR-IRSL and $^{40}Ar/^{39}Ar$ chronologies indicate that the sequence of strath terraces was formed between 316 ± 28 and 31 ± 6 ka (with a maximum age of 358 ± 26 kyr), and are all chronologically consistent with their elevation (Extended Data Figs. 2, 8, Supplementary Figs. 1, 2, Supplementary Tables 6, 7, 12).

Our Ngandong excavations yielded a composite cross-section with five lithofacies comprising the Ngandong terrace fill: these lithofacies could be related to terrace-fill descriptions from excavations at the site in the 1930s, which yielded the *H. erectus* calvaria and tibiae[3,15] (Fig. 2, Extended Data Fig. 5, Supplementary Table 1, Supplementary Information section 2). All *H. erectus* fossils recovered in the original excavations were associated with facies C (gravelly sand bars). Our excavations yielded 867 in situ disarticulated non-hominin fossils—mostly isolated teeth and bone fragments, but largely complete elements were also observed[3,17] (Extended Data Fig. 6c, f, g). Usually, these fossils were

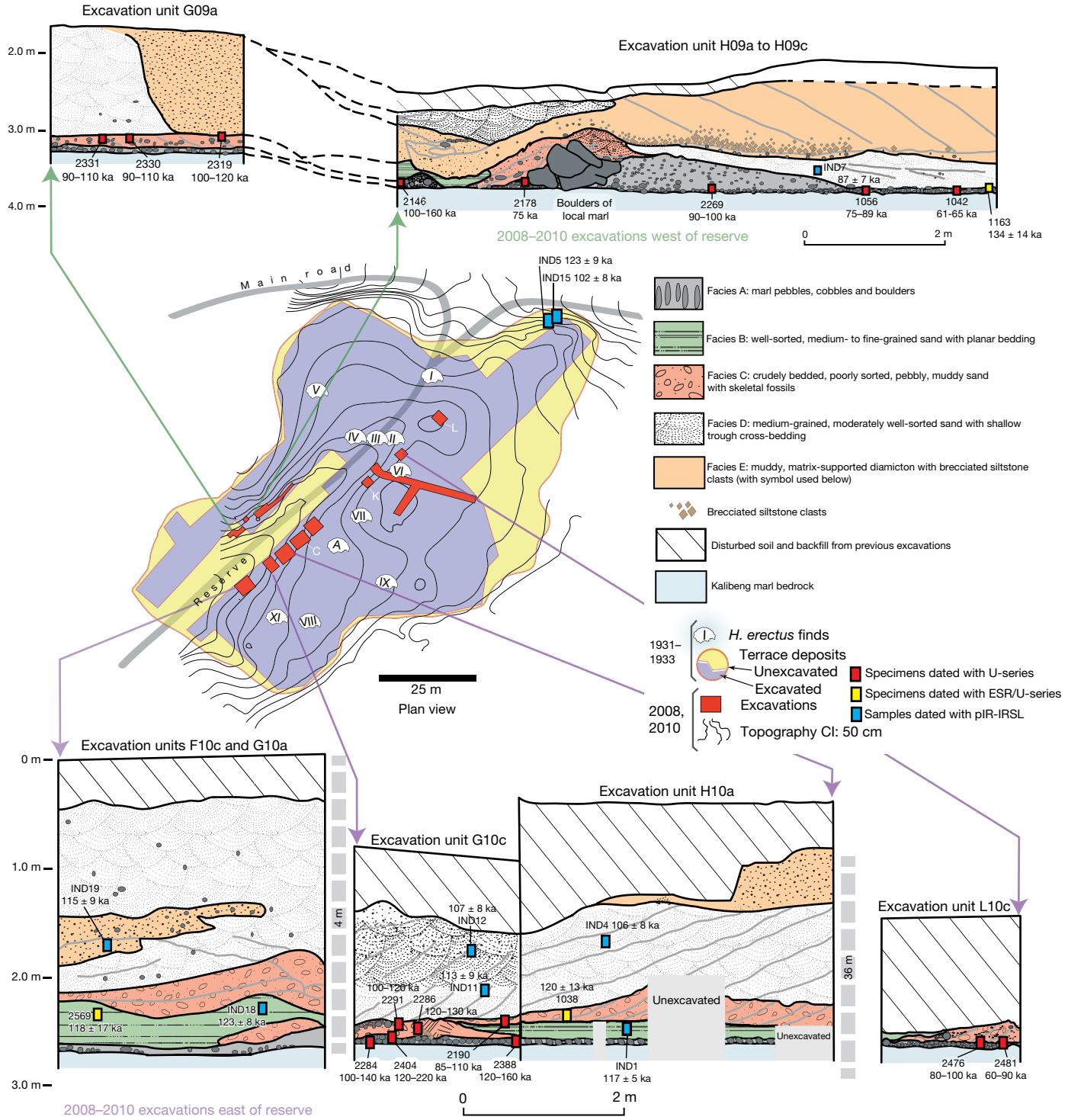


Fig. 2 | Cross-sections of Ngandong site, showing the stratigraphic context and the location of our dating samples. Depositional facies A–E, exposed in excavation bulkheads with collection points for pIR-IRSL samples (IND codes), US–ESR specimens and U-series diffusion–absorption–decay specimens (four-digit specimen numbers) (Supplementary Tables 6, 9, 10). Dated fossils not shown in the figure are 1026 and 1110 from excavation pit C (C on the plan-view map); 1075, 1076 and 1095 from pit L (L); and 1088 from pit K (K). Distances between pits east of the reserve are indicated on the grey dashed columns. The facies are present on the west and east sides of the archaeological reserve, but in different relative abundances. The Ngandong bone bed in facies C was generally excavated away in 1931–1933, but the underlying bone bed in facies A appears to be widely present at the site. The Ngandong *H. erectus* finds are labelled on the plan view map, following a previous publication[3]. I–XI represent the calvaria, and A represents one of the tibiae. Facies A is commonly one or two marl-cobbles thick, but also forms thicker bars. Facies B is moderately well-sorted, fine- to medium-grained sand with shallow-trough and ripple cross-laminations. Facies C is very coarse-grained, very poorly sorted, crudely cross-bedded and partially carbonate-cemented sand and pebbly granule conglomerate. Facies D is moderately well-sorted, medium- to coarse-grained, trough cross-bedded sand. Facies E is sandy gravelly muddy diamicton, which fills channels cut into facies B–D (and into which the bedding inclines). Extended Data Figure 6 and Supplementary Information section 3 provide additional lithological information. Scale bars apply to vertical and horizontal distances. CI, contour interval.

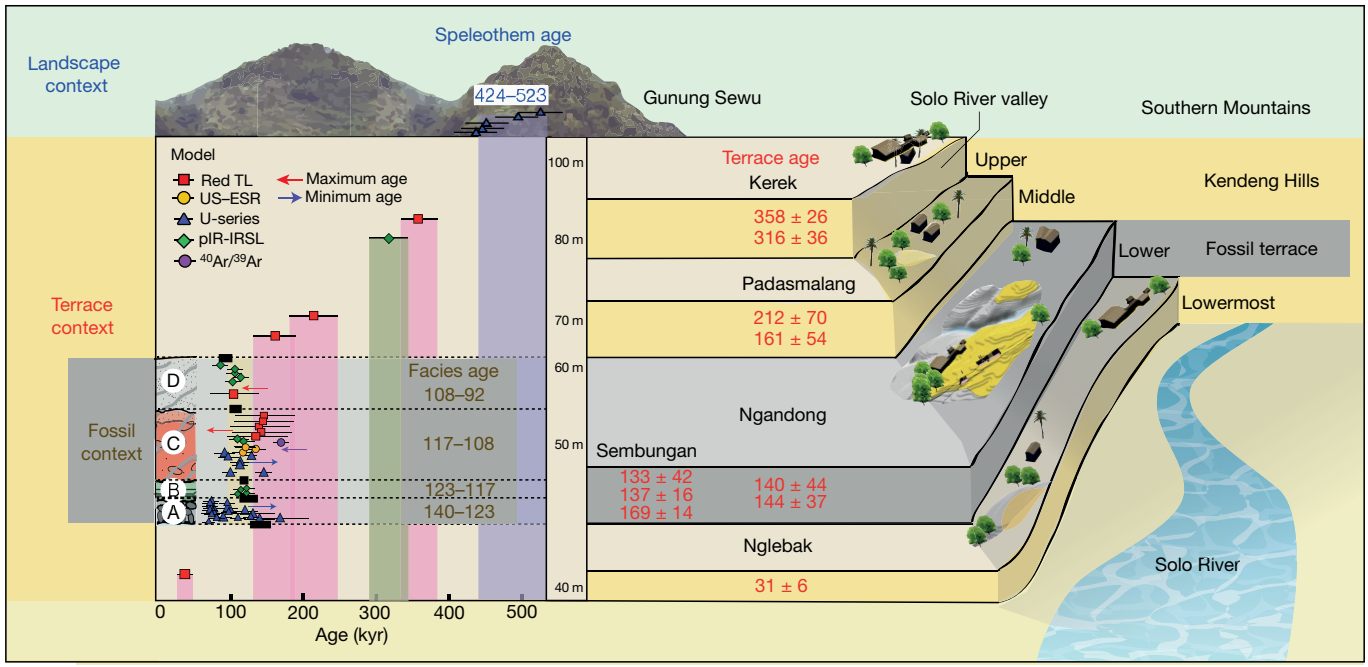


Fig. 3 | A regional chronology for the Ngandong evidence, summarizing the results of our approach. Composite chronology for the landscape, terrace and fossil context for the Ngandong site. All age ranges and errors are presented in kyr. Landscape context: constraining the evolution of the landscape from U-series dating of speleothems ($n = 5$) from the Gunung Sewu region of the Southern Mountains at an altitude of between 340–600 m (mean ages, with s.d. at 2σ uncertainties). Terrace context: from the red thermoluminescence and pIR-IRSL dating of quartz and feldspars, and $^{40}Ar/^{39}Ar$ dating of hornblende from the terrace deposits (mean ages with s.d. at 1σ uncertainties). Five terraces were dated in the region, from the oldest (Kerek; upper) down through Padasmalang (middle), Ngandong (lower), and Sembungan (lower) to Nglebak (lowermost), the youngest ($n = 21$). Relative terrace elevation in metres above mean sea level is shown, but is not to scale. Fossil context: this was provided by the excavations at Ngandong, in which four dating techniques were applied to the fossils and sediments ($n = 26$, mean ages with s.d. at 2σ uncertainties). The composite stratigraphy of the Ngandong terrace is shown. Facies A, B, C and D referring to the same facies shown in Fig. 2, with a thickness of about 2.5 m. All three contexts have been modelled to provide a Bayesian age for the boundaries between the facies at Ngandong (depicted as black rectangles with dashed lines in the model) with the resulting mean age ranges presented at 1σ uncertainties: 140 ± 24 to 123 ± 9 kyr (facies A), 123 ± 9 to 117 ± 6 kyr (facies B), 117 ± 6 to 108 ± 9 kyr (facies C) and 108 ± 9 to 92 ± 16 kyr (facies D). A larger version of this model can be found in Supplementary Information section 11. Symbols correspond to dating techniques: red thermoluminescence, red squares; US–ESR, yellow circles; U-series, blue triangles; pIR-IRSL, green diamonds; $^{40}Ar/^{39}Ar$, purple circle. Red and blue arrows denote maximum and minimum ages, respectively.

encased in a 10–25-cm-thick lens of poorly sorted fossil-rich muddy-pebble conglomerate that was deposited in a sediment-charged river (Fig. 2). Most of the 232 specimens that we analysed were broken before deposition, but more than 90% of them exhibit only minor abrasional rounding (Extended Data Fig. 7). Surface cracking and exfoliation indicative of substantial surface exposure is rare. No fossils show evidence of being reworked from a considerably older formation. Fossils from facies A and facies C have a similar taphonomy but fossils from facies C are larger, and more complete. No stone tools were discovered in this excavation. However, a concentration of 89 artefacts (dated to about 130 ka) was discovered in a contemporaneous Sembungan excavation located upstream of Ngandong (Extended Data Fig. 3, Supplementary Information section 3), and—when combined with the *Elephas* specimen discovered in the older Menden terrace, located downstream of Ngandong (Extended Data Fig. 4, Supplementary Table 5, Supplementary Information section 4)—this evidence provides an occupational context for the Ngandong hominins.

Laser-ablation U-series analysis yielded minimum age estimates of about 120 to 80 kyr and about 140 to 60 kyr for the mammalian long bones and eight bovid teeth, respectively (Extended Data Fig. 9, Supplementary Tables 10, 11). US–ESR dating of three additional bovid teeth provided age estimates corresponding to 134–118 ka (Extended Data Fig. 10, Supplementary Tables 8, 9). These age estimates for the Ngandong fauna agree with the age of deposition of the Ngandong terrace (144 ± 37 to 111 ± 9 kyr), the age of the upper and middle terraces (316 to 161 kyr), the maximum age for the lower terrace at Sembungan (169 ± 14 kyr) and the age of the lowermost terrace (31 ± 6 kyr), according to the red thermoluminescence, pIR-IRSL and $^{40}Ar/^{39}Ar$ dating. When these 52 dating results are entered into a Bayesian model (Fig. 3, Supplementary Tables 14, 15), an age range of 140–92 kyr is established for the deposition of the entire Ngandong terrace sequence, and a range of 117–108 kyr for the bone bed in facies C (Fig. 3), which contained the *H. erectus* material discovered in the 1930s.

Our modelled age range for the Ngandong terrace is substantially older than the direct $^{230}Th/^{234}U$ determinations (40 to 60–70 kyr) that have been reported for the Ngandong *H. erectus* calvaria[13], and is similar to previously reported combined U-series and ESR ages (corresponding to 77 to 143 kyr) for faunal teeth in the terrace at Jigar[14]. However, the upper age limit for the Ngandong site (of about 500 kyr) that was previously suggested on the basis of $^{40}Ar/^{39}Ar$ analyses of water-lain pumice from the Ngandong formation[14], and the age for Ngandong *H. erectus* calvaria of >200 kyr based on gamma-spectrometric U-series techniques[13], are at odds with our proposed age range for the bone bed (117–108 kyr) and our age for the next-oldest terrace in the sequence (162 ± 33 kyr). We believe that our bone-bed chronology is much closer to the actual age of Ngandong *H. erectus*.

Sedimentary and taphonomic observations at Ngandong are best explained by a single flood event, during which facies B, C and D accumulated in rapid succession[17] (Supplementary Information sections 2, 10). A reliable age estimate for the formation of the facies and the non-hominin fossils at Ngandong establishes a depositional age for the *H. erectus* remains (Fig. 2, Supplementary Information sections 5–9). The fossils show only incipient weathering and transport damage, despite being deposited in a river (Extended Data Fig. 7). The

preservation of delicate bony structures[3,17] and soft tissues (Supplementary Table 3) indicate limited exposure. The demise of *H. erectus* and other vertebrates evidently occurred upriver of Ngandong—possibly caused by the changing environmental conditions[17]. The skeletonized and disarticulated remains were then entrained by lahar flows[17] and monsoonal flooding of the Solo River (Supplementary Information section 10). The remains accumulated within large in-channel debris jams[21], owing to the narrowing of the valley at Ngandong, and triggered deposition in channel bars (facies A) and gravelly sand bars (facies C), shortly before sandy bedforms (facies D) and channelized mudflows (facies E) buried the bone beds.

This dated sedimentary and taphonomic framework for the Ngandong bone bed does not support an overlap between modern humans and *H. erectus* in this region[9,18,20]. Instead, the Ngandong fauna in facies A (140 ± 24 ka) pre-dates the rainforest-associated site of Punung (between 128 ± 15 and 118 ± 3 ka)[22], which agrees with the proposed biostratigraphical sequence of Java based on the palaeoenvironmental and associated faunal changes[23]. The *H. erectus* bone bed (facies C) overlaps with Punung and falls within the sea level lowstand at the onset of termination II (around 120 ka)[24]. Thus, it represents the last, dying remnants of the archaic fauna and open woodland environments that were superseded by the impeding rainforest flora and fauna associated with Punung (Supplementary Information section 10).

Furthermore, we can place Ngandong into a regional framework for Island Southeast Asia. *H. erectus* continuously inhabited the island, with dates on Java that start at 1.51 to 0.93 million years ago at Sangiran[1,2], then 540 to 430 ka at Trinil[25] and ending with 117 to 108 ka at Ngandong. *H. erectus* was dispersed widely by 700 ka, as shown by archaeological evidence for hominins at Mata Menge (Flores, Indonesia)[26] and Cagayan Valley (Luzon, Philippines)[27]. Two insular dwarf hominins are found on these outlying islands: *Homo floresiensis* at 100 to 60 ka[28] and *Homo luzonensis* at 66.7 ± 1 ka[29]. Phylogenetic relationships have yet to be determined for these two hominins, but they show morphological similarities with *H. erectus*[29]. Sharing similar temporal ranges, Ngandong *H. erectus*, *H. floresiensis* and *H. luzonensis* represent three evolutionary trajectories of *Homo* in Island Southeast Asia, each of which ended in extinction.

Genomic evidence from modern populations in New Guinea provides estimates for the dates of the arrival of another early hominin in Island Southeast Asia. Two Denisovan lineages diverged from the Altai Denisovans, one at about 363 ka and the other at about 283 ka[30]. These deep divergence dates provide evidence for the early arrival of Denisovans in Island Southeast Asia. Dispersing *Homo sapiens* encountered Denisovan lineages in Island Southeast Asia at about 45.7 ka[30] and at about 29.8 ka[30]. Additionally, a residual signal of approximately 1% archaic DNA in modern regional populations lies outside the human–Neanderthal–Denisovan clade[30]. This may reflect a past introgression event with *H. erectus* and provide evidence that these Denisovans encountered a late-surviving *H. erectus* population.

An increasingly complex picture of hominin evolution in Pleistocene Island Southeast Asia is emerging from fossil and genomic evidence. The chronology of Ngandong *H. erectus* is critical for this narrative. We have approached the age of the Ngandong site in three increasingly precise contexts: the Kendeng Hills landscape, the Solo River terraces and the Ngandong bone bed. Our age estimates for the vertebrate fossils—including *H. erectus*—at Ngandong are, therefore, firmly anchored within their regional chronological and geomorphical contexts. With modelled ages of 117 to 108 kyr, the Ngandong bone bed can finally assume its correct position in the hominin biostratigraphical sequence of Island Southeast Asia.

Online content

Any methods, additional references, Nature Research reporting summaries, source data, extended data, supplementary information, acknowledgements, peer review information; details of author contributions and competing interests; and statements of data and code availability are available at https://doi.org/10.1038/s41586-019-1863-2.

1. Larick, R. et al. Early Pleistocene $^{40}Ar/^{39}Ar$ ages for Bapang Formation hominins, Central Jawa, Indonesia. *Proc. Natl Acad. Sci. USA* **98**, 4866–4871 (2001).
2. Zaim, Y. et al. New 1.5 million-year-old *Homo erectus* maxilla from Sangiran (Central Java, Indonesia). *J. Hum. Evol.* **61**, 363–376 (2011).
3. Huffman, O. F., de Vos, J., Berkhout, A. W. & Aziz, F. Provenience reassessment of the 1931–1933 Ngandong *Homo erectus* (Java), confirmation of the bonebed origin reported by the discoverers. *Paleoanthropology* **2010**, 1–60 (2010).
4. Oppenoorth, W.F.F. Een nieuwe fossiele mensch van Java. *Tijdschrift van het Koninklijk Nederlandsch Aardrijkskundig Genootschap* **XLIX**, 704–708 (1932).
5. Frankel, M. Notes from an excavation. *Nature* https://doi.org/10.1038/news.2010.377 (2010).
6. Santa Luca, A. P. *The Ngandong Fossil Hominids: A Comparative Study of a Far Eastern* Homo erectus *Group* Yale University Publications in Anthropology 78 (Yale Peabody Museum, 1980).
7. Rightmire, G. P. *The Evolution of* Homo erectus: *Comparative Anatomical Studies of an Extinct Human Species* (Cambridge Univ. Press, 1990).
8. Schwartz, J. H. & Tattersall, I. *The Human Fossil Record: Volume Four – Craniodental Morphology of Early Hominids (Genera* Australopithecus, Paranthropus, Orrorin*) and Overview* (Wiley, 2005).
9. Swisher, C. C. III et al. Latest *Homo erectus* of Java: potential contemporaneity with *Homo sapiens* in southeast Asia. *Science* **274**, 1870–1874 (1996).
10. Bartstra, G.-J. et al. Ngandong man: age and artifacts. *J. Hum. Evol.* **17**, 325–337 (1988).
11. Rizal, Y. *Die Terrasse Entlang des Solo-Flusses in Mittel und Ost-Java, Indonesien.* PhD thesis, Universität zu Köln (1998).
12. Grün, R. & Thorne, A. Dating the Ngandong humans. *Science* **276**, 1575–1576 (1997).
13. Yokoyama, Y., Falguères, C., Sémah, F., Jacob, T. & Grün, R. Gamma-ray spectrometric dating of late *Homo erectus* skulls from Ngandong and Sambungmacan, Central Java, Indonesia. *J. Hum. Evol.* **55**, 274–277 (2008).
14. Indriati, E. et al. The age of the 20 meter Solo River terrace, Java, Indonesia and the survival of *Homo erectus* in Asia. *PLoS ONE* **6**, e21562 (2011).
15. Ciochon, R. L. et al. Rediscovery of the *Homo erectus* bed at Ngandong: site formation of a late Pleistocene hominin site in Asia. *Am. J. Phys. Anthropol.* **48**, 106 (2009).
16. Sambridge, M., Grün, R. & Eggins, S. U-series dating of bone in an open system: the diffusion-absorption-decay model. *Quat. Geochronol.* **9**, 42–53 (2012).
17. Huffman, O. F. et al. Mass death and lahars in the taphonomy of the Ngandong *Homo erectus* bonebed, and volcanism in the hominin record of eastern Java. *Paleoanthropology* **2010**, abstr. A14 (2010).
18. Westaway, M. C. Preliminary observations on the taphonomic processes at Ngandong and some implications for a late *Homo erectus* survivor model. *Tempus* **7**, 189–193 (2002).
19. Westaway, M., Jacob, T., Aziz, F., Otsuka, H. & Baba, H. Faunal taphonomy and biostratigraphy at Ngandong, Java, Indonesia and its implications for the late survival of *Homo erectus*. *Am. J. Phys. Anthropol.* **120**, abstr. 222–223 (2003).
20. Westaway, M. C. & Groves, C. P. The mark of ancient Java is on none of them. *Archaeol. Ocean.* **44**, 84–95 (2009).
21. Jenkins, K. et al. New excavations of a Late Pleistocene bonebed and associated MSA artifacts from Rusinga Island, Kenya. *Paleoanthropology* **2012**, abstr. A17 (2012).
22. Westaway, K. E. et al. Age and biostratigraphic significance of the Punung rainforest fauna, East Java, Indonesia, and implications for *Pongo* and *Homo*. *J. Hum. Evol.* **53**, 709–717 (2007).
23. de Vos, J. The *Pongo* faunas from Java and Sumatra and their significance for biostratigraphical and paleo-ecological interpretations. *Proc. Koninklijke Nederlandse Akademie van Wetenschappen, Series B* **86**, 417–425 (1983).
24. Railsback, L. B., Gibbard, P. L., Head, M. J., Voarintsoa, N. R. G. & Toucanne, S. An optimized scheme of lettered marine isotope substages for the last 1.0 million years, and the climatological nature of isotope stages and substages. *Quat. Sci. Rev.* **111**, 94–106 (2015).
25. Joordens, J. C. et al. *Homo erectus* at Trinil on Java used shells for tool production and engraving. *Nature* **518**, 228–231 (2015).
26. Brumm, A. et al. Age and context of the oldest known hominin fossils from Flores. *Nature* **534**, 249–253 (2016).
27. Ingicco, T. et al. Earliest known hominin activity in the Philippines by 709 thousand years ago. *Nature* **557**, 233–237 (2018).
28. Sutikna, T. et al. Revised stratigraphy and chronology for *Homo floresiensis* at Liang Bua in Indonesia. *Nature* **532**, 366–369 (2016).
29. Détroit, F. et al. A new species of *Homo* from the Late Pleistocene of the Philippines. *Nature* **568**, 181–186 (2019).
30. Jacobs, G. S. et al. Multiple deeply divergent Denisovan ancestries in Papuans. *Cell* **177**, 1010–1021 (2019).
31. Suminto, M. M., Sidarto, Maryanto, S., Susanto, E. E., Aziz, S. F., Christiana, I., & Fitriani, E. *A Study of the Solo River Terraces from Kerek to Karsono: Ngawi and Bojonegoro Regions, East Java* (Geological Research and Development Centre, 2004).
32. Sidarto & Morwood, M. J. Solo River terrace mapping in the Kendeng Hills area, Java: use of landsat imagery and digital elevation model overlays. *J. Sumber Daya Geologi* **14**, 196–207 (2004).

Publisher's note Springer Nature remains neutral with regard to jurisdictional claims in published maps and institutional affiliations.

© The Author(s), under exclusive licence to Springer Nature Limited 2019

Methods

To constrain age range of the Ngandong fossils, we considered three interrelated components: a landscape context, a terrace context and a fossil context.

Establishing the landscape context

The landscape evolution of central Java followed this sequence of events: (1) the seismic uplift of the Southern Mountains, (2) the northward diversion of the Solo River through the Kendeng Hills and (3) the resulting terrace formation, including that of the Ngandong terrace[33,34]. The timing of these events can be constrained by establishing the age of the oldest speleothem deposits in the Gunung Sewu (Fig. 1b) using U-series dating, which provides a minimum age for the uplift of the Southern Mountains, the diversion of the Solo River and the subsequent uplift of the Kendeng anticlinorium (which created the Kendeng Hills)—and thus a maximum age for terrace formation in the Solo River valley.

U-series dating of speleothems. U-series dating of flowstones and stalagmites provides minimum ages for the karstification of the Gunung Sewu, which was initiated by the uplift of the Southern Mountains. Calcite was sampled from the outer edges of the stalagmites using a hammer and chisel. Calcite crystals that were free of any weathered surfaces were extracted from each of these samples, and cleaned ultrasonically to remove as much sediment contamination as possible before they were subjected to chemical treatment and isotopic measurements by mass spectrometry[35]. U-series dating of the speleothem samples was conducted in the Radiogenic Isotope Facility (The University of Queensland), using a VG Sector 54 thermal ionization mass spectrometer (TIMS) and a Nu Plasma multi-collector inductively coupled mass spectrometer (MC-ICP-MS). Analytical procedures followed previous publications for TIMS and MC-ICP-MS[35–37]. $^{230}Th/^{234}U$ ages were calculated using Isoplot EX 3.75 (ref. [38]), and half-lives of 75,690 years (^{230}Th) and 245,250 years (^{234}U)[39].

Establishing the terrace context

As strath river terraces form in a sequence (with the oldest at the highest elevation and the youngest at the lowest), the age of the oldest Solo River terraces at Kerek (upper) and the youngest in Nglebak (lowermost) provide a maximum and minimum age range for the Ngandong terrace.

Strategy for identifying and dating the terraces. Initial mapping work in this region involved the use of digital elevation maps of the terraces created from a Landsat image (ETM7+ using bands 4, 5 and 7 merged with band 8) overlying a 1:25,000 topographical map, to produce a 15-m resolution digital elevation model[31,32]. Suitable sites were then chosen from each of the four identified terraces (lowermost, lower, middle and upper) within a designated study section from Kerek village in the south to Sunggun village in the north (Fig. 1c, Extended Data Fig. 1f). Compared to Sangiran and Mojokerto, the site of Ngandong is within much-younger clastic terrace deposits, which presents an opportunity to constrain the age of the deposition of the terrace using luminescence dating. This technique has yet to be successfully applied to this river system. The nature of the quartz and feldspar grains in this volcanic province is challenging, with no usable blue signal and high anomalous fading, respectively. This necessitates the use of red thermoluminescence dating techniques on quartz grains[40,41] and pIR-IRSL on feldspars[42]. This is supported by $^{40}Ar/^{39}Ar$ techniques on in situ pumice lens in the alluvium at Sembungan (low terrace).

Luminescence dating of quartz and feldspar grains from the fluvial terraces. At each site, a suitable sampling location was chosen, a section was dug to expose the terrace sediments and the stratigraphic characteristics were recorded. Sampling for luminescence dating was conducted using either opaque PVC pipes banged into the terrace (laboratory codes IND1–18 and NGD1–3) or—for the more-cemented terrace sediments—bulk sampling was conducted at night using subdued red-light conditions (laboratory code KER1). Quartz and feldspars grains of 90–125 μm were separated using standard purification procedures, including a final etch in 40% hydrofluoric acid for 45 min and 10% for 10 min, respectively, to remove the external alpha-dosed rinds[43]. The Solo River terraces yielded small amounts of quartz: 60 mg, with about 20 mg used for aliquots A and B of the dual-aliquot protocol (DAP) procedure[44] to derive the D_e estimates (Supplementary Table 6), and only about 40 mg remaining for additional testing. Therefore, feldspars were also analysed to support the sedimentary chronology, which also yielded small—but usable—amounts. All luminescence analysis was conducted at the 'Traps' luminescence dating facility at Macquarie University.

Using a DAP[44], isothermal red thermoluminescence emissions from quartz were detected using a red-sensitive photomultiplier tube (Electron Tubes S20 9658B). Quartz grains were mounted on stainless-steel discs using silicone oil spray; each large aliquot was composed of about 5,000 grains (around 10 mg). The isothermal red thermoluminescence emissions[45–47] were measured using a red-sensitive photomultiplier tube (Electron Tubes 9658B) and cooling tower (LCT50 liquid-cooled thermoelectric housing) with Kopp 2-63 and BG-39 filter combination[45]. Laboratory irradiations were conducted using a calibrated $^{90}Sr/^{90}Y$ beta source. D_e values were estimated from the 20–30-s interval of isothermal decay (which was bleachable by >380-nm illumination) using the final 160 s as background. Aliquots were heated to 260 °C at a heating rate of 5 K s^{-1} and then held at 260 °C for 1,000 s to minimize the unwanted thermoluminescence from incandescence.

To overcome the problems of anomalous fading[48], we adopted a standard pIR-IRSL protocol for single aliquots of feldspars using a 300 °C preheat and 270 °C pIR-IRSL stimulation combination, following a standard 50-°C infrared stimulation. The use of single-grain feldspar techniques was investigated but low sample sensitivities yielded very low acceptance rates (<0.5%) that were not practical considering the small amounts of sample yield. pIR-IRSL measurements were thus conducted on single aliquots of feldspars using infrared (875-nm) light-emitting diodes at 80% power for 200 s (to enable a long stimulation), and the emissions were detected using Schott BG-39 and Corning 7-59 filters to transmit wavelengths of 320–480 nm (ref. [49]). Four procedural tests were applied to small aliquots of about 1,000 grains using the following preheat and infrared stimulation combinations: (1) 250 and 225 °C (refs. [48,50]), (2) 280 and 250 °C (ref. [51]), (3) 300 and 270 °C (ref. [51]) and (4) 320 and 290 °C (refs. [52,53]). The tests were: (1) a preheat plateau test using 3 discs; (2) fading tests, including a prompt, 1-h, 10-h and 1-week delay; (3) bleaching tests using 1 fresh aliquot per temperature to determine the amount of residual IRSL after an extended bleach of 4 h in a solar simulator; and (4) dose recovery tests using 8 bleached aliquots (bleached using a solar simulator for 4 h) and a surrogate dose of 200 Gy. From these tests, it was determined that the 270-°C stimulation and 300-°C preheat combination plotted within the flattest part of the preheat plateau, provided the best recovery of the surrogate dose, with the least fading of all of the pIR-IRSL signals (g value = between 1.6–2.2% per decade) and lowest residual value (<10 Gy). In total, 24 aliquots were used to conduct a modified single-aliquot regenerative-dose (SAR) procedure. These resulting age estimates were corrected according to the results of the anomalous fading tests (using a weighted mean fading rate of 1.9 ± 0.3% per decade), but no residual corrections were undertaken.

Measurements of ^{238}U, ^{235}U, ^{232}Th (and their decay products) and ^{40}K were estimated using Geiger–Muller multi-counter beta-counting of dried and powdered sediment samples in the laboratory, and a portable gamma spectrometer in the field. The corresponding (dry) beta and gamma dose rates were obtained using previously published conversion factors[54] and beta-dose attenuation factors[55]. An effective internal

alpha dose rate of 0.03 Gy kyr^{-1} (ref. [56]) and 0.72 Gy kyr^{-1} (refs. [57,58]) were used for the 90–125-μm quartz and feldspar samples, respectively (owing to the radioactive decay of ^{40}K and ^{87}Rb), which were made assuming K (12.5 ± 0.5%)[57] and ^{87}Rb (400 ± 100 μg g^{-1})[58] concentrations, and was included in the total dose rate. Cosmic-ray dose rates were estimated from published relationships[59], making allowance for the sediment overburden at the sample locality (about 0.5-4.0 m), the altitude (around 60 m above sea level) and geomagnetic latitude and longitude (7° and 111°) of the sampling site. The total dose rate was calculated using a long-term water content of 5–15 ± 2%, which is close to the measured (field) water content of 5–15%. High-resolution gamma spectrometry of the powdered sediment samples was also conducted to test for disequilibrium within the uranium decay chain (Supplementary Table 7).

^{40}Ar/^{39}Ar dating of a pumice lens in the Sembungan terrace. ^{40}Ar/^{39}Ar dating of single and multiple hornblende crystals was conducted on a pumice lens (sample SS59B) taken from the middle of the Sembungan terrace, to provide the eruption age of the pumice and a maximum age of deposition for the terrace. The 10-cm-thick pumice lens was exposed in the western quarry wall over a length of 2.2 m at a depth of 2.0 m below datum, and 2.1 m above the base of the terrace fill. Euhedral hornblende crystals up to 1 mm in length were hand-picked under a binocular microscope and loaded into wells in aluminium sample discs (diameter 18 mm) for neutron irradiation, along with the astronomically calibrated 1.185-million-year-old Alder Creek sanidine[60] as the neutron fluence monitor. Neutron irradiation was performed for 0.25 h in the cadmium-shielded CLICIT facility at the Oregon State University TRIGA reactor.

Argon isotopic analyses of the gas released by laser fusion of hornblende crystals (Supplementary Table 12) was done on a fully automated, Nu Instruments Noblesse multi-collector noble-gas mass spectrometer, using previously documented instrumentation and procedures[61,62].

Estimating downcutting rates. We used the terrace chronology to establish downcutting rates for the Solo Valley in the Kendeng Hills. These rates were established by dividing the age of each alluvial terrace (in thousands of years) (Supplementary Table 6), by the distance of downcutting between each terrace (mm) to provide a downcutting rate (in millimetres per thousand years (mm kyr^{-1})) for each terrace level. Then, the age of the highest terrace was divided by the total distance to the river (66 m) to estimate an overall rate of downcutting (in mm kyr^{-1}) for the entire valley (Supplementary Information section 15). The mean errors associated with these red thermoluminescence and pIR-IRSL ages have been propagated through to the final downcutting rate, to obtain an error margin of ±8%.

Establishing the fossil context

The strategy for the Ngandong excavation consisted of locating the backfilled edges of the original excavated area along the margins of the original Netherlands Indies Survey reserve, using maps produced during the 1931–1933 excavations[3]. Our 115-m^2 excavation footprint encompassed several pits that paralleled the edges of the excavation reserve. We identified five lithofacies, comprising the terrace fill at Ngandong, and developed a composite cross-section that illustrated lateral facies relationships and the context of the bone bed within the sequence of deposits (Fig. 2, Supplementary Table 2). Attempts to date fossil teeth from facies A and facies C using radiocarbon were unsuccessful, as was initial optically stimulated luminescence dating of quartz from sediments. However, red thermoluminescence and pIR-IRSL dating of quartz and feldspars, respectively, from overbank terrace deposits, and U-series dating of fossil teeth and bones proved effective.

Laser-ablation U-series dating of fossil bone and teeth. Fifteen bone samples for U-series dating were collected during the 2010 field season (sample numbers 2146, 2178, 2190, 2216, 2269, 2284, 2286, 2291, 2319, 2330, 2331, 2388, 2404, 2476 and 2481) from facies A and facies C. Figure 2 gives the relative positions of these samples. Laser-ablation mass spectrometry to measure U-series isotopes along the cross-sections of these dense, mammalian long-bone fossils was carried out at the Australian National University[39,63–66] (Extended Data Fig. 9). Uranium and thorium concentrations were derived from repeated measurements of the NBS-610 standard, uranium-isotope ratios from the dentine of a rhinoceros tooth from Hexian[67]. Spot analyses were used, which have the advantages over continuous tracks by being able to avoid pores and optimize measurement conditions as well as counting statistics for each analysis. The laser was kept in one position for 100 s, ablating a small pit (132 μm in diameter, approximately 50 to 100-μm deep) in the bone. To address U-series age issues related to uncertainties in open-system uranium uptake, the ^{230}Th/^{238}U and ^{234}U/^{238}U datasets for each bone were fitted using a diffusion–absorption–decay model[68].

Coupled US–ESR dating of fossil teeth. Bovid molars were collected for US–ESR direct dating, and sectioned using a large diamond-blade rotating saw and polished to a 100-μm surface smoothness. Samples NDG-1038, NDG-1163, NDG-2074, NDG-2562, NDG-2566 and NDG-2569 were first analysed by laser-ablation ICP-MS (LA-ICPMS) quadrupole for uranium distribution, to assess the suitability of the samples for US–ESR dating. Only the samples NDG-1038, NDG-1163 and NDG-2569 were found to be suitable, and these samples were prepared following a previously developed protocol[66] (Extended Data Fig. 10). Each fragment was then measured at Southern Cross University on a Freiberg MS5000 ESR X-band spectrometer, and irradiated with the Freiberg X-ray irradiation chamber. ESR intensities were extracted from the merged spectra obtained from angular variation measurements[69,70] (for an example, see Extended Data Fig. 10b), after correcting for baseline, subtraction of isotropic signals and assessment of the contribution of non-oriented CO_2^- radicals (NOCORs) using previously published protocols[66,70] (for an example, see Extended Data Fig. 10c). Dose–response curves were obtained using the MCDOSE 2.0 software[71] (Extended Data Fig. 10a). U-series dating was conducted on both dentine and enamel at the University of Wollongong, using an ESI NW193 ArF Excimer laser coupled to a MC-ICP-MS Neptune Plus to calculate the internal dose rate. All age calculations were carried out with the US–ESR program[72], which uses previously published[73] dose rate conversion factors.

Modelling of landscape, terrace and excavation chronologies

To evaluate the uncertainties of the integrated dating approach of the landscape, terrace and fossil contexts (Supplementary Tables 6, 9, 10, 12, 13), Bayesian modelling was performed on all independent age estimates using the OxCal (version 4.2) software[74] available at https://c14.arch.ox.ac.uk/oxcal.html (Supplementary Tables 14, 15). The analysis incorporated the probability distributions of individual ages, and constraints imposed by stratigraphic relationships and the reported minimum or maximum nature of some of the individual age estimates. Each individual age was included as a Gaussian distribution (with mean and s.d. defined by the age estimate and their associated uncertainties). The U-series profiling ages on the fossil bone yielded a range of ages (160–60 kyr) and these were incorporated as a uniform distribution over this interval.

Data reporting

No statistical methods were used to predetermine sample size. The experiments were not randomized and investigators were not blinded to allocation during experiments and outcome assessment.

Reporting summary

Further information on research design is available in the Nature Research Reporting Summary linked to this paper.

Data availability

The data that support the findings of this study are included in the Supplementary Information. Additional data are available from the corresponding authors upon reasonable request.

Code availability

The Oxcal code used for the Bayesian model in this study is included in Supplementary Table 15.

33. Simandjuntak, T. O. & Barber, A. J. in *Tectonic Evolution of Southeast Asia (Geological Society Special Publication No. 106)* (eds Hall, R. & Blundell, D. J.) 185–201 (Geological Society of London, 1996).
34. Berghuis, H. W. K. & Troelstra, S. R. Plio-Pleistocene foraminiferal biostratigraphy of the eastern Kendeng zone (Java, Indonesia): the Marmoyo and Sumberingin sections. *Palaeogeogr. Palaeoclimatol. Palaeoecol.* **528**, 218–231 (2019).
35. Zhou, H. Y., Zhao, J. X., Wang, Q., Feng, Y. X. & Tang, J. Speleothem-derived Asian summer monsoon variations in central China during 54–46 ka. *J. Quat. Sci.* **26**, 781–790 (2011).
36. Clark, T. R. et al. Discerning the timing and cause of historical mortality events in modern *Porites* from the Great Barrier Reef. *Geochim. Cosmochim. Acta* **138**, 57–80 (2014).
37. Ludwig, K. R. *User's Manual for Isoplot 3.75. A Geochronological Toolkit for Microsoft Excel (Berkeley Geochronology Center Special Publication No. 5)* (Berkeley Geochronological Center, 2012).
38. Cheng, H. et al. The half-lives of uranium-234 and thorium-230. *Chem. Geol.* **169**, 17–33 (2000).
39. Eggins, S. M. et al. In situ U-series dating by laser-ablation multi-collector ICPMS: new prospects for Quaternary geochronology. *Quat. Sci. Rev.* **24**, 2523–2538 (2005).
40. Morwood, M. J. et al. Archaeology and age of a new hominin from Flores in eastern Indonesia. *Nature* **431**, 1087–1091 (2004).
41. Morwood, M. J. et al. Further evidence for small-bodied hominins from the Late Pleistocene of Flores, Indonesia. *Nature* **437**, 1012–1017 (2005).
42. Westaway, K. E. et al. An early modern human presence in Sumatra 73,000–63,000 years ago. *Nature* **548**, 322–325 (2017).
43. Huntley, D. J., Godfrey-Smith, D. I. & Thewalt, M. L. W. Optical dating of sediments. *Nature* **313**, 105–107 (1985).
44. Westaway, K. E. & Roberts, R. G. A dual-aliquot regenerative-dose protocol (DAP) for thermoluminescence (TL) dating of quartz sediments using the light-sensitive and isothermally stimulated red emissions. *Quat. Sci. Rev.* **25**, 2513–2528 (2006).
45. Spooner, N. A. & Franklin, A. D. Effect of the heating rate on the red TL of quartz. *Radiat. Meas.* **35**, 59–66 (2002).
46. Murray, A. S. & Mejdahl, V. Comparison of regenerative-dose single-aliquot and multiple-aliquot (SARA) protocols using heated quartz from archaeological sites. *Quat. Sci. Rev.* **18**, 223–229 (1999).
47. Huot, S., Buylaert, J.-P. & Murray, A. S. Isothermal thermoluminescence signals from quartz. *Radiat. Meas.* **41**, 796–802 (2006).
48. Thomsen, K. J., Murray, A. S., Jain, M. & Botter-Jensen, L. Laboratory fading rates of various luminescence signals from feldspar-rich sediment extracts. *Radiat. Meas.* **43**, 1474–1486 (2008).
49. Hütt, G., Jaek, I. & Tchonka, J. Optical dating: K-feldspars optical response stimulation spectra. *Quat. Sci. Rev.* **7**, 381–385 (1988).
50. Buylaert, J. P., Murray, A. S., Thomsen, K. J. & Jain, M. Testing the potential of an elevated temperature IRSL signal from K-feldspar. *Radiat. Meas.* **44**, 560–565 (2009).
51. Murray, A. S., Buylaert, J. P., Thomsen, K. J. & Jain, M. The effect of preheating on the IRSL signal from feldspar. *Radiat. Meas.* **44**, 554–559 (2009).
52. Thiel, C. et al. Luminescence dating of the Stratzing loess profile (Austria)—testing the potential of an elevated temperature post-IR IRSL protocol. *Quat. Int.* **234**, 23–31 (2011).
53. Thomsen, K. J., Murray, A. S. & Jain, M. Stability of IRSL signals from sedimentary K-feldspar samples. *Geochronometria* **38**, 1–13 (2011).
54. Stokes, S. et al. Alternative chronologies for late Quaternary (last interglacial–Holocene) deep sea sediments via optical dating of silt-sized quartz. *Quat. Sci. Rev.* **22**, 925–941 (2003).
55. Mejdahl, V. Thermoluminescence dating: beta-dose attenuation in quartz grains. *Archaeometry* **21**, 61–72 (1979).
56. Feathers, J. K. & Migliorini, E. Luminescence dating at Katanda—a reassessment. *Quat. Sci. Rev.* **20**, 961–966 (2001).
57. Huntley, D. J. & Baril, M. R. The K content of the K-feldspars being measured in optical dating or in thermoluminescence dating. *Ancient TL* **15**, 11–13 (1997).
58. Huntley, D. J. & Hancock, R. G. V. The Rb contents of the K-feldspars being measured in optical dating. *Ancient TL* **19**, 43–46 (2001).
59. Prescott, J. R. & Hutton, J. T. Cosmic-ray contributions to dose rates for luminescence and ESR dating: large depths and long-term time variations. *Radiat. Meas.* **23**, 497–500 (1994).
60. Rivera, T. A., Storey, M., Schmitz, M. D. & Crowley, J. L. Age intercalibration of $^{40}Ar/^{39}Ar$ sanidine and chemically distinct U/Pb zircon populations from the Alder Creek Rhyolite Quaternary geochronology standard. *Chem. Geol.* **345**, 87–98 (2013).
61. Brumm, A. et al. Hominins on Flores, Indonesia, by one million years ago. *Nature* **464**, 748–752 (2010).
62. Storey, M., Roberts, R. G. & Saidin, M. Astronomically calibrated $^{40}Ar/^{39}Ar$ age for the Toba supereruption and global synchronization of late Quaternary records. *Proc. Natl Acad. Sci. USA* **109**, 18684–18688 (2012).
63. Eggins, S., Grün, R., Pike, A. W. G., Shelley, A. & Taylor, L. ^{238}U, ^{232}Th profiling and U-series isotope analysis of fossil teeth by laser ablation-ICPMS. *Quat. Sci. Rev.* **22**, 1373–1382 (2003).
64. Grün, R. et al. U-series and ESR analyses of bones and teeth relating to the human burials from Skhul. *J. Hum. Evol.* **49**, 316–334 (2005).
65. Grün, R. et al. ESR and U-series analyses of enamel and dentine fragments of the Banyoles mandible. *J. Hum. Evol.* **50**, 347–358 (2006).
66. Grün, R., Aubert, M., Joannes-Boyau, R. & Moncel, M. H. High resolution analysis of uranium and thorium concentrations as well as U-series isotope distributions in a Neanderthal tooth from Payre using laser ablation ICP-MS. *Geochim. Cosmochim. Acta* **72**, 5278–5290 (2008).
67. Grün, R. et al. ESR and U-series analyses of teeth from the palaeoanthropological site of Hexian, Anhui Province, China. *J. Hum. Evol.* **34**, 555–564 (1998).
68. Grün, R., Eggins, S., Kinsley, L., Moseley, H. & Sambridge, M. Laser ablation U-series analysis of fossil bones and teeth. *Palaeogeogr. Palaeoclimatol. Palaeoecol.* **416**, 150–167 (2014).
69. Joannes-Boyau, R. & Grün, R. A comprehensive model for CO_2^- radicals in fossil tooth enamel: implications for ESR dating. *Quat. Geochronol.* **6**, 82–97 (2011).
70. Joannes-Boyau, R. Detailed protocol for an accurate non-destructive direct dating of tooth enamel fragment using electron spin resonance. *Geochronometria* **40**, 322–333 (2013).
71. Joannes-Boyau, R., Duval, M. & Bodin, T. MCDoseE 2.0 A new Markov chain Monte Carlo program for ESR dose response curve fitting and dose evaluation. *Quat. Geochronol.* **44**, 13–22 (2018).
72. Shao, Q., Bahain, J. J., Dolo, J. M. & Falguères, C. Monte Carlo approach to calculate US-ESR age and age uncertainty for tooth enamel. *Quat. Geochronol.* **22**, 99–106 (2014).
73. Guérin, G., Mercier, N. & Adamiec, G. Dose rate conversion factors: update. *Ancient TL* **29**, 5–8 (2011).
74. Bronk Ramsey, C. Radiocarbon calibration and analysis of stratigraphy: the OxCal program. *Radiocarbon* **37**, 425–430 (1995).

Acknowledgements This research, including the Solo River survey and the Sembungan and Menden terrace excavations, was funded by the Australian Research Council Discovery grant (DP1093049) to K.E.W. and (DP0343334 and DP0770234) to M.J.M. The 2008–2010 excavations at Ngandong were supported by the Wenner-Gren Foundation for Anthropological Research (ICRG-92), University of Iowa (UI) Center for Global and Regional Environmental Research (CGRER), UI Office of the President, UI Dean of the College of Liberal Arts and Sciences and the UI Office of the Vice-President for Research (to R.L.C.). The Menden excavations were financially supported by the Geological Survey Institute in Bandung (GSI). Laboratory costs were funded, in part, by the Human Evolution Research Fund at the University of Iowa Foundation. The $^{40}Ar/^{39}Ar$ dating was funded by the Villum Foundation. The authors acknowledge the invaluable support provided by A. D. Wirakusaman, and the support of E. A. Subroto. Excavations at Sembungan were undertaken under a recommendation letter from the Provincial Government of West Java to the Governor of the Central Java Province no. 070.10/237; a recommendation letter from the latter to the local government of the Blora Regency no. 070.10/237; and a research permit issued by the Blora Regency no. 071/457/2005. Excavations at Ngandong were carried out with the permission and recommendation of Wahyu, Head of the Foreign Researchers Licensing Secretariat of the State Ministry of Research and Technology (SMRT), which issued research permits 03799/SU/KS/2006, 1718/FRP/SM/VII/2008, and 04/TKPIPA/FRP/SM/IV/2010 for the fieldwork at Ngandong. The excavations at Sembungan and the Menden Terrace site in the Blora Regency were carried out under research permit no. 2785/FRP/SM/XI/2008. We thank K. M. Patel for help with figure creation and editorial assistance with the manuscript.

Author contributions Y.R., Y.Z., E.A.B. III, O.F.H., R.L.C., R.G., A., M.E.S., R.L., R.S. and S.P. carried out the 2008 and 2010 excavations at Ngandong, organized by Y.Z. and R.L.C. The Solo River survey and Sembungan and Menden terrace excavations were carried out by K.E.W., M.J.M., G.D.v.d.B., Sidarto, I.K., M.W.M., F.A. and Suminto. Dating of samples and age modelling was conducted by K.E.W., R.G., R.J.-B., R.M.B., M.S., J.-x.Z. and faunal analysis by R.S., J.-P.Z. and G.D.v.d.B. M.W.M. analysed the stone artefacts from Sembungan. This manuscript was written and edited by K.E.W., R.L.C., M.C.W., O.F.H., G.D.v.d.B., E.A.B. III and R.L. with sections of the Methods and Supplementary Information written by K.E.W., O.F.H., R.L.C., E.A.B. III, R.G., R.M.B., J.-x.Z., M.W.M. and M.S. All authors commented on and contributed to the manuscript.

Competing interests The authors declare no competing interests.

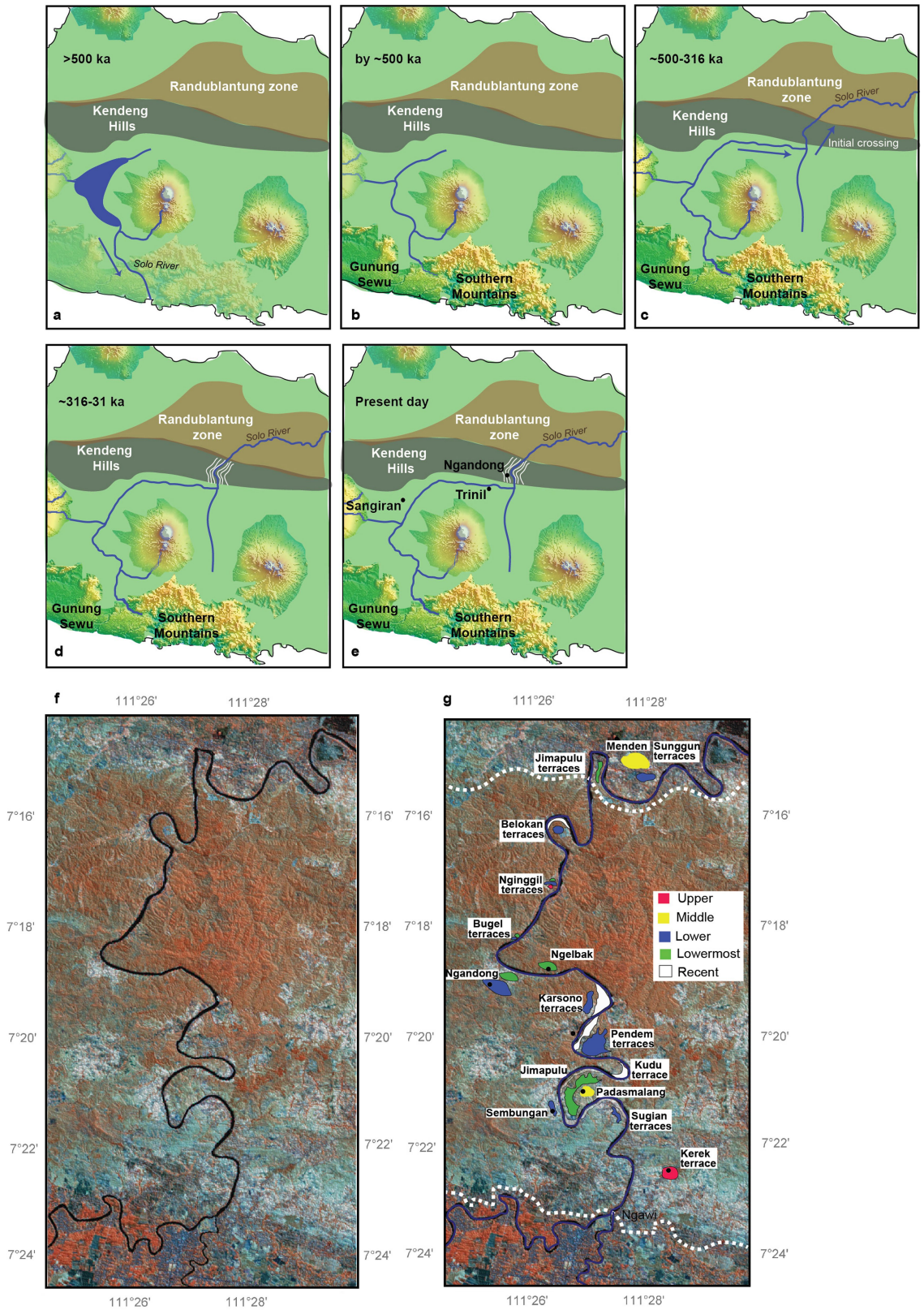
Additional information

Supplementary information is available for this paper at https://doi.org/10.1038/s41586-019-1863-2.

Correspondence and requests for materials should be addressed to K.E.W. or R.L.C.

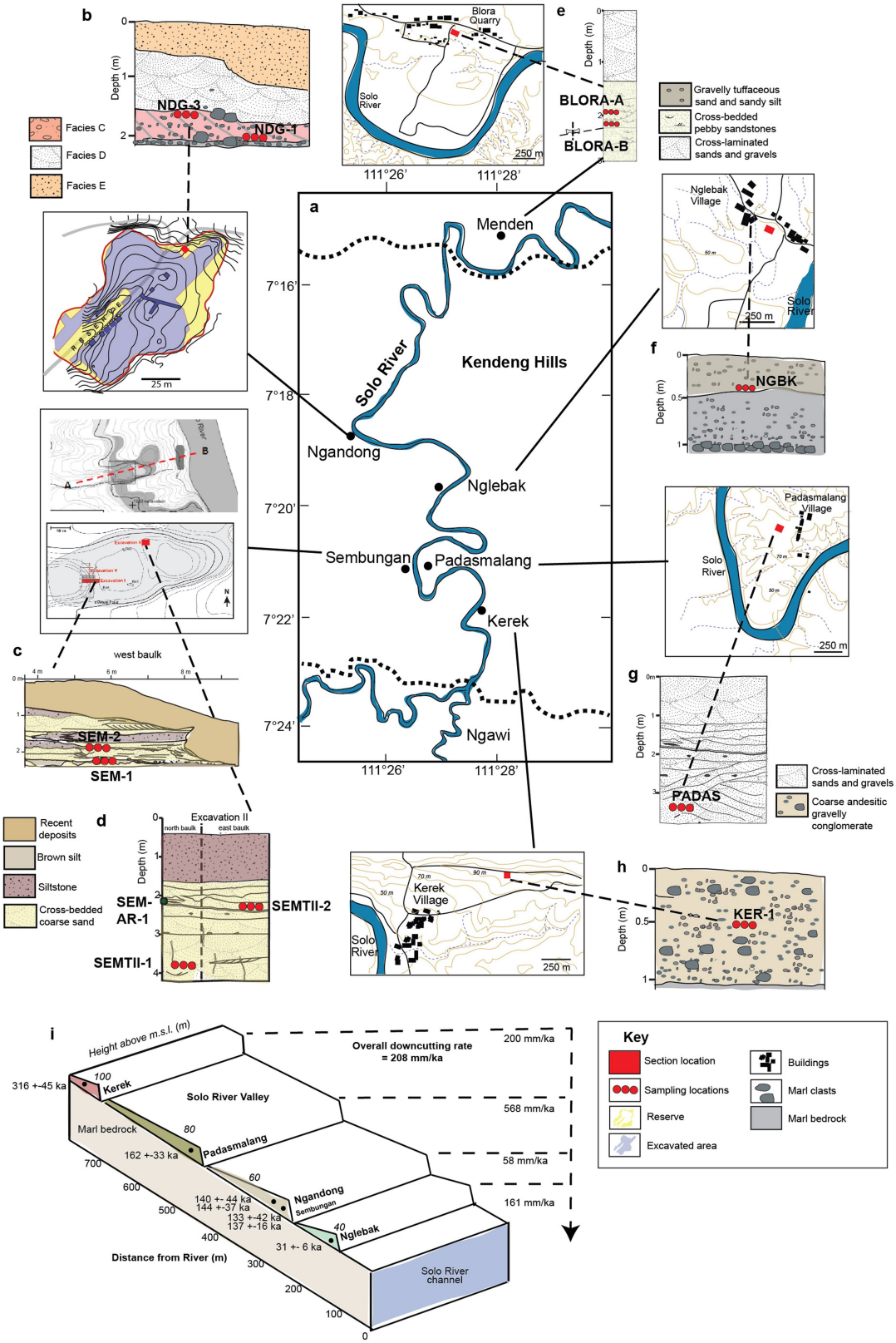
Peer review information *Nature* thanks Robin Dennell, James K. Feathers, Edward J. Rhodes and the other, anonymous, reviewer(s) for their contribution to the peer review of this work.

Reprints and permissions information is available at http://www.nature.com/reprints.

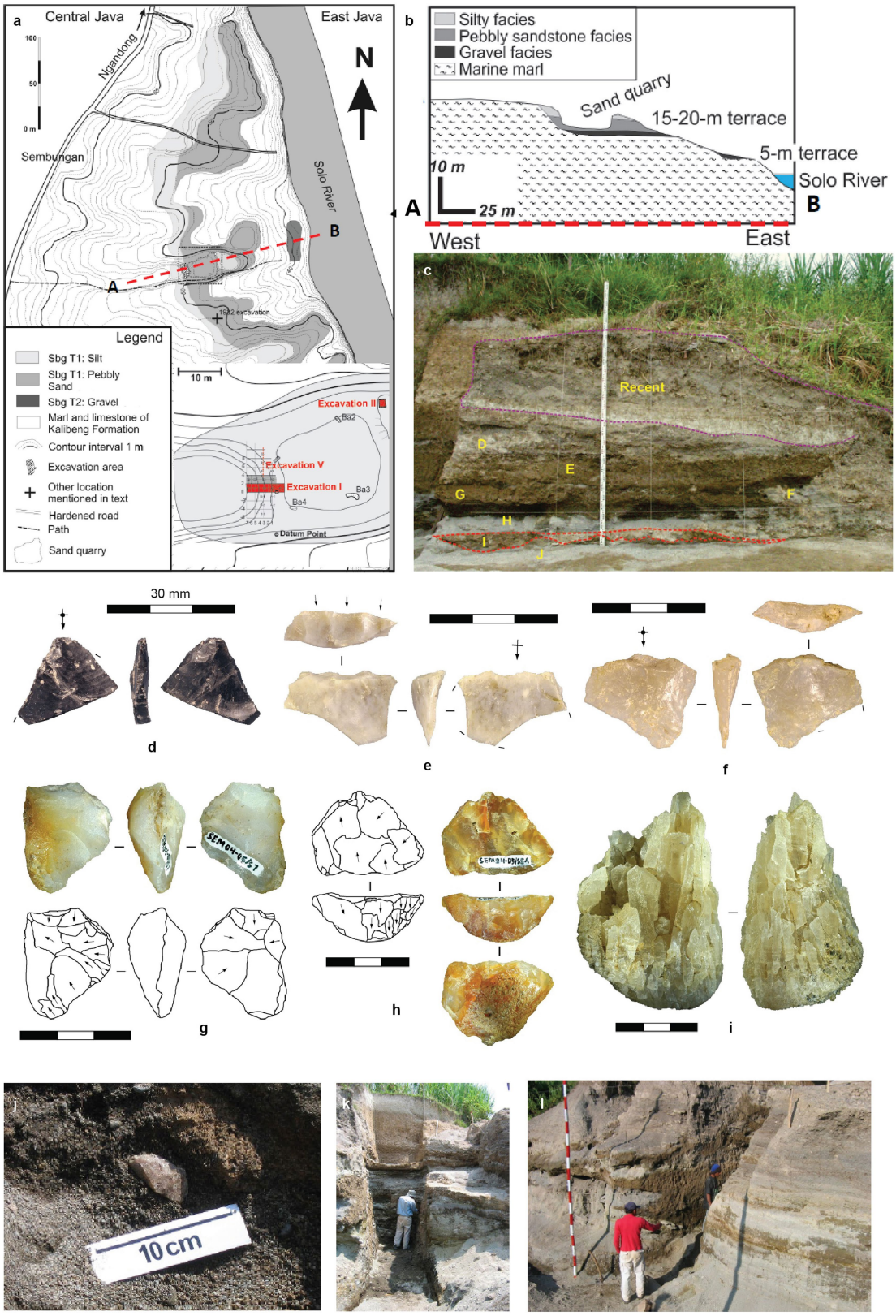


Extended Data Fig. 1 | See next page for caption.

Extended Data Fig. 1 | Evolutionary and geomorphical history of region. The landscape evolutionary stages that created the Solo River terraces. Drawn from refs. [2,3] on a topographical map from the USGS EROS. **a**, More-than 500-ka drainage from the proto-Merapi and Lawu volcanic highlands formed a lake or lagoon from which the proto-Solo River drained to the south (blue arrow), close to the present-day Pacitan region, and another branch flowed to the north of Lawu. By at least 1.5 million years ago, the Southern Mountains to the south and the Kendeng anticlinorium to the north were slowly emerging, forming the Gunung Sewu, and the Kendeng Hills (previously the Randublantung marine embayment[2]), respectively. **b**, By about 500 ka, the seismically uplifted Southern Mountains had blocked the southern exit of the Solo River to the ocean, and the area was dominated by trunk streams of the Solo River. **c**, Between about 500 and 316 ka, the Solo River abandons its southern trunk stream and extends its northern branch, where it is diverted to the west and northeast and carves an initial crossing through the Kendeng Hills to form the Solo River gap, and drain into the ocean to the north of Surabaya. **d**, Between about 316 and 31 ka, the uplifting Kendeng anticlinorium and the drainage from the Madiun Basin energized the Solo River, causing incision and forming the Solo River sequence of terraces (white parallel lines). **e**, Present-day Solo Basin and known fossil sites on exposed terraces. **f**, A digital elevation model[31,32], comprising a satellite image overlying a topographical map of the section of the Solo River system from Kerek village in the south to Sunggun village in the north (USGS Landsat). **g**, The same digital elevation model, with the classification scheme for the Solo River terraces with the upper, middle, lower and lowermost terraces identified. This image includes the key terrace sites that are sampled in this study; Kerek (upper), Padasmalang (middle), Sembungan (lower), Nglebak (lowermost) and Menden (outside of the Kendeng Hills, but contemporaneous with the upper and middle terraces), and the key fossil site of Ngandong (lower). The white dashed line indicates the limits of the Kendeng Hills. The Menden terrace lies outside of this divide, as does the westward-bearing Solo River and the site of Trinil.

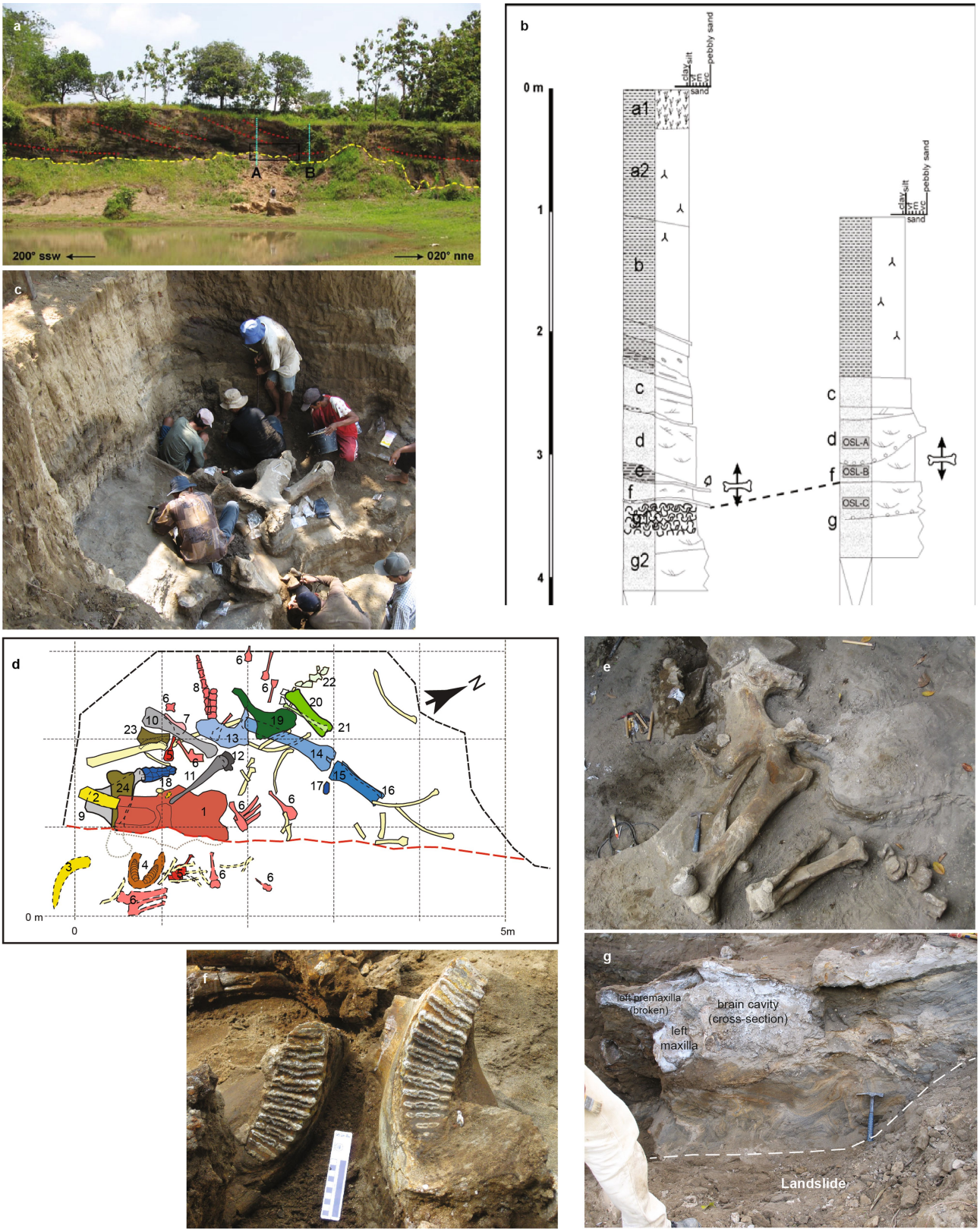


Extended Data Fig. 2 | Terrace-site stratigraphy and luminescence sampling. **a**, Map of the Kendeng Hills section of the Solo River from Ngawi to Menden, displaying the location of the six studied sites. Each site has a smaller inset showing the site locations, stratigraphic sections of the strath terraces and sampling locations for luminescence dating. **b**, Ngandong; the inset for the Ngandong site is shown in more detail to identify the exact location of the sampling site within the context of previous excavations. **c**, Sembungan excavation I. **d**, Sembungan excavation II. **e**, Menden. **f**, Nglebak. **g**, Padasmalang. **h**, Kerek. **i**, Three-dimensional slice of the Solo River valley, showing the terrace sequences and resulting downcutting rates (derived from 21 terrace samples ($n = 21$), mean ages with uncertainties presented at 1σ) plotted according to elevation and distance away from the river. The associated downcutting rates have been presented for each terrace, and for the river system as a whole.



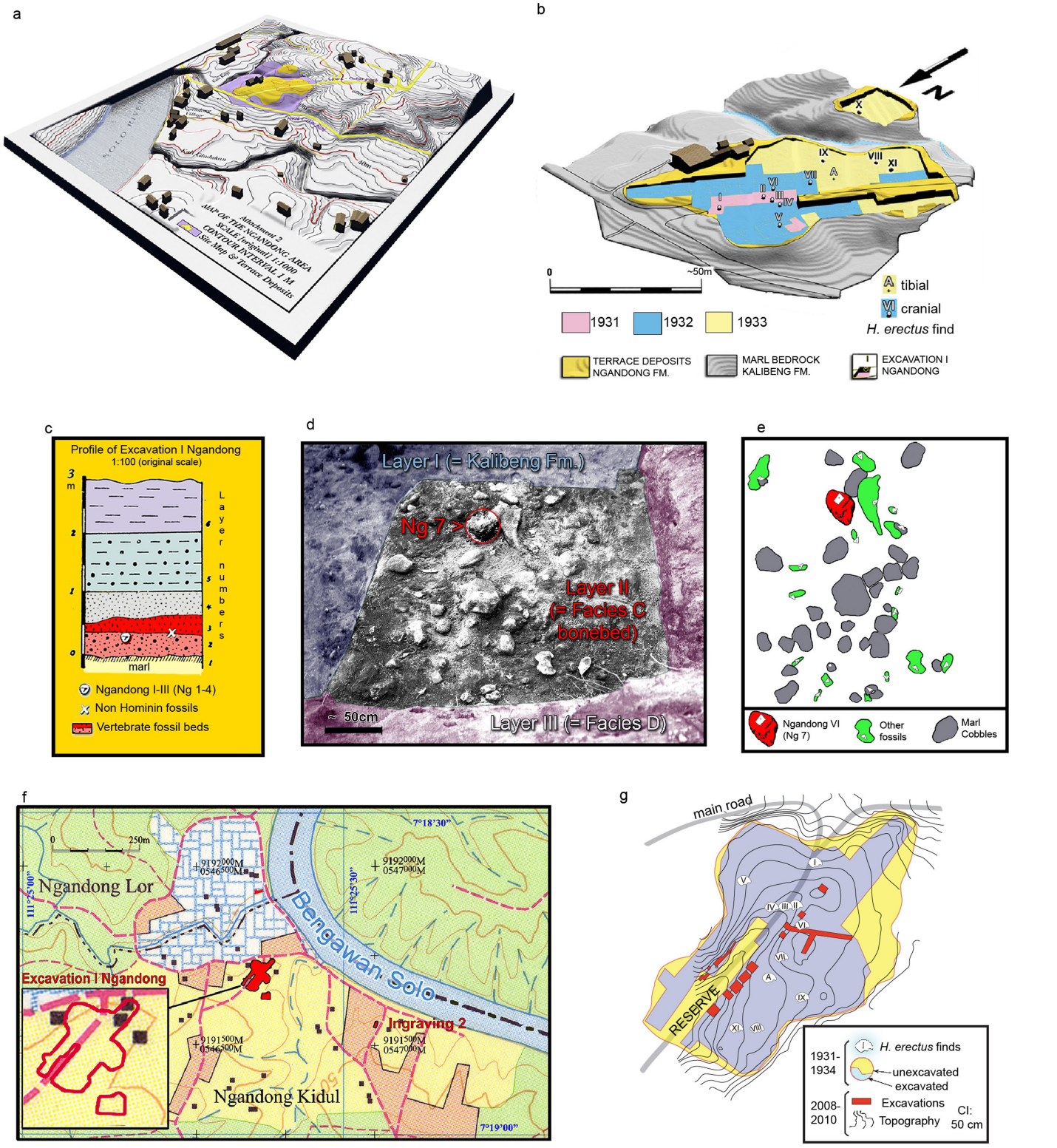
Extended Data Fig. 3 | See next page for caption.

Extended Data Fig. 3 | Stratigraphy and artefacts of the Sembungan excavations. a, Map of the Sembungan terrace, showing the lithology of the terrace and the location of the terrace rise in relation to the Solo River. The bottom-right inset shows the locations of the excavations I, II and V. **b**, A profile of the terrace along the A–B transect from A (marked by a red dashed line), showing the location of the sand quarry excavations in relation to the river. **c**, The west baulk of excavation I (marked on the inset in A), showing the stratigraphic layers and location of the stone artefact concentration (red dashed line at the base of the section). Layer J, very coarse sand; layer I, brown silt; layer H, cross-bedded coarse pebbly sand; layer G, lenses of siltstone; layer F, disturbed; layer E, massive siltstone; layer D, caliche palaeosol. **d**–**i**, Stone artefacts excavated in situ from Sembungan. **d**, Obsidian flake. **e**, Chert flake with unifacial retouching to the ventral surface across the proximal end, removing the point of force application. **f**, Chalcedony flake. **g**, **h**, Chalcedony centripetal cores. **i**, Quartz crystal cluster. Scale bars, 30 mm. **j**, A stone tool in situ from the Sembungan excavation V. **k**, Excavation I (inset in **a**). **l**, Excavation II (inset in **a**).



Extended Data Fig. 4 | See next page for caption.

Extended Data Fig. 4 | Menden stratigraphy and fossils. a, The quarry site of Blora on the Menden terrace near Sunggu (Central Java, Indonesia), to the north of the Kendeng Hills. The red dashed lines depict mega cross-bedding in the fluvial terrace. The vertical blue lines correspond to the stratigraphic section shown in **b** the yellow dashed line depicts the landslide scarp, and the black box shows the location of an almost-complete elephant skeleton. **b**, The stratigraphy of the Menden terrace according to logs A and B (marked on **a**). The upper a1, a2 and b layers represent cross-laminated sands and gravels, and the lower c–g layers represent cross-bedded pebbly sandstones. The relative location of the elephant skeleton can be seen by the fossil symbol. **c**, The excavation of the Menden terrace to recover the elephant skeleton (*Elephas hysudrindicus*)—a rare elephant species, endemic to Java. **d**, Site plan of the partial *E. hysudrindicus* skeleton excavated from the Menden terrace. Thick dashed line indicates extension of the excavation. Red dashed line indicates the boundary of the quarry wall at the time the fossil was discovered. All fossils recovered south of this boundary were found in a landslide at the foot of the quarry wall. 1, partial skull; 2, right tusk; 3, left tusk; 4, mandible; 5, cervical vertebrae; 6, thoracic vertebrae; 7, lumbar vertebrae; 8, caudal vertebrae; 9, right scapula; 10, right humerus; 11, right radius; 12, right carpals; 13, right pelvis; 14, right femur; 15, right tibia; 16, right fibula; 17, right patella; 18, right pes (articulated); 19, left pelvis; 20, left tibia; 21, left radius; 22, left tarsals; 23, left scapula fragment; 24, left humerus; pale yellow bones are ribs. **e**, The right pelvis and femur of the elephant in articulation, lying next to the left tibia and fibula and tarsals. **f**, The broken lower jaw of the elephant, with teeth, recovered from the landslide. **g**, The skull of the elephant in cross-section, as found in the landslide scar. Convoluted sediment layers can be seen below the skull.



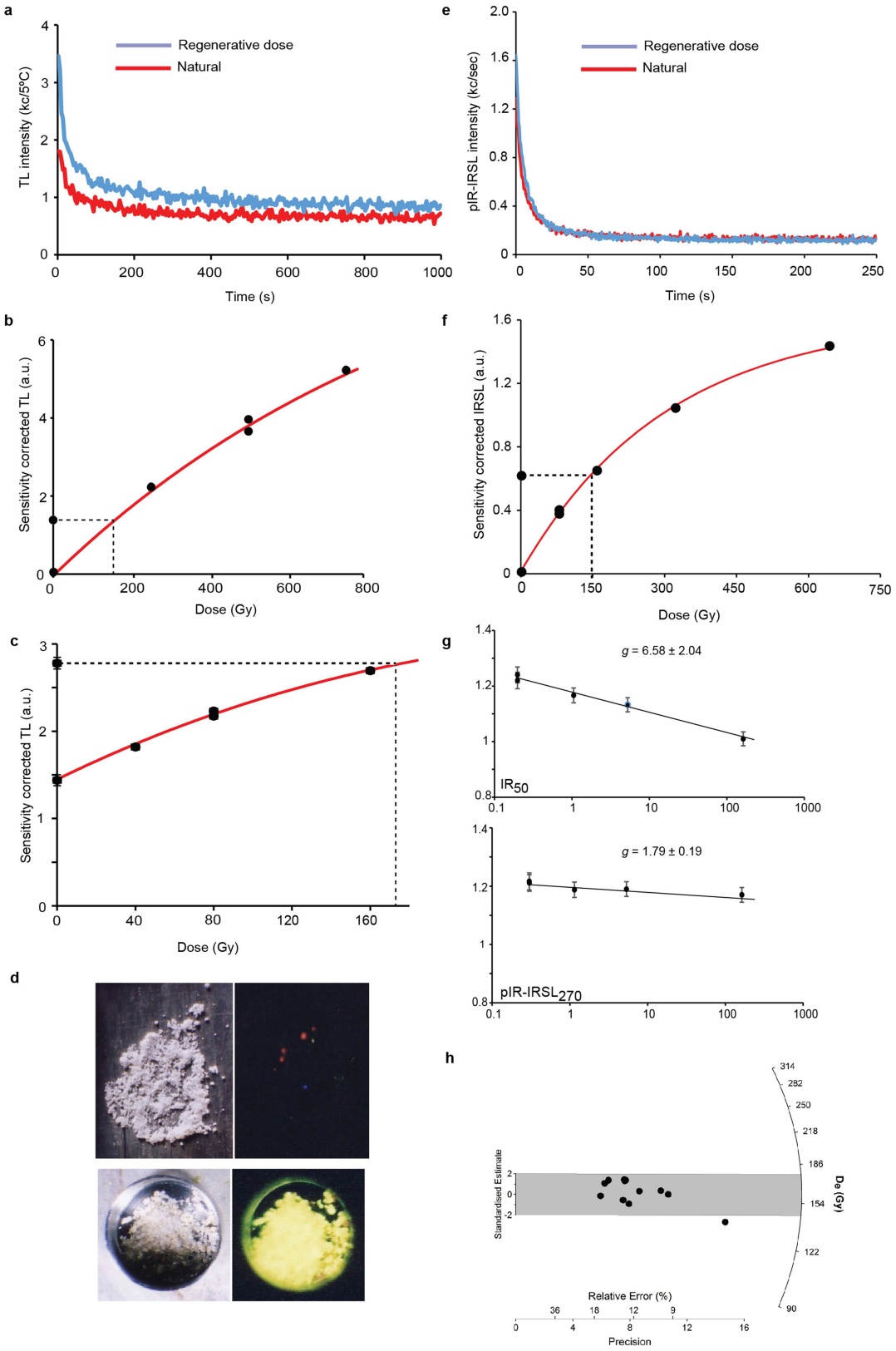
Extended Data Fig. 5 | History of *H. erectus* excavations at Ngandong. **a**, Aerial view of Ngandong, created from an unpublished map produced by the Geological Survey of the Netherlands Indies, who discovered the site and documented the unearthing of 14 *H. erectus* specimens. **b**, Extent of the 27-month-long, 1931–1933 excavations, including *H. erectus* finds[3]. The excavations produced about 25,000 fossils from the Ngandong terrace (originally referred to as the 20-m terrace) deposits[3]. **c**, Redisplay and translation of an original stratigraphic profile, published by the Geological Survey of the Netherlands Indies, showing the first four *H. erectus* discoveries made in 1931[3,4]. **d**, Day-of-discovery photograph of Ngandong VI (Ng 7), which is a whole fossil calvaria[3]. **e**, Plan-view drawing of the excavation square that included Ngandong VI, embedded in a river deposit of very coarse-grained volcaniclastic sand, along with marl cobbles and other vertebrate fossils[3]. **f**, Location of the site in the greater Ngandong area. **g**, Total data station mapping allowed the 1931–1933 excavated area to be repositioned on the landscape, including the 1931–1933 *H. erectus* discovery points (Extended Data Fig. 6). Panels **a**–**f** are redrawn from a previous publication[3].



Extended Data Fig. 6 | Photographs of 2008 and 2010 excavations at Ngandong including fossil discoveries. a, View of Ngandong site before the 2008 excavation, facing northwest. The orange string line marks the extent of the 1931–1933 excavations[3]. **b**, Collection of samples for optically stimulated luminescence dating, from facies B and C in pit A from 2008 (excavation unit H10a of the 2010 excavation). **c**, Bovid scapula and other fossils found in facies C in H10a from 2010. **d**, Excavations underway in excavation units H10a (foreground) and H10c (being dug) in 2010. **e**, Stratigraphy seen in the northwest wall of excavation unit H10a in 2010. Facies E is seen above the remnant of facies A, B, C and D, which are visible in the bottom half of this section. **f**, Exposed bone bed in facies A and C in excavation unit G09 from 2010. **g**, Fossils collected during 2010 excavation. Photographs **a**, **c** and **e** are by O.F.H. All other photographs are by R.L.C.

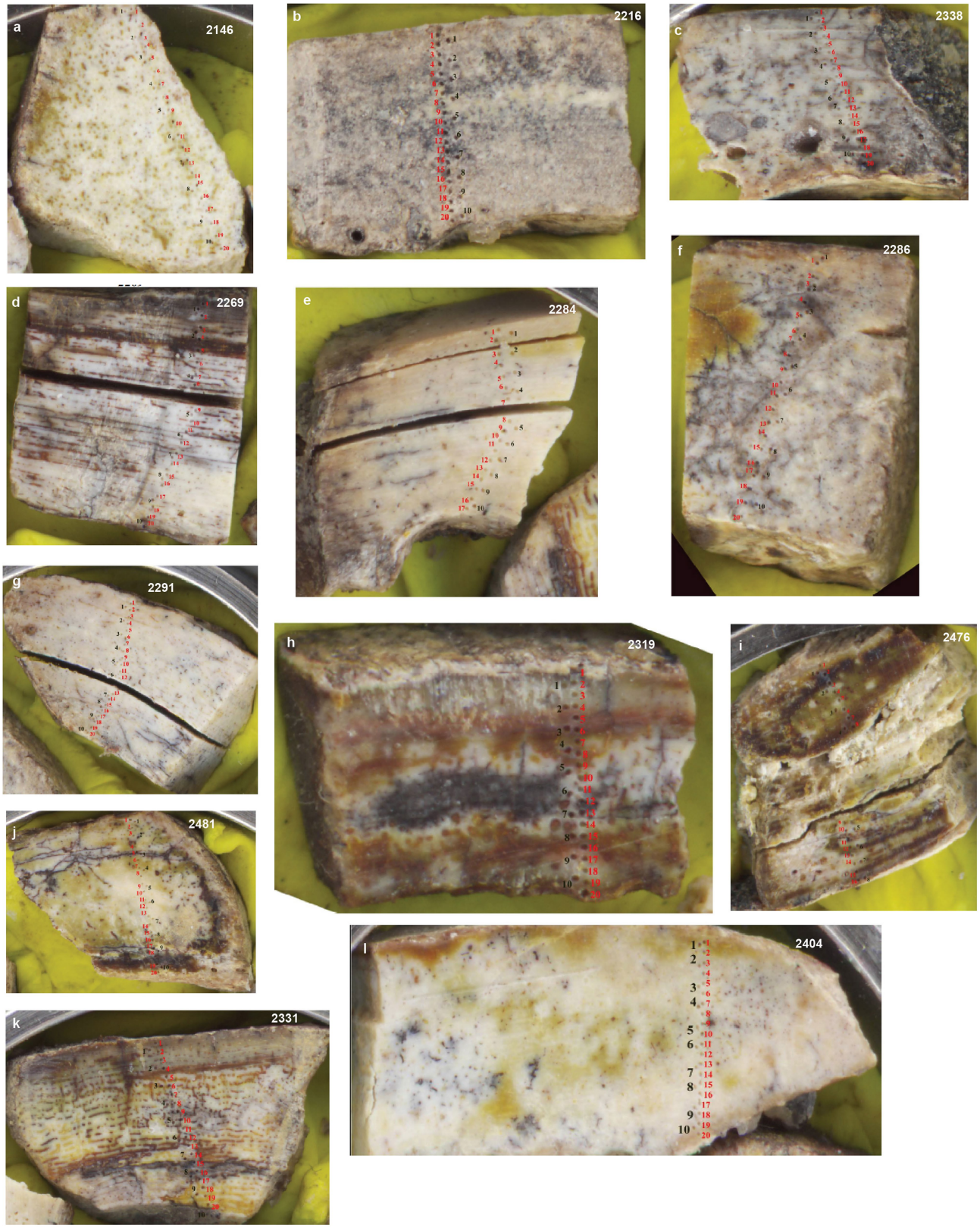


Extended Data Fig. 7 | Fauna from Ngandong recovered during the 2008–2010 excavations. a, Cervid antler, cf. *Axis* sp., specimen NDG 2306. **b**, Lower right M3, cf. *Bos* sp., specimen NDG 1134. **c**, Bovid incisor (Ix), cf. *Bubalus* sp. NDG 1106. **d**, Bovid cervical vertebra (atlas), specimen NDG 2149. **e**, Bovid tooth (*Bubalus* sp.), specimen NDG 1131. **f**, Cervid tooth, cf. *Cervus* sp., specimen NDG 2074. **g**, Bovid tooth (*Bubalus* sp.), specimen NDG 1038. **h**, Bovid tooth (*Bubalus* sp.), specimen NDG 2569. **i**, Bovid tooth (*Bubalus* sp.), specimen NDG 1163. **j**, Artiodactyl canon bone, specimen NDG 2148. **k**, Artiodactyl hoof, specimen NDG 2199. Specimens NDG-1038, NDG-1163 and NDG-2569 (**e**, **g** and **i**) provided results for US–ESR age calculations (Extended Data Fig. 10). All photographs are by J.-P.Z.

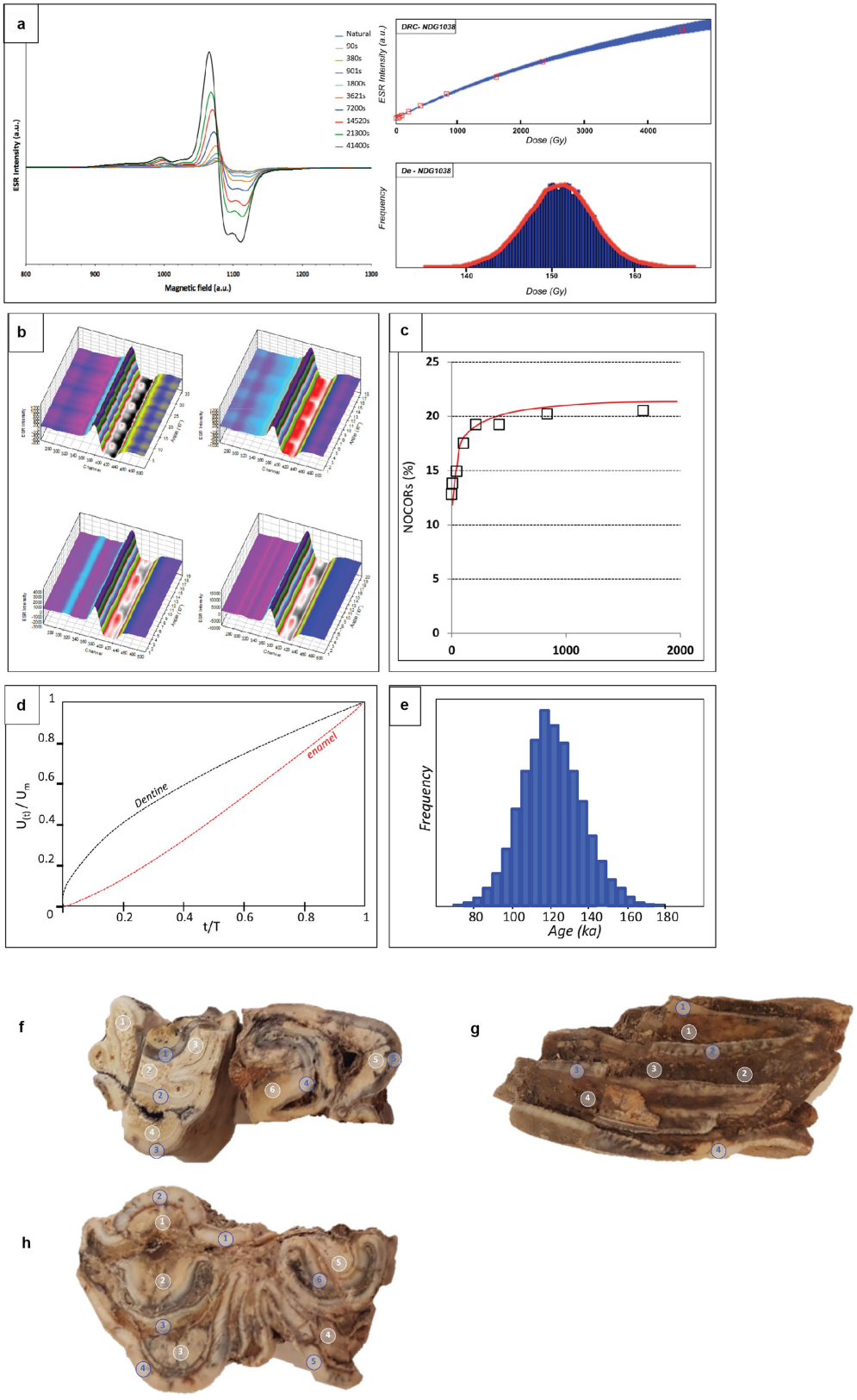


Extended Data Fig. 8 | See next page for caption.

Extended Data Fig. 8 | A comparison of red thermoluminescence and pIR-IRSL luminescence data for sample NDG-1. a, Quartz red thermoluminescence isothermal decays, showing a natural and regenerative decay. **b**, The dose response of aliquot A of the DAP technique with a D_e value of 185 ± 53 Gy. The points represent the mean with s.d. uncertainties (too small to see at this scale). **c**, The dose response of the subtracted aliquot B of the DAP technique with a D_e value of 170 ± 53 Gy. The points represent the mean value with an error as a s.d. of the fit (too small to see at this scale). **d**, Photographs of the luminescence emitted by a sample from the Ngandong terrace (NDG-1) compared to a sample from the Wae Raceng terrace in Flores (WR-1). The Flores terrace is so bright it has bleached the photographic paper, whereas the Ngandong terrace is much dimmer but the red luminescence emissions are clearly visible. **e**, Feldspar pIR-IRSL decays for sample NDG-1, showing the natural and regenerative decays. A long stimulation time is required to remove all of the pIR-IRSL signal. **f**, A dose–response curve for the sample NDG-1 with a D_e value of 150 ± 4 Gy. Each dose point represents the mean value with s.d. uncertainties (too small to see at this scale). **g**, Fading tests for the sample NDG-1, comparing the fading of the infrared signal at 50 °C (IR_{50}) with the fading with the pIR-IRSL signal at 270 °C ($pIR\text{-}IRSL_{270}$)—demonstrating the isolation of a very small fading signal. The points represent the median value with a standard error. **h**, Radial plot of the NDG-1 single-aliquot data.



Extended Data Fig. 9 | U-series-age depth dating of bone. a–l, Fossil bone recovered from the Ngandong excavations in 2010, displaying the track lines created by the LA-ICP-MS for U-series-age depth modelling. Bones were recovered from facies A and C. Figure 2 gives the locations of the bones. Specimen numbers (NDG) for each bone are listed in white in the top right corner.



Extended Data Fig. 10 | See next page for caption.

Extended Data Fig. 10 | Summary of the US–ESR dating protocol, and results for sample NDG-1038. a, Left, spectra of the merged signal increasing with irradiation steps. Top right, double saturated exponential dose–response curve of NDG-1038, using the MCDoseE 2.0 program[71]. Bottom right, dose equivalent distribution, using the MCDoseE 2.0 program[71]. **b**, Angular response of the enamel fragment in the ESR spectrometer at various irradiation steps from left to right and top to bottom: natural, 380 s, 1,800 s and 7,200 s. **c**, Determination of the NOCOR percentage in the angular response after subtracting the natural signal[70]. **d**, Uranium-uptake model in both enamel (red) and dentine (black) used to calculate the US–ESR dating of NDG-1038. **e**, US–ESR age distribution for NDG-1038 using a previously published program[72]. **f**–**h**, Photographs of the three bovid molar teeth. **f**, NDG-1038. **g**, NDG-11163. **h**, NDG-2569. These teeth were used for the direct dating by US–ESR of the Ngandong bone bed, with indication of U-series measurement locations. Teeth were sectioned to expose the various dental tissues. Numbers in white circles correspond to the dentine, and numbers in blue circles correspond to the enamel measurements. Results for each laser spot can be found in the Supplementary Table 8.

nature research

Corresponding author(s): Ciochon

Last updated by author(s): Oct 7, 2019

Reporting Summary

Nature Research wishes to improve the reproducibility of the work that we publish. This form provides structure for consistency and transparency in reporting. For further information on Nature Research policies, see Authors & Referees and the Editorial Policy Checklist.

Statistics

For all statistical analyses, confirm that the following items are present in the figure legend, table legend, main text, or Methods section.

n/a	Confirmed	
☐	☒	The exact sample size (*n*) for each experimental group/condition, given as a discrete number and unit of measurement
☐	☒	A statement on whether measurements were taken from distinct samples or whether the same sample was measured repeatedly
☐	☒	The statistical test(s) used AND whether they are one- or two-sided *Only common tests should be described solely by name; describe more complex techniques in the Methods section.*
☒	☐	A description of all covariates tested
☐	☒	A description of any assumptions or corrections, such as tests of normality and adjustment for multiple comparisons
☐	☒	A full description of the statistical parameters including central tendency (e.g. means) or other basic estimates (e.g. regression coefficient) AND variation (e.g. standard deviation) or associated estimates of uncertainty (e.g. confidence intervals)
☒	☐	For null hypothesis testing, the test statistic (e.g. *F*, *t*, *r*) with confidence intervals, effect sizes, degrees of freedom and *P* value noted *Give P values as exact values whenever suitable.*
☐	☒	For Bayesian analysis, information on the choice of priors and Markov chain Monte Carlo settings
☒	☐	For hierarchical and complex designs, identification of the appropriate level for tests and full reporting of outcomes
☒	☐	Estimates of effect sizes (e.g. Cohen's *d*, Pearson's *r*), indicating how they were calculated

Our web collection on statistics for biologists contains articles on many of the points above.

Software and code

Policy information about availability of computer code

Data collection	All software used for data collection is commercially available or described in the published literature (citations included). Software used includes: Microsoft Excel and MCDoseE (version 2.0) (for ESR dating).
Data analysis	All software used for data collection is commercially available or described in the published literature. Software used includes: Microsoft Excel, Isoplot EX (version 3.75) (U-series), MATHLAB USESR (US-ESR), OxCal (version 4.2) (Bayesian modeling), Riso Sequence Pro and Analyst. Full OxCal code for the Bayesian modeling is provided in Supplementary Table 15.

For manuscripts utilizing custom algorithms or software that are central to the research but not yet described in published literature, software must be made available to editors/reviewers. We strongly encourage code deposition in a community repository (e.g. GitHub). See the Nature Research guidelines for submitting code & software for further information.

Data

Policy information about availability of data

All manuscripts must include a data availability statement. This statement should provide the following information, where applicable:

- Accession codes, unique identifiers, or web links for publicly available datasets
- A list of figures that have associated raw data
- A description of any restrictions on data availability

The data that support the findings of this study are included in the Supplementary Information. Additional data is available from the corresponding author upon reasonable request.

Field-specific reporting

Please select the one below that is the best fit for your research. If you are not sure, read the appropriate sections before making your selection.

☐ Life sciences ☐ Behavioural & social sciences ☒ Ecological, evolutionary & environmental sciences

For a reference copy of the document with all sections, see nature.com/documents/nr-reporting-summary-flat.pdf

Ecological, evolutionary & environmental sciences study design

All studies must disclose on these points even when the disclosure is negative.

Study description	To determine the age of the hominin site of Ngandong, we considered three interrelated components; a landscape context, a terrace context, and a fossil context. Samples were dated using Uranium-series dating of speleothems, red TL, pIR-IRSL, 40Ar/39Ar, U-series on fossils, and ESR on fossil teeth. In total, we provide a modelled site age using 52 radiometric ages estimates. The study also includes the analysis of fossils and artefacts recovered from the contemporary sites of Ngandong, Sembungan, and Menden.
Research sample	To constrain the site of Ngandong we choose samples from a landscape, regional and local perspective. We chose speleothem samples from the 5 highest individual cave systems in the Gunung Sewu region. We chose optimum terrace sites from a large terrace survey conducted by the GRDC. Finally we determined excavation locations at Ngandong from extensive analysis of previous excavation to determine the original in situ locations and conducted multiple excavation baulks in these locations to optimise the sampling potential.
Sampling strategy	To establish a statistically significant sample size our sampling strategy was to sample from multiple locations in the Ngandong region as described above. Five speleothem samples were collected from the highest (therefore the oldest) caves sites in the Gunung Sewu – this number allows the oldest age range of speleothem precipitation to be estimated. We collected 21 luminescence and Ar-Ar samples from six different terraces in six different locations in the Ngandong area. By sampling this widely, we were able to robustly constrain each of the steps of terrace evolution in the Solo Valley. The chronology of the terraces were tested with independent age estimates from three different luminesce dating techniques (Red TL heat reset, Red TL light reset and pIR-IRSL techniques) and Ar-Ar dating. To constrain the fossil assemblage in the Ngandong terrace were conducted 26 direct dating age estimates of the bone and teeth from throughout the terrace across all four of the named Facies (A-D). Samples were chosen according to the weathering state of the enamel/dentine or collagen. Particular emphasis was placed on dense, thick bones without cortical sections. Such bones come closest to conform to the general assumption of the diffusion adsorption model. By developing a comprehensive sedimentological and fossil context, our dating strategy produces a robust chronology for the Ngandong evidence. In regards to the sampling strategy for the excavation at Ngandong, we excavated pits on both sides of the 1930's archaeological reserve (5 pit in 2008 and 12 pits in 2010) across the Ngandong terrace and collected 867 specimens. In respect to the specimens collected by previous excavations, our sample is limited to the published literature and a small collection of fossils because the majority of the 1930's collection was lost during World War II.
Data collection	The Ngandong excavation data was recorded by the members of ITB including palaeontologists and archaeologists over two field periods (2008 and 2010). The Solo Terrace data was collected by GSI over a five year period. All data pertaining to the dating techniques were collected by the appropriate dating specialists during collection in 2008 and during laboratory analysis from 2008-2019.
Timing and spatial scale	Excavations and field data collection were conducted between 2005 and 2010 at multiple sites in the Solo River Valley, Central Java, Indonesia.
Data exclusions	Samples were excluded if they failed predetermined tests for each dating method. These tests and exclusion criteria are outlined for each dating method in the Methods Summary and Supplementary Information. Fragmentary fossils that could not be identified were excluded from analysis for the excavations. For the US-ESR dating of three teeth samples NDG-2074, NDG-2562 and NDG-2566 were excluded from the dating as no enamel layer offered a uranium concentration <5 ppm, which has been described as the maximum acceptable concentration within the enamel layer to obtain a reliable equivalent dose. The ESR dating of the 15 bone samples did not yield any meaningful results as porous bones often display considerably more complex U-migration paths. For the luminescence dating single-aliquots were rejected according to a rejection criteria devised by cited reference.
Reproducibility	Multiple samples (52) and dating methods (seven) were used to determine a chronology for the Ngandong evidence. For both the sedimentological and fossil context independent ages estimates were employed to guarantee that the results are reliable and reproducible. Age estimates are consistent and stratigraphically correct between samples.
Randomization	Samples were collected for a specific dating method. Fossil specimens were allocated into taxonomical groups.
Blinding	Blinding was not relevant to the sample dating or the archaeological and paleontological research.

Did the study involve field work? ☒ Yes ☐ No

Field work, collection and transport

Field conditions	Field sample collection and excavations took place at multiple location and times in the Solo River Valley, Central Java, Indonesia (tropical climate).

Location	Field sample collection and excavations took place at multiple sites in the Solo River Valley, Central Java, including Ngandong, Sembungan, Menden, Padasmalang, Kerek, and Nglebak as well Song Gupuh in Gunung Sewu, East Java (see Figure 1 for locations).
Access and import/export	Excavations at Sembungan were undertaken under a recommendation letter from the Provincial Government of West Java to the Governor of the Central Java Province No. 070.10/237; a recommendation letter from the latter to the local government of the Blora Regency No. 070.10/237; and a research permit issued by the Blora Regency No. 071/457/2005. Excavations at Ngandong were carried out with the permission and recommendation of Mr. Wahyu, Head of the Foreign Researchers Licensing Secretariat of the State Ministry of Research and Technology (SMRT) that issued research permits 03799/SU/KS/2006, 1718/FRP/SM/VII/2008, and 04/TKPIPA/FRP/SM/IV/2010 for the fieldwork at Ngandong. The excavations at Sembungan and the Menden Terrace site in the Blora Regency were carried out under Research Permit Number 2785/FRP/SM/XI/2008.
Disturbance	Excavation procedures and techniques followed national and local regulations.

Reporting for specific materials, systems and methods

We require information from authors about some types of materials, experimental systems and methods used in many studies. Here, indicate whether each material, system or method listed is relevant to your study. If you are not sure if a list item applies to your research, read the appropriate section before selecting a response.

Materials & experimental systems

n/a	Involved in the study
☒	☐ Antibodies
☒	☐ Eukaryotic cell lines
☐	☒ Palaeontology
☒	☐ Animals and other organisms
☒	☐ Human research participants
☒	☐ Clinical data

Methods

n/a	Involved in the study
☒	☐ ChIP-seq
☒	☐ Flow cytometry
☒	☐ MRI-based neuroimaging

Palaeontology

Specimen provenance	Fossils were recovered from excavations at Ngandong, Sembungan, and Menden. More details about the provenance of these fossils is included in the Supplementary Information. A full list of permits for the excavations can be found in the Acknowledgments and in "Access and import/export" above. Permits were obtained for all specimens that were removed from Java, Indonesia, for laboratory analysis.
Specimen deposition	Fossils recovered from the 2008-2010 excavations at Ngandong are housed at the Institut Teknologi Bandung, Indonesia. Fossils and arefacts from the Sembungan and Menden excavations are under the care of the GSI, Indonesia.
Dating methods	The Methods Summary and Supplementary Information provides detailed descriptions of each dating method. Uranium-series dating of the speleothem samples was conducted in the Radiogenic Isotope Facility of The University of Queensland using VG Sector 54 thermal ionisation mass spectrometer (TIMS) and a Nu Plasma multi-collector inductively coupled mass spectrometer (MC-ICP-MS). All luminescence analysis, red TL and pIR-IRSL, was conducted at the "Traps" luminescence dating facility at Macquarie University in Sydney, Australia using a TL-DA-20 Luminescence reader. Neutron irradiation for 40AR/39Ar dating of hornblende crystals was conducted in the cadmium-shielded CLICIT facility at the Oregon State University TRIGA reactor. Laser ablation mass spectrometry to measure U-series isotopes along the cross-sections of these dense, mammalian long-bone fossils were carried out at the Australian National University. U-series analysis of fossil teeth was conducted at the Australian National University. Additional U-series measurements and ESR measurements were undertaken at Southern Cross University.

☒ Tick this box to confirm that the raw and calibrated dates are available in the paper or in Supplementary Information.

Article

Cortical pattern generation during dexterous movement is input-driven

https://doi.org/10.1038/s41586-019-1869-9

Received: 15 February 2018

Accepted: 29 October 2019

Published online: 25 December 2019

Britton A. Sauerbrei[1,3], Jian-Zhong Guo[1,3], Jeremy D. Cohen[1,3], Matteo Mischiati[1], Wendy Guo[1], Mayank Kabra[1], Nakul Verma[2], Brett Mensh[1], Kristin Branson[1] & Adam W. Hantman[1]*

The motor cortex controls skilled arm movement by sending temporal patterns of activity to lower motor centres[1]. Local cortical dynamics are thought to shape these patterns throughout movement execution[2–4]. External inputs have been implicated in setting the initial state of the motor cortex[5,6], but they may also have a pattern-generating role. Here we dissect the contribution of local dynamics and inputs to cortical pattern generation during a prehension task in mice. Perturbing cortex to an aberrant state prevented movement initiation, but after the perturbation was released, cortex either bypassed the normal initial state and immediately generated the pattern that controls reaching or failed to generate this pattern. The difference in these two outcomes was probably a result of external inputs. We directly investigated the role of inputs by inactivating the thalamus; this perturbed cortical activity and disrupted limb kinematics at any stage of the movement. Activation of thalamocortical axon terminals at different frequencies disrupted cortical activity and arm movement in a graded manner. Simultaneous recordings revealed that both thalamic activity and the current state of cortex predicted changes in cortical activity. Thus, the pattern generator for dexterous arm movement is distributed across multiple, strongly interacting brain regions.

Reaching, grasping and object manipulation have a central role in the lives of mammals with prehensile forelimbs. Motor cortex is a key brain hub involved in the control of skilled movements of the arm and hand. In primates and rodents, lesions of motor cortex can impair dexterity[7–9], stimulation of cortical neurons evokes movements[10–15], the activity of these neurons is closely linked to movement parameters[1,16–25], and optogenetic perturbations have a range of effects on different forelimb behaviours[14,22,26–28]. Recent work has emphasized that the motor cortex is a dynamical system in which neural firing rates evolve over time as a result of both the local cortical dynamics and external inputs from other areas, such as the thalamus and other cortical regions[2,3] (Fig. 1a). The dynamical principles governing the cortical system, however, remain largely unknown.

External inputs to motor cortex carry sensory information about the arm[29] as well as signals from the cerebellum, basal ganglia and higher cortical areas. The inputs are known to be important for movement preparation[5,6,30–33] and sensory-based corrections[29], but how do these inputs work together with local dynamics to produce motor cortical output during the execution of an unperturbed movement? One possibility is that once motor cortex has been set to the appropriate initial condition by external input, strong local dynamics generate the output during execution, whereas external inputs are weak; that is, the motor cortical dynamical system is largely autonomous during movement[4] (Fig. 1b, left). However, previous studies have shown movement-locked patterns in many brain areas providing input to motor cortex, coherence between motor cortex and these regions[34,35], and disrupted cortical activity following cerebellar cooling[36] or in animal models of Parkinson's disease[37]. A second possibility is that external inputs are needed to maintain the motor cortical dynamics in a pattern-generating regime, but the precise temporal pattern of these inputs is not critical to producing the correct output pattern[38]. A third possibility is that local dynamics within motor cortex must receive a strong, time-varying input pattern to produce the appropriate output (Fig. 1b, right). Although firing rates in thalamus are modulated on a kinematic timescale[39–43], the hypothesis that this temporal modulation is required for the generation of time-varying output within cortex has not been tested directly. Here we dissect the contribution of external inputs to cortical dynamics controlling dexterous behaviour by combining optogenetic perturbations of motor cortex and thalamus with high-density electrophysiology and movement tracking.

Recovery from perturbed initial states

To study cortical dynamics during dexterous movement, we trained mice to perform a reach-to-grasp movement, which we have previously shown to depend on motor cortex[26] (Fig. 1c), and extracted arm kinematics and behavioural waypoints from high-speed video (Fig. 1d, Supplementary Video 1). Using silicon probes, we recorded activity from neural ensembles in contralateral forelimb motor cortex (Fig. 1d). Whereas the responses of individual cells were highly consistent across trials, we observed a wide diversity of patterns across neurons, including increases, decreases, and multi-phasic responses (Fig. 1e, f). These

[1]Janelia Research Campus, Howard Hughes Medical Institute, Ashburn, VA, USA. [2]Department of Computer Science, Columbia University, New York, NY, USA. [3]These authors contributed equally: Britton A. Sauerbrei, Jian-Zhong Guo, Jeremy D. Cohen. *e-mail: hantmana@janelia.hhmi.org

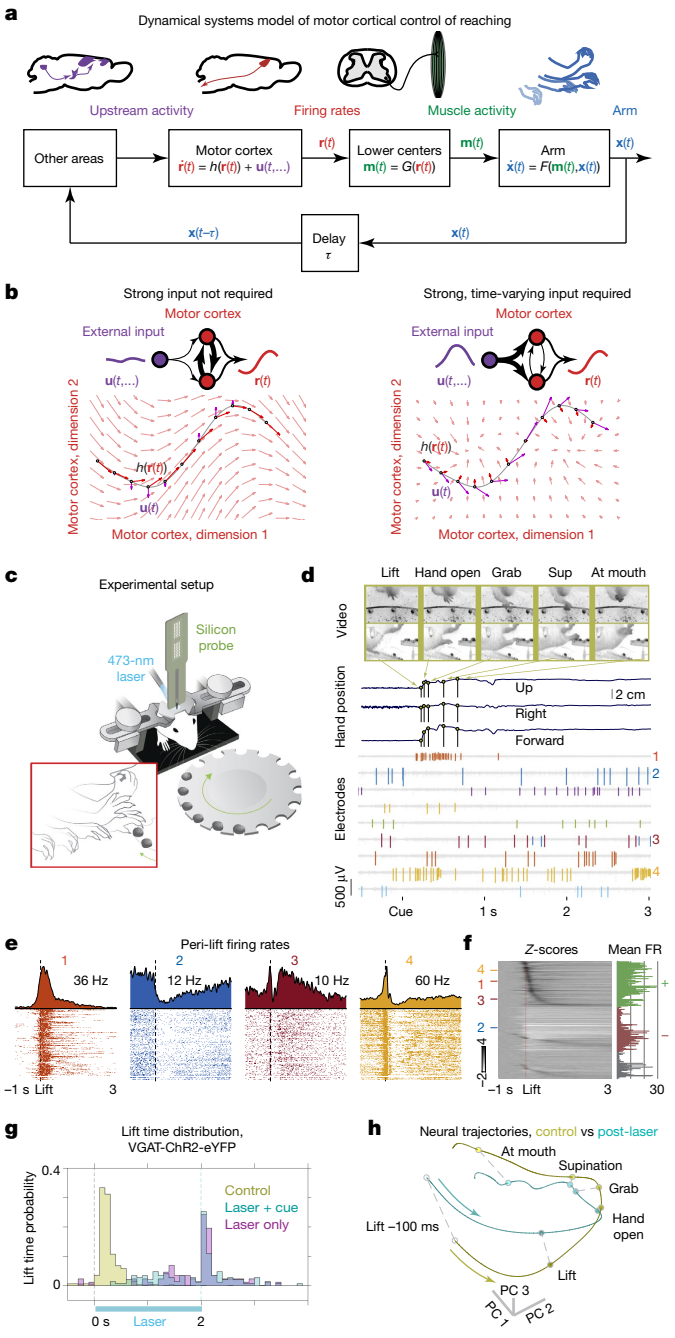


Fig. 1 | Motor cortex as a dynamical system controlling the arm. a, The dynamical systems model for motor cortical control of reaching (see Methods). **b**, Left, generation of firing-rate patterns $\mathbf{r}(t)$ if motor cortex were driven by strong recurrent dynamics $h(\mathbf{r}(t))$, with external inputs $\mathbf{u}(t)$ exerting a limited influence and not necessary for pattern generation. Right, generation of firing-rate patterns if motor cortex were dependent on strong temporally patterned external inputs, $\mathbf{u}(t)$. **c**, Experimental setup. Head-fixed mice reached for a pellet of food following an acoustic cue during recording and optogenetic perturbation of cortical activity. **d**, Raw video, electrophysiological recording and mouse behaviour in a single trial. Three-dimensional hand trajectories and the timing of each waypoint in the behavioural sequence were extracted from video using computer vision methods. Sup, supination. **e**, Spike raster plots and peri-event time histograms for four example neurons recorded in **d**, centred on lift. Numbers indicate the maximum value on the *y* axis, in spikes per second. **f**, Average *z*-scored firing rates (FR) and mean firing rates for all motor cortical neurons ($n = 19$ mice, $n = 39$ sessions and $n = 843$ neurons). During prehension, most neurons exhibited increases (39%) or decreases (37%) in spike counts around lift (two-sided rank sum test with Benjamini–Hochberg correction, $q < 0.05$). **g**, Distribution of lift times on control (yellow), laser plus cue (blue) and laser-only (magenta) trials for VGAT-ChR2-eYFP mice ($n = 5$ mice, $n = 7$ sessions). Cue starts at time 0, and the blue bar indicates the laser-on epoch. **h**, Neural population activity from lift −100 ms to lift +425 ms in control (yellow) and post-laser (blue) reaches in VGAT-ChR2-eYFP mice, obtained using trial-averaged principal component analysis (PCA) ($n = 4$ mice, $n = 6$ sessions and $n = 144$ neurons).

patterns are consistent with previous findings in the primary motor cortex of nonhuman primates[1,16,17] and rodents[18–23] performing dexterous behaviours.

If motor cortex were largely autonomous during movement execution (Fig. 1b, left), then the initial pre-movement state of cortex, which is set by external inputs, should determine the subsequent evolution of activity during execution. Thus, in this model, if cortex were perturbed to an aberrant state, it would need to be reset to the appropriate initial condition by external inputs before the initiation of movement, and this reset would probably increase the animal's reaction time. To examine how cortex recovers from aberrant initial states, we performed three cell-type-specific manipulations of the cortical network by activating either inhibitory interneurons (VGAT-ChR2-eYFP mice), intratelencephalic neurons (Tlx3-Cre x Ai32) or pyramidal tract neurons (Sim1-Cre x Ai32). Each of these perturbations had a large effect on cortical activity (Extended Data Fig. 1a, b) and blocked the initiation of reaching (Fig. 1g, Extended Data Fig. 1c, d). Following the release of each motor cortical perturbation, we frequently observed kinematically normal post-laser reaches (Extended Data Fig. 1c–f). The reaches occurred with a shorter reaction time than in control trials following the VGAT and Tlx3 perturbations (Extended Data Fig. 1e), contrary to the predictions of the autonomous model, and they also occurred following laser stimulation in the absence of a cue (Fig. 1g, Extended Data Fig. 1c–e). In post-perturbation reaches, the neural population activity, estimated using dimensionality reduction, did not return to the initial state observed in control trials, but immediately generated patterns that largely recapitulated those observed in control trials (Fig. 1h, Extended Data Figs. 1g, 2, Supplementary Videos 2, 3). Furthermore, it was possible to decode the post-laser hand trajectories using a decoder trained on control trials (Extended Data Fig. 3). This suggests that cortex does not need to return to a specific pre-movement state, as required by the autonomous model (Fig. 1b, left).

In the dynamical systems view, the contribution of local dynamics depends only on the current state of cortex. We observed that silencing motor cortex in VGAT-ChR2-eYFP mice fixes motor cortex to a constant state across trials (Extended Data Fig. 4a). Thus, unless the network is extremely sensitive to small differences in initial state[44] (as in a chaotic system), trial-to-trial variability in neural activity following the release of the laser will reflect variability in external inputs. When we compared trials on which a post-laser reach occurred with trials with no reach (Fig. 2a), we found that the two trial types started in the same initial state, but rapidly diverged after the release of the laser (Fig. 2b, c, Extended Data Fig. 5c), suggesting a difference in external input between reach and no-reach trials (Fig. 2d). We estimated this difference in inputs by subtracting the firing-rate derivatives of the two conditions (Fig. 2e; see Methods). The result of this experiment suggests that external input is critical to producing the correct reaching pattern.

Input is required for pattern generation

If the motor cortex requires external input throughout movement execution, then blocking or interrupting the input pattern should perturb both motor cortical activity and arm kinematics. To test this directly, we implanted optical fibres above motor thalamus contralateral to the arm in VGAT-ChR2-eYFP mice. This enabled us to activate inhibitory

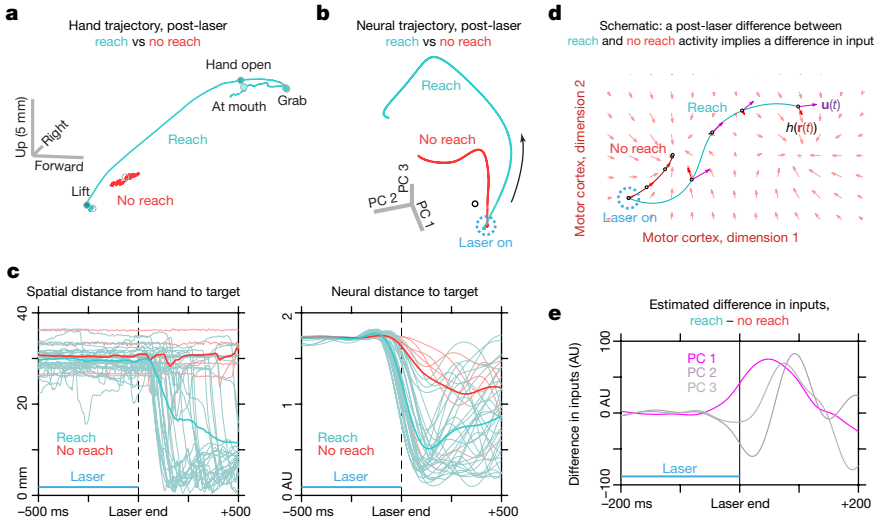


Fig. 2 | Divergence of neural trajectories from the same initial state. **a**, Average hand trajectory for trials with (blue) and without (red) post-laser reaches in VGAT-ChR2-eYFP mice ($n = 4$ mice and $n = 6$ sessions). **b**, Neural population activity aligned to the end of the laser for trials with (blue) and without (red) a post-laser reach ($n = 128$ neurons). Time limits are 250 ms before the end of the laser to 250 ms after the end of the laser. Black dot indicates baseline activity before the start of the trial. **c**, Spatial (left) and neural (right) distance to target, centred on the end of the laser, for trials with (blue) and without (red) post-laser reaches. **d**, Schematic illustrating that a divergence in neural trajectories from the same initial state implies a difference in external inputs. **e**, Estimated difference in external inputs between reach and no-reach conditions (see Methods). The divergence of the traces shortly before the end of the laser is owing to smoothing (Extended Data Fig. 5a–d).

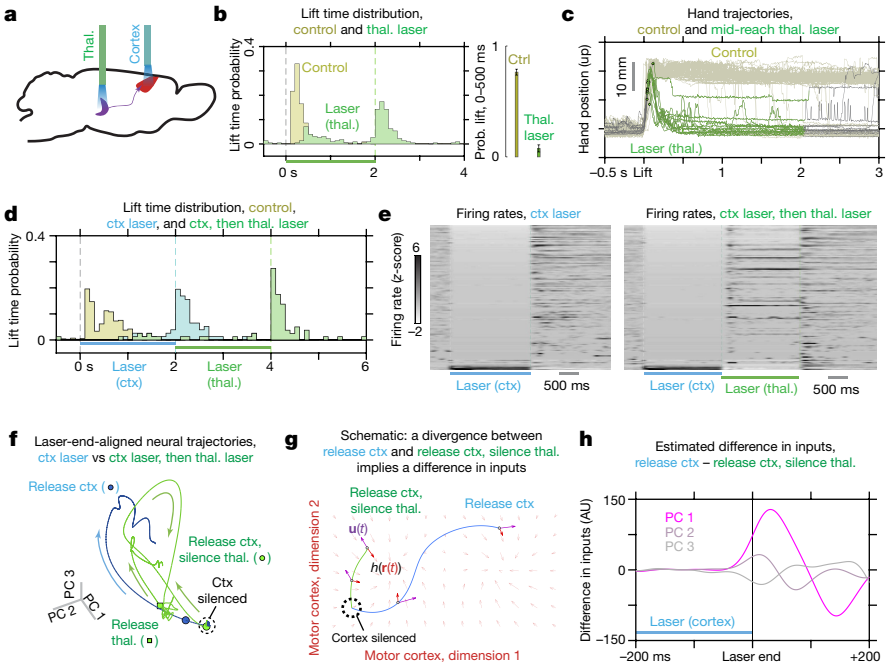


Fig. 3 | External inputs are required for the motor cortical pattern during reaching. **a**, Experimental schematic. Placement of fibres over motor cortex and thalamus (thal). **b**, Distribution of lift times on control (yellow) and thalamic inactivation (green) trials; $n = 3$ mice (VGAT-ChR2-eYFP) and $n = 7$ sessions. Right inset shows the probability of a lift within the first 500 ms following the cue for control and thalamus inactivation trials. **c**, Hand position in the upper direction centred on lift on control trials (light yellow) and mid-reach thalamic inactivation trials (black; green indicates laser on) for a single dataset. Dots indicate the start of the laser. Data from all mice ($n = 4$ mice and $n = 6$ sessions) are shown in Extended Data Fig. 6. **d**, Lift times for control trials (yellow), cortical inactivation (blue) and sequential inactivation of cortex (ctx) and thalamus (green); $n = 3$ mice (VGAT-ChR2-eYFP) and $n = 4$ sessions. **e**, Average firing rate z-scores for all recorded neurons under inactivation of cortex alone (left) and sequential inactivation of cortex and thalamus (right); $n = 3$ mice, $n = 4$ sessions and $n = 127$ neurons. **f**, Population activity following the end of cortical inactivation for trials with cortical inactivation only (blue) and inactivation of thalamus after cortex (green). Plotting limits start 500 ms before the end of cortical inactivation and finish 500 ms after the cortical inactivation (blue trace) and 500 ms after the thalamic inactivation (green trace). The divergence of the trajectories shortly before the end of cortical inactivation results from smoothing (Extended Data Fig. 5e–h), and inhibitory interneurons were excluded. **g**, Schematic illustrating that the divergence from the cortex-inactivated state reveals differences in input. **h**, Estimated difference in external inputs following the end of cortical inactivation between thalamus inactivated ($\mathbf{u}_{-\mathrm{th}}(t)$) and not inactivated ($\mathbf{u}_{+\mathrm{th}}(t)$) conditions. The difference is given by $\mathbf{u}_{+\mathrm{th}}(t) - \mathbf{u}_{-\mathrm{th}}(t)$.

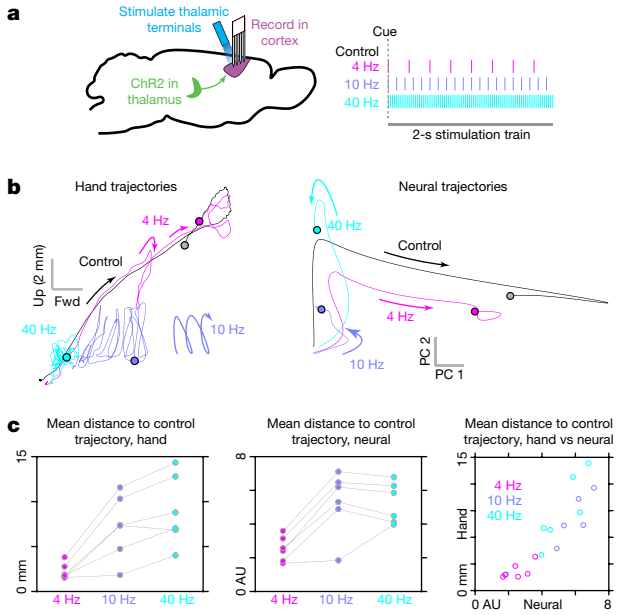


Fig. 4 | Modification of the temporal pattern of inputs perturbs cortical activity and movement. a, Experimental design. Mice expressing ChR2 in thalamic neurons performed the task during recording of cortical activity and optogenetic stimulation of thalamocortical terminals. **b**, Left, example average hand trajectory on control trials and stimulation trials with stimulation frequencies of 4, 10 and 40 Hz from a single experimental session. Data from all mice ($n = 3$ mice and $n = 6$ sessions) are shown in Extended Data Fig. 9. Time limits are cue −250 ms to cue +1,000 ms. Right, average neural activity (first two principal components) in the same session. Dots indicate the end of the trajectory at cue +1,000 ms. **c**, Left, average Euclidean distance from the hand position in each stimulation condition to the control hand position at the same time point. Each curve shows a single experimental session ($n = 3$ mice and $n = 6$ sessions). Middle, Euclidean distance from the neural state in the stimulated conditions to the neural state in the control condition. Right, distance from hand trajectory to control versus distance from the neural trajectory to control.

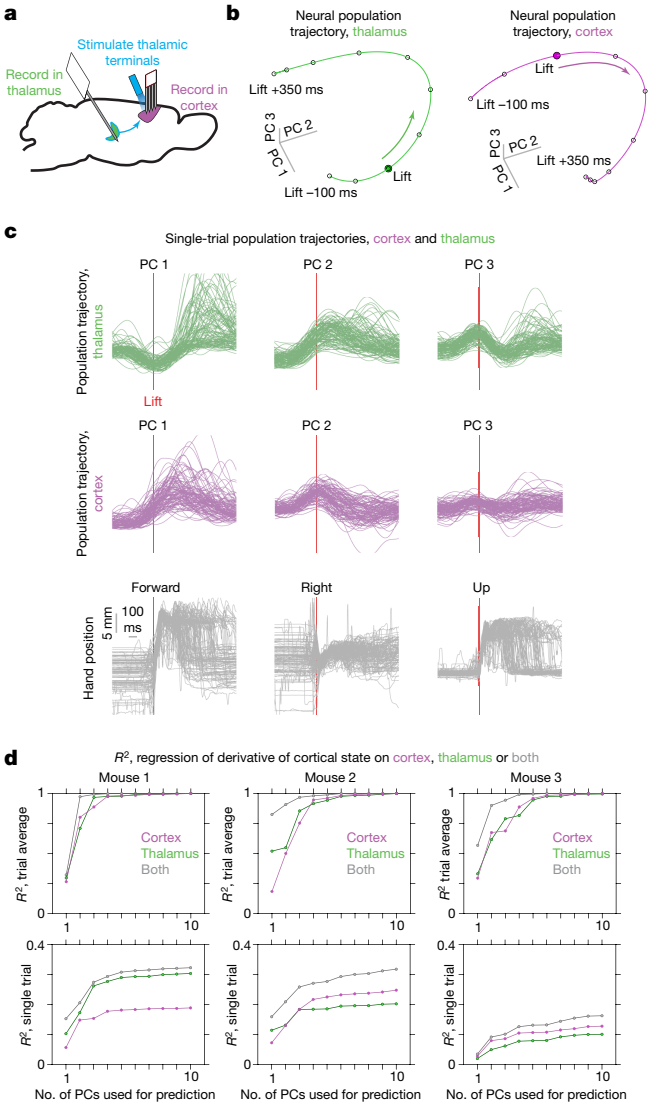


Fig. 5 | Relationship between population activity in motor thalamus and motor cortex. a, Experimental setup. Spiking activity was simultaneously recorded in motor cortex with a four-shank, 64-channel probe and in thalamus with a 384-channel Neuropixels probe ($n = 3$ mice and $n = 3$ sessions). The thalamic region projecting to motor cortex was identified by optogenetic stimulation of thalamocortical terminals. **b**, Population trajectories for thalamus (left, green) and cortex (right, magenta) obtained with trial-averaged PCA. **c**, Single-trial population activity in thalamus (top) and cortex (middle), along with hand position (bottom). **d**, Goodness-of-fit of regression models (coefficient of determination, R^2). The dependent variable was the derivative of the cortical population state for the first three principal components. The independent variable was the cortical state (magenta), the thalamic state (green) or both (grey) for the first N principal components, where N was varied between 1 and 10. The top row shows the goodness-of-fit for trial-averaged data, and the bottom for single-trial data.

terminals in this region, which has been shown to suppress activity in the projections to motor cortex[31] (Fig. 3a). Thalamic inactivation at the start of the trial blocked the initiation of coordinated reaching (Fig. 3b), and inactivation in the middle of the reach interrupted the progression of the hand to the target (Fig. 3c, Extended Data Fig. 6). These results demonstrate that external inputs are required to control the hand throughout the entire movement.

To isolate the effect of inputs from local dynamics, we first set the motor cortical network—and thus the contribution of local dynamics—to the same initial state by silencing cortex in VGAT-ChR2-eYFP mice. Then, when we removed the motor cortical inactivation, we allowed the network to recover in some trials, but immediately silenced the thalamus in other trials. This thalamic inactivation blocked reaching following the removal of motor cortical suppression (Fig. 3d). Thalamic inactivation did not act by merely silencing motor cortical spiking; firing rates during this epoch fluctuated extensively (Fig. 3e, Extended Data Fig. 7c). The mouse frequently reached to the target after the removal of thalamic inactivation (Fig. 3d, Extended Data Fig. 7a). These post-thalamic-inactivation reaches were generated by the same neural pattern that drove reaching in control trials and post-motor-cortical-inactivation trials (Extended Data Fig. 7b). Population activity with and without thalamic inactivation began with the same initial state, but rapidly diverged after the end of motor cortical suppression (Fig. 3f, Extended Data Fig. 5g, Supplementary Video 4). When thalamus was inactivated, the cortical trajectory exhibited a brief transient and then converged to a new fixed point, which could reflect the influence of local dynamics. Because the difference between the two trial types was whether or not we silenced thalamus, the rapid divergence of the corresponding trajectories from the cortex-inactivated state resulted from differences in external inputs, rather than extreme sensitivity to initial conditions (Fig. 3g). We estimated the difference in external inputs between the two conditions (see Methods), revealing a strong influence of inputs on the first principal component of neural activity (Fig. 3h).

Graded disruption of the input patterns

Our thalamic inactivation results showed that inputs are necessary to produce the correct cortical output. We next investigated whether a precise temporal pattern in these inputs is required (Fig. 1b, right). To address this question, we corrupted the input pattern by expressing ChR2 in thalamic neurons and stimulating thalamocortical terminals at frequencies of 4 Hz, 10 Hz and 40 Hz while recording from motor cortex during reaching (Fig. 4a). Stimulation of the terminals entrained spiking activity in motor cortex (Extended Data Fig. 8a), but produced relatively small changes in mean postsynaptic firing rates (Extended Data Fig. 8b) compared with the changes induced by direct stimulation of cortical neurons (Extended Data Fig. 1b). Stimulation partially blocked the initiation of reaching, and the blocking effect was dependent on the frequency of the stimulus (Extended Data Fig. 8d; $P = 6.7 \times 10^{-6}$, $F = 18.0$; one-way ANOVA). At 4 Hz stimulation, the mouse was able to reach to the pellet, and the hand and neural trajectories largely recapitulated the control trajectories (Fig. 4b, Extended Data Fig. 8c, 9, Supplementary Video 5), although the hand trajectory was transiently perturbed at the pulse times (Extended Data Fig. 9a). At 10 Hz stimulation, the mouse often initiated a movement, but was usually unable to reach to the pellet, and in some cases, the limb oscillated at the stimulation frequency. At 40 Hz stimulation, the initiation and execution of reaching were severely impaired. The neural and hand trajectories were more different from the control trajectories at higher stimulation frequencies ($P = 0.0040$ and 0.0052, $F = 8.2$ and 7.6, respectively, one-way ANOVA; Fig. 4c, left and centre), and the magnitude of the difference was correlated for the neural and hand activity (Spearman's $\rho = 0.94$, $P = 1.7 \times 10^{-6}$; Fig. 4c, right). Thus, our data suggest that the temporal pattern of inputs directly influences cortical activity and hand kinematics.

Thalamocortical coupling

We have shown that time-varying thalamic inputs are required for cortical pattern generation. We next investigated the contribution of these inputs relative to local dynamics. We simultaneously recorded activity in motor cortex and motor thalamus using a 384-channel Neuropixels probe[45] and verified the targeting of thalamus with optogenetic tagging and histology (Extended Data Fig. 10a–c). Most thalamic neurons were modulated around movement onset (Extended Data Fig. 10d; increases in $n = 73$ out of 98, decreases in $n = 11$ out of 98), consistent with previous reports in both rodents[39,42] and nonhuman primates[40,41,43]. Population activity in thalamus and cortex exhibited strong modulation in trial-averaged (Fig. 5b) and single-trial activity (Fig. 5c).

In the dynamical systems model, the derivative of the cortical state is a function of both external input and the current cortical state (Fig. 1a). Thus, we numerically differentiated the cortical population activity (single-trial or trial-averaged) and regressed it on the cortical state, the thalamic state, or both. If local dynamics were strong during movement execution, then the model using the cortical state as the independent variable should provide a better fit. However, if inputs were much stronger than local dynamics, then the model using thalamic state as the independent variable should provide a better fit. We found that the cortical derivative was predicted by both variables, with either thalamic state or cortical state providing a better fit, depending on the individual mouse (Fig. 5d). This suggests that the cortical state does not evolve as a purely autoregressive process or simply integrate thalamic input; rather, both local dynamics and inputs contribute to generating the cortical pattern.

Discussion

Studies in nonhuman primates have emphasized the role of external inputs in setting up a specific initial state in motor cortex that allows the appropriate activity pattern to unfold during the execution of a movement[4–6], though this state may be bypassed under certain conditions[46]. Under this view, the subsequent evolution of cortical activity may be strongly guided by autonomous dynamics, unless the cortex needs to correct for errors or perturbations[4]. After we optogenetically set cortex to aberrant initial states, it rapidly produced the appropriate pattern for reaching without returning to the initial state observed on control trials, provided the inputs were intact. This suggests that a specific initial state is not required for cortical pattern generation. Contrary to the predictions of the autonomous model (Fig. 1b, left), silencing or stimulating thalamus severely disrupted cortical pattern generation and arm movement. Thus, temporally patterned inputs are critical for producing the cortical output pattern during movement execution (Fig. 1b, right).

Our data reveal experimental conditions in which the temporal pattern of external inputs drives the pattern in motor cortex, and in which this output pattern is required to skilfully control the arm and hand. These findings complement previous studies, which have suggested that dexterous behaviours that require precise coordination of the fingers and interaction with objects, such as grasping[7–9,14,22,26], may be one class of cortically dependent movement. The execution of other forelimb behaviours—such as locomotion[14,47], pulling a grasped lever[14] or timing a sequence of lever taps[48]—does not appear to require cortex. The source, modality, and function of inputs may also differ across species; it is possible, for instance, that long-range inputs from other cortical regions may be more important in primates, which have a highly differentiated cortical network for planning and executing reaching and grasping[49]. Species differences in sensorimotor delays[50] and moment of inertia of limb segments, which are related to body size, could also affect the timescale on which peripheral inputs influence cortex.

We have shown that the cortical pattern that controls reaching can be produced only if temporally patterned inputs are maintained throughout the entire movement. Thus, while motor cortex is a bottleneck for descending motor commands, its activity patterns during movement are crucially moulded by its embedding within a vast and distributed network, which incorporates muscles, the sensory periphery, subcortical regions and other cortical areas.

Online content

Any methods, additional references, Nature Research reporting summaries, source data, extended data, supplementary information, acknowledgements, peer review information; details of author contributions and competing interests; and statements of data and code availability are available at https://doi.org/10.1038/s41586-019-1869-9.

1. Porter, R. & Lemon, R. *Corticospinal Function and Voluntary Movement* (Oxford University Press, 1995).
2. Churchland, M. M. et al. Neural population dynamics during reaching. *Nature* **487**, 51–56 (2012).
3. Shenoy, K. V., Sahani, M. & Churchland, M. M. Cortical control of arm movements: a dynamical systems perspective. *Annu. Rev. Neurosci.* **36**, 337–359 (2013).
4. Pandarinath, C. et al. Latent factors and dynamics in motor cortex and their application to brain–machine interfaces. *J. Neurosci.* **38**, 9390–9401 (2018).
5. Kaufman, M. T., Churchland, M. M., Ryu, S. I. & Shenoy, K. V. Cortical activity in the null space: permitting preparation without movement. *Nat. Neurosci.* **17**, 440–448 (2014).
6. Afshar, A. et al. Single-trial neural correlates of arm movement preparation. *Neuron* **71**, 555–564 (2011).
7. Lawrence, D. G. & Kuypers, H. G. The functional organization of the motor system in the monkey. I. The effects of bilateral pyramidal lesions. *Brain* **91**, 1–14 (1968).
8. Whishaw, I. Q., Pellis, S. M., Gorny, B., Kolb, B. & Tetzlaff, W. Proximal and distal impairments in rat forelimb use in reaching follow unilateral pyramidal tract lesions. *Behav. Brain Res.* **56**, 59–76 (1993).
9. Whishaw, I. Q. Loss of the innate cortical engram for action patterns used in skilled reaching and the development of behavioral compensation following motor cortex lesions in the rat. *Neuropharmacology* **39**, 788–805 (2000).
10. Grünbaum, A. S. F. & Sherrington, C. S. Observations on the physiology of the cerebral cortex of some of the higher apes. *Proc. R. Soc. Lond.* **69**, 206–209 (1902).
11. Penfield, W. & Boldrey, E. Somatic motor and sensory representation in the cerebral cortex of man as studied by electrical stimulation. *Brain* **60**, 389–443 (1937).
12. Graziano, M. S. A., Taylor, C. S. R. & Moore, T. Complex movements evoked by microstimulation of precentral cortex. *Neuron* **34**, 841–851 (2002).

13. Harrison, T. C., Ayling, O. G. S. & Murphy, T. H. Distinct cortical circuit mechanisms for complex forelimb movement and motor map topography. *Neuron* **74**, 397–409 (2012).
14. Miri, A. et al. Behaviorally selective engagement of short-latency effector pathways by motor cortex. *Neuron* **95**, 683–696.e11 (2017).
15. Brown, A. R. & Teskey, G. C. Motor cortex is functionally organized as a set of spatially distinct representations for complex movements. *J. Neurosci.* **34**, 13574–13585 (2014).
16. Evarts, E. V. Pyramidal tract activity associated with a conditioned hand movement in the monkey. *J. Neurophysiol.* **29**, 1011–1027 (1966).
17. Scott, S. H. The role of primary motor cortex in goal-directed movements: insights from neurophysiological studies on non-human primates. *Curr. Opin. Neurobiol.* **13**, 671–677 (2003).
18. Lemke, S. M., Ramanathan, D. S., Guo, L., Won, S. J. & Ganguly, K. Emergent modular neural control drives coordinated motor actions. *Nat. Neurosci.* **22**, 1122–1131 (2019).
19. Hyland, B. Neural activity related to reaching and grasping in rostral and caudal regions of rat motor cortex. *Behav. Brain Res.* **94**, 255–269 (1998).
20. Wagner, M. J. et al. Shared cortex–cerebellum dynamics in the execution and learning of a motor task. *Cell* **177**, 669–682 (2019).
21. Wang, X. et al. Deconstruction of corticospinal circuits for goal-directed motor skills. *Cell* **171**, 440–455 (2017).
22. Galiñanes, G. L., Bonardi, C. & Huber, D. Directional reaching for water as a cortex-dependent behavioral framework for mice. *Cell Rep.* **22**, 2767–2783 (2018).
23. Isomura, Y., Harukuni, R., Takekawa, T., Aizawa, H. & Fukai, T. Microcircuitry coordination of cortical motor information in self-initiation of voluntary movements. *Nat. Neurosci.* **12**, 1586–1593 (2009).
24. Georgopoulos, A. P., Kalaska, J. F., Caminiti, R. & Massey, J. T. On the relations between the direction of two-dimensional arm movements and cell discharge in primate motor cortex. *J. Neurosci.* **2**, 1527–1537 (1982).
25. Kakei, S., Hoffman, D. S. & Strick, P. L. Muscle and movement representations in the primary motor cortex. *Science* **285**, 2136–2139 (1999).
26. Guo, J.-Z. et al. Cortex commands the performance of skilled movement. *eLife* **4**, e10774 (2015).
27. Otchy, T. M. et al. Acute off-target effects of neural circuit manipulations. *Nature* **528**, 358–363 (2015).
28. Bollu, T., Whitehead, S. C., Prasad, N. & Walker, J. R. Motor cortical inactivation reduces the gain of kinematic primitives in mice performing a hold-still center-out reach task. Preprint at *bioRxiv* https://doi.org/10.1101/304907 (2018).
29. Scott, S. H. Optimal feedback control and the neural basis of volitional motor control. *Nat. Rev. Neurosci.* **5**, 532–545 (2004).
30. Churchland, M. M., Yu, B. M., Ryu, S. I., Santhanam, G. & Shenoy, K. V. Neural variability in premotor cortex provides a signature of motor preparation. *J. Neurosci.* **26**, 3697–3712 (2006).
31. Guo, Z. V. et al. Maintenance of persistent activity in a frontal thalamocortical loop. *Nature* **545**, 181–186 (2017).
32. Li, N., Daie, K., Svoboda, K. & Druckmann, S. Robust neuronal dynamics in premotor cortex during motor planning. *Nature* **532**, 459–464 (2016).
33. Gao, Z. et al. A cortico-cerebellar loop for motor planning. *Nature* **563**, 113–116 (2018).
34. Soteropoulos, D. S. & Baker, S. N. Cortico-cerebellar coherence during a precision grip task in the monkey. *J. Neurophysiol.* **95**, 1194–1206 (2006).
35. Murthy, V. N. & Fetz, E. E. Coherent 25- to 35-Hz oscillations in the sensorimotor cortex of awake behaving monkeys. *Proc. Natl Acad. Sci. USA* **89**, 5670–5674 (1992).
36. Meyer-Lohmann, J., Conrad, B., Matsunami, K. & Brooks, V. B. Effects of dentate cooling on precentral unit activity following torque pulse injections into elbow movements. *Brain Res.* **94**, 237–251 (1975).
37. Costa, R. M. et al. Rapid alterations in corticostriatal ensemble coordination during acute dopamine-dependent motor dysfunction. *Neuron* **52**, 359–369 (2006).
38. Yuste, R., MacLean, J. N., Smith, J. & Lansner, A. The cortex as a central pattern generator. *Nat. Rev. Neurosci.* **6**, 477–483 (2005).
39. Bosch-Bouju, C., Smither, R. A., Hyland, B. I. & Parr-Brownlie, L. C. Reduced reach-related modulation of motor thalamus neural activity in a rat model of Parkinson's disease. *J. Neurosci.* **34**, 15836–15850 (2014).
40. Strick, P. L. Activity of ventrolateral thalamic neurons during arm movement. *J. Neurophysiol.* **39**, 1032–1044 (1976).
41. Horne, M. K. & Porter, R. The discharges during movement of cells in the ventrolateral thalamus of the conscious monkey. *J. Physiol.* **304**, 349–372 (1980).
42. Gaidica, M., Hurst, A., Cyr, C. & Leventhal, D. K. Distinct populations of motor thalamic neurons encode action initiation, action selection, and movement vigor. *J. Neurosci.* **38**, 6563–6573 (2018).
43. van Donkelaar, P., Stein, J. F., Passingham, R. E. & Miall, R. C. Neuronal activity in the primate motor thalamus during visually triggered and internally generated limb movements. *J. Neurophysiol.* **82**, 934–945 (1999).
44. Russo, A. A. et al. Motor cortex embeds muscle-like commands in an untangled population response. *Neuron* **97**, 953–966 (2018).
45. Jun, J. J. et al. Fully integrated silicon probes for high-density recording of neural activity. *Nature* **551**, 232–236 (2017).
46. Ames, K. C., Ryu, S. I. & Shenoy, K. V. Neural dynamics of reaching following incorrect or absent motor preparation. *Neuron* **81**, 438–451 (2014).
47. Orlovsky, G. N., Deliagina, T. G. & Grillner, S. *Neuronal Control of Locomotion: from Mollusc to Man* (Oxford University Press, 1999).
48. Kawai, R. et al. Motor cortex is required for learning but not for executing a motor skill. *Neuron* **86**, 800–812 (2015).
49. Schaffelhofer, S. & Scherberger, H. Object vision to hand action in macaque parietal, premotor, and motor cortices. *eLife* **5**, e15278 (2016).
50. More, H. L. & Donelan, J. M. Scaling of sensorimotor delays in terrestrial mammals. *Proc. Biol. Sci.* **285**, 20180613 (2018).

Publisher's note Springer Nature remains neutral with regard to jurisdictional claims in published maps and institutional affiliations.

© The Author(s), under exclusive licence to Springer Nature Limited 2019

Methods

No statistical methods were used to predetermine sample size. The experiments were not randomized. The investigators were not blinded to allocation during experiments and outcome assessment.

Dynamical systems model for motor cortical control of reaching

In this model[2,3], depicted in Fig. 1a, the firing rates of motor cortical neurons, $\mathbf{r}(t)$, change as a result of two distinct influences. First, the local architecture intrinsic to motor cortex imposes a change, $h(\mathbf{r}(t))$, based on the current firing rates. Second, brain regions outside motor cortex provide external input, $\mathbf{u}(t)$. This input is not identical to the firing rates of the neurons in upstream brain regions; rather, it represents the effect those upstream firing rates have on the firing rates of postsynaptic neurons in motor cortex. The firing rates evolve according to $\mathbf{r}'(t) = h(\mathbf{r}(t)) + \mathbf{u}(t)$. These firing rates control the muscle activation, $\mathbf{m}(t) = G(\mathbf{r}(t))$, through circuits in the lower motor centres, including the spinal cord. In turn, the muscles change the positions and velocities of the joint centres, $\mathbf{x}(t)$, through a function describing the musculoskeletal mechanics: $\mathbf{x}'(t) = F(\mathbf{m}(t),\mathbf{x}(t))$. Delayed sensory feedback from the arm ascends into the brain and influences the external inputs $\mathbf{u}(t)$, closing the loop.

The additive interaction between inputs and local dynamics makes the model intuitive and tractable for estimating the difference in external input contributions across experimental conditions (Figs. 2e, 3h). However, it is likely that the network dynamics are nonlinear. That is, the evolution of cortical activity over time might be described by $\mathbf{r}'(t) = \phi(\mathbf{r}(t),\mathbf{u}(t))$, and thus local connectivity in motor cortex may amplify or distort simple changes in input, including changes in tonic drive. Modelling such complex, nonlinear interactions will require powerful new analysis tools, such as those that use deep learning to capture cortical dynamics[51].

Behavioural task and video analysis

Mice of either sex aged 8–25 weeks were fitted with head posts, food restricted, and trained to reach for food pellets, as described previously[26]. All data in this manuscript, including those from the behavioural experiments, are previously unpublished. WaveSurfer (http://wavesurfer.janelia.org/) was used to control the behavioural stimuli. Video of the behaviour was recorded at 500 Hz using BIAS software (IO Rodeo, available at https://bitbucket.org/iorodeo/bias) and two high-speed cameras (PointGrey, Flea3), which were calibrated to allow 3D triangulation of hand position (Caltech Camera Calibration Toolbox for Matlab; http://www.vision.caltech.edu/bouguetj/calib_doc/). Two types of information were extracted from video: ethograms labelling the frames in which lift, hand open, grab, supination, hand at mouth, and chew occurred, obtained using the Janelia Automatic Animal Behavior Annotator (https://github.com/kristinbranson/JAABA), and the position of the hand in space, obtained using the Animal Part Tracker (APT) (https://github.com/kristinbranson/APT). All procedures were approved by the Institutional Animal Care and Use Committee at Janelia Research Campus (protocols 13-99, 16-139 and 19-177).

Automatic behaviour characterization

Using an adaptation of the Janelia Automatic Animal Behaviour Annotator (JAABA), we trained automatic behaviour classifiers that input information from the video frames and output predictions of the behaviour category–lift, hand-open, grab, supination, at-mouth, and chew. We adapted JAABA to use Histogram of Oriented Gradients[52] and Histogram of Optical Flow[53] features derived directly from the video frames, instead of features derived from animal trajectories. The automatic behaviour predictions were post-processed as described previously[26] to find the first lift-hand-open-grab and supination-at-mouth-chew sequences. For the mid-reach thalamic perturbation experiments (Fig. 3c, Extended Data Fig. 6), we used the last lift detected before laser onset for aligning data. Tracking of hand position was performed using the APT software package (https://github.com/kristinbranson/APT). Hand position was annotated manually for a set of training frames, and the cascaded pose regression[54] algorithm was used to estimate the position of the hand in each remaining video frame. For the thalamus recordings and stimulation (Figs. 4, 5), APT was used with the DeepLabCut algorithm[55], and lifts were detected using threshold crossings of the upward hand velocity (threshold of 75 mm s^{-1}).

Electrophysiological recordings in motor cortex

Neural recordings were performed using the Whisper acquisition system (Janelia Applied Physics and Instrumentation Group) and 64-channel silicon probes (NeuroNexus A4×16-Poly2–5 mm-23 s-200-177-A64 or Janelia 4×16 probes). These probes consisted of four shanks with 16 contacts at the tip of each, over a depth of 345 µm (NeuroNexus) or 320 µm (Janelia probes). The electrode contacts were coated with PEDOT to lower their impedance, and in some cases, the tip of the probe was sharpened with a spinning hard disk to enable easier insertion. On the day before the experiment, a small craniotomy was made over motor cortex contralateral to the limb, and a stainless steel reference wire was implanted in visual cortex. During the recording session, the probe tips were positioned at approximately bregma +0.5 mm, 1.7 mm lateral, and slowly lowered to a depth of ~900 µm from the cortical surface, and a silicone elastomer (Kwik-Sil, World Precision Instruments) was applied to seal the craniotomy. At the end of the session, the probe was removed, and the craniotomy was re-sealed with silicone to allow a subsequent session on the following day. Signals were amplified with a gain of 200 and digitized to 16 bits at 25–50 kHz, and spike sorting was performed with JRClust (https://github.com/JaneliaSciComp/JRCLUST)[56].

Optogenetic manipulations

Cell-type-specific expression of ChR2 for cortical perturbations was achieved by either using VGAT-ChR2-eYFP mice[57] expressing ChR2 in inhibitory neurons (Slc32a1-COP4*H134R/eYFP, The Jackson Laboratory), or by crossing a Cre driver line to a Cre-dependent ChR2 reporter mouse, Ai32[58] (Rosa-CAG-LSL-ChR2(H134R)-eYFP-WPRE, The Jackson Laboratory). Experiments were performed in VGAT-ChR2-eYFP (n = 13), Tg(Tlx3-Cre)PL56Gsat x Ai32 (n = 3), Tg(Sim1-Cre)KJ18Gsat X Ai32 (n = 3), or Tg(Rbp4-Cre)KL100Gsat x Ai32 (n = 2) mice[59]. Rbp4-Cre x Ai32 mice were used for control trials only, as they provide poorer marking of pyramidal tract neurons than Sim1-Cre x Ai32. Experiments were attempted in three additional mice (VGAT-ChR2-eYFP, n = 2, and Tg(Sim1-Cre)KJ18Gsat x Ai32, n = 1), but were aborted owing to the poor quality of the electrophysiological signals. An optical fibre (200 µm or 400 µm, NA 0.39, Thorlabs) was coupled to a 473-nm laser (LuxX 473-80, Omikron Laserage) and positioned 2–4 mm over motor cortex in the head fixation apparatus, as described previously[26]. Five VGAT-ChR2-eFYP mice were implanted with an optical fibre over motor thalamus (bregma −1.1 mm, lateral 1.3 mm, depth 3.3 mm). A blue light-emitting diode array was directed at the animal's eyes throughout the session in order to mask the laser stimulus. Three trial types were used: control trials, in which the cue was presented with no laser stimulation; laser + cue trials, in which both were presented; and laser-only trials, in which the laser was turned on without a cue or food administration. A two-second laser stimulus (40 Hz sine wave) was initiated synchronously with the cue for VGAT-ChR2-eYFP mice, or 200 ms before cue onset for Tlx3-Cre x Ai32 and Sim1-Cre x Ai32 mice. Laser power was calibrated to the minimum level necessary to block reaching in probe experiments in the final days of training; this ranged from 10–50 mW at the fibre tip for VGAT mice, and 0.5–6 mW for Tlx3 and Sim1 mice. In mid-reach interruption experiments, a region of the video frame between the average lift and hand open locations was identified using BIAS software, and a contrast change in this region was used to open the laser shutter for 2 s. All optogenetic perturbations were unilateral, on the side opposite the

reaching arm. For mice with simultaneous recordings in motor cortex and thalamus ($n = 3$), ChR2 expression was driven in thalamus either by injecting a ChR2 reporter mouse Ai32 with AAV-2/9-Syn-Cre ($n = 2$), or by injecting a Vglut2-ires-Cre mouse (The Jackson Laboratory) with AAV-2/5-EF1a-DIO-hChR2(H134R)-mCherry ($n = 1$). For mice with cortical recording during the stimulation of thalamocortical terminals ($n = 3$), we used Vglut2-ires-Cre mice (The Jackson Laboratory) with AAV-2/5-EF1a-DIO-hChR2(H134R)-mCherry injected into motor thalamus, and stimulus trains consisting of 5 ms pulses at 4 Hz, 10 Hz or 40 Hz for 2 s were initiated synchronously with the cue.

Simultaneous electrophysiological recordings in motor cortex and thalamus

Mice expressing ChR2 in motor thalamus were head-fixed and trained on the reaching task. On the day before recording, craniotomies were performed to allow access to motor cortex (bregma +0.5 mm, 1.7 mm lateral) and thalamus (bregma −2.3 mm, 1.3 mm lateral), and were sealed with silicone elastomer (Kwik-Sil). On the day of recording, a four-shank, 64-channel silicon probe was inserted vertically into motor cortex at a depth of 800 μm, and a 960-site, 384-channel Neuropixels probe[45] (Option 3A) was inserted with a caudal tilt of 23 degrees from vertical to target thalamus. Once the thalamic probe was in position at ~4.6 mm from the surface, a pulse train of 473 nm light (40 Hz, 5 ms pulses, 2–12 mW) was applied through a fibre-coupled laser positioned over motor cortex. This pulse train stimulated thalamic terminals in motor cortex, and enabled identification of a region of the Neuropixels probe positioned in a thalamic region projecting to motor cortex (Extended Data Fig. 10a). The position of the Neuropixels probe was further verified by examining the probe track in a histological section (Extended Data Fig. 10b). The behavioural task was run as in the cortical recording experiments. Spike sorting was performed with Kilosort2[60] (https://github.com/MouseLand/Kilosort2) and Phy GUI (https://github.com/kwikteam/phy).

Data analysis

Peri-lift firing rates. For each neuron, lift-centred spike trains were smoothed with a Gaussian kernel ($\sigma = 50$ ms) and averaged across trials and z-scored. Lift modulation was assessed using a rank sum test comparing the raw spike counts in a 500-ms window centred at lift +200 ms with counts in a 500-ms window centred at lift −750 ms. Multiple comparisons were corrected using the Benjamini–Hochberg false discovery rate framework ($q < 0.05$), and all statistical tests in the study were two-sided (Fig. 1f, Extended Data Fig. 10d).

Trial-averaged PCA. Peri-lift firing rates were extracted by smoothing the spike trains with a Gaussian kernel ($\sigma = 25$ ms for Figs. 2b, 3f, $\sigma = 100$ ms in Fig. 4b and Extended Data Fig. 9c, and $\sigma = 50$ ms in the other analyses), z-scored, and averaged within each trial type for each neuron. The window used was −100 ms to 425 ms around each lift (Fig. 1h, Extended Data Fig. 1g), −100 ms to 350 ms around lift (Fig. 5b, Extended Data Fig. 7b), −250 ms to +250 ms from the end of cortical inactivation (Fig. 2b), −500 ms to +500 ms of the end of the cortical inactivation (Fig. 3f, blue), or −500 ms from the start of cortical inactivation to +500 ms from the end of the thalamic inactivation (Fig. 3f, green). Interneurons that increased their firing during cortical silencing were excluded in Figs. 2b, 3f, and one session in which no post-laser reaches occurred was excluded in Fig. 2. Principal component coefficients were fit using control trials only for lift-centred analyses (Fig. 1h, Extended Data Fig. 1g), or cortex inactivation only (Fig. 3f), and scores were then extracted for all trial types. For the lift-aligned PCA analyses, a control trial was included if lift and grab occurred within 500 ms following the cue, and a laser trial was included if lift and grab occurred within 500 ms of the end of the laser. We excluded one VGAT dataset and one Sim1 dataset from this analysis, as they had only 0 and 1 post-laser trial meeting this criterion, respectively. In order to examine the time of the divergence of neural trajectories from the cortex-inactivated state, we also smoothed the laser-aligned data with causal filters that used spikes only from the past (Extended Data Fig. 5). This resulted in trajectories that were causal, but not differentiable (as required by the analyses in Figs. 2e, 3h), so we used Gaussian smoothing for all other analyses (Figs. 1h, 2b, 3f, 4b, 5b, Extended Data Figs. 1g, 2, 5, 7b, 9c).

Single-trial PCA. Spike trains were smoothed with a Gaussian kernel ($\sigma = 100$ ms) and z-scored using the baseline mean and standard deviation, and principal components were extracted from trial-averaged, lift-aligned data. Z-scores from individual trials were then projected onto these components to obtain single-trial population activity (Fig. 5c, Extended Data Fig. 8c, lower two rows). Trial-averaged data in Fig. 4b (right) and Extended Data Fig. 9c were obtained by averaging these single-trial estimates (Fig. 5c, Extended Data Fig. 8c).

Gaussian-process factor analysis and neural distance. Neural population activity was reduced to a five-dimensional latent variable space using Gaussian-process factor analysis (GPFA)[61] (bin size 20 ms). A region of the dataset in which the recordings were stable was selected by finding the time interval and subset of neurons that maximized the quantity (usable neurons) × (usable seconds). The target spatial and neural states were defined using the three-dimensional position of the hand, and the five-dimensional latent variable representation of motor cortical activity obtained using GPFA, respectively. In both cases, the states were sampled at grab times, and the target state was defined to be the central location of the grab-triggered states, computed using convex hull peeling. Only 50% of the control trials were used to calculate the target states. The Euclidean distance from the target was then computed for each trial and time point, and the resulting distance curves were centred on the end of the laser (Fig. 2c, Supplementary Videos 2, 3).

Estimation of difference in external input contributions. We used the dynamical systems model, $\mathbf{r}'(t) = h(\mathbf{r}(t)) + \mathbf{u}(t)$, to calculate the difference in the contribution of external inputs between conditions following the end of cortical inactivation in VGAT-ChR2-eYFP mice. Suppose we have two types of trial, A and B. In Fig. 2e, these types correspond to trials in which a post-laser reach occurred or did not occur, and in Fig. 3h, they correspond to trials in which thalamus was perturbed following the end of cortical inactivation and trials in which the thalamus was not perturbed. Let $\mathbf{r}_A(t)$ and $\mathbf{r}_B(t)$ denote the population activity (principal component scores) on these trial types, and suppose the cortical inactivation ends at $t = 0$.

For $t \le 0$, we have fixed $\mathbf{r}_A(t) = \mathbf{r}_B(t) = \mathbf{0}$. Let $\varepsilon > 0$. According to the dynamical systems model,

$$\mathbf{r}_A'(t) - \mathbf{r}_B'(t) = (h(\mathbf{r}_A(t)) + \mathbf{u}_A(t)) - (h(\mathbf{r}_B(t)) + \mathbf{u}_B(t))$$

$$h(\mathbf{r}_A(0)) = h(\mathbf{0}) = h(\mathbf{r}_B(0))$$

Thus, for small ε, $h(\mathbf{r}_A(\varepsilon)) \approx h(\mathbf{r}_B(\varepsilon))$, so

$$\mathbf{u}_A(\varepsilon) - \mathbf{u}_B(\varepsilon) = \mathbf{r}_A'(\varepsilon) - \mathbf{r}_B'(\varepsilon) - (h(\mathbf{r}_A(\varepsilon)) - h(\mathbf{r}_B(\varepsilon))) \approx \mathbf{r}_A'(\varepsilon) - \mathbf{r}_B'(\varepsilon)$$

Thus, subtracting the derivative of population activity for the two conditions allows us to estimate the difference in the contributions of external inputs shortly after the end of cortical inactivation. This approximation relies on two assumptions. First, the firing rate derivative is additive in the autonomous and input-dependent contributions. Second, ε is small; that is, $h(\mathbf{r}(0)) = h(\mathbf{0})$ must be close to $h(\mathbf{r}(\varepsilon))$.

Direction of neural trajectories. This analysis addresses the question of whether neural activity for post-laser reaches first returned to the control baseline state. For each perturbation (VGAT, Tlx3 and Sim1), we estimated the population activity on control reaches, $\mathbf{r}_c(t)$, and

post-laser reaches, $\mathbf{r}_i(t)$, using the first six principal component scores. These captured 98%, 99% and 97% of the variance in control reaches for VGAT, Tlx3 and Sim1, respectively. At each point in time around the lift, we computed the derivative and divided by the norm of the derivative. This yielded the direction in population activity for control and laser reaches (see Extended Data Fig. 2a), shown for the first two principal components by the yellow and blue arrows in Extended Data Fig. 2b–d. We compared the similarity between the control and laser directions at each point in time by computing the inner product between them. This yielded the yellow curves in the right panels in Extended Data Fig. 2a–d. We then computed the difference between the population activity in the laser condition and the initial control state and normalized it to have unit length; this resulted in the direction from the state in the laser condition to the initial control state at each point in time, shown by the red arrows in the left panels of Extended Data Fig. 2b–d. We then found the similarity between this direction and the direction of the laser trajectory by computing their inner product, shown in the red curves in the right panels of Extended Data Fig. 2b–d. This analysis suggests that following the perturbations, the neural population recapitulated the pattern for reaching without returning to the control initial state.

Neural decoding. A linear filter was designed to decode 3D hand velocities from neural activity during reaches. The decoded hand velocities were then used as proxies for the components of neural activity relevant to movement in order to assess the effect of different types of pre-lift perturbations (VGAT, Tlx3, Sim1) on the neural activity during reach (Extended Data Fig. 3).

For decoding, both the 3D hand trajectories (500 Hz, see 'Behavioural task and video analysis') and the multiunit neural activity (counts of all detected spikes on each recording channel with 2-ms bins, no single unit identification) were smoothed with the same Gaussian kernel ($\sigma = 25$ ms). Velocities were numerically derived from smoothed hand trajectories using a central difference filter of order 8. Firing rates were z-scored with respect to the activity at rest, computed combining 1.5-s windows preceding the start of each trial. Channels with mean absolute z-scores greater than 100 during movement (for example, for units with standard deviations very close to zero) were excluded from further analysis. The z-scores of neural activity were then processed with PCA for denoising and dimensionality reduction, with the principal components computed from the lift-aligned trial-averaged activity in control trials (window −100 ms to 300 ms around lift). The decoding results with this method were better than with any alternative choices we tried (Extended Data Fig. 3m, n), which included: (1) computing the PCA components from the data matrix obtained concatenating all lift-aligned control and post-laser neural trajectories (after end of perturbation) rather than from trial-averaged control activity, (2) using only identified single-unit activity instead of multiunit activity, (3) using GPFA instead of PCA for dimensionality reduction, and (4) smoothing the firing rates with different Gaussian kernels (ranging from $\sigma = 2$ms to $\sigma = 500$ms) before Z-scoring and dimensionality reduction.

The decoder uses time-invariant coefficients to decode the hand velocity at any given time as a linear combination of the 15 most recent samples of PCA-reduced neural activity (hence up to 28 ms in the past). The decoder coefficients were obtained by regressing (ordinary least square sense, implemented via QR factorization in Matlab) velocity data against PCA-reduced neural data in a subset of trials (training set). Hand velocities were decoded during reaches in which the lift-to-grab sequence occurred within the first 500 ms after the cue (for control trials) or within the first 500 ms after the end of perturbation (for laser trials). Sessions without post-perturbation reaches satisfying these criteria (1 Vgat, 1 Sim1 session) or with only one such reach (1 Sim1 session) were excluded from the neural decoding analysis. The decoding window was extended by 50 ms before lift and 50 ms after grab, to include the beginning and the end of the reaching movement. Within each dataset, the training set used in fitting the decoder coefficients was comprised of a majority of control trials (three fifths). An additional subset of control trials (one fifth) was used to cross-validate the optimal choice of the number of PCA components to use in the decoder, as follows. For any choice of number of components to keep, a decoder was computed from the training control trials and used to decode the hand velocities in the validation control trials. The performance of each decoder was compared in terms of mean squared error between observed and decoded velocities. The minimum number of PCA dimensions that guaranteed performance within 1% of the overall minimum mean squared error across all choices was selected (using this 1% margin considerably reduced the dimensionality of the data in some sessions without compromising decoding performance). Finally, the selected decoder was used to decode hand velocities in the remaining testing subset of control trials (one fifth), which were not used for training or cross-validation, and on the laser trials in which reaches occurred at the end of the perturbation.

We found that the decoder performance was not uniform across the three directions (forward, lateral, upward), but was consistently worse in the lateral direction than in the other two directions. This may reflect the smaller extent to which the reaching trajectories sample lateral movements of the hand, or may reflect an insufficient sampling of the neural population of motor cortical cells responsible for the lateral movement of the hand. We thus showed the decoding performance in each direction separately, and primarily used the coefficient of determination (R^2) between decoded and observed hand velocities in each direction as the summary performance metric, except for the comparisons of decoding quality across trial types (Extended Data Fig. 3c, g, k) and choices of the decoder (Extended Data Fig. 3m, n) in which all directions were pooled together before computing the coefficient of determination. In most of the datasets, the velocity decoding accuracy was higher for control testing trials than laser trials. Nevertheless, in most sessions the decoder trained only on control trials still performed reasonably well on laser trials (at least in some of the directions).

Analysis of simultaneous recordings from thalamus and cortex. For analysis of trial-averaged cortical and thalamic firing rates, and for the identification of lift-modulated thalamic units, analyses were performed as described above for the cortical recording experiments (Fig. 5b, Extended Data Fig. 10d). For single-trial analysis of population activity, lift-aligned thalamic and cortical spiking was smoothed with a $\sigma = 100$ ms Gaussian kernel and z-scored using the baseline firing rates from lift −500 ms to lift −100 ms. Activity was first averaged across trials, and PCA was performed on the trial-averaged data matrix to obtain the principal component coefficients. Next, activity from individual trials was multiplied by this coefficient matrix, resulting in estimates of the single-trial population trajectories for cortex and thalamus (Fig. 5c).

According to the dynamical systems model, the derivative of the cortical state can be expressed as $\mathbf{r}'(t) = h(\mathbf{r}(t)) + \mathbf{u}(t)$. In the linear case, considering inputs from the thalamus, this corresponds to $\mathbf{r}'(t) = A\mathbf{r}(t) + B\mathbf{s}(t)$, where $\mathbf{s}(t)$ is the thalamic state. Because we measured cortical and thalamic activity simultaneously, we attempted to fit models of this form by regression. The cortical population trajectories (either the single-trial or trial-averaged estimates) for the first three principal components were numerically differentiated. We took these estimates of the derivative of the cortical state as the dependent variables for regression analyses using three different sets of independent variables: (1) thalamic population trajectories (first N principal components, with N ranging from 1 to 10), (2) cortical population trajectories (first N components), and (3) both thalamic and cortical population trajectories (first N components). These regression models were fit with ordinary least squares for both the trial-averaged (Fig. 5d, top row) and single-trial data (Fig. 5d, bottom row), with the goodness-of-fit of each model given by the coefficient of determination (R^2 value).

All analyses were performed with custom-written software in Matlab, except where otherwise noted.

Reporting summary

Further information on research design is available in the Nature Research Reporting Summary linked to this paper.

Data availability

The data generated in this study are available from the corresponding author on reasonable request.

Code availability

Code for automatic annotation of behaviour and behavioural waypoint estimation is available at https://github.com/kristinbranson/JAABA. Code for hand tracking is available at https://github.com/kristinbranson/APT. Code for spike sorting is available at https://github.com/JaneliaSciComp/JRCLUST, https://github.com/MouseLand/Kilosort2, and https://github.com/kwikteam/phy. Other code is available from the corresponding author on reasonable request.

51. Pandarinath, C. et al. Inferring single-trial neural population dynamics using sequential auto-encoders. *Nat. Methods* **15**, 805–815 (2018).
52. Dalal, N. & Triggs, B. in *International Conference on Computer Vision and Pattern Recognition 1* (IEEE Computer Society, 2005).
53. Laptev, I., Marszałek, M., Schmid, C. & Rozenfeld, B. in *International Conference on Computer Vision and Pattern Recognition 1–8* (IEEE Computer Society, 2008).
54. Dollár, P., Welinder, P. & Perona, P. Cascaded pose regression. In *International Conference on Computer Vision and Pattern Recognition 1* (IEEE Computer Society, 2010).
55. Mathis, A. et al. DeepLabCut: markerless pose estimation of user-defined body parts with deep learning. *Nat. Neurosci*. **21**, 1281–1289 (2018).
56. Jun, J. J. et al. Real-time spike sorting platform for high-density extracellular probes with ground-truth validation and drift correction. Preprint at *bioRxiv* https://doi.org/10.1101/101030 (2017).
57. Guo, Z. V. et al. Flow of cortical activity underlying a tactile decision in mice. *Neuron* **81**, 179–194 (2014).
58. Madisen, L. et al. A toolbox of Cre-dependent optogenetic transgenic mice for light-induced activation and silencing. *Nat. Neurosci*. **15**, 793–802 (2012).
59. Gerfen, C. R., Paletzki, R. & Heintz, N. GENSAT BAC cre-recombinase driver lines to study the functional organization of cerebral cortical and basal ganglia circuits. *Neuron* **80**, 1368–1383 (2013).
60. Stringer, C. et al. Spontaneous behaviors drive multidimensional, brainwide activity. *Science* **364**, eaav7893 (2019).
61. Yu, B. M. et al. Gaussian-process factor analysis for low-dimensional single-trial analysis of neural population activity. *J. Neurophysiol*. **102**, 614–635 (2009).

Acknowledgements We thank B. Yu and the Yu laboratory, S. Edgley, J. Dudman, A. K. Lee, M. Ahrens, A. Finkelstein, J. Fitzgerald and K. Shan for discussions and comments on an earlier version of the manuscript; A. Lee for tracking software; T. Harris, B. Barbarits, B. Karsh, S. Sawtelle, P. Polidoro, D. Flickinger and the Neuropixels Project for instrumentation development and support; W. Sun for probe sharpening and PEDOT application; A. Taylor for development of WaveSurfer; J. Jun and M. Pachitariu for spike-sorting software; S. Chung for assistance with video labelling; S. DiLiso for fibre implantation surgeries; K. Ritola and the Janelia Virus Tools facility for providing viruses; J. Kuhl for the mouse drawings; and the Janelia Vivarium, Histology and Scientific Computing facilities for support.

Author contributions B.A.S., J.-Z.G., J.D.C. and A.W.H. designed the experiments. B.A.S. and J.-Z.G. performed electrophysiological recordings in motor cortex. J.-Z.G. performed recordings in cortex with thalamic inactivation. J.D.C. performed simultaneous recordings in cortex and thalamus and recordings in cortex during stimulation of thalamic terminals. J.-Z.G. performed behavioural experiments. B.A.S. analysed electrophysiology and behaviour data and generated the figures. J.-Z.G. and W.G. analysed behaviour data. M.M. developed and performed the neural decoding analyses. B.A.S., M.M. and A.W.H. interpreted the results. N.V. and K.B. developed preliminary analyses for decoding of behavioural waypoints. M.K. and K.B. developed computer vision algorithms and software. B.A.S., A.W.H., M.M., B.M. and K.B. wrote the paper with input from all authors. A.W.H. supervised the project.

Competing interests The authors declare no competing interests.

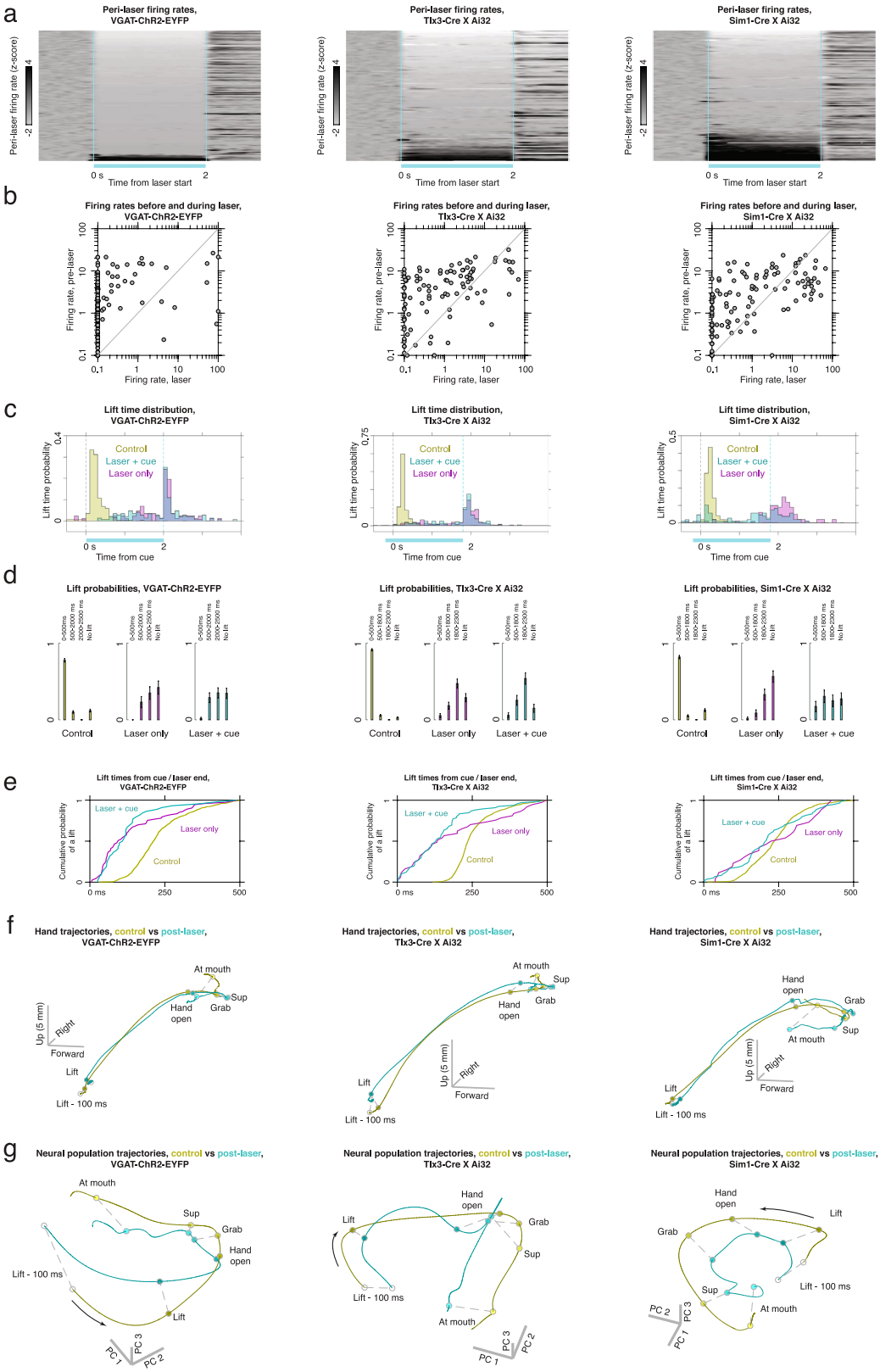
Additional information

Supplementary information is available for this paper at https://doi.org/10.1038/s41586-019-1869-9.

Correspondence and requests for materials should be addressed to A.W.H.

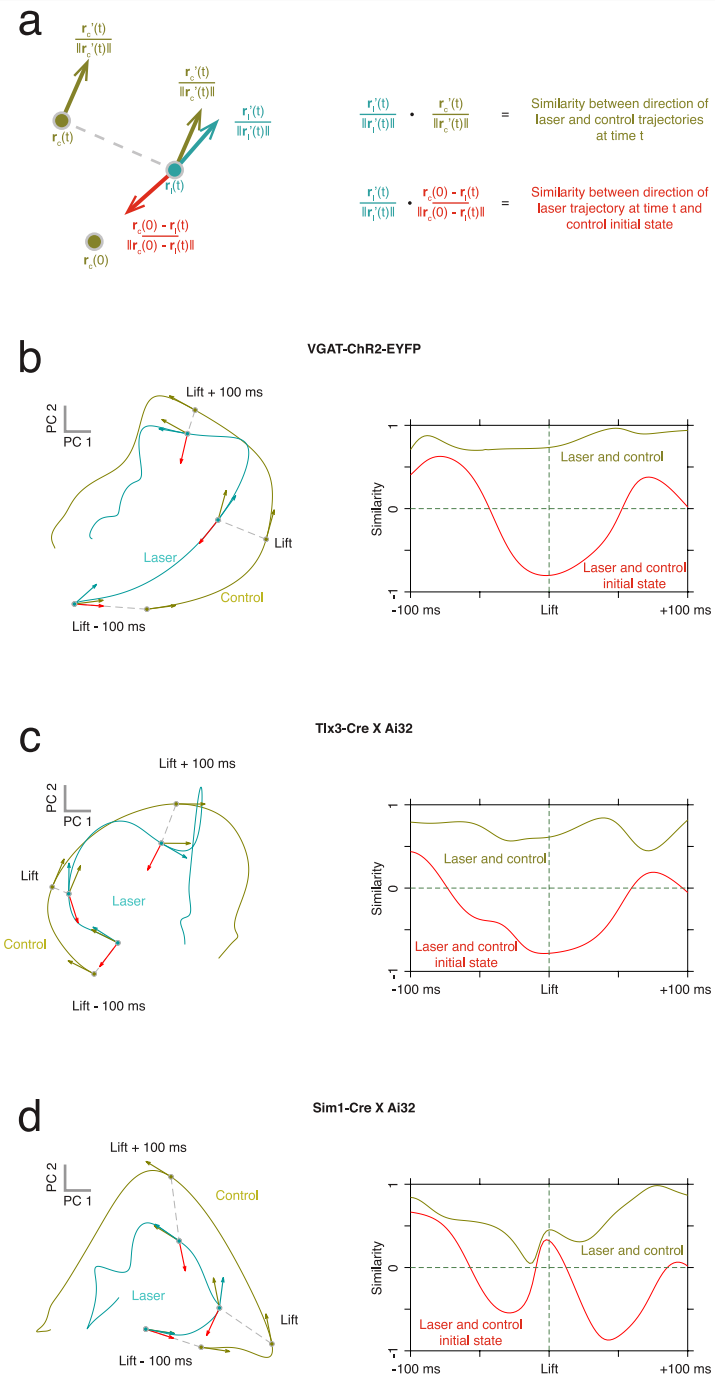
Peer review information *Nature* thanks Jesse Goldberg and the other, anonymous, reviewer(s) for their contribution to the peer review of this work.

Reprints and permissions information is available at http://www.nature.com/reprints.

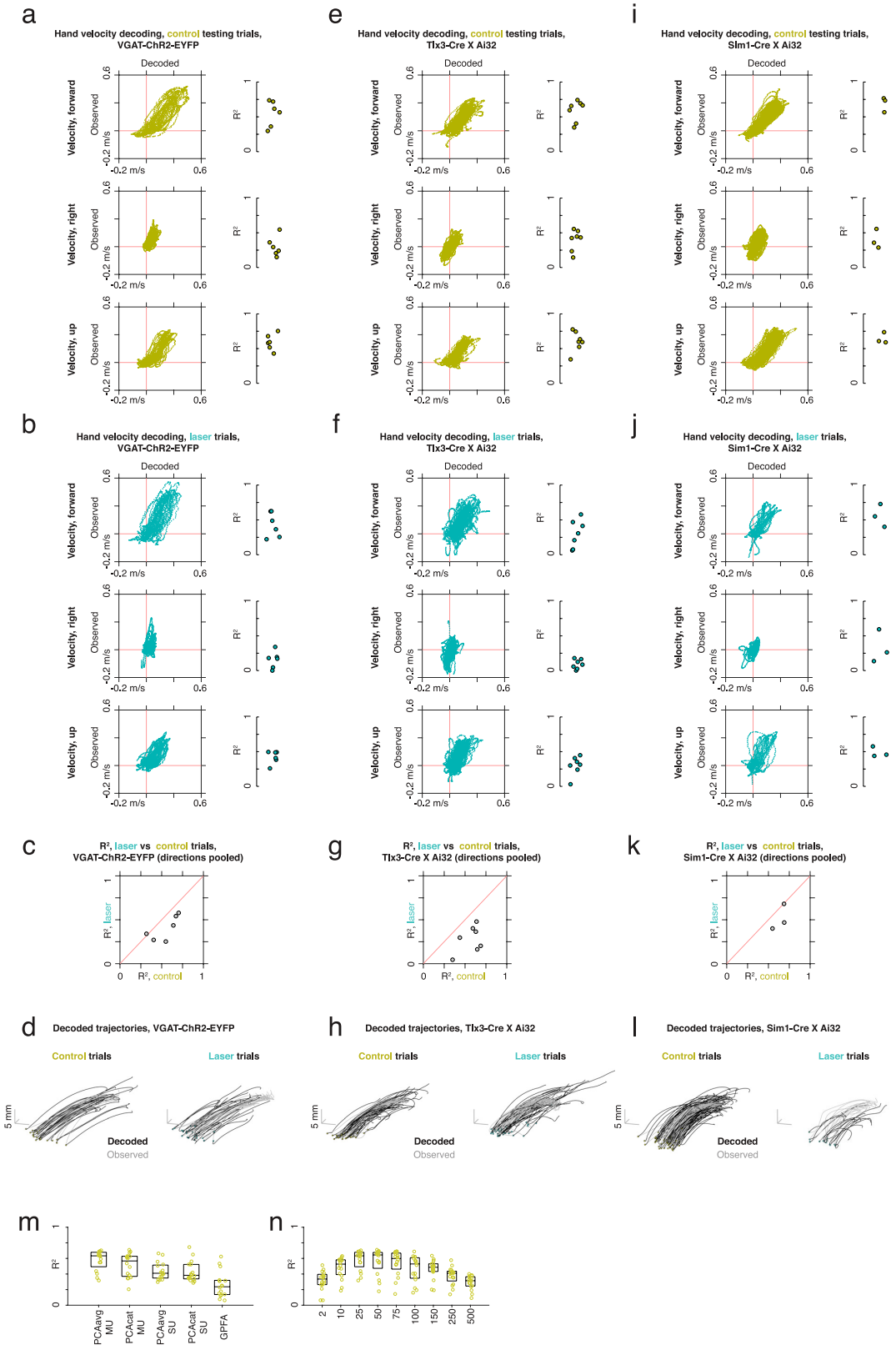


Extended Data Fig. 1 | See next page for caption.

Extended Data Fig. 1 | Summary of effects of optogenetic perturbations of motor cortex. Each of the three columns shows data from one mouse type: left, VGAT-ChR2-eYFP ($n = 5$ mice, $n = 7$ sessions); middle, Tlx3-Cre x Ai32 ($n = 3$ mice, $n = 7$ sessions); right, Sim1-Cre x Ai32 ($n = 3$ mice, $n = 5$ sessions). **a**, Average *z*-scored firing rates of motor cortical neurons before, during and after optogenetic activation of inhibitory interneurons (left), intratelencephalic neurons (middle) and pyramidal tract neurons (right). The blue bars under the *x* axes represent laser-on epochs. Left, black bands at the bottom are putative inhibitory interneurons. **b**, Firing rates before and during laser stimulation for each mouse type. Firing rates outside the range 0.1–100 were plotted at these values owing to the log-log scale. **c**, Distribution of lift times on control (yellow), laser + cue (blue) and laser-only (magenta) trials for each mouse type. Histograms show data only for trials where a lift occurred. **d**, Probability of a lift in each time bin (binomial maximum likelihood estimate) for control (yellow), laser-only (magenta) and laser + cue (blue) trials. Error bars show 95% binomial confidence intervals. **e**, Distribution of lift times for trials in which a lift occurred within 500 ms of either the cue (for control trials, yellow) or following the end of the laser (blue for laser + cue trials and magenta for laser only trials). **f**, Average hand trajectories on control (yellow) and post-laser (blue) reaches. **g**, Neural population activity from lift −100 ms to lift +425 ms on control (yellow) and post-laser (blue) reaches, obtained using trial-averaged PCA. For **f** and **g**, one session was removed for VGAT ($n = 4$ mice, $n = 6$ sessions), and one was removed for Sim1 ($n = 2$ mice, $n = 4$ sessions), owing to the absence of post-laser reaches for alignment.

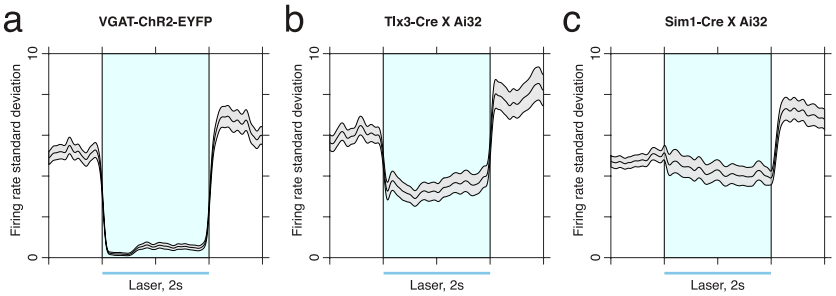


Extended Data Fig. 2 | Comparison of the direction of neural trajectories for post-laser reaches with the direction of control trajectories, and with the direction to the initial cortical state on control trials. a, Explanation of the analysis method. We represent the population trajectory on control trials, $\mathbf{r}_c(t)$, and laser trials, $\mathbf{r}_l(t)$, using the first six principal component scores, which account for 98%, 99% and 97% of the variance on control trials for VGAT, Tlx3 and Sim1, respectively. For each time point along the peri-lift neural trajectory $\mathbf{r}_l(t)$ for post-laser reaches, we obtain the direction of the neural trajectory by computing the derivative and dividing by the norm of the derivative (blue). We perform the same calculation for the control trajectory $\mathbf{r}_c(t)$ (yellow), and also compute the direction from the neural state in the laser trajectory to the initial control state (red). We then compare the direction of the laser trajectory with the control direction and the direction to the initial control state by taking the inner product with each. **b**, Left, neural population trajectories (first two principal components) for control (yellow) and post-laser (blue) reaches in VGAT-ChR2-eYFP mice ($n = 4$ mice, $n = 6$ sessions). The direction of the trajectories for control (yellow arrows) and laser (blue arrows) trajectories along the first two principal components are shown, along with the direction from the laser trajectory to the control initial state (red arrows). Right, similarity (inner product) between the direction of the laser trajectory and the direction of the control trajectory (yellow curve), and similarity between the direction of the laser trajectory and the control initial state (red curve). **c**, As in **b**, but for Tlx3-Cre x Ai32 mice ($n = 3$ mice, $n = 7$ sessions). **d**, As in **b**, but for Sim1-Cre x Ai32 mice ($n = 2$ mice, $n = 4$ sessions).

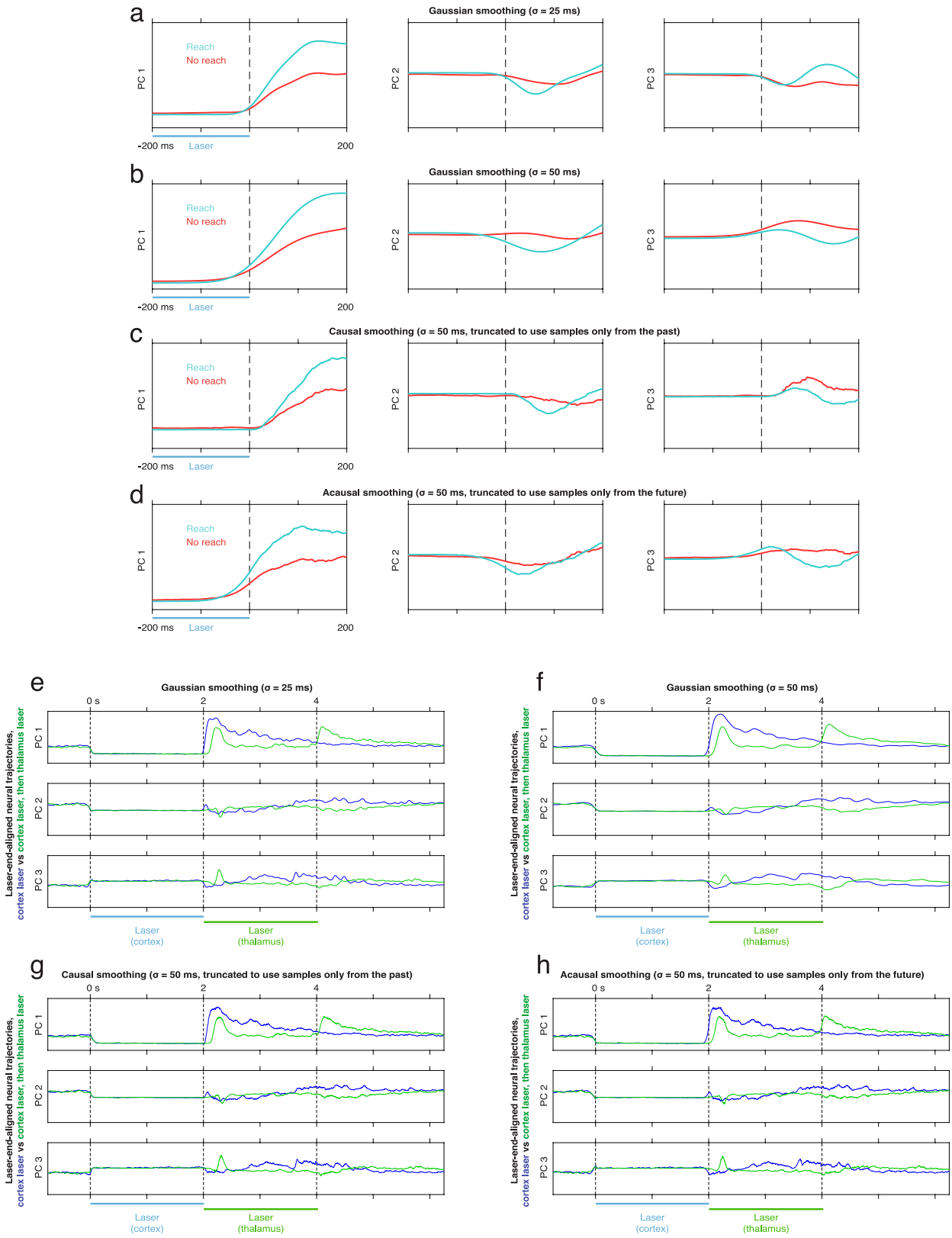


Extended Data Fig. 3 | See next page for caption.

Extended Data Fig. 3 | Decoding of hand velocity from motor cortical activity on control and post-perturbation reaches. a, Left, scatterplots of decoded versus observed hand velocity in the forward, right, and upward directions on control reaches in an example session from a VGAT-ChR2-eYFP mouse. Only testing trials not used for training the decoder were used. Right, R^2 values for the regression of observed on decoded velocities for control reaches in each VGAT-ChR2-eYFP dataset ($n = 4$ mice, $n = 6$ sessions). **b**, Left, scatter plots of decoded versus observed hand velocity for post-laser reaches in the dataset from **a**. Right, R^2 values for the regression of observed on decoded velocities for post-laser reaches in each VGAT-ChR2-eYFP dataset. **c**, Comparison of the decoder performance in control versus post-laser reaches for the dataset from **a**, **b** assessed using the R^2 computed after pooling across directions. **d**, Decoded position trajectories obtained by upsampling and numerically integrating (Simpson's rule) the decoded velocity for control trials (left) and laser trials (right) for the dataset in **a**, **b. e**–**h**, Decoder performance for Tlx3-Cre x Ai32 mice ($n = 3$ mice, $n = 7$ sessions), organized as in **a**–**d. i**–**l**, Decoder performance for Sim1-Cre x Ai32 mice ($n = 2$ mice, $n = 3$ sessions), organized as in **a**–**d. m**, Decoding performance for control testing trials on all sessions, by decoding method used ($n = 9$ mice, $n = 16$ sessions; all perturbation types aggregated). PCAavg refers to PCA coefficients extracted on lift-aligned trial averages with single trials projected onto these coefficients; PCAcat refers to PCA coefficients extracted on concatenated trial data; MU refers to multiunit activity; and SU refers to single units. For each method, the number of neural dimensions used for decoding was cross-validated (see Methods). Box plot shows the median and the 25th and 75th percentiles. **n**, Decoding performance for the PCAavg MU method, by the standard deviation of the Gaussian kernel used to extract firing rates ($n = 9$ mice, $n = 16$ sessions).

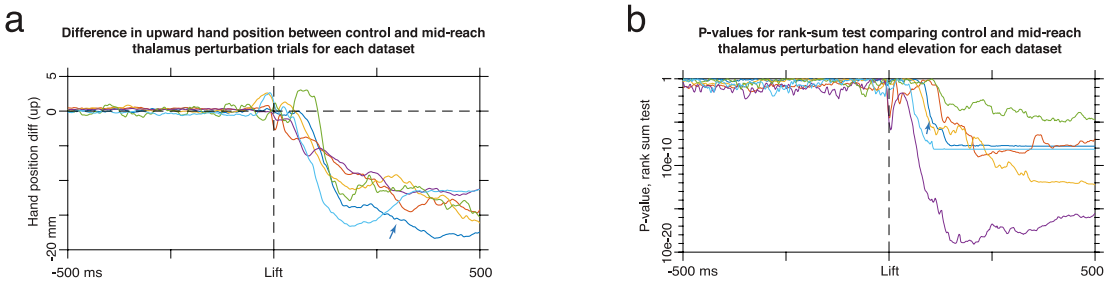


Extended Data Fig. 4 | Variability of firing rates during optogenetic perturbations to the cortical state. a, Standard deviation of firing rates across trials during laser stimulation in VGAT-ChR2-eYFP mice. The black curve is the standard deviation (over trials), averaged over all neurons ($n = 5$ mice, $n = 7$ sessions, $n = 155$ neurons). Error bars show s.e.m. Identified inhibitory neurons, which exhibited a firing-rate increase during the laser, were excluded. Smoothing was applied with a 50-ms Gaussian kernel for each trial. **b**, Standard deviation of firing rates across trials during laser stimulation in Tlx3-Cre x Ai32 mice, as in **a** ($n = 3$ mice, $n = 7$ sessions, $n = 100$ neurons). **c**, Standard deviation of firing rates across trials during laser stimulation in Sim1-Cre x Ai32 mice ($n = 3$ mice, $n = 5$ sessions, $n = 115$ neurons). Because it wasn't possible to identify inhibitory neurons when excitatory neurons were stimulated, all cells were included in **b** and **c**.

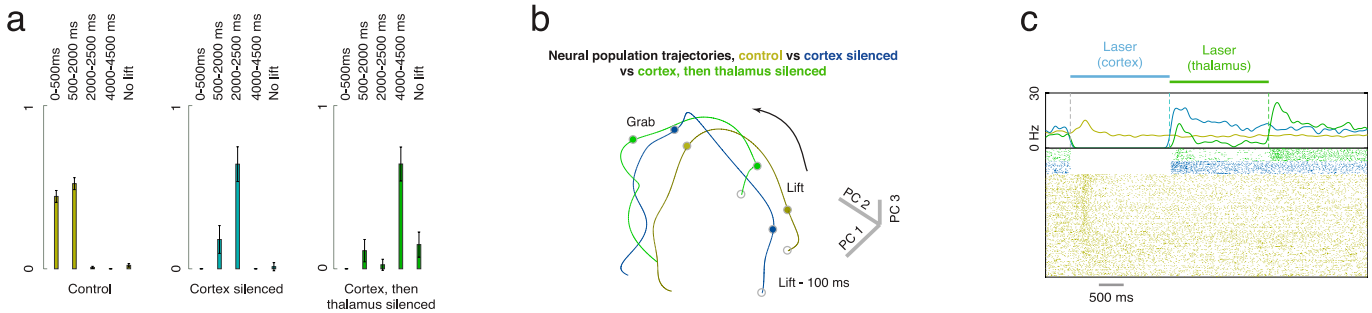


Extended Data Fig. 5 | See next page for caption.

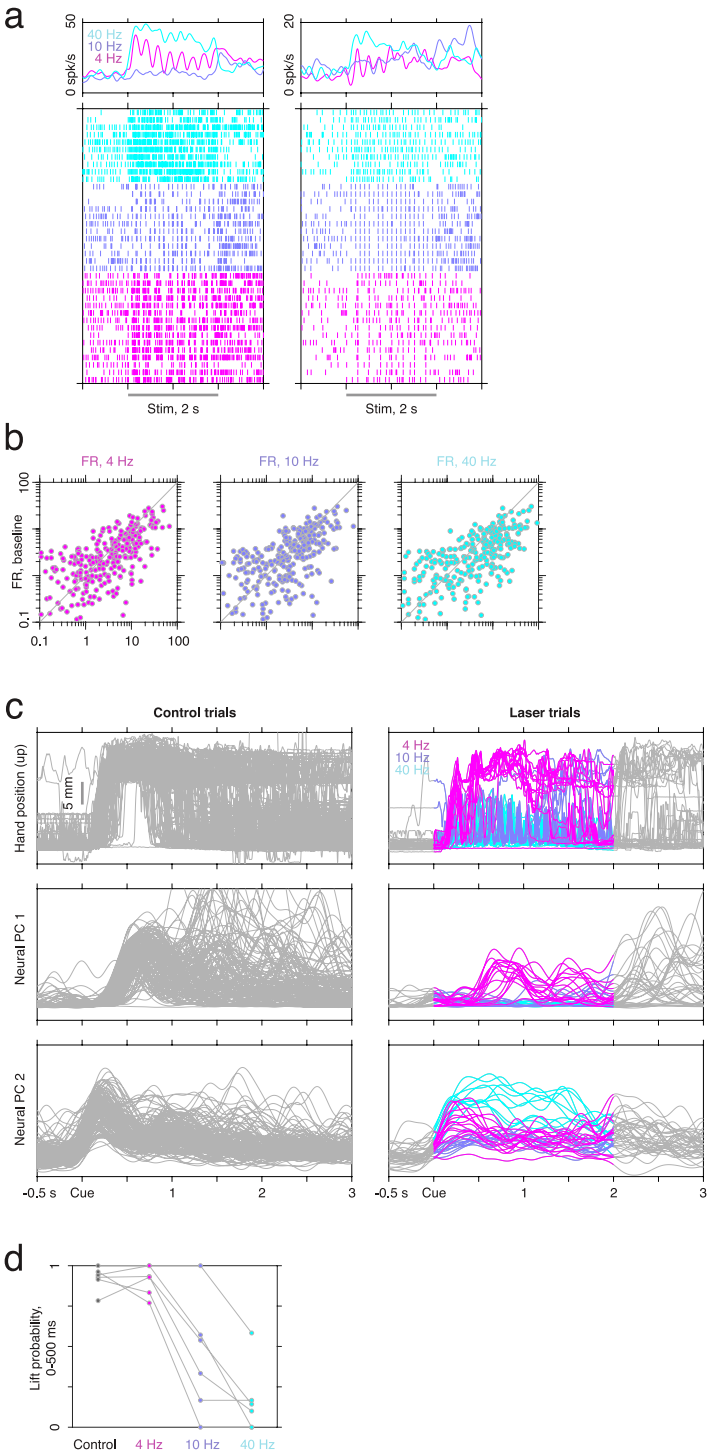
Extended Data Fig. 5 | Effect of different spike-train smoothing methods. **a**, Gaussian smoothing with a kernel width of $\sigma = 25$ ms for the reach–no-reach experiment, as shown in Fig. 2b. Note that the activity appears to change from the constant perturbed state slightly before the end of the laser. This is because the kernel smooths forward into the post-laser epoch. **b**, Gaussian smoothing with $\sigma = 50$ ms. The divergence from the perturbed state begins earlier owing to a higher level of smoothing. **c**, Causal smoothing with a half-Gaussian kernel, truncated to use samples only from the past. Neural activity diverges from the perturbed state only after the end of the laser. **d**, Acausal smoothing with a half-Gaussian kernel, truncated to use samples only from the future. **e**, Gaussian smoothing in the sequential inactivation experiment with a kernel width of $\sigma = 25$ ms, as shown in Fig. 3f. Note that the activity appears to change from the constant perturbed state slightly before the end of the cortical inactivation. There is also a delay from the start of the cortical inactivation to the arrival of the neural state at the constant value. **f**, Gaussian smoothing with $\sigma = 50$ ms. **g**, Causal smoothing with a half-Gaussian kernel, truncated to use samples only from the past. Neural activity diverges from the perturbed state only after the end of the laser. However, there is still a lag from the start of cortical inactivation to the arrival of neural activity at the constant perturbed state. **h**, Acausal smoothing with a half-Gaussian kernel, truncated to use samples only from the future. Neural activity again diverges from the perturbed state before the end of the cortical inactivation. At the start of the cortical inactivation, neural activity has already arrived at the perturbed state.



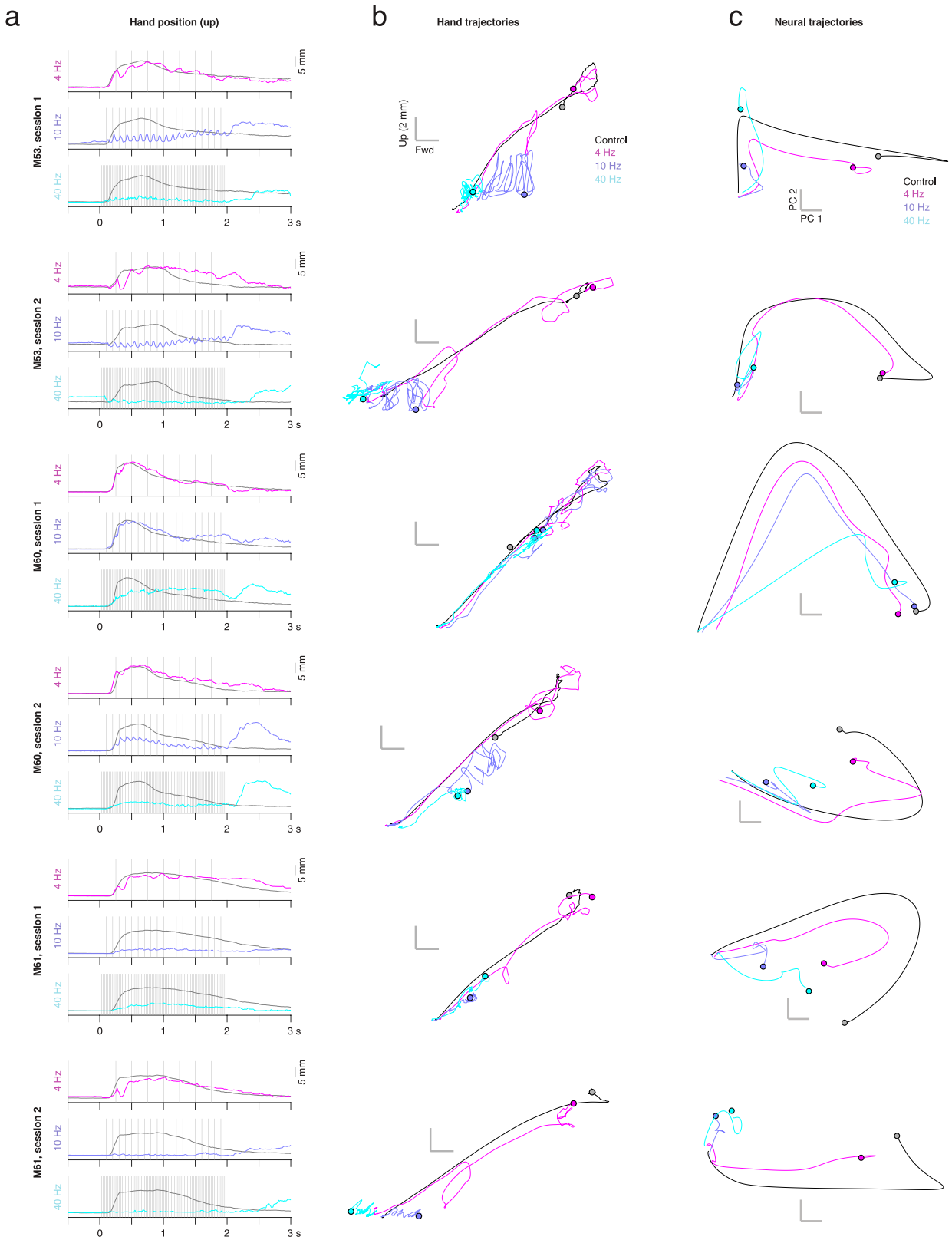
Extended Data Fig. 6 | Effect of mid-reach thalamic perturbation on hand trajectory in VGAT-ChR2-eYFP mice. a, Average difference in hand elevation between mid-reach perturbation trials and control trials for each dataset ($n = 4$ mice, $n = 6$ sessions). The example dataset shown in Fig. 3c is marked with the blue arrow. **b**, *P* values from two-sided rank sum tests at each time point, comparing the upward hand position on control and mid-reach thalamic inactivation trials.



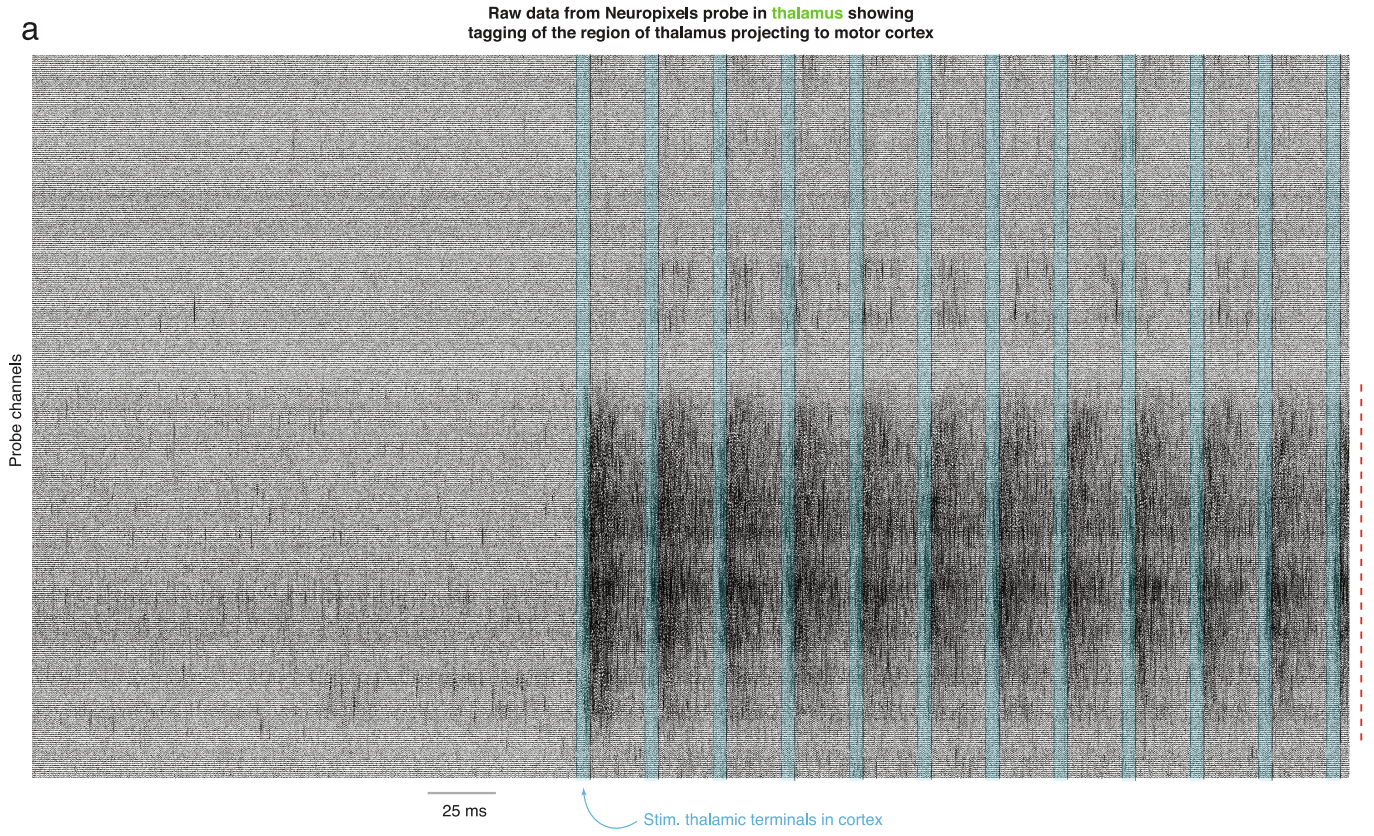
Extended Data Fig. 7 | Sequential inactivation of cortex and thalamus. **a**, Fraction of trials with lifts in each epoch for control trials (yellow), cortical inactivation only (blue) and sequential inactivation of cortex and thalamus (green) ($n = 3$ mice, $n = 4$ sessions). The cortical inactivation ends at 2,000 ms from the start of the trial, and the thalamic inactivation ends at 4,000 ms. Bars show maximum likelihood estimates of the binomial probability, with 95% confidence intervals. Corresponding data in Fig. 3d–f. **b**, Lift-locked neural population activity from lift −100 ms to lift +350 ms for control (yellow), post-cortex-inactivation (blue) and post-sequential-inactivation reaches (green), obtained using trial-averaged PCA; $n = 3$ mice, $n = 4$ sessions, $n = 127$ neurons. Circles indicate lift −100 ms, lift and grab times. **c**, Firing rates and spike rasters for an example cortical neuron on control trials (yellow), cortical inactivation (blue) and sequential inactivation of cortex and thalamus (green).



Extended Data Fig. 8 | Effects of stimulation of thalamocortical terminals on cortical firing rates and behaviour. a, Firing rates and spike rasters for two example neurons at each stimulation frequency. **b**, Firing rates in the 2 s before stimulation versus the 2 s during stimulation at each stimulation frequency. Each point is a single neuron ($n = 288$ cells). **c**, Left, single-trial hand position and neural activity (first two principal components) for control trials in the dataset shown in Fig. 4b. Right, hand position and neural activity in the same session under optogenetic stimulation of thalamocortical terminals at 4 Hz, 10 Hz and 40 Hz. **d**, Probability that a lift is initiated within the first 500 ms of the cue on control trials and at each stimulation frequency. Each curve shows a single session ($n = 6$ sessions, $n = 3$ mice). Corresponding data in Fig. 4.



Extended Data Fig. 9 | Hand kinematics and neural activity during thalamocortical stimulation for each dataset. a, Trial-averaged hand position aligned to the cue under 4 Hz, 10 Hz and 40 Hz stimulation. The control position is shown in grey. Vertical lines indicate the times of laser pulses. Each row corresponds to a single experimental session. **b**, Hand trajectories for control and laser trials for each dataset in **a**. Time limits are cue −250 ms to cue +1,000 ms, and the dot marks the end of the trajectory. **c**, Neural trajectories for each dataset in **a**. Corresponding data in Fig. 4; $n = 3$ mice, $n = 6$ sessions.



Extended Data Fig. 10 | Simultaneous recording in thalamus and motor cortex. a, Raw data from the thalamic Neuropixels probe aligned to motor cortex stimulation (cyan). A band of channels (red dotted line) exhibited activity locked to motor cortical stimulation, indicating projections to motor cortex. **b**, Histological section showing targeting of probe to motor thalamus. The bright region in the thalamus indicates ChR2 expression (eYFP) in an Ai32 mouse with an injection of AAV-2/9-Syn-Cre. The Neuropixels probe in the thalamus was coated with a green dye (DiO). The red dotted line corresponds approximately to the red dotted line in **a**. **c**, Spike rasters from cortical and thalamic neurons on a single reaching trial. **d**, Peri-lift firing rates for thalamic neurons ($n = 3$ mice, $n = 3$ sessions).

nature research

Corresponding author(s): Adam Hantman

Last updated by author(s): Sep 26, 2019

Reporting Summary

Nature Research wishes to improve the reproducibility of the work that we publish. This form provides structure for consistency and transparency in reporting. For further information on Nature Research policies, see Authors & Referees and the Editorial Policy Checklist.

Statistics

For all statistical analyses, confirm that the following items are present in the figure legend, table legend, main text, or Methods section.

n/a	Confirmed	
☐	☒	The exact sample size (*n*) for each experimental group/condition, given as a discrete number and unit of measurement
☐	☒	A statement on whether measurements were taken from distinct samples or whether the same sample was measured repeatedly
☐	☒	The statistical test(s) used AND whether they are one- or two-sided *Only common tests should be described solely by name; describe more complex techniques in the Methods section.*
☐	☒	A description of all covariates tested
☐	☒	A description of any assumptions or corrections, such as tests of normality and adjustment for multiple comparisons
☐	☒	A full description of the statistical parameters including central tendency (e.g. means) or other basic estimates (e.g. regression coefficient) AND variation (e.g. standard deviation) or associated estimates of uncertainty (e.g. confidence intervals)
☐	☒	For null hypothesis testing, the test statistic (e.g. *F*, *t*, *r*) with confidence intervals, effect sizes, degrees of freedom and *P* value noted *Give P values as exact values whenever suitable.*
☒	☐	For Bayesian analysis, information on the choice of priors and Markov chain Monte Carlo settings
☒	☐	For hierarchical and complex designs, identification of the appropriate level for tests and full reporting of outcomes
☐	☒	Estimates of effect sizes (e.g. Cohen's *d*, Pearson's *r*), indicating how they were calculated

Our web collection on statistics for biologists contains articles on many of the points above.

Software and code

Policy information about availability of computer code

Data collection	Video acquisition software is available at https://bitbucket.org/iorodeo/bias/src/default/. Behavioral control software is available at https://wavesurfer.janelia.org/.
Data analysis	Code for automatic annotation of behavior and behavioral waypoint estimation is available at https://github.com/kristinbranson/JAABA. Code for hand tracking is available at https://github.com/kristinbranson/APT. Code for spike sorting is available at https://github.com/JaneliaSciComp/JRCLUST, https://github.com/MouseLand/Kilosort2, and https://github.com/kwikteam/phy.

For manuscripts utilizing custom algorithms or software that are central to the research but not yet described in published literature, software must be made available to editors/reviewers. We strongly encourage code deposition in a community repository (e.g. GitHub). See the Nature Research guidelines for submitting code & software for further information.

Data

Policy information about availability of data

All manuscripts must include a data availability statement. This statement should provide the following information, where applicable:

- Accession codes, unique identifiers, or web links for publicly available datasets
- A list of figures that have associated raw data
- A description of any restrictions on data availability

Data and code are available from the corresponding author on reasonable request.

Field-specific reporting

Please select the one below that is the best fit for your research. If you are not sure, read the appropriate sections before making your selection.

☒ Life sciences ☐ Behavioural & social sciences ☐ Ecological, evolutionary & environmental sciences

For a reference copy of the document with all sections, see nature.com/documents/nr-reporting-summary-flat.pdf

Life sciences study design

All studies must disclose on these points even when the disclosure is negative.

Sample size	No statistical methods were used to predetermine sample size. At least n = 3 mice were used for each type of experiment, and experiments were performed over several days for each animal, as is typical in electrophysiological studies of motor control in vertebrates. Due to the lack of post-laser reaches in one Sim1-Cre X Ai32 mouse, this animal was not included for the subset of analyses focusing on post-laser reaches (leaving n = 2 mice for these analyses, but n = 3 mice for the other analyses).
Data exclusions	Cortical recordings were aborted when the quality of the raw signals was very poor (n = 2 VGAT-ChR2-EYFP mice and n = 1 Sim1-Cre X Ai32 mouse). For the simultaneous recordings in thalamus and cortex, sessions were excluded when the raw signals were poor in one or both regions or when either histology or optogenetic tagging attempts indicated that the first probe was not in motor thalamus (n = 15 sessions).
Replication	The main results from each experiment were identified in a subset of sessions and replicated in subsequent sessions. In cases where some differences were observed between mice or sessions (e.g. the limb oscillation under 10 Hz stimulation in Fig. E9), this is stated in the text and shown in the figures.
Randomization	Not applicable: all experimental manipulations were performed at the level of trials within each session, and there was no allocation of animals into different treatment groups.
Blinding	Because the experimental manipulations occurred at the level of trials (laser stimulation vs no stimulation), it was not possible to blind the experimenter to the trial type. There was no allocation of animals into different treatment groups.

Reporting for specific materials, systems and methods

We require information from authors about some types of materials, experimental systems and methods used in many studies. Here, indicate whether each material, system or method listed is relevant to your study. If you are not sure if a list item applies to your research, read the appropriate section before selecting a response.

Materials & experimental systems

n/a	Involved in the study
☒	☐ Antibodies
☒	☐ Eukaryotic cell lines
☒	☐ Palaeontology
☐	☒ Animals and other organisms
☒	☐ Human research participants
☒	☐ Clinical data

Methods

n/a	Involved in the study
☒	☐ ChIP-seq
☒	☐ Flow cytometry
☒	☐ MRI-based neuroimaging

Animals and other organisms

Policy information about studies involving animals; ARRIVE guidelines recommended for reporting animal research

Laboratory animals	Mice of either sex were used, at age 8-25 weeks. The following mouse lines were used: (1) VGAT-ChR2-EYFP (Slc32a1-COP4*H134R/EYFP) (2) Vglut2-IRES-Cre (3) Ai32 (Rosa-CAG-LSL-ChR2(H134R)-EYFP-WPRE) (4) Ai32 (Rosa-CAG-LSL-ChR2(H134R)-EYFP-WPRE) crossed to one of the following driver lines: (4a) Tlx3-Cre PL56Gsat (4b) Sim1-Cre KJ18Gsat (4c) Rbp4-Cre KL100Gsat
Wild animals	N/A
Field-collected samples	N / A
Ethics oversight	All procedures were approved by the Institutional Animal Care and Use Committee at Janelia Research Campus (protocols 13-99, 16-139, and 19-177).

Note that full information on the approval of the study protocol must also be provided in the manuscript.

Article

The emergence of transcriptional identity in somatosensory neurons

https://doi.org/10.1038/s41586-019-1900-1

Received: 17 April 2019

Accepted: 6 November 2019

Published online: 8 January 2020

Nikhil Sharma[1,2], Kali Flaherty[1,2], Karina Lezgiyeva[1,2], Daniel E. Wagner[3], Allon M. Klein[3] & David D. Ginty[1,2*]

More than twelve morphologically and physiologically distinct subtypes of primary somatosensory neuron report salient features of our internal and external environments[1–4]. It is unclear how specialized gene expression programs emerge during development to endow these subtypes with their unique properties. To assess the developmental progression of transcriptional maturation of each subtype of principal somatosensory neuron, we generated a transcriptomic atlas of cells traversing the primary somatosensory neuron lineage in mice. Here we show that somatosensory neurogenesis gives rise to neurons in a transcriptionally unspecialized state, characterized by co-expression of transcription factors that become restricted to select subtypes as development proceeds. Single-cell transcriptomic analyses of sensory neurons from mutant mice lacking transcription factors suggest that these broad-to-restricted transcription factors coordinate subtype-specific gene expression programs in subtypes in which their expression is maintained. We also show that neuronal targets are involved in this process; disruption of the prototypic target-derived neurotrophic factor NGF leads to aberrant subtype-restricted patterns of transcription factor expression. Our findings support a model in which cues that emanate from intermediate and final target fields promote neuronal diversification in part by transitioning cells from a transcriptionally unspecialized state to transcriptionally distinct subtypes by modulating the selection of subtype-restricted transcription factors.

Decades of analyses have identified more than twelve functionally distinct subtypes of dorsal root ganglia (DRG) somatosensory neuron that collectively enable the detection of a broad range of salient features of the internal and external world[1–4]. A fundamental question in sensory and developmental biology is how somatosensory neuron subtypes acquire their characteristic physiological, morphological, and synaptic properties during development, enabling animals to detect and respond to innocuous and noxious thermal, chemical, and mechanical stimuli. Classical studies of embryonic development have indicated that migrating multipotent neural crest progenitors, originating from the dorsal neural tube, populate nascent DRG[5]. During ganglia formation, dedicated progenitors that express either neurogenin-1 (NEUROG1) or neurogenin-2 (NEUROG2) have been proposed to give rise to distinct somatosensory neuron subtypes[6], which then innervate peripheral target fields where they form morphologically distinct types of axonal endings[1]. Current models of somatosensory neuron development have primarily been inferred from studies that have analysed changes in expression of individual genes or types of axonal ending in loss-of-function models[1,7,8]. Here, we use genome-wide transcriptomic analyses coupled with molecular genetic approaches to define the transcriptional mechanisms by which somatosensory neuron subtypes diversify.

scRNA-seq of somatosensory neurons

To begin to define the transcriptional cascades that underlie the specification of somatosensory neuron subtypes, we performed single-cell RNA sequencing (scRNA-seq) at embryonic day 11.5 (E11.5), which is shortly after DRG formation, and at critical developmental milestones during somatosensory neuron development: at E12.5, when virtually all DRG neurons are postmitotic[9] and have extended axons well into the periphery; at E15.5, when peripheral and central target fields of somatosensory neurons are being innervated[10,11]; at postnatal day 0 (P0), when maturation of sensory neuron endings within the skin and other targets is occurring[12,13]; at P5, when most peripheral endings have refined into their mature morphological states and central projection terminals are properly organized within select spinal cord laminae[8,14,15]; and in early adulthood (P28–42) (Fig. 1a, Extended Data Fig. 1a–f). We first examined primary sensory neurons in young adult DRG from all axial levels (Fig. 1a, Extended Data Fig. 1a). We used principal component analysis (PCA) and *t*-distributed stochastic neighbour embedding (t-SNE) to cluster adult DRG neurons on the basis of transcriptome similarity (Fig. 1a). Each cluster was classified as a subtype on the basis of previous studies that have described markers and functions for individual somatosensory neuron subtypes, confirmation by in situ

[1]Department of Neurobiology, Harvard Medical School, Boston, MA, USA. [2]Howard Hughes Medical Institute, Harvard Medical School, Boston, MA, USA. [3]Department of Systems Biology, Harvard Medical School, Boston, MA, USA. *e-mail: david_ginty@hms.harvard.edu

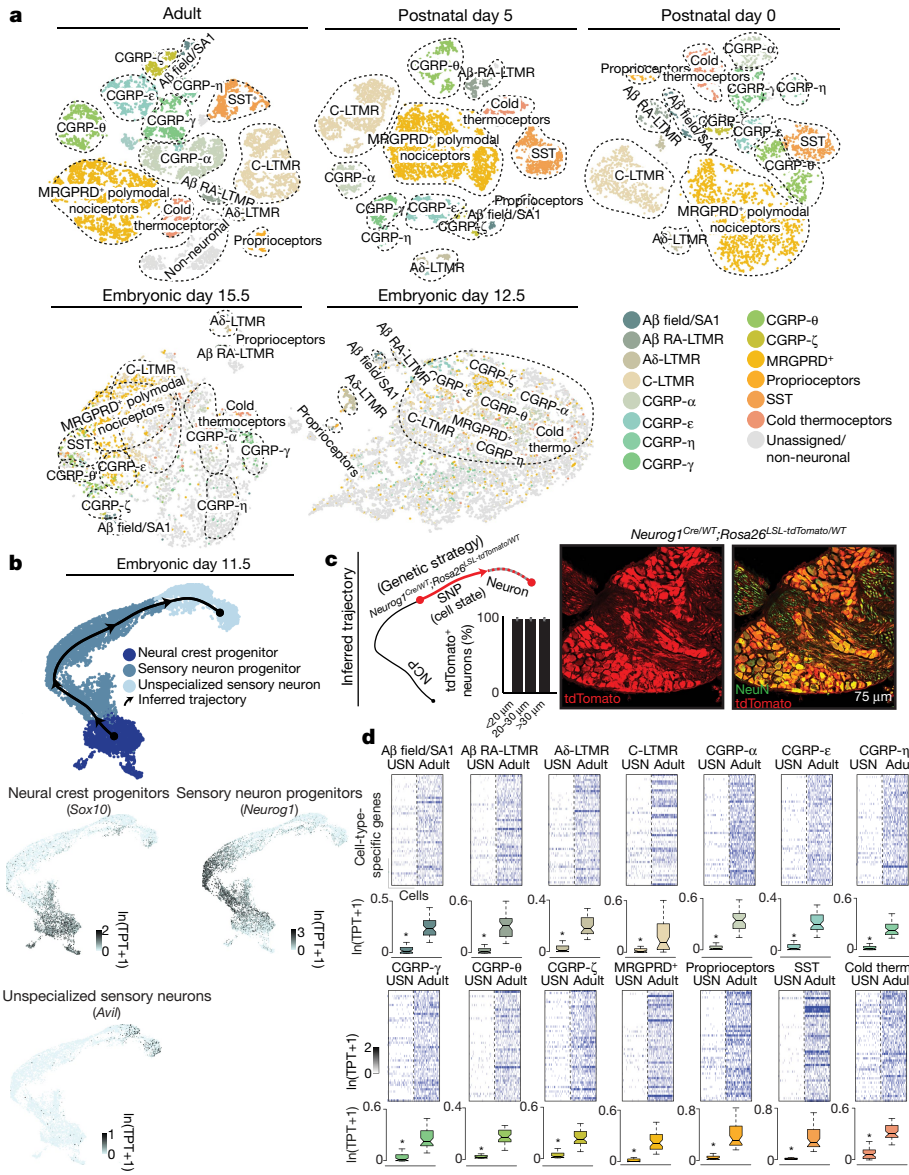


Fig. 1 | scRNA-seq of developing and mature DRG sensory neurons. a, t-SNE visualizations of DRG scRNA-seq data. SST, somatostatin. **b**, UMAP visualization of DRG scRNA-seq data from E11.5 with developmental trajectory and gene expression information overlaid. TPT, tags per ten thousand. **c**, Quantification (mean ± s.e.m.) of tdTomato$^+$ neurons and representative image (right). **d**, Heat map and quantification of genes enriched in each somatosensory neuron subtype as well as their expression levels in unspecialized sensory neurons (USNs). Boxes represent interquartile range (IQR), whiskers represent minimum and maximum values, and notches represent the 95% confidence interval of the median. *P < 0.0001, two-sided Wilcoxon rank-sum test with Bonferroni correction. For n values, see Methods.

analysis, and comparison to scRNA-seq data from adult trigeminal ganglia (see Methods, Extended Data Figs. 2a, b, 3a–d, Supplementary Data 1). These cell-type classifications are consistent with previously published RNA-seq findings of adult DRG and trigeminal ganglia[16–19].

We next sought to determine how the transcriptional identities of mature somatosensory neuron subtypes compare to those of newborn sensory neurons by analysing the transcriptomes of cells from DRG at E11.5 (Fig. 1b). We visualized the E11.5 scRNA-seq data using uniform manifold approximation and projection (UMAP)[20]. Mapping historically defined marker genes onto the UMAP representation revealed three principal cell types in E11.5 ganglia: 1) multipotent neural crest progenitors (NCPs), marked by *Sox10*[21,22]; 2) sensory neuron progenitors (SNPs), marked by *Neurog1* and *Neurog2*[23]; and 3) nascent, postmitotic sensory neurons marked by expression of the somatosensory neuron gene advillin (*Avil*[24]) and concomitant loss of expression of cell-cycle-associated genes (Fig. 1b, Extended Data Fig. 4a). Monocle 3[25] was then used to infer developmental relationships between NCPs, SNPs, and nascent *Avil*$^+$ sensory neurons. This analysis revealed a single continuous trajectory connecting NCPs, SNPs, and *Avil*$^+$ sensory neurons, suggesting a lack of transcriptional diversity in sensory neuron progenitors populating the *Avil*$^+$ compartment. Unexpectedly, labelled descendants of *Neurog1*$^+$ SNPs from *Neurog1*^{Cre}; *Rosa26*$^{LSL\text{-}tdTomato}$ mice had a broad range of cell diameters (Fig. 1c), consistent with the previous finding that in vitro directed differentiation with *Neurog1* overexpression leads to the generation of both small- and large-diameter DRG sensory neuron subtypes[26]. Moreover, genes that were highly enriched in E11.5 *Avil*$^+$ sensory neurons, relative to progenitors, generally remained expressed in adult somatosensory neuron subtypes (Extended Data Fig. 4b). On the other hand, the majority of genes whose expression was restricted to individual terminal somatosensory subtypes of adult ganglia were expressed at trace levels in E11.5 *Avil*$^+$ sensory neurons (Fig. 1d), suggesting that upon cell-cycle exit sensory neurons are transcriptionally

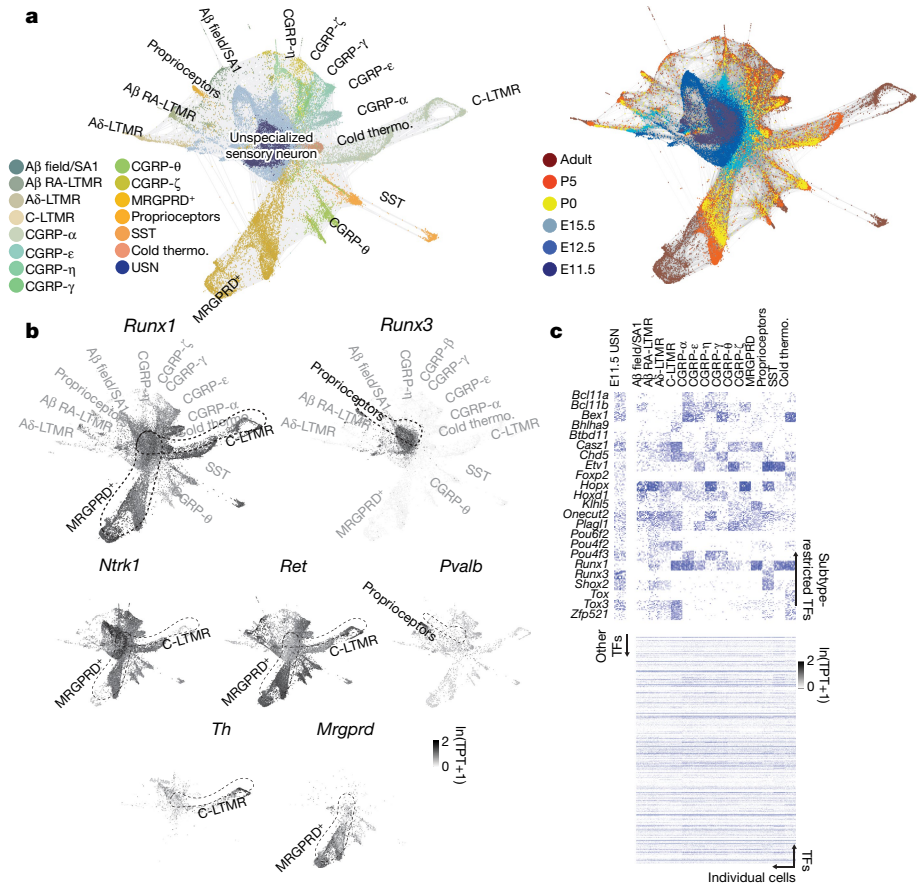


Fig. 2 | Transcriptional development of subtypes of DRG neurons. a, Force-directed layout of DRG sensory neurons overlaid with time point or cell-type information. **b**, Force-directed layout of DRG development overlaid with expression of indicated genes. **c**, Heat map of subtype-restricted TFs in each somatosensory neuron subtype of adult ganglia. For *n* values, see Methods.

unspecialized, specifically with respect to subtype-specific genes. These observations led us to consider whether a 'transcriptionally unspecialized state' serves as the starting point for somatosensory subtype diversification.

To investigate this idea, we compared scRNA-seq transcriptomes generated from sensory neurons between E11.5 and adulthood. Prospective identities of sensory neurons at each developmental stage were assigned on the basis of transcriptional similarity using canonical correlation analysis[27] (Fig. 1a, Extended Data Fig. 1f) and a graph-based strategy for locally embedding consecutive time points based on the transcriptional variation they share. We constructed single-cell *k*-nearest neighbour graphs for each time point (t_i) with nodes representing cells and edges linking neighbours. These graphs were then joined by identifying neighbouring cells in adjacent time points using a coordinate system learned from the subsequent time point (t_{i+1}; see Methods). The resulting graph forms a branching network that can be visualized using a force-directed layout. This representation spans all developmental stages and provides a consolidated view of the transcriptional maturation of each principal somatosensory neuron subtype from E11.5 to adulthood (Fig. 2a).

We next tested whether this graph-based representation of developmental gene expression profiles of sensory neuron subtypes recapitulates known developmental relationships. We inspected the gene expression patterns of the transcription factors (TFs) *Runx1* and *Runx3*, which have been implicated in the development of select unmyelinated (C-fibre) neuron subtypes and proprioceptors, respectively[28–30]. *Runx1* expression was prominent in unmyelinated sensory neuron subtypes, whereas *Runx3* expression was restricted to mature proprioceptors of adult ganglia, as previously described[28,29] (Fig. 2b). Furthermore, the graph-based representation accurately depicts the developmental switch from *Ntrk1*$^+$ to *Ret*$^+$ that occurs in subsets of non-peptidergic C-fibre neurons[30] (Fig. 2b). To facilitate exploration of this dataset by the community, we created an HTML-based interactive interface to enable visualization of the expression pattern of any gene at each developmental time point, from E11.5 to adulthood, for each of the somatosensory neuron subtypes (interactive somatosensory neuron browser: https://kleintools.hms.harvard.edu/tools/springViewer_1_6_dev.html?datasets/Sharma2019/all).

TFs in sensory neuron development

One observation from our initial analysis of the graph-based representation of developmental transcriptomes of sensory neurons is that the TFs *Runx1* and *Runx3*, which have been implicated in the development of sensory neuron subtypes, are broadly co-expressed in nascent E11.5 *Avil*$^+$ sensory neurons, in contrast to their mutually exclusive expression patterns in terminally differentiated subtypes of adult DRG (Fig. 2b). This is consistent with the finding that RUNX1 and RUNX3 proteins are colocalized in embryonic DRG[31]. This observation led us to consider whether other TFs that are subtype-restricted in adult ganglia may be co-expressed in nascent, transcriptionally unspecialized sensory neurons. To address this possibility, we identified TFs other than *Runx1* and *Runx3* that are expressed in select subtypes of somatosensory neurons from mature ganglia by inspecting 1,152 neuronally expressed TFs, and found that 23 are expressed in distinct subsets of adult somatosensory neurons (Fig. 2c). Strikingly, the scRNA-seq data revealed that several TFs expressed in select subtypes of sensory neurons of mature DRG are co-expressed in newborn E11.5 sensory

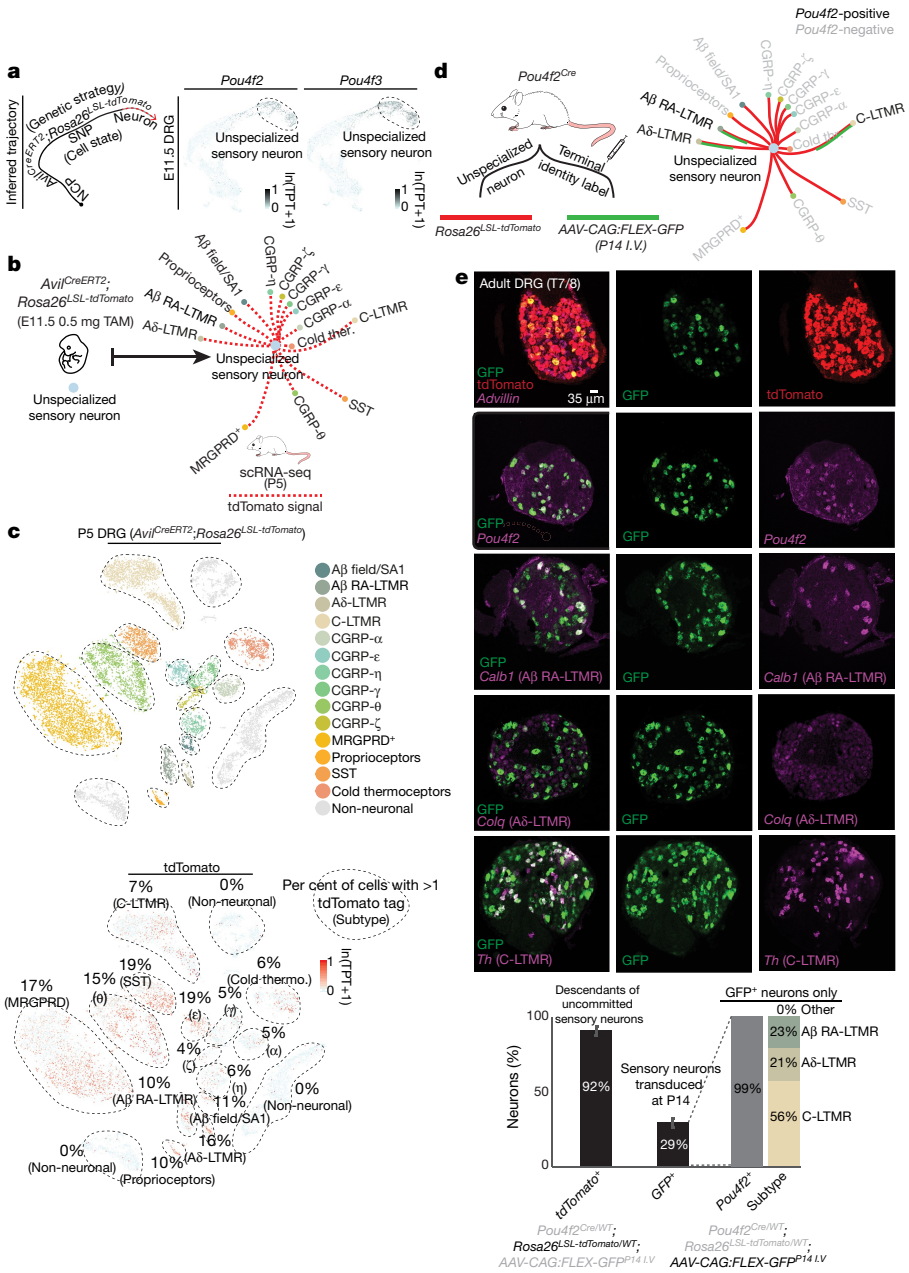


Fig. 3 | The unspecialized sensory neuron compartment gives rise to most or all somatosensory neuron subtypes. a, Developmental trajectory of sensory neurons (left) and t-SNE visualization with TF expression overlaid (right). **b**, Schematic description of the *Avil*^{CreERT2}*Rosa26*$^{LSL\text{-}tdTomato}$ labelling strategy. **c**, t-SNE visualization of *Avil*^{CreERT2}*Rosa26*$^{LSL\text{-}tdTomato}$ scRNA-seq with cell-type identity or tdTomato expression overlaid. **d**, Schematic representing strategy for labelling neurons in *Pou4f2*$^{Cre/WT}$ mice. **e**, smRNA-FISH and quantification for the indicated transcripts (mean ± s.e.m.). For *n* values, see Methods.

neurons (Extended Data Fig. 5a), like *Runx1* and *Runx3*. These scRNA-seq findings were verified using double single-molecule RNA fluorescent in situ hybridization (smRNA-FISH), with *Runx1* and *Runx3* as well as *Pou4f2* and *Pou4f3* serving as test cases. smRNA-FISH measurements showed that *Runx1* and *Runx3* as well as *Pou4f2* (Aβ rapidly adapting (RA)-low-threshold mechanoreceptors (LTMRs), Aδ-LTMRs, C-LTMRs) and *Pou4f3* (calcitonin gene-related peptide (CGRP)-αs and CGRP-ηs) are co-expressed in the majority of E11.5 *Avil*$^{+}$ sensory neurons, despite their mutually exclusive expression patterns in neurons from P0 and adult ganglia (Extended Data Fig. 5b, c). These observations suggest that all somatosensory neuron subtypes transit through a postmitotic transcriptionally unspecialized state. To further address this, we genetically labelled descendants in the *Avil*$^{+}$ cell compartment at E11.5 by administering a low dose of tamoxifen (0.5 mg) at E11.5 to *Avil*^{CreERT2}; *Rosa26*$^{LSL\text{-}tdTomato}$ mice and found *tdTomato* transcripts to be present in 5–19% of cells in each somatosensory neuron subtype of adult ganglia by scRNA-seq (Fig. 3a–c). In addition, we labelled all descendants of one of the 'broad early'-to-'subtype restricted late' TFs, *Pou4f2*, with tdTomato using a *Pou4f2*^{Cre}; *Rosa26*$^{LSL\text{-}tdTomato}$ mouse line, and transduced terminally differentiated *Pou4f2*$^{+}$ DRG subtypes in the same mouse using an adeno-associated virus (AAV) carrying a Cre-dependent GFP reporter delivered at P14 (Fig. 3d). smRNA-FISH analysis revealed *tdTomato* transcripts in more than 90% of DRG sensory neurons in adult *Pou4f2*^{Cre}; *Rosa26*$^{LSL\text{-}tdTomato}$; *AAV-CAG:FLEX-GFP*$^{P14\ I.V.}$ mice; by contrast, *GFP* transcripts were restricted to Aβ RA-LTMRs, Aδ-LTMRs and C-LTMRs (mature *Pou4f2*$^{+}$ populations) (Fig. 3e). Notably, a developmental analysis of subtype-specific gene expression revealed that, in general, large-diameter neurons achieved transcriptional maturity

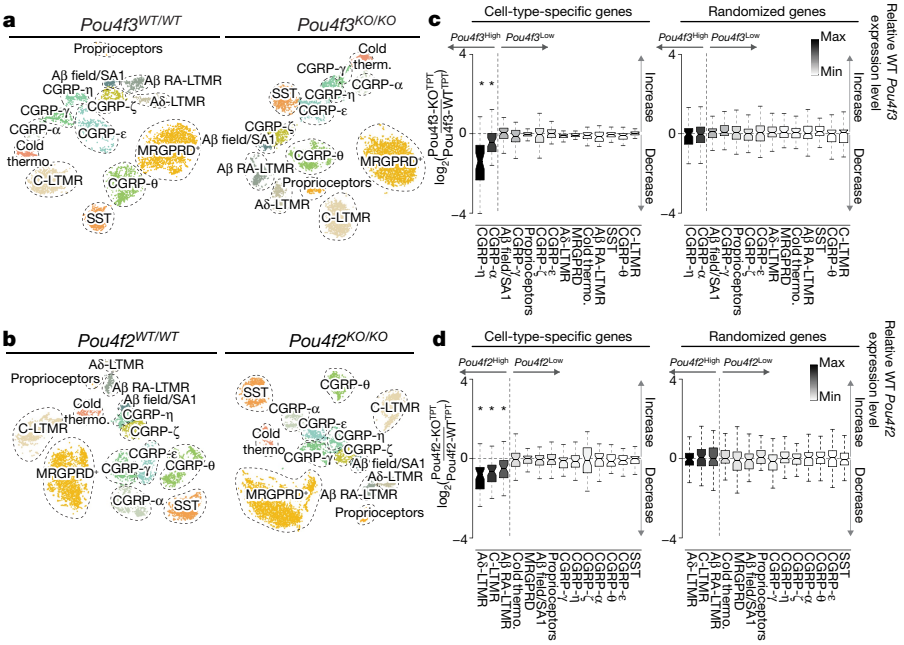


Fig. 4 | *Pou4f2* and *Pou4f3* regulate select somatosensory neuron subtype maturation. a, t-SNE visualizations of scRNA-seq data for neurons generated from $Pou4f3^{WT/WT}$ and $Pou4f3^{KO/KO}$ littermates. **b**, t-SNE visualizations of scRNA-seq data for neurons generated from $Pou4f2^{WT/WT}$ and $Pou4f2^{KO/KO}$ littermates. **c**, Fold-change distribution of cell-type-specific genes when comparing $Pou4f3^{KO/KO}$ and $Pou4f3^{WT/WT}$ littermate control samples. **d**, Fold-change distribution of cell-type-specific genes when comparing $Pou4f2^{KO/KO}$ and $Pou4f2^{WT/WT}$ littermates. **c**, **d**, Boxes represent IQR, whiskers represent minimum and maximum values, and notches represent the 95% confidence interval of the median. $^*P < 0.01$, two-sided Wilcoxon rank-sum test with Bonferroni correction. For *n* values, see Methods.

before small-diameter neurons, consistent with the historical view[32,33] (Extended Data Fig. 6a, b). Together, these results indicate that cells in the transcriptionally unspecialized compartment express a broad array of TFs that become restricted to select subsets of sensory neurons as development proceeds.

Specification of subtype identity

We next investigated whether broad-to-restricted TFs contribute to sensory neuron diversification during the transcriptionally unspecialized state, thus broadly influencing the transcriptional maturation of sensory neurons, or whether these TFs primarily influence the subtypes in which their expression is maintained. We collected DRG from neonatal (P0–5) pups containing null alleles of either *Pou4f2* or *Pou4f3*, which are representative broad-to-restricted TFs, and generated scRNA-seq transcriptomes from $Pou4f2^{KO(Cre)/KO(Cre)}$ mice and $Pou4f2^{+/+}$ littermate controls as well $Pou4f3^{-/-}$ mice and $Pou4f3^{+/+}$ littermate controls. Initial inspection of the scRNA-seq data from both *Pou4f2* and *Pou4f3* mutant mice revealed clusters corresponding to each somatosensory subtype (Fig. 4a, b). We found that cell numbers were not compromised, as representative ganglia (T7 and T8) from *Pou4f2* or *Pou4f3* knockouts had similar numbers of neurons to ganglia from littermate controls (Extended Data Fig. 7a, b). Notably, genes that were preferentially expressed in either $Pou4f2^+$ or $Pou4f3^+$ neurons showed reduced expression in the respective knockouts, compared to littermate controls, whereas the expression of randomly selected genes was unchanged (Fig. 4c, d). By contrast, somatosensory neuron subtypes in which expression of *Pou4f2* and *Pou4f3* was normally extinguished after E11.5 generally exhibited less marked alterations to subtype-specific gene expression or subtype-restricted TF expression in knockout mice when compared to controls (Fig. 4c, d, Extended Data Fig. 7a, b). Given the reduction in subtype-specific gene expression in *Pou4f2* and *Pou4f3* mutants, we also determined the consequences of *Pou4f2* or *Pou4f3* ablation on the unique axonal endings associated with mature somatosensory neuron subtypes. Although the axonal endings associated with $Pou4f2^+$ subtypes are known to form longitudinal lanceolate endings around hair follicles[1], the axonal ending morphologies associated with the $Pou4f3^+$ subtypes were not known. Genetic labelling experiments using newly generated Cre lines for each $Pou4f3^+$ subtype revealed that the axons of CGRP-α neurons have free nerve endings that penetrate the epidermis, whereas those of CGRP-η neurons form circumferential endings associated with hair follicles (Extended Data Fig. 8a–d). Longitudinal lanceolate endings and $CGRP^+$ circumferential axonal endings were partially compromised in *Pou4f2* and *Pou4f3* knockout mice, respectively (Extended Data Fig. 8e–k). Furthermore, postnatal depletion of *Pou4f3* using short hairpin RNA (shRNA) altered subtype-specific gene expression and function. Together, these results show that two representative subtype-restricted TFs, *Pou4f2* and *Pou4f3*, control transcriptional maturation of the sensory neuron subtypes in which they remain expressed.

Extrinsic control of subtype identity

We next investigated whether differential maintenance or extinction of TFs in emerging subtypes of neurons occurs via a process that is entirely intrinsic to developing sensory neurons or is guided by extrinsic cues. The mesenchymal and epidermal environments through which embryonic somatosensory axons extend are rich sources of extrinsic signals, including neuronal growth factors[8]. Therefore, we tested whether nerve growth factor (NGF), an extrinsic cue that is crucial for the growth and survival of embryonic somatosensory neurons expressing the NGF receptor NTRK1 (TRKA)[34]—which represent about 80% of adult DRG—may control the TF selection process. We performed scRNA-seq on DRG neurons from neonatal mice containing a targeted mutation in the *Ngf* gene. This genome-wide analysis of *Ngf*-dependent gene expression was carried out on the apoptosis-deficient *Bax*-knockout genetic background to circumvent the apoptotic cell death of DRG neurons associated with developmental loss of NGF[35]. Clustering analysis of the scRNA-seq data revealed that all somatosensory neuron subtypes were present in $Bax^{-/-}$ controls (Fig. 5a), but there were

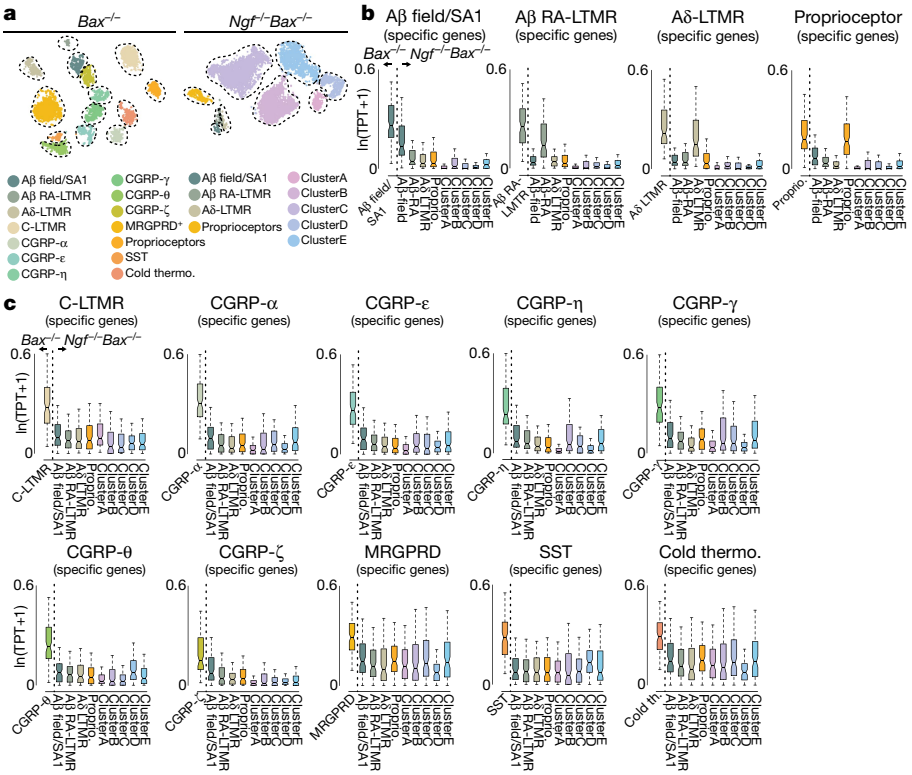


Fig. 5 | The extrinsic cue NGF is required for subtype-specific gene expression patterns. a, t-SNE visualizations of scRNA-seq data for neurons generated from P0 *Bax*$^{-/-}$ and *Ngf*$^{-/-}$*Bax*$^{-/-}$ littermates. **b**, Cell-type-specific gene expression in proprioceptor and A-fibre mechanoreceptor sensory neuron subtypes in *Bax*$^{-/-}$ and *Ngf*$^{-/-}$*Bax*$^{-/-}$ littermates. **c**, Cell-type-specific gene expression in all other sensory neuron subtypes in *Bax*$^{-/-}$ and *Ngf*$^{-/-}$*Bax*$^{-/-}$ littermates. Boxes represent IQR, whiskers represent minimum and maximum values, and notches represent the 95% confidence interval of the median. **b**, **c**, All clusters are different from controls by two-sided Wilcoxon rank-sum test with Bonferroni correction; $P < 0.01$. For *n* values, see Methods.

fewer transcriptionally distinct neuronal populations in *Ngf*$^{-/-}$*Bax*$^{-/-}$ double mutants (Fig. 5a). *Ntrk1*-negative neurons (proprioceptors and A-fibre mechanoreceptors) were not markedly transcriptionally compromised in *Ngf*$^{-/-}$*Bax*$^{-/-}$ mutants compared to *Bax*$^{-/-}$ controls (Fig. 5b), as expected. However, the subtype-specific gene expression patterns that are normally present in *Ntrk1*$^{+}$ sensory neuron subtypes were markedly altered in neurons from *Ngf*$^{-/-}$*Bax*$^{-/-}$ mutants (Fig. 5c). Notably, examination of the aforementioned subtype-restricted TFs showed that the combinations of TFs expressed in the unidentified neuronal clusters in *Ngf*$^{-/-}$*Bax*$^{-/-}$ mutants bore no resemblance to the TF combinations observed in neuronal subtypes in control mice, and this was confirmed using smRNA-FISH (Extended Data Fig. 9a, b). Furthermore, members of the NEUROD family of TFs, which are normally extinguished during embryonic development, remained expressed at P0 in *Ngf*$^{-/-}$*Bax*$^{-/-}$ mutants (Extended Data Fig. 9b, c). These findings indicate that the selection of somatosensory neuron subtype-restricted TFs is controlled, at least in part, by extrinsic cues acting on nascent sensory neurons.

Discussion

Our genome-wide transcriptomic analyses of cells traversing the developmental stages of somatosensory neurons support a model in which newborn somatosensory neurons are unspecialized with respect to expression of subtype-restricted TFs, and differential maintenance of unique combinations of these subtype-restricted TFs enables nascent sensory neurons to resolve into mature subtypes (Extended Data Fig. 9d). Early co-expression, and subsequent resolution, of TFs has been proposed to underlie the diversification of stem cells in the haematopoietic lineage[36–38], neural crest progenitors before lineage commitment[39], and developing spinal motor neurons[40–42]—although this view has been challenged in the case of the haematopoietic system[43]. The diversification of somatosensory neurons shares commonalities and differences with these systems. We propose that, unlike cells of the early neural crest and the haematopoietic lineages, somatosensory neuron subtypes emerge following cell-cycle exit and, unlike other progenitor types, newborn, postmitotic *Avil*$^{+}$ somatosensory neurons are not migratory but rather are permanent residents of sensory ganglia. Therefore, nascent sensory neurons cannot rely on cell division or migration to encounter new environments. Rather, a feature of nascent somatosensory neurons is that they immediately extend axons along intermediate targets, such as large blood vessels, en route to target organs, such as the skin, where they encounter extrinsic cues, including NGF and other secreted factors. We propose a model in which multiple distinct extrinsic cues act on axons of transcriptionally unspecialized sensory neurons, depending on the timing and trajectories of their projection patterns. These cues function, in part, to resolve TF expression patterns from a co-expressed state to a subtype-restricted state to promote the transcriptional specializations that underlie the unique molecular, morphological, and physiological properties of somatosensory neuron subtypes.

Online content

Any methods, additional references, Nature Research reporting summaries, source data, extended data, supplementary information, acknowledgements, peer review information; details of author contributions and competing interests; and statements of data and code availability are available at https://doi.org/10.1038/s41586-019-1900-1.

1. Abraira, V. E. & Ginty, D. D. The sensory neurons of touch. *Neuron* **79**, 618–639 (2013).
2. Julius, D. TRP channels and pain. *Annu. Rev. Cell Dev. Biol.* **29**, 355–384 (2013).

3. Basbaum, A. I., Bautista, D. M., Scherrer, G. & Julius, D. Cellular and molecular mechanisms of pain. *Cell* **139**, 267–284 (2009).
4. Julius, D. & Basbaum, A. I. Molecular mechanisms of nociception. *Nature* **413**, 203–210 (2001).
5. Le Douarin, N. *The neural crest* (Cambridge University Press, 1982).
6. Anderson, D. J. Lineages and transcription factors in the specification of vertebrate primary sensory neurons. *Curr. Opin. Neurobiol.* **9**, 517–524 (1999).
7. Marmigère, F. & Ernfors, P. Specification and connectivity of neuronal subtypes in the sensory lineage. *Nat. Rev. Neurosci.* **8**, 114–127 (2007).
8. Lallemend, F. & Ernfors, P. Molecular interactions underlying the specification of sensory neurons. *Trends Neurosci.* **35**, 373–381 (2012).
9. Kitao, Y., Robertson, B., Kudo, M. & Grant, G. Neurogenesis of subpopulations of rat lumbar dorsal root ganglion neurons including neurons projecting to the dorsal column nuclei. *J. Comp. Neurol.* **371**, 249–257 (1996).
10. Hasegawa, H., Abbott, S., Han, B. X., Qi, Y. & Wang, F. Analyzing somatosensory axon projections with the sensory neuron-specific Advillin gene. *J. Neurosci.* **27**, 14404–14414 (2007).
11. Ozaki, S. & Snider, W. D. Initial trajectories of sensory axons toward laminar targets in the developing mouse spinal cord. *J. Comp. Neurol.* **380**, 215–229 (1997).
12. Mirnics, K. & Koerber, H. R. Prenatal development of rat primary afferent fibers: II. Central projections. *J. Comp. Neurol.* **355**, 601–614 (1995).
13. Mirnics, K. & Koerber, H. R. Prenatal development of rat primary afferent fibers: I. Peripheral projections. *J. Comp. Neurol.* **355**, 589–600 (1995).
14. Woodbury, C. J., Ritter, A. M. & Koerber, H. R. Central anatomy of individual rapidly adapting low-threshold mechanoreceptors innervating the "hairy" skin of newborn mice: early maturation of hair follicle afferents. *J. Comp. Neurol.* **436**, 304–323 (2001).
15. Woodbury, C. J. & Koerber, H. R. Widespread projections from myelinated nociceptors throughout the substantia gelatinosa provide novel insights into neonatal hypersensitivity. *J. Neurosci.* **23**, 601–610 (2003).
16. Zeisel, A. et al. Molecular architecture of the mouse nervous system. *Cell* **174**, 999–1014 (2018).
17. Usoskin, D. et al. Unbiased classification of sensory neuron types by large-scale single-cell RNA sequencing. *Nat. Neurosci.* **18**, 145–153 (2015).
18. Zheng, Y. et al. Deep sequencing of somatosensory neurons reveals molecular determinants of intrinsic physiological properties. *Neuron* **103**, 598–616.e597, (2019).
19. Nguyen, M. Q., Wu, Y., Bonilla, L. S., von Buchholtz, L. J. & Ryba, N. J. P. Diversity amongst trigeminal neurons revealed by high throughput single cell sequencing. *PLoS One* **12**, e0185543 (2017).
20. McInnes, L., Healy, J. & Melville, J. UMAP: Uniform manifold approximation and projection for dimension reduction. Preprint at https://arxiv.org/abs/1802.03426 (2018).
21. Kim, J., Lo, L., Dormand, E. & Anderson, D. J. SOX10 maintains multipotency and inhibits neuronal differentiation of neural crest stem cells. *Neuron* **38**, 17–31 (2003).
22. Britsch, S. et al. The transcription factor Sox10 is a key regulator of peripheral glial development. *Genes Dev.* **15**, 66–78 (2001).
23. Ma, Q., Fode, C., Guillemot, F. & Anderson, D. J. Neurogenin1 and neurogenin2 control two distinct waves of neurogenesis in developing dorsal root ganglia. *Genes Dev.* **13**, 1717–1728 (1999).
24. Zurborg, S. et al. Generation and characterization of an Advillin-Cre driver mouse line. *Mol. Pain* **7**, 66 (2011).
25. Cao, J. et al. The single-cell transcriptional landscape of mammalian organogenesis. *Nature* **566**, 496–502 (2019).
26. Blanchard, J. W. et al. Selective conversion of fibroblasts into peripheral sensory neurons. *Nat. Neurosci.* **18**, 25–35 (2015).
27. Mayer, C. et al. Developmental diversification of cortical inhibitory interneurons. *Nature* **555**, 457–462 (2018).
28. Inoue, K. et al. *Runx3* controls the axonal projection of proprioceptive dorsal root ganglion neurons. *Nat. Neurosci.* **5**, 946–954 (2002).
29. Levanon, D. et al. The Runx3 transcription factor regulates development and survival of TrkC dorsal root ganglia neurons. *EMBO J.* **21**, 3454–3463 (2002).
30. Chen, C. L. et al. Runx1 determines nociceptive sensory neuron phenotype and is required for thermal and neuropathic pain. *Neuron* **49**, 365–377 (2006).
31. Yoshikawa, M. et al. Coexpression of Runx1 and Runx3 in mechanoreceptive dorsal root ganglion neurons. *Dev. Neurobiol.* **73**, 469–479 (2013).
32. Lawson, S. N. & Biscoe, T. J. Development of mouse dorsal root ganglia: an autoradiographic and quantitative study. *J. Neurocytol.* **8**, 265–274 (1979).
33. Lawson, S. N., Caddy, K. W. & Biscoe, T. J. Development of rat dorsal root ganglion neurones. Studies of cell birthdays and changes in mean cell diameter. *Cell Tissue Res.* **153**, 399–413 (1974).
34. Crowley, C. et al. Mice lacking nerve growth factor display perinatal loss of sensory and sympathetic neurons yet develop basal forebrain cholinergic neurons. *Cell* **76**, 1001–1011 (1994).
35. Patel, T. D., Jackman, A., Rice, F. L., Kucera, J. & Snider, W. D. Development of sensory neurons in the absence of NGF/TrkA signaling *in vivo*. *Neuron* **25**, 345–357 (2000).
36. Miyamoto, T. et al. Myeloid or lymphoid promiscuity as a critical step in hematopoietic lineage commitment. *Dev. Cell* **3**, 137–147 (2002).
37. Hu, M. et al. Multilineage gene expression precedes commitment in the hemopoietic system. *Genes Dev.* **11**, 774–785 (1997).
38. Orkin, S. H. Diversification of haematopoietic stem cells to specific lineages. *Nat. Rev. Genet.* **1**, 57–64 (2000).
39. Soldatov, R. et al. Spatiotemporal structure of cell fate decisions in murine neural crest. *Science* **364**, eaas9536 (2019).
40. Dasen, J. S., Tice, B. C., Brenner-Morton, S. & Jessell, T. M. A Hox regulatory network establishes motor neuron pool identity and target-muscle connectivity. *Cell* **123**, 477–491 (2005).
41. Dasen, J. S., Liu, J. P. & Jessell, T. M. Motor neuron columnar fate imposed by sequential phases of Hox-c activity. *Nature* **425**, 926–933 (2003).
42. Briscoe, J., Pierani, A., Jessell, T. M. & Ericson, J. A homeodomain protein code specifies progenitor cell identity and neuronal fate in the ventral neural tube. *Cell* **101**, 435–445 (2000).
43. Hoppe, P. S. et al. Early myeloid lineage choice is not initiated by random PU.1 to GATA1 protein ratios. *Nature* **535**, 299–302 (2016).

Publisher's note Springer Nature remains neutral with regard to jurisdictional claims in published maps and institutional affiliations.

© The Author(s), under exclusive licence to Springer Nature Limited 2020

Methods

No statistical methods were used to predetermine sample size. The experiments were not randomized and the investigators were not blinded to allocation during experiments and outcome assessment.

Animals

All mouse experiments in this study were approved by the National Institutes of Health and the Harvard Medical School IACUC. Experiments followed the ethical guidelines outlined in the NIH Guide for the care and use of laboratory animals (https://grants.nih.gov/grants/olaw/guide-for-the-care-and-use-of-laboratory-animals.pdf). *Avpr1a*$^{T2a\text{-}Cre}$ and *Bmpr1b*$^{T2a\text{-}Cre}$ mice were generated using standard homologous recombination techniques in embryonic stem (ES) cells. Chimaeras were generated by blastocyst injection and subsequent germline transmission was confirmed by tail PCR. The neo selection cassette was excised using a Flp-deleter strain for the *Avpr1a*$^{T2a\text{-}Cre}$ line but left intact for the *Bmpr1b*$^{T2a\text{-}Cre}$ line. Mice were housed under standard conditions and given chow and water ad libitum. Plug date was considered E0.5 and date of birth was considered P0. *Pou4f3* null mice were obtained from Jax (Stock No. 008645). *Pou4f2* null(Cre) mice were obtained from Jax (Stock No. 030357). ROSA26 Cre-dependent tdTomato reporter mice were obtained from Jax (Stock No. 007914). *Avil*^{CreERT2} mice were obtained from Jax (Stock No. 032027). All experiments with wild-type animals were conducted with mice on the C57Bl/6J background obtained from Jackson Laboratory.

Dissociation and purification of isolated single sensory neurons

The dissection strategy used was nearly identical for all ages presented in this study. Specifically, animals were killed, and spinal columns were removed and placed on a tray of ice. Individual DRG with central and peripheral nerves attached were removed from all axial levels and placed into ice-cold DMEM:F12 (1:1) supplemented with 1% pen/strep and 12.5 mM D-glucose. A fine dissection was performed to remove the peripheral and central nerve roots, resulting in only the sensory ganglia remaining. We collected 200–400 individual ganglia for the DRG and 20–30 ganglia for the trigeminal for each bioreplicate of single-cell sequencing. All scRNA-seq experiments in this study were performed with >2 bioreplicates. Sensory ganglia were dissociated in 40 units papain, 4 mg/ml collagenase, 10 mg/ml BSA, 1 mg/ml hyalurdonidase, 0.6 mg/ml DNase in DMEM:F12 + 1% pen/strep + 12.5 mM glucose for 10 min at 37 °C. Digestion was quenched using 20 mg/ml ovomucoid (trypsin inhibitor), 20 mg/ml BSA in DMEM:F12 + 1% pen/strep + 12.5 mM glucose. Ganglia were gently triturated with fire-polished glass pipettes (opening diameter of approx. 150–200 µm). Neurons were then passed through a 70-µm filter to remove cell doublets and debris. Neurons were pelleted and washed 4–8× in 20 mg/ml ovomucoid (trypsin inhibitor), 20 mg/ml BSA in DMEM:F12 + 1% pen/strep + 12.5 mM glucose followed by 2× washes with DMEM:F12 + 1% pen/strep + 12.5 mM glucose all at 4 °C. After washing, cells were resuspended in 50–200 µl of DMEM:F12 + 1% pen/strep + 12.5 mM glucose. Cells were counterstained with trypan blue, visually inspected and counted with a haemocytometer. Dissociated ganglia preparations were considered to pass quality control and used for scRNA-seq if >90% of cells were viable, as measured by exclusion of trypan blue, and virtually no cellular debris was visible.

Tissue processing for RNA-FISH

For sample preparation, individual DRG from mice were rapidly dissected and the axial level was identified by identifying specific DRG using the T12 DRG as a landmark. The T12 DRG was defined as the ganglion immediately caudal to the last rib. DRG were frozen in dry-ice-cooled 2-metylbutane and stored at −80 °C until they were sectioned. DRG were sectioned at a thickness of 15–20 µm and RNAs were detected by RNAscope (Advanced Cell Diagnostics) using the manufacturer's protocol. Total numbers of neurons per section of DRG were estimated by counting neuronal nuclei as measured by DAPI and counts were confirmed as reasonable estimates by comparison to counts obtained by measuring *Avil* or *Pou4f1*, which are both pan-somatosensory neuron markers. The numbers of somatosensory neurons per section were similar for DAPI compared with *Avil* or *Pou4f1* measurements. The following probes were used: Mm-*Th*TH (Cat#: 317621), Mm-*Calb1* (Cat#-428431), Mm-*Pou4f2* (custom made), Mm-*Pou4f3* (custom made), Mm-*Avil* (Cat#: 498531), Mm-*Asic1* (Cat#: 480581), Mm-*Mrgpra3* (Cat#: 548161), Mm-*Pou4f1* (Cat#: 414671), Mm-*Colq* (Cat#: 496211), Mm-*Sst* (Cat#: 404631), Mm-*Pvalb* (Cat#: 421931), Mm-*Ikzf1* (Cat#: 511201), Mm-*Avpr1a* (Cat#: 418061), Mm-*Oprk1* (Cat#: 316111), Mm-*Mrgprd* (Cat#: 417921), Mm-*Bmpr1b* (custom made), Mm-*Vcan* (Cat#: 486231), Mm-*Trpm8* (Cat#: 420451), Mm-*Neurod1* (Cat#: 416871), Mm-*Neurod6* (Cat#: 444851), Mm-*Shox2* (Cat#: 554291), Mm-*Hopx* (Cat#: 405161), Mm-*Runx1* (Cat#: 406671), Mm-*Runx3* (Cat#: 451271), *GFP* (Cat#: 400281), *tdTomato* (Cat#: 317041).

Single-cell RNA library preparation, sequencing, and analysis

Single-cell RNA-seq was performed with the 10× Genomics Chromium Single Cell Kit (v2 and v3). Approximately 1,000–8,000 cells were added to the reverse transcription mix before loading on the microfluidic chip. Downstream reverse transcription, cDNA synthesis/amplification, and library preparation were performed according to the manufacturer's instructions. All samples were sequenced on a NextSeq 500 with 58 bp sequenced into the 3′ end of the mRNAs. Initial gene expression tables for individual barcodes were generated using the cellranger pipeline according to instructions provided by 10× Genomics. All gene expression tables were then imported into R and analysed with Seurat (v.2.3) with standard procedures.

Cluster identification. Clusters were classified into transcriptionally distinct somatosensory neuron subtypes: Aβ RA-LTMRs[44–46], Aβ field-LTMRs/Aβ SA1-LTMRs[46,47], Aδ-LTMRs[46,48], C-LTMRs[46,49], CGRP$^+$ neurons[50,51] (containing six transcriptionally discrete subtypes), MRGPRD$^+$ polymodal nociceptors[46,52–54], proprioceptors[55,56], SST$^+$ pruriceptors (somatostatin/NPPB$^+$)[57,58], cold-sensitive thermoceptors[50,59,60], and two main classes of support cell (endothelial and Schwann cells). A transcriptionally distinct cluster uniquely corresponding to Merkel cell-associated Aβ SA1-LTMRs was not detected. However, based on bulk RNA-seq analysis of genetically defined and fluorescence-activated cell sorting (FACS)-purified LTMR subtypes, Aβ SA1-LTMRs contain transcriptomes with a striking resemblance to those of Aβ field-LTMRs[46]; therefore, these two Aβ LTMR subtypes are likely to be embedded within the same cluster in our t-SNE plot. We confirmed that marker genes for each of the sensory neuron subtypes were expressed in subsets of DRG neurons and noted that the relative proportions of certain sensory neuron subtypes varied across ganglia located at different axial levels (Extended Data Fig. 2a, b). Moreover, the somatosensory neuron subtypes identified in this adult DRG analysis were remarkably similar to those identified in scRNA-seq analysis of 5,556 somatosensory neurons obtained from adult trigeminal ganglia (TG) (Extended Data Fig. 3a–d). The cell types identified by our scRNA-seq findings are largely consistent with previously published adult DRG/TG scRNA-seq datasets[16,17,19,61,62].

Exclusion criteria. As a first quality control filter, individual cells were removed from the dataset if they had fewer than 1,000 discovered genes, fewer than 1,000 unique molecule identifiers (UMIs) or more than 5% of reads mapping to mitochondrial genes (several datasets use a 10% threshold for this parameter and this is indicated in the respective Figures). Preparing single-cell suspensions of DRG/TG sensory neurons often results in a population of non-neuronal–neuronal doublets. To circumvent this, we defined individual cells showing expression of Schwann cell markers (*Sox2* or *Ednrb*) and neuronal markers as neurons that did not resolve into single cells during the dissociation process.

Cells matching these criteria were removed before performing subsequent analysis and this analysis was applied to all datasets presented in this study. Lastly, for simplicity, most displays exclude non-neuronal cells (Schwann and endothelial). Generally, we found that <10% of cells in any given dataset were classified as non-neuronal.

General analysis parameters. Raw UMI counts were normalized to 10,000 UMIs per cell. Highly variable genes were calculated using the FindVariableGenes function with mean.function = ExpMean, dispersion.function = LogVMR, x.low.cutoff = 0, and y.cutoff = 0.5. PCA and t-SNE analyses were used for dimensionality reduction and elbow plots were generated to determine which principal components to include in the analysis. This corresponded to roughly the first 20 principal components. Canonical correlation analysis (CCA) and matching of cell types through development were performed as previously described[27].

Identification of differentially expressed genes. Differential gene expression analysis was performed on all expressed genes using the FindMarker function in Seurat using the Wilcoxon rank-sum test and a pseudocount of 0.001 was added to each gene to prevent infinite values. P values $<10^{-322}$ were defined as 0, as the R environment does not handle numbers $<10^{-322}$. Each identified cell type was compared against an outgroup which corresponded to all other cells in the dataset at the respective time point. All genes identified were spot checked by overlaying the expression levels on the t-SNE plot to ensure the computational method was faithfully identifying genes with the prescribed features. For subtype-specific gene expression analysis, subtype-specific genes were first defined using the littermate control mice because knockout mice were not always available on a pure C57/Bl6 background. The subtype-specific genes identified in littermate control mice were nearly identical to those observed in C57/Bl6 control animals. Of the top 100 subtype-specific genes, 50 were randomly selected from this group and compared to the knockout controls. Fifty expression-matched genes that were not included in the subtype-specific gene list were selected as randomized control genes.

Monocle 3 analysis (for E11 trajectory analysis). The Monocle 3 workflow was performed in a similar fashion as previously described[25]. In brief, the Monocle 3 pipeline offers several key advantages. First, this pipeline allows the generation of trajectories over potentially discontinuous underlying data. This is first accomplished by performing dimensionality reduction with the recently proposed UMAP algorithm[20], instead of t-SNE. Notably, UMAP provides comparable visualization quality to t-SNE and UMAP also performs better at preserving global relationships, which is a noted shortcoming of the t-SNE algorithm. Furthermore, the UMAP algorithm is more efficient [$O(N)$] compared to t-SNE [$N\log(N)$], making UMAP a more computationally friendly option for large datasets, as used in this study. The UMAP parameters used in this study are comparable to those previously applied[25] (reduction.use = 'PCA', max.dim = 2L, neighbours = 50, min_dist = 0.1, cosine distance metric). Similar parameters have been used to finely resolve subtrajectories[25] and therefore we argue that these parameters provide the greatest sensitivity for identifying branches, if they exist, within our dataset.

STITCH analysis. Although UMAP provides an advance in gene expression-based trajectory inference, more complex changes in gene expression space, as are often observed during development[63], continue to provide a marked challenge to identifying underlying trajectories. A recently proposed algorithm, STITCH[63], provides an alternative strategy, which is described here in brief. Instead of projecting all the data into a single low-dimensional space, STITCH assembles a manifold that is defined by a series of independent PCA subspaces corresponding to each individual time point with nodes representing cells and edges linking transcriptionally similar cells in a low-dimensional space. This allows connections between cells to be identified even if cells are optimally described by differing underlying PC subspaces. From here, each cell in time point t_i, where $i \in$ (E11.5, E12.5, E15.5, P0, P5, adult) forms an outgoing edge from $t_i \rightarrow t_i$ and $t_i \rightarrow t_{i-1}$, $\forall i \in$ (time points) where all cells are projected into the PC subspace defined by t_i alone. In essence, edges connect each cell to its closest transcriptional neighbour within a time point and the preceding time point. Edges are then subjected to local neighbourhood restriction such that an outgoing edge from a cell was maintained if its neighbours were at most threefold as far as the cell's closest neighbour. To avoid spurious connections that may form, edges were next subjected to a global neighbourhood restriction where edges are maintained if they were below the average edge distance across all cells between time points (t_i, t_{i-1}) or within 1 standard deviation of the average edge distance within the time point. The graph was further reduced by retaining at most 20 mutual nearest neighbour edges.

Cloning, production, purification, concentration and quality control of AAV

AAV backbones were generated using standing cloning and molecular biology techniques. The following sequences were used for shRNAs: luciferase (GCGCGATAGCGCTAATAATTT) and *Pou4f3* (TATCCCTTGGAGAAAAGCCTTGTT). AAVs included GFP, tagged with haemagglutinin (TACCCATACGATGTTCCAGATTACGCT), as a reporter to monitor infectivity. Each individual preparation of AAV (2/9) and (2/PHP.S[64]) was produced by transient transfection of pRC9, pHelper, and AAV-genome plasmid into 6-12 T225 flasks of HEK 293T cells. Viral medium was collected and replaced at 72 h. 293T cells and a second round of viral medium were collected at 120 h post transfection. AAVs were extracted from cell pellets using Salt Active Nuclease (Articzymes) in 40 mM Tris, 500 mM NaCl and 2 mM $MgCl_2$ pH 8 (SAN buffer). AAVs in supernatant were precipitated with 8% PEG/500 mM NaCl and resuspended in SAN buffer. Viral suspensions were loaded onto an iodixanol gradient (OptiPrep) and subsequently concentrated using Amicon filters with a 100-kD cutoff to a volume of 25–30 µl (1 × PBS + 0.001% F-68) per 6 T225 flasks transfected. Viral titres were normalized to 1×10^{14} µg/ml and stored at −80 °C in 5–10-µl aliquots. AAVs (2/9) were injected intraperitoneally (IP) into pups at P0. Pups were transiently anaesthetized by hypothermia and bevelled pipettes were used to deliver 10^{12} viral genomes in a volume of 10 µl (0.01% Fast Green, 1 × PBS). After mice were injected, they were returned to ambient temperature and upon regaining full mobility were cross fostered with nursing CD1 females. Approximately seven days after transduction, DRG were extracted for subsequent experimental analysis. Upon dissection, all DRG were visualized and monitored for GFP expression. For behavioural experiments, a minimum of 10^{12} viral genomes of AAV (2/PHP.S) were delivered to P21 mice via intravenous injection (retroorbital vein).

Immunostaining analysis

DRG. For immunostaining analysis, mice (P28–42) were anaesthetized with isoflurane and transcardially perfused with 10 ml of 1 × PBS (with heparin) followed by 10 ml of 1 × PBS/4% paraformaldehyde at room temperature. Spinal columns were then removed and rinsed in 1 × PBS and then cryoprotected overnight in 1 × PBS/30% sucrose at 4 °C, then embedded in NEG50 and stored at −70 °C. For cryosectioning, tissue blocks were equilibrated to −20 °C for 1 h and then sectioned onto glass slides at a thickness of 20–25 µm. Slides were stored at −70 °C until they were ready for staining. Slides with sections were taken from freezers and immediately placed into 1 × PBS and washed 3× with 1 × PBS for 5 min each at room temperature. Tissue was blocked using 1 × PBS/5% normal donkey serum/0.05% Triton X-100 for 1 h at room temperature. Tissue was then washed with 1 × PBS 3 × 5 min each at room temperature. Tissue was then incubated in primary antibody (rabbit anti-NEUN, Millipore: MAB377, 1:1,000; goat anti-mCherry/tdTomato, CederLane: AB0040-200, 1:1,000) in 1 × PBS/5% normal donkey serum/0.05% Triton X-100 overnight at 4 °C. Tissue was washed in 1 × PBS 3× for 5 min at room

temperature followed by secondary antibody (donkey anti-rabbit 488, 1:1,000; donkey anti-goat 555, 1:1,000) diluted in 1 × PBS/5% normal donkey serum/0.05% Triton X-100 for 1 h at room temperature. Lastly, tissue was washed in 1 × PBS 3× for 5 min at room temperature followed by application of mounting medium and glass coverslip.

Skin sections. Skin sections were immunostained as described for DRG sections with the following differences: Section thickness was 55–60 µm. Primary antibodies used were chicken anti-GFP, Aves: GFP-1020, 1:1,000; goat anti-mCherry/tdTomato, CederLane: AB0040-200, 1:1,000; and rabbit anti-CGRP, Immunostar: 24112, 1:1,000). All images were obtained as z-stacks using a Zeiss LSM 700 confocal microscope using a 10× or 20× objective.

Two-plate temperature choice assay

Animals were habituated to the behavioural apparatus for 30 min before experimental analysis. Animals were placed into the centre of two identical chambers with one chamber randomly set to 30 °C and the other to the test temperature indicated. Animals were recorded as they freely explored the arena while automatic tracking software was used to track animals over a 5-min period. Time spent in each temperature chamber was quantified as a fraction of total time tested and one temperature was tested per day.

RNA isolation, reverse transcription, and qRT–PCR

DRG were dissected as described above; however, instead of subjecting ganglia to dissociation, they were directly lysed by gentle agitation in Trizol at room temperature for 10 min. The RNeasy Mini (Qiagen) kit was used according to the manufacturer's instructions to purify DNA-free RNA. RNA was converted to cDNA using 200–250 ng of RNA with the high-capacity cDNA reverse transcription kit (Thermo Fisher Scientific). qRT–PCR was performed with technical triplicates and mapped back to relative RNA concentrations using a standard curve built from a serial dilution of cDNA. Data were collected using the LightCycler 480 SYBR Green I Master mix (Roche) on a QuantStudio 3 qPCR machine (Applied Biosystems).

Statistics and reproducibility

For all scRNA-seq data shown all individual cells for the labelled cell type are shown with no downsampling or subsetting implemented unless explicitly indicated. Differential and comparative gene expression analysis was conducted using a two-sided Wilcoxon rank-sum test with Bonferroni corrected *P* values. Immunostaining and cell counting comparisons were done using a two-sided *t*-test. Behavioural analysis was compared using a two-way ANOVA followed by a Tukey's post-hoc test. All scRNA-seq samples were derived from $n = 2$ biologically independent samples with the exception of the adult (P28–42) sample which was derived from $n = 6$ biologically independent samples. The sample sizes (cell numbers) for each cell type and samples sizes for other analyses were as follows: Fig. 1a Adult: 257 Aβ-field-LTMR cells, 273 Aβ-RA-LTMR cells, 182 Aδ-LTMR cells, 1,554 C-LTMR cells, 1,440 CGRP-α cells, 850 CGRP-ε cells, 270 CGRP-η cells, 705 CGRP-γ cells, 758 CGRP-θ cells, 333 CGRP-ζ cells, 2,817 MRGPRD cells, 234 proprioceptors, 761 SST cells, 488 cold thermoceptor cells; P0: 209 Aβ-field-LTMR cells, 297 Aβ-RA-LTMR cells, 237 Aδ-LTMR cells, 1,392 C-LTMR cells, 445 CGRP-α cells, 473 CGRP-ε cells, 153 CGRP-η cells, 334 CGRP-γ cells, 640 CGRP-θ cells, 243 CGRP-ζ cells, 3,019 MRGPRD cells, 104 proprioceptors, 787 SST cells, 405 cold thermoceptor cells; P0: 214 Aβ-field-LTMR cells, 163 Aβ-RA-LTMR cells, 165 Aδ-LTMR cells, 739 C-LTMR cells, 284 CGRP-α cells, 188 CGRP-ε cells, 122 CGRP-η cells, 216 CGRP-γ cells, 359 CGRP-θ cells, 122 CGRP-ζ cells, 1,704 MRGPRD cells, 103 proprioceptors, 397 SST cells, 284 cold thermoceptor cells; E15.5: 61 Aβ-field-LTMR cells, 33 Aβ-RA-LTMR cells, 96 Aδ-LTMR cells, 383 C-LTMR cells, 144 CGRP-α cells, 45 CGRP-ε cells, 26 CGRP-η cells, 97 CGRP-γ cells, 208 CGRP-θ cells, 63 CGRP-ζ cells, 670 MRGPRD cells, 40 proprioceptors, 61 SST cells, 128 cold thermoceptor cells, 3,196 unlabelled cells; E12.5: 30 Aβ-field-LTMR cells, 20 Aβ-RA-LTMR cells, 30 Aδ-LTMR cells, 122 C-LTMR cells, 57 CGRP-α cells, 87 CGRP-ε cells, 48 CGRP-η cells, 60 CGRP-γ cells, 9 CGRP-θ cells, 37 CGRP-ζ cells, 555 MRGPRD cells, 37 proprioceptors, 24 SST cells, 105 cold thermoceptor cells, 7,909 unlabelled cells; Fig. 1b E11.5: 1,951 unspecialized sensory neurons, 5,402 sensory neuron progenitors, 2,781 neural crest progenitors; Fig. 1c $n = 3$ biologically independent samples; Fig. 1d 1,951 unspecialized sensory neurons, 257 Aβ-field-LTMR cells, 273 Aβ-RA-LTMR cells, 182 Aδ-LTMR cells, 1,554 C-LTMR cells, 1,440 CGRP-α cells, 850 CGRP-ε cells, 270 CGRP-η cells, 705 CGRP-γ cells, 758 CGRP-θ cells, 333 CGRP-ζ cells, 2,817 MRGPRD cells, 234 proprioceptors, 761 SST cells, 488 cold thermoceptor cells; Fig. 2a, b 696 Aβ-field LTMR cells, 734 Aβ-RA-LTMR cells, 659 Aδ-LTMR cells, 3,750 C-LTMR cells, 2,072 CGRP-α cells, 1,503 CGRP-ε cells, 555 CGRP-η cells, 1,377 CGRP-γ cells, 1,895 CGRP-θ cells, 743 CGRP-ζ cells, 7,498 MRGPRD cells, 462 proprioceptors, 1,733 SST cells, 1,246 cold thermoceptor cells, 1,951 unspecialized sensory neurons, 14,982 cells with unmatched identity; Fig. 2c 1,951 unspecialized sensory neurons, 257 Aβ-field-LTMR cells, 273 Aβ-RA-LTMR cells, 182 Aδ-LTMR cells, 1,554 C-LTMR cells, 1,440 CGRP-α cells, 850 CGRP-ε cells, 270 CGRP-η cells, 705 CGRP-γ cells, 758 CGRP-θ cells, 333 CGRP-ζ cells, 2,817 MRGPRD cells, 234 proprioceptors, 761 SST cells, 488 cold thermoceptor cells; Fig. 3a 10,321 cells from E11.5; Fig. 3c 159 Aβ-field-LTMR cells, 385 Aβ-RA-LTMR cells, 203 Aδ-LTMR cells, 1,827 C-LTMR cells, 441 CGRP-α cells, 334 CGRP-ε cells, 348 CGRP-η cells, 417 CGRP-γ cells, 1,665 CGRP-θ cells, 196 CGRP-ζ cells, 3,666 MRGPRD cells, 185 proprioceptors, 802 SST cells, 717 cold thermoceptor cells; Fig. 3e $n = 3$ biologically independent samples; Fig. 4a, c control/knockout 776/435 Aβ-field-LTMR cells, 728/1,114 Aβ-RA-LTMR cells, 667/927 Aδ-LTMR cells, 2,928/2,486 C-LTMR cells, 478/656 CGRP-α cells, 990/582 CGRP-ε cells, 721/589 CGRP-η cells, 711/540 CGRP-γ cells, 1,845/2,381 CGRP-θ cells, 417/230 CGRP-ζ cells, 5,556/7,508 MRGPRD cells, 446/654 proprioceptors, 1,747/1,460 SST cells, 493/675 cold thermoceptor cells; Fig. 4b, d control/knockout 191/254 Aβ-field-LTMR cells, 246/332 Aβ-RA-LTMR cells, 170/236 Aδ-LTMR cells, 917/800 C-LTMR cells, 706/545 CGRP-α cells, 495/365 CGRP-ε cells, 279/330 CGRP-η cells, 559/429 CGRP-γ cells, 907/605 CGRP-θ cells, 292/341 CGRP-ζ cells, 1,977/2,960 MRGPRD cells, 123/213 proprioceptors, 724/835 SST cells, 427/392 cold thermoceptor cells; Fig. 5a–c in 159 controls, 342 Aβ-field-LTMR cells, 122 Aβ-RA-LTMR cells, 413 Aδ-LTMR cells, 783 C-LTMR cells, 363 CGRP-α cells, 314 CGRP-ε cells, 320 CGRP-η cells, 418 CGRP-γ cells, 460 CGRP-θ cells, 352 CGRP-ζ cells, 1,162 MRGPRD cells, 368 proprioceptors, 149 SST cells, 442 cold thermoceptor cells; in $Ngf^{-/-};Bax^{-/-}$, 82 Aβ-field-LTMR cells, 162 Aβ-RA-LTMR cells, 124 Aδ-LTMR cells, 395 proprioceptors, 2,558 ClusterA cells, 1,878 ClusterB cells, 362 ClusterC cells, 1,461 ClusterD cells, 714 ClusterE cells; Extended Data Fig. 1a 257 Aβ-field-LTMR cells, 273 Aβ-RA-LTMR cells, 182 Aδ-LTMR cells, 1,554 C-LTMR cells, 1,440 CGRP-α cells, 850 CGRP-ε cells, 270 CGRP-η cells, 705 CGRP-γ cells, 758 CGRP-θ cells, 333 CGRP-ζ cells, 2,817 MRGPRD cells, 234 proprioceptors, 761 SST cells, 488 cold thermoceptor cells; Extended Data Fig. 1b 209 Aβ-field-LTMR cells, 297 Aβ-RA-LTMR cells, 237 Aδ-LTMR cells, 1,392 C-LTMR cells, 445 CGRP-α cells, 473 CGRP-ε cells, 153 CGRP-η cells, 334 CGRP-γ cells, 640 CGRP-θ cells, 243 CGRP-ζ cells, 3,019 MRGPRD cells, 104 proprioceptors, 787 SST cells, 405 cold thermoceptor cells; Extended Data Fig. 1c 214 Aβ-field-LTMR cells, 163 Aβ-RA-LTMR cells, 165 Aδ-LTMR cells, 739 C-LTMR cells, 284 CGRP-α cells, 188 CGRP-ε cells, 122 CGRP-η cells, 216 CGRP-γ cells, 359 CGRP-θ cells, 122 CGRP-ζ cells, 1,704 MRGPRD cells, 103 proprioceptors, 397 SST cells, 284 cold thermoceptor cells; Extended Data Fig. 1d 61 Aβ-field-LTMR cells, 33 Aβ-RA-LTMR cells, 96 Aδ-LTMR cells, 383 C-LTMR cells, 144 CGRP-α cells, 45 CGRP-ε cells, 26 CGRP-η cells, 97 CGRP-γ cells, 208 CGRP-θ cells, 63 CGRP-ζ cells, 670 MRGPRD cells, 40 proprioceptors, 61 SST cells, 128 cold thermoceptor cells; Extended Data Fig. 1e 30 Aβ-field-LTMR cells, 20 Aβ-RA-LTMR cells, 30 Aδ-LTMR cells, 122 C-LTMR cells, 57 CGRP-α cells, 87 CGRP-ε cells, 48 CGRP-η cells, 60 CGRP-γ cells, 9

CGRP-θ cells, 37 CGRP-ζ cells, 555 MRGPRD cells, 37 proprioceptors, 24 SST cells, 105 cold thermoceptor cells; Extended Data Fig. 1f Mature/P5 merge, P5/P0 merge, E15.5/P0 merge, E15.5/E12.5 merge; Extended Data Fig. 2a, b $n = 15$ biologically independent sections for each in situ at each axial level; Extended Data Fig. 3a–c 293 Aβ-RA-LTMR cells, 106 Aδ-LTMR cells, 408 C-LTMR cells, 225 CGRP-α cells, 595 CGRP-ε cells, 127 CGRP-η cells, 329 CGRP-γ cells, 199 CGRP-θ cells, 96 CGRP-ζ cells, 1,103 MRGPRD cells, 131 SST cells, 656 cold thermoceptor cells; Extended Data Fig. 4a–e 257 Aβ-field-LTMR cells, 273 Aβ-RA-LTMR cells, 182 Aδ-LTMR cells, 1,554 C-LTMR cells, 1,440 CGRP-α cells, 850 CGRP-ε cells, 270 CGRP-η cells, 705 CGRP-γ cells, 758 CGRP-θ cells, 333 CGRP-ζ cells, 2,817 MRGPRD cells, 234 proprioceptors, 761 SST cells, 488 cold thermoceptor cells, 1,951 unspecialized sensory neurons, 5,402 sensory neuron progenitors, 2,781 neural crest progenitors; Extended Data Fig. 5a 696 Aβ-field-LTMR cells, 734 Aβ-RA-LTMR cells, 659 Aδ-LTMR cells, 3,750 C-LTMR cells, 2,072 CGRP-α cells, 1,503 CGRP-ε cells, 555 CGRP-η cells, 1,377 CGRP-γ cells, 1,895 CGRP-θ cells, 743 CGRP-ζ cells, 7,498 MRGPRD cells, 462 proprioceptors, 1,733 SST cells, 1,246 cold thermoceptor cells, 1,951 unspecialized sensory neurons, 14,982 cells with unmatched identity; Extended Data Fig. 5b 257 Aβ-field-LTMR cells, 273 Aβ-RA-LTMR cells, 182 Aδ-LTMR cells, 1,554 C-LTMR cells, 1,440 CGRP-α cells, 850 CGRP-ε cells, 270 CGRP-η cells, 705 CGRP-γ cells, 758 CGRP-θ cells, 333 CGRP-ζ cells, 2,817 MRGPRD cells, 234 proprioceptors, 761 SST cells, 488 cold thermoceptor cells; Extended Data Fig. 5c $n = 3$ biologically independent samples; Extended Data Fig. 6a, b adult: 257 Aβ-field-LTMR cells, 273 Aβ-RA-LTMR cells, 182 Aδ-LTMR cells, 1,554 C-LTMR cells, 1,440 CGRP-α cells, 850 CGRP-ε cells, 270 CGRP-η cells, 705 CGRP-γ cells, 758 CGRP-θ cells, 333 CGRP-ζ cells, 2,817 MRGPRD cells, 234 proprioceptors, 761 SST cells, 488 cold thermoceptor cells; P5 209 Aβ-field-LTMR cells, 297 Aβ-RA-LTMR cells, 237 Aδ-LTMR cells, 1,392 C-LTMR cells, 445 CGRP-α cells, 473 CGRP-ε cells, 153 CGRP-η cells, 334 CGRP-γ cells, 640 CGRP-θ cells, 243 CGRP-ζ cells, 3,019 MRGPRD cells, 104 proprioceptors, 787 SST cells, 405 cold thermoceptor cells; P0 214 Aβ-field-LTMR cells, 163 Aβ-RA-LTMR cells, 165 Aδ-LTMR cells, 739 C-LTMR cells, 284 CGRP-α cells, 188 CGRP-ε cells, 122 CGRP-η cells, 216 CGRP-γ cells, 359 CGRP-θ cells, 122 CGRP-ζ cells, 1,704 MRGPRD cells, 103 proprioceptors, 397 SST cells, 284 cold thermoceptor cells; E15.5 61 Aβ-field-LTMR cells, 33 Aβ-RA-LTMR cells, 96 Aδ-LTMR cells, 383 C-LTMR cells, 144 CGRP-α cells, 45 CGRP-ε cells, 26 CGRP-η cells, 97 CGRP-γ cells, 208 CGRP-θ cells, 63 CGRP-ζ cells, 670 MRGPRD cells, 40 proprioceptors, 61 SST cells, 128 cold thermoceptor cells; E12.5 30 Aβ-field-LTMR cells, 20 Aβ-RA-LTMR cells, 30 Aδ-LTMR cells, 122 C-LTMR cells, 57 CGRP-α cells, 87 CGRP-ε cells, 48 CGRP-η cells, 60 CGRP-γ cells, 9 CGRP-θ cells, 37 CGRP-ζ cells, 555 MRGPRD cells, 37 proprioceptors, 24 SST cells, 105 cold thermoceptor cells; Extended Data Fig. 7a $n = 3$ biologically independent samples for the *Avil* in situ, control/knockout 776/435 Aβ-field-LTMR cells, 728/1,114 Aβ-RA-LTMR cells, 667/927 Aδ-LTMR cells, 2,928/2,486 C-LTMR cells, 478/656 CGRP-α cells, 990/582 CGRP-ε cells, 721/589 CGRP-η cells, 711/540 CGRP-γ cells, 1,845/2,381 CGRP-θ cells, 417/230 CGRP-ζ cells, 5,556/7,508 MRGPRD cells, 446/654 proprioceptors, 1,747/1,460 SST cells, 493/675 cold thermoceptor cells; Extended Data Fig. 7b $n = 3$ biologically independent samples for the in situ, control/knockout 191/254 Aβ-field-LTMR cells, 246/332 Aβ-RA-LTMR cells, 170/236 Aδ-LTMR cells, 917/800 C-LTMR cells, 706/545 CGRP-α cells, 495/365 CGRP-ε cells, 279/330 CGRP-η cells, 559/429 CGRP-γ cells, 907/605 CGRP-θ cells, 292/341 CGRP-ζ cells, 1,977/2,960 MRGPRD cells, 123/213 proprioceptors, 724/835 SST cells, 427/392 cold thermoceptor cells; Extended Data Fig. 8e, f t-SNE plots represent 257 Aβ-field-LTMR cells, 273 Aβ-RA-LTMR cells, 182 Aδ-LTMR cells, 1,554 C-LTMR cells, 1,440 CGRP-α cells, 850 CGRP-ε cells, 270 CGRP-η cells, 705 CGRP-γ cells, 758 CGRP-θ cells, 333 CGRP-ζ cells, 2,817 MRGPRD cells, 234 proprioceptors, 761 SST cells, 488 cold thermoceptor cells; Extended Data Fig. 8h $n = 3$ biologically independent samples for the immunostaining; Extended Data Fig. 8j $n = 3$ biologically independent samples for the immunostaining; Extended Data Fig. 8k $n = 3$ biologically independent samples for the immunostaining and the in situ; Extended Data Fig. 9a control 342 Aβ-field-LTMR cells, 122 Aβ-RA-LTMR cells, 413 Aδ-LTMR cells, 783 C-LTMR cells, 363 CGRP-α cells, 314 CGRP-ε cells, 320 CGRP-η cells, 418 CGRP-γ cells, 460 CGRP-θ cells, 352 CGRP-ζ cells, 1,162 MRGPRD cells, 368 proprioceptors, 149 SST cells, 442 cold thermoceptor cells; *Ngf*$^{-/-}$;*Bax*$^{-/-}$ 82 Aβ-field-LTMR cells, 162 Aβ-RA-LTMR cells, 124 Aδ-LTMR cells, 395 proprioceptors, 2,558 ClusterA cells, 1,878 ClusterB cells, 362 ClusterC cells, 1,461 ClusterD cells, 714 ClusterE cells; Extended Data Fig. 9c $n = 3$ biologically independent samples for each in situ; Supplementary Data 1 257 Aβ-field-LTMR cells, 273 Aβ-RA-LTMR cells, 182 Aδ-LTMR cells, 1,554 C-LTMR cells, 1,440 CGRP-α cells, 850 CGRP-ε cells, 270 CGRP-η cells, 705 CGRP-γ cells, 758 CGRP-θ cells, 333 CGRP-ζ cells, 2,817 MRGPRD cells, 234 proprioceptors, 761 SST cells, 488 cold thermoceptor cells.

Reporting summary

Further information on research design is available in the Nature Research Reporting Summary linked to this paper.

Data availability

Sequence data from this study have been deposited in the Gene Expression Omnibus with accession code GSE139088. The scRNA-seq data are also available for browsing and analysis on reasonable request or via the HTML interface at https://kleintools.hms.harvard.edu/tools/springViewer_1_6_dev.html?datasets/Sharma2019/all.

Code availability

The computational code used in the study is available at GitHub (https://github.com/wagnerde) or upon request.

44. Wende, H. et al. The transcription factor c-Maf controls touch receptor development and function. *Science* **335**, 1373–1376 (2012).
45. Ichikawa, H., Deguchi, T., Nakago, T., Jacobowitz, D. M. & Sugimoto, T. Parvalbumin, calretinin and carbonic anhydrase in the trigeminal and spinal primary neurons of the rat. *Brain Res.* **655**, 241–245 (1994).
46. Zheng, Y. et al. Deep sequencing of somatosensory neurons reveals molecular determinants of intrinsic physiological properties. *Neuron* **103**, 598–616.e7 (2019).
47. Bai, L. et al. Genetic identification of an expansive mechanoreceptor sensitive to skin stroking. *Cell* **163**, 1783–1795 (2015).
48. Rutlin, M. et al. The cellular and molecular basis of direction selectivity of Aδ-LTMRs. *Cell* **159**, 1640–1651 (2014).
49. Li, L. et al. The functional organization of cutaneous low-threshold mechanosensory neurons. *Cell* **147**, 1615–1627 (2011).
50. Kobayashi, K. et al. Distinct expression of TRPM8, TRPA1, and TRPV1 mRNAs in rat primary afferent neurons with aδ/c-fibers and colocalization with trk receptors. *J. Comp. Neurol.* **493**, 596–606 (2005).
51. Rosenfeld, M. G. et al. Production of a novel neuropeptide encoded by the calcitonin gene via tissue-specific RNA processing. *Nature* **304**, 129–135 (1983).
52. Dong, X., Han, S., Zylka, M. J., Simon, M. I. & Anderson, D. J. A diverse family of GPCRs expressed in specific subsets of nociceptive sensory neurons. *Cell* **106**, 619–632 (2001).
53. Zylka, M. J., Dong, X., Southwell, A. L. & Anderson, D. J. Atypical expansion in mice of the sensory neuron-specific Mrg G protein-coupled receptor family. *Proc. Natl Acad. Sci. USA* **100**, 10043–10048 (2003).
54. Zylka, M. J., Rice, F. L. & Anderson, D. J. Topographically distinct epidermal nociceptive circuits revealed by axonal tracers targeted to *Mrgprd*. *Neuron* **45**, 17–25 (2005).
55. Arber, S., Ladle, D. R., Lin, J. H., Frank, E. & Jessell, T. M. ETS gene *Er81* controls the formation of functional connections between group Ia sensory afferents and motor neurons. *Cell* **101**, 485–498 (2000).
56. de Nooij, J. C., Doobar, S. & Jessell, T. M. Etv1 inactivation reveals proprioceptor subclasses that reflect the level of NT3 expression in muscle targets. *Neuron* **77**, 1055–1068 (2013).
57. Stantcheva, K. K. et al. A subpopulation of itch-sensing neurons marked by Ret and somatostatin expression. *EMBO Rep.* **17**, 585–600 (2016).
58. Mishra, S. K. & Hoon, M. A. The cells and circuitry for itch responses in mice. *Science* **340**, 968–971 (2013).
59. Bautista, D. M. et al. The menthol receptor TRPM8 is the principal detector of environmental cold. *Nature* **448**, 204–208 (2007).
60. McKemy, D. D., Neuhausser, W. M. & Julius, D. Identification of a cold receptor reveals a general role for TRP channels in thermosensation. *Nature* **416**, 52–58 (2002).
61. Hockley, J. R. F. et al. Single-cell RNAseq reveals seven classes of colonic sensory neuron. *Gut* **68**, 633–644 (2018).

62. Li, C. L. et al. Somatosensory neuron types identified by high-coverage single-cell RNA-sequencing and functional heterogeneity. *Cell Res*. **26**, 967 (2016).
63. Wagner, D. E. et al. Single-cell mapping of gene expression landscapes and lineage in the zebrafish embryo. *Science* **360**, 981–987 (2018).
64. Chan, K. Y. et al. Engineered AAVs for efficient noninvasive gene delivery to the central and peripheral nervous systems. *Nat. Neurosci*. **20**, 1172–1179 (2017).

Acknowledgements We thank all members of the Ginty laboratory for discussions and critical feedback during the course of this work. We thank L. Yap, A. Rodrigues, A. Shyer, B. Shrestha, C. Santiago, C. Harwell, D. Paul, G. Fishell, L. Orefice, L. Goodrich, M. Pecot, and R. Wolfson for feedback and critical evaluation of the data and manuscript. We thank L. Yap and M. Greenberg for providing the base construct for AAV-mediated shRNA delivery. We thank M. Greenberg for access to the NextSeq 500 sequencing platform. This work was supported by NIH grant NS97344 (D.D.G.), Howard Hughes Medical Institute–Life Sciences Research Foundation postdoctoral fellowship (D.E.W.), NIH grant 1K99GM121852 (D.E.W.), NIH grant 5R33CA212697 (A.M.K.), the Bertarelli Foundation (D.D.G.), a Fix Fund Postdoctoral Fellowship (N.S.), and the Edward R. and Anne G. Lefler Center for Neurodegenerative Disorders. D.D.G. is an investigator of the Howard Hughes Medical Institute.

Author contributions N.S. and D.D.G. conceived and designed the project. N.S. designed, executed and analysed all experiments with assistance and guidance from D.E.W. and A.M.K. on the STITCH/SPRING analysis. N.S., K.F. and K.L. designed, prepared, and validated AAV constructs. N.S. and D.D.G. wrote the manuscript with input from all authors.

Competing interests The authors declare no competing interests.

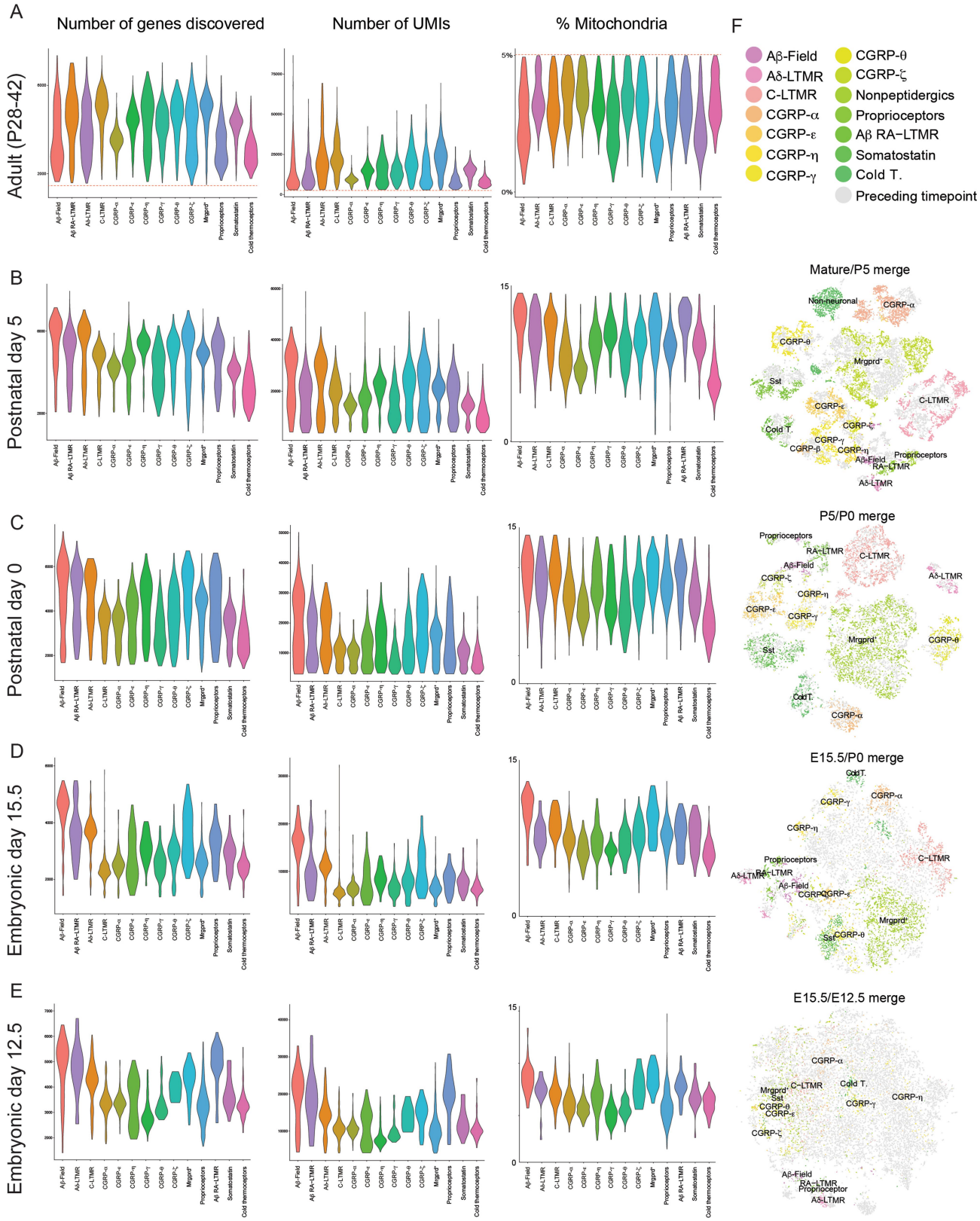
Additional information

Supplementary information is available for this paper at https://doi.org/10.1038/s41586-019-1900-1.

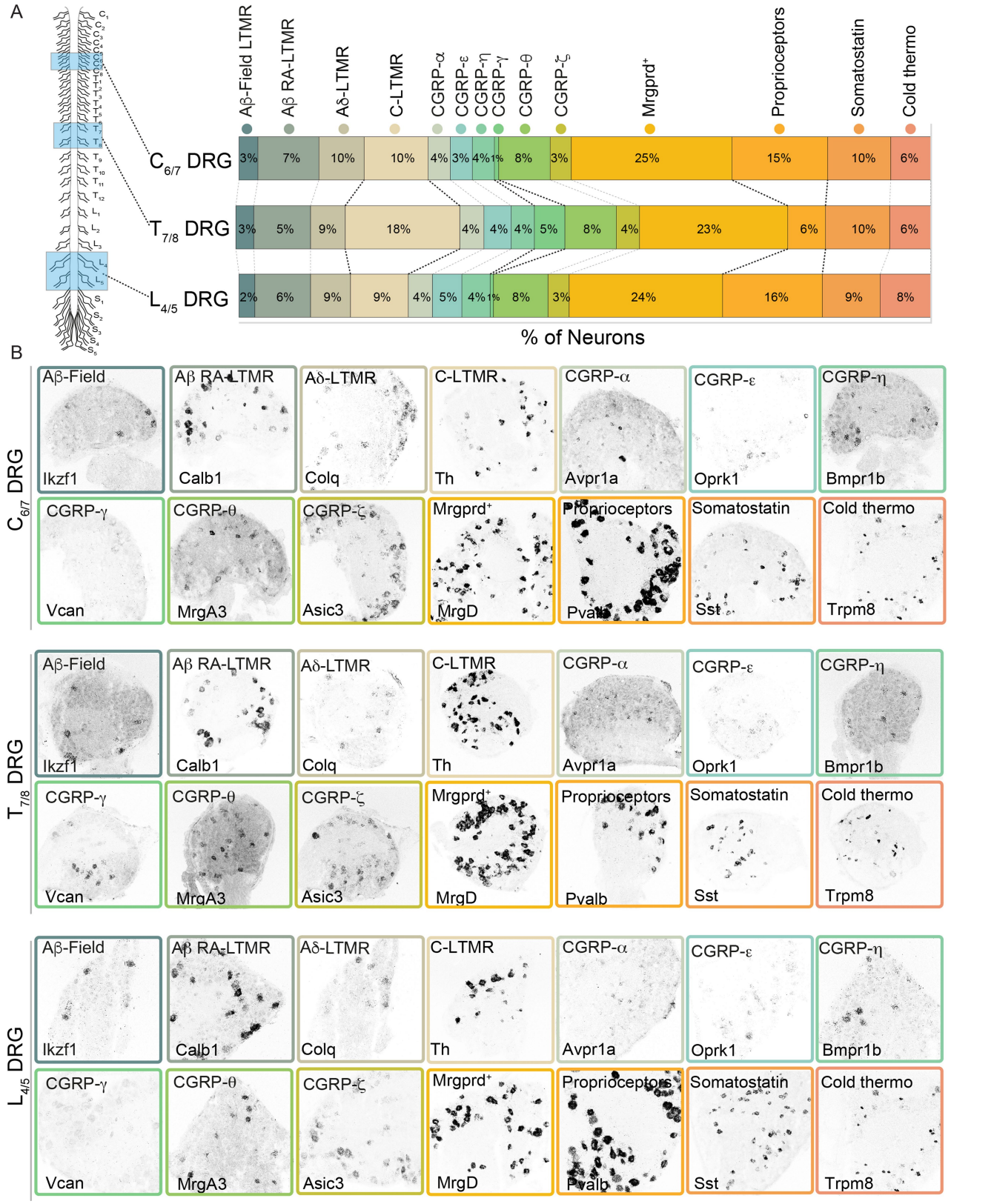
Correspondence and requests for materials should be addressed to D.D.G.

Peer review information *Nature* thanks Jeremy Dasen and the other, anonymous, reviewer(s) for their contribution to the peer review of this work.

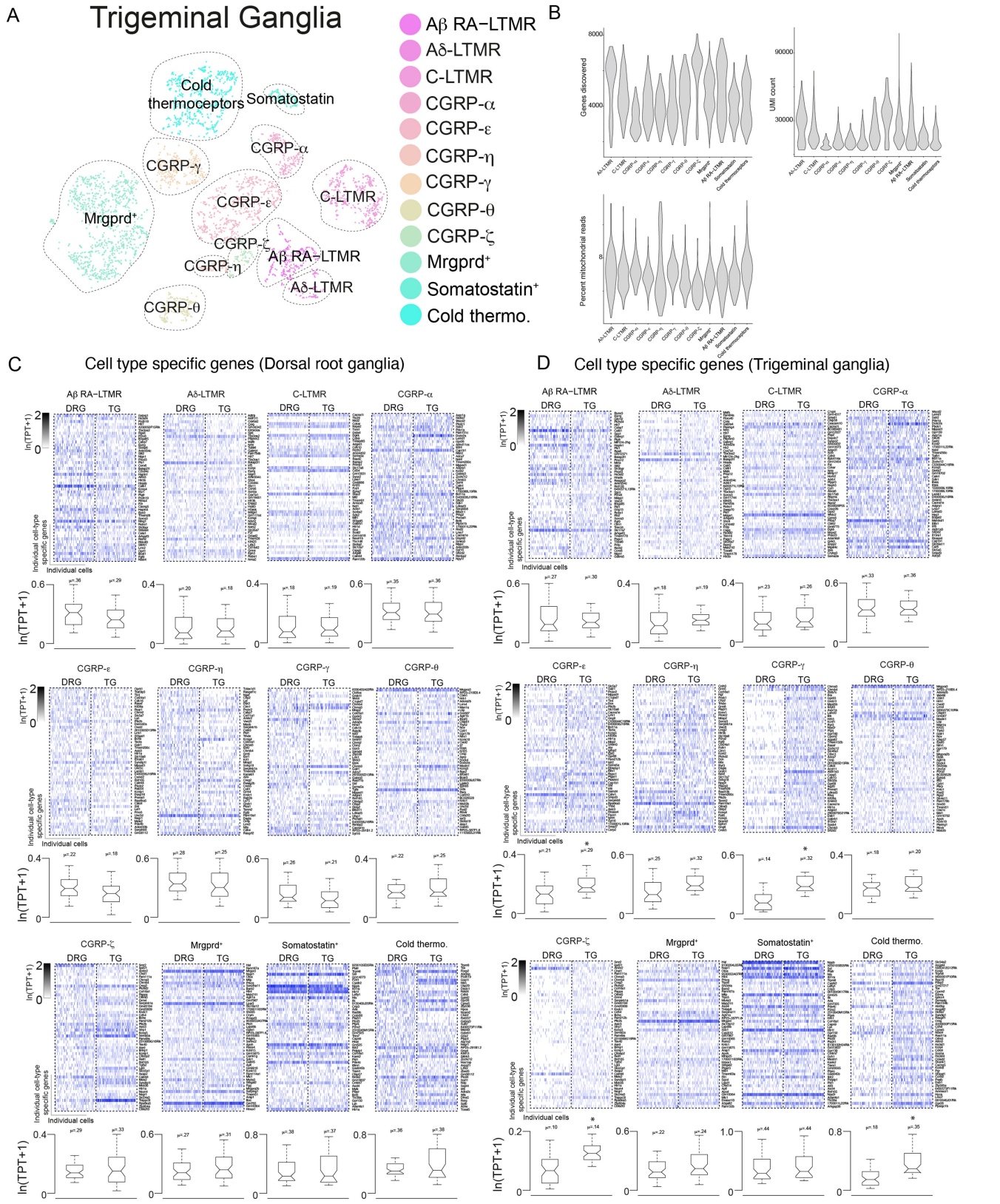
Reprints and permissions information is available at http://www.nature.com/reprints.



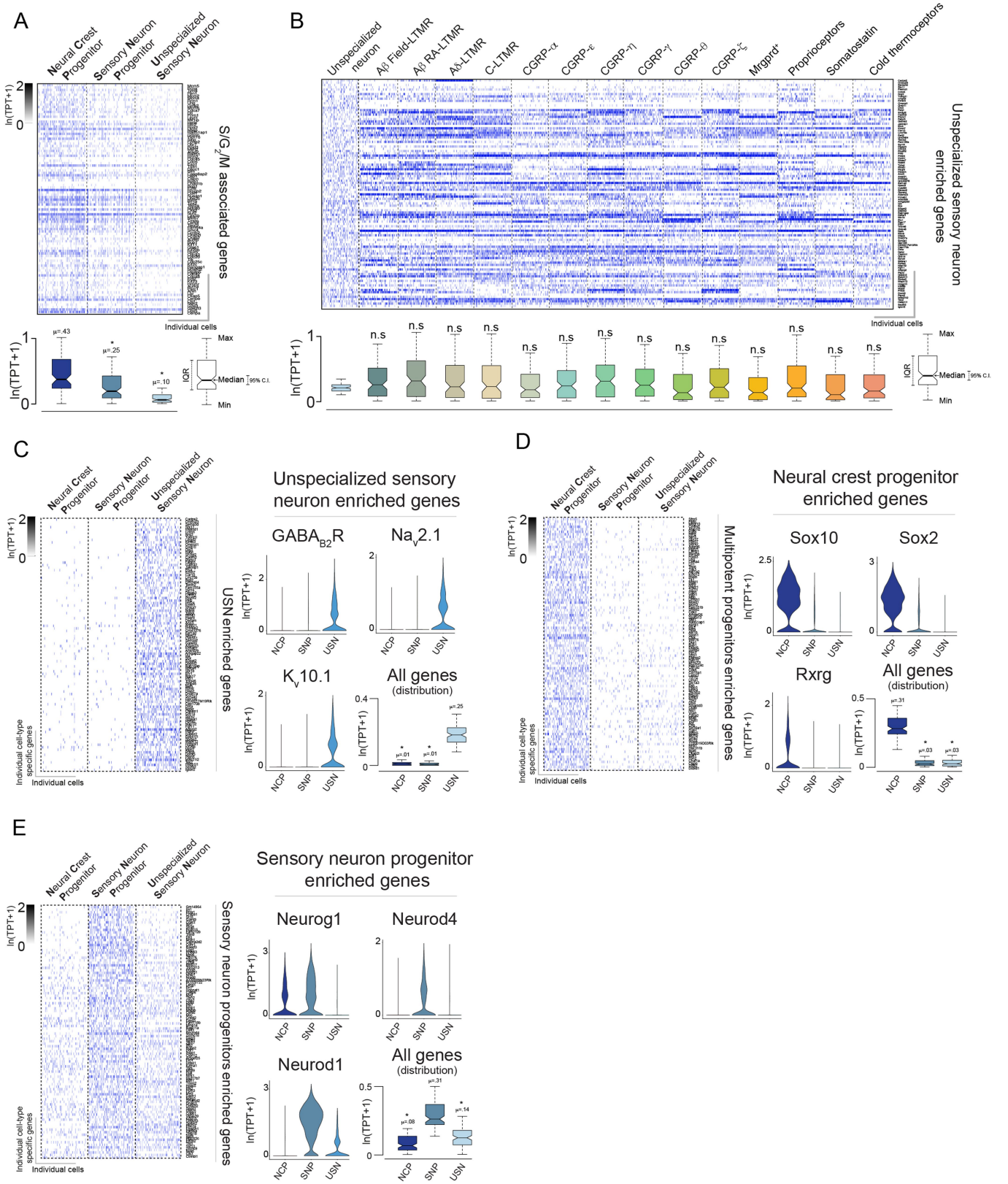
Extended Data Fig. 1 | Quality control metrics for DRG sensory neuron scRNA-seq data and canonical correlation analysis. a–**e**, Distribution of the number of genes discovered in each cell (individual points) in each population of sensory neuron (underlying violin plot) in adult mice (**a**), P5 (**b**), P0 (**c**), E15.5 (**d**), and E12.5 (**e**). Individual cells with fewer than 1,000 genes (considered to be low quality) or more than 10,000 genes (considered likely to be doublets) were eliminated from subsequent analysis. Individual cells with fewer than 1,000 UMIs (considered to be low quality) were excluded from subsequent analysis. **f**, Integration of adult/P5 (first plot), P5/P0 (second plot), P0/E15.5 (third plot), and E15.5/E12.5 (fourth plot) using canonical correlation analysis to find common sources of variation between time points. Single cells are labelled as individual points, with colour representing identified cell types and grey representing cells in the preceding time point. For *n* values, see Methods.



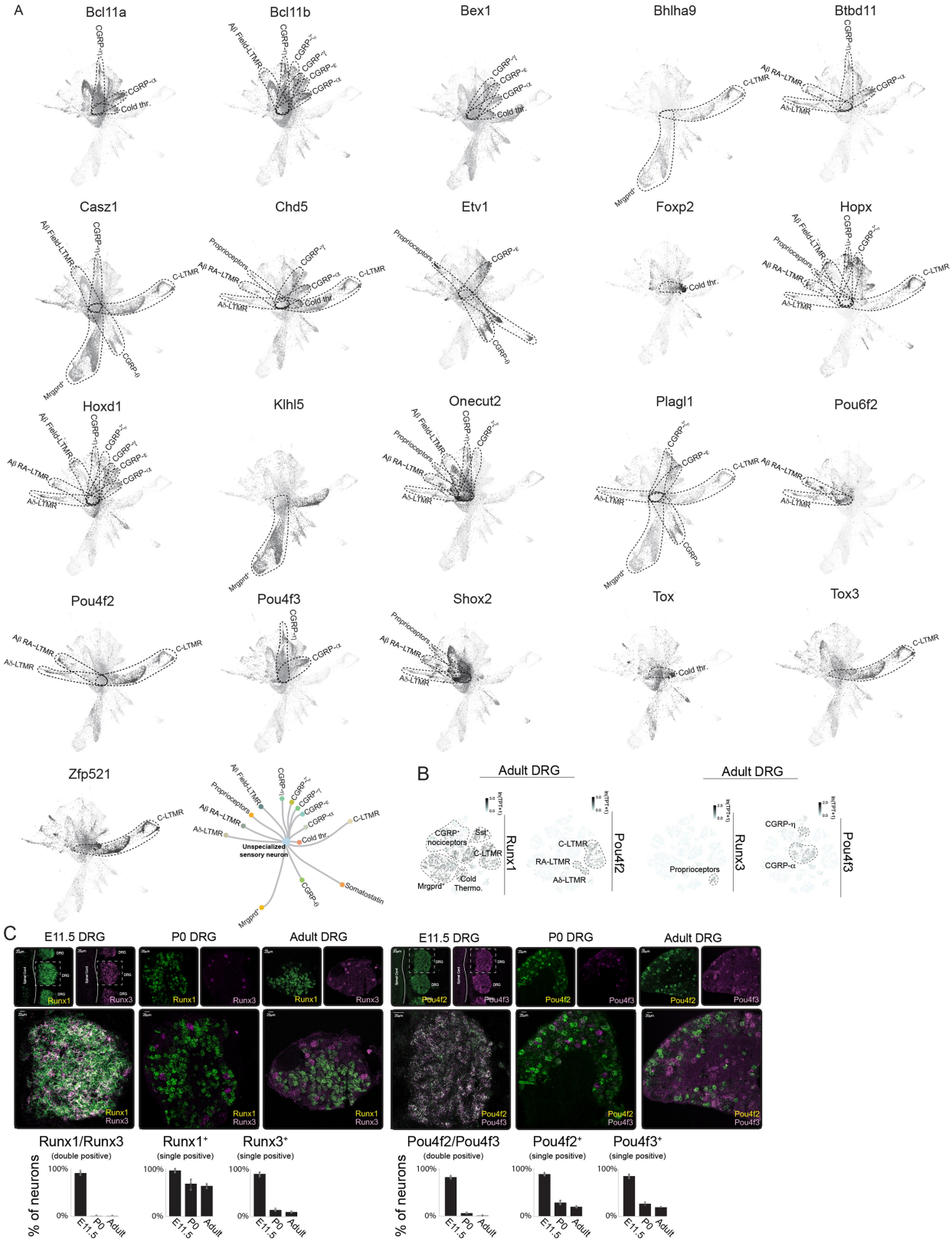
Extended Data Fig. 2 | Somatosensory neuron subtype composition varies across axial levels. a, Left, schematic representing which axial levels were quantified. Right, quantification of smRNA-FISH to determine the percentage of C6/7, T7/8, and L4/5 DRG neurons that corresponds to each transcriptionally defined somatosensory neuron subtype. Black dotted lines highlight the subtypes present at different percentages at different axial levels. **b**, Example images of smRNA-FISH for transcriptionally distinct somatosensory neuron subtypes in C6/7 (top), T7/8 (middle) and L4/5 (bottom) DRG. For *n* values, see Methods.



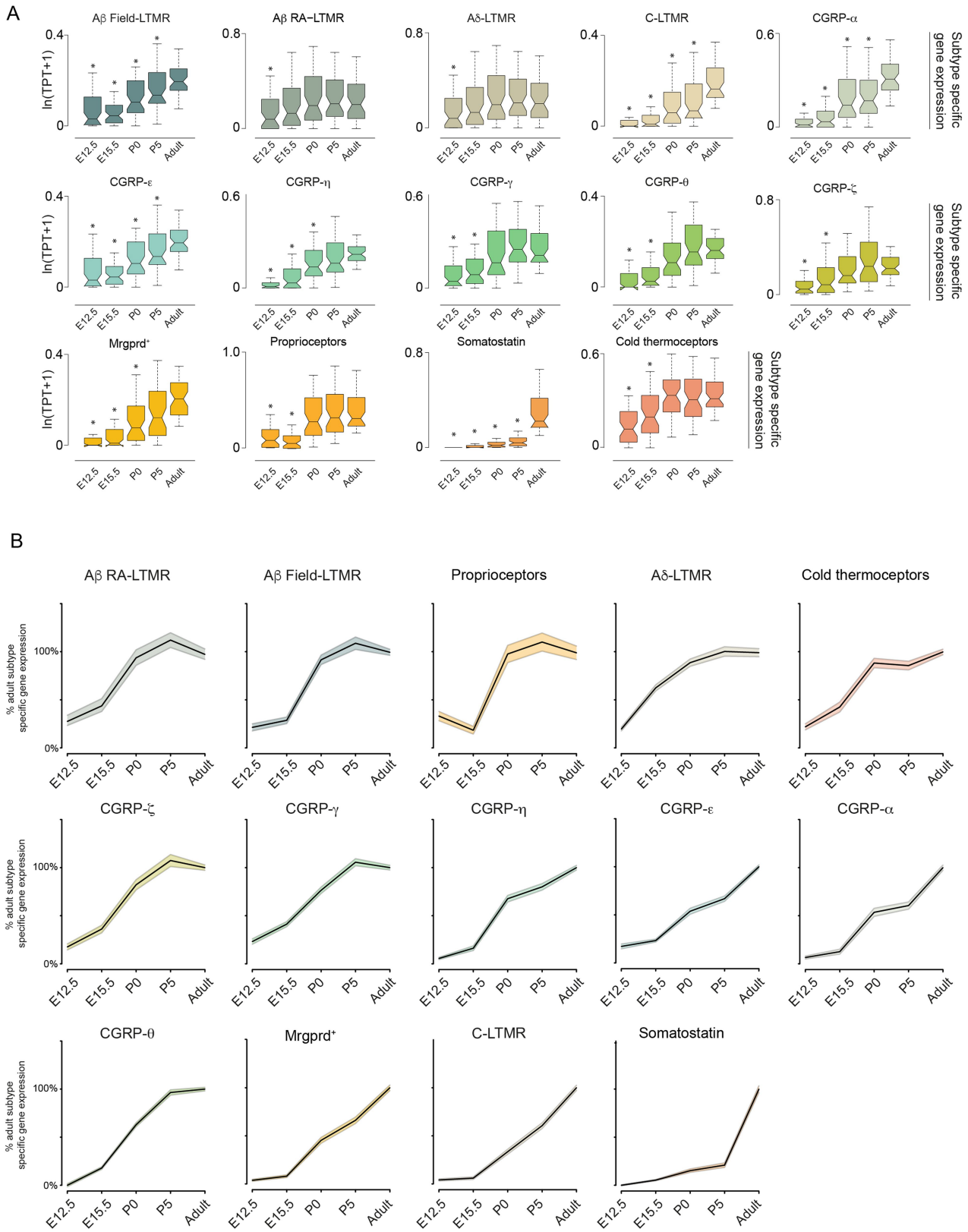
Extended Data Fig. 3 | Dorsal root ganglia and trigeminal ganglia comprise similar subtypes of somatosensory neurons. a, t-SNE visualization of trigeminal ganglia scRNA-seq data obtained from adult (P28–42) mice. Colours denote principal cell types and dotted circles were added to aid in visualization of principal cell types. **b**, Distribution of the number of genes discovered in each population of sensory neuron in adult trigeminal ganglia displayed as violin plots. **c**, Heat map depicting expression of genes that are enriched in somatosensory neuron subtypes resident in DRG as well as their expression levels in cognate subtype counterparts in trigeminal ganglia. **d**, Heat map depicting expression of genes that are enriched in somatosensory neuron subtypes resident in the trigeminal ganglia as well as their expression levels in cognate subtype counterparts in DRG. **c**, **d**, Boxes represent IQR, whiskers represent minimum and maximum values, and notches represent the 95% confidence interval of the median. *$P < 0.01$, two-sided Wilcoxon rank-sum test with Bonferroni correction. For n values, see Methods.



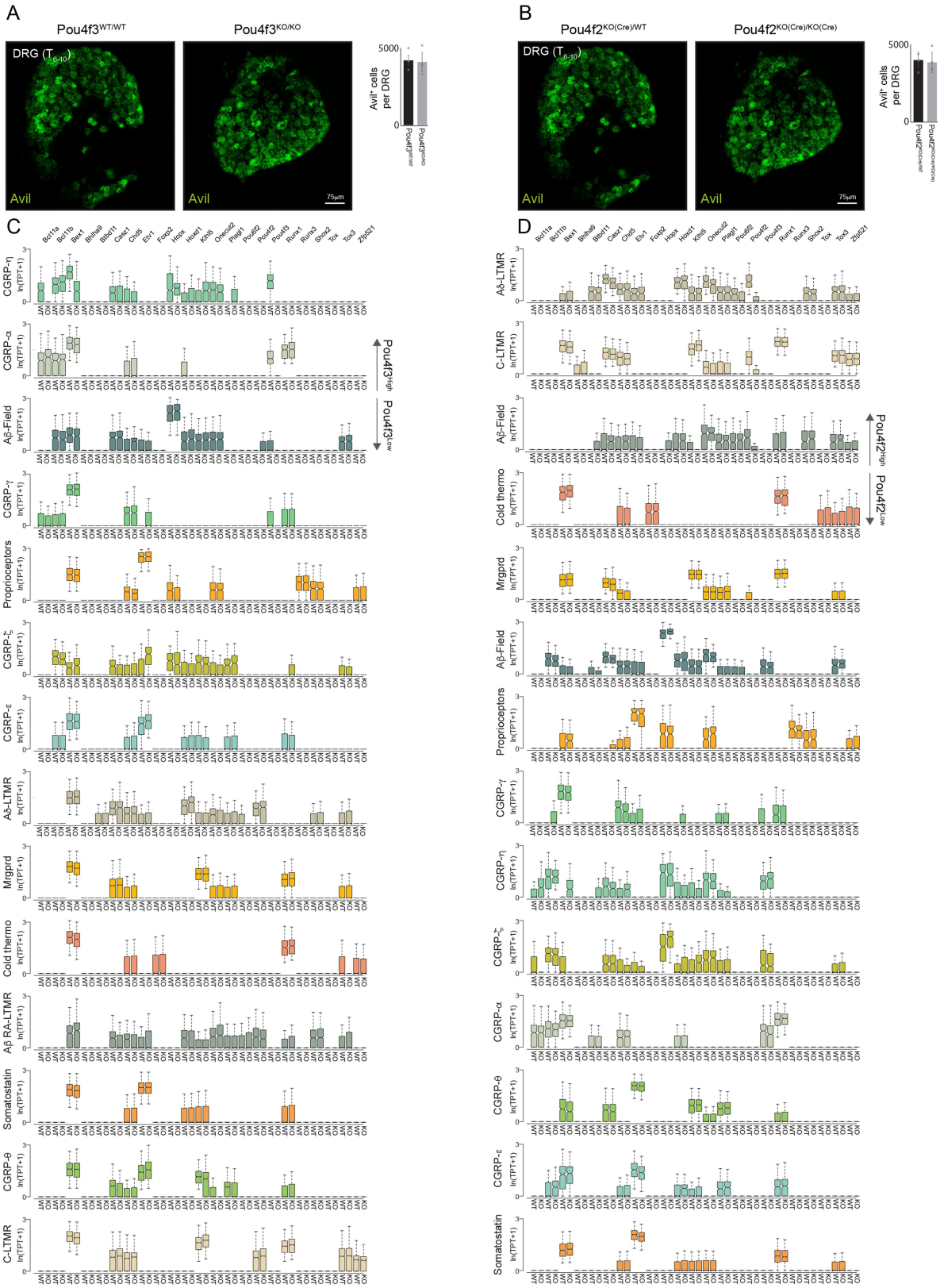
Extended Data Fig. 4 | Neural crest progenitors, sensory neuron progenitors and unspecialized sensory neurons express highly distinct gene programs. **a**, Heat map depicting cell cycle (S/G_2/M)-associated genes for the principal subtypes identified at E11.5. **b**, Heat map depicting expression of genes enriched in USNs in both mature somatosensory neuron subtypes and USNs. **c**, Left, heat map depicting expression of genes enriched in USNs as well as their expression in NCPs and SNPs. Right, violin and box plots depicting example genes enriched in USNs. **d**, Left, heat map depicting expression of genes enriched in NCPs as well as their expression in SNPs and USNs. Right, violin and box plots depicting example genes enriched in NCPs. **e**, Left, heat map depicting expression of genes enriched in SNPs as well as their expression in NCPs and USNs. Right, violin and box plots depicting example genes enriched in SNPs. **a**–**e**, Boxes represent IQR, whiskers represent minimum and maximum values, and notches represent the 95% confidence interval of the median. *P < 0.01, two-sided Wilcoxon rank-sum test with Bonferroni correction. For n values, see Methods.



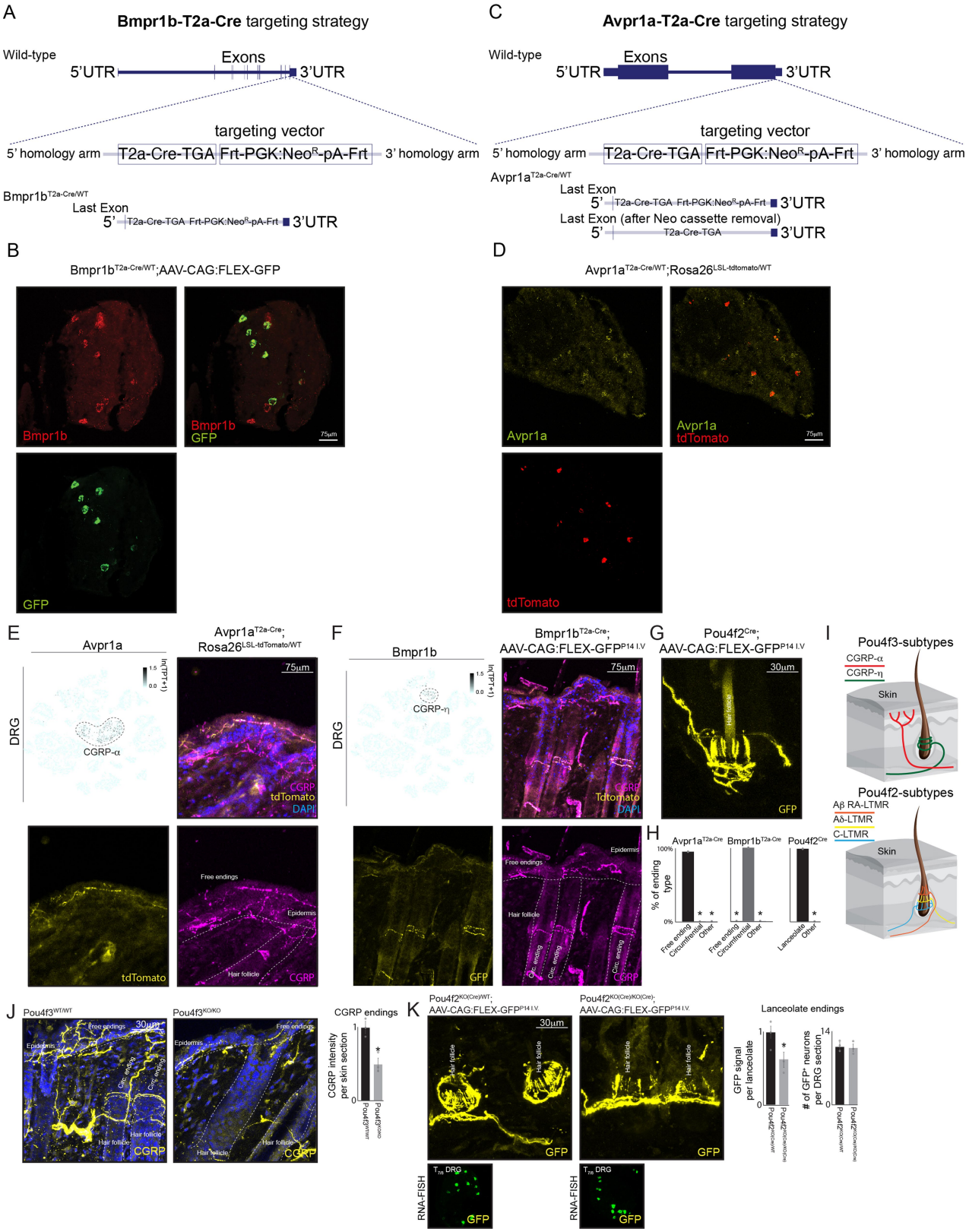
Extended Data Fig. 5 | Force-directed layout of putative subtype-restricted transcription factors. a, Force-directed layout representation of DRG with expression patterns displayed for the remaining putative subtype-restricted transcription factors. **b**, t-SNE visualization of expression of *Runx1*, *Runx3*, *Pou4f2* and *Pou4f3* in the adult DRG. **c**, Left, smRNA-FISH for *Runx1* and *Runx3* in E11.5, P0 or adult DRG. For E11.5, the spinal cord and DRG are labelled as references. Right, smRNA-FISH for *Pou4f2* and *Pou4f3* in E11.5, P0 or adult DRG. For E11.5, the spinal cord and DRG are labelled as references. Bottom, quantification of the smRNA-FISH. For *n* values, see Methods.



Extended Data Fig. 6 | Expression of somatosensory neuron subtype-specific genes during development. a, Box plots representing subtype-specific genes at E12.5, E15.5, P0, P5 and adult (P28–42) for each identified somatosensory neuron subtype. Boxes represent IQR, whiskers represent minimum and maximum values, and notches represent the 95% confidence interval of the median. *$P < 0.01$, two-sided Wilcoxon rank-sum test with Bonferroni correction. **b**, Normalized line plots showing what percentage of adult levels of subtype-specific gene expression are detected at E12.5, E15.5, P0, and P5. The black line represents the median of each time point with adult being defined as 100%. Upper and lower bands represent 95% confidence intervals (defined as $\pm 1.87 \times \mathrm{IQR}/\sqrt{n}$, where n is sample size). For n values, see Methods.

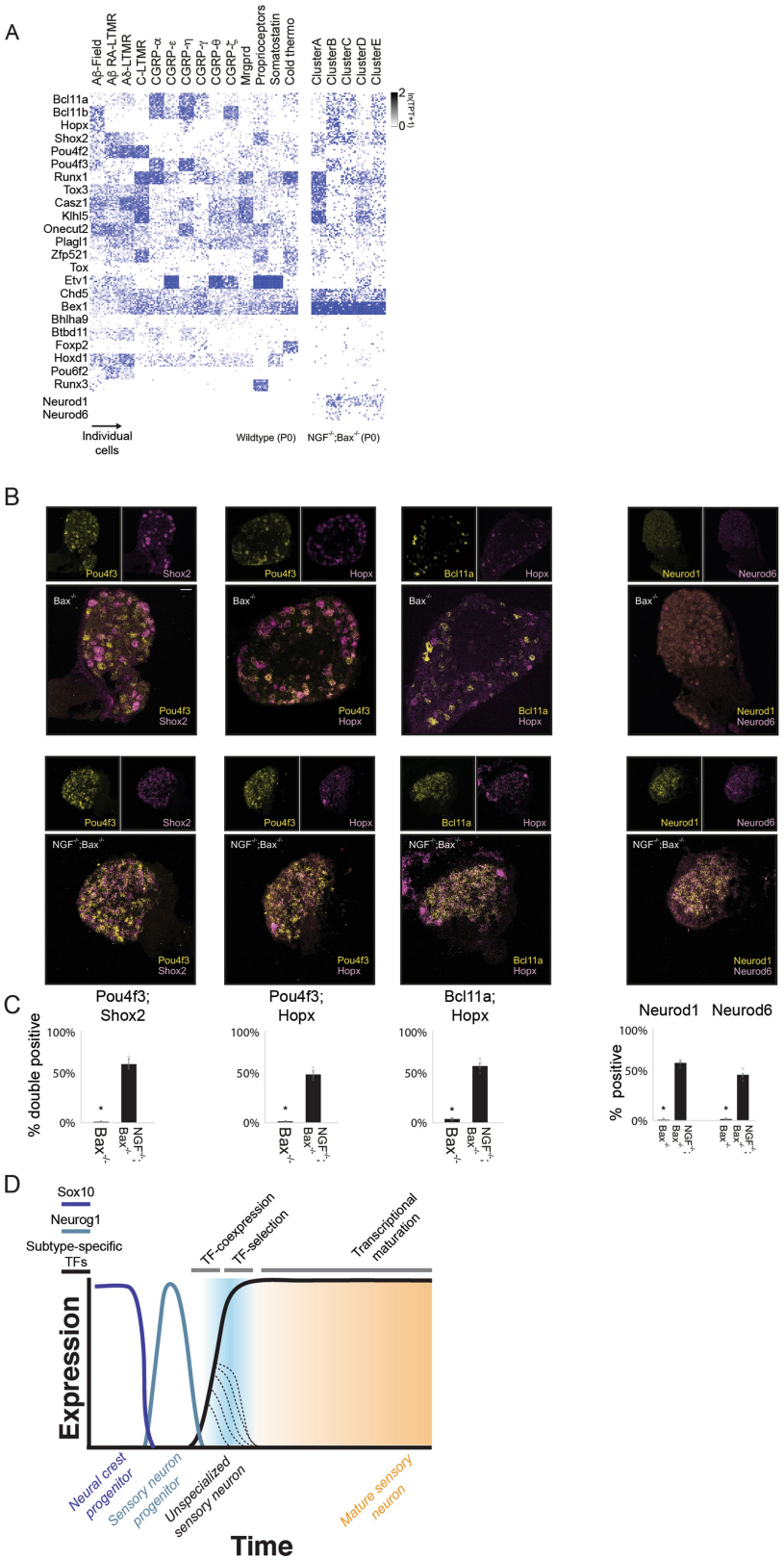


Extended Data Fig. 7 | DRG counts and TF analysis in *Pou4f2* and *Pou4f3* mutants. a, Representative images of *Avil* smRNA-FISH from T7/8 DRG in *Pou4f3*$^{WT/WT}$ (left) or *Pou4f3*$^{KO/KO}$ (right) littermate DRG. Right of images, quantification of estimated cell count per DRG. **b**, Representative images of *Avil* smRNA-FISH from T7/8 DRG in *Pou4f2*$^{KO(Cre)/WT}$ (left) or *Pou4f2*$^{KO(Cre)/KO(Cre)}$ (right) littermate DRG. Right of images, quantification of estimated cell count per DRG. **c**, Box plots displaying the expression of subtype-restricted TFs in each somatosensory neuron subtype in *Pou4f3*$^{WT/WT}$ (left) or *Pou4f3*$^{KO/KO}$ (right) littermates. **d**, Box plots displaying the expression of subtype-restricted TFs in each somatosensory neuron subtype in *Pou4f2*$^{WT/WT}$ (left) or *Pou4f2*$^{KO(Cre)/KO(Cre)}$ (right) littermates. **c**, **d**, Boxes represent IQR, whiskers represent minimum and maximum values, and notches represent the 95% confidence interval of the median. For *n* values, see Methods.



Extended Data Fig. 8 | See next page for caption.

Extended Data Fig. 8 | Generation and validation of *Bmpr1b*$^{T2a\text{-}Cre}$ and *Avpr1a*$^{T2a\text{-}Cre}$ mouse lines. a, Targeting strategy for inserting a T2a-Cre-TGA$^{STOP\ codon}$; Frt-PGK:Neo^{R}-pA-Frt cassette immediately upstream of the stop codon in *Bmpr1b*. **b**, smRNA-FISH for both *Bmpr1b* and *GFP* in *Bmpr1b*^{T2aCre} *AAV-CAG:FLEX-GFP*$^{P14I.V}$ mice to confirm the specificity and utility of the *Bmpr1b*$^{T2a\text{-}Cre}$ allele. **c**, Targeting strategy for inserting a T2a-Cre-TGA$^{STOP\ codon}$; Frt-PGK:Neo^{R}-pA-Frt cassette immediately upstream of the stop codon in *Avpr1a*. **d**, smRNA-FISH for both *Avpr1a* and *tdTomato* in *Avpr1a*$^{T2a\text{-}Cre(\Delta Neo)}$ *Rosa26*$^{LSL\text{-}tdTomato/WT}$ mice to confirm the specificity and utility of the *Avpr1a*$^{T2\text{-}aCre}$ allele. **e**, Top left, t-SNE representation of transcriptionally mature DRG overlaying the expression pattern of *Avpr1a*. Remaining images, representative immunostaining images of tdTomato and CGRP in skin sections obtained from *Avpr1a*$^{T2a\text{-}Cre}$ *Rosa26*$^{LSL\text{-}tdTomato}$ animals. **f**, Top left, t-SNE representation of transcriptionally mature DRG overlaying the expression pattern of *Bmpr1b*. Remaining images, representative immunostaining images of GFP and CGRP in skin sections obtained from *Bmpr1b*$^{T2a\text{-}Cre}$ *AAV-CAG:FLEX-GFP*$^{P14I.V}$ animals. **g**, Representative immunostaining images of GFP in skin sections obtained from *Pou4f2*$^{KO(Cre)}$*;AAV-CAG:FLEX-GFP*$^{P14I.V}$ animals. **h**, Quantification of ending morphology for CGRP-α (*Avpr1a*$^{T2a\text{-}Cre}$*Rosa26*$^{LSL\text{-}tdTomato}$) and CGRP-η (*Bmpr1b*$^{T2a\text{-}Cre}$*AAV-CAG:FLEX-GFP*$^{P14I.V}$) somatosensory neuron subtypes, as well as *Pou4f2* subtypes. **i**, Schematic representation of the skin with the distinct morphological ending types of CGRP-α and CGRP-η neurons displayed, as well as *Pou4f2* subtypes. **j**, Representative images of CGRP immunostaining in skin samples from 2–3-week-old *Pou4f3*$^{WT/WT}$ (left) or *Pou4f3*$^{KO/KO}$ (right) littermate controls. $^{*}P < 0.01$, two-tailed *t*-test. **k**, Representative images of GFP immunostaining in skin samples from 3–4-week-old *Pou4f2*$^{KO(Cre)/WT}$ (top left) or *Pou4f2*$^{KO(Cre)/KO(Cre)}$ (right) littermates; representative RNA-FISH for *GFP* in *Pou4f2*$^{KO(Cre)/WT}$ and *Pou4f2*$^{KO(Cre)/KO(Cre)}$ littermate controls are displayed below the skin immunostaining images. $^{*}P < 0.01$, two-way ANOVA with Tukey's HSD post-hoc analysis (**h**); two-sided *t*-test (**j**, **k**). Bar graphs in **h**, **j**, **k** show mean ± s.e.m. For *n* values, see Methods.



Extended Data Fig. 9 | Subtype-restricted TF expression profiles in *Ngf*$^{-/-}$ *Bax*$^{-/-}$ cell clusters. a, Heat map depicting expression of the subtype-restricted TFs in P0 somatosensory neuron subtypes (left) and clusters from *Ngf*$^{-/-}$*Bax*$^{-/-}$ mutants (right). **b**, smRNA-FISH for pairs of subtype-restricted TFs in *Bax*$^{-/-}$ (top) or littermate *Ngf*$^{-/-}$*Bax*$^{-/-}$ mutants (bottom). **c**, Quantification of the smRNA-FISH data showing the number of *Pou4f3*/*Shox2* double-positive, *Pou4f3*/*Hopx* double-positive, *Bcl11a*/*Hopx* double-positive, *Neurod1* single-positive or *Neurod6* single-positive neurons. **d**, Schematized model of gene expression programs as cells traverse development milestones. Transcriptionally unspecialized sensory neurons that emerge from *Sox10*$^{+}$ and *Neurog1*$^{+}$ progenitors co-express multiple TFs, which become restricted to select subtypes as neurons mature. These TFs are responsible for establishing the transcriptional specializations found in each neuronal subtype. **c**, $^{*}P < 0.01$, two-sided *t*-test. For *n* values, see Methods.

nature research

Corresponding author(s): David Ginty

Last updated by author(s): Oct 17, 2019

Reporting Summary

Nature Research wishes to improve the reproducibility of the work that we publish. This form provides structure for consistency and transparency in reporting. For further information on Nature Research policies, see Authors & Referees and the Editorial Policy Checklist.

Statistics

For all statistical analyses, confirm that the following items are present in the figure legend, table legend, main text, or Methods section.

n/a	Confirmed	
☐	☒	The exact sample size (*n*) for each experimental group/condition, given as a discrete number and unit of measurement
☐	☒	A statement on whether measurements were taken from distinct samples or whether the same sample was measured repeatedly
☐	☒	The statistical test(s) used AND whether they are one- or two-sided *Only common tests should be described solely by name; describe more complex techniques in the Methods section.*
☒	☐	A description of all covariates tested
☐	☒	A description of any assumptions or corrections, such as tests of normality and adjustment for multiple comparisons
☐	☒	A full description of the statistical parameters including central tendency (e.g. means) or other basic estimates (e.g. regression coefficient) AND variation (e.g. standard deviation) or associated estimates of uncertainty (e.g. confidence intervals)
☐	☒	For null hypothesis testing, the test statistic (e.g. *F*, *t*, *r*) with confidence intervals, effect sizes, degrees of freedom and *P* value noted *Give P values as exact values whenever suitable.*
☒	☐	For Bayesian analysis, information on the choice of priors and Markov chain Monte Carlo settings
☒	☐	For hierarchical and complex designs, identification of the appropriate level for tests and full reporting of outcomes
☒	☐	Estimates of effect sizes (e.g. Cohen's *d*, Pearson's *r*), indicating how they were calculated

Our web collection on statistics for biologists contains articles on many of the points above.

Software and code

Policy information about availability of computer code

Data collection	Basespace (Illumina) was used to handle bcl files extracted from NextSeq500 reads. Behavioral experiments were conducted using custom codes written in Bonsai and Arduino software, which are available upon request.
Data analysis	STITCH/SPRING analysis was implemented in Matlab and underlying code has been previously published and available on github, The CellRanger (v3.0.0) pipeline was also used to map scRNA-seq and generate Count tables data (10x Genomics). Monocle 3 and Seurat (v2 and v3) were used with standard commands in the R environment to further analyze data and generate heatmaps and gene expression plots and generate plots for scRNA-seq data, ImageJ (Fiji) was used to analyze confocal images

For manuscripts utilizing custom algorithms or software that are central to the research but not yet described in published literature, software must be made available to editors/reviewers. We strongly encourage code deposition in a community repository (e.g. GitHub). See the Nature Research guidelines for submitting code & software for further information.

Data

Policy information about availability of data

All manuscripts must include a data availability statement. This statement should provide the following information, where applicable:

- Accession codes, unique identifiers, or web links for publicly available datasets
- A list of figures that have associated raw data
- A description of any restrictions on data availability

All data is available online via https://kleintools.hms.harvard.edu/tools/springViewer_1_6_dev.html?datasets/Sharma2019/all . All raw read count tables for each time point is available via the gene expression omnibus.

Field-specific reporting

Please select the one below that is the best fit for your research. If you are not sure, read the appropriate sections before making your selection.

☒ Life sciences ☐ Behavioural & social sciences ☐ Ecological, evolutionary & environmental sciences

For a reference copy of the document with all sections, see nature.com/documents/nr-reporting-summary-flat.pdf

Life sciences study design

All studies must disclose on these points even when the disclosure is negative.

Sample size	No sample size pre-determination was performed. The largest number of cells that could be practically sequenced from an mice were done in all conditions. This study does not claim to saturate the discovery of all possible cell types nor saturate the detection of all possible difference. However, given the number of cell sequenced, we were able to confidently characterize cell types based on previously published literature as well as generate new Cre drivers that labeled morphologically homogenous cell types. This suggests that the number of cells sequenced is sufficient to support the claims of the study.
Data exclusions	Individual cells with high mitochondrial read count or low gene discovery were excluded from further analysis and predetermined based on standards previously determined - a common practice for single cell studies. The number of cells excluded were roughly equal across all time points and experimental conditions.
Replication	All replication attempts were successful by our best efforts. To validate scRNA-seq experiments we performed strategic in situ validation. To validate the faithfulness of the mouse reporter lines, we performed double in situs with the reporter and the endogenous gene driving Cre to confirm that the cell type of interest was properly labeled.
Randomization	Animals used for behavior were litter mates (test and control groups) and randomly selected. All time points for scRNA-seq were performed in random orders.
Blinding	Blinding was not possible in our study as all conditions were sequenced in parallel so the investigator could not be aware of the results until after completion of the experiment.

Reporting for specific materials, systems and methods

We require information from authors about some types of materials, experimental systems and methods used in many studies. Here, indicate whether each material, system or method listed is relevant to your study. If you are not sure if a list item applies to your research, read the appropriate section before selecting a response.

Materials & experimental systems

n/a	Involved in the study
☐	☒ Antibodies
☐	☒ Eukaryotic cell lines
☒	☐ Palaeontology
☐	☒ Animals and other organisms
☒	☐ Human research participants
☒	☐ Clinical data

Methods

n/a	Involved in the study
☒	☐ ChIP-seq
☒	☐ Flow cytometry
☒	☐ MRI-based neuroimaging

Antibodies

Antibodies used	Rabbit Anti-NeuN, Millipore: MAB377, 1:1000. Goat Anti-mCherry/tdtomato, CederLane: AB0040-200, 1:1000, Chicken Anti-GFP, Aves: GFP-1020, 1:1000, Rabbit Anti-GFP, ThermoFisher: A6455, 1:1000, Rabbit Anti-CGRP, Immunostar: 24112, 1:1000. Secondary antibodies included Alexa 488 or 546 conjugated goat anti-rabbit antibodies, goat anti-chicken antibodies, All secondary antibodies were purchased from Life Technologies except for Alexa 488 conjugated donkey anti-chicken antibodies, which was purchased from Jackson ImmunoResearch, and all were used at 1:500 dilution
Validation	All antibodies were validated in previous studies from our lab and others.

Eukaryotic cell lines

Policy information about cell lines

Cell line source(s)	293T cells (ATCC)
Authentication	Cells lines were not authenticated in this study - they were only used as a tool to generate adeno-associated virus

Mycoplasma contamination	Cell lines were not tested for myco contamination
Commonly misidentified lines (See ICLAC register)	No commonly misidentified cell lines were used

Animals and other organisms

Policy information about studies involving animals; ARRIVE guidelines recommended for reporting animal research

Laboratory animals	All data presented used mice on the C57Bl/6N or C57Bl/6J background. When possible littermate controls were used. Most animals were used in the 1-6 week old range, with a few labeled exceptions.
Wild animals	This study did not involve the use of wild animals
Field-collected samples	This study did not involve the use of wild animals
Ethics oversight	Harvard Medical School IACUC

Note that full information on the approval of the study protocol must also be provided in the manuscript.

Article

Clonally expanded CD8 T cells patrol the cerebrospinal fluid in Alzheimer's disease

https://doi.org/10.1038/s41586-019-1895-7

Received: 30 May 2018

Accepted: 2 December 2019

Published online: 8 January 2020

David Gate[1,2*], Naresha Saligrama[3], Olivia Leventhal[1], Andrew C. Yang[4,5], Michael S. Unger[6,7], Jinte Middeldorp[1,2,8], Kelly Chen[1], Benoit Lehallier[1,2], Divya Channappa[1], Mark B. De Los Santos[1], Alisha McBride[1,2], John Pluvinage[1,9,10], Fanny Elahi[11], Grace Kyin-Ye Tam[1,12], Yongha Kim[1,12], Michael Greicius[1,12], Anthony D. Wagner[13,14], Ludwig Aigner[6,7], Douglas R. Galasko[15], Mark M. Davis[3,16,17] & Tony Wyss-Coray[1,2,5,14,18*]

Alzheimer's disease is an incurable neurodegenerative disorder in which neuroinflammation has a critical function[1]. However, little is known about the contribution of the adaptive immune response in Alzheimer's disease[2]. Here, using integrated analyses of multiple cohorts, we identify peripheral and central adaptive immune changes in Alzheimer's disease. First, we performed mass cytometry of peripheral blood mononuclear cells and discovered an immune signature of Alzheimer's disease that consists of increased numbers of $CD8^+$ T effector memory $CD45RA^+$ (T_{EMRA}) cells. In a second cohort, we found that $CD8^+$ T_{EMRA} cells were negatively associated with cognition. Furthermore, single-cell RNA sequencing revealed that T cell receptor (TCR) signalling was enhanced in these cells. Notably, by using several strategies of single-cell TCR sequencing in a third cohort, we discovered clonally expanded $CD8^+$ T_{EMRA} cells in the cerebrospinal fluid of patients with Alzheimer's disease. Finally, we used machine learning, cloning and peptide screens to demonstrate the specificity of clonally expanded TCRs in the cerebrospinal fluid of patients with Alzheimer's disease to two separate Epstein–Barr virus antigens. These results reveal an adaptive immune response in the blood and cerebrospinal fluid in Alzheimer's disease and provide evidence of clonal, antigen-experienced T cells patrolling the intrathecal space of brains affected by age-related neurodegeneration.

Neuroinflammation is a pathological hallmark of Alzheimer's disease (AD). Although much effort has been dedicated to understanding innate inflammation in AD, little is known about the adaptive immune response. The lymphatic system of the brain carries immune cells from the cerebrospinal fluid (CSF) and connects to the deep cervical lymph nodes[3], enabling peripheral T cells to respond to brain antigens. However, whether T cells enter the brain to perpetuate neuroinflammation in AD is unknown.

Interaction between the T cell receptor (TCR) and antigen presented by the major histocompatibility complex (MHC) is critical to adaptive immunity. When T cells recognize cognate antigen, they clonally expand[4]. TCR sequences are so diverse that they are essentially unique to an individual T cell. Thus, finding two or more T cells with the same TCR sequence is evidence of clonal expansion[5]. Several small studies have reported changes in the distribution[6–9], function and cytokine secretion of peripheral T cells[10–12] in AD (Supplementary Table 1), but the antigens that drive these changes are unknown.

We integrated analyses of multiple cohorts and used several methods to assess adaptive immunity in AD (Fig. 1a). First, we used mass cytometry to study peripheral blood mononuclear cells (PBMCs) from patients with AD and patients with prodromal mild cognitive impairment (MCI) (cohort 1; Fig. 1a, Supplementary Table 2). We age-matched patients to cognitively typical, healthy control individuals (Extended Data Fig. 1a). In addition, we confirmed diagnoses as MCI or AD by: (1) reduced cognitive scores (Extended Data Fig. 1b); (2) reduced ratios of amyloid-β (Aβ):phosphorylated tau and Aβ:total tau within the CSF (Extended Data Fig. 1c, d); and (3) volumetric loss of brain regions as measured by magnetic resonance imaging (MRI) (Extended Data Fig. 1e). We developed a panel of immune markers (Supplementary Table 3) that enabled major subsets of PBMCs to be identified (Extended

[1]Department of Neurology and Neurological Sciences, Stanford University School of Medicine, Stanford, CA, USA. [2]Veterans Administration Palo Alto Healthcare System, Palo Alto, CA, USA. [3]Department of Microbiology and Immunology, School of Medicine, Stanford University, Stanford, CA, USA. [4]Department of Bioengineering, Stanford University, Stanford, CA, USA. [5]Chemistry, Engineering and Medicine for Human Health, Stanford University, Stanford, CA, USA. [6]Institute of Molecular Regenerative Medicine, Paracelsus Medical University, Salzburg, Austria. [7]Spinal Cord Injury and Tissue Regeneration Center Salzburg, Paracelsus Medical University, Salzburg, Austria. [8]Department of Translational Neuroscience, University Medical Center Utrecht Brain Center, Utrecht University, Utrecht, The Netherlands. [9]Medical Scientist Training Program, Stanford University School of Medicine, Stanford, CA, USA. [10]Stem Cell Biology and Regenerative Medicine Graduate Program, Stanford University School of Medicine, Stanford, CA, USA. [11]Department of Neurology, Memory and Aging Center, University of California at San Francisco, San Francisco, CA, USA. [12]Functional Imaging in Neuropsychiatric Disorders Laboratory, Department of Neurology and Neurological Sciences, Stanford University School of Medicine, Stanford, CA, USA. [13]Department of Psychology, Stanford University, Stanford, CA, USA. [14]Wu Tsai Neurosciences Institute, Stanford University, Stanford, CA, USA. [15]Department of Neurosciences, University of California at San Diego, La Jolla, CA, USA. [16]Institute for Immunity, Transplantation and Infection, Stanford University School of Medicine, Stanford, CA, USA. [17]Howard Hughes Medical Institute, Stanford University School of Medicine, Stanford, CA, USA. [18]Paul F. Glenn Center for the Biology of Aging, Stanford University School of Medicine, Stanford, CA, USA.
*e-mail: dgate@stanford.edu; twc@stanford.edu

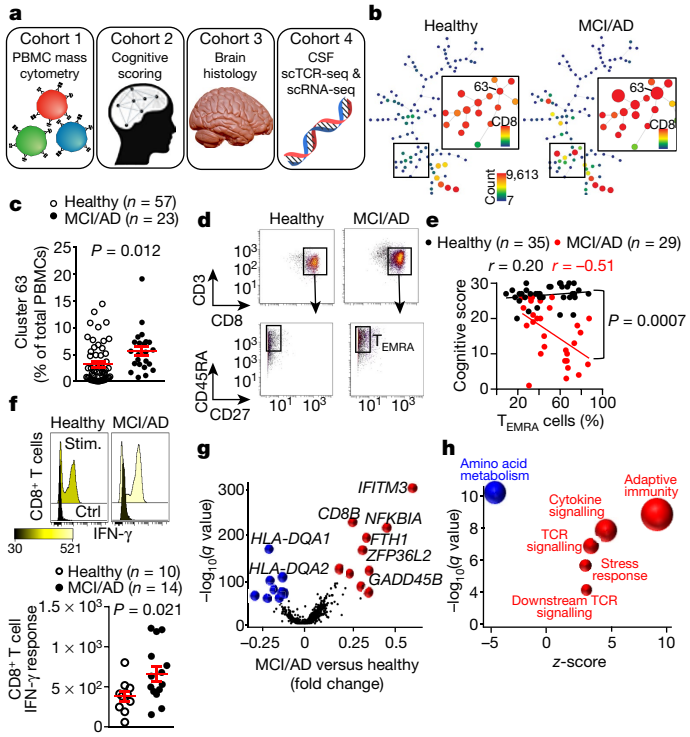


Fig. 1 | Peripheral CD8$^+$ T_{EMRA} cells are increased in AD and are negatively associated with cognition. a, Four cohorts were used to assess adaptive immunity in AD. **b**, Representative SPADE trees of PBMCs from healthy individuals and patients with MCI or AD in cohort 1 show an increased abundance of a CD8$^+$ cluster (cluster 63) in patients with MCI or AD. Background tree nodes are sized according to cell counts. Insets are coloured according to CD8 expression. **c**, Quantification of cluster 63 as a percentage of total PBMCs. The percentage of cluster 63 cells is significantly higher in patients with MCI or AD than healthy control individuals. Mean ± s.e.m.; unpaired two-sided *t*-test with Welch's correction. **d**, Marker expression analysis of cluster 63 corresponds to a CD3$^+$CD8$^+$CD45RA$^+$CD27$^-$ T_{EMRA} population. Data in **c**, **d** were pooled from seven independent experiments with similar results. **e**, Linear regression showing the inverse correlation between cognitive score and the percentage of CD8$^+$ T_{EMRA} cells in individuals from cohort 2. Pearson's correlation *r* values are shown for each group. The significance of the difference between the two data sets was measured by ANCOVA. **f**, Stimulation with PMA and ionomycin (stim.) induces increased expression of IFN-γ in CD8$^+$ T cells from patients with MCI or AD. Mean ± s.e.m.; unpaired two-sided *t*-test with Welch's correction. **g**, Differential expression analysis (scRNA-seq) of CD8$^+$ T_{EMRA} cells from healthy individuals ($n = 7$) and patients with MCI or AD ($n = 6$) shows upregulated TCR signalling. Model-based analysis of single-cell transcriptomics (MAST) differential expression test with Benjamini–Hochberg correction. **h**, Pathway analysis of differentially expressed genes in CD8$^+$ T_{EMRA} cells from patients with MCI or AD ($n = 6$ subjects) versus healthy individuals ($n = 7$ subjects) shows increased antigenic stimulation of CD8$^+$ T_{EMRA} cells in patients with MCI or AD. Fisher's exact test with Benjamini–Hochberg correction. Pathways (circles) with positive *z*-scores are coloured red; those with negative *z*-scores are coloured blue. The size of the circle corresponds to the size of the *z*-score (two-sided).

Data Fig. 2). We then used spanning-tree progression analysis of density-normalized events (SPADE) to perform unsupervised clustering (Extended Data Fig. 3a). Notably, we detected an increase in a population of CD8$^+$ cells in patients with MCI or AD (cluster 63; Fig. 1b). Plotting all SPADE clusters for *P* value versus fold change, the cluster that was most highly increased among patients was cluster 63 (Extended Data Fig. 3b). Quantification of individual subjects revealed higher values for this cluster in patients with MCI or AD than controls (Fig. 1c). Finally, marker expression for this cluster corresponded to CD3$^+$CD8$^+$CD27$^-$ T effector memory CD45RA$^+$ (T_{EMRA}) cells (Fig. 1d)—a T cell population with potent effector functions that include the secretion of proinflammatory cytokines and cytotoxic molecules[13].

We next used cluster identification, characterization and regression (CITRUS)[14] to determine whether clusters could predict disease status. Notably, CITRUS identified a significantly altered cluster (arbitrarily numbered 229992) that corresponds to CD3$^+$CD8$^+$CD45RA$^+$ T cells (Extended Data Fig. 3c). Quantification revealed higher percentages of this population in patient PBMCs than controls (Extended Data Fig. 3d). Moreover, marker expression again pointed to T_{EMRA} cells (Extended Data Fig. 3e). Next, we used a regularized supervised learning algorithm from CITRUS to determine populations of T cells that predicted whether a sample belonged to healthy groups or those with disease. Notably, cluster 229992 combined with nine additional clusters was 80% predictive of disease (Extended Data Fig. 3f, Supplementary Table 4). Next, we used our mass cytometry dataset to derive 41 immune variables, which showed differences between patients and healthy controls in relation to CD8$^+$ T cells (Supplementary Table 5). Specifically, we detected an increase in CD8$^+$ T cells in patients versus controls (Extended Data Fig. 4a), with a concomitant decrease in the ratio of CD4$^+$ to CD8$^+$ T cells (Extended Data Fig. 4b). Subsets of CD8$^+$ T cells were also altered in PBMCs from patients with MCI or AD: effector cells were overrepresented (Extended Data Fig. 4c), whereas memory cells were underrepresented (Extended Data Fig. 4d). Together, these results demonstrate an adaptive immune signature of AD that consists of increased peripheral CD8$^+$ T_{EMRA} cells.

To further investigate the role of CD8$^+$ T cells in MCI and AD, we assessed the relationship between cognition and populations of memory T cells in a separate cohort (cohort 2) (Fig. 1a, Extended Data Fig. 5a). This revealed a negative correlation in MCI and AD between CD8$^+$ T_{EMRA} cells and cognition (Fig. 1e), whereas percentages of T central memory (T_{CM}) and T effector memory (T_{EM}) cells were positively correlated (Extended Data Fig. 5b). Age did not influence the levels of CD8$^+$ T_{EMRA} cells in either group (Extended Data Fig. 5c). We next tested whether functional differences exist in the peripheral CD8$^+$ T cells of patients with MCI or AD. We stimulated PBMCs with phorbol 12-myristate 13-acetate (PMA) and ionomycin, and then measured the levels of two effector cytokines: interferon-γ (IFN-γ) and tumour necrosis factor (TNF) (Extended Data Fig. 5d). After stimulation with PMA, CD8$^+$ T cells from patients with MCI or AD had significantly higher levels of IFN-γ than did control CD8$^+$ T cells (Fig. 1f), and TNF also trended towards significance (Extended Data Fig. 5e). Overall, these data identify an antigen-experienced population of CD8$^+$ T_{EMRA} cells that has potent effector functions—including the ability to secrete proinflammatory cytokines—in the peripheral immune system of patients with MCI or AD.

The proinflammatory effector phenotype of peripheral antigen-experienced CD8$^+$ T_{EMRA} cells in MCI and AD prompted us to test whether CD8$^+$ T_{EMRA} cells from patients with MCI and AD were transcriptionally distinct. We performed droplet-based single-cell RNA sequencing (scRNA-seq) on sorted CD8$^+$ T_{EMRA} cells from populations of PBMCs from patients with MCI or AD and control individuals (Extended Data Fig. 6a). Differential expression and pathway analysis revealed a significant decrease in amino acid metabolism and an increase in TCR and cytokine signalling in CD8$^+$ T_{EMRA} cells in MCI and AD (Fig. 1g, h, Extended Data Fig. 6b, c). Collectively, these results indicate greater antigenic stimulation of peripheral CD8$^+$ T_{EMRA} cells in patients with MCI and AD than controls.

We next sought to determine whether CD8$^+$ T cells were present in the brain of patients with AD. We assessed post-mortem brains from a third cohort (cohort 3) comprising control individuals (no neurological disease) and patients with AD (Supplementary Table 6) by using immunohistochemistry to examine the expression of CD8 and Aβ and analyse the proximity of CD8$^+$ T cells to the cerebral vasculature. We noted numerous extravascular CD8$^+$ T cells in the perivascular space of blood vessels with cerebral amyloid angiopathy in the hippocampi of three AD brains (Fig. 2a); by contrast, CD8$^+$ T cells were not observed

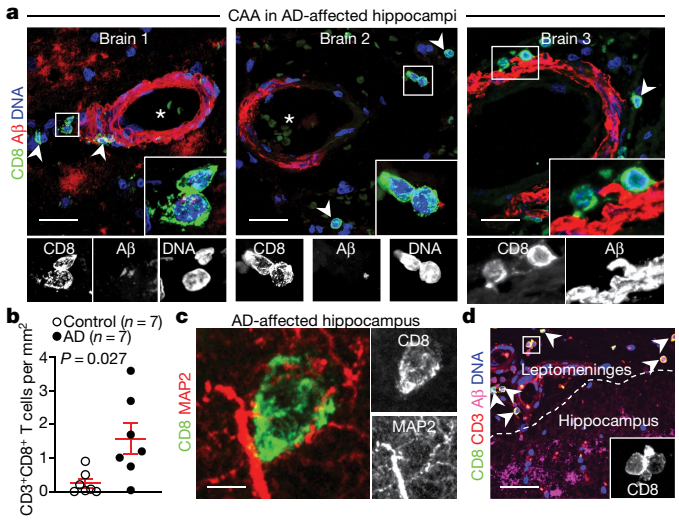


Fig. 2 | CD8⁺ T cells enter the brain in patients with AD. a, Confocal imaging of cerebral amyloid angiopathy (CAA) in the post-mortem brain of a patient with AD from cohort 3 shows CD8⁺ T cells in the perivascular space of Aβ⁺ blood vessels with cerebral amyloid angiopathy in three AD-affected hippocampi. Arrowheads indicate CD8⁺ T cells; asterisks indicate blood vessel lumen. Scale bars, 20 µm. **b**, Higher numbers of CD8⁺ T cells were detected in AD-affected than control hippocampi. Mean ± s.e.m.; unpaired two-sided *t*-test with Welch's correction. **c**, A CD8⁺ T cell is shown associated with MAP2⁺ neuronal processes. **d**, CD8⁺ T cells are localized to the leptomeninges and adjacent to hippocampal Aβ plaques. Scale bar, 100 µm. Data in **c**, **d** were replicated in three independent experiments.

surrounding blood vessels in control brains (Extended Data Fig. 7a). Notably, we detected CD8⁺ T cells adjacent to Aβ plaques (Extended Data Fig. 7b–d). We also detected significantly more $CD3^+CD8^+$ T cells in AD-affected hippocampi than control hippocampi (Fig. 2b, Extended Data Fig. 7e). CD8⁺ T cells associated with microtubule associated protein 2 $(MAP2)^+$ neuronal processes in AD-affected hippocampi (Fig. 2c). We also noted an association of CD8⁺ T cells with neurofilament heavy $(NEFH)^+$ neuronal processes in an APP/PS1 mouse model of AD (Extended Data Fig. 7f), and confirmed this association by electron microscopy (Extended Data Fig. 7g). Finally, we also detected $CD3^+CD8^+$ T cells in the leptomeninges adjacent to the hippocampus in brains from patients with AD (Fig. 2d).

The localization of CD8⁺ T cells to brain leptomeninges led us to investigate whether antigen-specific cells also patrol the CSF. CSF immunity is relatively uncharacterized in healthy elderly individuals[15,16]. Therefore, we enumerated immune cells in CSF from ten healthy elderly subjects (Extended Data Fig. 8a). We found that CSF from these individuals contained mostly T cells, with a minority of innate immune cells and an undetectable amount of B cells (Extended Data Fig. 8b). Notably, the CD8⁺ T cell repertoire of CSF from elderly individuals was composed almost exclusively of T_{EM} cells, and T_{EMRA} cells made up around 20% of this T_{EM} population (Extended Data Fig. 8c).

As T_{EMRA} cells are associated with immunological memory, we investigated whether clonally expanded T cells patrol the CSF in healthy individuals, patients with AD and patients with Parkinson's disease (PD; used as a control because antigen-specific T cells were recently discovered in vitro in PBMC samples from patients with PD[17]) in a separate cohort (cohort 4; Fig. 3a, Supplementary Table 2). We used two methods to assess clonal expansion: plate-based sequencing (plate-seq) and droplet-based sequencing (drop-seq). We first performed plate-seq of TCRs from CSF T cells of healthy controls ($n = 5$), patients with AD ($n = 3$) and patients with PD ($n = 2$) (Extended Data Fig. 8d). Clonally expanded cells were mostly CD8⁺ T cells, although we also detected $CD4^+$ T cell clones in nearly all subjects (Extended Data Fig. 8e, Supplementary Table 7). Strikingly, one patient with AD had a massively expanded clone that comprised 44% of all CD8⁺ TCRs (Fig. 3b). Analysis of marker expression identified this clone as $CD8^+CD45RA^+CD27^-$ T_{EMRA} cells (Fig. 3c). Together, these results provide the first evidence (to our knowledge) that clonally expanded CD8⁺ T cells patrol the CSF in brains that are affected by age-related neurodegeneration.

To examine potential changes in gene expression in clonal CD8⁺ T cell populations in AD, we sorted live cells of the CSF (Extended Data Fig. 8f) and used drop-seq to validate our plate-seq findings. Multidimensional reduction and visualization with *t*-distributed stochastic neighbour embedding (*t*-SNE) showed that most CSF cells were T cells (Fig. 3d, e). This cellular and molecular characterization of the CSF in elderly individuals and patients with AD indicates that the intrathecal immune compartment contains almost exclusively T cells of the T_{EM} subtype. Clusters were composed of a mixture of groups, sexes and patients (Extended Data Fig. 8g). We next performed single-cell TCR sequencing (scTCR-seq) on these cells, which showed that clonal T cells colocalized with CD8⁺ T cells (Fig. 3f). We observed numerous highly expanded CD8⁺ clones in CSF from patients with MCI or AD, whereas this expansion occurred less frequently in CSF from control individuals (Fig. 3g). Quantification of the most highly expanded (maximum) clone for each subject revealed that the percentages of the maximum clone were higher in patients with MCI or AD than in control individuals (Fig. 3h). Differential expression analysis of clones that were highly expanded in MCI and AD (that is, more than five T cells with the same TCRαβ sequence) revealed increased expression of cytotoxic effector genes, including natural killer cell granule protein 7 (*NKG7*) and granzymes A, H and K (*GZMA*, *GZMH* and *GZMK*) (Fig. 3i). We then quantified the percentages of T cells that corresponded to highly expanded clones, which showed that 49.13% were CD8⁺ T_{EMRA} cells (Fig. 3j). Differential expression analysis of clonally expanded CD8⁺ T_{EMRA} cells also revealed increased expression of cytotoxic effector genes including *NKG7* and *GZMA* in MCI and AD (Fig. 3k). Notably, CD8⁺ T_{EMRA} cells from patients with MCI or AD also expressed higher levels of the MHC genes human leukocyte antigen C (*HLA-C*) and beta-2-microglobulin (*B2M*)—a pro-ageing factor that impairs cognition[18]—compared with control cells (Fig. 3k). In addition, differential expression of highly expanded clones from patients with MCI or AD showed that these clones were CD8-positive and that they upregulated their expression of cytotoxic granules, proteases and proinflammatory cytokines (Extended Data Fig. 9a), many of which are associated with AD (Supplementary Table 8). Although it is not clear whether cells enter the brain parenchyma via the CSF, we localized GZMA expression to CD8⁺ T cells (Fig. 3l) and detected higher percentages of $GZMA^+CD8^+$ cells in hippocampi from patients with AD than in hippocampi from control individuals (Fig. 3m). Collectively, these results reveal the proinflammatory, cytotoxic function of clonal CD8⁺ T_{EMRA} cells in the CSF of patients with AD, and demonstrate the utility of combining scRNA-seq and scTCR-seq datasets.

We next pooled TCRαβ sequences from plate-seq and drop-seq experiments in cohort 4 to broadly assess clonality in neurodegeneration. We first separately analysed the maximum clones (defined as comprising 3% or more of all TCRαβ sequences) from healthy subjects and patients with MCI, AD and PD, which revealed a highly expanded clone in only one out of ten healthy subjects, compared with four out of six patients with AD, two out of six patients with PD and one out of five patients with MCI (Extended Data Fig. 9b). We next measured overall clonality (defined as the percentage of total TCRαβ sequences that are identical to one or more TCRαβ sequences), which revealed that the levels of clonality were highest in AD and PD (Extended Data Fig. 9c). Notably, when we integrated CSF cells from patients with PD into our analysis (Extended Data Fig. 9d), we observed increased expression of genes analogous to those observed in AD clones (Extended Data Fig. 9e). Together, these results demonstrate the clonal expansion of

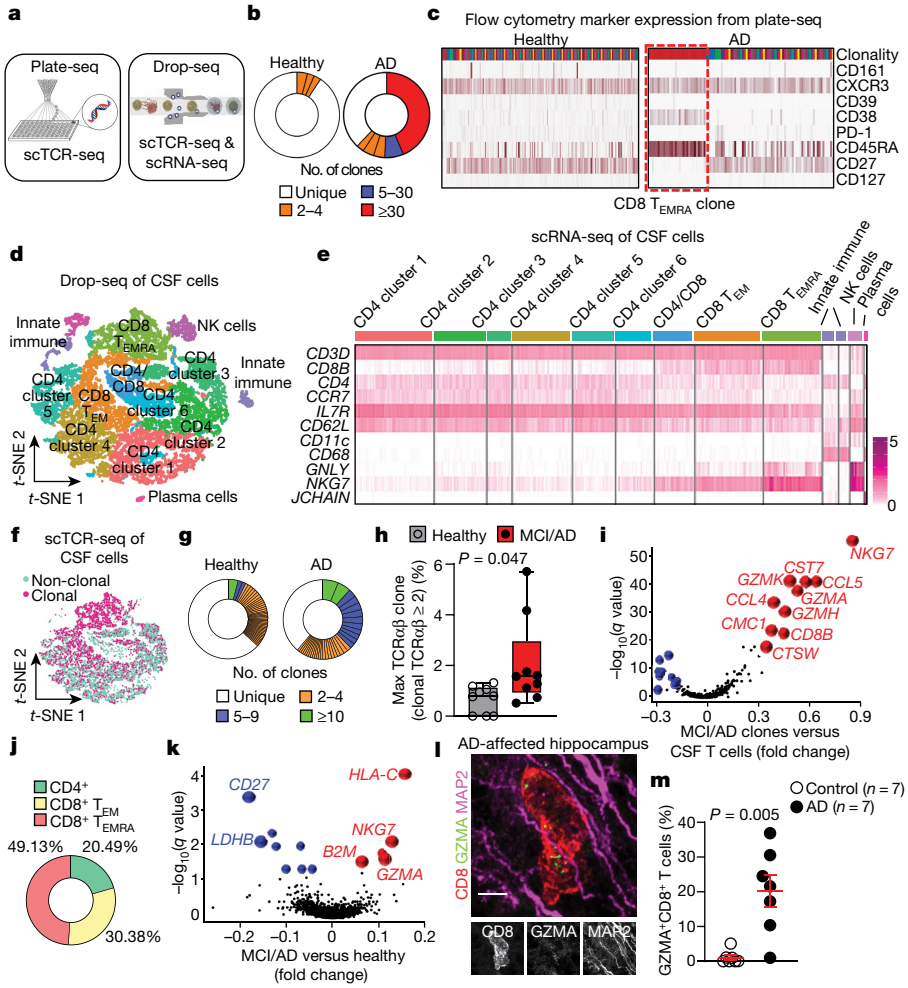


Fig. 3 | Clonal expansion of CD8$^+$ T$_{EMRA}$ cells in the CSF of patients with AD. **a**, Plate-seq and drop-seq methods used for scTCR-seq and scRNA-seq of immune cells of the CSF in patients from cohort 4. **b**, CD8$^+$ TCRαβ clonality (plate-seq) in the CSF of patients with AD and healthy control individuals. **c**, The top (most expanded) clone in AD had a marker expression profile of CD8$^+$CD45RA$^+$CD27$^-$ T$_{EMRA}$ cells. Data were replicated in two independent experiments. **d**, CSF cells analysed by drop-seq and clustered by multidimensional reduction with *t*-SNE, showing populations of immune cells that include CD8$^+$ T$_{EMRA}$ cells ($n = 9$ healthy control individuals (10,876 cells); $n = 9$ patients with MCI or AD (10,391 cells)). **e**, Marker expression of CSF clusters, including CD8$^+$ T$_{EMRA}$ cells. *CD62L* is also known as *SELL*; *CD11c* is also known as *ITGAX*. Data were pooled from three independent experiments. **f**, Concentration of clonal cells in locations of CD8$^+$ T cell clusters ($n = 9$ subjects per group). **g**, Representative plots of CD8$^+$ TCRαβ clonality (drop-seq) in age-matched subjects shows enhanced clonal expansion and more highly expanded clones in AD. Clones are coloured by proportion of the total TCRαβ sequences. **h**, Quantification of maximum clones (% TCRαβ sequences) shows a higher percentage in patients with MCI or AD than healthy control individuals ($n = 9$ subjects per group). Samples lacking clonal cells were scored as zero. Box plots show median and 25th to 75th percentiles, and whiskers indicate the minimum and maximum values. Unpaired two-sided *t*-test with Welch's correction. **i**, Differential expression of highly expanded clones (clonal TCRαβ > 5) revealed increased expression of cytotoxic effector genes. MAST differential expression test with Benjamini–Hochberg correction ($n = 9$ patients with MCI or AD). **j**, Quantification of highly expanded clones (clonal TCRαβ > 5) showed that 49.13% of them are CD8$^+$ T$_{EMRA}$ cells ($n = 9$ patients with MCI or AD). **k**, Increased expression of *B2M*, *NKG7* and *GZMA* in clonal CD8$^+$ T cells from patients with MCI or AD. MAST differential expression test with Benjamini–Hochberg correction ($n = 9$ subjects/group). **l**, A hippocampal CD8$^+$ T cell in an AD-affected brain (cohort 3) shows expression of GZMA adjacent to MAP2$^+$ neuronal processes. Scale bar, 5 µm. Data were replicated in three independent experiments. **m**, Percentages of CD8$^+$ T cells that express GZMA in control and AD-affected hippocampi. Mean ± s.e.m.; unpaired two-sided *t*-test with Welch's correction.

cytotoxic proinflammatory CD8$^+$ T$_{EMRA}$ cells in the CSF of patients with age-related neurodegeneration.

We next sought to determine the antigens that drive clonal expansion of CD8$^+$ T$_{EMRA}$ cells in the CSF of patients with MCI or AD. We created unweighted networks of our clonal TCRαβ sequences to detect shared clones within and between groups. Although we did not identify shared TCRαβ sequences in healthy subjects within or between groups, we detected a shared TCRαβ clone between a patient with MCI and a patient with AD (Fig. 4a). Notably, a third patient with AD shared this TCRβ sequence (CASSLGQAYEQYF), which has known specificity for the *Herpesviridae* Epstein–Barr nuclear antigen 3 (EBNA3A)[19] (Fig. 4b). We then assessed the gene-expression profile of this Epstein–Barr virus (EBV) EBNA3A-specific clone, and found that the expression of cytotoxic effector genes was increased (Fig. 4c).

To determine the antigen specificity of unknown TCRs, we applied HLA haplotyping within our GLIPH (grouping of lymphocyte interactions by paratope hotspots) algorithm[20] to our plate-seq TCRs. GLIPH can analyse large numbers of TCR sequences and define specificity groups that are shared by TCRs. Notably, GLIPH identified a shared TCRβ chain between patients with AD (CASSLAGGYNEQFF); this chain also shared homology with a TCRβ chain from a third patient (CASSLGTGNNEQFF) (Fig. 4d, Supplementary Table 9). To test for antigen specificity of GLIPH-derived TCRs, we generated two cell lines—termed TCRαβ 1 and TCRαβ 2—that express TCRαβ sequences

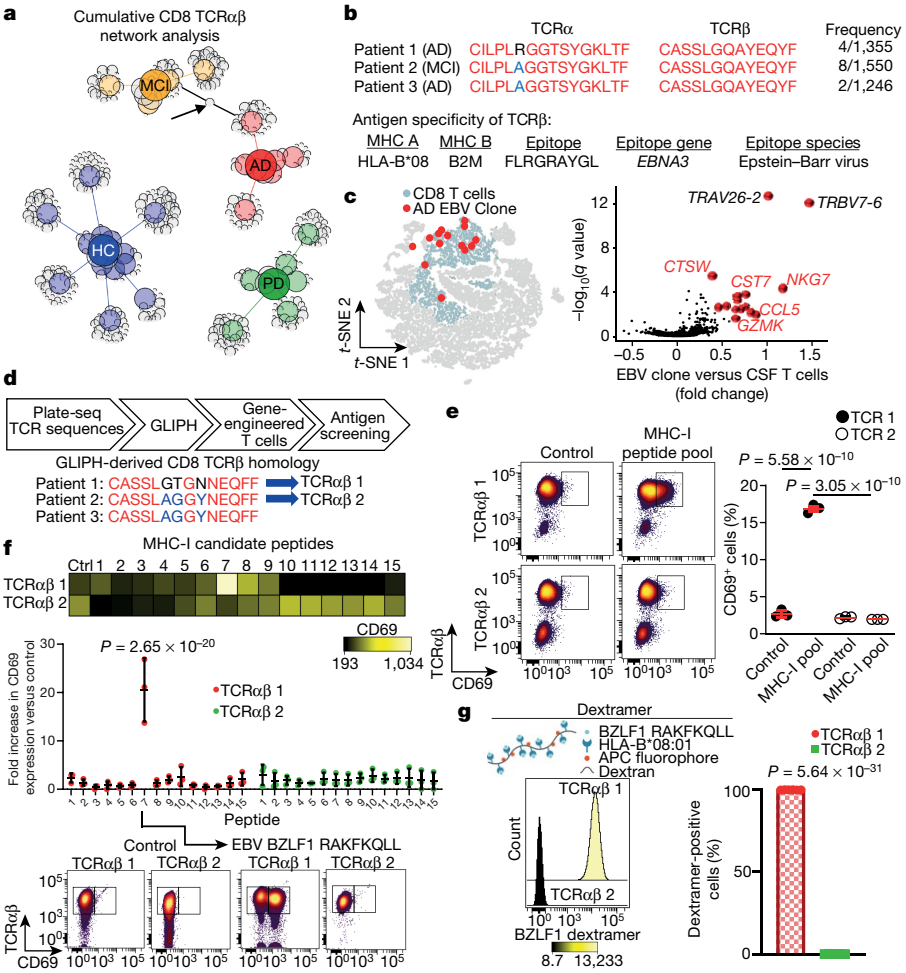


Fig. 4 | Antigen identification of clonally expanded TCRs in the CSF of patients with AD. a, Unweighted network analysis of CD8 TCRαβ sequences combined from plate-seq and drop-seq experiments. Group node IDs with individual TCRαβ clones are depicted as circles and sized according to the proportion of total sequences of each clone. Arrow indicates a shared clonal TCRαβ sequence with specificity for EBV EBNA3A. Note that several healthy control (HC) subjects have no clones. **b**, Shared TCRαβ sequences among patients with MCI or AD. Three patients had identical TCRβ chains with specificity for EBV EBNA3A. The antigen specificity of TCRβ is shown below[19]. **c**, Differential expression of EBV-specific clones in MCI and AD (from $n = 3$ subjects) versus all CSF T cells shows enhanced expression of cytotoxic effector genes. MAST differential expression test with Benjamini–Hochberg correction. **d**, Workflow for antigen identification of CSF TCRs. GLIPH was applied to TCR sequencing to derive homologous TCR sequences between patients. GLIPH identified two patients with AD who had identical TCRβ chains and a third patient with a similar sequence. The TCRαβ sequences derived from GLIPH were introduced into SKW-3 cells. **e**, Autologous fibroblasts were used to present antigens to TCRαβ 1 and TCRαβ 2 cells. Only TCRαβ 1 cells showed significant upregulation of CD69 following antigen presentation. Data are averages from three separate experiments performed in triplicate. Mean ± s.e.m.; one-way analysis of variance (ANOVA) ($F(3, 8) = 1{,}050$, $P = 1.01 \times 10^{-10}$) with Tukey's multiple comparisons test. **f**, Peptide 7 (RAKFKQLL) of the EBV trans-activator BZLF1 protein activates TCRαβ 1 but not TCRαβ 2 cells. Two-way ANOVA ($F(14, 60) = 14.06$, $P = 4.8 \times 10^{-14}$) followed by Sidak's multiple comparisons test. Data were pooled from $n = 3$ independent experiments. The P value shown is from comparing peptide 7 values for each cell line. Mean ± s.d. **g**, A fluorescent dextramer composed of HLA-B*08:01 presenting the BZLF1 peptide RAKFKQLL shows nearly 100% positivity with TCRαβ 1 but no positivity with TCRαβ 2 cells. Unpaired two-sided t-test with Welch's correction ($n = 6$ per group).

from these two patients with AD (patients 1 and 2) (Fig. 4d, Extended Data Fig. 10a). Both TCRαβ 1 and TCRαβ 2 cells showed upregulation of the activation marker CD69 when stimulated in a cell-free manner (Extended Data Fig. 10b). We then used dermal fibroblasts from patients 1 and 2 as autologous antigen-presenting cells to screen a pool of 80 known MHC-I restricted epitopes (Supplementary Table 10) for reactivity. Notably, TCRαβ 1 cells responded to the MHC-I peptide pool, whereas TCRαβ 2 cells were non-responsive (Fig. 4e, Extended Data Fig. 10c). TCR activation depended on autologous antigen presentation, as non-autologous presentation did not stimulate TCRαβ 1 cells—demonstrating MHC restriction (Extended Data Fig. 10d).

We then narrowed this MHC-I pool to 15 peptides that could activate TCRαβ 1 cells, by filtering for peptides restricted to an HLA that matched patient 1 (HLA-A*01:01 or HLA-B*08:01) (Supplementary Table 11). We used TCRαβ 2 as a control, given the sequence similarity of its β chain, separate patient HLA and inability to become activated by the MHC-I peptide pool. Only one peptide activated TCRαβ 1 cells: peptide 7—RAKFKQLL of the EBV trans-activator protein BZLF1 (Fig. 4f, Extended Data Fig. 10e). To verify the antigenicity of BZLF1 to TCRαβ 1 cells, we designed a dextramer to present RAKFKQLL on HLA-B*08:01 (Fig. 4g). Notably, the dextramer bound to TCRαβ 1 cells with 100% positivity, whereas TCRαβ 2 cells did not bind (Fig. 4g, Extended Data Fig. 10f). These results demonstrate BZLF1 peptide RAKFKQLL as a cognate antigen presented by HLA-B*08:01 for a previously undescribed TCR (TCRα: CAASEGGFKTIF; TCRβ: CASSLGTGNNEQFF). In summary, our TCRαβ cloning strategy led to the discovery of a novel TCR in AD, with specificity for the EBV trans-activator protein BZLF1.

Overall, these results demonstrate antigen-specific clonal expansion of $CD8^+$ T cells in AD and signify the need for a greater understanding of the role of adaptive immunity in this disease. Although we detected EBV-specific TCRs in CSF from patients with AD, we caution that these data are not evidence of a causal link between EBV infectivity and AD. In fact, the EBV-specific clones detected in this study were not the most highly expanded and were not enriched among patients. However, it remains tenable that the most highly expanded clones observed in patient CSF are specific for non-self antigens that were not identified in our search. Several different antigens may activate and promote $CD8^+$ T cell trafficking in AD, with a potential effect on neurodegeneration through their cytotoxic effector function. Identifying the self and non-self antigens that clonal TCRs recognize in amyloidogenic brain disorders such as AD and PD will provide a new approach to investigate adaptive immunity in neurodegenerative disease.

Online content

Any methods, additional references, Nature Research reporting summaries, source data, extended data, supplementary information, acknowledgements, peer review information; details of author contributions and competing interests; and statements of data and code availability are available at https://doi.org/10.1038/s41586-019-1895-7.

1. Ransohoff, R. M. How neuroinflammation contributes to neurodegeneration. *Science* **353**, 777–783 (2016).
2. Lindestam Arlehamn, C. S., Garretti, F., Sulzer, D. & Sette, A. Roles for the adaptive immune system in Parkinson's and Alzheimer's diseases. *Curr. Opin. Immunol.* **59**, 115–120 (2019).
3. Louveau, A. et al. Structural and functional features of central nervous system lymphatic vessels. *Nature* **523**, 337–341 (2015).
4. Sallusto, F., Lenig, D., Förster, R., Lipp, M. & Lanzavecchia, A. Two subsets of memory T lymphocytes with distinct homing potentials and effector functions. *Nature* **401**, 708–712 (1999).
5. Han, A., Glanville, J., Hansmann, L. & Davis, M. M. Linking T-cell receptor sequence to functional phenotype at the single-cell level. *Nat. Biotechnol.* **32**, 684–692 (2014).
6. Schindowski, K. et al. Increased T-cell reactivity and elevated levels of $CD8^+$ memory T-cells in Alzheimer's disease-patients and T-cell hyporeactivity in an Alzheimer's disease-mouse model: implications for immunotherapy. *Neuromolecular Med.* **9**, 340–354 (2007).
7. Tan, J. et al. CD45 isoform alteration in $CD4^+$ T cells as a potential diagnostic marker of Alzheimer's disease. *J. Neuroimmunol.* **132**, 164–172 (2002).
8. Togo, T. et al. Occurrence of T cells in the brain of Alzheimer's disease and other neurological diseases. *J. Neuroimmunol.* **124**, 83–92 (2002).
9. Lombardi, V. R., García, M., Rey, L. & Cacabelos, R. Characterization of cytokine production, screening of lymphocyte subset patterns and in vitro apoptosis in healthy and Alzheimer's Disease (AD) individuals. *J. Neuroimmunol.* **97**, 163–171 (1999).
10. Bongioanni, P., Boccardi, B., Borgna, M., Castagna, M. & Mondino, C. T-cell interferon gamma binding in patients with dementia of the Alzheimer type. *Arch. Neurol.* **54**, 457–462 (1997).
11. Monsonego, A. et al. Increased T cell reactivity to amyloid β protein in older humans and patients with Alzheimer disease. *J. Clin. Invest.* **112**, 415–422 (2003).
12. Monsonego, A., Imitola, J., Zota, V., Oida, T. & Weiner, H. L. Microglia-mediated nitric oxide cytotoxicity of T cells following amyloid β-peptide presentation to Th1 cells. *J. Immunol.* **171**, 2216–2224 (2003).
13. Sallusto, F., Geginat, J. & Lanzavecchia, A. Central memory and effector memory T cell subsets: function, generation, and maintenance. *Annu. Rev. Immunol.* **22**, 745–763 (2004).
14. Bruggner, R. V., Bodenmiller, B., Dill, D. L., Tibshirani, R. J. & Nolan, G. P. Automated identification of stratifying signatures in cellular subpopulations. *Proc. Natl Acad. Sci. USA* **111**, E2770–E2777 (2014).
15. Kivisäkk, P. et al. Human cerebrospinal fluid central memory $CD4^+$ T cells: evidence for trafficking through choroid plexus and meninges via P-selectin. *Proc. Natl Acad. Sci. USA* **100**, 8389–8394 (2003).
16. Giunti, D. et al. Phenotypic and functional analysis of T cells homing into the CSF of subjects with inflammatory diseases of the CNS. *J. Leukoc. Biol.* **73**, 584–590 (2003).
17. Sulzer, D. et al. T cells from patients with Parkinson's disease recognize α-synuclein peptides. *Nature* **546**, 656–661 (2017).
18. Smith, L. K. et al. β2-microglobulin is a systemic pro-aging factor that impairs cognitive function and neurogenesis. *Nat. Med.* **21**, 932–937 (2015).
19. Argaet, V. P. et al. Dominant selection of an invariant T cell antigen receptor in response to persistent infection by Epstein–Barr virus. *J. Exp. Med.* **180**, 2335–2340 (1994).
20. Glanville, J. et al. Identifying specificity groups in the T cell receptor repertoire. *Nature* **547**, 94–98 (2017).

Publisher's note Springer Nature remains neutral with regard to jurisdictional claims in published maps and institutional affiliations.

© The Author(s), under exclusive licence to Springer Nature Limited 2020

Methods

Study participants

Samples were acquired through the Stanford Brain Rejuvenation Program, the NIA funded Stanford Alzheimer's Disease Research Center (ADRC), the University of California at San Francisco ADRC and the University of California at San Diego ADRC. Collection of brain tissue, plasma, PBMCs and CSF was approved by the Institutional Review Board of each university, and written consent was obtained from all subjects. A total of 164 living subjects from three separate cohorts (cohorts 1, 2 and 4) were used in this study. The 164 subjects included 97 healthy individuals, 31 patients with MCI, 28 patients with AD and 8 patients with PD. The average age of subjects was 72.52 ± 6.96 (mean ± s.d.) for healthy individuals; 70.97 ± 7.82 for patients with MCI; 70.74 ± 7.01 for patients with AD; and 67.25 ± 7.01 for patients with PD. The average cognitive score was 27.17 ± 2.32 for healthy individuals; 23.39 ± 4.31 for patients with MCI; 11.05 ± 7.32 for patients with AD; and 27.29 ± 1.70 for patients with PD. All subjects were free from acute infectious diseases and in good physical condition. Patients were confirmed to have neurodegeneration by measurement of biomarkers including neurofilament, Aβ and tau (Quanterix). Group characteristics, including demographic, genetic, clinical and biomarker data for each group, are presented in Supplementary Table 12.

Tissue collection

PBMCs were isolated from blood by layering diluted blood (1:1 in PBS) on top of an equal volume of Ficoll, followed by centrifugation and isolation of the buffy coat. CSF was collected by lumbar puncture, then centrifuged at 300*g* to pellet immune cells. CSF samples were checked for blood contamination by resuspending the pelleted cells in 100 µl CSF and mixing 10 µl (10%) CSF with 10 µl trypan blue to assess red blood cell content and viability. Cells were visualized on a TC20 automated cell counter (BioRad) and cell viability and the presence or absence of red blood cells was recorded. CSF samples that were contaminated with blood were not used in the study. The resuspended cells were then mixed with 900 µl recovery cell culture freezing medium (Thermo Fisher Scientific). All samples were frozen overnight at −80 °C in a Mr. Frosty freezing container (Thermo Fisher Scientific) and transferred the following day to liquid nitrogen for storage. PBMC samples were stored over the course of a three-year period. The average PBMC viability for patient samples following sample thawing was 79%, and that for control samples was 77%. CSF samples were stored less than 6 months before analysis.

Cognitive testing

Study subjects underwent a battery of neuropsychological assessments to determine group status, including cognitive examination, evaluation of cerebellar function, deep tendon reflexes, sensory input and motor function. The Montreal Cognitive Assessment (MoCA)[21] examination was used to test study subjects for cognitive impairment. The MoCA assesses several cognitive domains: short-term memory recall (5 points), visuospatial abilities (4), executive functions (4), attention (1), concentration (3), working memory (1), language (6) and orientation to time and space (6). MoCA scores range between 0 and 30.

Structural brain MRI

T1-weighted MRI scans were acquired using an Axial 3D fast spoiled gradient sequence (GE Discovery 750). The imaging parameters were optimized for grey and white matter tissue contrast with a repetition time of 5.9 ms, echo time 2 ms, flip angle 15°, field of view 220 mm, matrix size 256 × 256, slice thickness 1 mm and 2 NEX. Image analysis was conducted using FreeSurfer 6.0. For subcortical segmentation, we used the 'recon-all' command. For hippocampal segmentation, we appended the flag '-hippocampal-subfields-T1' to the 'recon-all' command for each patient. To correct for sex differences, we normalized all volumetric measurements to the total intracranial volume for each patient.

Flow cytometry

Flow cytometry was conducted using an LSRFortessa (BD Biosciences). A panel consisting of antibodies conjugated to six different fluorophores was used to classify subsets of memory T cells and for drop-seq. Antibodies used were: CD8α-Pacific blue (BioLegend), CD3-BV650 (BD Biosciences), CD45RA-APC-Cy7 (BioLegend), CCR7-488 (BioLegend), IL-7Rα-PE (BioLegend) and CD27-PE-Cy7 (BioLegend). For characterization of CSF cells, this same panel was used, but CD19-PE-Cy5 (BioLegend) and CD14-Qdot-705 (Thermo Fisher Scientific) were included. For sorting CSF T cells for TCR plate-seq, the following antibodies were used: CD8α-PE (BioLegend), CD161-PE-Cy7 (BioLegend), CXCR3-APC (BioLegend), CD4-APC-Alexa700 (Thermo Fisher Scientific), CD39-APC-Cy7 (BioLegend), CD38-FITC (BioLegend), PD-1-BV421 (BD Biosciences), CD45RA-BV605 (BD Biosciences), CD3-BV650 (BD Biosciences), CD27-BV786 (BD Biosciences) and CD127-BUV395 (BD Biosciences). For each experiment, a compensation matrix was developed using singly stained and unstained controls or fluorescent beads, and all analysis was conducted in Cytobank.

Cell stimulation

PBMCs were thawed and plated at a density of 1×10^6 cells per well in a 24-well plate. The medium consisted of RPMI with 10% fetal bovine serum and 1× penicillin–streptomycin. After overnight incubation at 37 °C with 20 U ml^{-1} IL-2, cells were stimulated with a cocktail containing PMA, ionomycin and brefeldin A (BioLegend). Cells were then incubated an additional 5 h before performing intracellular flow cytometry analysis.

Mass cytometry

Mass cytometry was performed as previously described[22]. In brief, cells were thawed in complete medium containing RPMI with 10% fetal bovine serum (FBS), 1% penicillin–streptomycin and 0.1 mg ml^{-1} DNase. After washing in Maxpar Cell Staining Buffer (Fluidigm) cells were resuspended in 50 µl filtered antibody cocktail (Fluidigm) and incubated for 60 min on ice. Cells were again rinsed, then resuspended in 100 µl of 1:3,000-diluted In115-DOTA maleimide in buffer. Following additional rinses, cells were resuspended in 100 µl of 2% paraformaldehyde in buffer and incubated at 4 °C overnight. Cells were then washed twice with permeabilization buffer (eBioscience) and incubated on ice for 45 min. After rinsing, cells were resuspended in Ir-Interchelator in buffer and incubated for 20 min at room temperature. Cells were then washed with buffer, then MilliQ water and finally resuspended in MilliQ water for running on a Helios mass cytometer. To normalize mass cytometry data, the same lot of EQ Four Element Calibration Beads (Fluidigm) was used for all experiments to control for signal variation that may have occurred in the instrument over time. Normalization of mass cytometry data was achieved using the Matlab bead normalization tool.

SPADE and CITRUS analyses

SPADE and CITRUS analyses were conducted using Cytobank. For SPADE conducted on mass cytometry data, we established a target number of nodes of 100 for our immunophenotyping assay. We based this number on empirical evaluation of results from multiple runs on the same dataset, which showed comparable results. The SPADE population for immunophenotyping (live CD45$^+$ cells) was selected on the basis of the gating strategy shown in Extended Data Fig. 3. Cells were clustered on all markers except those used to exclude platelets or endothelial cells. For CITRUS, the same population of cells and same clustering channels were used as in SPADE to quantify the abundance of various populations. Results are from 5×10^3 events per sample, with a false discovery rate of 2%, minimum cluster size of 1% and cross validation folds set to 10. The predictive nearest shrunken centroid PAMR association model was

used. To avoid spurious results, we ran CITRUS with minimum cluster sizes of 1–4%, cross validation folds 5–10 and false discovery rate 1–5% for 1×10^4, 1.5×10^4 and 2×10^5 events, totalling 17 individual runs. For SPADE conducted on flow cytometry data, $CD3^+CD8^+$ cells were gated and clustered with a target number of nodes of 30.

Immunohistochemistry

Paraffin-embedded brain tissues were sectioned at 5-µm thickness. Deparaffinization was achieved by washing slides through a series of xylenes and decreasing concentrations of ethanol. Tissue sections were then subjected to antigen retrieval using citrate buffer, pH 6.0 (Sigma-Aldrich) at 95 °C for 30 min. Following rinsing with PBS, sections were incubated in blocking buffer containing PBS with 10% normal donkey serum and 0.03% Triton-X (Sigma-Aldrich) for 2 h at room temperature. Slides were then incubated with primary antibody in blocking buffer overnight at 4 °C. The following day, slides were rinsed with PBS then incubated in appropriate Alexa Fluor secondary antibodies (Thermo Fisher Scientific). Sections were then rinsed and stained with Hoechst DNA dye (Thermo Fisher Scientific) before being coverslipped with ProLong mounting medium (Invitrogen). Primary antibodies included rat anti-human CD3 (Abcam), rabbit anti-human CD8α (Cell Signaling), mouse anti-Aβ (Cell Signaling), chicken anti-human MAP2 (Abcam), mouse anti-human granzyme-A (Abcam), rat anti-mouse CD8a (eBioscience) and rabbit anti-mouse NEFH (Abcam). For mouse Aβ plaque staining, ThioflavinS (1 mg ml^{-1}, 1:625, Sigma) was added to the secondary antibody solution.

Confocal microscopy and image processing

For human tissue, the LSM880 confocal laser scanning microscope (Zeiss) was used to acquire images using 40× and 63× objectives. For mouse tissue imaging, the LSM700 and LSM710 confocal laser scanning microscopes (Zeiss) were used, which were provided by the microscopy core facility of the Spinal Cord Injury and Tissue Regeneration Center Salzburg (SCI-TReCS). For all Z-stacks, images were acquired using optical sectioning then combined into maximum intensity projections. 3D reconstructions were performed using Imaris v.9.1.2 (Bitplane).

Quantitative histology

For quantification of human $CD3^+CD8^+$ and $GZMA^+CD8^+$ T cells, homologous sections of the hippocampal dentate gyrus were cut at 10-µm thickness using a microtome (Leica Biosystems). Plot sampling was conducted by using CA3 as a boundary to draw a rectangular area of approximately 2 mm^2 that encompassed the molecular layer, granule cell layer and hilus. Three separate sections were sampled using a 20× objective. $CD3^+CD8^+$ T cells were then manually counted by a blinded observer in ZEN 2 Blue Edition (Zeiss).

Mice

APP/PS1 mice[23,24] expressing a chimaeric mouse/human mutant amyloid precursor protein (Mo/HuAPP695swe) and a mutant human presenilin 1 (PS1-dE9) directed to CNS neurons under the prion protein promoter were used (The Jackson Laboratory). Mice were housed at the Paracelsus Medical University Salzburg in groups under standard conditions at a temperature of 22 °C and a 12 h light/dark cycle with ad libitum access to standard food and water. Over 10 mice aged 12–13 months comprising both sexes were randomly analysed in an unblinded manner. Animal care, handling, genotyping and experiments were approved by Paracelsus Medical University Salzburg ethical committees.

Electron microscopy

For ultrastructure analysis, 12-13-month-old APP/PS1 mice and wild-type controls were transcardially perfused with 4% PFA and 0.5% glutaraldehyde in 0.1 M phosphate buffer (PB). Brains were removed and 50-µm sagittal sections were cut using a vibratome (Leica) and stored in 0.1 M PB with 0.05% sodium azide. Sections with brain areas of interest were selected and pre-embedding 3,3′-diaminobenzidine (DAB)-immunostaining was performed as described previously[25,26]. Rat anti-CD8 (eBioscience) primary antibody was used and incubated for 2 days at 4 °C. After several washes in PBS, sections were incubated for 2 days with biotinylated rabbit anti-rat antibody (Vector) at 4 °C. To increase staining signal, sections were incubated in the Vectastain ABC Hrp Kit (Vector) for 1 h. After rinsing three times in PBS, sections were transferred to DAB using the Peroxidase Substrate Kit (Vector). Sections were rigorously washed and osmificated by incubating in 1% OsO4 (EMS) in 0.1 M PB for 1 h. Following 3 washes for 10 min in distilled water, sections were incubated in Uranyl Acetate Replacement Stain-UAR (EMS) for 30 min. Sections were dehydrated by incubation in an increasing series of ethanol and transferred to propylenoxide (EMS) before embedding in araldite durcupan (four component resin, Sigma) overnight in aluminium foil cups at room temperature. The following day, slices were transferred to acetate slides (100 micron colour laser printer film, 5 Star Office Supplies), covered with small amounts of araldite, coated with a second acetate slide and hardened in an oven at 60 °C for 3 days. Hippocampal and cortical regions with $CD8^+$ T cells were identified using light microscopy and regions of interest were cut out of embedded sections. One side of the acetate slide was removed and samples were glued onto an araldite durcupan block with cyanoacrylate adhesive (UHU). This protocol was performed with small modifications according to previously reported protocols[27,28]. After removing the acetate slides and careful trimming of the samples into a trapezial shape, semi-thin sections of 1–1.5 µm were generated using an Ultracut Reichert E (Leica). Semi-thin sections were transferred to object slides and were stained with 1% Toluidine blue for orientation. After identification of stained cells, ultra-thin sections of 70 nm were directly cut using a diamond knife (Diatome). Sections were stretched with chloroform and subsequently collected with 50 or 75 mesh copper grids of 3 mm diameter coated with 0.2% Formvar solution. Grids were dried and analysed with a LEO 912 transmission electron microscope (Zeiss) equipped with an in-column energy filter, at 100 kV by using a Slow Scan Dual Speed CCD camera TRS Sharpeye (Troendle). The imaging software used was Image SP v.1.2.7.31 (SIS, Soft Image System).

TCR amplification by nested PCR plate-seq

TCR sequencing was conducted according to our previously established protocols[5,29]. In brief, TCR sequences from live $CD3^+$ single cells were obtained by a series of three nested PCR reactions. For all phases of PCR reactions, HotStarTaq DNA polymerase (Qiagen) was used. The phase 1 PCR reaction was a multiplexed PCR with multiple Vα, Vβ, Cα and Cβ region primers in a 16-µl reaction. For the phase 1 PCR reaction, the final concentration of each TCR V-region primer was 0.06 µM and each C-region primer was 0.3 µM. A PCR reaction was done using the following conditions: 95 °C 15 min; 94 °C 30 s, 62 °C 1 min, 72 °C 1 min × 16 cycles; 72 °C 10 min; 4 °C. Thereafter, a 1-µl aliquot of the phase 1 product was used as a template for the 12-µl phase 2 PCR reaction. The following cycling conditions were used for phase 2 PCR: 95 °C 15 min; 94 °C 30 s, 64 °C 1 min, 72 °C 1 min × 25 cycles; 72 °C 5 min; 4 °C. For the phase 2 reaction, multiple internally nested TCRVα, TCRVβ, TCRCα and Cβ primers were used (V primers 0.6 µM, C primers 0.3 µM). The phase 2 primers of TCR V-region contained a common 23-base sequence at the 5′ end to enable amplification during the phase 3 reaction with a common 23-base primer. A 1-µl aliquot of the phase 2 PCR product was used as a template for the 14-µl phase 3 PCR reaction, which incorporated barcodes and enabled sequencing on the Illumina MiSeq platform. For the phase 3 PCR reaction, amplification was performed using a 5′ barcoding primer (0.05 µM) containing the common 23-base sequence and a 3′ barcoding primer (0.05 µM) containing the sequence of a third internally nested Cα and/or Cβ primer, and Illumina Paired-End primers (0.5 µM each). The following cycling

conditions were used for phase 3 PCR: 95 °C 15 min; 94 °C 30 s, 66 °C 30 s, 72 °C 1 min × 25 cycles; 72 °C 5 min; 4 °C. The final phase 3 barcoding PCR reactions for TCRα and TCRβ were done separately. For the phase 3 reaction, 0.5 μM of the 3′ Cα barcoding primer and the 3′ Cβ barcoding primer were used. In addition to the common 23-base sequence at the 3′ end (that enables amplification of products from the second reaction) and a common 23-base sequence at the 5′ end (that enables amplification with Illumina Paired-End primers), each 5′ barcoding primer contains a unique 5-base barcode that specifies plate and a unique 5-base barcode that specifies row within the plate. These 5′ barcoding primers were added with a multichannel pipette to each of 12 wells within a row within a plate. In addition to the internally nested TCR C-region sequence and a common 23-base sequence at the 3′ end (that enables amplification with Illumina Paired-End primers), each 3′ barcoding primer contained a unique 5-nucleotide barcode that specified column. These 3′ barcoding primers were added with a multichannel pipette to each of eight wells within a column within all plates. After the phase 3 PCR reaction, each PCR product should have had a unique set of barcodes incorporated that specified plate, row and column and had Illumina Paired-End sequences that enabled sequencing on the Illumina MiSeq platform. The PCR products were combined at equal proportion by volume and run on a 1.2% agarose gel, and a band around 350 to 380 bp was excised and gel purified using a Qiaquick gel extraction kit (Qiagen). This purified product was then sequenced.

TCR plate-seq analysis

TCR sequencing data were analysed as previously described[5,29]. Raw sequencing data were processed and demultiplexed using a custom software pipeline to separate reads from every well in every plate as per specified barcodes. All paired ends were assembled by finding a consensus of at least 100 bases in the middle of the read. The resulting paired-end reads were then assigned to wells according to barcode. Primer dimers were filtered out by establishing a minimum length of 100 bases for each amplicon. A consensus sequence was obtained for each TCR gene. Because multiple TCR genes might be present in each well, our software establishes a cut-off of >95% sequence identity within a given well. All sequences exceeding 95% sequence identity are assumed to derive from the same TCR gene and a consensus sequence is determined. The 95% cut-off conservatively ensures that all sequences derived from the same transcript are properly assigned.

Drop-seq of peripheral $CD8^+$ T_{EMRA} and CSF cells

For $CD8^+$ T_{EMRA} scRNA-seq, base call files from a HiSeq 4000 Sequencer (Illumina) were generated by the Stanford Genomics Core. For CSF and peripheral $CD8^+$ T_{EMRA} scRNA-seq, FASTQ files from a Novoseq S4 sequencer were generated by Novogene. For CSF scTCR-seq, base call files from a NextSeq550 Sequencer (Illumina) were generated in-house. Single cell V(D)J and 5′ gene-expression analysis (10X Genomics) was used for peripheral $CD8^+$ T_{EMRA} and CSF cells. Cell Ranger v.3.0.2 was used to generate gene-expression matrices for both peripheral T_{EMRA} and CSF cells. The Cell Ranger mkfastq pipeline generated FASTQ files for both the 5′ expression library and the V(D)J libraries. Reads from the 10X v.2 5′ paired library were mapped to the human genome build GRCh38 3.0.0. Reads from the 10X V(D)J kit were mapped to the vdj-GRCh38 alts ensemble 2.0.0 (available from 10X Genomics). The 5′ gene-expression libraries were then analysed with the Cell Ranger count pipeline and the resulting expression matrix was used for further analysis in the Seurat package v.3.0. The V(D)J FASTQ files were analysed with the Cell Ranger vdj pipeline, which produced single cell V(D)J sequences and determined clonotypes. Clonotypes were determined by grouping of cell barcodes that shared the same set of productive CDR3 nucleotide sequences. The sequences of all contigs from all cells within a clonotype were then assembled to produce a clonotype consensus sequence. Clonality was integrated into the Seurat gene-expression analysis by adding clonality information to the metadata.

Clustering of peripheral $CD8^+$ T_{EMRA} and CSF cells

Individual sample expression matrices were loaded into R using the function Read10x under the Matrix package v.1.2-15. The expression matrix for each sample was merged into one Seurat object using the CreateSeuratObject and MergeSeurat functions. The Seurat package v.3.0[30,31] was used for filtering, variable gene selection, normalization, scaling, dimensionality reduction, clustering and visualization. For $CD8^+$ T_{EMRA} cells, genes were excluded if they were expressed in fewer than 10 cells, and cells were excluded if they expressed fewer than 200 genes. Cells that expressed more than 2,500 genes, more than 10,000 unique molecular identifiers (UMIs) and more than 10% mitochondrial genes were excluded. Regularized negative binomial regression using the sctransform normalization method was used to normalize, scale, select variable genes and regress out experimental batch, mitochondrial mapping percentage and the number of UMIs. After filtering and normalization, there were 15,330 genes across 18,203 cells. Following principal component analysis (PCA), 10 principle components were selected for clustering the cells. A resolution of 0.4 was used with *t*-SNE visualization. For CSF cells, genes were excluded if they were expressed in fewer than 10 cells and cells were excluded if they expressed fewer than 200 genes. Cells that expressed more than 1,800 genes, more than 7,500 UMIs and more than 10% mitochondrial genes were excluded from the analysis. The sctransform normalization method was used to normalize, scale, select variable genes and regress out sequencing and experimental batch, mitochondrial mapping percentage and the number of UMIs. After filtering and normalization, there were 212,267 samples and 14,734 features. Following PCA, four principle components were selected for clustering. A resolution of 0.3 was used with *t*-SNE visualization.

Analysis of scRNA-seq data

For differential expression analysis, markers for each cluster were determined by comparing the cells of each cluster to all other cells using the FindMarkers function in Seurat with the MAST algorithm from the R package MAST (v.1.8.2). For all comparisons between groups and clusters, only genes expressed by at least 10% of cells were included. The R package ggplot2 (v.3.1.0) was used to plot the results of differential expression analyses, showing the average log-transformed fold change of each gene and the −log10 of the adjusted *P* value (Benjamini–Hochberg correction). Seurat was used to produce violin plots of the expression of selected genes. For pathway analysis, Panther was used to perform Reactome pathway analysis with genes that were identified from differential expression analysis ($q < 0.05$) and with all genes in the dataset as background. Fisher's exact test was used with Bonferroni correction for multiple testing. *Z*-scores for each pathway were calculated using the R package GOPlot.

Determination of antigen specificity of V(D)J sequences

To determine whether TCR sequences identified in our scTCR-seq experiments on peripheral T_{EMRA} and CSF cells had known antigen specificity, the CDR3b region of each β chain was compared to the CDR3b repertoire from the VDJdb at https://vdjdb.cdr3.net/.

TCR clonality analysis

For CSF cells sequenced by plate-seq, analysis of clonality was performed using Excel. TCRs with two or more identical CDR3b regions and CDR3a regions were defined as clonal. R was used to calculate a proportion of the sum of reads of the clonotypes to the overall number of reads in a repertoire (∑reads of top clonotypes)/(∑reads for all clonotypes). For TCRs sequenced using single-cell V(D)J technology (10X Genomics), clonality was determined by the Cell Ranger vdj pipeline as previously described. Clonotypes were determined from grouping of cell barcodes that shared the same set of productive CDR3 nucleotide sequences.

The sequences of all contigs from all cells within a clonotype were then assembled to produce a clonotype consensus sequence. Clonality was integrated into the Seurat gene-expression analysis by adding clonality information to the metadata. For TCR network analysis, to depict connections between diagnosis groups, patients and clonotypes, we used the qgraph package for R. Only TCRs with full α and β chain sequences were included in the analysis. Unweighted networks were generated with all subjects and split per diagnosis group.

Gene-engineered T cell lines

The two TCRs identified from patients with AD by GLIPH were cloned into a pHR vector using the signal peptides of the TCR variable genes and full-length, unmodified constant regions from IMGT/V-QUEST. Packaging vectors pMD2G and pPAX were used to allow for human mammalian tropism and viral generation. Lentivirus was generated for each TCRα and TCRβ separately in Lenti-X 293T cells (Takara). Cells were cultured with 10% fetal bovine serum (FBS) in Dulbecco's modified Eagle's medium (DMEM) and viruses were collected at 48 h, filtered with 0.45-mM syringe filters (Thermo Fisher Scientific), and frozen at −80 °C or used immediately to infect the TCR-deficient SKW-3 cell line (Creative Bioarray; these cells were verified to lack TCRs using an antibody against TCRαβ and confirmed negative for mycoplasma contamination). TCRαβ 1 expressed TCRα: CAASEGGFKTIF and TCRβ: CASSLGTGNNEQFF. TCRαβ 2 expressed TCRα: CAADRTGGGNKLTF and TCRβ: CASSLAGGYNEQFF. Combined TCRα and TCRβ viruses were used to infect 2×10^6 SKW-3 cells at a multiplicity of infection of five by spinning for 1 h at 2,500 rpm at 32 °C, and cells were then placed back in culture. After 48 h, cells were collected, rinsed with PBS then incubated with live/dead near infrared dead cell dye (Thermo Fisher Scientific), stained for TCRαβ (IP26, BioLegend) and sorted on a FACSAria II cell sorter (BD). TCRαβ$^+$ cells were sorted before each experiment and cultures were maintained in DMEM containing 10% FBS and 1× penicillin–streptomycin supplemented with recombinant human IL-2 (20 IU ml^{-1}; R&D Systems).

TCR stimulation

For αCD2/CD3/CD28 TCR stimulation, anti-biotin particles loaded with the biotinylated antibodies were used to mimic antigen-presenting cells and activate TCRs. Transduced SKW-3 cells were incubated with biotinylated antibodies against human CD2, CD3 and CD28 (Miltenyi) in DMEM containing 10% FBS and 1× penicillin–streptomycin. Data were analysed using Cytobank and samples were gated on SKW-3 cells by forward and side scatter before analysis for TCRαβ and CD69 expression.

Autologous fibroblast antigen presentation

T cell lines were co-cultured with autologous fibroblasts in a 2:1 ratio during antigen presentation. For MCH-I peptide pool stimulation, a mix of 80 known MHC-I antigenic peptides (CEFX Ultra SuperStim Pool MHC-I Subset; JPT Peptides) were used to screen for reactive TCRs. Fibroblasts were plated at 5×10^4 cells per well in 24-well plates. The peptide mix contained 0.3–1.2 μg per peptide per μl (dependent on each peptide's molecular weight) dissolved in DMSO and had a purity of each peptide of greater than 70% as determined by high-performance liquid chromatography (HPLC). Peptide pools were added to fibroblast plates at 1:100 dilution in 250 μl medium. Control wells contained DMSO only. For individual peptide stimulations, peptides were produced at a purity of greater than 90% as determined by HPLC (JPT Peptides). Following 18 h of incubation at 37 °C, fibroblasts were heat-shocked at 41 °C for 30 min to increase antigen presentation. Fibroblasts were then rinsed with PBS and 1×10^5 cells from each T cell line were added in medium containing purified no azide/low endotoxin mouse anti-human CD28 antibody (2 μg ml^{-1}; BD Biosciences) and IL-2 (20 IU ml^{-1}). After 18 h, cells were analysed for activation by flow cytometry for TCRαβ and CD69 expression.

Statistical methods

All statistical analyses were performed using commercially available software (Prism, SPSS or Excel). All values are expressed as the mean ± SEM. Differences in means between two groups were analysed using unpaired two-sided heteroscedastic *t*-tests with Welch's correction, unless otherwise noted. For regression analyses, the significance of the difference between two datasets was measured by ANCOVA. Differences in means among multiple datasets were analysed using one- or two-way analysis of variance (ANOVA). When ANOVA showed significant differences, pair-wise comparisons between means were tested by Sidak's or Tukey's multiple comparisons test. For scRNA-seq analyses, we corrected for multiple comparisons and report adjusted P values using Benjamini–Hochberg correction. For pathway analyses, Fisher's exact test was used with Bonferroni correction for multiple testing. No statistical methods were used to predetermine sample size.

Reporting summary

Further information on research design is available in the Nature Research Reporting Summary linked to this paper.

Data availability

scRNA-seq and scTCR-seq datasets have been deposited online in the Gene Expression Omnibus (GEO) under accession number GSE134578.

21. Nasreddine, Z. S. et al. The Montreal Cognitive Assessment, MoCA: a brief screening tool for mild cognitive impairment. *J. Am. Geriatr. Soc.* **53**, 695–699 (2005).
22. Leipold, M. D., Newell, E. W. & Maecker, H. T. Multiparameter phenotyping of human PBMCs using mass cytometry. *Methods Mol. Biol.* **1343**, 81–95 (2015).
23. Jankowsky, J. L. et al. Co-expression of multiple transgenes in mouse CNS: a comparison of strategies. *Biomol. Eng.* **17**, 157–165 (2001).
24. Jankowsky, J. L. et al. Mutant presenilins specifically elevate the levels of the 42 residue β-amyloid peptide in vivo: evidence for augmentation of a 42-specific γ secretase. *Hum. Mol. Genet.* **13**, 159–170 (2004).
25. Marschallinger, J. et al. The L-type calcium channel Cav1.3 is required for proper hippocampal neurogenesis and cognitive functions. *Cell Calcium* **58**, 606–616 (2015).
26. Unger, M. S. et al. Doublecortin expression in CD8$^+$ T-cells and microglia at sites of amyloid-β plaques: a potential role in shaping plaque pathology? *Alzheimers Dement.* **14**, 1022–1037 (2018).
27. Gil-Perotin, S., Alvarez-Buylla, A. & Garcia-Verdugo, J. M. *Identification and Characterization of Neural Progenitor Cells in the Adult Mammalian Brain*. Advances in Anatomy, Embryology and Cell Biology Vol. 203 (Springer, 2009).
28. Sirerol-Piquer, M. S. et al. GFP immunogold staining, from light to electron microscopy, in mammalian cells. *Micron* **43**, 589–599 (2012).
29. Han, A. et al. Dietary gluten triggers concomitant activation of CD4$^+$ and CD8$^+$ αβ T cells and γδ T cells in celiac disease. *Proc. Natl Acad. Sci. USA* **110**, 13073–13078 (2013).
30. Butler, A., Hoffman, P., Smibert, P., Papalexi, E. & Satija, R. Integrating single-cell transcriptomic data across different conditions, technologies, and species. *Nat. Biotechnol.* **36**, 411–420 (2018).
31. Stuart, T. et al. Comprehensive integration of single-cell data. *Cell* **177**, 1888–1902 (2019).

Acknowledgements We thank M. Leipold, S. Douglas and H. Maecker from the Stanford Human Immune Monitoring Core for helpful discussion and assistance with mass cytometry experiments; B. Dulken and A. Brunet of Stanford University for sharing related mouse research; B. Carter of the Palo Alto Veterans Affairs FACS facility; V. Henderson and the entire Stanford Alzheimer's disease Reserach Center team; G. Kerchner and S. Sha for CSF collection; G. Deutsch, C. Litovsky and M. Thieu for assistance with cognitive assessments; and V. Carr, S. Guerin, A. Trelle and the Stanford Aging and Memory Study (SAMS) team for MRI data collection. This work was supported by a Glenn/American Federation for Aging Research (AFAR) Postdoctoral Fellowship for the Biology of Aging (D.G.), a National Institutes of Health National Institute on Aging (NIA) F32 Fellowship (AG055255-01A1) (D.G.), an Irene Diamond Fund/AFAR Postdoctoral Transition Award in Aging (D.G.), a National Multiple Sclerosis Society Postdoctoral Fellowship (N.S.), the National Institutes of Health Institute for Allergy, Infectious Diseases and Immunology (U19-AI057229), the Howard Hughes Medical Institute (N.S. and M.M.D.), the Austrian Science Funds Special Research Program F44 (F4413-B23) (M.S.U.), NIA R01 AG048076 (A.D.W.), the Dana Foundation (A.D.W.), the Cure Alzheimer's Fund (T.W.-C.), the NOMIS Foundation (T.W.-C.), the Stanford Brain Rejuvenation Project (an initiative of the Stanford Neurosciences Institute), NIA R01 AG045034 05 (T.W.-C.) and the NIA funded Stanford Alzheimer's Disease Research Center (P50AG047366).

Author contributions D.G. and T.W.-C. planned the study. D.G. performed the experiments, analysed the data and wrote the manuscript with help from T.W.-C. N.S. performed TCR plate-seq and analysis. M.M.D. guided TCR plate-seq and GLIPH experiments. B.L. independently analysed the dataset and performed TCR network analysis. M.S.U. and L.A. performed mouse

histology, 3D rendering and electron microscopy. F.E., M.G., A.D.W. and D.R.G. recruited study subjects and oversaw the acquisition of samples and clinical data. O.L., A.C.Y., J.M., K.C., D.C., M.B.D.L.S., A.M., J.P., G.K.-Y.T. and Y.K. assisted with experiments and/or sample processing.

Competing interests D.G., N.S., M.M.D. and T.W.-C. are co-inventors on a patent application related to this work. Patent STDU2-36496/US-1/PRO is for compositions and methods for measuring T cell markers associated with Alzheimer's disease.

Additional information
Supplementary information is available for this paper at https://doi.org/10.1038/s41586-019-1895-7.
Correspondence and requests for materials should be addressed to D.G. or T.W.-C.
Peer review information *Nature* thanks Michael T. Heneka, Paul Thomas and the other, anonymous, reviewer(s) for their contribution to the peer review of this work.
Reprints and permissions information is available at http://www.nature.com/reprints.

Corresponding author(s): Tony Wyss-Coray
twc@stanford.edu

Reporting Summary

Nature Research wishes to improve the reproducibility of the work that we publish. This form provides structure for consistency and transparency in reporting. For further information on Nature Research policies, see Authors & Referees and the Editorial Policy Checklist.

Statistical parameters

When statistical analyses are reported, confirm that the following items are present in the relevant location (e.g. figure legend, table legend, main text, or Methods section).

n/a	Confirmed	
☐	☒	The exact sample size (*n*) for each experimental group/condition, given as a discrete number and unit of measurement
☐	☒	An indication of whether measurements were taken from distinct samples or whether the same sample was measured repeatedly
☐	☒	The statistical test(s) used AND whether they are one- or two-sided *Only common tests should be described solely by name; describe more complex techniques in the Methods section.*
☐	☒	A description of all covariates tested
☐	☒	A description of any assumptions or corrections, such as tests of normality and adjustment for multiple comparisons
☐	☒	A full description of the statistics including central tendency (e.g. means) or other basic estimates (e.g. regression coefficient) AND variation (e.g. standard deviation) or associated estimates of uncertainty (e.g. confidence intervals)
☐	☒	For null hypothesis testing, the test statistic (e.g. *F*, *t*, *r*) with confidence intervals, effect sizes, degrees of freedom and *P* value noted *Give P values as exact values whenever suitable.*
☒	☐	For Bayesian analysis, information on the choice of priors and Markov chain Monte Carlo settings
☐	☒	For hierarchical and complex designs, identification of the appropriate level for tests and full reporting of outcomes
☐	☒	Estimates of effect sizes (e.g. Cohen's *d*, Pearson's *r*), indicating how they were calculated
☐	☒	Clearly defined error bars *State explicitly what error bars represent (e.g. SD, SE, CI)*

Our web collection on statistics for biologists may be useful.

Software and code

Policy information about availability of computer code

Data collection	Brain MRI quantifications were conducted using FreeSurfer 6.0. Confocal images were acquired using ZEN 2 Blue Edition (Zeiss). Electron microscopy images were acquired with Imaging software was Image SP v1.2.7.31 (SIS, Soft Image System). Clonality measurements were calculated using R Studio. Mass cytomtery analysis was conducted using Cytobank. For TCR network analysis, to depict connections between diagnosis groups, patient IDs and clonotypes, we used the qgraph package for R (Epskamp et al. 2012). Only TCRs with alpha and beta chain sequenced were included in the analysis and non-clonal cells were filtered out. Unweighted networks were generated with all subjects and split per diagnosis group. Sacha Epskamp, Angelique O. J. Cramer, Lourens J. Waldorp, Verena D. Schmittmann, Denny Borsboom (2012). qgraph: Network Visualizations of Relationships in Psychometric Data. Journal of Statistical Software, 48(4), 1-18. URL http://www.jstatsoft.org/v48/i04/.
Data analysis	Normalization of mass cytometry data was achieved using the Matlab bead normalization tool.

Data analysis

3D reconstructions of mouse CD8 T cells were performed using Imaris v9.1.2 (Bitplane).

For volumetric measurements in Extended Data Figure 1: for subcortical segmentation, we used the "recon-all" command. For hippocampal segmentation, we appended the flag "-hippocampal-subfields-T1" to the "recon-all" command for each patient. To correct for sex differences, we normalized all volumetric measurements to total intracranial volume for each patient.

TCR clonality analysis of CSF cells by plate-seq, we used Excel. TCRs with two or more identical CDR3b regions and CDR3a regions were defined as clonal. R was used to calculate a proportion of clonotypes' sum of reads to the overall number of reads in a repertoire (∑ reads of clonotype)/(∑ reads for all clonotypes). For TCRs sequenced using Single cell V(D)J technology (10X Genomics), clonality was determined by the cellranger vdj pipeline as previously described. Clonotypes were determined from grouping of cell barcodes that shared the same set of productive CDR3 nucleotide sequences. The sequences of all contigs from all cells within a clonotype were then assembled to produce a clonotype consensus sequence. Clonality was integrated into the Seurat gene expression analysis by adding clonality information to the metadata. For TCR network analysis, to depict connections between diagnosis groups, patients and clonotypes, we used the qgraph package for R. Only TCRs with full α and β chain sequences were included in the analysis. Unweighted networks were generated with all subjects and split per diagnosis group.

Analysis of scRNAseq data
Differential Expression
Markers for each cluster were determined by comparing the cells of each cluster to all other cells using the FindMarkers function in Seurat with the Model-based Analysis of Single Cell Transcriptomics (MAST) algorithm from the R package 'MAST' version 1.8.2. For all comparisons between groups and clusters, only genes expressed by at least 10% of cells were included. The R package 'ggplot2' version 3.1.0 was used to plot the results of the differential expression analysis, showing the average log fold change of each gene on the x axis and the -log10 of the p value adjusted (Benjamini-Hochberg correction). Seurat was used to produce violin plots of the expression of select genes.

Pathway analysis
Panther was used to perform Reactome pathway analysis with genes identified from differential expression analysis ($q<0.05$) and with all genes in the dataset as background. Fisher's Exact test was with the Bonferroni correction for multiple testing. Z-scores for each pathway were calculated using the R package 'GOPlot'.

Determination of Antigen Specificity of V(D)J Sequences
To determine whether TCR sequences identified in our scTCRseq experiments on peripheral TEMRA and CSF cells had known antigen specificity, the CDR3b region of each beta chain was compared to the CDR3b repertoire from the VDJdb at https://vdjdb.cdr3.net/.

Clustering of peripheral CD8+ TEMRA and CSF cells
Individual sample expression matrices were loaded into R using the function Read10x under the 'Matrix' package v1.2-15. The expression matrix for each sample was merged into one Seurat object using the CreateSeuratObject and MergeSeurat functions. Seurat package v3.043,44 was utilized for filtering, variable gene selection, normalization, scaling, dimensionality reduction, clustering and visualization.

For manuscripts utilizing custom algorithms or software that are central to the research but not yet described in published literature, software must be made available to editors/reviewers upon request. We strongly encourage code deposition in a community repository (e.g. GitHub). See the Nature Research guidelines for submitting code & software for further information.

Data

Policy information about availability of data

All manuscripts must include a data availability statement. This statement should provide the following information, where applicable:

- Accession codes, unique identifiers, or web links for publicly available datasets
- A list of figures that have associated raw data
- A description of any restrictions on data availability

Source data for figures are provided within Extended Data Figures.

RNA-seq datasets have been deposited online in the Gene Expression Omnibus (GEO) under accession number GSE134578.

Field-specific reporting

Please select the best fit for your research. If you are not sure, read the appropriate sections before making your selection.

☒ Life sciences ☐ Behavioural & social sciences ☐ Ecological, evolutionary & environmental sciences

For a reference copy of the document with all sections, see nature.com/authors/policies/ReportingSummary-flat.pdf

Life sciences study design

All studies must disclose on these points even when the disclosure is negative.

Sample size

Our mass cytometry study measured two independent study groups (healthy vs. MCI/AD) with continuous primary endpoints. We used power analyses to determine the minimum number of study subjects required per group, which was calculated to be 42 healthy and 14 MCI/AD. We

exceded these numbers in the study by analyzing 57 healthy and 23 MCI/AD samples. We established anticipated means for our healthy cohort based on preliminary experiments and considered an enrollment ratio of 3:1 (healthy:MCI/AD) based on enrollment data from the clinic. We measured group sizes to account for a 20% increase in our MCI/AD group. Our type II error rate was set to 0.05 and our power level set to 90%. Following the study, we performed a post-hoc power analysis with our sample sizes and found our mass cytometry study to have 92.3% power.

Data exclusions

Subjects who progressed from a clinical diagnosis of mild cognitive impairment to any form of dementia besides Alzheimer's were removed from the mass cytometry analysis.

Replication

All experiments in this study were successfully replicated at least twice.

Randomization

Study participants were allocated into groups following data acquisition. Study subjects underwent a battery of neuropsychological assessments to determine group status, including: cognitive examination, evaluation of cerebellar function, deep tendon reflexes, sensory input, and motor function. The Montreal Cognitive Assessment (MoCA) examination was used to test study subjects for cognitive impairment. The MoCA assesses several cognitive domains: short-term memory recall (5 points), visuospatial abilities (4), executive functions (4), attention (1), concentration (3), working memory (1), language (6) and orientation to time and space (6). MoCA scores range between 0 and 30. A score of 26 or over is considered to be cognitively typical.

Blinding

All experimenters were blinded to group allocation during data acquisition and analysis.

Reporting for specific materials, systems and methods

Materials & experimental systems

n/a	Involved in the study
☐	☒ Unique biological materials
☐	☒ Antibodies
☐	☒ Eukaryotic cell lines
☒	☐ Palaeontology
☐	☒ Animals and other organisms
☐	☒ Human research participants

Methods

n/a	Involved in the study
☒	☐ ChIP-seq
☐	☒ Flow cytometry
☐	☒ MRI-based neuroimaging

Unique biological materials

Policy information about availability of materials

Obtaining unique materials

Fresh human brain samples are difficult to obtain under a short post-mortem window and are thus not readily available. CSF samples contain very few cells and can only be analyzed once and are thus not readily available.

Antibodies

Antibodies used

Flow cytometry was conducted using an LSRFortessa (BD Biosciences). A panel consisting of antibodies conjugated to six different fluorophores was used to classify subsets of memory T cells and for droplet-based sequencing. Antibodies used were: CD8α-Pacific blue (Clone SK1; BioLegend cat #344718), CD3-BV650 (Clone UCHT1; BD Biosciences cat #563851), CD45RA-APC-Cy7 (Clone HI100; BioLegend cat #304128), CCR7-488 (Clone 4B12; BioLegend cat #120110), IL-7Rα-PE (Clone A019D5; BioLegend cat #351304), CD27-PE-Cy7 (Clone M-T271; BioLegend #356412). For CSF cell characterization, this same panel was used, but CD19-PE-Cy5 (Clone HIB19 BioLegend cat #302210) and CD14-Qdot-705 (Clone TüK4; ThermoFisher cat #Q22137) were included. For sorting CSF T cells for TCR plate sequencing, the following antibodies were used: CD8α-PE (Clone SK1; BioLegend cat #344706), CD161-PE-Cy7 (Clone HP-3G10; BioLegend #339917), CXCR3-APC (Clone CXCR3-173; BioLegend cat #126512), CD4-APC-Alexa700 (Clone RM4-5; ThermoFisher cat #56-0042-82), CD39-APC-Cy7 (Clone A1; BioLegend cat #328226), CD38-FITC (Clone HIT2; BioLegend cat #303504), PD-1-BV421 (Clone EH12.1; BD Biosciences cat #562516), CD45RA-BV605 (Clone 5H9; BD Biosciences cat #740424), CD3-BV650 (Clone UCHT1; BD Biosciences cat #563851), CD27-BV786 (Clone L128; BD Biosciences cat #563328), CD127-BUV395 (Clone HIL-7R-M21; BD Biosciences cat #742547). All antibodies were used at 1:250 dilution. For each experiment, a compensation matrix was developed using singly stained and unstained controls or fluorescent beads, and all analysis was conducted in Cytobank.

For immunohistochemistry, primary antibodies included polyclonal rat anti-human CD3 (1:200; Abcam cat #ab28364), rabbit anti-human CD8α (1:200; Clone D8A8Y; Cell Signaling), mouse anti-Aβ (1:2000; Clone D54D2; Cell Signaling), polyclonal chicken anti-human MAP2 (1:500; Abcam cat #ab5392), mouse anti-human granzyme-A (1:200; Clone GA6; Abcam), rat anti-mouse CD8a (Clone 4SM15; eBioscience cat #14-0808-82) and polyclonal rabbit anti-mouse NEFH (Abcam cat #ab8135). For mouse Aβ plaque

staining, ThioflavinS (1 mg/mL, 1:625, Sigma) was added to the secondary antibody solution.

Validation

Each primary antibody was validated using proper fluorophore controls and positive signal was evaluated versus an unstained sample. All antibodies have been previously published by our group (Han et al., Nat. Biotech., 2014). All antibodies are from reputable vendors and come with validation statements on the manufacturer's website.

Eukaryotic cell lines

Policy information about cell lines

Cell line source(s)

SKW-3 cells were provided by Mark Davis' lab (Stanford). Lenti-X 293T cell line was acquired from Takara (cat #632180).

Authentication

Verification of TCR deficiency in SKW-3 cells line was conducted by flow cytometry against TCRab. 293T cells were not authenticated, but functionally produced lenti viruses.

Mycoplasma contamination

Negative for mycoplasma

Commonly misidentified lines
(See ICLAC register)

SKW-3 cells are commonly misidentified as KE-37 cells. Our cells were verified to lack TCRs and functionally behave like T cells when transduced with T cell receptors.

Animals and other organisms

Policy information about studies involving animals; ARRIVE guidelines recommended for reporting animal research

Laboratory animals

APP/PS1 mice expressing a chimeric mouse/human mutant amyloid precursor protein (Mo/HuAPP695swe) and a mutant human presenilin 1 (PS1-dE9) directed to CNS neurons under the prion protein promoter were used (The Jackson Laboratory). Mice were housed at the Paracelsus Medical University Salzburg in groups under standard conditions at a temperature of 22°C and a 12 h light/dark cycle with ad libitum access to standard food and water. Over 10 mice aged 9-10 months comprising both sexes were randomly analyzed in an unblinded manner. Animal care, handling, genotyping and experiments were approved by Paracelsus Medical University Salzburg ethical committees.

Wild animals

The study did not involve wild animals.

Field-collected samples

The study did not involve samples collected from the field.

Human research participants

Policy information about studies involving human research participants

Population characteristics

A total of 164 subjects from four separate cohorts were used in this study. The 164 subjects used in this study included 97 healthy, 31 MCI, 28 AD and 8 PD. The average age for healthy subjects was 72.52 ± 6.96 (mean±standard deviation), for MCI subjects: 70.97 ± 7.82, for AD subjects: 70.74 ± 7.01 and for PD subjects: 67.25 ± 7.01. Average cognitive score for healthy subjects was 27.17 ± 2.32, MCI: 23.39 ± 4.31, AD: 11.05 ± 7.32 and PD: 27.29 ± 1.70. All subjects were free from acute infectious diseases and in good physical condition. Patients were confirmed to have neurodegeneration by measurement of biomarkers, including neurofilament, Aβ and tau (Quanterix). Group characteristics, including demographic, genetic, clinical and biomarker data for each group are presented in Extended Data Table 10.

Recruitment

Study subjects were recruited through Stanford's NIH-funded Alzheimer's Disease Research Center (ADRC), the UC San Diego ADRC and the UC San Francisco ADRC by general solicitation. The racial makeup of study subjects reflects that of the Stanford area and should be considered when analyzing these results.

Flow Cytometry

Plots

Confirm that:

☒ The axis labels state the marker and fluorochrome used (e.g. CD4-FITC).

☒ The axis scales are clearly visible. Include numbers along axes only for bottom left plot of group (a 'group' is an analysis of identical markers).

☒ All plots are contour plots with outliers or pseudocolor plots.

☒ A numerical value for number of cells or percentage (with statistics) is provided.

Methodology

Sample preparation

PBMCs were isolated from blood by layering diluted blood (1:1 in PBS) on top of an equal volume of Ficoll, followed by centrifugation and isolation of the buffy coat. PBMC samples were stored over the course of a three-year period. Average PBMC viability for patient samples following sample thawing was 79% while the average viability for control samples was 77%.

CSF was collected by lumbar puncture, then centrifuged at 300G to pellet immune cells. CSF samples were checked for blood

contamination by resuspending the pelleted cells in 100 µl of CSF and mixing 10 µl (10%) CSF with 10 µl trypan blue to assess red blood cell content and viability. Cells were visualized on a TC20 automated cell counter (BioRad) and cell viability and presence/absence of red blood cells was recorded. CSF samples contaminated with blood were removed from the study. The resuspended cells were then mixed with 900 µl Recovery Cell Culture Freezing Medium (Thermo Fisher). All Samples were frozen overnight at -80°C in a Mr. Frosty freezing container (Thermo Fisher) and transferred the following day to liquid nitrogen for storage. CSF samples were stored <6 months prior to analysis.

Instrument	BD LSRFortessa
Software	Cytobank v6.3.0.5
Cell population abundance	10,000 live leukocytes were gated for downstream SPADE analysis for mass cytomtery. For peripheral TEMRA scRNAseq, 50,000 peripheral cells were sorted then loaded into a 10X controller at 1,000 cells/ul. For CSF plate-seq, cells were sorted into individual wells of a 96-well plate. For CSF cell drop-seq, all cells from each CSF sample were live sorted, pelleted then loaded into the 10X controller. Since CSF cells are in low abundance (approximately 1 cell per ul), processing of samples (i.e. repetitive centrifugation) was carefully limited to achieve greater numbers of cells.
Gating strategy	Cells were distinguished from debris by SSC/FSC, then signlets were selected on a FSC-H/FSC-W plot. Cells doubly positive for CD3 and CD8 were gated (~10^3 expression in each channel)

☒ Tick this box to confirm that a figure exemplifying the gating strategy is provided in the Supplementary Information.

Magnetic resonance imaging

Experimental design

Design type	T1 weighted MRI Scans were acquired using Axial 3D fast spoiled gradient sequence (GE Discovery 750).
Design specifications	n/a (this is structural MRI data, not functional)
Behavioral performance measures	n/a

Acquisition

Imaging type(s)	Structural
Field strength	3 Tesla
Sequence & imaging parameters	The imaging parameters were optimized for gray/white matter tissue contrast with a repetition time of 5.9ms, echo time 2ms, flip angle 15, field-of-view 220mm, matrix size 256 x 256, slice thickness 1mm and 2 NEX.
Area of acquisition	Whole brain

Diffusion MRI ☐ Used ☒ Not used

Preprocessing

Preprocessing software	All the suggested T1-weighted scans use GE's "BRAVO" sequence. It is an IR-prep, fast SPGR sequence with parameters tuned to optimize brain tissue contrast.
Normalization	To correct for sex differences, we normalized all volumetric measurements to total intracranial volume for each patient.
Normalization template	MNI305 atlas was used for normalization. First stage was affine registration, followed by initial volumetric labeling. The variations due to biasing were corrected. Finally, a high dimensional nonlinear volumetric alignment to the MNI305 atlas was performed, and once preprocessing completed, the volume was labeled.
Noise and artifact removal	n/a These are structural data, not fMRI data
Volume censoring	n/a These are structural data, not fMRI data

Statistical modeling & inference

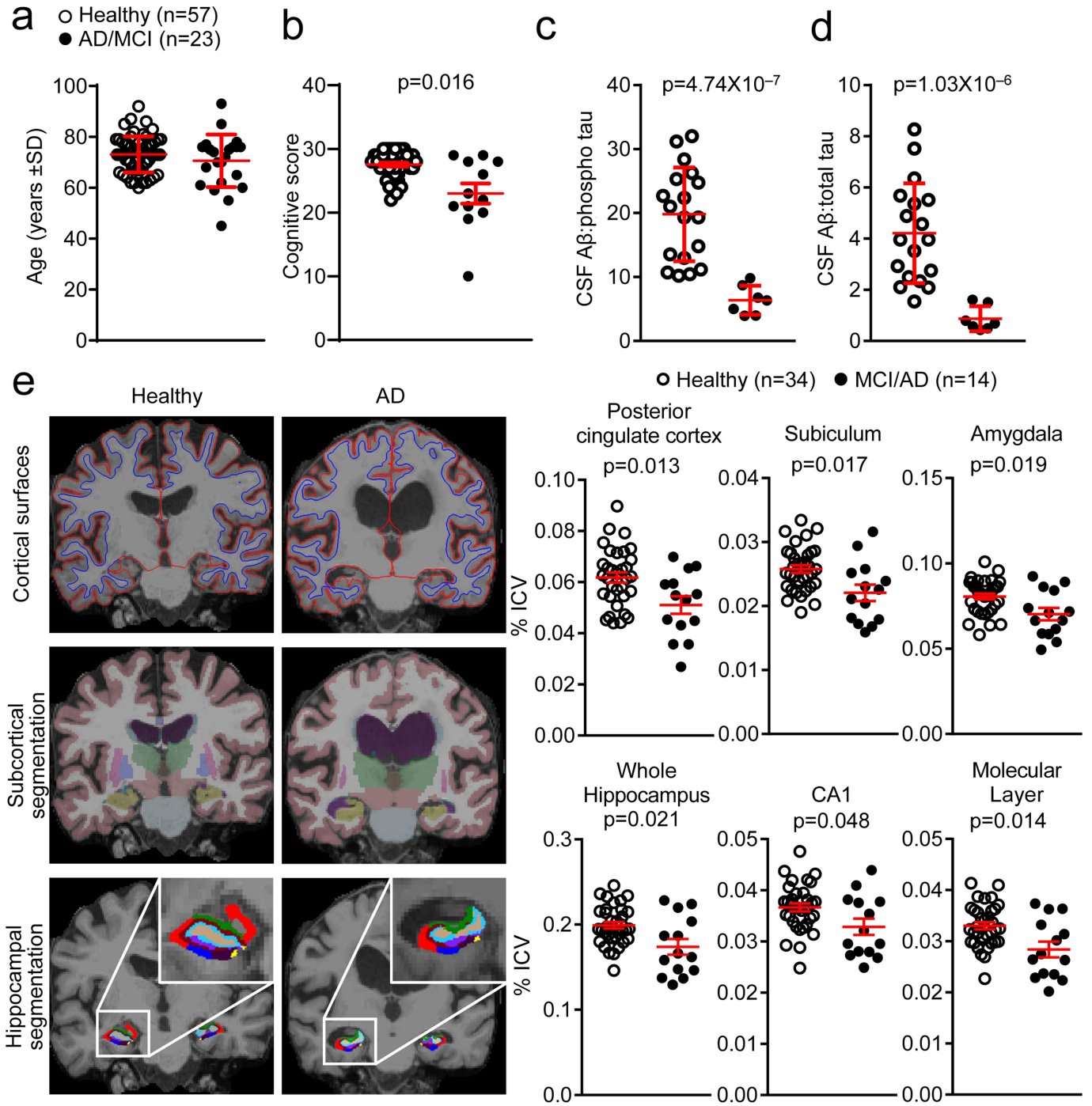
Model type and settings	Comparisons between groups of subjects were performed using multivariate analysis of covariance, where age served as a covariate.
Effect(s) tested	Increase/decrease in brain region volume

Specify type of analysis: ☐ Whole brain ☒ ROI-based ☐ Both

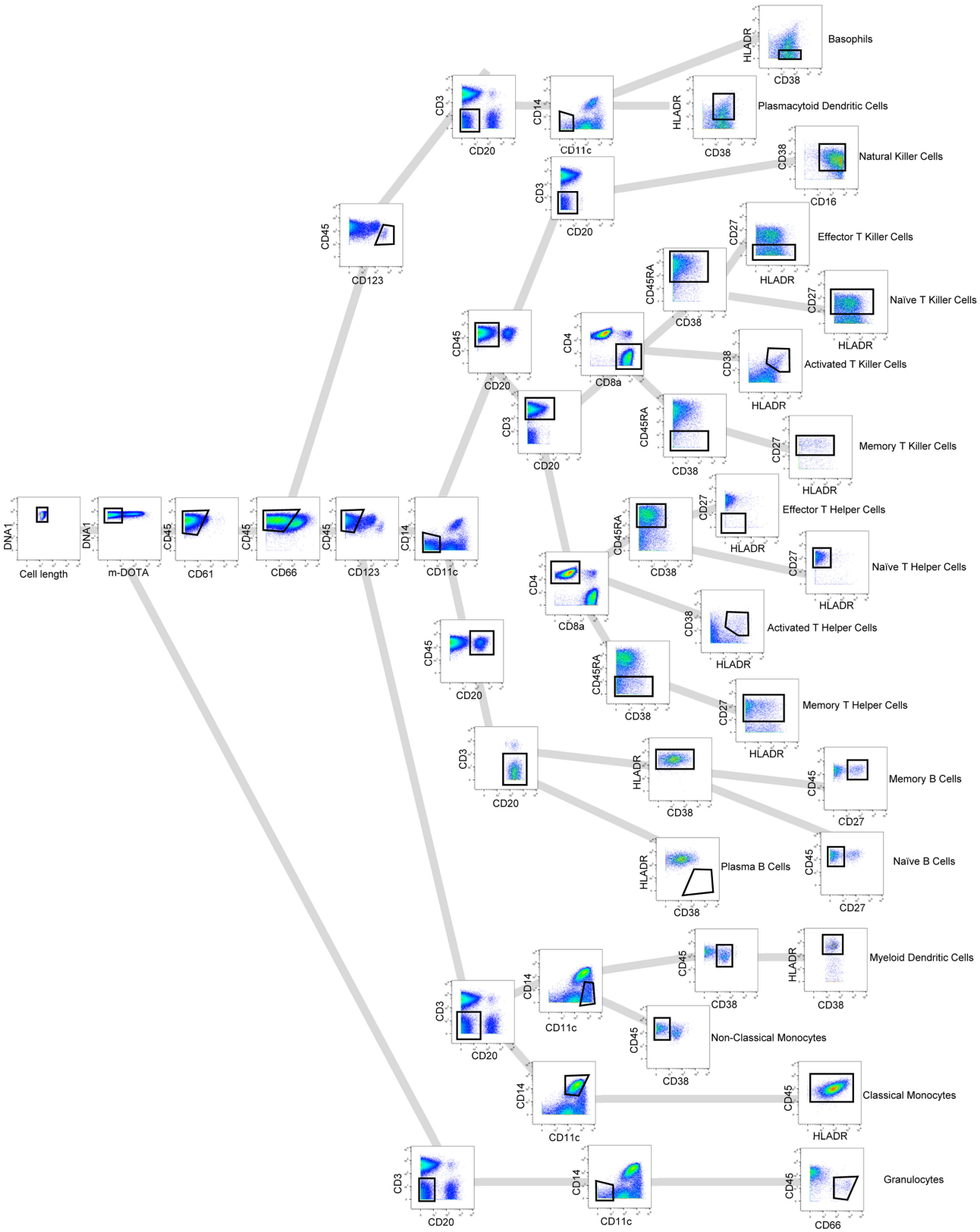
Anatomical location(s)	Subcortical segmentation including both left and right of Cerebral White Matter, Cerebral Cortex, Lateral Ventricle, Inferior Lateral Ventricle, Cerebellum White Matter, Cerebellum Cortex, Thalamus, Caudate, Putamen, Pallidum, Hippocampus, Amygdala, Lesion, Accumbens area, Vessel, Third Ventricle, Fourth Ventricle, Brain Stem, Cerebrospinal Fluid
Statistic type for inference (See Eklund et al. 2016)	n/a
Correction	n/a

Models & analysis

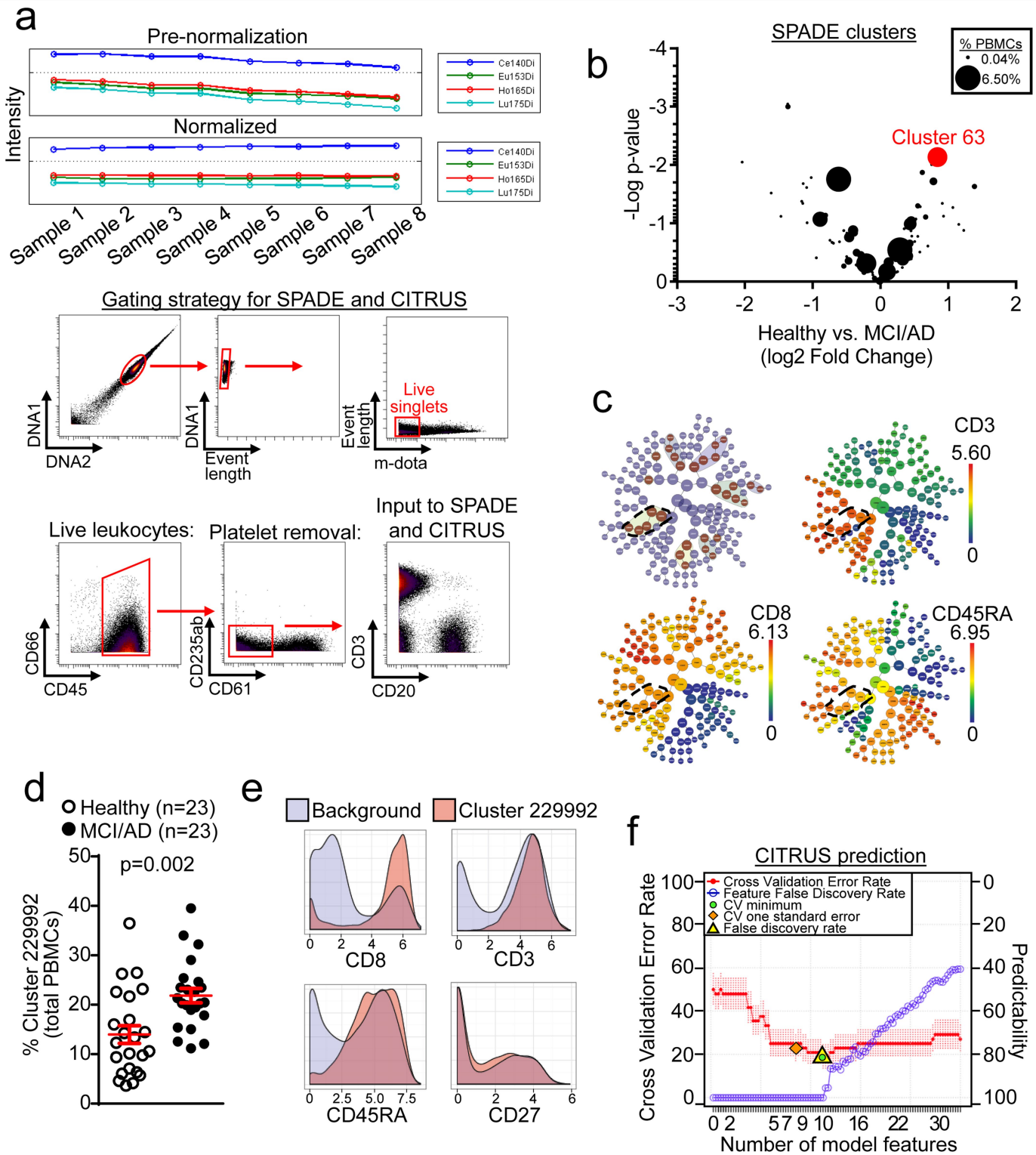
n/a	Involved in the study
☒	☐ Functional and/or effective connectivity
☒	☐ Graph analysis
☒	☐ Multivariate modeling or predictive analysis



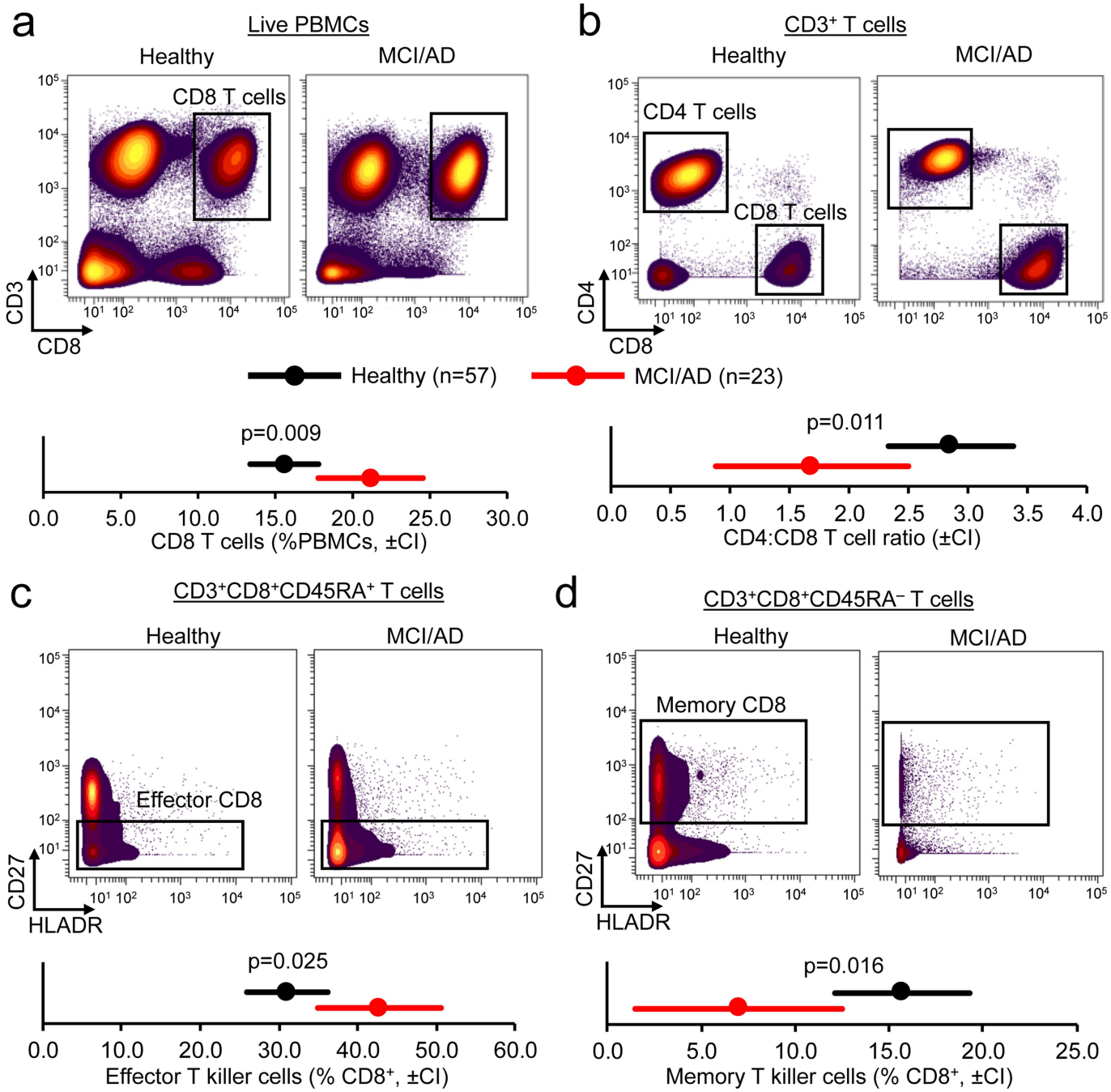
Extended Data Fig. 1 | Clinical measures of subjects from mass cytometry experiments. a, Cohort 1 groups were age-matched and included 57 healthy subjects and 23 patients with MCI or AD. **b**, Cognitive scoring shows significantly decreased cognitive scores in patients with MCI or AD. Note that not all patients with MCI or AD could complete a cognitive exam and these patients are thus not included in this analysis. Unpaired two-sided *t*-test with Welch's correction ($n = 51$ healthy; $n = 12$ MCI or AD); mean ± s.e.m. **c**, **d**, Quantification of CSF Aβ as a ratio to phosphorylated tau (**c**) or total tau (**d**) reveals significantly reduced ratios in patients with MCI or AD. Unpaired two-sided *t*-test with Welch's correction ($n = 18$ healthy, $n = 7$ MCI or AD); mean ± s.e.m. **e**, Top, representative MRI images show reduction in cortical grey matter in patients with AD. Middle, bottom, representative MRI images of several brain regions as measured by subcortical segmentation and hippocampal segmentation. Right, quantification of MRI images of patients with MCI or AD compared to control individuals shows significant reductions in the percentage of the intracranial volume (ICV) of brain regions classically associated with AD pathology. CA1, cornu ammonis area 1. Unpaired two-sided *t*-test; mean ± s.e.m.



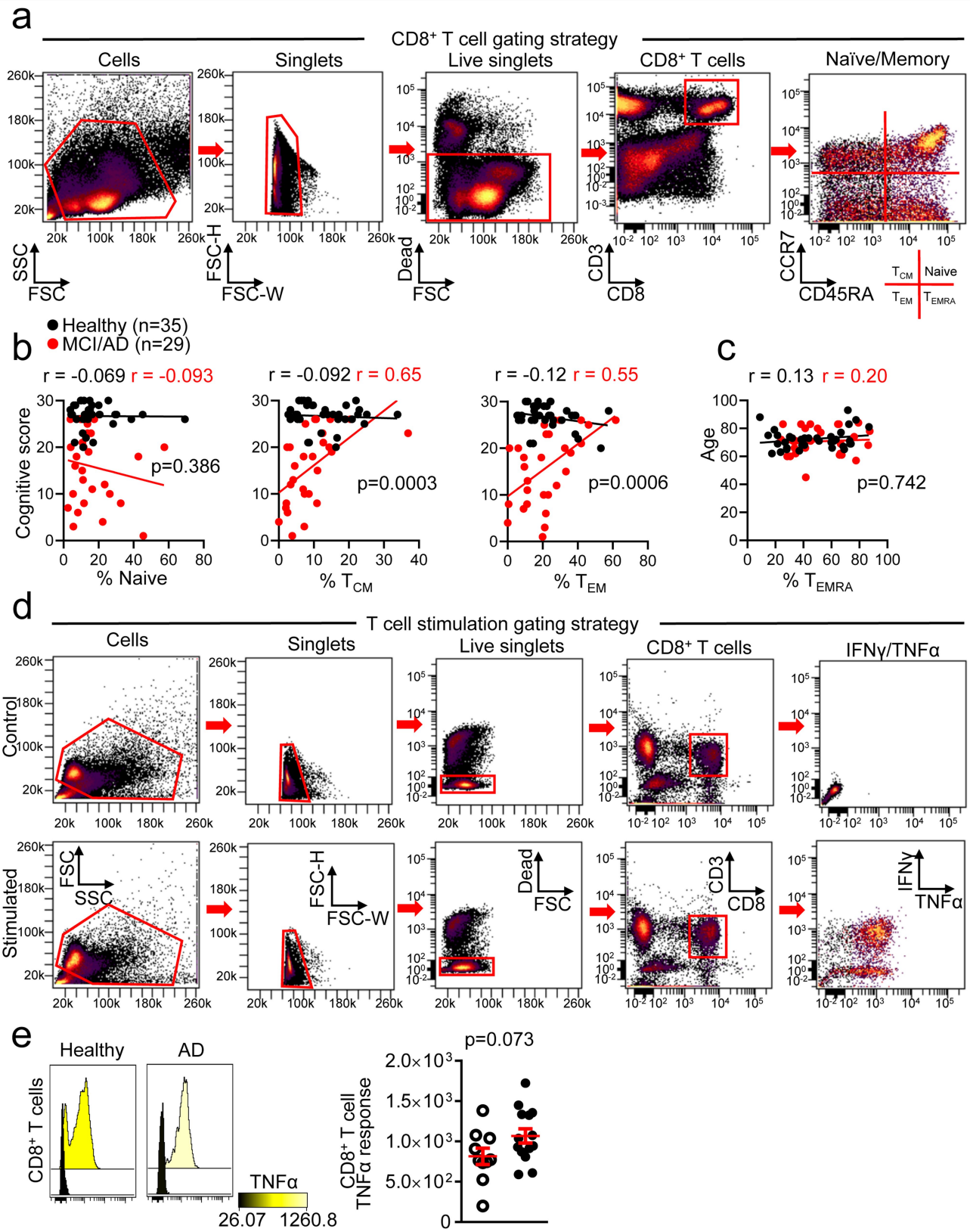
Extended Data Fig. 2 | Gating strategy for identifying immune cell populations from mass cytometry data. A gating strategy was used to identify populations of immune cells by mass cytometry.



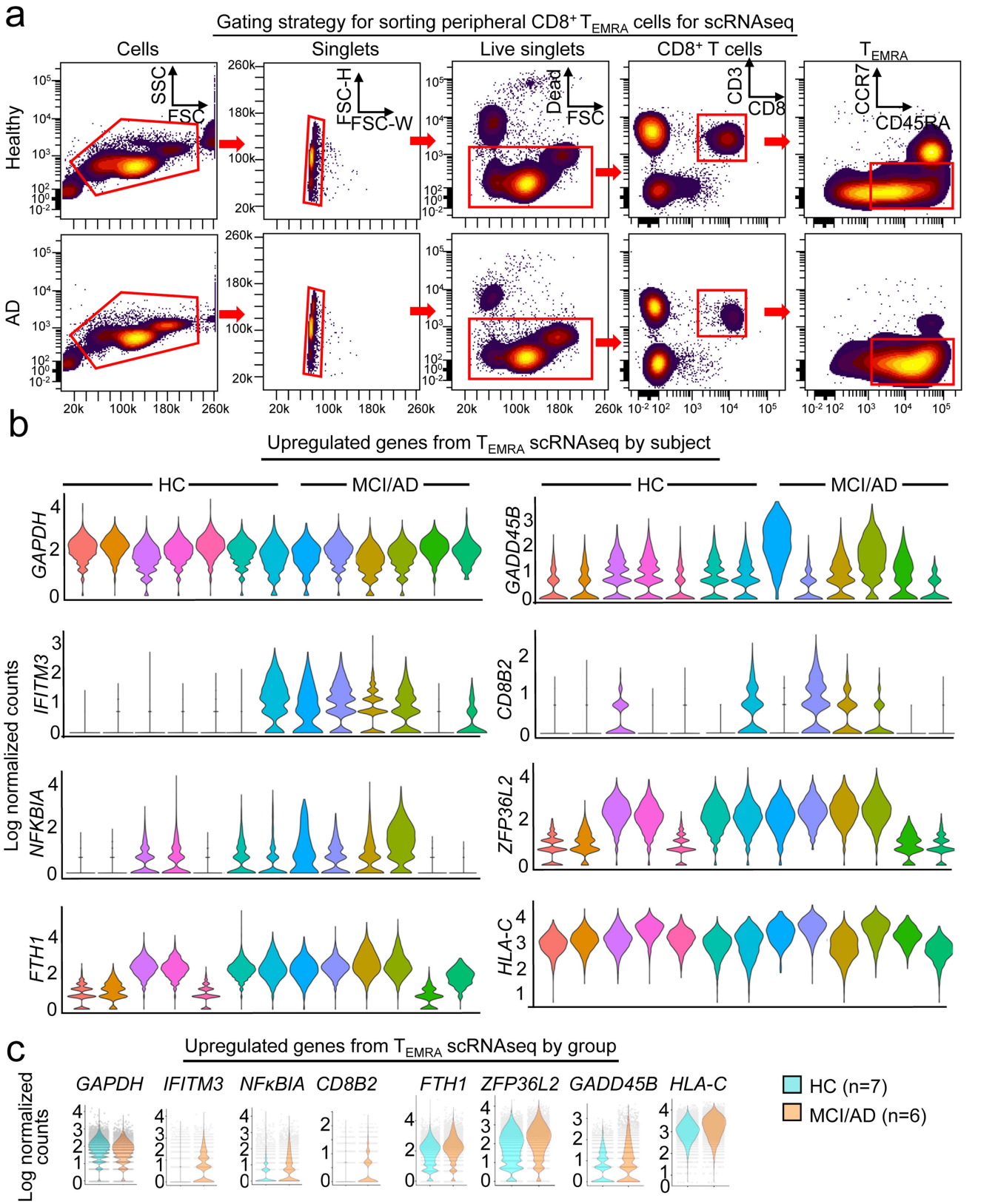
Extended Data Fig. 3 | Mass cytometry SPADE and CITRUS clustering shows increased numbers of CD8$^+$ T_{EMRA} cells in MCI or AD. a, Normalization of mass cytometry data was performed before all analyses. A gating strategy for input into downstream analyses is shown. Live, single leukocytes were selected for analysis. **b**, Plotting of clusters by *P* value and fold change of each cluster reveals cluster 63 as the most highly increased cluster among patients with MCI or AD. Clusters are sized according to their percentage of total PBMCs. Unpaired two-sided *t*-test ($n = 57$ healthy; $n = 23$ MCI or AD). **c**, CITRUS clustering showing significant differentiating populations (top left). Cluster 229992 and its significant daughter populations are outlined. Expression of CD3, CD8 and CD45RA shows that cluster 229992 corresponds to CD8$^+$ T_{EMRA} cells. **d**, Quantification of cluster 229992 cells as a percentage of total PBMCs for individual subjects. Percentages of this cluster are significantly higher in patients with MCI or AD than healthy control individuals. Unpaired two-sided *t*-test with Welch's correction; mean ± s.e.m. **e**, Marker expression of cluster 229992 shows it to be a CD3$^+$CD8$^+$CD45RA$^+$CD27$^-$ T_{EMRA} population. **f**, The regularized supervised learning algorithm from CITRUS predicts disease group with a 20% error rate (80% positive predictability). The number of model features increases from left to right. The most predictive model is shown as the lowest cross validation error rate (red line) constrained by the false discovery rate (yellow triangle).



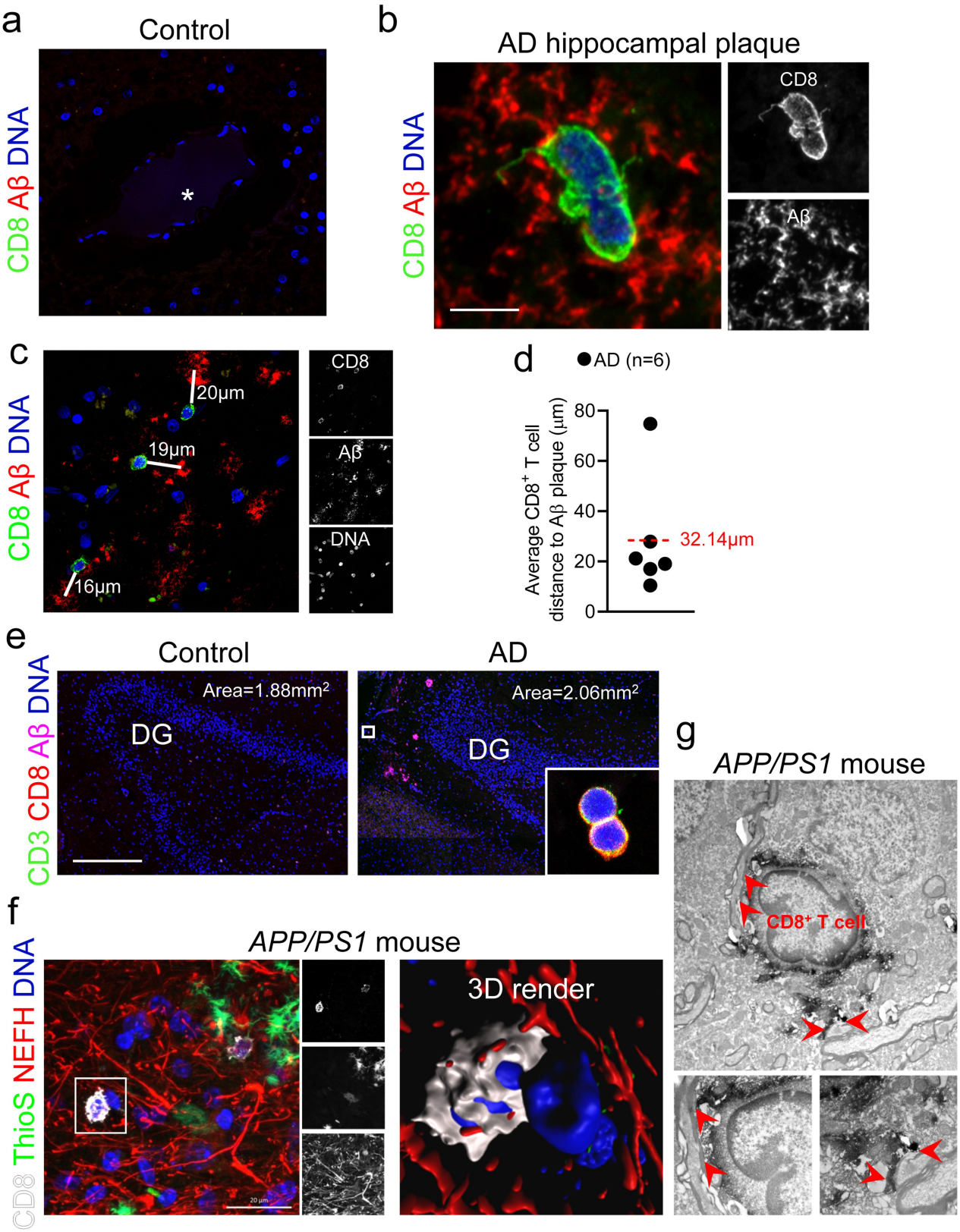
Extended Data Fig. 4 | Altered CD8⁺ T cell subsets in PBMCs from patients with MCI or AD. a, Mass cytometry plots of live PBMCs show increased abundance of $CD3^+CD8^+$ T cells in patients with MCI or AD. **b**, Gating of $CD3^+$ T cells into CD4 and CD8 populations shows increased prevalence of $CD8^+$ T cells in patients with MCI or AD. **c**, **d**, Significantly increased effector $CD8^+$ T cells (**c**) and significantly reduced memory $CD8^+$ T cells (**d**) in patients with MCI or AD. Multivariate analysis of covariance (MANCOVA) using age as a covariate, followed by post-hoc pairwise comparisons of estimated marginal means by unpaired two-sided *t*-test. Bonferroni correction for multiple comparisons. Confidence intervals (CI) of 95% are shown.



Extended Data Fig. 5 | Correlations of memory T cell populations with cognitive scores. a, Gating strategy for measuring memory T cell populations. **b**, Linear regression analysis correlating CD8$^+$ T cell populations with cognitive scores indicates a positive relationship between T_{EM} and T_{CM} CD8$^+$ T cells and no relationship with naive cells. The significance of the difference between datasets was measured by ANCOVA. **c**, The relationship between the percentage of CD8$^+$ T_{EMRA} cells and cognitive score was not influenced by age. The significance of the difference between the two datasets was measured by analysis of covariance (ANCOVA). Pearson's correlation *r* values are shown for each group (**b**, **c**). **d**, Gating strategy for T cell stimulation experiments. **e**, Increased intracellular TNF cytokine response in PMA–ionomycin-stimulated CD8$^+$ T cells from patients with MCI or AD. Unpaired two-sided *t*-test with Welch's correction ($n = 10$ healthy; $n = 14$ MCI or AD); mean ± s.e.m.

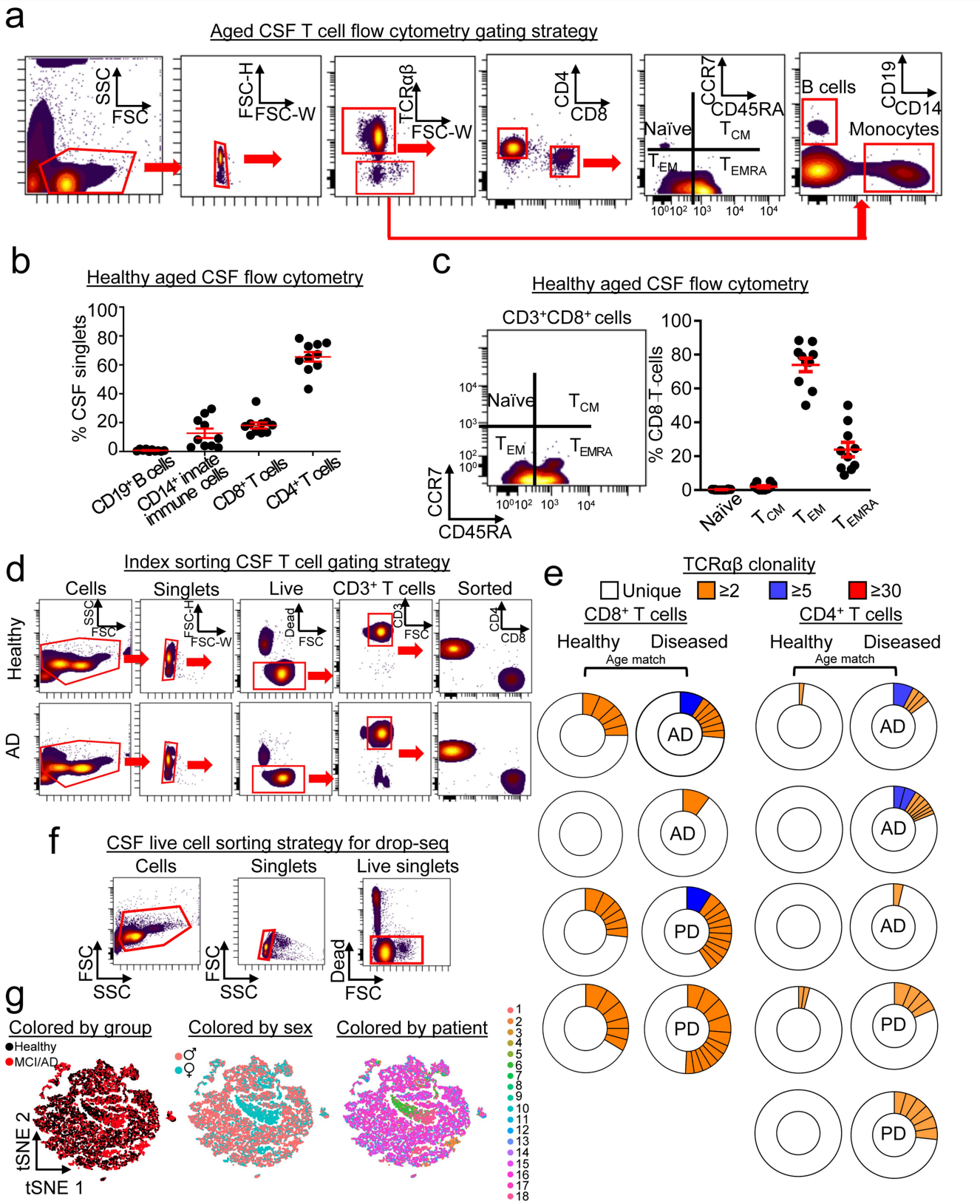


Extended Data Fig. 6 | Analysis of peripheral CD8$^+$ T_{EMRA} cells by scRNA-seq. **a**, Gating strategy for sorting peripheral CD8$^+$ T_{EMRA} cells for scRNA-seq. **b**, Differential expression analysis by scRNA-seq of CD8$^+$ T_{EMRA} cells from patients with MCI or AD versus CD8$^+$ T_{EMRA} cells from healthy individuals shows significantly increased expression of genes that are involved in T cell signalling, including *IFITM3*, *NFKBIA* and *CD8B2*. Violin plots show average log-normalized counts for significantly upregulated genes in MCI or AD CD8$^+$ T_{EMRA} cells by individual patient ($n = 7$ healthy; $n = 6$ MCI or AD). **c**, Violin plots show average log-normalized counts for significantly upregulated genes in MCI or AD CD8$^+$ T_{EMRA} cells by group. *GAPDH* is shown as a control. Each dot represents a single cell.

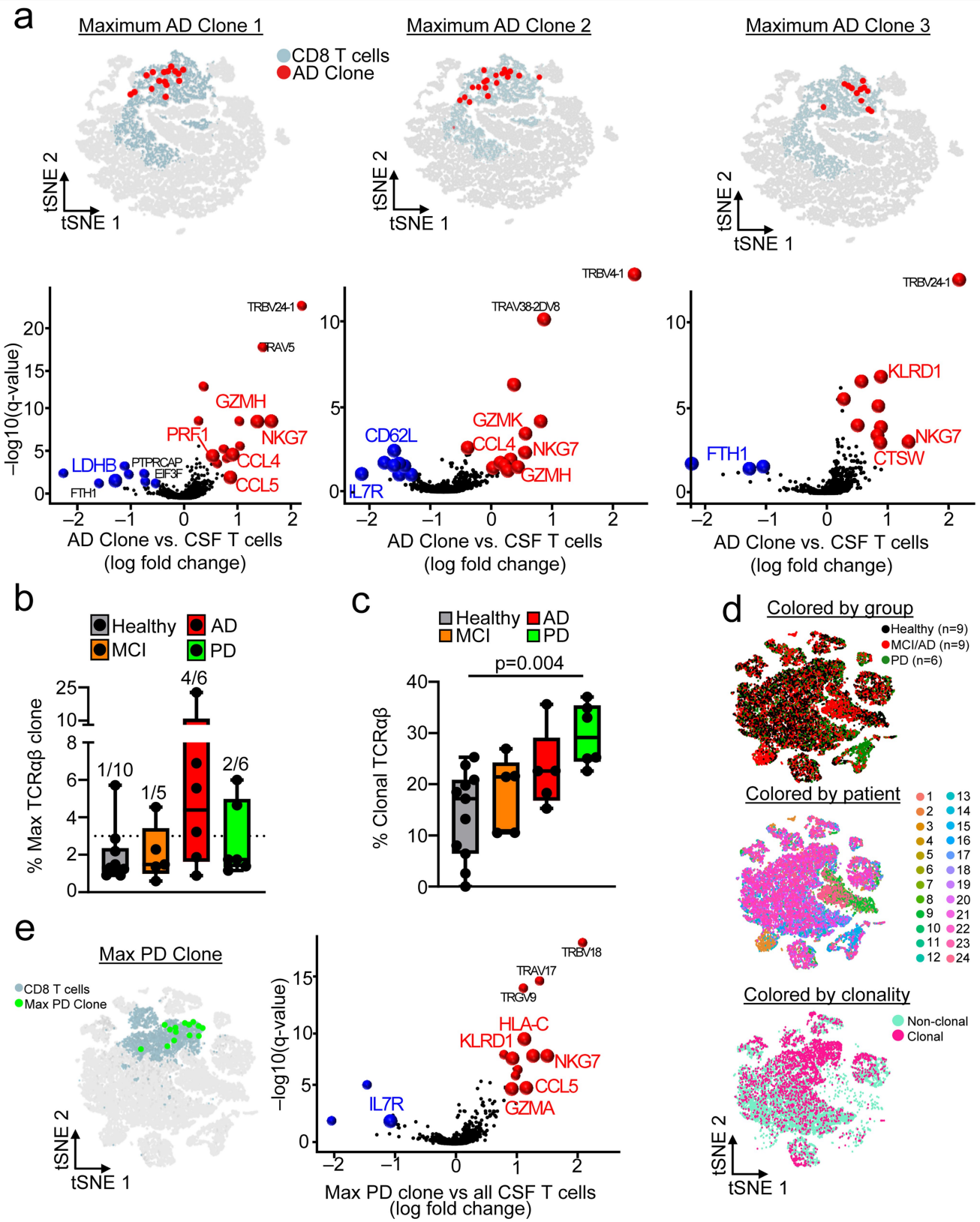


Extended Data Fig. 7 | See next page for caption.

Extended Data Fig. 7 | Histological analysis of CD8$^+$ T cells in hippocampi from patients with AD and from APP/PS1 mice. a, A blood vessel in the brain of a control (non-neurological disease) patient shows a lack of extravascular CD8$^+$ T cells. Asterisk indicates the blood vessel lumen. **b**, A CD8$^+$ T cell within an Aβ plaque. Scale bar, 5 µm. **c**, CD8$^+$ T cells in the AD-affected hippocampus in close proximity to Aβ plaques. White lines measure the distances from each cell to the nearest plaque centre. Data in **a**, **b** were replicated in at least three independent experiments. **d**, Quantification of the average distance from CD8$^+$ T cells to the nearest Aβ plaque. The dashed red line indicates the average of all cells. **e**, Representative images of the dentate gyrus that were used to quantify CD3$^+$CD8$^+$ T cells in the hippocampi of control individuals and patients with AD. Inset shows two CD3$^+$CD8$^+$ T cells. Sizes of the area plots used for quantification are shown for each image. Scale bar, 500 µm. **f**, Association of a CD8$^+$ T cell with NEFH$^+$ neuronal processes by immunohistochemistry and 3D modelling in the APP/PS1 mouse model of cerebral amyloidosis. **g**, Electron microscopy showing an association of a CD8$^+$ T cell with neuronal processes. Red arrowheads indicate areas in which the CD8$^+$ T cell associates with neuronal processes. Data in **e**–**g** were replicated in at least two independent experiments.

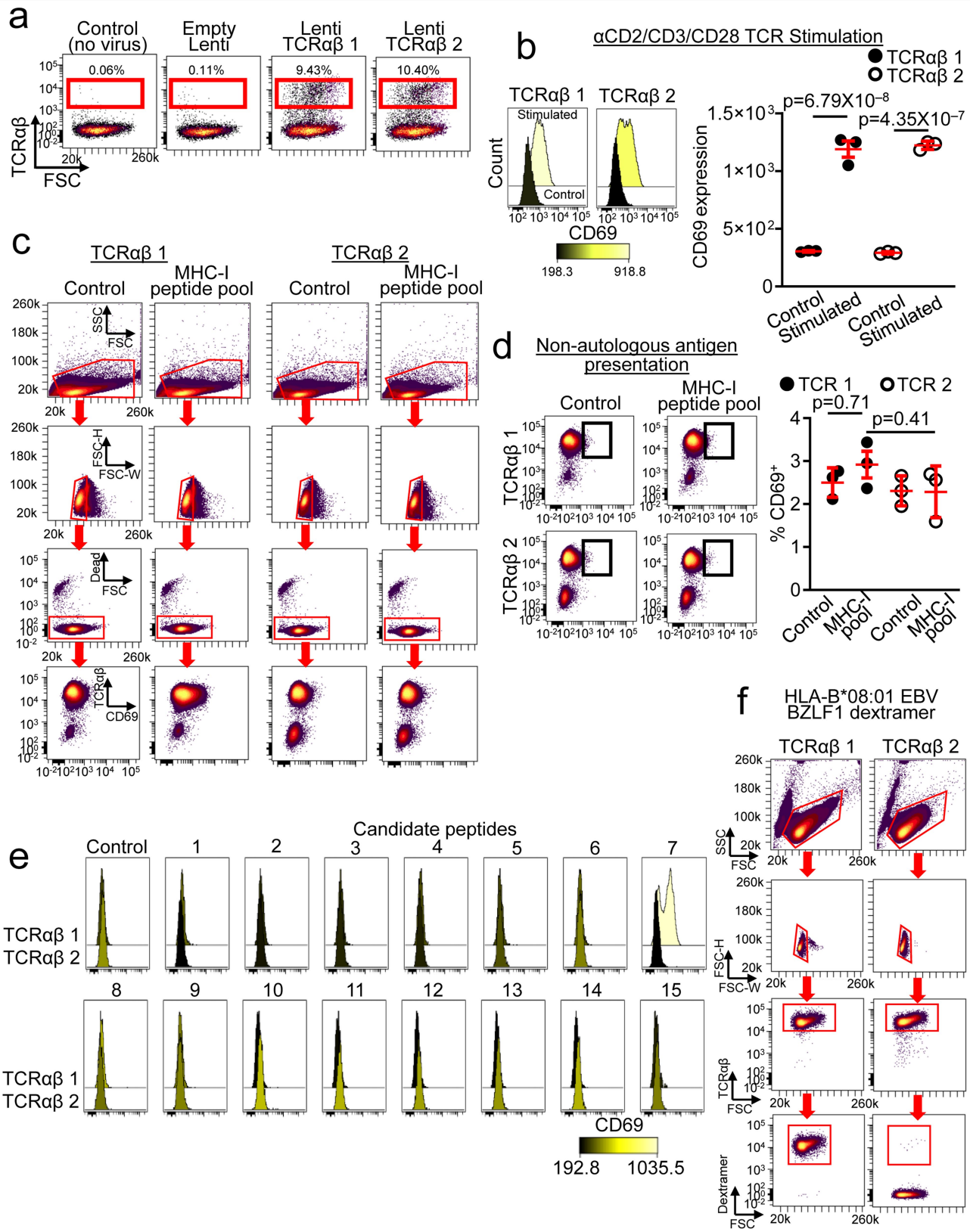


Extended Data Fig. 8 | Clonal expansion of T cells in the CSF. a, Gating strategy for enumerating T cell subtypes in CSF from healthy elderly individuals. **b**, Quantification of CSF cells shows that the majority of cells are T cells, with a minority population of $CD14^+$ monocytes and a quantifiably minor number of $CD19^+$ B cells ($n = 10$ healthy subjects); mean ± s.e.m. **c**, Quantification of $CD8^+$ T cell subsets shows that the majority of cells are T_{EM} or T_{EMRA} cells ($n = 10$ healthy subjects); mean ± s.e.m. **d**, Single-cell sorting of CSF cells shows that CD4 and CD8 T cells were sorted from control individuals and patients with AD. Data were replicated in two independent experiments. **e**, Donut plots depicting CSF clonality in plate-seq samples. Clones are coloured by their proportion of the total TCRαβ sequences for each subject. **f**, Gating strategy for drop-seq experiments. Live CSF cells were sorted using a live/dead marker. **g**, Multidimensional reduction and visualization by *t*-SNE shows distribution of CSF cells by group, sex and patient ($n = 9$ healthy, $n = 9$ MCI or AD).



Extended Data Fig. 9 | See next page for caption.

Extended Data Fig. 9 | Clonally expanded CD8$^+$ T cells in CSF from patients with AD and patients with PD. a, The top individual clones in AD were assessed by combining scRNA-seq and scTCR-seq datasets. A MAST differential expression test with Benjamini–Hochberg correction was conducted to compare CD8$^+$ T cell maximum clones (n = 12–18 cells) from patients with MCI or AD against all CSF T cells. Note the colocalization of AD clones with CD8$^+$ clusters on the t-SNE plots. **b**, Separate analysis of patients with MCI, AD and PD by percentages of maximum clones revealed an enrichment of highly expanded clones (defined as comprising 3% or more of all TCRαβ sequences; indicated by dotted line) in patients with these diseases. Only one out of ten healthy subjects had a highly expanded clone in their CSF, versus four out of six patients with AD, two out of six patients with PD and one out of five patients with MCI. **c**, Quantification of overall clonality (defined as the percentage of total TCRαβ sequences that are identical to one or more TCRαβ sequences) in the four groups of cohort 4. Significance was measured by two-way ANOVA followed by Tukey's multiple comparisons test. Only samples with detectable clones were included in the analysis (n = 11 healthy; n = 5 MCI; n = 5 AD; n = 6 PD). Box plots in **b**, **c** Box plots show median and 25th to 75th percentiles, and whiskers indicate the minimum and maximum values. **d**, Gene-expression analysis was conducted on all 24 samples and clustered by t-SNE. Clusters were composed of a mixture of groups, patients, clonal and non-clonal cells. **e**, Genes (encoding cytotoxic effector proteins) that showed increased expression in a maximum PD clone (n = 14 cells) were analogous to those observed to be overexpressed in AD clones. MAST differential expression test with Benjamini–Hochberg correction.



Extended Data Fig. 10 | See next page for caption.

Extended Data Fig. 10 | EBV BZLF1 antigen identification in the CSF of patients with AD. a, TCRβ chains derived from GLIPH were used to clone two full TCRαβ TCRs that were introduced into TCR-deficient SKW-3 cells by lentiviral transduction. TCRαβ 1 and TCRαβ 2 cell lines expressed TCRαβ by flow cytometry but controls (no virus and empty lenti viral vector) did not express TCRαβ. Data were replicated in three independent experiments. **b**, Both TCRαβ 1 and TCRαβ 2 cells upregulate the activation marker CD69 after stimulation with αCD2/CD3/CD28 beads ($n = 3$ per group). One-way ANOVA ($F(3,8) = 204.02$, $P = 6.78 \times 10^{-8}$) with Tukey's test for multiple comparisons; mean ± s.e.m. **c**, Gating strategy for MHC-I peptide pool experiments. **d**, TCRαβ 1 and TCRαβ 2 were presented with antigens in a non-autologous fashion (mismatch between fibroblast and TCR). No significant differences in reactivity were detected in either cell line. One-way ANOVA ($F(3,8) = 1.16$, $P = 0.38$) with Tukey's test for multiple comparisons; mean ± s.e.m. **e**, Individual histograms of autologous candidate peptide stimulations. CD69 expression is shown for control DMSO and each peptide for both cell lines. Note the increased expression of CD69 induced by peptide 7 in TCRαβ 1 cells. Data were replicated in three independent experiments. **f**, Gating strategy for quantifying HLA-B*08:01 EBV BZLF1 dextramer positivity.

Corresponding author(s): Tony Wyss-Coray
twc@stanford.edu

Reporting Summary

Nature Research wishes to improve the reproducibility of the work that we publish. This form provides structure for consistency and transparency in reporting. For further information on Nature Research policies, see Authors & Referees and the Editorial Policy Checklist.

Statistical parameters

When statistical analyses are reported, confirm that the following items are present in the relevant location (e.g. figure legend, table legend, main text, or Methods section).

n/a	Confirmed	
☐	☒	The exact sample size (*n*) for each experimental group/condition, given as a discrete number and unit of measurement
☐	☒	An indication of whether measurements were taken from distinct samples or whether the same sample was measured repeatedly
☐	☒	The statistical test(s) used AND whether they are one- or two-sided *Only common tests should be described solely by name; describe more complex techniques in the Methods section.*
☐	☒	A description of all covariates tested
☐	☒	A description of any assumptions or corrections, such as tests of normality and adjustment for multiple comparisons
☐	☒	A full description of the statistics including central tendency (e.g. means) or other basic estimates (e.g. regression coefficient) AND variation (e.g. standard deviation) or associated estimates of uncertainty (e.g. confidence intervals)
☐	☒	For null hypothesis testing, the test statistic (e.g. *F*, *t*, *r*) with confidence intervals, effect sizes, degrees of freedom and *P* value noted *Give P values as exact values whenever suitable.*
☒	☐	For Bayesian analysis, information on the choice of priors and Markov chain Monte Carlo settings
☐	☒	For hierarchical and complex designs, identification of the appropriate level for tests and full reporting of outcomes
☐	☒	Estimates of effect sizes (e.g. Cohen's *d*, Pearson's *r*), indicating how they were calculated
☐	☒	Clearly defined error bars *State explicitly what error bars represent (e.g. SD, SE, CI)*

Our web collection on statistics for biologists may be useful.

Software and code

Policy information about availability of computer code

Data collection	Brain MRI quantifications were conducted using FreeSurfer 6.0. Confocal images were acquired using ZEN 2 Blue Edition (Zeiss). Electron microscopy images were acquired with Imaging software was Image SP v1.2.7.31 (SIS, Soft Image System). Clonality measurements were calculated using R Studio. Mass cytomtery analysis was conducted using Cytobank. For TCR network analysis, to depict connections between diagnosis groups, patient IDs and clonotypes, we used the qgraph package for R (Epskamp et al. 2012). Only TCRs with alpha and beta chain sequenced were included in the analysis and non-clonal cells were filtered out. Unweighted networks were generated with all subjects and split per diagnosis group. Sacha Epskamp, Angelique O. J. Cramer, Lourens J. Waldorp, Verena D. Schmittmann, Denny Borsboom (2012). qgraph: Network Visualizations of Relationships in Psychometric Data. Journal of Statistical Software, 48(4), 1-18. URL http://www.jstatsoft.org/v48/i04/.
Data analysis	Normalization of mass cytometry data was achieved using the Matlab bead normalization tool.

Data analysis

3D reconstructions of mouse CD8 T cells were performed using Imaris v9.1.2 (Bitplane).

For volumetric measurements in Extended Data Figure 1: for subcortical segmentation, we used the "recon-all" command. For hippocampal segmentation, we appended the flag "-hippocampal-subfields-T1" to the "recon-all" command for each patient. To correct for sex differences, we normalized all volumetric measurements to total intracranial volume for each patient.

TCR clonality analysis of CSF cells by plate-seq, we used Excel. TCRs with two or more identical CDR3b regions and CDR3a regions were defined as clonal. R was used to calculate a proportion of clonotypes' sum of reads to the overall number of reads in a repertoire (∑ reads of clonotype)/(∑ reads for all clonotypes). For TCRs sequenced using Single cell V(D)J technology (10X Genomics), clonality was determined by the cellranger vdj pipeline as previously described. Clonotypes were determined from grouping of cell barcodes that shared the same set of productive CDR3 nucleotide sequences. The sequences of all contigs from all cells within a clonotype were then assembled to produce a clonotype consensus sequence. Clonality was integrated into the Seurat gene expression analysis by adding clonality information to the metadata. For TCR network analysis, to depict connections between diagnosis groups, patients and clonotypes, we used the qgraph package for R. Only TCRs with full α and β chain sequences were included in the analysis. Unweighted networks were generated with all subjects and split per diagnosis group.

Analysis of scRNAseq data
Differential Expression
Markers for each cluster were determined by comparing the cells of each cluster to all other cells using the FindMarkers function in Seurat with the Model-based Analysis of Single Cell Transcriptomics (MAST) algorithm from the R package 'MAST' version 1.8.2. For all comparisons between groups and clusters, only genes expressed by at least 10% of cells were included. The R package 'ggplot2' version 3.1.0 was used to plot the results of the differential expression analysis, showing the average log fold change of each gene on the x axis and the -log10 of the p value adjusted (Benjamini-Hochberg correction). Seurat was used to produce violin plots of the expression of select genes.

Pathway analysis
Panther was used to perform Reactome pathway analysis with genes identified from differential expression analysis ($q<0.05$) and with all genes in the dataset as background. Fisher's Exact test was with the Bonferroni correction for multiple testing. Z-scores for each pathway were calculated using the R package 'GOPlot'.

Determination of Antigen Specificity of V(D)J Sequences
To determine whether TCR sequences identified in our scTCRseq experiments on peripheral TEMRA and CSF cells had known antigen specificity, the CDR3b region of each beta chain was compared to the CDR3b repertoire from the VDJdb at https://vdjdb.cdr3.net/.

Clustering of peripheral CD8+ TEMRA and CSF cells
Individual sample expression matrices were loaded into R using the function Read10x under the 'Matrix' package v1.2-15. The expression matrix for each sample was merged into one Seurat object using the CreateSeuratObject and MergeSeurat functions. Seurat package v3.043,44 was utilized for filtering, variable gene selection, normalization, scaling, dimensionality reduction, clustering and visualization.

For manuscripts utilizing custom algorithms or software that are central to the research but not yet described in published literature, software must be made available to editors/reviewers upon request. We strongly encourage code deposition in a community repository (e.g. GitHub). See the Nature Research guidelines for submitting code & software for further information.

Data

Policy information about availability of data

All manuscripts must include a data availability statement. This statement should provide the following information, where applicable:

- Accession codes, unique identifiers, or web links for publicly available datasets
- A list of figures that have associated raw data
- A description of any restrictions on data availability

Source data for figures are provided within Extended Data Figures.

RNA-seq datasets have been deposited online in the Gene Expression Omnibus (GEO) under accession number GSE134578.

Field-specific reporting

Please select the best fit for your research. If you are not sure, read the appropriate sections before making your selection.

☒ Life sciences ☐ Behavioural & social sciences ☐ Ecological, evolutionary & environmental sciences

For a reference copy of the document with all sections, see nature.com/authors/policies/ReportingSummary-flat.pdf

Life sciences study design

All studies must disclose on these points even when the disclosure is negative.

Sample size

Our mass cytometry study measured two independent study groups (healthy vs. MCI/AD) with continuous primary endpoints. We used power analyses to determine the minimum number of study subjects required per group, which was calculated to be 42 healthy and 14 MCI/AD. We

exceded these numbers in the study by analyzing 57 healthy and 23 MCI/AD samples. We established anticipated means for our healthy cohort based on preliminary experiments and considered an enrollment ratio of 3:1 (healthy:MCI/AD) based on enrollment data from the clinic. We measured group sizes to account for a 20% increase in our MCI/AD group. Our type II error rate was set to 0.05 and our power level set to 90%. Following the study, we performed a post-hoc power analysis with our sample sizes and found our mass cytometry study to have 92.3% power.

Data exclusions

Subjects who progressed from a clinical diagnosis of mild cognitive impairment to any form of dementia besides Alzheimer's were removed from the mass cytometry analysis.

Replication

All experiments in this study were successfully replicated at least twice.

Randomization

Study participants were allocated into groups following data acquisition. Study subjects underwent a battery of neuropsychological assessments to determine group status, including: cognitive examination, evaluation of cerebellar function, deep tendon reflexes, sensory input, and motor function. The Montreal Cognitive Assessment (MoCA) examination was used to test study subjects for cognitive impairment. The MoCA assesses several cognitive domains: short-term memory recall (5 points), visuospatial abilities (4), executive functions (4), attention (1), concentration (3), working memory (1), language (6) and orientation to time and space (6). MoCA scores range between 0 and 30. A score of 26 or over is considered to be cognitively typical.

Blinding

All experimenters were blinded to group allocation during data acquisition and analysis.

Reporting for specific materials, systems and methods

Materials & experimental systems

n/a	Involved in the study
☐	☒ Unique biological materials
☐	☒ Antibodies
☐	☒ Eukaryotic cell lines
☒	☐ Palaeontology
☐	☒ Animals and other organisms
☐	☒ Human research participants

Methods

n/a	Involved in the study
☒	☐ ChIP-seq
☐	☒ Flow cytometry
☐	☒ MRI-based neuroimaging

Unique biological materials

Policy information about availability of materials

Obtaining unique materials

Fresh human brain samples are difficult to obtain under a short post-mortem window and are thus not readily available. CSF samples contain very few cells and can only be analyzed once and are thus not readily available.

Antibodies

Antibodies used

Flow cytometry was conducted using an LSRFortessa (BD Biosciences). A panel consisting of antibodies conjugated to six different fluorophores was used to classify subsets of memory T cells and for droplet-based sequencing. Antibodies used were: CD8α-Pacific blue (Clone SK1; BioLegend cat #344718), CD3-BV650 (Clone UCHT1; BD Biosciences cat #563851), CD45RA-APC-Cy7 (Clone HI100; BioLegend cat #304128), CCR7-488 (Clone 4B12; BioLegend cat #120110), IL-7Rα-PE (Clone A019D5; BioLegend cat #351304), CD27-PE-Cy7 (Clone M-T271; BioLegend #356412). For CSF cell characterization, this same panel was used, but CD19-PE-Cy5 (Clone HIB19 BioLegend cat #302210) and CD14-Qdot-705 (Clone TüK4; ThermoFisher cat #Q22137) were included. For sorting CSF T cells for TCR plate sequencing, the following antibodies were used: CD8α-PE (Clone SK1; BioLegend cat #344706), CD161-PE-Cy7 (Clone HP-3G10; BioLegend #339917), CXCR3-APC (Clone CXCR3-173; BioLegend cat #126512), CD4-APC-Alexa700 (Clone RM4-5; ThermoFisher cat #56-0042-82), CD39-APC-Cy7 (Clone A1; BioLegend cat #328226), CD38-FITC (Clone HIT2; BioLegend cat #303504), PD-1-BV421 (Clone EH12.1; BD Biosciences cat #562516), CD45RA-BV605 (Clone 5H9; BD Biosciences cat #740424), CD3-BV650 (Clone UCHT1; BD Biosciences cat #563851), CD27-BV786 (Clone L128; BD Biosciences cat #563328), CD127-BUV395 (Clone HIL-7R-M21; BD Biosciences cat #742547). All antibodies were used at 1:250 dilution. For each experiment, a compensation matrix was developed using singly stained and unstained controls or fluorescent beads, and all analysis was conducted in Cytobank.

For immunohistochemistry, primary antibodies included polyclonal rat anti-human CD3 (1:200; Abcam cat #ab28364), rabbit anti-human CD8α (1:200; Clone D8A8Y; Cell Signaling), mouse anti-Aβ (1:2000; Clone D54D2; Cell Signaling), polyclonal chicken anti-human MAP2 (1:500; Abcam cat #ab5392), mouse anti-human granzyme-A (1:200; Clone GA6; Abcam), rat anti-mouse CD8a (Clone 4SM15; eBioscience cat #14-0808-82) and polyclonal rabbit anti-mouse NEFH (Abcam cat #ab8135). For mouse Aβ plaque

staining, ThioflavinS (1 mg/mL, 1:625, Sigma) was added to the secondary antibody solution.

Validation

Each primary antibody was validated using proper fluorophore controls and positive signal was evaluated versus an unstained sample. All antibodies have been previously published by our group (Han et al., Nat. Biotech., 2014). All antibodies are from reputable vendors and come with validation statements on the manufacturer's website.

Eukaryotic cell lines

Policy information about cell lines

Cell line source(s)

SKW-3 cells were provided by Mark Davis' lab (Stanford). Lenti-X 293T cell line was acquired from Takara (cat #632180).

Authentication

Verification of TCR deficiency in SKW-3 cells line was conducted by flow cytometry against TCRab. 293T cells were not authenticated, but functionally produced lenti viruses.

Mycoplasma contamination

Negative for mycoplasma

Commonly misidentified lines
(See ICLAC register)

SKW-3 cells are commonly misidentified as KE-37 cells. Our cells were verified to lack TCRs and functionally behave like T cells when transduced with T cell receptors.

Animals and other organisms

Policy information about studies involving animals; ARRIVE guidelines recommended for reporting animal research

Laboratory animals

APP/PS1 mice expressing a chimeric mouse/human mutant amyloid precursor protein (Mo/HuAPP695swe) and a mutant human presenilin 1 (PS1-dE9) directed to CNS neurons under the prion protein promoter were used (The Jackson Laboratory). Mice were housed at the Paracelsus Medical University Salzburg in groups under standard conditions at a temperature of 22°C and a 12 h light/dark cycle with ad libitum access to standard food and water. Over 10 mice aged 9-10 months comprising both sexes were randomly analyzed in an unblinded manner. Animal care, handling, genotyping and experiments were approved by Paracelsus Medical University Salzburg ethical committees.

Wild animals

The study did not involve wild animals.

Field-collected samples

The study did not involve samples collected from the field.

Human research participants

Policy information about studies involving human research participants

Population characteristics

A total of 164 subjects from four separate cohorts were used in this study. The 164 subjects used in this study included 97 healthy, 31 MCI, 28 AD and 8 PD. The average age for healthy subjects was 72.52 ± 6.96 (mean±standard deviation), for MCI subjects: 70.97 ± 7.82, for AD subjects: 70.74 ± 7.01 and for PD subjects: 67.25 ± 7.01. Average cognitive score for healthy subjects was 27.17 ± 2.32, MCI: 23.39 ± 4.31, AD: 11.05 ± 7.32 and PD: 27.29 ± 1.70. All subjects were free from acute infectious diseases and in good physical condition. Patients were confirmed to have neurodegeneration by measurement of biomarkers, including neurofilament, Aβ and tau (Quanterix). Group characteristics, including demographic, genetic, clinical and biomarker data for each group are presented in Extended Data Table 10.

Recruitment

Study subjects were recruited through Stanford's NIH-funded Alzheimer's Disease Research Center (ADRC), the UC San Diego ADRC and the UC San Francisco ADRC by general solicitation. The racial makeup of study subjects reflects that of the Stanford area and should be considered when analyzing these results.

Flow Cytometry

Plots

Confirm that:

☒ The axis labels state the marker and fluorochrome used (e.g. CD4-FITC).

☒ The axis scales are clearly visible. Include numbers along axes only for bottom left plot of group (a 'group' is an analysis of identical markers).

☒ All plots are contour plots with outliers or pseudocolor plots.

☒ A numerical value for number of cells or percentage (with statistics) is provided.

Methodology

Sample preparation

PBMCs were isolated from blood by layering diluted blood (1:1 in PBS) on top of an equal volume of Ficoll, followed by centrifugation and isolation of the buffy coat. PBMC samples were stored over the course of a three-year period. Average PBMC viability for patient samples following sample thawing was 79% while the average viability for control samples was 77%.

CSF was collected by lumbar puncture, then centrifuged at 300G to pellet immune cells. CSF samples were checked for blood

contamination by resuspending the pelleted cells in 100 µl of CSF and mixing 10 µl (10%) CSF with 10 µl trypan blue to assess red blood cell content and viability. Cells were visualized on a TC20 automated cell counter (BioRad) and cell viability and presence/absence of red blood cells was recorded. CSF samples contaminated with blood were removed from the study. The resuspended cells were then mixed with 900 µl Recovery Cell Culture Freezing Medium (Thermo Fisher). All Samples were frozen overnight at -80°C in a Mr. Frosty freezing container (Thermo Fisher) and transferred the following day to liquid nitrogen for storage. CSF samples were stored <6 months prior to analysis.

Instrument	BD LSRFortessa
Software	Cytobank v6.3.0.5
Cell population abundance	10,000 live leukocytes were gated for downstream SPADE analysis for mass cytomtery. For peripheral TEMRA scRNAseq, 50,000 peripheral cells were sorted then loaded into a 10X controller at 1,000 cells/ul. For CSF plate-seq, cells were sorted into individual wells of a 96-well plate. For CSF cell drop-seq, all cells from each CSF sample were live sorted, pelleted then loaded into the 10X controller. Since CSF cells are in low abundance (approximately 1 cell per ul), processing of samples (i.e. repetitive centrifugation) was carefully limited to achieve greater numbers of cells.
Gating strategy	Cells were distinguished from debris by SSC/FSC, then signlets were selected on a FSC-H/FSC-W plot. Cells doubly positive for CD3 and CD8 were gated (~10^3 expression in each channel)

☒ Tick this box to confirm that a figure exemplifying the gating strategy is provided in the Supplementary Information.

Magnetic resonance imaging

Experimental design

Design type	T1 weighted MRI Scans were acquired using Axial 3D fast spoiled gradient sequence (GE Discovery 750).
Design specifications	n/a (this is structural MRI data, not functional)
Behavioral performance measures	n/a

Acquisition

Imaging type(s)	Structural
Field strength	3 Tesla
Sequence & imaging parameters	The imaging parameters were optimized for gray/white matter tissue contrast with a repetition time of 5.9ms, echo time 2ms, flip angle 15, field-of-view 220mm, matrix size 256 x 256, slice thickness 1mm and 2 NEX.
Area of acquisition	Whole brain

Diffusion MRI ☐ Used ☒ Not used

Preprocessing

Preprocessing software	All the suggested T1-weighted scans use GE's "BRAVO" sequence. It is an IR-prep, fast SPGR sequence with parameters tuned to optimize brain tissue contrast.
Normalization	To correct for sex differences, we normalized all volumetric measurements to total intracranial volume for each patient.
Normalization template	MNI305 atlas was used for normalization. First stage was affine registration, followed by initial volumetric labeling. The variations due to biasing were corrected. Finally, a high dimensional nonlinear volumetric alignment to the MNI305 atlas was performed, and once preprocessing completed, the volume was labeled.
Noise and artifact removal	n/a These are structural data, not fMRI data
Volume censoring	n/a These are structural data, not fMRI data

Statistical modeling & inference

Model type and settings	Comparisons between groups of subjects were performed using multivariate analysis of covariance, where age served as a covariate.
Effect(s) tested	Increase/decrease in brain region volume

Specify type of analysis: ☐ Whole brain ☒ ROI-based ☐ Both

Anatomical location(s)	Subcortical segmentation including both left and right of Cerebral White Matter, Cerebral Cortex, Lateral Ventricle, Inferior Lateral Ventricle, Cerebellum White Matter, Cerebellum Cortex, Thalamus, Caudate, Putamen, Pallidum, Hippocampus, Amygdala, Lesion, Accumbens area, Vessel, Third Ventricle, Fourth Ventricle, Brain Stem, Cerebrospinal Fluid
Statistic type for inference (See Eklund et al. 2016)	n/a
Correction	n/a

Models & analysis

n/a	Involved in the study
☒	☐ Functional and/or effective connectivity
☒	☐ Graph analysis
☒	☐ Multivariate modeling or predictive analysis

An acute immune response underlies the benefit of cardiac stem cell therapy

https://doi.org/10.1038/s41586-019-1802-2

Received: 20 March 2018

Accepted: 8 November 2019

Published online: 27 November 2019

Ronald J. Vagnozzi[1], Marjorie Maillet[1], Michelle A. Sargent[1], Hadi Khalil[1], Anne Katrine Z. Johansen[1], Jennifer A. Schwanekamp[2], Allen J. York[1], Vincent Huang[1], Matthias Nahrendorf[3], Sakthivel Sadayappan[2] & Jeffery D. Molkentin[1,4]*

Clinical trials using adult stem cells to regenerate damaged heart tissue continue to this day[1,2], despite ongoing questions of efficacy and a lack of mechanistic understanding of the underlying biological effect[3]. The rationale for these cell therapy trials is derived from animal studies that show a modest but reproducible improvement in cardiac function in models of cardiac ischaemic injury[4,5]. Here we examine the mechanistic basis for cell therapy in mice after ischaemia–reperfusion injury, and find that—although heart function is enhanced—it is not associated with the production of new cardiomyocytes. Cell therapy improved heart function through an acute sterile immune response characterized by the temporal and regional induction of CCR2$^+$ and CX3CR1$^+$ macrophages. Intracardiac injection of two distinct types of adult stem cells, cells killed by freezing and thawing or a chemical inducer of the innate immune response all induced a similar regional accumulation of CCR2$^+$ and CX3CR1$^+$ macrophages, and provided functional rejuvenation to the heart after ischaemia–reperfusion injury. This selective macrophage response altered the activity of cardiac fibroblasts, reduced the extracellular matrix content in the border zone and enhanced the mechanical properties of the injured area. The functional benefit of cardiac cell therapy is thus due to an acute inflammatory-based wound-healing response that rejuvenates the infarcted area of the heart.

Initial animal studies with adult stem cells reported improved heart function through the formation of new cardiomyocytes by transdifferentiation of the injected cells[6,7]. However, adult stem cell transdifferentiation was not observed in later studies[4,5,8], and clinical trials using adult stem cells in patients with acute myocardial infarction injury or decompensated heart failure have been indeterminate[1,9]. The mechanistic basis for cell therapy therefore remains unclear, although a paracrine hypothesis has previously been proposed[10]. Here we focused on two types of primary adult stem cell: fractionated bone marrow mononuclear cells (MNCs)—which have extensively been used in human clinical trials[2]—and cardiac mesenchymal cells that express the receptor tyrosine kinase KIT, originally termed and referred to here as cardiac progenitor cells (CPCs)[7,10]. We also examined the effect of injecting zymosan, a non-cellular and potent activator of the innate immune response[11]. Isolated MNCs were a heterogeneous cell population that comprised all the major haematopoietic lineages—although monocytes and granulocytes were predominant (Extended Data Fig. 1a). CPCs expressed mesenchymal cell-surface markers but were negative for markers of haematopoietic or endothelial cells (Extended Data Fig. 1b).

Uninjured eight-week-old male and female C57Bl/6J mice received an intracardiac injection of strain-matched MNCs, zymosan or saline (Fig. 1a). Histological foci of acute inflammation were observed within areas of cell or zymosan injection, as examined by confocal microscopy from heart sections three days, seven days or two weeks post-injection (Fig. 1b). Activated CD68$^+$ macrophages were significantly increased within the area of injection after three and after seven days, with a diminishing effect by two weeks as the cells or zymosan were cleared (Fig. 1b, c). We did not observe any differences in neutrophil levels from dissociated hearts at three days after injection (Extended Data Fig. 1c).

To further profile the induction of macrophages owing to injection of MNCs or zymosan, we used *Ccr2-RFP*[12] and *Cx3cr1-GFP*[13] knock-in mice to broadly distinguish the major subtypes of macrophage in the heart[14,15]. We delivered unlabelled MNCs or zymosan into eight-week-old *Ccr2-RFP* × *Cx3cr1-GFP* mice by intracardiac injection (Fig. 1d). Uninjured (that is, noninjected) adult hearts showed GFP$^+$ (CX3CR1$^+$) macrophages throughout the myocardium, whereas RFP$^+$ (CCR2$^+$) macrophages were largely absent at baseline (Fig. 1e). After one day, areas of the heart injected with MNCs or zymosan showed a robust accumulation of CCR2$^+$ macrophages, and CX3CR1$^+$ macrophages began to expand in the periphery of the injected area (Fig. 1e). At three days, these CX3CR1$^+$ macrophages had also expanded within the injection area along with the CCR2$^+$ macrophages; this began to resolve by seven days after injection. Flow cytometry analysis from these mice at three days after injection also indicated a shift in the overall content of the macrophage subtypes from a largely CX3CR1$^+$CCR2$^-$ population in the naive state to a mix of

[1]Department of Pediatrics, University of Cincinnati, Cincinnati Children's Hospital Medical Center, Cincinnati, OH, USA. [2]Department of Internal Medicine, Heart, Lung and Vascular Institute, University of Cincinnati, Cincinnati, OH, USA. [3]Center for Systems Biology, Department of Imaging, Cardiovascular Research Center, Massachusetts General Hospital of the Harvard Medical School, Boston, MA, USA. [4]Howard Hughes Medical Institute, Cincinnati Children's Hospital Medical Center, Cincinnati, OH, USA. *e-mail: jeff.molkentin@cchmc.org

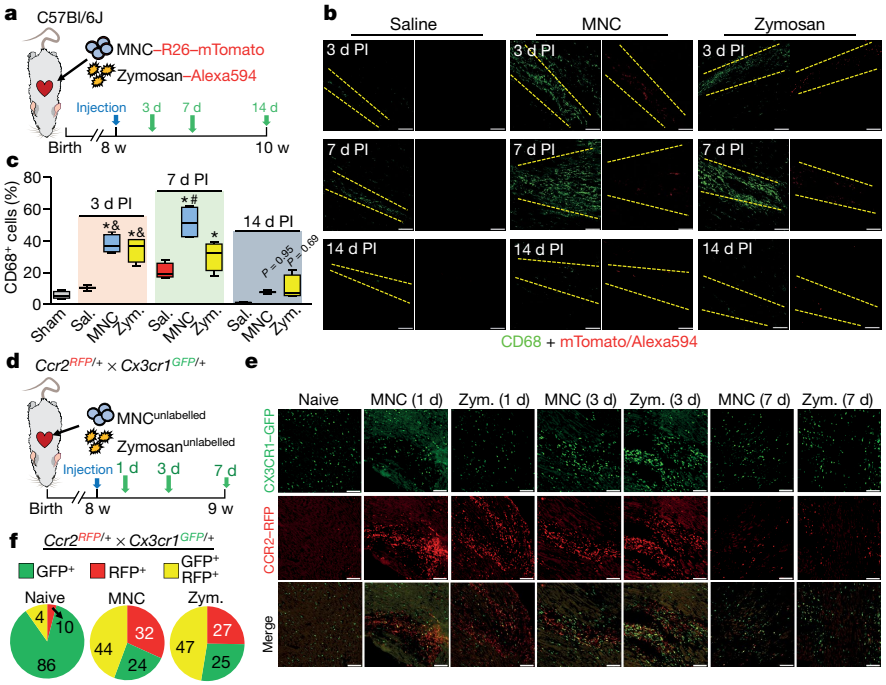


Fig. 1 | Cardiac cell injection causes local inflammation with the accumulation of distinct subtypes of macrophage. a, Experimental scheme using eight-week-old male and female C57Bl/6J mice subjected to intracardiac injection of strain-matched MNCs, Alexa Fluor 594-conjugated zymosan (zym.) or sterile saline (sal.). Sham-treated mice received thoracotomy, but no intracardiac injection. MNCs were isolated from *Rosa26-mTomato* mice on the C57Bl/6J background. **b**, Representative confocal immunohistochemistry micrographs of hearts showing activated CD68 macrophages (green), or the injected MNCs or zymosan (red). Dashed lines show injection sites. Images are from a minimum of 18 histological sections per mouse heart, assessed from $n = 3$ (saline at 3 days post-injection (PI), saline at 14 days post-injection and MNCs at 14 days post-injection) or $n = 4$ mice (all other groups). Scale bars, 100 µm. **c**, Quantification of $CD68^+$ cells as a percentage of total cells ($DAPI^+$), imaged at areas of injection from the groups described in **b**. Sample sizes for all groups are listed above in **b**. At 3 days, $^*P < 0.0001$ versus sham, $^{\&}P = 0.0003$ (MNC versus saline), $^{\&}P = 0.0015$ (zymosan versus saline). At 7 days, $^*P < 0.0001$ (MNC versus sham), $^*P = 0.0005$ (zymosan versus sham), $^{\#}P < 0.0001$ (MNC versus saline). Significance was determined by one-way analysis of variance (ANOVA) with Tukey's post hoc test. Data are summarized as box-and-whisker plots, indicating the median value (black bar inside box), 25th and 75th percentiles (bottom and top of box, respectively), and minimum and maximum values (bottom and top whisker, respectively). **d**, Experimental scheme using eight-week-old male and female *Ccr2-RFP* × *Cx3cr1-GFP* knock-in mice to simultaneously visualize $CCR2^+$ and $CX3CR1^+$ subtypes of macrophage, after injection of MNCs or zymosan. **e**, Representative confocal micrographs from cardiac histological sections from MNC- or zymosan-injected mice, versus naive (non-injected) controls (minimum of 30 sections assessed per mouse heart from $n = 2$ naive control mice and $n = 3$ MNC- or zymosan-injected mice), showing endogenous RFP and GFP immunofluorescence from $CCR2^+$ or $CX3CR1^+$ cells, respectively, at the injection site over a seven-day time course. Scale bars, 100 µm. **f**, Distribution of $CCR2^+$ and $CX3CR1^+$ subtypes of macrophage in hearts at three days after injection. Pie charts reflect the proportion of RFP ($CCR2^+$)- or GFP ($CX3CR1^+$)-expressing cells, as well as $CCR2^+CX3CR1^+$ double-positive (yellow) cells detected by flow cytometry, as a percentage of total macrophages identified by staining for F4/80 and CD64. Data are from $n = 6$ MNC- and zymosan-injected mice or $n = 2$ naive (non-injected) mice.

enhanced numbers of $CCR2^+$ and $CCR2^+CX3CR1^+$ (double-positive) macrophages with injection of MNCs or zymosan (Fig. 1f).

We also used immunohistochemistry to evaluate the ability of injected MNCs or zymosan to induce the formation of new cardiomyocytes ($PCM1^+$) in the heart (Fig. 2a, b). We observed no appreciable increase in cardiomyocyte cell-cycle activity ($Ki67^+$) versus saline-injected controls at the areas of injection, or distally across the entire tissue (Fig. 2c). Another proposed effect of cell therapy is the activation of endogenous CPCs; it has previously been determined that these can contribute to cardiac endothelial cell content after myocardial infarction injury[16]. We used a tamoxifen-inducible, $Kit^{MerCreMer/+}$ × *Rosa26-eGFP* lineage-tracing mouse strategy to examine endothelial cell formation from endogenous CPCs after injection of cells or zymosan (Figs. 2d, e). Notably, we did not observe transdifferentiation of injected MNCs or CPCs into cardiomyocytes or endothelial cells (Fig. 2f). However, two and six weeks after injection, $eGFP^+$ endothelial cells were significantly increased at the injection sites in zymosan-treated hearts, but not in hearts injected with MNCs or CPCs (Fig. 2g, h). Zymosan persisted the longest within these hearts, whereas CPCs and MNCs were essentially cleared by two weeks after injection (Fig. 2e), which potentially explains why zymosan was more effective. None of the treatments increased KIT^+-derived endothelial cells in the distal areas of the heart.

We next injected strain-matched MNCs, CPCs, zymosan or saline on each side of the infarct border zone in C57Bl/6J mice one week after ischaemia–reperfusion (I–R) injury (Fig. 3a). Importantly, the injection of cells or zymosan into uninjured hearts did not alter left ventricular structure or function (Extended Data Fig. 2a–f). Injection of MNCs, CPCs or zymosan each significantly improved cardiac ventricular performance after I–R by two weeks after their injection, when compared with saline-injected controls (Fig. 3b). Of note, although the intracardiac injection procedure itself (saline) produced a mild inflammatory response (Extended Data Fig. 3a–e), it did not improve cardiac function after I–R (Extended Data Fig. 3f–i). Injection of cells or zymosan was also associated with improvements in left ventricular end-systolic volume, consistent with better cardiac function (Extended Data Fig. 4a). By contrast, there was no change in left ventricular end-diastolic volume (Extended Data Fig. 4b) or heart rate (Extended Data Fig. 4c) across any of the treatment groups at two weeks after therapy. Importantly, the observed functional benefit persisted for at least eight weeks after the injection of MNCs or zymosan (Fig. 3c).

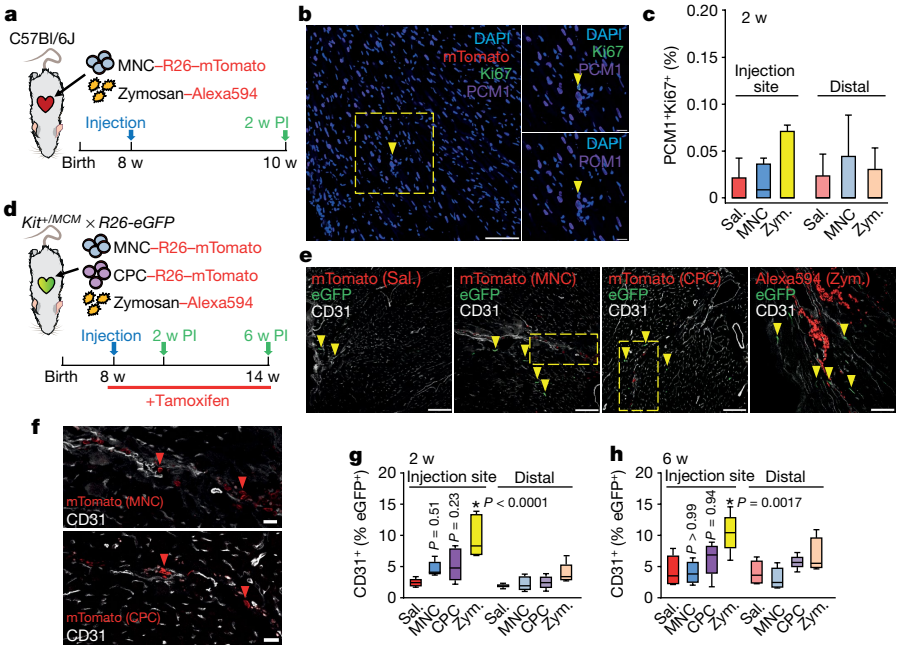


Fig. 2 | Cell or inflammatory therapy induces endothelial cell, but not cardiomyocyte, formation. a, Schematic of experiments performed in **b**, **c** in eight-week-old male and female C57Bl/6J mice that received intracardiac injection of MNCs, zymosan or saline, and were analysed two weeks later. **b**, Representative cardiac immunohistochemistry for Ki67 (green) and PCM1 (purple) from MNC-injected hearts. DAPI (blue) shows nuclei. A minimum of 45 histological sections were analysed per mouse heart from $n = 4$ MNC-treated mice, or $n = 5$ mice for all other groups. The yellow box denotes an area shown at a higher magnification in the insets on the right. The yellow arrowhead denotes a cardiomyocyte with cell-cycle activity. Scale bars, 100 µm (left), 10 µm (right). **c**, Quantification of cardiomyocytes with cell-cycle activity ($PCM1^+Ki67^+$) as a percentage of all cardiomyocytes imaged ($PCM1^+$) at two weeks after injection. Data are from a minimum of 45 cardiac histological sections analysed per mouse. $n = 4$ (MNC and at the injection site) or $n = 5$ mice for all other groups. **d**, Schematic of experiments performed in **e**–**h** using KIT lineage-tracing mice ($Kit^{MerCreMer/+} \times Rosa26\text{-}eGFP$) injected with MNCs, CPCs, zymosan or saline, then analysed two or six weeks later. Tamoxifen was administered continuously (in chow), starting one day before cell injection. **e**, Representative confocal immunohistochemistry images from hearts showing $CD31^+$ endothelial cells (white) and injected MNCs, CPCs or zymosan (red). eGFP (green) shows *Kit*-allele-derived endothelial cells. Yellow arrowheads denote $CD31^+$ endothelial cells that are also $eGFP^+$. Scale bars, 100 µm. **f**, Larger insets of images shown in **e**, (within the boxed areas). Injected MNCs (top) or CPCs (bottom, rotated 90°) are shown with red arrowheads indicating $mTomato^+$ cells that are negative for CD31 and lack known cardiomyocyte morphology. Scale bars, 20 µm. **g**, **h**, Quantification of the percentage of $eGFP^+$ endothelial cells relative to total endothelial cells counted, either two weeks (**g**) or six weeks (**h**) post-injection. All data in **e**–**h** are from $n = 6$ (six weeks after zymosan injection) or $n = 5$ mice (all other groups). All *P* values in **g**, **h** were determined by one-way ANOVA with Tukey's post hoc test. All numerical data in this figure (**c**, **g**, **h**)are summarized as box-and-whisker plots, indicating the median value (black bar inside box), 25th and 75th percentiles (bottom and top of box, respectively), and minimum and maximum values (bottom and top whisker, respectively). Data and representative micrographs in **e**–**h** are from a minimum of 45 histological sections analysed per individual mouse heart from the numbers of mice indicated above.

We next treated mice with a high dosage of the broad-spectrum immunosuppressant cyclosporine A (CsA), which abrogated the restorative effects on cardiac function that were seen with injections of MNCs or zymosan after I–R injury (Fig. 3d). Administering clodronate liposomes acutely depleted macrophages and abolished the protective effect of the MNC injection after I–R in a similar manner to CsA treatment (Fig. 3e). Finally, injecting cellular debris from MNCs killed by freezing and thawing also improved cardiac function after I–R (Extended Data Fig. 4d).

Cardiac I–R injury itself is associated with a robust, temporal recruitment of discrete myeloid cell populations[17], which we also observed using *Ccr2-RFP* × *Cx3cr1-GFP* mice (Fig. 3f). Of note, characterization of *Ccr2-RFP* × *Cx3cr1-GFP* mice at baseline using flow cytometry showed that over 90% of the $CX3CR1^+CCR2^-$ cells in the heart were tissue-resident $CD169^+$ macrophages[14], with a minor contribution of dendritic cells and neutrophils (Extended Data Fig. 5a–f). We also used $Ccr2^{-/-}$ or $Cx3cr1^{-/-}$ gene-targeted mice, and—although initial infarct sizes after I–R were not different among $Ccr2^{-/-}$ or $Cx3cr1^{-/-}$ mice and their strain-matched wild-type controls (not shown)—*Ccr2* deficiency partially improved cardiac function after I–R (Fig. 3h), consistent with previous reports[18,19]. Moreover, cell therapy by MNC injection in mice that lack *Ccr2* imparted no further functional benefit beyond the improvement seen in these mice after I–R (Fig. 3h). The loss of *Ccr2* led to a reduction in overall $CD68^+$ cell content, specifically at the border zone of hearts after I–R—both with and without cell therapy (Fig. 3i). By comparison, *Cx3cr1*-null mice showed left ventricular dysfunction after I–R injury that was similar to wild-type controls, but these *Cx3cr1*-null mice no longer benefitted from MNC therapy and showed a much greater total inflammatory response (Fig. 3h, i). This result is consistent with a recent study that has shown that ablation of $CX3CR1^+$ macrophages increases mortality and peri-infarct fibrosis after myocardial infarction in mice[15]. However, *Cx3cr1*-null mice show a GFP^+ (expressed from the *Cx3cr1-GFP* allele) macrophage content after permanent occlusion myocardial infarction injury that is similar to that of control mice, as well as the same content of activated $CD68^+$ macrophages in the infarct border zone at three days after myocardial infarction (Extended Data Fig. 6a–c). This observation is consistent with previous analyses of *Cx3cr1*-null mice, in which monocyte extravasation during peritonitis is unaffected[13] and trafficking of tissue macrophages from the yolk sac during development is unaltered[20]. Given these previous observations, the most likely explanation for our results is that CX3CR1 deficiency does not compromise tissue-resident macrophage content, but instead affects the function of these macrophages—resulting in greater tissue inflammation. Finally, the acute monocyte and neutrophil responses at three days after myocardial infarction were also not different between *Cx3cr1*-null mice and heterozygous *Cx3cr1-GFP* controls

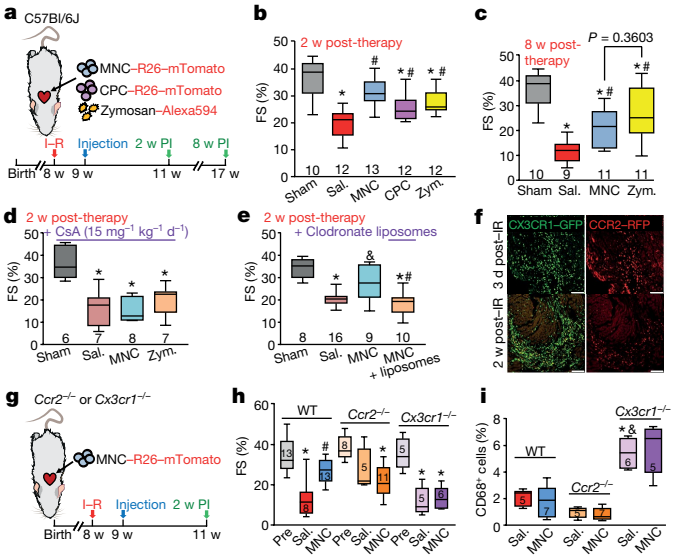


Fig. 3 | Cell or inflammatory therapy rejuvenates heart function after I–R. **a**, Schematic of experiments performed in **b**, **c**, in which eight-week-old male and female C57Bl/6J mice received 120 min of myocardial I–R injury, then (1 week later) intracardiac injection of MNCs, CPCs, zymosan or sterile saline flanking the injury area, followed by analysis two or eight weeks later. **b**, Fractional shortening (FS) as measured by echocardiography in the groups indicated, two weeks after cell or zymosan therapy. $^{*}P < 0.0001$ (saline versus sham), $^{*}P = 0.0002$ (CPC versus sham), $^{*}P = 0.0019$ (zymosan versus sham), $^{\#}P < 0.0001$ (MNC versus saline), $^{\#}P = 0.0157$ (CPC versus saline), $^{\#}P = 0.0019$ (zymosan versus saline). **c**, Fractional shortening at eight weeks after cell or zymosan therapy. $^{*}P < 0.0001$ (saline versus sham), $^{*}P = 0.0002$ (MNC versus sham), $^{*}P = 0.0086$ (zymosan versus sham), $^{\#}P = 0.0194$ (MNC versus saline), $^{\#}P = 0.0005$ (zymosan versus saline). Significance in **b**, **c** was determined by one-way ANOVA with Dunnett's post hoc test. The same sham group is shown in **b** and **c**, as these experiments were performed in parallel. **d**, Fractional shortening in post-I–R male and female mice that received CsA (15 milligrams per kilogram body weight per day) delivered by osmotic minipump, starting one day before MNC, zymosan or saline injection and continuing for two weeks after injection. $^{*}P = 0.0004$ (saline versus sham), $^{*}P = 0.0006$ (MNC versus sham), $^{*}P = 0.0018$ (zymosan versus sham), all by one-way ANOVA with Dunnett's post hoc test. **e**, Fractional shortening in post-I–R male and female mice that received two injections of clodronate liposomes delivered intraperitoneally one day before MNC injection, and again five days after MNC injection. No difference between control and liposome treatment was observed in mice that received intracardiac injection of saline after I–R, so these groups were combined (denoted as saline). $^{*}P < 0.0001$ (saline versus sham, or MNC + liposomes versus sham), $^{\&}P = 0.0276$ (MNC versus saline), $^{\#}P = 0.0042$ (MNC + liposomes versus MNC), all determined by one-way ANOVA with Dunnett's post hoc test. **f**, Confocal micrographs of histological sections at the infarct border zone of hearts from male and female *Ccr2-RFP* × *Cx3cr1-GFP* knock-in mice ($n = 2$ mice per group and time point, with a minimum of 10 sections assessed per mouse heart) at either three days or two weeks after I–R. Scale bars, 100 μm. **g**, Schematic of experiments performed in **h**, **i** in male and female $Ccr2^{-/-}$ or $Cx3cr1^{-/-}$ mice in the C57Bl/6J background that were subjected to I–R, and then injected with MNCs or sterile saline one week later. **h**, Fractional shortening in $Ccr2^{-/-}$ or $Cx3cr1^{-/-}$ mice or wild-type (WT) C57Bl/6J mice two weeks after cell injection, or non-injured mice (pre). $^{*}P < 0.0001$ (wild type, saline versus pre), $^{*}P = 0.0004$ ($Ccr2^{-/-}$, MNC versus pre), $^{*}P = 0.0001$ ($Cx3cr1^{-/-}$, saline versus pre), $^{*}P = 0.0002$ ($Cx3cr1^{-/-}$, MNC versus pre), $^{\#}P = 0.0030$ (wild type, MNC versus saline), all by one-way ANOVA with Tukey's post hoc test. **i**, Quantification of $CD68^{+}$ cells as a percentage of total cells ($DAPI^{+}$) imaged at the infarct border zone, three weeks after I–R. $^{*}P = 0.0001$ versus wild type and saline, $^{\&}P < 0.0001$ versus $Ccr2^{-/-}$ and saline, all by one-way ANOVA with Tukey's post hoc test. The number of mice in each of the experimental groups is indicated below or within the respective graphs. All numerical data are summarized as box-and-whisker plots, indicating the median value (black bar inside box), 25th and 75th percentiles (bottom and top of box, respectively), and minimum and maximum values (bottom and top whisker, respectively).

(Extended Data Fig. 6d). However, we observed significantly greater mortality after myocardial infarction in *Cx3cr1*-null mice (Extended Data Fig. 6e), which suggests that $CX3CR1^{+}$ cells have an important role in the later stages of infarct maturation (after day 3) and/or in the modulation of the fibrotic response, as has also recently been proposed[15]

Mechanistically, extracellular matrix content in the peri-infarct border zone was noticeably decreased with injection of MNCs around the I–R injury area (Fig. 4a, b). We also observed this decrease with the injection of non-viable MNCs, which suggests that it was primarily due to immunoreactivity—and not to active paracrine signalling (Fig. 4c). Notably, infarct strips from MNC-injected hearts produced a significantly greater change in passive force over increasing stretch, a profile that was more similar to that of the uninjured heart (change in initial length (L_0)) (Fig. 4d). This profile was also associated with a decrease in gene expression of several components of the extracellular matrix and genes that underlie the fibrotic response in MNC- versus saline-treated hearts after I–R injury (Fig. 4e). We repeated the force-lengthening assay on infarct strips from post-I–R hearts injected with zymosan, which showed an even larger improvement in passive force dynamics compared with the saline or MNC treatment (Extended Data Fig. 7a).

We next isolated bone marrow-derived macrophages or peritoneal macrophages from naive mice and cultured them on prefabricated collagen patches, followed by second harmonic generation microscopy to examine collagen organization (Fig. 4f). Bone marrow-derived macrophages and peritoneal macrophages each generated different patterns of collagen reorganization. To extend these observations, we used a collagen hybridizing peptide[21] reagent, which detects immature or denatured collagen and areas of active remodelling, on injured mouse hearts (Extended Data Fig. 7b). Hearts from MNC- or zymosan-treated mice showed reactivity to the collagen hybridizing peptide that was coincident with regional localization of $CCR2^{+}$ versus $CX3CR1^{+}$ macrophages within the microenvironment of the infarct border zone (Extended Data Fig. 7c). Finally, we isolated $CCR2^{+}$ or $CX3CR1^{+}$ macrophages from hearts at seven days after I–R (Fig. 4g) and cultured them with freshly isolated cardiac fibroblasts for 72 h. Gene expression analysis revealed that $CCR2^{+}$ macrophages increased fibroblast expression of smooth muscle α-actin (*Acta2*), lysyl oxidase (*Lox*) and collagen type I α 2 (*Col1a2*) (Fig. 4h, i, k). By contrast, $CX3CR1^{+}$ macrophages slightly reduced the expression of these genes but increased fibroblast expression of connective tissue growth factor (*Ctgf*, also known as *Ccn2*)[22] (Fig. 4j). Together, these results demonstrate that specific subtypes of macrophage mobilized by cell therapy differentially affect the passive mechanical properties of the cardiac infarct area by influencing the activity of cardiac fibroblasts.

As suggested over a decade ago[23], we observed that the acute inflammatory response is a primary beneficial effect that underlies cell therapy in the injured heart after myocardial infarction. We identified a mechanism by which temporary stimulation of the intrinsic wound-healing cascade and select subtypes of macrophage positively affect the extracellular matrix around and within the infarcted region of the heart, such that functional performance is improved. These results are consistent with recent reports that demonstrate key functional distinctions between $CCR2^{+}$ and $CX3CR1^{+}CCR2^{-}$ macrophages in cardiac wound healing[14,15]. In conclusion, our data suggest a need for the re-evaluation of current and planned clinical trials based on cardiac cell therapy to maximize the effects of the most prevalent underlying biological mechanism of action.

Online content

Any methods, additional references, Nature Research reporting summaries, source data, extended data, supplementary information, acknowledgements, peer review information; details of author contributions and competing interests; and statements of data and code availability are available at https://doi.org/10.1038/s41586-019-1802-2.

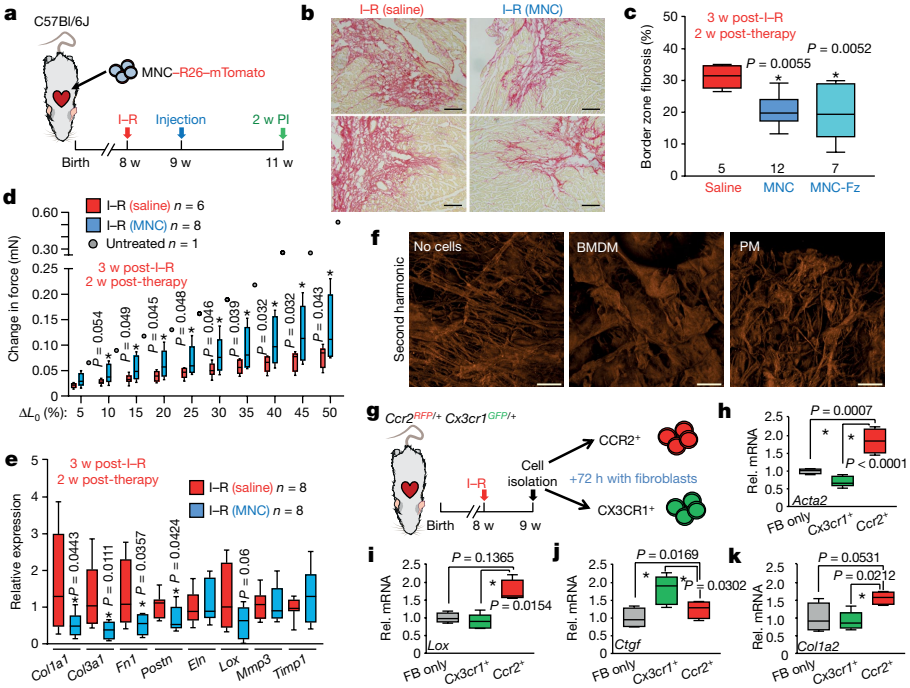


Fig. 4 | Cell therapy benefits the mechanical properties of the infarct via remodelling of the extracellular matrix. a, Schematic of experiments performed in **b**–**e**. **b**, Representative cardiac histological images stained with picrosirius red from the infarct border zone of mice three weeks after I–R, subjected to MNC or saline injection. Fibrosis is shown in red. Scale bars, 100 µm. **c**, Quantification of fibrotic area at the infarct border zone in hearts treated with MNCs, MNCs killed by freezing and thawing (-Fz) or saline, three weeks after I–R. *P* values are shown in the panel and were calculated by one-way ANOVA with Tukey's post hoc test. Images in **b** and quantification in **c** are from $n = 5$ saline-treated mice, $n = 12$ MNC-treated mice or $n = 7$ mice treated with MNCs killed by freezing and thawing, with a minimum of 20 histological sections assessed from each individual mouse heart. **d**, Change in passive force generation over increasing stretch lengthening (per cent of L_0) in isolated infarct strips from MNC- or saline-treated hearts, three weeks after I–R. Exact *P* values are shown in the panel versus I–R and saline, and were calculated by Student's two-tailed *t*-test. Data from one untreated control heart (no I–R or cell therapy) are shown for comparison. **e**, mRNA expression levels by PCR with reverse transcription (RT–PCR) for selected genes associated with fibrosis and the extracellular matrix in isolated infarct regions from MNC or saline-treated hearts, three weeks after I–R. Exact *P* values are shown in the panel versus I–R and saline, by Student's two-tailed *t*-test. **f**, Representative confocal micrographs of prefabricated collagen patches that were seeded and cultured for five days with either bone marrow-derived macrophages (BMDM) or peritoneal macrophages (PM) isolated from wild-type male and female mice, versus cell-free control patches cultured in medium. Fluorescence signal is from native type I and type II collagen using second harmonic generation microscopy. Scale bars, 100 µm. **g**, Schematic of experiments using activated cardiac macrophages isolated from post-I–R *Ccr2-RFP* × *Cx3cr1-GFP* knock-in mice that were then cultured with isolated cardiac fibroblasts for 72 h. **h**–**k**, Fibroblast (FB) mRNA was used for RT–PCR to assess expression of *Acta2* (**h**), *Lox* (**i**), *Ctgf* (**j**) or *Col1a2* (**k**). Rel. mRNA, relative levels of mRNA. For **i**, $^*P < 0.05$ by Kruskal–Wallis with Dunn's multiple comparisons test. For all other panels, $^*P < 0.05$ by one-way ANOVA with Tukey's post hoc test (exact *P* values are shown in the panels). All numerical data are summarized as box-and-whisker plots, indicating the median value (black bar inside box), 25th and 75th percentiles (bottom and top of box, respectively), and minimum and maximum values (bottom and top whisker, respectively). Micrographs in **f** are representative of five collagen patches seeded with cells pooled from $n = 4$ mice (2 male and 2 female). Data in **g**–**k** are from 4–5 replicates generated from fibroblasts isolated from $n = 10$ wild-type mice (6 male and 4 female) and macrophages isolated from $n = 6$ *Ccr2-RFP* × *Cx3cr1-GFP* heterozygous knock-in mice (3 male and 3 female).

1. Nguyen, P. K., Rhee, J. W. & Wu, J. C. Adult stem cell therapy and heart failure, 2000 to 2016: a systematic review. *JAMA Cardiol.* **1**, 831–841 (2016).
2. Fernández-Avilés, F. et al. Global position paper on cardiovascular regenerative medicine. *Eur. Heart J.* **38**, 2532–2546 (2017).
3. Epstein, J. A. A time to press reset and regenerate cardiac stem cell biology. *JAMA Cardiol.* **4**, 95–96 (2019).
4. Zwetsloot, P. P. et al. Cardiac stem cell treatment in myocardial infarction: a systematic review and meta-analysis of preclinical studies. *Circ. Res.* **118**, 1223–1232 (2016).
5. Tompkins, B. A. et al. Preclinical studies of stem cell therapy for heart disease. *Circ. Res.* **122**, 1006–1020 (2018).
6. Orlic, D. et al. Bone marrow cells regenerate infarcted myocardium. *Nature* **410**, 701–705 (2001).
7. Beltrami, A. P. et al. Adult cardiac stem cells are multipotent and support myocardial regeneration. *Cell* **114**, 763–776 (2003).
8. Eschenhagen, T. et al. Cardiomyocyte regeneration: a consensus statement. *Circulation* **136**, 680–686 (2017).
9. A futile cycle in cell therapy. *Nat. Biotechnol.* **35**, 291 (2017).
10. Sanganalmath, S. K. & Bolli, R. Cell therapy for heart failure: a comprehensive overview of experimental and clinical studies, current challenges, and future directions. *Circ. Res.* **113**, 810–834 (2013).
11. Pillemer, L., Blum, L., Pensky, J. & Lepow, I. H. The requirement for magnesium ions in the inactivation of the third component of human complement (C'3) by insoluble residues of yeast cells (zymosan). *J. Immunol.* **71**, 331–338 (1953).
12. Saederup, N. et al. Selective chemokine receptor usage by central nervous system myeloid cells in CCR2-red fluorescent protein knock-in mice. *PLoS ONE* **5**, e13693 (2010).
13. Jung, S. et al. Analysis of fractalkine receptor CX_3CR1 function by targeted deletion and green fluorescent protein reporter gene insertion. *Mol. Cell. Biol.* **20**, 4106–4114 (2000).
14. Bajpai, G. et al. Tissue resident CCR2$^-$ and CCR2$^+$ cardiac macrophages differentially orchestrate monocyte recruitment and fate specification following myocardial injury. *Circ. Res.* **124**, 263–278 (2019).
15. Dick, S. A. et al. Self-renewing resident cardiac macrophages limit adverse remodeling following myocardial infarction. *Nat. Immunol.* **20**, 29–39 (2019).
16. van Berlo, J. H. et al. c-kit$^+$ cells minimally contribute cardiomyocytes to the heart. *Nature* **509**, 337–341 (2014).
17. Nahrendorf, M. et al. The healing myocardium sequentially mobilizes two monocyte subsets with divergent and complementary functions. *J. Exp. Med.* **204**, 3037–3047 (2007).
18. Kaikita, K. et al. Targeted deletion of CC chemokine receptor 2 attenuates left ventricular remodeling after experimental myocardial infarction. *Am. J. Pathol.* **165**, 439–447 (2004).
19. Leuschner, F. et al. Therapeutic siRNA silencing in inflammatory monocytes in mice. *Nat. Biotechnol.* **29**, 1005–1010 (2011).
20. Stremmel, C. et al. Yolk sac macrophage progenitors traffic to the embryo during defined stages of development. *Nat. Commun.* **9**, 75 (2018).
21. Hwang, J. et al. In situ imaging of tissue remodeling with collagen hybridizing peptides. *ACS Nano* **11**, 9825–9835 (2017).
22. Brigstock, D. R. Regulation of angiogenesis and endothelial cell function by connective tissue growth factor (CTGF) and cysteine-rich 61 (CYR61). *Angiogenesis* **5**, 153–165 (2002).
23. Thum, T., Bauersachs, J., Poole-Wilson, P. A., Volk, H. D. & Anker, S. D. The dying stem cell hypothesis: immune modulation as a novel mechanism for progenitor cell therapy in cardiac muscle. *J. Am. Coll. Cardiol.* **46**, 1799–1802 (2005).

Publisher's note Springer Nature remains neutral with regard to jurisdictional claims in published maps and institutional affiliations.

© The Author(s), under exclusive licence to Springer Nature Limited 2019

Methods

Mice

This study was performed entirely in mice, using transgenic models that are commercially available as described later in this section. No human subjects or human material were used. All experiments involving mice were approved by the Institutional Animal Care and Use Committee (IACUC) at Cincinnati Children's Hospital under protocol IACUC2018-0047. All procedures were performed in compliance with institutional and governmental regulations under PHS Animal Welfare Assurance number D16-00068 (A3108-01). The generation and characterization of mice carrying the tamoxifen-inducible MerCreMer recombinase cDNA within the *Kit* allele (*Kit*$^{MerCreMer/+}$), and reporter mice carrying the Cre-regulated loxP-stop cassette and eGFP within the *Rosa26* gene locus, *Rosa26-eGFP* (R-GFP), have previously been described[16]. All the other mouse strains were purchased from The Jackson Laboratory, as follows: C57Bl/6J; (no. 000664), constitutive mTomato-expressing mice targeted in the *Rosa26* locus for MNC or CPC isolation; (*B6.129(Cg)-Gt(ROSA)26Sortm4(ACTB-tdTomato,-EGFP)Luo/J*, no. 007676), *Ccr2*-gene-deleted mice; (*B6.129S4-Ccr2tm1Ifc/J*, no. 004999), *Cx3cr1-GFP* knock-in mice (*Cx3cr1* homozygotes are nulls); *B6.129P-Cx3cr1tm1Litt/J*, no. 005582) and *Ccr2* RFP knock-in mice; (*B6.129(Cg)-Ccr2tm2.1Ifc/J*, no. 017586). Both male and female mice were used in all experiments, at age ranges indicated in the figures and text for each experiment. Mice were housed with mice of the same sex at a maximum of 4 mice per cage in a specific-pathogen-free, temperature-controlled vivarium under a 12-h light–dark cycle with ad libitum access to food and water. Randomization was not performed, because mice are genetically identical, housed together and of the same age ranges and sex ratios.

Preparation of cell or inflammatory therapies

To generate MNCs for injection, whole bone marrow was first isolated by flushing dissected femurs and tibiae of 10–12-week-old *Rosa26-mTomato*-expressing mice or C57Bl/6J mice with 10 ml of sterile Hanks Balanced Salt Solution (HBSS, Fisher Scientific no. SH3058801) + 2% bovine growth serum (BGS, Fisher Scientific, no. SH3054103) + 2 mM EDTA, as previously described[24]. This suspension was then filtered through a 40-µm mesh strainer (Fisher Scientific no. 22-363-547), centrifuged at 400*g* for 10 min at 4 °C, resuspended in 3 ml of sterile saline and layered on top of 4 ml of Ficoll Paque Plus (GE Healthcare no. 17-1440-02). Cells were then centrifuged at 2,500*g* for 30 min at 4 °C in a swinging bucket rotor centrifuge without brakes. MNCs were isolated by removal of the resulting thin mononuclear cell layer (the second layer from the top). Total MNCs were counted with a haemocytometer, washed twice with sterile saline and resuspended in sterile saline at a final concentration of either 2.5×10^6 cells per millilitre (for injection into uninjured hearts, a final dose 50,000 cells) or 7.5×10^6 cells per millilitre (for injection into post-I–R hearts, a final dose 150,000 cells). A higher dose of cells (MNCs or CPCs, see 'Mouse procedures') was used in post-I–R hearts to account for greater cell loss in the setting of damaged myocardium and to align with previous studies[4,5]. The full intracardiac injection procedure is described in 'Mouse procedures'. Cell viability was tested by incubating an aliquot of the MNC suspension with eFluor 450 Fixable Viability Dye (eBioscience no. 65-0863-18) and was found to be over 90% viable at the time of injection. All MNC preparations for injection were combined from an equal number of male and female mice. For experiments that used non-viable MNCs (frozen and thawed), this final MNC suspension was split into two equal aliquots. One aliquot was placed immediately at −80 °C for 10 min, followed immediately by incubation at 55 °C for 10 min, and this was repeated for a total of 3 freeze–thaw cycles.

To generate CPCs for injection, hearts from 10–12-week-old *Rosa26-mTomato*-expressing male and female mice were rapidly excised and briefly rinsed in cold 1× PBS. Single-cell suspensions from these hearts were prepared according to previously published protocols[25,26] with minor modifications. The atria were removed, and the ventricles were minced on ice using surgical scissors into approximately 2-mm pieces (8–10 pieces per mouse heart). Each dissociated ventricle was transferred into 2 ml of digestion buffer in 1 well of a 12-well tissue culture plate. Digestion buffer consisted of 2 mg/ml collagenase type IV (Worthington, no. LS004188), 1.2 U/ml dispase II (Roche, no. 10165859001) and 0.9 mM $CaCl_2$, in 1× HBSS. Tissues were incubated at 37 °C for 20 min with gentle rotation followed by manual trituration 12–15 times with a 10-ml serological pipette, such that all the tissue pieces were able to pass through the pipette. The tissues were settled by sedimentation and the supernatant was passed through a 40-µm mesh strainer and stored on ice. Two millilitres of fresh digestion buffer was added, followed by 2 additional rounds of incubation, trituration and replacement of supernatant with fresh digestion buffer, except trituration was performed with a 5-ml serological pipette for round 2 and a 1-ml p1000 pipette tip (USA Scientific, no. 1112-1720) for round 3. The pooled supernatant from the 3 rounds of digestion was washed with sterile PBS and centrifuged at 200*g* for 20 min at 4 °C in a swinging bucket rotor centrifuge without brakes. The pellet was resuspended in flow cytometry sorting buffer, consisting of 1× HBSS supplemented with 2% BGS and 2 mM EDTA, and incubated with anti-KIT microbeads (Miltenyi Biotec no. 130-091-224) for 20 min at 4 °C with gentle rotation. The suspensions were washed twice with sorting buffer and KIT$^+$ cells were enriched via positive selection over Miltenyi Biotec LS columns (no. 130-042-401) using benchtop magnetic cell separation (MACS) according to the manufacturer's instructions. Cells isolated via positive MACS selection for KIT were cultured in DMEM–F12–Glutamax medium (Gibco no. 10565-018) supplemented with 10% fetal bovine serum (Sigma, no. F2442), 0.2% insulin–transferrin–selenium (Lonza, no. 17-838Z), 20 ng/ml basic recombinant human fibroblast growth factor (Promega, no. G5071), 10^3 U/ml leukaemia inhibitor factor (Millipore, no. ESG1106), 20 ng/ml epidermal growth factor (Sigma, no. E9644) and 1% penicillin–streptomycin (Fisher Scientific, no. 30-002-CI).

KIT$^+$ isolated cells from the heart are referred to as CPCs (as previously named), although recent data would suggest that these cells transdifferentiate only into endothelial cells, and not cardiomyocytes, in vivo[3,8,16]. KIT$^+$ isolated cells were expanded in culture for 12–15 passages before being used for injection, at which point cells were washed 3 times with sterile saline, trypsinized, counted and resuspended in sterile saline at a final concentration of either 2.5×10^6 cells per millilitre (for injection into uninjured hearts, a final dose 50,000 cells) or 7.5×10^6 cells per millilitre (for injection into post-I–R hearts, a final dose 150,000 cells). As with MNCs, suspensions comprised pooled CPCs from an equal number of male and female mice.

Alexa Fluor 594-conjugated zymosan, or unconjugated zymosan, were purchased from Thermo Fisher (zymosan A (*Saccharomyces cerevisiae*) BioParticles, Alexa Fluor 594 conjugate, no. Z-23374, zymosan A (*S. cerevisiae*) BioParticles, unlabelled, no. Z2849). A suspension of either 1 mg/ml (for injection into uninjured hearts, a final dose of 10 µg) or 2 mg/ml (for injection into post-I–R hearts, a final dose of 20 µg) was prepared for injection in sterile saline according to the manufacturer's instructions. Zymosan dosing was extrapolated from a previous study using injection into neonatal mouse hearts[27]. A higher dose of zymosan was used in post-I–R hearts to enable comparisons with MNC- and CPC-treated animals.

Mouse procedures

To deliver cell or inflammatory therapies by intracardiac injection, mice were anaesthetized using isoflurane inhalation (to effect) and intubated, and a left lateral thoracotomy was performed. A 25-µl gastight syringe (Hamilton, no. 7654-01) fitted with a 33-gauge needle (Hamilton, no. 7803-05) was used for injections. For experiments in mice without injury, 20 µl of MNCs at a concentration of 2.5×10^6 cells per millilitre (50,000 cells in total) was injected over 3 regions of the left ventricle (6.7 µl per injection). For experiments with zymosan,

10 µl of a 1 mg/ml suspension was injected over 3 regions of the left ventricle (3.3 µl per injection, 10 µg zymosan in total). Injections were equidistant along the anterior wall of the left ventricle, with the needle entering just parallel to the long axis of the ventricle to avoid entering the left ventricular chamber. For experiments with injections occurring after cardiac injury, two injections were performed, one on either side of the infarct zone. Twenty microlitres total of MNCs or CPCs at a concentration of 7.5×10^6 cells per millilitre (150,000 cells total) was injected (10 µl per injection). For experiments with zymosan, 10 µl total of a 2 mg/ml suspension was injected (5 µl per injection, 20 µg zymosan in total). A greater number of cells and higher amount of zymosan were injected into the injured heart compared with the uninjured (naive) heart, because of less retention and a greater turnover of the cells or zymosan owing to the infarction injury. The sham procedure for intracardiac injection consisted of anaesthesia, intubation and thoracotomy as performed for the previously described myocardial infarction procedure[28]. The chest was then immediately closed, and mice recovered.

To induce cardiac injury, we used a modified surgical model of I–R via temporary left coronary artery ligation as previously described[28], in which 120 min of ischaemia was used before inducing reperfusion, which gave more complete killing of the ischaemic zone and greater reproducibility. After each surgical procedure (I–R or intracardiac injection), animals were given post-operative analgesics (buprenorphine, 0.1 milligram per kilogram body weight) and allowed to recover until the experimental time points indicated, at which point mice were then further analysed, or tissue was collected. For experiments with permanent-occlusion myocardial infarction, the same procedure was performed except the ligature was not released. Randomization was not performed because the mice used here are genetically identical, housed together and of the same age ranges and sex ratios. A discussion of blinding and sample elimination considerations can be found in 'Statistical information and experimental rigour (blinding)'.

Infarct size and area-at-risk after I–R was determined using triphenyl tetrazolium chloride and Evans blue staining, as previously described[28]. In experiments using immunosuppression via CsA, mice were anaesthetized with 2% isoflurane inhalation to effect, and osmotic minipumps (Alzet, no. 1002) were implanted subcutaneously on the left lateral side of the mouse. Minipumps were loaded with CsA (Neoral, Novartis, NDC 0078-0274-22) dissolved in Cremophor EL (Sigma, no. C5135) such that 15 milligrams CsA per kilogram of body weight was delivered per day[29]. In experiments using acute macrophage ablation, mice were administered 2 doses of 0.2 ml each of clodronate liposomes (Clophosome, no. F70101C-N) via intraperitoneal injection, one day before cell therapy and again on day 5 after cell therapy. Liposomes were kept on ice until administration and were rapidly mixed by inversion to deliver a uniform suspension. Control mice were injected with 0.2 ml of sterile saline. In experiments using *Kit*$^{MerCreMer/+}$ × *Rosa26-eGFP* genetic lineage-tracing mice, tamoxifen was administered as previously described[16] via ad libitum feeding with premanufactured tamoxifen chow (tamoxifen citrate 40 milligrams per kilogram body weight per day, Envigo, no. TD.1308603) for the time indicated in each individual experiment. For echocardiographic analysis of cardiac structure and function, mice were anaesthetized with 2% isoflurane inhalation to effect and analysed using a Vevo2100 instrument (VisualSonics) with an 18–38-MHz transducer as previously described[30]. Randomization was not performed because mice are genetically identical and of the same age ranges. A discussion of blinding and sample elimination considerations can be found in 'Mice' and 'Statistical information and experimental rigour (blinding)'.

Histology and immunohistochemistry

Primary antibodies and dilutions used for immunohistochemistry are listed in Supplementary Table 1. For histological analysis, mice were anaesthetized by isoflurane inhalation and killed by cervical dislocation. The chest was opened, and the heart was flushed with cold cardioplegia solution (1 M KCl in 1× PBS) via cardiac apical insertion of a 25-gauge needle. The left atrium was cut to allow drainage of blood from the heart, and mice were briefly perfused with cold fixative (4% paraformaldehyde in sodium phosphate buffer, pH 7.4) through the apex of the heart. Tissues were excised, flushed with fixative and incubated in cold fixative for 3.5 h at 4 °C with gentle rotation. Tissues were washed 3 times in cold 1× PBS and then cryopreserved by incubation in 30% sucrose in 1× PBS overnight at 4 °C with gentle rotation. Tissues were then embedded in TissueTek optimal cutting temperature medium (VWR, no. 25608-930) and flash-frozen at −80 °C. Five-micrometre cryosections were cut using a Leica CM1860 cryostat.

Picrosirius red staining was performed with a kit from Abcam (ab150681), as per the manufacturer's instructions. High-magnification images of hearts stained with picrosirius red were captured at 200× magnification using an Olympus BX51 microscope equipped with a single chip colour CCD camera (DP70) and DP controller software (Olympus America, v.3.1.1.). Border zone fibrosis was quantified as the percentage of picrosirius red-stained area over total tissue area analysed, as previously described[31].

All detection of genetic reporter-driven mTomato, RFP, GFP or eGFP expression was performed using endogenous fluorescence without antibody labelling. Immunohistochemistry was performed on cardiac cryosections as previously described[16,26] with the following modifications (see Supplementary Table 1 for primary antibodies and dilutions). Alexa Fluor fluorochrome-conjugated secondary antibodies were used at a 1:200 dilution for visualization (Life Technologies). For immunohistochemistry using antibodies against PCM1, antigen retrieval was first performed by incubation with 1% SDS for 5 min at room temperature with gentle rotation. PCM1 antibody was used to specifically identify cardiomyocytes in heart tissue sections. Histological cardiac sections were washed thoroughly in 1× PBS before proceeding. For immunohistochemistry using the collagen hybridizing peptide (CHP) (3Helix, no. BIO300), a stock solution of 15 µm biotin-conjugated CHP was prepared according to the manufacturer's instructions. The solution was heated to 80 °C for 5 min to denature the peptide, as previously described[21], followed by rapid cooling on ice and incubation on tissue sections overnight at 4 °C. Sections were then washed and processed for secondary antibody staining with fluorophore-conjugated streptavidin antibody used at a 1:200 dilution for visualization (Life Technologies). Confocal microscopy and image acquisition were performed using a Nikon Eclipse Ti inverted microscope equipped with a Nikon A1R confocal running NIS Elements AR 4.50.

Passive force measurements

Tissue strips from the infarct region of the left ventricle (or the left ventricular free wall for uninjured hearts) were dissected using a Zeiss Discovery V8 dissection microscope. Tissues were cut into 3 mm (length) × 2-mm (width) strips, and 3 or 4 strips were cut from each infarct region of the left ventricle. These strips contained scar and a small region of border zone on each end. Tissue strips were maintained in M199 media (Corning Cellgro, 10-060-CV) with no supplementation throughout the procedure of force measurements. Tissue strips were attached to aluminium t-clips (Kem-Mil, no. 1870) and mounted onto a permeabilized muscle fibre test apparatus (Aurora Scientific, Model: 802D-160-322) initially set to zero tension. Cardiac tissue length was then increased 5% over 50 ms, held for 450 ms and then stretched again from 5% to 50% in intervals of 5% with no period of relaxation, and force was monitored using DMC v600A software (Aurora Scientific). Change in force was calculated as the difference between maximum force generated after the 50-ms pull and the minimum force achieved after each time period. Minimum force was calculated when the rate of force decay was zero by solving for the derivative of the best-fit trend line, which was a second-degree polynomial equation.

RT–PCR from isolated infarct tissues

Tissue strips isolated from the infarct region as described in 'Passive force measurements' were homogenized with a Precellys 24 homogenizer (Bertin Instruments no. 03119.200.RD000) and RNA was isolated by using the RNeasy fibrous tissue kit according to the manufacturer's instructions (Qiagen no. 74704). One microgram of total RNA was reverse-transcribed using random oligo-dT primers and a Verso cDNA synthesis kit (Thermo Fisher Scientific no. AB1453A) according to the manufacturer's instructions. Real-time PCR was performed using Sso Advanced SYBR Green (BioRad no. 1725274) according to the following programme: one cycle of 95 °C for 10 min, one cycle of 95 °C for 15 s, 40 cycles of 95 °C for 15 s, 57 °C for 10 s and 62 °C for 30 s, and one cycle of 62 °C for 30 s. *Gapdh* expression was used for normalization. Primer sequences used are included in Supplementary Table 2.

Flow cytometry and cell sorting

For analysis of surface markers on MNCs or CPCs, cells were resuspended in 1× HBSS supplemented with 2% BGS and 2 mM EDTA and incubated with fluorophore- or biotin-conjugated primary antibodies (Supplementary Table 1) for 20 min at 4 °C with gentle rotation. Cells were then washed twice with 1× HBSS + 2% BGS and 2 mM EDTA. For detection of biotinylated antibodies, cells were incubated with streptavidin-conjugated BV421 (BD Horizon no. 563259) for 15 min at 4 °C with gentle rotation and then washed twice with 1× HBSS + 2% BGS and 2 mM EDTA. Samples were analysed using a BD FACSCanto running BD FACSDiVa V.8.0 software (BD Biosciences) and using the following laser configuration: blue (488 nm), yellow–green (561 nm) and red (635 nm). Analysis and quantification were performed using FlowJo v.10 (Tree Star).

For flow cytometry analysis of whole heart cardiac immune cell content, single-cell suspensions were first prepared using enzymatic dissociation and trituration as described in 'Preparation of cell or inflammatory therapies'. Mice were anaesthetized by 2% isoflurane inhalation to effect and killed by cervical dislocation. Hearts were rapidly excised and briefly rinsed in cold cardioplegic solution (1M KCl in 1× PBS) before enzymatic dissociation. The pellet resulting from dissociation was resuspended in 1 ml of red blood cell lysis buffer (150 mM NH_4Cl, 10 mM $KHCO_3$ and 0.1 mM Na_2EDTA) and incubated at room temperature for 5 min. Samples were then centrifuged at 400*g* for 10 min at 4 °C and resuspended in 1× HBSS supplemented with 2% BGS and 2 mM EDTA. Cells were incubated with fluorophore-conjugated primary antibodies for 20 min at 4 °C with gentle rotation, washed twice with 1× HBSS and analysed using a BD LSRFortessa running BD FACSDiVa v.8.0 software (BD Biosciences) and using the following laser configuration: UV (355 nm), violet (405 nm), blue (488 nm), yellow–green (561 nm) and red (635 nm) to detect fluorophore-conjugated antibodies and/or endogenous RFP and GFP signal from *Ccr2-RFP* × *Cx3cr1-GFP* mice. Analysis and quantification were performed using FlowJo v.10 (Tree Star.).

For isolation of cardiac $CCR2^+$ or $CX3CR1^+$ macrophages by fluorescence-activated cell sorting, hearts from *Ccr2-RFP* × *Cx3cr1-GFP* mice at 7 days after I–R injury were isolated and dissociated to single-cell suspensions as described in 'Preparation of cell or inflammatory therapies' for isolation of CPCs, except that the digestion solution was made in DMEM + 2% BGS and 1% penicillin–streptomycin instead of HBSS. Isolated cells were sorted by fluorescence-activated cell sorting using a Sony SH800S benchtop cell sorter in a BSL-2 biosafety cabinet. Endogenous RFP and GFP fluorescence were detected using 4 collinear lasers and $CCR2^+$ (RFP^+GFP^-) or $CX3CR1^+$ (GFP^+RFP^+ or RFP^-) cells were sorted into 1.5-ml Eppendorf tubes containing DMEM + 10% BGS and 1% penicillin–streptomycin. Cells were then cultured on isolated cardiac fibroblasts as described in 'Cardiac fibroblast and macrophage co-culture'.

Cardiac fibroblast isolation

Hearts were excised from ten eight-week-old male and female C57Bl/6J mice, and the ventricles and septum were isolated, rinsed in ice-cold PBS and minced into small pieces using sterile microscissors. Tissue fragments were digested in DMEM + 2% BGS and 1% penicillin–streptomycin containing type 2 collagenase (100 units per millilitre; LS004177, Worthington) for 20 min at 37 °C under gentle agitation. The digested tissue was triturated repeatedly to promote tissue dissociation. Dense fragments settled for 2 min and the supernatant, containing the cardiac fibroblasts, was collected and spun at 100*g* for 5 min. The cell pellet was resuspended in 10 ml of DMEM + 10% BGS and 1% penicillin–streptomycin and kept on ice. This process was repeated three times, until all the tissue was adequately digested. To remove cardiomyocytes and cell debris, cell suspensions were spun at 30*g*, followed by centrifugation of the supernatant at 100*g*. The final cell pellet containing the cardiac fibroblasts was resuspended in DMEM + 10% BGS and 1% penicillin–streptomycin and pre-incubated on 0.1% gelatin-coated plates for 2 h to allow fibroblast adherence before replenishment of the cell culture medium.

Cardiac fibroblast and macrophage co-culture

Isolated cardiac fibroblasts were split into 24-well 0.1% gelatin-coated plates at a seeding density of 15,000 cells per well and allowed to adhere overnight. Macrophage subtypes ($CCR2^+$ and $CX3CR1^+$ cells) isolated as described in 'Flow cytometry and cell sorting' were then seeded onto these cardiac fibroblasts at a density of 10,000 macrophages per 15,000 fibroblasts. Control fibroblasts received an equivalent amount of culture medium containing no macrophages. Adherence was verified the following day by fluorescence microscopy for RFP or GFP. Cells were isolated 72 h later for mRNA quantification.

mRNA isolation and qRT–PCR from cultured cardiac fibroblasts

Total RNA was purified from cultured cells with TRIzol reagent (Fisher Scientific no. 15596018) according to the manufacturer's instructions. Two hundred nanograms of RNA was reverse-transcribed to cDNA using the Verso cDNA synthesis kit (Thermo Fisher Scientific no. 277.97). Quantitative PCR was performed using SsoAdvanced Universal SYBR Green Supermix (BioRad no. 1725274) and assayed in duplicate, according to the manufacturer's instructions in a CFX96 PCR system. Primer sequences are included in Supplementary Table 2. All data were normalized to *Gapdh* (verified to not deviate between samples).

Macrophage culture on fibrillar collagen patches

Pre-sterilized resorbable collagen membranes (Ace Surgical Supply no. 509-3040) were cut into circles of a uniform thickness and a diameter of 6 mm, and then placed into 96-well plates. Bone marrow or peritoneal macrophages were isolated as previously described[32,33] and cultured in DMEM + 10% BGS and 1% penicillin–streptomycin. Cells were then seeded onto the collagen patches at a density of 10,000 cells per patch. Control patches were incubated in culture medium without macrophages. Five biological replicates were performed per group. After five days in culture, fibrillar collagen assembly was analysed by second harmonic generation microscopy using a Nikon A1R multiphoton upright confocal microscope equipped with a tuneable Coherent Chameleon II TiSapphire IR laser set to 840 nm. Three images were randomly taken per patch and assessed by a blinded investigator to select the representative images for each group.

Statistical information and experimental rigour (blinding)

All statistical tests used and graphical depictions of data (means and error bars, or box and whisker plots) are defined within the figure legends for the respective data panels. Exact *n* values for all experiments with statistical analysis are included in the figure legends or within the figure itself. For comparisons between two groups, unpaired or

Student's two-tailed *t*-tests were performed as noted within figure legends. For comparisons between more than two groups, a one-way ANOVA with Tukey's or Dunnett's post hoc test was performed as noted within figure legends. $P < 0.05$ was considered as statistically significant. Data in Fig. 4i used a Kruskal–Wallis test with Dunn's multiple comparisons test, as these data did not follow a normal distribution. All other data were found to follow a normal distribution as determined by the Shapiro–Wilk normality test or Kolmogorov–Smirnov test ($\alpha = 0.05$). For experiments involving I–R surgery, the number of mice that received surgery was determined based on previous experimentation in the laboratory, which demonstrated a peri-operative surgical mortality rate of 20%. Only mice that did not survive a given surgical procedure, or which were found at the time of I–R surgery to have incomplete reperfusion (failure of slipknot suture release), were excluded from analysis; otherwise no exclusions occurred. Randomization of mice within a group to receive a given surgical procedure (I–R versus sham) or treatment (saline versus cells or zymosan) was not needed because the mice were genetically identical and were littermates, although equal sex ratios and age ranges were maintained. Echocardiographic analysis, quantification of $eGFP^+$ endothelial cells, quantification of cardiomyocytes in cell cycle, measures of fibrosis, measures of tissue passive force, in vivo and in vitro gene expression analysis, and analysis of collagen organization in culture were conducted by investigators blinded to experimental treatment or procedure. Quantification of macrophage content by immunohistochemistry was performed using automated fluorescence threshold analysis in NIS Elements 4.50.

Reporting summary

Further information on research design is available in the Nature Research Reporting Summary linked to this paper.

Data availability

All raw data generated or analysed in this study are available from the corresponding author upon reasonable request. Original source data used to generate graphs in each of the figures and Extended Data figures are available as Microsoft Excel data sheet files from the corresponding author.

24. Schwanekamp, J. A., Lorts, A., Vagnozzi, R. J., Vanhoutte, D. & Molkentin, J. D. Deletion of periostin protects against atherosclerosis in mice by altering inflammation and extracellular matrix remodeling. *Arterioscler. Thromb. Vasc. Biol*. **36**, 60–68 (2016).
25. Pinto, A. R. et al. Revisiting cardiac cellular composition. *Circ. Res*. **118**, 400–409 (2016).
26. Vagnozzi, R. J. et al. Genetic lineage tracing of Sca-1$^+$ cells reveals endothelial but not myogenic contribution to the murine heart. *Circulation* **138**, 2931–2939 (2018).
27. Han, C. et al. Acute inflammation stimulates a regenerative response in the neonatal mouse heart. *Cell Res*. **25**, 1137–1151 (2015).
28. Kaiser, R. A. et al. Targeted inhibition of p38 mitogen-activated protein kinase antagonizes cardiac injury and cell death following ischemia-reperfusion in vivo. *J. Biol. Chem*. **279**, 15524–15530 (2004).
29. Sussman, M. A. et al. Prevention of cardiac hypertrophy in mice by calcineurin inhibition. *Science* **281**, 1690–1693 (1998).
30. Liu, R. et al. Cardiac-specific deletion of protein phosphatase 1β promotes increased myofilament protein phosphorylation and contractile alterations. *J. Mol. Cell. Cardiol*. **87**, 204–213 (2015).
31. Khalil, H. et al. Fibroblast-specific TGF-β-Smad2/3 signaling underlies cardiac fibrosis. *J. Clin. Invest*. **127**, 3770–3783 (2017).
32. Zhang, X., Goncalves, R. & Mosser, D. M. The isolation and characterization of murine macrophages. *Curr. Protoc. Immunol*. **14**, 14.1.1–14.1.14 (2008).
33. Davies, L. C., Jenkins, S. J., Allen, J. E. & Taylor, P. R. Tissue-resident macrophages. *Nat. Immunol*. **14**, 986–995 (2013).

Acknowledgements This work was supported by grants from the National Institutes of Health to J.D.M., S.S. and M.N. J.D.M. was supported by the Howard Hughes Medical Institute and the American Heart Association (19MERIT34370048). R.J.V. was supported by a National Research Service Award from the NIH (F32 HL128083) and a Career Development Award from the American Heart Association (19CDA34670044). All flow cytometric data were acquired using equipment maintained by the Research Flow Cytometry Core in the Division of Rheumatology at Cincinnati Children's Hospital Medical Center.

Author contributions J.D.M. and R.J.V. conceived the study. R.J.V., M.M., M.A.S., H.K., A.K.J., J.A.S., A.J.Y. and V.H. performed experiments and generated all the data shown in the manuscript. S.S. provided oversight and technical help along with J.A.S. in measuring myocardial scar mechanical properties. M.N. provided theoretical assessment of the project and advice in experimental design. J.D.M. and R.J.V interpreted the data and wrote the manuscript.

Competing interests The authors declare no competing interests.

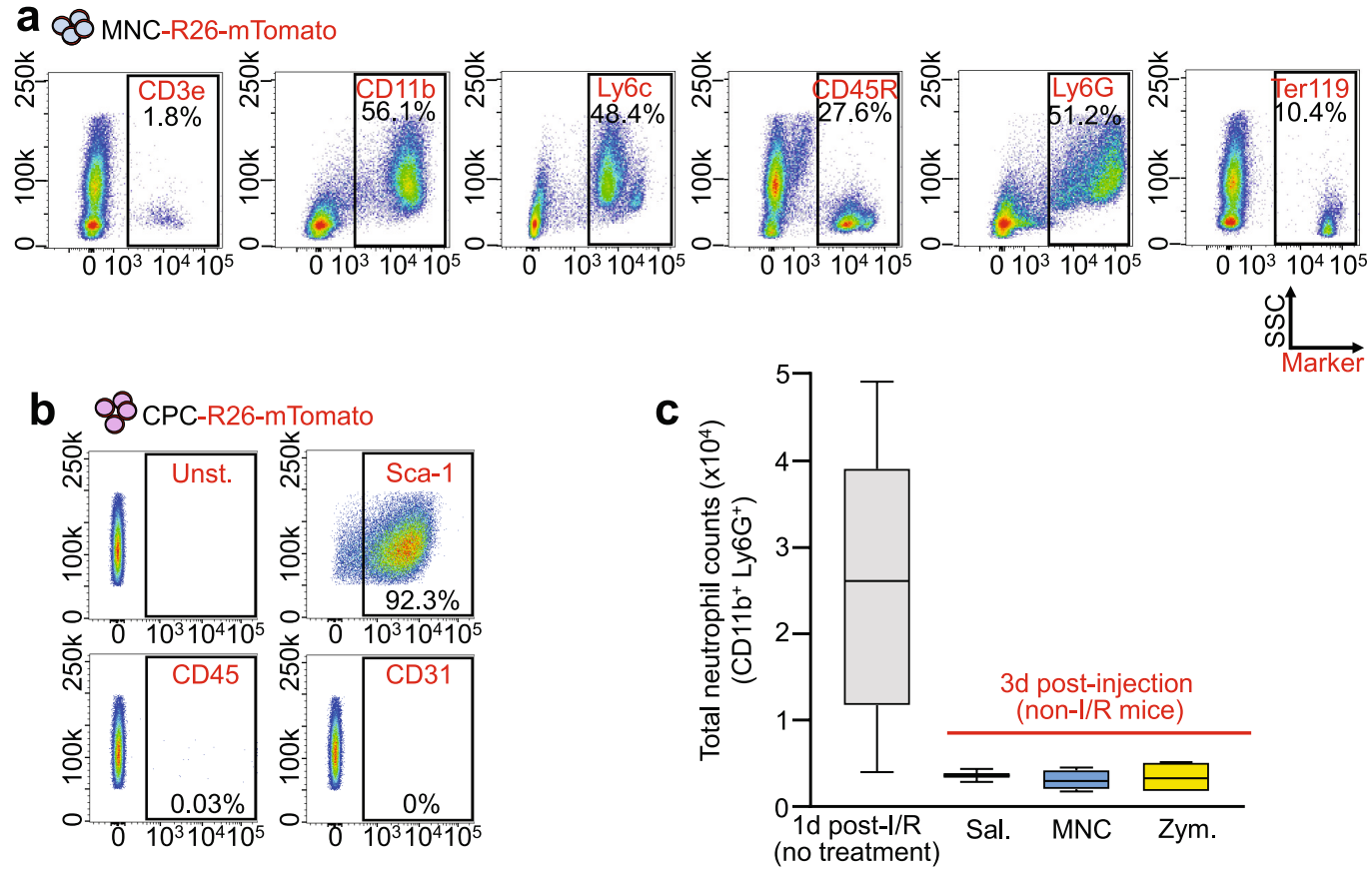
Additional information

Supplementary information is available for this paper at https://doi.org/10.1038/s41586-019-1802-2.

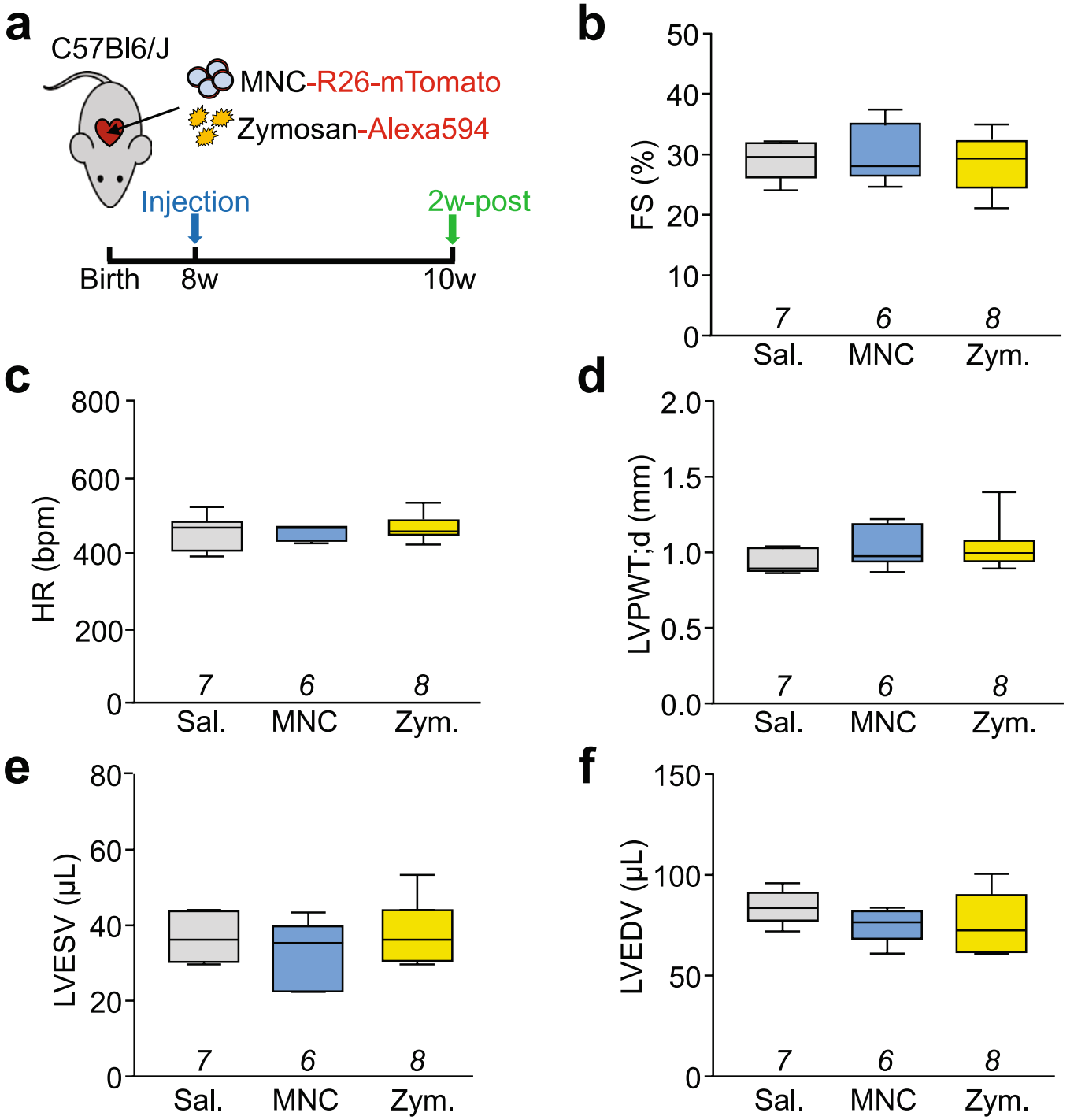
Correspondence and requests for materials should be addressed to J.D.M.

Peer review information *Nature* thanks Merry Lindsey, Christine Mummery and the other, anonymous, reviewer(s) for their contribution to the peer review of this work.

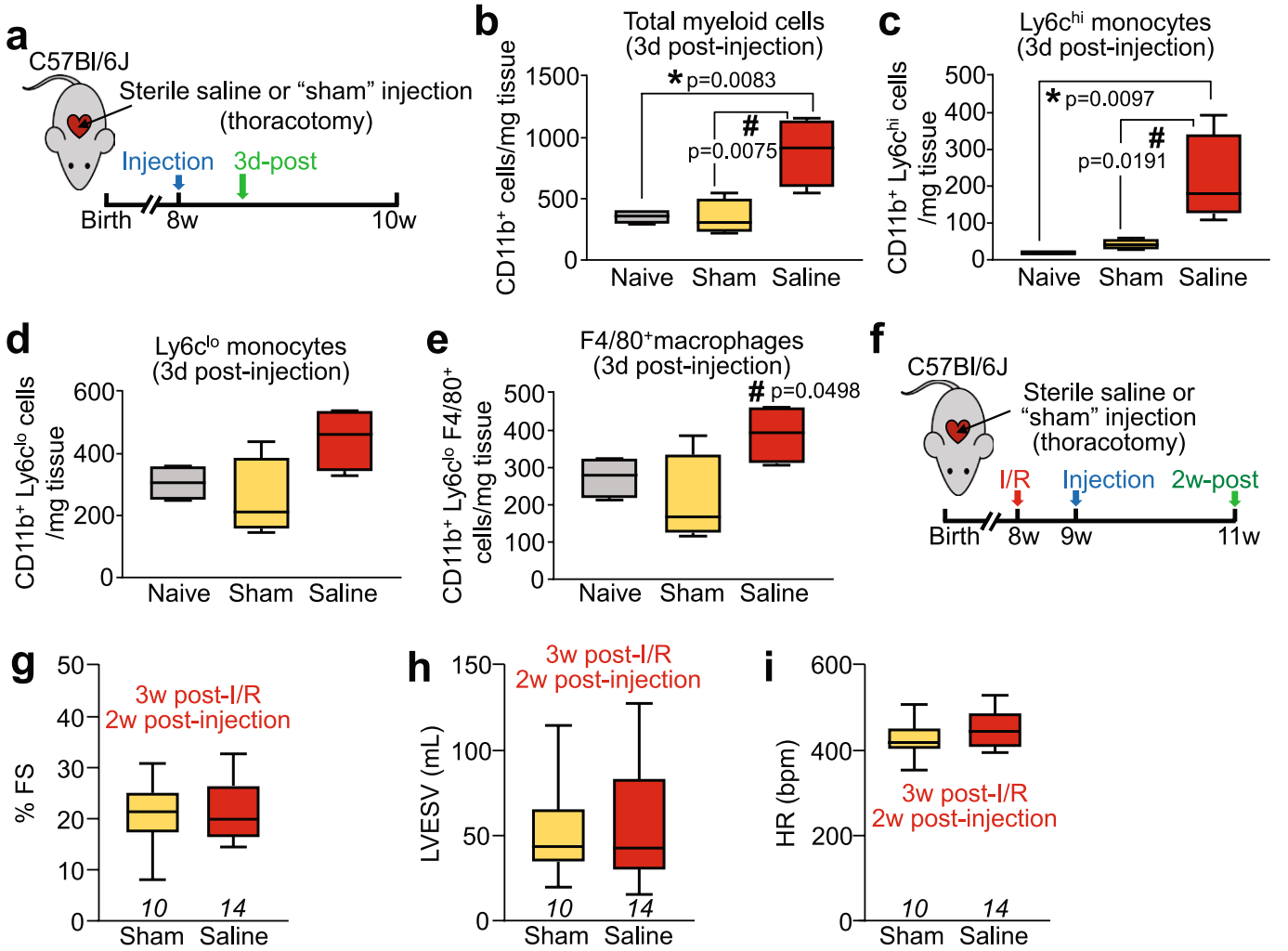
Reprints and permissions information is available at http://www.nature.com/reprints.



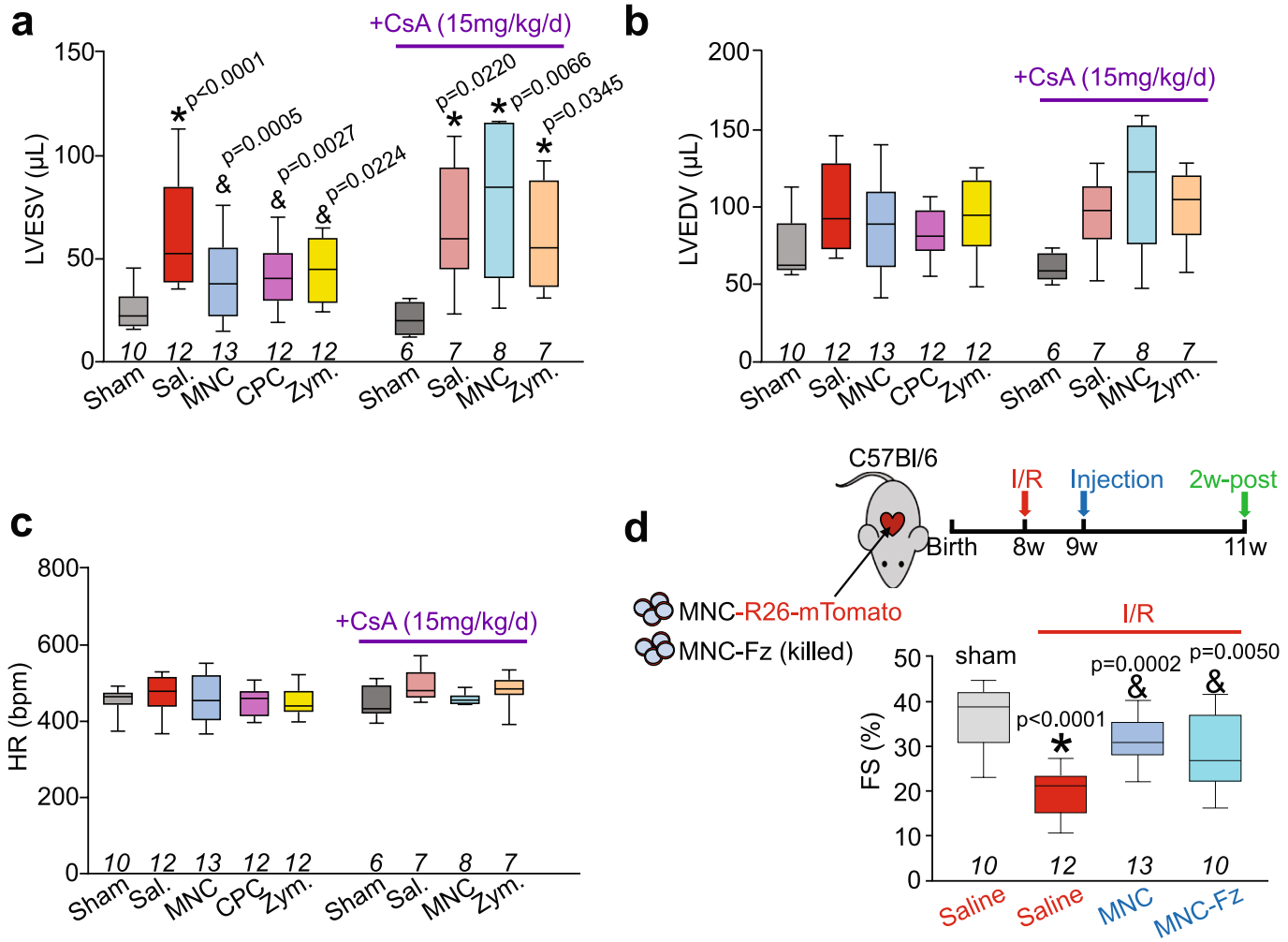
Extended Data Fig. 1 | Characterization of cells used in the injection studies and initial neutrophil response to injections. a, Flow cytometry analysis of MNCs isolated from *Rosa26-mTomato* mice for intracardiac injection. Singlet cells were selected by forward and side scatter properties followed by mTomato-positivity. mTomato$^+$ cells were then assessed for surface expression of CD3e, CD11b, Ly6c, CD45R, Ly6G or Ter119 via antibodies. **b**, Flow cytometry plots for CPCs immunolabelled with antibodies against mesenchymal (Sca1), endothelial (CD31) or haematopoietic (CD45) lineage markers as indicated in the plots. An unstained negative control (unst.) plot is also shown. Gating was determined versus unstained negative controls. Similar results in **a**, **b** were obtained from at least three independent cell preparations. **c**, Quantification via flow cytometry of total neutrophil levels in dissociated hearts from MNC-, zymosan- or saline-injected male and female C57Bl/6J mice, three days after injection. As a comparison, data from $n = 5$ C57Bl/6J mice isolated one day after I–R injury are also shown when neutrophil levels are high. Data are from $n = 4$ (MNC and zymosan) or $n = 2$ (saline) mice. Numerical data are summarized as box-and-whisker plots, indicating the median value (black bar inside box), 25th and 75th percentiles (bottom and top of box, respectively), and minimum and maximum values (bottom and top whisker, respectively).



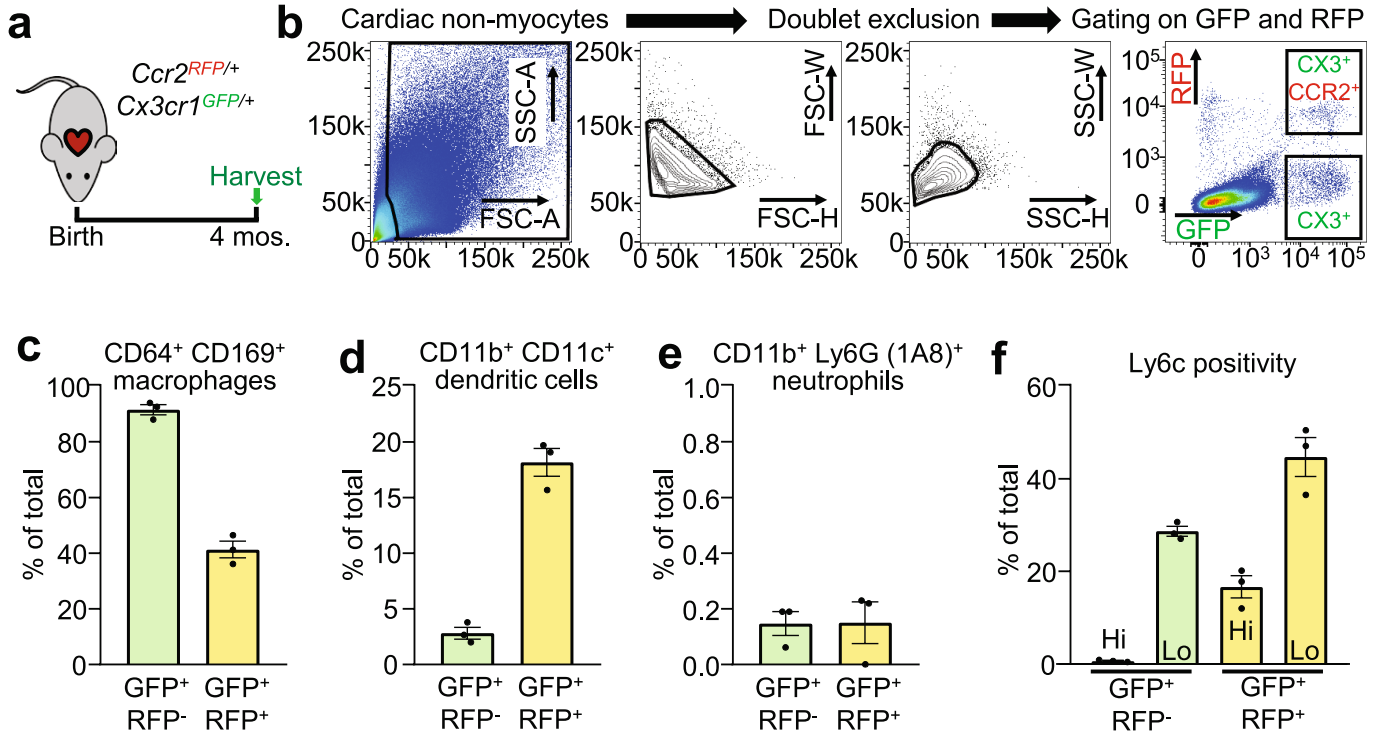
Extended Data Fig. 2 | Basal cardiac structure and function after cell or zymosan injection in uninjured mice. a, Schematic of all experiments performed in this figure, in which C57Bl/6J eight-week-old male and female mice received intracardiac injection of mTomato-labelled MNCs, Alexa 594-labelled zymosan or sterile saline and were assessed by echocardiography after two weeks. **b**–**f**, Echocardiography-measured fractional shortening (FS) percentage (**b**), heart rate (HR) as beats per minute (bpm) under isoflurane anaesthesia (**c**), left ventricular posterior wall thickness in diastole (LVPWT;d) in millimetres (**d**), left ventricular end-systolic volume (LVESV) in microlitres (**e**) and left ventricular end-diastolic volume (LVEDV) in microlitres (**f**). All values in **b**–**f** were unchanged with injection of MNCs or zymosan versus saline. All numerical data are summarized as box-and-whisker plots, indicating the median value (black bar inside box), 25th and 75th percentiles (bottom and top of box, respectively), and minimum and maximum values (bottom and top whisker, respectively). The number of mice for each group in **b**–**f** is indicated below each respective box-and-whisker plot.



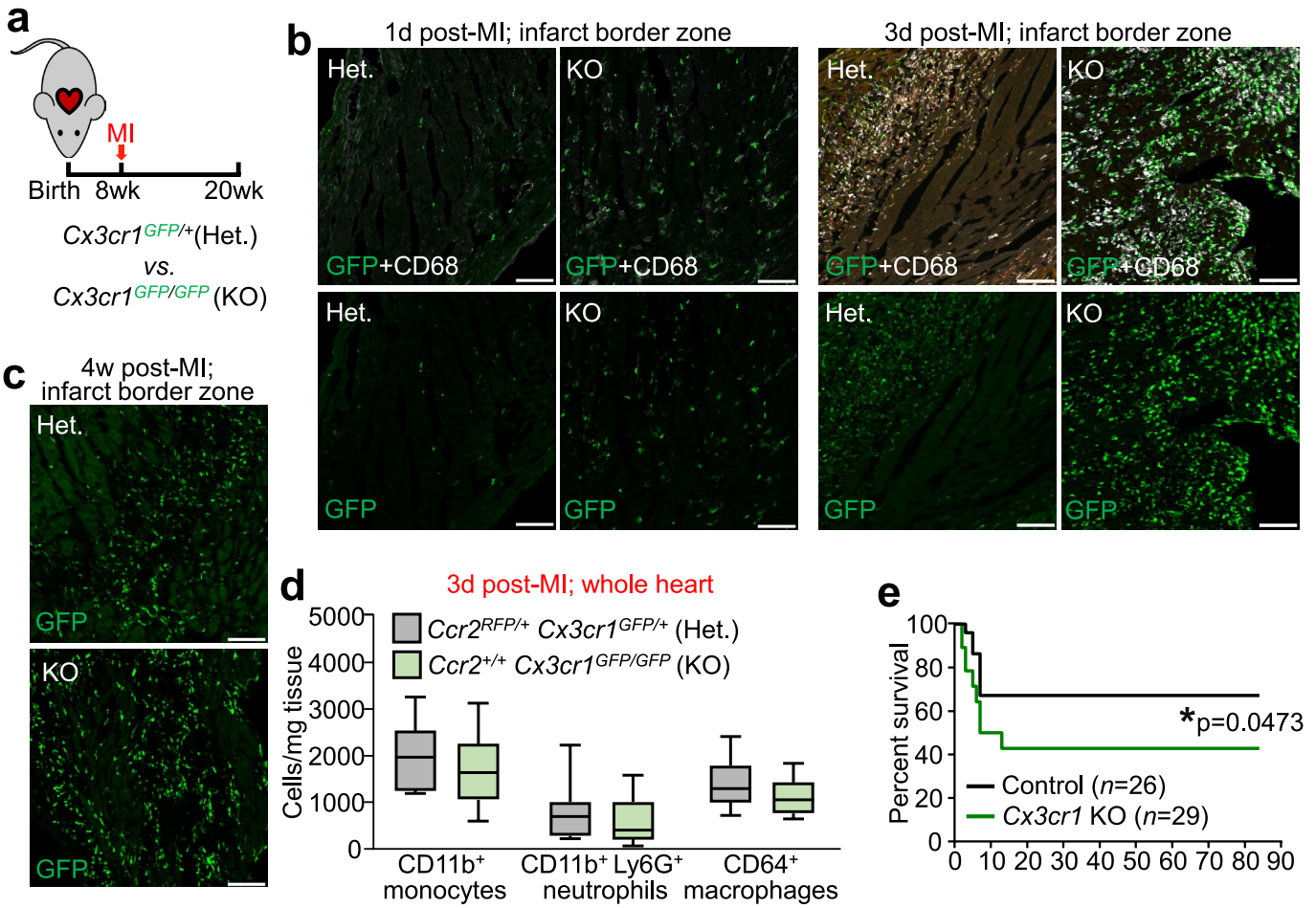
Extended Data Fig. 3 | Characterization of inflammatory and functional effects of the intracardiac injection protocol. a, Schematic of experiments performed in **b**–**e**. Eight-week-old C57Bl/6J (uninjured) male and female mice received intracardiac injection of sterile saline, or a sham procedure in which the heart was exposed by thoracotomy but no intracardiac injections were done. Naive mice without surgery served as an additional control. **b**–**e**, Quantification via flow cytometry of immune cells from enzymatically dissociated hearts from the above groups of mice. Total $CD11b^+$ myeloid cells (**b**), $CD11b^+Ly6C^{high}$ (**c**) or $CD11b^+Ly6C^{low}$ (**d**) monocytes, and $CD11b^+F4/80^+$ macrophages (**e**) from $n = 4$ mice per group are shown, normalized to the starting weight of dissociated tissue. $^*P < 0.05$ versus naive and $^{\#}P < 0.05$ versus sham by one-way ANOVA with Tukey's post hoc test (exact P values are shown in the panel). **f**, Schematic of experiments performed in **g**–**i** in which eight-week-old male and female C57Bl/6J mice received I–R injury followed by either intracardiac injection of saline or thoracotomy (sham) after one week, and then were assessed by echocardiography two weeks later. **g**–**i**, Fractional shortening (**g**), left ventricular end-systolic volume (**h**) and heart rate under isoflurane anaesthesia (**i**), as measured by echocardiography in the groups indicated. The number of mice for each group is indicated in each graph in **g**–**i**. All numerical data in this figure are summarized as box-and-whisker plots, indicating the median value (black bar inside box), 25th and 75th percentiles (bottom and top of box, respectively), and minimum and maximum values (bottom and top whisker, respectively).



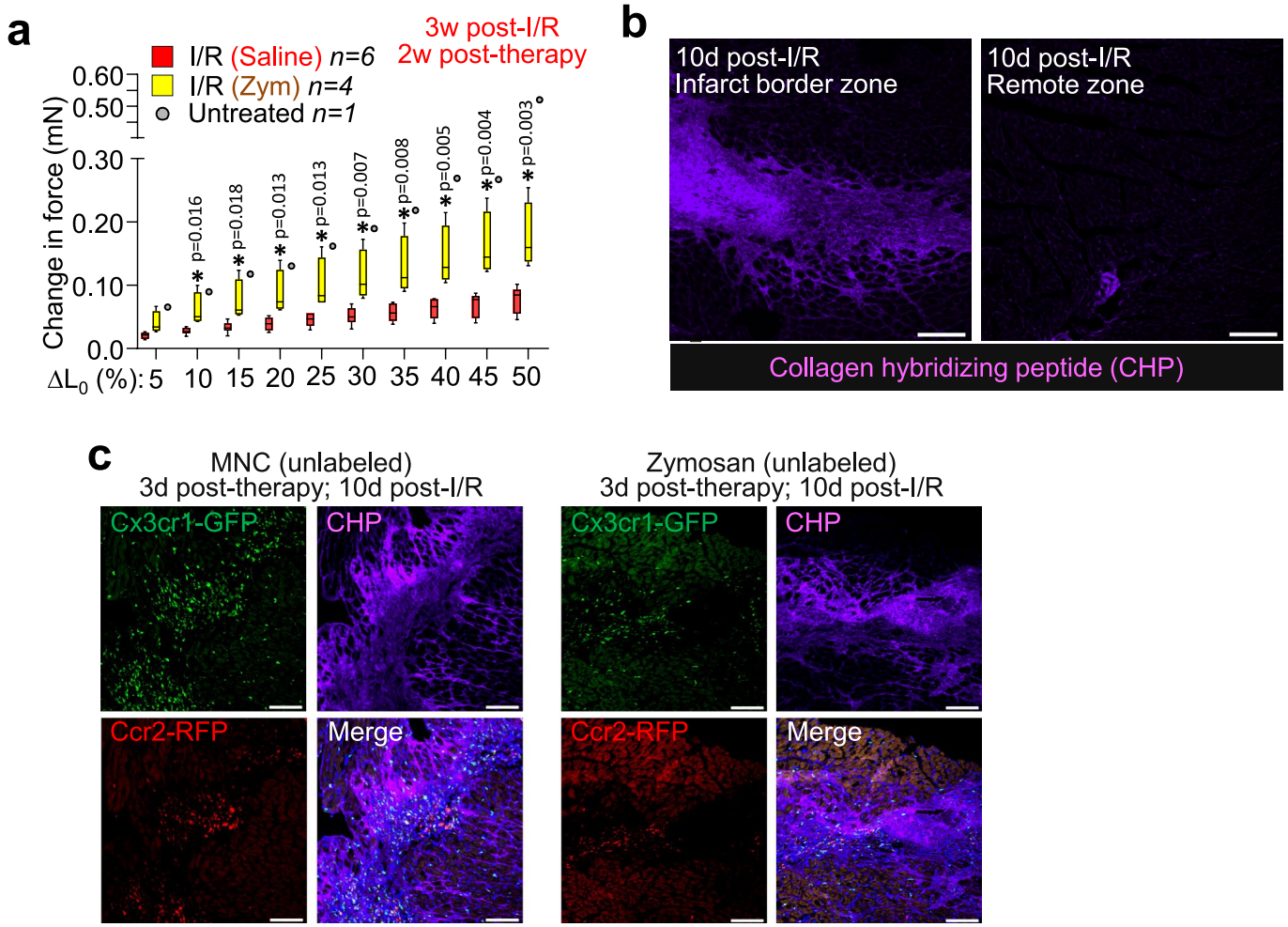
Extended Data Fig. 4 | Additional echocardiographic parameters and effect of treatment with MNCs killed by freezing and thawing, after I–R injury. **a**–**c**, Echocardiography to measure left ventricular end-systolic volume in microlitres (**a**), left ventricular end-diastolic volume in microlitres (**b**) or heart rate under isoflurane anaesthesia (**c**) in mice that received an intracardiac injection of MNCs, CPCs, zymosan or sterile saline, three weeks after I–R. These data were collected in the same group of mice shown in Fig. 3b, d. Data in **a** are significantly different, as assessed by one-way ANOVA with Dunnett's post hoc test (exact *P* values are shown in the panels). **d**, Schematic of experiment in which mice received an intracardiac injection of mTomato$^+$ MNCs or MNCs killed by freezing and thawing one week after I–R, and then two weeks later the cardiac ventricular fractional shortening percentage was measured by echocardiography. Exact *P* values are shown in the panel versus I–R and saline, which involved one-way ANOVA with Dunnett's post hoc test to examine significance. The sham, I–R and saline, and I–R and MNC groups shown here in **d** are the same data as also shown in Fig. 3, as these studies were performed in parallel. All numerical data are summarized as box-and-whisker plots, indicating the median value (black bar inside box), 25th and 75th percentiles (bottom and top of box, respectively), and minimum and maximum values (bottom and top whisker, respectively). The number of mice for each group is indicated below the respective plot.



Extended Data Fig. 5 | Characterization of cell types labelled from *Ccr2-RFP* × *Cx3cr1-GFP* knock-in mice. a, Schematic of experiments in which hearts from male and female double-heterozygous *Ccr2-RFP* × *Cx3cr1-GFP* knock-in mice ($n = 3$) were isolated and analysed by flow cytometry at 4 months of age. **b**, Representative flow cytometry plots with the gating strategy shown, in which singlet cells were first selected by forward and side scatter properties followed by gating on endogenous GFP and RFP fluorescence for $CX3CR1^+CCR2^-$ (GFP^+RFP^-) or $CX3CR1^+CCR2^+$ (GFP^+RFP^+) cells. **c**–**f**, Cells within the GFP^+RFP^- or GFP^+RFP^+ gates as shown in **b** were then assessed for surface marker expression via antibodies. $CD64^+CD169^+$ macrophages (**c**), $CD11b^+CD11c^+$ dendritic cells (**d**) or $CD11b^+Ly6G^+$ neutrophils (**e**) are shown as a percentage of all GFP^+RFP^- or GFP^+RFP^+ cells. **f**, Ly6c positivity in the total GFP^+RFP^- or GFP^+RFP^+ populations is also shown. All data are represented as the mean ± s.e.m. from $n = 3$ mice.



Extended Data Fig. 6 | Response of *Cx3cr1* global gene-deleted mice to myocardial infarction injury. a, Schematic of experiments in which eight-week-old male and female *Cx3cr1-GFP* heterozygous (het.) or *Cx3cr1-GFP/GFP* homozygous (knockout, KO) mice received myocardial infarction (MI) via permanent occlusion of the left coronary artery and were then followed out for 12 weeks. **b**, **c**, Representative confocal immunohistochemistry images from hearts of mice described in **a** at one day, three days or four weeks after myocardial infarction, showing endogenous GFP fluorescence from the *Cx3cr1* knock-in allele. Immunohistochemistry for activated CD68 macrophages (white) is also shown in **b**. Micrographs are representative of $n = 3$ mice per time point. Scale bars, 100 µm. **d**, Quantification via flow cytometry of total monocyte, neutrophil and macrophage levels in dissociated whole hearts from *Cx3cr1* heterozygous or knockout mice at three days after myocardial infarction. Data are from $n = 11$ (heterozygous) or $n = 12$ (knockout) mice. Numerical data are summarized as box-and-whisker plots, indicating the median value (black bar inside box), 25th and 75th percentiles (bottom and top of box, respectively), and minimum and maximum values (bottom and top whisker, respectively). **e**, Survival curve for *Cx3cr1-GFP/GFP* mice versus controls over 12 weeks (*x* axis shows days) after myocardial infarction injury. Control mice in this experiment included both *Cx3cr1-GFP* heterozygous and C57Bl/6J animals. The number (*n*) of mice for each group is indicated in the figure. *$P = 0.0473$ by two-sided Gehan–Breslow–Wilcoxon test.



Extended Data Fig. 7 | Mechanical and structural improvements in cell-therapy- or zymosan-treated hearts after I–R. a, Change in passive force generation over increasing stretch lengthening (per cent of L_0) in isolated infarct strips from zymosan- or saline-injected hearts, analysed three weeks after surgical injury (injection of zymosan or saline occurred two weeks before collecting from mice). Exact *P* values are shown in the panel, which were determined by unpaired two-tailed *t*-test. The I–R and saline, and untreated control, data shown here are the same as in Fig. 4, as these studies were performed in parallel. Numerical data are summarized as box-and-whisker plots, indicating the median value (black bar inside box), 25th and 75th percentiles (bottom and top of box, respectively), and minimum and maximum values (bottom and top whisker, respectively), from the number (*n*) of mice indicated in the panels. **b**, Representative confocal micrographs from heart histological sections from *Ccr2-RFP* × *Cx3cr1-GFP* mice at ten days after I–R, showing the infarct border zone versus remote myocardium, and labelled with a biotin-conjugated CHP that detects immature or denatured collagen. CHP labelling was detected with a streptavidin-conjugated Alexa 647 secondary antibody (purple). **c**, Representative confocal micrographs of heart histological sections from the post-I–R border zone of *Ccr2-RFP* × *Cx3cr1-GFP* mice that received intracardiac injection of MNCs or zymosan at seven days after I–R, analysed after an additional three days. Endogenous RFP (red) or GFP (green) fluorescence shows $CCR2^+$ or $CX3CR1^+$ macrophages, respectively. Sections were treated with CHP (purple) as in **b** to visualize immature collagen and areas of active remodelling versus areas in which subtypes of macrophage differentially localize. Images in **b**, **c** are representative of $n = 2$ mice per group. Scale bars, 100 µm.

Corresponding author(s): Jeffery D. Molkentin (jeff.molkentin@cchmc.org)

Life Sciences Reporting Summary

Nature Research wishes to improve the reproducibility of the work that we publish. This form is intended for publication with all accepted life science papers and provides structure for consistency and transparency in reporting. Every life science submission will use this form; some list items might not apply to an individual manuscript, but all fields must be completed for clarity.

For further information on the points included in this form, see Reporting Life Sciences Research. For further information on Nature Research policies, including our data availability policy, see Authors & Referees and the Editorial Policy Checklist.

Please do not complete any field with "not applicable" or n/a. Refer to the help text for what text to use if an item is not relevant to your study.
For final submission: please carefully check your responses for accuracy; you will not be able to make changes later.

ü Experimental design

1. Sample size

Describe how sample size was determined.

Sample sizes were chosen based on extensive prior experience of the lab in characterizing cardiac injury models in the mouse, including observed post-operative surgical mortality rates for myocardial infarction and ischemia/reperfusion injury.

2. Data exclusions

Describe any data exclusions.

Data exclusions were only made in the case of animals that either did not survive a given surgical procedure (intra-cardiac injection and/or myocardial infarction with reperfusion; I/R) or were insufficiently reperfused at the time of surgery (failure of surgical slipknot release). In these cases, any previously recorded data from these animals (for example at timepoints prior to death), were not excluded.

3. Replication

Describe the measures taken to verify the reproducibility of the experimental findings.

The results of all in vivo experiments were reproducible as shown across multiple animals (exact n values indicated in the text and figures) over multiple surgical cohorts. Cohorts of mice for intra-cardiac injection of cells/zymosan included age, strain, and sex-matched controls (saline injection) for comparison.

4. Randomization

Describe how samples/organisms/participants were allocated into experimental groups.

All experimental groups were allocated to provide a roughly equal mix of males and females. Randomization of mice within a group to receive a given surgical procedure (I/R or MI vs sham) or treatment (saline vs cells vs zymosan) was not needed because the mice within a given genotype or treatment group were genetically identical and were littermates.

5. Blinding

Describe whether the investigators were blinded to group allocation during data collection and/or analysis.

Full blinding during intra-cardiac injection and/or I/R injury and collection of echocardiographic data was not performed due to logistical issues of animal handling and post-operative care. Analysis of echocardiographic data, all histological analyses, gene expression analysis, and analysis of tissue passive force properties were performed by investigators blinded to experimental treatment or procedure.

Note: all in vivo studies must report how sample size was determined and whether blinding and randomization were used.

6. Statistical parameters

For all figures and tables that use statistical methods, confirm that the following items are present in relevant figure legends (or in the Methods section if additional space is needed).

n/a	Confirmed
☐	☒ The exact sample size (*n*) for each experimental group/condition, given as a discrete number and unit of measurement (animals, litters, cultures, etc.)
☐	☒ A description of how samples were collected, noting whether measurements were taken from distinct samples or whether the same sample was measured repeatedly
☐	☒ A statement indicating how many times each experiment was replicated
☐	☒ The statistical test(s) used and whether they are one- or two-sided *Only common tests should be described solely by name; describe more complex techniques in the Methods section.*
☐	☒ A description of any assumptions or corrections, such as an adjustment for multiple comparisons
☐	☒ Test values indicating whether an effect is present *Provide confidence intervals or give results of significance tests (e.g. P values) as exact values whenever appropriate and with effect sizes noted.*
☐	☒ A clear description of statistics including central tendency (e.g. median, mean) and variation (e.g. standard deviation, interquartile range)
☐	☒ Clearly defined error bars in all relevant figure captions (with explicit mention of central tendency and variation)

See the web collection on statistics for biologists for further resources and guidance.

ü Software

Policy information about availability of computer code

7. Software

Describe the software used to analyze the data in this study.

Quantitation of immunohistochemistry images was performed using NIS Elements v4.50 (Nikon Instruments). Quantitation of histological images of fibrosis was performed using Adobe Photoshop CS5. Analysis of echocardiographic data was performed using VevoLAB v1.7.1. (VisualSonics). Analysis of analytical flow cytometry data was performed using FlowJo V.10 (Tree Star, Inc). Acquisition of passive tissue force measurements was performed using DMC v600A (Aurora Scientific). For statistical analysis, two-tailed t-tests (Figures 4d, 4e) were performed using Microsoft Excel, Office365 version. All other tests, including one-way analysis of variance (ANOVA), survival curve analysis, and normality tests, were performed using GraphPad Prism version 8.0.1.

For manuscripts utilizing custom algorithms or software that are central to the paper but not yet described in the published literature, software must be made available to editors and reviewers upon request. We strongly encourage code deposition in a community repository (e.g. GitHub). *Nature Methods* guidance for providing algorithms and software for publication provides further information on this topic.

ü Materials and reagents

Policy information about availability of materials

8. Materials availability

Indicate whether there are restrictions on availability of unique materials or if these materials are only available for distribution by a third party.

Kit-MerCreMer x R-GFP mice used for lineage tracing will be made available under a materials transfer agreement (MTA) between the requesting institution and Cincinnati Children's Hospital. All other materials and reagents were obtained from commercial sources (see Online Methods for full description).

9. Antibodies

Describe the antibodies used and how they were validated for use in the system under study (i.e. assay and species).

All antibodies used in this study are commercially available. Antibody validation was performed by the individual manufacturer; validation information can be found on the manufacturers' web pages via the links provided below. Please also see Supplementary Table 1 and Online Methods for further description of antibodies, including dilutions used. Staining of samples in this study was also compared to unstained or secondary antibody-only controls processed in the same way.

Individual validation statements:
Abcam: https://www.abcam.com/primary-antibodies/improving-reproducibility-with-better-antibodies
Thermo Fisher: https://www.thermofisher.com/us/en/home/life-science/antibodies/invitrogen-antibody-validation.html
Novus: https://www.novusbio.com/5-pillars-validation
BioLegend: https://www.biolegend.com/reproducibility
eBioscience: https://www.thermofisher.com/us/en/home/life-science/antibodies/invitrogen-antibody-validation.html

Assay: Immunohistochemistry

CD68 - Figures 1b, 1c, 3i, Extended Data Figure 6b.
Supplier: Abcam, #ab53444
Monoclonal, clone FA-11
Lot: GR3241798-1
Manufacturer's validation information: https://www.abcam.com/cd68-antibody-fa-11-ab53444.pdf
Dilution used here: 1:100

Detected with:
Goat anti-rat IgG Alexa Fluor 488 (Figures 1b, 1c)
Supplier: Life Technologies, #A-11006
Lot: 1887148
Manufacturer's validation information: https://assets.thermofisher.com/TFS-Assets/LSG/certificate/Certificates-of-Analysis/1887148_A11006.pdf
Dilution used here: 1:200

or

Goat anti-rat IgG Alexa Fluor 647 (Figure 3i, Extended Data Figure 6b)
Supplier: Life Technologies, #A-21247
Lot: 2043368
Manufacturer's validation information: https://assets.thermofisher.com/TFS-Assets/BID/certificate/Certificates-of-Analysis/A21247%20Lot%202043368%20CofA.pdf
Dilution used here: 1:200

Ki-67 - Figures 2b, 2c.
Supplier: Thermo Fisher, #14-5698-82
Monoclonal, clone SolA15
Lot: 4328926
Manufacturer's validation information: https://www.thermofisher.com/order/genome-database/dataSheetPdf?producttype=antibody&productsubtype=antibody_primary&productId=14-5698-82&version=65
Dilution used here: 1:100

Detected with:
Goat anti-rat IgG Alexa Fluor 647
Supplier: Life Technologies, #A-21247
Lot: 2043368
Manufacturer's validation information: https://assets.thermofisher.com/TFS-Assets/BID/certificate/Certificates-of-Analysis/A21247%20Lot%202043368%20CofA.pdf
Dilution used here: 1:200

PCM1- Figures 2b, 2c.
Supplier: Novus Biologicals, #NBP1-87196
Polyclonal
Lot: F117419
Manufacturer's validation information: https://www.novusbio.com/PDFs/NBP1-87196.pdf
Dilution used here: 1:100

Detected with:
Goat anti-rabbit IgG Alexa Fluor 488

Life Sciences Reporting Summary (Antibodies section did not have enough room)

9. Antibodies

Describe the antibodies used and how they were validated
for use in the system under study (i.e. assay and species).

All antibodies used in this study are commercially available. Antibody validation was performed by the individual manufacturer; validation information can be found on the manufacturers' web pages via the links provided below. Please also see Supplementary Table 1 and Online Methods for further description of antibodies, including dilutions used. Staining of samples in this study was also compared to unstained or secondary antibody-only controls processed in the same way.

Individual validation statements:
Abcam: https://www.abcam.com/primary-antibodies/improving-reproducibility-with-better-antibodies
Thermo Fisher: https://www.thermofisher.com/us/en/home/life-science/antibodies/invitrogen-antibody-validation.html
Novus: https://www.novusbio.com/5-pillars-validation
BioLegend: https://www.biolegend.com/reproducibility
eBioscience: https://www.thermofisher.com/us/en/home/life-science/antibodies/invitrogen-antibody-validation.html

Assay: Immunohistochemistry

CD68 - Figures 1b, 1c, 3i, Extended Data Figure 6b.
Supplier: Abcam, #ab53444
Monoclonal, clone FA-11
Lot: GR3241798-1
Manufacturer's validation information: https://www.abcam.com/cd68-antibody-fa-11-ab53444.pdf
Dilution used here: 1:100

Detected with:
Goat anti-rat IgG Alexa Fluor 488 (Figures 1b, 1c)
Supplier: Life Technologies, #A-11006
Lot: 1887148
Manufacturer's validation information: https://assets.thermofisher.com/TFS-Assets/LSG/certificate/Certificates-of-Analysis/1887148_A11006.pdf
Dilution used here: 1:200

or

Goat anti-rat IgG Alexa Fluor 647 (Figure 3i, Extended Data Figure 6b)
Supplier: Life Technologies, #A-21247
Lot: 2043368
Manufacturer's validation information: https://assets.thermofisher.com/TFS-Assets/BID/certificate/Certificates-of-Analysis/A21247%20Lot%202043368%20CofA.pdf
Dilution used here: 1:200

Ki-67 - Figures 2b, 2c.

Supplier: Thermo Fisher, #14-5698-82
Monoclonal, clone SolA15
Lot: 4328926
Manufacturer's validation information: https://www.thermofisher.com/order/genome-database/dataSheetPdf?producttype=antibody&productsubtype=antibody_primary&productId=14-5698-82&version=65
Dilution used here: 1:100

Detected with:
Goat anti-rat IgG Alexa Fluor 647
Supplier: Life Technologies, #A-21247
Lot: 2043368
Manufacturer's validation information: https://assets.thermofisher.com/TFS-Assets/BID/certificate/Certificates-of-Analysis/A21247%20Lot%202043368%20CofA.pdf
Dilution used here: 1:200

PCM1- Figures 2b, 2c.
Supplier: Novus Biologicals, #NBP1-87196
Polyclonal
Lot: F117419
Manufacturer's validation information: https://www.novusbio.com/PDFs/NBP1-87196.pdf
Dilution used here: 1:100

Detected with:
Goat anti-rabbit IgG Alexa Fluor 488
Supplier: Life Technologies, #A-11008
Lot: 1853312
Manufacturer's validation information: https://assets.thermofisher.com/TFS-Assets/LSG/certificate/Certificates%20of%20Analysis/1853312_A11008.pdf
Dilution used here: 1:200

CD31 – Figures 2e, 2f.
Supplier: BD Biosciences, #553370
Monoclonal, clone MEC 13.3
Lot: 6196687
Manufacturer's validation information: http://www.bdbiosciences.com/ds/pm/tds/553370.pdf
Dilution used here: 1:100

Detected with:
Goat anti-rat IgG Alexa Fluor 647
Supplier: Life Technologies, #A-21247
Lot: 2043368
Manufacturer's validation information: https://assets.thermofisher.com/TFS-Assets/BID/certificate/Certificates-of-Analysis/A21247%20Lot%202043368%20CofA.pdf
Dilution used here: 1:200

Collagen Hybridizing Peptide, Biotin Conjugate (B-CHP) - Extended Data Figures 7b, 7c
Supplier: 3Helix #BIO300

Biotin-conjugated peptide
Manufacturer's validation information: https://www.3helix.com/wp-content/uploads/2019/04/3Helix_CHP_user_guide_20190326.pdf
Dilution used here: 15uM per tissue section

Detected with:
Alexa Fluor 647 Streptavidin
Supplier: Life Technologies, #S-21374
Lot: 1990312
Manufacturer's validation information: https://www.thermofisher.com/document-connect/document-connect.html?url=https%3A%2F%2Fassets.thermofisher.com%2FTFS-Assets%2FBID%2Fcertificate%2FCertificates-of-Analysis%2FS21374%2520Lot%25201990312%2520CofA.pdf&title=MTk5MDMxMg==
Dilution used here: 1:200

Assay: Flow Cytometry

CD3e, CD11b, CD45R, Ly-6G, or Ter119 (eBioscience #88-7774-75, as a biotinylated panel). Extended Data Figure 1a.

CD3e: Lot # E02344-1633
CD11b: Lot # 4283483
CD45R: Lot # 4291976
Ly6G: Lot # E03072-1632
Ter199: Lot # 4283598

Supplier: eBioscience, #88-7774-75
Manufacturer's validation information: https://assets.thermofisher.com/TFS-Assets/LSG/manuals/88-7774.pdf
Dilution used here: 1:50 for CD3e, 1:100 for each of the other antibodies

Detected with:
Streptavidin-conjugated Brilliant Violet 421
Supplier: BD Biosciences, #563259
Lot: 6077614
Manufacturer's validation information: http://www.bdbiosciences.com/ds/pm/tds/563259.pdf
Dilution used here: 1:200

Brilliant Violet 421™ anti-mouse CD11b - Extended Data Figure 3b-e.
Supplier: BioLegend, #101251
Monoclonal
Lot: B260574
Manufacturer's validation information: https://www.biolegend.com/en-us/products/brilliant-violet-421-anti-mouse-human-cd11b-antibody-7163
Dilution used here: 1:100
Visualized directly with conjugated fluorophore.

Brilliant Violet 510™ anti-mouse Ly6c - Extended Data Figure 3c-d
Supplier: BioLegend #128033
Monoclonal

Lot: B251849
Manufacturer's validation information: https://www.biolegend.com/en-us/products/brilliant-violet-510-anti-mouse-ly-6c-antibody-8726
Dilution used here: 1:100
Visualized directly with conjugated fluorophore

Brilliant Violet 421™ anti-mouse CD64 (FcγRI) - Figure 1f, Extended Data Figure 5c, Extended Data Figure 6d.
Manufacturer: BioLegend, #139309
Monoclonal
Lot: B254355
Manufacturer's validation information: https://www.biolegend.com/en-us/products/brilliant-violet-421-anti-mouse-cd64-fcgammari-antibody-8992
Dilution used here: 1:100
Visualized directly with conjugated fluorophore

APC anti-mouse F4/80 [BM8] - Figure 1f, Extended Data Figure 3e.
Manufacturer: BioLegend, #123116
Monoclonal
Lot: B268075
Manufacturer's validation information: https://www.biolegend.com/en-us/products/apc-anti-mouse-f4-80-antibody-4071
Dilution used here: 1:100
Visualized directly with conjugated fluorophore

eFluor660 CD169 (Siglec-1) - Extended Data Figure 5c.
Manufacturer: Thermo Fisher Scientific, #50-5755-82
Monoclonal
Clone: SER-4
Lot: 1917798
Manufacturer's validation information: https://www.thermofisher.com/order/genome-database/dataSheetPdf?producttype=antibody&productsubtype=antibody_primary&productId=50-5755-82&version=65
Dilution used here: 1:100
Visualized directly with conjugated fluorophore

APC anti-mouse CD11b - Extended Data Figure 5d-e, Extended Data Figure 6d.
Manufacturer: eBioscience, #17-0112-82
Monoclonal
Clone: M1/70
Lot: 4339583
Manufacturer's validation information: https://www.thermofisher.com/order/genome-database/dataSheetPdf?producttype=antibody&productsubtype=antibody_primary&productId=17-0112-82&version=65
Dilution used here: 1:100
Visualized directly with conjugated fluorophore

BUV395 Hamster Anti-Mouse CD11c - Extended Data Figure 5d.

Manufacturer: BD Biosciences, #564080
Monoclonal
Clone: HL3
Lot: 8206832
Manufacturer's validation information: http://www.bdbiosciences.com/ds/pm/tds/564080.pdf
Dilution used here: 1:100
Visualized directly with conjugated fluorophore

Brilliant Violet 421™ anti-mouse LY-6G - Extended Data Figure 5e, Extended Data Figure 6d.
Manufacturer: BD Biosciences, #562737
Monoclonal
Clone: 1A8
Lot: 7270577
Manufacturer's validation information: http://www.bdbiosciences.com/ds/pm/tds/562737.pdf
Dilution used here: 1:100
Visualized directly with conjugated fluorophore

Brilliant Violet 421™ anti-mouse Ly6c - Extended Data Figure 5f.
Manufacturer: BioLegend, #128031
Monoclonal
Clone: HK 1.4
Lot: B266457
Manufacturer's validation information: https://www.biolegend.com/en-ie/products/brilliant-violet-421-anti-mouse-ly-6c-antibody-8586
Dilution used here: 1:100
Visualized directly with conjugated fluorophore

Pacific Blue anti-mouse Ly-6A/E (Sca-1) - Extended Data Figure 1b.
Manufacturer: BioLegend, #108120
Monoclonal
Clone: D7
Lot: B181741
Manufacturer's validation information: https://www.biolegend.com/en-us/global-elements/pdf-popup/pacific-blue-anti-mouse-ly-6a-e-sca-1-antibody-3140
Dilution used here: 1:100
Visualized directly with conjugated fluorophore

CD45-APC - Extended Data Figure 1b.
Manufacturer: BD Biosciences, #559864
Monoclonal
Clone: 30-F11
Lot: 6203964
Manufacturer's validation information: http://www.bdbiosciences.com/ds/pm/tds/559864.pdf
Dilution used here: 1:100
Visualized directly with conjugated fluorophore

Brilliant Violet 421™ anti-mouse CD31 [390] - Extended Data Figure 1b.
Manufacturer: BioLegend, #102423

Monoclonal
Clone: 390
Lot: B231773
Manufacturer's validation information: https://www.biolegend.com/en-us/products/brilliant-violet-421-anti-mouse-cd31-antibody-8599
Dilution used here: 1:100
Visualized directly with conjugated fluorophore

Article

Microbial bile acid metabolites modulate gut RORγ$^+$ regulatory T cell homeostasis

https://doi.org/10.1038/s41586-019-1865-0

Received: 15 March 2019

Accepted: 7 November 2019

Published online: 25 December 2019

Xinyang Song[1,5], Ximei Sun[1,5], Sungwhan F. Oh[1,2], Meng Wu[1], Yanbo Zhang[1], Wen Zheng[1], Naama Geva-Zatorsky[1,4], Ray Jupp[3], Diane Mathis[1], Christophe Benoist[1] & Dennis L. Kasper[1]*

The metabolic pathways encoded by the human gut microbiome constantly interact with host gene products through numerous bioactive molecules[1]. Primary bile acids (BAs) are synthesized within hepatocytes and released into the duodenum to facilitate absorption of lipids or fat-soluble vitamins[2]. Some BAs (approximately 5%) escape into the colon, where gut commensal bacteria convert them into various intestinal BAs[2] that are important hormones that regulate host cholesterol metabolism and energy balance via several nuclear receptors and/or G-protein-coupled receptors[3,4]. These receptors have pivotal roles in shaping host innate immune responses[1,5]. However, the effect of this host–microorganism biliary network on the adaptive immune system remains poorly characterized. Here we report that both dietary and microbial factors influence the composition of the gut BA pool and modulate an important population of colonic FOXP3$^+$ regulatory T (T_{reg}) cells expressing the transcription factor RORγ. Genetic abolition of BA metabolic pathways in individual gut symbionts significantly decreases this T_{reg} cell population. Restoration of the intestinal BA pool increases colonic RORγ$^+$ T_{reg} cell counts and ameliorates host susceptibility to inflammatory colitis via BA nuclear receptors. Thus, a pan-genomic biliary network interaction between hosts and their bacterial symbionts can control host immunological homeostasis via the resulting metabolites.

FOXP3$^+$ T_{reg} cells residing in the gut lamina propria are critical in regulating intestinal inflammation[6,7]. A distinct T_{reg} cell population expressing the transcription factor RORγ is induced in the colonic lamina propria by colonization with gut symbionts[8–13]. Unlike thymic T_{reg} cells, colonic RORγ$^+$ T_{reg} cells have a distinct phenotype (Helios$^-$ and NRP1$^-$), and their accumulation is influenced by enteric factors derived from diet or commensal colonization[8,9]. We hypothesized that intestinal bacteria facilitate the induction of RORγ$^+$ T_{reg} cells by modifying metabolites resulting from the host's diet, and analysed RORγ$^+$Helios$^-$ cells in the colonic T_{reg} cell population from specific pathogen-free (SPF) mice fed different diets—that is, a nutrient-rich diet or a minimal diet (Supplementary Table 1). We compared RORγ$^+$ T_{reg} cells in these groups with those in germ-free (GF) mice fed a nutrient-rich diet (Fig. 1a). Both minimal-diet SPF mice and rich-diet GF mice had a lower number of RORγ$^+$Helios$^-$ cells in the colonic T_{reg} cell population than did rich-diet SPF mice (Fig. 1a and Extended Data Fig. 1a). The effect of diet on T_{reg} cell homeostatic proportions was limited to the colon and was not observed in other regions of the intestinal tract (the duodenum, jejunum or ileum) or in other lymphoid organs (the thymus, spleen, lymph nodes or Peyer's patches) (Extended Data Fig. 1b, c). When diets were switched from minimal to nutrient-rich, colonic RORγ$^+$ T_{reg} cell frequency was reversed (Extended Data Fig. 1d–f). This finding suggested that dietary components or their resulting products biotransformed by the host and its bacterial symbionts are probably responsible for the induction of colonic RORγ$^+$ T_{reg} cells. Consistent with our previous findings[8], we determined that, in our mouse colony, short-chain fatty acids (SCFAs) alone appear to be irrelevant to the accumulation of colonic RORγ$^+$ T_{reg} cells (Extended Data Fig. 1g–j).

As intestinal BAs are important metabolites affected by the host's diet and modified by gut bacteria, we checked the intestinal BA contents of these mice (Supplementary Table 2). The level of murine conjugated primary BAs (the taurine-conjugated species of cholic acid, chenodeoxycholic acid, muricholic acids and ursodeoxycholic acid (TCA, TCDCA, TMCAs and TUDCA, respectively)[14]) was greatly reduced in the faeces of minimal-diet SPF mice (Fig. 1b). Not surprisingly, the GF mice had accumulated conjugated primary BAs (Fig. 1b). However, along with the reduced RORγ$^+$ T_{reg} cell population, the levels of faecal deconjugated primary BAs and secondary BAs were significantly lower in both minimal-diet SPF mice and rich-diet GF mice than in rich-diet SPF mice (Fig. 1c, d). These results suggested that host BAs generated in response to diet and biotransformed by bacteria may induce colonic RORγ$^+$ T_{reg} cells.

To directly test whether BA metabolites regulate colonic RORγ$^+$ T_{reg} cells, we supplemented the drinking water of minimal-diet SPF mice with either individual or combinations of BAs (Fig. 1e). Neither individual primary nor secondary BAs rescued the counts of colonic RORγ$^+$ T_{reg} cells or total FOXP3$^+$ T_{reg} cells. However, mixtures of certain murine primary BAs (cholic/ursodeoxycholic acids,

[1]Department of Immunology, Blavatnik Institute, Harvard Medical School, Boston, MA, USA. [2]Center for Experimental Therapeutics and Reperfusion Injury, Department of Anesthesiology, Perioperative and Pain Medicine, Brigham and Women's Hospital, Harvard Medical School, Boston, MA, USA. [3]UCB Pharma, Slough, UK. [4]Present address: Department of Cell Biology and Cancer Science, Rappaport Faculty of Medicine, Technion Integrated Cancer Center, Technion–Israel Institute of Technology, Haifa, Israel. [5]These authors contributed equally: Xinyang Song, Ximei Sun. *e-mail: dennis_kasper@hms.harvard.edu

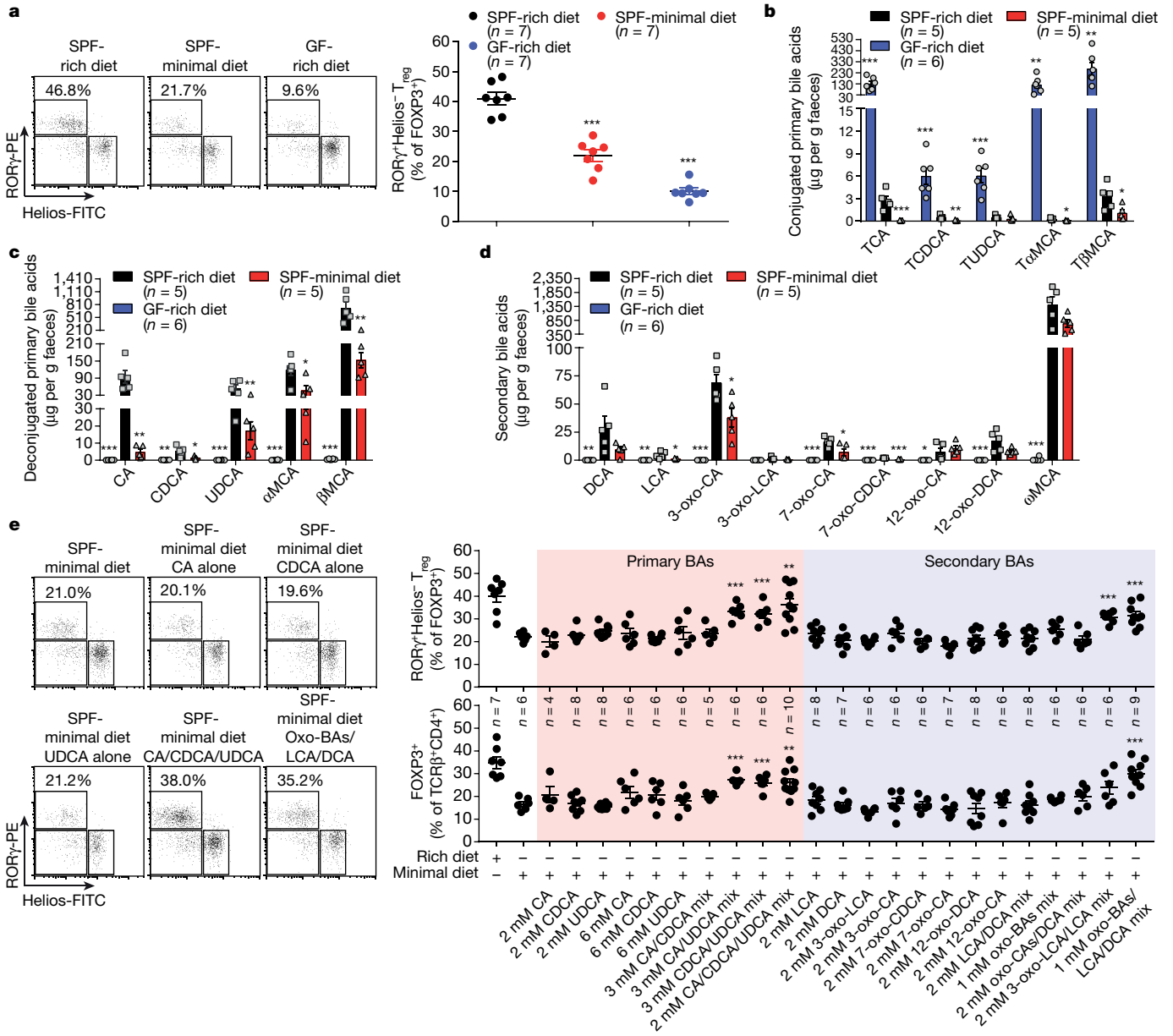


Fig. 1 | Gut BA metabolites are essential for colonic RORγ$^+$ T$_{reg}$ cell maintenance. a, Beginning at 3 weeks of age, three groups of mice were fed special diets for 4 weeks. SPF mice were fed either a nutrient-rich or a minimal diet, and GF mice were fed the nutrient-rich diet. Representative plots and frequencies of RORγ$^+$Helios$^-$ in the FOXP3$^+$CD4$^+$TCRβ$^+$ T$_{reg}$ cell population are shown. **b**–**d**, Liquid chromatography–mass spectrometry (LC–MS) quantification of faecal conjugated primary BAs (**b**), deconjugated primary BAs (**c**) and secondary BAs (**d**) from groups of mice fed as in **a**. The BAs determined were cholic acid (CA), chenodeoxycholic acid (CDCA), ursodeoxycholic acid (UDCA), α-muricholic acid (αMCA), βMCA, deoxycholic acid (DCA), lithocholic acid (LCA), 3-oxo-CA, 3-oxo-LCA, 7-oxo-CA, 7-oxo-CDCA, 12-oxo-CA, 12-oxo-DCA, ωMCA and taurine-conjugated species (TCA, TCDCA, TUDCA, TαMCA and TβMCA). **e**, Three-week-old SPF mice were fed a nutrient-rich diet, a minimal diet, or a minimal diet supplemented with one or more primary or secondary BAs in drinking water for 4 weeks. Representative plots and frequencies of colonic RORγ$^+$Helios$^-$ in the FOXP3$^+$CD4$^+$TCRβ$^+$ T$_{reg}$ cell population and of colonic FOXP3$^+$ in the CD4$^+$TCRβ$^+$ cell population are shown. The BAs used in the feed were CA, CDCA, UDCA, DCA, LCA, 3-oxo-CA, 3-oxo-LCA, 7-oxo-CA, 7-oxo-CDCA, 12-oxo-CA, 12-oxo-DCA and various indicated BA combinations. Data are representative of at least two independent experiments in **a**–**d**. Data are pooled from three independent experiments in **e**. *n* represents biologically independent animals. Data are mean ± s.e.m. $^*P < 0.05$, $^{**}P < 0.01$, $^{***}P < 0.001$, one-way analysis of variance (ANOVA) followed by the Bonferroni post hoc test.

chenodeoxycholic/ursodeoxycholic acids or cholic/chenodeoxycholic/ursodeoxycholic acids) restored colonic frequencies of both RORγ$^+$ T$_{reg}$ cells and FOXP3$^+$ T$_{reg}$ cells close to that in rich-diet mice (Fig. 1e and Extended Data Fig. 2a, b). Similarly, a mixture of eight representative secondary BAs from bacterial oxidation and dehydroxylation pathways significantly increased the number of colonic RORγ$^+$ T$_{reg}$ cells and FOXP3$^+$ T$_{reg}$ cells in minimal-diet mice (Fig. 1e and Extended Data Fig. 2a, b). We tested several more combinations of secondary BAs and found that only a combination of lithocholic/3-oxo-lithocholic acids restored colonic RORγ$^+$ T$_{reg}$ counts (Fig. 1e). No similar effect of these BAs was found on colonic type 17 T helper (T$_H$17) cells (Extended Data Fig. 2c), or on RORγ$^+$ T$_{reg}$ cells or T$_H$17 cells from the spleen, mesenteric lymph node or small intestine (Extended Data Fig. 2d, e). These results indicated that certain primary and secondary BA species within a BA pool preferentially regulate RORγ$^+$ T$_{reg}$ cells and that modulation of this T$_{reg}$ cell population by BAs is both cell-type and tissue-type specific.

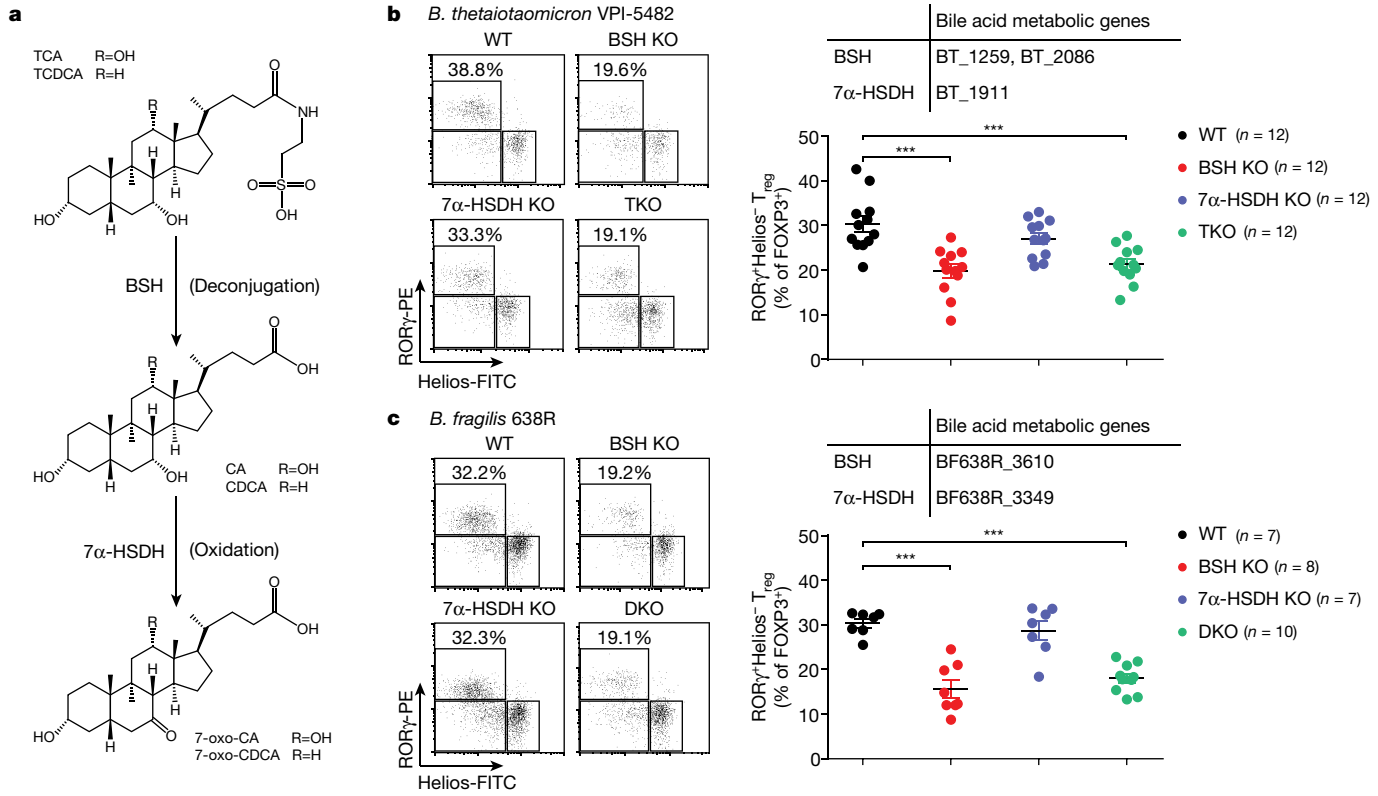


Fig. 2 | Gut bacteria control colonic RORγ$^+$ T$_{reg}$ cells through their BA metabolic pathways. a, Schematic diagram of BA metabolic pathways in *B. thetaiotaomicron* and *B. fragilis*. **b**, Each of the four groups of GF mice was colonized with one of the following microorganisms for 2 weeks: (1) a wild-type (WT) strain of *B. thetaiotaomicron*; (2) a BSH-mutant strain (BSH KO, in which both the BT_1259 and BT_2086 genes are deleted); (3) a 7α-HSDH-mutant strain (7α-HSDH KO, in which the BT_1911 gene is deleted); or (4) a triple-mutant strain (TKO; in which all three genes are deleted). Representative plots and frequencies of RORγ$^+$Helios$^-$ in the colonic FOXP3$^+$CD4$^+$TCRβ$^+$ T$_{reg}$ cell population are shown. **c**, Each of the four groups of GF mice was colonized with one of the following microorganisms for 2 weeks: (1) a wild-type strain of *B. fragilis*; (2) a BSH-KO strain (in which the BF638R_3610 gene is deleted); (3) a 7α-HSDH-KO strain (in which the BF638R_3349 gene is deleted); or (4) a double-mutant strain (DKO; in which both genes are deleted). Colonic T$_{reg}$ cells were analysed as in **b**. Data are pooled from three independent experiments in **b** and **c**. *n* represents biologically independent animals. Data are mean ± s.e.m. (**b** and **c**). ***$P < 0.001$, one-way ANOVA followed by the Bonferroni post hoc test.

As colonic BAs are derived mainly from bacterial biomodifications[2], we sought to determine how BA-producing bacteria regulate colonic RORγ$^+$ T$_{reg}$ cells. Although the composition of the gut microbiota reorganized in minimal-diet mice (Extended Data Fig. 3a–c), BA-metabolizing bacteria—for example, Bacteroidetes and Firmicutes—remained the dominant phyla within the minimal-diet mouse intestine (Extended Data Fig. 3d). Neither dietary alteration nor BA supplementation affected the level of recognized secondary BA-generating bacteria—that is, *Clostridium* cluster IV or XIVα—in the colons of these mice (Extended Data Fig. 3e), which suggests that the decrease in the number of RORγ$^+$ T$_{reg}$ cells in minimal-diet mice is not due to the loss of BA-producing bacteria. Minimal-diet GF mice had low numbers of colonic RORγ$^+$ T$_{reg}$ cells, as did rich-diet GF mice (Extended Data Fig. 3f). Transferring the gut microbiota from minimal-diet SPF mice into rich-diet GF mice—but not transfer into minimal-diet GF mice—fully restored the frequencies of colonic RORγ$^+$ T$_{reg}$ cells (Extended Data Fig. 3f). These results suggested that switching diet alone is insufficient to tune RORγ$^+$ T$_{reg}$ cells, while, in response to dietary stimuli, bacteria within the gut modulate this T$_{reg}$ cell population.

Several phyla and genera of human gastrointestinal bacteria can induce RORγ$^+$ T$_{reg}$ cells, and these same microorganism can also salvage conjugated BAs escaping from active transport in the ileum and convert them into various BA derivatives[2,15,16]. We hypothesized that BA metabolic pathways in these bacteria are involved in the induction of colonic RORγ$^+$ T$_{reg}$ cells. We chose two RORγ$^+$ T$_{reg}$ cell inducers—*Bacteroides thetaiotaomicron* and *Bacteroides fragilis*—to test this hypothesis, as they harbour simple BA metabolic pathways and are genetically tractable[17] (Fig. 2a). Using the suicide vector pNJR6 for *Bacteroides*[18], we knocked out the genes that encode proteins involved in both BA deconjugation (bile salt hydrolase (BSH)) and oxidation of hydroxy groups at the C-7 position (7α-hydroxysteroid dehydrogenase (7α-HSDH)) (Extended Data Fig. 4a, b). A genetic deficiency of the BA metabolic genes in these two species did not affect the ability of bacteria to colonize GF mouse colons (Extended Data Fig. 4c, d). Knockout of genes encoding BSH in these species altered the BA pool in monocolonized GF mice and impaired in vivo deconjugation of BAs (Extended Data Fig. 4e, f). These results were consistent with a recent report on the functions of BSH in *Bacteroides*[15]. Notably, we detected no BA level changes after deletion of the genes encoding 7α-HSDH, indicating that in these bacterial species, 7α-oxidation may not have a major role in BA metabolism. Elimination of BSH or the entire BA metabolic pathway in *Bacteroides*—a triple knockout (TKO) in *B. thetaiotaomicron* or a double knockout (DKO) in *B. fragilis*—dampened bacterial ability to induce colonic RORγ$^+$ T$_{reg}$ cells (Fig. 2b, c and Extended Data Fig. 5a, c). By contrast, 7α-HSDH mutants elicited counts of colonic RORγ$^+$ T$_{reg}$ cells comparable to those induced by wild-type *Bacteroides* (Fig. 2b, c and Extended Data Fig. 5a, c). As *Bacteroides* do not harbour typical biotransformation pathways for secondary BA generation[2], the decrease in the number of RORγ$^+$ T$_{reg}$ cells in BSH-mutant-associated GF mice indicated a direct role for primary BAs in regulating this T$_{reg}$ cell population. Deletion of BA biotransformation pathways in *Bacteroides* did not alter the ability of these species to induce colonic total FOXP3$^+$ T$_{reg}$ cells, colonic T$_H$17 cells (Extended

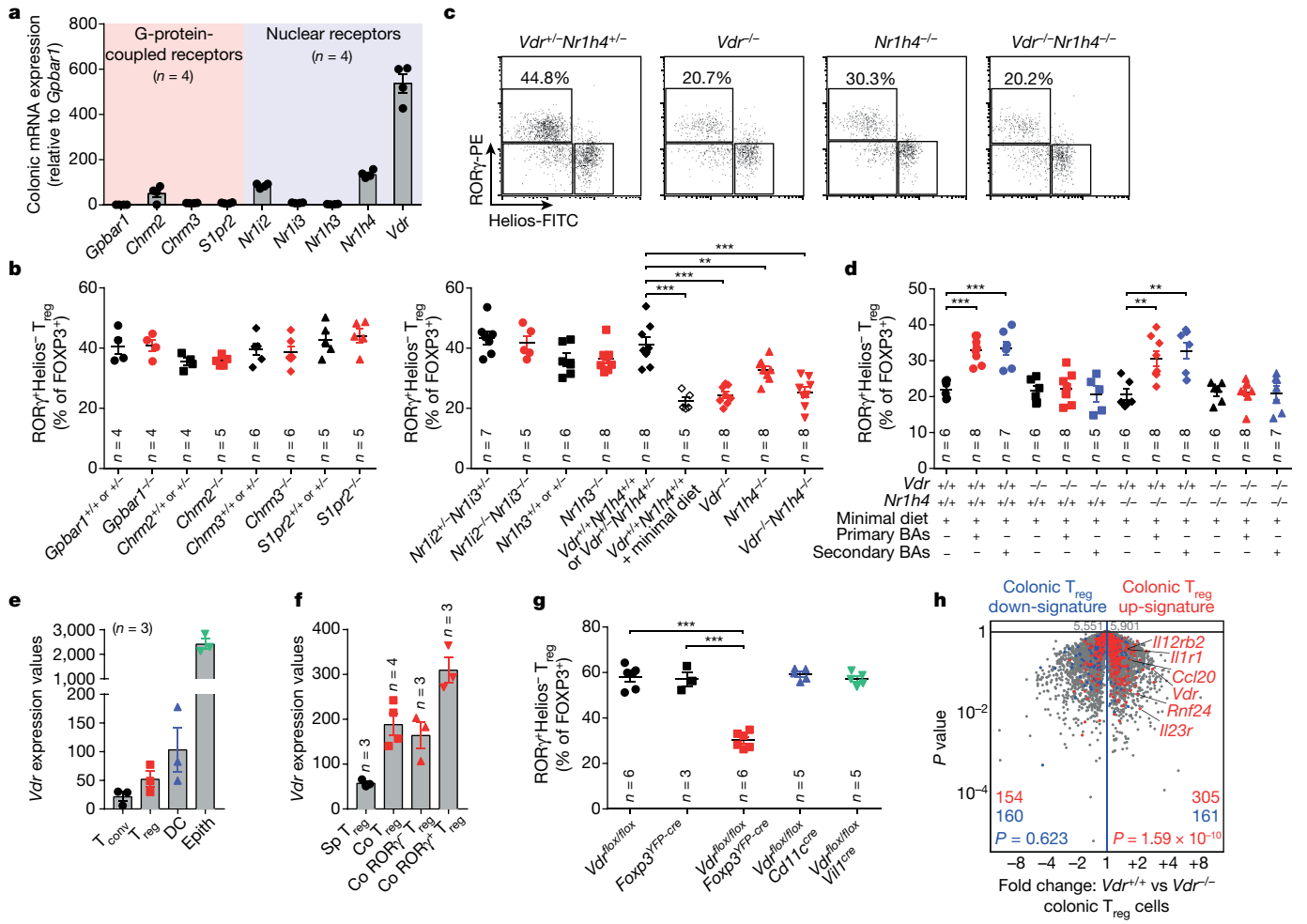


Fig. 3 | BA metabolites modulate colonic RORγ$^+$ T_{reg} cells via BARs. **a**, Quantitative mRNA expression of BARs in the colon of SPF mice. **b**, Frequencies of colonic RORγ$^+$Helios$^-$ in the FOXP3$^+$CD4$^+$TCRβ$^+$ T_{reg} cell population from mice deficient in G-protein-coupled receptors (*Gpbar1*$^{-/-}$, *Chrm2*$^{-/-}$, *Chrm3*$^{-/-}$ and *S1pr2*$^{-/-}$) and their littermate controls. **c**, Representative plots and frequencies of colonic RORγ$^+$Helios$^-$ in the FOXP3$^+$CD4$^+$TCRβ$^+$ T_{reg} cell population from mice deficient in nuclear receptors (*Nr1i2*$^{-/-}$*Nr1i3*$^{-/-}$, *Nr1h3*$^{-/-}$, *Vdr*$^{-/-}$, *Nr1h4*$^{-/-}$ and *Vdr*$^{-/-}$*Nr1h4*$^{-/-}$), their littermate controls and minimal-diet *Vdr*$^{+/+}$*Nr1h4*$^{+/+}$ mice. **d**, Three-week-old *Vdr*$^{+/+}$*Nr1h4*$^{+/+}$, *Vdr*$^{-/-}$, *Nr1h4*$^{-/-}$ and *Vdr*$^{-/-}$*Nr1h4*$^{-/-}$ mice were fed a minimal diet or a minimal diet supplemented with primary BAs (CA/CDCA/UDCA, 2 mM of each) or secondary BAs (DCA/LCA/3-oxo-CA/3-oxo-LCA/7-oxo-CA/7-oxo-CDCA/12-oxo-CA/12-oxo-DCA, 1 mM of each) in their drinking water for 4 weeks. Frequencies of colonic RORγ$^+$Helios$^-$ in the FOXP3$^+$CD4$^+$TCRβ$^+$ T_{reg} cell population are shown. **e**, Normalized expression values of *Vdr* in colonic T_{conv} cells, FOXP3$^+$ T_{reg} cells, dendritic cells (DCs) and epithelial cells (Epith). **f**, Normalized expression values of *Vdr* in splenic T_{reg} cells (Sp T_{reg}), colonic T_{reg} cells (Co T_{reg}), colonic RORγ$^-$ T_{reg} cells (Co RORγ$^-$ T_{reg}) and colonic RORγ$^+$ T_{reg} cells (Co RORγ$^+$ T_{reg}). **g**, Frequencies of colonic RORγ$^+$Helios$^-$ in the FOXP3$^+$CD4$^+$TCRβ$^+$ T_{reg} cell population from *Vdr*$^{flox/flox}$*Foxp3*$^{YFP\text{-}cre}$, *Vdr*$^{flox/flox}$*Cd11c*^{cre} and *Vdr*$^{flox/flox}$*Vil1*^{cre} mice and from *Vdr*$^{flox/flox}$ and *Foxp3*$^{YFP\text{-}cre}$ mice. **h**, Volcano plots comparing transcriptomes of colonic T_{reg} cells from *Vdr*$^{+/+}$*Foxp3*^{mRFP} or *Vdr*$^{-/-}$*Foxp3*^{mRFP} mice ($n = 3$). Colonic T_{reg} cell signature genes are highlighted in red (upregulated) or blue (downregulated). Data are pooled from two or three independent experiments. *n* represents biologically independent animals. Data are mean ± s.e.m. $^{**}P < 0.01$, $^{***}P < 0.001$, one-way ANOVA followed by the Bonferroni post hoc test (**c**, **d** and **g**) or χ^2 test (**h**).

Data Fig. 5b, d–h), or T_{reg} cells and T_H17 cells in the spleen, mesenteric lymph node and small intestine (Extended Data Fig. 5i–l).

Host BAs are metabolically modified by microorganisms and used as signalling molecules, serving as ligands that activate BA receptors (BARs)[4]. Thus, we explored whether BARs modulate gut RORγ$^+$ T_{reg} cell homeostasis. By comparing mouse colonic tissue expression of various BARs, we found that nuclear receptors, especially vitamin D receptor (VDR), were more abundant (Fig. 3a and Extended Data Fig. 6a). Next, we compared the numbers of colonic RORγ$^+$ T_{reg} cells in mice genetically deficient in each of several BARs. G-protein-coupled receptor deficiency did not affect the number of colonic RORγ$^+$ T_{reg} cells (Fig. 3b). The nuclear receptors NR1I2/3 (also known as PXR/CAR) and NR1H3 (also known as LXRα) were also non-contributory (Fig. 3c and Extended Data Fig. 6b). However, deficiency in either of the two BA-sensing nuclear receptors—VDR and NR1H4 (also known as FXR)[19,20]—compromised the number of colonic RORγ$^+$ T_{reg} cells (Fig. 3c and Extended Data Fig. 6b). The colonic RORγ$^+$ T_{reg} cell phenotype of mice with loss of both of these genes resembled that of mice with loss of only *Vdr* or in minimal-diet littermate controls (Fig. 3c and Extended Data Fig. 6b). This result indicated a prominent role for VDR signalling in modulating this colonic T_{reg} cell population. That all BAR-deficient mice had normal colonic counts of total FOXP3$^+$ T_{reg} cells and T_H17 cells (Extended Data Fig. 6c–g) as well as RORγ$^+$ T_{reg} cells in the spleen, mesenteric lymph node and small intestine (Extended Data Fig. 6h–n) indicated that BAR signalling control of RORγ$^+$ T_{reg} cells is tissue dependent.

To determine whether intestinal BAs modulate colonic RORγ$^+$ T_{reg} cells via VDR or NR1H4, we treated nuclear receptor-deficient mice with a mixture of three murine primary BAs (cholic/chenodeoxycholic/ursodeoxycholic acids) or a mixture of eight murine secondary BAs (deoxycholic acid/lithocholic acid/oxidized BAs). Both mixtures of

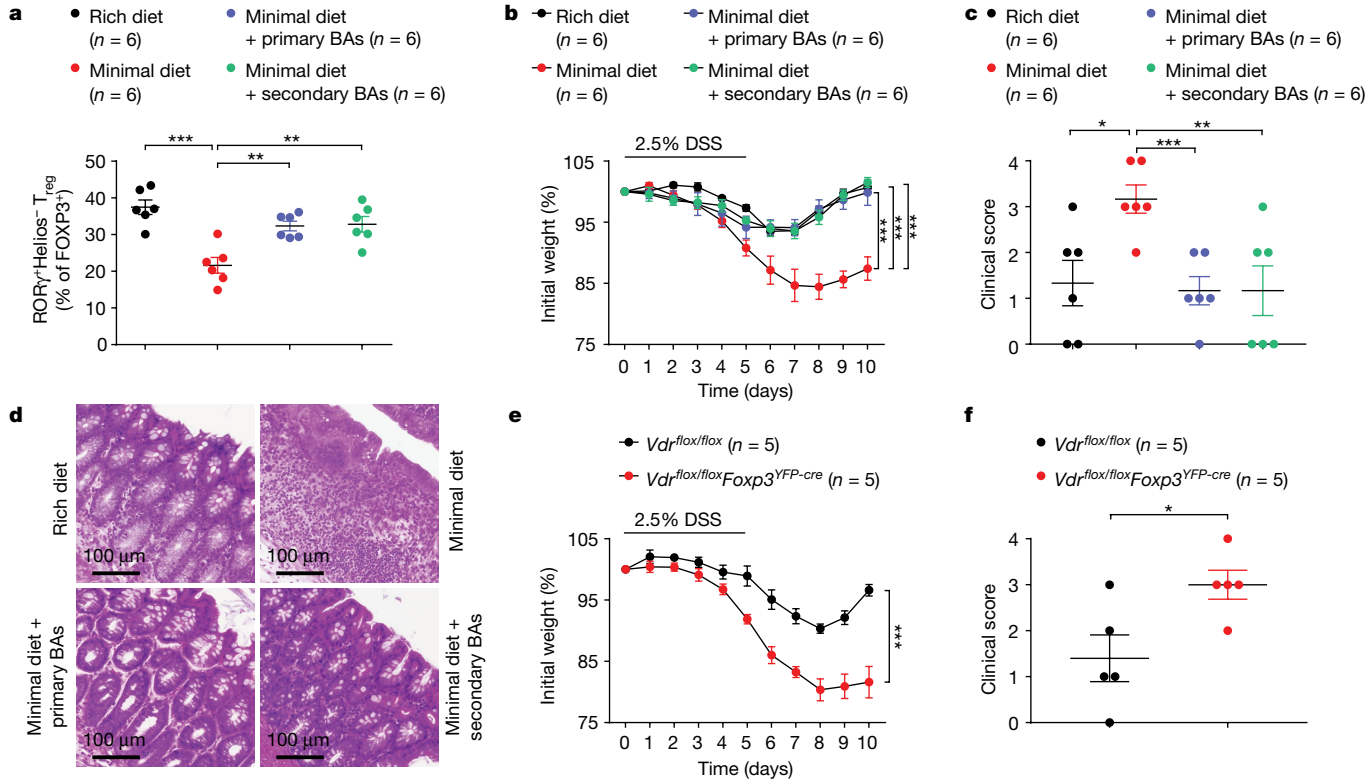


Fig. 4 | BAs ameliorate gut inflammation. a, Frequencies of RORγ$^+$Helios$^-$ in the colonic FOXP3$^+$CD4$^+$TCRβ$^+$ T_{reg} cell population on day 2 of DSS-induced colitis in mice fed a nutrient-rich diet, a minimal diet, or a minimal diet supplemented with mixtures of primary or secondary BAs in drinking water. The primary BAs were CA, CDCA and UDCA (2 mM of each). The secondary BAs were DCA, LCA, 3-oxo-CA, 3-oxo-LCA, 7-oxo-CA, 7-oxo-CDCA, 12-oxo-CA and 12-oxo-DCA (1 mM of each). **b**, Daily weight loss of mice described in **a** during the course of DSS-induced colitis. **c**, **d**, Clinical scores (**c**) and haematoxylin and eosin-stained histological sections (**d**) for representative colons on day 10 of colitis (see **b**). **e**, Daily weight loss of *Vdr*$^{flox/flox}$ and *Vdr*$^{flox/flox}$*Foxp3*$^{YFP\text{-}cre}$ mice during the course of DSS-induced colitis. **f**, Clinical scores for representative colons on day 10 of colitis (see **e**). Data are representative of two or three independent experiments. *n* represents biologically independent animals. Data are mean ± s.e.m. (**a**–**c**, **e** and **f**). $^*P < 0.05$, $^{**}P < 0.01$, $^{***}P < 0.001$, one-way ANOVA (**a** and **c**) or two-way ANOVA (**b** and **e**) followed by the Bonferroni post hoc test, or two-tailed Student's *t*-test (**f**).

BAs were sufficient to rescue colonic frequencies of RORγ$^+$ T_{reg} cells in minimal-diet NR1H4-deficient mice and their littermate controls (Fig. 3d). However, the failure of BA supplementation to restore colonic RORγ$^+$ T_{reg} cell counts in both minimal-diet VDR-deficient mice and minimal-diet mice deficient in both VDR and NR1H4 (Fig. 3d) implied a major role for the microbial BA–VDR axis in the regulation of colonic RORγ$^+$ T_{reg} cell populations.

As 1,25-dihydroxyvitamin D_3 can also activate VDR[19], we compared its levels in sera and colonic tissues from rich-diet and minimal-diet SPF mice and rich-diet GF mice. We found comparable levels among these three groups of mice (Extended Data Fig. 7a, b). We also found that, as previously reported[9], dietary vitamin A deficiency led to a decrease in the number of colonic RORγ$^+$ T_{reg} cells, while the absence of dietary vitamin D_3 did not have a similar effect (Extended Data Fig. 7c, d). These data indicated that the BA–VDR axis, not the vitamin D_3–VDR axis, is crucial in modulating RORγ$^+$ T_{reg} cells in the gut.

Next, we investigated which cell type responds to BA by affecting the upregulation of RORγ$^+$ T_{reg} cells. RNA sequencing (RNA-seq) performed on colonic-sorted cell fractions revealed high *Vdr* expression in epithelial and dendritic cells but also in FOXP3$^+$ T_{reg} cells—at a higher level than in T conventional (T_{conv}) cells (Fig. 3e). Indeed, *Vdr* expression is higher in colonic T_{reg} cells than in splenic T_{reg} cells, especially in RORγ$^+$ T_{reg} cells (Fig. 3f). This result is consistent with our earlier single-cell analysis highlighting VDR as a transcriptional regulator in colonic T_{reg} cells but not in other tissue T_{reg} cells[21]. To directly assess relevance, we crossed *Vdr*$^{flox/flox}$ conditional knockout mice with different Cre drivers to excise *Vdr* in distinct cell types. Colonic RORγ$^+$ T_{reg} cell counts were markedly reduced in *Vdr*$^{flox/flox}$*Foxp3*$^{YFP\text{-}cre}$ mice, while loss of VDR in dendritic or epithelial cells (*Cd11c*^{cre} and *Vil1*^{cre}; *Cd11c* is also known as *Itgax*) had no effect (Fig. 3g), demonstrating that VDR modulates colonic RORγ$^+$ T_{reg} cells in an intrinsic manner. RNA-seq profiling of colonic T_{reg} cells from VDR-deficient mice or control littermates showed a marked reduction in the transcriptional signature of colonic T_{reg} cells[8] in the absence of VDR (Fig. 3h); the RORγ$^+$ T_{reg} cell-specific signature was also downregulated, as expected (Extended Data Fig. 8). These data suggest that VDR is important in determining the RORγ-dependent program in colonic T_{reg} cells.

RORγ$^+$ T_{reg} cells have been reported to maintain colonic homeostasis and minimize colitis severity[8,11,22,23]. We investigated whether intestinal BAs modulate colonic inflammatory responses in a dextran sodium sulfate (DSS)-induced murine model of colitis. We saw no sign of inflammation in the colons of unchallenged mice fed a nutrient-rich diet, a minimal diet, or a minimal diet supplemented with primary or secondary BA mixtures in drinking water (Extended Data Fig. 9a–c). However, at the onset of colitis, challenged minimal-diet mice had a reduced proportion of colonic RORγ$^+$ T_{reg} cells (Fig. 4a)—an indication that they might be predisposed to severe colitis. Indeed, as DSS-induced colitis progressed, minimal-diet mice lost more weight and experienced more-severe colitis than rich-diet mice (Fig. 4b–d). Notably, both primary and secondary BA supplementation increased RORγ$^+$ T_{reg} cell counts in minimal-diet mice (Fig. 4a) and alleviated their colitis symptoms and signs (Fig. 4b–d). However, after colitis onset, BA supplementation barely alleviated colitis in minimal-diet mice (Extended Data Fig. 9d, e), suggesting that maintenance of an RORγ$^+$ T_{reg} cell pool by BAs during homeostasis is crucial to host resistance to DSS colitis. We next explored whether the BA–VDR axis is involved in regulating colitis in

mice. As in minimal-diet mice, deficiency of VDR in mice worsened the DSS-induced colitis phenotype (Extended Data Fig. 10a–c). The protective role of VDR signalling was also consistently observed in another mouse colitis model: naive $CD4^+$ T cell adaptive transfer into RAG1-deficient mice (Extended Data Fig. 10d–g). Importantly, severe DSS-induced colitis developed in $Vdr^{flox/flox}Foxp3^{YFP\text{-}cre}$ mice (Fig. 4e, f), implying that the BA–VDR axis has an intrinsic role in T_{reg} cell control of colonic inflammation.

As important molecular mediators, intestinal BAs are critical in maintaining a healthy colonic $ROR\gamma^+$ T_{reg} cell pool through BARs. Gut bacteria differ in the types and quantities of BA derivatives they can generate. For instance, across different phyla, many gut bacterial species harbour genes encoding BSH that are involved in the primary BA deconjugation process. As their regulation and substrate specificity may vary, both primary and secondary BA metabolic profiles of these bacteria are likely to be affected[2,15]. In addition, the microbial diversity of secondary BA metabolism adds another layer of complexity to BA derivative production in individual species that may ultimately affect their capacity for $ROR\gamma^+$ T_{reg} cell induction.

In view of the complexity of BA derivatives, our study suggests that dominant intestinal primary BA species—for example, cholic/chenodeoxycholic/ursodeoxycholic acids—along with certain potent secondary BA species—for example, lithocholic/3-oxo-lithocholic acids—modulate $ROR\gamma^+$ T_{reg} cells through the BAR VDR. Dysregulation of intestinal BAs has been proposed as a mediator of the pathogenesis of human inflammatory bowel diseases and colorectal cancers[1,24]. The essential role of VDR in modulating peripheral $ROR\gamma^+$ T_{reg} cells and colitis susceptibility raises the interesting possibility that human *VDR* genetic variants associated with inflammatory bowel diseases[25] might affect disease susceptibility through improper control of the intestinal T_{reg} cell pool. Mechanistically, it is intriguing to speculate that the nuclear receptor VDR—a colonic T_{reg} cell-preferring transcription factor[21]—may modulate colonic T_{reg} cell homeostasis by coordinating BA signals with transcription factor activity. An understanding of the molecular mechanisms underlying the regulation of colonic T_{reg} cells by this biliary network between hosts and their associated microorganisms will be valuable in improving therapy for human gastrointestinal inflammatory disorders.

Online content

Any methods, additional references, Nature Research reporting summaries, source data, extended data, supplementary information, acknowledgements, peer review information; details of author contributions and competing interests; and statements of data and code availability are available at https://doi.org/10.1038/s41586-019-1865-0.

1. Postler, T. S. & Ghosh, S. Understanding the holobiont: how microbial metabolites affect human health and shape the immune system. *Cell Metab.* **26**, 110–130 (2017).
2. Ridlon, J. M., Kang, D. J. & Hylemon, P. B. Bile salt biotransformations by human intestinal bacteria. *J. Lipid Res.* **47**, 241–259 (2006).
3. Wahlström, A., Sayin, S. I., Marschall, H. U. & Bäckhed, F. Intestinal crosstalk between bile acids and microbiota and its impact on host metabolism. *Cell Metab.* **24**, 41–50 (2016).
4. Fiorucci, S. & Distrutti, E. Bile acid-activated receptors, intestinal microbiota, and the treatment of metabolic disorders. *Trends Mol. Med.* **21**, 702–714 (2015).
5. Brestoff, J. R. & Artis, D. Commensal bacteria at the interface of host metabolism and the immune system. *Nat. Immunol.* **14**, 676–684 (2013).
6. Tanoue, T., Atarashi, K. & Honda, K. Development and maintenance of intestinal regulatory T cells. *Nat. Rev. Immunol.* **16**, 295–309 (2016).
7. Panduro, M., Benoist, C. & Mathis, D. Tissue Tregs. *Annu. Rev. Immunol.* **34**, 609–633 (2016).
8. Sefik, E. et al. Mucosal immunology. Individual intestinal symbionts induce a distinct population of $ROR\gamma^+$ regulatory T cells. *Science* **349**, 993–997 (2015).
9. Ohnmacht, C. et al. Mucosal immunology. The microbiota regulates type 2 immunity through $ROR\gamma t^+$ T cells. *Science* **349**, 989–993 (2015).
10. Geva-Zatorsky, N. et al. Mining the human gut microbiota for immunomodulatory organisms. *Cell* **168**, 928–943 (2017).
11. Xu, M. et al. c-MAF-dependent regulatory T cells mediate immunological tolerance to a gut pathobiont. *Nature* **554**, 373–377 (2018).
12. Yissachar, N. et al. An intestinal organ culture system uncovers a role for the nervous system in microbe–immune crosstalk. *Cell* **168**, 1135–1148 (2017).
13. Kim, K. S. et al. Dietary antigens limit mucosal immunity by inducing regulatory T cells in the small intestine. *Science* **351**, 858–863 (2016).
14. Sayin, S. I. et al. Gut microbiota regulates bile acid metabolism by reducing the levels of tauro-beta-muricholic acid, a naturally occurring FXR antagonist. *Cell Metab.* **17**, 225–235 (2013).
15. Yao, L. et al. A selective gut bacterial bile salt hydrolase alters host metabolism. *eLife* **7**, e37182 (2018).
16. Devlin, A. S. & Fischbach, M. A. A biosynthetic pathway for a prominent class of microbiota-derived bile acids. *Nat. Chem. Biol.* **11**, 685–690 (2015).
17. Wexler, A. G. & Goodman, A. L. An insider's perspective: *Bacteroides* as a window into the microbiome. *Nat. Microbiol.* **2**, 17026 (2017).
18. Stevens, A. M., Shoemaker, N. B. & Salyers, A. A. The region of a *Bacteroides* conjugal chromosomal tetracycline resistance element which is responsible for production of plasmidlike forms from unlinked chromosomal DNA might also be involved in transfer of the element. *J. Bacteriol.* **172**, 4271–4279 (1990).
19. Makishima, M. et al. Vitamin D receptor as an intestinal bile acid sensor. *Science* **296**, 1313–1316 (2002).
20. Makishima, M. et al. Identification of a nuclear receptor for bile acids. *Science* **284**, 1362–1365 (1999).
21. DiSpirito, J. R. et al. Molecular diversification of regulatory T cells in nonlymphoid tissues. *Sci. Immunol.* **3**, eaat5861 (2018).
22. Yang, B. H. et al. $Foxp3^+$ T cells expressing RORγt represent a stable regulatory T-cell effector lineage with enhanced suppressive capacity during intestinal inflammation. *Mucosal Immunol.* **9**, 444–457 (2016).
23. Britton, G. J. et al. Microbiotas from humans with inflammatory bowel disease alter the balance of gut Th17 and $ROR\gamma t^+$ regulatory T cells and exacerbate colitis in mice. *Immunity* **50**, 212–224 (2019).
24. Staley, C., Weingarden, A. R., Khoruts, A. & Sadowsky, M. J. Interaction of gut microbiota with bile acid metabolism and its influence on disease states. *Appl. Microbiol. Biotechnol.* **101**, 47–64 (2017).
25. Xue, L. N. et al. Associations between vitamin D receptor polymorphisms and susceptibility to ulcerative colitis and Crohn's disease: a meta-analysis. *Inflamm. Bowel Dis.* **19**, 54–60 (2013).

Publisher's note Springer Nature remains neutral with regard to jurisdictional claims in published maps and institutional affiliations.

© The Author(s), under exclusive licence to Springer Nature Limited 2019

Methods

Mice and dietary treatments

C57BL/6J wild-type mice were obtained from Jackson, as were *Vdr*$^{-/-}$, *Nr1h3*$^{-/-}$, *Nr1h4*$^{-/-}$, *Chrm2*$^{-/-}$, *Chrm3*$^{-/-}$, *Rag1*$^{-/-}$, *Foxp3*$^{YFP\text{-}cre}$, *Cd11c*^{cre}, *Vil1*^{cre} and *Foxp3*^{mRFP} mice. *Nr1i2*$^{-/-}$*Nr1i3*$^{-/-}$ mice were obtained from Taconic. *Gpbar1*$^{-/-}$ mice were purchased from KOMP Repository. *S1pr2*$^{-/-}$ mice were provided by T. Hla (Boston Children's Hospital). *Vdr*$^{flox/flox}$ mice[26] were provided by D. Gardner (University of California, San Francisco) and then crossed with *Foxp3*$^{YFP\text{-}cre}$, *Cd11c*^{cre} or *Vil1*^{cre} mice to generate the corresponding cell-type-specific knockout mice. *Vdr*$^{-/-}$*Nr1h4*$^{-/-}$ mice were obtained by crossing *Vdr*$^{+/-}$ with *Nr1h4*$^{+/-}$ mice. *Vdr*$^{+/+}$*Foxp3*^{mRFP} or *Vdr*$^{-/-}$*Foxp3*^{mRFP} reporter mice were generated by crossing *Vdr*$^{+/-}$ with *Foxp3*^{mRFP} reporter mice. Sterilized vitamin A-deficient, vitamin D_3-deficient and control diets on a nutrient-rich diet background were purchased from TestDiet. For dietary treatment experiments with BA supplementation, 3-week-old C57BL/6J wild-type mice were fed either a sterilized nutrient-rich diet (LabDiet 5K67) or a minimal diet (TestDiet AIN-76A) for 4 weeks. Some groups of the mice fed a minimal diet were also treated with various BAs (sodium salt form) in drinking water for 4 weeks as described below. The primary BAs tested were cholic acid, chenodeoxycholic acid and ursodeoxycholic acid (2 mM or 6 mM of a single BA); a mixture of cholic acid and chenodeoxycholic acid (3 mM of each, 6 mM in total); a mixture of cholic acid and ursodeoxycholic acid (3 mM of each, 6 mM in total); a mixture of chenodeoxycholic acid and ursodeoxycholic acid (3 mM of each, 6 mM in total); and a mixture of cholic acid, chenodeoxycholic acid and ursodeoxycholic acid (2 mM of each, 6 mM in total). The secondary BAs tested were deoxycholic acid, lithocholic acid, 3-oxo-cholic acid, 3-oxo-lithocholic acid, 7-oxo-cholic acid, 7-oxo-chenodeoxycholic acid, 12-oxo-cholic acid and 12-oxo-deoxycholic acid (2 mM of a single BA); a mixture of deoxycholic acid and lithocholic acid (2 mM of each, 4 mM in total); a mixture of lithocholic acid and 3-oxo-lithocholic acid (2 mM of each, 4 mM in total); a mixture of deoxycholic acid, 3-oxo-cholic acid, 7-oxo-cholic acid and 12-oxo-cholic acid (2 mM of each, 8 mM in total); a mixture containing the oxo-BAs (1 mM of each, 6 mM in total); and a mixture containing the oxo-BAs, deoxycholic acid and lithocholic acid (1 mM of each, 8 mM in total). Three-week-old mice fed a minimal diet were also treated with SCFAs (sodium salt form) in drinking water. The SCFAs tested were acetate and propionate (36 mM or 150 mM of either SCFA); butyrate (36 mM or 100 mM); and a combination of acetate, propionate and butyrate (36 mM of each, 108 mM in total). Fresh drinking water was supplied each week. Pregnant C57BL/6J wild-type mice were also fed a sterilized nutrient-rich diet or a minimal diet during gestation and nursing, and their offspring were exposed to the same diet until weaning at approximately 3 weeks of age. The offspring were then fed the same diet as their dams or switched to the opposite diet for another 4 weeks before phenotype analysis. Occasional growth restriction in mice fed a minimal diet necessitated their exclusion from all experiments. All mice were housed under the same conditions in SPF facilities at Harvard Medical School (HMS), and littermates from each mouse line were bred as strict controls. GF C57BL/6 mice were obtained from the National Gnotobiotic Rodent Resource Center at the University of North Carolina at Chapel Hill and were maintained in GF isolators at HMS. Animal protocol IS00000187-3 and COMS protocol 07-267 were approved by the HMS Institutional Animal Care and Use Committee and the Committee on Microbiological Safety, respectively. All animal studies were performed in compliance with the guidelines of ARRIVE.

Anaerobic bacterial culture

B. thetaiotaomicron VPI-5482 and *B. fragilis* 638R were grown either on basal medium (protease peptone, 20 g l^{-1}; yeast extract, 5 g l^{-1}; and NaCl, 5 g l^{-1}) supplemented with 0.5% glucose, 0.5% K_2HPO_4, 0.05% L-cysteine, 5 mg l^{-1} haemin and 2.5 mg l^{-1} vitamin K_1, or on BBL Brucella agar with 5% sheep blood, haemin and vitamin K_1. The bacteria were then cultured under strictly anaerobic conditions (80% N_2, 10% H_2 and 10% CO_2) at 37 °C in an anaerobic chamber.

Genetical manipulation of bacteria

Deletion mutants of *B. thetaiotaomicron* VPI-5482 were created by removal of the genes encoding BSHs (BT_1259 and BT_2086), the gene encoding 7α-HSDH (BT_1911) or all three genes. Deletion mutants of *B. fragilis* 638R were created by removal of the gene encoding BSH (BF638R_3610), the gene encoding 7α-HSDH (BF638R_3349) or both genes. DNA segments (1 kb) upstream and downstream of the region to be deleted were PCR amplified with the following primers: BT_1259 up forward: 5′-TTTGTCGACTTATATTTTCTTCCAAAACT-3′; BT_1259 up reverse: 5′-CAAGCTGCTATCAATAATTTCGATTTTTAGTTATA-3′; BT_1259 down forward: 5′-CTAAAAATCGAAATTATTGATAGCAGCTTGCTGCA-3′; BT_1259 down reverse: 5′-TTTGGATCCGGGAGGATTCCACATAATAT-3′; BT_2086 up forward: 5′-TTTGTCGACCATCCAAACCCAGTGTGAAC-3′; BT_2086 up reverse: 5′-ATAACTAACTATCGAATTACTTCCAAATTAAATAG-3′; BT_2086 down forward: 5′-TAATTTGGAAGTAATTCGATAGTTAGTTATGTGGT-3′; BT_2086 down reverse: 5′-TTTGGATCCAAGAGCATAAAGAGCTGTTG-3′; BT_1911 up forward: 5′-TTTGTCGACTAGGAAAAGAAAAAGTGATC-3′; BT_1911 up reverse: 5′-CTGTCCGGGGTATATATATGTTGAGAATTTGATGA-3′; BT_1911 down forward: 5′-AAATTCTCAACATATATATACCCCGGACAGTACAT-3′; BT_1911 down reverse: 5′-TTTGGATCCAATTTGATATAAGCGTACGA-3′; BF638R_3610 up forward: 5′-TTTGTCGACTATAGCTGGATGGCTGTTGC-3′; BF638R_3610 up reverse: 5′-CCTCGGTAGACATTTACTCTTTATATTAAAATGGT-3′; BF638R_3610 down forward: 5′-TTTAATATAAAGAGTAAATGTCTACCGAGGCAGAT-3′; BF638R_3610 down reverse: 5′-TTTGGATCCAGAAGAAGAGATTGGTTCAC-3′; BF638R_3349 up forward: 5′-TTTGTCGACATCCCCGCCTGAGCAAGAAG-3′; BF638R_3349 up reverse: 5′-TTGATAAGATTCTTTAATAGGATGGTTTTGAGGAT-3′; BF638R_3349 down forward: 5′-CAAAACCATCCTATTAAAGAATCTTATCAAGTTAC-3′; BF638R_3349 down reverse: 5′-TTTGGATCCCCTGAGGGGTGGGAGAAACT-3′. PCR products from upstream and downstream regions were further fused together by fusion PCR to generate 2-kb PCR products, which were digested with BamHI and SalI. The digested products were cloned into the appropriate site of the *Bacteroides* suicide vector pNJR6. The resulting plasmids were conjugally transferred into *Bacteroides* strains by the helper plasmid R751, and *Bacteroides* strains integrated with the plasmids were selected by erythromycin resistance. The integrated *Bacteroides* strains were passaged for ten generations without erythromycin selection, and cross-out mutants were determined by PCR with primers targeting the two flanking regions of the indicated genes. PCR of an intact gene plus its flanking regions generated a product of approximately 1,150–1,500 bp, while successful deletion of the gene of interest resulted in a PCR amplicon of only 350–450 bp of its two flanking regions. The DKO mutant of *B. fragilis* and the TKO mutant of *B. thetaiotaomicron* were created by subsequent deletion of the indicated genes.

Generation of monocolonized mice

GF C57BL/6J mice were orally inoculated by gavage with a broth-grown single bacterial strain at 4 weeks of age. Each group of mice was then maintained in a gnotobiotic isolator under sterile conditions for 2 weeks. Faecal material was collected and plated 2 weeks after bacterial inoculation to determine colonization levels (colony-forming unit per gram of faeces) and to ensure colonization by a single bacterial strain.

BA extraction and quantification

Faecal contents from the distal colons of mice were collected and weighed before BA extraction[27]. In brief, one weighed faecal pellet was resuspended with 500 µl sterile ddH_2O in a 1.5-ml screw-cap conical tube and sonicated for 10 min. The homogenates were centrifuged at 300*g* for 5 min, and the supernatants were transferred to a new tube. The remaining material was resuspended in 250 µl LC–MS-grade methanol

containing internal standards and subjected to sonication for another 10 min. The homogenates were also centrifuged at 300*g* for 5 min and the supernatants were collected and combined, after which another 500-µl volume of sterile ddH_2O was added to make a final 1.25-ml solution. The solution was acidified with acetic acid (Sigma) and then loaded onto a methanol-activated C18 column. The column was subsequently washed with 1 ml of 85:15 (vol/vol) H_2O/methanol solution, and the BAs were eluted with 2 ml of 25:75 (vol/vol) H_2O/methanol solution. The eluted solutions were dried under nitrogen and resuspended in 200 µl of 50:50 (vol/vol) H_2O/acetonitrile solution. The samples were kept at −20 °C until analysed. Nineteen synthetic standards (taurocholic acid, taurochenodeoxycholic acid, tauroursodeoxycholic acid, cholic acid, chenodeoxycholic acid, ursodeoxycholic acid, lithocholic acid and deoxycholic acid from Sigma; tauro-α-muricholic acid, tauro-β-muricholic acid, β-muricholic acid and ω-muricholic acid from Santa Cruz; and α-muricholic acid, 3-oxo-cholic acid, 3-oxo-lithocholic acid, 7-oxo-cholic acid, 7-oxo-chenodeoxycholic acid, 12-oxo-cholic acid and 12-oxo-deoxycholic acid from Steraloids) were run, and a calibration curve was generated for quantification. All standards were resuspended in LC–MS-grade acetonitrile and prepared in-phase for analysis. All samples and standards were analysed by ultra-performance liquid chromatography coupled to electrospray ionization tandem mass spectrometry (UPLC–ESI-MS/MS; Thermo Scientific Orbitrap Q Exactive with Thermo Vanquish UPLC) with a Phenomenex Kinetex C8 (100 mm × 3 mm × 1.7 µm) column; a 20–95% gradient of H_2O-acetonitrile was used as eluent, with 0.1% formic acid as an additive. Mass spectral data were acquired by a cycle of MS1 scan (range 300–650), followed by data-dependent MS/MS scanning (ddMS2) of the top 5 ions in the pre-generated inclusion list. D_4-glycocholic acid and D_4-deoxycholic acid served as internal standards for conjugated and unconjugated BAs, respectively.

SCFA extraction and quantification

Faecal contents from the distal colons of mice were collected and weighed before SCFA extraction. Faecal contents were resuspended in 75% acetonitrile containing three deuterated internal standards (D_3-acetate, D_5-propionate and D_7-butyrate). Samples were sonicated for 10 min, vortexed and centrifuged at 8,000*g* for 5 min. Supernatant was collected and treated with activated charcoal to remove non-polar lipids by re-centrifuging. Supernatant was then collected, dried under nitrogen and resuspended in 95% acetonitrile solution. The samples were kept at −20 °C until analysed. All standards were resuspended in UPLC-grade methanol. For hydrophilic interaction liquid chromatography (HILIC)–ESI-MS/MS analysis, a Waters BEH amide HILIC column (2.1 mm × 100 mm × 2.5 µm) was used with a linear gradient of acetonitrile:H_2O = 95:5 to 60:40 (vol/vol) with 2 mM ammonium formate at pH 9.0. Deprotonated anion ($[M-H]^-$) of each SCFA (acetate, propionate and butyrate) was quantitated in negative-ion mode.

MS data acquisition and processing

Each individual species has been matched with its (1) accurate MS1 anion ($[M-H]^-$ or $[M+HCOO^-]$), (2) isotope ratio, and (3) LC retention time of authentic standard, for suitable identification and quantification of level 1 metabolite[28]. Thermo Xcalibur Suite version 3.0 was used for peak identification and area integration as well as generation of a calibration curve for all synthetic standards. Raw data (integrated ion counts) were converted to absolute amounts by the calibration curve of individual species. Recovery of internal standards of individual samples was also calculated in same procedure. The calculated value was normalized by sample weight and the proportion of the injected sample for analysis to generate the desired final concentration (µg per g or µmol per g sample).

Isolation of mouse lymphocytes and flow cytometry

For isolation of lamina propria lymphocytes, colonic and small-intestinal tissues were dissected and fatty portions discarded. Peyer's patches were also removed from the small intestines for isolation of lymphocytes. The excised intestinal tissues were washed in cold PBS buffer, and epithelia were removed by 500-r.p.m. stirring at 37 °C in RPMI medium (Gibco) containing 1 mM EDTA (Ambion), 1 mM dithiothreitol (Sigma) and 2% (vol/vol) FBS (GemBio). After 15 min of incubation, the epithelium-containing supernatants were discarded, and the remaining intestinal tissues were washed in RPMI medium with 5% (vol/vol) FBS, further minced into small pieces, and digested by 500-r.p.m. stirring at 37 °C in RPMI medium containing collagenase type II (1.5 mg ml^{-1}, Invitrogen), Dispase II (0.5 mg ml^{-1}, Invitrogen) and 1.2% (vol/vol) FBS for 40 min. The digested tissues were filtered, and the solutions were centrifuged at 500*g* for 10 min to collect lamina propria cells. The pellets were resuspended, and the lamina propria lymphocytes were isolated by GE Healthcare Percoll (40%/80%) gradient centrifugation. For isolation of Peyer's patch lymphocytes, the excised Peyer's patches were digested in the same medium by 500-r.p.m. stirring at 37 °C for 10 min, the digested Peyer's patches were filtered, the solutions were centrifuged at 500*g* for 10 min and lymphocytes were collected. Lymph nodes, spleens and thymuses were mechanically disrupted. Single-cell suspensions were subjected to flow cytometric analysis by staining with antibodies against CD45 (30-F11, BioLegend), CD4 (GK1.5, BioLegend), TCRβ (H57-597, BioLegend), Helios (22F6, BioLegend), RORγ (AFKJS-9, eBioscience) and FOXP3 (FJK-16s, eBioscience). For intracellular staining of transcription factors, cells were blocked with an antibody against CD16/32 (2.4G2, BD Pharmingen) and stained for surface and viability markers. Fixation of cells in eBioscience Fix/Perm buffer for 50 min at room temperature was followed by permeabilization in eBioscience permeabilization buffer for 50 min in the presence of antibodies at room temperature. Cells were acquired with a Miltenyi MACSQuant Analyzer, and analysis was performed with FlowJo software.

Murine colitis models and histology

Three-week-old C57BL/6J wild-type mice were fed a sterilized nutrient-rich diet or a minimal diet for 4 weeks. Some groups of the mice fed a minimal diet were also pre-treated with a bile-salt mixture in drinking water for 4 weeks. The mice were next treated with 2.5% DSS (MP Biomedicals) in drinking water for 5 days and then switched back to regular water or bile salt-containing water for another 5 days[29]. *Vdr*$^{+/+}$, *Vdr*$^{-/-}$, *Vdr*$^{flox/flox}$ and *Vdr*$^{flox/flox}$*Foxp3*$^{YFP\text{-}cre}$ mice were treated with 2.5% DSS by the same protocol. The mice were weighed throughout the course of experimental colitis and were killed at specific time points, after which colonic tissue was obtained for histopathological and FACS analyses. For the T cell-adoptive transfer model of colitis[29], the indicated splenic naive T cells ($TCR\beta^+CD4^+CD25^-CD45RB^{hi}$) were sorted from 8-week-old *Vdr*$^{+/+}$ and *Vdr*$^{-/-}$ mice by flow cytometry (Astrios, BD Biosciences). Cells (5×10^5 in 200 µl sterile PBS) were then intraperitoneally injected into *Rag1*$^{-/-}$ recipient mice. The mice were weighed throughout the T cell colitis model to assess their weight loss. Colonic tissues from both colitis models were dissected and immediately fixed with Bouin's fixative solution (RICCA) for histological analyses. Paraffin-embedded sections of colonic tissue were stained with haematoxylin and eosin, and clinical scores were determined by light microscopy[30].

RNA isolation and quantitative PCR

Total RNA was extracted from mouse colonic tissues with TRIzol reagent (Invitrogen) according to the manufacturer's instructions. RNA samples were reverse-transcribed into cDNA with a TaKaRa PrimeScript RT Reagent Kit. The cDNA samples were amplified by quantitative PCR with a KAPA SYBR FAST qPCR kit on an Eppendorf Realplex^2 Mastercycler. The primers for quantitative PCR were as follow: *Vdr* forward: 5′-CACCTGGCTGATCTTGTCAGT-3′; *Vdr* reverse: 5′-CTGGTCATCAGAGG TGAGGTC-3′; *Nr1h3* forward: 5′-TGTGCGCTCAGCTCTTGT-3′; *Nr1h3* reverse: 5′-TGGAGCCCTGGACATTACC-3′; *Nr1h4* forward: 5′-GAAAATCC AATTCAGATTAGTCTTCAC-3′; *Nr1h4* reverse: 5′-CCGCGTGTTCTGTT AGCAT-3′; *Nr1i2* forward: 5′-TCTCAGGTGTTAGGTGGGAGA-3′; *Nr1i2*

reverse: 5′-GCACGGGGGTACAACTGTTA-3′; *Nr1i3* forward: 5′-AAATGTTGGCATGAGGAAAGA-3′; *Nr1i3* reverse: 5′-CTGATTCAGTTGCAAAGATGCT-3′; *Gpbar1* forward: 5′-ATTCCCATGGGGGTTCTG-3′; *Gpbar1* reverse: 5′-GAGCAGGTTGGCGATGAC-3′; *Chrm2* forward: 5′-AAAGGCTCCTCGCTCCAG-3′; *Chrm2* reverse: 5′-AGTCAAGTGGCCAAAGAAACA-3′; *Chrm3* forward: 5′-ACTGGACAGTCCGGGAGATT-3′; *Chrm3* reverse: 5′-TGCCATTGCTGGTCATATCT-3′; *S1pr2* forward: 5′-CCCAACTCCGGGACATAGA-3′; *S1pr2* reverse: 5′-ACAGCCAGTGGTTGGTTTTG-3′; *Rpl13a* forward: 5′-GGGCAGGTTCTGGTATTGGAT-3′; *Rpl13a* reverse: 5′-GGCTCGGAAATGGTAGGGG-3′. Expression of the indicated genes was normalized to the expression of housekeeping gene *Rpl13a*.

16S rRNA profiling of the gut microbiota

Faecal DNA was extracted from faecal pellets of the indicated mice with a QIAGEN QIAamp Fast DNA Stool Mini Kit (ref. no. 51604) according to the manufacturer's instructions. The DNA samples were stored at −80 °C before processing. Purified DNA samples were quantified with a Qubit dsDNA HS Assay Kit (Invitrogen, Q32854) and normalized to 6 ng μl^{-1}, with subsequent amplification with barcoded primer pairs: 515f PCR forward primer: 5′-AATGATACGGCGACCACCGAGAT CTACACGCT TATGGTAATT GT GTGCCAGCMGCCGCGGTAA-3′; 806r PCR reverse primer: 5′-CAAGCAGAAGACGGCATACGAGAT XXXXXXXXXXXXAGTCAGTCAG CC GGACTACHVGGGTWTCTAAT-3′ (with XXXXXXXXXXXX representing the barcodes). PCR products were quantified with the above Qubit kit and then combined into a pool library with equal mass to each sample. The pooled library was purified by AMpure beads (Beckman Coulter, A63880) and then subjected to agarose gel electrophoresis. A DNA band of approximately 390 bp was dissected and purified with a QIAquick Gel Extraction Kit (Qiagen, 28704). The concentration of the pooled library was measured and normalized to 10 nM. The purified pooled DNA library was qualified by an Agilent High Sensitivity DNA Chip on a bioanalyzer. The quantitated library was then subjected to multiplex sequencing (Illumina MiSeq, 251 nt × 2 pair-end reads with 12-nt index reads). Raw sequencing data were analysed by QIIME2. In brief, the data were imported into QIIME2 and demultiplexed, a DADA2 pipeline was used for sequencing quality control, and a feature table was constructed with the following options: qiime dada2 denoise-paired−i-demultiplexed-seqs demux.qza−o-table table−o-representative-sequences rep-seqs−p-trim-left-f 0−p-trim-left-r 0−p-trunc-len-f 150−p-trunc-len-r 150. The feature table of the gut microbiota was used for alpha and beta diversity analysis as well as for taxonomic analysis and differential abundance testing.

Faecal bacterial DNA extraction and quantitative PCR analysis

Faecal DNA was extracted from the faecal pellets of indicated mice with a QIAGEN QIAamp Fast DNA Stool Mini Kit (51604) according to the manufacturer's instructions. Quantitative PCR analysis was performed with an Eppendorf Realplex^2 Mastercycler and a KAPA SYBR FAST qPCR Kit. The 16S rRNA gene primers for real-time quantitative PCR were as follows[31]: total bacteria forward: 5′-GGTGAATACGTTCCCGG-3′; total bacteria reverse: 5′-TACGGCTACCTTGTTACGACTT-3′; *Clostridium* cluster IV forward: 5′-CCTTCCGTGCCGSAGTTA-3′; *Clostridium* cluster IV reverse: 5′-GAATTAAACCACATACTCCACTGCTT-3′; *Clostridium* cluster XIVα forward: 5′-AAATGACGGTACCTGACTAA-3′; *Clostridium* cluster XIVα reverse: 5′-CTTTGAGTTTCATTCTTGCGAA-3′. The relative quantity of the indicated *Clostridium* clusters was normalized to the total bacteria.

RNA-seq and microarray analysis of splenic and colonic cells

Mouse colonic lymphocytes form $Vdr^{+/+}Foxp3^{mRFP}$ or $Vdr^{-/-}Foxp3^{mRFP}$ reporter mice were isolated as described above. Single-cell suspensions were blocked with an antibody against CD16/32 (2.4G2) and stained with antibodies against BioLegend CD45 (30-F11), CD4 (GK1.5), TCRβ (H57-597), CD8α (53-6.7), CD19 (1D3/CD19), CD11c (N418), F4/80 (BM8) and TER-119 (TER-119) and with viability dye. Live FOXP3$^+$ T_{reg} cells (CD45$^+$CD19$^-$CD11c$^-$F4/80$^-$TER-119$^-$TCRβ$^+$CD8α$^-$CD4$^+$mRFP$^+$) were double-sorted by flow cytometry (Astrios, BD Biosciences) to achieve 99% purity and directly lysed with TCL buffer (Qiagen, 1031576) containing 1% 2-mercaptoethanol (Sigma-Aldrich, M6250). Colonic live T_{conv} cells (CD45$^+$CD19$^-$CD11c$^-$F4/80$^-$TER-119$^-$TCRβ$^+$CD8α$^-$CD4$^+$mRFP$^-$) and CD11c$^+$ dendritic cells (CD45$^+$CD19$^-$TCRβ$^-$TER-119$^-$F4/80$^-$CD11c$^+$) were double-sorted at the same time. Colonic epithelial cells (CD45$^-$EpCAM$^+$) were also isolated as previously described[32]. Samples lysed in TCL buffer (Qiagen, 1031576) were kept on ice for 5 min, frozen by dye ice and stored at −80 °C before processing. Smart-Seq2 libraries for low-input RNA-seq were prepared by the Broad Technology Labs and were subsequently sequenced through the Broad Genomics Platform. In brief, total RNA was extracted and purified by Agencourt RNAClean XP beads (Beckman Coulter, A66514). mRNA was polyadenylated and selected by an anchored oligo (dT) primer and converted to cDNA by reverse transcription. First-strand cDNA was amplified by PCR followed by transposon-based fragmentation with the Nextera XT DNA Library Preparation Kit (Illumina, FC-131-1096). Samples were then amplified with barcoded primers (Illumina P5 and P7 barcodes) by PCR. Pooled samples were subjected to sequencing on an Illumina NextSeq500 (2 × 25-bp reads). Transcripts were quantified by the Broad Technology Labs computational pipeline (Cuffquant version 2.2.1[33]). Normalized reads were further filtered and analysed by Multiplot Studio in the GenePattern software package. The colonic T_{reg} cell signatures (fold change > 2 and $P < 0.05$) and RORγ$^+$ T_{reg} cell signatures (fold change > 1.5 and $P < 0.05$)[8] were used in the present study. Loss of VDR functional transcripts in all VDR-deficient cells was confirmed by analysis of a deletion of *Vdr* exon 3 transcripts in the cells[34].

Microarray analysis of splenic and colonic T_{reg} cells was described in our previous report (GEO accession: GSE68009)[8], and the expression of VDR within these populations is shown in the present study.

ELISA of mouse 1,25-dihydroxyvitamin D_3

SPF mice were fed either a nutrient-rich or a minimal diet, and GF mice were fed the nutrient-rich diet as described above. Whole blood was collected in a serum separation tube and allowed to clot for 2 h at room temperature. The serum was then collected by centrifugation at 10,000 r.p.m. for 15 min. Colonic tissues were dissected, weighed and then homogenized in 500 μl PBS on ice. The cells were lysed by freeze (liquid nitrogen)−thaw (room temperature) for three cycles, and the supernatants were collected by centrifugation at 13,000 r.p.m. for 15 min. Serum and colonic levels of 1,25-dihydroxyvitamin D_3 in the indicated mice were determined with a mouse 1,25-dihydroxyvitamin D_3 ELISA kit (LifeSpan BioSciences, LS-F28132) according to the manufacturer's instructions.

Immunoblot analysis

Mouse colonic tissues were directly lysed with Triton buffer (0.5% Triton X-100 and 20 mM HEPES, pH 7.6) on ice, and the lysates were separated by NuPAGE 4–12% Bis-Tris gel (Invitrogen). Separated proteins were transferred onto iBlot 2 NC Mini Stacks (Invitrogen) with an iBlot 2 Dry Blotting System (Invitrogen). The filters were then blocked with TBS with 5% non-fat dry milk (Rockland) plus 0.1% Tween 20 for 1 h at room temperature. After blocking, the filters were incubated overnight at 4 °C with primary antibodies (1:1,000 dilution) against VDR (sc-13133, Santa Cruz), NR1H4 (sc-25309, Santa Cruz), GPBAR1 (PA5-23182, Invitrogen) or actin (sc-8432, Santa Cruz), and were subsequently washed three times with TBS (Bio-Rad) containing 0.1% Tween 20 (Bio-Rad). The filters were then incubated with IRDye 680LT secondary antibodies (1:5,000 dilution) (LI-COR Biosciences) for 1 h at room temperature in the dark. After three washes with TBS containing 0.1% Tween 20, the indicated signals were detected with an Odyssey CLx Fluorescence Imaging System (LI-COR).

Statistical analysis

Results were shown as mean ± s.e.m. Differences between groups were evaluated by analysis of variance followed by a Bonferroni post hoc test or by two-tailed Student's *t*-test with 95% confidence intervals. To determine the enrichment of certain gene signatures in RNA-seq datasets, we used a χ^2 test. $P < 0.05$ was considered statistically significant.

Reporting summary

Further information on research design is available in the Nature Research Reporting Summary linked to this paper.

Data availability

The microarray, RNA-seq and 16S rRNA profiling data are available in the NCBI database under accession numbers GSE68009, GSE137405 and PRJNA573477, respectively. The MS data are available in the MetaboLights database with the identifier MTBLS1276.

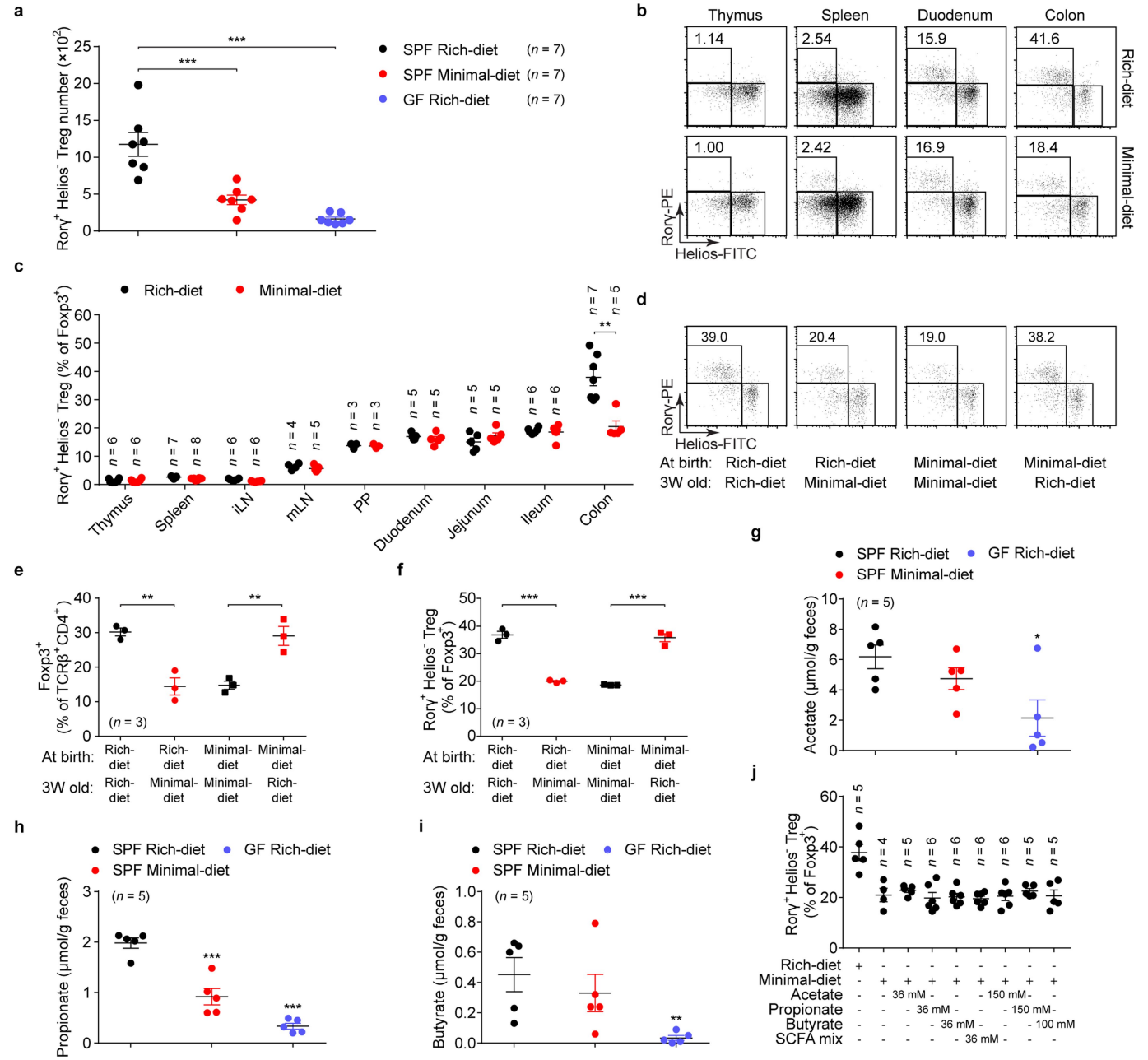
26. Chen, S. et al. Cardiomyocyte-specific deletion of the vitamin D receptor gene results in cardiac hypertrophy. *Circulation* **124**, 1838–1847 (2011).
27. Persson, E. et al. Simultaneous assessment of lipid classes and bile acids in human intestinal fluid by solid-phase extraction and HPLC methods. *J. Lipid Res.* **48**, 242–251 (2007).
28. Sumner, L. W. et al. Proposed minimum reporting standards for chemical analysis Chemical Analysis Working Group (CAWG) Metabolomics Standards Initiative (MSI). *Metabolomics* **3**, 211–221 (2007).
29. Song, X. et al. Growth factor FGF2 cooperates with interleukin-17 to repair intestinal epithelial damage. *Immunity* **43**, 488–501 (2015).
30. Wirtz, S., Neufert, C., Weigmann, B. & Neurath, M. F. Chemically induced mouse models of intestinal inflammation. *Nat. Protocols* **2**, 541–546 (2007).
31. Atarashi, K. et al. Induction of colonic regulatory T cells by indigenous *Clostridium* species. *Science* **331**, 337–341 (2011).
32. Haber, A. L. et al. A single-cell survey of the small intestinal epithelium. *Nature* **551**, 333–339 (2017).
33. Trapnell, C. et al. Differential gene and transcript expression analysis of RNA-seq experiments with TopHat and Cufflinks. *Nat. Protocols* **7**, 562–578 (2012).
34. Li, Y. C. et al. Targeted ablation of the vitamin D receptor: an animal model of vitamin D-dependent rickets type II with alopecia. *Proc. Natl Acad. Sci. USA* **94**, 9831–9835 (1997).

Acknowledgements We thank D. Gardner, Y. Li and T. Hla for providing mouse strains, and C. Fu for help with microscope. We also thank T. Sherpa and J. Ramos for help with GF mice and J. McCoy for manuscript editing. This work was supported in part by a Sponsored Research Agreement from UCB Pharma and Evelo Biosciences. S.F.O. was supported by NIH K01 DK102771.

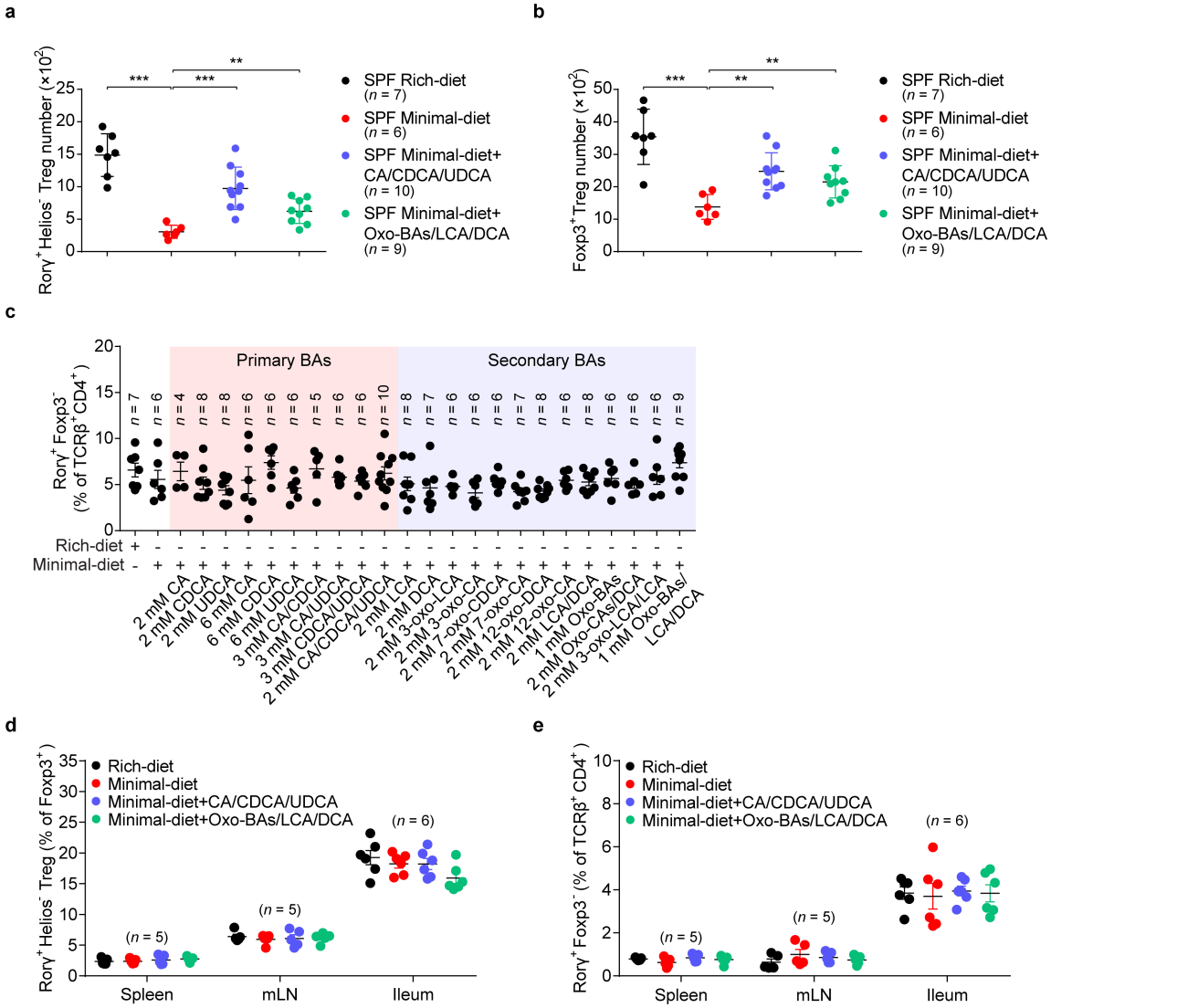
Author contributions D.L.K. and X. Song designed the experiments and wrote the manuscript. X. Song, X. Sun, S.F.O., M.W., Y.Z., W.Z. and N.G.-Z. conducted or helped with the experiments. X. Song, X. Sun and Y.Z. analysed the data. R.J., D.M. and C.B. were involved in data discussions and edited the manuscript. D.L.K. supervised the study.

Competing interests The authors declare no competing interests.

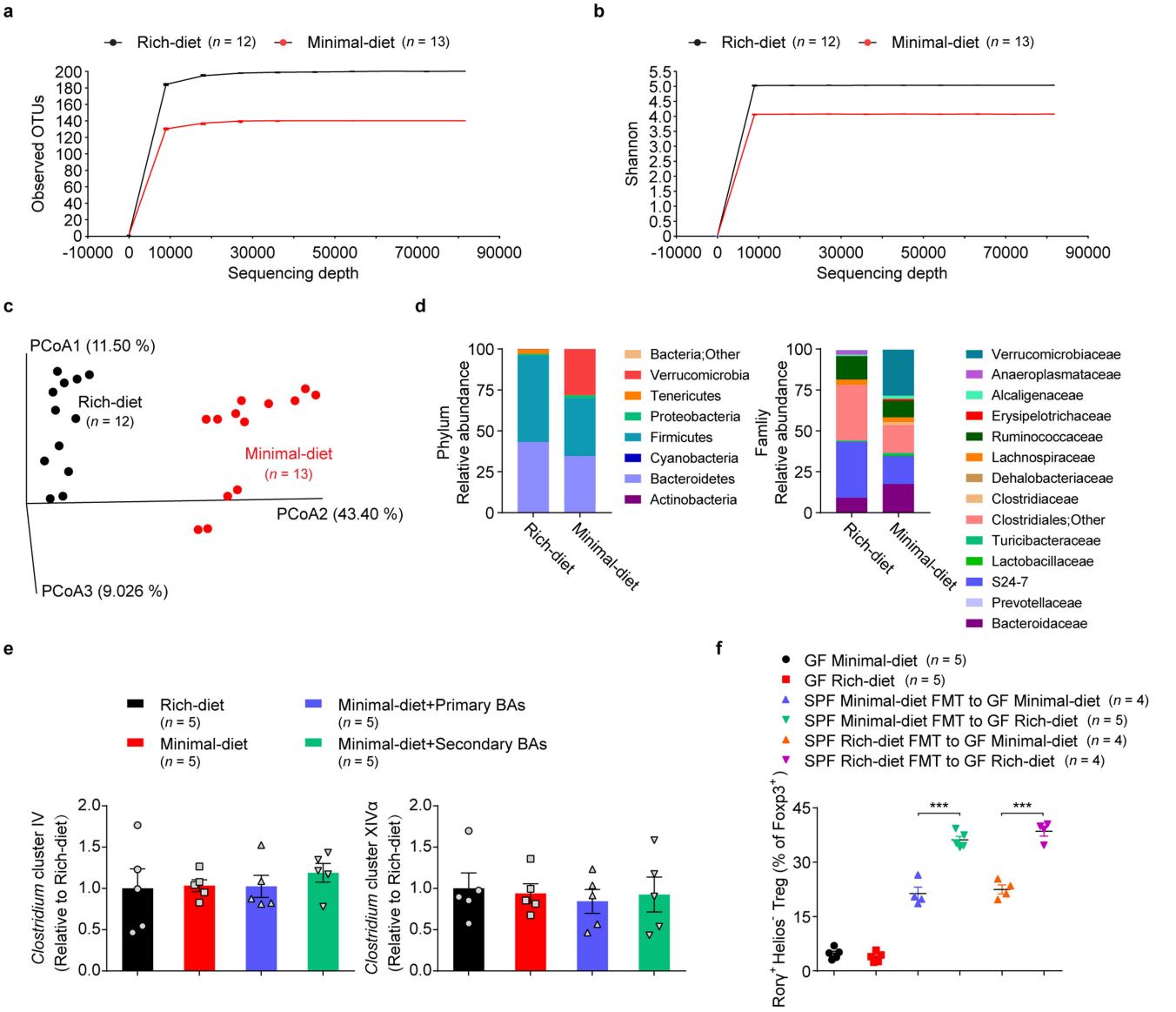
Additional information
Supplementary information is available for this paper at https://doi.org/10.1038/s41586-019-1865-0.
Correspondence and requests for materials should be addressed to D.L.K.
Peer review information *Nature* thanks Pieter Dorrestein, Hiroshi Ohno and the, other, anonymous reviewer(s) for their contribution to the peer review of this work.
Reprints and permissions information is available at http://www.nature.com/reprints.



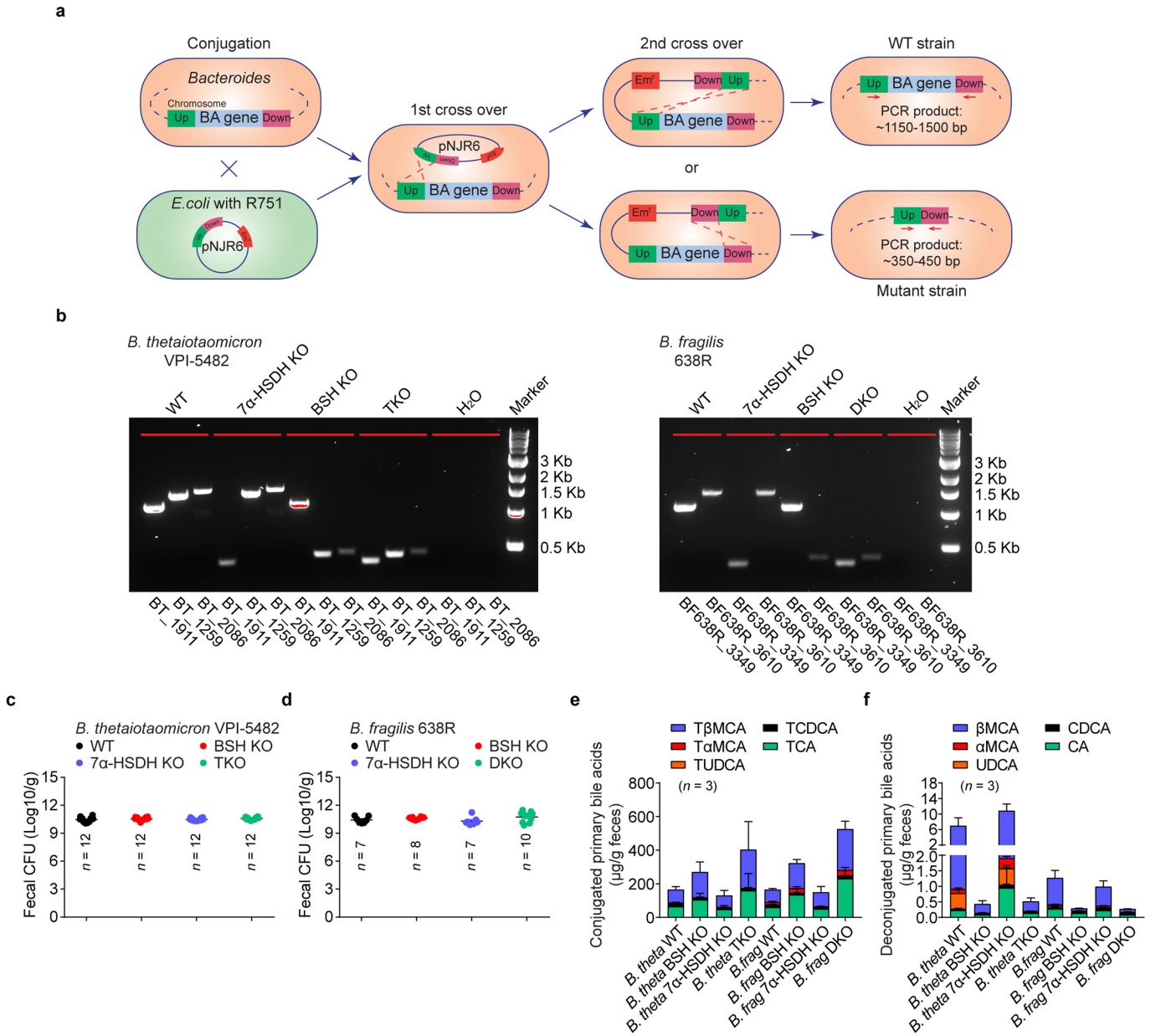
Extended Data Fig. 1 | Both dietary and microbial factors control the number of colonic RORγ$^+$T$_{reg}$ cells. a, Beginning at 3 weeks of age, three groups of mice were fed special diets for 4 weeks. SPF mice were fed either a nutrient-rich or a minimal diet, and GF mice were fed the nutrient-rich diet. Colonic T$_{reg}$ cells were analysed, and absolute numbers of RORγ$^+$Helios$^-$ in the FOXP3$^+$CD4$^+$TCRβ$^+$T$_{reg}$ cell population are shown. **b**, **c**, Three-week-old SPF mice were fed as in **a**, and T$_{reg}$ cells in different tissues were analysed after 4 weeks. Representative plots (**b**) and frequencies of RORγ$^+$Helios$^-$ in the FOXP3$^+$CD4$^+$TCRβ$^+$T$_{reg}$ cell population (**c**) are shown. iLN, inguinal lymph node. **d**–**f**, SPF mice were fed a nutrient-rich or a minimal diet at birth and were either maintained on that diet or switched to the opposite diet at 3 weeks of age. Colonic T$_{reg}$ cells were analysed after 4 weeks. Representative plots of RORγ$^+$Helios$^-$ in the FOXP3$^+$CD4$^+$TCRβ$^+$T$_{reg}$ cell population (**d**), and the frequencies of FOXP3$^+$ in the CD4$^+$TCRβ$^+$ cell population (**e**) and RORγ$^+$Helios$^-$ in the colonic FOXP3$^+$CD4$^+$TCRβ$^+$T$_{reg}$ cell population (**f**) are shown. **g**–**i**, LC–MS quantification of faecal acetate (**g**), propionate (**h**) and butyrate (**i**) from SPF mice fed a nutrient-rich or a minimal diet, and from GF mice fed a nutrient-rich diet. **j**, Three-week-old SPF mice were fed a nutrient-rich diet, a minimal diet, or a minimal diet supplemented with individual or mixed SCFAs in drinking water. Colonic T$_{reg}$ cells were analysed after 4 weeks. Frequencies of RORγ$^+$Helios$^-$ in the FOXP3$^+$CD4$^+$TCRβ$^+$T$_{reg}$ cell population are shown. Data are representative of two independent experiments. *n* represents biologically independent animals. Data are mean ± s.e.m. (**a**, **c** and **e**–**j**). $^*P < 0.05$, $^{**}P < 0.01$, $^{***}P < 0.001$, one-way ANOVA followed by the Bonferroni post hoc test (**a**, **e**–**i**) or two-tailed Student's *t*-test (**c**).



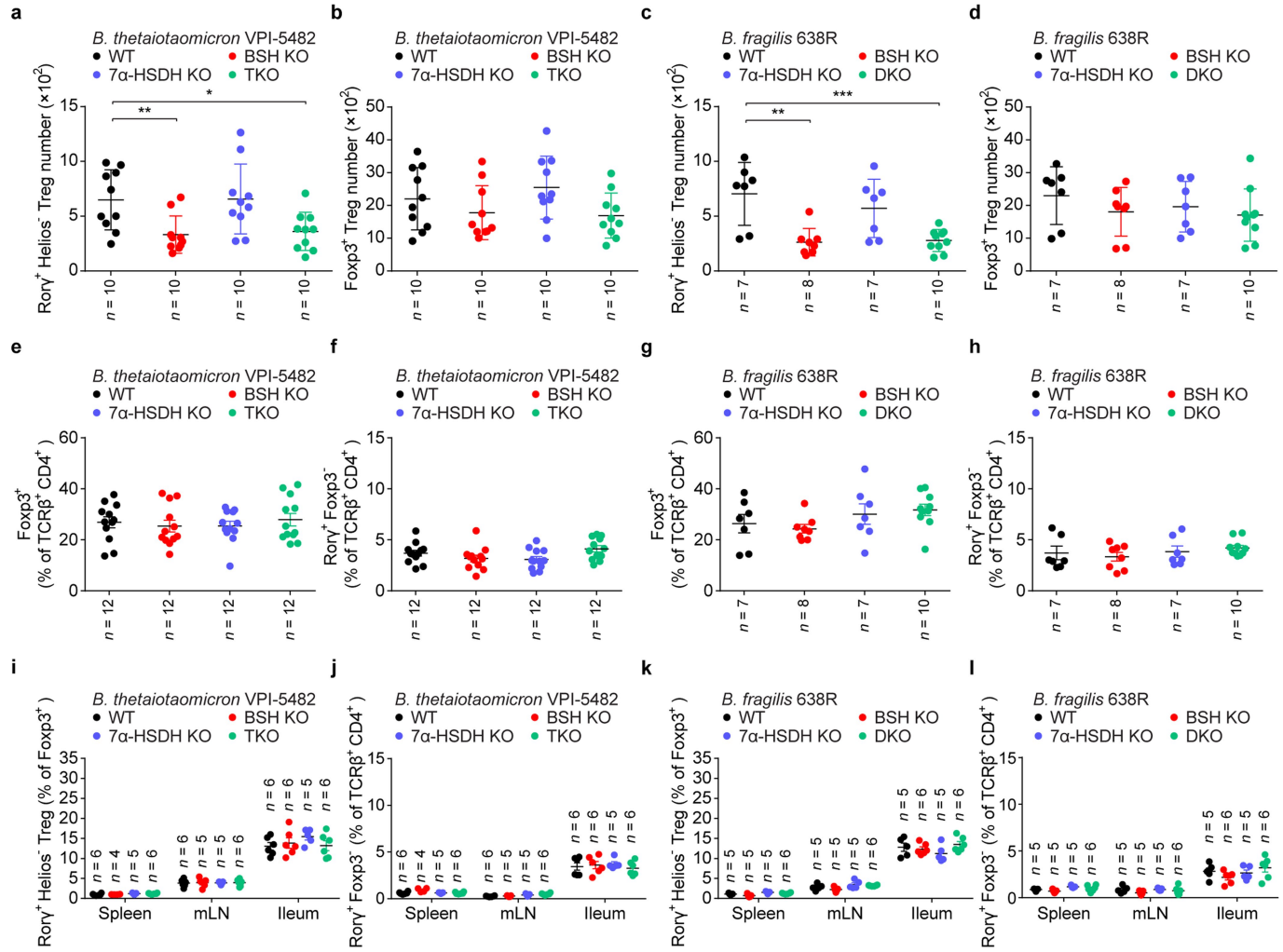
Extended Data Fig. 2 | Intestinal BAs regulate the number of colonic T_{reg} cells. a, **b**, Absolute numbers of RORγ$^+$Helios$^-$ in the colonic FOXP3$^+$CD4$^+$TCRβ$^+$ T_{reg} cell population (**a**) and of FOXP3$^+$ T_{reg} cells in the CD4$^+$TCRβ$^+$ population (**b**) in SPF mice fed a nutrient-rich diet, a minimal diet, or a minimal diet supplemented with mixtures of primary or secondary BAs in drinking water. The primary BAs were CA, CDCA and UDCA (2 mM of each). The secondary BAs were 3-oxo-CA, 3-oxo-LCA, 7-oxo-CA, 7-oxo-CDCA, 12-oxo-CA, 12-oxo-DCA, DCA and LCA (1 mM of each). **c**, Three-week-old SPF mice were fed a nutrient-rich diet, a minimal diet, or a minimal diet supplemented with one or more primary or secondary BAs in drinking water. Colonic T_H17 cells were analysed after 4 weeks. CA, CDCA, UDCA, DCA, LCA, 3-oxo-CA, 3-oxo-LCA, 7-oxo-CA, 7-oxo-CDCA, 12-oxo-CA, 12-oxo-DCA and the indicated BA combinations were tested. Frequencies of RORγ$^+$FOXP3$^-$ in the CD4$^+$TCRβ$^+$ cell population are shown. **d**, **e**, Three-week-old SPF mice were fed a nutrient-rich diet, a minimal diet, or a minimal diet supplemented with the indicated primary BAs (CA/CDCA/UDCA, 2 mM of each) or the secondary BAs (oxo-BAs/LCA/DCA, 1 mM of each) in drinking water. T_{reg} cells and T_H17 cells in the spleen, mesenteric lymph node and ileum were analysed after 4 weeks. Frequencies of RORγ$^+$Helios$^-$ in the FOXP3$^+$CD4$^+$TCRβ$^+$ T_{reg} cell population (**d**) and of RORγ$^+$FOXP3$^-$ in the CD4$^+$TCRβ$^+$ cell population (**e**) are shown. Data are pooled from two or three independent experiments. *n* represents biologically independent animals. Data are mean ± s.e.m. $^{**}P < 0.01$, $^{***}P < 0.001$, one-way ANOVA followed by the Bonferroni post hoc test.



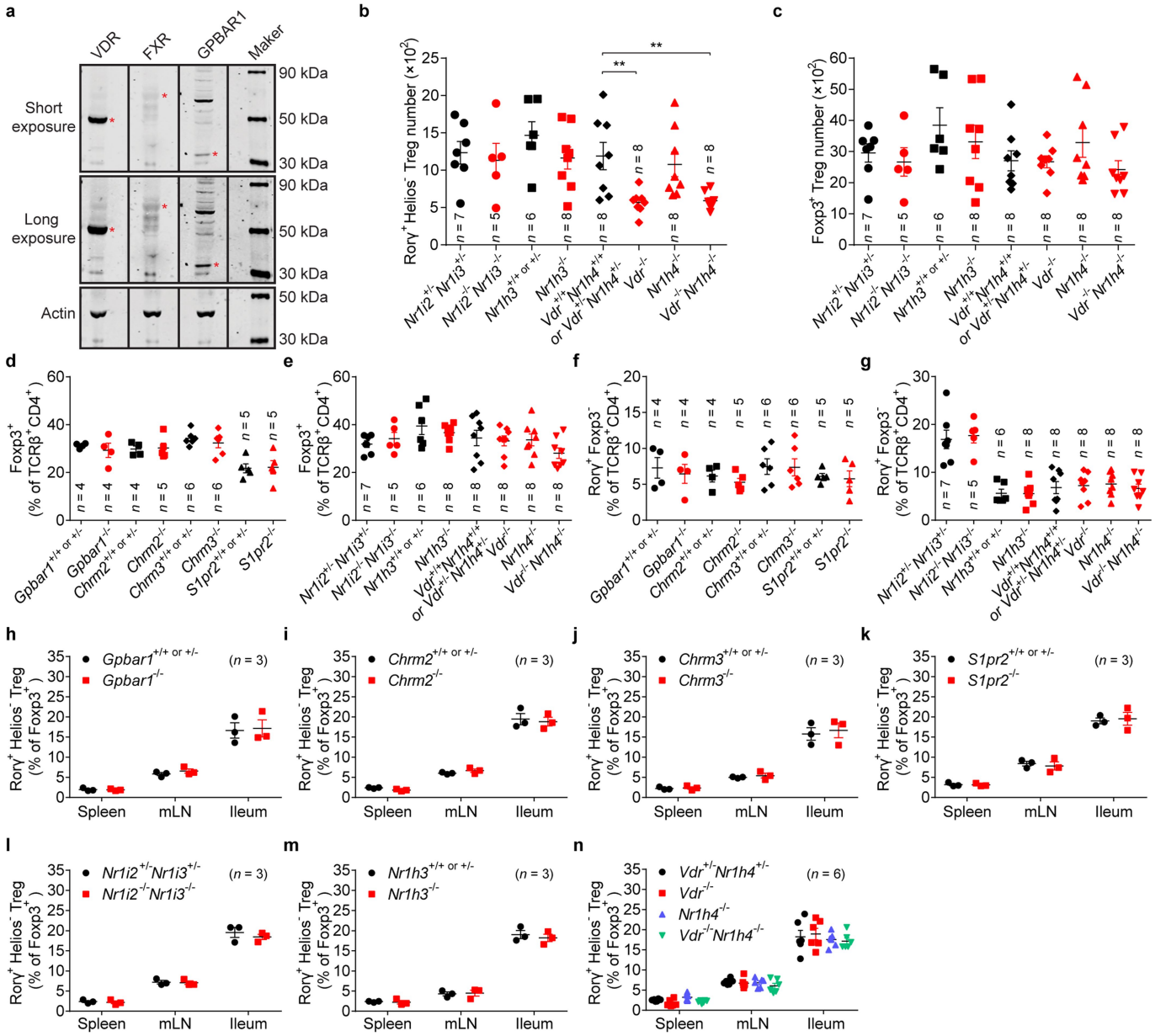
Extended Data Fig. 3 | Colonic microbial profiling of rich-diet mice versus minimal-diet mice. a–**d**, Three-week-old SPF mice were fed a nutrient-rich or a minimal diet, and the microbial compositions in the colonic lumen were analysed after 4 weeks by 16S rRNA sequencing. Observed operational taxonomic units (OTUs) (**a**), Shannon index (**b**), principal coordinates analysis (PCoA) (**c**) and the relative abundance of bacteria at the phylum and family levels (**d**) are shown. **e**, Quantitative PCR analysis of 16S rDNA of *Clostridium* cluster IV and *Clostridium* cluster XIVα in colonic luminal specimens from SPF mice fed a nutrient-rich diet, a minimal diet, or a minimal diet supplemented with the indicated primary BAs (CA/CDCA/UDCA, 2 mM of each) or the secondary BAs (oxo-BAs/LCA/DCA, 1 mM of each) in drinking water. **f**, Four-week-old GF mice or GF mice receiving transferred faecal materials (FMTs) from minimal-diet or rich-diet SPF mice were fed a nutrient-rich diet or a minimal diet, and colonic T_{reg} cells were analysed after 2 weeks. Frequencies of colonic RORγ$^+$Helios$^-$ in the FOXP3$^+$CD4$^+$TCRβ$^+$ T_{reg} cell population are shown. Data are pooled from three independent experiments in **a**–**d**. Data are representative of two independent experiments in **e** and **f**. *n* represents biologically independent animals. Data are mean ± s.e.m. ***$P < 0.001$, one-way ANOVA followed by the Bonferroni post hoc test.



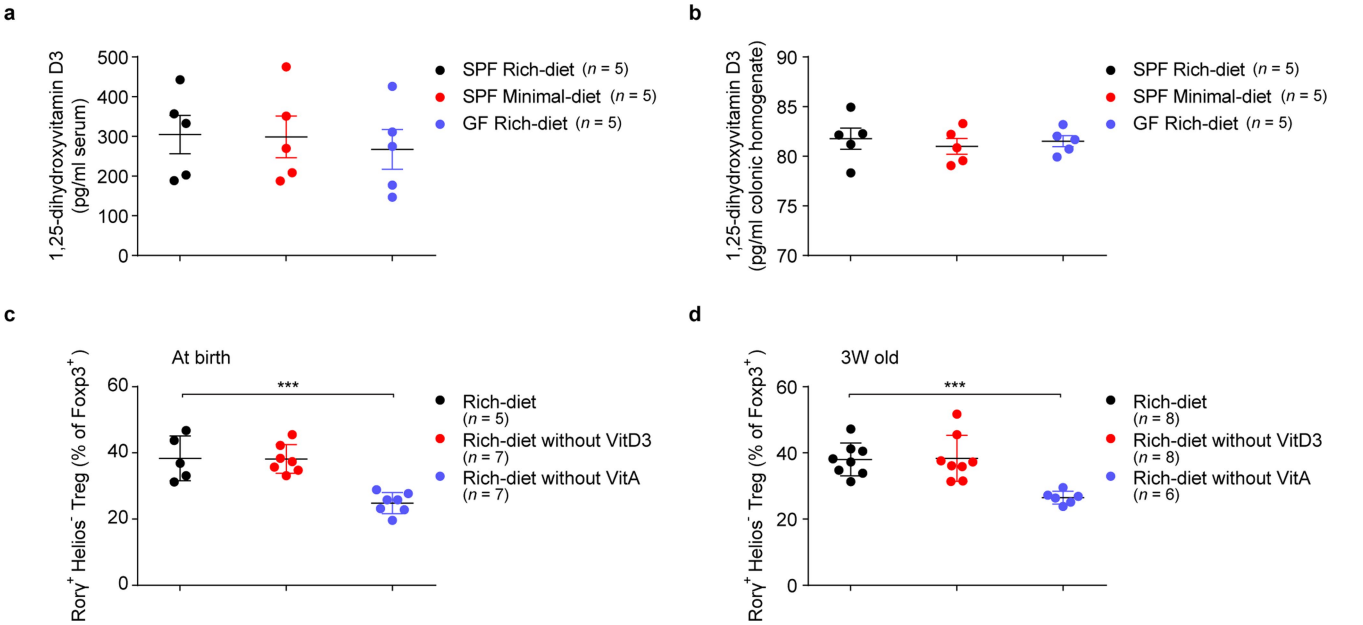
Extended Data Fig. 4 | Generation of BA metabolic pathway mutants in *Bacteroides*. **a**, Schematic diagram of pNJR6 suicide vector-mediated BA gene deletion in *Bacteroides*. **b**, Genotyping of *B. thetaiotaomicron* and *B. fragilis* BA metabolic pathway mutants by PCR. PCR primers were designed to target the flanking regions of an intact gene. PCR of an untouched gene plus its flanking regions generated a PCR product of around 1,150–1,500 bp, while deletion of an interested BA metabolic gene resulted in only an approximately 350–450-bp PCR amplicon of its two flanking regions. **c**, **d**, Bacterial load (measured as colony-forming unit (CFU) per gram of faeces) of *B. thetaiotaomicron* (**c**) and *B. fragilis* (**d**) BA metabolic pathway mutants and their wild-type control strains in monocolonized GF mice. **e**, **f**, LC–MS quantification of faecal conjugated primary BAs (**e**) and deconjugated primary BAs (**f**) in GF mice monocolonized with *B. thetaiotaomicron* or *B. fragilis* BA metabolic pathway mutants and their wild-type control strains. Data are representative of two independent experiments in **b**, **e** and **f**. Data are pooled from three independent experiments in **c** and **d**. *n* represents biologically independent animals. Data are mean ± s.e.m. (**c**–**f**).



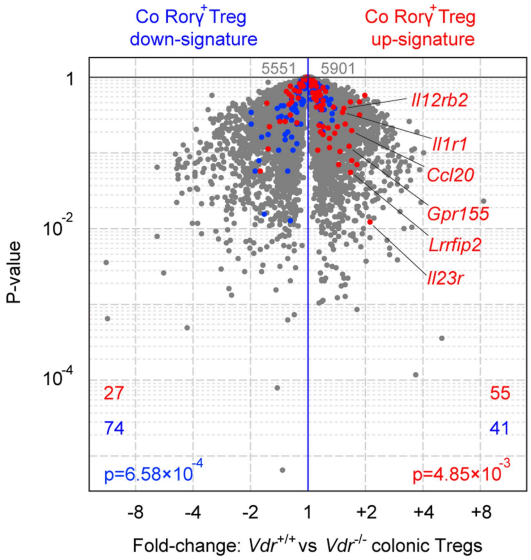
Extended Data Fig. 5 | Gut bacteria modulate colonic RORγ$^+$ T_{reg} cells via their BA metabolic pathways. a, **b**, Each of four groups of GF mice was colonized with one of the following microorganisms: (1) a wild-type strain of *B. thetaiotaomicron*; (2) a BSH-mutant strain; (3) a 7α-HSDH-mutant strain; or (4) a triple-mutant (TKO) strain. Colonic T_{reg} cells were analysed after 2 weeks. Absolute numbers of RORγ$^+$Helios$^-$ in the colonic FOXP3$^+$CD4$^+$TCRβ$^+$ T_{reg} cell population (**a**) and of FOXP3$^+$ T_{reg} cells in the CD4$^+$TCRβ$^+$ population (**b**) are shown. **c**, **d**, Each of four groups of GF mice was colonized with one of the following microorganisms: (1) a wild-type strain of *B. fragilis*; (2) a BSH-KO strain; (3) a 7α-HSDH-KO strain; or (4) a double-mutant (DKO) strain. Absolute numbers of colonic T_{reg} cells are shown as in **a** and **b**. **e**, **f**, GF mice were colonized with *B. thetaiotaomicron* BA metabolic pathway mutants or their wild-type control strains. Colonic T_{reg} cells and T_H17 cells were analysed after 2 weeks. Frequencies of FOXP3$^+$ in the CD4$^+$TCRβ$^+$ cell population (**e**) or RORγ$^+$FOXP3$^-$ in the CD4$^+$TCRβ$^+$ cell population (**f**) are shown. **g**, **h**, GF mice were colonized with *B. fragilis* BA metabolic pathway mutants or their wild-type control strains. Frequencies of colonic T_{reg} cells and T_H17 cells are shown as in **e** and **f**. **i**, **j**, GF mice were colonized with *B. thetaiotaomicron* BA metabolic pathway mutants or their wild-type control strains. T_{reg} cells and T_H17 cells in the spleen, mesenteric lymph node and ileum were analysed after 2 weeks. Frequencies of RORγ$^+$Helios$^-$ in the FOXP3$^+$CD4$^+$TCRβ$^+$ T_{reg} cell population (**i**) and RORγ$^+$FOXP3$^-$ in the CD4$^+$TCRβ$^+$ cell population (**j**) are shown. **k**, **l**, GF mice were colonized with *B. fragilis* BA metabolic pathway mutants or their wild-type control strains. Frequencies of T_{reg} cells and T_H17 cells in the spleen, mesenteric lymph node and ileum are shown as in **i** and **j**. Data are pooled from two or three independent experiments. *n* represents biologically independent animals. Data are mean ± s.e.m. $^*P < 0.05$, $^{**}P < 0.01$, $^{***}P < 0.001$, one-way ANOVA followed by the Bonferroni post hoc test.



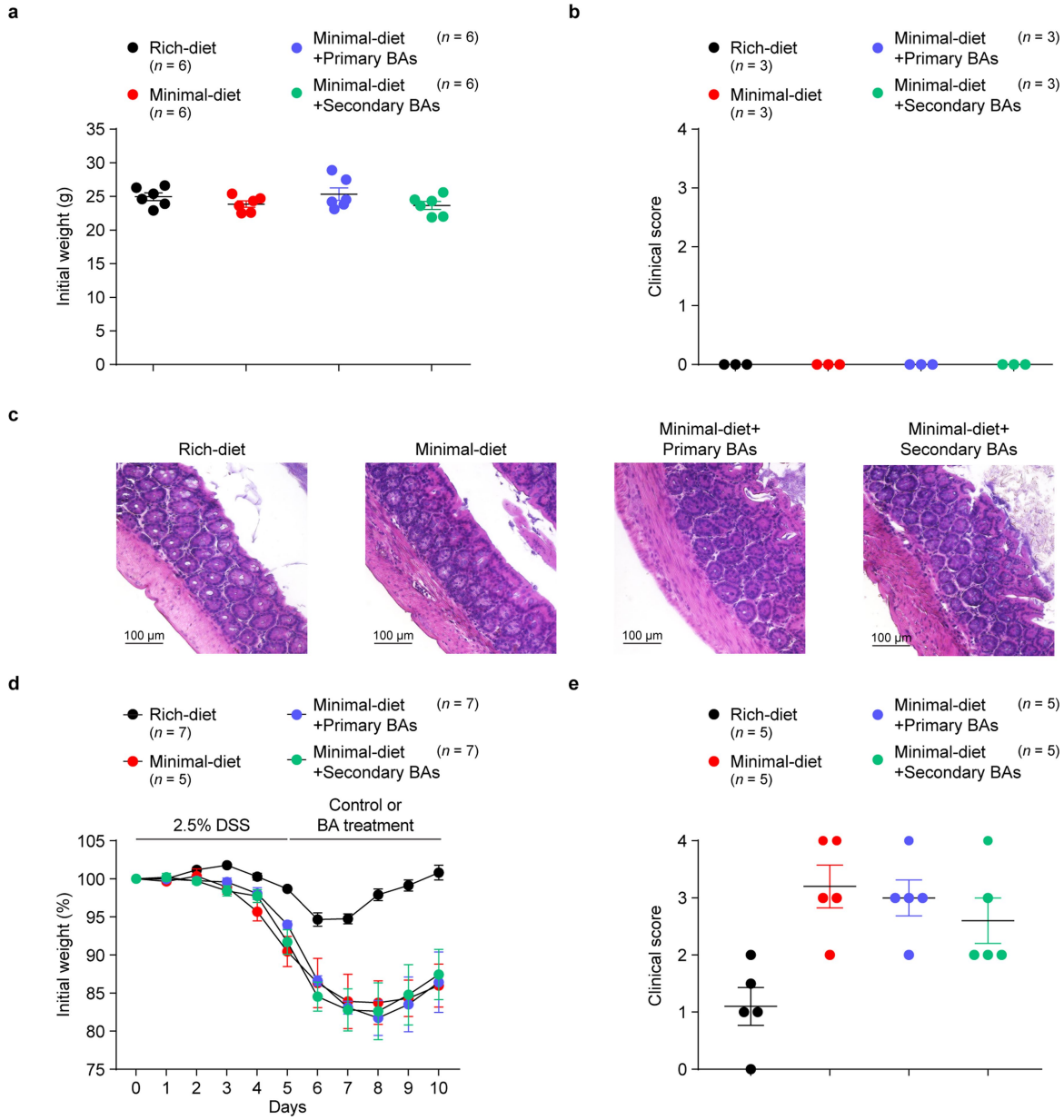
Extended Data Fig. 6 | The effect of BAR deficiency on T_{reg} cells or T_H17 cells in gut and peripheral lymphoid organs. a, Protein expression of VDR, FXR (also known as NR1H4) and GPBAR1 in the colonic tissue of SPF C57BL/6J mice was analysed by western blot. The red asterisks indicate the corresponding molecular weight of VDR (53 kDa), FXR (69 kDa) and GPBAR1 (33 kDa). For gel source data, see Supplementary Fig. 1. **b**, **c**, Absolute numbers of RORγ$^+$Helios$^-$ in the colonic FOXP3$^+$CD4$^+$TCRβ$^+$ T_{reg} cell population (**b**) and of FOXP3$^+$ T_{reg} cells in the CD4$^+$TCRβ$^+$ population (**c**) from mice deficient in nuclear receptors (*Nr1i2*$^{-/-}$*Nr1i3*$^{-/-}$, *Nr1h3*$^{-/-}$, *Vdr*$^{-/-}$, *Nr1h4*$^{-/-}$ and *Vdr*$^{-/-}$*Nr1h4*$^{-/-}$) and their littermate controls. **d**, **e**, Frequencies of FOXP3$^+$ in the colonic CD4$^+$TCRβ$^+$ cell population from mice deficient in G-protein-coupled receptors (*Gpbar1*$^{-/-}$, *Chrm2*$^{-/-}$, *Chrm3*$^{-/-}$ and *S1pr2*$^{-/-}$) and their littermate controls (**d**) and from mice deficient in nuclear receptors (*Nr1i2*$^{-/-}$*Nr1i3*$^{-/-}$, *Nr1h3*$^{-/-}$, *Vdr*$^{-/-}$, *Nr1h4*$^{-/-}$ and *Vdr*$^{-/-}$*Nr1h4*$^{-/-}$) and their littermate controls (**e**). **f**, **g**, Frequencies of RORγ$^+$FOXP3$^-$ in the colonic CD4$^+$TCRβ$^+$ cell population from mice described in **d** and **e**. **h**–**n**, T_{reg} cells in the spleen, mesenteric lymph node and ileum from the indicated mice were analysed. Frequencies of RORγ$^+$Helios$^-$ in the FOXP3$^+$CD4$^+$TCRβ$^+$ T_{reg} cell population from *Gpbar1*$^{-/-}$ (**h**), *Chrm2*$^{-/-}$ (**i**), *Chrm3*$^{-/-}$ (**j**), *S1pr2*$^{-/-}$ (**k**), *Nr1i2*$^{-/-}$*Nr1i3*$^{-/-}$ (**l**), *Nr1h3*$^{-/-}$ (**m**), and *Vdr*$^{-/-}$, *Nr1h4*$^{-/-}$ and *Vdr*$^{-/-}$*Nr1h4*$^{-/-}$ (**n**) mice and their littermate controls are shown. Data are representative of two or three independent experiments in **a** and **d**–**n**, or are pooled from two or three independent experiments in **b** and **c**. *n* represents biologically independent animals. Data are mean ± s.e.m. $^{**}P < 0.01$, one-way ANOVA followed by the Bonferroni post hoc test.



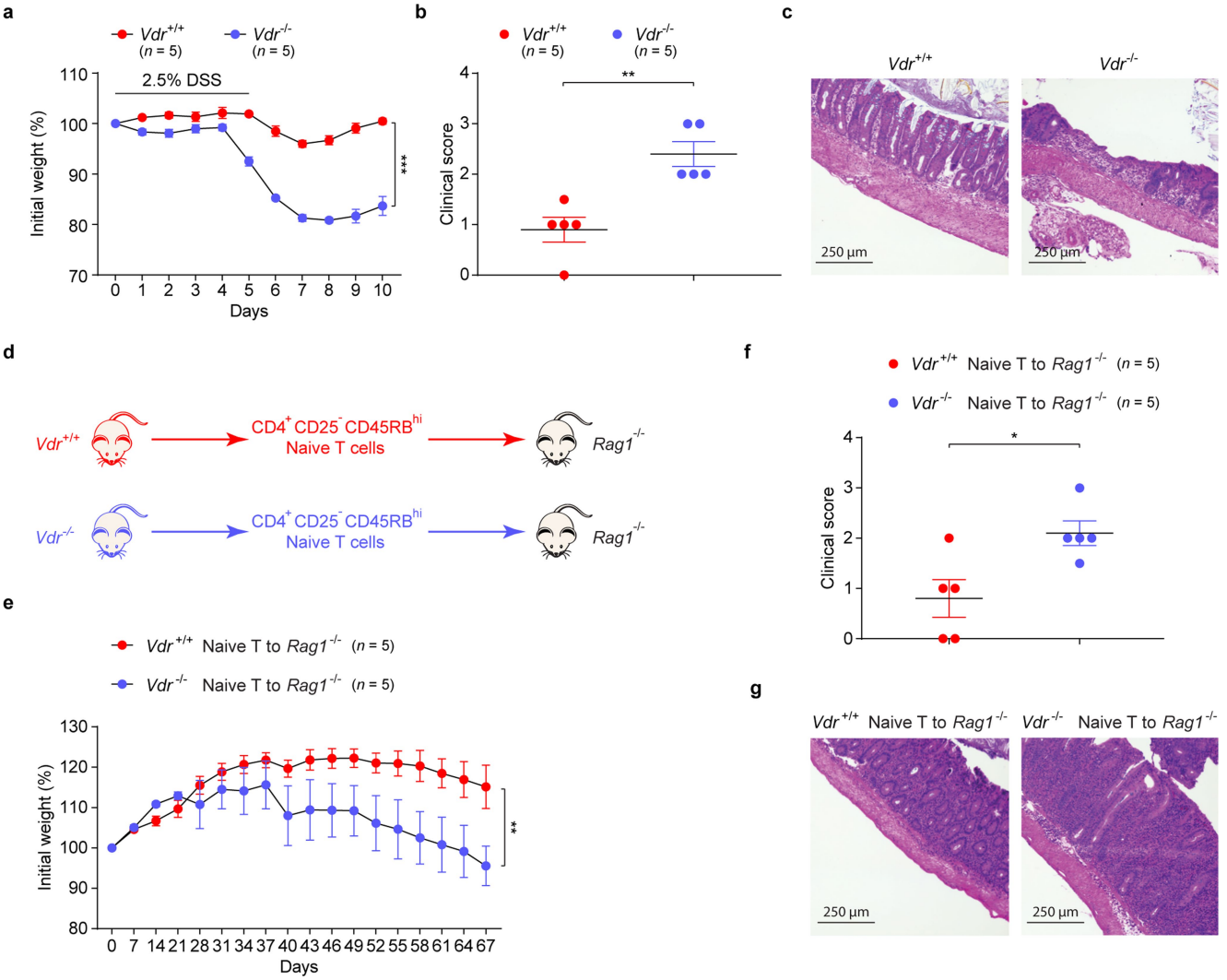
Extended Data Fig. 7 | Dietary vitamin D_3 does not alter the frequency of colonic RORγ$^+$ T_{reg} cells. a, **b**, Beginning at 3 weeks of age, three groups of mice were fed special diets for 4 weeks. SPF mice were fed either a nutrient-rich or a minimal diet, and GF mice were fed the nutrient-rich diet. The levels of 1,25-dihydroxyvitamin D_3 in serum (**a**) and the colon (**b**) of these mice were determined by ELISA. **c**, SPF mice were fed a nutrient-rich diet, or a rich diet deficient in vitamin D_3 (VitD3) or vitamin A (VitA) at birth. Colonic T_{reg} cells were analysed after 7 weeks. Frequencies of RORγ$^+$Helios$^-$ in the colonic FOXP3$^+$CD4$^+$TCRβ$^+$ T_{reg} cell population are shown. **d**, SPF mice were fed a nutrient-rich diet at birth and were either maintained on that diet or switched to a rich diet deficient in vitamin D_3 or vitamin A at 3 weeks of age. Colonic T_{reg} cells were analysed after 4 weeks. Frequencies of RORγ$^+$Helios$^-$ in the colonic FOXP3$^+$CD4$^+$TCRβ$^+$ T_{reg} cell population are shown. Data are representative of two independent experiments. *n* represents biologically independent animals. Data are mean ± s.e.m. ***$P < 0.001$, one-way ANOVA followed by the Bonferroni post hoc test.



Extended Data Fig. 8 | Comparison of RORγ$^+$ T_{reg} cell signature genes of colonic T_{reg} cells from *Vdr*$^{+/+}$ and *Vdr*$^{-/-}$ mice. Volcano plots comparing transcriptomes of colonic T_{reg} cells from *Vdr*$^{+/+}$*Foxp3*^{mRFP} and *Vdr*$^{-/-}$*Foxp3*^{mRFP} mice ($n = 3$). Colonic RORγ$^+$ T_{reg} cell signature genes are highlighted in red (upregulated) or blue (downregulated). The number of genes from each signature preferentially expressed by one or the other population is shown at the bottom. Data are pooled from two independent experiments. *n* represents biologically independent animals. To determine the enrichment of certain gene signatures in RNA-seq datasets, a χ^2 test was used. $P < 0.05$ was considered statistically significant.



Extended Data Fig. 9 | BA supplementation does not cause gut inflammation and cannot ameliorate gut inflammation after the development of colitis. **a**–**c**, Three-week-old SPF mice were fed a nutrient-rich diet, a minimal diet, or a minimal diet supplemented with mixtures of primary BAs (CA/CDCA/UDCA, 2 mM of each) or secondary BAs (oxo-BAs/LCA/DCA, 1 mM of each) in drinking water. Initial body weights were recorded before DSS challenge (**a**). Clinical scores (**b**) and haematoxylin and eosin histology (**c**) for representative colons from mice not challenged with DSS are shown. **d**, **e**, Three-week-old SPF mice fed a nutrient-rich or a minimal diet for 4 weeks were then challenged in the DSS-induced colitis model. After the development of colitis at day 5 of the model, the DSS containing drinking water was switched to regular drinking water or to drinking water supplemented with mixtures of primary or secondary BAs. The primary BAs were CA, CDCA and UDCA (2 mM of each). The secondary BAs were 3-oxo-CA, 3-oxo-LCA, 7-oxo-CA, 7-oxo-CDCA, 12-oxo-CA, 12-oxo-DCA, DCA and LCA (1 mM of each). Daily weight loss (**d**) of mice during the course of DSS-induced colitis and clinical scores (**e**) on day 10 of colitis are shown. Data are representative of two independent experiments. *n* represents biologically independent animals. Data are mean ± s.e.m. in **a**, **b**, **d** and **e**.



Extended Data Fig. 10 | VDR signalling controls gut inflammation. a–**c**, Daily weight loss (**a**) of *Vdr*$^{+/+}$ and *Vdr*$^{-/-}$ mice during the course of DSS-induced colitis. Clinical scores (**b**) and haematoxylin and eosin histology (**c**) of representative colons on day 10 of colitis are shown. **d**, Schematic representation of the T cell-adaptive transfer model of colitis. Either *Vdr*$^{+/+}$ or *Vdr*$^{-/-}$ naive T cells are transferred to *Rag1*$^{-/-}$ mice. **e**–**g**, Weight loss (**e**) of *Rag1*$^{-/-}$ mice in **d** during the course of T cell-adaptive transfer-induced colitis. Clinical scores (**f**) and haematoxylin and eosin histology (**g**) of representative colons on day 67 of colitis are shown. Data are representative of two independent experiments. *n* represents biologically independent animals. Data are mean ± s.e.m. in **a**, **b**, **e** and **f**. *$P < 0.05$, **$P < 0.01$, ***$P < 0.001$, two-way ANOVA followed by the Bonferroni post hoc test (**a** and **e**) or two-tailed Student's *t*-test (**b** and **f**).

nature research

Corresponding author(s): Dennis Kasper

Last updated by author(s): Oct 26, 2019

Reporting Summary

Nature Research wishes to improve the reproducibility of the work that we publish. This form provides structure for consistency and transparency in reporting. For further information on Nature Research policies, see Authors & Referees and the Editorial Policy Checklist.

Statistics

For all statistical analyses, confirm that the following items are present in the figure legend, table legend, main text, or Methods section.

n/a	Confirmed	
☐	☒	The exact sample size (*n*) for each experimental group/condition, given as a discrete number and unit of measurement
☐	☒	A statement on whether measurements were taken from distinct samples or whether the same sample was measured repeatedly
☐	☒	The statistical test(s) used AND whether they are one- or two-sided *Only common tests should be described solely by name; describe more complex techniques in the Methods section.*
☐	☒	A description of all covariates tested
☐	☒	A description of any assumptions or corrections, such as tests of normality and adjustment for multiple comparisons
☐	☒	A full description of the statistical parameters including central tendency (e.g. means) or other basic estimates (e.g. regression coefficient) AND variation (e.g. standard deviation) or associated estimates of uncertainty (e.g. confidence intervals)
☐	☒	For null hypothesis testing, the test statistic (e.g. *F*, *t*, *r*) with confidence intervals, effect sizes, degrees of freedom and *P* value noted *Give P values as exact values whenever suitable.*
☒	☐	For Bayesian analysis, information on the choice of priors and Markov chain Monte Carlo settings
☒	☐	For hierarchical and complex designs, identification of the appropriate level for tests and full reporting of outcomes
☒	☐	Estimates of effect sizes (e.g. Cohen's *d*, Pearson's *r*), indicating how they were calculated

Our web collection on statistics for biologists contains articles on many of the points above.

Software and code

Policy information about availability of computer code

Data collection	MACSQuantify™ Software was used to collect data from flow cytometry; Eppendorf MasterCycler was used to collect real-time PCR data; Thermo Scientific Orbitrap Q Exactive with Thermo Vanquish UPLC (UPLC-MS/MS) was used to collect MS data; Odyssey® CLx Fluorescence Imaging System was used to collect Immunoblot images; Zeiss Light Microscope was used to collect histological data; Illumina MiSeq was used to collect 16S rRNA profiling data; Illumina NextSeq500 was used to collect RNAseq data; BioTek® microplate reader was used to collect ELISA data.
Data analysis	Flow cytometric analyses were performed with the FlowJo 10.4.1; Thermo Xcalibur suite software version 3.0 was used to analysis the bile acid and SCFA data generated by UPLC-MS/MS (Thermo Scientific Orbitrap Q Exactive with Thermo Vanquish UPLC); 16S rRNA profiling data were analyzed by QIIME2; RNAseq data were analyzed by Cuffquant 2.2.1 and Multiplot Studio 1.5.60 in the GenePattern software package; ELISA data were obtained by BioTek® Gen5 software; Statistical analyses were performed with the GraphPad Prism 7.0 and Excel 2016.

For manuscripts utilizing custom algorithms or software that are central to the research but not yet described in published literature, software must be made available to editors/reviewers. We strongly encourage code deposition in a community repository (e.g. GitHub). See the Nature Research guidelines for submitting code & software for further information.

Data

Policy information about availability of data

All manuscripts must include a data availability statement. This statement should provide the following information, where applicable:

- Accession codes, unique identifiers, or web links for publicly available datasets
- A list of figures that have associated raw data
- A description of any restrictions on data availability

The authors declare that the data supporting the findings of this study are available within the paper and its supplementary information files. Accession codes will be available along with publication.

Field-specific reporting

Please select the one below that is the best fit for your research. If you are not sure, read the appropriate sections before making your selection.

☒ Life sciences ☐ Behavioural & social sciences ☐ Ecological, evolutionary & environmental sciences

For a reference copy of the document with all sections, see nature.com/documents/nr-reporting-summary-flat.pdf

Life sciences study design

All studies must disclose on these points even when the disclosure is negative.

Sample size	Sample sizes were based on a combination of the resource equation method, limited availability of gnotobiotic mice, and prior lab experience to ensure statistical and biological significance.
Data exclusions	No data was excluded from the analysis. Occasional growth restriction in mice fed a minimal diet (AIN-76A) necessitated their exclusion from all experiments. The exclusion criteria for growth restricted mice were pre-established.
Replication	Replicate experiments were preformed successfully at least two to three times. The number of replicates for each experiment is listed in the figure legends. If group size was small (due to limited availability of mouse strains), data from replicate experiments were pooled for graphical representation.
Randomization	Mice were randomized between groups when feasible. Age- and sex-matched littermates from each mouse line were bred as strict controls.
Blinding	Investigators were not blinded to the experimental groups given different housing conditions required. Clinical scores of hematoxylin/eosin stained colonic tissue sections were determined by a pathologist who was blinded to the nature of the mice under analysis.

Reporting for specific materials, systems and methods

We require information from authors about some types of materials, experimental systems and methods used in many studies. Here, indicate whether each material, system or method listed is relevant to your study. If you are not sure if a list item applies to your research, read the appropriate section before selecting a response.

Materials & experimental systems

n/a	Involved in the study
☐	☒ Antibodies
☒	☐ Eukaryotic cell lines
☒	☐ Palaeontology
☐	☒ Animals and other organisms
☒	☐ Human research participants
☒	☐ Clinical data

Methods

n/a	Involved in the study
☒	☐ ChIP-seq
☐	☒ Flow cytometry
☒	☐ MRI-based neuroimaging

Antibodies

Antibodies used	Following FACS antibodies were used in the study:PB-CD45 (30-F11, Biolegend, 103126), PE/Cy7-CD45 (30-F11, Biolegend, 103114), BV605-CD4 (GK1.5, Biolegend, 100451), PerCP/Cy5.5-CD4 (GK1.5, Biolegend, 100434), PE/Cy7-TCR-β (H57-597, Biolegend, 109222), FITC-TCR-β (H57-597, Biolegend, 109206), FITC-Helios (22F6, Biolegend, 137214), PE-RORγ (AFKJS-9, eBioscience™, 50-112-9700), APC-Foxp3 (FJK-16s, eBioscience™, 50-112-8936), APC/Cy7-Cd11c (N418, Biolegend, 117324), APC-CD8a (53-6.7, Biolegend, 100712), APC-CD19 (1D3/CD19, Biolegend, 152410), APC-F4/80 (BM8, Biolegend, 123116), APC-TER-119 (TER-119, Biolegend, 116212), PE-EpCAM (G8.8, Biolegend, 118206), PE-CD45RB (C363-16A, Biolegend, 103308), APC-CD25 (3C7, Biolegend, 101910), and anti-CD16/32 (2.4G2,BD Pharmingen™, 553142). Following WB antibodies were used in the study: Anti-VDR (sc-13133, Santa Cruz), Anti-FXR (sc-25309, Santa Cruz), Anti-GPBAR1 (PA5-23182, Invitrogen), Anti-Actin (sc-8432, Santa Cruz), IRDye® 680LT Goat anti-Rabbit IgG Secondary Antibody (P/N: 926-68021, LI-COR Biosciences), and IRDye® 680LT Goat anti-Mouse IgG Secondary Antibody (P/N: 926-68020, LI-COR Biosciences).
Validation	All the antibodies used in this study were validated by manufactures and used according to supplied instructions. The WB antibodies were re-validated by immunoblot performed in this study, and the FACS antibodies were determined by testing them with splenocyte staining.

Animals and other organisms

Policy information about studies involving animals; ARRIVE guidelines recommended for reporting animal research

Laboratory animals	C57BL/6J wild-type mice were obtained from Jackson, as were Vdr–/–, Nr1h4–/–, Nr1h3–/–, Chrm2–/–, Chrm3–/–, Rag1–/–, Foxp3YFP-cre, Cd11ccre, Vil1cre, and Foxp3mRFP mice. Nr1i2–/–Nr1i3–/– mice were obtained from Taconic. Gpbar1–/– mice were from KOMP Repository. S1pr2–/– mice were kindly provided by Dr. Timothy Hla at Boston Children's Hospital. Vdrflox/flox mice were kindly provided by Dr. David Gardner at University of California, San Francisco, and then crossed with Foxp3YFP-cre, Cd11ccre, or Vil1cre mice to generate the corresponding cell type specific knockout mice. Vdr–/–Nr1h4–/– mice were obtained by crossing Vdr+/– with Nr1h4+/– mice. Vdr–/–Foxp3mRFP or Vdr+/+Foxp3mRFP reporter mice were generated by crossing Vdr +/– with Foxp3mRFP reporter mice. All genetically modified mice and their control mice were subjected to experiments at the ages of 6-8 weeks old. For dietary treatment experiments, 3-week-old C57BL/6J wild-type mice or genetically deficient mice were fed either a sterilized nutrient-rich diet (LabDiet 5K67) or a minimal diet (TestDiet AIN-76A) for 4 weeks. Some groups of the mice fed a minimal diet were also treated with various BAs or SCFAs (sodium salt form) in drinking water for 4 weeks. GF C57BL/6J mice were orally inoculated by gavage with a broth-grown single bacterial strain or a collection of fecal material at 4 weeks of age. Each group of mice was then maintained in a gnotobiotic isolator under sterile conditions for 2 weeks.
Wild animals	The study did not involve wild animals.
Field-collected samples	The study did not involve samples collected from the field.
Ethics oversight	Harvard Medical School Institutional Animal Care and Use Committee and the Committee on Microbiological Safety.

Note that full information on the approval of the study protocol must also be provided in the manuscript.

Flow Cytometry

Plots

Confirm that:

☒ The axis labels state the marker and fluorochrome used (e.g. CD4-FITC).

☐ The axis scales are clearly visible. Include numbers along axes only for bottom left plot of group (a 'group' is an analysis of identical markers).

☐ All plots are contour plots with outliers or pseudocolor plots.

☒ A numerical value for number of cells or percentage (with statistics) is provided.

Methodology

Sample preparation	For isolation of LP lymphocytes, colonic and small intestinal tissues were dissected and fatty portions discarded. PPs were also removed from small intestines for isolation of lymphocytes. The excised intestinal tissues were washed in cold PBS buffer, and epithelia were removed by 500-rpm stirring at 37°C in RPMI medium containing 1 mM EDTA, 1 mM DTT, and 2% (vol/vol) FBS. After 15 min of incubation, the epithelium-containing supernatants were discarded, and the remaining intestinal tissues were washed in RPMI medium with 5% (vol/vol) FBS, further minced into small pieces, and digested by 500-rpm stirring at 37°C in RPMI medium containing collagenase type II (1.5 mg/ml), Dispase II (0.5 mg/ml), and 1.2% (vol/vol) FBS for 40 min. The digested tissues were filtered, and the solutions were centrifuged at 500 g for 10 min in order to collect LP cells. The pellets were resuspended, and the LP lymphocytes were isolated by Percoll (40%/80%) gradient centrifugation. For isolation of PP lymphocytes, the excised PPs were digested in the same medium by 500-rpm stirring at 37°C for 10 min, the digested PPs were filtered, the solutions were centrifuged at 500 g for 10 min, and lymphocytes were collected. Lymph nodes, spleens, and thymuses were mechanically disrupted.
Instrument	Miltenyi MACSQuant Analyzer and BD Biosciences MoFlo Astrios EQ.
Software	FlowJo 10.4.1.
Cell population abundance	All the cells were double sorted by flow cytometry (Astrios, BD Biosciences) to achieve 99% purity.
Gating strategy	The gating strategies used in this study: 1. FSC-A/SSC-A---FSC-A/FSC-H--- CD45-PB/Viability Dye-APC/Cy7---TCR-β-PE/Cy7/CD4-PerCP/Cy5.5---Foxp3-APC---RORγ-PE/ Helios-FITC. 2. FSC-A/SSC-A---FSC-A/FSC-H--- CD45-PE/Cy7/Viability Dye-DAPI---TCR-β-FITC/CD4-BV605---Foxp3-mRFP+/-. 3. FSC-A/SSC-A---FSC-A/FSC-H--- CD45-PE/Cy7/Viability Dye-DAPI---Cd11c-APC/Cy7. 4. FSC-A/SSC-A---FSC-A/FSC-H--- CD45-PB/Cy7-/Viability Dye-APC/Cy7---EpCAM-PE. 5. FSC-A/SSC-A---FSC-A/FSC-H--- CD45-PB/Viability Dye-AmCycan---TCR-β-PE/Cy7/CD4-PerCP/Cy5.5---CD25-APC-/CD45RB-PE high.

☐ Tick this box to confirm that a figure exemplifying the gating strategy is provided in the Supplementary Information.

Article

A GPR174–CCL21 module imparts sexual dimorphism to humoral immunity

https://doi.org/10.1038/s41586-019-1873-0

Received: 17 August 2018

Accepted: 31 October 2019

Published online: 25 December 2019

Ruozhu Zhao[1,2,3,4], Xin Chen[1,2,3,4], Weiwei Ma[1,2,3,9], Jinyu Zhang[2,3,5], Jie Guo[6], Xiu Zhong[4], Jiacheng Yao[4], Jiahui Sun[1,2,3], Julian Rubinfien[2,10], Xuyu Zhou[6], Jianbin Wang[4] & Hai Qi[1,2,3,4,7,8]*

Humoral immune responses to immunization and infection and susceptibilities to antibody-mediated autoimmunity are generally lower in males[1–3]. However, the mechanisms underlying such sexual dimorphism are not well understood. Here we show that there are intrinsic differences between the B cells that produce germinal centres in male and female mice. We find that antigen-activated male B cells do not position themselves as efficiently as female B cells in the centre of follicles in secondary lymphoid organs, in which germinal centres normally develop. Moreover, GPR174—an X-chromosome-encoded G-protein-coupled receptor—suppresses the formation of germinal centres in male, but not female, mice. This effect is intrinsic to B cells, and correlates with the GPR174-enhanced positioning of B cells towards the T-cell–B-cell border of follicles, and the distraction of male, but not female, B cells from S1PR2-driven follicle-centre localization. Biochemical fractionation of conditioned media that induce B-cell migration in a GPR174-dependent manner identifies CCL21 as a GPR174 ligand. In response to CCL21, GPR174 triggers a calcium flux and preferentially induces the migration of male B cells; GPR174 also becomes associated with more Gαi protein in male than in female B cells. Male B cells from orchidectomized mice exhibit impaired GPR174-mediated migration to CCL21, and testosterone treatment rescues this defect. Female B cells from testosterone-treated mice exhibit male-like GPR174–Gαi association and GPR174-mediated migration. Deleting GPR174 from male B cells causes more efficient positioning towards the follicular centre, the formation of more germinal centres and an increased susceptibility to B-cell-dependent experimental autoimmune encephalomyelitis. By identifying GPR174 as a receptor for CCL21 and demonstrating its sex-dependent control of B-cell positioning and participation in germinal centres, we have revealed a mechanism by which B-cell physiology is fine-tuned to impart sexual dimorphism to humoral immunity.

We began by comparing the formation of germinal centres by specific B cells from male and female MD4 mice. These particular B cells recognize hen egg lysozyme (HEL). We transferred MD4 B cells into the same male host mice together with OT-II helper T cells, which recognize the major histocompatibility complex (MHC) molecule I-A^b in complex with chicken ovalbumin-derived peptide ($OVA_{323–339}$). Five days after immunization with HEL–OVA, female MD4 B cells made a substantially larger contribution to germinal centres than male cells (Extended Data Fig. 1a, b). Interestingly, at day 4 before visible germinal-centre formation, female MD4 cells were more concentrated in the follicular centre occupied by the follicular dendritic cell network, whereas male cells in the same follicle were more dispersed across the entire follicle (Extended Data Fig. 1c, d), suggesting that differential follicle-centre localization may underlie the differential germinal-centre formation by male and female B cells.

A series of guidance receptors—including the chemokine receptors CXCR5 (refs. [4,5]) and CCR7 (refs. [6,7]), the sphingosine-1-phosphate receptor 2 (S1PR2; ref. [8]) and the G-protein-coupled receptor GPR183 (refs. [9,10])—orchestrates the sequential localization of antigen-activated B cells during a germinal-centre response. However, we did not detect differences in the expression of these receptors between the two sexes (Extended Data Fig. 2a). In a survey of additional G-protein-coupled receptors (GPCRs), we found that X-linked GPR174 was expressed by naive and germinal-centre B cells (Extended Data Fig. 2b). When

[1]Tsinghua-Peking Center for Life Sciences, Tsinghua University, Beijing, China. [2]Laboratory of Dynamic Immunobiology, Institute for Immunology, Tsinghua University, Beijing, China. [3]Department of Basic Medical Sciences, School of Medicine, Tsinghua University, Beijing, China. [4]School of Life Sciences, Tsinghua University, Beijing, China. [5]Department of Microbiology and Biochemical Pharmacy, College of Pharmacy, Third Military Medical University, Chongqing, China. [6]Institute of Microbiology, Chinese Academy of Sciences, Beijing, China. [7]Beijing Key Laboratory for Immunological Research on Chronic Diseases, Tsinghua University, Beijing, China. [8]Beijing Frontier Research Center for Biological Structure, Tsinghua University, Beijing, China. [9]Present address: Centre for Immunology and Vaccinology, Chelsea and Westminster Hospital, Faculty of Medicine, Imperial College, London, UK. [10]Present address: Yale University, New Haven, CT, USA. *e-mail: qihai@tsinghua.edu.cn

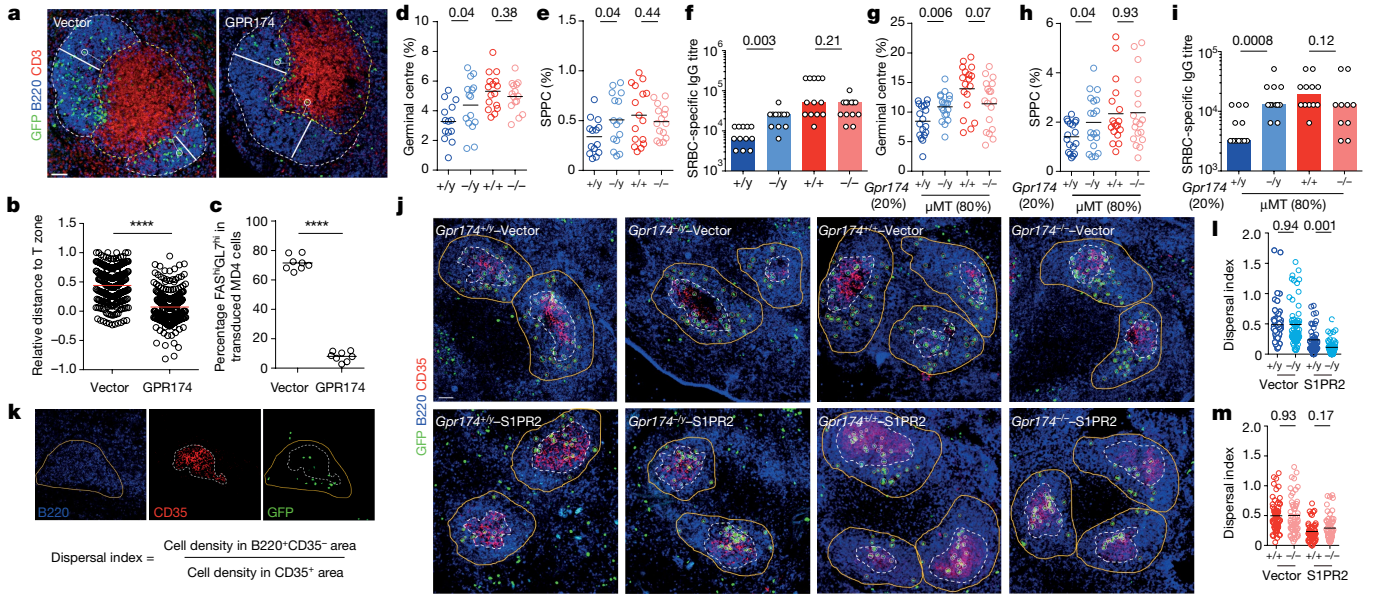


Fig. 1 | GPR174 regulates B-cell positioning and suppresses germinal-centre formation in male, but not female, mice. a, Splenic distribution patterns of mouse B cells retrovirally transduced with vector that expresses GFP alone or in combination with GPR174, 24 h after adoptive transfer. B220, the follicle; CD3, the T-cell zone. **b**, Summary statistics of the relative distance to the T-cell zone, defined as the ratio between the shortest distance from GFP$^+$ B cells to the T-zone edge (yellow dashed lines in **a**) and the maximum depth of the follicle (white lines), with negative values indicating T-zone locations. Each symbol denotes one B cell (n = 218 and 232), with data pooled from three experiments. Scale bar, 50 μm. **c**, Germinal-centre (FAS^{hi}GL7^{hi}) frequencies of transduced MD4 B cells five days after immunization. Each symbol denotes one mouse (n = 8 mice), with data pooled from two experiments. **d**, **e**, Statistics for germinal centres (**d**) and spleen plasma cells (SPPCs) (**e**) in mice of the indicated genotypes and sexes seven days after SRBC immunization. Blue and cyan symbols, males; red and pink symbols, females. Each symbol denotes one mouse (n = 14, 15, 16 and 15 from left to right). Data pooled from four experiments. **f**, SRBC-specific IgG titres in sera from mice of the indicated genotypes and sexes 14 days after SRBC immunization. Each symbol denotes one mouse (n = 12, 12, 13 and 13); data pooled from two experiments. **g**, **h**, Statistics of germinal centres (**g**) and SPPCs (**h**) in mixed bone-marrow chimeric mice seven days after SRBC immunization. Each symbol denotes one mouse (n = 18, 19, 18 and 18), with data pooled from four experiments. **i**, SRBC-specific IgG titres in sera of mixed bone-marrow chimaeras 14 days after SRBC immunization. Each symbol denotes one mouse (n = 12, 12, 12 and 10), with data pooled from two experiments. **j**, Distribution patterns of B cells of the indicated genotypes and sexes, transduced to express control vector (top) or S1PR2 (bottom), 12 h after transfer into sex-matched B6 recipients. Yellow lines outline follicle borders; white dashed lines outline CD35$^+$ follicular dendritic cell regions in each follicle; yellow circles highlight transferred B cells in the IgD$^+$ CD35$^-$ area; white circles highlight transferred B cells in the CD35$^+$ region. Scale bar, 50 μm. **k**, Definition of the dispersal index. **l**, **m**, Summary statistics of dispersal indices for male (**l**) and female (**m**) cells. Each symbol represents one follicle (n = 55, 58, 44, 48 biological replicates for males; n = 58, 49, 46, 49 for females). Data were pooled from two independent experiments. **b**–**e**, **g**–**h**, **l**–**m**, Short horizontal lines indicate mean. Two-tailed unpaired Student's t-tests were used. **f**, **i**, Column height indicates median. Two-tailed Mann–Whitney U-tests were used. P values are given in graphs; ****P < 0.0001.

retrovirally overexpressed, GPR174 promoted B-cell localization towards the T-cell–B-cell border of secondary lymphoid organs (Fig. 1a, b) without increasing CCR7 expression (Extended Data Fig. 2c), and markedly inhibited germinal-centre formation (Fig. 1c and Extended Data Fig. 3a). To test whether GPR174 differentially regulates germinal-centre responses in the two sexes, we examined germinal-centre formation in GPR174-deficient male and female mice. Seven days after immunization with sheep red blood cells (SRBCs), the size of germinal centres was lower in males than in females; GPR174 deficiency led to a marked recovery of the germinal-centre size in males but did not affect females (Fig. 1d and Extended Data Fig. 3b). Males had lower levels of splenic plasma cells and anti-SRBC immunoglobulin G (IgG) titres, which also recovered substantially in the absence of GPR174 (Fig. 1e, f and Extended Data Fig. 3c). In a model of acute viral infection, GPR174 also differentially impinged on germinal-centre formation in different sexes (Extended Data Fig. 3d). Next, we constructed mixed bone-marrow chimaeras comprising 80% of bone-marrow cells from μMT mice (which cannot generate B cells) and 20% of wild-type or GPR174-deficient donor bone-marrow cells. One week after SRBC immunization, germinal-centre formation by *Gpr174*$^{-/y}$ B cells was higher than that by *Gpr174*$^{+/y}$ counterparts in male chimaeras, whereas female *Gpr174*$^{+/+}$ and *Gpr174*$^{-/-}$ B cells did not differ in female chimaeras (Fig. 1g and Extended Data Fig. 3e). Splenic plasma cells and anti-SRBC titres followed the same trend (Fig. 1h, i and Extended Data Fig. 3f). Thus, GPR174 suppresses the intrinsic ability of male, but not female, B cells to form germinal centres and produce plasma cells.

We observed no difference in the follicular distribution of naive B cells sufficient or deficient in GPR174, and no difference in localization to the T-cell–B-cell border following acute activation[9] (Extended Data Fig. 4). Upregulation of S1PR2 on activated B cells promotes follicle-centre localization before germinal-centre formation[11], a process that can be mimicked with S1PR2 overexpression[8]. To examine whether endogenous GPR174 regulates this process in a sex-dependent manner, we transduced S1PR2 into male and female B cells. Following transfer into B6 mice, wild-type male and female B cells concentrated towards the follicular centre comparably; by contrast, this process was exaggerated by GPR174 deficiency for male, but not female, B cells (exemplified in Fig. 1j and quantified with a dispersal index in Fig. 1k–m). These data suggest that in male, but not female, mice endogenous GPR174 guides activated B cells away from the follicular centre, and thereby inhibits germinal-centre formation.

Previous studies have suggested that lysophosphoserine (LysoPS) is a GPR174 ligand[12], and that GPR174 plays a part in regulating the functions of regulatory T cells[13]. However, we found that LysoPS does not induce GPR174-dependent migration, whereas culture medium conditioned by a crude preparation of splenic stromal elements contained a strong chemoattractant activity for GPR174, irreplaceable by LysoPS (Extended Data Fig. 5a, b). Because this chemoattractant activity was

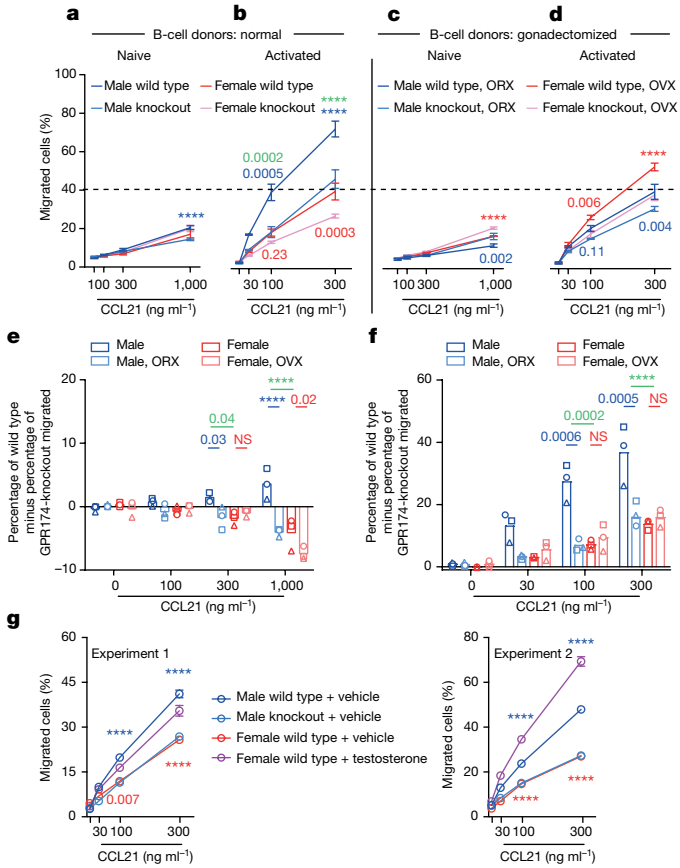


Fig. 2 | Sexually dimorphic GPR174-mediated B-cell migration to CCL21. **a**–**d**, Transwell migration in response to the indicated CCL21 concentrations by naive B cells (**a**, **c**) or B cells that were stimulated with anti-IgM (10 μg ml^{-1}) and anti-CD40 (10 μg ml^{-1}) antibodies for 48 h (**b**, **d**), from GPR174-sufficient or -deficient littermates that were either unmanipulated (**a**, **b**) or gonadectomized, six weeks after surgery (**c**, **d**). The dashed line at 40% aids cross-panel comparison. ORX, orchidectomized; OVX, ovariectomized. Data represent three biological replicates for each condition from one of three independent experiments with similar results. Blue asterisks, wild-type versus GPR174-knockout male; red asterisks, wild-type versus GPR174-knockout female; green asterisks, wild-type male versus wild-type female. **e**, **f**, Summary statistics from the three experiments, showing GPR174-dependent migration of naive B cells (**e**) or activated B cells (**f**) in response to CCL21, calculated by subtracting the mean percentage migrated of GPR174-knockout B cells from the mean percentage migrated of corresponding wild-type B cells. Mean values from individual experiments are indicated with different symbols, and bar heights indicate averages of the three experiments. Blue asterisks, male versus male ORX; red asterisks, female versus female OVX; green asterisks, male versus female. **g**, Transwell migration of activated B cells that were isolated from GPR174-sufficient or -deficient male or GPR174-sufficient female littermate mice treated with either vehicle or testosterone. Data represent three biological replicates for each condition, from two independent experiments. Blue asterisks, male wild type versus knockout plus vehicle; red asterisks, female wild type vehicle versus testosterone. All statistical comparisons were made by two-way analysis of variance (ANOVA) with Bonferroni's multiple comparisons; ****$P < 0.0001$. NS, not significant.

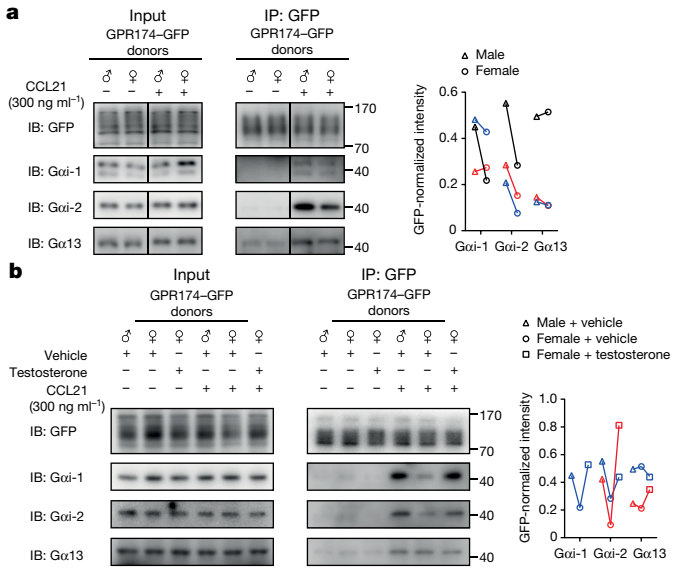


Fig. 3 | Sex and hormone dependence of CCL21-induced GPR174–Gαi association. **a**, Left and centre, immunoblots (IBs) of lysates (left) or GFP immunoprecipitates (centre) of B cells isolated from male or female GPR174–GFP BAC transgenic mice, activated with anti-IgM and anti-CD40, and left untreated or stimulated with 300 ng ml^{-1} CCL21. Right, normalized quantities of indicated Gα proteins in co-immunoprecipitation (IP) products from three similar experiments, each represented by a different colour and a connecting line. **b**, Left and centre, immunoblots of lysates or GFP immunoprecipitates of B cells from the indicated sources and treatments, as in **a**. Right, normalized quantities of indicated Gα proteins in co-immunoprecipitation products from two experiments, each represented by a different colour and a connecting line. Gαi-1 was probed in one of the two experiments. Vehicle, mice treated with sunflower seed oil; testosterone, mice treated with testosterone dissolved in sunflower seed oil. For gel source data, see Supplementary Fig. 1.

lost after heating at 100 °C or incubation with proteinase K (Extended Data Fig. 5c), it is likely that GPR174 sensed a protein. GPR174 is highly conserved in mammalian species, and we confirmed that the mouse receptor responded to ligands from rat (data not shown) and porcine (Extended Data Fig. 5d) spleens. Subsequently, through a 6-step isolation procedure (Extended Data Fig. 5e), we concentrated from 16 porcine spleens sufficient amounts of ligand activities for mass-spectrometry-based protein identification (Extended Data Fig. 5f–k). Fraction 5 from the final mono-S purification step contained the strongest chemoattractant activity and gave rise to bands with enhanced intensities on silver-stained gels (Extended Data Fig. 5k–l). By mass spectrometry, we identified numerous peptides that collectively cover 50% of the porcine CCL21 sequence.

To verify that CCL21 and potentially CCL19 are chemokine ligands for GPR174, we neutralized CCL21 and CCL19 in splenic-stroma-conditioned medium. We found that blocking either CCL21 or CCL19 reduced, and blocking both abrogated, the migration of GPR174-transduced B cells to stroma-conditioned medium (Extended Data Fig. 6a). GPR174-transduced B cells also vigorously migrated towards recombinant CCL21 or CCL19 (Extended Data Fig. 6b). GPR174 or CCR7 transfection of 293T cells—which do not endogenously express these proteins—conferred a comparable binding capacity to CCL21 (Extended Data Fig. 6c). Finally, GPR174- or CCR7-expressing 293T cells responded to CCL21 with calcium fluxes in a dose-dependent manner (Extended Data Fig. 6d, e). The estimated half maximal effective concentration (EC_{50}) for CCL21 to trigger either GPR174 or CCR7 was around 15 nM (with 95% confidence intervals of 9–23 nM for GPR174 and 8–28 nM for CCR7). Therefore, similarly to CCR7, GPR174 is a binding and signalling receptor for CCL21. This is consistent with the fact that CCL21 is produced by stromal cells in the T-cell zone, and that GPR174 overexpression led B cells to position towards the T-cell–B-cell border (Fig. 1a, b).

To test whether endogenous GPR174 contributes to CCL21-directed B-cell migration differently between the two sexes, we first examined naive B cells. As shown in Fig. 2a, naive B cells migrated to CCL21 weakly in general, with barely 20% migrating at CCL21 concentrations of 1,000 ng ml^{-1}. GPR174 deficiency did not have any effect on female naive B cells (compare the red and pink titration curves in Fig. 2a); for male naive cells, however, GPR174 deficiency led to a slight but discernible

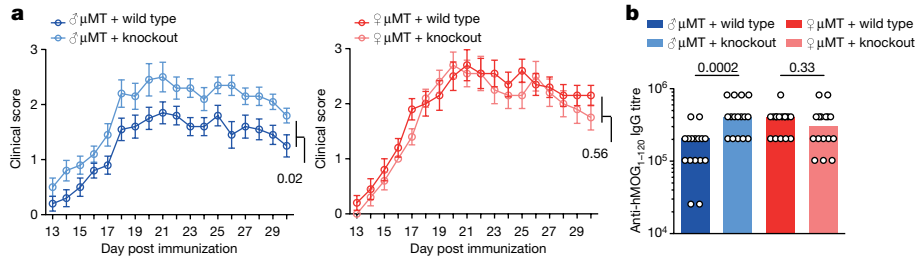


Fig. 4 | B-cell GPR174 reduces EAE susceptibility and autoantibody titres in male mice. a, EAE disease scores of 12-week-old mixed bone-marrow chimaeras of the indicated sexes, constructed with 80% μMT and 20% GPR174-sufficient or -deficient bone-marrow cells. Data ($n = 10$ mice each group) are from one of two independent experiments with similar results. **b**, Anti-MOG IgG titres in the indicated chimaera on day 30 after EAE induction. Data ($n = 16$ mice each group) are pooled from two independent experiments. Data are plotted as mean ± s.e.m., compared by two-way ANOVA with Bonferroni's multiple comparisons (**a**), or as individual mice with bars indicating median and compared by two-tailed Mann–Whitney *U*-test (**b**). *P* values are given in the graph.

reduction in migration to 1,000 ng ml^{-1} CCL21 (wild type, 20.5 ± 1.0% migrated; knockout, 14.5 ± 1.3%; $P < 0.0001$).

Next, we examined activated B cells. As shown in Fig. 2b, activated male B cells migrated more strongly than female B cells towards CCL21, reaching twice as high a percentage migrated as the female cells at all CCL21 concentrations (compare the blue and red curves). GPR174 deficiency led to a roughly 50% reduction in migration by male cells (blue and cyan curves), down to a level comparable to that seen with wild-type female cells (the cyan and red curves); GPR174 deficiency in female activated B cells also led to a reduction, but of a smaller magnitude (compare the red and pink curves).

To test whether sex hormones are responsible, we further examined B cells from gonadectomized male and female mice. GPR174-deficient naive B cells isolated from orchidectomized mice actually migrated more in response to 1,000 ng ml^{-1} CCL21 (Fig. 2c) (wild type, 12.0 ± 0.9%; knockout, 16.8 ± 1.8%; $P = 0.0017$). GPR174-deficient female naive B cells also migrated more than wild-type cells following ovariectomy (compare the red and pink curves in Fig. 2a, c). For activated male B cells, isolated from orchidectomized mice, CCL21-induced migration was down to a level similar to that of female B cells isolated from normal mice (compare the blue curve in Fig. 2d with the red curve in Fig. 2b) and, notably, to a level similar to that of GPR174-deficient B cells from normal or orchidectomized mice (compare the blue curve in Fig. 2d to the cyan curves in Fig. 2b, d). Thus, orchidectomy substantially reduced GPR174-mediated migration to CCL21 in male activated B cells. On the other hand, ovariectomy did not change the comparatively smaller effect of GPR174 on female B cells (red and pink curves in Fig. 2b, d).

The data presented in Fig. 2a–d are from one experiment. Summary statistics from three such independent experiments are presented in Fig. 2e, f, in which the migrated fraction in each GPR174-deficient group is subtracted from that in the corresponding wild-type group to quantify GPR174-dependent migration. For naive B cells, GPR174 mediates a small response only to high concentrations of CCL21 in the male, but this effect is absent in female cells or in male cells from orchidectomized mice (Fig. 2e). For activated B cells, GPR174 mediates much stronger migration (more so in males than in females), and orchidectomy abrogates the margin by which male outperform female cells (Fig. 2f).

Although testosterone treatment in vitro for up to two days did not alter B-cell migration to CCL21 (data not shown), two-week testosterone treatment of orchidectomized mice rescued their B-cell migration to CCL21 (Extended Data Fig. 7a). Furthermore, B cells isolated from testosterone-treated female mice became much more efficient in migrating to CCL21 (Fig. 2g). We did not detect any difference in GPR174 or CCR7 expression by B cells from male, female, gonadectomized or testosterone-treated mice (Extended Data Fig. 7b–g). Transcriptomic analyses of B cells from sham-operated or gonadectomized male or female mice revealed no differential expression of known guidance receptors (R.Z. et al., unpublished observations). GPR174 expression did not differ between male and female B cells during an active response in vivo (Extended Data Fig. 7h). Therefore, the male hormone conditions GPR174-mediated B-cell migration to CCL21, although receptor expression is not the point of regulation.

GPCR-mediated chemotaxis depends on coupling with Gαi proteins, and coupling to Gα12/13 proteins inhibits directional migration towards ligands. The same GPCR can couple to different Gα proteins in different cell types or in the same cell type of different sexes, as in the case of the corticotropin-releasing-hormone receptor[14]. To test whether GPR174 is differentially coupled to Gαi and/or Gα12/13 proteins in male and female B cells, we created a transgenic mouse line in which bacterial artificial chromosomes (BACs) were used to express a functionally validated construct consisting of GPR174 fused to green fluorescent protein (GFP) (Extended Data Fig. 8). We then immunoprecipitated GPR174–GFP-associated proteins from primary B cells using the GFP as a tag. B cells did not markedly express Gαi-3 or Gα12 (data not shown), and our analyses thus focused on Gαi-1, Gαi-2 and Gα13. As shown in Fig. 3a, GPR174 in activated male or female B cells was associated with Gα13 but minimally with Gαi-1 or Gαi-2, consistent with Gα13 activation by GPR174 in an assay of transforming growth factor-α (TGFα) shedding[12]. We also found that, upon CCL21 stimulation, GPR174 association with Gα13 became higher and association with Gαi-1 and Gαi-2 was markedly increased, consistent with GPR174-promoted migration to CCL21; notably, the GPR174–Gαi association was stronger in male than in female B cells, whereas the GPR174–Gα13 association showed no difference between the sexes. For B cells isolated from female GPR174–GFP mice that were treated with testosterone, the profile of Gα association became similar to that of male B cells, exhibiting overtly increased CCL21-dependent Gαi association and unchanged Gα13 association (Fig. 3b). These data show that ligand-engaged GPR174 is differentially coupled to Gαi in male and female B cells, and reveal a likely mechanism for the sexual dimorphism of GPR174-mediated migration to CCL21.

In an active immune response, GPR174-deficient male B cells became more concentrated within the follicular dendritic cell network and made a much larger contribution to germinal-centre formation (Extended Data Fig. 9), whereas GPR174 made no difference to B-cell localization or germinal-centre magnitude in females (Extended Data Fig. 10 and data not shown). This indicates that the sexually dimorphic GPR174 response to CCL21 is one reason why humoral responses are weaker in males than in females. To test whether this GPR174 effect impinges on susceptibility to B-cell-dependent autoimmune diseases, we resorted to experimental autoimmune encephalomyelitis (EAE), which is induced in mice by immunization with human myelin oligodendrocyte glycoprotein ($MOG_{1–120}$)—a model that recapitulates the requisite role of B cells in human multiple sclerosis[15–17]. We immunized male μMT:*Gpr174*$^{+/y}$, male μMT:*Gpr174*$^{-/y}$, female μMT:*Gpr174*$^{+/+}$ and

female µMT:*Gpr174*$^{-/-}$ bone-marrow (80/20) chimaeras with human $MOG_{1–120}$ protein and followed the disease course. All mice developed symptoms of EAE, with females suffering a more severe disease course; GPR174 deletion did not change the disease course in females but did exacerbate it in males (Fig. 4a). Correlating with this finding, male µMT:*Gpr174*$^{+/y}$ chimaeras produced the lowest $MOG_{1–120}$-specific antibody titres, which were increased in male µMT:*Gpr174*$^{-/y}$ chimaeras to a level similar to that in females (Fig. 4b). Therefore, the sexually dimorphic functions of GPR174 in B cells contribute substantially to different disease susceptibilities in the two sexes.

Our study identifies GPR174 as a receptor for CCL21, and reveals its chemotactic effects on activated B cells as a mechanism for sexual dimorphism in humoral responses and autoimmunity. Testosterone-conditioned differential coupling to Gαi proteins underlies the different effects of GPR174 on male and female B-cell migration to CCL21. Given the well-established role of CCR7 in CCL21-mediated chemotaxis, it is an intriguing possibility that CCL21 binding might induce GPR174–CCR7 heterodimerization and achieve a signalling outcome that these two receptors cannot attain individually. When CCR7 is ablated in B cells, CCL21-induced GPR174–Gαi coupling and GPR174-mediated migration are markedly reduced (R.Z. et al., unpublished observations), suggesting a dual role for CCR7 in governing the B-cell migratory response to CCL21 via itself and GPR174. LysoPS restrains regulatory T cells in a GPR174-dependent manner[13]. Future studies will need to elucidate how tripartite CCL21–GPR174–CCR7 interactions regulate Gαi coupling and downstream signals in a testosterone-dependent manner, and whether and how LysoPS and CCL21 might compete or collaborate in triggering GPR174-dependent functions. Although the functions of GPR174 in humans remain to be validated, antagonists that selectively target GPR174 binding to CCL21 or selectively inhibit GPR174–Gαi coupling in B cells might boost vaccine outcomes in otherwise poorly responding men.

Online content

Any methods, additional references, Nature Research reporting summaries, source data, extended data, supplementary information, acknowledgements, peer review information; details of author contributions and competing interests; and statements of data and code availability are available at https://doi.org/10.1038/s41586-019-1873-0.

1. Whitacre, C. C. Sex differences in autoimmune disease. *Nat. Immunol.* **2**, 777–780 (2001).
2. Klein, S. L. & Flanagan, K. L. Sex differences in immune responses. *Nat. Rev. Immunol.* **16**, 626–638 (2016).
3. Ghosh, S. & Klein, R. S. Sex drives dimorphic immune responses to viral infections. *J. Immunol.* **198**, 1782–1790 (2017).
4. Ansel, K. M. et al. A chemokine-driven positive feedback loop organizes lymphoid follicles. *Nature* **406**, 309–314 (2000).
5. Förster, R. et al. A putative chemokine receptor, BLR1, directs B cell migration to defined lymphoid organs and specific anatomic compartments of the spleen. *Cell* **87**, 1037–1047 (1996).
6. Nakano, H. et al. A novel mutant gene involved in T-lymphocyte-specific homing into peripheral lymphoid organs on mouse chromosome 4. *Blood* **91**, 2886–2895 (1998).
7. Förster, R. et al. CCR7 coordinates the primary immune response by establishing functional microenvironments in secondary lymphoid organs. *Cell* **99**, 23–33 (1999).
8. Green, J. A. et al. The sphingosine 1-phosphate receptor $S1P_2$ maintains the homeostasis of germinal center B cells and promotes niche confinement. *Nat. Immunol.* **12**, 672–680 (2011).
9. Pereira, J. P., Kelly, L. M., Xu, Y. & Cyster, J. G. EBI2 mediates B cell segregation between the outer and centre follicle. *Nature* **460**, 1122–1126 (2009).
10. Gatto, D., Paus, D., Basten, A., Mackay, C. R. & Brink, R. Guidance of B cells by the orphan G protein-coupled receptor EBI2 shapes humoral immune responses. *Immunity* **31**, 259–269 (2009).
11. Pereira, J. P. P., Kelly, L. M. & Cyster, J. G. Finding the right niche: B-cell migration in the early phases of T-dependent antibody responses. *Int. Immunol.* **22**, 413–419 (2010).
12. Inoue, A. et al. TGFα shedding assay: an accurate and versatile method for detecting GPCR activation. *Nat. Methods* **9**, 1021–1029 (2012).
13. Barnes, M. J. et al. The lysophosphatidylserine receptor GPR174 constrains regulatory T cell development and function. *J. Exp. Med.* **212**, 1011–1020 (2015).
14. Bangasser, D. A. et al. Sex differences in corticotropin-releasing factor receptor signaling and trafficking: potential role in female vulnerability to stress-related psychopathology. *Mol. Psychiatry* **15**, 896–904 (2010).
15. Lyons, J. A., San, M., Happ, M. P. & Cross, A. H. B cells are critical to induction of experimental allergic encephalomyelitis by protein but not by a short encephalitogenic peptide. *Eur. J. Immunol.* **29**, 3432–3439 (1999).
16. Genain, C. P., Cannella, B., Hauser, S. L. & Raine, C. S. Identification of autoantibodies associated with myelin damage in multiple sclerosis. *Nat. Med.* **5**, 170–175 (1999).
17. Mulero, P., Midaglia, L. & Montalban, X. Ocrelizumab: a new milestone in multiple sclerosis therapy. *Ther. Adv. Neurol. Disorder*. https://doi.org/10.1177/1756286418773025 (2018).

Publisher's note Springer Nature remains neutral with regard to jurisdictional claims in published maps and institutional affiliations.

© The Author(s), under exclusive licence to Springer Nature Limited 2019

Methods

Mice

The following mice were originally from the Jackson Laboratory: C57BL/6 (Jax664), μMT (Jax2288), GFP-expressing (Jax4353), cyan fluorescent protein (CFP)-expressing (Jax 4218), dsRed-expressing (Jax 6051), $OVA_{323–339}$-specific T-cell-receptor transgenic OT-II (Jax 4194) and HEL-specific Ig-transgenic MD4 (Jax2595). GPR174-deficient mice were generated by standard gene-targeting procedures to replace the *Gpr174* open reading frame with a LacZ/neo cassette using the 129SvEvBrd embryonic stem cell line (Texas A&M Institute for Genomic Medicine, TG0128). These GPR174-deficient mice were backcrossed to C57BL/6 mice for 12 generations. Relevant mice on the C57BL/6 background were interbred to obtain GFP-expressing MD4 mice and dsRed-expressing GPR174-sufficient or -deficient MD4 mice. Age-matched littermates between 6 and 12 weeks of age and of the indicated sexes were used for experiments. Sample sizes for mouse experiments were empirically determined, and mice were randomly assigned to control or experimental group. No blinding was necessary for the mouse experiments presented here. All mice were maintained under specific-pathogen-free conditions and were used in accordance with governmental and Tsinghua Institutional Animal Care and Use Committee guidelines for animal welfare.

GPR174–GFP BAC transgenic mice

Sequences coding for the glycine–glycine–glycine–serine (GGGS) linker (repeated four times) and enhanced GFP (EGFP) were inserted immediately before the stop codon of the GPR174 open reading frame in the mouse BAC clone RP23-206J14 by homologous recombination. The modified BAC was purified and microinjected into the pronuclei of fertilized ova to generate transgenic reporters. A founder mouse that was screened positive for GFP-expressing B cells in the blood was used to further breed with B6 mice to establish the GPR174–GFP BAC strain.

Cell culture, retrovirus and in vitro transduction

Naive T cells or B cells were isolated using the Negative CD4 T-cell Isolation Kit or the Naive B-cell Isolation Kit (Miltenyi Biotec) according to the manufacturer's protocols. To overexpress target genes in B cells, purified B cells were activated with 1 μg ml^{-1} lipopolysaccharide (Sigma) for 1 day before being spin-infected with retroviral supernatants at 1,500*g* for 2 h, as described[18].

Construction of bone-marrow chimaeras

B6 recipient mice were lethally irradiated by X-ray (5.5 Gy, twice) and then given an intravenous transfer of 3×10^6 sex-matched bone-marrow cells, consisting of 80% μMT cells and 20% GPR174-sufficient or -deficient cells. Chimaeras were used for experiments six to eight weeks after reconstitution.

Gonadectomy

Mice after weaning were anaesthetized with avertin (2.5%, 0.015 ml g^{-1} body weight) intraperitoneally. For ovariectomy of female mice, ovaries on both sides were exposed and removed through bilateral dorsal incisions. For orchidectomy in male mice, a median abdominal incision was made to expose and remove testicles on both sides. Sham-operated control mice underwent surgery including bilateral dorsal incisions or a median abdominal incision without removal of ovaries or testicles. Surgical wound openings were sutured, and antibiotics and analgesics were applied locally. Mice were allowed to recover for eight weeks before subsequent experiments.

Testosterone treatment

Six- to eight-week-old mice were subcutaneously injected with testosterone (10 mg kg^{-1} body weight) dissolved in sunflower seed oil every other day for two weeks. Vehicle control mice were treated with sunflower seed oil alone.

Adoptive transfer, immunization and viral infection

To measure germinal-centre formation by MD4 B cells, 10^5 OT-II T cells and 5×10^5 MD4 B cells of indicated genotypes were intravenously transferred into male B6 recipients, which were subsequently immunized subcutaneously with 0.5 μg lipopolysaccharide and 30 μg HEL–OVA conjugate antigen in alum (Thermo Scientific). The HEL–OVA was made by chemical crosslinking with a HydraLink conjugation kit (SoluLink) as previously described[19]. To measure germinal-centre formation in response to SRBC immunization or lymphocytic choriomeningitis virus (LCMV) infection, mice were injected intraperitoneally with 5×10^8 SRBCs (from Z. Baiji) or 2×10^5 plaque-forming units of the LCMV Armstrong virus (from L. Ye and R. Ahmed).

EAE by MOG protein immunization

The sequence encoding the first 120 amino acids of human MOG was amplified by polymerase chain reaction (PCR) from a human brain complementary DNA library, and cloned between the *Nde*I and *Xho*I sites of the pET22b+ expression vector (Novagen). Human MOG protein was expressed in BL21(DE3) *Escherichia coli* and purified by its carboxy-terminal histidine (His) tag. Protein purity and concentration were assessed by SDS–PAGE and bicinchoninic acid (BCA) protein assay, respectively. Recombinant proteins were stored at −80 °C until use. To induce EAE, bone-marrow-chimeric animals of indicated types were immunized subcutaneously at the flank with 200 μg recombinant human MOG protein emulsified in complete Freund's adjuvant on day 0. Mice were injected intravenously with 200 ng of pertussis toxin (Invitrogen) on days 0 and 2. Mice were monitored daily in a blind manner for disease progression from day 1. Disease severity was scored as following: 0, no clinical signs; 1, paralysed tail; 2, loss of coordinated movement and paresis of hind limbs; 2.5, paralysis of one hind limb; 3, paralysis of both hind limbs; 3.5, paralysis of both hind limbs and weakness in forelimbs; 4, paralysis of forelimbs; and 5, moribund. To compare disease severity, we studied ten mice per condition per experiment, and analysed disease scores over time with two-way ANOVA.

Flow cytometry

Single-cell suspensions were incubated in MACS buffer (phosphate-buffered saline (PBS) supplemented with 1% fetal bovine serum (FBS) and 5 mM EDTA) containing 20 μg ml^{-1} 2.4G2 (BioXcell) for 20 min before being stained with indicated monoclonal antibodies. Staining reagents included: BV421-anti-CD4 (GK1.5), APC-Cy7-anti-CD19 (1D3), PE-Cy7-anti-CD95 (Jo2), AlexaFluor-700-anti-B220 (RA3-6B2), eFlour450-anti-B220 (RA3-6B2) and APC-anti-CD138 (281-2) from BD Biosciences; and eFlour450-anti-GL7 (GL-7) and FITC-anti-GL7 (GL-7) from eBioscience; PerCP Cy5.5 anti-IgD (HK1.4), biotinylated anti-CCR7 (4B12), and streptavidin-APC (405207) from Biolegend. Dead cells were excluded from analysis by staining with 7-AAD (Biotium) or using the Zombie Yellow Fixable Viability kit (Biolegend). All cytometry data were collected on an LSR II or FACSAria III cytometer (BD Biosciences) and analysed with FlowJo software (TreeStar).

Measurement of antigen-specific antibody titres

To measure SRBC-specific antibody titres, we lysed 5×10^8 SRBCs with 1 ml double-distilled water and centrifuged them at 15,000 r.p.m. for 20 min. The pellet was resuspended in PBS and used to coat MaxiSorp enzyme-linked immunosorbent assay (ELISA) plates (Nunc Maxisorp) overnight at 4 °C. To measure MOG-specific serum antibodies, we used 2 μg ml^{-1} purified recombinant human MOG to coat the ELISA plates. Nonspecific binding was blocked with 1% bovine serum albumin (BSA) in PBS with Tween-20 (PBST) for 2 h at 37 °C, followed by incubation with 2× serial dilutions of serum samples of immunized mice for 1 h at 37 °C. Plates were washed and incubated with horseradish peroxidase (HRP)-conjugated anti-mouse IgG secondary antibody (1/20,000) for 1 h at 37 °C. Plates were washed, developed with

3,3′,5,5′-tetramethylbenzidine (TMB) and stopped with 1 M HCl. We set blank wells as zero, and recorded absorbance at 450 nm. We used sera from unimmunized mice as the negative control; the cut-off value was the optical density at 450 nm (OD_{450}) of the negative control multiplied by 2.1. A well with an OD_{450} value of no less than the cut-off value was considered positive. The highest dilution of a sample that gave positivity is the titre of the sample.

Distribution of B cells by immunohistochemistry

For various experiments, naive B cells, B cells activated for 1 h with 10 μg ml^{-1} F(ab′)$_2$ goat anti-mouse IgM (Jackson Immunoresearch), or B cells transduced with retrovirus were transferred into B6 recipients. When required, these cells were labelled with 1 μM tetramethylrhodamine (TAMRA), 4-chloromethyl-6,8-difluoro-7-hydroxycoumarin (CMF2HC) or 5-chloromethylfluorescein diacetate (CMFDA) (Invitrogen). Spleens or inguinal lymph nodes of the recipient mice were fixed with 1% paraformaldehyde for 12 h and then dehydrated in 30% sucrose solution for 12 h at 4 °C. To ensure maximum representation of different organ regions in the final dataset, we processed nonconsecutive tissue sections and stained them with indicated antibodies. Staining reagents included eFluor450-IgD (eBioscience), APC-CD35 (BD), PE-CD3 (BD), eFluor450-B220 (eBioscience), rabbit anti-GFP (abcam), and AF488 goat anti-rabbit IgG (Invitrogen). Slides were mounted with the ProlongGold Antifade reagent (Invitrogen) and examined with an Olympus FV1000 upright microscope. Images were analysed with Imaris (Bitplane) and ImageJ 1.46r (National Institutes of Health).

Splenic stroma preparation

Spleens from mice, rats or pigs were repeatedly pressed and ground against a metal mesh to release red blood cells and lymphocytes. The remaining unsuspendable, amorphic stromal tissue elements were thoroughly washed with PBS before being placed in B27 serum-free culture medium (Invitrogen) and incubated at 37 °C for 12 h. For mice, stromal elements from three animals were cultured in 1 ml medium. For pigs, stromal elements from 1 spleen were cultured in 80 ml. The resultant culture was centrifuged at 10,000 r.p.m. for 60 min to obtain the conditioned medium, which was either immediately used for experiments or frozen at −20 °C until use.

Transwell assay

B cells activated with 1 μg ml^{-1} lipopolysaccharide for 60 h were used to assay different fractions resulting from biochemical fractionation. Naive B cells or B cells activated with 10 μg ml^{-1} F(ab′)$_2$ goat anti-mouse IgM (Jackson Immunoresearch) and 10 μg ml^{-1} anti-CD40 (clone FGK4.5, Bio X Cell) were used to assay CCL21-induced migration. When B cells of different genotypes were compared, at least three donor mice of each genotype and treatment were used to isolate B cells in each experiment, and littermates were always used. B cells were suspended at 10^6 cells per millilitre and rested in RPMI medium containing 1% FBS at 37 °C for 1 h. Next a total of 100 μl cell suspension was added to the upper chamber in a 5-μm-pore Transwell (Corning Costar), and a total of 150 μl attractant-containing solutions was added to the bottom chamber. These solutions included culture medium conditioned with crude mouse splenic stroma preparation, culture medium conditioned with crude porcine splenic stroma preparation, elution fractions from chromatography, culture medium containing recombinant CCL21 and CCL19 (Peprotech), or 18/0 LysoPS (Avanti Polar Lipids) of indicated concentrations. For some experiments, murine stroma-conditioned medium was first supplemented with a final concentration of 5 μg ml^{-1} neutralizing antibodies against mouse CCL21 or CCL19 (R&D system) or goat IgG isotype control, and incubated at 4 °C for 3 h before being used for the transwell assay. The antibody dose was at least sufficient to neutralize 100 ng ml^{-1} CCL21 or CCL19, as determined in preliminary experiments. Cells were allowed to transmigrate for 3 h at 37 °C in an incubator. Cells that had migrated to the bottom wells were enumerated by flow cytometry, with fluorescent A20 cells of known numbers added immediately before reading as an internal counting standard. Each condition was measured in triplicate wells unless indicated otherwise.

Biochemical fractionation

Chromatography was carried out using an ÄKTApurifer 10 fast protein liquid chromatography (FPLC) system (GE Healthcare) at 4 °C, with the exception of the last step, which was carried out using an ÄKTAmicro FPLC system (GE Healthcare). A total of 1,200 ml porcine stroma-conditioned medium was applied to an anion-exchange column (250 ml bed volume) equilibrated with buffer I (25 mM Hepes, pH 7.0). The column was washed with three column volumes before being eluted with three column volumes of buffer I supplemented with 1 M NaCl. The flow-through was buffer-changed with buffer II (25 mM Tris-HCl, pH 8.5) into 100 ml and reapplied to an anion-exchange column equilibrated with buffer II. The column was washed with two column volumes of buffer II and eluted with two column volumes of a 0.1–0.5 M linear NaCl gradient. Fractions of 10 ml each were collected, and aliquots were buffer-changed with RPMI 1640 for the transwell assay. Active fractions were pooled and buffer-changed into 10 ml with buffer II and loaded onto a heparin column (5 ml bed volume) equilibrated with buffer II. The column was washed with 12 column volumes of buffer II and eluted with 4 column volumes of 0–2 M linear NaCl gradient. Fractions of 2 ml each were collected and aliquots were buffer-changed with RPMI 1640 for the transwell assay. Active fractions were again pooled, buffer-changed into 0.5 ml buffer I and loaded onto a Superdex-75 column (24 ml bed volume) equilibrated with buffer I. The column was then eluted with one-column volume of buffer I. Fractions of 0.5 ml each were collected, and aliquots were buffer-changed with RPMI 1640 for the transwell assay. Active fractions were pooled and concentrated into 0.5 ml to load onto a Mono S column (1 ml bed volume) equilibrated with buffer I. The column was washed with 12 column volumes of buffer I and eluted with 25 column volumes of 0–0.5 M linear NaCl gradient. Fractions of 1 ml each were collected, and aliquots were buffer-changed with RPMI 1640 for the transwell assay. Active fractions were pooled, buffer-changed and concentrated into 50 μl with buffer I, and reloaded onto the Mono S column equilibrated with buffer I. The column was washed with three column volumes of buffer I containing 0.3 M NaCl, and eluted with 24 column volumes of 0.3–0.4 M linear NaCl gradient. Fractions of 1 ml each were collected, and aliquots were buffer-changed with RPMI 1640 for the final transwell assay to identify the fraction that contained the strongest chemoattractant activity.

Mass spectrometry analysis

Fractions from the last purification step were concentrated into 50 μl and analysed on 12% NuPAGE gels (Invitrogen). Gels were stained with the Pierce silver stain for mass spectrometry (Thermo Fisher Scientific) according to the manufacturer's protocol. Bands of increased intensities in the fraction containing the strongest chemoattractant activity were excised and subjected to in-gel digestion before being analysed with a Q Exactive HF mass spectrometer (Thermo Fisher Scientific). Mass spectrometry data were analysed using the Swissprot database with the MASCOT search engine.

His-tagged recombinant CCL21 and binding assay

The mouse CCL21 coding sequence was amplified from C57BL/6 mouse spleen cDNA and cloned between the *Nde*I and *Xho*I sites of the pET22b+ expression vector (Novagen), which provides a C-terminal His tag. The recombinant protein was expressed in BL21(DE3) mice and purified by its His tag. Protein purity and concentration were assessed by SDS–PAGE and BCA assay, respectively, and bioactivity was verified using a calcium mobilization assay. Recombinant proteins were stored at −80 °C until use. To measure CCL21–His binding to GPR174, with CCR7 as a positive control, 293T cells were transfected with GPR174–GFP or CCR7–GFP fusion constructs. Aliquots of transfected cells were then

incubated with CCL21–His protein at indicated concentrations at 37 °C for 30 min, washed twice with cold PBS, and fixed immediately with 4% paraformaldehyde. After washings in PBS, the fixed cells were stained with a phycoerythrin-conjugated anti-His antibody (clone J095G46, Biolegend) and analysed by flow cytometry. GFP^- cells in each sample served as a nonspecific background staining internal control, and the mean fluorescence intensity (MFI) of GFP^+ cells stained with phycoerythrin-conjugated anti-His antibody, with the MFI of corresponding GFP^- cells subtracted, was used to quantify specific CCL21 binding.

Measurement of chemokine-triggered calcium fluxes

Mouse *Gpr174* and *Ccr7* were amplified by PCR and cloned into the pRK5 plasmid. HEK293T cells were transiently transfected with GPR174-expressing, CCR7-expressing or control plasmid. Cells were physically detached from the culture vessel 48 h after transfection, washed twice with PBS, and stained with 1 μM Indo-1 (Invitrogen) in PBS at 37 °C for 30 min. After being washed twice with PBS, cells were resuspended with Hanks' balanced salt solution (Invitrogen) containing 25 mM Hepes and 1% FBS, and kept on ice. When subjected to chemokine stimulation, cells were first brought into a water batch at 37 °C for 5 min of incubation, and then assessed on an LSR II cytometer (BD Biosciences) to establish the baseline for the unstimulated state. Cells were stimulated with a concentration series of recombinant CCL21 ranging from 0.1 ng ml^{-1} to 10 μg ml^{-1}. Cells at each condition were continuously monitored and recorded for 2 min. At the end, ionomycin (Sigma) was further added to the sample at a final concentration of 1 μg ml^{-1}, and the sample was further monitored and recorded for 1 min. Indo-1(bound)/Indo-1(free) ratios were used to indicate intracellular Ca^{2+} concentrations, as analysed in FlowJo (TreeStar). The highest Ca^{2+} concentration stimulated by ionomycin was used as 100% to normalize the calcium response induced by CCL21. The EC_{50} was estimated in GraphPad by fitting a three-parameter, nonlinear dose–response curve.

Immunoprecipitation and western blotting

Freshly isolated mouse B cells from GPR174–GFP BAC transgenic mice were activated with 10 μg ml^{-1} $F(ab')_2$ goat anti-mouse IgM and 10 μg ml^{-1} anti-CD40 for 48 h. These activated B cells were then suspended at 2×10^7 cells per millilitre in RPMI medium containing 1% FBS, and left untreated or stimulated with 300 ng ml^{-1} CCL21 at 37 °C for 30 min. B cells were then immediately lysed in 1% NP-40 lysis buffer (25 mM Tris-HCl, pH 7.4, 137 mM NaCl, 1% Nonidet P-40, 20% glycerol and protease inhibitors). For immunoprecipitation of GFP-tagged GPR174, lysates of 10^8 B cells were incubated overnight with 20 μl of GFP–Trap beads (ChromoTek). After repeated washings, immunoprecipitates were eluted by incubation in 0.2 M Glycine buffer (pH 3.0) for 10 min at room temperature, and then neutralized with 1 M Tris-HCl (pH 8.5). Proteins were separated by SDS–PAGE and transferred to polyvinylidene membrane (Millipore). Membranes were blocked with Tris-buffered saline containing 5% BSA and 0.1% Tween 20. To detect target molecules by immunoblotting, we used rabbit anti-GFP (Abcam), rabbit anti-Gαi-1 (Abcam), rabbit anti-Gαi-2 (Abcam) and rabbit anti-Gα13 (Abcam) antibodies. HRP-conjugated goat anti-rabbit antibody was purchased from Bioeasytech. Immunoblots were detected using enhanced chemiluminescence (Thermo Fisher Scientific), and images were analysed with ImageJ software.

Quantitative PCR

Cells of desired types were sorted with a FACSAria III and subjected to total RNA extraction with the RNeasy Plus Mini or Micro kit (Qiagen) according to the manufacturer's instructions. RNA was reverse-transcribed with All-In-One RT MasterMix (Abm). Quantitative PCR was performed with qPCR MasterMix (Abm) on a 7500 Real-Time PCR system (Applied Biosystems). Primers used were as follows: *Gapdh* sense 5′-TGTTCCTACCCCCAATGTGTC, antisense 5′-TAGCCCAAGATGCCCTTCAGT; *Gpr174* sense 5′-AGGCCACACACCTTTTTCCC, antisense 5′-CAGGCCAGGACATCATGGAA; *S1pr2* sense 5′-CAACTCCGGGACATAGACCG, antisense 5′-CCAGCGTCTCCTTGGTGTAA; *Gpr183* sense 5′- CATAAAAGGACGCCTGCTCG, antisense 5′- TTTCCCACCAGCCCAATGAT; *Ccr7* sense 5′-GGTGGCTCTCCTTGTCATTTTC, antisense 5′- TACGTCAGTATCACCAGCCC; *Cxcr5* sense 5′- ACTACCCACTAACCCTGGACA, antisense 5′- CGAGGTGGAACAGGAAGGTC. Relative expression of target genes among different samples was compared after normalization against expression of the housekeeping genes *Actb* or *Gapdh*.

Statistical data analysis

Statistics and graphing were conducted in Prism (Graphpad). Unless indicated otherwise, two-tailed unpaired Student's *t*-tests were used to compare endpoint means of different groups.

Reporting summary

Further information on research design is available in the Nature Research Reporting Summary linked to this paper.

Data availability

Data generated here are included within the paper (and its Supplementary Information files) or available from the corresponding author upon reasonable request. Source Data for Figs. 1–4 and Extended Data Figs. 1–10 are provided with the paper.

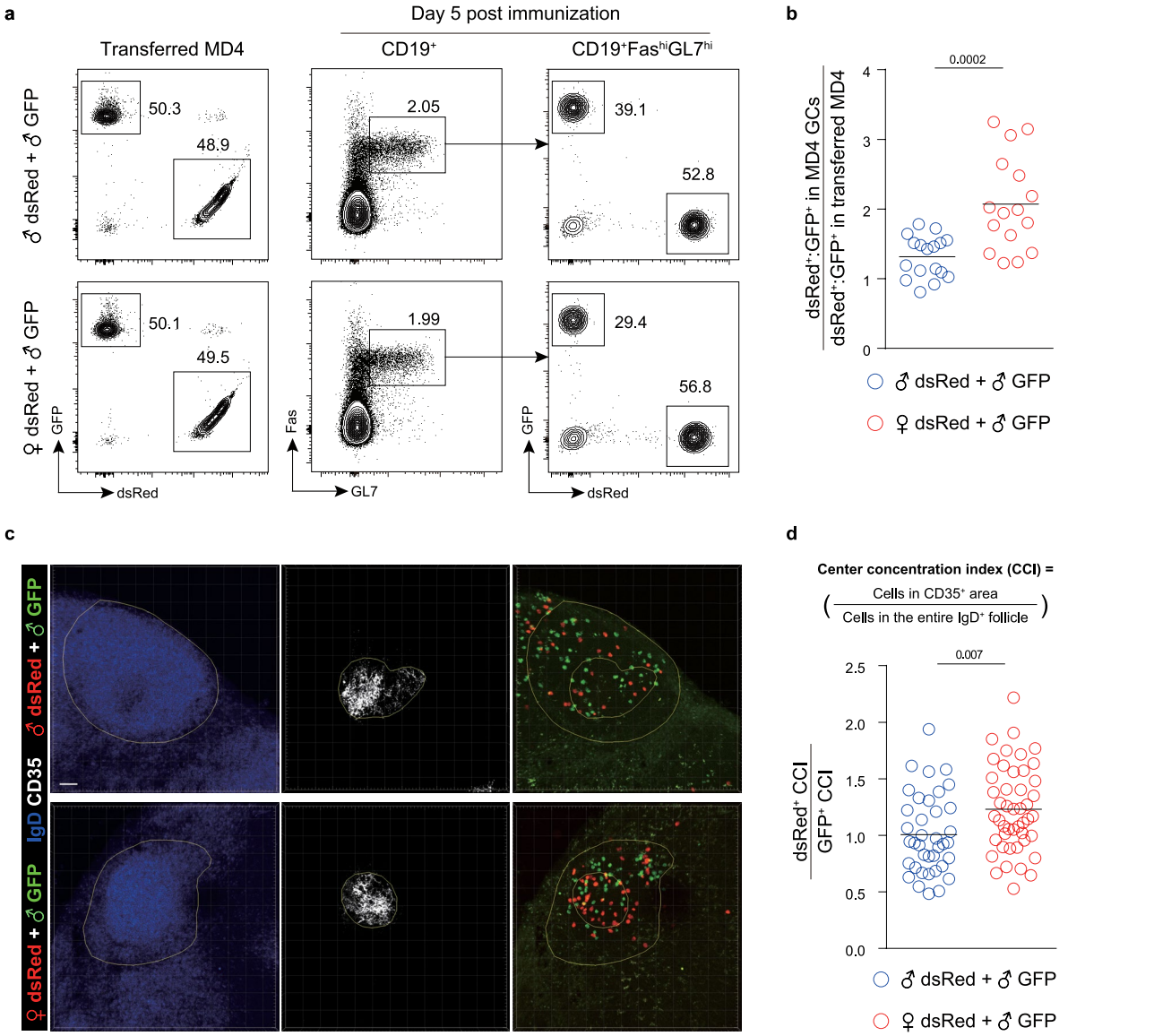
18. Wang, Y. et al. Germinal-center development of memory B cells driven by IL-9 from follicular helper T cells. *Nat. Immunol.* **18**, 921–930 (2017).
19. Xu, H. et al. Follicular T-helper cell recruitment governed by bystander B cells and ICOS-driven motility. *Nature* **496**, 523–527 (2013).

Acknowledgements We thank the Protein Preparation and Characterization Core Facility at the Tsinghua University Branch of the China National Center for Protein Sciences for chromatography support; and T. Li, K. He and H. Wang at the National Center of Biomedical Analysis for expert advice and assistance with mass spectrometry. This work was funded in part by the National Natural Science Foundation of China (grants 81621002, 31830023, 81761128019 and 81425011), the Tsinghua-Peking Center for Life Sciences and the Beijing Municipal Science and Technology Commission. This work was also funded in part by the Bill and Melinda Gates Foundation and the Howard Hughes Medical Institute. The findings and conclusions within are those of the authors and do not necessarily reflect the positions or policies of the Bill and Melinda Gates Foundation or the Howard Hughes Medical Institute.

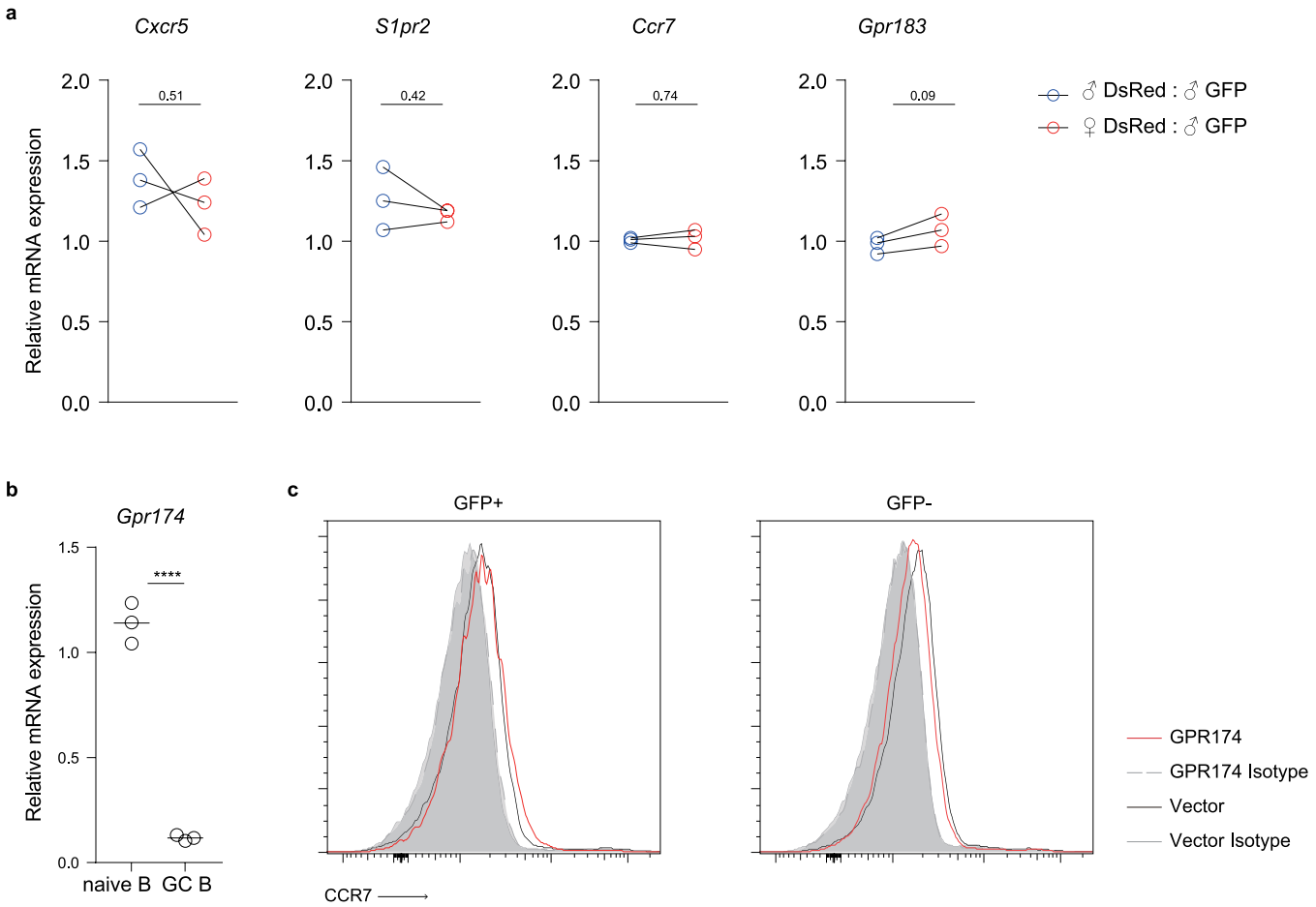
Author contributions R.Z. conducted a majority of the experiments and designed parts of the study. X.C. made the initial observation of GPR174-mediated positioning effects, developed conditioned media for ligand identification and, together with W.M., conducted baseline characterization of GPR174-deficient mice. X.C., J.G. and X. Zhou generated GPR174–GFP BAC transgenic mice. J.Z. conducted antibody titre analyses. J.Y., J.S. and J.W. conducted RNA-sequencing analyses. X. Zhong and J.R. helped with transwell and immunohistochemistry analyses, respectively. H.Q. conceptualized the study, supervised the work and wrote the paper with R.Z.

Competing interests The authors declare no competing interests.

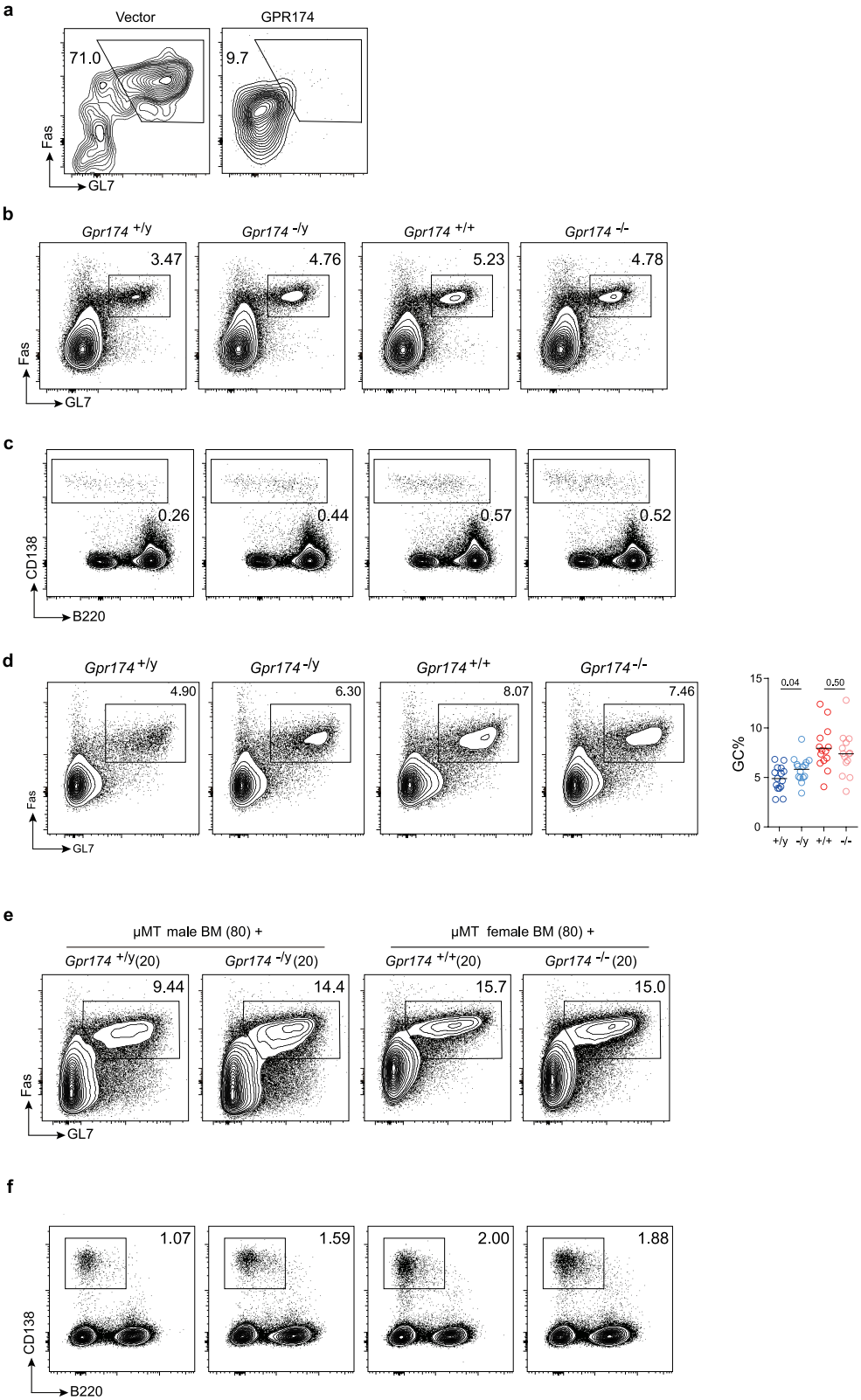
Additional information
Supplementary information is available for this paper at https://doi.org/10.1038/s41586-019-1873-0.
Correspondence and requests for materials should be addressed to H.Q.
Peer review information *Nature* thanks Andrew Luster, Charles Mackay and the other, anonymous, reviewer(s) for their contribution to the peer review of this work.
Reprints and permissions information is available at http://www.nature.com/reprints.



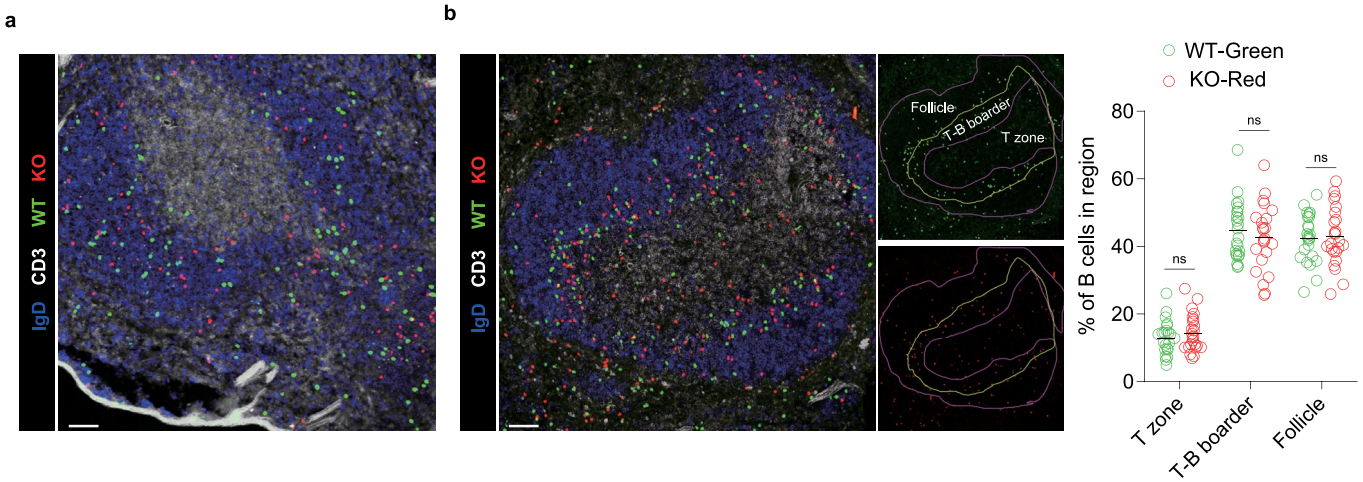
Extended Data Fig. 1 | Intrinsic differences between male and female B cells in forming geminal centres. a, Representative contour plots and frequencies of dsRed-expressing and GFP-expressing MD4-derived cells of the indicated sexes, found in the initial transfer inoculum (left panels) or in the germinal-centre compartment in draining lymph nodes five days after subcutaneous immunization (middle and right panels) of male recipient mice. **b**, Summary statistics of the dsRed/GFP ratio in MD4 germinal centres (GCs), normalized against the dsRed/GFP ratio in transfer inoculum. Each symbol represents one mouse ($n = 17$ and 16); data were pooled from three independent experiments with similar results. **c**, Representative distribution patterns of dsRed-expressing and GFP-expressing MD4 cells of the indicated sexes in follicles 90 h after immunization. Scale bar, 50 µm. **d**, Definition of the centre concentration index (CCI) and summary statistics of the CCI of dsRed$^+$ tester cells of the indicated sexes, normalized against the CCI of GFP$^+$ male control cells in the same follicle. Each symbol denotes one follicle ($n = 38$ and 46). Data pooled from two independent experiments with similar results. Scatter plots have horizontal lines denoting mean (**b**, **d**); two-tailed unpaired Student's *t*-tests were used to calculate the *P* values at the top of each graph.



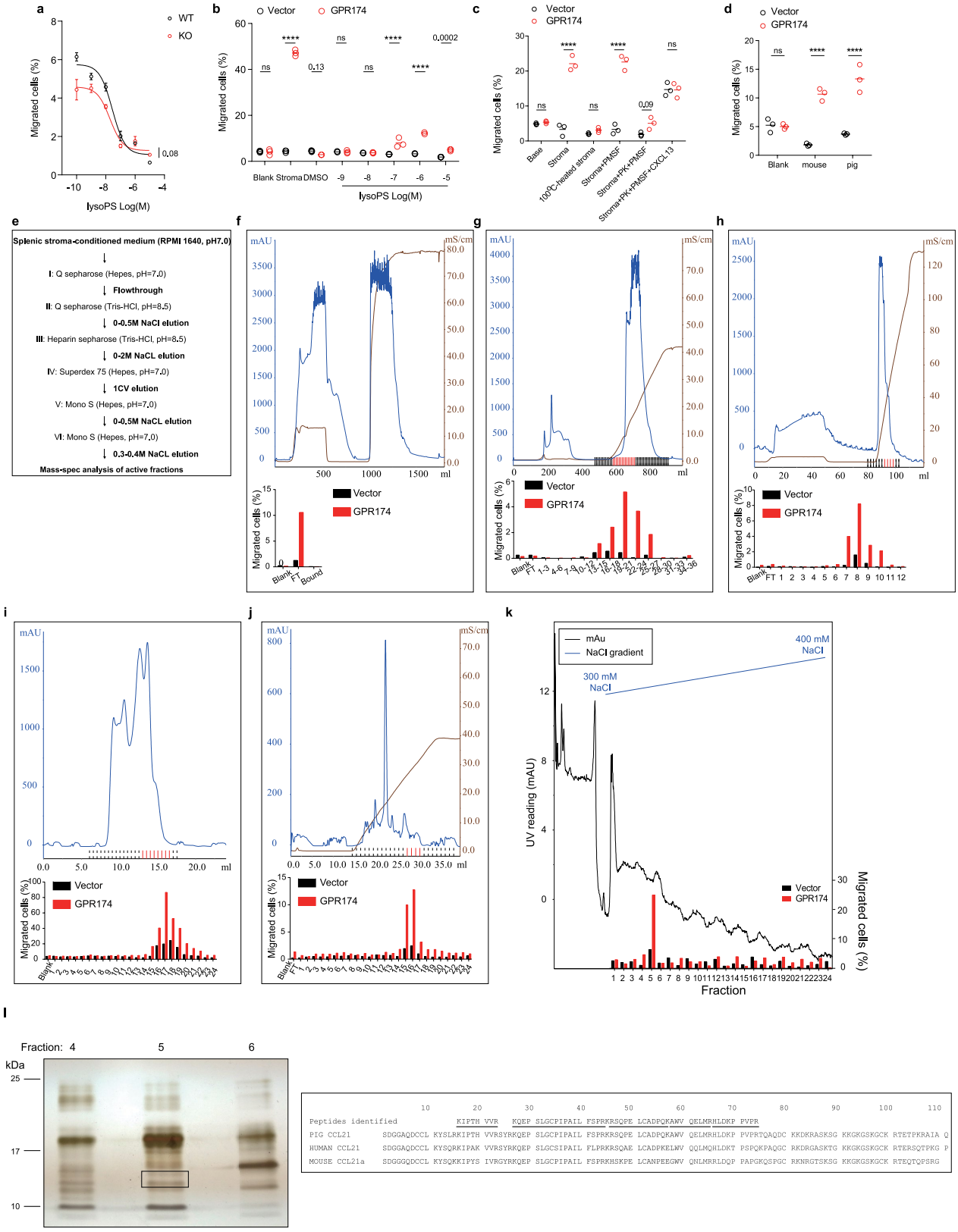
Extended Data Fig. 2 | Expression of guidance GPCRs in male and female cells, differential GPR174 expression by naive and germinal-centre B cells, and lack of influence on CCR7 expression. a, Relative mRNA expression of *Cxcr5*, *S1pr2*, *CCR7* and *Gpr183* in male or female dsRed-expressing MD4 B cells, normalized against that in cotransferred male GFP-expressing MD4 B cells (Extended Data Fig. 1), 90 h after immunization. Data are shown as pairs of three individual experiments. **b**, Relative *Gpr174* mRNA levels in indicated splenic B cell subsets, normalized against *Gapdh* expression. The results are shown as scatter plots of three biological replicates, with lines indicating mean, and are representative of two independent experiments with similar results. **c**, Surface CCR7 levels on B cells that were retrovirally transduced with a control or GPR174-expressing vector. GFP^+, infected cells after transduction; GFP^-, uninfected cells after transduction; representative of three independent experiments. Two-tailed paired (**a**) or unpaired (**b**) Student's *t*-tests were used to calculate *P* values, given at the top of each graph; ****$P < 0.0001$.



Extended Data Fig. 3 | GPR174 suppresses germinal-centre formation in male, but not female, mice. a, Representative cytometric profiles of $FAS^{hi}GL7^{hi}$ frequencies of transduced MD4 B cells in B6 recipients five days after immunization. **b**, **c**, Representative cytometric profiles of germinal centres (**b**) and SPPCs (**c**) in mice of the indicated genotypes and sexes seven days after SRBC immunization, matching the summary statistics presented in Fig. 1d, e, respectively. **d**, Representative cytometric profiles (left panels) and summary statistics (right panel) of germinal centres in littermate mice of the indicated genotypes and sexes, eight days after infection with LCMV Armstrong (10^5 plaque-forming units per mouse). The scatter plot (right) shows individual mice with lines denoting mean ($n = 15, 15, 14$ and 14 mice, from left to right). Data pooled from three independent experiments with similar results. A two-tailed unpaired Student's *t*-test was used. **e**, **f**, Representative cytometric profiles of germinal centres (**e**) and SPPCs (**f**) in mixed bone-marrow (BM) chimeric mice of indicated types seven days after SRBC immunization, matching the summary statistics presented in Fig. 1g, h, respectively.

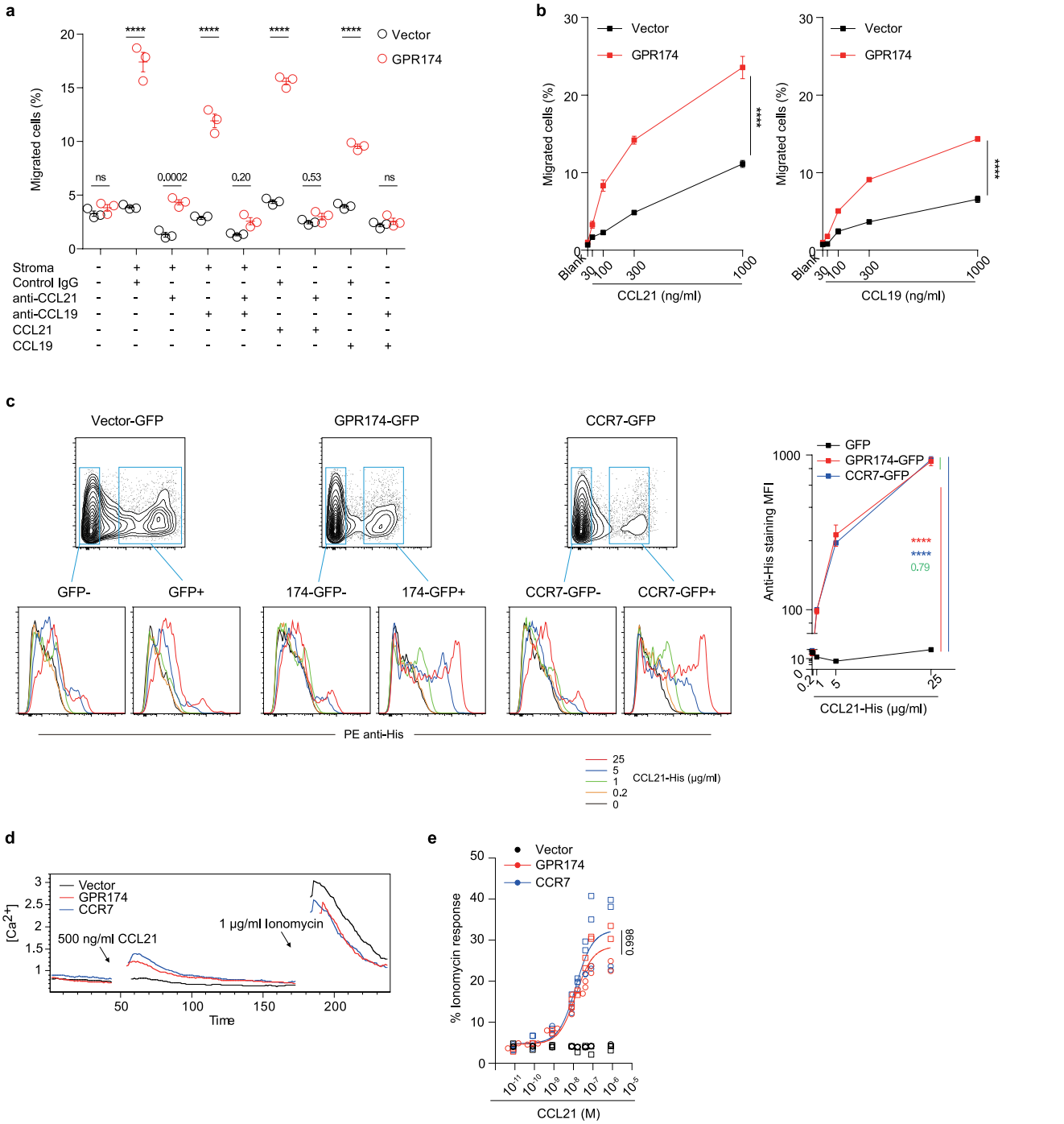


Extended Data Fig. 4 | Endogenous GPR174 does not affect the follicular distribution of naive B cells or the accumulation of freshly activated B cells to the T-cell–B-cell border. a, Splenic distribution of GPR174-sufficient and -deficient naive B cells 24 h after adoptive transfer. WT, wild type; KO, knockout. Data are representative of two independent experiments involving either male or female cells. Scale bars, 50 µm. **b**, Left, splenic distribution of GPR174-sufficient or -deficient B cells that were stimulated with anti-IgM, 6 h after adoptive transfer. Scale bar, 50 µm. Middle, definitions of follicular area, the T-cell–B-cell border and the T-cell zone, based on IgD and CD3 staining. Right, relative abundance of transferred B cells in the indicated regions. Data ($n = 24$ biological replicates) represent two independent experiments with similar results. Lines in scatter plots denote mean. We used two-way ANOVA with Bonferroni's multiple comparisons; ns, not significant.

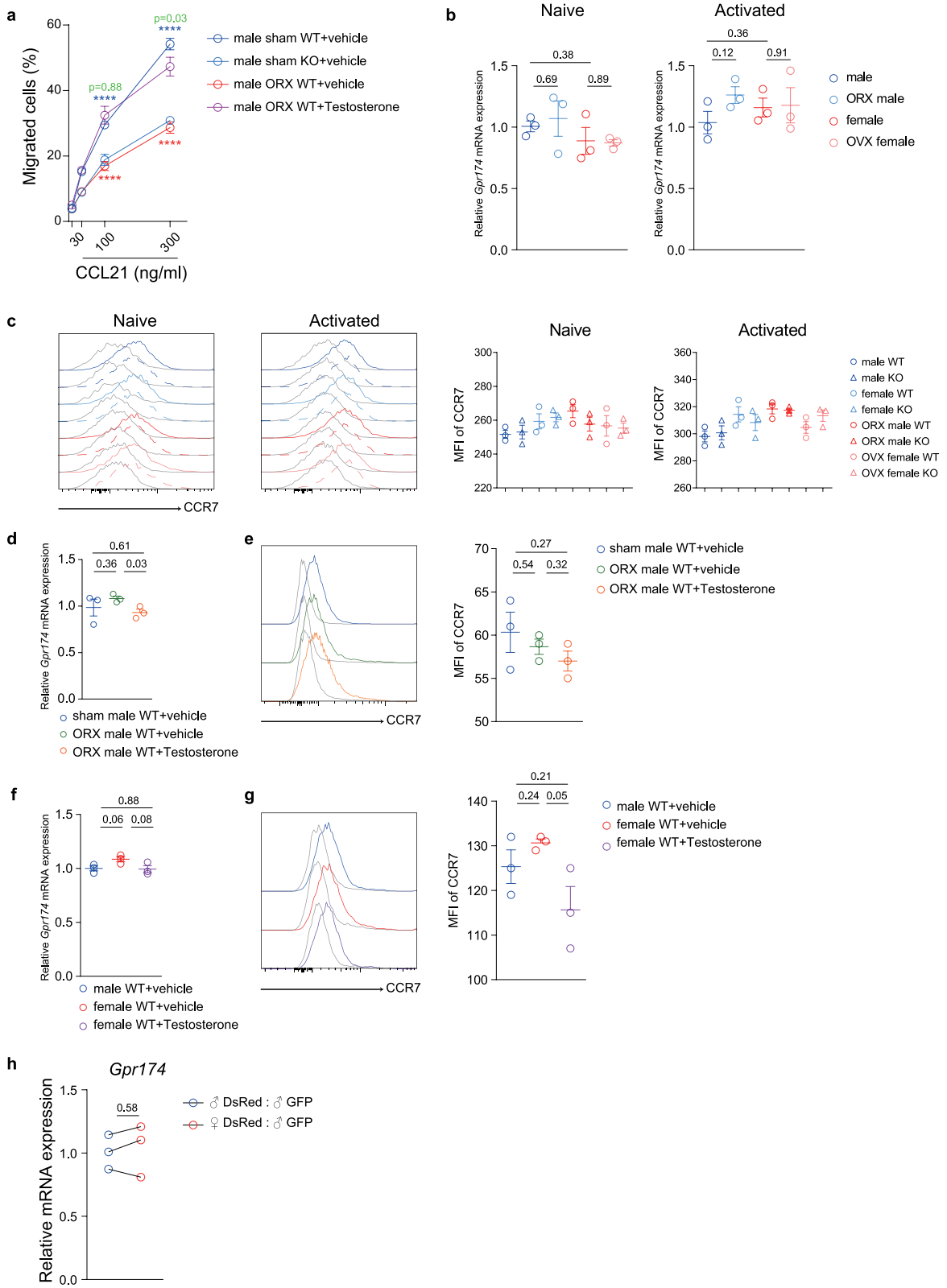


Extended Data Fig. 5 | See next page for caption.

Extended Data Fig. 5 | Minimal LysoPS effects on GPR174-dependent B-cell migration and GPR174 ligand identification. a, Transwell migration of lipopolysaccharide-activated GPR174-sufficient or -deficient B cells in response to LysoPS of indicated concentrations. Data are plotted as mean ± s.e.m. of the percentage of cells that migrated in triplicated wells at each concentration, fitted with three-parameter log dose–response curves; two-way ANOVA was used to compare the two groups. One of two independent experiments with similar results is shown. **b**–**d**, Transwell migration of lipopolysaccharide-activated B cells that were transduced with a control or GPR174-expressing vector, in response to stroma-conditioned medium (stroma), dimethylsulfoxide (DMSO) control or LysoPS of indicated concentrations (**b**); or in response to stroma-conditioned medium (stroma), conditioned medium heated at 100 °C for 10 min (heated), conditioned medium treated with the proteinase K inhibitor PMSF alone (PMSF), conditioned medium treated with proteinase K and then PMSF (PK + PMSF), or conditioned media treated as above and then further supplemented with 300 ng ml^{-1} CXCL13 (PK + PMSF + CXCL13) to exclude cell damage owing to remaining proteinase activity (**c**); or in response to blank culture medium, or mouse or porcine stroma-conditioned media (**d**). All data are plotted as the mean percentages of cells that migrated in triplicated wells, from one experiment representative of three with similar results. Two-way ANOVA with Bonferroni's multiple comparison tests were used to compare vector and GPR174 groups, with *P* values given in the graphs. ****$P < 0.0001$; ns, not significant. **e**, Workflow showing the six-step biochemical fractionation method for identifying GPR174 ligands in splenic stroma-conditioned medium. See Methods for details. CV, column volume. **f**–**k**, Chromatography traces and putative ligand activities as detected by the transwell assay in **d** in relevant fractions during the six steps of **e**. AU, arbitrary units; mS, millisiemens. **l**, Left, silver staining of the indicated fractions from **k** resolved on 12% SDS–PAGE; the black box on fraction 5 marks bands subjected to liquid chromatography-mass spectrometry (LC-MS)/MS analysis. Right, identified unique porcine CCL21-derived peptides (solid underlines) aligned against porcine, human and murine CCL21 protein sequences. For gel source data, see Supplementary Fig. 1. Data shown in **f**–**l** are from one of two independent experiments with similar results. FT, flow-through.

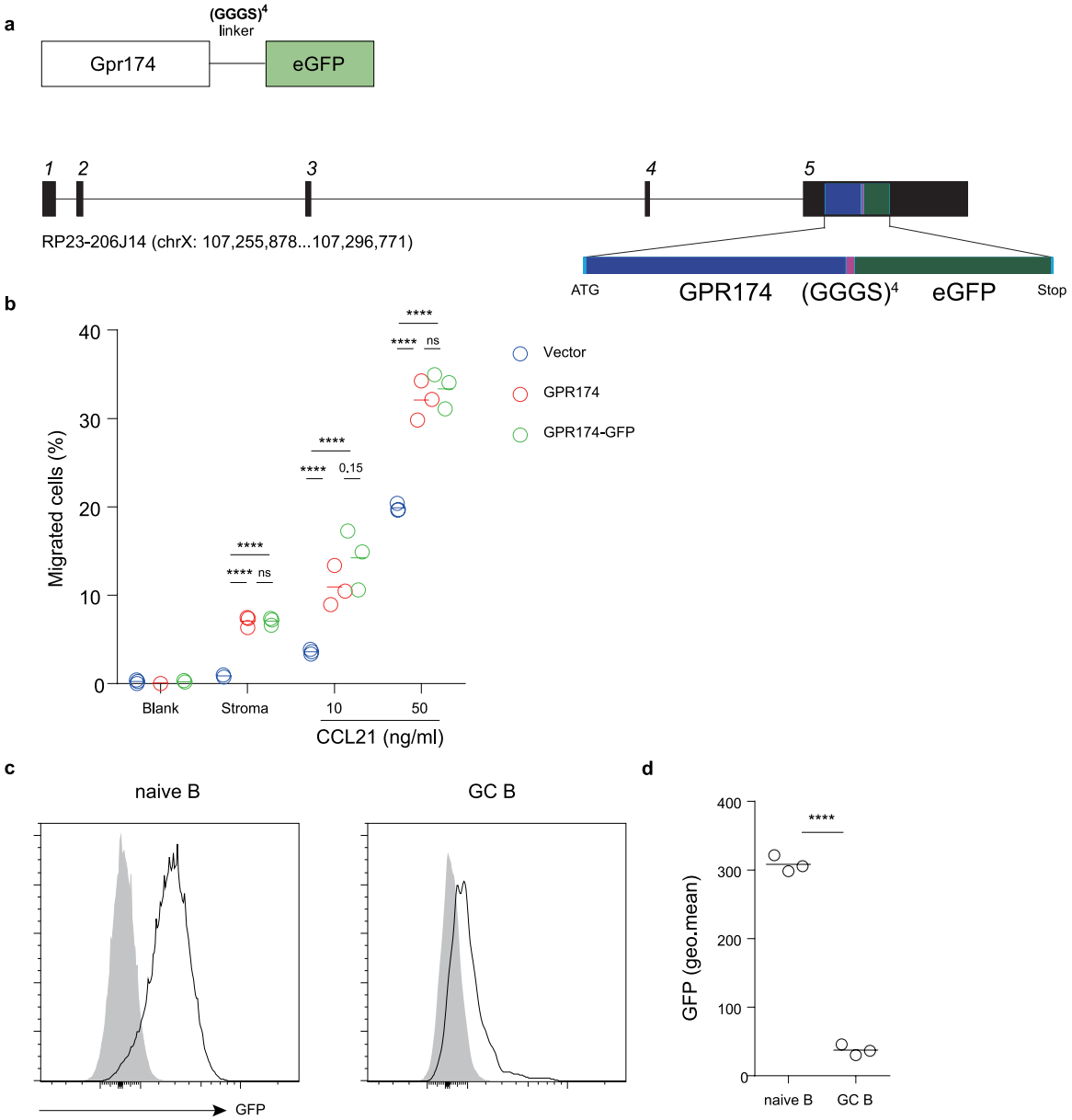


Extended Data Fig. 6 | CCL21 and CCL19 are chemoattractant ligands of GPR174. a, **b**, Transwell migration of lipopolysaccharide-activated B cells that were transduced with a control or GPR174-expressing vector: **a**, in response to stroma-conditioned medium (stroma) or 100 ng ml^{-1} recombinant CCL21 or CCL19, in the presence of control IgG or 5 μg ml^{-1} CCL21- or CCL19-blocking antibody, individually or in combination; **b**, in response to recombinant mouse CCL21 (left) or CCL19 (right). Data represent triplicated wells for each condition from one of three independent experiments with similar results. Two-tailed unpaired Student's *t*-tests; ****$P < 0.0001$. **c**, Cytometric profiles and MFI of CCL21 binding to HEK293T cells transfected with control GFP, GPR174–GFP or CCR7–GFP fusion constructs, with background staining on the GFP$^-$ fraction subtracted from the corresponding GFP$^+$ fraction. Left, gating of GFP$^-$ and GFP$^+$ cells in each group (top) and histograms of anti-His staining (bottom) of cells that were incubated with different doses of His-tagged recombinant CCL21. PE, phycoerythrin. Right, data represent three biological replicates for each condition, from one of three independent experiments with similar results. Two-way ANOVA tests were used to compare groups, with *P* values given in the graph; red asterisks, GFP versus GPR174–GFP; blue asterisks, GFP versus CCR7–GFP; green asterisks, GPR174–GFP versus CCR7–GFP; ****$P < 0.0001$. **d**, **e**, Exemplary calcium responses of HEK293T cells transfected with vector, GPR174 or CCR7, following stimulation with CCL21 or the calcium ionophore ionomycin at the indicated concentrations (**d**); and the magnitude of CCL21-triggered calcium responses as a fraction of the ionomycin-triggered maximum of the same cells, overlaid with three-parameter log dose–response curves on top (**e**). The two different symbols indicate data from two independent experiments. *P* values obtained from an extra sum-of-squares *F*-test of the null hypothesis that the GPR174 and CCR7 curves have the same EC_{50}.

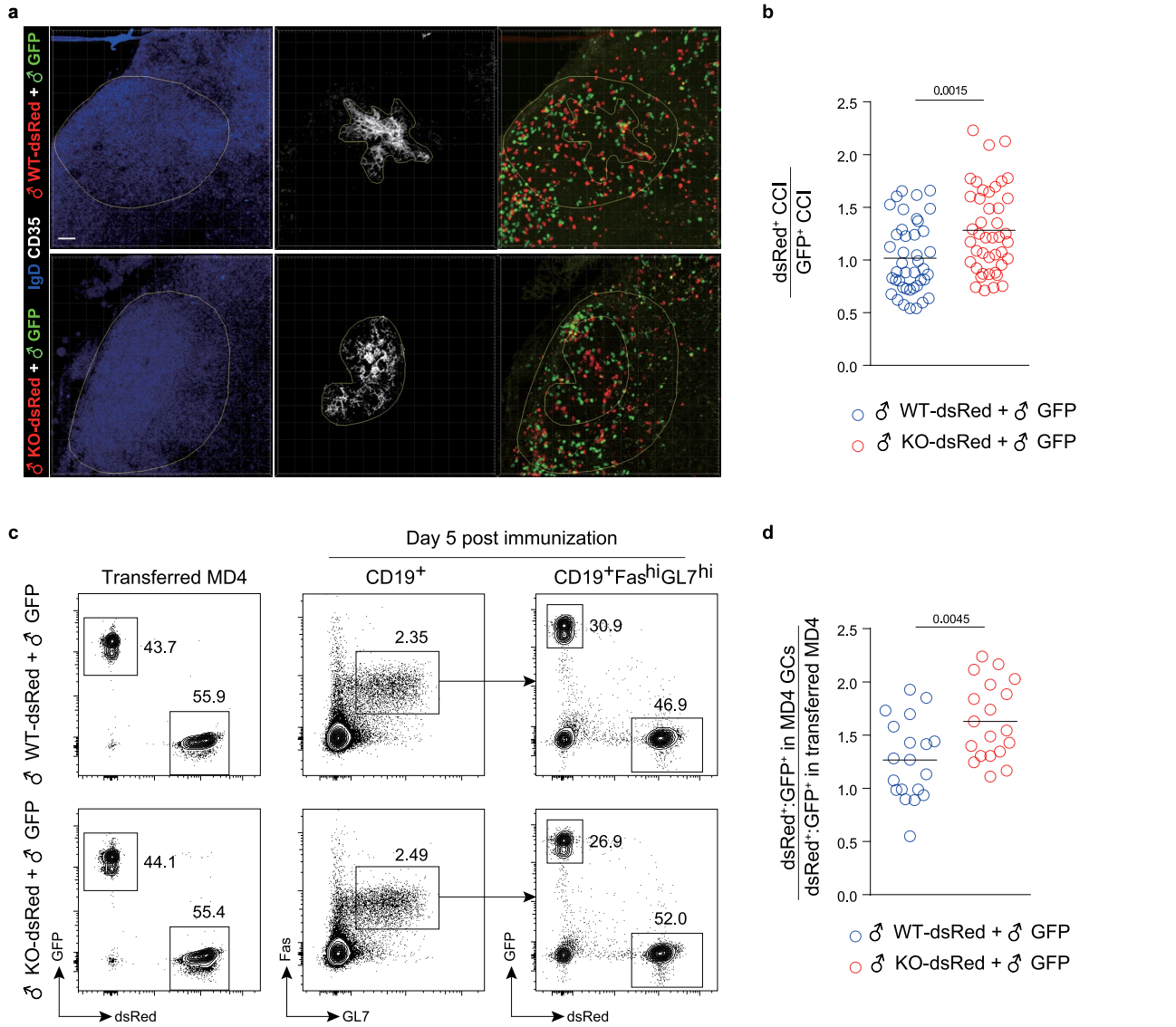


Extended Data Fig. 7 | See next page for caption.

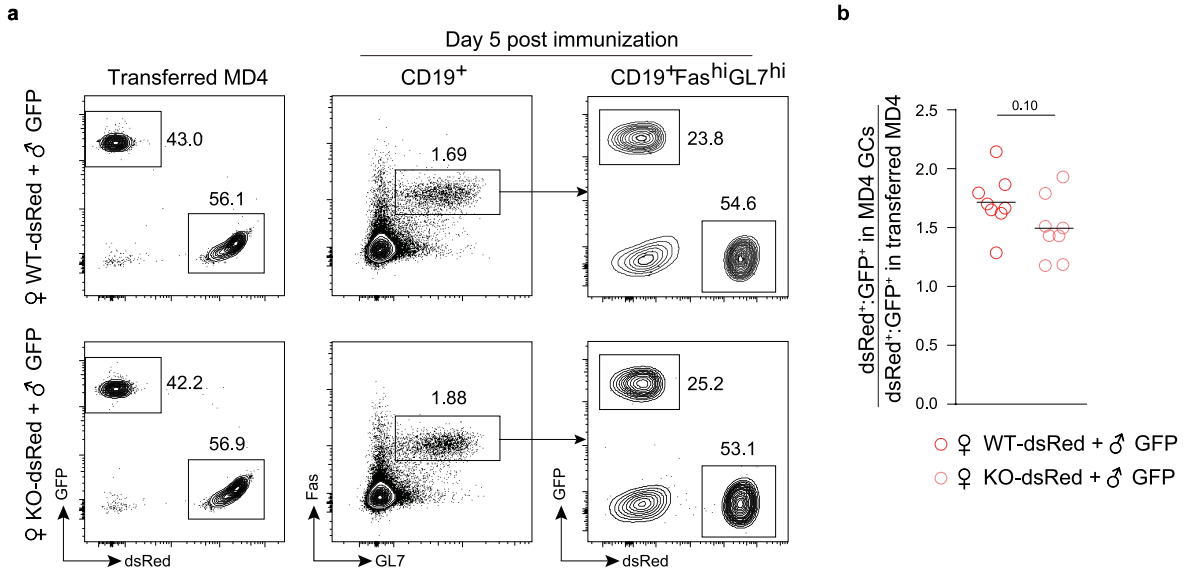
Extended Data Fig. 7 | Testosterone dependence of the GPR174-mediated migratory response to CCL21 does not involve modulation of GPR174 or CCR7 expression. a, CCL21-induced transwell migration of B cells from GPR174-sufficient (WT) or -deficient (KO) male littermate mice that were sham-operated (sham) or orchidectomized (ORX), allowed to recover for six weeks, and then treated with either vehicle or testosterone for two weeks. Data represent three biological replicates from one of two independent experiments with similar results. Blue asterisks, male sham wild type plus vehicle versus sham GPR174-knockout plus vehicle; red asterisks, male ORX wild type plus vehicle versus male ORX wild type plus testosterone; green asterisks, male sham wild type plus vehicle versus male ORX wild type plus testosterone. **b**, Relative *Gpr174* mRNA levels normalized to *Gapdh* expression in naive and activated B cells from male or female mice that were either sham-operated or gonadectomized. Data ($n = 3$ biological replicates) represent three independent experiments with similar results. **c**, Surface CCR7 levels on naive or activated B cells isolated from mice of the indicated GPR174 genotypes, sexes and gonadectomies. Data shown are histogram overlays (coloured lines, CCR7; grey lines, isotype staining control) and CCR7 MFIs after isotype staining background subtraction. Each symbol in the MFI data represents one mouse, and data represent three independent experiments with similar results. **d**, **e**, Relative *Gpr174* mRNA levels (**d**) and surface CCR7 levels (**e**) on activated B cells from male mice that were sham-operated or orchidectomized and then treated with either vehicle or testosterone. Data represent three mice per group from one of three independent experiments with similar results. **f**, **g**, Relative *Gpr174* mRNA levels (**f**) and surface CCR7 levels (**g**) on activated B cells from male or female mice that were treated with either vehicle or testosterone. Data represent three mice per group from one of three independent experiments with similar results. **h**, Relative expression of *Gpr174* mRNA in male or female dsRed-expressing MD4 B cells normalized against that in cotransferred male GFP-expressing MD4 B cells 90 h after activation by HEL–OVA immunization (as in Extended Data Fig. 1); three line-connected pairs indicate three independent experiments. Two-way ANOVA with Bonferroni's multiple comparisons (**a**) or two-tailed unpaired (**b**–**g**) or paired (**h**) Student's *t*-tests were used for statistical comparisons, with *P* values given in the graph.



Extended Data Fig. 8 | Characterization of GPR174–GFP transgenic mice. **a**, Diagrams of the GPR174–GFP fusion (top) and GPR174–GFP BAC construct (bottom) in the context of the *Gpr174* genomic locus, with the five exons numbered in italics. **b**, Transwell migration of lipopolysaccharide-activated B cells that were transduced with a control, GPR174-expressing or GPR174-GFP-expressing vector in response to stroma-conditioned medium (stroma) or 10 ng ml^{-1} or 50 ng ml^{-1} recombinant CCL21. Data represent three biological replicates from one of two independent experiments with similar results. **c**, **d**, Histograms (**c**) and geometric MFI (geo.mean) (**d**) of GFP fluorescence from naive and germinal-centre B cells in B6 (grey histograms) or GPR174–GFP BAC (open histograms) transgenic mice. Each symbol in the MFI plot represents one mouse, and data represent two independent experiments with similar results. Two-way ANOVA with Bonferroni's multiple comparisons (**b**) or two-tailed unpaired Student's *t*-test (**d**) was used for comparisons between groups. ****$P < 0.0001$; ns, not significant.



Extended Data Fig. 9 | GPR174 retards follicular-centre localization and germinal-centre formation by male B cells. a, Representative distribution patterns of dsRed-expressing and GFP-expressing MD4 cells of the indicated genotypes in follicles of the draining lymph nodes 90 h after immunization of male recipient mice. Scale bar, 50 µm. **b**, Summary statistics of ratios between CCIs, as defined in Extended Data Fig. 1d, of dsRed$^+$ cells and GFP$^+$ cells of the indicated genotypes in the same follicles. Each symbol denotes one follicle (n = 42 and 43), with lines denoting mean. Data are pooled from two independent experiments with similar results. **c**, Representative contour plots and frequencies of dsRed-expressing and GFP-expressing cells of the indicated genotypes in the transferred MD4 (left panels) or in the germinal-centre compartment five days after immunization (middle and right panels). **d**, Summary statistics of the dsRed/GFP ratio in MD4 germinal centres normalized against the dsRed/GFP ratio in transferred MD4. Each symbol denotes one mouse (n = 19 and 19), with lines denoting mean. Data are pooled from three independent experiments with similar results. Two-tailed unpaired Student's t-tests were used to compare groups, with P values given in the graph.



Extended Data Fig. 10 | GPR174 does not affect germinal-centre formation by female B cells. a, Representative contour plots and frequencies of dsRed-expressing and GFP-expressing cells of the indicated genotypes in the transferred MD4 (left panels) or in the germinal-centre compartment five days after immunization (middle and right panels) of male recipient mice. **b**, Summary statistics of the dsRed/GFP ratio in MD4 germinal centres, normalized against the dsRed/GFP ratio in transferred MD4 cells. Each symbol denotes one mouse, with lines showing mean. Data ($n = 8$ and 8) are pooled from two independent experiments with similar results. Two-tailed unpaired Student's t-test was used to compare groups.

nature research

Corresponding author(s): Hai Qi

Last updated by author(s): 2019/10/19

Reporting Summary

Nature Research wishes to improve the reproducibility of the work that we publish. This form provides structure for consistency and transparency in reporting. For further information on Nature Research policies, see Authors & Referees and the Editorial Policy Checklist.

Statistics

For all statistical analyses, confirm that the following items are present in the figure legend, table legend, main text, or Methods section.

n/a	Confirmed
☐	☒ The exact sample size (*n*) for each experimental group/condition, given as a discrete number and unit of measurement
☐	☒ A statement on whether measurements were taken from distinct samples or whether the same sample was measured repeatedly
☐	☒ The statistical test(s) used AND whether they are one- or two-sided *Only common tests should be described solely by name; describe more complex techniques in the Methods section.*
☐	☒ A description of all covariates tested
☐	☒ A description of any assumptions or corrections, such as tests of normality and adjustment for multiple comparisons
☐	☒ A full description of the statistical parameters including central tendency (e.g. means) or other basic estimates (e.g. regression coefficient) AND variation (e.g. standard deviation) or associated estimates of uncertainty (e.g. confidence intervals)
☐	☒ For null hypothesis testing, the test statistic (e.g. *F*, *t*, *r*) with confidence intervals, effect sizes, degrees of freedom and *P* value noted *Give P values as exact values whenever suitable.*
☒	☐ For Bayesian analysis, information on the choice of priors and Markov chain Monte Carlo settings
☒	☐ For hierarchical and complex designs, identification of the appropriate level for tests and full reporting of outcomes
☒	☐ Estimates of effect sizes (e.g. Cohen's *d*, Pearson's *r*), indicating how they were calculated

Our web collection on statistics for biologists contains articles on many of the points above.

Software and code

Policy information about availability of computer code

Data collection	Flowcytometry data were collected using BD FACSDIVA V8.0.1. Imaging data were collected using FV10-ASW V3.1. Protein purification data were collected using UNICORN V7.0.
Data analysis	Flowcytometry data were processed and analyzed using FlowJo V10. Imaging data were processed and analyzed using Imaris V7.6.5 and ImageJ 1.52. Protein purification data were processed and analyzed using UNICORN V7.0

For manuscripts utilizing custom algorithms or software that are central to the research but not yet described in published literature, software must be made available to editors/reviewers. We strongly encourage code deposition in a community repository (e.g. GitHub). See the Nature Research guidelines for submitting code & software for further information.

Data

Policy information about availability of data

All manuscripts must include a data availability statement. This statement should provide the following information, where applicable:

- Accession codes, unique identifiers, or web links for publicly available datasets
- A list of figures that have associated raw data
- A description of any restrictions on data availability

Data generated during this study are included in this published article (and its supplementary information files) or available from the corresponding author upon reasonable request.

Field-specific reporting

Please select the one below that is the best fit for your research. If you are not sure, read the appropriate sections before making your selection.

☒ Life sciences ☐ Behavioural & social sciences ☐ Ecological, evolutionary & environmental sciences

For a reference copy of the document with all sections, see nature.com/documents/nr-reporting-summary-flat.pdf

Life sciences study design

All studies must disclose on these points even when the disclosure is negative.

Sample size	The sample size for each experiment is indicated in the figure legend. The sample size was chosen empirically to provide a sufficient level of statistical power for detecting indicated biological effects. No statistical methods were used to pre-determine the sample size.
Data exclusions	No data were excluded from analyses.
Replication	All experimental findings were reproducible across multiple independently repeated experiments, as indicated.
Randomization	Where applicable, littermate animals of desired genotypes were randomly assigned into experimental and control groups.
Blinding	Imaging analyses were conducted in a blinded manner.

Reporting for specific materials, systems and methods

We require information from authors about some types of materials, experimental systems and methods used in many studies. Here, indicate whether each material, system or method listed is relevant to your study. If you are not sure if a list item applies to your research, read the appropriate section before selecting a response.

Materials & experimental systems

n/a	Involved in the study
☐	☒ Antibodies
☐	☒ Eukaryotic cell lines
☒	☐ Palaeontology
☐	☒ Animals and other organisms
☒	☐ Human research participants
☒	☐ Clinical data

Methods

n/a	Involved in the study
☒	☐ ChIP-seq
☐	☒ Flow cytometry
☒	☐ MRI-based neuroimaging

Antibodies

Antibodies used	Antibodies included BV421-anti-CD4 (GK1.5, 562891), APC-Cy7-anti-CD19 (1D3, 557655), PE-Cy7-anti-CD95 (Jo2, 557653), AlexaFluor-700-anti-B220 (RA3-6B2, 557957), eFlour450-anti-B220 (RA3-6B2, 558108), APC-anti-CD138 (281-2, 558626) from BD Biosciences; eFlour450-anti-GL7 (GL-7, 48-5902-82) and FITC-anti-GL7 (GL-7, 53-5902-82) from eBioscience; PerCP Cy5.5 anti-IgD (HK1.4, 405709), biotinylated anti-CCR7 (4B12, 120103), and streptavidin-APC (405207) from Biolegend. Antibodies were used at 1:200 dilution for staining cells or tissue sections.
Validation	Based on information provided by commercial vendors.

Eukaryotic cell lines

Policy information about cell lines

Cell line source(s)	A20 and 293T cell lines were originally from the American Type Culture Collection (Manassas, VA, USA).
Authentication	No specific procedure was taken to authenticate the cell line identity.
Mycoplasma contamination	The cell lines have been tested negative for mycoplasma contamination.
Commonly misidentified lines (See ICLAC register)	No cell lines used are in the database of commonly misidentified cell lines.

Animals and other organisms

Policy information about studies involving animals; ARRIVE guidelines recommended for reporting animal research

Laboratory animals	C57BL/6 (Jax664), µMT (Jax2288), GFP-expressing (Jax4353), CFP-expressing (Jax 4218), dsRed-expressing (Jax 6051), OVA323–339-specific T-cell receptor transgenic OT-II (Jax 4194), and HEL-specific Ig-transgenic MD4 (Jax2595) mice were originally from the Jackson Laboratory. GPR174-deficient mice were generated by standard gene targeting procedures to replace the Gpr174 open reading frame with a lacZ/neo cassette using 129SvEvBrd embryonic stem cell line (Texas A&M Institute for Genomic Medicine, TG0128). These mutant mice were backcrossed to C57BL/6 for 12 generations. Relevant mice on the C57BL/6 background were interbred to obtain GFP-expressing MD4 mice and dsRed-expressing GPR174-sufficient or -deficient dsRed MD4 mice. Age-matched littermates between 6 and 12 weeks of age and of indicated sexes were used for experiments. All mice were maintained under specific-pathogen free conditions and were used in accordance of governmental and Tsinghua guidelines for animal welfare.
Wild animals	The study did not involve wild animals.
Field-collected samples	The study did not involve samples collected from the field.
Ethics oversight	*Identify the organization(s) that approved or provided guidance on the study protocol, OR state that no ethical approval or guidance was required and explain why not.*

Note that full information on the approval of the study protocol must also be provided in the manuscript.

Flow Cytometry

Plots

Confirm that:

☒ The axis labels state the marker and fluorochrome used (e.g. CD4-FITC).

☒ The axis scales are clearly visible. Include numbers along axes only for bottom left plot of group (a 'group' is an analysis of identical markers).

☒ All plots are contour plots with outliers or pseudocolor plots.

☒ A numerical value for number of cells or percentage (with statistics) is provided.

Methodology

Sample preparation	Spleen and LN single-cell suspension was incubated in MACS buffer (phosphate-buffered saline (PBS) supplemented with 1% fetal bovine serum (FBS) and 5 mM EDTA) containing 20 µg/ml 2.4G2 (BioXcell) for 20 min before being stained with indicated monoclonal antibodies.
Instrument	LSR II or FACSAria III cytometer (BD Biosciences)
Software	Flowcytometry data were processed and analyzed using FlowJo V10.
Cell population abundance	At least 10000 events were acquired for cells in the defined gate.
Gating strategy	For all experiments FSC-A/ SSC-A gates of the starting cell population were used to identify viable cells. Singlet cells were identified using FSC-H/ FSC-W gating. Isotype control was used to distinguish between background and marker-positive events.

☒ Tick this box to confirm that a figure exemplifying the gating strategy is provided in the Supplementary Information.

Article

Rapid non-uniform adaptation to conformation-specific KRAS(G12C) inhibition

https://doi.org/10.1038/s41586-019-1884-x

Received: 7 May 2019

Accepted: 31 October 2019

Published online: 8 January 2020

Jenny Y. Xue[1,2,9], Yulei Zhao[1,9], Jordan Aronowitz[1], Trang T. Mai[1], Alberto Vides[1], Besnik Qeriqi[3], Dongsung Kim[1], Chuanchuan Li[1], Elisa de Stanchina[3], Linas Mazutis[4], Davide Risso[5,6] & Piro Lito[1,2,7,8]*

KRAS GTPases are activated in one-third of cancers, and KRAS(G12C) is one of the most common activating alterations in lung adenocarcinoma[1,2]. KRAS(G12C) inhibitors[3,4] are in phase-I clinical trials and early data show partial responses in nearly half of patients with lung cancer. How cancer cells bypass inhibition to prevent maximal response to therapy is not understood. Because KRAS(G12C) cycles between an active and inactive conformation[4–6], and the inhibitors bind only to the latter, we tested whether isogenic cell populations respond in a non-uniform manner by studying the effect of treatment at a single-cell resolution. Here we report that, shortly after treatment, some cancer cells are sequestered in a quiescent state with low KRAS activity, whereas others bypass this effect to resume proliferation. This rapid divergent response occurs because some quiescent cells produce new KRAS(G12C) in response to suppressed mitogen-activated protein kinase output. New KRAS(G12C) is maintained in its active, drug-insensitive state by epidermal growth factor receptor and aurora kinase signalling. Cells without these adaptive changes—or cells in which these changes are pharmacologically inhibited—remain sensitive to drug treatment, because new KRAS(G12C) is either not available or exists in its inactive, drug-sensitive state. The direct targeting of KRAS oncoproteins has been a longstanding objective in precision oncology. Our study uncovers a flexible non-uniform fitness mechanism that enables groups of cells within a population to rapidly bypass the effect of treatment. This adaptive process must be overcome if we are to achieve complete and durable responses in the clinic.

KRAS(G12C) undergoes nucleotide cycling between its active (GTP-bound) and inactive (GDP-bound) states in cancer cells[4,5,7]. First-in-class mutant GTPase inhibitors target KRAS(G12C) in a conformation-specific manner: they bind only to the inactive state and trap the oncoprotein by preventing its reactivation by nucleotide exchange[3–5,8,9]. Upon treatment with a KRAS(G12C)-specific inhibitor (G12Ci), KRAS(G12C)-mutant cells had an initial inhibition that was followed by a reaccumulation of active KRAS (KRAS–GTP) and reactivation of its downstream signalling (Extended Data Fig. 1), a pattern that is consistent with adaptation[10–12]. The KRAS(G12C) nucleotide cycle and the conformation-specific nature of inhibition led us to test whether adaptation to treatment with G12Ci occurs in a non-uniform manner across cancer cells in a population (see Methods for rationale).

To this end, we performed single-cell RNA sequencing (scRNA-seq)[13,14] on three models of KRAS(G12C) lung cancer, treated with the G12Ci for 0, 4, 24 and 72 h (Methods). After controlling for potentially confounding variables (Extended Data Fig. 2a–e) and reducing the dimensionality of the dataset with an algorithm[15] that accounts for the zero-inflated nature of scRNA-seq data (Extended Data Fig. 2f), cells were clustered and projected in a two-dimensional space using either *t*-distributed stochastic neighbour embedding (*t*-SNE) or diffusion component mapping (Extended Data Fig. 2g–j). We used trajectory inference analysis[16,17] to order cells along a process (that is, pseudotime) and identify cell fates in an unsupervised manner. This analysis revealed three trajectories (paths 1–3 in Fig. 1a, Extended Data Fig. 2k). Two of these represented a shift from an initial state (grey cluster) to a drug-induced state (path 1, red clusters and arrow in Fig. 1a), and then back (path 2, blue clusters and arrow in Fig. 1a). The distribution of clusters over treatment time (Fig. 1b) suggested that paths 1 and 2 represent inhibited and adapting cell states, respectively.

To test this, we used about 200 KRAS(G12C)-dependent genes to derive a KRAS(G12C)-specific transcriptional output score (Methods), which was used as an indicator of KRAS signalling across single cells. At baseline most cells had high output, as evidenced by their high G12C-induced scores (reflecting genes downregulated upon treatment with G12Ci) and low G12C-suppressed scores (reflecting genes upregulated

[1]Human Oncology and Pathogenesis Program, Memorial Sloan Kettering Cancer Center, New York, NY, USA. [2]Tri-Institutional MD-PhD Program, Weill Cornell Medical College and Rockefeller University and Memorial Sloan Kettering Cancer Center, New York, NY, USA. [3]Antitumor Assessment Core Facility, Memorial Sloan Kettering Cancer Center, New York, NY, USA. [4]Computational and Systems Biology, Memorial Sloan Kettering Cancer Center, New York, NY, USA. [5]Department of Statistical Sciences, University of Padova, Padua, Italy. [6]Department of Healthcare Policy and Research, Weill Cornell Medical College, New York, NY, USA. [7]Department of Medicine, Memorial Sloan Kettering Cancer Center, New York, NY, USA. [8]Department of Medicine, Weill Cornell Medical College, New York, NY, USA. [9]These authors contributed equally: Jenny Y. Xue, Yulei Zhao. *e-mail: litop@mskcc.org

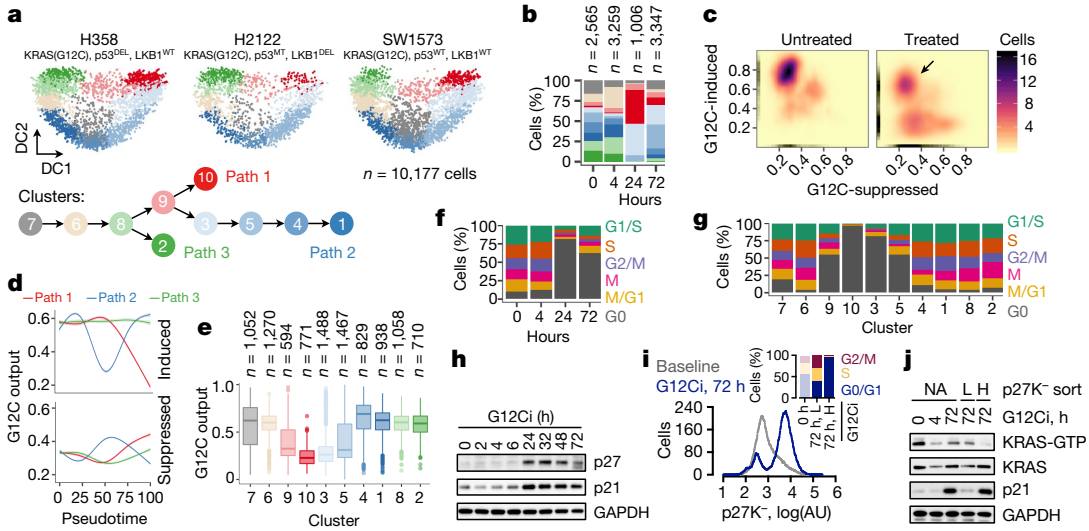


Fig. 1 | Divergent single-cell fates after conformation-specific KRAS(G12C) inhibition. a, Diffusion component (DC) analysis of single cells from models of KRAS(G12C) tumours, treated with a G12Ci for 0, 4, 24 and 72 h. The arrows indicate inhibitory trajectories derived by the Slingshot algorithm. **b**, Cluster composition across treatment time. **c**, The distribution of KRAS(G12C)-dependent transcriptional output score across single cells. **d**, The trend in G12C output as a function of pseudotime was established by fitting a spline to single-cell data. The 95% confidence interval is shown. $n = 4{,}759$, $n = 8{,}653$ and $n = 4{,}050$ in path 1, path 2 and path 3, respectively; n, number of cells. **e**, G12C output score across clusters. Median, upper and lower quartiles, and outliers are shown. **f**, **g**, Cell-cycle-phase distribution over time (**f**) or across clusters (**g**). **h**, Extracts from drug-treated KRAS(G12C)-mutant cells (H358) were analysed to determine the expression of the indicated proteins. **i**, H358 cells expressing the quiescence biosensor (mVenus–p27K$^-$) were analysed by fluorescence-activated cell sorting (FACS). Inset, cell-cycle distribution of the indicated populations. **j**, Biosensor-expressing cells were treated, sorted and analysed to determine the levels of active and total KRAS. A representative of three independent experiments is shown in **h**–**j**. H, high p27K$^-$ expression; L, low p27K$^-$ expression; NA, not applicable.

upon treatment with G12Ci) (Fig. 1c, Extended Data Fig. 3a, b). Treatment with G12Ci sequestered most cells in a state with low output. Some drug-treated cells had high output (arrow in Fig. 1c), indicating diverging responses across the population. The change in output score revealed different fates along the trajectories (Fig. 1d, e, Extended Data Fig. 3c–e): cells in path 1 had inhibited output, and cells in path 2 had an initial inhibition followed by reactivation.

The trajectories correlated with changes in cell-cycle-specific expression signatures (Extended Data Fig. 4a). By classifying cells along the cell cycle, we found that treatment with G12Ci induced a quiescent state (G0) that was transcriptionally distinct from G1 (Fig. 1f, Extended Data Fig. 4b–d). This induction mirrored the inhibition of KRAS(G12C) output along the trajectories (Fig. 1g). Treatment with G12Ci also led to higher levels of protein expression for p21 and p27 (Fig. 1h, Extended Data Fig. 4e), two markers of quiescence[18]. Consistent with this, cell-cycle analysis of double-thymidine-synchronized cells showed that the G12Ci treatment arrests cells in a G0 or G1 state (Extended Data Fig. 4f).

We used a quiescence biosensor[19] based on a cyclin-dependent-kinase binding-defective p27 mutant (p27K$^-$) to monitor the subpopulations and to validate the results of the scRNA-seq analysis (Fig. 1i, Extended Data Fig. 5a). As predicted, the G12Ci treatment led to a bimodal cell distribution, comprising a subpopulation of quiescent cells with high p27K$^-$ (about 80% of the total population) and a subpopulation of rapidly adapting cells with low p27K$^-$ (about 20%). This differed from the effect of inhibitors that target MEK or ERK, two kinases that are downstream of KRAS(G12C) (Extended Data Fig. 5b, c). Although exposed to the G12Ci treatment for the same duration, cells with low p27K$^-$ had higher active KRAS than cells with high p27K$^-$ (Fig. 1j, Extended Data Fig. 5d) and were able to progress past the G1 restriction point (Fig. 1i, inset). Rechallenge with the G12Ci attenuated the adapting response to some degree, but it could not eliminate this population (Extended Data Fig. 5a, e). Furthermore, the inhibition of levels of KRAS–GTP by the G12Ci during rechallenge was less than its initial effect (Extended Data Fig. 5f).

To identify the adaptive signals that are responsible for the divergent response to the G12Ci treatment, we used two orthogonal approaches (Methods). A differential expression analysis, which contrasted single cells from the inhibited and adapting trajectories, revealed many transcripts with trajectory-specific expression (Extended Data Fig. 6a). A genome-wide knockout screen identified single-guide RNA (sgRNA) targets that enhanced the effect of treatment with G12Ci (Extended Data Fig. 6b). After integrating the results from both approaches, we focused on genes with subpopulation-specific expression that were also functionally related to proliferation on treatment (Fig. 2a, b, Extended Data Fig. 6c–e). Of these, heparin-binding epidermal growth factor (*HBEGF*), aurora kinase A (*AURKA*) and *KRAS* were studied in more detail.

The expression of *HBEGF* mRNA—which encodes a ligand of the epidermal growth factor receptor (EGFR)[20]—was downregulated shortly after treatment with G12Ci, but rebounded at 48–72 h (Extended Data Fig. 7a). The single-cell analysis 'localized' this rebound to a cluster of quiescent cells (Fig. 2a, b, Extended Data Fig. 6d). This change was associated with an approximately twofold increase in secreted HBEGF during the G12Ci treatment (Extended Data Fig. 7a). Consistent with a potential role in mediating adaptation to the G12Ci treatment, sgRNAs targeting EGFR signalling intermediates were depleted on treatment with G12Ci (Fig. 2c). Likewise, siRNA-mediated knockdown of *HBEGF* enhanced the antiproliferative effect of the drug (Extended Data Fig. 7b).

The secretion of HBEGF could affect a broader population of cells in an autocrine and/or paracrine fashion by activating EGFR, which—similar to other receptor tyrosine kinases—drives nucleotide exchange to activate RAS[20]. Indeed, adapting cells had higher levels of EGFR pathway activation than quiescent cells (Fig. 2d). Stimulation with recombinant EGF induced KRAS activation in sorted quiescent cells and enhanced signalling in an EGFR- and SHP2-dependent manner (Extended Data Fig. 7c–e). EGF also enhanced the escape from quiescence (Fig. 2e) when the ligand was added during the adaptive phase of the G12Ci treatment (24–48 h), but not when it was added at the beginning. This

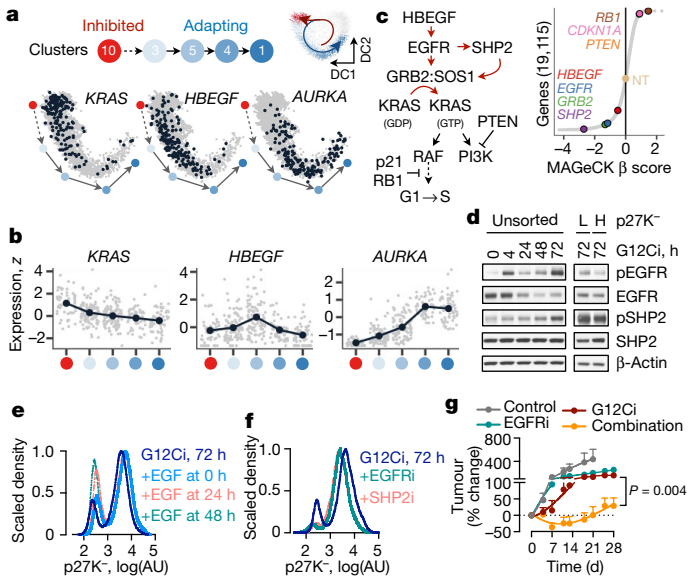


Fig. 2 | Adaptation to the G12Ci treatment is dependent on EGFR signalling. **a**, **b**, The peak (**a**) or mean (**b**) expression of genes with trajectory-specific expression. **a**, Cells from the indicated clusters were projected in their diffusion component coordinates. Cells with peak expression in the indicated genes are shown in navy. **b**, Cells were grouped by cluster, ordered in pseudotime and the mean expression was calculated for pools of 15 cells (grey) or the entire cluster (navy). **c**, A genome-wide CRISPR–Cas9 screen in H358 cells identified EGFR signalling intermediates as potential regulators of the G12Ci treatment. NT, non-targeting sgRNAs. *SHP2* is also known as *PTPN11*. **d**, Immunoblots of extracts from G12Ci-treated and FACS-sorted H358 p27K$^-$ cells. **e**, **f**, The cells were treated with the G12Ci for 72 h alone, in the presence of EGF stimulation at the indicated times (**e**) or in the presence of the indicated EGFR signalling inhibitors (**f**). **g**, Mice bearing xenografts of H2122 cells were treated as shown, to determine the effect on tumour growth. Mean + s.e.m, $n = 4$ mice. A two-sided *t*-test *P* value is shown. A representative of two independent experiments is shown in **d**–**f**.

suggests that EGFR signalling is required for the escape from drug-induced quiescence.

Inhibition of EGFR signalling, either by targeting EGFR or SHP2, attenuated the adaptive reactivation of KRAS–GTP in KRAS(G12C)-mutant lung cancer cells and 'RASless'[21] mouse embryonic fibroblasts (Extended Data Fig. 7f–i). Cotargeting EGFR or SHP2 together with KRAS(G12C) attenuated the escape from drug-induced quiescence (Fig. 2f) and enhanced the antiproliferative and/or antitumour effect (Fig. 2g, Extended Data Fig. 7j). Broad suppression of receptor tyrosine kinases by serum deprivation enhanced the antiproliferative effect of G12Ci in several models (Extended Data Fig. 7k), which suggests that additional growth factors may contribute in a tumour- or subpopulation-specific manner. Thus, EGFR signalling coordinates—at least in part—the heterogeneous response to the G12Ci treatment.

Although it is predominantly activated in G2M to control cell division, AURKA has also previously been implicated in the regulation of mitogenic signalling[22–25] (Fig. 3a) and acquired resistance to EGFR or PI3K inhibition[26,27]. AURKA was upregulated along the adapting trajectory (Extended Data Fig. 6) and expressed at higher levels in sorted adapting cells than in sorted quiescent cells (Fig. 3b). sgRNAs against *AURKA* ranked highly in the screen (Fig. 3a). Individual knockout of *AURKA* augmented the antiproliferative effect of the G12Ci and prevented the reactivation of KRAS over time (Fig. 3c, d). Inhibitors targeting AURKA[28] suppressed the reactivation of KRAS–GTP during the G12Ci treatment, both in KRAS(G12C)-mutant cancer cells (Extended Data Fig. 8a) and RASless mouse embryonic fibroblasts (Extended Data Fig. 8b). Doxycycline-inducible AURKA expression not only enhanced the adaptive reactivation of KRAS–GTP and CRAF–MEK–ERK signalling during the G12Ci treatment, but also attenuated the antiproliferative effect of treatment with G12Ci (Extended Data Fig. 8c, d).

AURKA interacts with wild-type HRAS in non-malignant cells to enhance its interaction with CRAF[24]. Here we found that AURKA also interacts with KRAS(G12C) in cancer cells (Extended Data Fig. 8e). Treatment with G12Ci or an AURKA inhibitor (AURKAi) displaced only CRAF or only AURKA, respectively, from KRAS(G12C). Treatment with a combination of G12Ci and AURKAi displaced both interactions to enhance pCRAF and pERK inhibition, relative to treatment with each drug alone (Extended Data Fig. 8f, g). This suggests that AURKA complexes with KRAS to stabilize its interaction with downstream effector CRAF. As expected, targeting AURKA prevented the escape from G12Ci-induced quiescence (Fig. 3e). Combined inhibition of AURKA and KRAS(G12C) had a synergistic antiproliferative effect across KRAS(G12C)-mutant models (Extended Data Fig. 8h) and resulted in a stronger antitumour effect in vivo, as compared to G12Ci monotherapy (Fig. 3f, Extended Data Fig. 8i, j). Thus, the heterogeneous bypass of G12Ci-induced quiescence also depends on the AURKA-mediated adaptive reactivation of KRAS.

The non-uniform response to the G12Ci treatment may occur in a KRAS(G12C)-dependent or KRAS(G12C)-independent manner. Unlike treatment with G12Ci, treatment with a *KRAS*^{G12C}-specific siRNA (*KRAS*^{G12C} siRNA)[29] yielded a uniform induction of quiescence (Fig. 4a). The *KRAS*^{G12C} siRNA differs from the inhibitor in that it suppresses signalling in a manner that is not dependent upon conformation, but is otherwise susceptible to KRAS(G12C)-independent adaptive pressures. The uniform effect of the *KRAS*^{G12C} siRNA suggests that reactivation

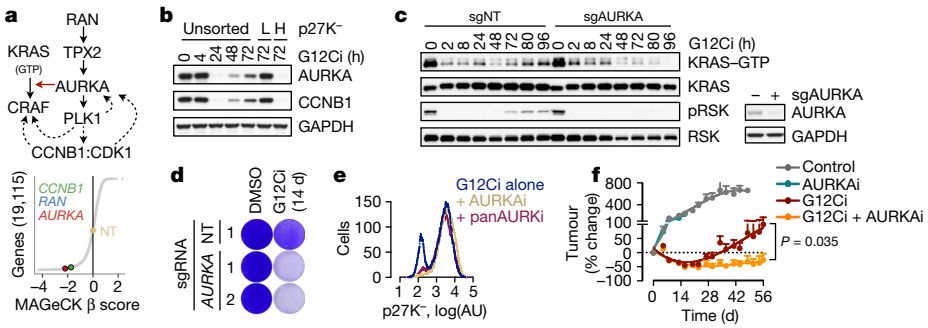


Fig. 3 | AURKA is involved in the adaptive reactivation of KRAS and escape from drug-induced quiescence. **a**, AURKA signalling intermediates identified in the CRISPR–Cas9 screen as potential regulators of the response to the G12Ci treatment. **b**, Immunoblots of extracts from FACS-sorted H358 p27K$^-$ cells. **c**, **d**, KRAS(G12C)-mutant lung cancer cells (H358) that express a non-targeting (NT) sgRNA or *AURKA*-specific sgRNAs were treated with the G12Ci and analysed by immunoblotting (**c**) or by crystal violet staining (**d**). **e**, Cells were treated with the indicated inhibitors for 72 h and analysed by FACS. **f**, Mice bearing xenografts of H358 cells were treated with the indicated inhibitors to determine the effect on tumour growth. Mean + s.e.m, $n = 4$ mice. A two-sided *t*-test *P* value is shown. A representative of three independent experiments is shown in **b**–**e**.

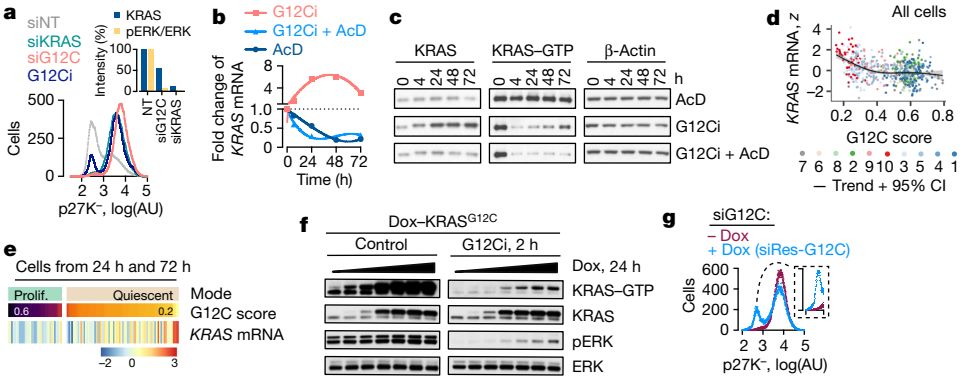


Fig. 4 | Newly synthesized KRAS(G12C) escapes trapping by the drug. a, Cells expressing the quiescence biosensor (H358 p27K$^-$, *KRAS*$^{G12C+/-}$) were transfected with *KRAS*-specific siRNAs targeting both wild-type and G12C alleles (siKRAS), or only the G12C allele (siG12C), for 72 h and analysed by FACS. The effect of a 72-h G12Ci treatment is shown. Inset, cell extracts were immunoblotted and quantified to determine the intensity of KRAS expression and ERK phosphorylation. **b**, Effect of the indicated treatments on *KRAS* mRNA. AcD, actinomycin D. **c**, Inhibitor-treated cell extracts were analysed by immunoblotting. **d**, **e**, Normalized KRAS expression across single cells as a function of KRAS(G12C) output score (**d**) or in quiescent versus proliferating (prolif.) cells (**e**). CI, confidence interval. **f**, H358 cells engineered to express haemagglutinin (HA)-tagged KRAS(G12C) under a doxycycline (dox) -inducible promoter were treated with the G12Ci in the presence of doxycycline (0–2 μg ml^{-1}). **g**, Cells expressing the quiescence biosensor, engineered to stably express doxycycline-inducible siRes-G12C, were transfected with *KRAS*^{G12C} siRNA, followed by doxycycline treatment (100 ng ml^{-1}). A representative of three independent experiments is shown in **a**–**c**, **f**, **g**.

of KRAS(G12C) is sufficient for the divergent response. However, drug-bound KRAS(G12C) cannot undergo nucleotide exchange to the active state[3–5]. We therefore considered how KRAS(G12C) might be reactivated, when almost the entire initial pool is covalently bound and inhibited by the drug.

The G12Ci treatment induced *KRAS* mRNA and KRAS protein expression (Fig. 4b, c, Extended Data Fig. 9a). This induction was heterogeneous across the population (Fig. 2a, b, Extended Data Fig. 6). It was inversely proportional to KRAS–RAF–MEK–ERK signalling activity (Extended Data Fig. 9a), and was most pronounced in clusters of quiescent cells with maximal inhibition of G12C output (Fig. 4d, e). Inhibiting new KRAS synthesis with the transcription inhibitor actinomycin D or *KRAS*-specific siRNAs prevented the KRAS–GTP rebound during the G12Ci treatment (Fig. 4b, c, Extended Data Fig. 9b). Conversely, doxycycline-induced KRAS(G12C) expression attenuated the effect of drug treatment (Fig. 4f, Extended Data Fig. 9c).

To confirm that KRAS(G12C) is sufficient for the divergent response to the G12Ci treatment, we used the *KRAS*^{G12C} siRNA to mimic the initial inhibitory phase, and doxycycline-induced expression of siRNA-resistant *KRAS*^{G12C} (siRes-G12C) to mimic the adaptive phase triggered by new KRAS(G12C). As evidenced in Fig. 4g and Extended Data Fig. 9d, expression of siRes-G12C led to a bimodal distribution in cells transfected with *KRAS*^{G12C} siRNA, with about 30% of cells escaping quiescence. This phenocopies the effect of the G12Ci, even though no drug was added in this experiment.

The data suggest that some newly synthesized KRAS(G12C) undergoes nucleotide exchange to the active, drug-insensitive state before it is bound and inhibited by the drug. Indeed, EGF stimulation attenuated the inhibition of KRAS(G12C) when EGF was added before the G12Ci, but not when it was added afterwards (Extended Data Fig. 9e). This suggests that exposure to growth factors is the initial stimulus that affects the inhibitory fate of cells with new KRAS(G12C). AURKA probably operates later, to maintain active KRAS(G12C) and effector signalling.

Our study thus sheds light on why treatment with a KRAS(G12C) inhibitor results predominantly in partial responses in patients with lung cancer[30]. We identify an adaptive fitness mechanism that allows groups of cancer cells within a population to rapidly escape inhibition (Extended Data Fig. 10, Supplementary Discussion). The synthesis of new KRAS(G12C) and its distribution between the active or inactive states modulates the divergent response. Drug-induced quiescent cells without adequate expression of new KRAS(G12C) are eliminated from the population by treatment. Cells with new KRAS(G12C)—which is rapidly converted to the active, drug-insensitive state—escape inhibition and resume proliferation. This occurs through signals that act upstream of KRAS: receptor tyrosine kinases trigger nucleotide exchange, and AURK signalling facilitates effector activation and cell-cycle progression. In cells in which these signals are not active (or in cells in which the signals are pharmacologically suppressed), new KRAS(G12C) spends a longer time in its inactive conformation, in which it can be bound and inhibited by the drug. These cell-intrinsic events are sufficient for a rapid, multifactorial and non-uniform adaptive process that limits the therapeutic potential of conformation-specific KRAS(G12C) inhibition. This mechanism must be suppressed for complete and durable responses in the clinic.

Online content

Any methods, additional references, Nature Research reporting summaries, source data, extended data, supplementary information, acknowledgements, peer review information; details of author contributions and competing interests; and statements of data and code availability are available at https://doi.org/10.1038/s41586-019-1884-x.

1. Pylayeva-Gupta, Y., Grabocka, E. & Bar-Sagi, D. RAS oncogenes: weaving a tumorigenic web. *Nat. Rev. Cancer* **11**, 761–774 (2011).
2. Li, S., Balmain, A. & Counter, C. M. A model for RAS mutation patterns in cancers: finding the sweet spot. *Nat. Rev. Cancer* **18**, 767–777 (2018).
3. Ostrem, J. M., Peters, U., Sos, M. L., Wells, J. A. & Shokat, K. M. K-Ras(G12C) inhibitors allosterically control GTP affinity and effector interactions. *Nature* **503**, 548–551 (2013).
4. Patricelli, M. P. et al. Selective inhibition of oncogenic KRAS output with small molecules targeting the inactive state. *Cancer Discov.* **6**, 316–329 (2016).
5. Lito, P., Solomon, M., Li, L. S., Hansen, R. & Rosen, N. Allele-specific inhibitors inactivate mutant KRAS G12C by a trapping mechanism. *Science* **351**, 604–608 (2016).
6. Simanshu, D. K., Nissley, D. V. & McCormick, F. RAS proteins and their regulators in human disease. *Cell* **170**, 17–33 (2017).
7. Hunter, J. C. et al. Biochemical and structural analysis of common cancer-associated KRAS mutations. *Mol. Cancer Res.* **13**, 1325–1335 (2015).
8. Zeng, M. et al. Potent and selective covalent quinazoline inhibitors of KRAS G12C. Cell *Chem. Biol.* **24**, 1005–1016 (2017).
9. Janes, M. R. et al. Targeting KRAS mutant cancers with a covalent G12C-specific inhibitor. *Cell* **172**, 578–589 (2018).
10. Corcoran, R. B. et al. EGFR-mediated re-activation of MAPK signaling contributes to insensitivity of *BRAF* mutant colorectal cancers to RAF inhibition with vemurafenib. *Cancer Discov.* **2**, 227–235 (2012).
11. Prahallad, A. et al. Unresponsiveness of colon cancer to BRAF(V600E) inhibition through feedback activation of EGFR. *Nature* **483**, 100–103 (2012).
12. Lito, P., Rosen, N. & Solit, D. B. Tumor adaptation and resistance to RAF inhibitors. *Nat. Med.* **19**, 1401–1409 (2013).

13. Grün, D. & van Oudenaarden, A. Design and analysis of single-cell sequencing experiments. *Cell* **163**, 799–810 (2015).
14. Stuart, T. & Satija, R. Integrative single-cell analysis. *Nat. Rev. Genet*. **20**, 257–272 (2019).
15. Risso, D., Perraudeau, F., Gribkova, S., Dudoit, S. & Vert, J. P. A general and flexible method for signal extraction from single-cell RNA-seq data. *Nat. Commun*. **9**, 284 (2018).
16. Trapnell, C. et al. The dynamics and regulators of cell fate decisions are revealed by pseudotemporal ordering of single cells. *Nat. Biotechnol*. **32**, 381–386 (2014).
17. Street, K. et al. Slingshot: cell lineage and pseudotime inference for single-cell transcriptomics. *BMC Genomics* **19**, 477 (2018).
18. Cheung, T. H. & Rando, T. A. Molecular regulation of stem cell quiescence. *Nat. Rev. Mol. Cell Biol*. **14**, 329–340 (2013).
19. Oki, T. et al. A novel cell-cycle-indicator, mVenus–p27K^{-}, identifies quiescent cells and visualizes G0–G1 transition. *Sci. Rep*. **4**, 4012 (2014).
20. Lemmon, M. A. & Schlessinger, J. Cell signaling by receptor tyrosine kinases. *Cell* **141**, 1117–1134 (2010).
21. Drosten, M. et al. Genetic analysis of Ras signalling pathways in cell proliferation, migration and survival. *EMBO J*. **29**, 1091–1104 (2010).
22. Katayama, H. et al. Phosphorylation by aurora kinase A induces Mdm2-mediated destabilization and inhibition of p53. *Nat. Genet*. **36**, 55–62 (2004).
23. Lim, K. H. et al. Aurora-A phosphorylates, activates, and relocalizes the small GTPase RalA. *Mol. Cell. Biol*. **30**, 508–523 (2010).
24. Umstead, M., Xiong, J., Qi, Q., Du, Y. & Fu, H. Aurora kinase A interacts with H-Ras and potentiates Ras–MAPK signaling. *Oncotarget* **8**, 28359–28372 (2017).
25. Gong, X. et al. Aurora A kinase inhibition is synthetic lethal with loss of the *RB1* tumor suppressor gene. *Cancer Discov*. **9**, 248–263 (2019).
26. Donnella, H. J. et al. Kinome rewiring reveals AURKA limits PI3K-pathway inhibitor efficacy in breast cancer. *Nat. Chem. Biol*. **14**, 768–777 (2018).
27. Shah, K. N. et al. Aurora kinase A drives the evolution of resistance to third-generation EGFR inhibitors in lung cancer. *Nat. Med*. **25**, 111–118 (2019).
28. Keen, N. & Taylor, S. Aurora-kinase inhibitors as anticancer agents. *Nat. Rev. Cancer* **4**, 927–936 (2004).
29. Sunaga, N. et al. Knockdown of oncogenic KRAS in non-small cell lung cancers suppresses tumor growth and sensitizes tumor cells to targeted therapy. *Mol. Cancer Ther*. **10**, 336–346 (2011).
30. Fakih, M. et al. Phase 1 study evaluating the safety, tolerability, pharmacokinetics (PK), and efficacy of AMG 510, a novel small molecule *KRAS*^{G12C} inhibitor, in advanced solid tumors. *J. Clin. Oncol*. **37**, 3003 (2019).

Publisher's note Springer Nature remains neutral with regard to jurisdictional claims in published maps and institutional affiliations.

© The Author(s), under exclusive licence to Springer Nature Limited 2020

Methods

No statistical methods were used to predetermine sample size. The experiments were not randomized and investigators were not blinded to allocation during experiments and outcome assessment.

Cell culture and reagents

All cell lines used in this study were maintained in DMEM medium supplemented with 10% FBS, penicillin, streptomycin and 2mM L-glutamine. Cell lines were obtained from ATCC (H358: CRL-5807; H2122: CRL-5985; and SW1573: CRL-2170), expanded immediately and frozen in aliquots. The cell lines tested negative for mycoplasma. All experiments were performed within 20 passages. The KRAS(G12C) inhibitor (ARS1620) was obtained from ChemGood and administered at 10 μM, or as otherwise specified, in culture and at a dose of 200 milligrams per kilogram body weight (mpk) in mice. The maximum selective concentration for in vitro dosing was experimentally determined to be 10 μM. At concentrations greater than 10 μM, antiproliferative effects were observed in non-KRAS(G12C)-mutant cells, such as HEK293 cells. Inhibitors targeting AURKA (alisertib) and AURKA, AURKB and AURKAC (tozasertib) were obtained from Selleckem. These were administered at 10 μM, or as otherwise specified, in culture and at doses of 30 mpk twice a day for alisertib or of 50 mpk for tozasertib, in mice. Inhibitors targeting EGFR (gefitinib, 10 μM), pan-HER kinase (afatinib, 1 μM), SHP2 (SHP099, 10 μM), MEK (trametinib, 25 nM), ERK (SCH772984, 500 nM), PI3K (BYL719, 1 μM), AKT (MK-2206, 2 μM) or RAL (BQU57, 10 μM) were obtained from Selleckem, and were administered in culture at the above concentrations, unless otherwise indicated. Gefitinib was administered at a dose of 100 mpk in mice. Actinomycin D was purchased from Sigma Aldrich and used at a concentration of 2.5 μg/ml.

Rationale and approach

The goal of this study was to determine how KRAS(G12C)-mutant cancer cell populations adapt to treatment with a conformation-specific KRAS(G12C) inhibitor. These inhibitors bind only to the inactive conformation, and spare the active state of KRAS(G12C). They inactivate KRAS(G12C) by trapping the oncoprotein in its inactive state and preventing its reactivation by nucleotide exchange. Inhibition occurs because—rather than existing in a constitutively active state—KRAS(G12C) hydrolyses GTP to GDP and undergoes nucleotide cycling in cancer cells. We reasoned that cells across a population do not have synchronized KRAS(G12C) nucleotide cycles. Various perturbations (such as drug treatment) are likely to diversify the population, altering the distribution of cells with predominantly active or inactive KRAS(G12C). On the basis of this reasoning, we hypothesized that the adaptive reactivation during the G12Ci treatment occurs by shifting the KRAS(G12C) equilibrium to the active, drug-insensitive state and reflects a non-uniform behaviour of cancer cells, in a manner that is determined by the distribution of the nucleotide-bound states of KRAS(G12C) (that is, the distribution of cells with predominantly active or inactive KRAS(G12C) after treatment).

The cells were treated with the G12Ci for a short time to minimize the chance of acquired or selected genomic alterations. Treatment was carried out in the absence of the tumour microenvironment to minimize the potential confounding effect of stromal interactions. scRNA-seq was chosen because it allows for: (1) an analysis of thousands of single cells to determine phenotypic differences in treatment response; and (2) the determination of transcriptional changes across the population. It is well established that only the GTP-bound conformation of KRAS activates effector signalling, which in turn leads to changes in transcriptional output[1,2]. With this in mind, the collective expression of KRAS(G12C)-dependent genes was used to infer the activation status of KRAS signalling in each single cell.

scRNA-seq

Experiment. KRAS(G12C)-mutant tumour cell models (H358, H2122 and SW1573) were treated with the KRAS(G12C) inhibitor (ARS1620, 10 μM) for 0, 4, 24 and 72 h, followed by rapid collection of attached cells in cryopreservation medium. The cells were stored at −80 °C until the completion of the experiment. scRNA-seq was carried out using the Chromium 10X platform (3-prime v.1), following the manufacturer's protocol, as previously described[31–34]. In brief, single-cell suspensions were loaded on a GemCode single-cell instrument to generate single-cell gel bead emulsions (GEMs). Each GEM contains sequencing adapters and primers, a barcode used to index cells, a randomer or unique molecular identifier (UMI) used to count transcripts and an anchored oligo-dT to prime polyadenylated RNA transcripts. Cells were loaded at a limiting dilution to minimize the co-occurrence of two or more cells in the same GEM. The cells were lysed, and their mRNA was reverse-transcribed followed by disruption of the emulsions. Subsequently, barcoded cDNA was pooled followed by shearing, end repair and A-tailing, ligation of adaptors and another round of PCR amplification to generate samples carrying properly oriented adaptors. The libraries were then sequenced with HiSeq 2500 in paired-end mode. Alignment, barcode assignment and UMI counting were carried out using the Cell Ranger Single-Cell Software Suite. Then, sample demultiplexing was performed to generate FASTQ files for the 14-bp barcode, the 10-bp UMI tag and the cDNA insert. The latter was aligned to the human reference genome using STAR. Cell barcodes and UMIs were filtered to ensure correct assignment and elimination of mismatches, and PCR duplicates were marked and removed. The number of reads that provided meaningful information was calculated as the product of four metrics: valid barcodes, valid UMI, associated with a cell barcode and confidently mapped to exons.

Initial processing. The gene–cell count data matrices generated for each treatment collection time were consolidated into a single matrix representing each tumour cell line and assembled into a SingleCellExperiment object using R and Bioconductor tools[35]. A number of quality-control metrics were derived using the scater package[36]. Before merging the datasets from different KRAS(G12C) models, we performed quality control on each model separately. Cells that had a total UMI count, total gene count or per cent mitochondrial count greater or lower than 3 mean absolute s.d. were excluded from the analysis, as these cells may represent doublets or cell debris. To account for the possibility that differences in these variables may be treatment-related, filtering was carried out individually for each treatment time point. Despite two independent experimental replicates leading to sequencing of several thousand single cells, no good-quality cells (that is, suitable for downstream analysis) were identified from the 24-h treatment time point in H2122 cells. Genes expressed only in a small proportion of cells (that is, less than 5% of the cells) were excluded from downstream analysis. Once filtered, the datasets from each tumour model were joined together. Only genes detected in all three models were included in the joined dataset. Together, this filtering resulted in a dataset with 10,177 cells and 8,687 genes, in which each cell had an average of about 3,000 expressed transcripts.

Dimensionality reduction. This was carried out on the merged datasets from 'Initial processing', using a zero-inflated negative binomial-based wanted variation extraction (ZINB-WaVE) method[15,37]. In brief, the method fits a model that accounts for dropouts, overdispersion and the count nature of the data (such as those recorded in scRNA-seq experiments). The model enables both cell-level and gene-level intercepts, which serve as global-scaling normalization factors. With this in mind, we controlled for both gene-level (that is, per cent dropout) and cell-level (that is, batch or tumour of origin, transcript count, mitochondrial transcript count and ribosomal transcript count) effects, adding them as covariates in the model. The K parameter was chosen empirically, by evaluating $K = 10$, 5, 3 and 2. $K = 2$ was found to optimally reduce batch effects. The effect of the regression is shown in Extended Data Fig. 2a–f.

Normalization. Size factors were computed by using the scran normalization method[38]. In brief, cells were first clustered using the

quickCluster command. Cells in each cluster were normalized using a deconvolution method embedded in the scran package, which improves normalization accuracy by reducing pooling together cells in the same cluster. Only genes with a mean count of greater than 0.1 across the dataset were used in this process. The size factors generated through this approach were then used to compute normalized expression values as log-transformed count data (Supplementary Data 1–3).

Modelling technical variance. After normalization, we modelled technical noise by fitting a mean-dependent trend to the variances of a set of endogenous control genes (for example, ribosomal genes). This was carried out as previously described[38]. Genes with a variability that surpassed that expected on technical grounds alone were deemed to have a high degree of biological variability. Highly variable genes were used to construct two-dimensional projections.

Two-dimensional projections. To carry out downstream analysis and visualize the single cells, we used the two-dimensional output of ZINB-WaVE *t*-SNE or diffusion component analysis[39]. The latter two projections were carried out using commands embedded in the scatter package with default parameters, which included using the top 500 most-variable genes to carry out the projection. *t*-SNE was performed on low-rank approximations of the two-dimensional output of ZINB-WaVE (which controls for the potential confounding factors noted in 'Dimensionality reduction'). Initial runs were carried out with default parameters. The final projections were generated by using a perplexity parameter of 50 and a theta parameter of 0. A local sigma parameter was used for the diffusion component projection.

Clustering. The *t*-SNE projection was used to establish a distance matrix, followed by clustering of cells by density peaks, as previously described[40]. We then used rho and delta thresholds (200 and 15, respectively) to determine cluster peaks and assign single cells to these clusters (Supplementary Data 2). The performance of the clustering algorithm was examined by silhouette-width analysis (Extended Data Fig. 2j), which reported a mean width per cluster ranging between 0.18 to 0.52.

Trajectory inference analysis. The Slingshot algorithm[17] was used to order and project cells into principal curves representing distinct trajectories. The arc length along each principal curve represents pseudotime, a computational parameter denoting progress along a biological process[41]. To establish trajectories associated with KRAS(G12C) inhibition, the cells collected from all treatment time points were first clustered in the two-dimensional reduced space. The Slingshot algorithm was then used to reconstruct the clusters into trajectories. The algorithm was anchored by indicating a starting cluster—that is, the cluster with the greatest number of cells collected at 0 h (cluster 7). The trajectories and end points were otherwise estimated in an unsupervised manner and are graphically represented in Extended Data Fig. 2k. When comparing expression changes between trajectories (for example, Fig. 1d, Extended Data Fig. 6c) single cells were grouped by trajectory and assigned the pseudotime value corresponding to that trajectory. In this comparison, cells before the bifurcation points were assigned to both trajectories, and cells after the bifurcation were assigned to a single trajectory (Supplementary Data 4). When comparing expression changes between clusters or cell-cycle modes (for example, Fig. 1e, Extended Data Fig. 6d), the cells were grouped by these factors and pseudotime was not considered in the differential expression model (but was used for visualization, as described in 'Visualization'). In graphs, pseudotime was adjusted across trajectories (range of 0 to 100) to enable comparisons in expression trends.

Differential expression. Dropout events in scRNA-seq experiments make analysis of differential gene expression challenging. We used the zero-inflated negative binomial model described in 'Dimensionality reduction' to identify excess zero counts and generate gene- and cell-specific weights. These can be used to adapt bulk RNA-seq differential gene-expression pipelines for zero-inflated data[42]. With this mind, we applied methods from the limma package[43] to perform differential gene expression, using observational weights to adjust for zero inflation. First, we identified genes with an expression that differed as a function of pseudotime between inhibited (path 1) and adapting (path 2) trajectories. The cells were grouped by trajectory, and gene expression over pseudotime was contrasted between path 1 and path 2, while controlling for potentially confounding factors (batch, total features, total counts, per cent mitochondrial counts and per cent ribosomal counts) and correcting for multiple-hypothesis testing. The false discovery rates from this test are listed in the br.qval column in Supplementary Data 3. A similar analysis was carried out in the subset of cells collected only at 72 h, to determine whether the differences persisted in cells collected at the same treatment time. We also explored differences in gene expression between cell clusters or cell-cycle modes; that is, quiescent (G0) versus proliferating cells (G1S, S, G2M, M and MG1). Significant differences were tested using limma[38]. These results are listed in the cluster.qval and mode.qval columns in Supplementary Data 3. Key differentially expressed genes are mapped in Extended Data Fig. 6a, d. The false discovery rates corresponding to *KRAS*, *HBEGF* and *AURKA* are shown in Extended Data Fig. 6e. Given the limitations in performing differential gene-expression analysis in scRNA-seq datasets, efforts were made to experimentally validate key findings from this analysis.

Visualization. To visualize *KRAS*, *HBEGF* and *AURKA*, the cells were ordered by cluster and pseudotime and then the normalized expression values (see 'Normalization') were averaged across pools of n adjacent cells ($n = 15$ for the plots in Figs. 2b and 4d or $n = 40$ for the heat maps in Extended Data Fig. 6). In some instances, the last pool per cluster contained more than n, but fewer than $2n$, cells. This was done in an effort to compensate for random dropout events in each single cell and to minimize the risk of visualizing technical outliers. The averaged expression was scaled across all pools and then presented graphically. The projection of peak gene-expression levels into two-dimensional coordinates (Fig. 2a) was carried out by identifying and labelling the cells with scaled expression equal or greater than 2 s.d. from the mean of the entire dataset. Projections of expression signature scores (Extended Data Fig. 3) were carried out in a similar manner without a cut-off. The expression trend for a gene or a gene set was established by fitting a spline along with its 95% confidence interval to the single-cell data.

Bulk RNA sequencing and output score determination

Bulk RNA-seq. KRAS(G12C)-mutant lung cancer cells were treated with the G12Ci for 0, 4, 24 and 48 h in biological triplicates. RNA was extracted using the RNeasy Mini Kit (Qiagen catalogue no. 74104), according to the manufacturer's instructions. After RiboGreen quantification and quality control by Agilent BioAnalyzer, 500 ng of total RNA per sample underwent polyA selection and TruSeq library preparation according to instructions provided by Illumina (TruSeq Stranded mRNA LT Kit, catalogue no. RS-122-2102), with 8 cycles of PCR. Samples were barcoded and run on HiSeq 4000 in a 50-bp and 50-bp paired-end run, with an average of 30 million paired reads per sample. Ribosomal reads represented less than 0.5% of the total reads generated. The sequencing output files from different lanes were concatenated, aligned to GRCH38 using HISAT2 and transcripts were counted using HTSeq in Python. The count data matrix was then processed in R by using limma[43] and edgeR[44] from Bioconductor, as previously described[45]. In brief, the data were filtered by removing transcripts that were not detected in all replicates. Size-factor normalization was carried out and differential expression analysis was performed contrasting each time point to the untreated condition. The count data were transformed to $\log_2$-transformed counts per million followed by an estimation of the

mean-variance relationship, which was then used to compute appropriate observation-level weight data. The data for each gene were used to fit a linear model and to compute various statistical parameters for a given set of contrasts. Differentially expressed genes were considered to be those with $\log_2$-transformed fold change equal or greater than 2 in any contrast and an adjusted *P* value of less than 0.05. These genes (563 induced, and 447 suppressed, by KRAS(G12C)) comprised the lung-cancer-specific KRAS(G12C)-dependent gene-expression signature that was used to calculate the G12C output score across single cells (Supplementary Data 5).

Output score determination. The list of KRAS(G12C)-dependent genes was filtered to remove genes with undetected or very low expression in the single-cell dataset (that is, average log count of less than 0.1). The G12C output score in each single cell was the average log count expression of the remaining KRAS(G12C)-dependent genes (212 genes, Supplementary Data 6), normalized across all cells in the dataset. The G12C-induced and -suppressed scores were calculated from genes that were, respectively, down- or upregulated by the G12Ci treatment in the bulk RNA-seq experiment. When not specified, G12C output refers to the score derived from genes that were downregulated during the G12Ci treatment (these comprised the majority of the KRAS(G12C)-dependent genes detected in the scRNA-seq dataset). The trend in G12C output score as a function of pseudotime was visualized by fitting a spline and its 95% confidence interval (Fig. 1d). The G12C output score in each single cell is shown in Extended Data Fig. 3b–d. The rotation gene set test[46] was used to compare the G12C-induced or -suppressed gene sets across pseudotime in path 1 versus path 2 ($P = 0.001$ for the G12C-induced gene set and $P = 0.001$ for the G12C-suppressed gene set) (Fig. 1d). The G12C output score in clusters (Fig. 1e) was compared by using analysis of variance (ANOVA) ($P = 0.001$) and then in a pairwise fashion by using the Tukey test and correcting for multiple hypothesis testing ($P = 0.001$ for each of—but not limited to—the following cluster comparisons: 7 versus 9, 7 versus 10, and 10 versus any other). The difference in G12C output score between quiescent or proliferating cells (Extended Data Fig. 5d) was compared by a two-tailed *t*-test ($P < 0.001$, in each cell line). Again, these findings were validated experimentally.

Cell-cycle classification was performed by using published cell-cycle-phase-specific gene-expression signatures (G0, G1S, G2M, M and MG1)[19,32]. The overlap between the gene sets is shown in Extended Data Fig. 4b. These were used to calculate a phase-specific score, in a similar manner to that described for the G12C output score, followed by scaling the scores across cells and cell-cycle phases. The cells were classified by assigning the cell-cycle phase corresponding to the highest scaled value. The scaled values are graphically depicted in the heat map in Extended Data Fig. 4c.

Identification of candidate genes for further analysis

The objective of this part of the study was to identify the genes responsible for the divergent response to treatment. We identified a large number of genes that were differentially expressed between the inhibited and adapting single-cell trajectories. The zero-inflated nature of scRNA-seq data makes it difficult to reliably estimate the magnitude of changes in expression. With this in mind, in an effort to unbiasedly select candidate genes for further validation and analysis we resorted to a CRISPR–Cas9 screen. By integrating the results from the screen and single-cell analyses, we aimed to identify key genes and/or pathways that are differentially expressed between the single-cell trajectories and that are also functionally related to proliferation during the G12Ci treatment.

CRISPR–Cas9 screen

Library lentivirus production and purification. The Brunello human genome sgRNA library[47] was obtained from the gene editing and screening core facility at Memorial Sloan Kettering Cancer Center (MSKCC). This library consists of four sgRNAs per gene, optimized to reduce off-target effects. To produce the lentivirus expressing the sgRNA library, HEK293FT cells were transfected with the DNA library using XtremeGene HP (Sigma-Aldrich), according to the manufacturer's instructions. After 24 h, the medium was replaced with fresh complete DMEM. Following another 48-h incubation, the medium was collected and centrifuged at 500*g* at 4 °C for 5 min to pellet cell debris. The supernatant was passed through a 0.45-μm filter and was snap-frozen in aliquots for future use.

Establishment of Cas9-expressing cells. Lentivirus expressing spCas9 was produced as above and transduced into H358 cells at a multiplicity of infection of 1. Cells were sorted into 96-well plates at one cell per well and selected for growth in complete medium containing 10 μg/ml blasticidin. Cas9-expressing cell lines were validated for Cas9 expression, Cas9 activity and a similar sensitivity to the G12Ci as the parental cell line (data not shown).

Titration of the library-expressing virus. To determine the titre of the viral library, Cas9-expressing H358 cells were seeded in 15-cm dishes in complete medium and transduced with increasing amounts of virus. The number of viable cells after puromycin selection was determined and used to calculate titre.

G12Ci screen. Cas9-expressing H358 cells were transduced with the sgRNA-library-expressing virus at a multiplicity of infection of 0.3 and a coverage of 500×. Puromycin was added 2 days after transduction at a concentration of 2 μg/ml. Eight days after selection (set as t_0), live cells were collected and a portion (40 million cells, which represents a 500× coverage of the library) was collected for genomic DNA (gDNA) extraction (Qiagen Gentra Puregene Cell Kit). The remaining cells were reseeded into 150-mm^3 dishes at 4 million cells per dish and treated with DMSO or G12Ci (ARS1620, 10 μM). The medium was changed every three days. Cells were passaged at 80% confluence, and at least 500× coverage of the library was maintained at each passage. Fourteen days after treatment, cells were collected and gDNA was extracted.

Next-generation sequencing library preparation. The gDNA extracted in 'G12Ci screen' were used to generate next-generation sequencing libraries. The sgRNA sequences were amplified and prepared for deep sequencing through a two-step PCR. The first step was performed with 10 μg input gDNA in a 100-μl reaction (260 μg gDNA per sample) with 1 μl of Herculase polymerase (Agilent). The PCR primers included adapters: ATGGACTATCATATGCTTACCGTAACTTGAAAGTATTTCG (v2 adaptor forward) and CTTTAGTTTGTATGTCTGTTGCTATTATGTCTACT ATTCTTTCC (v2 adaptor reverse). The thermocycling parameters were: 95 °C for 5 min, then 95 °C for 20 s; 60 °C for 20 s; 72 °C for 30 s for 30 cycles, and 72 °C for 3 min. The number of cycles was tested to ensure it fell within the linear phase of amplification. Amplicons for each sample were pooled and the second step of PCR was performed with 8 ×100-μl reactions containing 5 μl of pooled first PCR amplicons to attach Illumina adaptors and indexes with NEBNext High-Fidelity 2× PCR Master Mix. The thermocycling parameters were: 98 °C for 3 min, then 98 °C for 20 s; 68 °C for 20 s; 72 °C for 20 s for 12 cycles, and 72 °C for 5 min. All parallel PCRs were pooled and purified by one round of phenol extraction using PhaseLock tubes (ref 2302820 VWR) according to the manufacturer's instruction. PCR products were eluted with 30 μl of EB buffer and resolved on a 2% agarose gel. Amplicons with desired size were purified from the gel with Qiagen's gel purification kit. Final next-generation sequencing amplicons were eluted from column with EB buffer and concentrations were determined via Qubit. Samples were diluted to 30 nM before sending for sequencing.

Data analysis. This was carried out using MAGeCK[48] in Python. MAGeCK uses the beta score to estimate gene dependencies: a positive beta indicates that a gene is positively selected, and a negative beta

indicates that a gene is negatively selected. The fold change in expression was also calculated to help interpret and filter the results. This approach was used to determine the sgRNAs that are depleted during treatment. Gene-specific values were calculated as the mean change in expression for the four sgRNAs in the library targeting that gene. The non-targeting average was calculated from 1,000 non-specific sgRNAs. We prioritized genes with 2 or more sgRNAs that were downregulated by 2-or-more-fold in the G12Ci versus t_0 comparison, and which were also identified as having trajectory-specific expression in the scRNA-seq analysis. Preference was given to pathways being represented by several intermediates. Key findings were validated by independent genetic or pharmacological approaches.

Cloning and plasmids

sgRNAs targeting *AURKA* (guide 1: 5′-CCATATAGAAAATAATCCTG and guide 2: 5′-CCTGAAAACTCACCGAAGGT) were cloned into lentiGuide-Puro vector (a gift from F. Zhang; Addgene plasmid no. 52963) using the BsmBI site. The pMXs-IP-mVenus-p27K$^-$ vector was a gift from T. Kitamura. siRNA-resistant *HA-KRAS^{G12C}* (that is, siRes-G12C) construct was generated by modifying the siRNA-targeted sequence (5′-G GTG GGT GCA TGC GGA GT-3′; the G12C codon is underlined), and the modified *HA-KRAS^{G12C}* was synthesized and cloned into the pENTR/D-TOPO vector (Invitrogen). The gene was then inserted into the pInducer20 vector (a gift from S, Elledge; Addgene plasmid no. 44012) or pLIX_403 vector (a gift from D. Root; Addgene plasmid no. 41395) using the Gateway LR Clonase II kit (Invitrogen). *AURKA* was amplified with primers (forward 5′-CACCATGG ACCGATCTAAAGAAAACT; reverse 5′-CTAAGACTGTTTGCTAGCTG) from the template pAuroraA-GFP-AURKA-mCherry (a gift from M. Tramier; Addgene plasmid no. 99878) and cloned into pInducer20 vector.

Virus production and generation of stable cell lines

HEK293T cells were seeded at 90% density in a 10-cm dish and transfected with the expression vector and packaging vectors pMD2.G and psPAX2 using Lipofectamine 3000 (Invitrogen) according to the manufacturer's instructions. Conditioned medium containing recombinant viruses was collected and filtered through 0.45-μm filters (Millipore). The virus-containing medium was added to cells with 8 μg/ml Polybrene (Millipore) overnight. Approximately 24 h after infection, the cells were selected with 2 μg/ml puromycin or 500 ng/ml G418.

Flow cytometry

Quiescence biosensor distribution. Three million H358 cells expressing the mVenus–p27K$^-$ biosensor[19] were plated in 6-cm dishes and treated with the indicated inhibitors for 72 h. For siRNA experiments, 5×10^5 cells were seeded in 6-cm dishes and transfected with 25 nM *KRAS^{G12C}* siRNA (sense: GUU GGA GCU UGU GGC GUA G-dTdT; antisense: CUA CGC CAC AAG CUC CAA C -dTdT; underline highlights the G12C codon) using Lipofectamine RNAiMAX (Invitrogen). Doxycycline was added to a final concentration of 100 ng/ml and cells were incubated for 72 h. Cells were collected with TrypLE Express (Gibco) and fixed for 10 min at room temperature with 4% paraformaldehyde. Samples were washed twice with PBS and filtered through 35-μm mesh-capped collection tubes. If cell-cycle analysis was performed, cells were subsequently treated with 70% ethanol and stained with 5 μg/ml DAPI. Cells were analysed on BD Biosciences LSR Fortessa. Forward and side scatter plots were used to exclude debris, damaged cells and doublets. Data analysis was performed with FCS Express 6 Flow and GraphPad Prism 7.0 software. Where indicated, the p27K$^-$ biosensor distribution was subjected to minimum and maximum normalization in Prism, to compare between different conditions. Cell sorting was performed on unfixed cells on BD Biosciences FACSAriaII. Post-sort purity was 95%+ and was determined by running a small aliquot of the collected sample.

Synchronization experiments. H358 cells were seeded at low density (10–20%) and incubated with 2 mM thymidine for 22 h. Next, the cells were released in complete medium supplemented with 25 μM 2′-deoxycytidine for 10 h, followed by another 20 h incubation with 2 mM thymidine. Following synchronization at the G1–S boundary, cells were released in complete medium containing either DMSO or G12Ci (10 μM), and collected for analysis at the indicated times. Cells were fixed in 70% ethanol, washed twice with PBS and stained in propidium iodide staining solution (PBS with 100 μg/ml RNase and 50 μg/ml propidium iodide). Samples were analysed as in 'Quiescence biosensor distribution'. Cell-cycle distribution was determined using the Multicycle DNA function embedded in FCS Express 6 Flow.

Clonogenic assay

The cells were seeded in 6-well plates at densities of 4×10^5 or 1×10^5 cells per well and treated as indicated for 6 or 12 days, respectively. Media was changed every 3 days. Cells were fixed with ice-cold methanol for 10 min and stained with 0.5% crystal violet solution for 30 min at room temperature on shaker. Plates were washed thoroughly and scanned.

KRAS(G12C)-expressing RASless mouse embryonic fibroblasts

RASless (that is, *NRAS$^{-/-}$HRAS$^{-/-}$*, *Lox-KRAS-Lox*, *4HT-cre*) mouse embryonic fibroblasts were generated and provided by M. Barbacid[21]. These were infected with a retrovirus expressing HA-tagged KRAS(G12C) (generated from a pBABEPuro DNA vector) followed by puromycin selection to establish mouse embryonic fibroblasts expressing exogenous KRAS(G12C) and endogenous wild-type KRAS. The cells were then treated with 4-hydroxy-tamoxifen for one week to ablate the endogenous *KRAS* allele. The latter were used to determine the effect of various treatments on KRAS(G12C) reactivation.

RAS activation assay

These assays were performed as previously described[49] using the Active Ras Pull-Down and Detection Kit (Thermo Fisher Scientific). In brief, whole-cell lysates were incubated with GST–RAF1 RAS-binding domain (RBD) and glutathione agarose resin for 1 h at 4 °C, followed by 3 washes and elution with SDS–PAGE loading buffer. The samples were then subjected to western blotting with a KRAS-specific antibody. When HA–KRAS(G12C) was exogenously expressed, an HA-specific antibody enabled specific determination of KRAS(G12C) in its GTP-bound conformation.

Immunoprecipitation

H358 doxycycline-inducible HA–KRAS(G12C) cells were plated in 6-cm dishes at 50% confluence. After induction with 2 μg/ml of doxycycline for 24 h, cells were treated with G12Ci or AURKAi or the combination for another 2 h. Cells were then collected and 200 μg of protein lysate was used to immunoprecipitate HA–KRAS(G12C) with Pierce Anti-HA magnetic beads according to the manufacturer's protocol (Thermo Scientific no. 88836). Beads were eluted with SDS–PAGE loading buffer and the immunoprecipitation product was subjected to western blotting analysis.

Immunoblotting

Immunoblotting was performed as previously described[49–51], with the antibodies listed in Supplementary Table 1. All antibodies have been validated either in our previous work (KRAS, HA-tag, pEGFR, EGFR, pCRAF, CRAF, pERK, ERK, pRSK, RSK and GAPDH) or in other publications (β-actin, pSHP2, SHP2, pAURKA, AURKA, PLK1, CCNB1, cleaved PARP, p21 and p27).

Cell viability assay

Cells were seeded in 96-well plates at 2×10^3 cells per well in (at minimum) triplicates and treated with the indicated concentrations of drugs. After 72 h, cell viability was assayed by CellTiter-Glo Luminescent Cell Viability Assay (Promega). For siRNA experiments, cells were reverse-transfected with 25 nM siRNA for 3 days before the addition of drug. siRNAs targeting *HBEGF* and *KRAS* are ON-TARGETplus Smartpool siRNA from Dharmacon, and the non-targeting siRNA (control siRNA-A)

is from Santa Cruz Biotechnology. Data analysis was performed with GraphPad Prism 7.0.

Synergy determination

To determine the presence of synergy between two drug treatments, cells were treated with increasing concentrations of either drug for 72 h, followed by determination of viable cells using the CellTiter-Glo Luminescent Cell Viability Assay (Promega). The experiment was carried out in biological triplicates. The data were expressed as percentage inhibition relative to baseline, and the presence of synergy was determined by the Bliss method using the synergy finder R package[52].

Quantitative RT–PCR

Cells were treated as shown and total RNA was extracted using the Quick-RNA Miniprep Kit (Zymo Research). One microgram of RNA was used for cDNA synthesis using the High-Capacity cDNA Reverse Transcription Kit (Applied Biosystems). qPCR reactions were performed using the Applied Biosystem PowerUP SYBR Green Master Mix (Applied Biosystems) on the QuantStudio 6 Flex Real-Time PCR System (Applied Biosystems). Samples were run in triplicate, and mRNA levels were normalized to *ACTB*. Primer sequences are: *KRAS* (forward, GGACTGGGGAGGGCTTTCT; reverse, GCCTGTTTTGTGTCTACTGTTCT), *HBEGF* (forward, ATCGTGGGGCTTCTCATGTTT; reverse, TTAGTCATGCCCAACTTCACTTT) and *ACTB* (forward, CATGTACGTTGCTATCCAGGC; reverse, CTCCTTAATGTCACGCACGAT).

Mouse studies

These studies were carried out as previously described[50,51]. In brief, 6-to-8-week-old female nu/nu athymic mice were obtained from the Envigo Laboratories and maintained in compliance with Institutional Animal Care and Use Committee (IACUC) guidelines under protocol 18-05-007 approved by MSKCC IACUC. The maximum tumour measurement permitted was 1.5 cm, and this was not exceeded in any of our experiments. Mice implanted with xenografts were chosen for efficacy studies in an unbiased manner. Once tumours reached 100-mm^3 volume, mice were randomized and treated with drug or the appropriate vehicle control. Treatments and tumour measurements were performed as previously described[51] in a non-blinded manner by a research technician who was not aware of the objectives of the study. Prism (GraphPad Software) was used for data analysis. For each study arm, the fractional difference in tumour growth relative to t_0 was plotted over time. Statistically significant differences were determined for each treatment time point by using the two-tailed *t*-test function embedded in Prism.

Reporting summary

Further information on research design is available in the Nature Research Reporting Summary linked to this paper.

Data availability

The data that support the findings of this study are available within the paper and its Supplementary Information files. Source Data for Figs. 1–4 and Extended Data Figs. 2–9 are provided with the paper. The scRNA-seq data have been deposited in the Gene Expression Omnibus (GEO) with the accession code GSE137912. Data or other materials are available from the corresponding author upon reasonable request.

Code availability

The analysis was performed using standard protocols with previously described computational tools. The scripts, along with the processed files described in the Methods, are available from the corresponding author upon reasonable request.

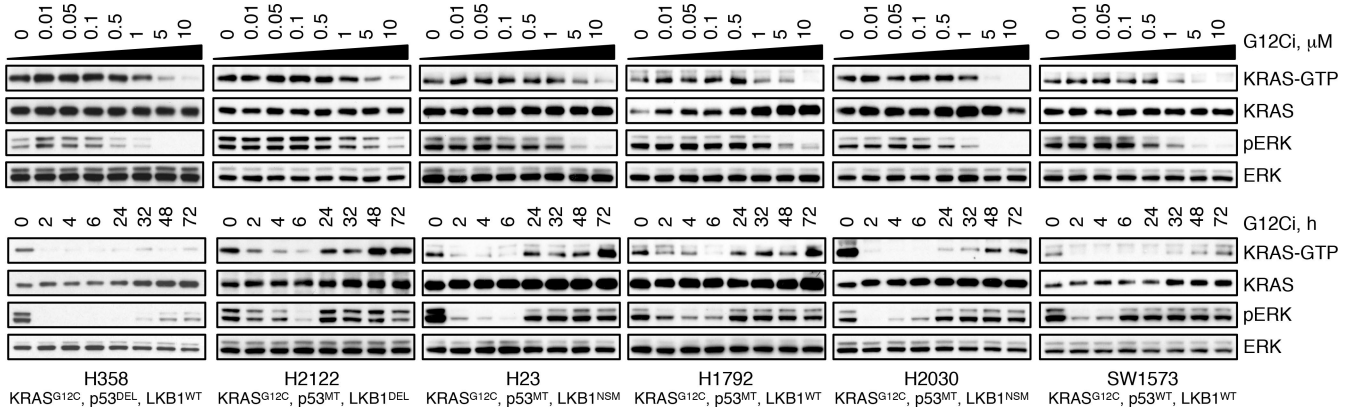
31. Klein, A. M. et al. Droplet barcoding for single-cell transcriptomics applied to embryonic stem cells. *Cell* **161**, 1187–1201 (2015).
32. Macosko, E. Z. et al. Highly parallel genome-wide expression profiling of individual cells using nanoliter droplets. *Cell* **161**, 1202–1214 (2015).
33. Azizi, E. et al. Single-cell map of diverse immune phenotypes in the breast tumor microenvironment. *Cell* **174**, 1293–1308 (2018).
34. van Dijk, D. et al. Recovering gene interactions from single-cell data using data diffusion. *Cell* **174**, 716–729 (2018).
35. Huber, W. et al. Orchestrating high-throughput genomic analysis with Bioconductor. *Nat. Methods* **12**, 115–121 (2015).
36. McCarthy, D. J., Campbell, K. R., Lun, A. T. & Wills, Q. F. Scater: pre-processing, quality control, normalization and visualization of single-cell RNA-seq data in R. *Bioinformatics* **33**, 1179–1186 (2017).
37. Vallejos, C. A., Risso, D., Scialdone, A., Dudoit, S. & Marioni, J. C. Normalizing single-cell RNA sequencing data: challenges and opportunities. *Nat. Methods* **14**, 565–571 (2017).
38. Lun, A. T., McCarthy, D. J. & Marioni, J. C. A step-by-step workflow for low-level analysis of single-cell RNA-seq data with Bioconductor. *F1000Res.* **5**, 2122 (2016).
39. Haghverdi, L., Buettner, F. & Theis, F. J. Diffusion maps for high-dimensional single-cell analysis of differentiation data. *Bioinformatics* **31**, 2989–2998 (2015).
40. Rodriguez, A. & Laio, A. Clustering by fast search and find of density peaks. *Science* **344**, 1492–1496 (2014).
41. Cannoodt, R., Saelens, W. & Saeys, Y. Computational methods for trajectory inference from single-cell transcriptomics. *Eur. J. Immunol.* **46**, 2496–2506 (2016).
42. Van den Berge, K. et al. Observation weights unlock bulk RNA-seq tools for zero inflation and single-cell applications. *Genome Biol.* **19**, 24 (2018).
43. Ritchie, M. E. et al. limma powers differential expression analyses for RNA-sequencing and microarray studies. *Nucleic Acids Res.* **43**, e47 (2015).
44. Robinson, M. D., McCarthy, D. J. & Smyth, G. K. edgeR: a Bioconductor package for differential expression analysis of digital gene expression data. *Bioinformatics* **26**, 139–140 (2010).
45. Risso, D., Ngai, J., Speed, T. P. & Dudoit, S. Normalization of RNA-seq data using factor analysis of control genes or samples. *Nat. Biotechnol.* **32**, 896–902 (2014).
46. Wu, D. et al. ROAST: rotation gene set tests for complex microarray experiments. *Bioinformatics* **26**, 2176–2182 (2010).
47. Sanson, K. R. et al. Optimized libraries for CRISPR–Cas9 genetic screens with multiple modalities. *Nat. Commun.* **9**, 5416 (2018).
48. Li, W. et al. MAGeCK enables robust identification of essential genes from genome-scale CRISPR/Cas9 knockout screens. *Genome Biol.* **15**, 554 (2014).
49. Lito, P. et al. Disruption of CRAF-mediated MEK activation is required for effective MEK inhibition in KRAS mutant tumors. *Cancer Cell* **25**, 697–710 (2014).
50. Lito, P. et al. Relief of profound feedback inhibition of mitogenic signaling by RAF inhibitors attenuates their activity in BRAFV600E melanomas. *Cancer Cell* **22**, 668–682 (2012).
51. Xue, Y. et al. An approach to suppress the evolution of resistance in BRAF^{V600E}-mutant cancer. *Nat. Med.* **23**, 929–937 (2017).
52. He, L. et al. Methods for high-throughput drug combination screening and synergy scoring. *Methods Mol. Biol.* **1711**, 351–398 (2018).

Acknowledgements The authors thank C. Sawyers and M. Mroczkowski for their insight on the manuscript; R. Garippa for his advice on the CRISPR screen; and P. Jallepalli for his help with the interpretation of the AURKA findings. This work has been supported in part by the NIH/NCI (1R01CA23074501 to P.L., 1R01CA23026701A1 to P.L., K08CA191082-01A1 to P.L. and 1F30CA232549-01 to J.Y.X.). P.L. is also supported in part by The Pew Charitable Trusts, the Damon Runyon Cancer Research Foundation and the American Lung Association. E.d.S. is supported in part by the MSKCC Pilot Center for Precision Disease Modeling program (U54 OD020355). D.R. is supported by Programma per Giovani Ricercatori Rita Levi Montalcini granted by the Italian Ministry of Education, University and Research. The authors acknowledge the Josie Robertson Investigator Program at MSKCC, a Medical Scientist Training Program grant to the Weill Cornell–Rockefeller–Sloan Kettering Tri-Institutional MD-PhD Program (T32GM007739) and the MSKCC Support Grant-Core Grant program (P30 CA008748).

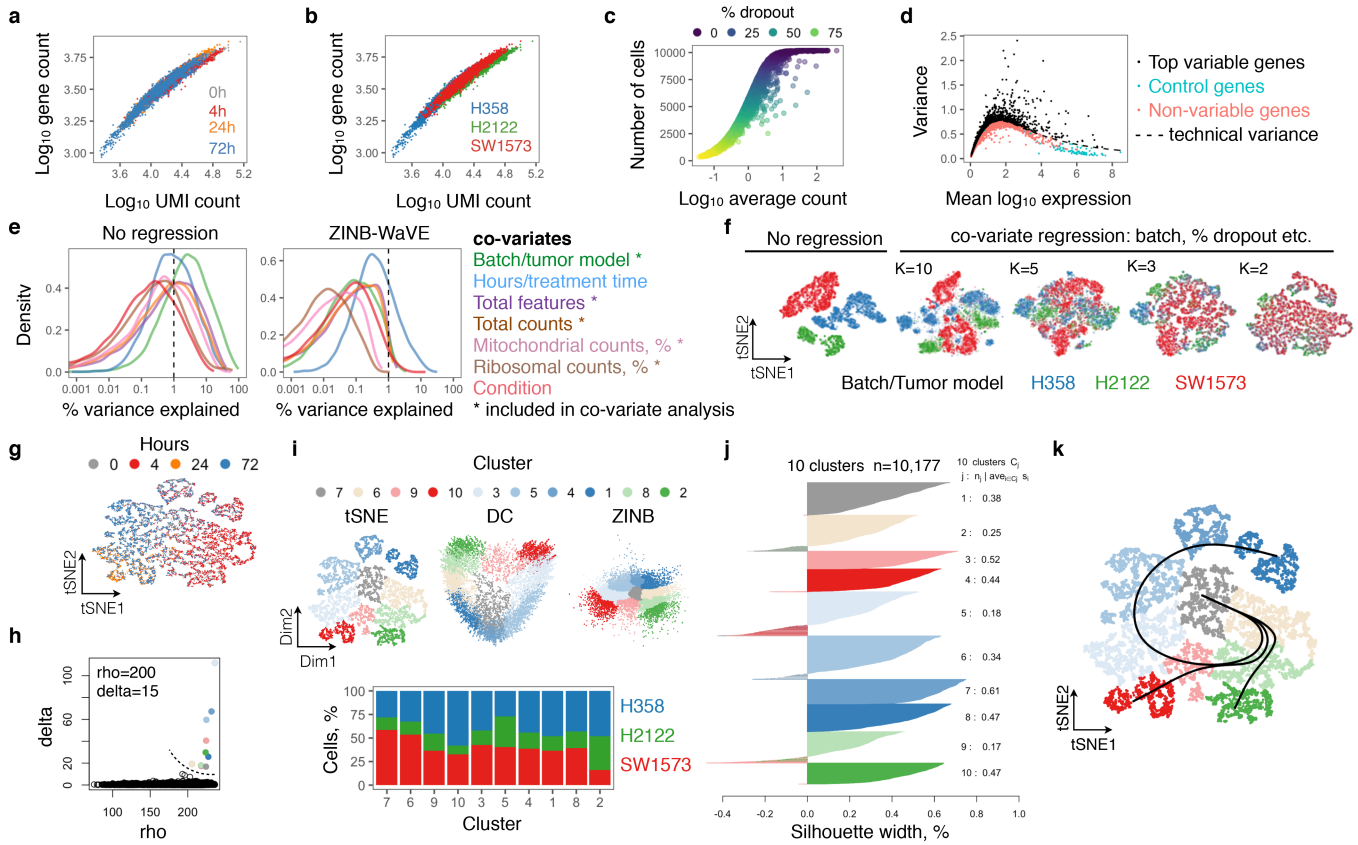
Author contributions J.Y.X., Y.Z. and P.L. designed the study and analysed data. J.Y.X., Y.Z., J.A., A.V., T.T.M., D.K. and C.L. performed experiments. B.Q. and E.d.S. helped to perform in vivo studies. L.M. and D.R. helped to carry out the scRNA-seq experiment and performed statistical data analysis, respectively. J.Y.X., Y.Z. and P.L. were the main writers of the manuscript, with considerable help from D.R. All other authors reviewed the manuscript and contributed to writing it. P.L. conceived and supervised the study.

Competing interests MSKCC has received research funds from companies developing G12C inhibitors and has confidentiality agreements with these companies. A part of these funds is allocated for research to be conducted under the supervision of P.L. These funds were not used to support the work in this paper. The experiments in this paper were performed with commercially available inhibitors. P.L. has not received honoraria, consultation fees, stock options or travel reimbursement from such companies.

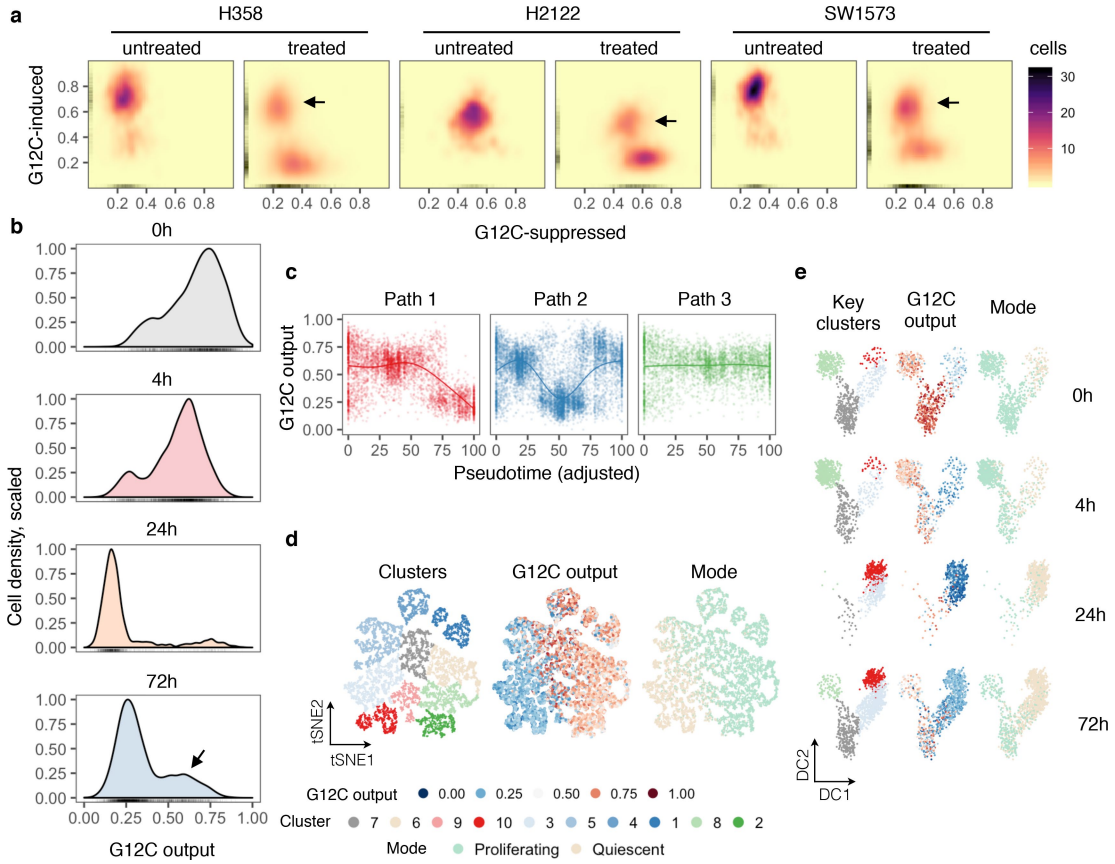
Additional information
Supplementary information is available for this paper at https://doi.org/10.1038/s41586-019-1884-x.
Correspondence and requests for materials should be addressed to P.L.
Peer review information *Nature* thanks Frank McCormick, Arjun Raj and the other, anonymous, reviewer(s) for their contribution to the peer review of this work.
Reprints and permissions information is available at http://www.nature.com/reprints.



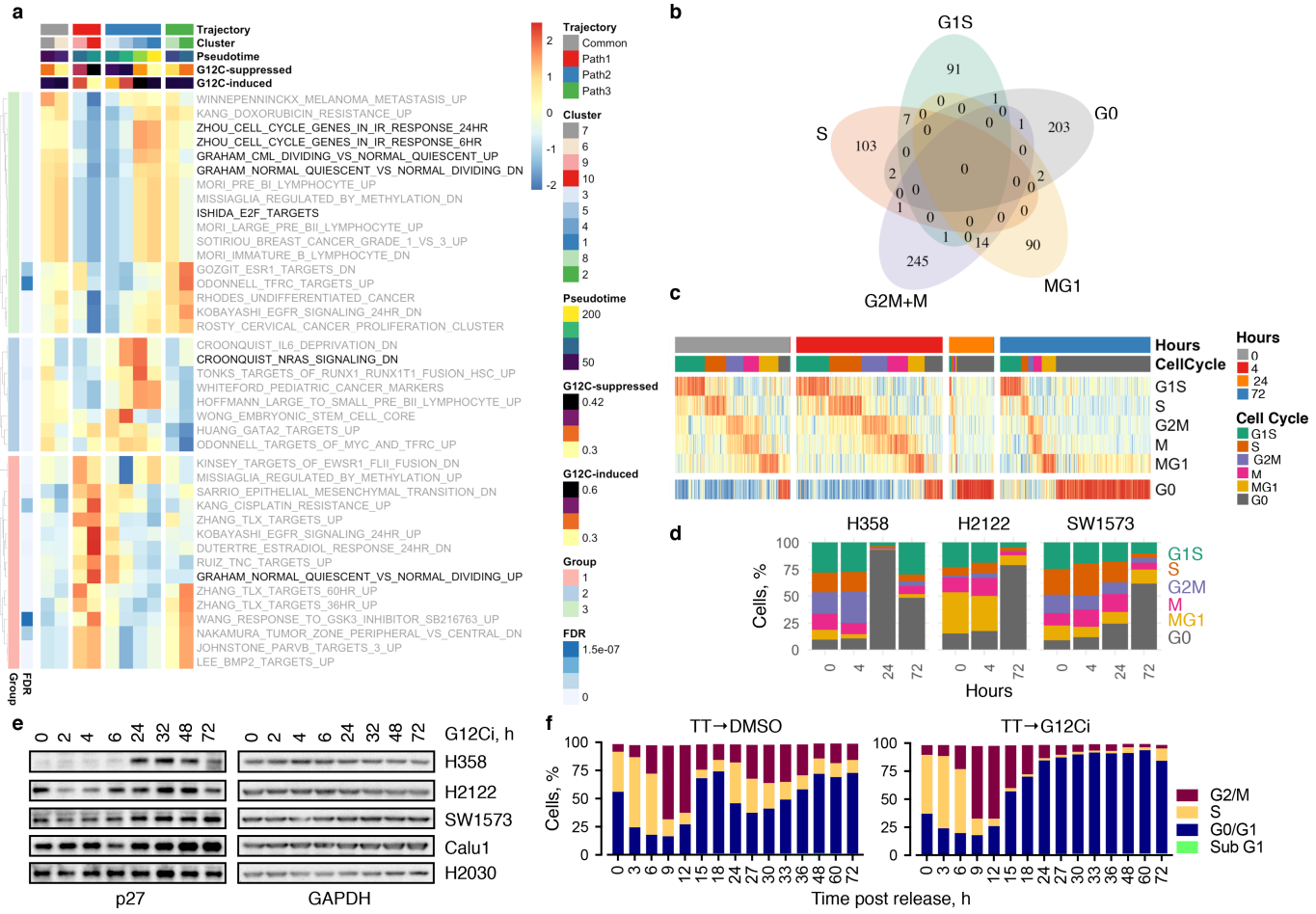
Extended Data Fig. 1 | The effect of the G12Ci treatment on KRAS signalling across lung cancer cell lines. The indicated models were treated with increasing concentrations of the G12Ci (ARS1620) for 2 h (top panels) or with 10 μM over time (bottom panels), and immunoblotted to determine the effect on KRAS signalling intermediates. Key genetic alterations found at baseline in the KRAS(G12C)-mutant cell lines used in this study are listed. A representative of two independent experiments for each cell line is shown.



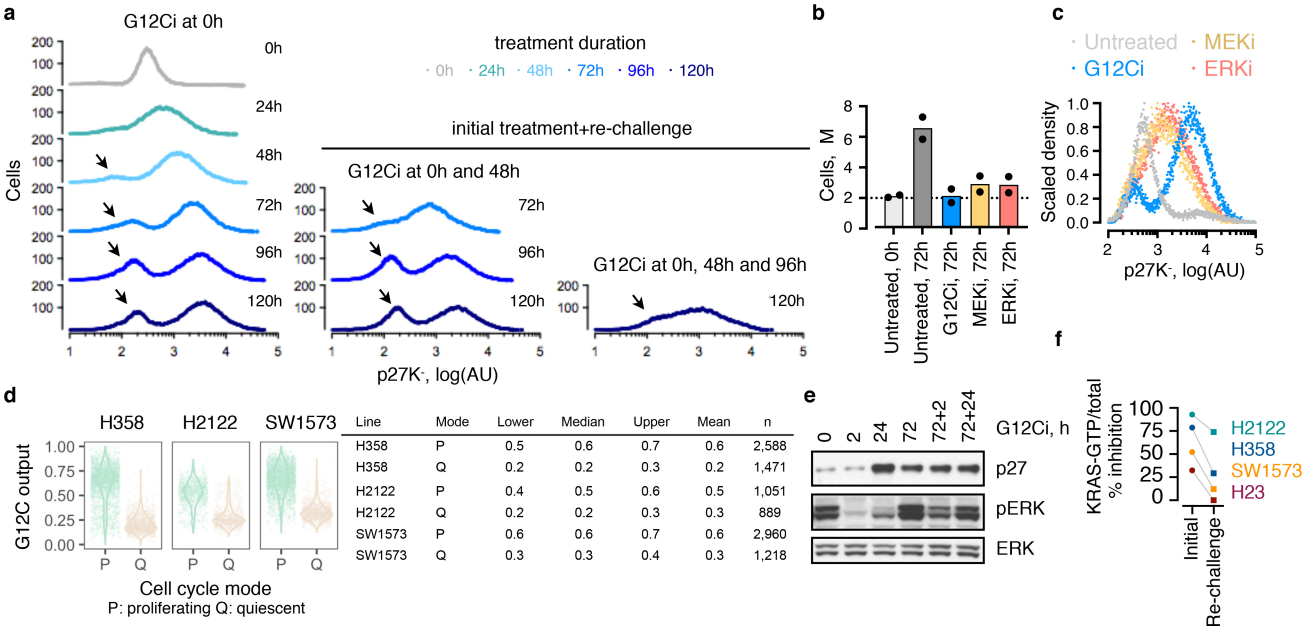
Extended Data Fig. 2 | Quality assessment and processing of scRNA-seq data. a, **b**, Gene counts as a function of UMI count. Cells are grouped by length of G12Ci treatment (**a**) or tumour model (**b**). **c**, The number of cells expressing a gene, as a function of its average count across the dataset. **d**, Variance as a function of mean expression. Technical variance (that is, variability attributed to technical factors) was calculated by the expression of ribosomal genes. $n = 10,177$ single cells in **a**–**d**. **e**, The per cent of variance explained by various experimental factors. A number of variables had a meaningful contribution to the variance of the dataset (that is, they accounted for greater than 1% of the variation), suggesting the need to correct for these potentially confounding factors in downstream analysis. **f**, Dimensionality reduction and covariate regression using the ZINB-WaVE algorithm. The *K* parameter of 2 was chosen, as this minimizes batch and other covariate effects. **g**, *t*-SNE projection showing single cells coloured by length of inhibitor treatment. **h**, Parameters used to cluster cells by using the Density Cluster algorithm. **i**, Cluster distribution in the indicated projections (top) and cell line composition of each cluster (bottom), showing a similar representation of cells from different tumour models in each cluster. **j**, Silhouette-width analysis to assess the appropriateness of clustering. Negative values indicate cells that have been inappropriately assigned. **k**, *t*-SNE projection of KRAS(G12C) single cells with the three inhibitory trajectories identified by the Slingshot algorithm.



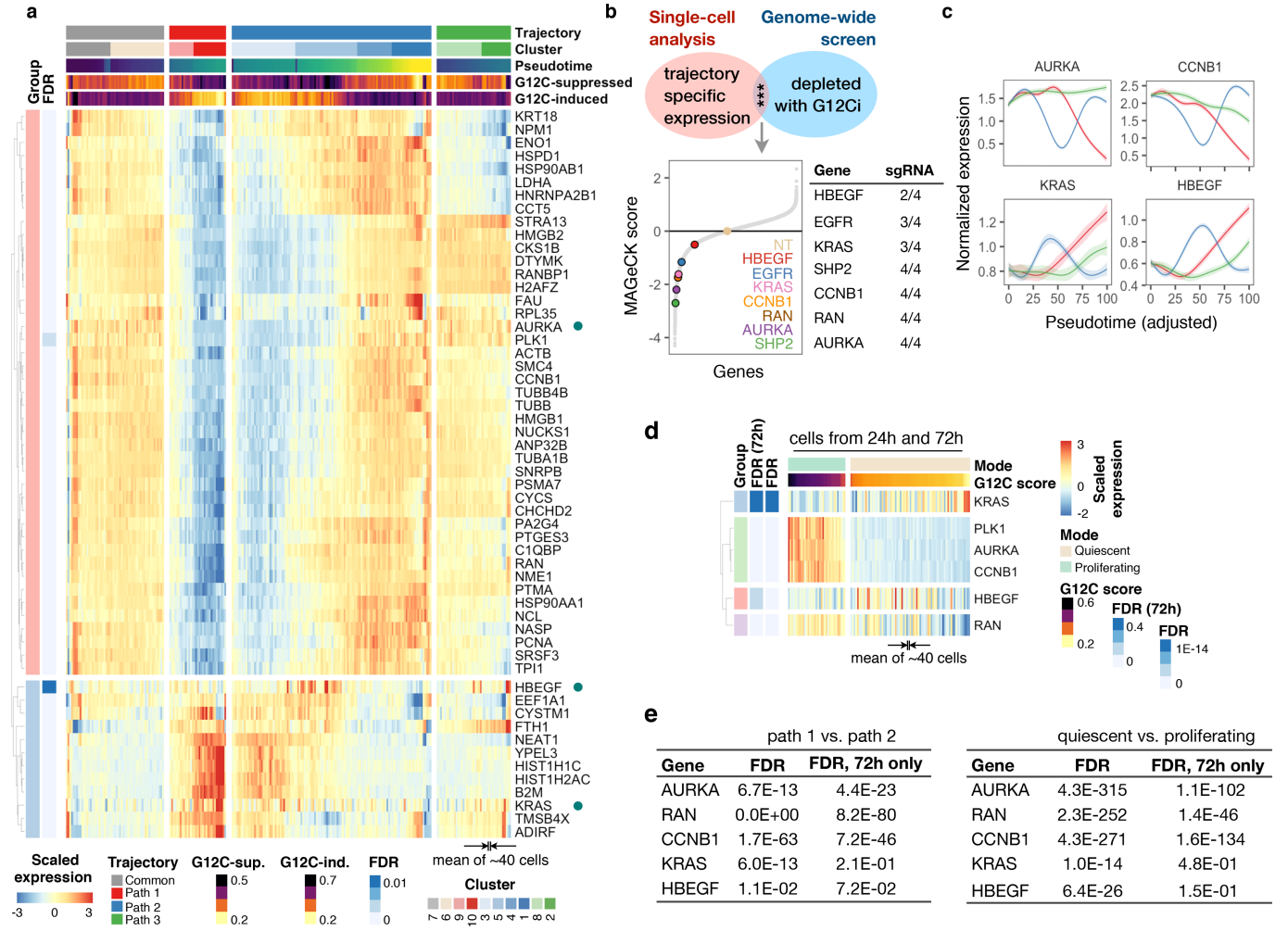
Extended Data Fig. 3 | KRAS(G12C)-dependent transcriptional output score in 10,177 lung cancer cells. a, The distribution of KRAS(G12C)-specific gene-expression output score across single cells in the three tumour models under study. The arrows denote cohorts of cells with high output despite treatment. **b**, Density plots showing the effect of G12Ci treatment on the KRAS(G12C) output score ($n = 2{,}565$ single cells from 0 h, $n = 3{,}259$ single cells from 4 h, $n = 1{,}006$ single cells from 24 h and $n = 3{,}347$ single cells from 72 h). At 72 h the cells assume an asymmetric distribution, suggesting that a subpopulation of KRAS(G12C) cells has adapted to treatment by reactivating KRAS(G12C)-dependent output (arrow). **c**, The KRAS(G12C) output score as a function of pseudotime (which was adjusted to allow comparisons between trajectories). The trend line was derived by fitting a spline to the G12C output score for each cell ($n = 4{,}759$ single cells in path 1, $n = 8{,}653$ single cells in path 2 and $n = 4{,}050$ single cells in path 3). **d**, **e**, The indicated variables are plotted for each cell in a two-dimensional *t*-SNE (**d**) or diffusion component (**e**) space. For simplicity, only the key clusters delineating each trajectory are shown in **e**.



Extended Data Fig. 4 | G12Ci treatment induces quiescence in a subpopulation of cancer cells. a, Single cells were analysed to determine gene-expression signatures that correlated with the inhibitory fates. The top 20 signatures in each direction are shown. **b**, The overlap in the cycle-specific gene-expression signatures used to classify cells along their cell-cycle phase. The G0 and G1 phase signatures comprise mostly non-overlapping genes. **c**, A heat map of cell-cycle-specific gene-expression scores across each cell. Values were scaled across columns. **d**, Effect of G12Ci on cell-cycle distribution across treatment time and tumour models. **e**, The cell lines were treated as shown, to determine the level of p27 expression by immunoblotting. A representative of two independent experiments is shown for all except H2030, which was assayed once. **f**, KRAS(G12C)-mutant cells (H358) were synchronized with double thymidine treatment and then released in the presence or absence of G12Ci treatment, followed by cell-cycle analysis using propidium iodide staining. This assay cannot distinguish G0 from G1. TT, double thymidine. A representative of two independent experiments is shown.



Extended Data Fig. 5 | Biosensor validation of the divergent response to G12Ci treatment. a, Cells expressing the quiescence biosensor (H358, p27K$^-$) were treated and rechallenged with the G12Ci to determine the effect on quiescence (that is, p27K$^-$ high peak) at the indicated times. **b**, **c**, The cells were treated with the indicated inhibitors for 72 h to determine the effect on cell number (**b**, $n = 2$ biological replicates) or the distribution of biosensor expression (**c**). **d**, Comparison of the KRAS(G12C) output score between proliferating and quiescent cells. The transcriptional output signature score derived from scRNA-seq analysis is similar to the KRAS–GTP levels determined by RBD pull-down in Fig. 1j. **e**, The cells were exposed to a single treatment (0–72 h) or drug rechallenge (+) for 2 h or 24 h. Cell extracts were evaluated by immunoblotting. **f**, The indicated KRAS(G12C)-mutant lung cancer cell lines were treated with the G12Ci for 72 h followed by drug rechallenge for 4 h. The percentage inhibition in KRAS–GTP/total was determined by comparing baseline versus 4-h G12Ci and 72-h G12Ci versus 72-h + 4-h G12Ci. A representative of two experimental repeats is shown in **a**, **e**.



e

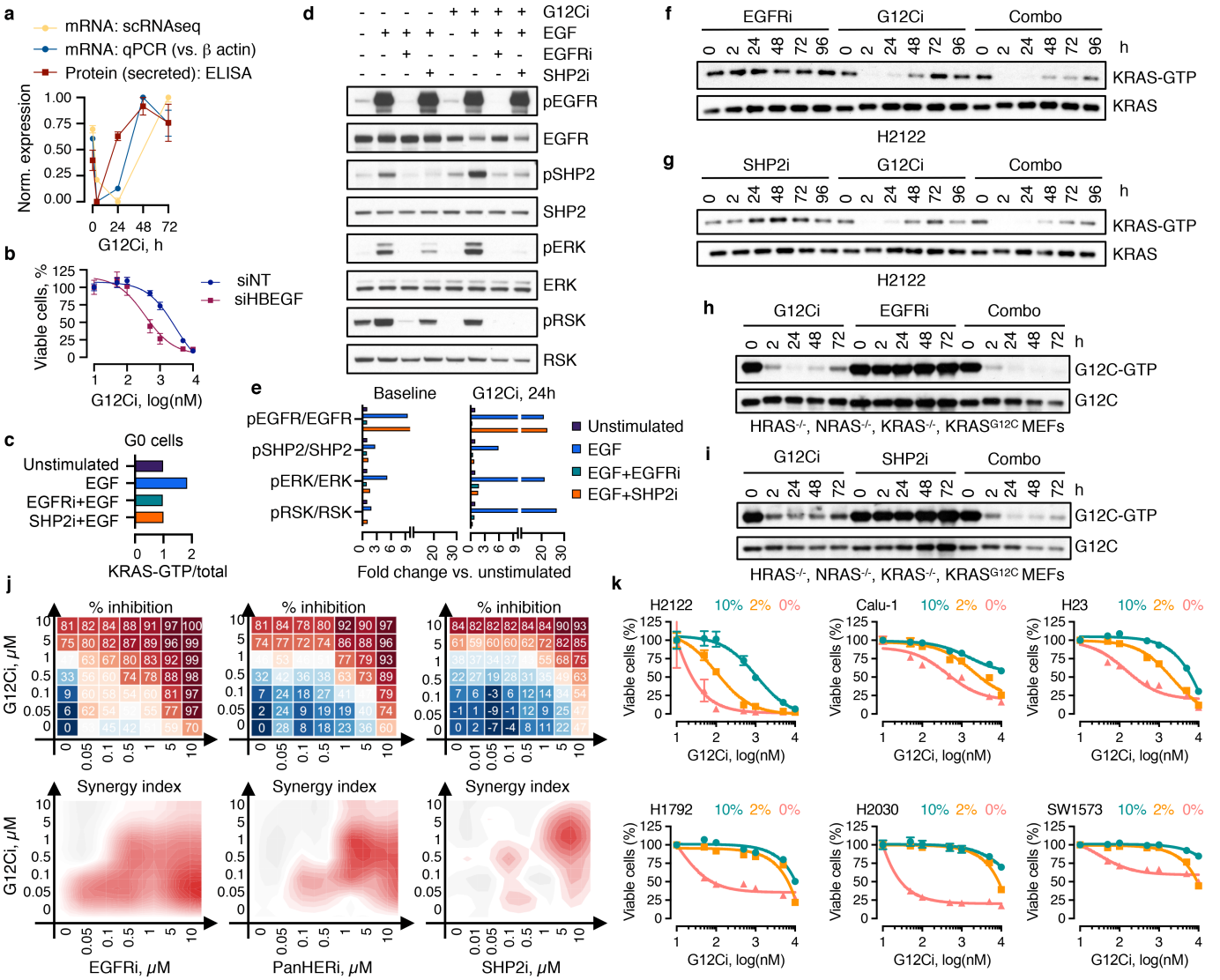
path 1 vs. path 2

Gene	FDR	FDR, 72h only
AURKA	6.7E-13	4.4E-23
RAN	0.0E+00	8.2E-80
CCNB1	1.7E-63	7.2E-46
KRAS	6.0E-13	2.1E-01
HBEGF	1.1E-02	7.2E-02

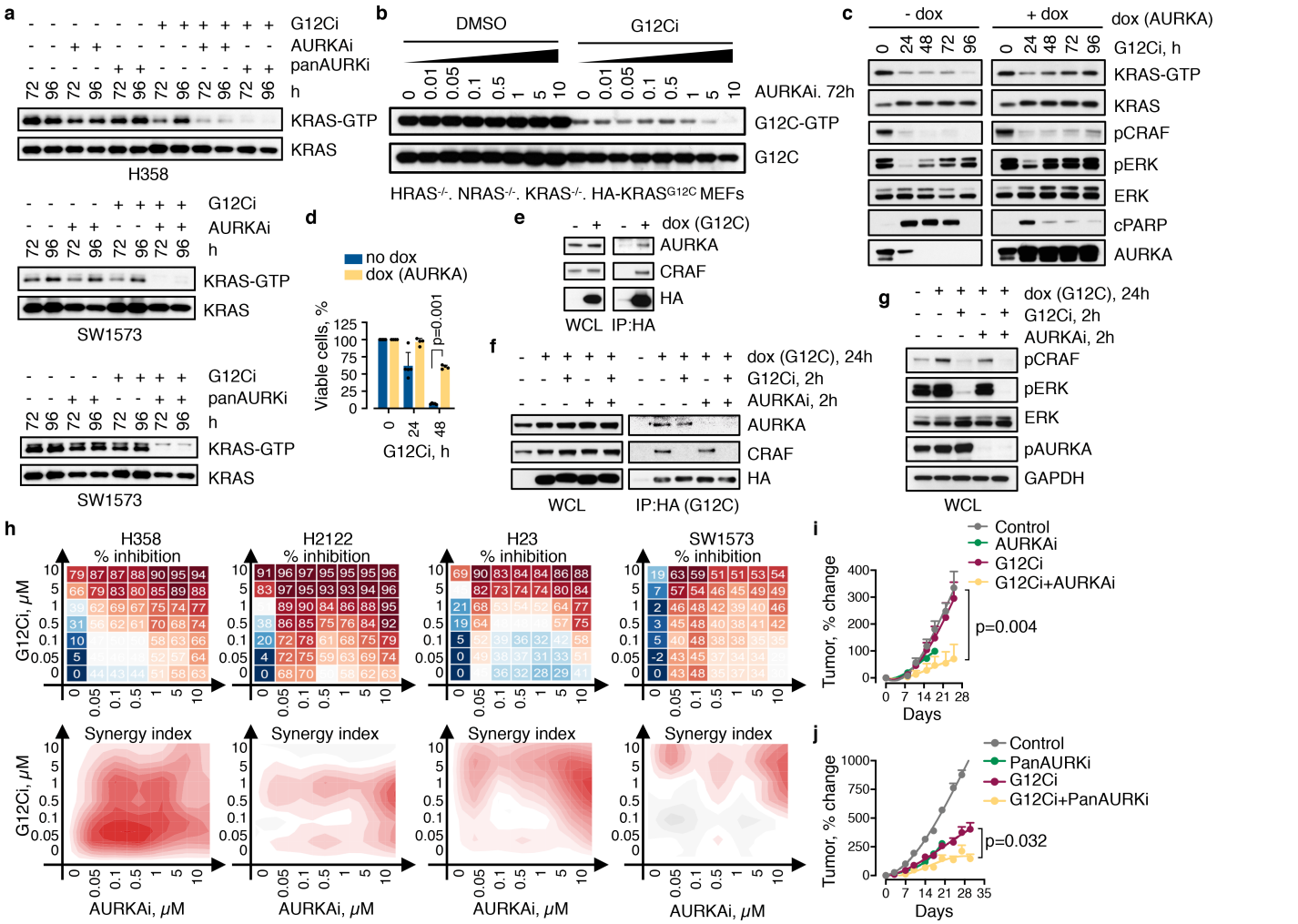
quiescent vs. proliferating

Gene	FDR	FDR, 72h only
AURKA	4.3E-315	1.1E-102
RAN	2.3E-252	1.4E-46
CCNB1	4.3E-271	1.6E-134
KRAS	1.0E-14	4.8E-01
HBEGF	6.4E-26	1.5E-01

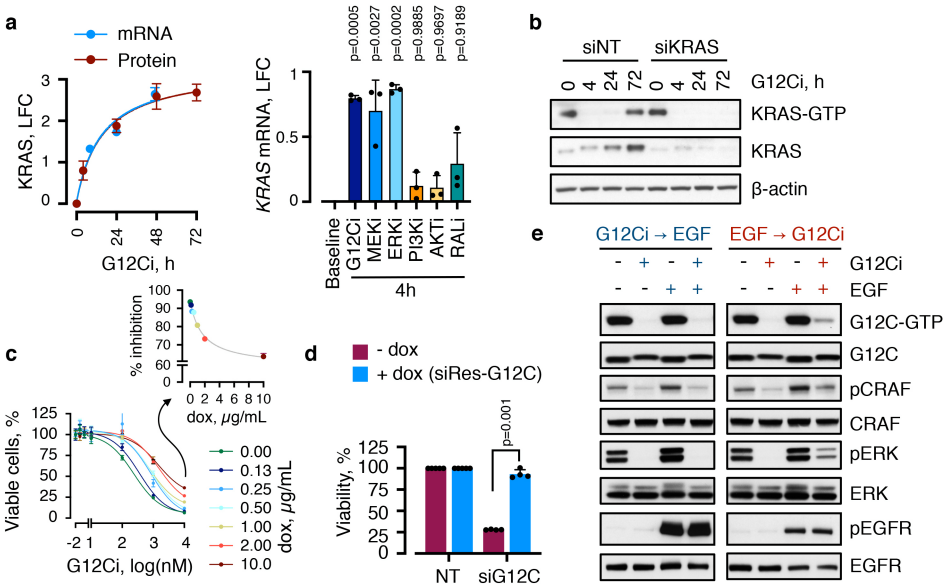
Extended Data Fig. 6 | Genes with trajectory-specific expression profiles. **a**, Single cells were analysed to identify differentially expressed genes by contrasting paths 1 and 2. The top 50 genes are shown. The teal dots indicate genes that were validated in subsequent experiments. **b**, A CRISPR–Cas9 screen was carried out in H358 cells to help to narrow down the list of genes with trajectory-specific expression (by identifying and focusing on genes modulating the antiproliferative effect of the G12Ci). The schematic is not drawn to scale. Preference was given to genes with two or more sgRNAs that were downregulated by at least twofold in the G12Ci versus t_0 comparison and that were also identified as having trajectory-specific expression in the scRNA-seq analysis. Pathways with several intermediates represented were prioritized. The number of gene-specific sgRNAs that were depleted during G12Ci treatment is also shown. NT, non-targeting control. **c**, The trend in expression for the indicated genes as a function of pseudotime was established by fitting a spline to single-cell data. The 95% confidence interval is shown. The pseudotime was adjusted to compare between trajectories. **d**, The expression of the indicated genes in proliferating or quiescent cells. Only cells collected during the adaptive phase (24–72 h) of G12Ci treatment are shown. **e**, The gene false discovery rate (FDR) in the indicated comparisons across either the entire cohort of cells or the subset of cells collected at the 72-h time point only (n = 4,759 single cells in path 1, n = 8,653 single cells in path 2, n = 4,050 single cells in path 3, n = 6,599 single cells in G1S, S, G2M, M or MG1 (proliferating) and n = 3,578 single cells in G0 (quiescent).



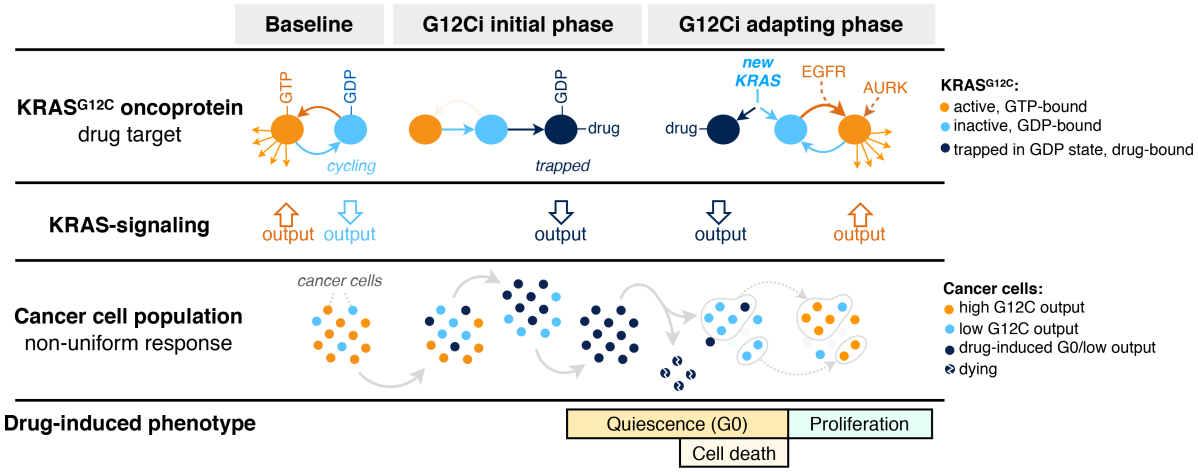
Extended Data Fig. 7 | The adaptive reactivation of KRAS during G12Ci treatment is dependent on EGFR signalling. a, The cells were treated with the G12Ci over time to determine the effect on HBEGF expression. mRNA expression was determined by scRNA-seq (mean, $n > 1{,}000$ single cells per time point, see Fig. 1b) or by quantitative PCR (qPCR, mean ± s.e.m., $n = 3$). The amount of protein secreted in the medium was quantified by enzyme-linked immunosorbent assay (mean ± s.e.m., $n = 3$). Norm., normalized (minimum–maximum). **b**, Cells transfected with *HBEGF*-specific siRNAs were treated with increasing concentrations of G12Ci for 72 h to determine the effect on viability (mean ± s.e.m., $n = 5$). **c**, Cells treated with the G12Ci for 72 h were stimulated with EGF for 10 min, alone or in combination with the indicated inhibitors. Quiescent cells ($p27K^-$ high) were isolated by FACS and their extracts were assayed for active KRAS by RBD pull-down. Immunoblots were quantified by densitometry and reported as fold change relative to unstimulated. **d**, **e**, Untreated or G12Ci-treated (24 h) H358 cells were stimulated with EGF (200 ng ml^{-1}) for 10 min alone or in combination with the indicated inhibitors. Cell extracts were analysed by immunoblotting (**d**). The effect of EGF stimulation at baseline (lanes 2–4 versus lane 1) or after G12Ci treatment (lanes 6–8 versus lane 5) was quantified by densitometry (**e**). **f**–**i**, The indicated *KRAS^{G12C}*-mutant lung cancer cells (**f**, **g**) or HA–KRAS(G12C)-expressing RASless mouse embryonic fibroblasts (**h**, **i**) were treated with the G12Ci alone or in combination with EGFR or SHP2 inhibitors, as shown. Cell extracts were subjected to RBD pull-down to determine the level of active (GTP-bound) and total KRAS. The HA tag was used to determine the specific effect on KRAS(G12C) (**h**, **i**). **j**, H358 cells were treated with the G12Ci alongside the EGFR inhibitor gefitinib (EGFRi), the pan-HER inhibitor afatinib (panHERi) or the SHP2 inhibitor SHP099 (SHP2i) to determine the effect on cancer cell growth (top) and the presence of treatment synergy (bottom), by using the Bliss index. Red denotes synergy. The mean of three biological replicates is shown on top. **k**, The indicated KRAS(G12C)-mutant cells were treated with increasing concentration of the G12Ci in the presence of 10%, 2% or 0% serum to determine the effect on cell viability (mean ± s.e.m., $n = 3$). A representative of two independent experiments is shown in **d**, **f**–**i**. Unless otherwise indicated, *n* denotes biological replicates.



Extended Data Fig. 8 | AURKA is involved in the reactivation of KRAS–GTP during G12Ci treatment. a, KRAS(G12C)-mutant lung cancer cells were treated with the G12Ci alone or in combination with AURKA inhibitor (AURKAi, alisertib, 10 μM) or panAURK inhibitor (tozasertib, 10 μM) to determine the effect on KRAS–GTP levels over time. There is no effect on KRAS–GTP levels with the AURKAi treatment in the absence of the G12Ci treatment. **b**, RASless mouse embryonic fibroblasts expressing KRAS(G12C) were treated as shown with the indicated concentrations of AURKAi (μM) to determine the effect on KRAS(G12C)–GTP. **c**, H358 cells stably transfected with doxycycline-inducible AURKA (dox AURKA) were treated with the G12Ci in the presence or absence of doxycycline (2 μg ml^{-1}). Extracts from cells were analysed by immunoblotting to determine the effect on the indicated intermediates. **d**, H358 doxycycline-inducible AURKA cells were treated as shown and assayed to determine the effect on cell viability (mean + s.e.m, $n = 5$). A two-tailed t-test P value is shown. **e**–**g**, H358 cells stably expressing HA-tagged KRAS G12C under a doxycycline-inducible promoter were treated with doxycycline for 24 h alone (**e**) or with the indicated inhibitors (**f**, **g**). Cell extracts were immunoprecipitated and immunoblotted as indicated. **h**, KRAS(G12C)-mutant cell lines were treated as shown to determine the effect on cancer cell growth (top) and the presence of treatment synergy (bottom), by using the Bliss index. Red denotes synergy. The mean of three biological replicates is shown on top. **i**,**j**, Mice bearing SW1573 (**i**) or H2122 (**j**) xenografts were treated with the indicated inhibitors to determine the effect on tumour growth (mean + s.e.m, $n = 6$ in SW1573, $n = 5$ in H2122). A two-tailed t-test P value is shown. A representative of at least two independent experiments is shown in **a**–**g**. Unless otherwise indicated, n denotes biological replicates.



Extended Data Fig. 9 | Inhibition of MAPK signalling stimulates new KRAS synthesis. a, The cells were treated with the indicated inhibitors and analysed to determine the level of *KRAS* mRNA or KRAS protein expression (mean ± s.e.m., $n = 3$). LFC, $\log_2$-transformed fold change, relative to 0 h. The indicated *P* values were determined by ANOVA ($P = 0.001$) followed by pairwise comparisons versus baseline, while correcting for multiple hypotheses (using Dunnett's test in Prism). **b**, SW1573 ($KRAS^{G12C+/+}$) cells were transfected with non-targeting (NT) or *KRAS*-specific siRNAs followed by treatment with the G12Ci and immunoblotting. **c**, H358 cells engineered to express HA–KRAS(G12C) under a doxycycline-inducible promoter were treated with the G12Ci, alone or in the presence of doxycycline, to determine the effect on cell viability at 72 h (mean ± s.e.m., $n = 3$). **d**, H358 p27K$^-$ cells were stably transfected with doxycycline-inducible siRes-G12C. The cells were transfected with $KRAS^{G12C}$ siRNA (siG12C) followed by doxycycline (2 μg ml^{-1}) induction. The effect on cell viability is shown as mean ± s.e.m. ($n = 5$ without doxycycline, $n = 4$ with doxycycline). A two-tailed *t*-test *P* value is shown. **e**, H358 cells with doxycycline-inducible HA–KRAS(G12C) were treated with doxycycline (2 μg ml^{-1}) for 24 h in serum-free medium. Then, the cells were exposed to either EGF (200 ng ml^{-1}) followed by the G12Ci (10 μM), or vice versa. Cell extracts were analysed by RBD pull-down and immunoblotting. The specific effect on KRAS(G12C) was determined by the HA tag. A representative of at least two independent experiments is shown in **b**, **d**, **e**. Unless otherwise indicated, *n* denotes biological replicates.



Extended Data Fig. 10 | Rapid non-uniform adaptation to conformation-specific KRAS(G12C) inhibition. Left, at baseline, KRAS(G12C) cycles between its active (GTP-bound) and inactive (GDP-bound) conformations. Active KRAS(G12C) engages effector signalling, which regulates a transcriptional repertoire (that is, KRAS output) that is responsible for controlling various cellular functions. Middle, shortly after exposure to G12Ci treatment, KRAS(G12C) is trapped in its inactive state, and eventually the cancer cell population is sequestered in a low-KRAS output state. These cells stop proliferating and enter quiescence (G0). Right, over time, some cells undergo cell death and others adapt to the G12Ci to reactivate KRAS transcriptional output, bypassing drug-induced quiescence to resume proliferation. Our model suggests that this occurs because cells with low-KRAS output produce new KRAS(G12C) protein, which is not bound by the drug. Then, upstream signals operating in distinct cancer cell subpopulations—such as those mediated by EGFR or AURKA—maintain the new protein in its active, drug-insensitive state. By comparison, in cells in which these upstream signals are not active (or in cells in which these signals are pharmacologically inactivated), the new KRAS(G12C) spends a longer time in its inactive conformation, in which it can be bound by the drug and inhibited. This multifactorial process gives rise to a non-uniform treatment response with diverging effects across the cancer cell population.

nature research

Corresponding author(s): Lito

Last updated by author(s): 09-27-19

Reporting Summary

Nature Research wishes to improve the reproducibility of the work that we publish. This form provides structure for consistency and transparency in reporting. For further information on Nature Research policies, see Authors & Referees and the Editorial Policy Checklist.

Statistics

For all statistical analyses, confirm that the following items are present in the figure legend, table legend, main text, or Methods section.

n/a	Confirmed	
☐	☒	The exact sample size (*n*) for each experimental group/condition, given as a discrete number and unit of measurement
☐	☒	A statement on whether measurements were taken from distinct samples or whether the same sample was measured repeatedly
☐	☒	The statistical test(s) used AND whether they are one- or two-sided *Only common tests should be described solely by name; describe more complex techniques in the Methods section.*
☐	☒	A description of all covariates tested
☐	☒	A description of any assumptions or corrections, such as tests of normality and adjustment for multiple comparisons
☒	☐	A full description of the statistical parameters including central tendency (e.g. means) or other basic estimates (e.g. regression coefficient) AND variation (e.g. standard deviation) or associated estimates of uncertainty (e.g. confidence intervals)
☒	☐	For null hypothesis testing, the test statistic (e.g. *F*, *t*, *r*) with confidence intervals, effect sizes, degrees of freedom and *P* value noted *Give P values as exact values whenever suitable.*
☒	☐	For Bayesian analysis, information on the choice of priors and Markov chain Monte Carlo settings
☒	☐	For hierarchical and complex designs, identification of the appropriate level for tests and full reporting of outcomes
☒	☐	Estimates of effect sizes (e.g. Cohen's *d*, Pearson's *r*), indicating how they were calculated

Our web collection on statistics for biologists contains articles on many of the points above.

Software and code

Policy information about availability of computer code

Data collection	Single cell RNA sequencing data was carried out on a 10X genomics platform as indicated in the methods. Bulk RNA sequencing was performed on a HiSeq instrument using the approach indicated in methods.
Data analysis	The data was analyzed using available open source as described in methods. Briefly, the tools used are as follows: Cell Ranger Single Cell Software Suite, Single Cell Experiment, Scran, Scater, Seurat, ZinBwave, iGraph, Density Cluster, Slingshot, HiSat2, HTSeq, Limma, EdgeR, Mageck and Synergy Finder. All of these can be found in Bioconductor.

For manuscripts utilizing custom algorithms or software that are central to the research but not yet described in published literature, software must be made available to editors/reviewers. We strongly encourage code deposition in a community repository (e.g. GitHub). See the Nature Research guidelines for submitting code & software for further information.

Data

Policy information about availability of data

All manuscripts must include a data availability statement. This statement should provide the following information, where applicable:

- Accession codes, unique identifiers, or web links for publicly available datasets
- A list of figures that have associated raw data
- A description of any restrictions on data availability

The data are deposited in GEO with the accession code GSE137912

Field-specific reporting

Please select the one below that is the best fit for your research. If you are not sure, read the appropriate sections before making your selection.

☒ Life sciences ☐ Behavioural & social sciences ☐ Ecological, evolutionary & environmental sciences

For a reference copy of the document with all sections, see nature.com/documents/nr-reporting-summary-flat.pdf

Life sciences study design

All studies must disclose on these points even when the disclosure is negative.

Sample size	scRNAseq was performed on three models and 10,177 cells were analyzed. Biosensor experiments analyzed at least 200 cells per condition. SiRNA experiments, western blotting, viability experiemnts were performed at least twice. Each viability experiement was performed on three biological replicates. In vivo tumor growth experiments were performed on 4 or 5 biological replicates as indicated.
Data exclusions	Single cells were excluded from analysis based on pre-established criteria indicating poor quality of sequencing or doublet reads as indicated in methods. FACS experiments were gated to analyze only live cells, others were omitted.
Replication	The experimental replcates are indicsted in the figure legends. All stated replicates indicate either biological replicates (e.g. viability studies, tumor growth measurements) or independent experimental repeats (e.g. western blotting, biosensor studies)
Randomization	In vivo tumor growth experiments: implanted mice were treated in a random manner with vehicle, single agent or drug combinations. Otherwise not applicable.
Blinding	Tumor growth measurements were carried out in a non blinded manner by a technician not aware of the goals of the experiment. Otherwise not applicable.

Reporting for specific materials, systems and methods

We require information from authors about some types of materials, experimental systems and methods used in many studies. Here, indicate whether each material, system or method listed is relevant to your study. If you are not sure if a list item applies to your research, read the appropriate section before selecting a response.

Materials & experimental systems

n/a	Involved in the study
☐	☒ Antibodies
☐	☒ Eukaryotic cell lines
☒	☐ Palaeontology
☐	☒ Animals and other organisms
☒	☐ Human research participants
☒	☐ Clinical data

Methods

n/a	Involved in the study
☒	☐ ChIP-seq
☐	☒ Flow cytometry
☒	☐ MRI-based neuroimaging

Antibodies

Antibodies used	These are described in methods.
Validation	All antibodies have been validated in our previous publications (KRAS, ERK, pERK, RSK, pRSK, GAPDH, EGFR, pEGFR and CCND1) or other studies (AURKA, PLK1, CCNB1, RAN and p27).

Eukaryotic cell lines

Policy information about cell lines

Cell line source(s)	ATCC
Authentication	The cell lines were obtained from ATCC and used withing 20 passages.
Mycoplasma contamination	The cell lines used in the study tested negative for mycoplasma.
Commonly misidentified lines (See ICLAC register)	NA

Animals and other organisms

Policy information about studies involving animals; ARRIVE guidelines recommended for reporting animal research

Laboratory animals	Athymic or NSG mice as indicated in the methods.
Wild animals	NA
Field-collected samples	NA
Ethics oversight	Animal experiments were carried out under IACUC approved protocols.

Note that full information on the approval of the study protocol must also be provided in the manuscript.

Flow Cytometry

Plots

Confirm that:

☒ The axis labels state the marker and fluorochrome used (e.g. CD4-FITC).

☒ The axis scales are clearly visible. Include numbers along axes only for bottom left plot of group (a 'group' is an analysis of identical markers).

☒ All plots are contour plots with outliers or pseudocolor plots.

☒ A numerical value for number of cells or percentage (with statistics) is provided.

Methodology

Sample preparation	Cells were harvested with TrypLE Express (Gibco) and fixed for 10 min at room temperature with 4% paraformaldehyde. Samples were washed twice with PBS and filtered through 35µm mesh-caped collection tubes.
Instrument	BD LSRFortessa
Software	FCS Express 6 Flow and GraphPad Prism 7.0a software
Cell population abundance	Attached cells were assayed to determine the distribution of the G0 biosensor. The entire distribution is shown.
Gating strategy	Forward and reverse scatter parameters were used for gating. The distribution of the entire cell population is shown for the G0 biosensor. See methods.

☐ Tick this box to confirm that a figure exemplifying the gating strategy is provided in the Supplementary Information.

Article

FACT caught in the act of manipulating the nucleosome

https://doi.org/10.1038/s41586-019-1820-0

Received: 11 July 2019

Accepted: 7 November 2019

Published online: 27 November 2019

Yang Liu[1,9], Keda Zhou[1,9], Naifu Zhang[2], Hui Wei[3], Yong Zi Tan[3,4,7], Zhening Zhang[3,5,8], Bridget Carragher[3], Clinton S. Potter[3], Sheena D'Arcy[2] & Karolin Luger[1,6]*

The organization of genomic DNA into nucleosomes profoundly affects all DNA-related processes in eukaryotes. The histone chaperone known as 'facilitates chromatin transcription' (FACT[1]) (consisting of subunits SPT16 and SSRP1) promotes both disassembly and reassembly of nucleosomes during gene transcription, DNA replication and DNA repair[2]. However, the mechanism by which FACT causes these opposing outcomes is unknown. Here we report two cryo-electron-microscopic structures of human FACT in complex with partially assembled subnucleosomes, with supporting biochemical and hydrogen–deuterium exchange data. We find that FACT is engaged in extensive interactions with nucleosomal DNA and all histone variants. The large DNA-binding surface on FACT appears to be protected by the carboxy-terminal domains of both of its subunits, and this inhibition is released by interaction with H2A–H2B, allowing FACT–H2A–H2B to dock onto a complex containing DNA and histones H3 and H4 (ref. [3]). SPT16 binds nucleosomal DNA and tethers H2A–H2B through its carboxy-terminal domain by acting as a placeholder for DNA. SSRP1 also contributes to DNA binding, and can assume two conformations, depending on whether a second H2A–H2B dimer is present. Our data suggest a compelling mechanism for how FACT maintains chromatin integrity during polymerase passage, by facilitating removal of the H2A–H2B dimer, stabilizing intermediate subnucleosomal states and promoting nucleosome reassembly. Our findings reconcile discrepancies regarding the many roles of FACT and underscore the dynamic interactions between histone chaperones and nucleosomes.

Nucleosomes are the basic repeating structural units of eukaryotic chromatin, consisting of two H2A–H2B dimers and one $(H3–H4)_2$ tetramer, wrapped by 147 base pairs (bp) of DNA[4]. They represent formidable barriers to the transcription and replication machinery, and therefore must be at least partially dismantled ahead of polymerases and reassembled in their wake, to maintain the structural and regulatory functions of chromatin[5]. Histone chaperones—a diverse group of structurally unrelated proteins—facilitate these processes[6]. FACT (Fig. 1a) is an essential histone chaperone[1,7,8] (reviewed in ref. [2]) that in vitro promotes nucleosome assembly by tethering histone and DNA components, and also facilitates nucleosome disassembly by displacing H2A–H2B and promoting the partial unravelling of DNA[3,8–13]. Although the structure of each individual domain in both FACT subunits (SPT16 and SSRP1) is known[2], the structure of the intact FACT heterodimer alone or with its relevant substrate(s) has been elusive, and insight into its mechanism is therefore largely indirect.

FACT–nucleosome complex resembles a unicycle

An intermediate state of FACT-mediated nucleosome assembly has previously been identified[3]. This complex can be biochemically reconstituted by combining 79 bp of the '601' DNA prebound to a $(H3–H4)_2$ tetramer ('tetrasome'), with FACT prebound to H2A–H2B (Fig. 1b). During grid preparation for our present cryo-electron-microscopy (cryo-EM) studies, very few particles of this intermediate complex escaped being damaged by the water–air interface in conventional blotting and plunge-freezing procedures. However, adding the zwitterionic detergent CHAPS, followed by sample aspiration and rapid freezing using Chameleon, a commerical version of 'Spotiton'[14], resulted in well-dispersed particles (Extended Data Fig. 1a).

Through extensive three-dimensional classification (Extended Data Figs. 1–3 and Extended Data Table 1), we obtained two maps at 4.9 Å (complex 1) and 7.4 Å (complex 2) resolution, which on first inspection differ in the number of H2A–H2B dimers bound to

[1]Department of Biochemistry, University of Colorado at Boulder, Boulder, CO, USA. [2]Department of Chemistry and Biochemistry, The University of Texas at Dallas, Dallas, TX, USA. [3]National Resource for Automated Molecular Microscopy Simons Electron Microscopy Center, New York Structural Biology Center, New York, NY, USA. [4]Department of Physiology and Cellular Biophysics, Columbia University, New York, NY, USA. [5]Biochemistry and Molecular Biophysics Department, Columbia University Medical Center, New York, NY, USA. [6]Howard Hughes Medical Institute, Chevy Chase, MD, USA. [7]Present address: Department of Physiology and Cellular Biophysics, Columbia University, New York, NY, USA. [8]Present address: Biochemistry and Molecular Biophysics Department, Columbia University Medical Center, New York, NY, USA. [9]These authors contributed equally: Yang Liu, Keda Zhou. *e-mail: karolin.luger@colorado.edu

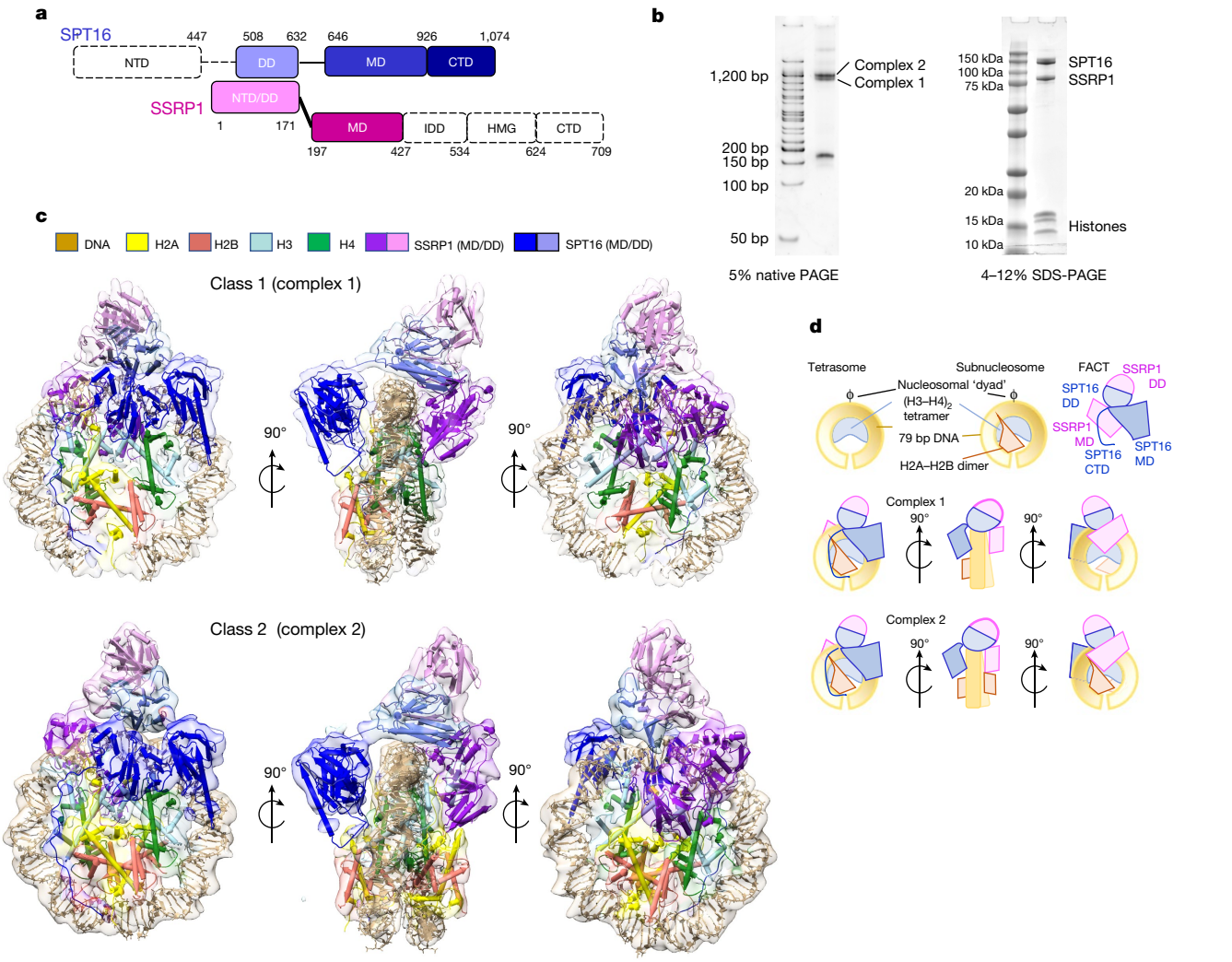


Fig. 1 | FACT forms two complexes with a partially assembled nucleosome. **a**, Domain structure of the two FACT subunits, SPT16 and SSRP1. DD, dimerization domain; CTD, C-terminal domain; HMG, HMG-box domain; IDD, intrinsically disordered domain; NTD, N-terminal domain; MD, middle domain. Domains for which no density is visible are shown in white with a dashed outline. **b**, Biochemical characterization of FACT–subnucleosome complexes by native PAGE and SDS–PAGE, stained by SYBR gold and Blazin blue, respectively. This experiment was repeated more than ten times with similar results. **c**, Ribbon diagram of DNA, histones and FACT domains fit into class 1 (top) and class 2 (bottom) electron-density maps (80% transparency) (see Methods for definitions of classes). **d**, Schematic of subnucleosomal particles and FACT (top row), and of the two complexes in the same orientations as in **c** (bottom two rows).

the $(H3–H4)_2$–DNA–FACT complex (Fig. 1c, d). In both structures, histones bind DNA and each other in a manner that is identical to their interactions in a complete nucleosome[4,15]. Although we used full-length FACT, we observed no density for the amino-terminal domain (NTD) of SPT16 and several of the C-terminal domains (CTDs) of SSRP1 (Fig. 1a).

The overall architecture of both structures resembles a unicycle, consisting of a saddle and fork formed by the FACT heterodimer, a wheel (the tetrasome) and one or two pedals (H2A–H2B dimers) (Fig. 1c, d and Supplementary Video 1). The SPT16 dimerization domain straddles nucleosomal DNA at the dyad, and the SSRP1 dimerization domain stacks on top of the SPT16 dimerization domain, together forming the saddle. The SPT16 and SSRP1 middle domains project down on either side of the tetrasome wheel and interact with DNA and histones, forming the fork. On the SPT16 side, one H2A–H2B dimer pedal is docked onto the tetrasome through a nucleosomal four-helix bundle arrangement between H2B and H4, and the SPT16 CTD wraps around the exposed H2A–H2B DNA-binding surface. The SSRP1 middle domain is located on the other side of the tetrasome wheel. Although no H2A–H2B is present on the SSRP1 side in complex 1, we observe clear electron density for a second H2A–H2B dimer in complex 2, comprising 20–30% of the intact particles (Fig. 1c, bottom). This second H2A–H2B dimer is also engaged with the tetrasome in the same manner as in a complete nucleosome, despite the absence of DNA, and is in close proximity with the rearranged SSRP1 middle domain. The presence of two complexes is consistent with biochemical data[3].

FACT has an extensive DNA-binding surface

The extensive interaction of both FACT subunits with nucleosomal DNA is surprising, as in absence of histones FACT (in its phosphorylated form) does not bind DNA (see below). We find that approximately 19 bp of DNA are contacted by FACT (Fig. 2a), burying a combined surface area of roughly 2,300 Å^2. Elements from the SPT16 dimerization domain and both middle domains contribute to DNA binding. The inner surface of the FACT saddle and fork is positively charged, and the tips of the fork are negatively charged, promoting FACT interactions with DNA and histones in the configuration of the tetrasome (Fig. 2a).

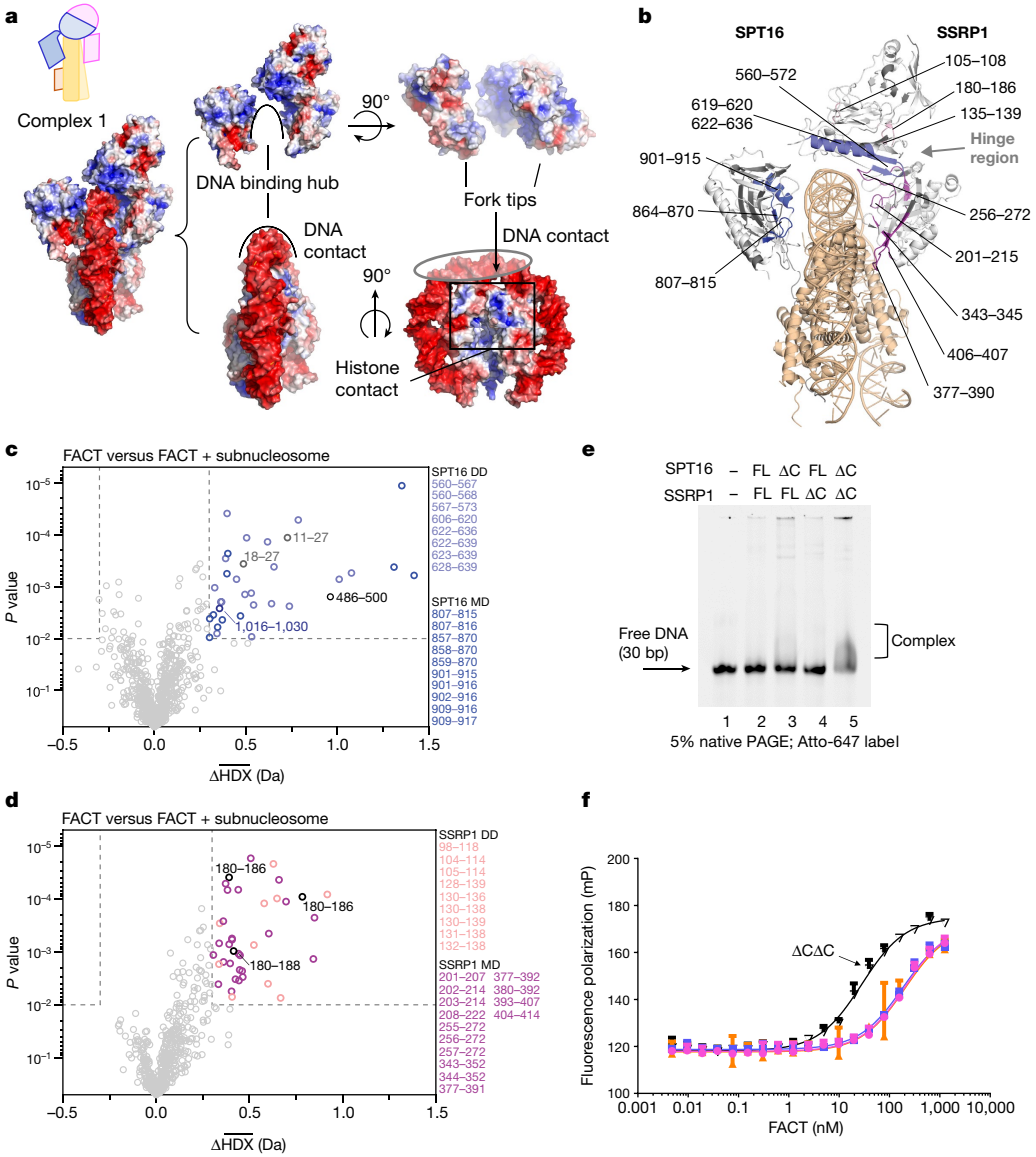


Fig. 2 | FACT makes extensive contacts with tetrasome DNA. a, Surface potential of the FACT–subnucleosome complex. Colouring changes from red for −5 kT e^{-1} to blue for +5 kT e^{-1}, generated with APBS Tools 2.1 (PyMOL 2.3.2). Histones are omitted from the top centre and right panels. **b**, Regions of significant ($P < 0.01$) changes in average HDX (ΔHDX, from **c**, **d**) are mapped onto complex 1. Notable regions are coloured according to domain location (Fig. 1a). Regions with no detectable change are in white; regions for which no peptides were recovered are in grey. The grey arrow denotes protected regions at the intersubunit interface. The subnucleosome is coloured wheat. Representative uptake plots are listed in Extended Data Fig. 5. **c**, Volcano plot comparing the average ΔHDX of SPT16 peptides in FACT and in FACT bound to subnucleosomes at all time points. Each time point was collected in triplicate ($n = 3$); the Welch's *t*-test was one-sided. **d**, Volcano plot comparing average ΔHDX of SSRP1 peptides in FACT and in FACT bound to subnucleosomes at all time points. Each time point was collected in triplicate ($n = 3$) and the Welch's *t*-test was one-sided. For **c**, **d**, dotted lines show significance cut-offs of Δ average HDX > 0.3 Da and $P < 0.01$ from a Welch's *t*-test. Insignificant peptides are in light grey, and significant peptides are coloured according to their domain location and listed. **e**, DNA binding by FACT CTD deletions. We incubated 400 nM FACT or deletion constructs with 100 nM Atto-647-labelled 30-bp DNA, and analysed the results by native PAGE, visualized by DNA fluorescence. This was repeated twice with similar results, and multiple times with DNA of different lengths. ΔC, ΔCTD; FL, full-length. **f**, Fluorescence polarization assay of FACT (0–2,500 nM) with 20 nM Alexa-488-labelled tetrasome. Dissociation constants (K_d) (in nM): full-length FACT (magenta) 204.2 ± 19 ($R^2 = 0.9723$); SPT16ΔC–SSRP1 (blue) 184.8 ± 14 ($R^2 = 0.9807$); SPT16–SSRP1ΔC (orange) 201.0 ± 50.6 ($R^2 = 0.8266$); and ΔCΔC (black) 28.15 ± 1.9 ($R^2 = 0.9843$). K_d and standard deviations were derived from four biological replicates.

Our map does not allow us to assign amino acids in FACT that directly participate in subnucleosome binding. To validate our structures, we used hydrogen–deuterium exchange (HDX) coupled to mass spectrometry, comparing deuterium uptake in FACT alone and in FACT bound to subnucleosomes (Extended Data Figs. 4, 5). On the basis of volcano plot analysis[16], we find a significant decrease in deuterium uptake (with a ΔHDX of more than 0.3 Da; $P < 0.01$) in regions of the dimerization and middle domains of SPT16 and SSRP1. These regions map primarily to the inner face of the fork that interfaces directly with DNA and histones (Fig. 2b–d). A decrease in deuterium is also observed at the interface between the SSRP1 middle domain and both dimerization domains (the hinge region) (Fig. 2b), suggesting decreased domain flexibility upon subnucleosome binding. These solution-based results are entirely consistent with the structures, and almost no changes in deuterium uptake are observed in regions outside those present in the structure.

Despite the extensive DNA interface, phosphorylated FACT purified from insect cells is unable to bind free DNA (Fig. 2e). We hypothesized

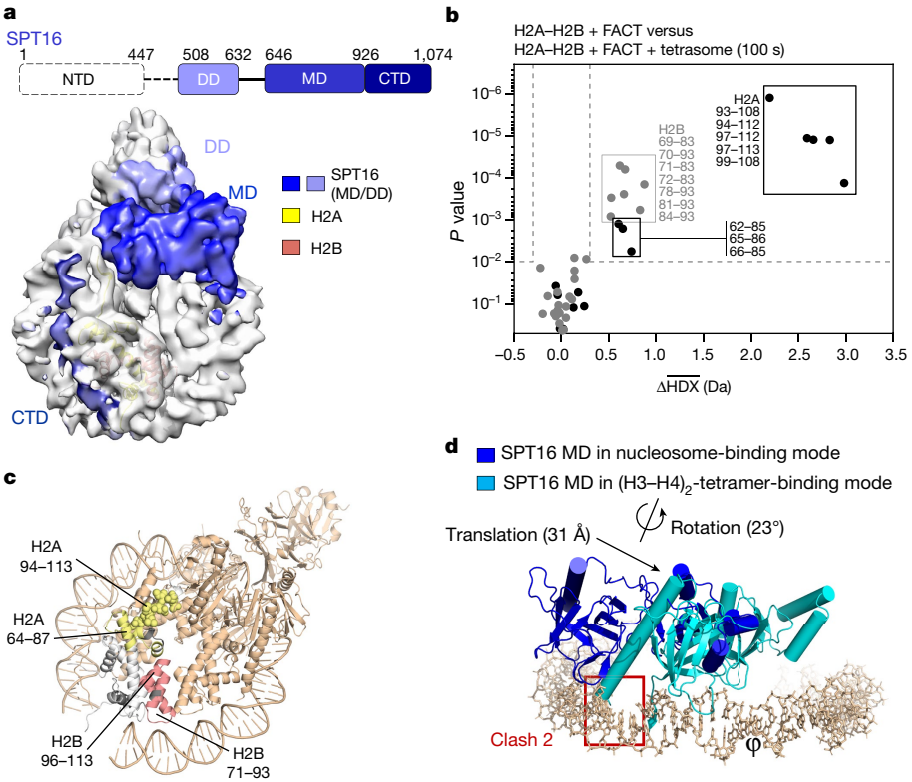


Fig. 3 | SPT16 interactions with the subnucleosome. a, All visible domains of SPT16 interact extensively with the subnucleosome. The SPT16 CTD occupies DNA-binding surface of H2A–H2B. **b**, Volcano plot comparing the average ΔHDX of H2A–H2B with FACT and H2A–H2B with FACT and tetrasomes after 100 s exposure to deuterium. Data were collected in triplicate ($n = 3$); Welch's *t*-test was one-sided. Dotted lines show significance cut-offs of Δ average HDX > 0.3 Da and $P < 0.01$ from a Welch's *t*-test. Peptides from H2A are black, and from H2B are grey. Notable peptides are listed. **c**, Regions of significant Δ average HDX (from **b**) mapped onto H2A–H2B from complex 1. Parts of the docking domain are shown in space-filling mode. For H2A–H2B, regions with an HDX change are in yellow (H2A) and red (H2B); regions with no peptide coverage are in grey. FACT and tetrasome are shown in wheat. **d**, Comparison of the SPT16 MD in complex 1, with the SPT16 MD bound to $(H3–H4)_2$ (RCSB Protein Data Bank (PDB) code 4Z2M). Only DNA and the SPT16 MD from complex 1 are shown; the two structures were aligned on the basis of the $(H3–H4)_2$ tetramer (root mean square deviation (r.m.s.d.) < 0.1 Å). φ represents the dyad (the central base pair) of the nucleosomal DNA.

that the disordered CTDs of one or both FACT subunits block DNA binding by preventing access to the concave side of the saddle, and that this autoinhibition could be relieved by H2A–H2B interaction, which is known to occur through either CTD[12]. To test this, we performed DNA-binding assays with FACT C-terminal deletion constructs (Fig. 2e and Extended Data Fig. 6a). Deletion of either the SPT16 CTD or the SSRP1 CTD alone had no effect, but deletion of both simultaneously enabled FACT to shift free DNA on a native gel. DNA interaction was also facilitated (to a lesser degree) when full-length FACT was prebound to an H2A–H2B dimer (Extended Data Fig. 6b). It has previously been found that FACT does not produce a gel shift with tetrasome[3]. To test whether this is also due to autoinhibition by FACT CTDs, we used fluorescence polarization binding assays. As was the case for DNA binding, deletion of both CTDs resulted in an enhanced affinity of FACT for the tetrasome (Fig. 2f).

SPT16 C-terminal tail shields H2A–H2B

The acidic SPT16 CTD (pI of 4.3) wraps around the DNA-binding surface of H2A–H2B (Figs. 1c, 3a). The precise SPT16 residues involved cannot be identified from the density or the HDX owing to the low coverage in that region (Extended Data Fig. 4a), but we observe a slight yet significant protection of residues 1016–1030 ($P < 0.01$) (Extended Data Fig. 4c). H2A–H2B interfaces can be identified by comparing the HDX of H2A–H2B that is bound by FACT, with H2A–H2B in the FACT-bound subnucleosome (Fig. 3b and Extended Data Fig. 7). Direct comparison with free H2A–H2B is convoluted by the global stabilization of histone folds upon protein interaction[17]. Volcano plot analysis shows a significant decrease in deuterium uptake (ΔHDX is more than 0.3 Da; $P < 0.01$) in H2A–H2B regions involved in nucleosome formation. In H2B the decrease is localized to its DNA-binding L2 loop and interface with H4, whereas in H2A it is localized to the docking domain that binds H3 αN and the SPT16 middle domain (see below) and to the L2 loop (Fig. 3c). Notably, H2A L2 binds the SPT16 CTD rather than DNA, supporting our interpretation that the SPT16 CTD acts the part of DNA[12] and might counteract the 'foreign DNA invasion' observed in transcription through nucleosomes[18,19].

SPT16 has two binding modes on $(H3–H4)_2$

A crystal structure of the SPT16 middle domain with the $(H3–H4)_2$ tetramer reveals two regions of contact, neither of which is possible in the context of the subnucleosome[10]. Our structures confirm the prediction[10] that one region of interaction is occluded by H3 αN and the H2A-docking domain, and the other is occupied by nucleosomal DNA. Consequently, the SPT16 middle domain (and with it the entire FACT complex) moves and rotates substantially by roughly 31 Å and 23° when the substrate transitions from free $(H3–H4)_2$ to tetrasome (Fig. 3d). This frees up space for the H2A-docking domain, while the SPT16 middle domain binds to the nearby DNA (interface 1) (Extended Data Fig. 8). It also displaces a segment of FACT that in the absence of DNA covers the DNA-binding L1 loop of histone H4. Instead, this FACT region is now near the H4 N-terminal tail and H3 α1 (interface

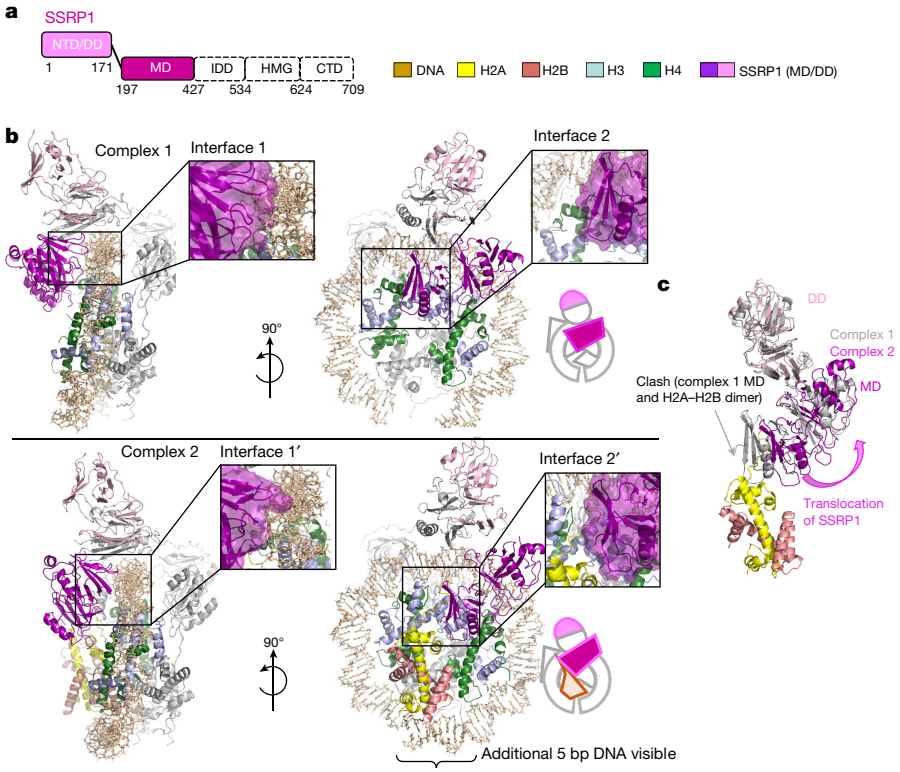


Fig. 4 | SSRP1 can assume two different positions on the subnucleosome, depending on the presence or absence of a second H2A–H2B dimer. a, The domain structure of SSRP1. **b**, Comparison of binding interfaces between SSRP1 and the sunucleosome in complex 1 (top) and complex 2 (bottom). Interfaces are enlarged in insets. The molecular surface of SSRP1 is shown by the main-chain trace. **c**, The SSRP1 MD and DD in complexes 1 and 2 undergo substantial rearrangement on the subnucleosome surface when superimposing the two complexes via the $(H3–H4)_2$ tetramer. The SSRP1 MD in complex 1 would clash with the H2A-docking domain.

2) (Extended Data Fig. 8). Overall, this massive rearrangement allows SPT16 middle domain to make interactions with nucleosomal DNA while also forging new interactions with histones—thereby stabilizing a subnucleosomal particle. Of note, the previously demonstrated interaction between the SPT16 middle domain and a fused H2A–H2B is not observed[12,20].

SSRP1 can exclude or hold a second H2A–H2B

The most substantial difference between our two structures is on the SSRP1 side of the complex: they differ in the absence (complex 1) or presence (complex 2) of a second H2A–H2B dimer, probably representing two stages of the assembly in equilibrium (Figs. 1b–d, 4 and Extended Data Fig. 9). In both structures, the SSRP1 middle domain (consisting of two pleckstrin homology (PH) domains[21]) interacts with both dimerization domains, and the PH1 domain makes numerous contacts with the DNA (interface 1 in Fig. 4b). Although the relative orientation of PH1 with respect to the DNA is slightly different in the two structures, the same structural elements are likely to be engaged with DNA (Fig. 4a, b; interfaces 1 and 1′). In complex 1, the SSRP1 PH2 domain is positioned across the $(H3–H4)_2$ four-helix bundle and on top of H3 α2, thereby precluding the placement of the second H2A–H2B and H3 αN in its rightful position in the nucleosome (interface 2 in Fig. 4b). In complex 2, a second H2A–H2B has successfully docked onto the histone core, facilitated by interactions with the PH2 domain of SSRP1 middle domain (interface 2′ in Fig. 4b). H3 αN and an additional 5 bp of DNA (which binds the L1L2 interface of the second H2A–H2B dimer) are clearly visible in the electron-density map for complex 2, but are absent in complex 1. The relocation of the SSRP1 PH2 domain on the tetrasome surface by 10.9 Å and 9.5° (upon addition of the second H2A–H2B dimer) (Fig. 4c) is partially transmitted to the dimerization domains, and also results in a subtle movement of the SPT16 middle domain (Supplementary Video 2).

Implications for FACT mechanism

The structures reported here and previously[10], together with HDX data, highlight a plasticity of FACT interactions (Supplementary Videos 2 and 3) that is likely to be required for its diverse functions. In the absence of DNA, FACT maintains the tetrameric conformation of $(H3–H4)_2$ during early steps of nucleosome (re)assembly. In this mode, FACT might also bind H2A–H2B dimers through the SPT16 CTD. DNA then binds the tetramer and displaces FACT, which assumes its position on top of nucleosomal DNA while forging new contacts with H3–H4. This promotes incorporation of the tethered H2A–H2B by freeing up H3–H4 to engage its H2A-docking domain. FACT maintains interactions with the H2A–H2B DNA-binding surface through the SPT16 CTD, thereby stabilizing the subnucleosome. A similar interaction between the SPT16 CTD and H2A–H2B has recently been observed, although no other FACT domains were visible in that structure[22].

Our structures also suggest a potential mechanism for FACT-mediated nucleosome disassembly[11,13] through a reversal of these steps. When the DNA at superhelix location −1 is peeled off from H3–H4 by DNA or RNA polymerase[18], the SPT16 middle domain protects the newly exposed sites on the histones on the proximal side of the nucleosome, allowing FACT to contact the H3–H4 four-helix bundle, and resulting in the displacement of the H2A-docking domain (Supplementary Video 3) to facilitate the passage of polymerase. Similarly, the SSRP1 middle domain can also switch between two binding modes to accommodate either addition or destabilization of H2A–H2B on the distal side of the nucleosome. This mechanism is consistent with observations of histone occupancy in an Spt16 or Ssrp1 knockdown in *Drosophila* cells[23].

Both processes might be facilitated by the HMG domain of SSRP1[24] and other domains not visible in our structure, and this is the topic of ongoing investigations.

Online content

Any methods, additional references, Nature Research reporting summaries, source data, extended data, supplementary information, acknowledgements, peer review information; details of author contributions and competing interests; and statements of data and code availability are available at https://doi.org/10.1038/s41586-019-1820-0.

1. Orphanides, G., LeRoy, G., Chang, C. H., Luse, D. S. & Reinberg, D. FACT, a factor that facilitates transcript elongation through nucleosomes. *Cell* **92**, 105–116 (1998).
2. Gurova, K., Chang, H. W., Valieva, M. E., Sandlesh, P. & Studitsky, V. M. Structure and function of the histone chaperone FACT—resolving FACTual issues. *Biochim. Biophys. Acta. Gene Regul. Mech.* **1861**, 892–904 (2018).
3. Wang, T. et al. The histone chaperone FACT modulates nucleosome structure by tethering its components. *Life Sci Alliance* **1**, e201800107 (2018).
4. Luger, K., Mäder, A. W., Richmond, R. K., Sargent, D. F. & Richmond, T. J. Crystal structure of the nucleosome core particle at 2.8 Å resolution. *Nature* **389**, 251–260 (1997).
5. Lai, W. K. M. & Pugh, B. F. Understanding nucleosome dynamics and their links to gene expression and DNA replication. *Nat. Rev. Mol. Cell Biol.* **18**, 548–562 (2017).
6. Das, C., Tyler, J. K. & Churchill, M. E. The histone shuffle: histone chaperones in an energetic dance. *Trends Biochem. Sci.* **35**, 476–489 (2010).
7. Belotserkovskaya, R. et al. FACT facilitates transcription-dependent nucleosome alteration. *Science* **301**, 1090–1093 (2003).
8. Hsieh, F. K. et al. Histone chaperone FACT action during transcription through chromatin by RNA polymerase II. *Proc. Natl Acad. Sci. USA* **110**, 7654–7659 (2013).
9. Winkler, D. D., Muthurajan, U. M., Hieb, A. R. & Luger, K. Histone chaperone FACT coordinates nucleosome interaction through multiple synergistic binding events. *J. Biol. Chem.* **286**, 41883–41892 (2011).
10. Tsunaka, Y., Fujiwara, Y., Oyama, T., Hirose, S. & Morikawa, K. Integrated molecular mechanism directing nucleosome reorganization by human FACT. *Genes Dev.* **30**, 673–686 (2016).
11. Valieva, M. E. et al. Large-scale ATP-independent nucleosome unfolding by a histone chaperone. *Nat. Struct. Mol. Biol.* **23**, 1111–1116 (2016).
12. Kemble, D. J., McCullough, L. L., Whitby, F. G., Formosa, T. & Hill, C. P. FACT disrupts nucleosome structure by binding H2A-H2B with conserved peptide motifs. *Mol. Cell* **60**, 294–306 (2015).
13. Chen, P. et al. Functions of FACT in breaking the nucleosome and maintaining its integrity at the single-nucleosome level. *Mol. Cell* **71**, 284–293 (2018).
14. Dandey, V. P. et al. Spotiton: new features and applications. *J. Struct. Biol.* **202**, 161–169 (2018).
15. Tachiwana, H. et al. Structural basis of instability of the nucleosome containing a testis-specific histone variant, human H3T. *Proc. Natl Acad. Sci. USA* **107**, 10454–10459 (2010).
16. Hageman, T. S. & Weis, D. D. Reliable identification of significant differences in differential hydrogen exchange-mass spectrometry measurements using a hybrid significance testing approach. *Anal. Chem.* **91**, 8008–8016 (2019).
17. D'Arcy, S. et al. Chaperone Nap1 shields histone surfaces used in a nucleosome and can put H2A-H2B in an unconventional tetrameric form. *Mol. Cell* **51**, 662–677 (2013).
18. Kujirai, T. et al. Structural basis of the nucleosome transition during RNA polymerase II passage. *Science* **362**, 595–598 (2018).
19. Ehara, H. et al. Structural insight into nucleosome transcription by RNA polymerase II with elongation factors. *Science* **363**, 744–747 (2019).
20. Hondele, M. et al. Structural basis of histone H2A–H2B recognition by the essential chaperone FACT. *Nature* **499**, 111–114 (2013).
21. Zhang, W. et al. Crystal structure of human SSRP1 middle domain reveals a role in DNA binding. *Sci. Rep.* **5**, 18688 (2015).
22. Mayanagi, K. et al. Structural visualization of key steps in nucleosome reorganization by human FACT. *Sci. Rep.* **9**, 10183 (2019).
23. Ramachandran, S., Ahmad, K. & Henikoff, S. Transcription and remodeling produce asymmetrically unwrapped nucleosomal intermediates. *Mol. Cell* **68**, 1038–1053 (2017).
24. McCullough, L. L. et al. Functional roles of the DNA-binding HMGB domain in the histone chaperone FACT in nucleosome reorganization. *J. Biol. Chem.* **293**, 6121–6133 (2018).

Publisher's note Springer Nature remains neutral with regard to jurisdictional claims in published maps and institutional affiliations.

© The Author(s), under exclusive licence to Springer Nature Limited 2019

Methods

Expression and purification of FACT and mutant FACT

We infected Sf9 cells with *Autographa californica* multiple nucleopolyhedrovirus (AcMNPV) to express either wild-type human FACT or FACT with C-terminal deletions (SPT16ΔC(Δ934–1,047)–SSRP1, SPT16–SSRP1ΔC(Δ625–709) or SPT16ΔC(Δ934–1,047)–SSRP1ΔC(Δ625-709)). We purified proteins as previously described[3], with minor modifications. We fused a ×6 histidine (His) tag to the N terminus of SPT16, and purified FACT over a 5-ml prepacked HisTrap HP column, followed by a 5-ml prepacked HiTrap Q HP column. The last step was a Superdex 200 10/300 size-exclusion column run in 200 mM NaCl, 20 mM Tris-Cl (pH 8.0), 0.01% CHAPS, 0.01% octylglucoside (OG), 5% glycerol and 1 mM tris(2-carboxyethyl)phosphine (TCEP). Columns were purchased from GE Healthcare.

Complex formation

We expressed and purified recombinant human histones as previously described[25]. We premixed 1 μM FACT with equimolar amounts of refolded H2A–H2B for 10 min at room temperature, and then added an equimolar amount of $(H3–H4)_2$ tetrasome reconstituted onto 79 bp 601 DNA[26] in 20 mM Tris-Cl (pH 8.0), 150 mM NaCl, 1 mM EDTA and 1 mM TCEP[25]. After a 30-min incubation, the complex was visualized with 5% native PAGE.

Binding assays

We mixed 400 nM FACT (wild type or deletion constructs) with 100 nM of Atto-647-labelled 30 bp DNA in 20 mM Tris-Cl (pH 8.0), 100 mM NaCl, 1 mM EDTA and 1 mM TCEP. After incubation for 10 min in room temperature, DNA shifting was analysed by 5% native PAGE.

To measure FACT–tetrasome interactions, we mixed varying amounts of FACT (up to 2,500 nM) with 20 nM Alexa-488-labelled H3–H4 tetrasome in 20 mM Tris-Cl (pH 8.0), 0.01% CHAPS, 0.01% NP40, 100 mM NaCl, 1 mM EDTA and 1 mM TCEP. The reaction was incubated in a 384-well microplate for 10 min at room temperature and fluorescence polarization data (obtained on a CLARIOstar microplate reader from BMG Labtech) were analysed by Graphpad Prism. Four replicates were done. Absolute K_d values obtained with labelled tetrasome have to be taken with caution because of known tetrasome heterogeneity between batches. Nevertheless, comparative values obtained with the same batch are reproducible. Original data can be found in Supplementary Table 1.

Single-particle cryo-EM sample vitrification

Reconstituted complexes were concentrated to 7–10 μM using an Amicon Ultra-4 centrifugal filter (Ultracel 50K, Millipore). Fresh detergent (CHAPS, 0.25–0.5%) was added before grid preparation. To minimize sample interaction with the air–water interface and to keep the complex intact[27], we vitrified the complex using a commercial prototype (from TTP Labtech) of the Chameleon robot based on the Spotiton robot[14,28,29]. The time between the sample being spotted onto the nanowire grid[30] and vitrification into liquid ethane was 133 ms. Grids were plasma-cleaned (Gatan Solarus) for 5 s using an H_2/O_2 mixture before vitrification. The robot chamber was operated at room temperature and roughly 80% humidity in the sample and plunging area.

Data acquisition

We recorded images on a Titan Krios electron microscope (FEI) equipped with a caesium corrector and a K2 summit direct detector with a quantum energy filter (Gatan) at 1.0961 Å per pixel in counting mode, using the Leginon software package[31]. Pixel size was calibrated in-house using a proteasome test sample. We used an energy-filter slit width of 30 eV during the collection, aligned automatically every hour using Leginon. The first data collection was performed using a dose of roughly 66.37 $e^- Å^{-2}$ across 50 frames (200 ms per frame) at a dose rate of roughly 8.0 $e^- pix^{-1} s^{-1}$, using a set defocus range of −1.9 μm to −2.0 μm. The second data collection was performed using a dose of roughly 63.61 $e^- Å^{-2}$ across 50 frames (200 ms per frame) at a dose rate of around 7.6 $e^- pix^{-1} s^{-1}$, using a set defocus range of −1.5 μm to −2.5 μm. We used a 100-μm-aperture objective. We recorded a total of 8,318 micrographs over two separate data-collection sessions using an image beam shift data collection strategy[32].

Data processing

Data from the two sessions were processed separately and combined towards the end of the processing pipeline. For the first dataset, movie frames were aligned using MotionCor2 (ref. [33]) with 5-by-5 patches and a *B*-factor of 100 using the Appion software package[34]. We carried out micrograph contrast transfer function (CTF) estimation using CTFFind4 (ref. [35]). We used DoG picker[36], a template-free particle-picking algorithm, to pick 744,552 particles (box size of 240, binned by 2) that were extracted in Relion 3.0 (refs. [37–39]) and transferred into CryoSPARC 2 (ref. [40]) for two-dimensional (2D) classification. We discarded 2D class averages that were clearly contaminated or showed no features. We then ran cryo-EM single-particle ab initio reconstruction and classification (CryoSPARC) using 2 classes iteratively for 5 rounds, keeping particles in the better class for the next iteration, producing a final stack of 17,369 particles. These particles were processed using nonuniform refinement to produce a map of around 6 Å resolution. We used the Euler angles and shifts to re-extract the particles in Relion 3.0, followed by CTF refinement and Bayesian polishing[41]. The particles were brought back into CryoSPARC 2 for nonuniform refinement. We then used improved Euler angles and shifts to re-extract the particles in Relion 3.0 for two more rounds of Bayesian polishing. The final nonuniform refinement of 17,369 particles (extracted using a 256 box size binned by a 1.28 to 200 box size) resulted in a map at 4.4 Å resolution based on the Fourier shell correlation (FSC) 0.143 criterion[42,43].

For the second dataset, movie frames were aligned using patch motion in CryoSPARC 2. CTF was estimated in a patch manner and particles were picked with the CryoSPARC 2 blob picker. A total of 522,050 picked particles were then extracted (256 box size binned by 2) and 2D classification was performed. Four rounds of iterative CryoSPARC ab initio using three classes were used to clean up the dataset—the particles in the best class after each round were carried forward to the next iteration. The remaining 8,399 particles were refined to around 8 Å resolution using nonuniform refinement. The Euler angles and shifts were then used to re-extract the particles in Relion 3.0, followed by CTF refinement and Bayesian polishing[41]. The particles were brought back into CryoSPARC 2.0 for nonuniform refinement. Improved Euler angles and shifts were then used to re-extract the particles in Relion 3.0 for two more rounds of Bayesian polishing. The final nonuniform refinement of 8,399 particles (extracted using 256 box size binned by 1.28 to 200 box size) resulted in a map at 7.4 Å resolution based on the FSC 0.143 criterion[42,43].

We carried out heterogeneous refinement using four classes for these particles. We identified two distinct classes, differing by the presence or absence of one of the histone dimers. Class 1, with 10,317 particles and without the second histone H2A–H2B dimer, resulted in a map at 6.6 Å resolution using nonuniform refinement; class 2, with 4,212 particles and the second H2A–H2B dimer, resulted in a map at 7.3 Å resolution using nonuniform refinement.

We then combined both datasets in CryoSPARC 2.0 and carried out a three-class ab initio run to sort out heterogeneity in the dataset. We identified two distinct classes, differing by the presence or absence of one of the histone dimers. Class 1, with 16,317 particles and without the second histone H2A–H2B dimer, resulted in a map at 4.9 Å resolution using nonuniform refinement; class 2, with 6,990 particles and the second H2A–H2B dimer, resulted in a map at 7.4 Å resolution using nonuniform refinement. We used the locally sharpened maps from CryoSPARC 2.0 for subsequent model building and analysis. The three-dimensional (3D) FSC and sphericity of the maps were calculated using the 3DFSC server[44].

All conversions between Relion and CryoSPARC were performed using D. Asarnow's pyem script (personal communication; https://github.com/asarnow/pyem).

Model building and refinement

The initial models were built by fitting published high-resolution crystal structures or homology models into the final 3D electron maps in University of California at San Francisco (UCSF) Chimera[45]. The crystal structures (with PDB identification code) used for initial modelling are: 3LZ0 ('601' Widom DNA), 3AFA (human histone core), 4Z2M (SPT16 middle domain) and 4IFS (SSRP1 middle domain). The initial model for dimerization domains was a combination of a crystal structure (5UMR, SSRP1; amino acids 1–100) and a homology model based on the crystal structure of the *Chaetomium thermophilum* Spt16 Pob3N heterodimer (4KHB) using SWISS-MODEL[46]. The initial models were then manually edited using COOT[47]. We used Poly-UNK to fit the visible density without assigning amino acids. We refined the models using real-space refinement in PHENIX[48].

HDX-MS

We prepared 7 µM H2A–H2B, FACT, FACT–H2A–H2B and FACT–subnucleosome in 20 mM Tris-HCl, 150 mM NaCl, 1 mM TCEP, pH 7.5 at 25 °C. Samples were diluted 1/6 with the same buffer containing H_2O for controls (pH_{read} = 7.5 at 25 °C) or D_2O (final D_2O concentration of 83% (v/v) with pH_{read} = 7.1 at 25 °C). After 10 s, 10^2 s, 10^3 s and 10^4 s, samples were mixed 1/1 with 1% formic acid, 3.84 M guanidinium chloride, pH 1.75 to give a final pH of 2.3 at 0 °C, and flash-frozen in liquid nitrogen for storage at −80 °C. Samples were thawed and liquid chromatography–mass spectrometry (LC–MS) performed using a Waters HDX manger and SYNAPT G2-Si Q-Tof. Three technical replicates of each sample were analysed in a random order. Samples were digested on-line using *Sus scrofa* pepsin A (Waters Enzymate BEH) at 15 °C, and peptides were trapped on a C4 pre-column (Waters Acquity UPLC Protein BEH C4) for 3 min at 100 µl min^{-1} and 1 °C. The liquid-chromatography buffer was 0.1% formic acid. Peptides were separated over a C18 column (Waters Acquity UPLC BEH) and eluted with a linear 3–40% (v/v) acetonitrile gradient for 7 min at 40 µl min^{-1} and 1 °C. Raw data from control samples were processed by PLGS (Waters Protein Lynx Global Server 3.0.2) using a database containing *Sus scrofa* pepsin A and *Homo sapiens* SSRP1, SPT16, H2A and H2B. In PLGS, the minimum fragment ion matches per peptide was 3, and methionine oxidation and serine/threonine/tyrosine phosphorylation were allowed. The low and elevated energy thresholds were 250 and 50 counts, respectively, and the overall intensity threshold was 750 counts. Labelled data were analysed in DynamX 3.0 with 0.3 products per amino acid and one consecutive product.

All mass-spectrometry data were acquired using positive-ion mode in either high-definition mass spectrometry (HDMS) or $HDMS^E$ mode, the latter being used to collect both low-energy (6 V) and high-energy (ramping 22–44 V) peptide-fragmentation data for peptide identification. HDMS mode was used to collect low-energy ion data for all deuterated samples. All samples were acquired in resolution mode. Capillary voltage was set to 2.8 kV for the sample sprayer. Desolvation gas was set to 650 l h^{-1} at 175 °C. The source temperature was set to 80 °C. Cone and nebulizer gas was flowed at 90 l h^{-1} and 6.5 bar, respectively. The sampling cone and source offset were both set to 30 V. Data were acquired at a scan time of 0.4 s with a m/z range of 100–2,000. Mass correction was done using [Glu1]–fibrinopeptide B as a reference mass. We include as Supplementary Information a summary of our HDX data (Supplementary Table 2) as well as the HDX data (Supplementary Table 3), as per consensus guidelines[49].

Sample size and randomization

No statistical methods were used to predetermine sample size. The experiments were not randomized and the investigators were not blinded to allocation during experiments and outcome assessment.

Reporting summary

Further information on research design is available in the Nature Research Reporting Summary linked to this paper.

Data availability

Raw HDX-MS data are available in Supplementary Tables 2 and 3 for Figs. 2b–d, 3b, c. Atomic coordinates and cryo-EM maps have been deposited in the PDB and Electron Microscopy Data Bank (EMDB) under accession codes EMDB-20840, PDB 6UPK and EMDB-20841, PDB 6UPL. Raw cryoEM images have been deposited in the Electron Microscopy Public Image Archive (EMPIAR-10333).

25. Dyer, P. N. et al. Reconstitution of nucleosome core particles from recombinant histones and DNA. *Methods Enzymol.* **375**, 23–44 (2004).
26. Thåström, A. et al. Sequence motifs and free energies of selected natural and non-natural nucleosome positioning DNA sequences. *J. Mol. Biol.* **288**, 213–229 (1999).
27. Noble, A. J. et al. Routine single particle cryoEM sample and grid characterization by tomography. *eLife* **7**, e34257 (2018).
28. Razinkov, I. et al. A new method for vitrifying samples for cryoEM. *J. Struct. Biol.* **195**, 190–198 (2016).
29. Jain, T., Sheehan, P., Crum, J., Carragher, B. & Potter, C. S. Spotiton: a prototype for an integrated inkjet dispense and vitrification system for cryo-TEM. *J. Struct. Biol.* **179**, 68–75 (2012).
30. Wei, H. et al. Optimizing "self-wicking" nanowire grids. *J. Struct. Biol.* **202**, 170–174 (2018).
31. Suloway, C. et al. Automated molecular microscopy: the new Leginon system. *J. Struct. Biol.* **151**, 41–60 (2005).
32. Cheng, A. et al. High resolution single particle cryo-electron microscopy using beam-image shift. *J. Struct. Biol.* **204**, 270–275 (2018).
33. Zheng, S. Q. et al. MotionCor2: anisotropic correction of beam-induced motion for improved cryo-electron microscopy. *Nat. Methods* **14**, 331–332 (2017).
34. Lander, G. C. et al. Appion: an integrated, database-driven pipeline to facilitate EM image processing. *J. Struct. Biol.* **166**, 95–102 (2009)
35. Rohou, A. & Grigorieff, N. CTFFIND4: fast and accurate defocus estimation from electron micrographs. *J. Struct. Biol.* **192**, 216–221 (2015).
36. Voss, N. R., Yoshioka, C. K., Radermacher, M., Potter, C. S. & Carragher, B. DoG Picker and TiltPicker: software tools to facilitate particle selection in single particle electron microscopy. *J. Struct. Biol.* **166**, 205–213 (2009).
37. Scheres, S. H. RELION: implementation of a Bayesian approach to cryo-EM structure determination. *J. Struct. Biol.* **180**, 519–530 (2012).
38. Kimanius, D., Forsberg, B. O., Scheres, S. H. & Lindahl, E. Accelerated cryo-EM structure determination with parallelisation using GPUs in RELION-2. *eLife* **5**, e18722 (2016).
39. Zivanov, J. et al. New tools for automated high-resolution cryo-EM structure determination in RELION-3. *eLife* **7**, e42166 (2018).
40. Punjani, A., Rubinstein, J. L., Fleet, D. J. & Brubaker, M. A. cryoSPARC: algorithms for rapid unsupervised cryo-EM structure determination. *Nat. Methods* **14**, 290–296 (2017).
41. Zivanov, J., Nakane, T. & Scheres, S. H. W. A Bayesian approach to beam-induced motion correction in cryo-EM single-particle analysis. *IUCrJ* **6**, 5–17 (2019).
42. Rosenthal, P. B. & Henderson, R. Optimal determination of particle orientation, absolute hand, and contrast loss in single-particle electron cryomicroscopy. *J. Mol. Biol.* **333**, 721–745 (2003).
43. Scheres, S. H. & Chen, S. Prevention of overfitting in cryo-EM structure determination. *Nat. Methods* **9**, 853–854 (2012).
44. Tan, Y. Z. et al. Addressing preferred specimen orientation in single-particle cryo-EM through tilting. *Nat. Methods* **14**, 793–796 (2017).
45. Pettersen, E. F. et al. UCSF Chimera—a visualization system for exploratory research and analysis. *J. Comput. Chem.* **25**, 1605–1612 (2004).
46. Waterhouse, A. et al. SWISS-MODEL: homology modelling of protein structures and complexes. *Nucleic Acids Res.* **46** (W1), W296–W303 (2018).
47. Emsley, P., Lohkamp, B., Scott, W. G. & Cowtan, K. Features and development of Coot. *Acta Crystallogr. D* **66**, 486–501 (2010).
48. Adams, P. D. et al. PHENIX: a comprehensive Python-based system for macromolecular structure solution. *Acta Crystallogr. D* **66**, 213–221 (2010).
49. Masson, G. R. et al. Recommendations for performing, interpreting and reporting hydrogen deuterium exchange mass spectrometry (HDX-MS) experiments. *Nat. Methods* **16**, 595–602 (2019).
50. Wlodawer, A., Li, M. & Dauter, Z. High-resolution cryo-EM maps and models: a crystallographer's perspective. *Structure* **25**, 1589–1597 (2017).

Acknowledgements This work was supported by the Howard Hughes Medical Institute (Y.L., K.Z. and K.L.), by start-up funds (S.D.) and by the National Institutes of Health (NIH) National Institute of General Medical Sciences (NIGMS) (GM133751 to S.D.). Screening of the initial cryo-EM condition was performed at the CU Boulder Electron Microscopy Service, with help from C. Page and G. P. Morgan. Some of this work was performed at the Simons Electron Microscopy Center and National Resource for Automated Molecular Microscopy, located at the New York Structural Biology Center, supported by grants from the Simons Foundation (SF349247) and the NIH NIGMS (GM103310), with additional support from Agouron Institute (F00316) and the NIH (OD019994). We thank D. Reinberg for assistance in initial stages of the project.

Author contributions Y.L. cloned and expressed all FACT constructs with the help of K.Z. K.Z. and Y.L. optimized sample and grid preparation and performed extensive screening. H.W. and Z.Z. (with B.C. and C.S.P.) optimized the conditions for Chameleon/Spotiton vitrification. H.W. collected the data. Y.Z.T., H.W. and K.Z. analysed the electron-microscopy data and obtained the electron-density maps, with input from B.C. and C.S.P. K.Z. modelled and refined the structures. K.Z., Y.L. and K.L. interpreted electron-microscopy structures and drafted the manuscript. Y.L. designed and performed all biochemical assays, with input from K.Z. and K.L. N.Z. (with input from Y.L.) designed HDX experiments, with the help of S.D. and K.L. N.Z. and S.D. performed HDX experiments and analysed HDX data. Y.L., K.Z., S.D. and K.L. wrote the manuscript and prepared the figures.

Competing interests B.C. and S.C.P. have an intellectual property licensing arrangement with TTP Labtech Ltd for the Chameleon sample vitrification instrument.

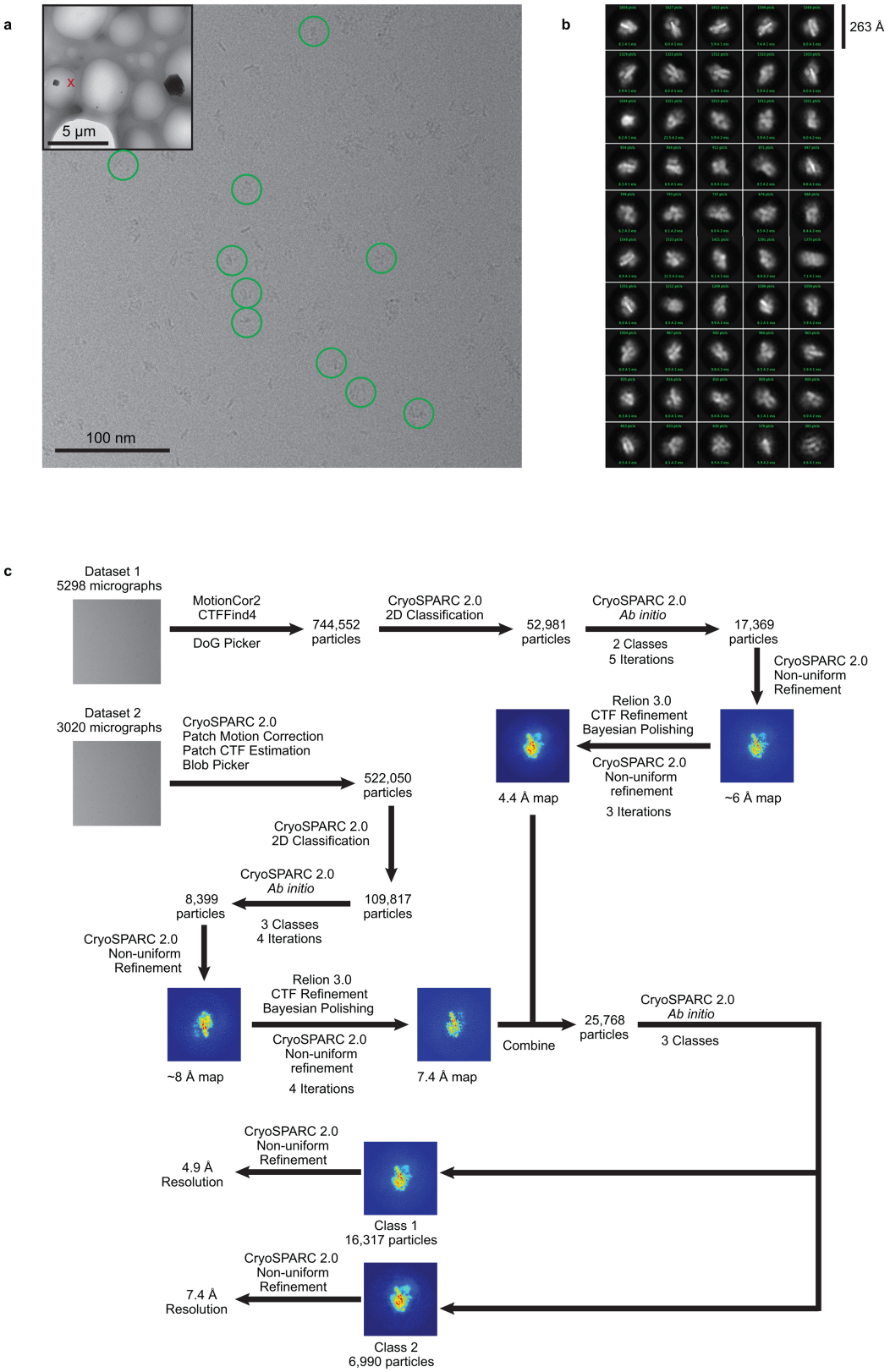
Additional information

Supplementary information is available for this paper at https://doi.org/10.1038/s41586-019-1820-0.

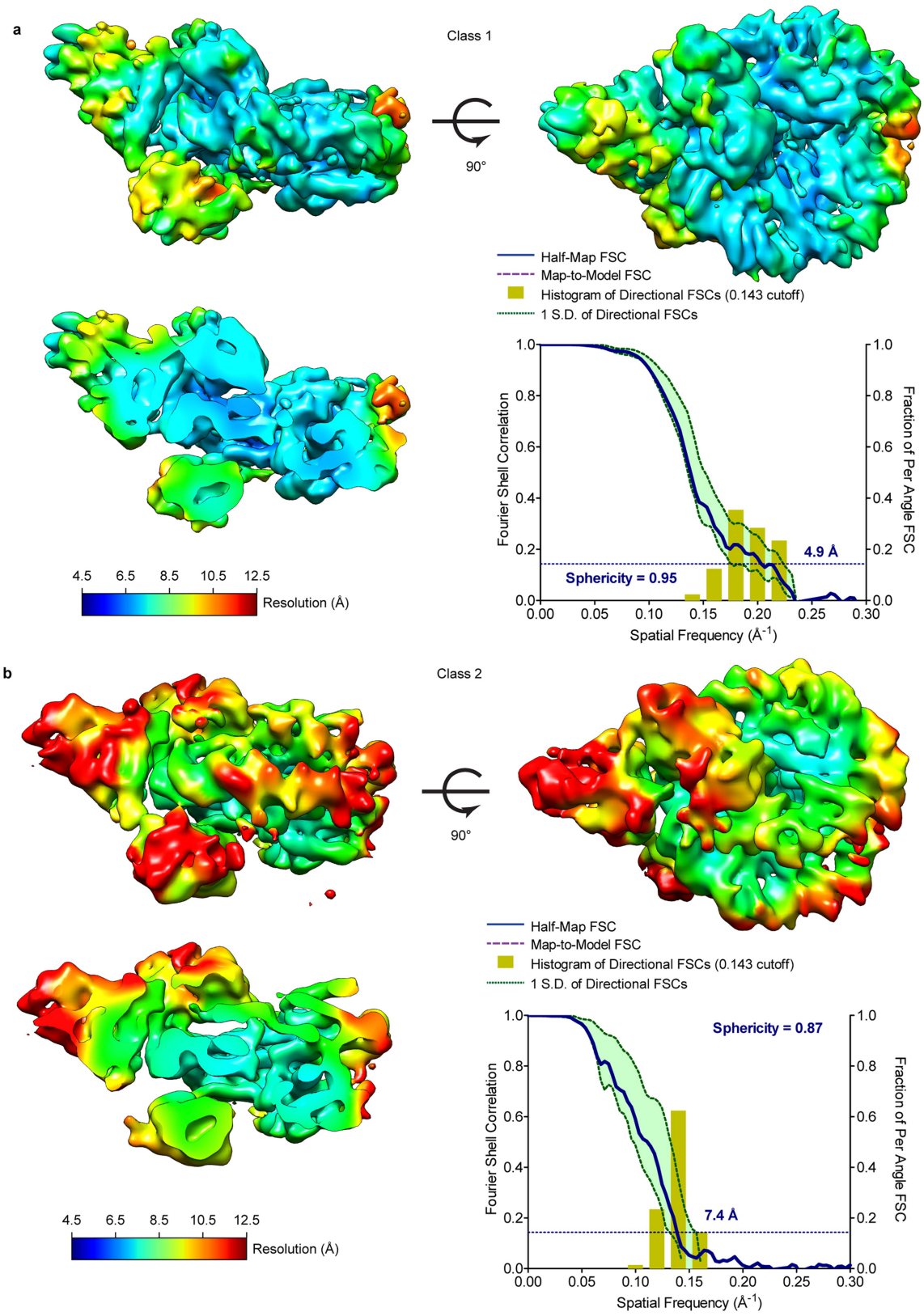
Correspondence and requests for materials should be addressed to K.L.

Peer review information *Nature* thanks Tim Formosa, Karl-Peter Hopfner, Hitoshi Kurumizaka and the other, anonymous, reviewer(s) for their contribution to the peer review of this work.

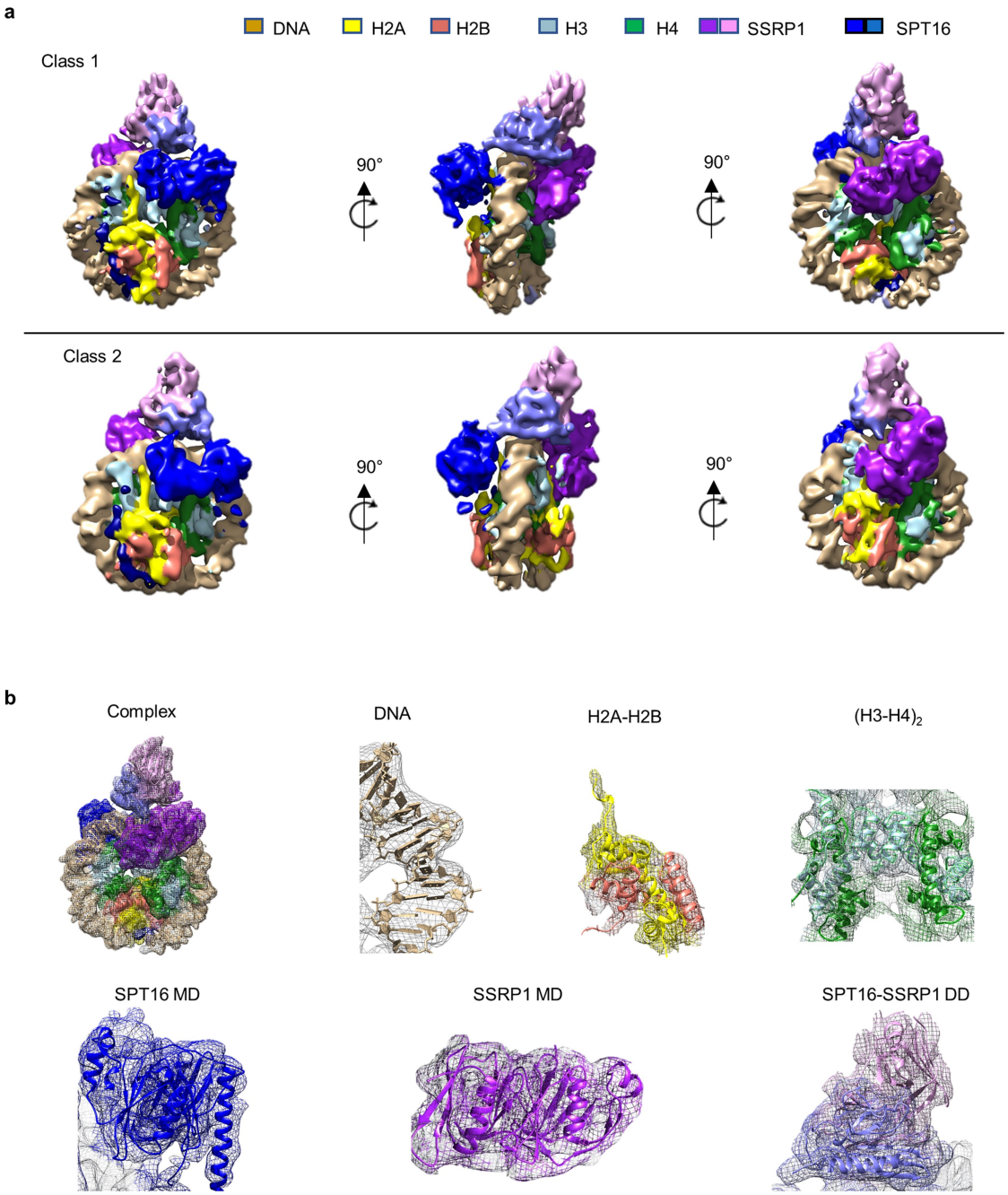
Reprints and permissions information is available at http://www.nature.com/reprints.



Extended Data Fig. 1 | Analysis of electron-microscopic data. **a**, Representative micrograph of particles containing 79 bp of 601 DNA prebound to a $(H3–H4)_2$ tetramer ('tetrasome'), with FACT prebound to H2A–H2B. The inset is a lower-magnification view showing the holy substrate. The red X marks the location of this micrograph in the low-magnification map. The particles in the final picking are circled in green. This experiment was repeated with six independent grids in two Krios sessions, with similar results. **b**, Two-dimensional class averages generated from the dataset obtained from CryoSPARC 2.0. **c**, Flowchart showing the data-processing strategy.

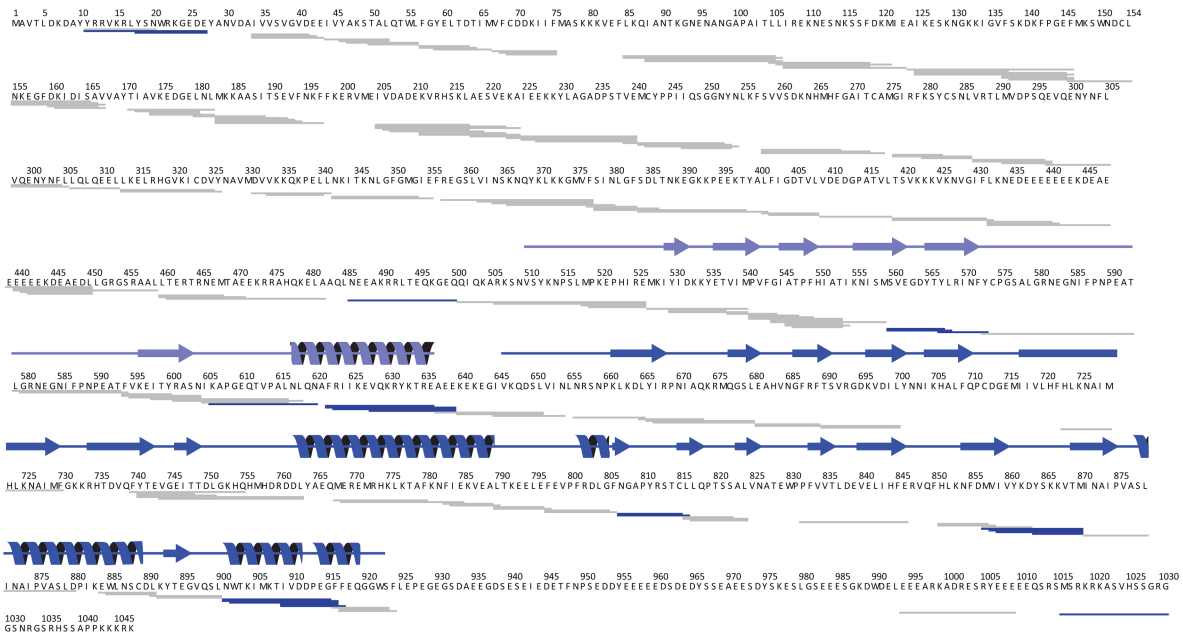


Extended Data Fig. 2 | Validation of electron-microscopic data. a, Local-resolution map and FSC curve for class 1 (complex 1). Local resolution was calculated in CryoSPARC 2.0 and 3DFSC was calculated using the 3DFSC server. **b**, Local-resolution map and FSC curve for class 2 (complex 2). Local resolution was calculated as in **a**.



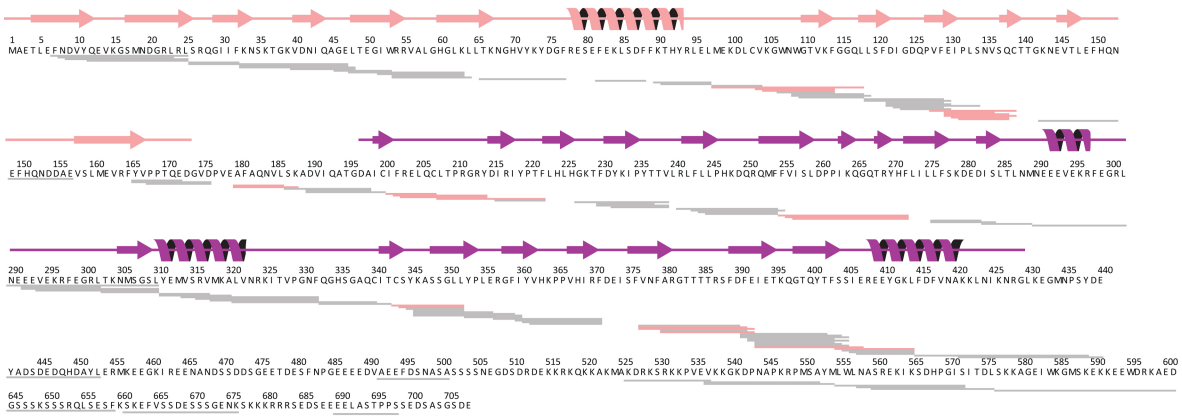
Extended Data Fig. 3 | Electron density and models. a, Density maps for class 1 and 2 particles in three orthogonal orientations. The subunits and domains are colour-coded as indicated. **b**, Representative views of models fit into electron-density maps for FACT–subnucleosome complex 1, DNA, H2A–H2B, $(H3–H4)_2$, SPT16 middle domain, SSRP1 MD and SPT16–SSRP1 dimerization domains.

a SPT16 Coverage Map



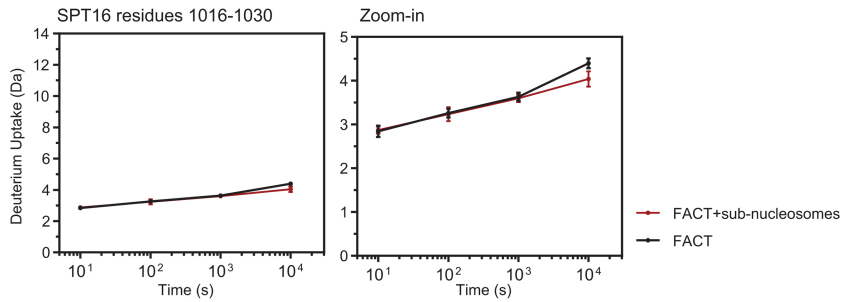
Residues with significant ΔHDX between FACT and FACT+sub-nucleosomes (Fig. 2b):
21-27, 486-500, 560-572, 619-620, 622-636, 807-815, 864-870, 901-915, 1016-1030.

b SSRP1 Coverage Map

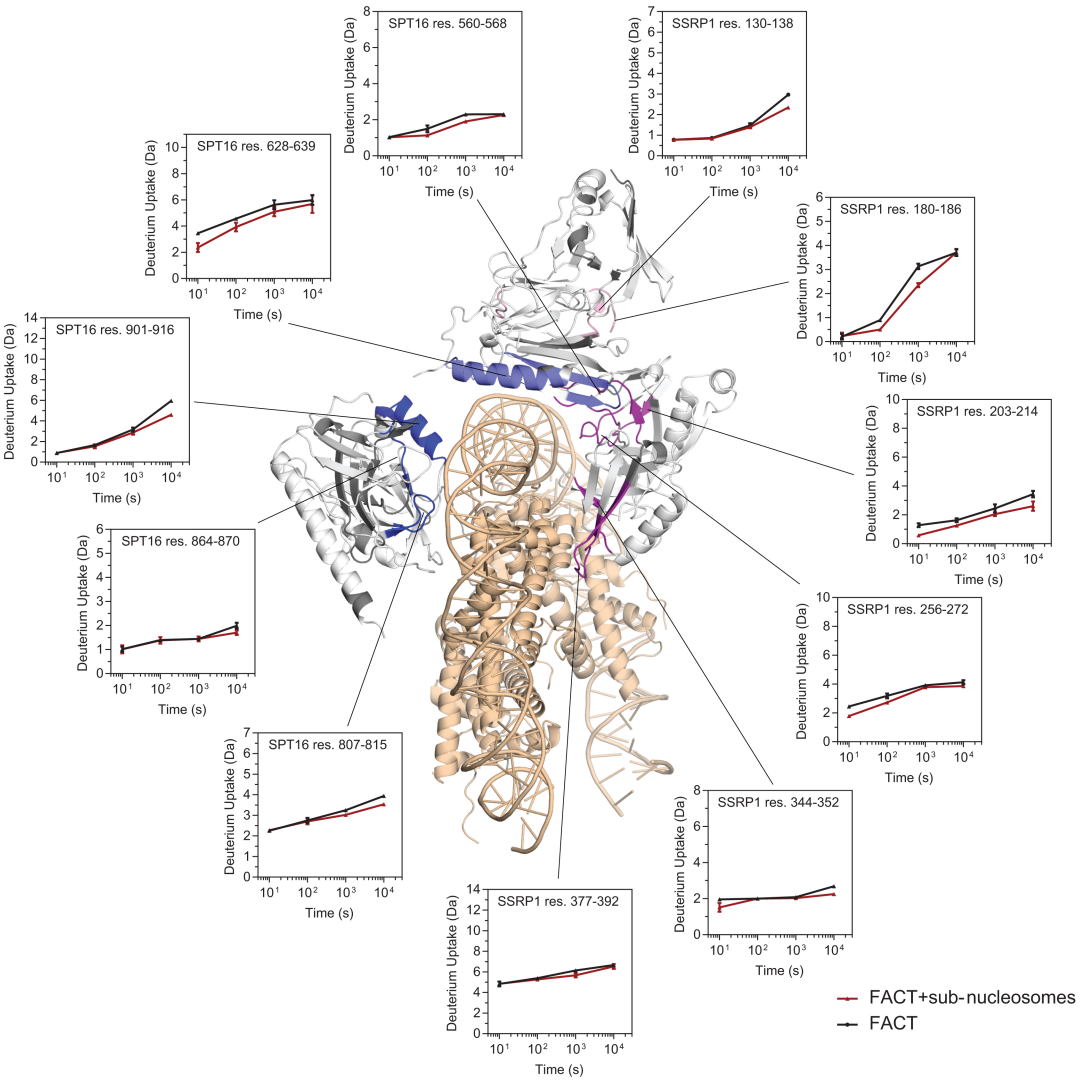


Residues with significant ΔHDX between FACT and FACT+sub-nucleosomes (Fig. 2c):
105-108, 135-139, 180-186, 201-215, 256-272, 343-345, 377-390, 406-407.

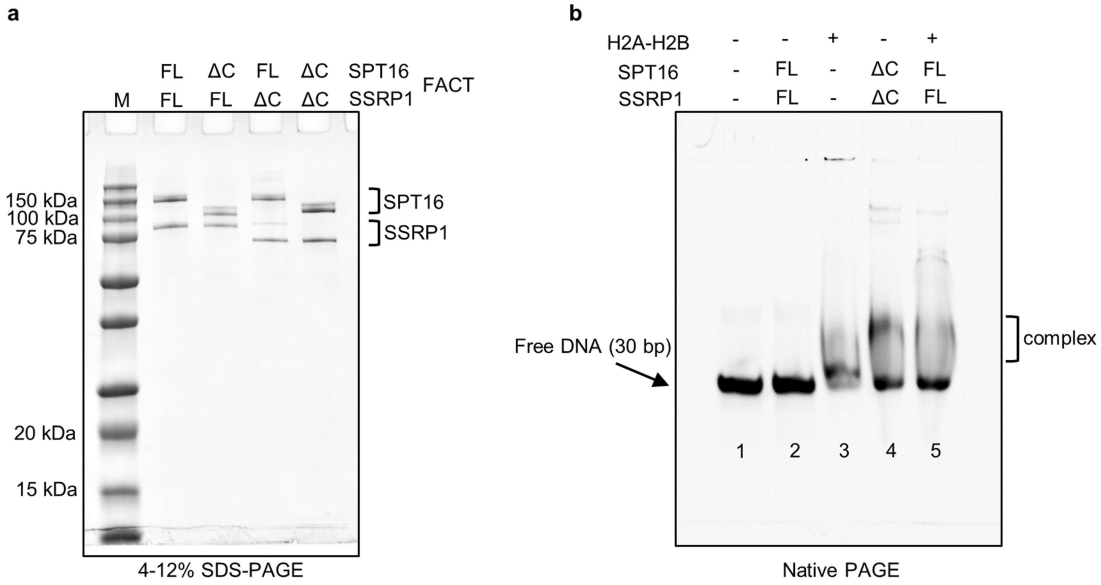
c



Extended Data Fig. 4 | Coverage maps from FACT HDX experiments. **a**, **b**, SPT16 and SSRP1 coverage maps from HDX experiments. Each rectangle represents one peptide, repeatably monitored through all time points and samples. Significant peptides ($P < 0.01$) (Fig. 2b) are coloured and listed at the bottom of each panel. Secondary-structure elements from the structures of the published domains that were used for fitting are also shown. **c**, Deuterium uptake plot for SPT16 residues 1016–1030, showing FACT (black) and FACT with subnucleosomes (red). Each data point is the average of 3 replicates with error bars of ± 2 s.d.

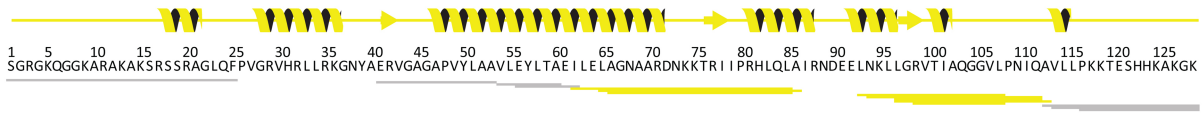


Extended Data Fig. 5 | Changes in deuterium uptake mapped onto complex 1. Deuterium-uptake plots are included for example peptides that show a significant change ($P < 0.01$) (Fig. 2c, d) when comparing FACT (black) with FACT plus subnucleosomes (red). Each data point is the average of 3 replicates, with error bars of ± 2 s.d. The subnucleosome is shown in wheat. For FACT, regions with no detectable change are in white; regions with a change are coloured according to their domain location (Fig. 1a); and regions with no peptide coverage are in grey.



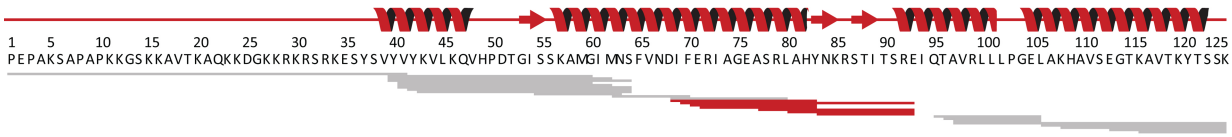
Extended Data Fig. 6 | Effects of FACT deletion mutants on DNA binding. **a**, Full-length (FL) FACT and FACT CTD deletions (SPT16ΔC–SSRP1, SPT16–SSRP1ΔC or SPT16ΔC–SSRP1ΔC) were purified from Sf9 cells and visualized on 4–12% SDS–PAGE, stained with Blazin blue. This particular gel was run only once, although proteins were purified and analysed by SDS–PAGE four times. **b**, As for Fig. 2e, except that full-length FACT was pre-incubated with an equimolar amount of H2A–H2B dimer at 400 nM. The pre-incubation of wild-type FACT with H2A–H2B dimer has a similar effect on DNA binding as FACT ΔCTDs. Visualized by Atto N (647). The experiment was done twice with similar results.

a H2A Coverage Map



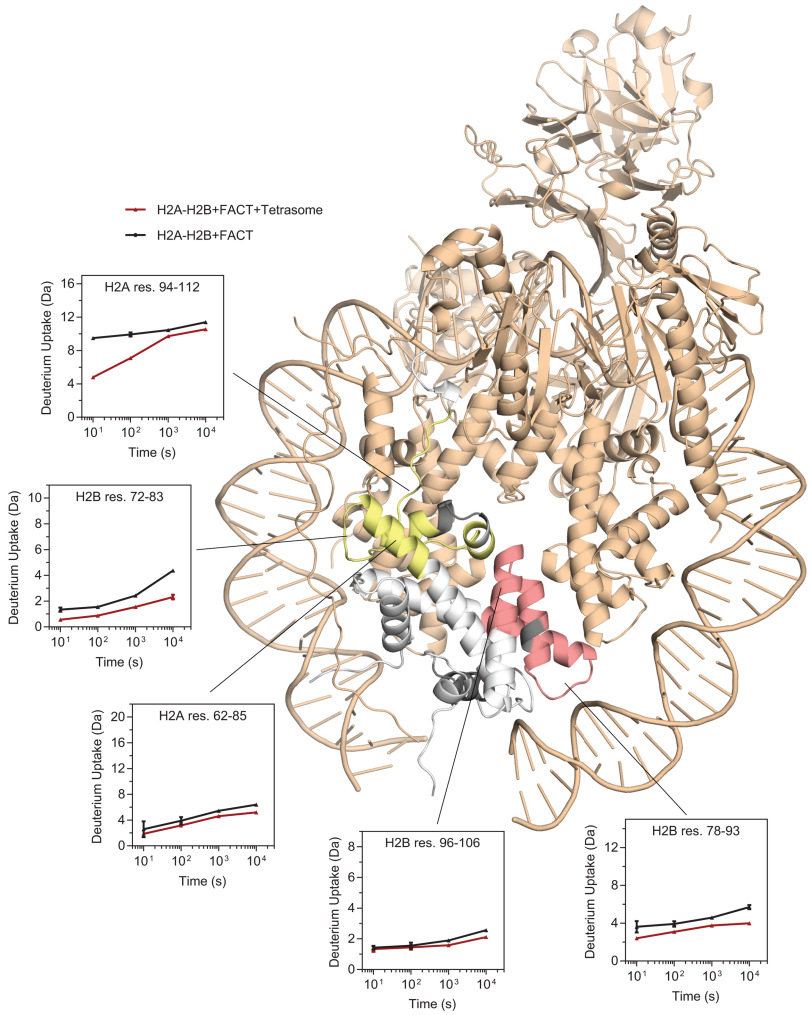
Residues with significant ΔHDX between H2A-H2B-FACT and H2A-H2B+FACT+tetrasome at 100 s (Fig. 3b): 64-87, 94-113.

b H2B Coverage Map

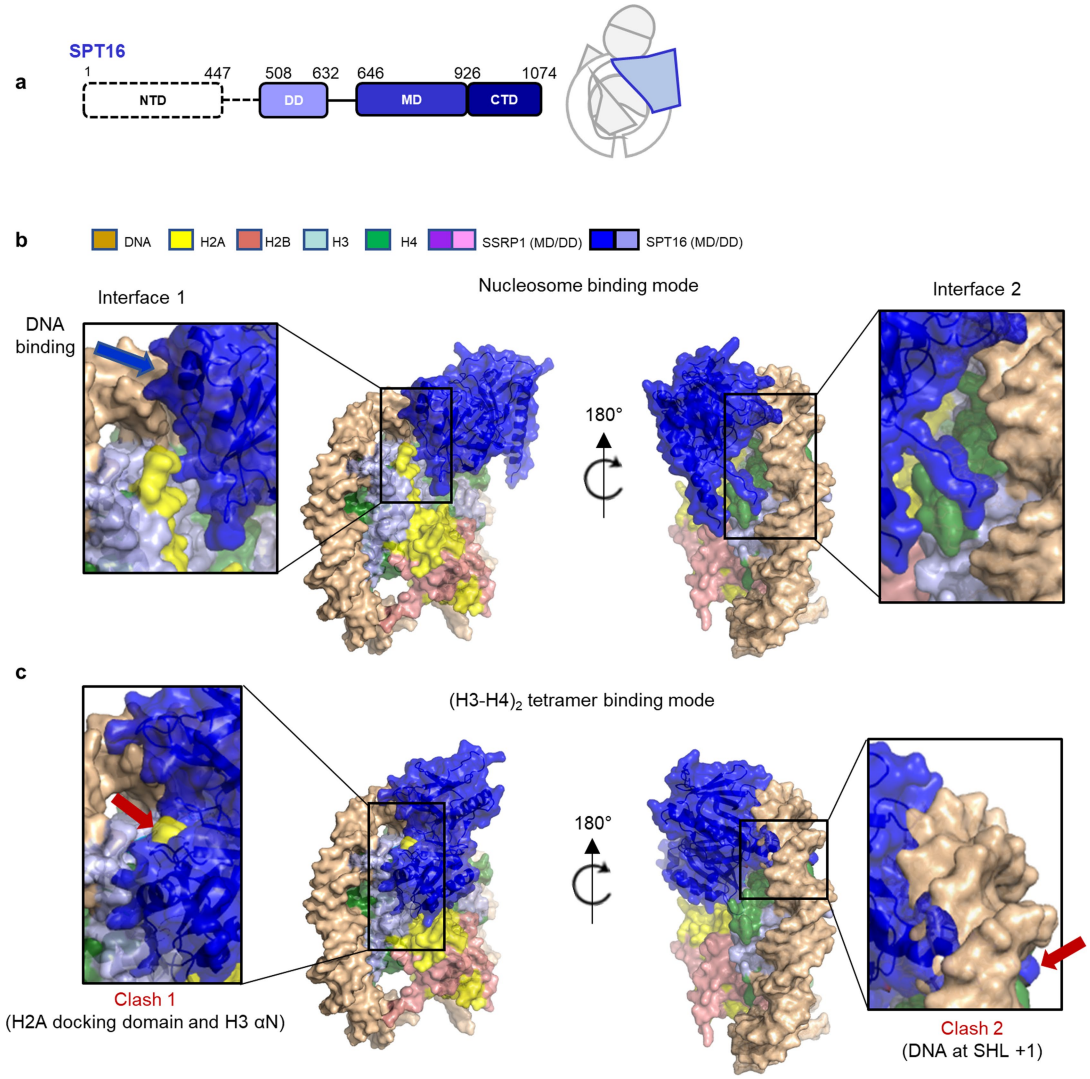


Residues with significant ΔHDX between FACT and FACT+sub-nucleosomes at 100 s (Fig. 3b): 71-93. Note residues 96-113 shows a change at ≥1000 s only.

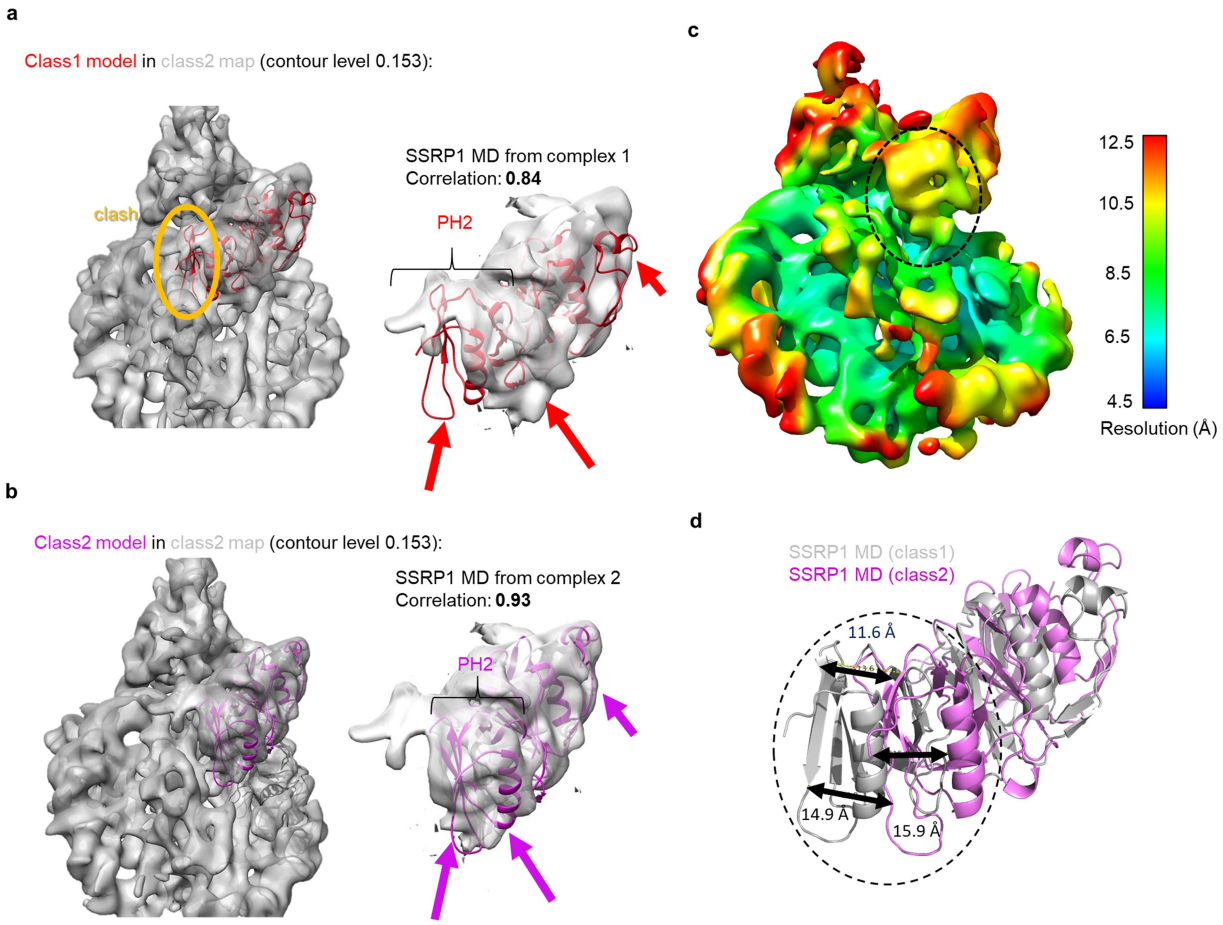
c



Extended Data Fig. 7 | Coverage maps from H2A–H2B HDX experiments. **a**, **b**, H2A and H2B coverage maps from HDX experiments. Each rectangle shows one peptide repeatably monitored through all time points and samples. Significant peptides ($P < 0.01$) (Fig. 3b) are coloured and listed. Secondary-structure elements are shown. **c**, Deuterium-uptake plots for example peptides that show a significant change ($P < 0.01$) (Fig. 3c) when comparing H2A–H2B with FACT (black) and H2A–H2B with FACT plus tetrasomes (red). Each data point is the average of 3 replicates with error bars of ± 2 s.d. FACT, H3–H4 and DNA are wheat. For H2A–H2B, regions with no detectable change are white; regions with a change are in yellow for H2A and red for H2B; and regions with no peptide coverage are in grey.



Extended Data Fig. 8 | Interactions between H3–H4 and the SPT16 middle domain are incompatible with FACT interactions made with the subnucleosome. a, Domain structure of SPT16, and cartoon showing the overall architecture. **b**, Interactions between H3–H4 and the SPT16 MD (PDB code 4Z2M) are incompatible with FACT interactions made with the subnucleosome. These structures are for complex 1, which shows only the SPT16 MD. Two sites of interaction with the subnucleosome are outlined (interface 1, near the H2A-docking domain and nearby DNA; interface 2, near the H4 N-tail and DNA). **c**, The presence of DNA and the H2A–H2B dimer completely occludes interactions between the SPT16 MD and the $(H3–H4)_2$ tetramer in the 4Z2M structure (clashes 1 and 2, indicated by red arrows).



Extended Data Fig. 9 | Model-to-map fitting for the class 2 map of the SSRP1 MD. a, The class 1 model of the SSRP1 MD (red ribbon) does not fit into the class 2 map (grey). The contour level of the map is 0.153. Left, the entire map. The orange oval highlights how the class 1 model overlaps with the density assigned to H2A–H2B. Right, close-up of the fit between the class 1 model and class 2 density for the SSRP1 MD. Arrows highlight problematic fits; a substantial part of the PH2 domain is outside of the density, and other parts of the density are empty. The correlation between model 1 (from class 1) and map 2 for the entire SSRP1 MD is 0.84 (calculated using UCSF Chimera). **b**, The class 2 model of the SSRP1 MD (purple ribbon) fits into the class 2 density map (grey). The contour level of the map is 0.153. Left, the entire map; no clashes are identified. Right, close-up of the fit between the model and density for the SSRP1 MD. Arrows indicate the same parts of the model or map as in **a**. The correlation between model 2 (from class 2) and map 2 for the entire SSRP1 MD is 0.93 (calculated using UCSF Chimera). **c**, Local-resolution heat map for the class 2 map. The resolution of the highlighted region (the PH2 domain from the SSRP1 MD at interface 2) is between 9 Å and 10 Å. The contour level is 0.177. **d**, Relative movement of the highlighted region (the PH2 domain of the SSRP1 MD at interface 2) between class 1 and 2 models. The distances or movements of the same amino acids in the two models (dotted ovals in **c**, **d**) are indicated.

Extended Data Table 1 | Summary of cryoEM data collection and refinement

Cryo-EM data collection, refinement and validation statistics

	Class 1 (EMDB-20840) (PDB 6UPK)	Class 2 (EMDB-20841) (PDB 6UPL)
Data collection and processing		
Magnification	105,000	
Voltage (kV)	300	
Electron exposure (e–/Å^2)	70	
Defocus range (μm)	1.5-2.5	
Pixel size (Å)	1.0961	
Symmetry imposed	C1	C1
Initial particle images (no.)	162,798	
Final particle images (no.)	16,317	6990
Map resolution (Å)	4.9	7.4
FSC threshold	0.143	
Map resolution range (Å)	4.9 – 12.3	6.5 – 20.0
Directional resolution range (Å)	4.4 – 6.7	6.2 – 9.4
Sphericity of 3DFSC	0.95	0.87
Refinement		
Initial model used (PDB code)	3LZ0,3AFA,4Z2M,4IFS	
Model resolution (Å)	5.25	7.3
FSC threshold	0.143	0.143
Model resolution range (Å)	4.8-7.1	6.6-7.9
Map sharpening *B* factor (Å^2)	151.0	382.7
Model composition		
Non-hydrogen atoms	13861	15882
Protein residues	1368	1589
Nucleotide	144	158
B factors (Å^2)*		
Protein	524	408
Nucleotide	470	411
R.m.s. deviations		
Bond lengths (Å)	0.006	0.005
Bond angles (°)	1.101	1.090
Validation		
MolProbity score	2.26	2.25
Clashscore	20.32	21.65
Poor rotamers (%)	0.00	0.23
Ramachandran plot		
Favored (%)	92.85	93.55
Allowed (%)	7.15	6.32
Disallowed (%)	0.00	0.13

To obtain the best fit between model and map, we applied real-space refinement of atomic displacement parameters (ADPs, or *B*-factors) in PHENIX. The *B*-factors increase substantially during ADP real-space refinement. These numbers do not represent the same physical
meaning of *B*-factors as in crystallography[50].

nature research

Corresponding author(s): Karolin Luger

Last updated by author(s): Oct 16, 2019

Reporting Summary

Nature Research wishes to improve the reproducibility of the work that we publish. This form provides structure for consistency and transparency in reporting. For further information on Nature Research policies, see Authors & Referees and the Editorial Policy Checklist .

Statistics

For all statistical analyses, confirm that the following items are present in the figure legend, table legend, main text, or Methods section.

n/a	Confirmed	
☐	☒	The exact sample size (*n*) for each experimental group/condition, given as a discrete number and unit of measurement
☐	☒	A statement on whether measurements were taken from distinct samples or whether the same sample was measured repeatedly
☒	☐	The statistical test(s) used AND whether they are one- or two-sided *Only common tests should be described solely by name; describe more complex techniques in the Methods section.*
☒	☐	A description of all covariates tested
☒	☐	A description of any assumptions or corrections, such as tests of normality and adjustment for multiple comparisons
☐	☒	A full description of the statistical parameters including central tendency (e.g. means) or other basic estimates (e.g. regression coefficient) AND variation (e.g. standard deviation) or associated estimates of uncertainty (e.g. confidence intervals)
☐	☒	For null hypothesis testing, the test statistic (e.g. *F*, *t*, *r*) with confidence intervals, effect sizes, degrees of freedom and *P* value noted *Give P values as exact values whenever suitable.*
☒	☐	For Bayesian analysis, information on the choice of priors and Markov chain Monte Carlo settings
☒	☐	For hierarchical and complex designs, identification of the appropriate level for tests and full reporting of outcomes
☒	☐	Estimates of effect sizes (e.g. Cohen's *d*, Pearson's *r*), indicating how they were calculated

Our web collection on statistics for biologists contains articles on many of the points above.

Software and code

Policy information about availability of computer code

Data collection	CryoEM data was collected by Leginon software package. HDX data was collected by HDMS and HDMSE modes in MassLynx v4.1. Florescence polarization assay data was collected by CLARIOstar.
Data analysis	CryoEM data analysis was performed by MotionCor2 (1.2.1), CTFFind4 (4.1), DoG picker (1), Appion (3.2), Relion 3.0, cryoSPARC (2), Daniel Asarnow's pyem script (unpublished, https://github.com/asarnow/pyem), UCSF Chimera 1.11.2, PHENIX 1.12-2829, Coot 0.8.9 and SWISS-MODEL. Electrostatic surfaces were calculated with Pymol 2.3.2 (Apbs Tools 2.1). HDX data analysis was carried out by Waters Protein Lynx Global SERVER 3.0.2 and DynamX 3.0. Florescence polarization data was analyzed by Graphpad Prism 7.

For manuscripts utilizing custom algorithms or software that are central to the research but not yet described in published literature, software must be made available to editors/reviewers. We strongly encourage code deposition in a community repository (e.g. GitHub). See the Nature Research guidelines for submitting code & software for further information.

Data

Policy information about availability of data

All manuscripts must include a data availability statement. This statement should provide the following information, where applicable:

- Accession codes, unique identifiers, or web links for publicly available datasets
- A list of figures that have associated raw data
- A description of any restrictions on data availability

HDX-MS raw data is available in SI tables 2 and 3. Atomic coordinates and cryo-EM maps have been deposited in the Protein Data Bank (PDB) and Electron Microscopy Data Bank (EMDB) under accession codes xxxx and xxxx, according to policies.

Field-specific reporting

Please select the one below that is the best fit for your research. If you are not sure, read the appropriate sections before making your selection.

☒ Life sciences ☐ Behavioural & social sciences ☐ Ecological, evolutionary & environmental sciences

For a reference copy of the document with all sections, see nature.com/documents/nr-reporting-summary-flat.pdf

Life sciences study design

All studies must disclose on these points even when the disclosure is negative.

Sample size	In binding assays (EMSA and FP), the concentrations for substrates and titrated proteins were determined based on the initial estimation of binding affinity from preliminary data. Number of biological replicates are listed in the figure legends
Data exclusions	Low quality data from cryoEM was excluded in Relion and cryoSPARC to reach high resolution with criteria pre-established in Relion and cryoSPARC. No data was excluded in both HDX and binding assays.
Replication	All experiments were performed with multiple biological replicates, indicated in figure legends. All of them are reproducible.
Randomization	This is not relevant in this study because protein structural data , HDX data and binding assays (EMSA and FP) could not be randomized.
Blinding	The investigators were not blinded on this study. No bias was introduced during data collection and data analysis in any assay in this study.

Reporting for specific materials, systems and methods

We require information from authors about some types of materials, experimental systems and methods used in many studies. Here, indicate whether each material, system or method listed is relevant to your study. If you are not sure if a list item applies to your research, read the appropriate section before selecting a response.

Materials & experimental systems

n/a	Involved in the study
☒	☐ Antibodies
☐	☒ Eukaryotic cell lines
☒	☐ Palaeontology
☒	☐ Animals and other organisms
☒	☐ Human research participants
☒	☐ Clinical data

Methods

n/a	Involved in the study
☒	☐ ChIP-seq
☒	☐ Flow cytometry
☒	☐ MRI-based neuroimaging

Eukaryotic cell lines

Policy information about cell lines

Cell line source(s)	SF9 insect cell lines for protein expression
Authentication	N.A.
Mycoplasma contamination	Cells were not tested for mycoplasma
Commonly misidentified lines (See ICLAC register)	none

Article

Activation of the GLP-1 receptor by a non-peptidic agonist

https://doi.org/10.1038/s41586-019-1902-z

Received: 10 May 2019

Accepted: 8 November 2019

Published online: 8 January 2020

Peishen Zhao[1,9], Yi-Lynn Liang[1,9], Matthew J. Belousoff[1,9], Giuseppe Deganutti[2,9], Madeleine M. Fletcher[1], Francis S. Willard[3], Michael G. Bell[3], Michael E. Christe[3], Kyle W. Sloop[3], Asuka Inoue[4], Tin T. Truong[1], Lachlan Clydesdale[1], Sebastian G. B. Furness[1], Arthur Christopoulos[1], Ming-Wei Wang[5,6], Laurence J. Miller[7], Christopher A. Reynolds[2], Radostin Danev[8]*, Patrick M. Sexton[1,6]* & Denise Wootten[1,6]*

Class B G-protein-coupled receptors are major targets for the treatment of chronic diseases, including diabetes and obesity[1]. Structures of active receptors reveal peptide agonists engage deep within the receptor core, leading to an outward movement of extracellular loop 3 and the tops of transmembrane helices 6 and 7, an inward movement of transmembrane helix 1, reorganization of extracellular loop 2 and outward movement of the intracellular side of transmembrane helix 6, resulting in G-protein interaction and activation[2–6]. Here we solved the structure of a non-peptide agonist, TT-OAD2, bound to the glucagon-like peptide-1 (GLP-1) receptor. Our structure identified an unpredicted non-peptide agonist-binding pocket in which reorganization of extracellular loop 3 and transmembrane helices 6 and 7 manifests independently of direct ligand interaction within the deep transmembrane domain pocket. TT-OAD2 exhibits biased agonism, and kinetics of G-protein activation and signalling that are distinct from peptide agonists. Within the structure, TT-OAD2 protrudes beyond the receptor core to interact with the lipid or detergent, providing an explanation for the distinct activation kinetics that may contribute to the clinical efficacy of this compound series. This work alters our understanding of the events that drive the activation of class B receptors.

Class B peptide G-protein-coupled receptors (GPCRs) regulate the control of glucose and energy homeostasis, bone turnover, and cardiovascular development and tone[1]. Several peptide agonists are clinically approved for disorders of energy and bone metabolism[1]; however, attempts to develop non-peptide, orally available analogues have yielded only limited success. Understanding the structural basis of class B GPCR activation is crucial to the rational development of peptidic and non-peptidic drugs. Recent structural determination of full-length, active class B receptors bound to peptide agonists[2–6] confirmed that the N terminus of the peptide ligands, required for receptor activation, binds deep within the seven-transmembrane helical bundle. This is associated with an outward movement of the tops of transmembrane helices (TM) 6 and 7 (and interconnecting extracellular loop (ECL) 3) and a large kink in the centre of TM6 that opens up the intracellular face of the receptor to allow G-protein coupling[2–4,7–10]. In parallel, a conformational reorganization of ECL2 and an inward movement of TM1 facilitates peptide interaction and receptor activation.

The GLP-1 receptor (GLP-1R) is an established therapeutic target for type 2 diabetes and obesity[11]. Despite their clinical success, GLP-1R peptide drugs are suboptimal owing to their route of administration and side-effect profiles, most notably nausea and vomiting that reduce patient compliance[11]. For many years, oral GLP-1R agonists have been pursued, with recent studies reporting promising clinical trial data for oral semaglutide—a new formulation of the approved peptide semaglutide[12,13]. However, it induced slightly greater severity of nausea and gastrointestinal side effects than those observed with injectable GLP-1 mimetics[13]. Future development of non-peptide drugs could offer more traditional small molecule absorption characteristics that may assure better long-term patient compliance with the potential for reduced gastrointestinal liability, especially for patients who are co-administering with other medications.

Several non-peptidic GLP-1R agonists have been identified[14]. One class form covalent interactions with C347$^{6.36}$ (in which the superscript denotes the Wootten class B GPCR numbering) and are predicted to allosterically disrupt polar networks at the base of the receptor, promoting activation[15], whereas other small molecule compounds bind to unknown sites at the receptor extracellular face[14,16,17]. However, it is assumed that these molecules may need to mimic key interactions of the peptide N terminus deep within the transmembrane core to initiate receptor activation, as is seen for short stabilized 11-mer peptides, that occupy an overlapping site to full-length peptides[18].

[1]Drug Discovery Biology, Monash Institute of Pharmaceutical Sciences, Monash University, Parkville, Victoria, Australia. [2]School of Biological Sciences, University of Essex, Colchester, UK. [3]Lilly Research Laboratories, Eli Lilly and Company, Indianapolis, IN, USA. [4]Graduate School of Pharmaceutical Sciences, Tohoku University, Sendai, Miyagi, Japan. [5]The National Center for Drug Screening and CAS Key Laboratory of Receptor Research, Shanghai Institute of Materia Medica, Chinese Academy of Sciences, Shanghai, China. [6]School of Pharmacy, Fudan University, Shanghai, China. [7]Mayo Clinic, Scottsdale, AZ, USA. [8]Graduate School of Medicine, University of Tokyo, Hongo, Bunkyo-ku, Tokyo, Japan. [9]These authors contributed equally: Peishen Zhao, Yi-Lynn Liang, Matthew J. Belousoff, Giuseppe Deganutti. *e-mail: rado@m.u-tokyo.ac.jp; patrick.sexton@monash.edu; denise.wootten@monash.edu

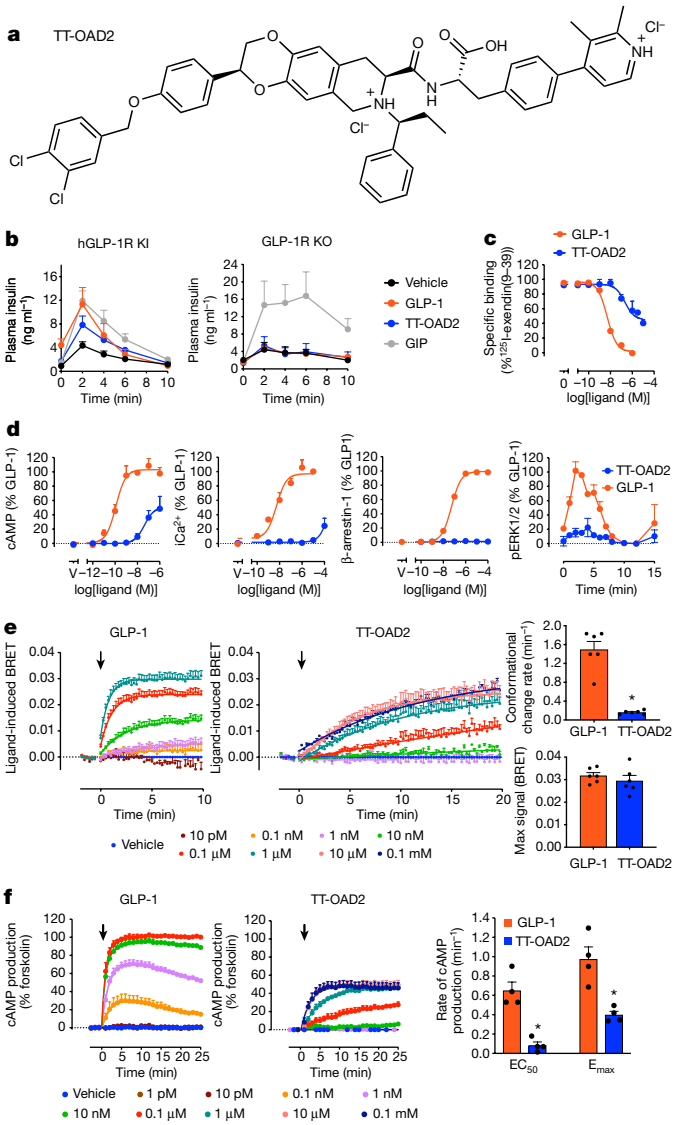


Fig. 1 | Pharmacology exhibited by TT-OAD2 relative to GLP-1. a, Chemical structure of TT-OAD2. **b**, Plasma insulin induced by GLP-1 (10 μg kg^{-1}), TT-OAD2 (3 mg kg^{-1}) or gastric inhibitory polypeptide (GIP; 25 μg kg^{-1}) in an acute IVGTT on humanized GLP-1R knock-in (KI) and GLP-1R knockout (KO) mice. **c**, Whole-cell binding assays showing the ability of GLP-1 and TT-OAD2 to displace ^{125}I-exendin(9-39). **d**, cAMP accumulation, intracellular calcium mobilization, β-arrestin-1 recruitment and ERK1/2 phosphorylation (pERK1/2). **e**, Agonist-induced changes in trimeric G_s conformation in cell plasma membrane preparations for GLP-1 (left) and TT-OAD2 (middle). Rates (top right) and plateau (bottom right) at saturating concentrations (1 μM GLP-1, 10 μM TT-OAD2) were quantified by applying a one-phase association curve. **f**, Kinetics of cAMP production measured by an EPAC biosensor for GLP-1 (left) and TT-OAD2 (middle). Rates were quantified using approximate EC_{50} and E_{max} concentrations (1 nM and 0.1 μM for GLP-1, 0.1 μM and 10 μM for TT-OAD2) by applying a one-phase association curve. In **e** and **f**, arrows refer to the time at which ligand or vehicle was added. Parameters derived from kinetic data are represented as scatter plots with each individual experiment shown by black circles. All experiments were performed in GLP-1R expressing HEK293A cells. Data in **b** are mean + s.e.m. from 4–5 mice per treatment, representative of 3 independent experiments. Data in **c**–**f** are mean + s.e.m. of 4–5 independent experiments (in duplicate or triplicate). *P < 0.05, Student's paired t-test.

Here we investigate TT-OAD2 (Fig. 1a), a non-peptidic compound reported in the patent literature and part of the chemical series that contains the vTv Therapeutics investigational drug candidate, TTP273. TTP273, an orally administered GLP-1R agonist, successfully completed phase IIa efficacy trials for type 2 diabetes (ClinicalTrials.gov Identifier: NCT02653599), in which it met its primary endpoint, reducing levels of glycated haemoglobin in patients with type 2 diabetes, with no reported cases of nausea[19], suggesting a potential clinical advantage for compounds of this series. Little has been disclosed about the molecular properties of this compound series; however, recent progression of TTP273 has been hampered by unexpected complexity in identifying optimal dosing that may be linked to a lack of understanding of its mechanism of action. Assessment of acute in vivo activity in humanized GLP-1R mice revealed that TT-OAD2 is insulinotropic and that this effect is dependent on the GLP-1R (Fig. 1b).

TT-OAD2 is a biased agonist with slow kinetics

In HEK293 cells that overexpress GLP-1R, TT-OAD2 only partially displaced the orthosteric probes ^{125}I-exendin(9–39) and ROX-exendin-4 (Fig. 1c, Extended Data Fig. 1a), consistent with an allosteric mode of interaction[16]. Although GLP-1R signals to several cellular pathways, TT-OAD2 activated only a subset of these responses; it was a low-potency partial agonist for cAMP accumulation, with only weak responses detected for mobilization of intracellular Ca^{2+} and phosphorylation of ERK1/2 at very high concentrations (100 μM) (Fig. 1d) and no detectable recruitment of β-arrestin-1. These data are indicative of bias towards cAMP and away from these other pathways relative to endogenous GLP-1. There is considerable interest in exploiting biased agonism at GPCRs to maximize the beneficial effects of receptor activation, while minimizing on-target side-effect profiles.

CRISPR-engineered HEK293 cells in which $G_{s/olf}$ or $G_{i/o/z}$ proteins were deleted revealed that G_s was essential for the production of cAMP; however, this response, for both ligands, was also dependent on the presence of $G_{i/o/z}$ proteins. (Extended Data Fig. 1b). Assessment of proximal activation of G_s and G_i transducers using split luciferase NanoBit G-protein sensors (Extended Data Fig. 1c) determined GLP-1-decreased luminescence in a bi-phasic, concentration-dependent, manner for both G proteins with similar potencies in each phase. For TT-OAD2, the G_i sensor gave a similar decrease in luminescence to GLP-1; however, enhanced luminescence was observed for the G_s sensor, which suggests a different mechanism of G_s activation. To probe these differences further, we used membrane-based assays of bioluminescence resonance energy transfer (BRET) G-protein sensors to assess the rate and nature of the G_s conformational change. In contrast to the rates of change in the conformation of G_i, which were similar for both ligands (Extended Data Fig. 1), there was a marked distinction in kinetics for G_s coupling. GLP-1 promoted a rapid conformational change in G_s protein, whereas for TT-OAD2 this was very slow (Fig. 1e). However, both agonists induced a similar plateau of the measured response (Fig. 1e) that was reversed by excess GTP (Extended Data Fig. 1d), indicative of a similar overall conformational rearrangement. Together, this suggests that slower G_s conformational transitions, required for the exchange of GDP for GTP and G_s activation, would result in lower turnover of G protein and rate of cAMP production by TT-OAD2. Direct kinetic measurements of cAMP production validated this hypothesis (Fig. 1f, Extended Data Fig. 1e). Overall, these data revealed TT-OAD2 as a biased agonist that can only activate a subset of pathways with limited efficacy and with distinct activation kinetics relative to peptide agonists.

TT-OAD2 has an unexpected binding mode

To understand how TT-OAD2 binds and activates the GLP-1R, we determined the GLP-1R structure bound to TT-OAD2 and the transducer heterotrimeric G_s protein (Fig. 2). Complex formation was initiated in *Tni* insect cells by stimulation with 50 μM TT-OAD2, and complexes were then solubilized and purified (Extended Data Fig. 2a). Vitrified complexes were imaged by single-particle cryo-electron microscopy (cryo-EM) on a Titan Krios. Following 2D and 3D classification, the most

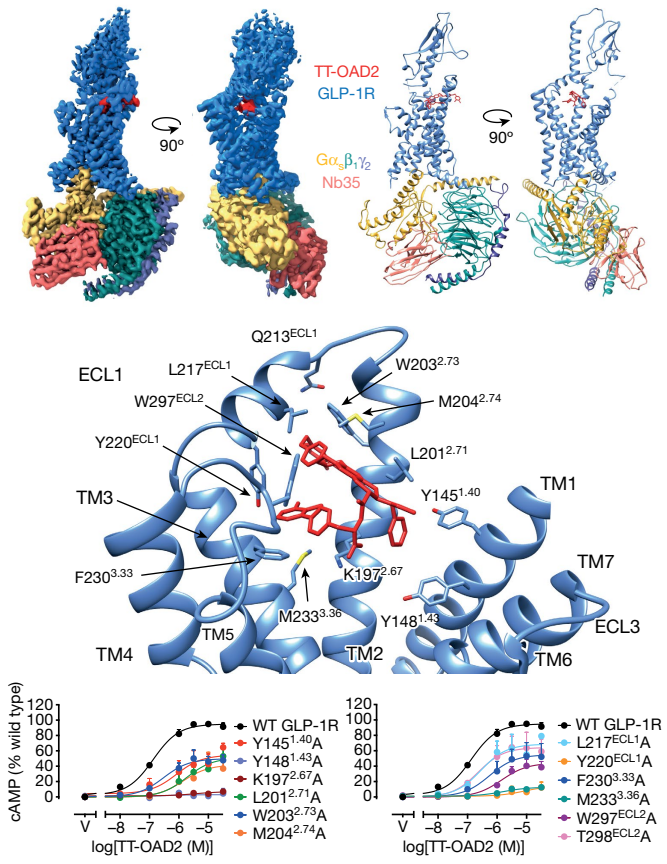


Fig. 2 | TT-OAD2–GLP-1R–G_s cryo-EM structure reveals non-peptide binding site. Top, orthogonal views of the TT-OAD2–GLP-1R–G_s complex cryo-EM map (left) and the structure after refinement in the cryo-EM map (right), colour-coded to protein chains; GLP-1R (blue), TT-OAD2 (red), heterotrimeric G_s (α: gold, β: dark cyan, γ: purple, Nb35: salmon). Middle, TT-OAD2 interacts with the top of the GLP-1R bundle. Interacting residues of GLP-1R (blue) with TT-OAD2 (red). Bottom, TT-OAD2-mediated cAMP production by receptors containing alanine mutants of key residues assessed in ChoFlpIn cells. Data are mean + s.e.m. of four independent experiments performed in duplicate. WT, wild type.

abundant class was resolved to 3.0 Å (Extended Data Fig. 2c–f, Supplementary Table 1). The cryo-EM density map allowed unambiguous assignment of the TT-OAD2-binding site and pose, and clear rotamer placement for most amino acids within the receptor core and G protein (Fig. 2, Extended Data Figs. 3, 4a, b). The GLP-1R extracellular domain (ECD) and the $G\alpha_s$ α-helical domain were not resolved at high resolution, consistent with their greater mobility. Rigid body fitting of an available X-ray structure of the GLP-1R ECD domain (PDB code 3C5T)[20] was performed into the density to generate a full-length model.

TT-OAD2 bound high up in the helical bundle interacting with residues within TM1, TM2, TM3, ECL1 and ECL2 (Fig. 2, Extended Data Fig. 4a). Most interactions are hydrophobic in nature (Fig. 2), including numerous π–π stacking interactions between receptor aromatic residues and phenolic regions within the ligand. Unexpectedly, TT-OAD2 adopts a 'boomerang-like' orientation within the binding site with the 3,4-dichloro-benzyl ring of TT-OAD2 protruding beyond the receptor core through transmembrane helices 2 and 3, interacting with $W203^{2.73}$, and embedding in the detergent micelle, consistent with probable interactions with the lipid bilayer in a native system. $F230^{3.33}$ and $W297^{ECL2}$ interact with the 2,3-dimethyl-pyridin-4-yl-phenol region, $Y220^{ECL1}$ forms a hydrogen bond with the 2,3-dimethyl-pyridine ring and $K197^{2.67}$ forms a polar interaction with the propionic acid part of the ligand. Additional hydrophobic contacts are formed with TT-OAD2 by $Y145^{1.40}$, $L201^{2.71}$, $I196^{2.69}$, $A200^{2.70}$, $L217^{ECL1}$, $V229^{3.32}$ and $M204^{3.36}$ (Fig. 2, Extended Data Fig. 4a). Molecular dynamics simulations of the TT-OAD2–GLP-1R–G_s complex predicted further transient interactions with TM1, TM2, TM3, ECL1, ECL2 and the ECD of GLP-1R (Extended Data Table 1). Assessment of TT-OAD2-induced cAMP production at alanine mutants of key receptor residues within the binding site revealed reduced potency (negative logarithm of the half-maximal effective concentration, pEC_{50}), reduced maximal responses (E_{max}) or both relative to the wild-type receptor (Fig. 2, Supplementary Table 2). Application of the operational model of agonism revealed these mutations directly alter TT-OAD2 functional affinity (K_A) and/or efficacy (τ) (Supplementary Table 2), which highlights the importance of these residues in TT-OAD2 function.

Peptide versus non-peptide binding sites

The TT-OAD2-binding pose has very limited overlap with full-length peptides, GLP-1 and exendin-P5 (ExP5)[3,6] (Fig. 3, Extended Data Fig. 5). Structural comparisons, combined with associated molecular dynamics simulations performed on models generated from the cryo-EM data, identified only 10 out of 29 residues that interact with both TT-OAD2 and GLP-1. Moreover, the persistence and nature of ligand interactions formed by common residues differed (Fig. 3c, Extended Data Table 1). In contrast to TT-OAD2, peptide ligands engage transmembrane helices 5–7 in addition to extensive interactions deep within the bundle in transmembrane helices 1–3 (Fig. 3, Extended Data Fig. 5, Extended Data Table 1).

The relatively limited overlap between the peptide- and TT-OAD2-binding sites suggests that this compound series may modulate peptide function in a physiological setting. To address this, we assessed the effect of TT-OAD2 on the signalling of two physiological ligands (Extended Data Fig. 6). TT-OAD2 inhibited GLP-1- and oxyntomodulin-mediated cAMP, calcium, pERK1/2 and β-arrestin responses in a concentration-dependent manner (Extended Data Fig. 6). This suggests that the profile of signalling observed from the GLP-1R when using TT-OAD2-like compounds as drugs may depend on the dose administered; at high concentrations, their presence would probably inhibit all endogenous peptide effects, biasing receptor responses primarily to cAMP formation mediated by the compound itself. However, at lower concentrations, some endogenous peptide signalling may still occur. Notably, TTP273 was reported to exhibit greater clinical efficacy at lower concentrations, indicating that maintenance of some aspects of physiological signalling may be important for clinical efficacy[19].

GLP-1R conformational changes and activation

At a gross level, the TT-OAD2-complexed GLP-1R helical bundle displays the key hallmarks of activated, peptide-occupied, class B GPCRs[2–6]. At the extracellular face, this includes the large outward movement of TM6, ECL3 and TM7, inward movements of TM1, helical extensions within TM2 and TM3, a reordering of ECL1, and conformational transitions within ECL2 that increases upward towards the extracellular side (Extended Data Fig. 5). At the intracellular side, there is an equivalent large outward movement of TM6 away from the centre of the helical bundle, and the smaller outward movement of TM5. It is important to note that the fully active state is driven in part by allosteric conformational changes, including those in the extracellular face, linked to G protein binding[21]. Nonetheless, all the GLP-1R structures are solved with the same G protein yet reveal conformational differences at their extracellular face, including within the extent of movement of TM6, ECL3, ECL7 and the conformation of the ECD, TM2–ECL1 and ECL2 that are linked to the bound agonists (Fig. 3a, b, Extended Data Fig. 5b, c). This suggests that distinct receptor activation triggers converge to common changes at the intracellular face that allow coupling to transducers.

Although the low resolution of the receptor ECD for the TT-OAD2 complex indicates extensive mobility, it occupied a distinct orientation

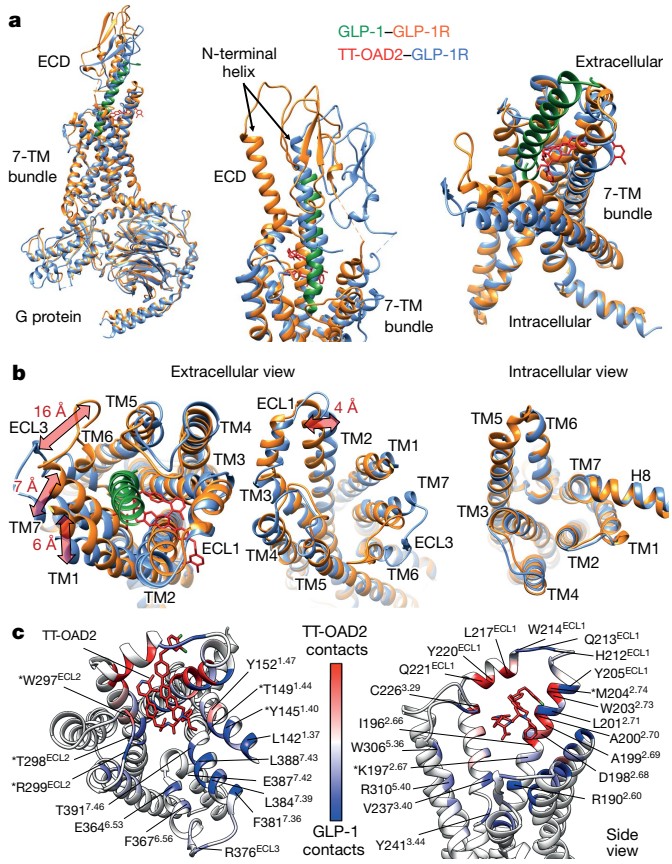


Fig. 3 | Comparisons of GLP-1R conformations induced by GLP-1 and TT-OAD2. a, **b**, Superimposition of the GLP-1R from PDB 5VAI (GLP-1R or G protein: orange, GLP-1: green) and the TT-OAD2 structure (GLP-1R or G protein: blue, TT-OAD2: red) reveals partial overlap of peptide- and TT-OAD2-binding sites and conformational differences in the receptor. **a**, Left, full complex; middle, close up of ECD and the top of the seven-transmembrane (7-TM) bundle; right, close up of the transmembrane bundle. **b**, Left, 16 Å, 7 Å and 6 Å differences occur in the location of TM6/ECL3, TM7 and TM1, respectively. Middle, a 4 Å shift in the location of the top of TM2 result in distinct conformations of ECL1. Right, the intracellular region of the GLP-1R helical bundles have similar overall backbone conformations. **c**, Comparison of the GLP-1R–TT-OAD2 and GLP-1R–GLP-1 contacts during molecular dynamics simulations performed on the GLP-1R–TT-OAD2–G_s and GLP-1R–GLP-1–G_s complexes. Top (left) and side (right) views of the GLP-1R transmembrane domain (ribbon representation, TT-OAD2 in red sticks, GLP-1 not shown). TT-OAD2 made contacts (red coloured ribbon) with ECL1 and residues located at the top of TM2 and TM3. GLP-1 was able to engage TM5, TM6 and TM7 of the receptor and side chains located deep in the bundle (blue coloured ribbon). Residues that are involved both in the GLP-1R–TT-OAD2–G_s and GLP-1R–GLP-1–G_s complexes are indicated by asterisks, and coloured according to the algebraic difference in occupancy (contact differences in percentage frames) between GLP-1R–TT-OAD2–G_s and GLP-1R–GLP-1–G_s. Red indicates regions more engaged by TT-OAD2 and blue more engaged by GLP-1. The ECD is not shown. Plotted data are summarized in Extended Data Table 1.

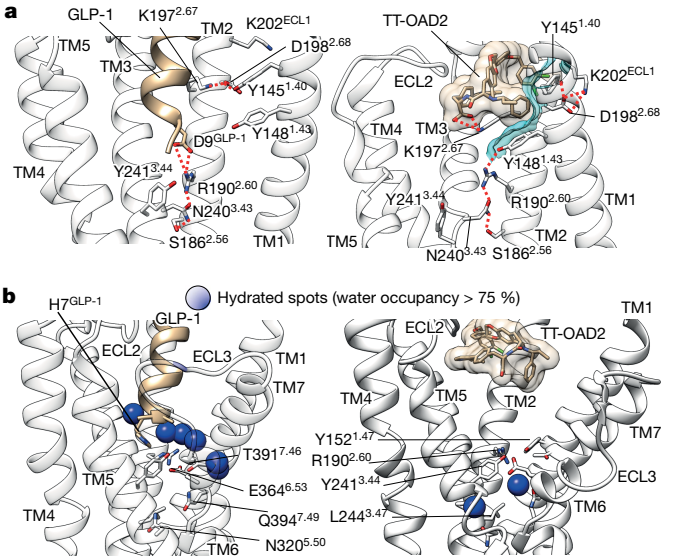


Fig. 4 | TT-OAD2 interactions lead to reorganization and stabilization of the central polar network via a distinct mechanism to GLP-1. Summaries of interactions observed in molecular dynamics simulations (Supplementary Video 2) on TT-OAD2- and GLP-1-bound GLP-1R that predict interactions stabilizing the active conformation of the central polar network. **a**, Left, GLP-1 (brown ribbon) residue D^9 (brown stick) forms an ionic interaction (red dotted lines) with $R190^{2.60}$, which is involved in key hydrogen bonds with $N240^{3.43}$ (in turn interacting with $S186^{2.56}$). At the top of TM2, $K197^{2.67}$, $D198^{2.68}$ and $Y145^{1.40}$ are stabilized in polar interactions (red dotted lines). Right, TT-OAD2 (brown stick and transparent surface) forms ionic interaction (red dotted lines) with $K197^{2.67}$ and hydrophobic contacts with $Y145^{1.40}$ and $Y148^{1.43}$ (cyan transparent surfaces) modifying the interaction network at the top of TM1. $Y148^{1.43}$ transiently interacts with $R190^{2.60}$ and partially reorients $N240^{3.43}$ and $S186^{2.56}$. TM6 and TM7 were removed for clarity. **b**, GLP-1R transmembrane helix sites are occupied by structural water molecules; blue spheres indicate receptor volumes occupied by low-mobility water molecules (occupancy more than 75% frames). Left, the GLP-1R–GLP-1–G_s complex stabilizes the central transmembrane polar residues by waters interacting with $Y152^{1.47}$, $T391^{7.46}$, $R190^{2.60}$ and $E364^{5.53}$ (Supplementary Video 1). Right, the GLP-1R–TT-OAD2–G_s complex is characterized by structural water molecules interacting with $N320^{5.50}$ and $E364^{6.53}$ (Supplementary Video 1).

relative to the transmembrane core in comparison to peptide-bound complexes, whereas both GLP-1- and ExP5-bound receptors stabilized a similar conformation[3,6] (Extended Data Fig. 5a). Similarly, the short 11-mer peptide HepP5 forms few interactions with the ECD[18] and occupies a distinct orientation relative to GLP-1 and ExP5, but this conformation also differs from that stabilized by TT-OAD2 (Extended Data Fig. 5c). The cryo-EM map of the TT-OAD2-bound receptor complex supports extended interactions of the ECD with ECL1 and ECL2 (Extended Data Fig. 4c) and this is supported by molecular dynamics simulations that predicts interactions of $R40^{ECD}$ with $D215^{ECL1}$ and $E34^{ECD}$ with $R299^{ECL2}$ (Extended Data Table 2). This later interaction is particularly important as $R299^{ECL2}$ directly, and stably interacts with peptide ligands, but in the TT-OAD2-bound receptor, stabilizes the N terminus of the ECD in a position that may have an analogous role to the peptide in stabilizing ECL2. Indeed, in our models, the position of the far N-terminal ECD helix overlapped with the location of the C-terminal region of GLP-1 and ExP5 when comparing the TT-OAD2- and peptide-bound structures (Fig. 3a). Thus, the ECD is likely to be important for both stabilizing the TT-OAD2-binding site and facilitating receptor activation, as previously proposed for different classes of peptide ligands[22,23].

Distinctions from peptide-bound receptors observed within TM2/ECL1 and ECL2 (Fig. 3b) are probably driven by direct ligand interactions by TT-OAD2 (Fig. 2), whereas those within TM6 and TM7 by direct interactions formed by peptide agonists. Molecular dynamics simulations also support a role of membrane lipid interactions in directly stabilizing both these regions within the TT-OAD2-bound structure (Extended Data Fig. 7). Notably, the helical bundle of the TT-OAD2-complexed receptor is in a more open conformation than the peptide-occupied receptors, largely owing to the top of TM6/ECL3, TM7 and TM1 residing 16 Å, 6 Å and 7 Å further outwards relative to the GLP-1-bound structure (measured from the Cα atoms of $D372^{6.62/ECL3}$, $F381^{7.37}$ and $P137^{1.32}$, respectively (Fig. 3b). The orientation of TM6, ECL3 and TM7 also differs between ExP5- and GLP-1-bound structures, with ExP5 adopting a more open conformation[3]; however, the outward positioning of ECL3 induced by TT-OAD2 is much larger (Extended Data Fig. 5b). Peptide-bound

structures of all solved class B GPCRs revealed direct interactions of the engaged peptide with residues within TM5, TM6, TM7 and ECL3 with the peptide volume (minimally) presumed to actively contribute to the outward conformational change in this region[2–4,8,9,24]. In the apo-state of the glucagon receptor, interactions occur between ECL3 and the ECD that contribute to maintenance of receptor quiescence[7,8,25,26]. Molecular dynamics simulations on the GLP-1R structures, performed after the removal of either TT-OAD2 or GLP-1, predict that the GLP-1R ECD also adopts both open and closed conformations in the apo-state, in which it can form transient interactions with both ECL2 and ECL3[25] (Extended Data Fig. 8). Combining this information with the GLP-1R active structures suggests that interactions, with either peptide or non-peptide agonists, can release ECL3-ECD constraints, lowering the energy barrier for receptor activation. However, the degree of ligand interaction with TM6–ECL3–TM7 determines the extent to which the transmembrane bundle opens, and this in turn directly contributes to G-protein efficacy and biased agonism, as these regions (TM6–ECL3–TM7 and TM1) have been identified as key drivers for these phenomena, particularly for the GLP-1R[3,27–29].

Despite the different binding modes, commonalities observed in interactions with TT-OAD2 and peptide with transmembrane helices 1–3 and stabilization of ECL2 are sufficient to initiate conformational transitions that propagate to a similar reorganization of the class B GPCR conserved central polar network that is linked to activation, albeit the mechanism for this differs for peptide agonists versus TT-OAD2 (Fig. 4a, Supplementary Video 1, Extended Data Fig. 9). Molecular dynamics simulations of the GLP-1-bound GLP-1R predicted persistent interactions between Y152$^{1.47}$, R190$^{2.60}$, Y241$^{3.44}$ and E364$^{6.53}$ and the N terminus of GLP-1 that directly engage the central polar network (Fig. 4a, Extended Data Tables 1, 2, Supplementary Video 1). By contrast, TT-OAD influences the central polar network allosterically via interactions with K197$^{2.67}$, Y145$^{1.40}$ and Y148$^{1.43}$. TT-OAD2 also promotes unique hydrogen bond networks with crucial residues in TM2 (Fig. 4a, Extended Data Table 2) that result in different interaction patterns at the top of TM1 and TM2 relative to peptide-occupied receptors. These effects propagate to the polar network through transient contacts between TT-OAD2 with Y148$^{1.43}$ and Y152$^{1.47}$ that in turn interact with R190$^{2.60}$ of the central polar network (Supplementary Video 2). When bound by GLP-1, the polar network is stabilized by ligand and a network of water molecules, whereas for TT-OAD2, this occurs via a distinct network of structural waters rather than by the ligand (Fig. 4b, Supplementary Video 1). These differences in the mechanism of conformational transitions and stabilization of conserved polar networks (summarized in Extended Data Fig. 9) may contribute to the different kinetic profiles of G-protein activation, as well as the full versus partial agonism for cAMP production.

Collectively, our work provides key advances in understanding the activation of class B GPCRs and G_s protein efficacy, identifying a non-peptide binding site within the GLP-1R that can promote distinct efficacy and biased signalling relative to peptide ligands, and this may extend to other class B GPCRs. The demonstration that non-peptide agonists of the GLP-1R are not required to mimic the extensive receptor contacts formed by peptides within the transmembrane cavity to promote receptor activation will advance the pursuit of non-peptide agonists for therapeutically important class B receptors.

Online content

Any methods, additional references, Nature Research reporting summaries, source data, extended data, supplementary information, acknowledgements, peer review information; details of author contributions and competing interests; and statements of data and code availability are available at https://doi.org/10.1038/s41586-019-1902-z.

1. Bortolato, A. et al. Structure of class B GPCRs: new horizons for drug discovery. *Br. J. Pharmacol.* **171**, 3132–3145 (2014).
2. Liang, Y. L. et al. Cryo-EM structure of the active, G_s-protein complexed, human CGRP receptor. *Nature* **561**, 492–497 (2018).
3. Liang, Y. L. et al. Phase-plate cryo-EM structure of a biased agonist-bound human GLP-1 receptor-Gs complex. *Nature* **555**, 121–125 (2018).
4. Liang, Y. L. et al. Phase-plate cryo-EM structure of a class B GPCR-G-protein complex. *Nature* **546**, 118–123 (2017).
5. Zhao, L. H. et al. Structure and dynamics of the active human parathyroid hormone receptor-1. *Science* **364**, 148–153 (2019).
6. Zhang, Y. et al. Cryo-EM structure of the activated GLP-1 receptor in complex with a G protein. *Nature* **546**, 248–253 (2017).
7. Siu, F. Y. et al. Structure of the human glucagon class B G-protein-coupled receptor. *Nature* **499**, 444–449 (2013).
8. Zhang, H. et al. Structure of the full-length glucagon class B G-protein-coupled receptor. *Nature* **546**, 259–264 (2017).
9. Zhang, H. et al. Structure of the glucagon receptor in complex with a glucagon analogue. *Nature* **553**, 106–110 (2018).
10. Song, G. et al. Human GLP-1 receptor transmembrane domain structure in complex with allosteric modulators. *Nature* **546**, 312–315 (2017).
11. Htike, Z. Z. et al. Efficacy and safety of glucagon-like peptide-1 receptor agonists in type 2 diabetes: A systematic review and mixed-treatment comparison analysis. *Diabetes Obes. Metab.* **19**, 524–536 (2017).
12. Aroda, V. R. et al. PIONEER 1: Randomized clinical trial comparing the efficacy and safety of oral semaglutide monotherapy with placebo in patients with type 2 diabetes. *Diabetes Care* **42**, dc190749 (2019).
13. Pratley, R. *et al*. Oral semaglutide versus subcutaneous liraglutide and placebo in type 2 diabetes (PIONEER 4): a randomised, double-blind, phase 3a trial. *Lancet* **394**, 39–50 (2019).
14. Wootten, D. et al. Differential activation and modulation of the glucagon-like peptide-1 receptor by small molecule ligands. *Mol. Pharmacol.* **83**, 822–834 (2013).
15. Nolte, W. M. et al. A potentiator of orthosteric ligand activity at GLP-1R acts via covalent modification. *Nat. Chem. Biol.* **10**, 629–631 (2014).
16. Freeman, J. W. S. et al. TTP273: Oral, G protein pathway selective clinical-stage GLP-1 receptor (GLP-1R) agonist. *Keystone Symposium, Keystone, CO February 22* http://vtvtherapeutics.com/wp-content/uploads/pdf/GLP1_poster_animation_Keystone_CO_FINAL.pdf (2016).
17. Chen, D. et al. A nonpeptidic agonist of glucagon-like peptide 1 receptors with efficacy in diabetic *db/db* mice. *Proc. Natl Acad. Sci. USA* **104**, 943–948 (2007).
18. Jazayeri, A. et al. Crystal structure of the GLP-1 receptor bound to a peptide agonist. *Nature* **546**, 254–258 (2017).
19. Freeman, J. D. C., Dunn, I. & Valcarce, C. TTP273, Oral (nonpeptide) GLP-1R agonist: improved glycemic control without nausea and vomiting in phase 2. *American Diabetes Association 77th Scientific Sessions, San Diego, CA, June 9–13, 2017* http://vtvtherapeutics.com/wp-content/uploads/pdf/ADA_Logra_study_results_poster_1220-P%20Final.pdf (2017).
20. Runge, S., Thøgersen, H., Madsen, K., Lau, J. & Rudolph, R. Crystal structure of the ligand-bound glucagon-like peptide-1 receptor extracellular domain. *J. Biol. Chem.* **283**, 11340–11347 (2008).
21. DeVree, B. T. et al. Allosteric coupling from G protein to the agonist-binding pocket in GPCRs. *Nature* **535**, 182–186 (2016).
22. Yin, Y. et al. An intrinsic agonist mechanism for activation of glucagon-like peptide-1 receptor by its extracellular domain. *Cell Discov.* **2**, 16042 (2016).
23. Zhao, L. H. et al. Differential requirement of the extracellular domain in activation of class B G protein-coupled receptors. *J. Biol. Chem.* **291**, 15119–15130 (2016).
24. Ehrenmann, J. et al. High-resolution crystal structure of parathyroid hormone 1 receptor in complex with a peptide agonist. *Nat. Struct. Mol. Biol.* **25**, 1086–1092 (2018).
25. Yang, L. et al. Conformational states of the full-length glucagon receptor. *Nat. Commun.* **6**, 7859 (2015).
26. Wootten, D., Simms, J., Miller, L. J., Christopoulos, A. & Sexton, P. M. Polar transmembrane interactions drive formation of ligand-specific and signal pathway-biased family B G protein-coupled receptor conformations. *Proc. Natl Acad. Sci. USA* **110**, 5211–5216 (2013).
27. dal Maso, E. et al. The molecular control of calcitonin receptor signaling. *ACS Pharmacol. Transl. Sci.* **2**, 31–51 (2019).
28. Wootten, D. et al. The extracellular surface of the GLP-1 receptor is a molecular trigger for biased agonism. *Cell* **165**, 1632–1643 (2016).
29. Lei, S. et al. Two distinct domains of the glucagon-like peptide-1 receptor control peptide-mediated biased agonism. *J. Biol. Chem.* **293**, 9370–9387 (2018).

Publisher's note Springer Nature remains neutral with regard to jurisdictional claims in published maps and institutional affiliations.

© The Author(s), under exclusive licence to Springer Nature Limited 2020

Methods

Data reporting

No statistical methods were used to predetermine sample size. The experiments were not randomized and investigators were not blinded to allocation.

TT-OAD2 synthesis

Several azoanthracene-based derivatives are reported as potent agonists of the GLP-1R (WO10114824), and a compound from this series known as OAD2 was selected for our studies (WO14113357). OAD2, (*S*)-2-{[(3S,8S)-3-[4-(3,4-dichloro-benzyloxy)-phenyl]-7-((*S*)-1-phenyl-propyl)-2,3,6,7,8,9-hexahydro-[1,4]dioxino[2,3-g]isoquinoline-8-carbonyl]-amino}-3-[4-(2,3-dimethyl-pyridin-4-yl)-phenyl]-propionic acid, was synthesized using procedures previously described (see example 179 in WO10114824), and a dihydrochloride salt form (OAD2.2HCl) was prepared by standard methods from the free base. Therefore, TT-OAD2 is the dihydrochloride salt of OAD2 in patent WO14113357. The purity of TT-OAD2 was determined by liquid chromatography–mass spectrometry (LC–MS) to be 98.62%.

Constructs

GLP-1R was modified to contain either a 2xcMyc-N-terminal epitope tag (for signalling and radioligand-binding assays) or a Nanoluc tag (with a 12xGly linker; for NanoBRET binding studies) after the native signal peptide. For β-arrestin recruitment assays, a C-terminal Rluc8 was fused to the C terminus of the receptor. For G-protein conformational assays, a Nanoluc flanked by SGGGGS linkers was inserted into $G\alpha_s$ and $G\alpha_{i2}$ after G(h1ha10) in $G\alpha_s$ or E(HA.03) in $G\alpha_{i2}$ as previously described[30,31]. These were used in conjunction with an N-terminally Nluc-labelled $G\gamma_2$. For G-protein steady-state assays, G-protein NanoBit-split luciferase constructs were generated by fusing the LgBIT after G(h1ha10) in $G\alpha_s$ or E(HA.29) in $G\alpha_{i2}$ and the SmBIT to $G\gamma_2$. For structural studies, human GLP-1R in the pFastBac vector was modified to include an N-terminal Flag tag epitope and a C-terminal 8×histidine tag; both tags are removable by 3C protease cleavage. These modifications did not alter the pharmacology of the receptor[3]. A dominant-negative $G\alpha_s$ construct was generated previously by site directed mutagenesis to incorporate mutations that alter nucleotide handling, stabilize the G_0 state and interactions with the βγ subunits[30].

Insect cell expression

GLP-1R, human dominant-negative $G\alpha_s$, His6-tagged human $G\beta_1$ and $G\gamma_2$ were expressed in *Tni* insect cells (Expression systems) using baculovirus. Cell cultures were grown in ESF 921 serum-free media (Expression Systems) to a density of 4 million cells per ml and then infected with three separate baculoviruses at a ratio of 2:2:1 for GLP-1R, dominant-negative $G\alpha_s$ and $G\beta_1\gamma_2$. Cells were obtained by centrifugation 60 h after infection and the cell pellet was stored at −80 °C.

Purification of the TT-OAD2–GLP-1R–G_s complex

Cell pellet was thawed in 20 mM HEPES, pH 7.4, 50 mM NaCl, 2 mM $MgCl_2$ supplemented with cOmplete Protease Inhibitor Cocktail tablets (Roche). Complex formation was initiated by addition of 50 μM TT-OAD2, Nb35–His (10 μg ml^{-1}) and apyrase (25 mU ml^{-1}, NEB) to catalyse hydrolysis of unbound GDP and allow for stabilization of the G_0 state; the suspension was incubated for 1 h at room temperature. Membrane was solubilized by 0.5% (w/v) lauryl maltose neopentyl glycol (LMNG, Anatrace) supplemented with 0.3% (w/v) cholesteryl hemisuccinate (CHS, Anatrace) for 2 h at 4 °C. Insoluble material was removed by centrifugation at 30,000*g* for 30 min and the solubilized complex was immobilized by batch binding to M1 anti-Flag affinity resin in the presence of 3 mM $CaCl_2$. The resin was packed into a glass column and washed with 20 column volumes of 20 mM HEPES pH 7.4, 100 mM NaCl, 2 mM $MgCl_2$, 3 mM $CaCl_2$, 1 μM OAD, 0.01% (w/v) MNG and 0.006% (w/v) CHS before bound material was eluted in buffer containing 5 mM EGTA and 0.1 mg ml^{-1} Flag peptide. The complex was then concentrated using an Amicon Ultra Centrifugal Filter (molecular mass cut off 100 kDa) and subjected to size-exclusion chromatography on a Superdex 200 Increase 10/300 column (GE Healthcare) that was pre-equilibrated with 20 mM HEPES pH 7.4, 100 mM NaCl, 2 mM $MgCl_2$, 1 μM OAD, 0.01% (w/v) MNG and 0.006% (w/v) CHS to separate complex from contaminants. Eluted fractions consisting of receptor and G-protein complex were pooled and concentrated. Final yield of purified complex was approximately 0.15 mg per litre of insect cell culture.

Electron microscopy

Samples (3 μl) were applied to a glow-discharged Quantifoil R1.2/1.3 CuRh 200 mesh holey carbon grid (Quantifoil GmbH) and were flash frozen in liquid ethane using the Vitrobot mark IV (Thermo Fisher Scientific) set at 100% humidity and 4 °C for the prep chamber. Data were collected on a Titan Krios microscope (Thermo Fisher Scientific) operated at an accelerating voltage of 300 kV with a 50 μm C2 aperture at an indicated magnification of 105 K in nanoprobe EFTEM mode. Gatan K3 direct electron detector positioned post a Gatan Quantum energy filter, operated in a zero-energy-loss mode with a slit width of 25 eV was used to acquire dose fractionated images of the GLP-1R TT-OAD2-bound sample without an objective aperture. Movies were recorded in hardware-binned mode (previously called counted mode on the K2 camera) yielding a physical pixel size of 0.826 Å pixel^{-1} with an exposure time of 3.715 s amounting to a total dose of 65.6 e^- Å^{-2} at a dose rate of 12.2 e^- pixel^{-1} s^{-1}, which was fractionated into 62 subframes. A second dataset of 1,568 micrographs was also recorded using the same microscope but in 'super-resolution' mode on the K3 detector, the physical pixel size was 0.413 Å with an exposure time of 4.015 s amounting to a total dose of 63.5 e^- Å^{-2}, which was fractionated into 67 subframes. Defocus range was set between −0.7 and −1.5 μm. A total of 3,158 plus 1,568 movies were collected in two data collection sessions.

Electron microscopy data processing

Movies were motion-corrected with UCSF MotionCor2[32] (movies collected in super-resolution mode were Fourier scaled by a factor of ×2 to match the pixel size of the larger data set). This was followed by CTF estimation sing the GCTF software packag[33]. Particles were picked from the micrographs using the automated reference-free procedure in RELION[34,35]. Reference free 2D and 3D classification (by generating multiple ab initio models with no structural identity enforced) was carried out in CryoSPARC (v.2.5.0)[36]. A homogeneous subset of particles was then subjected to movie refinement and Bayesian particle polishing as implemented in RELION (v.3.0). This homogeneous subset of polished particles was used in a 3D refinement in RELION and then further classified into 3D classes with alignment of Euler angles not taken into account. Particles belonging to the 3D class that yielded the best resolved map were then subjected to signal subtraction to subtract density due to the detergent micelle and the alpha domain of the G protein. Final 3D refinement was performed in RELION (3.0) yielded a map of resolutions 3.01 Å. Local resolution estimations were performed using the ResMAP software packag[37].

Atomic model refinement

Fitting the model to the cryoEM electron density map was achieved using the MDFF routine in namd[38]. The fitted model was further refined by rounds of manual model building in coot[39] and real space refinement as implemented in the Phenix software package[40], the model restraints for the TT ligand were prepared by using the coordinates generated from Chem3D and the ELBOW software package[41]. The ligands were fitted after the first round of real-space refinements, manually first in coot[39], then refined using Phenix real-space refinement[42]. Ramachandran, rotamer and secondary structure restraints were applied for the first round of real-space refinement, and after manual inspection and

adjustment of the model in coot further real-space refinements were carried out with only Ramachandran and rotamer restraints applied and the model/data weight was allowed to freely refine. The density around the extracellular domain was poorly resolved (local resolution estimated at >8 Å) and was not modelled.

Modelling methods for preparation of molecular dynamic simulations

The two missing receptor loops, namely the stalk region and ICL3, were generated using PLOP[43]; ICL3 was also minimized in the presence of Gα to eliminate steric clashes. On the basis of the electron density of our structures, TM1 for the GLP-1-bound 5VAI structure[6] was replaced by TM1 from the P5-bound structure (PDB code 6B3J)[3] by the method of molecular superposition. The missing residues in the stalk region were reconstructed using Modeller[44] subject to the constraint that the high variability positions[45] in the GLP-1R multiple sequence alignment (E133–R134) faced outwards. The missing loops in the G protein were generated by molecular superposition, using VMD[46], of the corresponding loops in the β_2-adrenergic receptor–G protein complex[47], PDB code 3SN6 to the flank either side of the gap, since this particular X-ray structure (with 99% identity to the G protein used in this study) generally gave a lower root mean squared deviation value on molecular superposition than plausible alternative G-protein structures (for example, PDB 5VAI). The joining point was taken as the closest atom pairs (usually separated by approximately 0.2 Å) that maintained an appropriate Cα–Cα distance (3.7–3.9 Å) across the join; selected residues spanning the join were minimized using PLOP where additional refinement was deemed necessary. The exception to this was the loop between A249–N264, which was completed using the shorter loop from the adenosine A_{2A} receptor–G-protein complex, PDB code 5G53[48]. The helical domain, between residues G47 and G207, which is not visible in the cryo-EM structure, was omitted as in earlier work.

Molecular dynamics methods

Four GLP-1R complexes (GLP-1R–TT-OAD2–G_s; GLP-1R–TT-OAD2; GLP-1R–GLP-1–G_s; and GLP-1R–GLP-1; Supplementary Table 3) and two apo GLP-1R structures (obtained by removing both the G_s protein and the ligands; Supplementary Table 3) were prepared for simulation with the CHARMM36 force field[49], through use of in-house python htmd[50] and TCL (Tool Command Language) scripts. The pdb2pqr[51] and propka[52] software were used to add hydrogen atoms appropriate for a pH of 7.0; the protonation of titratable side chains was checked by visual inspection. The coordinates were superimposed on the corresponding GLP-1R coordinates from the OPM database[53] so as to orient the receptor before insertion[54] in a rectangular pre-built 125 Å × 116 Å 1-palmitoyl-2-oleyl-*sn*-glycerol-3-phosphocholine (POPC) bilayer; lipid molecules overlapping the receptor were removed. TIP3P water molecules were added to the 125 Å × 116 Å × 195 Å simulation box using the VMD Solvate plugin 1.5 (Solvate Plugin, v.1.5; http://www.ks.uiuc.edu/Research/vmd/plugins/solvate/). Overall charge neutrality was maintained by adding Na^+ and Cl^- counter ions to a final ionic concentration of 150 mM using the VMD Autoionize plugin 1.3 (Autoionize Plugin, v.1.3; http://www.ks.uiuc.edu/Research/vmd/plugins/autoionize/). CGenFF force field parameters[55–57] and topology files for TT-OAD2 were retrieved from the Paramch[56] webserver. No further optimization was performed because the obtained parameters were associated to low penalty scores.

Systems equilibration and molecular dynamics simulation settings

ACEMD[58] was used for both equilibration and molecular dynamics productive simulations. Isothermal-isobaric conditions (Langevin thermostat[59] with a target temperature of 300 K and damping of 1 ps^{-1} and Berendsen barostat[60] with a target pressure 1 atm) were used to equilibrates the systems through a multi-stage procedure (integration time step of 2 fs). Initial steric clashes between lipid atoms were reduced through 3,000 conjugate-gradient minimization steps, then a 2 ns molecular dynamics simulation was run with a positional constraint of 1 kcal mol^{-1} $Å^{-2}$ on protein atoms and lipid phosphorus atoms. Subsequently, 20 ns of molecular dynamics simulations were performed constraining only the protein atoms. In the final equilibration stage, protein backbone alpha carbons constraints were applied for a further 60 ns.

Productive trajectories in the canonical ensemble (NVT) at 300 K (four 500-ns-long replicas for each GLP-1R complex; Supplementary Table 3) were computed using a thermostat damping of 0.1 ps^{-1} with an integration time step of 4 fs and the M-SHAKE algorithm[61] to constrain the bond lengths involving hydrogen atoms. The cut-off distance for electrostatic interactions was set at 9 Å, with a switching function applied beyond 7.5 Å. Long-range Coulomb interactions were handled using the particle mesh Ewald summation method (PME)[62] by setting the mesh spacing to 1.0 Å. Trajectory frames were written every 100 ps of simulations.

Molecular dynamics analysis

The first half (500 ns) of the molecular dynamics replicas involving GLP-1R–TT-OAD2, GLP-1R–GLP-1 complexes as well as the apo-GLP-1R (TT-OAD2), and apo-GLP-1R (GLP-1) systems (Supplementary Table 3) were considered as part of the equilibration stage and therefore not considered for analysis. Atomic contacts (atom distance less than 3.5 Å) were computed using VMD[46]. Hydrogen bonds were identified using the GetContacts analysis tool (https://getcontacts.github.io/), with the donor-acceptor distance set to 3.3 Å and the angle set to 150°. Videos were generated using VMD[46] and avconv (https://libav.org/avconv.html). Root mean square fluctuation (RMSF) values were computed using VM[46] after superposition of the molecular dynamic trajectories frames on the alpha carbon of the transmembrane domain (residues $E138^{1.33}$–$V404^{7.60}$). The orientation of the N-terminal helix of the ECD of GLP-1R was drawn in VMD considering a representative frame every 10 ns. To detect volumes within the transmembrane domain of GLP-1R occupied by water molecules with low mobility (structural water molecules), the AquaMMapS[63] analysis was performed on 10-ns-long molecular dynamics simulations of the GLP-1R–TT-OAD2–G_s and GLP-1R–GLP-1–G_s complexes (coordinates were written every 10 ps of simulation); all the alpha carbons were restrained in analogy with the approach proposed previously[64].

Whole-cell radioligand binding assays

HEK293 cells (confirmed mycoplasma negative) were seeded at 30,000 cells per well in 96-well culture plates and incubated overnight in DMEM containing 5% FBS at 37 °C, 5% CO_2. Media was replaced with HBSS containing 25 mM HEPES and 0.1% (w/v) BSA with 0.1 nM ^{125}I-exendin(9–39) and increasing concentrations of unlabelled agonist. Cells were incubated overnight at 4 °C, washed three times in ice-cold buffer and then solubilized in 0.1 M NaOH. Radioactivity was determined by gamma counting. Non-specific activity was defined using 1 μM exendin(9–39).

cAMP accumulation assays

HEK293 cells (confirmed mycoplasma negative) were seeded at a density of 30,000 cells per well into 96-well culture plates and incubated overnight in DMEM containing 5% FBS at 37 °C in 5% CO_2. cAMP detection was performed as previously described in the presence of the phosphodiesterase inhibitor 3-isobutyl-1-methylxanthin[65]. All values were converted to cAMP concentration using a cAMP standard curve performed in parallel and data were subsequently normalized to the response of 100 μM forskolin in each cell line. In one series of experiments, vehicle or increasing concentrations of TT-OAD2 was added 30 min before assay of peptide response.

cAMP kinetics studies

HEK293A cells (confirmed mycoplasma negative) were transfected with an Epac-cAMP sensor (CAMYEL) and human GLP-1R at an optimized

ratio. Ligand-mediated cAMP production was measured 48 h after transfection. In brief, culture media was replaced with assay buffer (1× HBSS, 10 mM HEPES, 0.1% BSA, pH 7.4). BRET signals were measured at 1 min intervals using a PHERAstar plate reader (BMG LabTech) in the absent or present of increasing concentration of ligands. Forskolin (100 μM) was used as a positive control, and data were normalized to the forskolin response.

β-arrestin recruitment assays

HEK293 cells (confirmed mycoplasma negative) were transiently transfected with GLP-1R-Rluc8 and β-arrestin1-Venus at a 1:4 ratio and seeded at a density of 30,000 cells per well into 96-well culture plates and incubated for 48 h in DMEM containing 5% FBS at 37 °C in 5% CO_2. β-arrestin recruitment was performed as previously described[66]. In one series of experiments, vehicle or increasing concentrations of TT-OAD2 was added 30 min before assay of peptide response.

ERK1/2 phosphorylation assays

HEK293 cells (confirmed mycoplasma negative) expressing stably expressing the GLP-1R were seeded at a density of 30,000 cells per well into 96-well culture plates and incubated overnight at 37 °C in 5% CO_2. Receptor-mediated pERK1/2 was determined using the AlphaScreen ERK1/2 SureFire protocol as previously described[14]. Data were normalized to the maximal response elicited by 10% FBS determined at 6 min. In one series of experiments, vehicle or increasing concentrations of TT-OAD2 was added 30 min before assay of peptide response.

Ca^{2+} mobilization assays

HEK293 cells (confirmed mycoplasma negative) stably expressing the GLP-1R were seeded at a density of 30,000 cells per well into 96-well culture plates and incubated overnight at 37 °C in 5% CO_2, and receptor- mediated intracellular calcium mobilisation determined as previously described[65]. Fluorescence was determined immediately after ligand addition, with an excitation wavelength set to 485 nm and an emission wavelength set to 520 nm, and readings taken every 1.36 s for 120 s. The peak value was used to create concentration-response curves. Data were normalized to the maximal response elicited by 100 μM ATP. In one series of experiments, vehicle or increasing concentrations of TT-OAD2 was added 30 min before assay of peptide response.

Generation of stable cell lines containing wild-type and mutant GLP-1R

Mutant receptors were generated in a 2xc-Myc epitope-tagged receptor using QuikChange site-directed mutagenesis (Invitrogen) and sequences confirmed. Wild-type and mutant receptors were stably expressed in CHOFlpIn cells (confirmed mycoplasma negative) using the FlpIn Gateway technology system and selected using 600 μg ml^{-1} hygromyocin B.

NanoBRET ligand binding

HEK293A cells were transiently transfected with Nluc-hGLP-1R. Forty-eight hours after transfection, cells were collected and plasma membrane was extracted as described previously[31]. Cell membrane (1 μg per well) was incubated with furimazine (1:1,000 dilution from stock) in assay buffer (1× HBSS, 10 mM HEPES, 0.1% (w/v) BSA, 1× P8340 protease inhibitor cocktail, 1 mM DTT and 0.1 mM PMSF, pH 7.4). RhodamineX-Ex4 (Rox-Ex4) was used as fluorescent ligand in the NanoBRET binding assay. BRET signal between Nluc-hGLP-1R and Rox-Ex4 was measured using PHERAstar (BMG LabTech) at 10 s interval (25 °C), a 2 min baseline was taken before addition of Rox-Ex4 (K_d concentration 3.16nM, determined previously), the measurement continued for 15 min followed by adding increasing concentration of TT-OAD2, or unlabelled Ex4 as a control. Data were corrected for baseline and vehicle treated samples.

G-protein conformation assays

HEK293AΔS/Q/12/13 cells stably expressing GLP-1R (tested and confirmed to be free from mycoplasma) were transfected with a 1:1:1 ratio of Nanoluc-$G\alpha_s$ (Nanoluc inserted at position 72): $G\beta_1$:Venus-$G\gamma_2$ 24 h before collection and preparation of cell plasma membranes. Cell membrane (5 μg per well) was incubated with furimazine (1:1,000 dilution from stock) in assay buffer (1× HBSS, 10 mM HEPES, 0.1% (w/v) BSA, 1× P8340 protease inhibitor cocktail, 1 mM DTT and 0.1 mM PMSF, pH 7.4). The GLP-1R-induced BRET signal between $G\alpha_s$ and Gγ was measured at 30 °C using a PHERAstar (BMG LabTech). Baseline BRET measurements were taken for 2 min before addition of vehicle or ligand. BRET was measured at 15-s intervals for a further 7 min. All assays were performed in a final volume of 100 μl.

G-protein NanoBIT assays

HEK293A wild-type cells stably express human GLP-1R were transiently transfected with Gα-LgBIT, $G\beta_1$, $G\gamma_2$-SmBIT (1:5:5) 48 h before the assays. Cells were then incubated with coelenterazine H (5 μM) for 1 h at room temperature. Luminescence signals were measured using a Clariostar plate reader (BMG LabTech) at 30 s intervals before and after ligand addition (25 °C). Data were corrected to baseline and vehicle treated samples.

In vivo IVGTT assays

Intravenous glucose tolerance tests were performed in male human GLP-1R knock-in and knockout mice (all on C57/BL6 background[67]). Catheters were placed in the right carotid artery and left jugular vein of mice 6–11 months of age. Approximately one week later, mice (n = 4–5 per group) were fasted overnight and the catheters were exteriorized as mice acclimated to test cages. Vehicle (5% DMSO, 20% Captisol in $NaHPO_4$, pH 2, 1 ml kg^{-1}), GLP-1(7-36)NH_2 at 10 μg kg^{-1}, GIP(1-42) at 25 μg kg^{-1}, or OAD2 at 3 mg kg^{-1} was administered intravenously one minute before glucose load (0.5 g kg^{-1}). Blood samples were collected at −10, 0, 2, 4, 6, 10, 20 and 30 min to determine blood glucose concentrations via glucometer (Roche, Aviva) and plasma insulin measurement (Alpco, 80-INSMSU-E10). All mouse experiments were performed in accordance with the Institutional Animal Care and Use Committee of Eli Lilly and Company and the NIH Guide for the Use and Care of Laboratory Animals.

Data analysis

Pharmacological data were analysed using Prism 7 (GraphPad). Concentration response signalling data were analysed using a three-parameter logistic equation, or via operational analysis. Changes in the rate of change in BRET kinetic data were fitted to one-phase association curve. Statistical analysis was performed with either one-way analysis of variance and a Dunnetts post-test or a paired t-test, and significance accepted at $P < 0.05$.

Graphics

Molecular graphics images were produced using the UCSF Chimera package from the Computer Graphics Laboratory, University of California, San Francisco (supported by NIH P41 RR-01081).

Reporting summary

Further information on research design is available in the Nature Research Reporting Summary linked to this paper.

Data availability

All relevant data are available from the authors and/or included in the manuscript or Supplementary Information. Atomic coordinates and the cryo-EM density map have been deposited in the Protein Data Bank

(PDB) under accession number 6ORV and Electron Microscopy Data Bank (EMDB) accession EMD-20179.

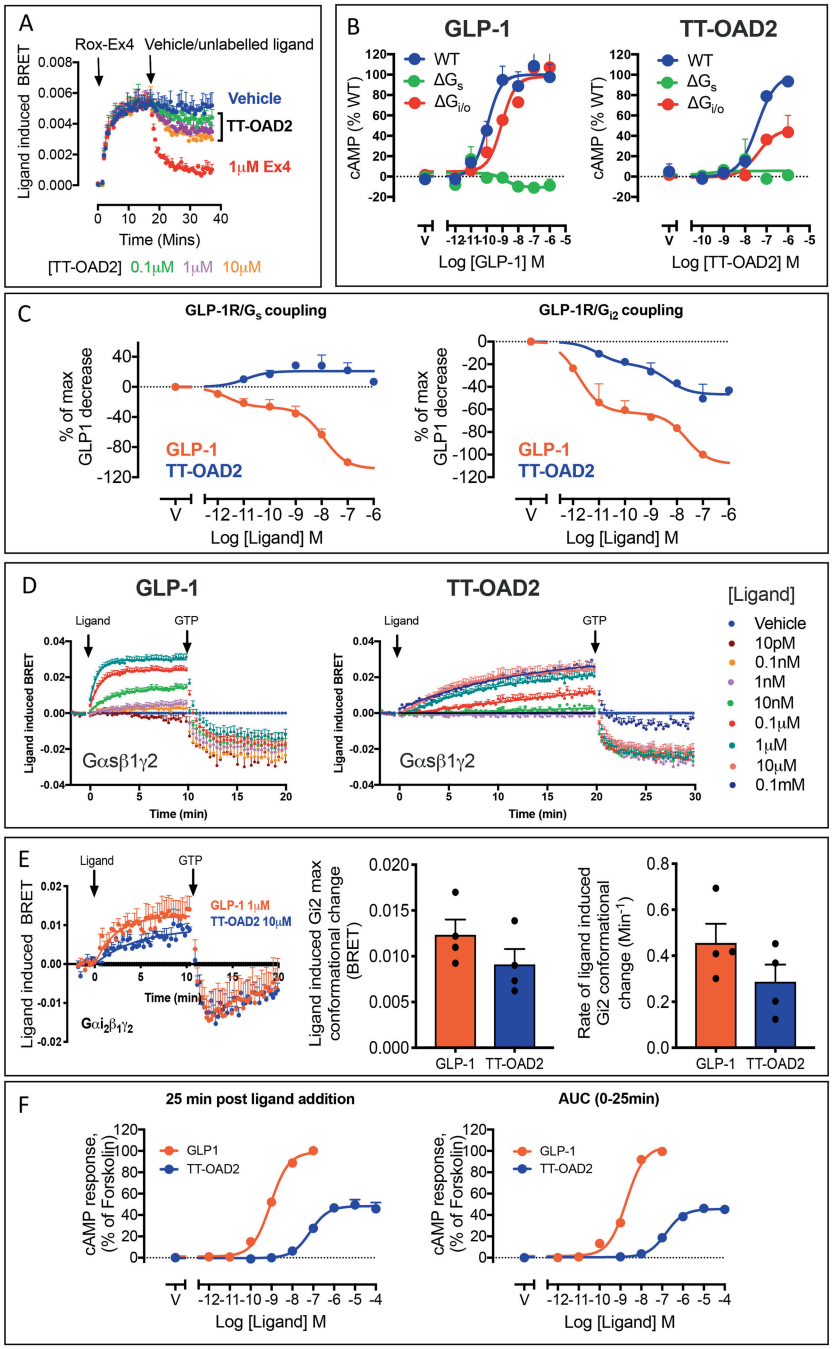
30. Liang, Y.-L. et al. Dominant negative G proteins enhance formation and purification of agonist-GPCR-G protein complexes for structure determination. *ACS Pharmacol. Transl. Sci.* **1**, 9 (2018).
31. Furness, S. G. B. et al. Ligand-dependent modulation of G protein conformation alters drug efficacy. *Cell* **167**, 739–749.e711 (2016).
32. Zheng, S. Q. et al. MotionCor2: anisotropic correction of beam-induced motion for improved cryo-electron microscopy. *Nat. Methods* **14**, 331–332 (2017).
33. Zhang, K. Gctf: Real-time CTF determination and correction. *J. Struct. Biol.* **193**, 1–12 (2016).
34. Nakane, T., Kimanius, D., Lindahl, E. & Scheres, S. H. Characterisation of molecular motions in cryo-EM single-particle data by multi-body refinement in RELION. *eLife* **7**, e36861 (2018).
35. Zivanov, J. et al. New tools for automated high-resolution cryo-EM structure determination in RELION-3. *eLife* **7**, e42166 (2018).
36. Punjani, A., Rubinstein, J. L., Fleet, D. J. & Brubaker, M. A. cryoSPARC: algorithms for rapid unsupervised cryo-EM structure determination. *Nat. Methods* **14**, 290–296 (2017).
37. Kucukelbir, A., Sigworth, F. J. & Tagare, H. D. Quantifying the local resolution of cryo-EM density maps. *Nat. Methods* **11**, 63–65 (2014).
38. Chan, K. Y., Trabuco, L. G., Schreiner, E. & Schulten, K. Cryo-electron microscopy modeling by the molecular dynamics flexible fitting method. *Biopolymers* **97**, 678–686 (2012).
39. Emsley, P., Lohkamp, B., Scott, W. G. & Cowtan, K. Features and development of Coot. *Acta Crystallogr. D* **66**, 486–501 (2010).
40. Adams, P. D. et al. PHENIX: a comprehensive Python-based system for macromolecular structure solution. *Acta Crystallogr. D* **66**, 213–221 (2010).
41. Moriarty, N. W., Grosse-Kunstleve, R. W. & Adams, P. D. electronic Ligand Builder and Optimization Workbench (eLBOW): a tool for ligand coordinate and restraint generation. *Acta Crystallogr. D* **65**, 1074–1080 (2009).
42. Afonine, P. V. et al. Real-space refinement in PHENIX for cryo-EM and crystallography. *Acta Crystallogr. D* **74**, 531–544 (2018).
43. Jacobson, M. P. et al. A hierarchical approach to all-atom protein loop prediction. *Proteins* **55**, 351–367 (2004).
44. Eswar, N. et al. Comparative protein structure modeling using Modeller. *Curr Protoc Bioinformatics* **Chapter 5**, Unit 5.6 (2006).
45. Vohra, S. et al. Similarity between class A and class B G-protein-coupled receptors exemplified through calcitonin gene-related peptide receptor modelling and mutagenesis studies. *J. R. Soc. Interface* **10**, 20120846 (2012).
46. Humphrey, W., Dalke, A. & Schulten, K. VMD: visual molecular dynamics. *J. Mol. Graph* **14**, 33–38 (1996).
47. Rasmussen, S. G. et al. Crystal structure of the β_2 adrenergic receptor–G_s protein complex. *Nature* **477**, 549–555 (2011).
48. Carpenter, B., Nehmé, R., Warne, T., Leslie, A. G. & Tate, C. G. Structure of the adenosine A_{2A} receptor bound to an engineered G protein. *Nature* **536**, 104–107 (2016).
49. Huang, J. & MacKerell, A. D. Jr. CHARMM36 all-atom additive protein force field: validation based on comparison to NMR data. *J. Comput. Chem.* **34**, 2135–2145 (2013).
50. Doerr, S., Harvey, M. J., Noé, F. & De Fabritiis, G. HTMD: high-throughput molecular dynamics for molecular discovery. *J. Chem. Theory Comput.* **12**, 1845–1852 (2016).
51. Dolinsky, T. J., Nielsen, J. E., McCammon, J. A. & Baker, N. A. PDB2PQR: an automated pipeline for the setup of Poisson–Boltzmann electrostatics calculations. *Nucleic Acids Res.* **32**, W665–W667 (2004).
52. Olsson, M. H., Søndergaard, C. R., Rostkowski, M. & Jensen, J. H. PROPKA3: consistent treatment of internal and surface residues in empirical pka predictions. *J. Chem. Theory Comput.* **7**, 525–537 (2011).
53. Lomize, M. A., Lomize, A. L., Pogozheva, I. D. & Mosberg, H. I. OPM: orientations of proteins in membranes database. *Bioinformatics* **22**, 623–625 (2006).
54. Sommer, B. Membrane packing problems: a short review on computational membrane modeling methods and tools. *Comput. Struct. Biotechnol. J.* **5**, e201302014 (2013).
55. Vanommeslaeghe, K. et al. CHARMM general force field: a force field for drug-like molecules compatible with the CHARMM all-atom additive biological force fields. *J. Comput. Chem.* **31**, 671–690 (2010).
56. Vanommeslaeghe, K. & MacKerell, A. D. Jr. Automation of the CHARMM General Force Field (CGenFF) I: bond perception and atom typing. *J. Chem. Inf. Model.* **52**, 3144–3154 (2012).
57. Vanommeslaeghe, K., Raman, E. P. & MacKerell, A. D. Jr. Automation of the CHARMM General Force Field (CGenFF) II: assignment of bonded parameters and partial atomic charges. *J. Chem. Inf. Model.* **52**, 3155–3168 (2012).
58. Harvey, M. J., Giupponi, G. & Fabritiis, G. D. ACEMD: Accelerating Biomolecular Dynamics in the Microsecond Time Scale. *J. Chem. Theory Comput.* **5**, 1632–1639 (2009).
59. Loncharich, R. J., Brooks, B. R. & Pastor, R. W. Langevin dynamics of peptides: the frictional dependence of isomerization rates of *N*-acetylalanyl-*N*'-methylamide. *Biopolymers* **32**, 523–535 (1992).
60. Berendsen, H. J. C., Postma, J. P. M., van Gunsteren, W. F., DiNola, A. & Haak, J. R. Molecular dynamics with coupling to an external bath. *J. Chem. Phys.* **81**, 3684 (1984).
61. Kräutler, V. G., van Gunsteren, W. F. & Hünenberger, P. H. A fast SHAKE algorithm to solve distance constraint equations for small molecules in molecular dynamics simulations. *J. Comput. Chem.* **22**, 501–508 (2001).
62. Essmann, U. P. & Berkowitz, L. M.L. A smooth particle mesh Ewald method. *J. Chem. Phys.* **103**, 8577 (1995).
63. Cuzzolin, A., Deganutti, G., Salmaso, V., Sturlese, M. & Moro, S. AquaMMapS: an alternative tool to monitor the role of water molecules during protein-ligand association. *ChemMedChem* **13**, 522–531 (2018).
64. Wall, M. E., Calabró, G., Bayly, C. I., Mobley, D. L. & Warren, G. L. Biomolecular solvation structure revealed by molecular dynamics simulations. *J. Am. Chem. Soc.* **141**, 4711–4720 (2019).
65. Koole, C. et al. Allosteric ligands of the glucagon-like peptide 1 receptor (GLP-1R) differentially modulate endogenous and exogenous peptide responses in a pathway-selective manner: implications for drug screening. *Mol. Pharmacol.* **78**, 456–465 (2010).
66. Savage, E. E., Wootten, D., Christopoulos, A., Sexton, P. M. & Furness, S. G. A simple method to generate stable cell lines for the analysis of transient protein-protein interactions. *Biotechniques* **54**, 217–221 (2013).
67. Jun, L. S. et al. A novel humanized GLP-1 receptor model enables both affinity purification and Cre-LoxP deletion of the receptor. *PLoS One* **9**, e93746 (2014).

Acknowledgements The work was supported by the Monash University Ramaciotti Centre for Cryo-Electron Microscopy, the Monash MASSIVE high-performance computing facility, the National Health and Medical Research Council of Australia (NHMRC) project grants (1061044, 1065410, 1120919 and 1126857) and NHMRC program grants (1055134 and 1150083), the Japan Society for the Promotion of Science (JSPS) KAKENHI no. 18H06043 and Japan Science and Technology Agency (JST) PRESTO no. 18069571 (to R.D.). P.M.S. and A.C. are NHMRC Senior Principal Research Fellows and D.W. is an NHMRC Senior Research Fellow. S.G.B.F. is an ARC Future Fellow. A.I. was funded by the PRIME JP17gm5910013 and the LEAP JP17gm0010004 from the Japan Agency for Medical Research and Development, and JSPS KAKENHI 17K08264. We are grateful to G. Christopoulos, V. Julita, T. Fields, C. Lafuente, J. M. Minguez, G. C. Sanz and F. Qu for assay and technical support.

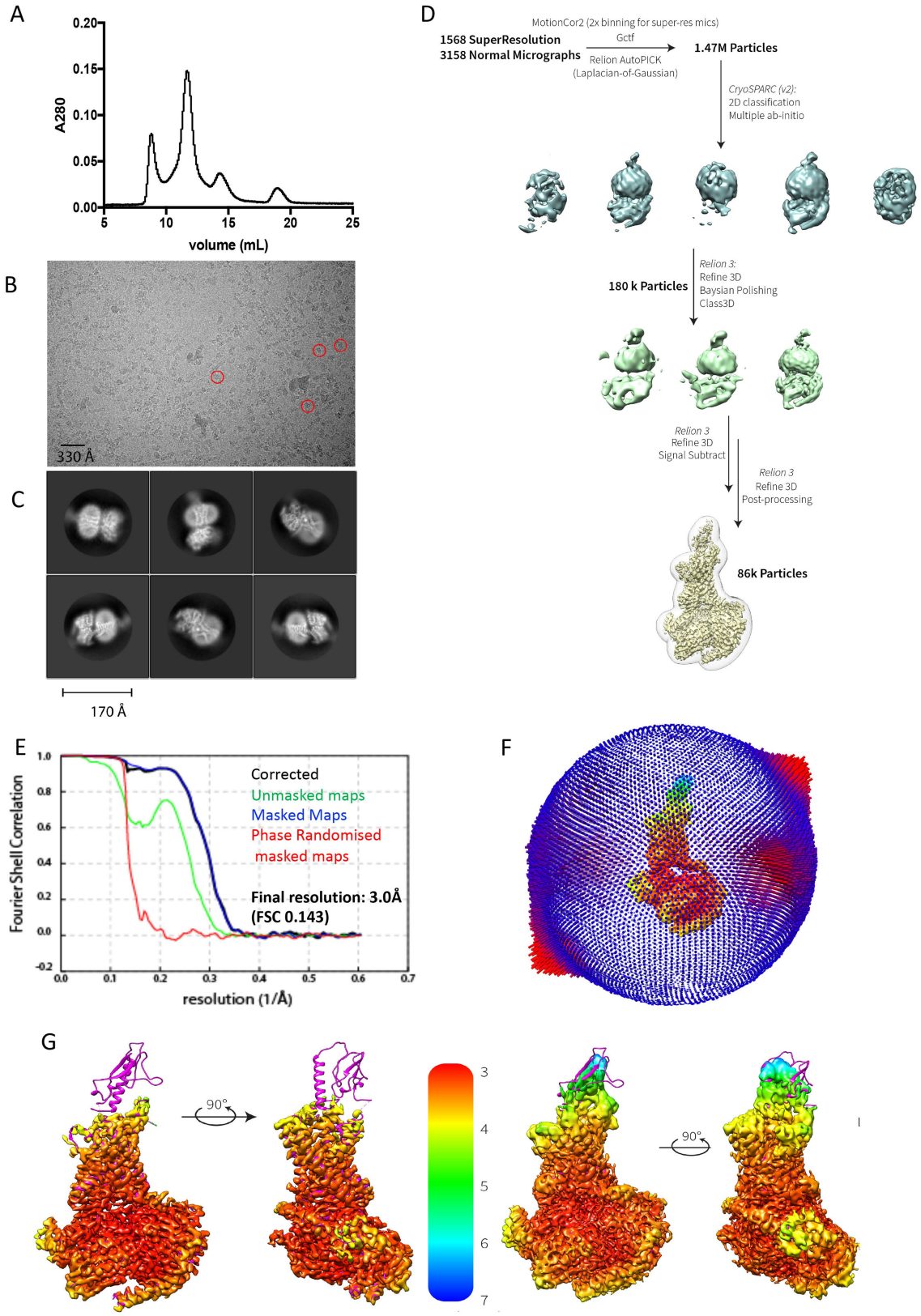
Author contributions P.Z. designed and performed most of the pharmacological studies with assistance from T.T.T.; Y.-L.L. expressed and purified the complex; R.D. performed cryo-sample preparation and imaging to acquire electron microscopy data; M.J.B. and R.D. processed the electron microscopy data and performed electron microscopy map calculations; M.J.B. built the model and performed refinement; M.M.F. performed the mutagenesis studies, L.C. performed studies in the HEK293 CRISPR-knockout cells; G.D. and C.A.R. designed, performed and analysed the molecular dynamics simulations; F.S.W. and M.G.B. provided TT-OAD2. M.E.C., M.G.B. and K.W.S. designed and oversaw the in vivo studies; P.Z., Y.-L.L., M.J.B., G.D., C.A.R., F.S.W., K.W.S., R.D., P.M.S. and D.W. performed data analysis; P.Z., Y.-L.L., M.J.B., G.D., C.A.R., F.S.W., K.W.S., A.C., L.J.M., M.-W.W. and R.D. assisted with data interpretation, figure and manuscript preparation; P.M.S. and D.W. designed and supervised the project, interpreted the data and wrote the manuscript.

Competing interests F.W.S., M.E.C. and K.W.S. are employees of Eli Lilly and Company.

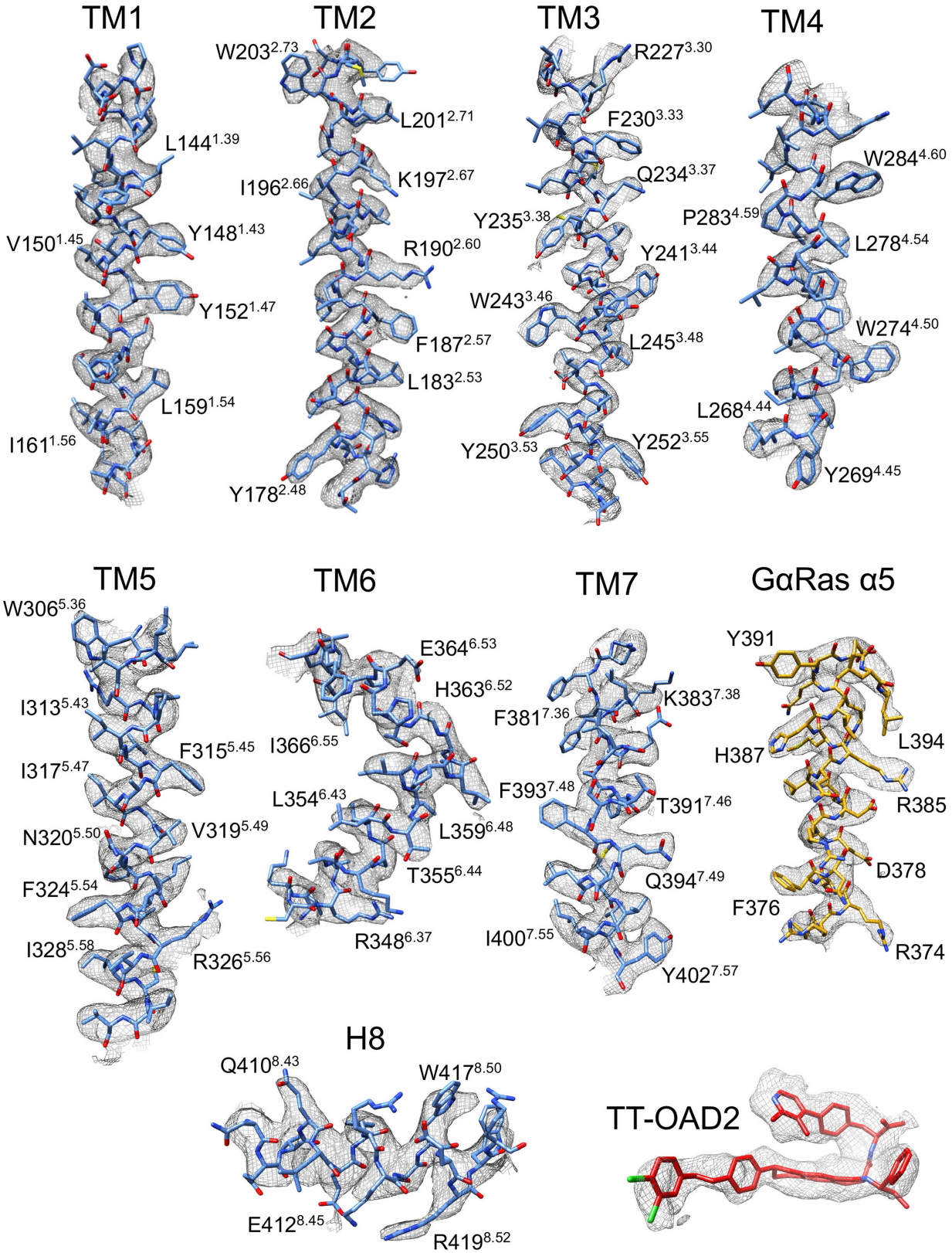
Additional information
Supplementary information is available for this paper at https://doi.org/10.1038/s41586-019-1902-z.
Correspondence and requests for materials should be addressed to R.D., P.M.S. or D.W.
Peer review information *Nature* thanks Doryen Bubeck, Dave D'Alessio, Nita R. Shah and the other, anonymous, reviewer(s) for their contribution to the peer review of this work.
Reprints and permissions information is available at http://www.nature.com/reprints.



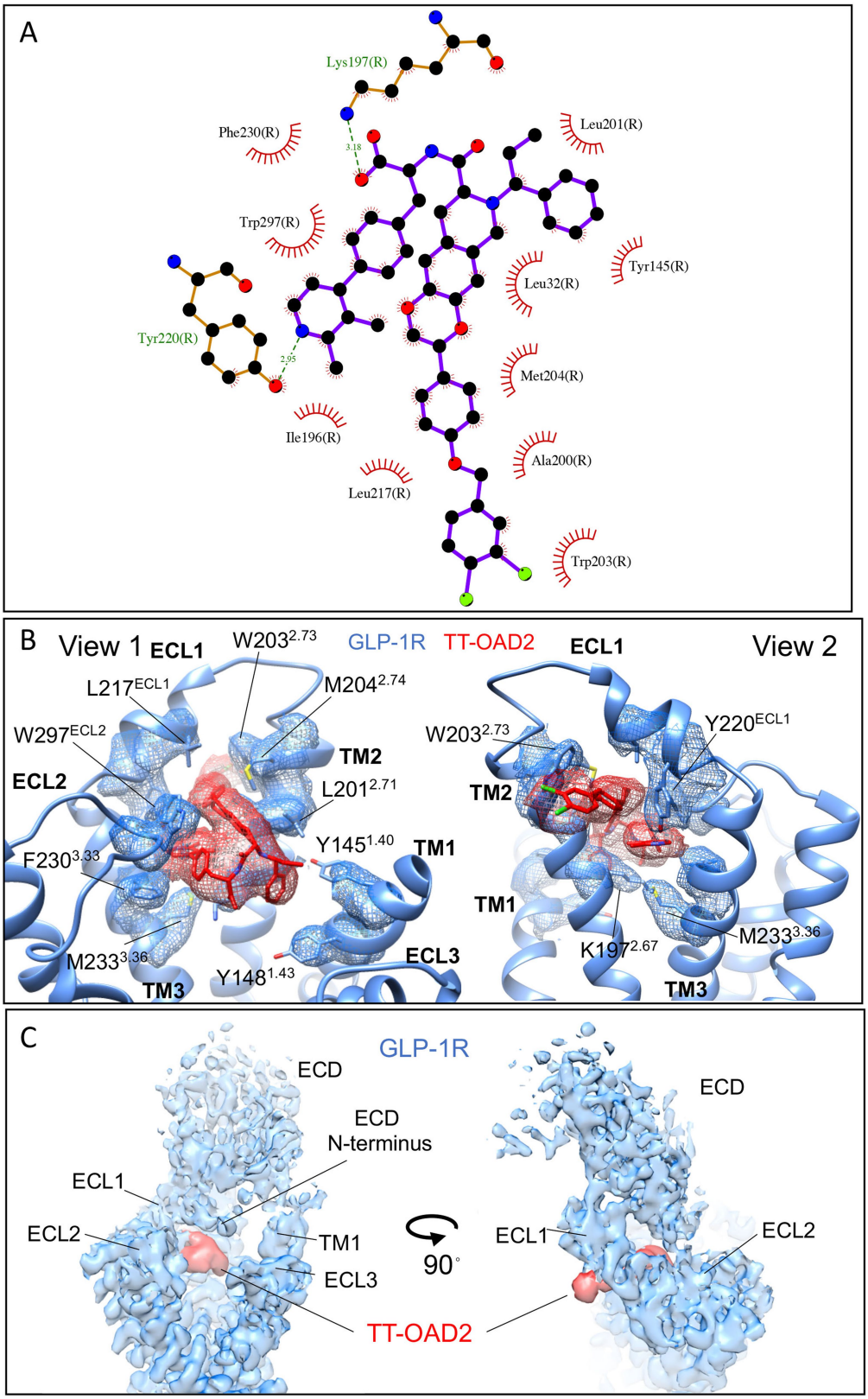
Extended Data Fig. 1 | Binding, transducer coupling and signalling mediated by TT-OAD2. a, Kinetic ligand-binding assay using ROX-exendin-4 as the fluorescent probe. TT-OAD2 is only able to partially displace the probe and with slower kinetics relative to exendin-4 that shows complete displacement of the probe with rapid kinetics. **b**, cAMP accumulation studies using GLP-1 and TT-OAD2 as the agonist in wild-type HEK293 cells and HEK293 cells in which $G_{s/olf}$ (ΔG_s) or all $G_{i/o/z}$ ($\Delta G_{i/o/z}$) have been depleted using CRISPR–Cas9. **c**, HEK293A cells transiently transfected with the GLP-1R and the NanoBit constructs for $G\alpha_s$ and $G\alpha_{i2}$ (Gα-LgBIT, $G\gamma_2$-SmBIT). Luminescence signal was assessed over time (0–20 min) in the presence of increasing concentrations of GLP-1 and TT-OAD2. Concentration response curves are expressed as AUC (0–20 min) for each concentration and normalized to the negative response observed by GLP-1 at 1 μM. **d**, Agonist-induced changes in trimeric G_s protein conformation. Ligand-induced changes in BRET were measured in plasma membrane preparations performed in kinetic mode until kinetic equilibrium was reached for vehicle or increasing concentrations of GLP-1 (left) and TT-OAD2 (right). The addition of GTP dissociated the trimeric G protein complex stabilized by GLP-1-occupied and TT-OAD2-occupied GLP-1R. **e**, Agonist-induced changes in trimeric G_{i2} protein conformation. Left, ligand-induced changes in BRET were measured in plasma membrane preparations performed in kinetic mode until kinetic equilibrium with a saturating concentration of GLP-1 and TT-OAD2. The BRET signal decreased in the presence of GTP, which suggests that GTP dissociated the G_{i2} protein complex stabilized by GLP-1-occupied and TT-OAD2-occupied GLP-1R. Quantification of the plateau (middle) and the rate of ligand-induced conformational change (right) for each agonist (1 μM GLP-1 and 10 μM TT-OAD2) was calculated by applying a one-phase association curve to the kinetic data with values from each individual experiment show in black circles. **f**, Concentration–response curves of production in live HEK293 cells expressing the GLP-1R and an EPAC BRET biosensor in the presence of different concentrations of GLP-1 and TT-OAD2. Left, cAMP response taken 25 min after ligand addition. Right, area under the curve (AUC) analysis of the response calculated as AUC across the full kinetic trace for each ligand concentration (from data in Fig. 2d). Data are mean + s.e.m. of 4–6 independent experiments performed in duplicate or triplicate.



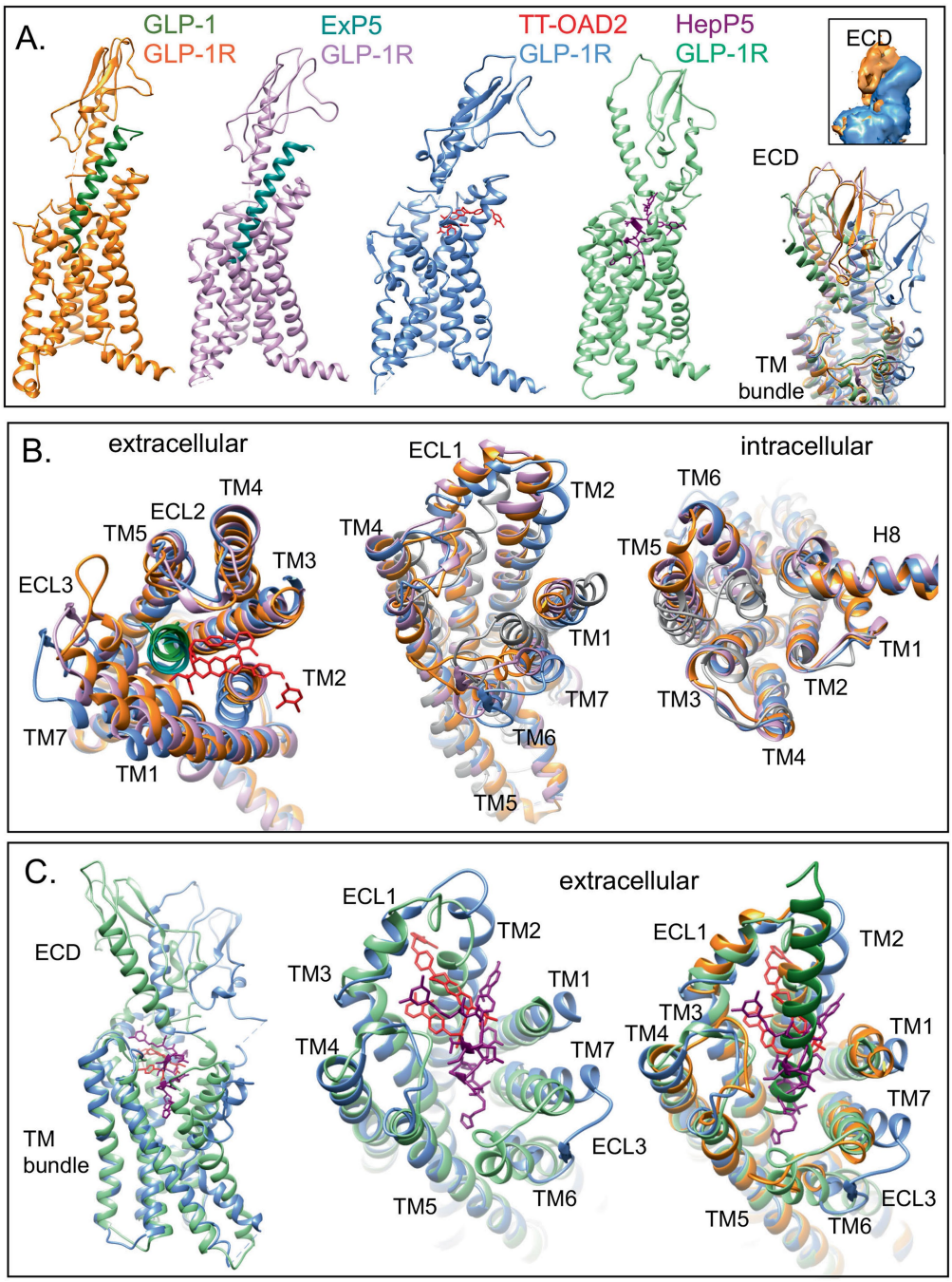
Extended Data Fig. 2 | Purification, cryo-EM data imaging and processing of the TT-OAD2–GLP-1R–G_s complex. a, Representative elution profile of Flag-purified complex on Superdex 200 Increase 10/30 SEC. **b**, Representative micrograph of the TT-OAD2–GLP-1R–G_s complex. Red circles highlight examples of individual particles. **c**, Two-dimensional class averages of the complex in maltose-neopentyl glycol (MNG) micelle. **d**, Cryo-EM data processing workflow. **e**, Gold-standard Fourier shell correlation (FSC) curves, showing the overall nominal resolution at 3.0 Å. **f**, 3D histogram representation of the Euler angle distribution of all the particles used for the in the reconstruction overlaid on the density map drawn on the same coordinate axis (map is coloured according to local resolution as in **g**). **g**, Cryo-EM density map coloured according to resolution. Left, map with the GLP-1R ECD masked; right, map including the ECD of GLP-1R.



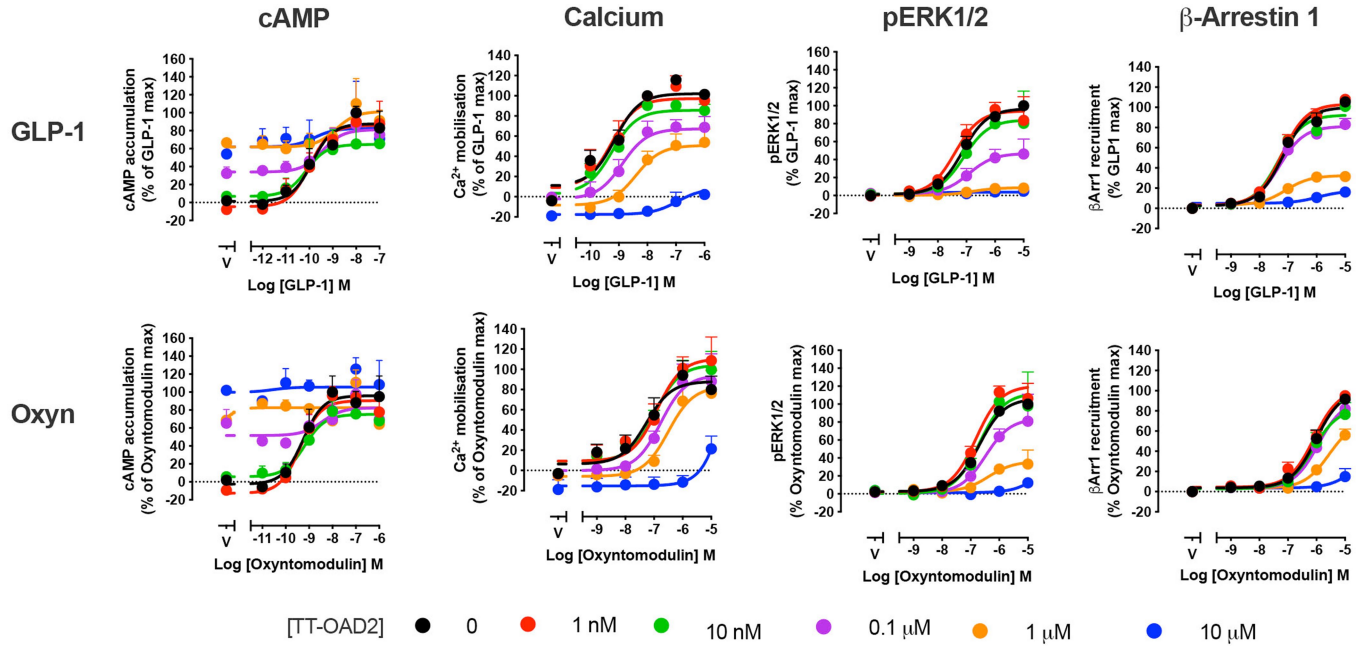
Extended Data Fig. 3 | The atomic resolution model of the TT-OAD2–GLP-1R–Gα_s heterotrimer in the cryo-EM density map. Electron microscopy density map and the model are shown for all seven transmembrane helices and helix 8 (H8) of the receptor, the α5 helix of the Gα_s Ras-like domain and TT-OAD2. All transmembrane helices exhibit good density, with TM6 that displays flexibility being the least well resolved region.



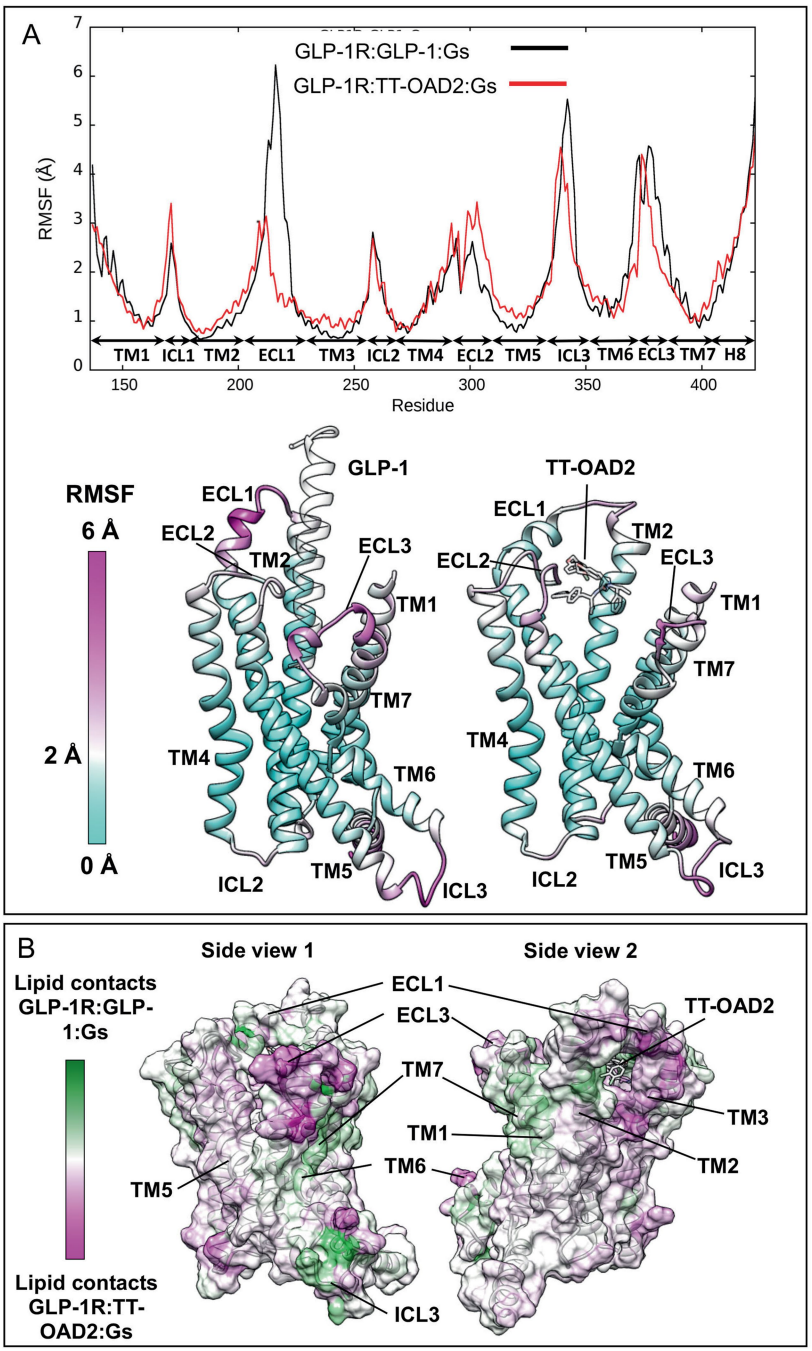
Extended Data Fig. 4 | Cryo-EM density supports ligand interactions in the TT-OAD2-binding site. a, Interacting residues predicted by LigPlot using the full-length model with ECD. **b**, The pose of TT-OAD2 and interactions with residues within TM1, TM2, TM3, ECL1 and ECL2 are supported by well-resolved density in the cryo-EM map. **c**, Density for the ECD was visible in the cryo-EM and supports extended interactions of the ECD with ECL1 and ECL2, as well as with the ligand TT-OAD2.



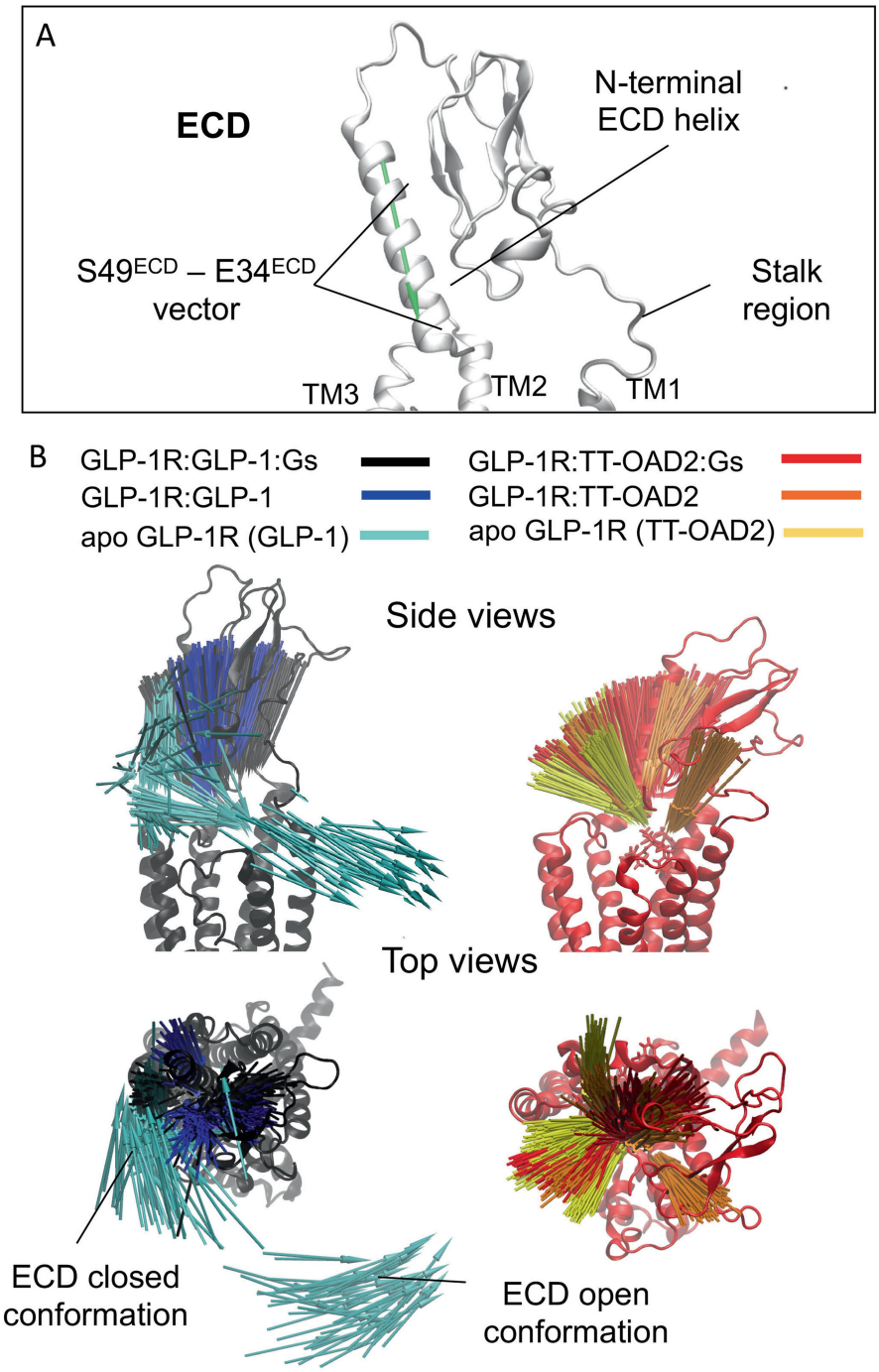
Extended Data Fig. 5 | Comparison of the TT-OAD2–GLP-1R–G_s complex with peptide agonist-bound GLP-1R structures and the inactive class B GPCR glucagon receptor transmembrane helices. a, Structures of agonist-bound GLP-1R; from left to right: GLP-1R (orange) bound to GLP-1 peptide (green) in an active conformation, GLP-1R (pink) bound to ExP5 peptide (cyan) in an active conformation, GLP-1R (blue) bound to non-peptide TT-OAD2 (red) in an active conformation, GLP-1R (pale green) bound to 11-mer peptide HepP5 (purple) in a partially active conformation. Far right, overlay of GLP-1R agonist-bound structures highlighting variations within the ECD position in the different structures. Inset, differences in the location of the ECD are supported by density in the cryo-EM maps; shown are the GLP-1-bound (orange) and TT-OAD2 bound (blue) GLP-1R. **b**, **c**, Various overlays of these structures (using the same colours) to compare conformational differences between the different structures. **b**, Overlay of TT-OAD2-bound GLP-1R G_s structure with the full-length peptide bound G_s structures and the inactive glucagon receptor (GCGR; grey) bundle reveals common conformational transitions occur in all agonist-bound structures relative to the inactive GCGR, but the extent of these movements differ. A more open helical bundle is observed for the TT-OAD2-bound GLP-1R than either GLP-1- or ExP5-bound owing to a distinction in the conformations of TM1, TM6, TM7 and ECL3 at the extracellular side of the receptor induced by the binding of the different ligands (left and middle). Middle, differences in the conformation of TM2 between the inactive and peptide-agonist-bound structures is also evident. Right, at the intracellular face all active structures display a similar large outward movement of TM6 and a smaller movement within TM5. **c**, Comparison of TT-OAD2-bound GLP-1R with the small peptide HepP5-bound GLP-1R structure. Left, TT-OAD2 and Hep-P5 occupy a partially overlapping binding site but promote distinct conformations of the ECD and transmembrane bundle of the GLP-1R. Middle, HepP5 engages deeper in the helical bundle than TT-OAD2 and promotes a more closed helical bundle owing to differences induced in the conformation of TM1, TM6, TM7 and ECL3. Right, overlay of the TT-OAD2-, Hep-P5- and GLP-1-bound GLP-1R transmembrane bundles reveals HepP5 induces a similar conformation of the helical bundle to GLP-1 whereas TT-OAD2 induces a distinct conformation.



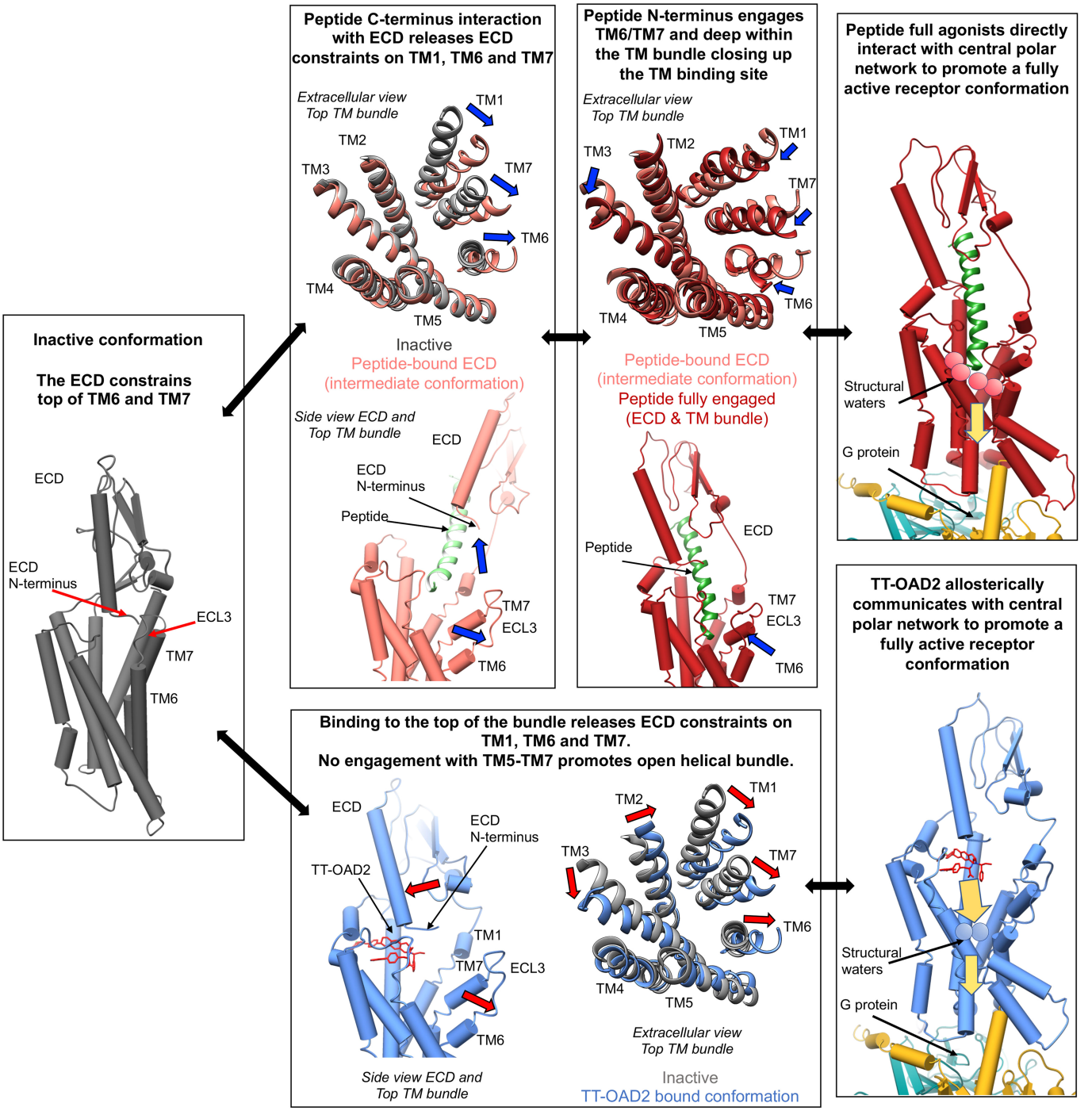
Extended Data Fig. 6 | Pharmacological responses exhibited by endogenous ligands GLP-1 and oxyntomodulin in the presence of TT-OAD2. Signalling profiles of GLP-1 and oxyntomodulin, after 30 min preincubation of vehicle (0) or increasing concentrations of TT-OAD2. Data were performed in HEK293A cells stably expressing the GLP-1R, and are mean + s.e.m. of 3–4 independent experiments performed in duplicate.



Extended Data Fig. 7 | GLP-1R domains are stabilized by either ligand contacts or lipid interactions. a, Top, RMSF values of alpha carbons computed during MD simulations of the GLP-1R–GLP-1–G_s complex (black line) and the GLP-1R–TT-OAD2–G_s complex (red line); transmembrane helices, intracellular loops (ICLs), and ECLs positions are indicated. Bottom left, RMSF values plotted on the GLP-1R structure bound to GLP-1 (transparent ribbon). Bottom right, RMSF values plotted on the GLP-1R structure bound to TT-OAD2 (transparent stick representation). ECL1 and ECL3 were more dynamic in the GLP-1-bound receptor than the TT-OAD2-bound structure. By contrast, ECL2 and the top end of TM5 were more mobile in the GLP-1R–TT-OAD2–G_s complex. **b**, GLP-1R contacts formed with membrane lipids during molecular dynamic simulations of the GLP-1R–TT-OAD2–G_s and the GLP-1R–GLP-1–G_s systems. Two sides views of the receptor are shown (ribbon and transparent surface). When bound to TT-OAD2, ECL1, TM3, the distal end of TM6, and ECL3 are more in contact with the membrane lipids (magenta). By contrast, TM1 and TM7 are more prone to interact with the membrane when GLP-1 is bound (green). The outward movement of ECL3 in the GLP-1R–TT-OAD2–G_s complex (stabilized by a hydrogen bond network different than GLP-1R–GLP-1–G_s; Extended Data Table 2) produces more interactions with the lipids, possibly further stabilizing the open conformation of TM6, ECL3 and TM7.



Extended Data Fig. 8 | Dynamics of the ECD of GLP-1R. a, The vector (shown here as a green arrow) connecting $S49^{ECD}$ and $E34^{ECD}$ alpha carbons (ECD N-terminal helix) are shown in the box. **b**, Left, ECD N-terminal helix orientations observed during the molecular dynamics simulation of the GLP-1R–GLP-1–G_s (black arrows), the GLP-1R–GLP-1 complex (obtained by removing G protein; blue arrows), and the apo-GLP-1R (obtained by removing both the G_s protein and GLP-1; cyan arrows) are shown on the left viewed from the top and side of the bundle. The receptor is shown as a dark grey ribbon. During molecular dynamic simulations with GLP-1 bound, the N-terminal helix was oriented vertically (black and blue arrows), whereas in the apo-form the ECD N-terminal helix was more dynamic and experienced both open and closed conformations (this is analogous to the suggested ECD dynamics for the glucagon receptor). Right, ECD N-terminal helix orientations of the GLP-1R–TT-OAD2–G_s (red arrows), the GLP-1R–TT-OAD2 complex (obtained by removing G protein; orange arrows), and the apo-GLP-1R (obtained by removing both the G_s protein and TT-OAD2; yellow arrows) are shown. The receptor is shown as a red ribbon. The distal end ($S49^{ECD}$) of the helix was more mobile than the proximal one ($E34^{ECD}$), which had an overall tendency to remain in the proximity of the TT-OAD2-binding site, driven by transient interactions with the ligand (Extended Data Table 1) and hydrogen bonds with the $R299^{ECL2}$ side chain (Extended Data Table 2). Molecular dynamics simulations therefore suggest a different behaviour for residue $R299^{ECL2}$, which is stably involved in interactions with the peptide in the GLP-1-R–GLP-1–G_s complex (Extended Data Table 1), and instead interacts with $E34^{ECD}$ and other residues located at the ECL2 ($E294^{ECD}$, $D293^{ECD}$ and $N300^{ECD}$) in the GLP-1R–TT-OAD2–G_s complex (Extended Data Table 2).



Extended Data Fig. 9 | Proposed activation mechanism of class B GPCRs. Left, in the inactive conformation, the top of the transmembrane domain is stabilized by interactions of the ECD with the TM6–ECL3–TM7 region. Top, activation of class B GPCRs by peptides occurs via a two domain mechanism. Top left, engagement of the peptide with the receptor ECD releases ECD constraints on the transmembrane domain promoting outward movements of TM1, TM6 and TM7 by peptide. Middle, interaction of the peptide N terminus in the bundle within TM1, TM2, TM3, TM5, TM6 and TM7 promotes TM1, TM6 and TM7 to close in around the peptide. Direct engagement of peptides with the central polar network facilitates conformational transitions required for G protein coupling and activation. Top right, the active conformation of the central polar network is stabilized by a series of structural waters. Bottom, interaction of the non-peptide TT-OAD2 at the top of the GLP-1R transmembrane bundle releases ECD constraints on the transmembrane bundle resulting in movements of TM1, TM6 and TM7 outwards. TT-OAD2 does not engage TM5–TM7 and the bundle remains open. TT-OAD allosterically promotes conformational rearrangement of the central polar network to stabilize the fully active receptor conformation that allows coupling to G protein. Bottom right, the central polar network is stabilized by a distinct network of structural waters relative to peptide-mediated activation.

Extended Data Table 1 | GLP-1R–TT-OAD2 and GLP-1R–GLP-1 contacts during molecular dynamics simulations performed on the GLP-1R–TT-OAD2–G_s and GLP-1R–GLP-1–G_s complexes

GLP-1R:TT-OAD2 (TM) Residues	Contacts occupancy (% frames)	GLP-1R:GLP-1 (TM) Residues	Contacts occupancy (% frames)
*K197$^{2.67}$	100.0	*R299^{ECL2}	302.9
A200$^{2.70}$	100.0	L388$^{7.43}$	288.0
Y220^{ECL1}	100.0	L201$^{2.71}$	273.2
*F230$^{3.33}$	99.9	L384$^{7.39}$	266.2
*M204$^{2.74}$	99.8	Y205^{ECL1}	261.3
*W297^{ECL2}	99.8	L142$^{1.37}$	222.5
W203$^{2.73}$	99.7	L141$^{1.36}$	196.2
C226$^{3.29}$	99.7	*Y145$^{1.40}$	193.2
*M233$^{3.36}$	99.5	F381$^{7.36}$	187.4
V229$^{3.32}$	99.2	R190$^{2.60}$	151.1
L201$^{2.71}$	98.9	*K197$^{2.67}$	140.8
L217^{ECL1}	98.1	*M233$^{3.36}$	139.1
I196$^{2.66}$	88.6	E387$^{7.42}$	132.1
*Y145$^{1.40}$	68.9	*Y148$^{1.43}$	131.2
Q221^{ECL1}	67.4	H212^{ECL1}	124.1
A199$^{2.69}$	52.4	Q213^{ECL1}	111.8
Q234$^{3.37}$	48.6	E364$^{6.53}$	103.7
D198$^{2.68}$	44.4	T391$^{7.46}$	101.3
T29^{ECD}	43.9	W214^{ECL1}	93.2
*Y148$^{1.43}$	43.4	V237$^{3.40}$	89.6
*V194$^{2.64}$	42.6	*F230$^{3.33}$	87.3
S31^{ECD}	41.5	*T298^{ECL2}	86.6
C296^{ECL2}	40.3	*V194$^{2.64}$	81.0
W33^{ECD}	38.7	Y241$^{3.44}$	80.3
A28^{ECD}	36.4	W306$^{5.36}$	76.6
L32^{ECD}	25.1	R376^{ECL3}	69.1
T149$^{1.44}$	23.6	*$^{\#}$W297^{ECL2}	67.0
*R299^{ECL2}	22.0	F367$^{6.56}$	62.6
*T298^{ECL2}	20.1	R310$^{5.40}$	59.6
		F385$^{7.40}$	57.0
		I313$^{5.43}$	56.7
		*M204^{ECL1}	52.7

Contacts involving the GLP-1R transmembrane domain are determined as the sum of the occupancy (reported as percentage of frames) of all the contacts involving each residue. Values higher than 100% indicate residues able to interact with more than one peptide side chain. A contact was considered productive if the distance between the residue and the ligand was less than 3.5 Å. Data are summarized in Fig. 4c. TT-OAD2 mainly interacted with TM2, ECL1 and TM3. Interactions with TM1 and ECL2 were present but not persistent (with the exception of W297^{ECL2}). The N-terminal helix of the ECD was engaged in (many) transient interactions. Overall, GLP-1 interacted with a different set of residues and was able to further involve TM5, TM6 and TM7. TT-OAD2 and GLP-1 common contact residues (indicated by an asterisk) were located at TM1, TM2 and ECL2. Ligand contacts formed via interaction with the receptor backbone rather than a side chain interaction are indicated by a hash symbol.

Extended Data Table 2 | Main GLP-1R–GLP-1R intramolecular hydrogen bonds during molecular dynamics simulation

GLP-1R residues involved in intramolecular hydrogen bonds		GLP-1R:TT-OAD2:Gs	GLP-1R:GLP-1:Gs	GLP-1R:GLP-1:Gs / GLP-1R:TT-OAD2:Gs Δ occupancy [a]
R40^{ECD}	D215^{ECL1}	38.2	68.6	30.4
R176$^{2.46}$	E408^{H8}	35.7		-35.7
R176$^{2.46}$	E247$^{3.50}$	46.7	97.9	51.2
N182$^{2.52}$	W274$^{4.50}$	73	81.4	8.4
R190$^{2.60}$	E364$^{6.53}$	4	5	1
R190$^{2.60}$	Y241$^{3.44}$	13.9	14.2	0.3
R190$^{2.60}$	N240$^{3.43}$	78,2	93.1	14.9
D198$^{2.68}$	K202^{ECL1}	60.2	18.8	-41.4
D198$^{2.68}$	Y145$^{1.40}$	74	59.2	-14.8
D198$^{2.68}$	K197$^{2.67}$	0.2	59.6	59.4
R227$^{3.30}$	D222^{ECL1}	4.1		-4.1
R227$^{3.30}$	D293^{ECL2}	63.5	31.9	-31.6
R227$^{3.30}$	S223^{ECL1}		37	37
N240$^{3.43}$	S186$^{2.56}$	54.9	69.1	14.2
E247$^{3.50}$	Y402$^{7.47}$	60.4	77.6	17.2
D293^{ECL2}	K288$^{4.64}$	23.4	4.9	-18.5
D293^{ECL2}	Y220^{ECL1}		13.6	13.6
E294^{ECL2}	S301^{ECL2}	0.8		-0.8
E294^{ECL2}	T298^{ECL2}	11.1		-11
E294^{ECL2}	K288$^{4.64}$	42.5	39	-3.5
R299^{ECL2}	E34^{ECD}	56.5	0.1	-56.4
R299^{ECL2}	E294^{ECL2}	26.5		-26.5
R299^{ECL2}	D293^{ECL2}	17.8		-17.8
R299^{ECL2}	N300^{ECL2}	16.2		-16.2
R299^{ECL2}	E373^{ECL3}		19.6	19.6
N300^{ECL2}	E292$^{4.68}$	13.9		-13.9
R310$^{5.40}$	E364$^{6.53}$	31.4	3.3	-28.1
R310$^{5.40}$	D372^{ECL3}		29,6	29.6
D344$^{6.33}$	K346$^{6.35}$	48.9	11,2	-37.7
H363$^{6.52}$	T391$^{7.46}$	38.5	0,5	-38
E364$^{6.53}$	Y241$^{3.44}$	48.6	59,6	11
D372^{ECL3}	K383$^{7.38}$	23.2	0,6	-22.6
R376^{ECL3}	D372^{ECL3}		21,2	21.2
R376^{ECL3}	E373^{ECL3}	13.4	42,7	29.3
R380$^{7.35}$	D372^{ECL3}	60.7	1	-59.7
R380$^{7.35}$	E387$^{7.42}$	2.4	44,7	42.3
E387$^{7.42}$	K383$^{7.38}$	62.6	2.2	-60.4

Data expressed as the occupancy (percentage of frames) in which the interactions were present in the GLP-1R–TT-OAD2–G_s and GLP-1R–GLP-1–G_s complexes. Differences between GLP-1R–GLP-1–G_s and GLP-1R–TT-OAD2–G_s are reported in the right column; green indicates more contacts in GLP-1 versus TT-OAD2, and red denotes more contacts in TT-OAD2 versus GLP-1. Grey cells indicate that hydrogen bonds were not present.

nature research

Corresponding author(s): Radostin Danev, Patrick M. Sexton, Denise Wootten

Reporting Summary

Nature Research wishes to improve the reproducibility of the work that we publish. This form provides structure for consistency and transparency in reporting. For further information on Nature Research policies, see Authors & Referees and the Editorial Policy Checklist.

Statistical parameters

When statistical analyses are reported, confirm that the following items are present in the relevant location (e.g. figure legend, table legend, main text, or Methods section).

n/a	Confirmed	
☐	☒	The exact sample size (*n*) for each experimental group/condition, given as a discrete number and unit of measurement
☐	☒	An indication of whether measurements were taken from distinct samples or whether the same sample was measured repeatedly
☐	☒	The statistical test(s) used AND whether they are one- or two-sided *Only common tests should be described solely by name; describe more complex techniques in the Methods section.*
☐	☒	A description of all covariates tested
☐	☒	A description of any assumptions or corrections, such as tests of normality and adjustment for multiple comparisons
☐	☒	A full description of the statistics including central tendency (e.g. means) or other basic estimates (e.g. regression coefficient) AND variation (e.g. standard deviation) or associated estimates of uncertainty (e.g. confidence intervals)
☐	☒	For null hypothesis testing, the test statistic (e.g. *F*, *t*, *r*) with confidence intervals, effect sizes, degrees of freedom and *P* value noted *Give P values as exact values whenever suitable.*
☐	☒	For Bayesian analysis, information on the choice of priors and Markov chain Monte Carlo settings
☒	☐	For hierarchical and complex designs, identification of the appropriate level for tests and full reporting of outcomes
☒	☐	Estimates of effect sizes (e.g. Cohen's *d*, Pearson's *r*), indicating how they were calculated
☒	☐	Clearly defined error bars *State explicitly what error bars represent (e.g. SD, SE, CI)*

Our web collection on statistics for biologists may be useful.

Software and code

Policy information about availability of computer code

Data collection	SerialEM
Data analysis	GraphPad Prism, UCSF Chimera, VMD, GetContacts analysis tool, avconv, AquaMMapS, ACEMD, Modeller, MDFF, Coot, Phenix, Chem3D, Relion 3.0, CryoSPARC 2.5.0, ResMAP, MotionCor2, Gctf, EMAN2

For manuscripts utilizing custom algorithms or software that are central to the research but not yet described in published literature, software must be made available to editors/reviewers upon request. We strongly encourage code deposition in a community repository (e.g. GitHub). See the Nature Research guidelines for submitting code & software for further information.

Data

Policy information about availability of data

All manuscripts must include a data availability statement. This statement should provide the following information, where applicable:

- Accession codes, unique identifiers, or web links for publicly available datasets
- A list of figures that have associated raw data
- A description of any restrictions on data availability

Atomic coordinates and the cryo-EM density map have been deposited in the Protein Data Bank under accession number 6ORV and EMDB entry ID 20179

Field-specific reporting

Please select the best fit for your research. If you are not sure, read the appropriate sections before making your selection.

☒ Life sciences ☐ Behavioural & social sciences ☐ Ecological, evolutionary & environmental sciences

For a reference copy of the document with all sections, see nature.com/authors/policies/ReportingSummary-flat.pdf

Life sciences study design

All studies must disclose on these points even when the disclosure is negative.

Sample size	Sample size calculation was not required
Data exclusions	No data were excluded
Replication	Experimental findings were reliably reproduced
Randomization	Randomization was not required
Blinding	Blinding was not performed

Reporting for specific materials, systems and methods

Materials & experimental systems

n/a	Involved in the study
☐	☐ Unique biological materials
☐	☒ Antibodies
☐	☒ Eukaryotic cell lines
☐	☐ Palaeontology
☐	☒ Animals and other organisms
☐	☐ Human research participants

Methods

n/a	Involved in the study
☐	☐ ChIP-seq
☐	☐ Flow cytometry
☐	☐ MRI-based neuroimaging

Unique biological materials

Policy information about availability of materials

Obtaining unique materials	*Describe any restrictions on the availability of unique materials OR confirm that all unique materials used are readily available from the authors or from standard commercial sources (and specify these sources).*

Antibodies

Antibodies used	rabbit anti-Gs C-18 antibody (cat no sc-383), Santa Cruz mouse Penta-His antibody (cat no 34660), QIAGEN 680RD goat anti-mouse antibody (LI-COR) 800CW goat anti-rabbit antibody (LICOR)
Validation	All antibodies were used for Western blot analysis and have been validated.

Eukaryotic cell lines

Policy information about cell lines

Cell line source(s)	Cells used in assays were obtained from ATCC
Authentication	No authentication required
Mycoplasma contamination	Cell lines were tested and are free from mycoplasma contamination

Commonly misidentified lines (See ICLAC register)	Cells are not listed in the database

Palaeontology

Specimen provenance	Not applicable
Specimen deposition	Not applicable
Dating methods	Not applicable

☐ Tick this box to confirm that the raw and calibrated dates are available in the paper or in Supplementary Information.

Animals and other organisms

Policy information about studies involving animals; ARRIVE guidelines recommended for reporting animal research

Laboratory animals	C57/Bl6
Wild animals	Not applicable
Field-collected samples	Not applicable

Human research participants

Policy information about studies involving human research participants

Population characteristics	Not applicable
Recruitment	Not applicable

ChIP-seq

Data deposition

☐ Confirm that both raw and final processed data have been deposited in a public database such as GEO.

☐ Confirm that you have deposited or provided access to graph files (e.g. BED files) for the called peaks.

Data access links *May remain private before publication.*	Not applicable
Files in database submission	Not applicable
Genome browser session (e.g. UCSC)	Not applicable

Methodology

Replicates	Not applicable
Sequencing depth	Not applicable
Antibodies	Not applicable
Peak calling parameters	Not applicable
Data quality	Not applicable
Software	Not applicable

Flow Cytometry

Plots

Confirm that:

☐ The axis labels state the marker and fluorochrome used (e.g. CD4-FITC).

☐ The axis scales are clearly visible. Include numbers along axes only for bottom left plot of group (a 'group' is an analysis of identical markers).

☐ All plots are contour plots with outliers or pseudocolor plots.

☐ A numerical value for number of cells or percentage (with statistics) is provided.

Methodology

Sample preparation	Not applicable
Instrument	Not applicable
Software	Not applicable
Cell population abundance	Not applicable
Gating strategy	Not applicable

☐ Tick this box to confirm that a figure exemplifying the gating strategy is provided in the Supplementary Information.

Magnetic resonance imaging

Experimental design

Design type	Not applicable
Design specifications	Not applicable
Behavioral performance measures	Not applicable

Acquisition

Imaging type(s)	Not applicable
Field strength	Not applicable
Sequence & imaging parameters	Not applicable
Area of acquisition	Not applicable

Diffusion MRI ☐ Used ☒ Not used

Preprocessing

Preprocessing software	Not applicable
Normalization	Not applicable
Normalization template	Not applicable
Noise and artifact removal	Not applicable
Volume censoring	Not applicable

Statistical modeling & inference

Model type and settings	Not applicable
Effect(s) tested	Not applicable

Specify type of analysis: ☐ Whole brain ☐ ROI-based ☐ Both

Statistic type for inference (See Eklund et al. 2016)	Not applicable

Correction	Not applicable

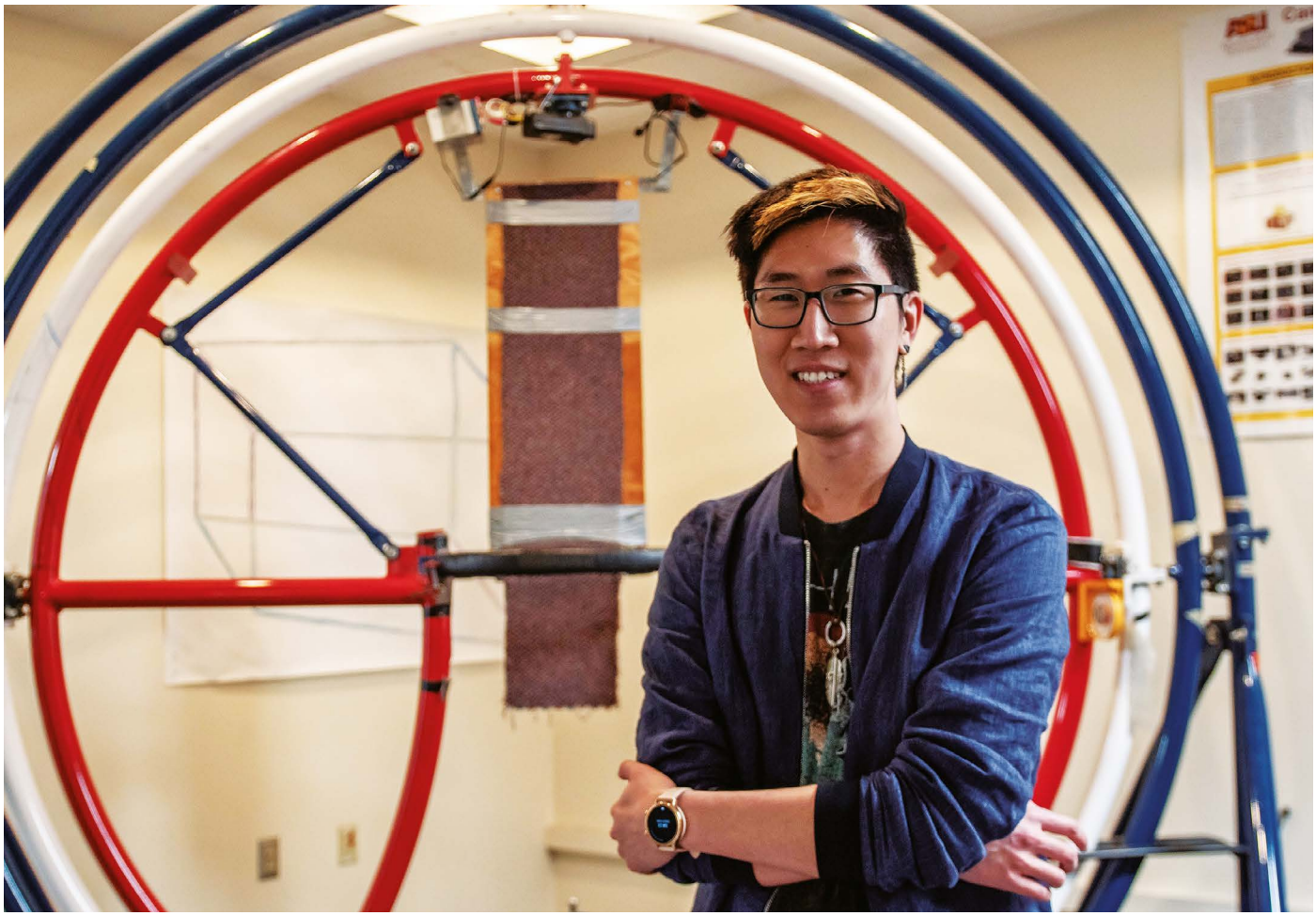
Models & analysis

n/a	Involved in the study
☒	☐ Functional and/or effective connectivity
☒	☐ Graph analysis
☒	☐ Multivariate modeling or predictive analysis

Work

Your story

Send your careers story to: naturecareerseditor@nature.com



ROBERT EWING/ASU

PhD student Ty Tang in a gyroscope lab at Arizona State University in Tempe.

WHAT I LEARNT FROM A STINT IN INDUSTRY

Two years of work before graduate school gave me confidence and technical skills, and made me certain that research was the right choice. **By Ty Tang**

"If you want to go to graduate school, don't go to work first. You'll get addicted to the money and you won't be able to go back."

I listened to these words of advice carefully. I had spent the past several months asking people about their experiences of graduate school. The overwhelming majority of advice related to money. "It's not worth the increase in salary", "you'll be so poor", "you'll envy your friends with jobs". But, I wondered, what about the love for research and learning?

Like many other students, I was confronted with a predicament: at a turbulent stage of my life, with uncertainty around every corner, I was torn between applying to graduate schools or for full-time jobs. Like many students, I was terrified of committing to one or the other, so I applied to both. And with some luck and persistence, I was offered opportunities for both, putting me back to square one.

One day, as my decision deadlines approached, I had a realization: if I started to work and became 'addicted to the money', then graduate school probably wasn't the right decision to start with. Why waste up to six years of my life on a career path I was uncertain about if, in the end, money was worth more to me than my passion for science? It wasn't exactly the intent behind the advice, but it nonetheless allowed me to proceed with some clarity. After finishing my last undergraduate term of a

© 2020 Springer Nature Limited. All rights reserved.



TY TANG

Ty Tang (second from right) made great friends at Epic Systems in Verona, Wisconsin.

bioengineering degree at the University of Illinois at Chicago, I embarked on a journey to work as an interface engineer at Epic Systems, a health-care software company in Verona, Wisconsin.

Defy expectations

Being an interface engineer at Epic Systems required new skills: project management, writing code, working with customers and troubleshooting problems. I also had to adjust to a lack of autonomy, because what I did at work depended on the customers' and the company's needs. In more cynical moments, I imagined that I might gradually begin to hate my job, be miserable for a while and regret ever choosing industry over academia.

I was surprised by how wrong I was. I had the good fortune to make great friends, be surrounded by smart and driven people and was finally able to buy groceries without financial stress. But the most incredible thing for me was that I actually enjoyed my job. Like everything, it had its ups and downs, but I was surprised by how engaging non-academic full-time employment could be. I applied the same discipline and creative problem-solving I had developed as an undergraduate researcher and taught myself new skills as I grew professionally. I made contributions that felt meaningful, and I enjoyed working with my peers and customers. I looked forward to the challenges and opportunities, and, overall, I felt happy. Working there made me realize some important things.

Graduate school is often overly romanticized. I'm as guilty of this as anyone, but now I understand that not all research is fun and stimulating, and that not all work is tedious and soulless.

"For me, taking a detour from research wasn't a waste of time – not by a long shot."

The people around you matter. Sometimes, even more than where you are. I found that being surrounded by smart, kind and passionate people makes everything easier. I learnt to cherish my personal relationships and the importance of prioritizing them over work.

Money can buy you a lot of happiness. Some might argue that happiness as a result of buying things is fleeting and shallow, but, for me, the value of removing financial burdens – of going out to eat without feeling guilty and being able to travel and have new experiences – can't be overstated. It's not that you can be happy only if you have money, but it certainly helps.

Money isn't everything. Everyone knows this, but sometimes it's hard to accept. When people look on social media and see their friends or colleagues going on extravagant holidays, it's easy to think that if you could just win the lottery, you'd never have to worry about anything ever again. But, of course, it's not that simple. There are things other than money that matter to us.

For me, what money couldn't buy was passion. Even though I was happy, I couldn't help but feel that something was missing, and that I wanted to do more. It wasn't long before I started looking into graduate programmes again. Having heard me talk passionately about my research experiences, my boss wasn't at all surprised to hear my decision.

Time to return

After 18 months at Epic, I started going for interviews at graduate schools, and a few months later, I accepted an offer from Arizona State University in Tempe to study cognitive science. Armed with my experience in project management and technical writing, I felt much more confident and prepared for the challenges that awaited me in graduate school than I had before. I also couldn't wait to apply the technical skills I'd picked up, and use my determination and ambition in another arena.

For me, taking a detour from research wasn't a waste of time – not by a long shot. Not only did I meet incredible people and improve my working habits, but I'm now certain that I am where I want to be.

When I was asking for advice about graduate school, I wish I'd been told that going to graduate school is not a decision you should rush: it's a huge commitment and can be financially stressful. If you're not sure whether you want to be a scientist, it's okay to take some time to do something else. You might end up realizing that graduate school wasn't the right decision for you, and that's absolutely fine.

I also wish someone had told me not to get tunnel vision too early in my career. I recommend you explore your options. Try things you think you might like, but also try things you might not like. Your experiences will give you perspectives and skills that can give you an edge over your competition.

No matter what you do, there are many opportunities to learn and to contribute to the world. Even if you don't work in research, the skills you develop as a student and a scientist will allow you to make positive changes. In the end, what you have to decide for yourself is where you want to make those changes and what really matters to you.

Taking a break before graduate school didn't weaken my resolve, it strengthened it, and I don't think I would have been able to achieve what I have without that experience.

Ty Tang is a cognitive-science PhD student at Arizona State University in Tempe.

© 2020 Springer Nature Limited. All rights reserved.

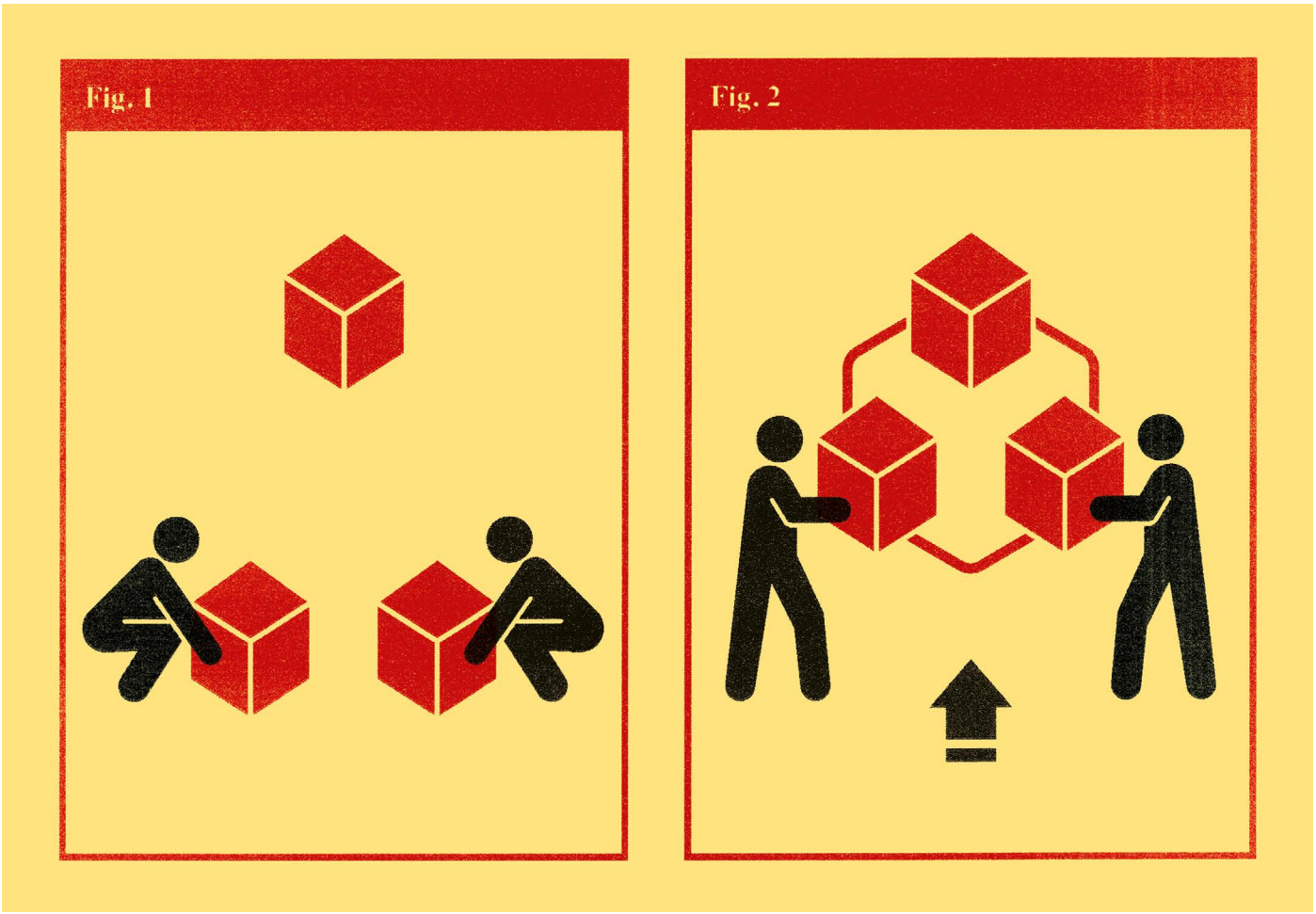


ILLUSTRATION BY THE PROJECT TWINS

ELEVEN TIPS FOR WORKING WITH LARGE DATA SETS

Big data are difficult to handle. These tips and tricks can smooth the way. **By Anna Nowogrodzki**

Big data are everywhere in research, and the data sets are only getting bigger — and more challenging to work with. Unfortunately, says Tracy Teal, it's a kind of labour that's too often left out of scientific training.

"It's a mindset," says Teal, "treating data as a first-class citizen." She should know: Teal was until last month the executive director of The Carpentries, an organization in Oakland, California, that teaches coding and data skills to researchers globally. She says there's a tendency in the research community to dismiss the time and effort needed to manage and share data, and not to regard it as a real part of science. But, she suggests, "we can shift our mindset to valuing that work as a part of the research process", rather than treating it as an afterthought.

Here are 11 tips for making the most of your large data sets.

Cherish your data. "Keep your raw data raw: don't manipulate it without having a copy," says Teal. She recommends storing your data somewhere that creates automatic backups and that other laboratory members can access, while abiding by your institution's rules on consent and data privacy.

Because you won't need to access these data often, says Teal, "you can use storage options where it can cost more money to access the data, but storage costs are low" — for instance, Amazon's Glacier service. You could even store the raw data on duplicate hard drives kept in different locations. Storage costs for large data files can add up, so budget accordingly.

"We can shift our mindset to valuing that work as a part of the research process."

Visualize the information. As data sets get bigger, new wrinkles emerge, says Titus Brown, a bioinformatician at the University of California, Davis. "At each stage, you're going to be encountering new and exciting messed-up behaviour." His advice: "Do a lot of graphs and look for outliers." Last April, one of Brown's students analysed transcriptomes — the full set of RNA molecules produced by a cell or organism — from 678 marine microorganisms such as plankton (L. K. Johnson *et al. GigaScience* **8**, giy158; 2019). When Brown and his student charted

© 2020 Springer Nature Limited. All rights reserved.

average values for transcript length, coverage and gene content, they noticed that some values were zero — showing where the computational workflow had failed and had to be re-run.

Show your workflow. When particle physicist Peter Elmer helps his 11-year-old son with his mathematics homework, he has to remind him to document his steps. "He just wants to write down the answer," says Elmer, who is executive director of the Institute for Research and Innovation in Software for High Energy Physics at Princeton University in New Jersey. Researchers working with large data sets can benefit from the same advice that Elmer gave his son: "Showing your work is as important as getting to the end."

This means recording your entire data workflow — which version of the data you used, the clean-up and quality-checking steps, and any processing code you ran. Such information is invaluable for documenting and reproducing your methods. Eric Lyons, a computational biologist at the University of Arizona in Tucson, uses the video-capture tool asciinema to record what he types into the command line, but lower-tech solutions can also work. A group of his colleagues, he recalls, took photos of their computer screen's display and posted them on the lab's group on Slack, an instant-messaging platform.

Use version control. Version-control systems allow researchers to understand precisely how a file has changed over time, and who made the changes. But some systems limit the sizes of the files you can use. Harvard Dataverse (which is open to all researchers) and Zenodo can be used for version control of large files, says Alyssa Goodman, an astrophysicist and data-visualization specialist at Harvard University in Cambridge, Massachusetts. Another option is Dat, a free peer-to-peer network for sharing and versioning files of any size. The system maintains a tamper-proof log that records all the operations you perform on your file, says Andrew Osheroff, a core software developer at Dat in Copenhagen. And users can direct the system to archive a copy of each version of a file, says Dat product manager Karissa McKelvey, who is based in Oakland, California. Dat is currently a command-line utility, but "we've been actively revamping", says McKelvey; the team hopes to release a more user-friendly front end later this year.

Record metadata. "Your data are not useful unless people — and 'future you' — know what they are," says Teal. That's the job of metadata, which describe how observations were collected, formatted and organized. Consider which metadata to record before you start collecting, Lyons advises, and store that information alongside the data — either in the software tool used to collect the observations or in a README or another dedicated file. The Open Connectome Project, led by Joshua Vogelstein, a neurostatistician at Johns Hopkins University in Baltimore, Maryland, logs its metadata in a structured plain-text format called JSON. Whatever your strategy, try to think long-term, Lyons says: you might one day want to integrate your data with those of other labs. If you're proactive with your metadata, that integration will be easier down the line.

Automate, automate, automate. Big data sets are too large to comb through manually, so automation is key, says Shoaib Mufti, senior director of data and technology at the Allen Institute for Brain Science in Seattle, Washington. The institute's neuroinformatics team, for instance, uses a template for brain-cell and genetics data that accepts information only in the correct format and type, Mufti says. When it's time to integrate those data into a larger database or collection, data-quality assurance steps are automated using Apache Spark and Apache Hbase, two open-source tools, to validate and repair data in real time. "Our entire suite of software tools to validate and ingest data runs in the cloud, which allows us to easily scale," he says. The Open Connectome Project also provides automated quality assurance, says Vogelstein — this generates visualizations of summary statistics that users can inspect before moving forward with their analyses.

"Our entire suite of software tools to validate and ingest data runs in the cloud, which allows us to easily scale."

Make computing time count. Large data sets require high-performance computing (HPC), and many research institutes now have their own HPC facilities. The US National Science Foundation maintains the national HPC network XSEDE, which includes the cloud-based computing network Jetstream and HPC centres across the country. Researchers can request resource allocations at xsede.org, and create trial accounts at go.nature.com/36ufhgh. Other options include the US-based ACI-REF network, NCI Australia, the Partnership for Advanced Computing in Europe and ELIXIR networks, as well as commercial providers such as Amazon, Google and Microsoft.

But when it comes to computing, time is money. To make the most of his computing time on the GenomeDK and Computerome clusters in Denmark, Guojie Zhang, a genomics researcher at the University of Copenhagen, says his group typically runs small-scale tests before migrating its analyses to the HPC network. Zhang is a member of the Vertebrate Genomes Project, which is seeking to assemble the genomes of about 70,000 vertebrate species. "We need millions or even billions of computing hours," he says.

Capture your environment. To replicate an analysis later, you won't just need the same version of the tool you used, says Benjamin Haibe-Kains, a computational pharmacogenomicist at the Princess Margaret Cancer Centre in Toronto, Canada. You'll also need the same operating system, and all the same software libraries that the tool requires. For this reason, he recommends working in a self-contained computing environment — a Docker container — that can be assembled anywhere. Haibe-Kains and his team use the online platform Code Ocean (which is based on Docker) to capture and share their virtual environments; other options include Binder, Gigantum and Nextjournal. "Ten years from now, you could still run that pipeline exactly the same way if you need to," Haibe-Kains says.

Don't download the data. Downloading and storing large data sets is not practical. Researchers must run analyses remotely, close to where the data are stored, says Brown. Many big-data projects use Jupyter Notebook, which creates documents that combine software code, text and figures. Researchers can 'spin up' such documents on or near the data servers to do remote analyses, explore the data, and more, says Brown. Jupyter Notebook is not particularly accessible to researchers who might be uncomfortable using a command line, Brown says, but there are more user-friendly platforms that can bridge the gap, including Terra and Seven Bridges Genomics.

Start early. Data management is crucial even for young researchers, so start your training early. "People feel like they never have time to invest," Elmer says, but "you save yourself time in the long run". Start with the basics of the command line, plus a programming language such as Python or R, whichever is more important to your field, he says. Lyons concurs: "Step one: get familiar with data from the command line." In November, some of his collaborators who were not fluent in command-line usage had trouble with genomic data because chromosome names didn't match across all their files, Lyons says. "Having some basic command-line skills and programming let me quickly correct the chromosome names."

Get help. Help is available, online and off. Start with the online forum Stack Overflow. Consult your institution's librarians about the skills you need and the resources you have available, Teal advises. And don't discount on-site training, Lyons says: "The Carpentries is a great place to start."

Anna Nowogrodzki is a journalist based near Boston, Massachusetts.

© 2020 Springer Nature Limited. All rights reserved.



Where I work
Carla Shatz

Photographed for *Nature* by Gabriela Hasbun.

This office is my hut, where I do lots of brainstorming to go over laboratory members' experiments and results. It's where ideas get put into action or put down onto paper. People say it's cosy.

Everyone would call me a compulsive person. My desk is clean, and so are my desk drawers. The order of my desk symbolizes an orderly mind. Because of that, my mind has room to notice things that don't fit the pattern. This is partly why my lab has been able to think outside the box and has worked on themes that don't fit the expected.

I am a neurobiologist who studies how mammalian brain circuits are tuned by experience and neural activity during development. People thought these circuits should all be hard-wired, so we were very surprised to find years ago that the adult patterning of a visual circuit in the brain is not there initially in the embryo. More recently, we got another shock when we found that these circuits are remodelled by molecules that are typically thought of as components of the immune system. Now, we are working on how these immune molecules are somehow being used by neurons to stabilize or prune their synapses, or connections.

Above my computer are pictures of my 'labsters', as I call my lab members from over the years, and some of my mentors. There's a special one of me and Eve Marder when we shared the 2016 Kavli Prize in Neuroscience, along with that year's seven other prizewinners in various fields – all men in tuxedos. I like mixing the plaques of recognition with my lab family, because you don't have one without the other.

We control so little in life, and it gives me a kind of perverse pleasure to have my office under control. Generally, my lab members are amused by my neat-freak mentality. But the best science is done when people are extremely careful and precise.

Carla Shatz is a biologist and neurobiologist and director of the Stanford Bio-X interdisciplinary centre at Stanford University in California. **Interview by Kendall Powell.**

© 2020 Springer Nature Limited. All rights reserved.

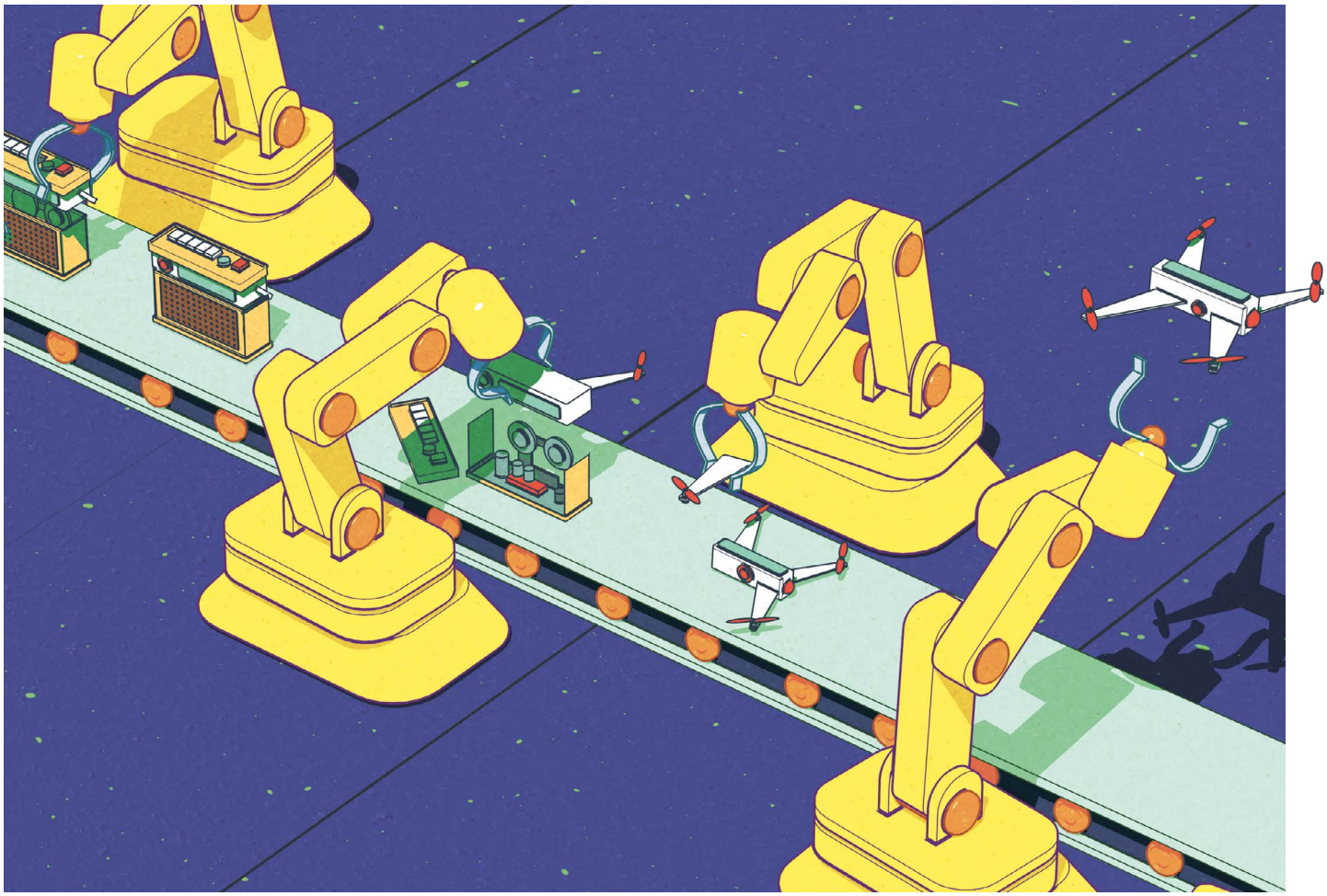


ILLUSTRATION BY GEOFFROY DE CRÉCY

TAIWAN'S TIME TO TRANSFORM

The government is betting its manufacturing future on smart machinery and artificial intelligence to improve product quality and flexibility. **By Sarah O'Meara**

In 2016, industrial engineer Chen-Fu Chien was asked to lead a university research centre in Taiwan that would develop new manufacturing technologies using artificial intelligence (AI).

Rather than aiming to publish academic papers, his brief was to produce ideas that could be quickly transferred into industrial settings, says Chien. His research at the National Tsing Hua University (NTHU) in Hsinchu City uses big-data analytics to make machines smarter through AI that lets them take decisions without human control. It is one of several approaches to creating 'smart factories' that use an interconnected, digital network of supply systems — part of Taiwan's push to improve the flexibility, quality and efficiency of its manufacturing.

"I am one of the few senior scientists in Taiwan who's worked extensively with business, as well as in public research. It's one of the reasons the government asked me to lead the project," says Chien, whose position at the NTHU is endowed by the US firm Micron Technology in Boise, Idaho, which develops computer memory and storage technologies.

Chien's mission is a sign of how Taiwan's government wants its manufacturing industry to change using technologies such as cloud computing, big data, the Internet of Things and smart robots — a shift in industrial practices that has been dubbed Industry 4.0. Once known as a hub for mass-produced cheap goods, such as toys and electronics carrying the ubiquitous 'Made in Taiwan' stamp, the island is looking to science to upgrade its image so it can become a destination for international companies searching for futuristic manufacturing solutions.

In 2018, Chien and his team opened the Artificial Intelligence for Intelligent

© 2020 Springer Nature Limited. All rights reserved.

Manufacturing Systems (known as AIMS) research centre in Hsinchu. The laboratory has more than 50 staff members and Chien is responsible for 10 related projects in other research institutes across Taiwan. It is part of a wider initiative begun in 2018 that includes three further facilities developing AI technologies in areas such as financial technology, health care and intelligent transportation systems. The whole initiative will cost the Taiwanese government around US$33 million over 5 years.

"The Ministry of Science and Technology wanted our centre to help create the next generation of intelligent manufacturing systems that could only be found in Taiwan," Chien says. The ministry's aim is "to use the region's strength in electronics manufacturing to its best advantage and establish Taiwan as a key high-tech manufacturing hub".

Taiwan's efforts to change its manufacturing model are timely. A global slowdown in trade since 2011 and a tariff war on goods traded between mainland China and the United States have pushed companies to look for alternative manufacturing options that are flexible, efficient and unaffected by such economic tussles.

Diverse development

Taiwan has been a leading manufacturer of electronic components since the 1990s. Its economy remains reliant on an industry that is led by the world's largest contract electronic chipmaker, Taiwan Semiconductor Manufacturing Company (TSMC), which supplies technology companies such as Apple and Huawei and contributed more than 4% to the region's gross domestic product in 2018.

However, the growth of consumer electronics has slowed across the world in the past few years: many people already have smartphones, and so fewer are being bought. In 2016, Taiwan's newly inaugurated president, Tsai Ing-wen, announced that the government would promote a new model of economic development. The idea was to encourage local technology firms to diversify their products and to become more innovative and self-sufficient to boost technology ties with the United States and Japan. Taiwan also wants to reduce its reliance on mainland China (see 'Moving money').

"Companies need to make manufacturing more intelligent so it can be more flexible."

Tsai's 2016 strategy was followed by a breakneck series of policy announcements to encourage investment in smart machinery — equipment that can work with less input from an expensive human controller — and in other manufacturing technologies (see 'Non-stop reforms').

When Taiwanese manufacturers began moving factories to mainland China in the 2000s, it harmed the development of smart manufacturing technology on the island, explains Stephen Su, who runs a centre at Taiwan's Industrial Technology Research Institute (ITRI), a government-funded research and development centre in Hsinchu. The institute, founded in 1973, has acted as an incubator for several Taiwanese companies, including the TSMC.

Now the government is "pouring resources" into smart manufacturing "because it's the future of production", Su says.

A conventional moving assembly line — many people using tools to complete small tasks in a much larger, complex process — was pioneered by Henry Ford to manufacture automobiles in the United States in 1913. Invented at the end of the 'second industrial revolution' that saw the global spread of technologies such as electrical power, the assembly line is still used in many factories today, says Chien.

Machines have largely replaced workers since the advent of the computer age, which saw a third revolution in industry involving robotics and greater automation. The next development, known as the fourth industrial revolution or Industry 4.0, will use advances in cyber-physical systems, such as optical-fibre sensors on machines. These will collect and exchange data that can be processed by big-data analytics and AI technologies, enabling manufacturers to make flexible decisions about how they operate and to allocate resources efficiently to empower smart production. Taiwan is betting that the products of the future will be made by such intelligent machinery.

Companies around the world are similarly re-evaluating where and how they make their products, says Jason Ho, general manager of Avectec in Zhubei City near Hsinchu, which offers conventional manufacturers a software platform to help create smart factories. In these, networked machines can detect their own faults, work more efficiently and reduce production costs.

"Particularly in high-tech areas such as the computer industry, information and communications technology and consumer electronics, companies don't need to focus on making more products more quickly. They need to make manufacturing more intelligent so it can be more flexible. That way, companies can quickly adjust the product to meet the demands of each customer," Ho says.

Talent base

Now that Taiwan is remaking itself as a destination for the next generation of manufacturers, there's one thing it requires more of: talent.

It is in urgent need of experienced engineers, both to design smart manufacturing technologies and to create the high-tech products of the future, says Su. "We must invest in our scientists and engineers. There are many countries in southeast Asia that are also becoming more sophisticated in terms of manufacturing, and to stay competitive, it's important to make investments in education," says Su.

NON-STOP REFORMS
TAIWAN'S POLICIES AIM TO BOOST TECH-BASED INDUSTRIES

May 2016
Taiwan's government announces its 'Five plus two' policy — a plan to innovate in the fields of biotechnology, defence, green energy, intelligent machinery and the Internet of Things.

November 2016
Launch of the Digital Nation and Innovative Economic Development Program (DIGI+), an initiative to make Taiwan a smart digital region by 2025. Policies include investment in start-up firms and development of the cybersecurity industry.

February 2017
The Smart Machinery Promotion Program is introduced. It aims to develop smart-machinery applications by combining manufacturing expertise with that from information and communications technologies.

July 2017
The Ministry of Science and Technology (MOST) unveils plans to establish four research centres in artificial intelligence (AI). The initiative will cost US$33 million annually over five years.

August 2017
MOST announces a 4-year, $132-million semiconductor programme to speed up the development of AI processor chips, and a 5-year, $517.5-million strategy to cultivate AI talent and research (2017 to 2021).

© 2020 Springer Nature Limited. All rights reserved.

Mark Liu, chair of the TSMC, says the region's shortage of qualified engineers and other professionals could hamper the industry's development more than technological barriers.

Taiwan's government has acknowledged the severity of its talent deficit, and in 2018 passed legislation to help recruit and attract foreign professionals to work in Taiwan. Measures include the introduction of an employment gold card, a type of visa that entitles the holder to tax breaks, pension contributions and flexible residency options for family members. Of the 500 cards that were issued by the end of November 2019, just under one-fifth went to specialists in science and technology.

Su also points to the 2018 launch of an industry-funded organization called the Taiwan AI Academy, which started as one of the 11 project teams at the AIMS centre. It now has four campuses across Taiwan and runs 12-week courses for technical professionals or business managers working in the field who want to sharpen their skills. "Smart manufacturing with AI applications is one focus for the training curriculum," Su says. "Many large manufacturing conglomerates such as AUO, MediaTek and the Formosa Plastics Group have sent their engineers and managers there." (The academy lists these firms as sponsors on its website.)

Other initiatives will also spur the need for talent. In January 2019, the government announced a programme to encourage Taiwanese businesses located overseas to relocate home by offering incentives such as financial subsidies and administrative support. As this article went to press, 168 companies had pledged to return from mainland China. William Tang, a spokesperson from InvesTaiwan — the government agency in Taipei that runs the project — says those companies will together invest $200 billion over three years in industrial infrastructure, such as factories, equipment and telecommunications technology, with an estimated $6.3 billion spent in 2019.

From the ground up

Mechavision in Taipei City, a spin-off company from ITRI that specializes in industrial robotic arms, is one of those hoping to capitalize on a growing need for more advanced production equipment both at home and abroad.

The three-year-old firm makes robotic tactile sensing technology for use where humans and robots collaborate in close quarters on the factory floor. For safety, the robots are fitted with an electronic skin that has tactile sensors, which allows the machines to detect workers nearby and so move away when necessary.

Mechavision's chief strategy officer and founder, Camus Su, says that one of the firm's main clients is Taiwanese company Qisda in Taoyuan City. It makes a variety of products, including computer monitors and mobile communication devices, so has opted for a mixed-line system that allows different models to be made on the same assembly line. The company needs "high flexibility in order to cope with different product sizes and specifications," he says, "and right now, our human–robot collaboration system is the best way to do this."

Min Sun, chief AI scientist at Appier, a Taiwanese company that uses AI to help enterprises solve business problems, says that in one respect, advanced computing technology has helped to transform the region's industrial model as computers get better at performing complex manufacturing tasks.

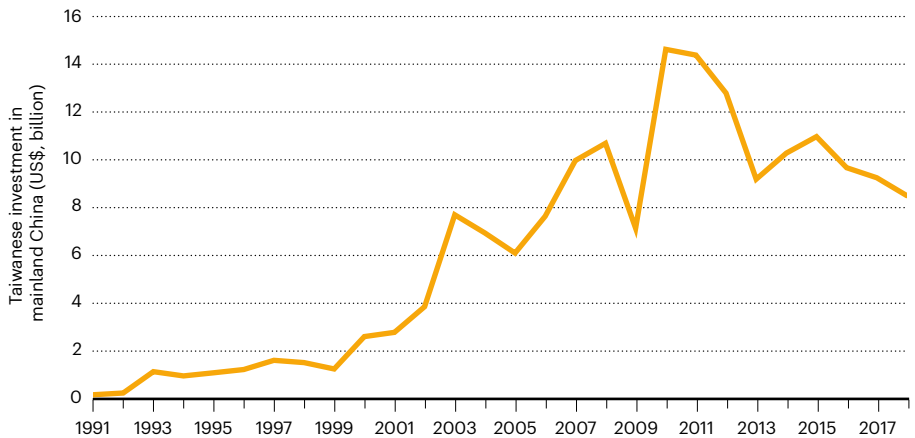
Unlike in the United States or mainland China, where one spoken language is dominant, Taiwan and its neighbours in southeast Asia operate in hundreds of languages, which makes it harder to collect surveys and feedback in a large, usable data set for developing new software and hardware, says Sun, who was previously a researcher in electrical engineering at the NTHU. "In recent years, it's made it harder to gather the market knowledge needed to create new products, such as consumer electronics like tablets or headphones," he says. "Now, you don't need so much human resource to convert the information into usable data. AI can understand all the different languages at once."

Sarah O'Meara is a writer and editor in London.

Publisher's note: Springer Nature remains neutral with regard to jurisdictional claims in institutional affiliations.

MOVING MONEY

Taiwan has increased its investment in mainland China over the past three decades.



SOURCE: MAINLAND AFFAIRS COUNCIL

January 2018
The government rolls out its three-year AI Taiwan Action Plan to establish the island as an AI leader. It aims to prioritize AI innovation and implementation in industry during 2018–21 and invest more than $300 million into the field.

February 2018
Taiwan relaxes regulations for the employment of foreign professionals to encourage talent recruitment.

March 2018
The government promotes policies to incentivize investment in start-ups. These aim to provide capital, relax visa and employment laws, encourage local and foreign cooperation and help investors to cash in on successes.

June 2018
MOST establishes the Taiwan Tech Arena to support start-ups in AI, semiconductors and software development and to help them to forge international links.

January 2019
Launch of a three-year scheme to relocate Taiwanese businesses back to the region. Policies involve assisting firms with resources such as land, water, electricity, labour, taxation and financing.

May 2019
Taiwan's cabinet approves a 4-year, $658-million spending plan for 5G technology to increase the region's digital competitiveness.

© 2020 Springer Nature Limited. All rights reserved.